21st Century COE Program

Evolution of Urban Earthquake Engineering

Fifth International Conference on Urban Earthquake Engineering

Center for Urban Earthquake Engineering

Tokyo Institute of Technology

Tokyo Tech

CUEE

21st Century COE Program

Evolution of Urban Earthquake Engineering

Fifth International Conference on Urban Earthquake Engineering

Center for Urban Earthquake Engineering

Tokyo Institute of Technology

Tokyo Tech

CUEE

PREFACE

I am very delighted to host the 5th International Conference on Urban Earthquake Engineering, inviting many distinguished guests and experts from around the world. Every year since our Center of Excellence (COE) Program titled "Evolution of Urban Earthquake Engineering" was adopted in 2003 by the Ministry of Education, Culture, Sport, Science, and Technology (MEXT), Japan, we have held this conference which has been the biggest annual event for the program. Thanks to not only wonderful presentations and fruitful discussions but also heartwarming support and encouragement from every participant, the conference has grown year on year; even exceeding the limit of the current conference proceeding. To accommodate the conference papers in one volume, we have newly introduced a condensed format of papers for this conference.

Despite the happy growth of the conference, we have experienced unhappy earthquake disasters even in the last 5 years during the course of this program. There is always something new to learn from every earthquake disaster. For example, oil tanker fires triggered by the long period ground motions during the 2003 Tokachi-oki earthquake, the pressing need for the earthquake education and real time information systems during the 2004 Sumatra earthquake which triggered the Indian Ocean tsunami, and long aftermath of damage to a nuclear power plant caused by the 2007 Niigata-chuetsu-oki earthquake. Moreover, in and around Japan, big earthquakes such as Nankai, To-nankai and Tokai earthquakes are supposedly imminent to occur. I wonder by what means these future earthquakes can be managed.

As a matter of fact, just like the Tokyo metropolitan area, almost every Asian metropolis displays concentration of population as well as information and facilities on a large scale. From earthquake engineering point of view, seismic risk of the metropolis is undeniably growing up to be a mega-risk. In my belief, we have to expand our research to find solutions to mitigate such mega-risk as soon as possible. In this context, although this conference is the last one to be held under the COE Program, it should be the first step to consolidated global research.

Tatsuo Ohmachi
Leader of the COE Program, and
Director of CUEE, Tokyo Tech

TABLE OF CONTENTS

Geotechnical Earthquake Engineering

Tsunami

Bridge Structures

Passive Control and Base Isolation

Steel Structures, Response Analysis of Structures

Socioeconomic Issues

Fifth International Conference on Urban Earthquake Engineering
March 4-5, 2008, Tokyo Institute of Technology, Tokyo, Japan

MANAGEMENT OF WORLDWIDE EARTHQUAKE RISKS FOR BUSINESS AND INDUSTRY, INCLUDING DIRECT LOSSES, BUSINESS INTERRUPTIONS, AND FINANCIAL LOSSES

Peter I. Yanev[1)]

1) Earthquake Engineering and Risk Management Consultant, Partner and Director, Global Risky Miyamoto, Inc. California USA
peter@yanev.com

1. INTRODUCTION

This paper has three purposes:

1. To increase awareness of the existing earthquake risk to business and industry in urban areas exposed to strong earthquakes.
2. To provide guidance to corporate managements (and to their consulting earthquake engineers) on how to analyze and manage the risk.
3. To encourage the inclusion of business and risk management studies in the education of all earthquake engineering professionals.

Many of the world's largest urban areas and their extensive industry are located in areas of high earthquake risk. These include San Francisco and its Silicon Valley, Tokyo and Japan's highly urbanized and industrialized other cities, Jakarta, Manila, Taipei and Beijing, Teheran and Istanbul, Athens and Naples, Mexico City, Caracas, Santiago de Chile, Los Angeles and Seattle-Vancouver. The risk includes direct damage to structures and plants and their equipment systems and infrastructure, business interruption and related financial losses – including loss of market share and decreased capitalization. The existing vulnerabilities, unless quantified and lowered, will lead to very large corporate losses in future earthquakes. The combined costs of such losses will be an order of magnitude, or more, higher than the cost of damage to buildings and their contents.

Very few companies and other organization around the world have analyzed adequately their earthquake risk. Even fewer have taken steps to manage that risk. Further, with the exception of several forward looking companies, almost all the effort spent to date has been targeted to prevent building damage and/or to purchase insurance. That is a thoroughly insufficient strategy for managing the earthquake risk of business and industry. A broader approach must be taken.

Such an approach would be structured to include:

- Deterministic and probabilistic assessment of existing and future risks
- Financial loss analyses and cost-benefit analyses to manage the risk
- Communicating the risk to corporate management at the Board and the CEO/COO/CFO levels
- Engineering loss control for existing and new facilities and their related infrastructure,
- Risk transfer through insurance and reinsurance, catastrophe bonds and other financial instruments.

Engineers, worldwide, should be driving the process of earthquake risk management – much like they drive the process of engineering education. Instead, they have abridged their responsibility to other professions that are not equipped technically to handle it. That includes corporate risk managers, who are found only in a few advanced countries, and who typically rely on their insurance brokers. The latter almost universally have no engineering knowledge or any interest in the subject, aside from the commissions generated. Further, earthquake risk management during the last decade has veered towards reliance on catastrophe (cat) software, most often run by insurance brokers. The software, with all of its sophistication, is not a substitute for engineering and produces unreliable results. Engineers must take control of the process of earthquake risk management if any further progress in risk control is to be made.

2. LESSONS FROM THE 2007 NIIGATA EARTHQUAKE IN RISK MANAGEMENT

The July 16, 2007 Niigata (Chuetsu Oki), Japan earthquake had a moderate magnitude of 6.8 and caused limited but concentrated damage in the vicinity of Kashiwazaki, just south of the City of Niigata. A few large industrial and commercial facilities were affected (References 1 and 2). They present ideal case studies for earthquake risk management. The names of the two companies that are discussed below, although well known, are not important for the purposes of this paper. Most large companies and organizations around the world would have done no better.

2.1 Automotive Industry Parts Manufacturer:

Kashiwazaki houses Japan's largest manufacturer of piston rings and other parts used in cars, trucks, etc. The very large facility is shown in Figure 1. The business media reported that the plant manufactures about 40% of all piston rings for the Japanese automobile industry. The plant is a sprawling, mostly older manufacturing facility, with dozens of buildings and mostly relatively low-tech manufacturing operations. For the most part, the structures performed adequately (Figure 2) and did not contribute significantly to the roughly 10 days of loss of operations. That business interruption was caused almost entirely by damage to equipment. The primary cause of damage was the inadequate anchorage of equipment. 1,240 out of 1,840 (70%) of heavy machinery slid or toppled during the earthquake. All of this damage could have been prevented with simple equipment anchorages and braces through an engineering loss control program.

The company's management described the earthquake motion as a series of strong lateral shocks, three or four which knocked down or pushed sideways the equipment. As the equipment fell, various components broke. As the equipment slide or fell over it also damaged attached piping, ducting, electrical conduits, etc. Equipment that was bolted down to its foundations, such as heavy rotating machinery that must be anchored in order to operate properly, was not damaged.

The biggest effect of the shutdown of production was that it affected most of Japan's auto industry. Most of Japan's major auto manufacturers, a;; of whom use just-in-time supply, could not manufacture cars without parts from their main supplier. That affected Toyota, Honda and most others. The auto manufactures, who are not located in Kashiwazaki and were not affected directly by the earthquake, sent quickly after the earthquake large teams of their own engineers and machinist to assist their supplier in Kashiwazaki with engineering and repair and helped it restart much quicker than it would have been able to do on its own. Nevertheless, all that resulted in the loss of production of a reported 120, 000 vehicles. That loss, in itself, is much greater that the direct damage to the plant.

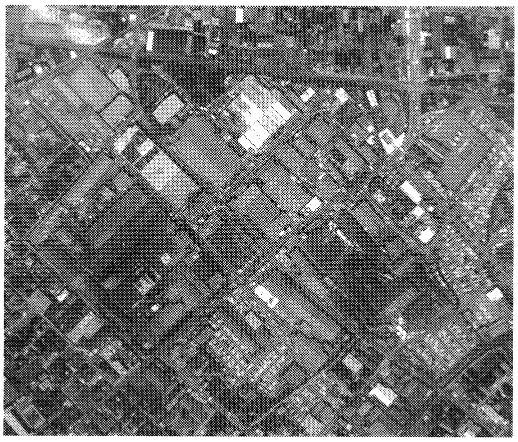

Figure 1 View of the large auto industry parts plant (Google Maps)

Figure 2 Some of the structures that were undamaged or lightly damaged at the prison ring manufacturing plant in Kashiwazaki City.

All of this happened in a moderate earthquake in one of the world's most sophisticated economies. What if the earthquake, for example, had a much larger magnitude, of 7. instead of 6.8? Building damage would have been extensive and equipment would have been much, much worse. The business interruption would have been several months instead of several days. Because of the just-in-time supply system, because of the lack of redundant suppliers, and because of inadequate earthquake risk management at just one company, Japan's automobile industry would have experienced a huge financial loss.

The same lesson applies to all industries, worldwide, that rely on just-in-time delivery and on sole-source or nearly sole-source suppliers located in earthquake areas. The potential loss of unprotected equipment and the resulting business interruption and financial losses lessons also apply to all industries and commercial operations in earthquake areas worldwide.

What is required for this particular case is (1) to protect the equipment and (2) to build redundancies in the system. It was recently announced by the company that because of the effects of this earthquake the company has decided to build at least two new additional plants for the production of piston rings elsewhere in Japan and abroad.

2.2 Power Generating Plant

The Kashiwazaki-Kariwa Nuclear Power Plant is one of the world's largest nuclear power generation facilities. It is located just a few miles from the earthquake's epicenter. It is owned and operated by the world's third largest electric utility company. As shown in Figure 3, the plant consists of seven reactors lined along the coastline. The electric output of the plant is over 8.200 MW. This amount is sufficient for approximately 16 million households or approximately 30% of Japanese households.

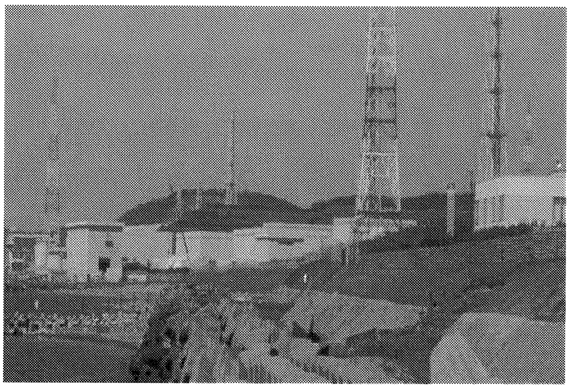

Figure 3 View of the nuclear power plant shortly after the earthquake.

All nuclear plants in Japan are required to have earthquake motion recording instrumentation, placed at different locations throughout the plant. As nuclear reactors in Japan are required to be built on rock, the instruments on the foundation slabs of the reactors recorded ground accelerations exceeding 0.50 g. That is the strongest ground motion ever affecting a nuclear reactor. The accelerations exceeded one of the design criteria for the plant by a factor of more than two. That was also a new experience for the nuclear power industry.

Three reactors were shut down at the time of the earthquake for maintenance. Three other units were operating at the time of the earthquake and were automatically and successfully shut down once the ground motion was detected. One unit was just starting up, after a maintenance shutdown, and was also successfully shutdown during the earthquake.

The plant experienced no significant damage to any structures or equipment related to nuclear safety. Nuclear safety-related structures and equipment are designed to very high earthquake criteria. Other portions of the plant, which are not important from a nuclear safety perspective, such as suspended ceilings in a cafeteria or an electrical transformer in the station outside on open ground, suffered moderate damage. These were designed to normal earthquake criteria like those for typical commercial buildings and systems. Ground settlement outside the nuclear safety-related parts of the plant caused damage to outside non-critical equipment, piping, etc. All of that was relatively minor. One such example of damage was a fire in a high-voltage transformer, shown in Figure 4. The fire was extinguished in two hours, but that image played on the international media for several days, and the implication was that a nuclear power plant was on fire (which it was not). The media had a field day with similar photographs, without ever explaining how unimportant for safety that fire was.

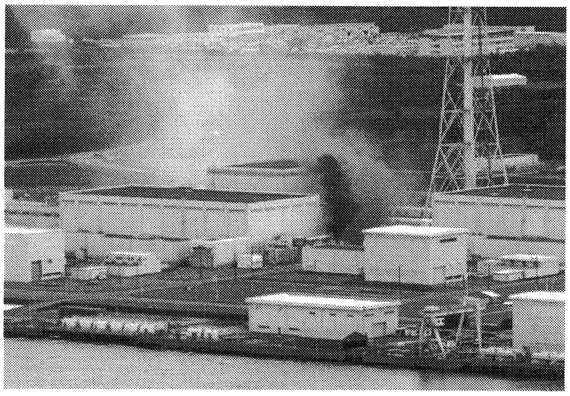

Figure 4 Transformer fire in the yard of one of the nuclear units. The non-safety related fire was extinguished in two hours but the image played on the international media for several days (Yahoo News)

It appears that the power company was simply unprepared to handle bad news regarding its major facilities. For about three days, the company did not release reports to the public while the international media, in particular, sensationalized the apparent minor damage. Then it released a flurry of reports, some of which turned out to be conflicting.

In effect, the inadequate communication and public relations response to the earthquake turned what was an engineering success into a major business failure – the largest single industrial financial loss from an earthquake ever. After a few days of conflicting reports and bad publicity, the government stepped in and shut down the plant, initially for the rest of 2007, possibly for much longer. The business interruption to the plant and the cost of the replacement generating capacity would now amount to several billion dollars. That number alone is much greater than the total damage caused by the earthquake in the stricken region of Japan. Further, the company expects a drop in profits for this year of over 70%. Next year's profit and revenue are also up in the air. The stock market reacted swiftly, compounding the already staggering loss. All this happened in a moderate Magnitude 6.8 earthquake. What if the earthquake had been bigger? What risk management program should have been in place?

4. ENGINEERING EDUCATION

Earthquake engineers (and scientists) are not generally trained to answer the last question. Those few that can address the question have arrived on the answer through experience and through working with corporate managements.

I believe that, in order for professional engineers to provide the correct answer, we need first to expand engineering education. Earthquake risk management requires technical solutions based on effective business practices and knowledge of financial management. It does not matter how good or cost effective an engineering solution is if the engineer cannot communicate both the technical results and the business solution to corporate management in the financial terms to which they are accustomed.

To be effective in today's world of earthquake risk management engineers must be educated in the rudimentary techniques of management and finance. The logic and the mathematics required to do that are much simpler than those required for a graduate course in structural dynamics or probabilistic risk analysis. Two well thought out and organized courses on business for practicing engineers, at the upper undergraduate or graduate levels, should provide the needed education. Only then should we expect engineers to drive the solutions for earthquake risk management worldwide.

An engineering business course could include, as a case study, one of several phased earthquake risk management programs. A typical Three Phase Corporate Earthquake Risk Management Program for business and industry is outlined below.

5. THE THREE PHASE CORPORATE EARTHQUAKE RISK MANAGEMENT PROGRAM

The initial phase is the **Risk Audit** of the corporate facilities. The risks are identified using state-of-the-art screening methods, walk-downs, risk assessment and analysis technology, and engineering experience. The screening and analyses are also based on Earthquake Experience Data collected from several hundred destructive earthquakes throughout the world.

In the second phase, the **Cost-Benefit Analysis**, recommendations for strengthening important buildings and key equipment (that controls business interruption) are developed. Engineering and business analyses are performed to evaluate the costs and economic benefits associated with such upgrades and the resulting decrease in Business Interruption, Loss of Market Share, etc.

The final phase of the Earthquake Risk Management Program is its **Implementation.** That includes, but is not limited to:

- Developing corporate standards of performance for earthquakes. These typically should exceed the requirements of the local building codes and should meet the specific needs of the company.
- Designing and constructing the recommended structural and equipment upgrades to existing facilities to achieve the desired levels of performance.
- Transferring earthquake risk through various financial vehicles such as property and casualty insurance, reinsurance, cat bonds, etc.
- Developing a business recovery program that includes planning scenarios, post-event operations, business and financial planning, public relations, etc.

6. HISTORY OF CORPORATE EARTHQUAKE RISK MANAGEMENT

Earthquake risk management for corporations started in earnest in the early 1980s in California with the introduction of probable maximum loss (PML) analyses coupled with overall corporate earthquake risk reduction programs, such as the one discussed above.

Since that time, thousands of companies, first in the United States (with facilities in earthquake regions such as California) and then throughout the world, have implemented some of the aspects of classical earthquake risk reduction programs. Few, however, have maintained these programs adequately over the years since their introductions. The first programs started in Silicon Valley in the San Francisco Area in 1981 because of the realization that business interruption, not just damage from shaking, would cause extended outages and loss of production. Such losses would dwarf the losses from building damage alone.

A few European companies, particularly the larger multinational companies, with properties in earthquake areas in and outside of Europe also became active after the 1989 San Francisco and the 1994 Los Angeles earthquakes. Following the early 1980's prediction of a major earthquake in the Shizuoka area south of Tokyo and especially after the 1995 Kobe earthquake, some Japanese companies also started to take earthquake risk seriously. However, most companies worldwide have done little to analyze or protect their facilities beyond the rudimentary requirements of the local building codes.

The analyses are conducted by earthquake and structural engineering companies with extensive experience with the effects of earthquakes, collected from damage observations and coupled with engineering analyses. Typically, corporate Risk Management, which is usually embedded in the CFO or Treasury offices, takes the lead in hiring the engineering companies. Sometimes the individual plants or facilities take the initiative and hire their own consultants. The analyses should address all possible losses from earthquakes, including building damage, equipment damage, inventory losses, interruptions due to damage to the facilities of suppliers, damage from fires following the earthquake, business interruption losses, and loss of market-share. Business interruptions due to general infrastructure damage, such as loss of electric power, water and gas are also analyzed in order to determine their impact on business interruption.

The nature of the analyses took a turn for the worse around 2000 with the widespread introduction of cat analysis software. The software was initially developed for the use of insurance and reinsurance companies who needed a tool for their own risk assessment. Their risk typically consists of hundreds or thousands of large individual risks with a wide geographic distribution; not just a typical single industrial portfolio of a few important facilities. The software and their analysis engines use very sophisticated probabilistic analyses based on the law of large numbers and generalized property damage data from catastrophes in the form of "damage or fragility" functions. The insurance industry, led by the larger broking companies, began to use the software to analyze individual risks; the work is now usually done by staff who are not earthquake engineers and have no significant field engineering experience. The software is not at all adequate for the analyses of individual facilities without detailed input from the field, even when used by engineers. Using engineers is a common practice in Japan, for example, but that too is not enough without field inspections. The software can and should only be used for probabilistic analyses to determine annualized loss costs, for example, for individual facilities such as a car manufacturing plant after detailed PML numbers are generated through field inspections. I have reviewed many computer based analyses and their reports for individual facilities or buildings over the last several years. Some were written by engineers; most were not worth the paper they were written upon. My conclusion is simple – if an engineer uses software, he or she should only use it in conjunction with detailed field inspections by competent and experienced earthquake engineers.

7. A CASE STUDY OF INDUSTRY EARTHQUAKE PREPAREDNESS IN A LARGE URBAN AREA: ISTANBUL, TURKEY

Istanbul has an enormous variety of commercial buildings and industrial facilities with different sizes, shapes, and structural systems built with highly variable construction practices over varied terrain. As of today, Istanbul houses almost one sixth of the total population and more than half of the industrial capacity of Turkey. The metropolitan area presents a typical example from around the world of earthquake risk to industry outside a few more advanced areas like California, Japan, New Zealand and Chile.

My first opportunity to view directly the effects of an earthquake in Turkey dates back to the 1975 Lice earthquake near Diarbakir in Eastern Turkey, which destroyed Lice and several nearby villages, with a heavy loss of life. I have led the investigations of several earthquakes in Turkey since 1975 and also had the opportunity to visit many industrial facilities in the strongly affected area of the 1999 earthquakes near Istanbul as part of the Earthquake Engineering Research Institute's investigating team. Following the earthquake, we worked on several of the damaged industrial facilities in the Izmit area. In 2002 the World Bank asked me to conduct an earthquake assessment of the Istanbul Metropolitan Region in preparation for the Bank's Istanbul Seismic Mitigation and Preparedness (ISMEP) Project (Reference 4). I have worked with the World Bank and others in Turkey since then, and continue to work there and in several neighboring countries that have high earthquake risks (References 5 and 6).

Since the 1999 earthquake, we visited, conducted risk reviews and assessments, and completed earthquake retrofit designs for over 60 companies and organizations and their facilities in the Istanbul region (Reference 3). That includes the following types of facilities and their associated structures, equipment, and infrastructure:

1. Pharmaceutical Plants
2. Automobile Manufacturing and Assembly Plants
3. Steel Plants
4. Beverage, Food, and Food Processing Plants
5. Chain Stores and Hypermarkets
6. Chemical Plants
7. Paint Manufacturing Plants
8. Oil and Gas Facilities, including Storage and Distribution
9. Ceramics Manufacturing Plants
10. Warehouses and other Storage Facilities
11. Residential Developments
12. Other Heavy and Light Industry Facilities and Plants
13. Commercial and Government Buildings (Industrial to High-rise)
14. Power Plants, Substations, etc.
15. Telecommunications Facilities
16. Large Bridges, Viaducts, Freeway Overpasses
17. Airports and Associated Structures

18. Ports
19. Fire Stations
20. Police Stations
21. Emergency Centers
22. Schools and Universities
23. Hospitals
24. Historical Buildings and Museums

For the above facilities we typically considered some or all of the following earthquake effects:

1. Building Damage
2. Equipment Damage
3. Inventory Damage
4. Fire Following the Earthquake
5. Business Interruption
6. Loss of Market Share
7. Infrastructure Damage
8. Damage to Clients and Suppliers

In almost all of these facilities we observed obvious structural vulnerabilities that could lead to partial or total collapses of buildings. In most cases facility management was unaware of the risks; actually management typically believes that the buildings were highly earthquake resistant (often because they were not damaged by the distant 1999 earthquake, as discussed further below).

In all facilities we also observed inadequately braced or totally unprotected (for earthquake) equipment, architectural features, and other components that will be damaged during a major earthquake and will cause prolonged business interruptions.

Since building codes contain few explicit provisions for the protection of equipment, proper earthquake resistant anchorages are usually ignored in Turkey during design and installation. Without proper anchorage and/or bracing, equipment can easily be damaged in even a moderate earthquake. However, if properly secured to prevent sliding and overturning, most equipment can withstand very strong ground shaking without any damage. In addition, damage to equipment during an earthquake often occurs due to the interaction of various nonstructural items within a facility. For example, a relatively unimportant storage rack that is not anchored could fall and damage an adjacent vital piece of manufacturing/process equipment. Most of this risk and the resultant damage can be easily mitigated if only management and their engineers will recognize the problem

Losses from fire following earthquake can equal or exceed those resulting from shaking at many of the reviewed facilities. For certain industrial facilities, this was observed to be a very serious problem. Sprinklers or piping is easily damaged if improperly braced, and most of it is not, even in new installations. Sprinkler leakage has also caused extensive damage to contents in buildings that had no structural damage in past earthquakes. Most of the risk and the resultant damage can be mitigated easily.

One of the problems that we encountered frequently was the interpretation of the lack of damage from the 1999 earthquakes in Istanbul. That lack of damage misled industry into thinking that the risk is not high. Following the 1999 earthquakes, many companies hired consulting engineers and university staff to survey their facilities. Most of the facilities that were evaluated were outside of the strongly shaken area and suffered minor or no damage. Management personnel that we met with often do not understand that the 1999 quake was almost 100 km. away from Central Istanbul; it was not in Istanbul. The damage reports usually stated that the facilities were not damaged significantly and could continue to operate without any immediate danger. Facility management typically interpreted and continues to interpret these post-earthquake assessment reports to be saying that the future earthquake risk to their facilities is low. In effect, the damage (or lack of damage) reports were misinterpreted to be risk analyses, which they were not. They also typically attributed the lack of damage in 1999 to adequate construction and earthquake preparedness, which usually was not the case. Further, most believe that their facilities will survive a future and even larger earthquake with little or no damage.

Another frequently observed problem was the poor quality of typical repairs and retrofits following the 1999 earthquakes. Numerous industrial and commercial buildings that were damaged in the 1999 earthquakes were repaired shortly after the earthquakes. Most of the observed repairs and "strengthening" features are simply repairs to bring buildings and systems to pre-earthquake conditions. We observed very few genuine strengthening features that actually reduced the risk.

Over the last seven years we have met with many dozens of senior executives of Turkish and multi-national companies in the Istanbul area. To date, we have found only two Risk Managers of Turkish companies, including the Turkish subsidiaries of multi-national companies and their joint-venture companies. Turkish companies and organizations have no in-house risk management organizations. Typically, the risk management function is handled by default by a financial officer of the company who has no risk management experience (other than, perhaps, buying insurance). Typically, we found that the companies do not even understand their earthquake insurance coverage.

Our overall observations of the risk to industrial facilities and many commercial buildings in Istanbul can be summarized rather simply:

- **Typically, plants and facilities have high existing risks. This is the case with both older and newer plants and facilities.**
- **Most companies and organizations, including some of the largest multinational companies operating in Turkey, have done nothing to understand and to manage the risk from**

earthquakes (other than buying some insurance).

A small number of companies in Istanbul have now completed some rudimentary equipment bracing programs; fewer have addressed their building problems. Several multinational companies, with operations in Turkey, lead that effort. On the public side, the Municipality of Istanbul, through the ISMEP Project with funding from the World Bank is currently strengthening over 400 school and hospital buildings and assessing many of the cultural heritage buildings in the city.

8. MULTINATIONAL COMPANIES AND DESIGN AND CONSTRUCTION STANDARDS

Much of the industry in earthquake areas around the world is owned and operated by multinational companies. These organizations face unique problems in managing their risk. Some are the only organizations in many countries that have addressed their earthquake risk. Japanese auto manufacturers in Turkey, for example, had the best performance, generally, during the 1999 Izmit earthquake.

Multinationals typically employ one of two management systems for their facilities around the world. Some have a concentrated risk management system, where the risk management group is responsible for addressing and managing risk at all facilities around the world. Under this system, the risk manager often is capable of initiating risk studies anywhere with a budget directly from headquarters. This is the system found most often in U.S. based multinationals. Other multinationals have decentralized risk management operations; the risk management office is located at their headquarters and is responsible for purchasing insurance worldwide, but any risk studies must be paid for and initiated by the local profit centers or plants. This is the system often used by multinationals based in Europe. Many multinationals operate throughout the world through joint ventures with local companies – that is most often the case in Turkey, for example. In those cases it is often very difficult to find out who is in charge of risk management.

Multinationals with concentrated risk management seem to have the most success so far in accomplishing some earthquake risk control at their facilities outside the home country. The least effective multinationals, as regards loss control, are those that typically operate joint ventures with local companies.

Even some of the world's best know companies have often done little to moderate or even study their risks in earthquake prone countries around the world. For example, that is the case with many of California's Silicon Valley companies that have facilities in Japan. Typically, the newer buildings meet the requirements of the strict building codes while the vital production equipment remains virtually unprotected because there are no code requirements for earthquakes. That has, and will continue to lead to costly business interruptions, as happened during the 2007 Niigata earthquake. I reviewed recently a multi-billion dollar new high-tech manufacturing facility outside Tokyo, owned by a California based company. The buildings had very low PMLs but the critical production equipment was mostly unanchored. The expected business interruption was more than 6 months – with effectively no expected building damage. A loss control program can reduce that interruption to a few days.

One of the major problems that multinationals (and the local companies) have to overcome is over-reliance on local codes and construction practices. Most code requirements around the world are based on the requirements of Japanese and Californian codes, particularly for buildings. Typically, they lag the newer Californian and Japanese requirements by several years; they usually tend to get updated only after major earthquakes point out local weaknesses. Thus, the codes are generally out of date. Further, they are typically much weaker in their requirements for the protection of architectural items and equipment. Typically they have no requirements for production equipment.

Design and construction practices and standards around the world's earthquake prone areas also vary widely. New Zealand and Chile, for example, have very high standards when compared to most other countries. Surprisingly, countries like Greece, Italy and Israel have far weaker standards. Asia's fast growing economies, including China, India, Taiwan, and Indonesia are rapidly building plants, structures and infrastructure in their far-flung earthquake regions that will require massive strengthening programs in the future. It is much more cost effective to provide the necessary earthquake resistance up-front and before the next earthquake.

9. RECOMMENDED RISK MANAGEMENT PROGRAM FOR INDUSTRY – BASED ON CALIFORNIA'S EXPERIENCE AND A SIMPLE BUSINESS APPROACH

Managing earthquake risk is an essential part of any business process in California and in several other earthquake prone regions. Earthquake risk management is a major concern for businesses operating in earthquake areas throughout the world; many have taken the typical business approach summarized below.

Californian companies started managing their earthquake risks in the 1980s. The work accelerated following the 1989 San Francisco and 1994 Los Angeles earthquakes, when it became obvious that businesses that had initiated programs to manage their earthquake risk suffered much less damage and business interruption than businesses that had done nothing more than buy earthquake insurance.

For an industrial facility there are several options for managing earthquake risk. These include:

1. **Do nothing and accept the risk.** This is usually the current situation in most countries.
2. **Manage some of the risk exclusively through earthquake insurance coverage for potential damage and business interruption.** Many companies have taken this route. This was also the situation in California before 1980 and Japan before 1995.
3. **Assess the risk and reduce it to an acceptable level.** This includes engineering analyses of the assets of the company and the strengthening of selected structures and equipment within its facilities to reduce the risk to an acceptable and predetermined level. Depending on the level of strengthening implemented, it is also appropriate to carry adequate earthquake insurance. ***This is the business approach now favored by industry in California and elsewhere and recommended for companies worldwide.***

Finally, any company that operates manufacturing facilities and/or owns or leases commercial buildings should develop its own earthquake risk management standards that meet its specific needs and apply them rigorously around the world.

References:

Global Risk Miyamoto (2007), "2007 Niigata Chuetsu-Oki Japan Earthquake – Reconnaissance Report", West Sacramento, California, USA

EQRM International (2007), "The July 16, 2007 Niigata, Japan Earthquake; Lessons for Industry and Business I Turkey", Istanbul, Turkey

Yanev, Peter I. and Rafael Alaluf (2006), "Earthquake Risk to Industry in Istanbul and How to Manage It", Istanbul, Turkey,

Yanev, Peter I. (2002), "Observations on Earthquake Risk and Engineering Practices in Romania", Report to the World Bank For the Romania Hazard Risk Mitigation and Emergency Preparedness Project (PO75163), Washington, D.C., May

Yanev, Peter I. (2002), "Observations on Earthquake Risk and Engineering Practices in Istanbul, Turkey", Report to the World Bank, Washington, D.C., December

ENEL (2004), "Catastrophe Risk Management in Bulgaria", Report No. RAT-1367/2004 to the World Bank, Bergamo, Italy, October

Fifth International Conference on Urban Earthquake Engineering
March 4-5, 2008, Tokyo Institute of Technology, Tokyo, Japan

SCALABLE WIRELESS SENSOR NETWORKS FOR STRUCTURAL MONITORING

Gregory L. Fenves[1] and Shamim N. Pakzad[2]

1) Professor, Department of Civil and Environmental Engineering, University of California, Berkeley, U.S.A.
2) Graduate Student Researcher, Department of Civil and Environmental Engineering, University of California, Berkeley, U.S.A.
fenves@berkeley.edu, shamimp@ce.berkeley.edu

Abstract: A wireless sensor network was designed, developed, and deployed for structural health monitoring with the goal of providing scalability of the network in terms of the number of sensor nodes. A standard microprocessor and operating system is extended for high-frequency sampling, reliable command dissemination, and data pipelining over a large number of hops (more than 40). The pipelining provided a communication bandwidth of 550 bytes/sec independent of the number of nodes and hops. Utilizing the ambient vibration data collected in the network, the vibration modes of the main span of the Golden Gate Bridge were identified with a high degree of confidence, including higher vibration modes. To achieve high spatial density, necessary for local damage detection over the life of a structure, the sensor networks need to be highly scalable to hundreds or even thousands of sensors. This will require an integrated approach to hardware for heterogeneous sensor networks, system software architecture based on a parallel computing abstraction or distributed database abstraction, and scalable structural health monitoring algorithms.

1. INTRODUCTION

Sensor networks have tremendous promise for monitoring the performance of structural systems and other critical components of the infrastructure. The information from a structural monitoring system can improve safety, reliability, and decrease long-term maintenance costs. Monitoring systems allow "virtual inspection" of a structure after an earthquake or other extreme event, which can bring the structure back into service sooner than traditional inspection and tagging procedures. Considering an entire urban region, there are many advantages of major structures providing diagnostic and prognostic information for prioritizing emergency response and resource allocation. Recovery will be more rapid with improved information about actual condition.

The advances in sensor networks for structural health monitoring and assessment have been driven by the rapid improvements in sensor technology, such as micro-electro-mechanical-system sensors (MEMS), fiber optic sensors, piezoelectric materials and other smart materials, and even video and laser imaging (Spencer, et al. 2004; Glaser et al., 2007). The most active area of research and development for structural health monitoring has been in the use of wireless communication with MEMS sensors, and recent developments and testbeds have provided valuable information (Mastroleon et al. 2004; Chung et al. 2005; Lynch and Loh, 2006; Ou et al. 2005).

The potential of wireless sensor networks is that they can provide fine-grained sensing with high spatial density in a structure. This is essential for identifying local processes of damage at any point in the structure, over its entire lifecycle. The use of high production volume, low cost sensors with minimal installation and maintenance can eventually allow hundreds to thousands of sensors to be deployed in a major structure. This is important for structural health monitoring applications because damage is a local phenomenon and in most structures it is not possible to a priori locate sensors in areas that may experience damage over the service life. To address the question of high spatial sampling density, the objective of this paper is to describe a scalable sensor network for structural monitoring, discuss development of scalable hardware, communication, operating system software, and applications, and outline future research to improve scalability for structural health monitoring sensor networks.

Scalability is a concept in communications and computation that means a measure of cost, complexity, and network performance of a system does not increase more than linearly as a function of the number of nodes or processors. For example, in the case of a cellular telephone network, the addition of one cell phone in the network generally has zero or little cost beyond the handset. Traditionally, wired sensors for structural systems are not considered scalable since the transducers are not only expensive, but also the wiring and recording (logging) costs generally increase substantially as more cables need to be installed, connected, and tested.

Scalability has another meaning in terms of parallel computing, which considers computational performance as a function of processor speed and inter-process communication. A broad view of scalability for structural health monitoring is based not only on network communication but also parallel computation. A unified view of a sensor network in terms of parallel processing of algorithms and as a distributed database of information related to structural health points towards future directions in research and development of wireless scalable networks.

2. EXAMPLE OF HIGH-SPATIAL SAMPLING DENSITY FOR STRUCTURAL MONITORING

2.1 Overview

To demonstrate the utility of high-spatial sampling density, recent results from measuring ambient vibration of the Golden Gate Bridge in San Francisco, California, U.S.A., are presented. The current seismic monitoring system for the bridge has more than 70 accelerometers (Stahl et al. 2007), but the 1280 m main span only has instruments at the mid-span and one quarter-span location. More than twenty years ago, Abdel-Ghaffar and Scanlan (1985) measured ambient vibrations using portable accelerometers and seismometers and identified vibration modes of the main span and other portions of the bridge.

Recently, a research team from the University of California, Berkeley, conducted a three-month deployment of an innovative sensor network using wireless communication. The sensor nodes and network were developed for measuring ambient accelerations in the main span and the south tower (Pakzad et al. 2008). Before discussing the hardware, software, and communication, and how they were designed for scalability, it is worthwhile to examine the vibration data for the main span and the importance of high-density spatial sampling. Fifty-three (53) sensor nodes were installed along the entire length of west side of the main span, and three (3) additional ones were on the east side. Each sensor node had two accelerometers in each transverse and vertical direction. The west-side nodes were mostly spaced at 30.5 m, depending on reception and interference of the low-power radios on the nodes. The east-side sensor nodes were placed at mid-span and the two quarter-span locations.

2.2 Ambient Vibration Data

Figure 1 shows typical ambient acceleration data in the vertical direction from the sensor node at mid-span. The sampling rate was 50 Hz and the run (172 in this case) collected data for 1600 sec. The amplitude of ambient acceleration is typically the order of 10 milli-g, but spikes of up to 20 milli-g are observed, presumably because of vehicle passage.

Figure 1 also shows the power spectral density (PSD) of the signal for this one run. The plot clearly has peaks that indicate amplification at the vibration frequencies for the vertical and torsional modes of the main-span. Examination of the entire data set shows consistent results in terms of peaks in the PSD for individual runs and among the runs. The PSD of the ambient acceleration signals also confirm that the low-frequency noise level is small compared with the peaks, which was one of the design goals for the low-cost sensor node hardware.

2.3 Vibration Mode Identification

Using the acceleration data from a single run, a multi-variate ARMA method is used to identify the vibration frequencies, damping ratios, and mode shapes (Pakzad et al. 2008). The ambient vibration data is low-passed filtered

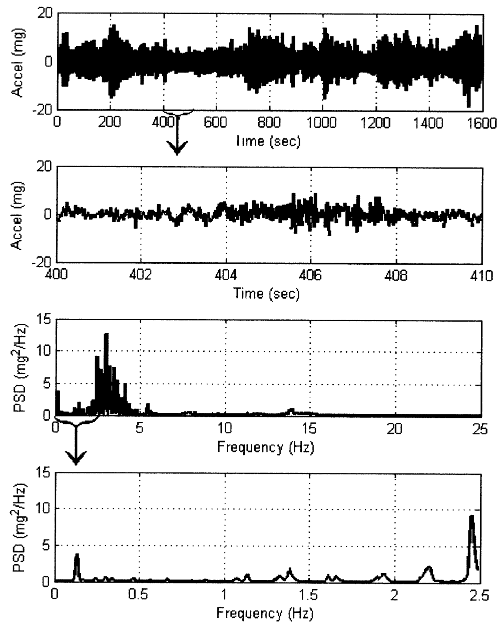

Figure 1 Time History and Power Spectrum Density for Vertical Accelerometer at West-Side Midspan (Run 172)

because the important vibration modes of the main-span have frequencies less than 5 Hz, far below the Nyquist frequency of 25 Hz. Modal phase collinearity (Pappa et al. 1993) was used to verify the spatial coherency of the identified vibration modes; most modes have a MPC value of at least 0.95.

An example of the results of the identification process using the ambient acceleration data from 49 sensors for one run is illustrated in Figure 2. Vertical vibration modes up to mode 23 were identified from the data, and the figure plots the main span mode shapes for mode 1 (f=0.11 Hz, ξ=1.4%), mode 11 (f=0.89 Hz, ξ=0.6%), and mode 23 (f=2.72 Hz, ξ=0.6%). It is important to note that even with relatively low-cost sensors, the high-density of spatial sampling allows identification of the higher vibration modes.

Further analysis shows that the data give the same identified vibration modes when different sets among the 56 sensors are used, thus demonstrating that the identification results are repeatable (Pakzad et al. 2008). Furthermore, the large number of samples provides statistical measures of the confidence of identified modes (Pakzad and Fenves, 2008). High-density spatial sampling is necessary for detecting changes in a structure caused by localized damage, and large number of samples improves the confidence in estimates of structural performance and ability to detect changes.

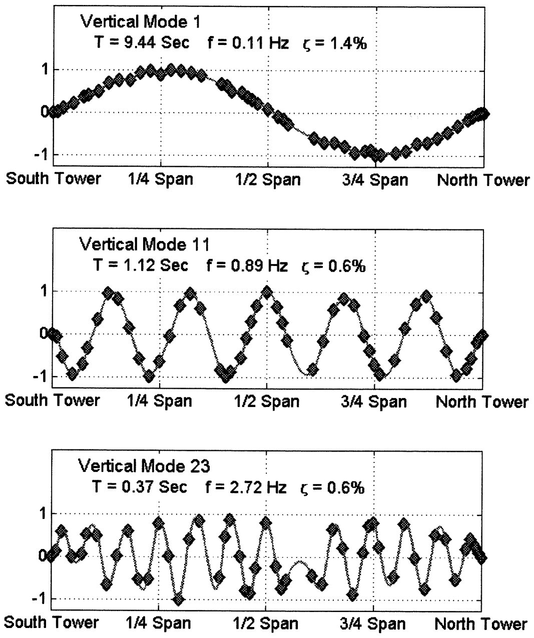

Figure 2 Identified Vibration Mode Shapes for Three Vertical Modes: 1, 11, and 23 (Run 172)

3. SYSTEM DESIGN FOR SCALABLE WIRELESS SENSOR NETWORK

3.1 System Requirements

A basic requirement for a scalable sensor network is that the nodes be fairly low cost using commercial off-the-shelf components and wireless communication. High data quality could have been provided with relatively expensive sensors and high-performance microprocessors. For scalability, low-cost components were selected, but they need to be significantly adapted through hardware and software to provide the data quality for modal identification (as illustrated in section 2). The nodes needed a battery power source since on-site power was not available at the bridge. Similarly, wireless communication was necessary because it would not have been possible to wire sensors along the length of the Golden Gate Bridge.

The following requirements were established for the wireless sensor network:

- Measure acceleration in the ambient range (order of 100 micro-g to 100 milli-g) and in the event of a strong earthquake (order of 1 g).
- High sampling rate (up to 200 Hz)
- Lossless communication of data in a large multi-hop wireless network.

These requirements imposed substantial challenges but were necessary for scalability and the structural health monitoring applications. The following subsections summarize how the design requirements were met using creative hardware, software, and communications solutions.

3.2 Sensor Node Hardware

The hardware design is shown schematically in Figure 3. The broad range of acceleration was not possible with a single MEMS accelerometer of reasonable cost, so two sets of accelerometers were selected for each direction. The high-level motion sensor is Analog Device's ADXL202 with a sensitivity of 1 milli-g at 25 Hz. For low-level motion Silicon Design's 1221L has high sensitivity with a hardware noise ceiling of 10 micro-g. Each MEMS sensor channel provides analog output, which is fed to a single-pole low-pass filter for anti-aliasing with a cutoff frequency of 25 Hz, and a 16-bit analog-to-digital converter (ADC). The analog output is sampled at 1 kHz and downsampled by averaging to reduce the noise even further.

The MicaZ mote from Crossbow is used as the microprocssor for controlling the MEMS sensors, local processing, data storage, and radio communication. Each mote has 512 kB flash memory, which can store up to 250,000 samples. The MicaZ radio uses the 2.4 GHz band with a bi-directional antenna. Power for the node is from four 6 V lantern batteries wired for 12 V and 15 A-h. The sensor node hardware is shown in Figure 4.

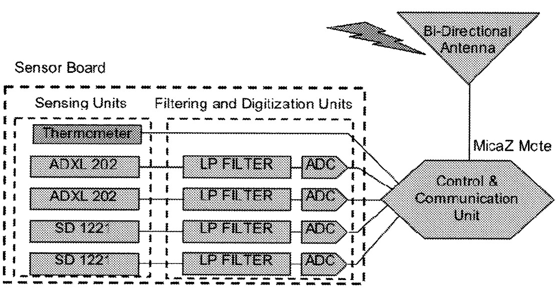

Figure 3 Schematic of Sensor Node Hardware

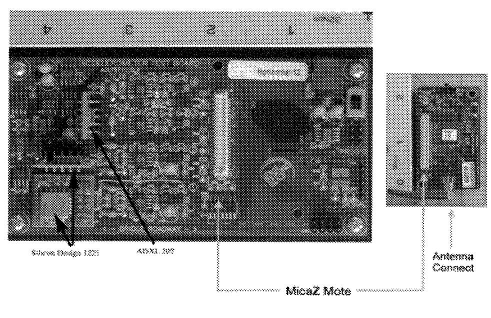

Figure 4 Sensor Node Hardware. Enclosure box and batteries not shown.

3.3 System Software

The system software is based on the TinyOS operating system (Hill et al. 2000), but with major extensions to address the requirements for a scalable network for structural health monitoring. Extensions of the system software were required for high-frequency sampling, multi-hop communication, reliable data transmission, and communication pipelining.

High-frequency sampling, up to 1 kHz for reducing noise and identifying dynamic response is necessary for structural health monitoring. Most wireless sensor applications, however, have used much lower sampling rates. High-frequency sampling introduces significant problems in timing of each node and synchronizing a large number of nodes in the network. A TinyOS component, Flooding Time-Synchronization Protocol (FTSP) provides time synchronization over the network (Maroti et al. 2004). Testing and analysis show that FTSP with the TinyOS timer gives a synchronization error of 10 micro-sec for a sampling rate of up to 6.67 kHz (Kim et al. 2007). Assuming an acceleration signal at 25 Hz with amplitude of 10 milli-g, the noise from timing error is 16 micro-g, which is less than the sensitivity of the MEMS accelerometers. This is excellent timing performance using the single clock on the MicaZ mote for all functions, including sampling the analog-digital converters, writing and erasing memory, and communication via the radio.

Multi-hop communication is essential since the physical size of structures is much larger than the radio range of motes. TinyOS provides the routing services necessary for multi-hop communication of data packets (Woo and Culler, 2003). To meet the system requirements, two significant extensions of the communication system were necessary for scalability. The standard TinyOS protocol does not guarantee delivery of a data packet, which could be lost because of radio interference or packet collision. The challenge is to provide reliable data transfer with minimal computation, memory, and power. A new protocol named Straw (Scalable Thin and Rapid Amassment Without loss) has been developed, tested, and deployed for multi-hop networks to provide this service (Kim et al. 2007). It is a selective-NACK (Negative ACKnowledgement) collection protocol, where the data transfer is initiated by the receiving node. The sender node transmits data packets upon request, then the receiver identifies and returns a list of missing packets back to the sender. The lost packets are resent until all packets are acknowledged.

Finally, once the routing of data packets in the network is established through routing tables, it is essential to maximize the bandwidth of the network. This is done by data pipelining in which a packet of data is sent by one node; after the packet has been transferred through at least five other nodes, a request initiates send of another packet. Testing has shown that a delay of five nodes provides a good balance between maximizing the capacity of the pipeline and minimizing the effects of radio interferences.

3.4 Network Performance

The routing and pipelining significantly increase the effective bandwidth of a large network regardless of the number of hops. On the Golden Gate Bridge deployment, the empirical data shows that the one-hop bandwidth is 1200 bytes/sec. Each additional hop reduces the bandwidth because a node has to receive the data, buffer it, and retransmit it (in addition to sending its own data). With the data pipelining the average bandwidth for the entire network is 550 bytes/sec and it remains nearly independent of the number of nodes. This is important because it indicates that the network would have reliable communication for even hundreds of nodes. The packet loss rate is 2.5%, which is acceptable for the low-power radios and noisy electromagnetic environment of the steel bridge.

4. EVALUATION AND FUTURE NEEDS FOR WIRELESS SENSOR NETWORKS

The wireless sensor network designed, deployed, and tested on the Golden Gate Bridge addressed several of the key issues in scalability of wireless networks for large number of sensors. The major contribution of the work is to develop high-frequency sampling, reliable command dissemination and data collection, and scalable communication bandwidth all within a multi-hop wireless network. The bandwidth achieved over more than forty hops on the linear network topology exceeds those of recent testbeds and demonstrations of wireless sensor technology for structural health monitoring. Ambient vibration data were transmitted from all sensor nodes to the base station and standard system identification methods used to identify vibration modes. The high spatial density of the nodes allowed the identification of higher vibration modes with statistical confidence, demonstrating the important role of spatial sampling.

The findings help identify several major issues for improving scalability of sensor networks. Wireless communication is necessary for scalability because of the difficulty and expense of cabling hundreds to thousands of sensor nodes. Additionally, a wireless infrastructure for a structure (or collection of structures) would leverage several applications in addition to structural monitoring, such as energy demand management, security, and occupant support (for buildings), or traffic management (for bridges).

Increasing the scalability of wireless sensor networks has to be addressed in terms of hardware, system software, and structural health monitoring applications.

4.1 Sensor Node Hardware

Sensor transducer research and development has made rapid progress in recent years, producing a wide range of low-power devices for measuring physical quantities, such as acceleration and strain, physio-chemical quantities, such as corrosion, or changes in condition such as cracking through MEMS devices, fiber optics, and smart materials. In the long run, structural health monitoring will employ heterogeneous sensor nodes to detect a wide range of operational or exceptional conditions. Communication and system software, and applications need to operate in such a heterogeneous environment, and have the ability to adapt to technology and applications over the lifecycle of a structure.

Power management is a key factor in highly scalable sensor networks since it would be an unrealistic expense and operational burden to provide power or to change batteries in sensor nodes, many of which may not be easily accessible after installation. Power harvesting from ambient environment, through photovoltaic, wind, thermal gradients, or other approaches require research and development.

Linking the issue of power with sensor network system design is the processing power, memory, and other computing resources of the microprocessor. In the Golden Gate Bridge sensor network, a standard microprocessor (Crossbow MicaZ) was used to simplify the node and limit power requirements. Much more capable processors are available (e.g. linux-on-a-chip, such as Intel Stargate) at the expense of larger power requirements. It is an open question about what is the optimal allocation of processing power to the network compared with a base station server for each structural health monitoring application.

4.2 System Software Architecture

Most structural health monitoring applications using wireless sensor networks are based on a server architecture in which all nodes transmit signals to the base station server, in a manner similar to traditional wired networks using data loggers. This was done for the application described in section 2 and 3, although advances were made in terms of reliable communication and re-use of bandwidth. Ultimately, the server model of a sensor network is not expandable because of the data volumes increase beyond what can be communicated wirelessly with limited power. It is noted that many of the issues related to system software for structural monitoring are similar to those for embedded computing in general.

Moving from the server model for sensor networks, there are two possible abstractions. The first is viewing the network as a parallel computer in which processing is highly distributed and inter-processor communication has limited bandwidth and high power requirements relative to local processor computation. Applications such as modal identification or damage detection would be distributed over the network and computed in parallel. This approach, however, combines well-known difficulties in developing parallel algorithms with the difficulty of programming sensor node microprocessors.

An alternative abstraction for a wireless sensor network is as a distributed and hierarchical database (Franklin et al. 2007). Data, either directly sensed, or locally processed, is distributed throughout the network. Operations on the data may be expressed in the form of a query, and the query is sent through the network, processed locally, and results returned. There are many advantages to this abstraction, including the ability to define aggregation of data hierarchically (including the important aggregation operation of correlation, such as for system identification), the ability to express queries as a declaration (as opposed to a procedural function), which simplifies programming, and the ability to isolate the particular characteristics of sensor nodes as virtual devices.

4.3 Structural Health Monitoring Applications

There is a rich literature and many examples of structural health monitoring applications. However, most work has been based on limited sensors and a server abstraction for the data collection and processing. There is an urgent need to reformulate existing algorithms, and develop completely new algorithms that are scalable to thousands of sensors. The role of the system software architecture, either the parallel computing abstraction or the distributed database abstraction, will be crucial in the computational performance of distributed structural health monitoring applications. This is an important area for further research.

5. CONCLUSIONS

An innovative wireless sensor network for structural monitoring was designed and developed to achieve scalability in terms of the number of sensor nodes. High-resolution accelerations were obtained using commercial MEMS accelerometers. The major conclusions are that standard microprocessors and operating system can be extended for high-frequency sampling, reliable data collection and command dissemination, and data pipelining over a large number of hops (more than 40). The pipelining provided a communication bandwidth of 550 bytes/sec independent of the number of nodes and hops.

Utilizing the ambient vibration data collected in the network, the vibration modes of the main span of the Golden Gate Bridge could be identified with a high degree of confidence even for the higher modes. The results demonstrate the ability of high spatial density in the sampling to identify local features of structural response.

The research points to new directions for the structural engineering research community with regards to structural health monitoring using sensor networks. To achieve high spatial density, necessary for local damage detection over the life of a structure, sensor networks need to be highly scalable to hundreds or even thousands of sensors. This will require an integrated approach to hardware for heterogeneous sensor networks, system software architecture based on a parallel computing abstraction or distributed and hierarchical database abstraction, and highly parallel structural health monitoring algorithms.

Acknowledgements:

The work described in this paper benefited from substantial contributions by Dr. Sukun Kim, and Professors David Culler, James Demmel, and Steven Glaser. The staff and management of Golden Gate Bridge District, in particular Dennis Mulligan, Jerry Kao and Jorge Lee provided unprecedented access and support for the sensor network deployment on the Golden Gate Bridge. This research was supported by the National Science Foundation under Grant No. EIA-0122599 and by the Center for Information Technology Research in the Interest of Society (CITRIS) at University of California, Berkeley.

References:

Abdel-Ghaffar, A.M., and Scanlan, R.H. (1985), "Ambient Vibration Studies of Golden Gate Bridge: I Suspended Structure," *Journal of Engineering Mechanics*, **111**(4), 463-482.

Chung, H.-C., Enomoto, T., Shinozuka, M., Chou, P., Park, C., Yokoi, I. and Morishita, S. (2004), "Real Time Visualization of Structural Response With Wireless MEMS Sensors," Proceedings of 13th World Conference on Earthquake Engineering, Paper No. 121, Vancouver, BC, Canada.

Franklin, M.J., Hellerstein, J.M., and Madden, S. (2007). "Thinking Big About Tiny Databases," *Bulletin of the IEEE Computer Society Technical Committee on Data Engineering.*

Glaser, S.D., Liu, H., Wang, M.L., Ou, J. (2007), "Sensor Technology Innovation for the Advancement of Structural Health Monitoring: A Strategic Program of US-China Research For The Next Decade," *Smart Structures and Systems*, **3**(2), 221-244.

Hill, J., Szewczyk, R., Woo, A., Hollar, S., Culler, D.E., and Pister, K.S.J. (2000), "System Architecture Directions for Networked Sensors," Proceedings, Ninth International Conference on Architectural Support for Programming Languages and Operating Systems, Cambridge, MA, 93-104.

Kim, S., Pakzad, S.N., Culler, D., Demmel, J., Fenves, G.L., Glaser, S., and Turon, M. (2007). "Health Monitoring of Civil Infrastructures Using Wireless Sensor Networks," Proceedings of the 6th International Conference on Information Processing in Sensor Networks (IPSN 2007), Cambridge, MA.

Lynch, J. P. and Loh, K. J. (2006), "A Summary Review of Wireless Sensors and Sensor Networks for Structural Health Monitoring," *Shock and Vibration*, **38**(2), 91-128.

Maróti, M., Kusy, B., Simon, G., and Lédeczi, Á. (2004), "The Flooding Time Synchronization Protocol," Proceedings of ACM Second International Conference on Embedded Networked Sensor Systems (SenSys 2004), Baltimore, MD, 39-49.

Mastroleon, L., Kiremidjian, A. S., Carryerb, E., and Law, K. H. (2004), "Design of A New Power-Efficient Wireless Sensor System for Structural Health Monitoring," SPIE, **5395**, 51-60.

Ou, J. P., Li, H. W., Xiao, Y. Q. M. and Li, Q. S. (2005), "Health Dynamic Measurement of Tall Building Using Wireless Sensor Network," SPIE, **5765**, 205-216.

Pakzad, S.N, Fenves, G.L., Kim, S., Culler, D.E., and Demmel, J. (2008), "Design and Implementation OF Scalable Wireless Sensor Network for Structural Monitoring," *Journal of Infrastructure Systems*, in press.

Pakzad, S.N., and Fenves, G.L. (2008) "Statistical Analysis of Vibration Properties of a Suspension Bridge Using Spatially Dense Wireless Sensor Network," under preparation.

Pappa, R.S., Elliott, K.B. and Schenck, A. (1993), "Consistent Mode Indicator for Eigen System Realization Algorithm," *Journal of Guidance, Control and Dynamics; **16(5)**:852–858.*

Spencer, B.F., Ruiz-Sandoval, M.E., Kurata, N. (2004). "Smart Sensing Technology: Opportunities and Challenges," *Journal of Structural Control and Health Monitoring.*

Stahl, F.L., Mohn, D.E., and Currie, M.C. (2007), *The Golden Gate Bridge, Report of the Chief Engineer, Volume II*, Ch. 7, 156-158.

Woo, A., Tong, T., and Culler, D. (2003), "Taming the Underlying Challenges of Reliable Multi-hop Routing in Sensor Networks," Proceedings of ACM First International Conference on Embedded Networked Sensor Systems (SenSys 2003), Los Angeles, CA.

Fifth International Conference on Urban Earthquake Engineering
March 4-5, 2008, Tokyo Institute of Technology, Tokyo, Japan

NEW DEVELOPMENTS OF STRONG MOTION PREDICTION LEARNING FROM RECENT DISASTROUS EARTHQUAKES

Kojiro Irikura[1], and Susumu Kurahashi[2]

1) Adjunct Professor, Aichi Institute of Technology, Japan
2) PhD candidate, Aichi Institute of Technology
irikura@geor.or.jp, g05801@aitech.ac.jp

Abstract: Strong motion prediction has been progressed for promoting earthquake countermeasures learning from severe disasters of the 1995 Kobe earthquake. "National Seismic Hazard Map" has been made as one of national projects integrating all fields of earthquake researches such as active fault, earthquake forecast and strong motion prediction studies after the Kobe earthquake. Ground motions from earthquakes caused to specified source faults are evaluated based on "recipe". Verification and applicability have been examined by comparing observed ground motions with synthesized ones estimated using the "recipe". The 2007 Chuetsu-oki earthquake happened very close to the Kasiwazaki-Kariwa Nuclear Power Plant. The active faults caused to the earthquake have not been specified for the aseismic design of the plant. Ground motions from the earthquake are found to be predictable as long as the source fault is specified through investigation of active folds and faults. Further improvements of the fault modeling are required to make more reliable evaluation of ground motions for earthquake safety designs.

1. INTRODUCTION

Importance of strong motion prediction has been widely recognized for promoting earthquake-counter measures as one of the lessons of the 1995 Kobe earthquake. The Headquarter of Earthquake Research Promotion established just after the earthquake have developed "National Seismic Hazard Maps" (Earthquake Research Committee 2005). It should be more precisely called to be "Maps of Strong Motion Prediction in Japan". The maps show results of prediction of strong ground motions from two different approaches, probabilistic and deterministic, integrating survey of active faults, long-term evaluation for earthquake activities, and evaluation of strong ground motion. The probabilistic hazard maps show the probability of ground motion larger than seismic intensity 6-lower, occurring within 30 years from the present. On the other hand, the deterministic hazard maps show the levels of ground motions from earthquakes caused to specific active faults, based on fault models obtained from the active fault information.

The procedures of fault modeling for the prediction of strong ground motion are proposed as a recipe combining the active fault information with scaling relations of fault parameters from the waveform inversion of source processes using strong ground motions. This technique is introduced to the "Regulatory Guide for Aseismic Design of Nuclear Power Reactor Facilities" revised in 2006 by the Nuclear Safety Commission of Japan.

The 2007 Niigata-ken Chuetsu-oki happened very close to the Kasiwazaki-Kariwa Nuclear Power Plant that has the largest electric output in the world. It triggered a fire at an electrical transformer and other problems in the Plant. However, no problems have been confirmed with regard to the safety of the nuclear reactors as four of the plant's seven reactors running at the time of the earthquake were all shut down automatically by a safety mechanism according to the reports by the International Atomic Energy Agency (IAEA 2007) as well as the Nuclear and Industrial Safety Agency in Japan (NISA 2007).

There was recorded ground acceleration of 680 gals on the base mat of Unit No.1 reactor, 2.5 times more than the ground motion levels for aseismic design of facilities. The active faults caused to the earthquake have not been specified in evaluating input ground motions for the aseismic design. We need to make careful examinations why the active faults have been missed and how the ground motions have been underestimated.

In this report, we outline strong motion prediction for active faults, verification of recipe for strong motion prediction for recent disastrous earthquakes, e.g. simulations of the 2007 Chuetsu-oki earthquake and some other earthquakes, and prospect of strong motion prediction for promoting earthquake-counter measures, and overviews of strong motion predictions.

2. OUTLINE OF STRONG MOTION PREDICTION

We have understood that strong ground motions are related to slip heterogeneity inside the source rather than average slip in the entire rupture area from recent studies of rupture process using strong motion data during large earthquakes. Asperities are characterized as regions that have a large slip relative to the average slip in the rupture area, based on heterogeneous slip distributions that are estimated from the waveform inversion (Somerville et al. 1999). We also found that strong motion generation areas coincide approximately with asperity areas, where a lot of stress is released (Miyake et al. 2001, Miyake et al. 2003). The asperity areas as well as the entire rupture areas scale with total seismic moments.

2.1 Scaling Relationships of Fault Parameters

One of the most important ideas for strong motion prediction is the scaling relationships of fault parameters. The conventional scaling relations of fault parameters such as rupture area and average slip on fault with seismic moment are mostly determined geologically from surface offsets and geophysically from forward source modeling using teleseismic data and geodetic data (e.g. Kanamori and Anderson 1975). Those fault parameters are only available for simulating very long period motions, but are not sufficiently available for near-source strong motions dominating short period motions of less than 1 sec of engineering interest.

We found new scaling relations of the asperity areas, as well as entire rupture areas, with respect to total seismic moment from the results of the waveform inversion mentioned above. Therefore, there are two kinds of the scaling relationships. One is the conventional scaling relations such as rupture area versus seismic moment and fault slip versus seismic moment. The other is the new ones such as asperity area versus seismic moment and asperity slip versus seismic moment. Based on the two kinds of scaling relationships for the entire rupture area and the asperity areas with respect to the total seismic moment, the source model for predicting strong ground motions is characterized by three parameters: outer, inner, and extra fault parameters.

The scaling for the outer fault parameters, i.e. relationship between seismic moment and rupture area, for inland crustal earthquakes are summarized as shown in Fig. 1 (Irikura 2004). For earthquakes with relatively small seismic moment less than 10^{19} Nm, the total fault area S seems to follow the self-similar scaling relation with constant static stress drop in proportion to the two-thirds power of seismic moment M0. For large earthquakes more than 10^{19} Nm, the scaling tends to depart from self-similar model (Irikura and Miyake 2001) corresponding to the saturation of fault width due to the seismogenic zone size. Further, one more stage should be added for extra large earthquakes more than 10^{21} Nm from the idea of Scholtz (2002) as changing from L-model into W-model. The scaling relationships in this study as shown by broken lines in Fig. 1 are drawn assuming the fault width saturates with 20 km long.

The inner fault parameters are introduced in this study as the combined area of asperities and stress drop of each asperity that define slip heterogeneity inside the source fault and that have much more influence on strong ground motions than the outer fault parameters. The relationships between rupture area S as the outer fault parameter and combined area of asperities S_a as the inner fault parameter are shown in Fig. 2 (Irikura 2004). The ratio S_a / S seems to be almost constant regardless of the rupture area, about 0.22 for the inland earthquake.

Then, stress drop on the asperities $\Delta\sigma_a$ is derived as a product of the average stress drop over the fault $\Delta\bar{\sigma}_c$ and the ratio of asperity area S_a to total rupture area S (e.g., Madariaga 1979).

$$\Delta\sigma_a = \Delta\bar{\sigma}_c \cdot S/S_a \tag{1}$$

Another empirical-relationship between seismic moment Mo and flat level of acceleration source spectrum A_o related to the inner source parameters is shown in Fig. 3, initially found by Dan et al. (2001) and confirmed by other authors (Morikawa and Fujiwara 2003, Satoh 2004).

$$A_0 = 2.46 \cdot 10^{17} \cdot (M_0 \cdot 10^7)^{1/3} \tag{2}$$

where the unit of M_0 is $N \cdot m$.

The acceleration level A_0^a generated from the asperities is theoretically proportional to the square root of the combined areas of asperities S_a and the stress drop in the asperities $\Delta\sigma_a$ by Madariaga (1977). A_0^a is replaced by acceleration level from theoretical level A_0 from the total criteria because short-period motions mostly are mostly generated from the asperities.

$$A_0^a = 4\sqrt{\pi}\beta v_r \Delta\sigma_a \sqrt{S_a} \tag{3}$$

where β and v_r are S wave velocity of the media and rupture velocity.

Then, S_a is estimated as follows.

$$S_a = \left(\frac{7\pi^2}{4}\beta v_r\right)^2 \cdot \frac{(M_0)^2}{S \cdot (A_0)^2} \tag{4}$$

In this case the stress drop of the asperities $\Delta\sigma_a$ is also given as a product of $\Delta\bar{\sigma}_c$ and S/S_a using (1).

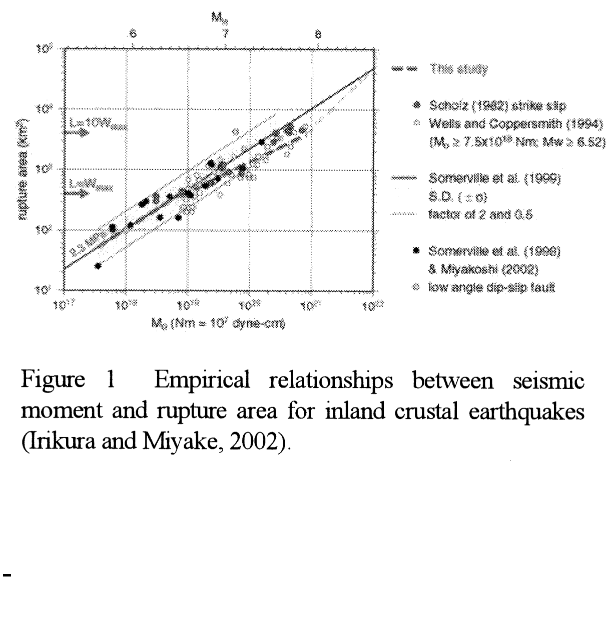

Figure 1 Empirical relationships between seismic moment and rupture area for inland crustal earthquakes (Irikura and Miyake, 2002).

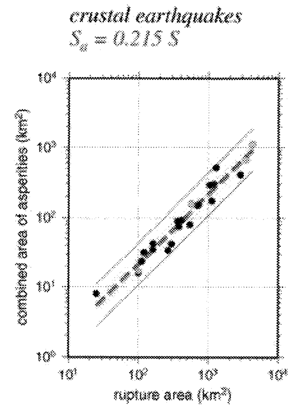

Figure 2 Empirical relationships between combined area of asperities and total rupture area (thick broken line) for inland crustal earthquakes (Irikura and Miyake, 2002). Shadow ranges (standard deviation). Thin solid lines show a factor of 2 and 1/2 for the average. Database obtained by the waveform inversions for the inland crustal earthquakes is Somerville et al. (1999) and Miyakoshi (2002)

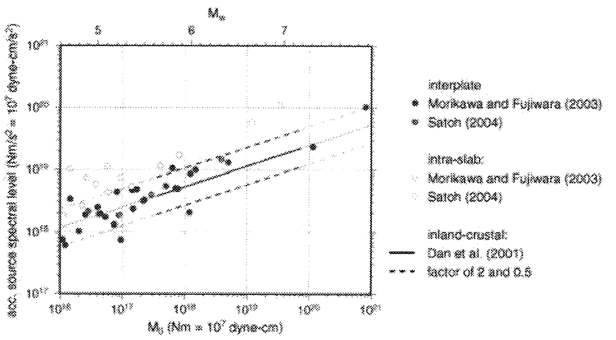

Figure 3 Empirical relationship between seismic moment and acceleration source spectral level for inland crustal earthquakes.

2.2 Recipe for Source Modeling

Strong motions for large earthquakes are simulated, based on characterized source models defined by three kinds of parameters, outer, inner, and extra fault parameters. We developed a "recipe" for predicting strong ground motions (Irikura and Miyake 2001, Irikura 2004) to characterize those fault parameters of source modeling for future large earthquakes.

The source model is constructed by the following procedure. First, the outer fault parameters are given as follows. Step 1: Total Rupture Area ($S = LW$) is given from investigations of active faults. Step 2: Total Seismic Moment (M_0) is given from the empirical scaling relation, M_0 versus S. Step 3: Average Stress Drop ($\Delta\overline{\sigma}_c$) on the source fault is estimated from the theoretical equation for circular crack model by Eshelby (1957) at the first stage of Fig. 1 (Mo < 10^{19} Nm) and another equation by Fujii and Matsu'ura (2000) at the second and third stages of Fig. 1.

Second, the inner fault parameters are given to characterize stress heterogeneity inside the fault area. Step 4: Combined Area of Asperities (S_a) is estimated from the acceleration source spectral level based on the empirical relation such as (2) or observed records. Step 5: Stress Drop on Asperities ($\Delta\sigma_a$) is derived as a product of $\Delta\overline{\sigma}_c$ as the outer fault parameter and S_a/S from Step 4. Step 6: Number of Asperities (N) is related to the segmentation of the active faults, e.g. two per a segment. Step 7: Average Slip on Asperities (D_a) given as $2.0 \cdot D$ based on the empirical relationship by Somerville et al. (1999). Step 8: Effective Stress on Asperity (σ_α) and Background Slip Areas (σ_β) is considered to be identical to stress drop on asperity $\Delta\sigma_\alpha$. Step 9: Parameterization of Slip-Velocity Time Functions is given to be the Kostrov-like slip-velocity time functions as a function of peak slip-velocity and rise time based on the results of dynamic simulation by Day (1982). The peak slip-velocity is given as a function of effective stress, rupture velocity and f_{max}.

The extra fault parameters are the rupture starting point and rupture velocity to characterize the rupture propagating pattern in the fault plane. For inland crustal earthquakes, rupture nucleation and termination are related to geomorphology of active faults (e.g., Nakata et al. 1998, Kame and Yamashita 2003).

3. APPLICABILITY OF STRONG MOTION PREDICTION RECIPE

Strong motions for large earthquakes are simulated, based on characterized source models defined by three kinds of parameters, outer, inner, and extra fault parameters. Those fault parameters are defined by the "recipe" of strong motion prediction. This "recipe" has been applying to deterministic seismic-hazard maps for specified seismic source faults with high probability of occurrence potential in the National Seismic Hazard Maps for Japan (2005). The availability of the "recipe" has been tested in each application by the comparison between PGV's of the synthesized motions and those derived from empirical attenuation relationship by Si and Midorikawa (1999). More detailed examination for strong motion prediction should be made, comparing simulated ground motions with observed ones for recent disastrous earthquakes.

3.1 Simulation of Ground Motions for the 2007 Niigata-ken Chuetsu-oki Earthquake (Mw=6.6)

This earthquake occurred on July 16, 2007, northwest off Kashiwazaki in Niigata Prefecture, Japan, causing severe damage such as ten people dead, about 1300 injured, about 1000 collapsed houses and major lifelines suspended to near-source region. In particular, strong ground motions from the earthquake struck the Kashiwazaki-Kariwa nuclear power plant (hereafter KKNPP), triggering a fire at an electric transformer and other problems such as leakage of water containing radioactive materials into air and the sea, although the radioactivity levels of the releases are as low as those of the radiation of the natural environment in a year.

We attempt to simulate strong ground motions during the 2007 Chuetsu-oki earthquake based on the characterized source model. It is to examine the predictability of the ground motions with specified source model given by the "recipe".

The source mechanism of this earthquake is supposed to be a reverse fault with the SW-NE strike and SE dip from the aftershock distribution re-determined using the OBS seismometers (ERI, Univ. of Tokyo 2008) as shown in Fig. 4. Results of the rupture processes inverted by using strong motion data show the source fault with the SW-NE strike and SE dip gives slip distribution to match well observed data (Hikima and Koketsu 2007).

The PGA attenuation-distance relationships in Fig. 5 generally follow the empirical relations in Japan obtained by Si and Midorikawa (1999) except the KKNPP. The strong ground motions in the site of the KKNPP had markedly large accelerations more than those expected from the empirical relations. The surface motions there had the PGA of more than 1200 gals and even underground motions on one of the base-mats of the reactors locating five stories below the ground had the PGS of 680 gals. The PGA's recorded at underground rock sites of the KKNPP are significantly larger than those expected from the empirical relationship by Fukushima and Tanaka (1990).

The observed records close to the mainshock had two or three distinctive pulses, in particular, three significant pulses at stations on the base-mats of the Nuclear Reactors of the KKNPP site. We estimated the locations of asperities using time differences between those pulses. We found that three asperities are located south-west and south of the hypocenter in Fig. 6. In this study, we called those asperities to be ASP1, ASP2 and ASP3. We chose appropriate records of aftershocks as the empirical Green's function, taking into account locations and fault mechanisms of the aftershocks. As a result, we adopted the record of Aftershock 1 on July 16 at 21:08 for ASP 1 and ASP2, and Aftershock 2 on August 4 at 0:16 for ASP3. Table 1 shows the source information about the mainshock and aftershocks and Table 2 shows the parameters of the fault plane used in this study.

We obtained the best-fit model by forward modeling to minimize the residuals between the observed and synthesized. The areas of three asperities were about 30 km^2 and stress drop were 20 – 24 MPa that are summarized in Table 3. The synthesized motions at KKZ1R2, KKZ5R2, NIG005 and NIG018 are compared with the observed ones in Fig. 7. The synthesized waveforms agree with the observed ones fairly well. In particular, three pulses appearing in the observed records at KKZ1R2 and KKZ5R2 located at B5F in underground of Unit 1 and Unit 5, respectively, are well reproduced in the synthesized velocity and displacement.

Table 1 The information of the mainshock and aftershocks used as the empirical Green's function.

	Mainshock	Aftershock(AFT1)	Aftershock(AFT2)
Origin time	07/07/16 10:13	07/07/16 21:08	07/08/04 00:16
Hypocenter	37.557, 138.609	37.509, 138.630	37.420, 138.537
Depth	12km	15.6km	13.1km
Mw	6.6	4.4	-
Mo	8.37E+16Nm	5.21E+16Nm	1.56E+14Nm

Table 2 The fault plane of the mainshock. The strike and dip were used from aftershock distributions by ERI, Univ. of Tokyo.

strike	dip	rake	Latitude	Longitude	depth
30	40	90	37.343	138.392	6.2km

Table 3 Source parameters for each asperity.

	Rupture start point	Depth (km)	Mo (Nm)
ASP1	(4,3)	12.3	1.69×10^{18}
ASP2	(5,5)	11.0	1.69×10^{18}
ASP3	(4,7)	12.0	1.02×10^{18}
	L (km) × W (km)	$\Delta\sigma$ (MPa)	Risetime (second)
ASP1	5.5×5.5 (N:5×5)	23.7	0.5
ASP2	5.5×5.5 (N:5×5)	23.7	0.5
ASP3	5.04×5.04 (N:9×9)	19.8	0.45

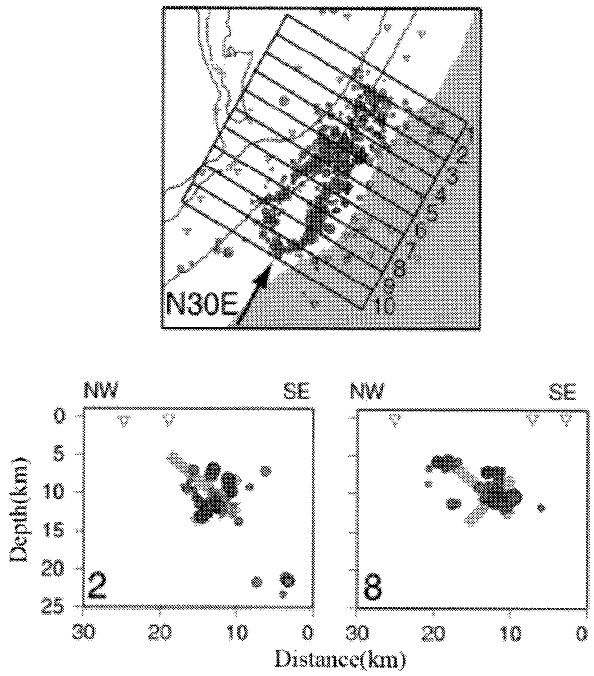

Figure 4 Aftershock distributions in the horizontal plane (upper) and cross section perpendicular to the strike (lower) using the OBS seismometers (ERI, Univ. of Tokyo,2008).

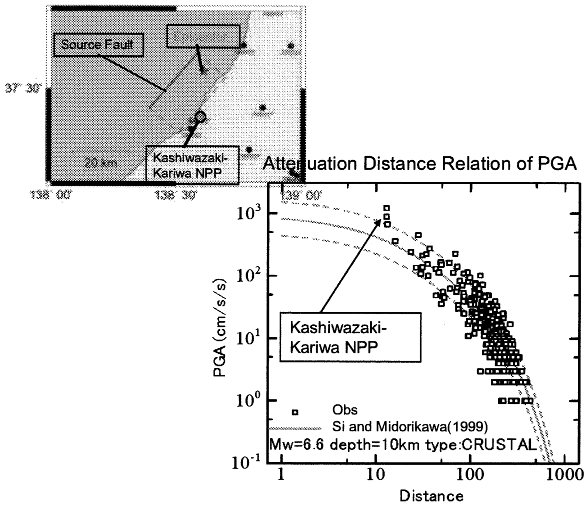

Figure 5 Upper: Map showing source fault by Horikawa (2007) and observation sites. Lower: Relationship of observed peak horizontal ground accelerations versus shortest distances to source fault (lower). Red solid and dotted curves show the empirical PGA attenuation distance relationship for surface data by Si and Midorikawa (1999) and its standard deviation

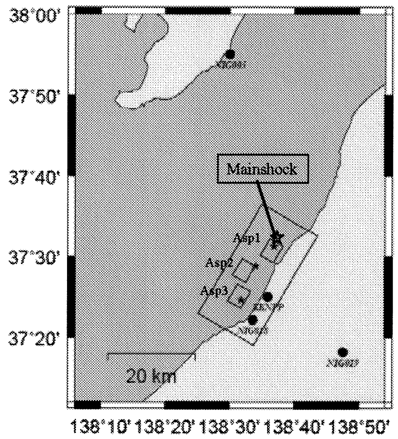

Figure 6 Map showing source model (rectangular) consisting of three asperities (Asp1, Asp2 and Asp3) in this study and the locations of K-net stations and KKNPP (circle) and the epicenter of the mainshock (red star).

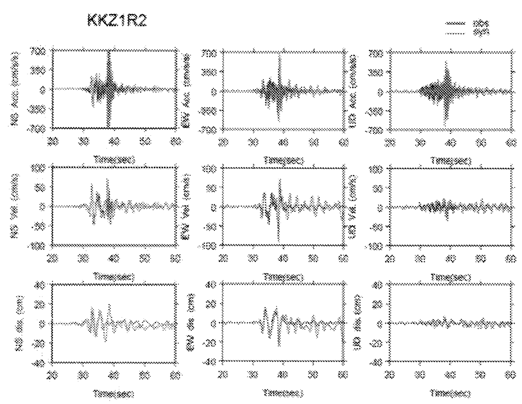

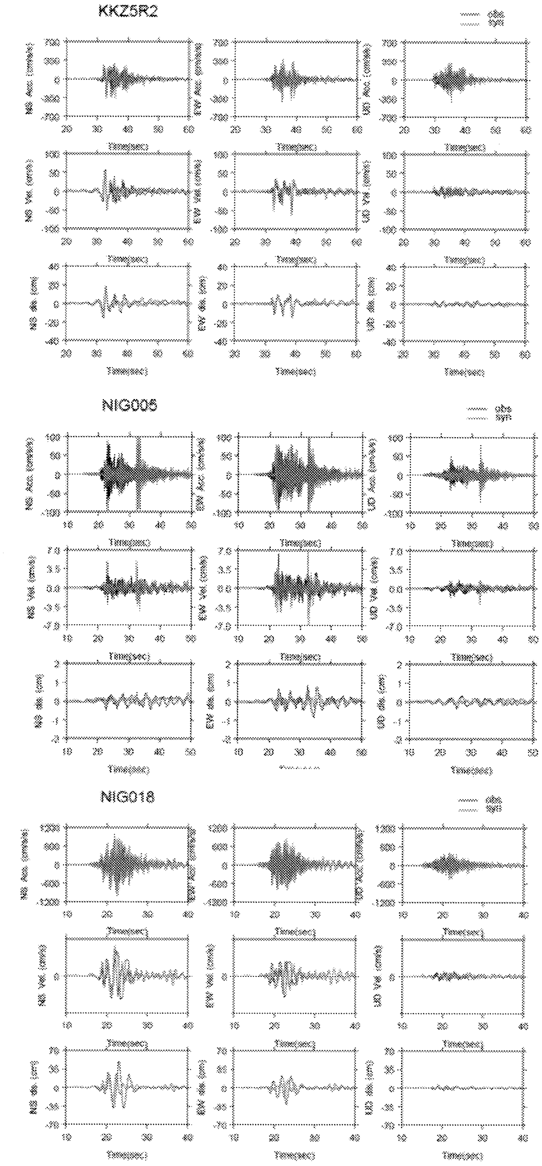

Figure 7 Comparison between the observed records (black) and synthesized motions (red). Acceleration (top), velocity (middle) and displacement (bottom) are shown at KKZ1R2, KKZ5R2, NIG005 and NIG018.

3.2 Verification of the "Recipe" for Recent Disastrous Earthquakes

We introduce two more examples, one is the 2007 Noto Hanto earthquake and the 2005 Fukuoka-ken Seiho-oki earthquake.

The 2007 Noto-Hanto earthquake (Mw=6.7) on March 25, 2007 occurred west off the Noto peninsula, Japan in Fig. 8. Strong ground motions with the JMA seismic intensity of 6-upper struck Wajima, Anamizu, and Nanao in the northern part of the Noto peninsula. The PGA's of this earthquake with shortest fault distance seem to be a little larger than the empirical attenuation-distance relationships by Si and Midorikawa (1999) as shown in Fig. 9.

The source slip model of the 2005 Noto Hanto earthquake was determined from the inversion of strong ground motion records by Horikawa (2007). His result is not always available for strong motion simulation because the inversion is done using only long-period motions more than 1 sec. The characterized source model with asperities inside the rupture area is needed to simulate broadband motions including short-period motions less than 1 sec. for accurate estimation of seismic intensity interest. The asperities are defined as rectangular regions where the slip exceeds in the same specified manner as Somerville et al. (1999). Resultant source model is shown in the left of Fig. 10. For comparison, we made a source model following the "recipe" as shown in the middle of Fig. 10, where the asperity area and stress parameters are estimated from the acceleration source spectral-level of observed data.

Further, we made a source model by forward modeling, comparing between the observed records and synthesized motions based on the characterized source model using the empirical Green's function method. The best-fit source model consists of two asperities with different size shown in Fig. 10. A large one is located just above the hypocenter with an area of 6.3 x 6.3 km^2 and stress drop of about 26 MPa. A smaller one is located north-east of the large one with an area of 3.6 x 3.6 km^2 and stress drop of about 10 MPa. The stress drops of the asperities are about two times higher than average values of inland crustal earthquakes so far estimated.

The outer and inner fault parameters of those three source models (waveform inversion, recipe and forward modeling) are summarized in Table 4 and 5, respectively. The stress drop of the asperity estimated from the waveform inversion is almost the same as those from the recipe. However, the asperities by the forward modeling have a little larger stress drop (ASP1:26MPa) than the empirical ones. This result is consistent with lager acceleration than the empirical attenuation distance relation in Fig. 9.

Observed motions at ISK001 and ISK003 are compared with synthesized motions for those three source models in Fig. 11. The synthesized waveforms for any models almost agree with the observed ones. Of course, the forward modeling gave the synthesized motions best-fit to the observed.

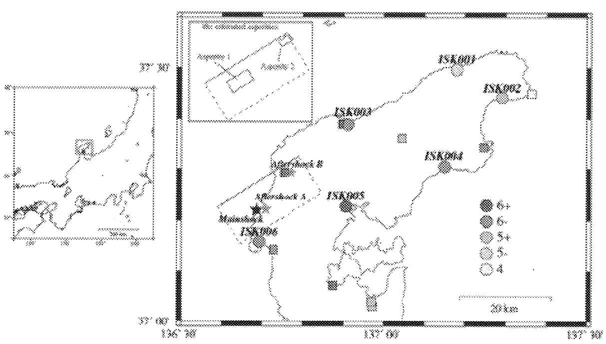

Figure 8 Map showing source fault of 2007 Noto Hanto earthquake (rectangular), the locations of stations used for analysis (circle), the other stations (square) and epicenter of the mainshock (star).

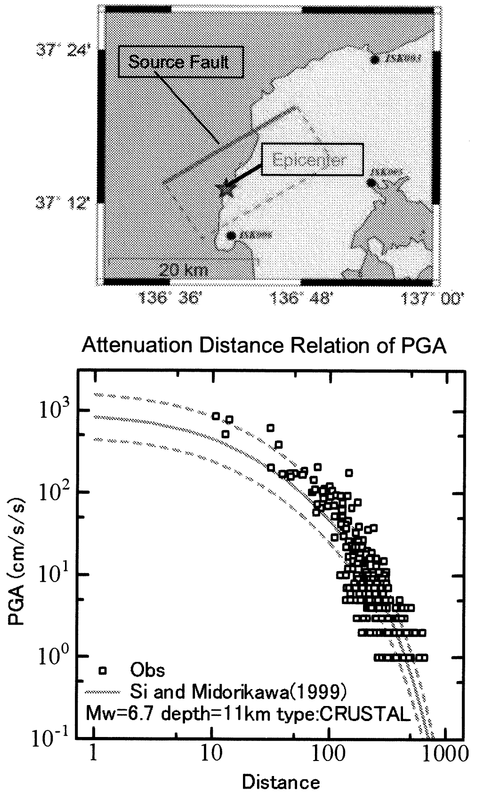

Figure 9 Upper: Map showing source fault by Horikawa (2007). Lower: Relationship of observed peak horizontal ground accelerations versus shortest distances to the source fault. Red solid and dotted curves show the empirical PGA attenuation distance relationship for surface data by Si and Midorikawa (1999) and its standard deviation (lower).

Table 4 Source parameters for slip model of the Noto-hanto earthquake estimated with the wave inversion using strong ground motions by Horikawa (2007).

Strike	Dip	Length	Width	Area
58	60	22km	20km	440km^2
Seismic Moment			Static Stress Drop	
1.08E+19 Nm			2.84 MPa	

Table 5 Source parameters for the characterized source model by three models.

	Waveform Inversion	Recipe	Forward Modeling
Total Area S (km^2)	90	90.6	52.65
Sa/S	20.45	20.59	11.97
Source Radius (km)	5.35	5.37	4.09
Seismic Moment (Nm)	4.41E+18	4.43E+18	2.90E+18
Stress Drop (MPa)	13.9	13.8	ASP1 : 26 ASP2 : 10

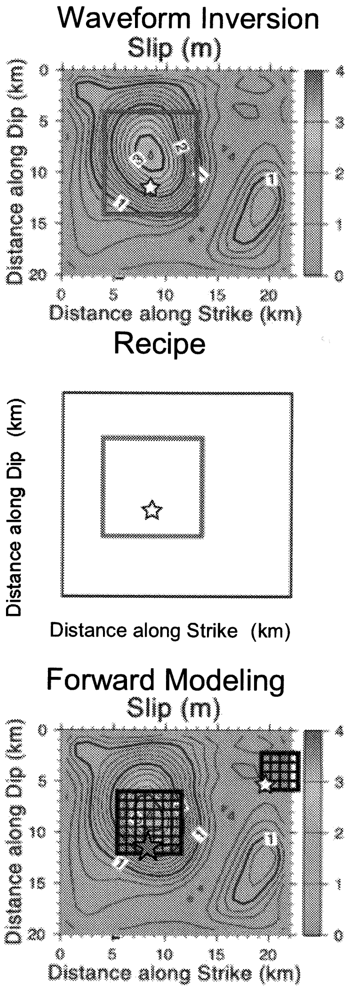

Figure 10 Characterized source models with asperities inside the rupture area. Upper is a model by waveform inversion result, Middle is that by recipe, and Bottom is that by forward modeling.

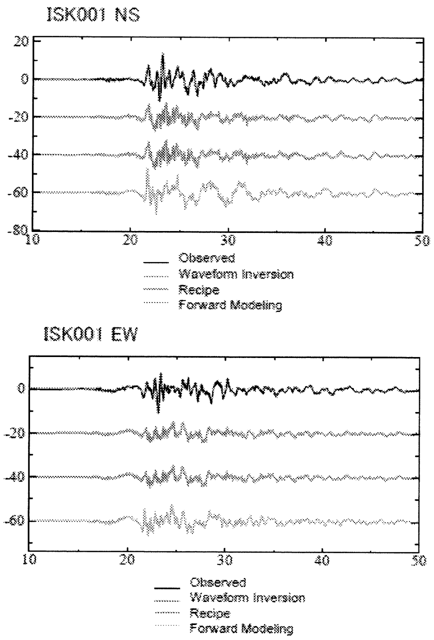

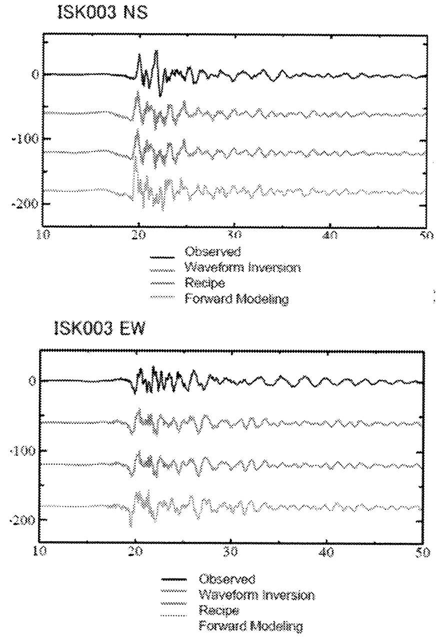

Figure 11 Comparison between observed records and synthesized motions for three source models by waveform inversion, recipe, and forward modeling at ISK001 and ISK003.

The 2005 Fukuoka-ken Seiho-oki earthquake (Mw=6.6) on March 20, 2005 occurred west off the Fukuoka peninsula, Japan. The fault plane projected to surface and observation sites are shown in Fig. 12. The source slip model of this earthquake was determined from the inversion of strong ground motion records by several authors (e.g. Kobayashi et al. 2006, Sekiguchi et al. 2006, Asano et al. 2006, and so on). The slip distribution on the fault plane is roughly similar each other, although there are some differences depending on frequency ranges of the data, smoothing techniques used there and etc. Even if the inverted source model is almost uniquely determined, it is not always available for strong motion simulation. Those inversions were done using only long-period motions more than 1 sec.

Verification of estimating strong ground motions for this earthquake based on "recipe" was made by Earthquake Research Committee (2007). We describe the outline of the verification mentioned above.

The characterized source model with asperities inside the rupture area is needed to simulate broadband motions including short-period motions less than 1 sec. for accurate estimation of seismic intensity interest. The asperities are defined as rectangular regions where the slip exceeds in the same specified manner as Somerville et al. (1999).

Three source models, Case 1, 2, and 3 are made for slip models inverted from strong motion data by Kobayashi et al. (2006), Sekiguchi et al. (2006), Asano et al. (2006) as shown in Fig. 13 (Strong Motion Evaluation Committee 2007). Another source model Case 4 is added following the "recipe". The locations of those three asperities are set referring the results from the other inverted models. The combined areas of asperities and the stress parameters for the inverted source models are 48 ~ 64 km^2 and 20 ~26 MPa, while those of the recipe model are 80 km^2 and 16 MPa, respectively. That is, in the recipe model the asperity is a little wider and the stress parameter is somewhat small.

The synthesized motions are calculated using a hybrid method (Irikura and Kamae 1999) with the crossover period of 1 sec, summing up longer period motions with a theoretical procedure and shorter period motions with the stochastic Green's function method. Synthesized velocity waveforms at engineering bed rock are compared with the observed ones at 10 sites in Fig. 14. We found that the synthesized motions agree well with the observe records, although the synthesized ones at some sites are a little smaller because the effects of surface geology are not considered.

We compiled the relationship between the combined areas of the asperities and total seismic moments for earthquakes so far analyzed in Fig. 15. The recent disastrous earthquakes introduced here almost follow the empirical relationship so far reported. Speaking more detailed, the asperity areas of the 2007 Noto Hanto earthquakes have a little smaller than those of the 2007 Chuetsu-oki earthquake, resultantly related to higher stress parameters on asperities and larger accelerations.

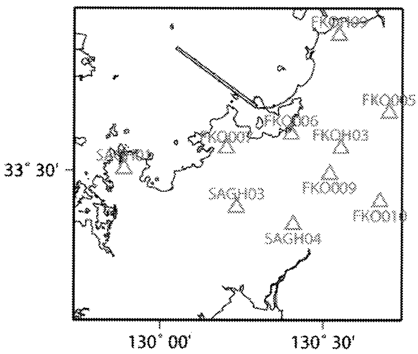

Figure 12 Map showing fault plane (rectangular) and the location of stations used for analysis (triangles).

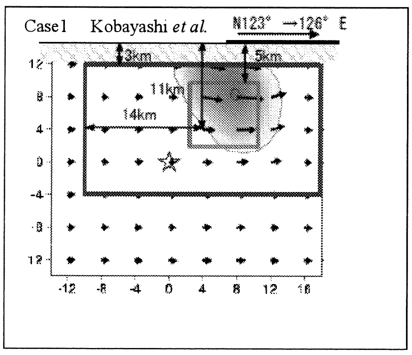

Figure 13 Four characterized source models (Case 1, Case 2, Case 3, Case 4) with asperities inside rupture area. Case 1 to 3 are from inversion results by Kobayashi et al. (2006), Asano et al. (2006), and Sekiguchi et al. (2006), respectively.

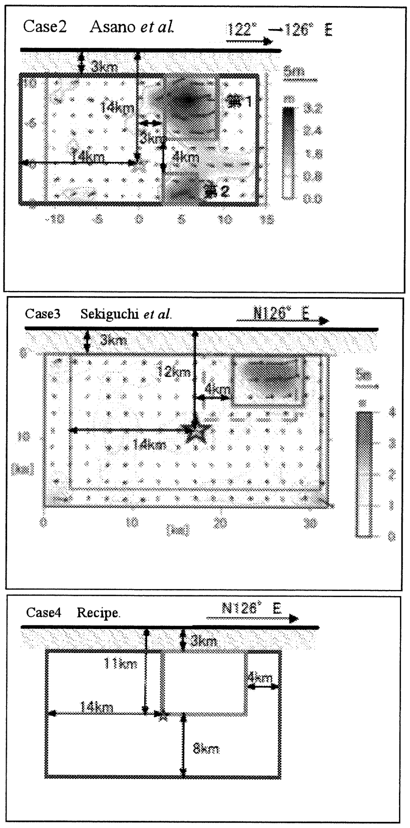

Figure 13 Continued.

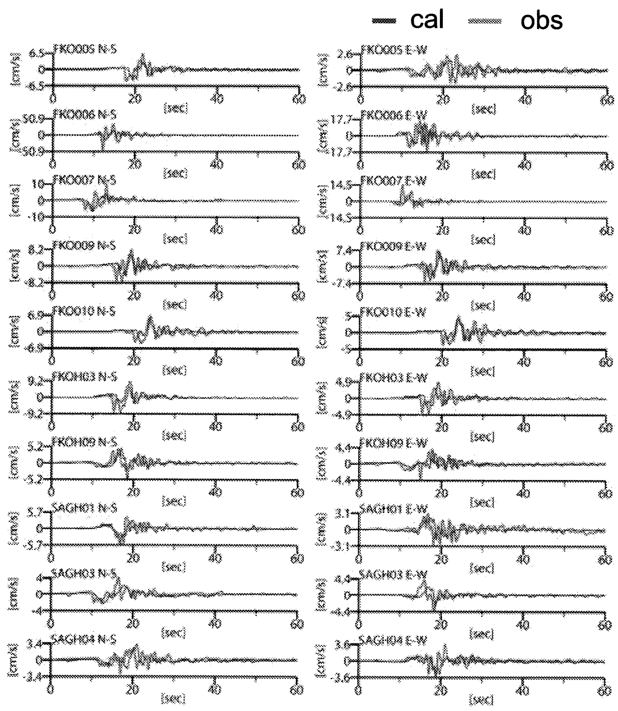

Figure 14 Comparison between observed records (red) and synthesized motions by a hybrid method (blue) at 10 stations.

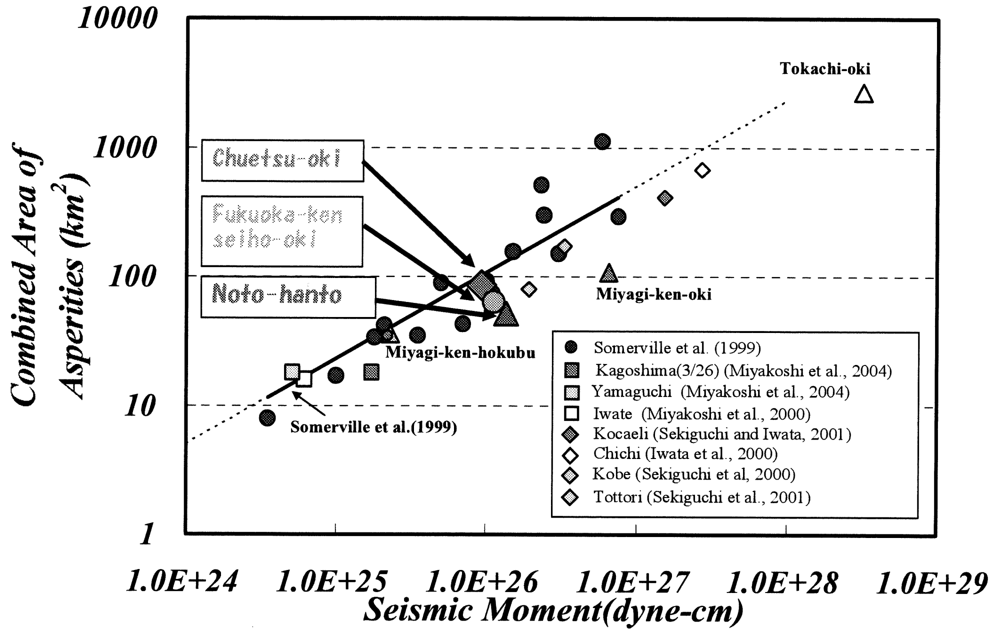

Figure 15 Relationship between combined areas of asperities and total seismic moments for earthquakes.

4. OVERVIEWS OF STRONG MOTION PREDICTIONS

One of the problems with strong motion maps is that recent disastrous earthquakes have occurred in regions where probability of ground motions is relatively small, for example, 2000 Tottori-ken Seibu earthquake, 2004 Chuetsu earthquake, 2005 Fukuoka-ken Seiho-oki earthquake, 2007 Noto-hanto earthquake, 2007 Chuetsu-oki earthquake. Therefore, the maps by themselves are not always responsible for people who expect seismologists and earthquake engineers to reduce earthquake damage for future large earthquakes.

These earthquakes are caused to inland and offshore active folds and faults. A reason is that high shaking areas in probabilistic sense are related to mainly subduction earthquakes, because probability of earthquake occurrence on inland active folds and faults are one order smaller than inland crustal earthquakes. It comes from lack of data for so far for active fault information on offshore. The Headquater of Earthquake Research Promotion has made evaluation of long-term earthquake predictions only for active faults and fault systems on land, but not on offshore. They have not systematically surveyed active tectonics on offshore. We need to promote such seismo-tectonics studies in offshore regions, source modeling for active folds as well as active fault systems, and strong motion predictions for potential earthquakes.

Another problem is associated with earthquake safety of important structure, in particular nuclear power plants.

The two earthquakes, 2007 Noto-hanto and 2007 Chuetsu-oki earthquakes happened very close to the Nuclear Power Plants and stroke extremely strong ground motions more than the levels accounted for in the aseismic design of the plants. In particular, ground motions from the Chetsu-oki earthquake exceeded 2.5 times of the design level. Although the level of the seismic input in the design of the plant was exceeded during the earthquake, "there is no visible significant damage because of the conservatisms introduced at different stages of the design process" as the IAEE report says. They also indicated that "a re-evaluation of the seismic safety for Kashiwazaki-Kariwa plant needs to be done with account taken of the lessons learned from the Chuetsu-oki earthquake and using updated criteria and methods." The re-evaluation of the seismic safety should also be done for all of other nuclear power plant in Japan. Detailed geo-morphological, geological, and geophysical investigations have to be made both on land and offshore for defining seismic input motions following revised regulatory guide fro aseismic design of nuclear power plants issued in September 2006. We have not to miss any earthquakes that jeopardize the safety of plants, investigating the potential existence of active faults near plants. To do that, it is necessary to establish methodology of reliable prediction of strong ground motions for earthquakes occurring underneath sites where active faults have not been specified.

Acknowledgements:

We appreciate National Research Institute for Earth Science and Disaster Prevention (NIED) for providing the K-NET, KiK-net and F-net data. We also thank to Tokyo Electric Power Company (TEPCO) for providing strong ground motion data at the Kashiwazaki-Kariwa nuclear power plant.

References:

Asano, K. and Iwata, T. (2006), "Source process and near-source ground motions of the 2005 West Off Fukuoka Prefecture earthquake," *Earth Planets Space,* **58** (1), pp. 93-98.

Dan, K., Watanabe, T., Sato, T. and Ishii, T. (2001), "Short-period source spectra inferred from variable-slip rupture models and modeling of earthquake fault for strong motion prediction," *Journal of Struct. Constr. Engng. AIJ,* **545**, pp. 51-62.

Day, S. M. (1982), "Three-dimensional simulation of spontaneous rupture: the effect of nonuniform prestress," *Bull. Seism. Soc. Am.,* **88**, pp. 512-522.

Earthquake Research Committee (2005), Report: 'National Seismic Hazard Map for Japan (2005), *MEXT, http://www.jishin.go.jp/ main/ index-e.html* .

Strong Motion Evaluation Research Committee (2007), "Verification of strong motion evaluation using observed records of the 2005 Fukuoka-ken Seiho-oki Earthquake (in Japanese)", *MEXT, http://www.jishin.go.jp/main/kyoshindo/07mar _fukuoka / index.htm.*

Earthquake Research Institute, Univ. of Tokyo (2008), "The aftershock distribution of 2007 Chuetsu-oki earthquake re-determined using the OBS seismometers," *Report published by Earthquake Research Committee 2008,* (in Japanese).

Eshelby, J. D. (1957), "The determination of the elastic field of an ellipsoidal inclusion, and related problems," *Proc. Roy Soc.,* **A241**, pp. 376-396.

Fujii, Y. and Matsu'ura, M. (2000), "Regional difference in scaling laws for large earthquakes and its tectonic implication," *PAGEOPH,* **157**, pp. 2283-2302.

Fukushima, Y. and Tanaka, T. (1990), "A new attenuation relation for peak horizontal acceleration of strong earthquake ground motion in Japan," *Bull. Seism. Soc. Am.,* **80**, pp. 757-783.

Hikima, K. and Koketsu, K. (2007), "Source process of the 2007 Chuetsu-oki Earthquake Inferred from far field waveforms and strong motions," *Programme and Abstracts for the Seismological Society of Japan, 2007 Fall Meeting,* P1-085, Poster. (in Japanese).

Horikawa, H. (2007), "Source rupture process of 2007 Noto-Hanto Earthquake,"*http://unit.aist.go.jp/actfault/katsudo/jishin/notohan to/hakaikatei2.htm.* (in Japanese).

IAEA (2007), IAEA Mission Report "Preliminary Findings and Lessons Learned from the 16 July 2007 Earthquake at Kashiwazaki-Kariwa NPP" Vol. I., http://www.nisa.meti.go.jp/ english/index.htm.

Irikura, K. (2004), "Recipe for predicting strong ground motion from future large earthquake," *Annuals of Disaster Prevention Research Institute.,* **47A**, pp. 25- 45. (in Japanese).

Irikura, K. and Kamae, K. (1999), "Strong ground motions during the 1948 Fukui earthquake," *Zisin,* **52**, pp. 129-150. (in Japanese with English abstract).

Irikura, K. and Miyake, H. (2001), "Prediction of strong ground motions for scenario earthquakes," *Journal of Geography,* **110**, pp. 849-875 (in Japanese with English abstract).

Irikura, K. and H. Miyake (2002). Source modeling for strong ground motion prediction, *Chikyu, Monthly,* extra issue **37**, 62 - 77 (in Japanese).

Kame, N. and Yamashita, T. (2003), "Dynamic branching, arresting of rupture and the seismic wave radiation in self-chosen crack path modeling," *Geophys. J. Int.,* **155**, pp. 1042-1050.

Kanamori, H. and Anderson, D. L. (1975), "Theoretical basis of some empirical relations in seismology," *Bull. Seism. Soc. Am.,* **86**, pp. 1073-1095.

Kobayashi, R., Miyazaki, S. and Koketsu, K. (2006), "Source processes of the 2005 West Off Fukuoka Prefecture earthquake and its largest aftershock inferred from strong motion and 1-Hz GPS data," *Earth Planets Space,* **58** (1), pp. 57-62.

Madariaga, R. (1977), "High frequency radiation from crack (stress drop) models of earthquake faulting," *Geophys. J. R. Astron. Soc.,* **51**, pp. 625-651.

Madariaga, R. (1979), "On the relation between seismic moment and stress drop in the presence of stress and strength heterogeneity," *J. Geophys. Res.,* **84**, pp. 2243-2250.

Miyake, H., Iwata, T. and Irikura, K. (2001), "Estimation of rupture propagation direction and strong motion generation area from azimuth and distance dependence of source amplitude spectra," *Geophys. Res. Lett.,* **28**, pp. 2727-2730.

Miyake, H., Iwata, T. and Irikura, K. (2003), "Source characterization for broadband ground-motion simulation: Kinematic heterogeneous source model and strong motion generation area," *Bull. Seism. Soc. Am.,* **93**, pp. 2531-2545.

Morikawa, N. and Fujiwara, H. (2003), "Source and path characteristics for off Tokachi-Nemuro earthquakes," *Programme and Abstracts for the Seismological Society of Japan, 2003 Fall Meeting,* **104**. (in Japanese).

Nakata, T., Shimazaki, K., Suzuki, Y. and Tsukuda, E. (1998), "Fault branching and directivity of rupture propagation," *Journal of Geography,* **107**, pp. 512-528. (in Japanese).

NISA (2007), "The Earthquakes in Niigata Prefecture and its Effects on Kashiwazaki-Kariwa Nuclear Power Station, http://www.nisa.meti.go.jp/english/index.htm.

Satoh, T. (2004), "Short-period spectral level of intraplate and interplate earthquakes occurring off Miyagi prefecture," *Journal of JAEE'2004.,* **4**, pp. 1-4. (in Japanese with English abstract).

Scholz, C. H. (2002), "The mechanics of earthquakes and faulting," *Cambridge University Press.*

Sekiguchi, H., Aoi, S., Honda, R., Morikawa, N., Kunugi, T. and Fujiwara, H. (2006), "Rupture process of the 2005 west off Fukuoka prefecture earthquake obtained from strong motion data of K-NET and KiK-net," *Earth Planets Space,* **58** (1), pp. 37-43.

Si, H. and Midorikawa, S. (1999), "New attenuation relationships for peak ground acceleration and velocity considering effects of fault type and site condition," *J. Struct. Constr. Eng., AIJ.,* **523**, pp. 63-70. (in Japanese with English abstract).

Somerville, P. G., Irikura, K., Graves, R., Sawada, S., Wald, D., Abrahamson, N., Iwasaki, T., Kagawa, T., Smith, N. and Kowada, A. (1999), "Characterizing crustal earthquake slip models for the prediction of strong ground motion," *Seism. Res. Lett.,* **70**, pp. 59-80.

Fifth International Conference on Urban Earthquake Engineering
March 4-5, 2008, Tokyo Institute of Technology, Tokyo, Japan

MODELING & MONITORING TALL BUILDINGS:

John W. Wallace[1] and Derek Skolnik[2]

1) Professor, Department of Civil Engineering, UCLA, USA
2) PhD Candidate, Department of Civil Engineering, UCLA, USA
wallacej@ucla.edu

Abstract: Tall building construction in urban centers along the US west coast has recently surged. A significant number of the proposed buildings are being designed using alternative structural systems citing UBC 1997. These designs typically involve nonlinear dynamic analyses of 3D finite element models, some including gravity systems, and require peer-review. This process has led to debate within the profession over appropriate ground motion selection, as well as modeling and acceptance criteria. Instrumented structures help address these fundamental questions as well as other related issues. Reinforced concrete walls are commonly used as the primary lateral-force-resisting- system for tall buildings. As the tools for conducting nonlinear response history analysis have improved and with the advent of performance-based seismic design, reinforced concrete walls and core walls are often employed as the only lateral-force-resisting-system. Proper modeling of the load versus deformation behavior of reinforced concrete walls and link beams is essential to accurately predict important response quantities. Given this critical need, an overview of modeling approaches appropriate to capture the lateral load responses of both slender and stout reinforced concrete walls, as well as link beams, is presented. Modeling of both flexural and shear responses is addressed, as well as the potential impact of coupled flexure-shear behavior. Model results are compared with experimental results to assess the ability of common modeling approaches to accurately predict both global and local experimental responses. Based on the findings, specific recommendations are made for general modeling issues, limiting material strains for combined bending and axial load, and shear backbone relations.

1. INTRODUCTION

Tall building construction in urban centers along the US west coast has recently surged. For example, within the City of Los Angeles, 61 buildings over 20 stories, and 23 over 40, are under development – note, currently there are only 20 buildings over 40 stories in downtown Los Angeles (Figure s 1 & 2). A significant number of the proposed buildings are being designed using alternative structural systems citing UBC 1997. These designs typically involve nonlinear dynamic analyses of 3D finite element models, some including gravity systems, and require peer-review. This process has led to debate within the profession over appropriate ground motion selection, as well as modeling and acceptance criteria. This debate has led to several important projects, one to develop modeling and acceptance criteria for tall buildings and another focused on updating instrumentation requirements. The first project is part of the Pacific Earthquake Engineering Research (PEER) Center Tall Buildings Initiative (TBI), whereas the second project involves collaboration between the NEES@UCLA Laboratory, the UCLA Center for Embedded Networked Sensing, the California Geological Survey, and the City of Los Angeles. An overview of each of these projects is discussed in the following sections.

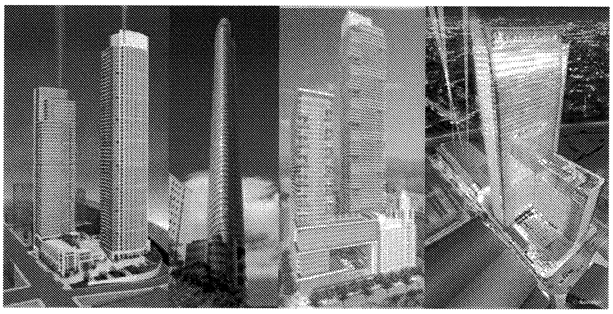

Figure 1 Existing and planned tall west coast buildings

2. MONITORING OF TALL BUILDINGS

The City of LA, quite fortuitously, requires instrumentation (e.g., accelerometers installed at the base, mid-level, and roof) to obtain building permits for all structures over ten stories (LA Building Code 2002). Instrumented structures help address fundamental questions related to modeling and response as well as other related issues such as podium effects. Monitoring a variety of response quantities, such as displacements and strains, offer further insight into the behavior of important structural elements, viz. RC core walls, coupling beams, and outriggers. Realizing this, we are working with the LA-DBS to update the instrumentation requirements.

The building surge as well as an updated instrumentation program provides a rich opportunity to collect unique data in both wind and earthquake events to address critical analysis and design issues. In the medium-term, the aim is to develop and implement a network for structural monitoring and performance-based assessment using LA tall buildings as a test-bed.

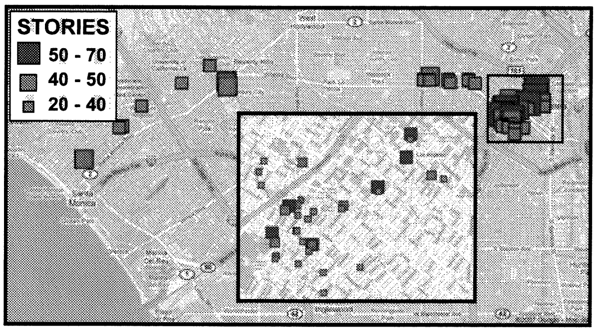

Figure 2 Proposed new tall buildings in Los Angeles

2.1 Monitoring Strategy

The boom in tall building construction provides a unique opportunity to employ monitoring equipment to measure structural responses for a variety of conditions (ambient, high-level wind, and earthquake). Ideally, a broad spectrum of sensor types capable of measuring floor accelerations, wind pressures, average concrete strains, rebar strains, and rotations should be employed. In addition to a broad spectrum of sensors, key attributes of a robust monitoring system include: rapid deployment, energy efficiency, event detection, robust analog-to-digital conversion, local storage, redundant time synchronization, mulit-hop wireless data transport, and remote sensor and network health monitoring. Recent developments in all of these areas reveal that robust structural health monitoring is likely to emerge over the next decade. Therefore, careful consideration should be given to increased use of sensors in existing and planned buildings. In general, more sensors are needed than are often employed in buildings, that is, only one triaxial accelerometer at the base, a mid-level, and the roof.

Given the complexity and geometry of tall buildings, laboratory studies, which are hindered by scale, materials, and appropriate boundary conditions, are unlikely to provide definitive results for a variety of these issues. For a given instrumented building, the details of the embedded sensor network design should be model-driven, i.e., sensor types and locations determined based on response quantities obtained from 3D dynamic finite element models (FEM) subjected to a suite of site-specific ground motions (Figure 3). For example, in moment frames, response quantities of interest might be interstory displacements at several floors (where maximum values are expected) along with base and roof accelerations. In cases where novel systems or materials are employed (e.g., high-performance concrete, headed reinforcement, unbonded braces), additional instrumentation could be used to measure very specific response quantities (e.g., headed bar strain, axial deformations, etc). In a concrete core wall system, response quantities of interest might be average core wall concrete strains within the plastic hinge (yielding) region and rotations imposed on coupling beams (or slab-wall connections). Other modeling and design issues could also be targeted, such as so-called podium effects and appropriate ground motion building inputs at subterranean levels (Stewart, 2007). Given the uncertainty associated with the response of structural systems to earthquake ground motions, a probabilistic distribution of response quantities of interest (e.g., interstory displacements, coupling beam deformations) should be determined for the structural model subjected to the suite of ground motions and the sensor layout should target specific regions versus a single response quantity.

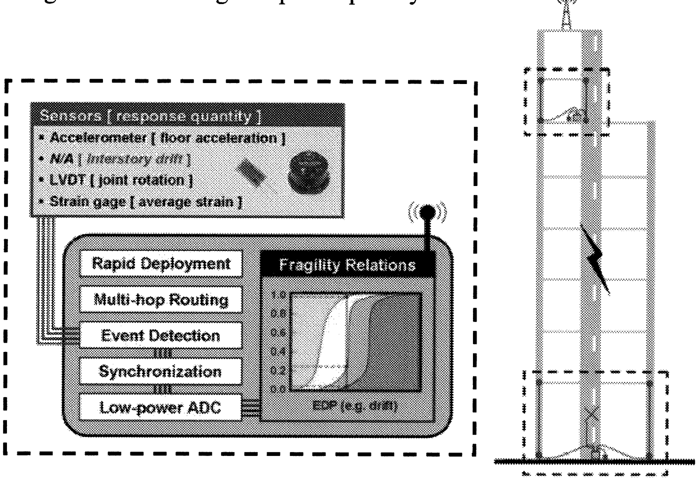

Figure 3 Model-driven SHM deployment and toolbox

2.3 Sensors and Data Acquisition

One particularly useful response quantity within the PBEE framework is interstory drift. However, current methods for measuring interstory displacements (e.g., double integration of acceleration) are problematic. Hence a new laser/photodiode-based prototype sensor is under development. Shortcomings in current data acquisition and wireless communications have lead to substantial research in developing new technologies. A toolbox is under development, based on a low-power LEAP2 platform (McIntire, 2006) with integrated 24bit ADC (Reftek, Inc.), field-tested software/hardware for robust wireless network access, and reliable RBS time synchronization (typically GPS is unavailable inside buildings). Results from bench top and shake-table testing, with a modest scale structure, for both sensor and toolbox prototypes are underway (Figure 4).

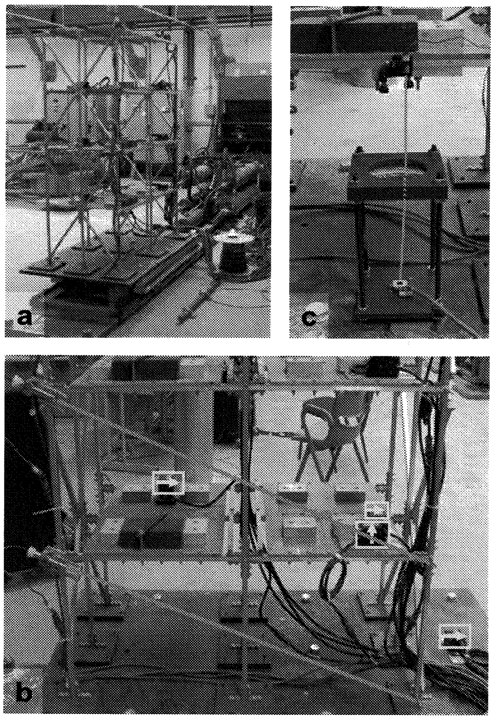

Figure 4 Scale structure on nees@UCLA linear shaker (a), close-up of traditional instrumentation for measuring interstory drift (b), preliminary prototype for laser/photodiode sensor (c).

As noted earlier, the city of Los Angeles requires instrumentation for many tall building construction permits. Presently, we are working with the LADBS and the California Strong Motion Instrumentation Program (CSMIP) on additional requirements for the 'special' projects involving peer review. These new buildings designed using nonlinear response histories (via "Seismic Response History Procedures" of Chapter 16 of ASCE 7) will be subject to a pending information bulletin tentatively titled; *Special Requirements and Specifications for Installation and Servicing of Structural Monitoring Instrumentation.* The goal is to increase the number and type of sensors installed in each structure. For example, general tall buildings are required to install three 3-channel instruments, typically at the base, mid-level, and roof. Special tall buildings will have requirements based on number of stories, vertically distributed in a meaningful fashion, e.g., to capture higher mode responses (Table 1).

3.2 Future Studies

Over the next six months prototype toolboxes and the capabilities will be assess via side-by-side comparisons with existing NEES@UCLA equipment.

Table 1 Periods, Participation Factors, and Damping Ratios of Space Frame with Dampers

Number of stories above ground	Minimum Number of channels
(6 – 10)*	12
10 – 20	15
20 – 30	21
30 – 50	24
> 50	30

* Instrumentation for buildings less than 10 stories is required only if the total aggregate floor area exceeds 60,000 square feet (5574 m2)

3. MODELING AND ACCEPTANCE CRITERIA

Reinforced concrete (RC) structural walls are effective for resisting lateral loads imposed by wind or earthquakes. They provide substantial strength and stiffness as well as the deformation capacity needed to meet the demands of strong earthquake ground motions. As the tools for conducting nonlinear response history analysis has improved and the application of performance-based seismic design approaches have become common, use of reinforced concrete walls and core walls for lateral-force resistance along with a slab-column gravity frame have emerged as one of the preferred systems for tall buildings.

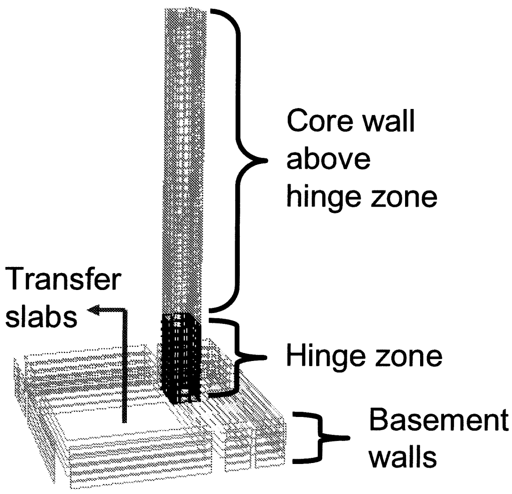

Figure 5 Representative tall core wall building

The lateral building strength is sometimes concentrated in relatively few walls distributed around the floor plate or within a central core wall to provide the lateral stiffness needed to limit the lateral deformations to acceptable levels. Although extensive research has been carried out to study the behavior of reinforced concrete walls and frame-wall systems, including development of very refined modeling approaches, use of relatively simple or course models is required for very tall buildings to reduce computer run times for the nonlinear response history analyses. Therefore, it is important to balance model simplicity with the ability to reliably predict the inelastic response both at the global and local levels under seismic loads to ensure that the analytical model captures the hysteretic wall behavior and the interaction between the wall and other structural members and the foundation reasonably well.

The most common modeling approach used for RC walls involves using a fiber beam-column element (e.g, PERFORM 3D, 2006) or the Multiple-Vertical-Line-Element Model, which is similar to a fiber model (Orakcal and Wallace, 2006). Use of either of these models allows for a fairly detailed description wall geometry, reinforcement, and materials, and accounts for important response features such as migration of the neutral axis along the wall cross-section during loading and unloading, interaction with the connecting components such as slabs and girders, both in the plane of the wall and perpendicular to the wall, as well as the influence of variation of axial load on wall flexural stiffness and strength. Important modeling parameters include the definition of the material properties for the longitudinal reinforcement, the core concrete enclosed by transverse reinforcement (i.e., confined concrete), and cover and web concrete (i.e., unconfined concrete). More complex model and material behavior also can be described that incorporates observed interaction between flexural/axial behavior and shear behavior (Massone et al, 2006; Orakcal et al., 2006); however, an uncoupled model, where flexure/axial behavior is independent of shear behavior, is commonly used for design.

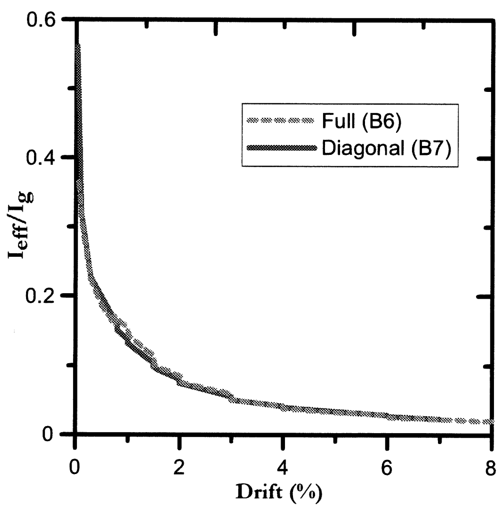

Figure 6 Link beam effective stiffness

Coupling or link beams exist due to the core wall configuration or they are needed to enhance the lateral stiffness of the building, and proper modeling of the load versus deformation behavior of reinforced concrete and coupling beams is essential to accurately predict important response quantities. Selection of appropriate flexural stiffness values for the coupling beams is particularly important, as use of one-half of the gross concrete inertia value generally produces higher shear stresses than are acceptable for design. Given this problem, it is common practice to reduce coupling beam stiffness to significantly lower values, on the order of 0.2Ig to 0.1Ig, or less, to achieve an acceptable level of shear stress for design actions. At issue is whether a reduction of this magnitude is appropriate at service or design loads, since relatively large cracks may form, or at DBE or MCE, where a significant stiffness reduction would appear appropriate, and spalling of relatively large chunks of concrete could potentially pose a hazard.

It is common for the footprint of the building at lower levels to be larger than the tower footprint to accommodate parking needs. This abrupt change in geometry can have a significant impact on the distribution of lateral forces at the discontinuity, where loads are shared between the core wall and the parking level walls. Parking level walls are typically stout, i.e., the wall height-to-length or aspect ratio is low; therefore, selection of the stiffness values for flexure and shear are important and can substantially impact the distribution of lateral forces between the core wall and perimeter basement level walls. Since the floor slabs in the region of the discontinuity are required to transfer forces from the core wall to the perimeter walls, selection of appropriate slab stiffness values and design of slab reinforcement are important issues. Variation of slab and wall stiffness values is typically required to determine the potential range of design values to ensure proper design. For embedded basement levels, response history analysis is further complicated by the need to define the level at which the ground acceleration records are applied (Stewart., 2007).

Slab-column framing provides an efficient system to resist gravity loads, with limited forming and relatively low story heights, as well as providing an open, flexible floor plan. Since the slab-column frame resists only gravity loads, it is not included in the lateral load analysis. However, the ability of the slab-column gravity frame to maintain support for gravity loads for the lateral deformations imposed on the gravity system by the lateral-force resisting system must be checked. The primary objectives of this "deformation compatibility" check are to verify that slab-column punching failures will not occur for service-level and design-level earthquakes, as well as to assess the need to place slab shear reinforcement adjacent to the column to enhance slab shear strength. Design requirements for these checks are included in ACI 318-05 §21.11.5 (Building, 2005). Detailing of the slab-wall connection also is an important design consideration, as the rotation of the core wall can impose relatively large rotation demands on the slab at the slab-wall interface (Klemencic et al., 2006). During construction, construction and concrete placement of the core wall typically precedes the slab, requiring special attention to slab shear and moment transfer at the slab-wall interface.

As noted in the preceding paragraphs, design of tall buildings utilizing reinforced concrete walls is complicated by the uncertainty associated with a variety of issues. Although analytical modeling studies and experimental studies are appropriate for improving our understanding of some issues (e.g., coupling beams), it is clear that other issues can only be answered by installation of sensors in actual buildings. Ideally, the sensors could be installed both during and after building construction to enable the broadest spectrum of data collection and follow-up analytical studies. Sensors to measure a wide variety of response quantities (acceleration, force/pressure, velocity, displacement, rotation, and strain) could be installed to collect critical data to improve our ability to model the dynamic responses of tall buildings. Data collection in for ambient, wind, low-level earthquakes, as well as the significant earthquakes would help improve our computer modeling capabilities, and ultimately the economy and safety of tall buildings.

The preceding paragraphs provide an overview of some of the important issues associated with analysis and design of tall reinforced concrete buildings. Each of these issues is being addressed in the PEER Center Tall Buildings Initiative as Applied Technology Council Project 72 (ATC-72). The 90% draft of the ATC-72 report is currently under review and should be published late in 2008.

4. SUMMARY

The boom in tall building design and construction along the west coast of the United States has generated significant interest in the use of alternative analysis and design approaches, including Performance-Based Seismic Design. Use of nonlinear response history analysis and three-dimensional computer models is becoming common. The PEER Center Tall Buildings Initiative was undertaken to summarize key issues and to develop consensus views for modeling and acceptance criteria. Work to improve equipment and interfaces for monitoring are being developed jointly by NEES@UCLA, the CENS at UCLA and industry partners, including the California Geological Survey and the City of Los Angeles.

Acknowledgements:

The authors gratefully acknowledge the support staff support provided by the NEES@UCLA Equipment Site with support Cooperative Agreement with NEESinc with National Science Foundation funding, as well as the support provided by the UCLA Center for Embedded Networked Sensing (CENS) (NSF Cooperative Agreement CCR-0120778). We also wish to acknowledge the fruitful collaboration with Dr. Robert Nigbor (NEES@UCLA); CENS faculty participants Dr. Deborah Estrin, Dr. William Kaiser, and Dr. Paul Davis; and CENS graduate students Martin Lukac, Dustin McIntire, Thanos Stathopoulos, and staff member and Dr. Vinayak Naik.

References:

ACI 318-05, "Building Code Requirements for Structural Concrete (ACI 318-05) and Commentary (ACI 318R-05)"; American Concrete Institute; Farmington Hills, Michigan; 2005.

Klemencic, R., Fry, J. A., Hurtado, G., Moehle, J. P., "Performance of Post-Tensioned Slab-Core Walls Connections," PTI Journal, Vol., No. 2, pp. 7 – 23, December 2006.

Los Angeles Building Code, §1635, 2002

McIntire, D., Ho, K., Yip, B., Singh, A., Wu, W. and Kaiser, W., The Low Power Energy Aware Processing (LEAP) System. IPSN Track on Sensor Platform, Tools and Design Methods for Networked Embedded Systems (SPOTS), pp:449-457, April 19-21, 2006, Nashville, TN, USA.

Orakcal, K. and Wallace, J. W., "Flexural Modeling of Reinforced Concrete Walls – Model Calibration," ACI Structural Journal, Vol. 103, No. 2, pp 196 – 206, March – April, 2006.

PERFORM-3D, "NONLINEAR ANALYSIS AND PERFORMANCE ASSESSMENT FOR 3D STRUCTURES," Version 4, Computer & Structures Inc., Berkeley, CA.

Reftek, Refraction Technology Inc. Plano, TX, US www.reftek.com

Stewart, J. P., "Input motions for buildings with embedment," Proceedings, Los Angeles Tall Buildings Structural Design Council, 2007 Annual Meeting, May 2007.

EARTHQUAKE EARLY WARNING
- PROVISION TO GENERAL PUBLIC AND FUTURE PROSPECT -

Osamu Kamigaichi

Senior Coordinator for Seismological Information, Dept. of Seismology and Volcanology, Japan Meteorological Agency, Tokyo, Japan
okamigai@met.kishou.go.jp

Abstract: Japan Meteorological Agency started Earthquake Early Warning provision to the general public in October 2007. In this article, outline of EEW, preparatory process for the provision, and future prospects are introduced

1. Introduction

Earthquake early warning of JMA is to enable advance countermeasures to the strong motion disaster by providing expected seismic intensity and arrival time of the strong motion before the S wave arrival. However, due to its very short available time, it is essential to well publicize the principle and technical limit of EEW, and proper actions to be taken when it is seen or heard, to utilize EEW effectively without causing unnecessary confusion. In this article, outline of EEW, necessary preparatory process to start EEW provision to the general public, and future prospects are briefly introduced.

2. Outline of EEW

The essential contents of EEW are, estimated origin time, hypocenter location, magnitude of the earthquake, and expected maximum seismic intensity (JMA scale) and earliest arrival time (second) of the strong motion for each sub-prefectural area. Considering the trade-off between the promptness and accuracy, EEWs are issued basically several times for one earthquake improving the accuracy as available data increases as time passes, securing the promptness of the first issuance at the same time. To realize it, JMA developed the method to estimate epicentral distance and azimuth by using first 2 seconds of waveform data in corporation with the Railway Technical Research Institute (Tsukada et al(2004)) to enable quick epicenter determination even for events occurring outside of the seismic network, as well as for those inside (Kamigaichi(2004)). To improve the accuracy, Not-yet-arrived method (Horiuchi et al(2005)) developed by the National Research Institute for Earth Science and Disaster Prevention is also incorporated. In total, about 1,000 seismic stations are used(JMA:200, NIED:800) for EEW.

On line connected computer can utilize such multiply issued information for automatic control. But, when they are transmitted to the public, it is impossible to respond properly, and moreover, it is impossible to transmit all by characters and voice. So, the content and issuance criterion of EEW had to be carefully designed when it is provided to the general public.

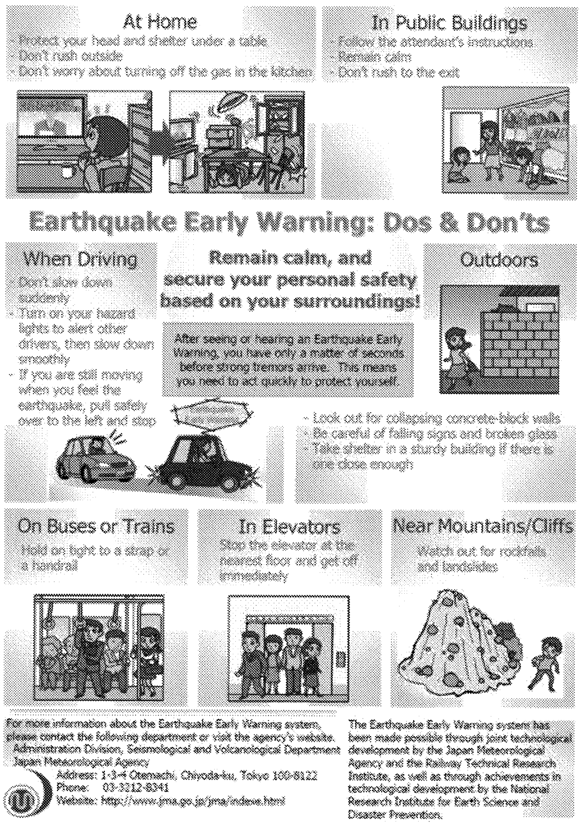

Figure 1 Leaflet(English version) to show proper response to EEW in various situations

3. Preparatory Process to Start EEW Provision to the General Public

1) Two Step Provision

JMA started to provide EEW to a limited number of users who understand the technical limit of EEW and can utilize it effectively, such as for automatic control on the 1st of August 2006. At that moment, EEW was not well known to the general public, so JMA decided to start provision to the general public after well publicizing the EEW principle and proper actions to be taken. For this purpose, JMA made leaflets to show a guideline for proper response to EEW in various situations (Figure 1: English version). JMA also distributed video material to explain technical principle and proper response, made posters, held seminars, and posted relevant information on EEW on the JMA's web page (http://www.jma.go.jp/jma/index.html). After confirming that the ratio of the people who understand EEW increased significantly by these public relations activities, JMA started to provide EEW to the general public on the 1st of October 2007.

2) Content and issuance criterion of EEW for general public

JMA considered the issuance criterion and contents of EEW when it is issued to the general public to meet the following conditions.

a) It should be issued on the best timing, avoiding the false alarm, securing the promptness as much as possible, and making the revised issuance as few as possible.

b) It should be issued when really a strong motion is expected, and the area where the safety actions must be taken should be made clear.

As a result,

- Issuance criterion : when the maximum seismic intensity 5 lower(JMA scale) or over is expected by using seismic records from more than one station.
- EEW contents : Origin time, epicentral region name, and names of areas(unit area is about 1/3 to 1/4 of one prefecture) where seismic intensity 4 or over is expected. Expected arrival time is not included because it differs substantially even in one unit area.

Figure 2 shows an example EEW for the general public when its issuance criterion is applied to the Niigata-ken Chuetsu-oki earthquake (M6.8) on the 16th of July, 2007(before the start of EEW provision to the general public). Left figure shows observed maximum seismic intensities in each sub-prefectural area, and right figure shows a spatial extent of warned area where seismic intensity 4 or over is expected, and contour circles denoting available time for taking action in seconds. As for the areas with expected and observed seismic intensity 4 or over, they show a good agreement. As for the time for taking action, although EEW was not in time for the S wave arrival for the area close to the epicenter due to the technical limit, 16 seconds were available at IIzuna-town in Nagano prefecture where seismic intensity 6 upper was observed. EEW is considered to work effectively for trench-type large earthquakes, but even for a shallow inland event, the area where EEW is valid can exist if the event is large.

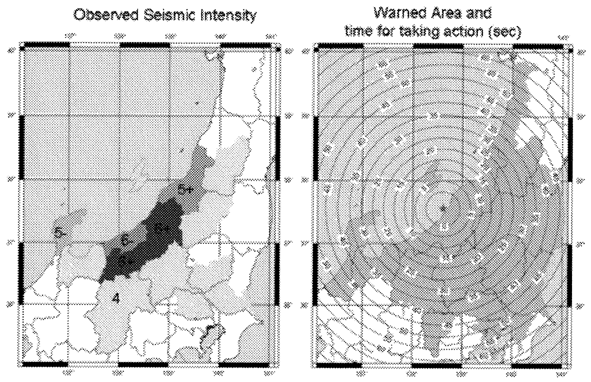

Figure 2 Example of EEW for the general public when its issuance criterion and content are applied to the Niigata-ken Chuetsu-oki Earthquake on the 16th of July, 2007.

4. Meteorological Service Law Amendment

Along with above mentioned public relations activities, JMA amended the Meteorological Service Law to

a) clearly define the issuance and transmission responsibilities of JMA and relevant organizations to secure prompt transmission of EEW to the people, and to

b) establish technical standard that the providers must satisfy when they issue expected seismic intensity and arrival time of strong motion at individual house and building, which is beyond the national agency's service, to secure their quality.

The technical standard is as below.

i) Hypocenter parameters(origin time, hypocenter location and magnitude) contained in the EEW issued from JMA must be used,

ii) Seismic intensity and arrival time estimation method must give values within certain deviations from those given by JMA's method. When different amplification coefficients of the surface layer are used from JMA's, its technical adequacy must be shown. A method that gives a smaller estimation residual than JMA's is also permitted.

The essence of setting the technical standard is not to prohibit superior method, but to avoid a low-quality service to be provided to the people.

On Site Warning based on P-wave sensor at the site is not an object of this technical standard.

The amended Law came into force on the 1st of December, 2007.

5. Future Prospects

1) Establishment of various transmission routes

To make EEW efficient for the disaster mitigation, it is very important to establish various transmission routes that can reach to the individual person promptly and surely. For the time being, TV and radio will be the main routes. Besides them, portable terminals like cellular phone that can receive EEW, EEW receivers through internet or dedicated line, combined system of J-Alert(Fire and Disaster Management Agency) and loud speaker(Municipality), announcement system in public places are being developed or introduced. For the promotion of these, JMA will keep close cooperation with relevant organizations.

2) Promotion of utilization

It is up to the manager's judgement to utilize EEW in the public facility. To help their consideration, JMA has been attending their meetings, and has made a guideline to introduce and utilize EEW in the public places, in which example of operation manual, way to conduct exercise are introduced, and posted on the JMA's web-page.

3) Improvement of the method

3-1) Reduction of false warning

Out of 1,713 EEWs issued in about three years before the start of provision to the general public, JMA issued 30 false warnings. Many of these were due to human error or initial defect of instruments, and they have been fixed. Still, there exists a possibility of false warning due to a lighting strike near a station, and JMA is considering the countermeasure. As for the EEW for the general public, by setting the issuance criterion so that signals must be detected at more than one station, no false warning will be issued.

3-2) Improvement of seismic intensity estimation

JMA has been making effort to improve the seismic intensity estimation accuracy. When the up-to-date(as of Oct.,2007) method is applied to the past events to meet the issuance criterion for general public, out of 322 sub-prefectural area for which seismic intensity 4 or over is expected, 37% gives identical maximum seismic intensity scale with the observation, and 83% falls within ±1.

The main future subjects will be as follows.

- Rapid estimation of spatial extent of rupture area

As of now, regression formula for the estimation of maximum velocity amplitude to use distance from the fault surface as an input parameter is used. But a distance from hypothetical sphere centered at the hypocenter is used instead of that from the fault surface, because it is difficult to estimate in a prompt manner. By this improvement, seismic intensity estimation accuracy at near distance can be improved.

- Development of technique that can incorporate different stress drop for each event, and different seismic wave attenuation characteristic for each region.

References:

Tsukada,S., T.Odaka, K.Ashiya, K.Ohtake and D.Nozaka(2004), "Analysis of the Envelope Waveform of the Initial Part of P-waves and its Application to Quickly Estimating the Epicentral Distance and Magnitude", Jishin2, vol.56, No.4, pp.351-361.

Horiuchi,S., H.Negishi, K.Abe, A.Kamimura and Y.Fujinawa (2005), "An Automatic Processing System for Broadcasting Earthquake Alarms", Bull. Seism. Soc. Am. Vol.95, pp.708-718.

Kamigaichi,O.(2004), " JMA earthquake early warning", Journal of Japan Association for Earthquake Engineering, vol.4(Special Issue), pp.134-137.

Fifth International Conference on Urban Earthquake Engineering
March 4-5, 2008, Tokyo Institute of Technology, Tokyo, Japan

EXPERIMENTS OF EARTHQUAKE EARLY WARNING TO EXPRESSWAY DRIVERS USING SYNCHRONIZED DRIVING SIMULATORS

Fumio Yamazaki[1], Yoshihisa Maruyama[2], and Masato Sakaya[3]

1) Professor, Graduate School of Engineering, Chiba University, Japan.
2) Assistant Professor, Graduate School of Engineering, Chiba University, Japan.
3) Former Student, School of Engineering, Chiba University, Japan.
yamazaki@tu.chiba-u.ac.jp, ymaruyam@tu.chiba-u.ac.jp

Abstract: To reduce casualties due to earthquakes, Japan Meteorological Agency (JMA) has introduced earthquake early warning (EEW) to general public on October 1, 2007. However, the possibility that EEW causes traffic accidents exists because EEW through car radio may not be transmitted to all the expressway drivers. Hence, the effects of early earthquake warning were investigated using plural driving simulators, connected together by a server. In the virtual experiments, three driving simulators were used, simulating three cars running together on an expressway. When EEW was transmitted to all the cars, the drivers reduced speed slowly and no trouble occurred. On the contrary, when EEW was transmitted to only one car, some drivers reduced speed suddenly, and accidents occurred in 2 cases out of 14 tests. These experiments show the necessity of public education how to react EEW on expressways. Turning on the hazard lights after receiving an EEW and then reduce speed gradually is suggested to avoid accidents.

1. INTRODUCTION

The Japan Meteorological Agency (JMA) started to provide the earthquake early warning (EEW), which contains the arrival time of S-wave and the intensity of seismic motion estimated by the P-wave detection near the hypocenter (Doi, 2001). It is expected that the preparations for strong shaking and tsunami can start based on an EEW and thus, emergency responses can be performed rapidly and efficiently.

The EEW has been under operation on a trial basis since August 2006. The EEW is transmitted to construction sites, railway companies and so on, where the EEW is expected to be utilized properly without confusions. Based on the results of trial operations, the JMA started to issue the EEW to general public through radio and TV on October 1, 2007 (JMA, 2007). On the other hand, it is pointed out that some troubles may be caused when the EEW is issued to the general public. For example, it is anticipated that many evacuees may go down like ninepins at the exits of theaters and department stores.

The JMA compiled dos and don’ts after receiving the EEW (JMA, 2007). The proper behaviors during automobile driving are mentioned in the dos and don’ts. The possibility that EEW causes traffic accidents exists because the EEW through car radio may not be transmitted to all the expressway drivers. Maruyama and Yamazaki (2004) showed the effects of EEW to drivers on an expressway using a driving simulator. In the study, no other vehicles were considered except for examinee’s. It is important to consider the interaction among vehicles on an expressway when the EEW is issued. In this study, the effects of EEW are investigated using three driving simulators, connected together by a server. The reactions of drivers are observed under various receiving conditions of EEW.

2. OUTLINE OF THE DRIVING SIMULATOR EXPERIMENTS

Figure 1 shows the driving simulators used in this study (Honda Motor Co., Ltd., 2001). Two regular driving simulators and one simple driving simulator that consists of only a steering wheel, brake and accelerator pedals were employed in the virtual tests. Figure 2 shows the scenario course in the experiment and the front view from the rear vehicle. The examinees were instructed to drive at the speed of 80 km/h in the left lane. In the right lane, the simple driving simulator, driven by a trained person, was assigned as a pace maker during the experiment.

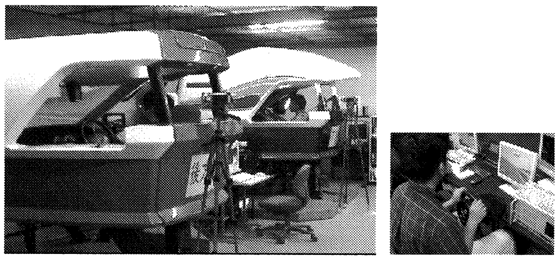

Figure 1. Synchronized driving simulators used in this study. Two regular simulators (left) and simple simulator (right).

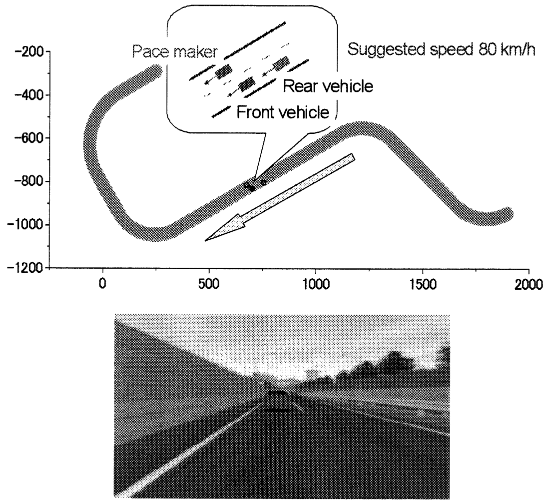

Figure 2. Scenario course in the experiment and the front view from the rear vehicle

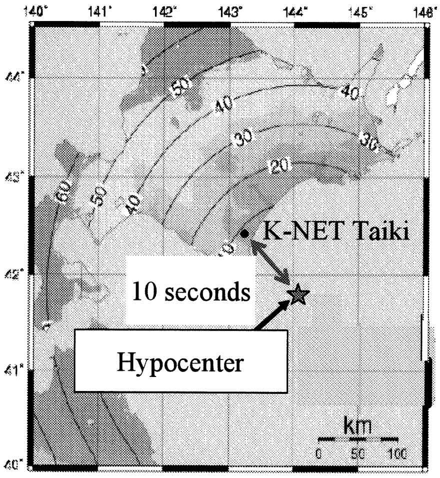

Figure 3. Scenario earthquake early warning for the 2003 Tokachi-oki EQ by JMA

The condition of an EEW was determined using the locations of the hypocenter and seismometers in the 26 September 2003 Tokachi-oki earthquake. According to the results of numerical simulation by JMA, the time between receiving the EEW and the arrival of S-wave is about 10 seconds in Taiki Town, which is located about 100 km away from the epicenter. Hence, the three-component acceleration record in K-NET Taiki Town with PGA=366.1cm/s^2 and JMA Instrumental Intensity=5.95 was used as an input seismic motion in the experiment.

The seismic response acceleration of a moving vehicle was calculated based on a vehicle response model (Maruyama and Yamazaki, 2002), and then the obtained response acceleration was applied to the driving simulators.

Three types of experiments were conducted in this study. The EEW was given neither the front vehicle nor the rear vehicle in Experiment 1 (14 pairs of drivers). The EEW was transmitted to the both vehicles in Experiment 2 (13 pairs). In Experiment 3, the EEW was given only to the front vehicle, and it was not given to the rear vehicle (14 pairs). The EEW was assumed to be transmitted by car radio, and it announced to the drivers that an earthquake has just occurred and strong motion will arrive soon.

3. RESULTS OF QUESTIONNAIRE SURVEY AFTER THE EXPERIMENTS

After the experiment, questionnaire survey was conducted to each examinee. Figure 4 shows the degree of recognition of the earthquake motion during the experiments. When the EEW was not transmitted to the drivers, about 40 % of examinees in Experiment 1 and about 70 % of examinees in Experiment 3 (rear vehicle) could not recognize the earthquake occurrence. Similar tendency was also pointed out under the actual earthquake environment (Maruyama and Yamazaki, 2006).

On the other hand, the examinees recognized the earthquake motion when the EEW was provided. If failures of road embankment or cracks of road surface are generated due to an earthquake, drivers that are unaware of the earthquake may run into the failures. The drivers that know the earthquake occurrence in advance by EEW can avoid such kind of traffic accidents. The EEW seems to be very effective in this regard.

In Experiment 3, the examinees of the front vehicle

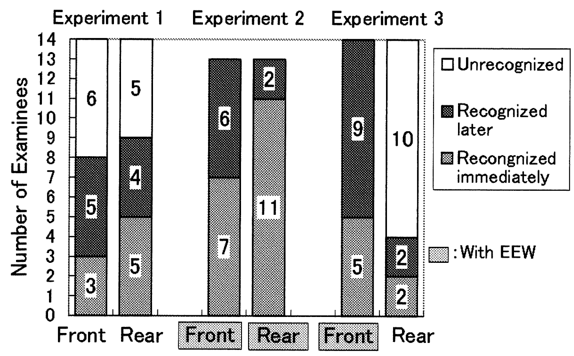

Figure 4. Degree of recognition of earthquake occurrence during the experiment

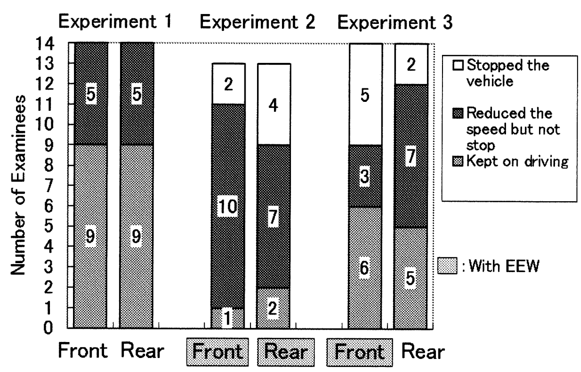

Figure 5. Reactions of the examinees during strong shaking

can recognize the earthquake occurrence owing to EEW. But the examinees of the rear vehicle may be unaware of the earthquake. The difference of earthquake recognition between the two drivers will affect drivers' behaviors during an earthquake.

Figure 5 shows the reactions of the examinees during strong seismic motion. In Experiment 1, more than half of the examinees kept on driving as usual even under strong shaking. On the contrary, many of the examinees in Experiment 2 reduced speed or stopped the car during strong shaking. Because of the EEW, the examinees in Experiment 2 recognized the earthquake. Hence, they reduced speed or stopped their vehicles to make ready for strong shaking. The results of Experiment 1 indicate that the drivers that are unaware of an earthquake may drive as usual. As for the rear vehicle in Experiment 3, less than half of the examinees kept on driving as usual though they did not recognize the earthquake. Because the examinee on the rear vehicle tried to keep the distance from the front vehicle, he reduced speed or stopped the vehicle without recognizing the earthquake.

4. RESULTS OF THE EXPERIMENTS

In the experiments, the moving speed of vehicle, the positions of brake and accelerator pedals, the angle of steering wheel and so forth were recorded to evaluate drivers' reactions during an earthquake.

Figure 6 shows the moving speeds of front vehicles in Experiments 1 and 2. The examinees in Experiment 1 drove at the speed of 80 km/h (22.2 m/s) as instructed even after main shaking because many of them did not recognize the earthquake occurrence. On the other hand, the examinees in Experiment 2 reduced the moving speed gradually after receiving the EEW. If the disorders on the road surface are generated because of strong ground shaking, the drivers with lower moving speed may avoid traffic accidents easily. According to these results, the EEW is effective for driving safety in this regard.

So far, the result of Experiment 1 when the EEW was given to neither the front vehicle nor the rear vehicle and that of Experiment 2 when the EEW was given to the both drivers were compared and discussed. If the EEW is broadcasted by TV and radio, some drivers on the expressway will receive the EEW and the others will not be informed.

Figure 7 shows the distance between the two vehicles in Experiment 3. The EEW was given only to the front vehicle in Experiment 3. The distance between the two vehicles become shorter during the EEW announcement (t = 0-5 s) in some cases. The driver on the front vehicle reduces the moving speed due to the EEW, however, the driver on the rear vehicle keeps on driving without reducing the moving speed. Two pairs of examinees out of 14 (dashed lines in Fig. 7) eventually crashed because of the information gap. In addition that, there are some cases that the distance between the two cars became too short and thought to be dangerous.

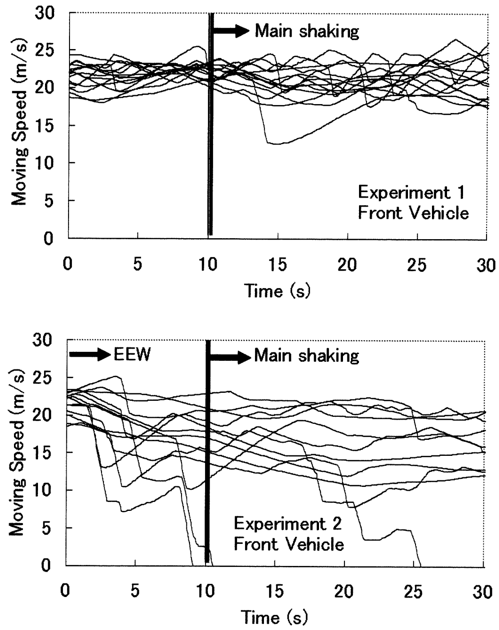

Figure 6. Comparison of moving speed in Experiments 1 and 2 (Front vehicle).

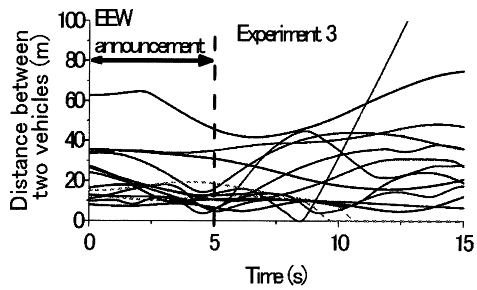

Figure 7. Distance between the two vehicles in Experiment 3

Figures 8 and 9 show examples of moving speeds of vehicles and positions of brake pedals observed in Experiments 2 and 3. When the EEW was given to the both examinees in Experiment 2 (Fig. 8), the front vehicle reduced speed gradually and the rear vehicle put on the brake in phase to keep the distance from the front vehicle.

When the EEW was given only to the front vehicle in Experiment 3 (Fig. 9), the examinee on the front vehicle put on the brake before the S-wave arrival (t = 10 s). Although the examinee on the rear vehicle tried to stop immediately, he eventually crashed to the front vehicle.

Four examinees on the front vehicle turned on hazard light before reducing the moving speeds in Experiment 3. In these cases, the rear vehicles could respond properly even though they did not receive an EEW. The intention to reduce speed of the front vehicle was conveyed to the rear vehicle by turning on hazard light. When the EEW is transmitted to general public through radio and TV, some drivers may receive the EEW and the others may not receive it at the present stage. Turning on the hazard lights by EEW

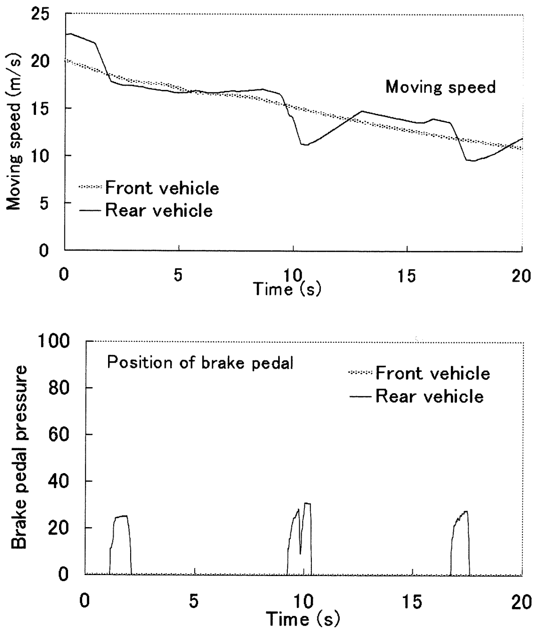

Figure 8. Examples of moving speeds and positions of brake pedals in Experiment 2

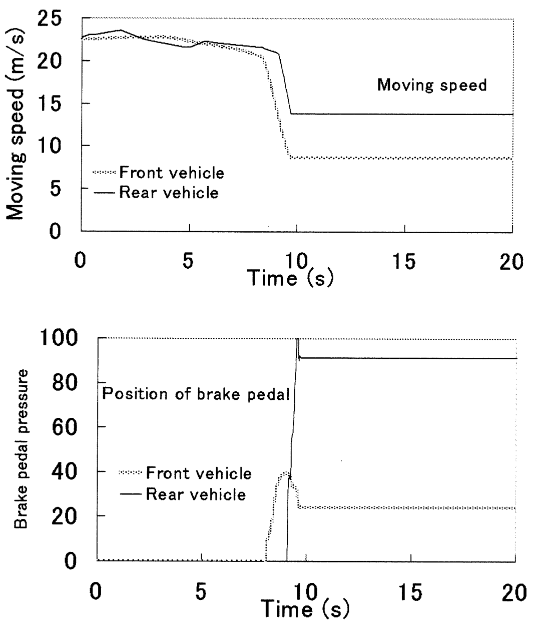

Figure 9. Examples of moving speeds and positions of brake pedals in Experiment 3

receivers is considered to be the most effective way to make the other drivers ready for an unknown hazard (a coming earthquake) on an expressway.

5. CONCLUSIONS

In this study, a series of virtual driving tests were conducted to realize the reactions of drivers under the earthquake early warning. When an EEW is given only to a part of vehicles running in close distances, the disagreement among drivers' reactions during an earthquake may cause traffic accidents. Such kind of expected events were actually occurred in the experiments using three driving simulators connected together by a server. Turning on the hazard lights by drivers that received the EEW is considered to be the effective way to make the drivers without receiving the EEW ready for unexpected hazards. To avoid accidents due to EEW from mass media, it is important to instruct drivers to turn on the hazard lights before reducing speed when receiving the EEW on an expressway.

References:

Doi K. (2002). "Earthquake early warning system in Japan", *Early Warning Systems for Natural Disaster Reduction,* Springer, 447-452.

Honda Motor Co., Ltd. (2001). "Honda introduces all-new automobile driving simulator", *http://world.honda.com/news/2001/printerfriendly/c010417_2.html*

Japan Meteorological Agency (2007). "Earthquake early warning", *http://www.jma.go.jp/jma/en/Activities/eew.html*

Maruyama Y., Yamazaki F. (2002). "Seismic response analysis on the stability of running vehicles", *Earthquake Engineering and Structural Dynamics*, **31**, 1915-1932.

Maruyama Y., Yamazaki F. (2004). "Driving simulator experiment on the effect of early warning of seismic motion to expressway drivers", *Proceedings of the 13th World Conference on Earthquake Engineering*, Paper No. 3487, 10p.

Maruyama Y., Yamazaki F. (2006). "Relationship between seismic intensity and drivers' reaction in the 2003 Miyagiken-Oki earthquake", *Structural Eng./Earthquake Eng.*, Japan Society of Civil Engineers, **23**(1), 69s-74s.

APPLICATION OF EARTHQUAKE EARLY WARNING SYSTEM TO A HIGH-RISE BUILDING IN TOKYO, JAPAN, CONSIDERING LONG-PERIOD STRONG GROUND MOTION

Hisada Y[1], T Kubo[2], S Horiuchi[3] and S Yamamoto[3]

1) Professor, Kogakuin University, Tokyo, Japan
2) ABSG Consulting, Tokyo, Japan
3) National Research Institute for Earth Science and Disaster Prevention, Ibaraki, Japan n
Author for correspondence, e-mail: hisada@cc.kogakuin.ac.jp

Abstract: We apply Earthquake Early Warning System (EEWS) and Real-time Strong-motion Monitoring System (RSMS) to reduce earthquake-related damage of the 29-story building of Kogakuin University in the downtown Tokyo, Shinjuku, Japan. EEWS, which is operated by NIED (National Research Institute for Earth Science and Disaster Prevention), is the system to provide earthquake information, such as the location and magnitude of an earthquake, the arrival time of the S-wave, and the estimated seismic intensities, before the actual arrivals of S-waves. For the case of subduction earthquakes (i.e., the Tokai and Tonankai earthquakes), we can expect a couple of minutes before the building's largest response, because it is shaken by the surface waves with a slow speed less than 1 km/s, which are exited in the Kanto sedimentary basin. Therefore, we apply EEWS to the emergency operation control system of elevators during earthquakes to stop them automatically at the nearest floors, and to the announcement system to secure safeties of students and staffs in the building. On the other hand, RSMS of Kogakuin University, which consists of 40 channels of accelerometers and data servers, is the system to monitor the building response and to estimate the building damage in real-time (i.e., the seismic intensities and the drift angles of the building floors). We apply the P-wave data of a borehole of RSMS to the emergency operation control system of elevators.

1. INTRODUCTION

The Shinjuku campus of Kogakuin University is located in the downtown Tokyo, and is a high-rise building of the 29-stories with 149m of height and about 3 s of the 1st natural period (see Picture 1 and Figure 1). The building needs to prepare for the two types of large earthquakes (The Headquarters for Earthquake Research Promotion, 2007): one is M7 earthquakes under the Tokyo area, and the other is M8 earthquakes from a rather far subduction zone. The Headquarters estimated about 70% of the occurrence probability of an M7 class earthquake in the southern Kanto area for the next 30 years. When this type of earthquake occurs, it is estimated disastrous damage in the Tokyo metropolitan area (The Central Disaster Prevention Council of Cabinet Office, 2004). On the other hand, the occurrence probability of the Tokai earthquake (M8.0) for the next 30 years is estimated at 86% (The Headquarters for Earthquake Research Promotion, 2007). When the earthquake occurs, the long-period strong ground motions, which are the surface waves excited in the Kanto sedimentary basin, will vigorously shake long-period structures in Tokyo, such as high-rise buildings and oil storage tanks.

In order to reduce earthquake related damage from those earthquakes, we apply EEWS (Early Earthquake Warning System) and RSMS (Real-time Strong-motion Monitoring System) to the elevator control system of the high rise building of Kogakuin University. The Japan Meteorological Agency (JMA) distributes the EEWS information to public users staring on 1st October 2007, which are the estimated seismic intensities and the expected arrival time. On the other hand, the National Research Institute for Earth Science and Disaster Prevention (NIED) also provide the EEWS information for academic users with more detail information than those of JMA, such as the magnitude, depth, location of an earthquake (Yamamoto et al., 2005), which we use for estimating the arrival time and amplitudes of the surface waves. On the other hand, the building has RSMS for monitoring its response during earthquakes, which is also used to estimate the building damage by computing the story drift angles and the seismic intensities on each floor in real-time.

2. Emergency Operation Control Systems of Elevators and RSMS

2.1 Emergency Operation Control Systems of Elevators of Kogakuin University

The campus building of Kogakuin University has 3 types of the elevators with different emergency operation control systems. Figure 1 shows the elevation plans of the building and the 1st floor plan together with the locations of the elevators. Table 1 shows the locations of the P- and S-wave sensors and their trigger levels for the emergency control during an earthquake. When the P-wave sensors are triggered, the elevators stop by the nearest floors for about 60 s to 90 s, and automatically restart their service, if nothing happens afterward. On the other hand, when the S-wave sensors are triggered at the lower levels, the elevators also stop by the nearest floors, but do not restart without confirming the safety by the maintenance company staffs. When the S-wave sensors are triggered at the highest level, the elevators stop immediately, and thus, the people in the elevators are probably trapped. Therefore, we apply EEWS and RSMS to prevent those worst situations.

2.2 RSMS of Kogakuin University and Observation Records

Figure 1 also shows the location floors of accelerometers of RSMS with the red boxes. We will apply them to estimate the building damage by computing seismic intensities and the drift angles of the floors. The elevators for higher and middle floors do not have P wave sensors (see Table 1). Thus, we use the P wave sensor of B6F for the emergency control systems of the elevators.

Figure 2 shows the locations of the Kogakuin building, the K-Net Shinjuku station (TKY007), and the epicenter of the 2004 Chuetsu Earthquake. Figure 3 shows the observed records of RSMS and the K-Net for the earthquake. The P- and the S-waves arrived at Shinjuku at about 37 s and 59 s, respectively, after the occurrence of the earthquake. On the other hand, the surface waves arrived at about 93 s, and shaken the building with the maximum response around at 125 s. Therefore, we will have enough time for controlling the elevators before their arrival.

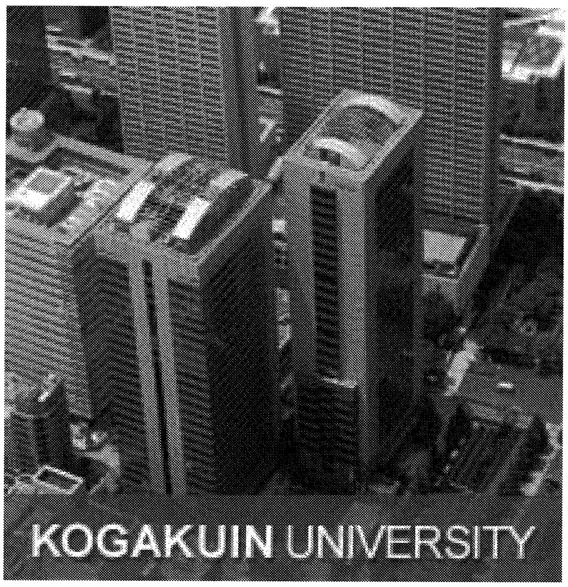

Picture 1 The Shinjuku campus building of Kogakuin University (Right) and the STEC office building (Left)

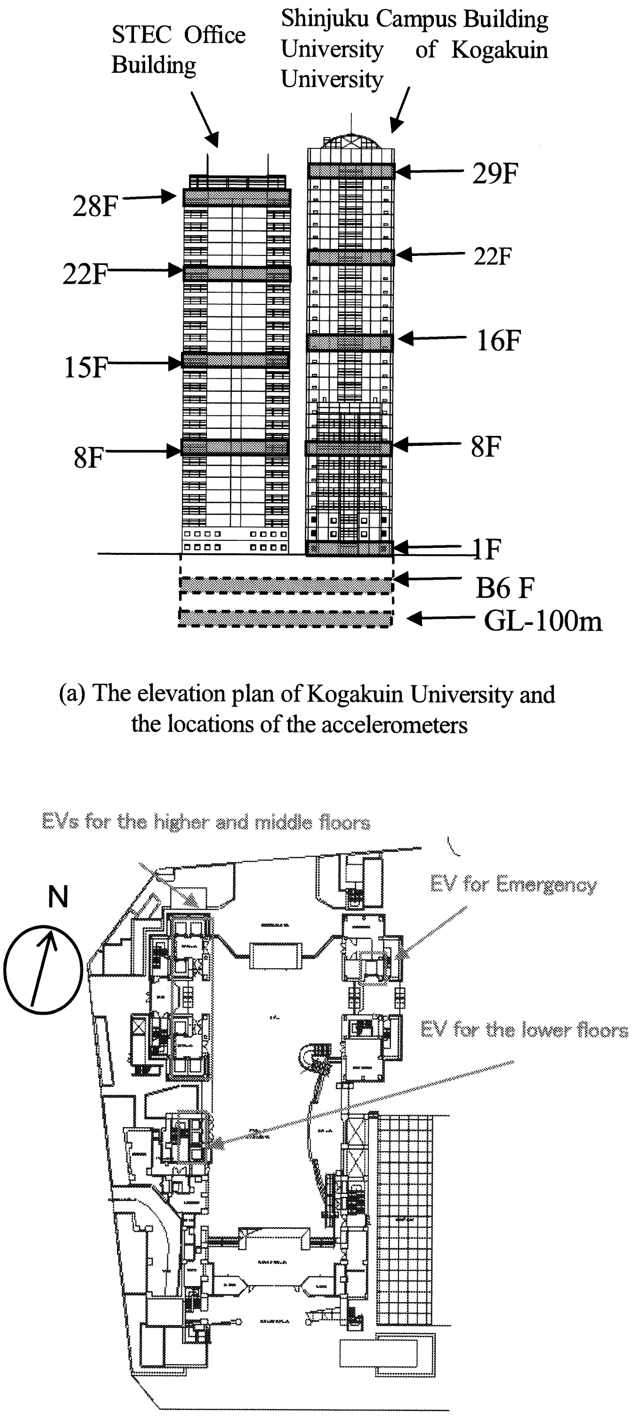

(a) The elevation plan of Kogakuin University and the locations of the accelerometers

(b) The locations of the elevators in floor plan

Figure 1 (a) The elevation plan of Kogakuin University and the locations of the accelerometers, and (b) the locations of the elevators in floor plan

Table 1 The P and S sensors, their locations and trigger levels for the emergency operation control systems of elevators of the Kogakuin University

EV type	Lowest trigger level P wave sensor	Low trigger level S Wave sensor	High trigger level S Wave sensor	Others
EVs for the higher and middle floors	No	80gal on penthouse	120gal on penthouse	Seismic Wave Energy sensor
EV for the lower floors	5gal on pit	150gal on 8th floor	No	
EV for Emergency	5gal on pit	40gal on penthouse	80gal on penthouse	

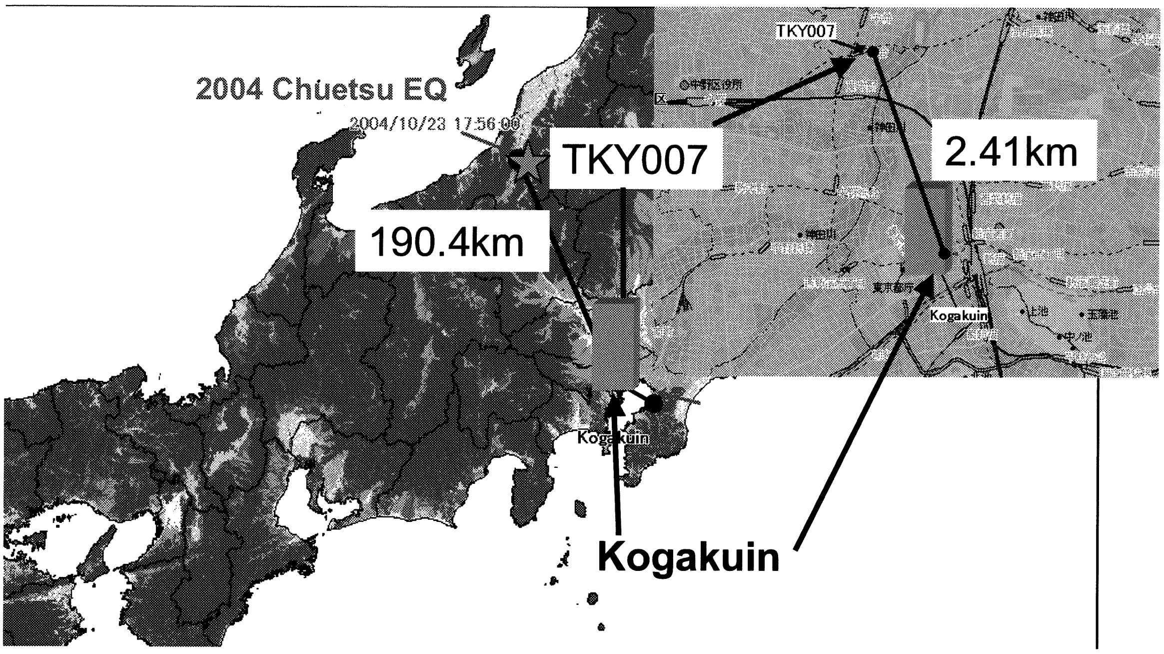

Figure 2 The location of Kogakuin Building, K-net and the seismic source in 2004 Chuetsu EQ

3. Quick Estimation of Strong Ground Motions using EEWS and Its Application to Emergency Operation Control System of Elevators

We roughly estimate the strong ground motions including the surface waves at the building site, and apply them to the emergency control systems of elevators. First we construct the librations of Green's functions for various seismic regions and the corresponding maximum response values of the building. Once an earthquake occurs, the maximum building response can be quickly computed using the source data of EEWS and the Green's function library. If the response is estimated over a certain threshold value, the EEWS server sends a signal to the emergency control systems of elevators as the lowest trigger level for stopping them at the nearest floors.

Figure 4 shows estimated strong motions for the 2004 Chuetsu Earthquake using the wavenumber integration method (Hisada, 1995) assuming the flat-layered ground structure model shown in Table 2; the model consists of the sedimentary layers of the Kanto basin (Yamada and Yamanaka, 2003) and the crustal layers of the traveltime database of NIED. Table 3 shows the source parameters from EEWS, in which the JMA magnitude is estimated using Takemura (1990) and the stress drop is the average value. Figure 4(a) shows the comparisons between the observed records by RSMS and the estimated waves, which are band pass filtered from 0.2 Hz to 1 Hz. Figure 4(b) shows the observed building response at the top floor and the simulated results using a 1-mass model, which is equivalent to 1st mode of the building (3 s of period and 2% of damping). Even though the methodology is very simple, the estimations show in good approximation in the first half of the observations (from 30s to 70s), not only in the arrival time, but also in the amplitudes. However, they do not agree well with the observed ones after 70s, probably because of the 3D basin effects. Since our purpose is to estimate the maximum building response quickly and roughly, the methodology is applicable to the emergency control systems of elevators.

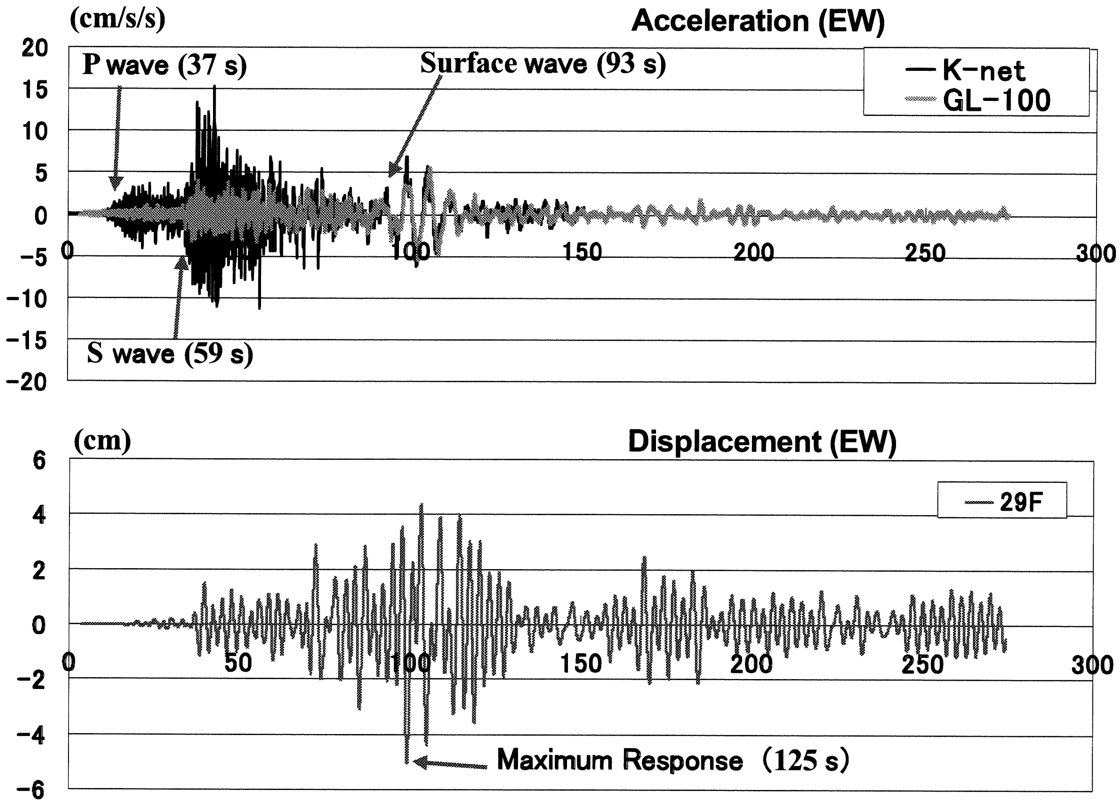

Figure 3 The observed ground accelerations (Top), and the building displacement at 29F (bottom) for the 2004 Chuetsu earthquake

Table 2 The layered structure model at the Shinjuku site

Layer Number	density(t/m3)	Vp(m/s)	Qp	Vs(m/s)	Qs	Thichness(m)	Data
1	1.85	1840	100	500	100	400	Sedimental layers at Shinjuku-ward. Yamada and Yamanaka (2003)
2	1.9	1900	100	750	100	800	
3	2	2200	200	1350	200	650	
4	2	3863	200	2287	200	650	
5	2.3	5527	300	3224	300	2500	Crustal Layers NIED traveltime database
6	2.3	5816	400	3392	400	3000	
7	2.3	6035	500	3521	500	4000	
8	2.3	6206	600	3620	600	3000	
9	2.3	6381	600	3722	600	3000	
10	2.3	6684	600	3899	600	5000	
11	2.3	7201	600	4200	600	8000	
12	2.3	7775	600	4364	600	9000	
13	2.3	7804	600	4380	600	10000	

Table 3 The point source parameter in 2004 Chuetsu Earthquake

Mjma	Depth(km)	Mo (dyne-cm)	Stress Drop (bar)	fmax (Hz)
6.8	13.2	4.74E+25	30	6

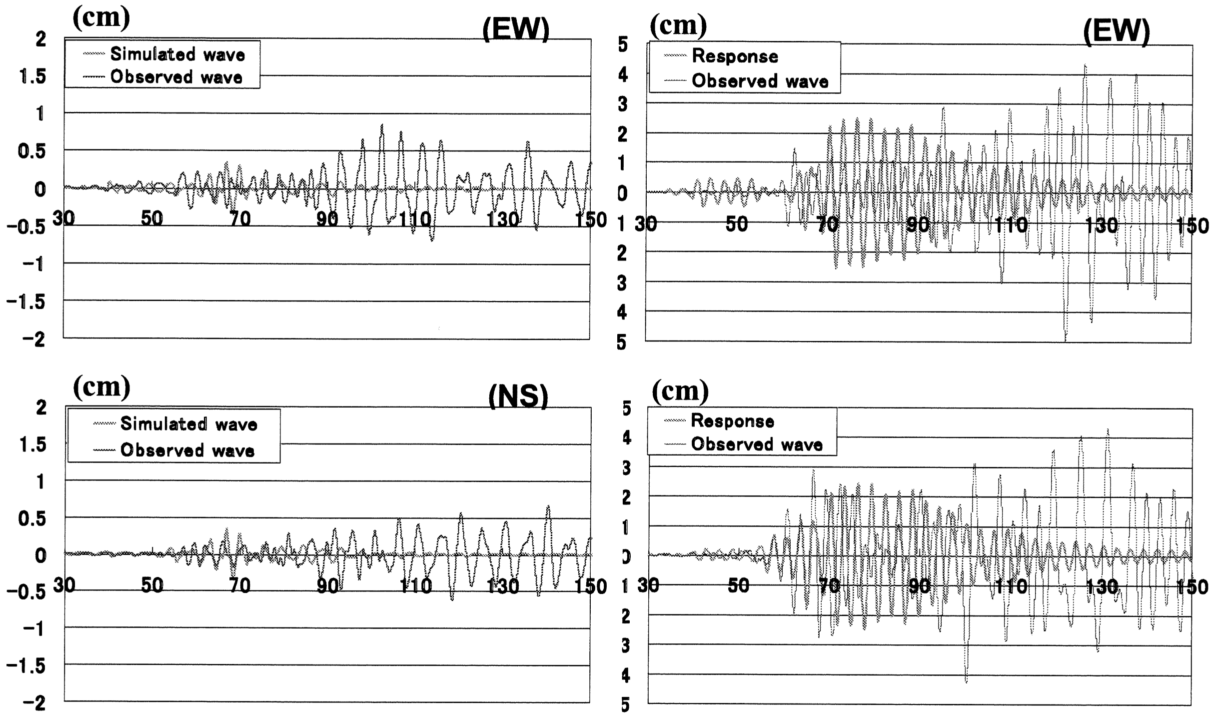

(a) Displacements at the -100 m level (b) Displacements at the 29-floor level

Figure 4 The comparison between the observed and simulated displacements for the 2004 Chuetsu earthquake

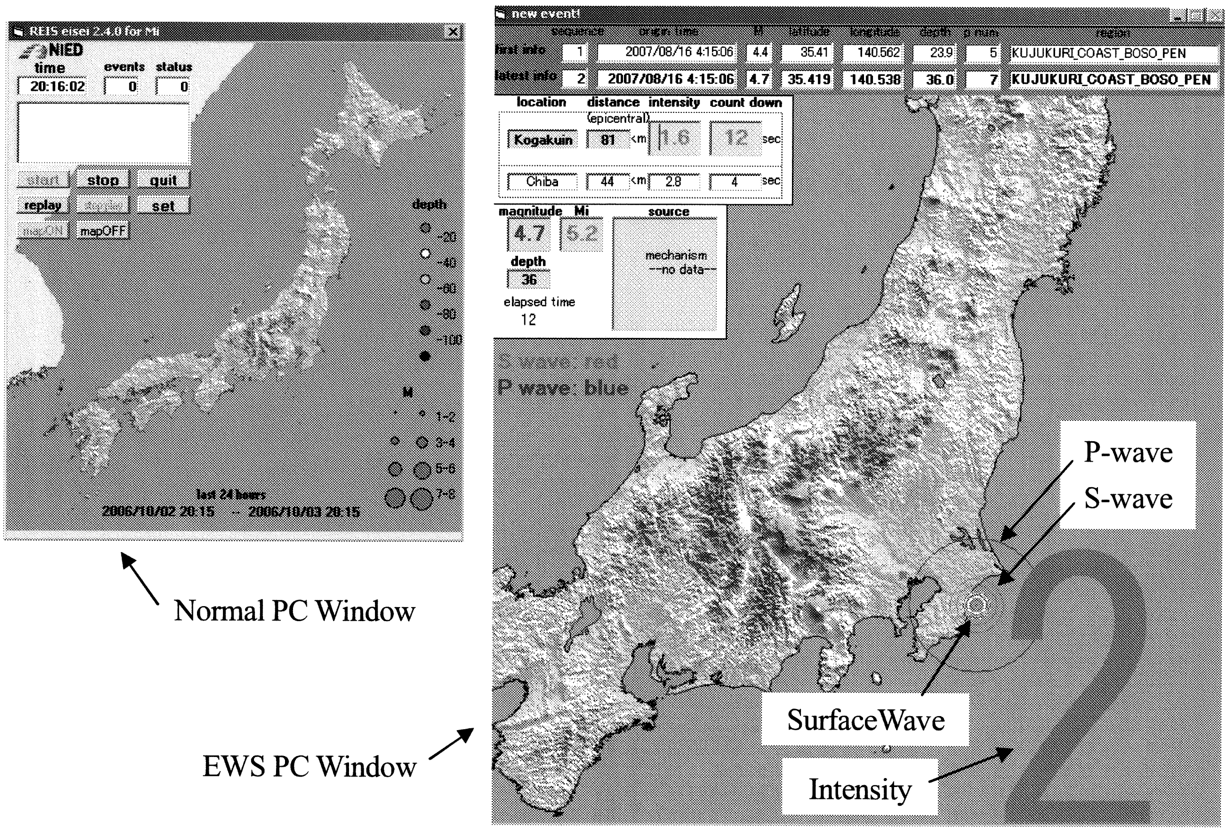

Figure 5 Early Warning System for informing the estimated seismic intensity, P-, S-, and surface waves

3. CONCLUSIONS

We applied EEWS and RSMS to the emergency operation control systems of the elevators of the high-rise campus building in downtown Tokyo by considering not only the P- and S-waves, but also the surface wave (see Figure 5). First, we used the P-wave sensor of RSMS as the lowest trigger level of the emergency control system for stopping the elevators at the nearest floors. Second, we confirmed that EEWS is especially useful for estimating the long-period strong ground motions from large earthquakes, because they are the surface waves with slow propagating speed, and thus we will have an enough time before the arrivals of the main motions. Secondly, we developed the methodology for estimating quickly the maximum building response using the source data of EEWS, a library of Green's functions, and the corresponding building response. Finally, we applied the methodology to the emergency operation control systems of the elevators. That is, once an earthquake occurs, the maximum building response can be quickly computed using the library data and the source data of EEWS. If the response is estimated over a certain threshold value, the EEWS server sends a signal to the emergency control systems of elevators as the lowest trigger level for stopping them at the nearest floors. In addition, we are planning to apply EEWS and RSMS to the announcement system to prevent a panic by providing the accurate information about the building's safety; this is important because the high-rise building will continue to shake vigorously for several minutes by the surface waves, especially for M8-class earthquakes.

Acknowledgements:

The authors acknowledge support from Japan Ministry of Education, Culture, Sport, Science, and Technology (MEXT) for establishing the Center for Urban Earthquake Engineering (CUEE) in Tokyo Institute of Technology. This research is supported by the Earthquake and Environmental Research Center of Kogakuin University funded by the Frontier Research Promotion Program of Ministry of Education, Culture, Sports, Science and Technology of Japan (MEXT), the Realtime Strong Motion Monitoring System of High-Rise building for Long-period ground motion funded by the MEXT, .a research project of Ministry of Land, Infrastructure and Transport Japan. The authors acknowledge the National Research Institute for Earth Science and Disaster Prevention for use of K-NET data.

References:

Hisada, Y., An Efficient Method for Computing Green's Functions for a Layered Half-Space with Sources and Receivers at Close Depths (Part 2), Bulletin of the Seismological Society of America, Vol.85, No.4, pp. 1080-1093, 1995

The Central Disaster Prevention Council of Cabinet Office, Conference for Shuto-Chokka Earthquake Disaster Mitigation, 2004, ((in Japanese))

http://www.bousai.go.jp/

The Headquarters for Earthquake Research Promotion, The long-term evaluation in Kanto Area, 2007, (in Japanese)

http://www.jishin.go.jp/main/choukihyoka/kaikou.htm

Takemura, M., Magnitude-Seismic Moment Relations for the Shallow Earthquakes in and around Japan, J. Seism. Soc. Jpn. (Zisin) Vol.43, pp 257-265, 1990 (in Japanese)

Yamada, N and Yamanaka, H, Ground Motion Simulation of Moderate Earthquakes for Comparison of Performance of 3D Subsurfaxe Structural Models in Kanto Plain for Strong Motion Prediction, Zisin, Vol.56, No.2, pp111-124, 2003 (in Japanese)

Yamamoto, S., Horiuchi, S., Negishi, H., and Urabe, T., Broadcasting and Receiving Systems for Earthquake Early Warning Using DVB Satellite Communication, J. Seism. Soc. Jpn. (Zisin), Vol.58, 71-76, 2005 (in Japanese)

ON-SITE ALARM – THE EFFECTIVE EARTHQUAKE EARLY WARNING

Yutaka Nakamura[1), 2)]

1) President, System and Data Research Co., Ltd., Japan
2) Visiting Professor, Dept. of Built Environment, Tokyo Institute of Technology, Japan
yutaka@sdr.co.jp

Abstract: The most important countermeasure against earthquake risk is to have all structures strong enough for the possible earthquake load. In this regard, an early warning system should be installed to reduce the possibility of earthquake disaster. An early warning system is required mainly to issue an alarm to have a time margin for evacuating or shutting down key facilities, and not to determine exact earthquake parameters. Thus the early warning system must be realized independently with On-Site alarm and the government and other public authorities must release accurate earthquake information immediately after the earthquake.

1. INTRODUCTION

There are two kinds of the earthquake alarm as in Fig.1. One is "On-Site Alarm" which is the alarm based on the observation at the side of the objects to be warned. The other is "Front Alarm" which is the alarm based on the observation near the epicentral area for the warning to possible damaged area. "Front Alarm" is transmitted by using communication networks, so the alarm is also called as "Network Alarm".

For each, there are two more kinds of alarm. One is the alarm exceeding the preset level, so-called "S-wave Alarm" or "Triggered Alarm". And the other one is the alarm during the preliminary motion, so-called "P-wave Alarm".

As the first stage of the earthquake alarm, the simple triggered alarm had been realized. This is the alarm seismometer observing the strong motion just near the objective for the alarm, and when the earthquake motion exceeds the preset level, the alarm seismometer issues the alarm. Although because of the anxiety of false alarm, it is not able to set the alarm level low and the alarm is issued almost same time to the severe strong motion, it is useful to stop the gas supply or other systems automatically.

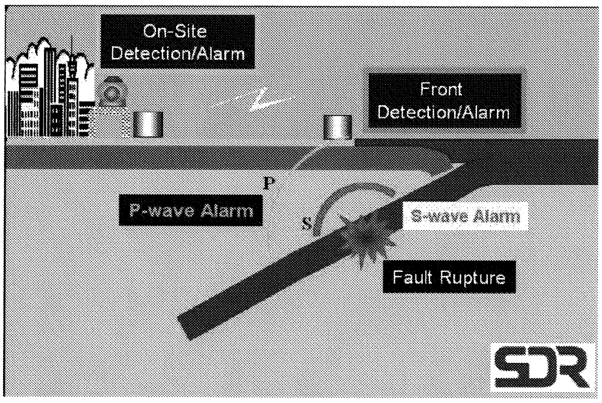

Fig.1 Comcept of Earthquake Early Warning

Next, to extend the margin time before the strong motion arrival, it was considered the way to observe the earthquake near the focal area, so-called "Front Alarm". This idea originally had been offered in 1868 by Dr. Cooper. He proposed to utilize the propagation time of the earthquake motion from the epicenter to alarmed area and support the activities for escape. More than 100 years after this original idea, the first system realizing the "Front Alarm" was developed as the coast line detection system for Tohoku Shinkansen line in 1982. After this, SAS, Sistema de Alerta Sísmica, for Mexico City started operation in 1991.

Then the next system was considered to detect the initial part of the earthquake motion and issue the alarm based on the risk of the earthquake. The first P wave detection system for practical use, UrEDAS, Urgent Earthquake Detection and Alarm System, was realized as the front alarm system for Tokaido Shinkansen line in 1992, and then almost same system was installed for Sanyo Shinkansen line in 1996.

The 1995 Great Hanshin Disaster triggered to develop earlier P wave alarm system because of the impression of necessity to make on-site P wave alarm. This is Compact UrEDAS and it was installed for Tohoku, Joetsu and Nagano Shinkansen lines and Tokyo metro subway network.

And then Wakayama prefecture decided to install UrEDAS for their own tsunami disaster prevention system and started test operation in 2000.

As the new generation of UrEDAS and Compact UrEDAS, the new small-sized instrument FREQL, Fast Response Equipment against Quake Load, is developed to shorten the processing time for alarm and to combine the functions of UrEDAS and Compact UrEDAS. After P wave detection, FREQL can issue the alarm within one second (minimum in 0.2 seconds) and estimate the earthquake parameters at one second. Since 2005, FREQL has been adopted for the hyper rescue team of Tokyo fire department to save the staffs from the large after shocks during their activity. The hyper rescue teams are famous of the salvage of the child from the land slide after the 2004 Niigataken Chuetsu Earthquake, and they were afraid of the hazard caused by the aftershocks at that time.

On the other hand, it is necessary for local facilities to grasp immediately their "own" strong motion index for the quick response. For this purpose, a simple seismometer "AcCo", Acceleration Collector, was developed. This unique palmtop seismometer has a bright indicator, memory and alarm buzzer and relay connecter.

On-Site alarm is more important than network alarm, because network alarm is sometime missed during data communication. From the view of this, it is not enough to receive the Earthquake Early Information from JMA, Japan Meteorological Agency, EEI. Contrary with this, FREQL has both functions of UrEDAS and Compact UrEDAS for On-Site Alarm and Network Alarm. And also AcCo has simple alarm functions for On-Site Alarm.

Fig.2 shows systems of EEW: UrEDAS, Compact UrEDAS, FREQL and AcCo.

2. Principal EEW: UrEDAS, Compact UrEDAS and FREQL

2.1 UrEDAS

Main UrEDAS functions are estimation of magnitude and location, vulnerability assessment and warning within a few seconds of initial P wave motion at a single station. Unlike the existing automatic seismic observation systems, UrEDAS does not have to transmit the observed waveform in real time to a remote processing or centralized system and thus the system can be considerably simplified.

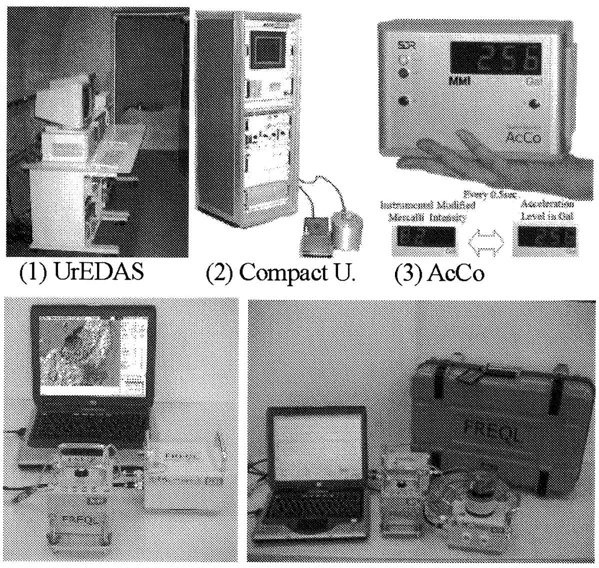

(1) UrEDAS (2) Compact U. (3) AcCo

(4) FREQL (5) FREQL of Portable Type

Fig.2 UrEDAS, Compact UrEDAS, FREQL and AcCo

UrEDAS calculates parameters such as back azimuth, predominant frequency for magnitude evaluation and vertical to horizontal ratio for discrimination between P and S waves, using amplitude level for each sampling in real time. These calculations are basically processed in real time without storing waveform data. UrEDAS processes these calculation continuously regardless of whether or not an earthquake occurs, and calculates just like filtering, so the number of procedures is not increased in the event of an earthquake. UrEDAS can detect earthquakes in P-wave triggering with the amplitude level, and then estimates earthquake parameters such as magnitude, epicentral and hypocentral distance, depth and back azimuth from the result of real-time calculation in a fixed period. UrEDAS can issue an alarm based on the M-Δ diagram as in Fig.3 immediately after earthquake detection. This new way of alarm is referred to as the M-Δ Alarm. Moreover UrEDAS can support restarting operation based on the detailed earthquake parameters.

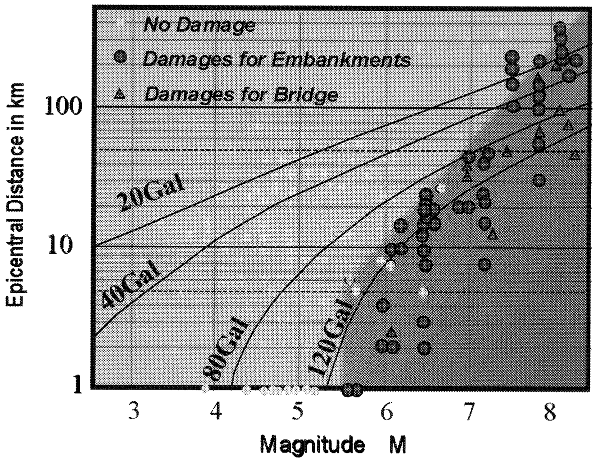

Fig.3 M-Δ Diagram

Fig.4 Video Photos examples at focal region

The 1995 Hyogoken-Nanbu Earthquake also provided the motivation for Compact-UrEDAS development. Fig.4 shows several pictures from the VTR shoot in the focal region, initial P-wave motion was detected as something happening, and then severe motion started. In an interview with victims, although there were only a few seconds between detection of something happening to earthquake recognition, there was anxiety and fear because they could not understand what was happening during this period and felt relieved after recognition of earthquake occurrence. To counter this kind of feeling, earlier earthquake alarm was required: Compact UrEDAS was developed to issue the alarm within one second of P-wave arrival.

2.2 Compact UrEDAS

Compact UrEDAS estimates the expected destructiveness of the earthquake immediately from the earthquake motion directly, not from the earthquake parameters as UrEDAS, and then issues the alarm if needed. To estimate earthquake dangerousness, the power of the earthquake motion is calculated from the inner product of acceleration vector and velocity vector, but this value will be large. Hence Destructive Intensity (DI) is defined as the logarithm of absolute value of this inner product as in Fig. 5.

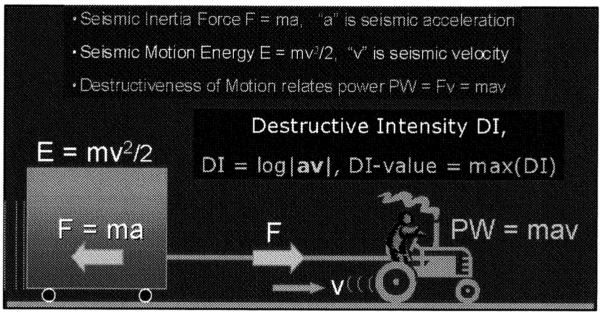

Fig.5 Definition of DI

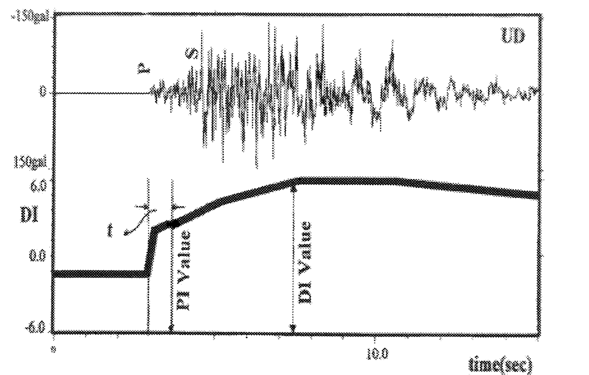

Fig.6 Change of DI

Fig. 6 shows the change of DI as a function of time. When the P wave arrives, DI increases drastically. PI value is defined as maximum DI within t seconds after P-wave detection. This value is suggested to be used for P-wave alarm. Subsequently, DI continues to increase slowly until the S-wave arrival, after which it reaches its maximum value which is called the DI value. This value relates to earthquake damage and is similar to the Instrumental Intensity scale of JMA or MMI, Modified Mercalli Intensity. Instrumental JMA seismic intensity can be determined only after the earthquake has terminated. On the other hand, DI has a very important practical advantage, because it can be calculated in real time soon after the P-wave arrival with physical meaning. In other words, with the continuous observations of DI, an earthquake alarm can be issued efficiently and damage can be estimated precisely.

2.3 FREQL

FREQL is integrated the functions of UrEDAS, Compact UrEDAS and AcCo. Which is to say that FREQL can estimate the earthquake parameters one second after the P wave detection faster than UrEDAS, can judge the dangerousness of the earthquake motion within one second, minimum in 0.2 seconds, after P wave detection faster than Compact UrEDAS, and can output the information and alarm based on both acceleration and RI, Realtime Intensity, in real time same as AcCo.

And the all components of seismometer, sensors, A/D converter, amplifier, CPU and so on, are put together in small aluminum die-cast vessel of almost 5 inches cube, and the system is electrical isolated. So the FREQL is easy to install and the structure of FREQL is noise proof.

FREQL also has functions to omit the influence of electrical thunder noise and to detect the P wave after rather small pre-shock. Thus it is able to say that FREQL solved the known problems of the ordinary earthquake early warning systems. It is known that there was a pre-shock at the time of the 1994 Northridge earthquake attacked Los Angels and the 1995 Hyogoken-Nanbu Earthquake attacked great Hanshin area. It seems to be failing for the early warning system except FREQL that it is not possible to issue the alarm for large earthquake motion if the pre-shock exists just before the destructive earthquake because the pre-shock is recognized as small event. And also it seems to be difficult for the huge system to keep running perfectly under the destructive earthquake motion. It is uncertain only with such remote systems because of information lack. It must be considered on installing the onsite warning system for the important facility.

FREQL is toward to the new field for the early warning system, as for the hyper rescue teams of Tokyo fire department under the severe situation with the risk of aftershocks (see Fig. 7).

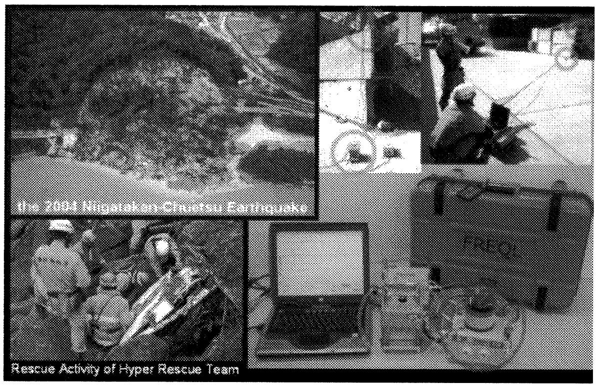

Fig.7 New Field for EEW

Hyper rescue teams made a miraculous activity but the activity was always in a risk of large after shocks. After the activity at the damaged area of the 2004 Niigataken-Chuetsu Earthquake, the Tokyo fire department approached us to adopt FREQL as a support system for the rescue activity, taking notice of the portability, rapidness and accuracy of the warning. FREQL for Tokyo fire department was consists of FREQL main body, power unit with backup battery for three hours, central monitoring system and the portable alarm instrument with more than 105dB loud alarm and rotary light.

Tokyo fire department has equipped the FREQL unit form spring of 2005, and since 2007, three hyper rescue teams is operating. At the time of their rescue activity after the 2005 Pakistan earthquake, they reported that FREQL works in right manner. Now, there are many FREQL of portable type equipped at local fire stations in Japan.

And the FREQL of permanent type are used in many field such as subway, nuclear power plant, high-rise building, semiconductor facilities, and etc., in Japan.

Now, in Berkeley and in Pasadena, FREQL has started test observation. These projects are doing under the support by UC Berkeley and Caltech. I hope this FREQL network growth to Pan-Pacific Tsunami Warning System.

2.4 AcCo

Because usual seismometers were expensive and required an expert of installation and maintenance, so they were installed for limited facilities. After the Kobe earthquake, the number of seismometer was increased but at most thousands sets for whole Japan. It is not so much because it means one set per several tens km^2 or per several ten thousands person. Even so there are many seismometers in Japan, but many hazardous countries have only a few seismometers. So it is difficult to take exact countermeasure against earthquake disasters because it is impossible to grasp and analysis the damage based on the strong motion records and to draw a plan of the city with certain strategy.

AcCo was developed to realize a simple seismometer to issue alarm and record the strong motion in low cost. Since AcCo is just a palmtop size instrument, it can indicate not only acceleration but also the world's first real time intensity. So AcCo can issue alarm with the trigger of both acceleration and intensity.

AcCo indicates acceleration and intensity if the 5HzPGA (5 Hz low passed peak ground acceleration) exceeds 5 Gals as in Fig.2(3). Intensity can be chose from RI, MMI or PEIS, Philippine Earthquake Intensity Scale. AcCo can output the digitized waveform via serial port and also record the waveform for the two largest events with delay memory. AcCo can work with AC power supply and backup battery for seven hours.

Because AcCo indicates acceleration as inertial force and RI as the power of the earthquake motion, it is useful to learn the sense for the meaning of acceleration and intensity from the experience. This sense is required for the exact image against the earthquake motion.

AcCo is applied for many fields as warning system, education, kindergarden, factory, train operation and so on. And also AcCo is used not only in Japan but also in out side of Japan for a instance, Taiwan, Philippine and etc..

2.5. Alarm timing and margin time gained by EEW

In case of the system requiring the earlier warning with no error or accidental warning, it is necessary to install a system with high reliability and sophisticated as FREQL. But in general, it seems to be useful even the simple warning system in general. This kind of system seems to be useful enough in many cases under the situation of several alarms per year even in higher seismic activity area of Japan. AcCo 10 Gals alarm or RI 2.0 alarm can play the role of this simple early warning. Fig.8 shows the relationship example between the alarm timings. Since the AcCo 10 Gals alarm or RI 2.0 alarm is a little later than the P wave alarm of FREQL, it is enough earlier than the ordinary triggered S wave alarm.

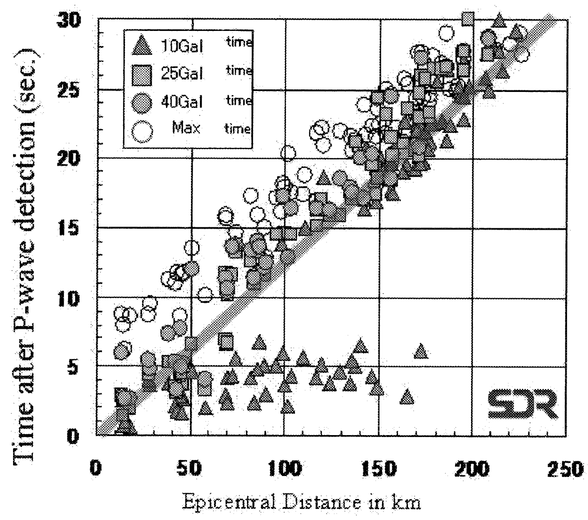

Fig.8 An example of alarm timings by simple triggers in case of the 2000 Tottoriken-Seibu Earthquake

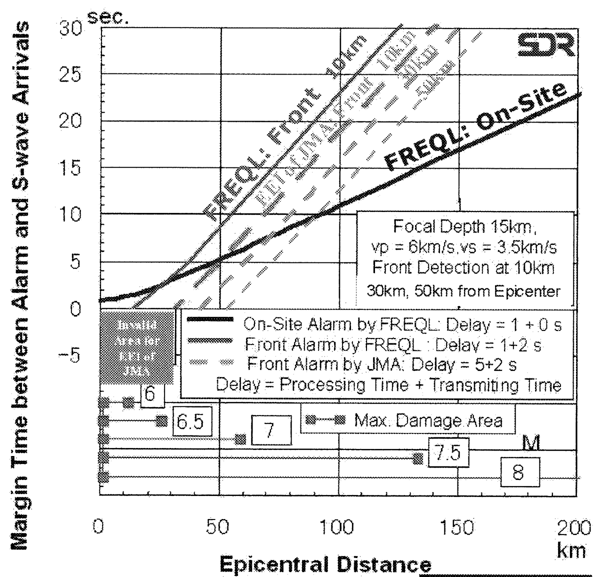

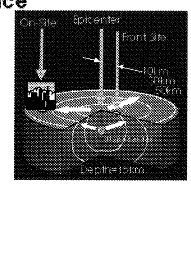

Fig.9 Margin time by EEW

Fig.9 shows gained margin time by EEW. Basic condition for calculating margin time is assumed as follows: focal depth is15km, velocity of P-wave and S-wave are vp = 6 km/s and vs = 3.5 km/s, respectively, front detection site at 10 km, 30 km and 50 km from the epicenter.

Based on the calculation for 10km, EEI of JMA comes after S wave arrival within a 30 km radius as confession by JMA. On-Site alarm by FREQL can keep at least more than one second even just above the epicenter; and more margin time than front alarm by JMA within about 55 km radius from the epicenter. This distance corresponds for out line of the damage area for over M7. It means that the EEI of JMA is not available the estimated damaged area up to M7, so it seems that it is not useful for the recent Japanese earthquake in this 20 years. Contrary to this, the on-site FREQL alarm is available even around the focal area; of course the margin time is just a few seconds. So we should take a hard look at the on-site alarm and put it into practical use. It is also useful for popularization of earthquake disaster mitigation. It seems that there are many fields not so effected by false alarm if reset easily. Official information as correct location and magnitude must be informed within few minutes for the exact clear of the alarm. And this kind of information must keep suitable redundancy so there must be informed from several organizations.

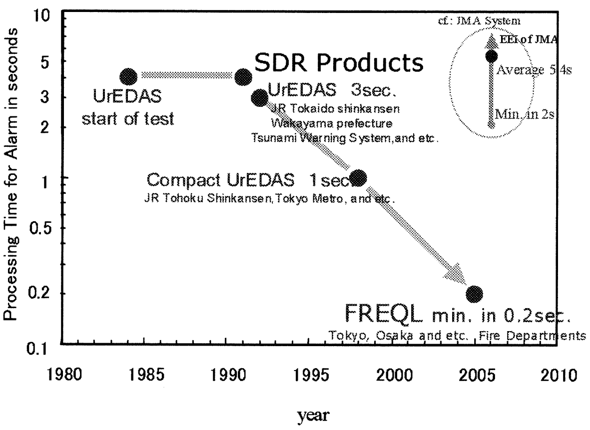

Fig.10 Change of processing time for EEW

3. Practical Operation Example of Compact UrEDAS

At the time of the 2004 Niigataken Chuetsu Earthquake, Mjma 6.8, there were four trains running in the focal area. There are four observatories called Oshikiri SP, Nagaoka SSP, Kawaguchi SS and Muikamachi SP, from north to south. Of these stations, Kawaguchi and Nagaoka issued both the P-wave and the S-wave alarms, and the others issued only the S-wave alarm. Every station issued the alarm for the section to the next station (see Fig.11). At first Kawaguchi and then Nagaoka issued the P-wave alarm. Subsequently, Oshikiri and Muikamachi issued the 40 Gals alarm. As the result, trains Toki #325 and #332 received the alarm 3.6 seconds after the earthquake occurred, Toki #406 4.5 seconds after and Toki #361 11.2 seconds. The

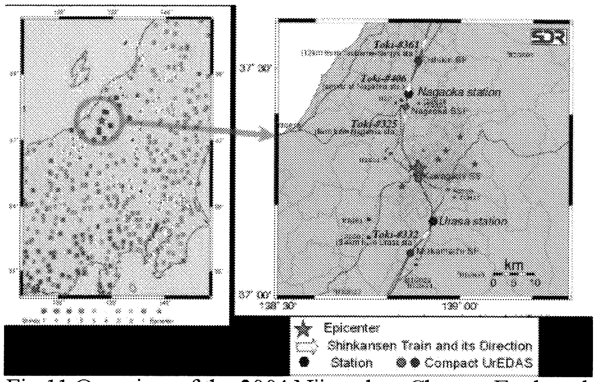

Fig.11 Overview of the 2004 Niigataken-Chuetsu Earthquake

section damaged was between Muikamachi and Nagaoka. Trains traveling on this section received the alarm immediately, proving that the alarm system settings were appropriate.

The UD component of earthquake motion predominate the high frequency more than 10 Hz. The Shinkansen line runs from north to south and the EW component seems to effect derailment. In the case of the EW component, there is a peak at 1.5 Hz and the range of 1 to 2.5 Hz predominates. The natural frequency of the Shinkansen vehicle is included this frequency range.

The Kawaguchi observatory detected the P wave 2.6 seconds after the earthquake occurred, and one second after that, or 3.6 seconds after the event, issued a P-wave alarm. When the derailed train, Toki #325, encountered the earthquake motion when traveling at 75 m from the Takiya tunnel exit of 206km000m, it was three seconds after earthquake occurrence. 3.6 seconds after the earthquake, the train received the alarm from the Compact UrEDAS and the power supply was interrupted. The Shinkansen train situated automatically to apply the break immediately at the interruption of power supply. The driver put on the emergency brake after recognizing the Compact UrEDAS alarm. The S-wave hit the train 2.5 seconds after the alarm, and more one second later, a strong motion with five seconds duration hit the train. Fig.12 shows the schematic

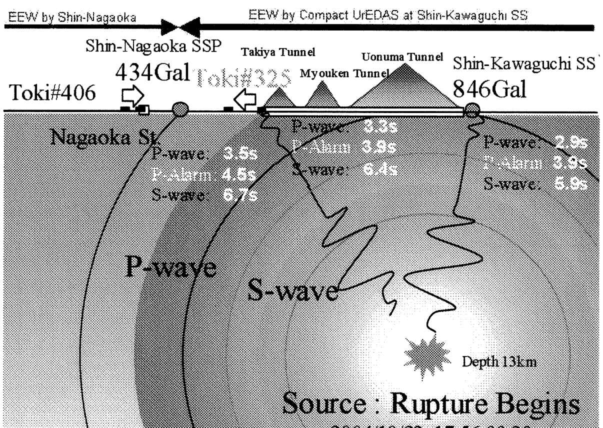

Fig.12 Schematic diagram for this earthquake

diagram for this earthquake.

As the result of simulation using the strong-motion records at Kawaguchi and Nagaoka, real-time intensity (RI) rose sharply with the earthquake motion arrival and immediately reached the P-wave alarm level. This RI is a real-time value and the maximum value fits the instrumental intensity of JMA. Because FREQL, the new generation of Compact UrEDAS, improves the reliability of P-wave distinction, FREQL can issue the alarm immediately after the P-wave alarm threshold is exceeded. If FREQL had been installed instead of Compact UrEDAS, both Kawaguchi and Nagaoka observatory would issued the P-wave alarm 0.2 and 0.6 seconds after P-wave detection, respectively. Table 1 summarizes the simulation results. In this case, the P-wave alarm reached the derailed section before P-wave arrival. Accordingly, FREQL minimizes

Table 1 Summarize the simulation results

Alarm and Accident Site	Kawaguchi	Tunnel Exit	Nagaoka
5HzPGA (Gal)	846		434
RImax (MMI)	6.6 (10.9)		5.8 (9.6)
Origin Time	17:56:00.3	17:56:00.3	17:56:00.3
Recorded Detecting Time	3 s		4 s
P-wave arrival Time	2.9	3.3	3.5
Time of RI >2	3.1		4.1
P-wave Alarm Time	3.9	3.9	4.5
Time of Max. Acc >10Gal	3.4		4.7
Time of Max. Acc >40Gal	4.2		5.9
Time of 5HzPGA	7.7		9.4
Time of RImax	8.1		9.5

the process time for alarm.

Fig.13 shows the details of the derailment. The derailed train, Toki #325, consisted of 10 cars, from car #10 to car #1 along the traveling direction. The number of derailed axles is 22 out of a total of 40 axles. The last car, #1, fell down the drain besides the track and tilted by about 30 degrees. The open circle indicates the location of broken window glass. The quantity of broken grass appears greater on the left due to the something bounce from the sound barrier, and tends to break one or two cars after the derailed car. The amount of broken glass from car #1 is exceeded by that of car #2.

If it is assumed that the glass broken of car #2 was caused by the derailment of cars #4 and #3, the paucity of broken glasses from car #1 suggests that car #2 did not derail during the earthquake motion. It is estimated that the frictional heat between the vehicle and the rails caused elongation and slightly rift up at the joints of 206km700m, and car #1 derailed, making car #2 derail.

Deformation performance of viaducts is specified within one cm under the loading of the seismic design force. Although the designed natural frequency corresponding to the deformation performance is 2.5 Hz, in practice it is 3.5 Hz. The viaduct may thus be considered to behave statically against the earthquake motion less than around 1.5 Hz. Fig.14 shows the relative deformation derived from the dimension of the viaduct columns. The meshed line shows the averaged deformation for each viaduct block, and it is estimated that the relative large occurred at the area

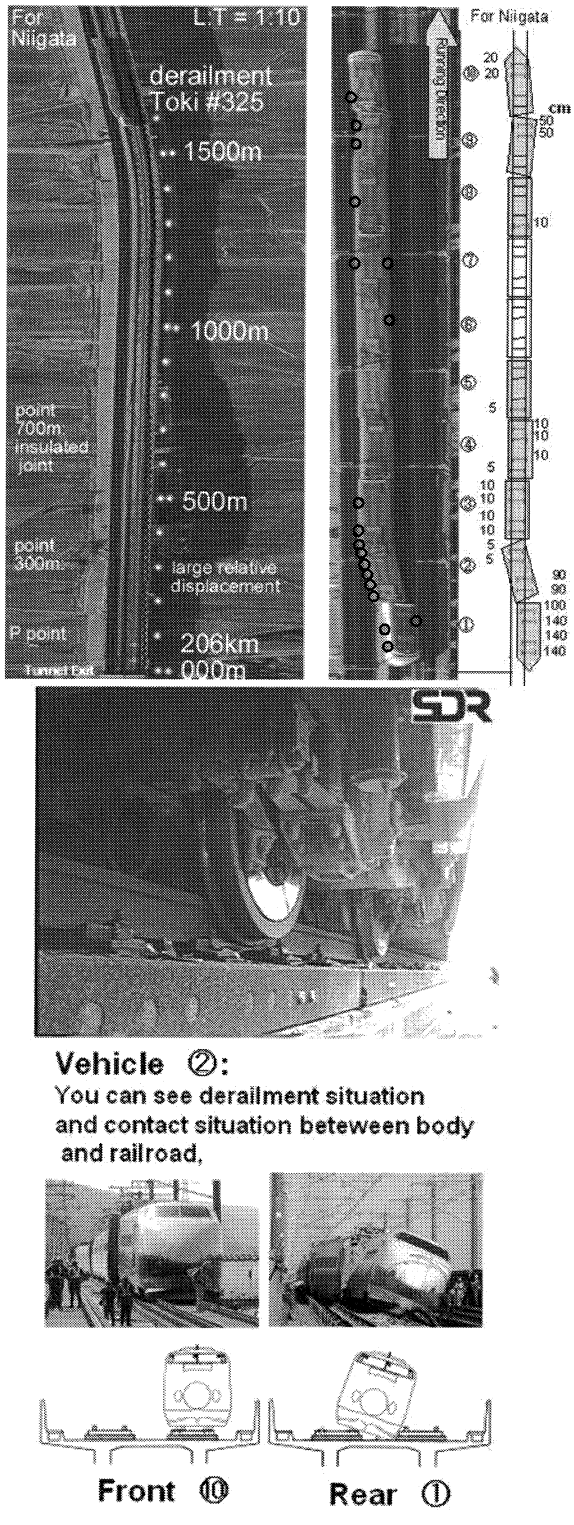

Fig.13 Detail of the derailment

farther from the tunnel exit. Taking into account the timing of earthquake occurrence, this is the point of derailment.

Fig.15 outlines the circumstances of the derailment. It seems that the derailed cars were on the large displacement section accidentally. The later the alarm reached, the more the number of derailed car, because of the risk of running the

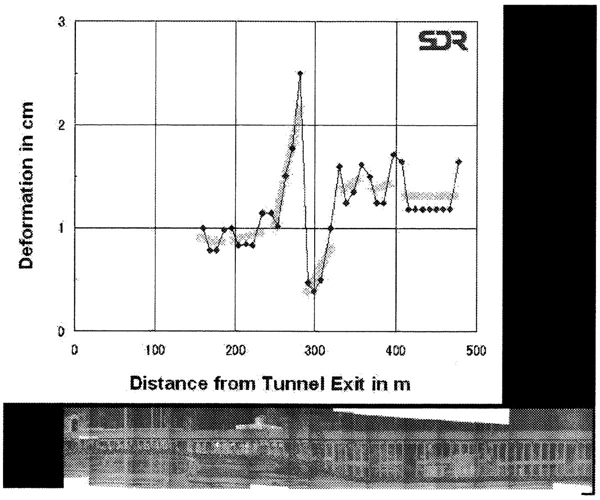

Fig. 14 Performance of the deformation

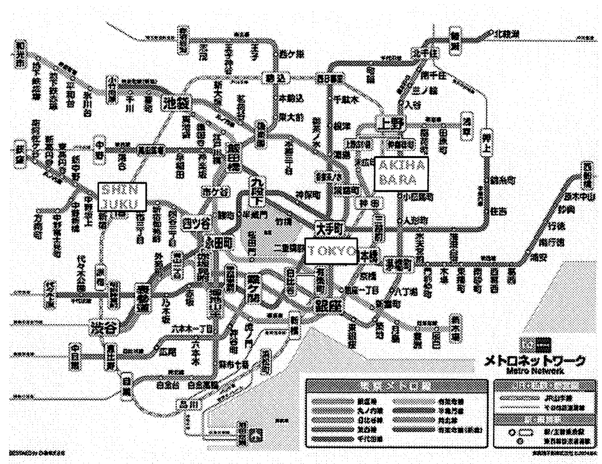

Fig. 16 Subway network of Tokyo Metro Company

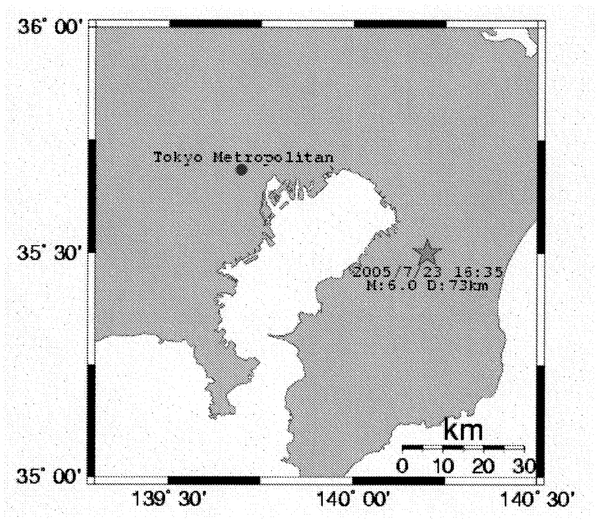

Fig. 17 The 2005 Chiba North-West Earthquake

large displacement section. As a result, if the friction heat release value were higher, the derailment situations were more severe. On the other hand, the early warning slows the train down, which means that the main shock hits the train before the large displacement section and decreases while the train travels the section. The number of the derailed cars is thus expected to decrease and the derailment damage must be minor. In this regard, the P-wave alarm of the Compact UrEDAS demonstrates its effectiveness at making the derailment non-catastrophic.

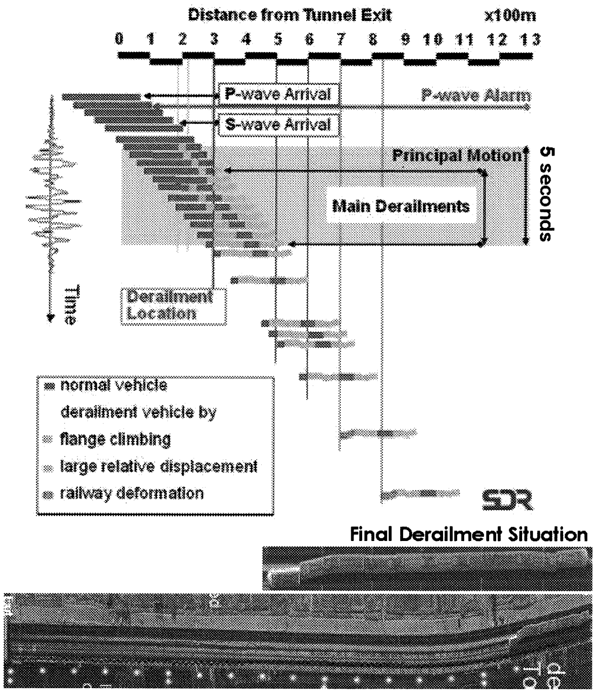

Fig. 15 Estimated situation of the derailment

4. An Example of Integrated Systems for EEW and Quick Response against Strong Motion

Tokyo Metro, Subway Company, built the new earthquake early warning/quick response system based on the experience of the 2005 Chiba north-west earthquake, Mjma 6.0. Tokyo Metro network is the core of the railway transportation system for the entire Tokyo metropolitan area as in Fig. 16.

In July 2005, the earthquake attacked the Tokyo metropolitan area as in Fig. 17. This earthquake occurred at 35.5N and 140.2E with about 73km in depth, and the maximum JMA intensity was 5+ corresponding to MMI VIII approximately. This earthquake occurred at north-west of Chiba prefecture and caused a traffic disturbance widely in Tokyo metropolitan area. All the train operation had been stopped for a long time after the earthquake, although a severe damage was not caused even in the area of high intensity. The longest down time for the train operation was more than seven hours. That of Tokyo Metro was four hours.

Tokyo Metro had to check all track on foot, because the control reference value for train operation exceeded.

The value of Tokyo Metro is 100Gal of 5HzPGA. This value varies by Train Company. To check the track on foot is the reason why had all train operation been stopped for a long time.

After the earthquake, we proposed a new system for early warning and quick response with basic idea as follows. It is necessary for the control against the earthquake to equip the system not only to issue the early warning but also to support the quick and rational recovery work after the earthquake. Tokyo Metro Company accepted our proposal, and replaced and built the new early warning/quick response system as followed.

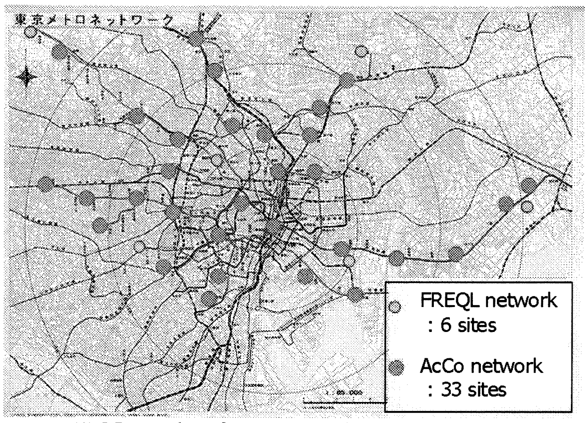

(1) Networks of FREQL and AcCo

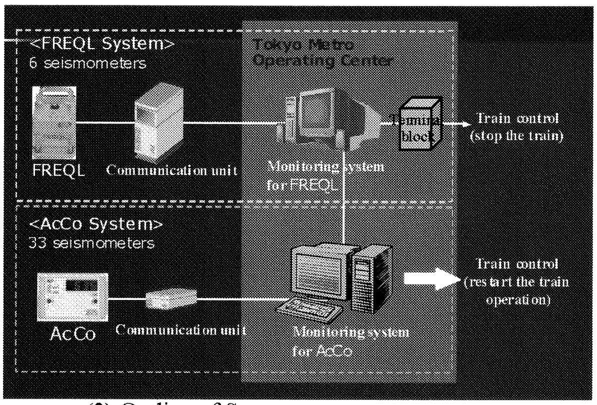

(2) Outline of Systems

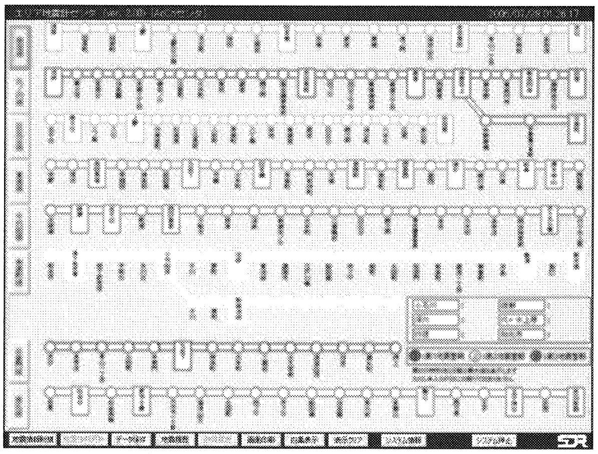
(3) Monitoring System for AcCo

Fig.18 New Earthquake Early Warning System

The system consists of two seismometer networks as shown in Fig.18. One is the early warning system network consisting six sets of FREQL to control or stop the train operation immediately after the earthquake occurrence. And the other is the network of the portable digital seismometer consisting of 33 sets of AcCo in every about three kilometers mesh to grasp more detailed seismic motion on their service area.

The information from both FREQL network and AcCo network are gathered to the operation center and displayed on the individual monitoring system. The monitoring system for AcCo can indicate the integrated information from AcCo and FREQL on the subway network image. The AcCo monitoring system is also installed on the control table for each subway line.

At the time of the earthquake, the early warning system detects at first the earthquake immediately and then the 33 local seismometers inform the actual earthquake motion of each site independently and rapidly as in Fig.19. This system realized quick response and restart of the train operation because the early warning became faster and checking zone after earthquake was optimized. This updated system is expected to realize quicker response during and after.

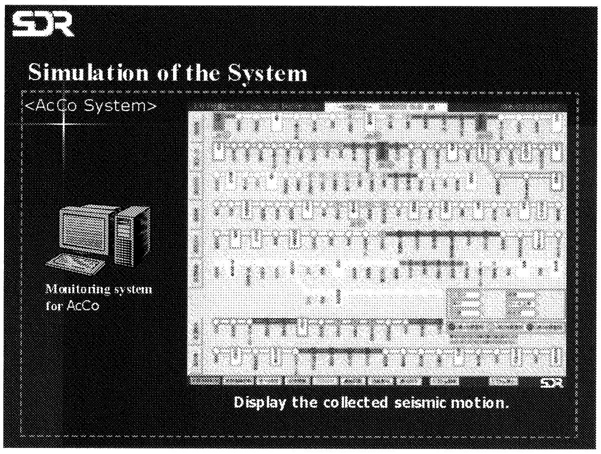

Fig.19 Display example when earthquake occurred

For the large system as the train operation, it is necessary for the control against the earthquake to equip the system not only to issue the early warning but also to support the quick and rational recovery work after the earthquake.

5. Discussion

It seems that the difference between real time seismology (RTS) and real time earthquake engineering (RTEE) is the way of contribution indirectly or directly for practical use, as same as the difference between science and engineering. RTS makes the countermeasure soon after the earthquake rational and prompt by sending information universally to be useful for public. And RTEE sends the information for certain customers as a trigger of the countermeasures against the earthquake disaster. From the view of time domain, RTS is required by the rational action after the earthquake terminated and RTEE is necessary for the immediate response just after the earthquake occurrence or earthquake motion arrival.

RTS needs high accuracy on the information but not immediate, so it is possible to utilize effectively the knowledge and experience on seismology and infrastructures as observation networks. The task are to be more accurate the information on the earthquake observation and to deliver rapidly to all people.

On the other hand, the most important aim of RTEE is to decrease the degree of the disaster or the possibility of the disaster occurrence so it is necessary to issue alarm rapidly and certainly. For this purpose, at first it must be concerned to install own observation system for the alarm, without relying the information from the other authorities. And then, it is possible to use the other information if it can be received. It is necessary to customize the way of issuing and utilizing the alarm depends on the situation for each customer and fields. Again, it is risky to rely to the information only from the other authorities using the data transmission network under the situation of earthquake.

In Japan, JMA has started delivering the EEI, Earthquake Early Information, on 1st October 2007. It is clear that EEI is belonging to RTS. So it is only a result of earthquake observation and must be delivered widely for public with no restriction for receiving. Since for some case, it may be possible to use it as alarm, but generally to say, EEI is mainly for the rational countermeasures after earthquake termination. It must be used for release of the EEW by the people quickly if the alarm is not needed. From the view of this, the most important is accuracy and the delay of few seconds is not a problem, because the error of this kind of information may cause a serious confusion. It is enough that the accurate information is delivered within one or two minutes after the event. Alarm must be released rationally and EEI may play an important role as one of the useful tools for this.

It is necessary to grasp the distribution of earthquake motion at the early stage. It is recommended to progress the earthquake disaster prevention with the combination of the public information such as EEI by JMA rather late and local dense and quick information by the people.

Acknowledgements:

Many thanks are due to those people and organizations involved in the our developing project for Earthquake Early Warning

References:

Nakamura Y., Earthquake Warning System of Japanese National Railways (in Japanese), Railway Technology, Vol.42, No.10, pp.371-376, 1985.

Cooper, J.D.: Earthquake Indicator, San Francisco Daily Evening Bulletin, 3rd November 1868.

Nakamura, Y.: Earthquake Early Warning and Derailment of Shinkansen at the 2004 Niigataken-Chuetsu Earthquake (in Japanese), Jishin Journal, No.41, pp25-37, Association for the Development of Earthquake Prediction, June 2006.

Nakamura Y., UrEDAS, Urgent Earthquake Detection and Alarm System, Now and Future, 13th WCEE, paper #908, 2004.

Nakamura Y., On a Rational Strong Motion Index Compared with Other Various Indices, 13th WCEE, paper #910, 2004.

Fifth International Conference on Urban Earthquake Engineering
March 4-5, 2008, Tokyo Institute of Technology, Tokyo, Japan

EFFECT OF LONG-DISTANCE SUMATRA EARTHQUAKES ON HIGH-RISE BUILDINGS IN SINGAPORE

Tso-Chien Pan[1], Kusnowidjaja Megawati[2], and Chee Leong Lim[3]

1) Professor, School of Civil & Environmental Engineering, Nanyang Technological University, Singapore
2) Assistant Professor, School of Civil & Environmental Engineering, Nanyang Technological University, Singapore
3) Research Fellow, School of Civil & Environmental Engineering, Nanyang Technological University, Singapore
cpan@ntu.edu.sg, kuno@ntu.edu.sg, cheeleong@ntu.edu.sg

Abstract: Singapore is located in a low-seismicity region. However, tremors caused by distant Sumatran earthquakes have reportedly been felt in Singapore for many years. This paper reports one the ground motions recorded in Singapore due to the recent Southern Sumatra earthquake (M_w = 8.4) of 12 September 2007. Based on previous studies for Singapore, the maximum credible earthquakes (MCEs) from Sumatra have been hypothesized to be a subduction earthquake (M_w = 9.0) and a strike-slip earthquake (M_w = 7.5). Response at a soft soil site in Singapore to the synthetic bedrock motions corresponding to these maximum credible earthquakes are simulated using a one-dimensional wave propagation method based on the equivalent-linear technique. A typical high-rise residential building in Singapore is analyzed to study its responses subjected to the MCE ground motions at both the rock site and the soft soil site. At the rock site, the earthquake ground motions are hardly a problem to the building. However, at a soft soil site, the MCEs may cause some columns being overstressed and cracking on the infill walls. Even though the base shear forces caused by the earthquake ground motions would exceed the notional horizontal load requirement in BS 8110 code, the capacity of column members designed under the gravity loads are sufficient to resist the lateral load.

1. INTRODUCTION

The 1985 Michoacan earthquake, in which a large earthquake (M_s = 8.1) along the coast of Mexico, caused destructions and loss of lives in Mexico City, 350 km away from the epicenter. Learning from the Michoacan earthquake, it has been recognized that urban areas located rather distantly from earthquake sources may not be completely safe from the far-field effects of earth tremors. Singapore is located in a low-seismicity region, where the closest active seismic sources are located more than 400 km away, along and off the western coast of Sumatra. Earthquakes in Sumatra, some of which had magnitudes as low as 6.0, have frequently shaken high-rise buildings in Singapore, especially those founded on Quaternary marine clay deposits and reclaimed lands. No structural damage, however, has been reported (Pan 1995, Pan et al. 2001). Although seismic hazard from such distant earthquakes in terms of ground shaking is considerably low, seismic risk in terms of damage potential to structures, loss of lives and assets cannot be ignored because of the high concentration of population and commercial activities taking place in structures that have not been designed specifically for seismic loads. Currently, building design code for structures in Singapore has been developed largely based on the BS8110 Code (BSI 1987), which does not provide seismic loadings.

A recent study by Megawati and Pan (2002) has identified the maximum credible earthquakes in Sumatra to be a subduction earthquake (M_w = 9.0) off the west coast of Sumatra and a strike-slip earthquake (M_w = 7.5) on the Sumatran fault. Synthetic bedrock motions corresponding to the maximum credible Sumatran subduction earthquake and the strike-slip earthquake have been simulated (Megawati and Pan 2002, Megawati et al. 2003, Pan and Megawati 2002). In addition, the study by Pan and Lee (2002) has considered site response at a soft soil site for a recorded Sumatra subduction earthquake (M_w = 7.0, epicentral distance = 540 km). The present study considers soil response at the same site to the synthetically generated maximum credible earthquake ground motions using the one-dimensional wave propagation method based on the equivalent-linear technique.

This paper starts with a brief description of the seismotectonics of Sumatra and the geological formation of Singapore. The geotechnical properties of the soft soil site are then described, which is followed by the procedure of the soil site response analysis. Finally, response spectrum analyses are carried out to study the seismic response of a typical high-rise residential building subjected to the maximum credible earthquakes.

2. GROUND MOTIONS RECORDED IN SINGAPORE

Sumatra is located adjacent to the Sunda trench (Figure 1), where the Indian-Australian plate subducts beneath the

Eurasian plate at a rate of 67 ± 7 mm per year towards N11°E ± 4° (Tregoning et al. 1994). The islands of Sumatra and Java lie on the over-riding plate, a few hundred kilometers from the trench. Convergence is nearly orthogonal to the trench axis near Java, but it is highly oblique near Sumatra, where the strain is strongly partitioned between dip slip on the subduction zone interface and right-lateral slip on the Sumatran fault along the western coast of the island. The earthquake focal mechanisms and the hypocentral distributions indicate that the subducting plate dips less than 15° beneath the outer arc ridge, and the dip angle becomes steeper to about 50° below the volcanic arc. The relatively shallow dip angle gives strong coupling between the over-riding and the subducting plates. As such, six giant earthquakes ($M_w \geq 8.0$) have occurred along the Sumatran megathrust during the last 210 years, to release the strain accumulated in the convergence between the two tectonic plates: 1797 ($M_w = 8.7$), 1833 ($M_w = 9.0$), 1861 ($M_w = 8.5$), 2004 ($M_w = 9.2$), 2005 ($M_w = 8.7$), and 2007 ($M_w = 8.4$). The rupture zone of the 1833 event, named as the Mentawai segment, is the closest segment to Singapore. It was estimated to have caused a long rupture which measured more than 400 km between Enggano and Batu islands (Figure 1). Singapore is located almost perpendicularly at about 720 km to the centre of the rupture zone (Figure 1). The earthquake, with an average M_w of 9.0, is selected to be the maximum credible earthquake that the Sumatra subduction zone is capable of generating (Megawati and Pan 2002).

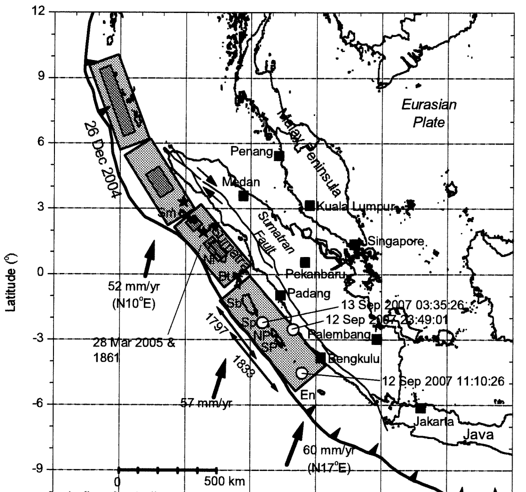

Figure 1 The Sumatran Fault and the Sunda Trench with epicenters of the maximum credible earthquakes

The Sumatran fault lies roughly 250 km northeast of the trench. The 1650 km long fault runs along the western side of the Sumatra Island, coinciding with the Bukit Barisan mountain chain. The Sumatran fault is highly segmented, composing of 19 major segments with cross-strike width of step-overs between adjacent segments of about 5 km to 12 km. The lengths of the segments range from 30 km to 220 km. Due to the fact that the fault is highly segmented, it has a limited capacity to generate very large earthquakes. However, the fault is located relatively close to Singapore than the subduction zone. Historical records show that the segments of the Sumatran fault have caused numerous major earthquakes but their magnitudes are limited to about 7.5 – 7.7 with rupture lengths not greater than 100 km (Sieh and Natawidjaja, 2000). Of the 19 segments of which the Sumatran fault is composed, the Suliti segment (1.75° – 1.0°S, length ≈ 95 km), the Sumani segment (1.0° – 0.5°S, length ≈ 60 km) and the Sianok segment (0.7°S – 0.1°N, length ≈ 90 km) are the closest segments to Singapore (Figure 1). Two major earthquakes have occurred in these segments. The first one was on 4 Aug 1926 ($M_s \approx 7.0$) and the second one was on 9 June 1943 ($M_s = 7.4$-7.6). Judging from the historical earthquake records and the geometrical segmentation of the Sumatran fault, the maximum credible earthquake that can be generated by the fault is a right-lateral event with a magnitude of $M_w = 7.5$ in the Sumani segment (Megawati et al. 2003).

2.1 Seismic Stations in Singapore

The location of seismic stations in Singapore is shown in Figure 2. The nine seismic stations include those at Beatty Secondary School (BES, 1.34°N, 103.85°E), Pulau Tekong (PTK, 1.40°N, 104.05°E), and Katong Park (KAP, 1.17° N, 103.53° E). The surface geological map of Singapore (Figure 3) shows that BES is located on soft quaternary deposit, while PTK is situated on weathered sedimentary rock. KAP is located on Kallang Formation, consisting predominantly of marine clay, which is soft, silty, and kaolinite-rich.

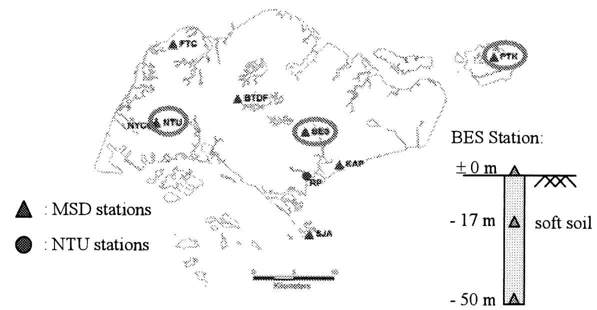

Figure 2 Seismic stations in Singapore

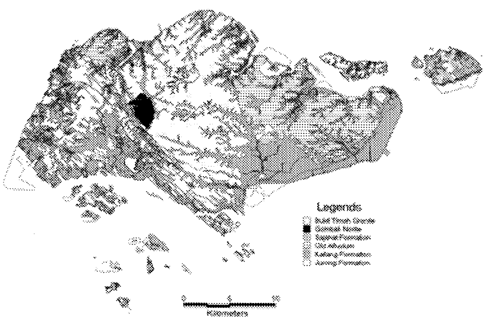

Figure 3 Surfacial geology map of Singapore

2.2 Southern Sumatra Earthquake (M_w = 8.4)

This section describes the ground motions recorded in Singpaore due to the recent Southern Sumatra earthquake (M_w = 8.4) of 12 September 2007. Between the hours of 12 September 11:10 UTC and 13 September 03:35 UTC, three large earthquakes struck off the western coast of Sumatra, between the cities of Bengkulu and Padang. The events, of magnitude M_w 8.4, 7.8 and 7.1, occurred approximately 530 km to 700 km from Singapore. The three earthquakes occurred along southern Sumatran megathrust, between the islands of Sipora and Enggano (Figure 1). According to the Earthquake Center of the United States Geological Survey, the first event (M_w = 8.4) occurred on the 12th, at 11:10:26 UTC, followed by the second (M_w = 7.8) at 23:49:01 UTC and the third (M_w = 7.1) on the following day, at 03:35:26 UTC. The respective epicentral distances to Singapore are 702 km, 532 km and 614 km.

The seismic stations located at BES and PTK recorded the ground motions from the three Sumatran events (Figure 2). Figure 2 shows the downhole array at BES, where three triaxial seismometers were installed at three different levels (at the surface and at depths of 17 m and 50 m). The purpose of installing the downhole array is to investigate amplification of seismic shear wave as it travels vertically through the soft-soil profile at the site. PTK station has only one triaxial seismometer on the ground surface.

Figure 4 shows ground accelerations from the M_w = 8.4 event of 12 September 2007, recorded at PTK and BES. The horizontal peak ground accelerations (PGAs) at PTK is 1.2 cm/s^2, while the value at the ground surface of BES is 2.9 cm/s^2, implying an amplification factor of about 2.2. The respective pseudo-velocity response spectra, with 5% damping ratio, are shown in Figure 5, where the spectra of the mean as well as the mean plus and minus one standard deviation, estimated using the attenuation relationship developed at NTU, are plotted for comparison. Figure 5 shows that the recorded spectra at PTK (rock), NTU (rock) and BES (at surface and -50 m level) largely fall within the band of the plus and minus one standard deviation, indicating that the attenuation relationship could reasonably estimate the actual response spectra. Figure 5 also shows that the surface spectrum at BES demonstrates a significant site effect within the natural period range of 0.5 – 2.0 sec.

News hotlines were barraged by alarmed callers who described swinging ceiling lamps, vibrating glasses, water oscillating in home aquariums (Ang Mo Kio and various locations, Xinming Ribao, 13 September 2007), while pieces of concrete were dislodged from the floor of an apartment in the East Coast (The Straits Times, 14 September 2007). Reports of dizziness and nausea during the tremors were widespread, but the extent of discomfort experienced in adjacent buildings, and even among individuals in the same building, varied greatly. Spontaneous mass evacuations from the NTUC building in Raffles Quay were mirrored islandwide – along the East Coast, Eunos and Bedok.

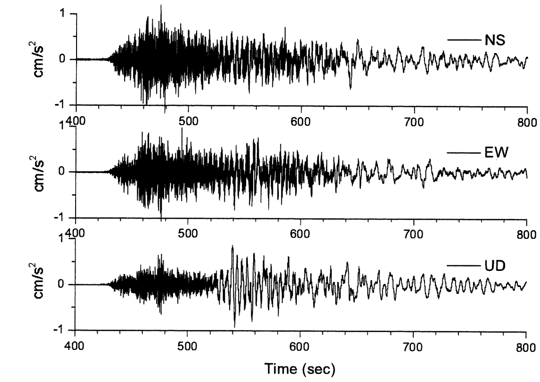

(a) Recorded at PTK

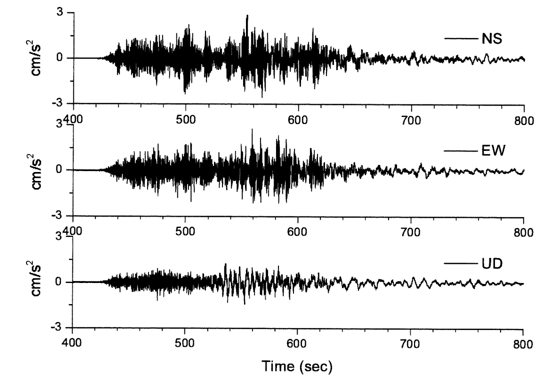

(b) Recorded at BES (ground surface)

Figure 4 Ground accelerations (in cm/sec^2) from the M_w = 8.4 event of 12 September 2007

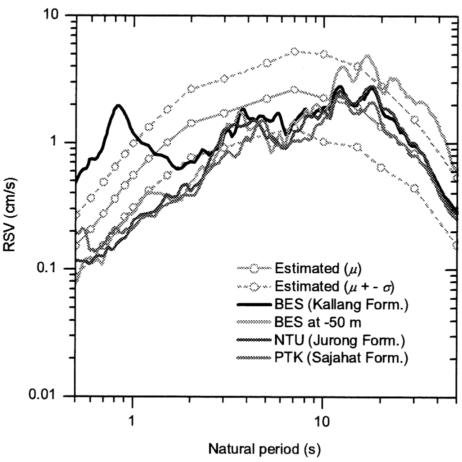

Figure 5 Pseudo-velocity response spectra based on the ground motions at BES, NTU and PTK, with 5 % damping ratio for the M_w = 8.4 event of 12 September 2007

Following the M_w = 8.4 event on 12 September 2007 there were 246 buildings inspected by engineers, and were found to be structurally sound. General advice was disseminated to the public by the Singapore Civil Defence Force through the mass media, suggesting that people take shelter under tables and away from windows or unstable objects (if indoors) and away from buildings and electrical cables (if outdoors). Members of the public were also discouraged from using elevators to escape buildings, to be wary of triggering explosions in the event of gas leaks, and were encouraged above all to remain calm during tremors.

3. MAXIMUM CREDIBLE GROUND MOTIONS

Megawati and Pan (2002), and Megawati et al. (2003) identified that the maximum credible ground motions in Singapore are likely to be caused by the two large earthquakes of different source mechanisms. One is a strike-slip earthquake (Sumani segment) with an epicentral distance of around 425 km and a moment magnitude of 7.5. The other is a Sumatra subduction earthquake with an epicentral distance of 723 km and a moment magnitude of 9.0 (Figure 1). The bedrock motions in Singapore due to these two earthquakes have been simulated using the extended reflectivity method (Kohketsu 1985), taking into account uncertainties in the source rupture process. Detailed descriptions of the MCEs and the simulation process can be found in separate publications (Megawati and Pan 2002, Megawati et al. 2003). One set of the simulated motions is used in this study. The three components of the strike-slip earthquake and the subduction earthquake are shown in Figures 6 and 7, respectively. The beginning of the signals corresponds approximately to the arrival in Singapore of the first P wave from the sources.

Response spectra of 5% damping ratio are shown in Figures 8 and 9, respectively, for the maximum credible earthquakes. The larger of the two horizontal components of the synthetic MCE ground motions are thus used in the convolution process to obtain the surface accelerations at the soft soil site. They are the tangential acceleration component of the Sumatra strike-slip earthquake and the perpendicular acceleration component of the Sumatra subduction earthquake.

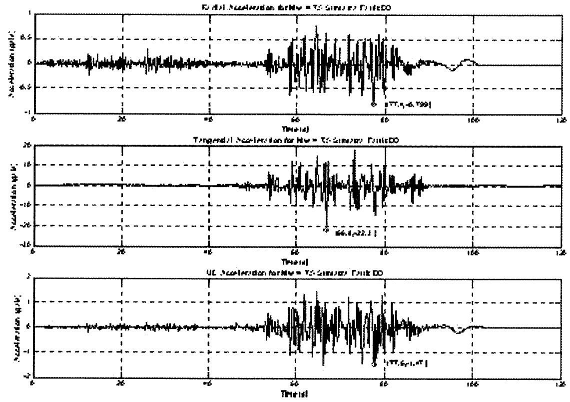

Figure 6 Three acceleration components for the maximum credible strike-slip earthquake

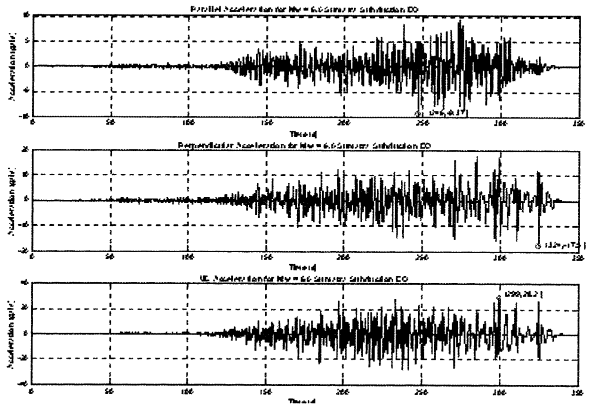

Figure 7 Three acceleration components for the maximum credible Sumatra subduction earthquake

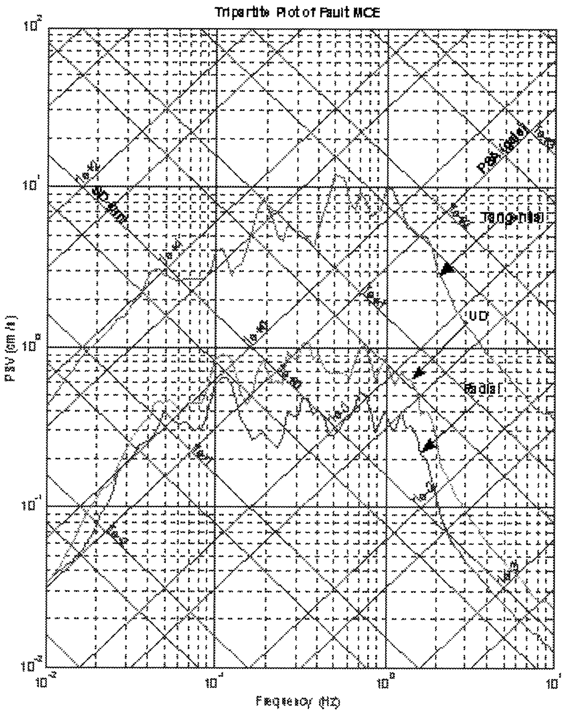

Figure 8 Tripartite plot of response spectra (5% damping ratio) for the strike-slip MCE

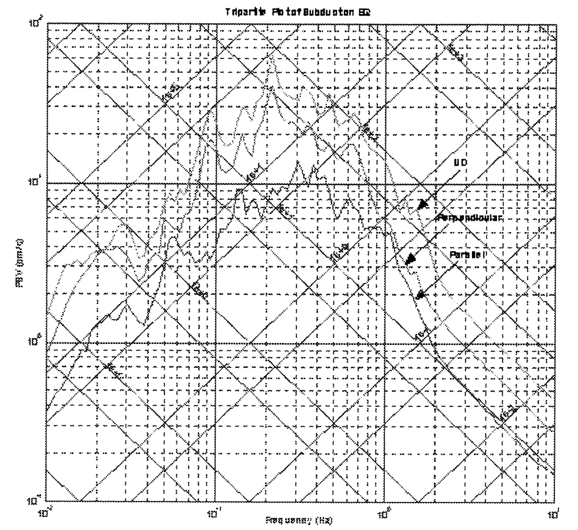

Figure 9 Tripartite plot of response spectra (5% damping ratio) for the subduction MCE

4. RESPONSE OF A HIGH-RISE RESIDENTIAL BUILDING

In this section, the responses of a typical high-rise residential building under the scenario earthquakes are studied. Both the rock and the soft soil site ground motions from the subduction and the strike-slip earthquakes described are used as the inputs. The responses to the different ground excitations are compared. Because of the unusual shape of the typical building, the effects of flexible diaphragms are significant and thus, included in the finite element (FE) modeling.

4.1 Building Descriptions

The structure under study is a typical 15-storey, reinforced concrete (RC) residential building. The overall height of the building is 42.8 m. Figure 10 shows a typical floor plan of the building. The dimensions of the floor plan are 94.5 m in the longitudinal direction and 11 m in the transverse direction. The RC building has a frame-shear wall dual structural system. No clear symmetry can be observed from the building drawings. The frame system consists of a series of two-bay frames spanning in the transverse direction. The frames are spaced at about 3 m along the longitudinal direction. The typical column sections are 0.3 m by 1.2 m for the first three stories, and 0.3 m by 0.9 m for the upper stories with the larger dimension along the transverse direction. Such wall-like columns are prohibited from the modern seismic design codes. The design provision for seismic loadings in ACI-318 (ACI 2002) requires a minimum width to length ratio of 0.4. The typical beam size is 0.3 m by 0.5 m. The walls are also aligned mainly along the transverse direction. Therefore, the longitudinal direction appears to be the weaker direction. The partition walls inside the frames are made of bricks. The floors are RC with 0.125 m thickness. Because of the large aspect ratio of the floor dimensions, the effects of flexible diaphragm may be significant on the building's seismic response.

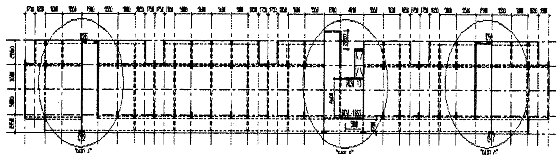

Figure 10 The floor plan of typical building

4.2 Finite Element Model

A three-dimensional (3D) FE model was constructed to study the dynamic characteristics of the building. The perspective view of the model is shown in Figure 12. In the model, the flexible floors were modeled using shell elements, and the brick partition walls were included via plane stress elements. The fundamental frequency is 1.27 Hz in the transverse direction, which is contrast to the original expectation. This may be due to the brick infill walls which increase the stiffness in the longitudinal direction greatly. The first 3 modes of the model are primarily the global longitudinal or rotational modes, while mode 4 is clearly a diaphragm deformation mode in the transverse direction where the floors are bent as a flexible deep beam.

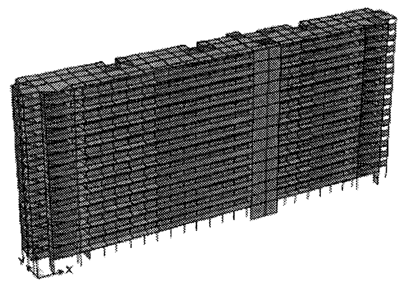

Figure 11 The perspective view of the FE model

4.3 Structural Response

Two specific response spectra of the rock ground motions mentioned in the previous sections, one from the subduction perpendicular component and the other from the strike-slip tangential component, and their corresponding ground motions at a soft soil site are used as the inputs to the FE model. The ground motions are applied separately in the longitudinal and the transverse directions. The responses are summarized as follows.

The total base shear forces of the FE model subjected to the MCEs are shown in Table 1 for both the longitudinal and the transverse directions. The maximum base shear force is 14,056 kN and is about 9.2 % of the total building dead weight. Even though the total base shear forces of the model are greater than 1.5% of the total building weight, which is the notional horizontal load required by BS 8110 (BSI 1987), they are all well below the base shear capacity of the building. The base shear capacities of the building are 22.4% and 35.3% of the building weight for the longitudinal and the transverse directions, respectively.

The individual column shear capability of the building structure is studied via the ratios of the base shear forces of individual frames over their corresponding shear capacities. The ratios were calculated for the strike-slip earthquake case using its soft soil ground motions, because it can be seen from Table 1 that this ground motion generates the maximum total base shear forces. For both directions, all the ratios are below 70%. Therefore, the shear forces should not be a problem for individual frames during the MCE events.

The moment responses of the vertical members were checked. It was found that when the building was loaded in the longitudinal direction, the moments in all the columns were below their capacities. However, when the building was loaded in the transverse direction, some columns were overstressed by the biaxial bending moments. The forces applied in the transverse direction may generate a relatively more significant response in the longitudinal direction.

Table 1 shows that, when the ground motions change from the bedrock motions to the soft soil motions, the base shear forces are amplified by two to four times. For example, when the building is subjected to the bedrock motion of the strike-slip earthquake, the total base shear force is only 6,014 kN, compared to 13,544 kN when subjected to the soft soil motion of the same earthquake. Therefore, the typical building would function very well during the MCE events when it is located at the rock sites. However, the MCE events might cause some damages to the building located at soft soil site, such as overstressing on members.

Table 1 Base shear forces of the building subjected to MCEs

Earthquake	Soil Type	Longitudinal Shear Force (kN)	Longitudinal Force/Weight (%)	Transverse Shear Force (kN)	Transverse Force/Weight (%)
Strike-Slip	Rock	6015	3.9%	5524	3.6%
	Soil	13544	8.9%	14056	9.2%
Subduction	Rock	3772	2.5%	4021	2.6%
	Soil	9873	6.5%	11020	7.2%

It is believed that the building was designed under the assumption of rigid diaphragms in spite of the large aspect ratio of the floors, i.e. the lateral forces were distributed according to the stiffness of the vertical members. However, the building under study does experience the diaphragm deformation. Therefore, it is worthy to investigate how much the structural responses are different from the original design values. A sub-model was constructed by rigidly constraining all the floors of the existing FE model. The percentage changes of the base shear forces of the individual frames from the rigid model to the flexible model are then calculated. It can be found that the maximum change in percentage is about 45% increase. The design force at this location calculated under the rigid diaphragm assumption would thus be underestimated. However, because the shear capacities of the columns designed under the gravity load are much larger than the shear force demands caused by the MCEs, the structure would still be safe in terms of the shear forces. A more detailed study on the effects of flexible diaphragms can be found in a separate publicaiton (Pan et al., 2006).

5. CONCLUSIONS

This paper reports one set of the ground motions recorded in Singapore due to the recent Southern Sumatra earthquake (M_w = 8.4) of 12 September 2007. Ground motions at a soft soil site in Singapore due to the MCE from Sumatra have been computed using a one-dimensional equivalent-linear ground response analysis technique. It has been shown that such maximum credible earthquakes are able to induce, at the soft soil site, spectral accelerations greater than 20 gals for a wide frequency range. The responses of a typical high-rise residential building subjected to the ground motions of MCEs were investigated. Even though the base shear forces caused by the earthquake ground motions would exceed the notional horizontal load requirement in BS 8110 code, the capacity of column members designed under the gravity loads are sufficient to resist them.

Acknowledgements:

The authors wish to acknowledge Mr X T You, ex-Research Scholar at NTU, and Professor James M W Brownjohn, Sheffield University, UK, for their contributions during the course of this reported work.

References:

ACI Committee 318 (2002). "Building code requirements for structural concrete and commentary".

British Standards Institution. (1987), "BS8110, Part 1: British Standard: structural use of concrete: code of practice for design and construction".

Kohketsu, K. (1985), "The extended reflectivity method for near-field seismograms." Journal of Physics of the Earth **33**: 121-131.

Megawati, K., and Pan, T-C. (2002), "Prediction of the maximum credible ground motion in Singapore due to a great Sumatran subduction earthquake: the worst-case scenario." J. Earthquake Engrg. Struct. Dyn **31:** 1501-1523.

Megawati, K., Pan, T-C., and Koketsu, K. (2003), "Response spectral attenuation relationships for Singapore and the Malay Peninsula due to distant Sumatran fault earthquakes." J. Earthquake Engrg. Struct. Dyn. **32**: 2241-2265.

Pan, T-C. (1995), "When the doorbell rings – a case of building response to a long distance earthquake." J. Earthquake Engrg. Struct. Dyn. **24**: 1343-1353.

Pan, T-C., and Lee, CL. (2002), "Site response in Singapore to long-distance Sumatra earthquakes." Earthquake Spectra **18**(2): 347-367.

Pan, T-C., Megawati, K, Brownjohn, JMW., and Lee, CL. (2001), "The Bengkulu, southern Sumatra, earthquake of 4 June 2000 (Mw = 7.7): Another warning to remote metropolitan areas." Seismological Research Letters **72**(2): 171 – 185.

Pan, TC., and Megawati, K. (2002), "Estimation of peak ground accelerations of the Malay Peninsula due to distant Sumatra earthquakes." Bull. Seis. Soc. America **92**: 1082-1094.

Pan, T-C., You, XT., and Brownjohn, JMW. (2006), "Effects of infill walls and floor diaphragms on the dynamic characteristics of a narrow-rectangle building." Earthquake Engineering and Structural Dynamics **35**(5): 637-651.

Sieh, K, and Natawidjaja, D. (2000), "Neotectonics of the Sumatran fault, Indonesia." Journal of Geophysical Research **105**: 28295-28326.

Tregoning, P., Brunner, FK., Bock, Y., Puntodewo, SSO., McCaffrey, R., Genrich, JF., Calais, E., Rais, J., and Subarya, C. (1994), "First Geodetic measurement of convergence across the Java Trench." Geophysical Research Letters **21**: 2135-2138.

Fifth International Conference on Urban Earthquake Engineering
March 4-5, 2008, Tokyo Institute of Technology, Tokyo, Japan

VERIFICATION OF THE NATIONAL SEISMIC HAZARD MAPS FOR JAPAN WITH ACTUAL OBSERVED STRONG MOTIONS BY K-NET IN LAST DECADE

Hiroyuki Fujiwara[1], Nobuyuki Morikawa[2], Yutaka Ishikawa[3], Toshihiko Okumura[4], Jun'ichi Miyakoshi[5], and Nobuoto Nojima[6]

1) Project Director, National Research Institute for Earth Science and Disaster Prevention, Japan
2) Researcher, National Research Institute for Earth Science and Disaster Prevention, Japan
3) General Manager, Shimizu Corporation, Japan
4) Senior Researcher, Shimizu Corporation, Japan
5) Researcher, Shimizu Corporation, Japan
6) Professor, Department of Civil Engineering, Gifu University
fujiwara@bosai.go.jp, morikawa@bosai.go.jp, yutaka.ishikawa@shimz.co.jp, oku@shimz.co.jp, miyakoshi@shimz.co.jp, nojima@gifu-u.ac.jp

Abstract: National seismic hazard maps for Japan were published by the Earthquake Research Committee of Japan in March 2005, and have been updated every year since then. As the first step to verifying the validity of the probabilistic seismic hazard maps, we compared the intensity records obtained through observations of strong motions over the past 10 years with the values shown in the probabilistic hazard maps, so as to analyze the frequency of strong motions that have occurred in Japan

1. INTRODUCTION

National seismic hazard maps for Japan were published by the Earthquake Research Committee of Japan in March 2005, and have been updated every year since then. Because the probabilistic seismic hazard maps focuses on estimates of such long-term periods as 30 years and even 50 years, data that cover a very long term are required to evaluate the validity of estimate results using strict probabilistic and statistical approaches.

In this research, as the first step to verifying the validity of the probabilistic seismic hazard maps, we compared the intensity records obtained through observations of strong motions over the past 10 years with the values shown in the probabilistic hazard maps, so as to analyze the frequency of strong motions that have occurred in Japan.

2. K-NET STATISTICS ON SEISMIC INTENSITY

We used all the records of strong motions recorded at K-NET observation sites for the 10 years from January 1, 1997, to December 31, 2006, for verification. K-NET is an observation network that covers the entire area of Japan uniformly, using a grid with meshes of about 25 kilometers. The network had 1,000 observation sites when it was first established, and new observation sites—many of which are in the Kanto area—have been added since then. The number of observation sites peaked at 1,035, a figure that included six sites for ocean-bottom seismographs, but as of the end of 2006, the number of observation sites stood at 1,028.

The operation rate was about 95% in the initial stage, rising to about 97% after the third year, and has remained at around 99% for the past five years. All of the K-NET stations are sited on the ground, and it was possible for us to calculate the JMA seismic intensity using the acceleration records obtained by K-NET.

Figure 1 shows the distribution of observation sites that have recorded events with a seismic intensity higher than a given value over the past 10 years. Figure 2 indicates the total number of records of seismic intensity at all observations sites during the 10-year period. Table 1 shows the cumulative times of values above each intensity level, and the number of observations.

3. CHARACTERISTICS OF K-NET OBSERVATION SITES

Morikawa et al. (2007) evaluated site-specific amplification characteristics of observation sites of the networks for strong motion and seismic intensity in Japan.

In Figure 3, we plotted seismic intensity amplification characteristics obtained by Morikawa et al. in ascending order for each observation site that recorded an event above a given degree of intensity. As we can see in Figure 3(a), the observation sites that recorded events of above intensity 3

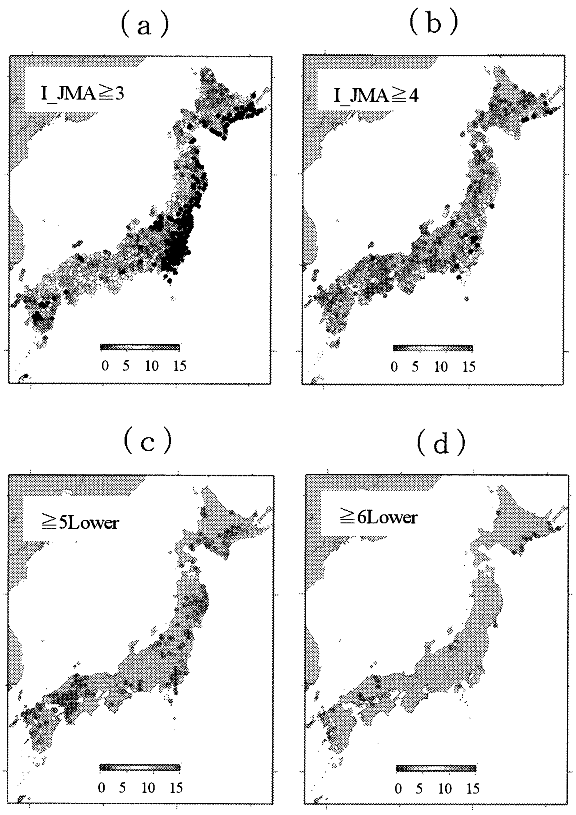

Figure 1. K-NET observations points and observation frequencies of (a) above intensity 3, (b) above intensity 4, (c) above intensity 5 lower, and (e) above intensity 6 lower observed in the 10 years from January 1997 to December 2006.

include most K-NET observation sites, and they are distributed evenly from those with large amplification to those with small amplification.

Observation sites with large amplification tend to record a higher value than a large intensity selectively. As shown in Figure 3(d), most intensity values higher than intensity 6 lower were recorded at observation sites with amplification larger than average amplification.

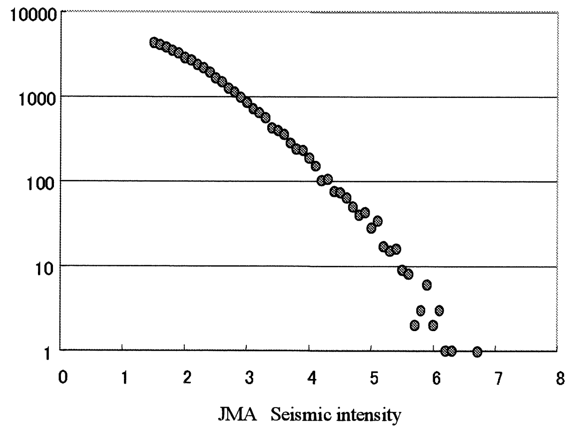

Figure 2. Number of records at all K-NET observation sites for the 10 years from January 1997 to December 2006.

Table 1. Cumulative number of records and number of sites observed JMA seismic intensity larger than a certain level for the 10-year period

I_JMA	Number of records	Number of sites
≧2	42,995	1,029
≧3	12,141	992
≧4	2,519	714
≧5Lower	412	232
≧5Upper	145	99
≧6Lower	36	29
≧6Upper	8	6

(Note) Records obtained from K-NET observation points exclude those obtained from the six ocean-bottom seismographs located in Sagami Bay.

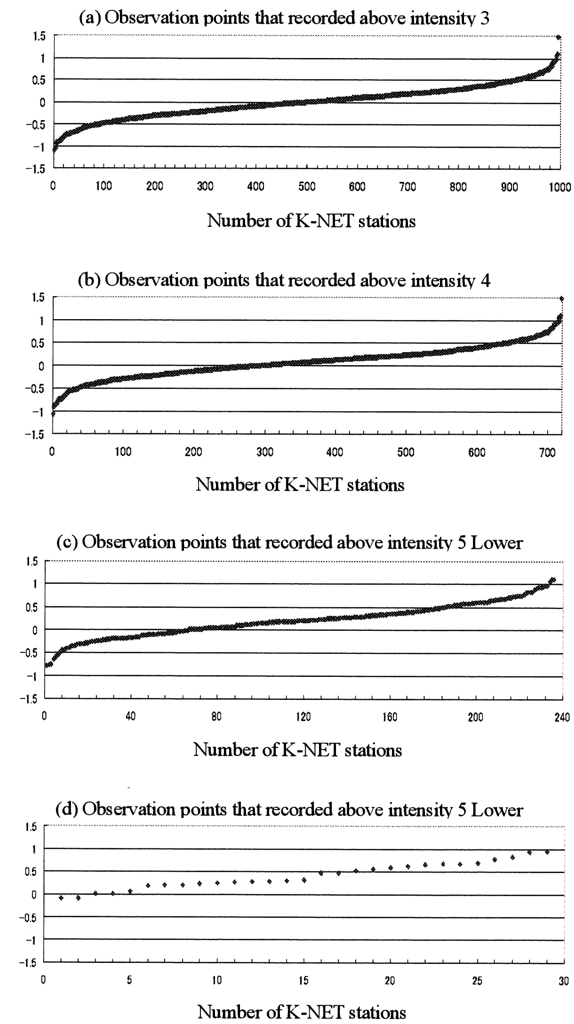

Figure 3. Intensity amplification characteristics estimated by K-NET records.

On the other hand, the probabilistic seismic hazard maps for Japan uses amplification characteristics based on geomorphologic classification. In Figure 4, we show a comparison between intensity amplification characteristics of meshes[2)] that include K-NET observations points and those of K-NET, as obtained by Morikawa et al. Although we found some positive correlation, the degree of correspondence varies greatly. It is important to estimate the site amplification characteristics to obtain a higher precision for the probabilistic seismic hazard maps.

With the above discussions, we consider geographic distribution by intensity. Most observation sites across the country recorded intensity 3. In particular, those on the Pacific Coast from Hokkaido to the Tohoku area, as well as those in the Kanto area recorded intensity 3 a large number of times. Intensity 4 was observed all across the country, with the exception of the northern part of Hokkaido and part of the coast along the Japan Sea. Additionally, intensity 4 was not observed characteristically in some parts of the Chubu area, where active faults are densely distributed.

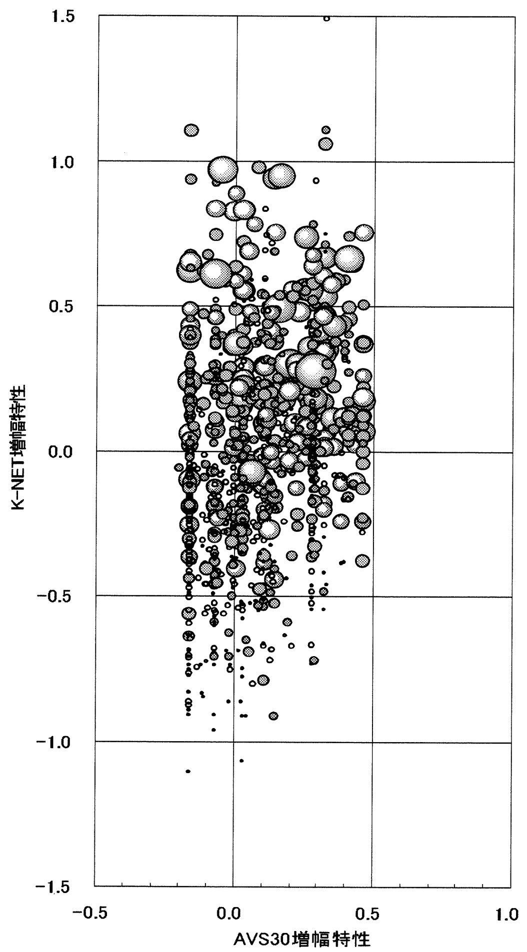

Figure 4. Comparison between amplification characteristics of intensity calculated from geomorphologic classification (horizontal axis) and those calculated from the observation records of K-NET (vertical axis). The size of the symbol corresponds to the number of observation records.

Contrary to the above, the influence of specific damaging earthquakes grows apparent in the map of above intensity 5 lower. It mainly comes from damaging earthquakes whose magnitude are around 7, including those in northwestern Kagoshima Prefecture (1997), western Tottori Prefecture (2000), the Geiyo earthquake (2001), the earthquakes off the coast of Miyagi Prefecture (2003 and 2005), the Tokachi Oki Earthquake (2003), the Niigata-Chuetsu Earthquake (2004), and one west off the coast of Fukuoka Prefecture (2005). In addition to these earthquakes, intensity 5 lower observed in the Kanto and Chubu areas was caused by steady earthquakes a little smaller in scale. Intensity 6 lower was mostly caused by the damaging earthquakes mentioned above, and selectively observed at the observation sites with large amplification as shown in Figure 3(d).

Currently, a map that covers all earthquakes is usually used as the probabilistic seismic hazard map of Japan. If we limit intensity 5 upper strong motions that cause damage, we need other maps that cover earthquakes by restricted evaluation criterion, or by susceptibility to ground motion.

4. CHARACTERISTICS OF SEISMIC HAZARD AT K-NET OBSERVATION SITES

First, we consider the probabilistic seismic hazard at K-NET observations sites. Figure 5(a) shows the distribution of cumulative relative frequency of 30-year exceedance probability (starting in 2007) of intensity 6 lower for the meshes of 1,028 that include all K-NET observation sites. For comparison, we attached an exceedance probability (for 30 years starting in 2005) to all meshes based on an analysis conducted by the Ishikawa et al. (2006) as well as meshes with a population of more than 1,000.

From this figure, we found that the characteristics of probabilistic seismic hazard at K-NET observations sites is more like the distribution for meshes with a population of more than 1,000 than the distribution for all meshes. This is because the majority of K-NET observations points are set up around inhabitable land, whereas N-NET covers the entire country.

In Figure 5(b), we show the cumulative relative frequency of 30-year exceedance probability of intensity 6 lower at 29 points that observed events above intensity 6 lower in the 10 years since 1997 with the distribution of all of K-NET's observations sites. We can see that intensity 6 lower was frequently observed during this 10-year period as a relative ratio at the observation sites that have a low hazard, and whose 30-year exceedance probability was lower than 3%.

The same trend was observed in the case of intensity 5 lower, although we did not attach a figure. This is partly because there were no large earthquakes in the Nankai Trough that have strongly affected areas with a high probabilistic earthquake hazard in the specified 10-year period.

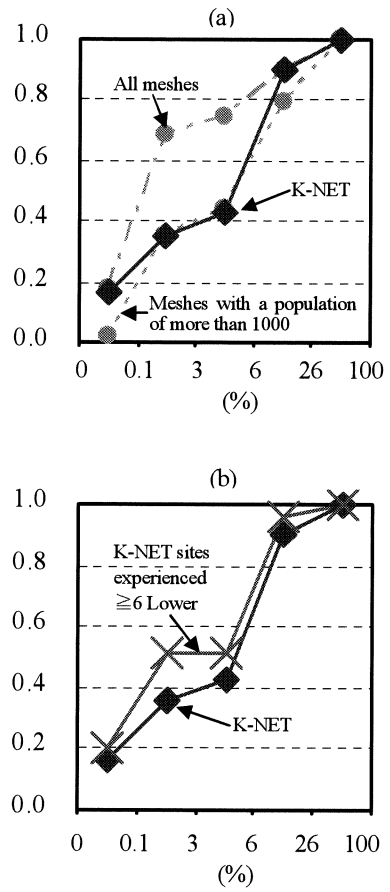

Figure 5. Seismic hazard at K-NET observation sites. (Cumulative relative frequencies of 30-year exceedance probability of intensity 6 lower)

5. PROBABILISTIC SEISMIC HAZARD MAPS FOR THE 10 YEARS SINCE 1997

In order to compare the frequency of strong motion between the K-NET observation data and the expected value based on the probabilistic seismic hazard map, we calculated the probabilistic seismic hazard maps for 10 years since 1997.

Table 2. Probability of occurrence of major subduction zone earthquakes

	Nankai	To-Nankai	Tokai	Miyagi-ken-oki
10 years since 1997	2.3%	5.2%	44%	8.2%
30 years since 2007	53%	64%	87%	Near100%
	Near Ocean trench of Southern Sanriku	Northern part off Sanriku	Tokachi-oki	Nemuro-oki
10 years since 1997	32%	Near 0%	15%	0.34%
30 years since 2007	80%	3.2%	0.32%	37%

5.1 Evaluation criteria

While the analytical method is corresponding to the national probabilistic seismic hazard maps from 2007, we modified the probabilities of earthquakes with non-stationary occurrence model beginning from 1997. The origin time of the Tokachi-oki earthquake was March 1952, because it has been occurred during the target period. Table 2 shows the probabilities of earthquakes occurring in the major subduction zone for 10 years since 1997. We also attached probabilities of occurrence for 30 years after 2007.

5.2 Evaluation results

Figure 6 shows the probabilistic seismic hazard maps for 10 years since 1997. Figure 6(a) shows the distribution of 10-years probability of exceedance of intensity 5 lower, and Figure 6(b) is that for intensity 6 lower. For comparison, we attached the probabilistic seismic hazard maps for 30 years after 2007 in Figure 7. The color-coded threshold of probabilities for 10-years maps was equivalent to that for 30-years maps.

The probabilistic seismic hazard maps after 2007 (Figure 7) are strongly affected by ocean-trench earthquakes shown in Table 2, but those from 1997 (Figure 6) show relatively low seismic hazard on the western Japan faced the Pacific coast. On the contrary, the seismic hazard in the southeast Hokkaido is relatively high for 1997 maps because the probability of the Tokachi-oki Earthquake has been relatively high.

6. COMPARISON BETWEEN K-NET DATA AND PROBABILISTIC SEISMIC HAZARD MAPS

We compared Figures 1(c) and (d) with Figure 2, and found that observation points on the Pacific Coast from Hokkaido to the Kanto area through the Tohoku area, those from the Chubu area to the Kinki area, and those in the western part of Shikoku, originally had a high probability of seismic hazard in 1997. However, intensity 5 lower was observed in areas with a relatively low seismic hazard in Niigata Prefecture, Tottori Prefecture, the Western part of the Chugoku area, and the northern part and southwestern part of Kyushu.

We found that of the observation points that observed intensity 6 lower, the probabilistic seismic hazard was relatively high in Hokkaido and Miyagi Prefecture in 1997, but that the seismic hazard was not so high at other observation points, supporting the results shown in Figure 5(b).

Next, we consider the ratio of land that experienced intensity 5 lower, intensity 5 upper, intensity 6 lower, and intensity 6 upper more than once in the 10 years.

Table 3 shows the ratio of land (the number of observation sites that experienced certain seismic intensity divided by the number of all observation sites) where K-NET observed the four intensity classes more than once in the 10 years since 1997. What corresponds to these values in the probabilistic seismic hazard maps is the average of the exceedance probability of each mesh. Therefore, we have

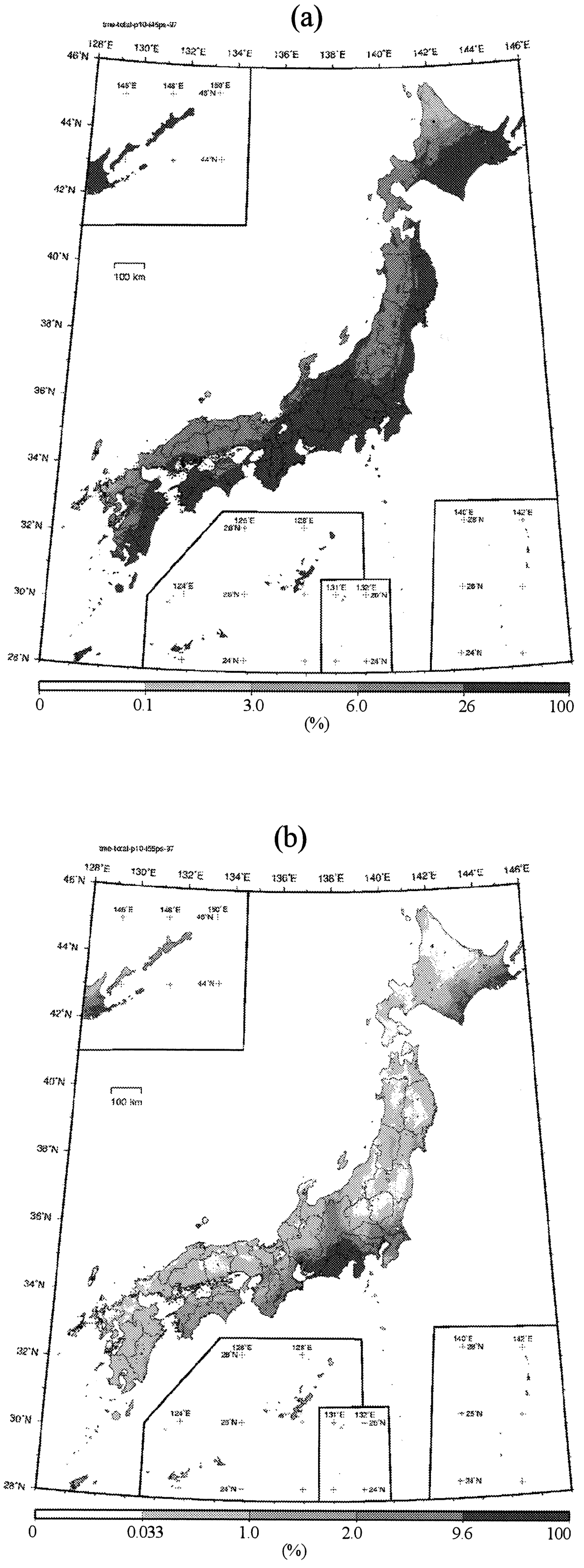

Figure 6. Probabilistic seismic hazard maps of Japan for 10 years since 1997. Figure (a) shows the distribution of exceedance probability of intensity 5 lower, and Figure (b) is that for intensity 6 lower.

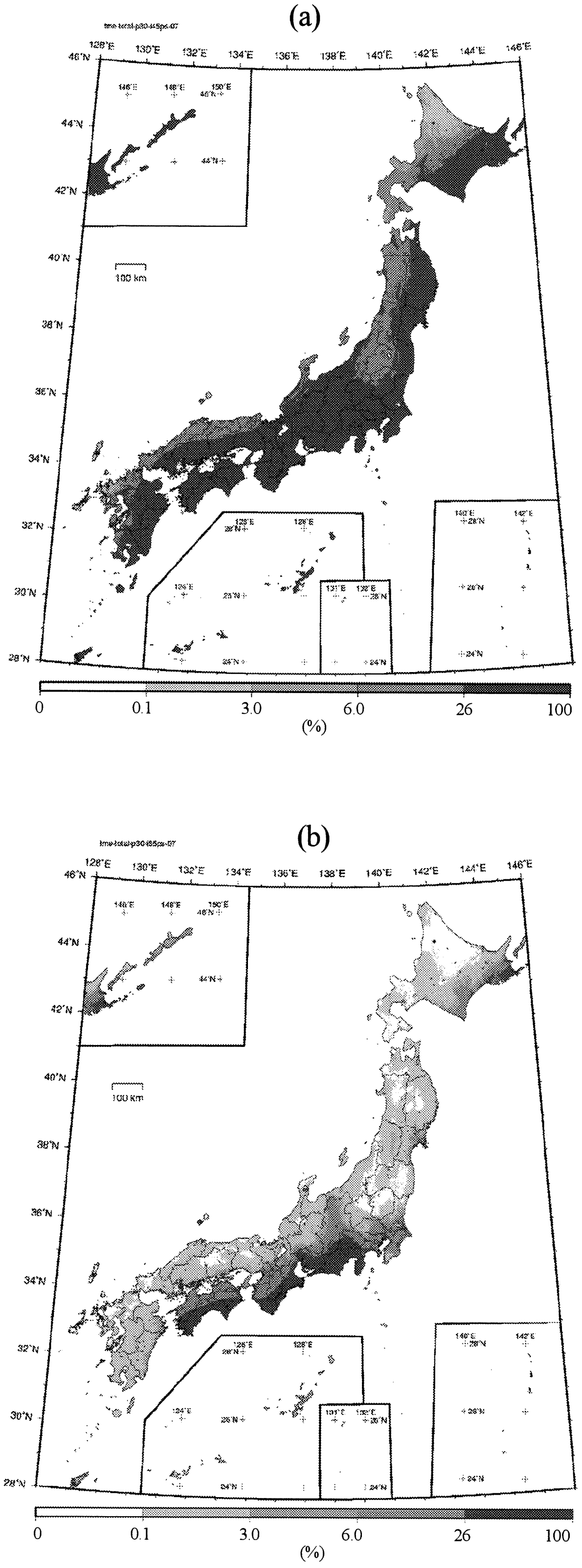

Figure 7. Probabilistic seismic hazard maps of Japan for 30 years after 2007. Figure (a) shows the distribution of exceedance probability of intensity 5 lower, and Figure (b) is that for intensity 6 lower.

Table 3. Total areas of Japan that experienced intensity 5 lower, intensity 5 upper, intensity 6 lower, and intensity 6 upper more than once in 10 years

	Ratio of area from K-NET	Probabilistic map (All meshes)	Probabilistic map (Popularity of more than 1000)
≧5Lower	0.232	0.21	0.39
≧5Upper	0.099	0.077	0.17
≧6Lower	0.029	0.021	0.051
≧6Upper	0.006	0.0028	0.010

(Note) Taking the operation rate into consideration, we used an approximation number of 1,000 for the total number of K-NET observation sites.

attached Table 3 that shows the national average of the 10-year exceedance probability of each intensity class. Based on an analysis of Figure 5(a), in addition to a case that covers all meshes, we have attached a case that covers meshes with a population of more than 1,000.

The ratio from K-NET observation data is somewhat smaller than the national average of exceedance probability of the probabilistic seismic maps for meshes with population of more than 1,000. However, in view of the fact that the Tokai earthquake that strongly affects the area with a high probabilistic seismic hazard in Figure 6 did not occur in the 10 years, it maintains some degree of compatibility as the national average.

7. CONCLUSIONS

To develop the probabilistic seismic hazard maps of Japan, it is of great significance to verify it regularly by means of observation information. We hope that this type of analysis will be conducted regularly in the future.

Acknowledgements:

We used strong motion data of K-NET.

References:

Morikawa, N., Fujiwara, H., Aoi, S., Kunugi, T., Nakamura, H., Adachi, S. (2007), "Site-specific amplification characteristics at observation sites – Evaluation by attenuation relation", *Proceedings of the 5the Annual Meeting of Japan Association for Earthquake Engineering*, 58-59, in Japanese.

National Research Institute for Earth Science and Disaster Prevention (2005), "Japan Seismic Hazard Information Station, J-SHIS", http://www.j-shis.bosai.go.jp/

Ishikawa Y., Okumura, T., Miyakoshi, J., Nojima, N. (2006), "National Statistics of Probabilistic Seismic Hazard (No. 1) Statistical distribution of intensity", *Proceedings of the 4the Annual Meeting of Japan Association for Earthquake Engineering*, in Japanese.

Fifth International Conference on Urban Earthquake Engineering
March 4-5, 2008, Tokyo Institute of Technology, Tokyo, Japan

DAMAGE AND GROUND MOTION OF THE DECEMBER 26, 2006 PINGTUNG EARTHQUAKE

Kou-Liang Wen[1], Yu-Wen Chang[2], Che-Min Lin[3], Hsien-Jen Chiang[3], and Ming-Wei Huang[4]

1) Professor, Institute of Geophysics, National Central University, Taiwan
Division Head, National Center for Research on Earthquake Engineering, NARL, Taiwan
2) Assistant Research Fellow, National Center for Research on Earthquake Engineering, NARL, Taiwan
3) PhD Student, Institute of Geophysics, National Central University, Taiwan
4) Associate Research Fellow, National S&T Center for Disaster Reduction, NARL, Taiwan
wenkl@earth.ncu.edu.tw, ywchang@ncree.org, cheminlin@gmail.com, s1642006@cc.ncu.edu.tw, mwhuang@ncdr.nat.gov.tw

Abstract: Two large consecutive earthquakes eight minutes apart occurred in the offshore areas of Hengchun, Pingtung County at night on December 26, 2006. The seismic intensity in the Kaohsiung and Pingtung areas reached 5 according to the Central Weather Bureau's intensity scale making them the strongest earthquakes in the Hengchun area in a century. These earthquakes were felt throughout Taiwan. Because the earthquakes were located offshore, but not far from the coast, seismic instruments at Taipower's Nuclear Power Plant No.3 (NPP3) recorded their largest motions since recording commenced at the site. As a result, Unit 2 of NPP3 was shut down while Unit 1 remained operating at full capacity. Other damage that occurred during this earthquake sequence included building collapse, rock falls, structure and non-structural damage to buildings, fire, and damage to utilities such as gas, electricity, and telephone lines; liquefaction was also noted. In this paper, we also predict the shakemap based on the source parameters and real-time observations, and compare this with the recorded shakemap. This analysis shows our shakemap prediction model to be extremely useful in predicting what emergency response units can expect after a large damaging earthquake. Strong motion data near a collapsed building was used to calculate the response spectrum and compared with the building code to check the reason why the building collapsed. This study presents the damage that occurred during this event and the results of the seismic assessment to discuss the reasons why so much damage occurred in the southern Taiwan area.

1. INTRODUCTION

A M_L7.0 earthquake took place at 20:26:21.0 (Taiwan local time, referred to as the 2026 Earthquake) on December 26, 2006 at about 38.4 km southwest of Kenting. The epicenter was located in the offshore area (Figure 1a). About eight minutes later at 20:34:15.1 (referred to as the 2034 Earthquake) another strong M_L7.0 shock occurred (Figure 1b). The epicenter of the first shock was located at 21.69°N and 120.56°E. Its focal depth was 44.1 km. The 2034 Earthquake, at a depth of 50.2 km, was also a deep earthquake located at 21.97°N and 120.42°E. It was felt over a wide area. The Seismology Center of the Central Weather Bureau (CWB) stated that according to its records there has never been such a large earthquake within 50 km of the epicenter. These earthquakes took place in an area where the Eurasian and Philippine Sea plates interact. The Philippine Sea plate subducts northward under the Eurasian plate after their collision along the eastern offshore areas of Taiwan. Meanwhile, in the southwestern offshore areas, the Eurasian plate begins to subduct eastward under the Philippine Sea plate. The latest earthquakes happened to occur in this area. Many aftershocks took place following the main shock. Up to 13:00 of December 27, 132 aftershocks has been recorded, among them nine were in the range M_L4.7 to 6.4. Most had focal depths less than 30 km. Figure 2 shows the epicenters of the main shock and larger aftershocks.

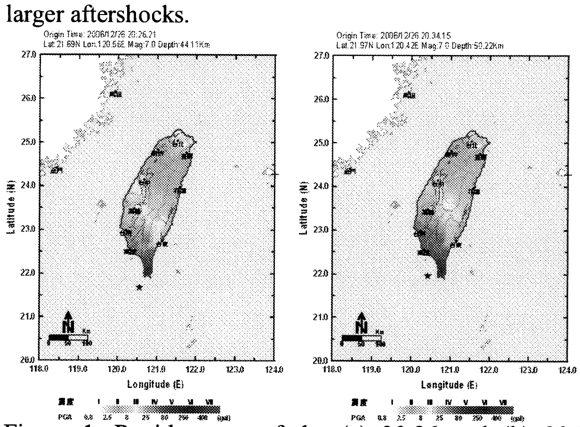

Figure 1. Rapid report of the (a) 20:26 and (b) 20:34 December 26, 2006 earthquake by the Central Weather Bureau.

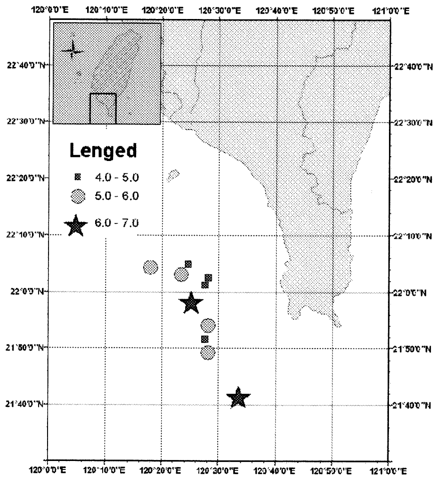

Figure 2. Epicenters of the mainshock of December 26, 2006 and its aftershocks.

We arranged a field survey after the earthquakes and in this paper report the damage and collected ground motion recordings of the Taiwan Strong Motion Instrumentation Program (TSMIP network: Kuo *et al.*, 1995; Liu *et al.*, 1999) operated by the Central Weather Bureau. We use this data to compare peak ground accelerations (PGAs) and the response spectra with the building code to better understand the reasons why such extensive damage occurred.

2. REGIONAL GEOLOGY AND BACKGROUND SEISMICITY

2.1 Regional Geology

The hills on the east side of Hengchun Peninsula are the southern extension of the Central Mountains. Their strikes are mostly in a north-south or northeast direction. Major rivers on the slopes facing east include Kangkou and Chioupeng creeks, both of which flow into the Pacific Ocean. Those on the slopes facing west include the Suchung, Baoli, and Wangsha creeks; all of these flow into the South China Sea. Several well-developed terraces are cut by these creeks. The coast of the Hengchun Peninsula is surrounded by coral reefs. Sand dunes and beaches are common. A narrow, low-lying valley running from north to south from Haikou to Nanwan is the most exceptional topographic feature. Along the valley's eastern flank are hills and highlands of varying elevations. Along its western flank are undulating plains with elevations between 5 and 100 meters.

Ho (1986) considered the Hengchun Peninsula as a very narrow section of the southernmost Central Mountain Range, forming the southernmost tip of Taiwan Island. The region is mainly composed of unmetamorphosed Miocene formations. On top of these Miocene formations are partially covered Pliocene-Pleistocene and more recent sediments. In terms of stratigraphy, the northern part of Hengchun Peninsula is composed of slightly metamorphosed argillites and slates, interspersed with small amounts of sandstones. These rocks are considered part of the Lushan Formation. The southern part of the Hengchun Peninsula is mainly composed of unmetamorphosed Tertiary formations, transitioning northward into the Lushan Formation. Tsan (1974a and 1974b) in his geological surveys of this area named the lower part of the Miocene formation as Changlo Formation, mostly consisting of dark gray shale. He named the upper layer as Loshui Formation, consisting of sandstone and shale, with some conglomerates. Pelletier et al. (1986) lumped together all Miocene rocks as the Suchunghsi Formation, including the Kenting melanges.

The Maanshan Formation is a west dipping monocline. Its dip angle averages about 45°, although it varies locally. These Pliocene-Pleistocene sediments are in unconformity with the Miocene formations on the east side of the NPP3 plant site. Many researchers inferred this boundary as a major fault structure (i.e. the so called Hengchun Fault). Regarding tectonic activities, it is generally agreed that available evidence for fault movements is confined to the Miocene formation. The fault movements are considered to be related to a regional stress field at the time. Available evidence suggests that the Hengchun Peninsula has not been subjected to major fault movements since the late Pliocene to early Pleistocene. Early researchers on the geology of the Hengchun Peninsula proposed the Hengchun Fault to be a major NS striking fault on the west side of the Peninsula. It is located along the contact zone between the Pliocene-Pleistocene sedimentary rocks on the west and the Miocene rocks on the east. It is generally considered now to be a fault which lacks of evidence of any recent activity.

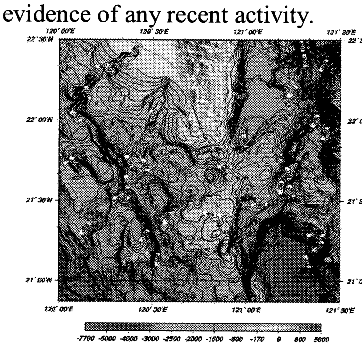

Figure 3. Bathometric map of the offshore area in southern Taiwan.

Although the Hengchun Fault in southernmost Taiwan is marked by an apparent topographical lineament on land, its offshore extension is not obvious (Figure 3). This is probably because the area is in an ongoing sedimentation environment. Regardless, the sea floor topography still shows a linear depression down to about 21°50', where it is cut by an EW submarine channel. Whatever the case, it is still hard to trace the offshore extension of Hengchun Fault with currently available data.

2.2 Background Seismicity

Monitoring of regional seismicity in Taiwan has been significantly improved since 1990 after the CWB installed dense networks of strong motion accelerographs and real-time velocity seismic stations. Figure 4 shows a map of earthquake epicenters in Taiwan area from 1973 to 2003. In the figure the size of dots represents magnitude, whereas the color represents focal depth (h): light black for h < 20 km, gray for 50>h>20 km, and dark black for h>50 km. We can see clearly from the figure most earthquakes occurred along the east coast and its offshore areas. They are apparently related to subduction of the Philippine Sea plate under Eurasian plate in northeastern Taiwan. There are significant earthquake activities under Taiwan Island due to collision of the two plates. It is evident from the figure that Hengchun area has relatively low seismicity as compared to other areas in Taiwan.

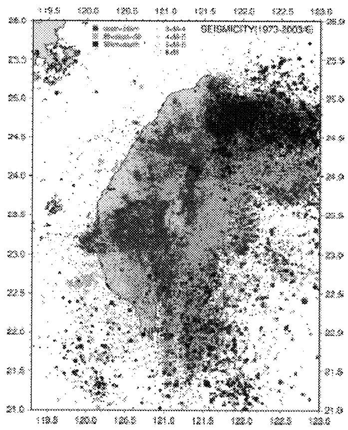

Figure 4. Seismicity map of Taiwan (1973 – 2003).

3. DAMAGE CAUSED BY THE PINGTUNG EARTHQUAKES

According to the field survey after the event occurred, three residential houses collapsed, and numerous others suffered cracks in their walls in the Hengchun area. Some fence walls collapsed. Ceilings in many old houses as well as in the Pingtung County Government Office fell leaving a mess on floor. A road next to the Shanhai Elementary School failed, resulting in piles of debris in the playground. Some classrooms suffered severe cracking and peeling on the walls. Some cracks extended for as long as 10 m. Figure 5 shows a photo of building damage. Rock falls in the Shanhai Elementary School are shown in Figure 6. In the Nanwan area two areas exhibited liquefaction, though this was due to back-fill soil not the original soil layer (Figure 7).

Figure 5. Building collapsed in the Hengchun area.

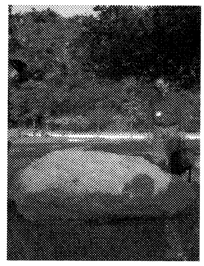

Figure 6. Rock fall in an elementary school.

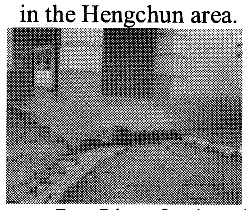

Figure 7a. Liquefaction in the Nanwan elementary school.

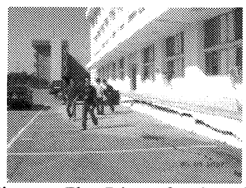

Figure 7b. Liquefaction in the Nanwan area.

Fires broke out at two stores in a shopping mall on Chungcheng Road in the old district of Hengchun. Figure 8 shows an example of how the fire occurred and the extent of fire. Two feeder lines between Pingtung and Chehcheng were broken, resulting in power outages for about 3,000 customers. Gas leaked in a cooking classroom of the Hengchun Vocational School. Unit 2 of Taipower's NPP3 was manually shut down and safety valves were tripped at the Taling Oil Refinery in Kaohsiung. In addition, fires broke out at two houses in Nantzu District of Kaohsiung. Twelve cases of people being trapped in elevators and one case of a gas leak were reported. The earthquakes also caused major submarine fiber-optic cable failures in the offshore areas of Hengchun, disrupting international telephone and Internet connections (Figure 9, Hsu, 2007).

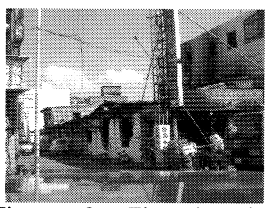

Figure 8. Fire in the Hengchun area.

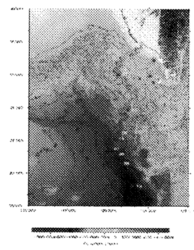

Figure 9. Submarine cable faults due to the Pingtung Earthquake (Hsu, 2007).

4. STRONG MOTION ANALYSIS

4.1 Analysis of Peak Acceleration Values

When an earthquake takes place seismic energy propagates by waves from the source rupture zone to the site. Depending on rock properties and geometric spreading of propagation paths the shaking intensity (in terms of PGA for example) will unavoidably attenuate. In engineering applications the attenuation of seismic intensity can be expressed as:

$$Y = f(M,R) \qquad (1)$$

where M and R represent earthquake magnitude and source distance, respectively. In practice, several functional forms are often used to represent attenuation. In this study, we adopt Campbell's form (Campbell, 1981) for regression. The result is as follow:

$$Y=0.003694e^{1.75377M}(R+0.122196e^{0.78315M})^{-2.056445} \qquad (2)$$

The results for Equation 2 are based on observed ground motion data (including the Chi-Chi earthquake and its aftershocks) from 1993 to 2000. The ground motion parameters are represented as the geometric mean of two orthogonal horizontal components. In regression for the attenuation coefficients we included all hard site stations except those in the Taipei Basin and Ilan Plain. Following typical seismic hazards analysis, the definition of closest distance to the fault is used for R. Thus, Equation 2 can be used to assess seismic hazards in the Taiwan area.

(a) (b)

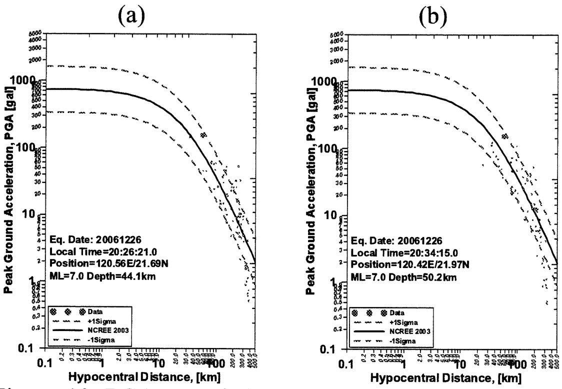

Figure 10. PGA recorded at CWB real time stations and expected curve for the (a) 2026 earthquake and (b) 2034 earthquake.

By substitution in Equation 2 with the magnitude and focal depth of the two earthquakes we can calculate the expected PGA values. The results are shown in Figure 10: the solid black curve is for the mean values and the dotted curves for the plus- and minus-one-standard-deviation values. The dot in each figure shows the geometric mean of horizontal PGA value recorded at the free-field station at NPP3. Also shown in red dots in the figures are the PGA values recorded at the CWB real-time strong motion stations. From the figures we can see that most of the observed PGA values are within one standard deviation, but some exceed the expected range due to site amplification at the alluvium plane in the southern Taiwan.

The predictive model for potential ground motions (Jean *et al.*, 2003, 2006; Wen *et al.*, 2006) is based on the attenuation relation for hard sites and takes into account the site conditions of individual strong motion stations. It can be used to calculate the expected PGA values with given magnitude and location of an earthquake. We first use Equation 2 to calculate the expected ground motion values. Next we incorporate the site amplification coefficients C_0 and C_1 in Equation 3 to obtain the corrected ground motion values at individual stations:

$$ln(Y_e)=C_0+C_1xln(y) \qquad (3)$$

in which y is calculated from Equation 2, C_0 and C_1 are site amplification coefficients for each individual station, and Y_e is the expected ground motion value after correction for local site effects. But the uniqueness was different for each earthquake, so the limited observations of the Real-Time Digital (RTD) stream output system can help to correct the source effect. The RTD system is capable of calculating the earthquake location and its magnitude about one minute after an earthquake occurs. The ground shaking information of the RTD site can also be automatically distributed at the same time (Jean et al., 2006). Using the expected ground motion values obtained by Equation 3 and observations of the RTD system, we can make shakemaps for potential earthquakes.

(a) (b)

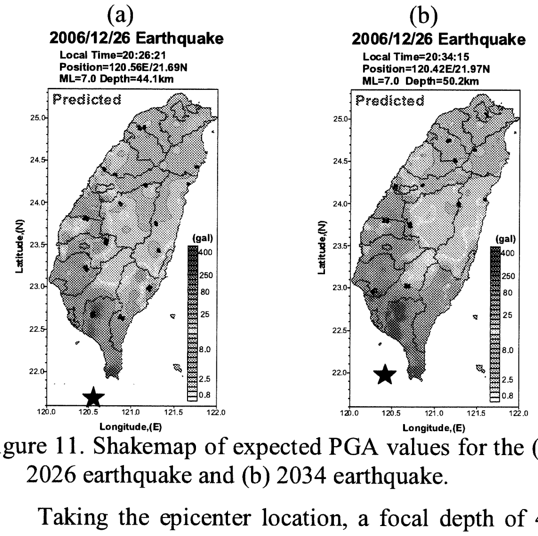

Figure 11. Shakemap of expected PGA values for the (a) 2026 earthquake and (b) 2034 earthquake.

Taking the epicenter location, a focal depth of 44.1 km and magnitude M_L7.0 for the 2026 Earthquake, we use Equations 2 and 3 and observations of the RTD system to assess the probable ground motion distribution, as shown in Figure 11a. It shows that the Hengchun area experienced CWB intensity 4. The results for the M_L7.0 2034 earthquake are shown in Figure 11b. A relatively large area in Pingtung suffered CWB intensity 5. These two expected ground motion maps show more large areas are greater than intensity 4 than those actually observed intensity values from the CWB real-time strong motion network shown in Figure 1 for the two earthquakes. After waiting several months to retrieve TSMIP records, the observation shakemaps of these two events were plotted in Figure 12. The maximum PGA occurred at the Station KAU046 reaching about 0.26 g (Figure 13). The two expected ground motion maps are quite consistent with what were actually observed intensity values from the TSMIP strong motion network shown in Figure 12. This shows that this predictive model for potential ground motions, which accounts for local site conditions, can reflect clearly the amplification effects of shaking intensity at soft soil sites in the Chianan area. And this predictive model can be used immediately after we receive the earthquake source parameters, meaning this shakemap can be used as a reference for loss estimation and emergency response.

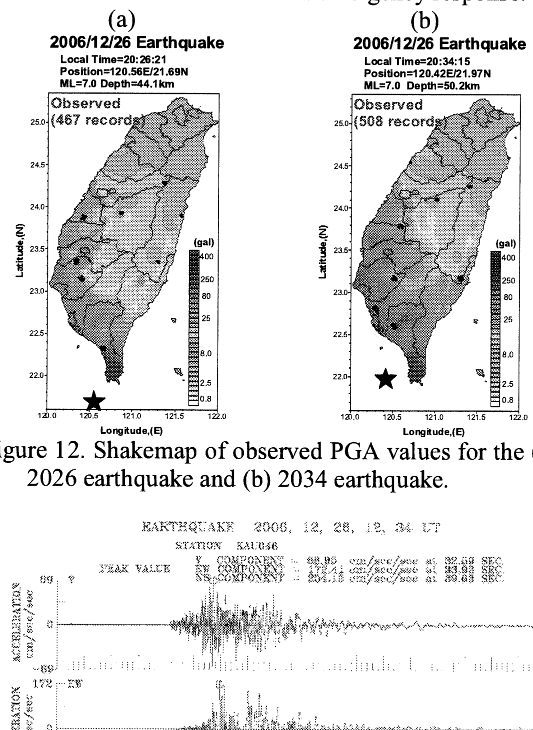

Figure 12. Shakemap of observed PGA values for the (a) 2026 earthquake and (b) 2034 earthquake.

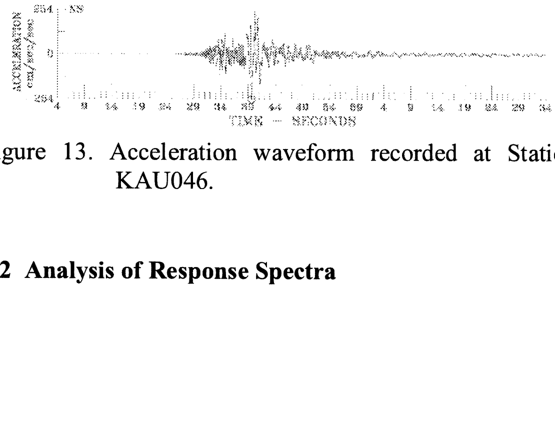

Figure 13. Acceleration waveform recorded at Station KAU046.

4.2 Analysis of Response Spectra

During this earthquake, most of the buildings, which collapsed or were damaged, were in the Hengchun area. On the basis of the building code, the design spectra parameters in the Hengchun, Pingtung area for class 2 sites are listed in Table 1 (The Committee for Architecture Technique, 2005). For the many buildings that are not newly constructed, so most structures need to consider the zoning parameter of 0.28 g (The Committee for Architecture Technique, 1995) in their design. The design code of code'1995 and code'2005 in 2500 years return period are similar design PGA value. It means the design code in 1995 year was considering high safety factor. The maximum PGA value recorded in the Hengchun area is about 0.26 g (254 gal) at KAU046 station for the 2034 Earthquake. Although it is not greater than the 0.28 g of the code'1995. Station KAU046 is the nearest strong motion station to the collapsed structure. We calculated a 5% damping response spectra from the acceleration time histories recorded at KAU046. The results are plotted in Figure 14 together with the corresponding design spectra in the same figure for comparison. From the observed spectral accelerations of 2026 earthquakes (Figure 14a), the observed response spectra fall below the corresponding design spectra of the code'1995 and code'2005 in 2500 years return period, except for the EW component at the period around 1~2 seconds, which has a larger response. Considering that it is typical for periods of 1~2 seconds to correspond to high rise buildings greater than 10 storeys, then the low-rise building collapses in the Hengchun area may not be directly due to the strong shaking of the 2026 Earthquake. For the 2034 Earthquake, except for the NS component having a larger response at around 1~2 seconds, the observed spectral accelerations at both components are already greater than the design spectrum at less than 1 second. The damage survey also shows that the building in Figure 5 collapsed during the second earthquake.

Table 1. Design spectra in the Hengchun, Pingtung area for class 2 sites (The Committee for Architecture Technique, 2005)

Year	EPA	S_{as}	S_{a1}
475	0.22 g	0.55 g	0.45 g
2500	0.28 g	0.7 g	0.52 g

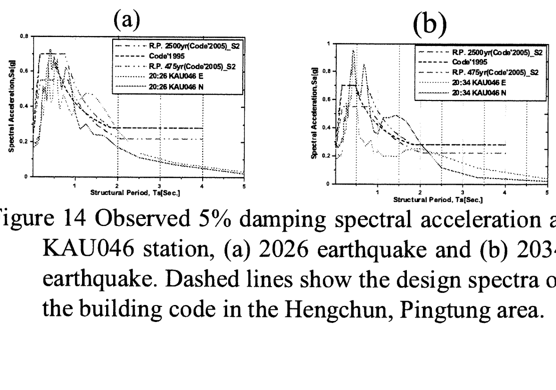

Figure 14 Observed 5% damping spectral acceleration at KAU046 station, (a) 2026 earthquake and (b) 2034 earthquake. Dashed lines show the design spectra of the building code in the Hengchun, Pingtung area.

5. RESULTS AND DISCUSSIONS

Two large M_L7.0 earthquakes occurred on December 26, 2006 in the offshore areas of Hengchun in Pingtung County. According to the CWB records, there has never been such a large earthquake in that area. In summary, these earthquakes caused 2 deaths, 42 injuries (2 deaths and 38 injuries in Pingtung County, 3 injuries in Kaohsiung County and 1 injury in Kaohsiung City), 3 houses to collapse, and 12 fires (10 in Kaohsiung City and 2 in Pingtung County). Liquefaction occurred in the Nanwan area due to local back-fill soil. The earthquakes also caused massive failures of major submarine fiber-optic cables in the offshore areas of Hengchun, resulting in severe disruption of international telephone and Internet connections. It is still hard to assess the economic losses caused by these earthquakes.

As for response spectra, we calculated a 5% damping response spectra from the records obtained near where the buildings collapsed. We further compared the observed response spectra with corresponding design spectra at the Hengchun, Pingtung area. With the exception that the NS component exceeded the design spectra at periods around 1~2 seconds, all other observed response spectra were below the design spectra for other periods of the 2026 Earthquake. The spectra of 1~2 seconds only correspond to high-rise building response. This shows that the low-rise building collapse in the Hengchun area was due to the strong shaking of the 2034 Earthquake at periods less than 1 second.

A total of 467 and 508 accelerographs were triggered by the 2026 and 2034 Earthquakes. The recorded PGA values generally agree with the expected values calculated from the attenuation relations for Taiwan area. Moreover, the distribution patterns of observed PGA values are also consistent with those of expected PGA values calculated based on existing ground motion prediction models. Due to the predictive models usefulness at estimating a potential shakemap for peak ground acceleration, we can use it as an early-stage reference for loss estimation and emergency response immediately after receiving the earthquake source parameters from the CWB. This will help with seismic hazard mitigation work.

Acknowledgements:

We would like to thank the Central Weather Bureau, Taiwan for providing the strong motion data. This study was supported by the National Science Council under the grant number NSC95-2745-M-008-003.

References:

Campbell, K. W. (1981), "Near-source attenuation of peak horizontal acceleration," *Bull. Seism. Soc. Am.*, 71(6), 2039-2070.

Ho, C. S. (1986), "An introduction to the geology of Taiwan – Explanatory text of the geologic map of Taiwan," Central Geological Survey, MOEA, 164pp.

Hsu, S. K. and MACHO Working Group (2007), "Tectonic and oceanic background of the MACHO site," Abstract and Presentations of the Workshop of the MACHO project: new earthquake and tsunami observation and expectation in Taiwan, Nov. 16-17, 921 Earthquake Museum of Taiwan.

Jean, W. Y., Chang, Y. W., and Loh, C. H. (2003), "Early estimation procedure of seismic hazard for major earthquake," Proceedings of the Joint NCREE/JRC Workshop International Collaboration on Earthquake Disaster Mitigation Research, Taipei, Taiwan, 435-440.

Jean, W. Y., Chang, Y. W., Wen, K. L., and Loh, C. H. (2006), "Early estimation of seismic hazard for strong earthquakes in Taiwan," *Natureal Hazards*, **37**, 39-53.

Kuo, K. W., Shin, T. C., and Wen, K. L. (1995), "Taiwan strong motion instrumentation program (TSMIP) and preliminary analysis of site effects in Taipei basin from strong motion data," In *Urban Disaster Mitigation: the Role of Engineering and Technology* (ed. F.-Y. Cheng and M.-S. Sheu), Elsevier Science Ltd., 47-62.

Liu, K. S., Shin, T. C., and Tsai, Y. B. (1999), "A Free-Field Strong Motion Network in Taiwan: TSMIP," *Ter. Atm. Oce.*, 10, 2, 31-50.

Pelletier, B. and Stephan, J. F. (1986), "Middle Miocene subduction and late Miocene beginning of collision registered in the Hengchun Peninsula: geodynamic implication for the evolution of Taiwan," *Tectonophysics*, 125, 1-3, 133-160.

Tsan, S. F. (1974a), "The Kenting Formation, a note on Hengchen peninsula stratigraphy," *Proc. Geol. Soc. China*, 17, 131-134.

Tsan, S. F. (1974b), "Stratigraphy and structure of the Hengchun peninsula, with special reference to a Miocene olistostrome," *Bull. Geol. Surv. Taiwan*, 24, 107-108.

The Committee for Architecture Technique (1995), "The building seismic design code," Ministry of the Interior, R.O.C.

The Committee for Architecture Technique (2005), "The building seismic design code," Ministry of the Interior, R.O.C.

Wen, K. L., Chang, Y. W., and Jean, W. Y. (2006), "Seismic potential estimation of the Maishan fault," Symposium for Centenary of Maishan earthquake, Chungcheng University, March 16~18.

(This Paper Already Submitted to Terr. Atm. Oce. Sci.)

SEISMIC BEHAVIOR OF OFFICE FURNITURE IN HIGH-RISE BUILDING DUE TO LONG-PERIOD GROUND MOTION

Saburoh Midorikawa[1], Toshiyuki Masatsuki[2]. Michihiro Ohori[3], and Hiroyuki Miura[4]

1) Professor, Dept. Built Environment, Tokyo Institute of Technology, Japan
2) Formerly Graduate Student, Dept. Built Environment, Tokyo Institute of Technology, Japan
3) Research Associate, Center for Urban Earthquake Engineering, Tokyo Institute of Technology, Japan
4) Assistant Professor, Dept. Built Environment, Tokyo Institute of Technology, Japan
smidorik@enveng.titech.ac.jp ,toshi-masatsuki@kke.co.jp, ohori@enveng.titech.ac.jp, hmiura@enveng.titech.ac.jp

Abstract: This paper examines the behavior of office furniture in a high-rise building due to long-period ground motion. In order to grasp fundamental characteristics of behavior of furniture, shaking table tests are conducted. The behavior of the furniture in the shaking table tests is simulated by a rigid body simulation program. Finally, we simulate the behavior of a number of office furniture in a super-high-rise building at Tokyo during the Tokai earthquake.

1. INTRODUCTION

The metropolitan areas in Japan are located on large basins where long-period ground motion is easily excited by a large shallow earthquake. In the metropolitan areas, many high-rise buildings have been built up and may vibrate largely by the long-period motion. For example, in Tokyo, more than 200 buildings higher than 100 m have been constructed as shown in Fig. 1. The vibration periods of the buildings range 2 to 6 second (see Fig. 2).

Some of the high-rise office buildings in Tokyo have about 10,000 occupants and high potential for seismic indoor risk. Therefore, seismic behavior of furniture in the buildings needs to be studied in order to evaluate risk of injuries and confusions by overturning or displacement of furniture.

The overturning of furniture during earthquakes has been examined (e.g. Ishiyama, 1982). The behavior due to long-period motion, however, has not been well discussed. In this paper, in order to evaluate seismic risk in office space, the behavior of office furniture is examined in an upper floor of a high-rise building due to the long-period motion by means of the shaking table test and simulation.

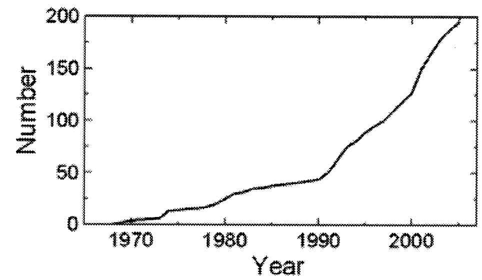

Figure 1 Number of High-rise Buildings in Tokyo

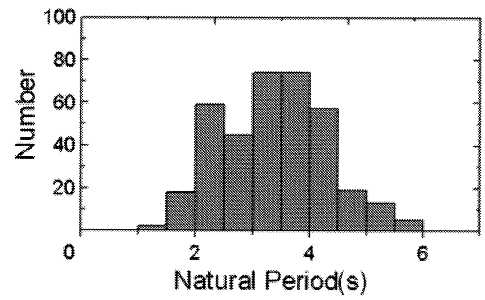

Figure 2 Vibration Periods of High-rise Buildings in Tokyo

2. SHAKING TABLE TESTS

In order to study fundamental characteristics of behavior of furniture, shaking table tests are conducted using a large-stroke shaking table with maximum displacement of 1m. The maximum acceleration and velocity are 1000 cm/s^2 and 150 cm/s, respectively. The shaking direction is two horizontal. The size of the table is 3.2 m by 2.5 m. The payload is one ton. The appearance of the table is shown in Photo 1.

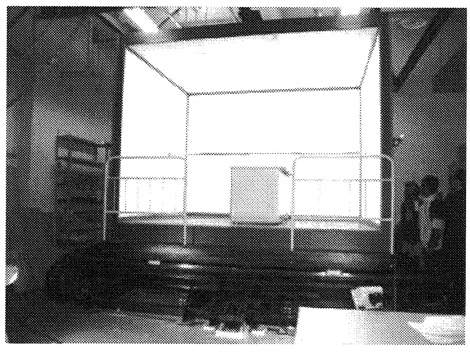

Photo 1 Appearance of Shaking Table

Table 1 Specifications of Models

Model	Size (cm)	Weight (kg)
Simple box	120×60×60	30
Cabinet	45×90×110	130
Desk	120×70×70	67
Caster chair with no weight	60×60×70	12
Caster chair with weight (50kg)	60×60×70	60
Box with caster	60×60×120	110
Desk with chair	120×100×70	127

Table 2 Shaking Cases

Without caster

Case	Period (s)	Acc.(cm/s/s)	Vel.(cm/s)	Dis.(cm)
A1	5	157.9	125.7	100
A2	2	197.4	62.8	20
A3	3	219.3	104.7	50
A4	2.5	252.7	100.5	40
A5	3	311.4	148.7	71
A6	2.5	372.7	125.7	59
A7	2	394.8	125.7	40
A8	2	463.8	147.7	47

With caster

Case	Period (s)	Acc.(cm/s/s)	Vel.(cm/s)	Dis.(cm)
B1	2.5	126.3	50.3	20
B2	3	87.7	41.9	20
B3	3	131.6	62.9	30
B4	5	142.1	113.0	90

The floor materials used in the tests are plywood and tile carpet. The test models are a simple wood box, a cabinet, a desk, a caster chair, a box on casters, and a desk with a chair. The box on 4 casters is assumed as a copy machine. The desk with a chair is assumed as a man in a sitting position who clings to desk during shaking. The specifications of the models are shown in Table 1.

The shaking is given to one horizontal direction with sinusoidal waves. The tests are conducted for twelve cases of shaking with acceleration of 90 to 460 cm/s^2 and period of 2 to 5 second, as shown in Table 2. The acceleration and relative displacement of the models are measured by sensors as shown in Fig. 3.

The results of the tests are summarized in Table 3. The results indicate that the caster chair and the box on casters move in the low acceleration level case of about 150 cm/s^2, and that the desk do not move in the highest acceleration level case of about 460 cm/s^2, but the desk with chair moves in the lower case of about 250 cm/s^2.

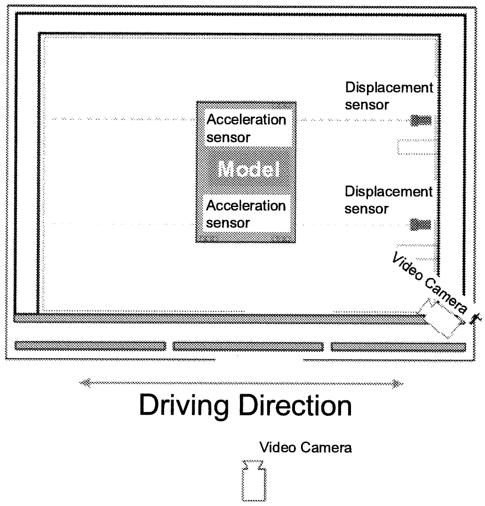

Figure 3 Locations of Sensors

Table 3 Results of Shaking Table Tests

C: Floor material is tile carpet. W: Floor material is plywood. ○: Moved, ×: Not moved, △: Overturned, −: Not tested

Case	Simple box		Cabinet				Desk				Caster chair with no weight		Caster chair with weight		Box with caster		Desk with chair			
			Longitudinal direction		Transverse direction		Longitudinal direction		Transverse direction								Longitudinal direction		Transverse direction	
	C	W	C	W	C	W	C	W	C	W	C	W	C	W	C	W	C	W	C	W
A1	×	×	×	×	−	−	×	×	×	×	○	−	○	−	○	○	×	×	×	×
A2	×	×	×	×	−	−	×	×	×	×	−	−	−	−	○	○	×	○	×	○
A3	×	×	×	×	×	−	×	×	×	×	−	−	−	−	○	○	×	○	×	○
A4	×	×	×	×	△	−	×	×	×	×	−	−	−	−	○	○	○	○	×	○
A5	○	○	○	×	△	×	×	×	×	○	−	−	−	−	○	○	○	○	○	○
A6	○	○	○	×	−	△	×	○	×	○	−	−	−	−	−	−	○	○	○	○
A7	○	○	○	○	−	△	×	○	×	○	−	−	−	−	−	−	○	○	○	○
A8	○	○	○	○	−	−	×	○	×	○	−	−	−	−	−	−	○	○	○	○
B1	−	−	−	−	−	−	−	−	−	−	○	○	○	○	−	×	−	−	−	−
B2	−	−	−	−	−	−	−	−	−	−	○	○	○	○	−	×	−	−	−	−
B3	−	−	−	−	−	−	−	−	−	−	○	○	○	○	−	×	−	−	−	−
B4	−	−	−	−	−	−	−	−	−	−	○	○	○	○	−	○	−	−	−	−

3. SIMULATION METHOD AND RESULTS

The behavior of the furniture in the shaking table tests is simulated by a rigid body simulation program called Springhead (Hasegawa and Sato, 2004). In Springhead, a contact area is divided into several triangle elements. Springs and dampers are set at the triangle element (See Fig. 4), and the reaction force for each element is computed and used in the simulation. Therefore, Springhead is able to calculate fast and accurately contact forces such as dynamic and static friction force. In the simulation, rolling mechanism such as a caster is also considered.

Dynamic parameters of the furniture used in the simulation such as friction, spring and damper coefficients are determined from the comparison of the computed behavior with the behavior in the shaking table tests. As the result of the parameter study, the behavior in the shaking table tests is well reproduced by the simulation as shown in Fig. 5.

Then the behavior of a number of furniture in an upper floor of a high-rise building is simulated at Tokyo due to the anticipated Tokai earthquake (See Fig. 6). The simulated ground motion by Hijikata et al.(2006) is used to calculate the floor response of the 30-story building as shown in Fig. 7. In this case, the maximum velocity and displacement of the floor response are 260 cm/s and 130 cm, respectively.

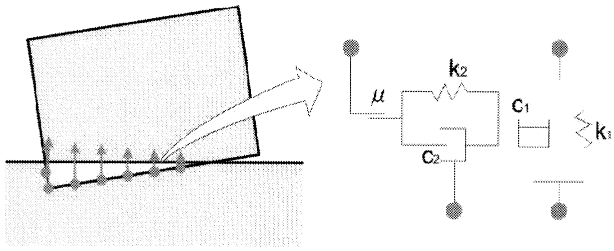

Figure 4 Scematic Figure of Springhead

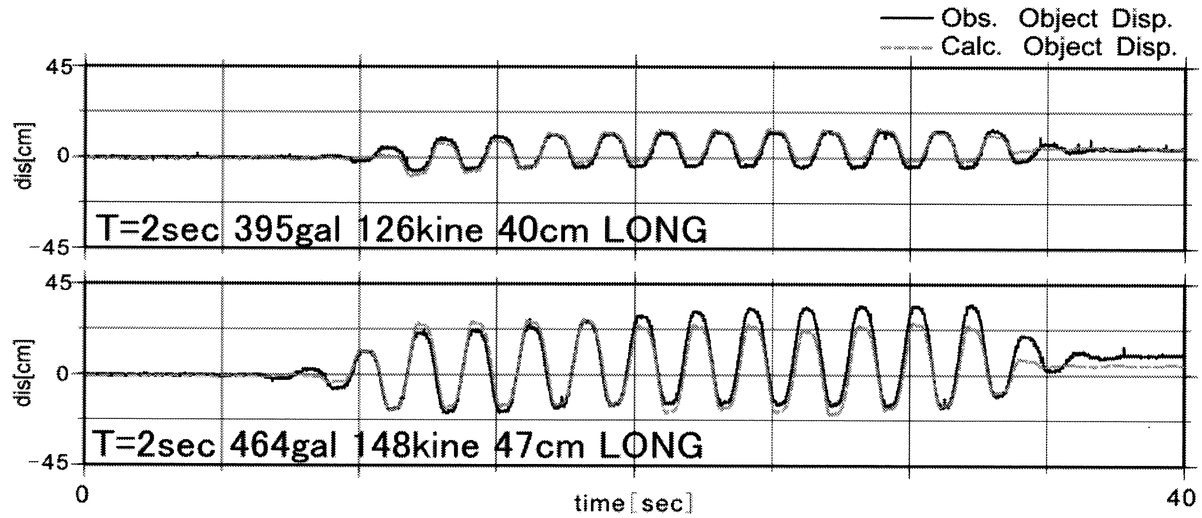

Figure 5 Comparison of Shaking Table Test and Simulation

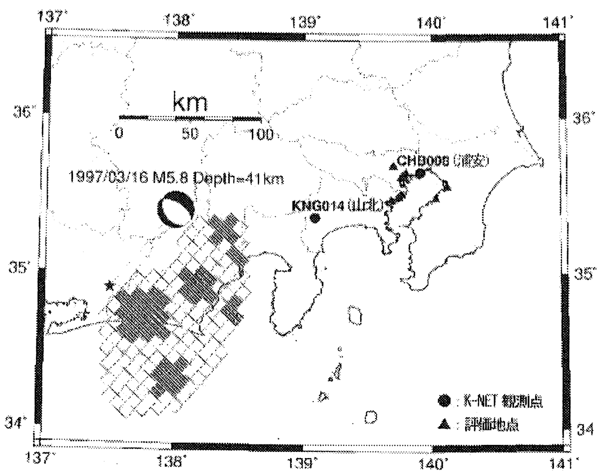

Figure 6 Locations of Tokai Earthquake and Tokyo (after Hijikata et al., 2006)

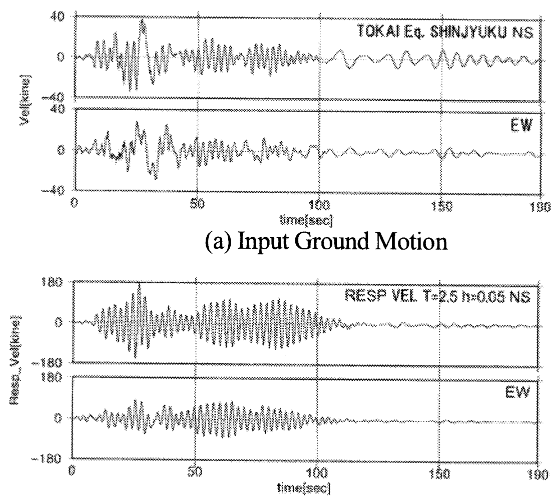

(a) Input Ground Motion

(b) Building Floor Response

Figure 7 Time Histories of Ground and Floor Responses

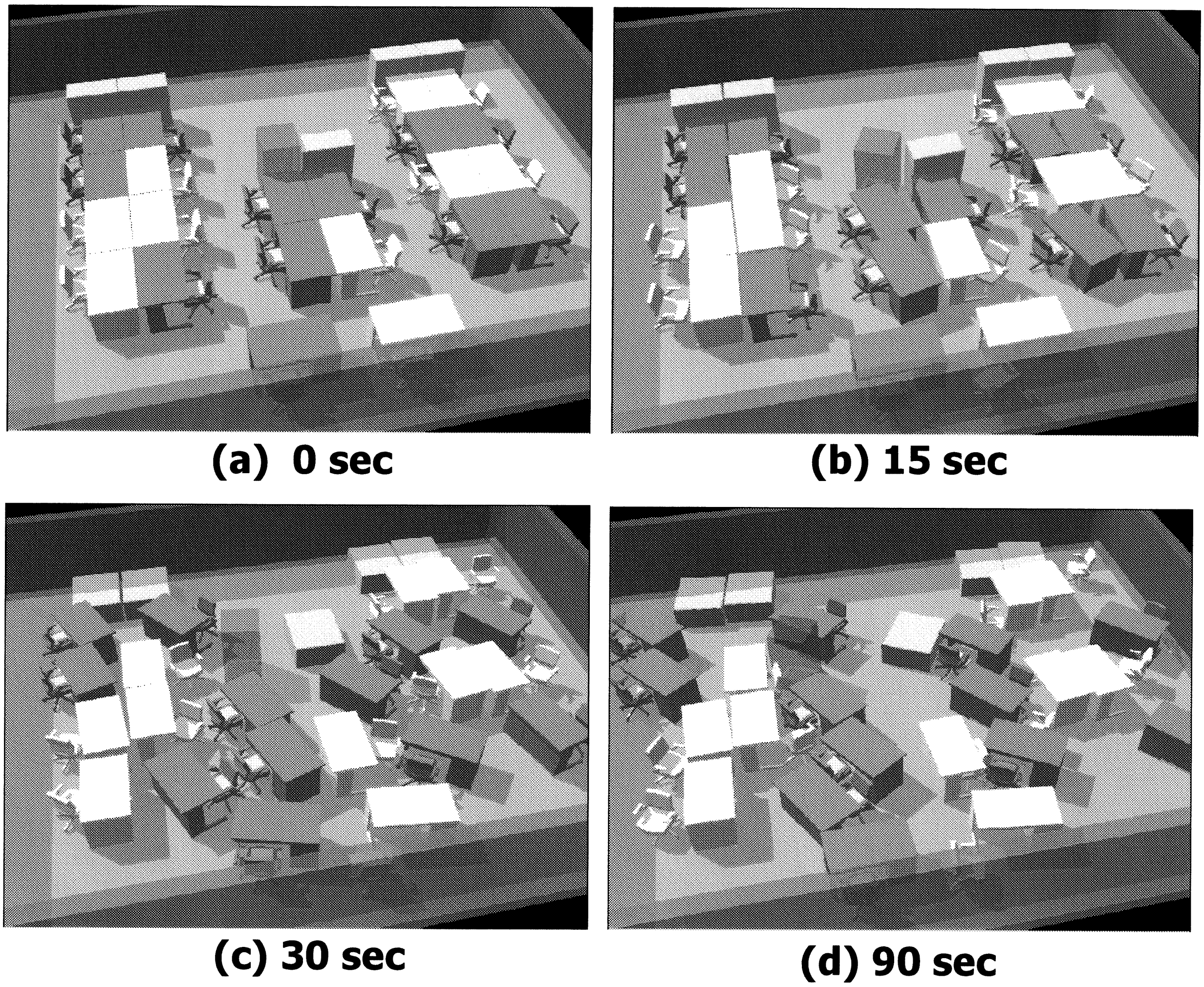

Figure 8 Behavior of Office Furniture on Upper Floor of High-rise Building

Figure 8 shows the result of the simulation, indicating that the furniture continues to move around and collide against each other during about 80 seconds. Desks with a chair and a box with casters are displaced about 1 m. The behavior of the furniture can cause fear and injury to people in the floor, and make the evacuation action difficult.

4. CONCLUSIONS

The behavior of office furniture in a high-rise building due to long-period ground motion is examined in order to evaluate risk of injuries and confusions by overturning or displacement of furniture. The shaking table tests are conducted. to grasp fundamental characteristics of behavior of furniture. The behavior of the furniture in the shaking table tests is well simulated by a rigid body simulation program, indicating validity of the simulation method used. Then the behavior of a number of furniture is simulated in an upper floor of a 30-story high-rise building at Tokyo due to the anticipated Tokai earthquake. The furniture continues to move around and collide against each other during about 80 seconds. Desks with a chair and a box with casters are displaced about 1 m. The behavior of the furniture can cause fear and injury to people in the floor, and make the evacuation action difficult.

Acknowledgements:

The study is partially supported by Grants-in-Aid for Scientific Research (Scientific Research (A) No.19201034) from Ministry of Education, Culture, Sport, Science, and Technology (MEXT).

References:

Hasegawa, S. and Sato, M. (2004), "Real-time rigid body simulation for haptic interactions based on contact volume of polygonal objects," *Eurographics 2004*, **23**, 529-538.

Hijikata, K. et al. (2006), "Simulation of broad-band ground motion in the Kanto basin due to the Tokai earthquake," *Proceedings of the Second Symposium on Large Subduction Earthquakes*, 83-90 (in Japanese).

Ishiyama, Y. (1982), "Criteria for overturning of bodies by earthquake excitations," *Transaction of A.I.J.*, 317, 1-14.

Fifth International Conference on Urban Earthquake Engineering
March 4-5, 2008, Tokyo Institute of Technology, Tokyo, Japan

MODIFIED SEMI EMPIRICAL TECHNIQUE FOR PREDICTION OF STRONG GROUND MOTION

A. Joshi[1], and K. Mohan[2]

1) Department of Earth Sciences, Indian Institute of Technology Roorkee, Roorkee 247 667, India
2) Institute of Seismological Research, Gandhinagar, 382218, Gujarat, India
anushijos@yahoo.co.in,

Abstract: This paper present modified semi empirical method for simulation of strong ground motion. In this paper simulation of strong ground motion due to a rupture buried in a earth medium consisting of several layers of different velocities and thicknesses is made by considering (1) transmission of energy at each layer; (2) frequency filtering properties of earth medium and earthquake source; (3) correction factor for slip of large and small magnitude earthquakes and (4) site amplification effects at various stations. To test the efficacy of the developed technique, strong motion records were simulated at different stations that have recorded the 2004 Niigata-ken Chuetsu, Japan earthquake (M_s 7.0). Comparison is made between the simulated and observed velocity and acceleration records and their response spectra. Efficacy of this technique has been established by comparison of synthetic with the observed records over wide range of frequencies. The simulation technique is further applied to predict the strong motion records due to M 8.0 earthquake at various sites in the central seismic gap region Kumaon Himalaya, India.

1. INTRODUCTION

The technique of semi empirical modeling of strong ground motion was initially started by Midorikawa (1993). The technique was based on the Empirical Greens Function (EGF) technique of Irikura (1983). Although the EGF technique predicts strong motion data in most reliable manner, it requires the records of small events at those stations at which simulation is desired. The records of small events are not easily available at all sites of interest. Therefore the estimation of the strong motion parameters using EGF techniques is a difficult task, especially in those regions where we have limited seismic information in hand. The semi empirical technique of Midorikawa (1993) uses the envelope of acceleration records in place of small events used in the EGF technique. Joshi et al. (2001) has incorporated the stochastic nature of the strong ground motion and use of envelope function based on kinematic model of rupture plane as shaping time window to simulate high frequency strong ground motion. Further modification in this technique has been made by Joshi and Midorikawa (2004) by placing the rupture in a layered earth model and considering the correction for slip duration of small and large earthquakes. This modified technique is tested with the strong motion data of Himalayan and Japanese earthquakes (Joshi, 2004, Joshi and Midorikawa, 2004, 2005). Although these refinements give reliable simulations in a wide frequency range, the component wise simulation of strong motion records is needed for reliable assessment of engineering parameters. The work presented in this paper is the modification of above technique to simulate the component of the strong motion records by using the site effects at various stations.

2. METHODOLOGY

The technique presented in this paper is based on semi empirical method proposed by Midorikawa (1993) and later modified by Joshi (1997); Joshi et al. (2001) and Joshi and Midorikawa (2005). In this method, the entire rupture plane is divided into several small rupture planes which are termed as elements or subfaults. The basis of the division is self-similarity laws given by Kanamori and Anderson (1975) that are discussed in detail by Joshi (2004). In this semi empirical method, we use the envelope function generated by subfault in a layered earth model which is mathematically given by Joshi et al. (2001). The formula for envelope function requires parameters like peak ground acceleration value, duration parameter and transmission factor. The detail of these parameters are given by Joshi et al. (2001) and Joshi and Midorikawa (2004). Detail discussion of this method is given by Joshi and Midorikawa (2004).

For simulation of time series having basic spectral properties of acceleration record we have used the modified form of stochastic simulation technique given by Boore (1983). In this modified form the envelope of accelerogram released by subfaults has been used as the shaping window. The record having basic spectral shape of accelerogram is obtained after the white gaussian noise is passed through number of filters representing the source property, near site attenuation of high frequencies and anealstic attenuation. Using the semi empirical approach the envelope of vertical peak ground acceleration is simulated. Hence, after windowing the filtered record obtained from stochastic simulation technique the vertical component of accelerogram is obtained. Site amplification curve plays important role in resolving the generated vertical component into horizontal component. In the present work we have used the NS and EW component of observed records of small events at each station to obtain H/V ratio. The H/V ratio is computed from the portion of record, which contain S-wave phase. At each station two H/V ratio curves are obtained i.e. one for NS and other for EW component. The simulated NS and EW component of strong motion records are obtained after multiplying the spectrum of simulated vertical component with these two H/V ratio curves. In order to compensate the appropriate difference in the slip of large and small earthquake, the simulated record is further convolved with the correction function 'F (t)'given by Irikura et al. (1997). The method of simulation used in this paper is shown in Fig 1.

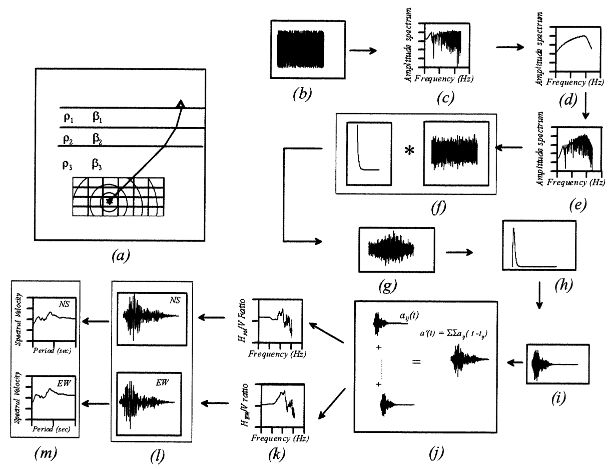

Figure 1 Complete method of simulation of strong ground motion showing (a) model of rupture plane in a layered earth medium. Radial rupture geometry is assumed. Star and triangle denotes nucleation point and the observation point, respectively, (b) white Gaussian noise, (c) spectrum of white Gaussian noise, (d) plot of the theoretical acceleration spectrum, (e) spectrum obtained after multiplying theoretical acceleration spectra with that of white noise, (f) The obtained sequence and its convolution with the correction function, (g) obtained sequence after convolution with the correction function, (h) shaping window used in the present approach, (i) obtained vertical component of record after windowing, (j) summation of records from each element to simulate the vertical component of acceleration record of the target earthquake, (k) site amplification curve (H/V) obtained from the NS and EW component of observed acceleration records, (l) the simulated NS and EW components of the records after filtering it with the site amplification curve and (m) The response curve at 5% damping.

3. CASE STUDY: 2004 NIIGATA-KEN CHUETSU EARTHQUAKE

On 23rd October 2004 at 17:56 (JST), an earthquake (M_{JMA} 6.8; Japan Meteorological Agency) struck mid Niigata prefecture, at 80 km south of Niigata city, on the West coast of Honshu, Japan (Bardet, 2004). The parameters of this earthquake are listed in Table 1. Kyoshin Net (K-NET) is a system which sends strong-motion data on the Internet. The earthquake of 23rd October, 2004 was recorded at 327 stations of Kyoshin network (K-NET) and 286 stations of KiK network (KiK-NET). The data used in this work is downloaded from the K-NET site maintained by NIED, Japan. In the present method of simulation we use the site amplification curves at each station. We have selected twenty-three stations at which we have performed the simulation. In order to have H/V curves at each of these twenty-three sites, we have selected at least six past events at each station. For simulation purpose, we are using the average H/V curve at each station.

Table 1 Parameter of the 23rd October 2004 Niigata-ken Chuetsu earthquake, Japan.

Hypocenter	Size	Fault Plane Solution	Ref.
8:56:4.8 (GMT) 37.31N, 138.83E 13 km	$m_b = 6.4$ $M_s = 7.0$ $M_W = 6.6$ $M_s = 6.3$ $M_{JMA} = 6.8$	NP1:φ=23, δ=39, λ=86 NP2:φ=209, δ=51, λ=93	CMT Harv.

In the present work the regression relation between vertical peak ground acceleration, magnitude and hypocentral distance given by Abrahamson and Litehiser (1989) has been used. Using data of the 2004 Niigata ken-Chuetsu earthquake, the duration parameter has been computed at various stations and the following modified form of regression relation for duration parameter has been obtained:

$$T_d = .0015\ 10^{.5M} + 1.79\ R^{0.037}$$

In this expression, M is the magnitude of earthquake and R is the hypocentral distance in km. In the present method we have used the frequency dependent Q relations given by Kiyono (1992) as it is an average relation for Japan and has been already tested earlier by Joshi and Midorikawa (2004) for simulation of strong ground motion of the Geiyo earthquake of 2001, Japan.

The modelling parameters of the 2004 Niigata-ken Chuetsu earthquake are kept similar to that assumed by Honda et al. (2004) for estimation of source parameters of this earthquake. In order to have simulations at different locations, we have selected 23 stations surrounding the rupture plane. The site amplification at each station is computed from the records of past events recorded by instrument placed at same station.

The rupture plane is placed at a depth of 13 km from surface of earth in a layered velocity model given by Honda et al. (2004). This rupture plane is divided into 12 subfaults each of magnitude 4.9. The NS and EW horizontal component of accelerogram due to target earthquake at 23 stations are simulated. The velocity, displacement and response spectra are calculated from observed and simulated acceleration records. Contour maps of acceleration, velocity and displacement have been prepared from both observed and simulated records and are shown in Fig 2. It is seen from Fig 2 that the general trend of distribution of peak ground acceleration from simulated records is matching closely with that from observed records in near field region. A good match is seen in the trend at far field stations in EW component (Fig 2(c) and d). Similar match in the distribution of peak ground velocity and peak ground displacement is seen in the nearfield regions. Among simulations at 23 stations, Fig 3 presents the result of simulations at three stations.

The station wise comparison shows that this technique is capable of simulating strong ground motion at nearfield as well as farfield stations in a frequency range 1- 50 Hz. Mismatch at many stations are evident at frequencies less than 1.0 Hz. In most of the cases contribution of simulated record is less in this low frequency range. This may be due to local heterogeneities present beneath the stations.

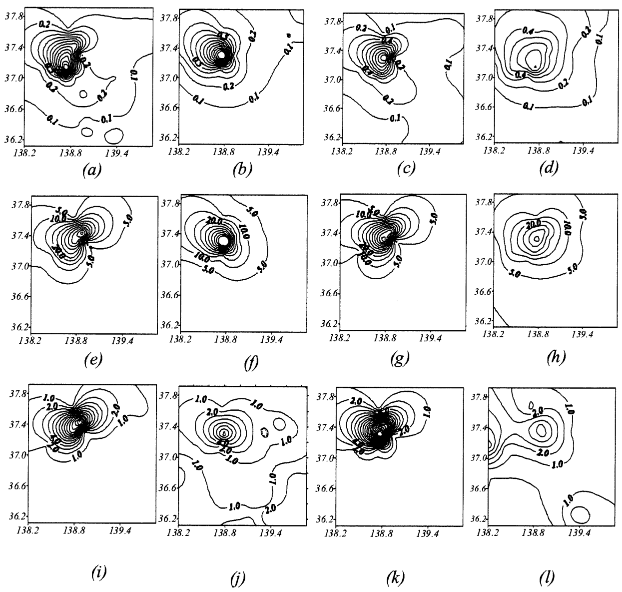

Figure 2 Contours of peak ground acceleration (in the % of g) computed from (a) observed NS component, (b) simulated NS component, (c) observed EW component and (d) simulated EW component of acceleration record. Contours of peak ground Velocity (in cm/sec) computed from (e) observed NS component, (f) simulated NS component, (g) observed EW component and (h) simulated EW component of velocity record. Contours of peak ground displacement (in cm) computed from (i) observed NS component, (j) simulated NS component, (k) observed EW component and (l) simulated EW component of displacement record.

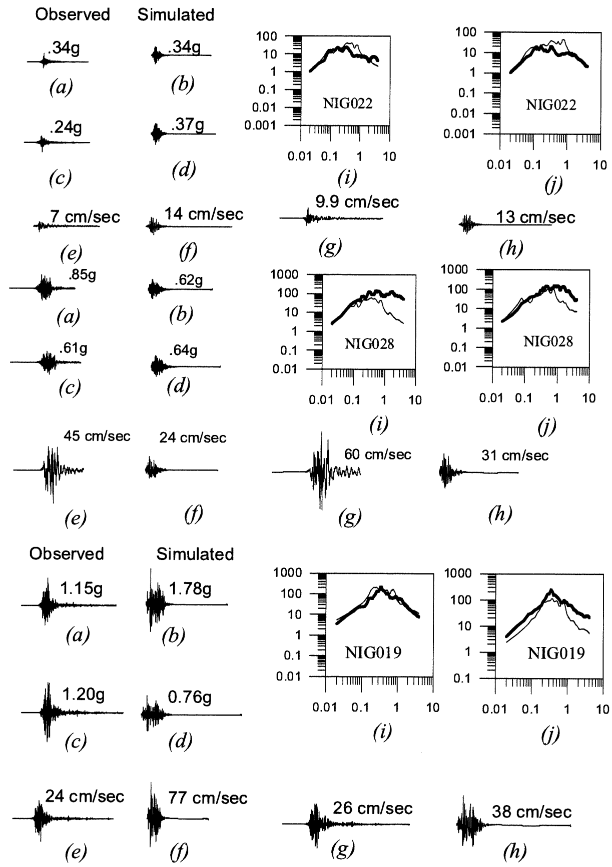

Figure 3 (a) Observed NS component and (b) simulated NS component, (c) observed EW component and (d) simulated EW component of acceleration record; (e) observed NS component and (f) simulated NS component, (g) observed EW component and (h) simulated EW component of velocity record. Comparison of response spectra prepared from (i) NS component and (j) EW component of observed and simulated records at NIG022, NIG028 and NIG019 stations. The x axis in the response spectra denotes period in second. The station names are shown inside the figure showing response spectra. The response spectra shown by thick black line represents that prepared from observed record.

4. PREDICTION FOR GREAT EARTHQUAKE IN KUMAON HIMALAYA

Uttarakhand Himalaya in India lies in the central seismic gap region identified by Khattri (1987). This region is among the seismically active regions. Most of the area in Uttarakhand state has been placed under zone V and zone IV of the seismic hazard map published by Bureau of Indian standard (BIS), Govt. of India. During last 100 years this region has been visited by 14 earthquakes of magnitude greater than 6.0. This region has witnessed two major earthquakes in the last decade. The 91.5 percent houses in the Uttarankhand state are made up of mud and adobe, brunt brick and stone and are weakest in strength during earthquake. According to census of India, 2001, the population of Uttarankhand state alone is 8,479,562 and the decadal growth rate (1991-2001) in population is 19.20%. Due to its enormous potential of hydroelectric power generation many project have been started in Uttarakhand. As this region of seismic gap in Himalaya has potential of generating great earthquake. A great earthquake in an hypothetical location along Main central Thrust in the central gap region has been modeled and the records are analysed in terms of strong motion parameters.

The attenuation relation of Abrahamson and Litehiser (1989) for estimation of vertical peak ground acceleration has been used in the present work. In the present work the duration relation modified by Joshi (2004) for its applicability for Himalayan earthquake has been used. For computing H/V ratio curve at various stations we have used the data of strong motion network of eight stations installed in the Pithoragarh region of Kumaon Himalaya. Data recorded by this network has been used for estimating site effect at each station using H/V method of Nakamura (1988). The rupture responsible for great earthquake in the Kumaon is modeled by placing it in the seismic gap region. Using the rupture length magnitude relationship of Araya and Kiureghian (1988), the length of rupture plane is calculated as 160 km. The downward extension of this rupture plane is computed as 66 km using the relation given by Kanamori and Anderson (1975). As the depth of detachment fault in this part of Himalaya is about 10-20 km and most of major earthquakes in this region are originating at the depth of 12 km, we have placed the rupture responsible for this hypothetical earthquake at a depth of 12 km. As most earthquakes in this part are originating from Main Central Thrust (MCT), which is a shallow dipping thrust, we have considered the dip of this rupture plane to be 15°. Considering rupture velocity to be 80% of shear wave velocity. rupture propagation with in the rupture plane is considered to be about 2.6 km/sec. The velocity structure used in the present work has been taken after Yu et al. (1995). The simulated NS and EW components of strong ground motion and the corresponding response spectra at 5% damping at stations Sobla, Dharchula, Didihat, Pithoragarh and Munsiari . The peak ground acceleration calculated from the scenario earthquake of Magnitude M=8 at a depth of 12km along the MCT at these five stations is very high and giving alarm for high devastations in this region for great earthquakes.

The present method is strongly dependent on scaling laws which are empirical in nature. Therefore, the successful prediction of strong ground motion parameters is entirely dependent on applicability of scaling laws in the region. Although the method of H/V ratio can be used for conversion of vertical component into horizontal components it still lacks the representation of radiation pattern.

5. CONCLUSIONS

This paper presents a simplified hybrid method for simulation of strong ground motion. Using the site amplification curve (H/V) at various sites, NS and EW component of strong ground motion are simulated for the 2004 Niigata-ken Chuetsu earthquake, Japan at numbers of stations. The parameters of synthetic strong motion records and their comparison establish the efficacy of the approach to model earthquake using simple regression relations and parameters not so difficult to estimate. Using same method strong ground motions for a great earthquake in Kumaon Himalaya has been simulated.

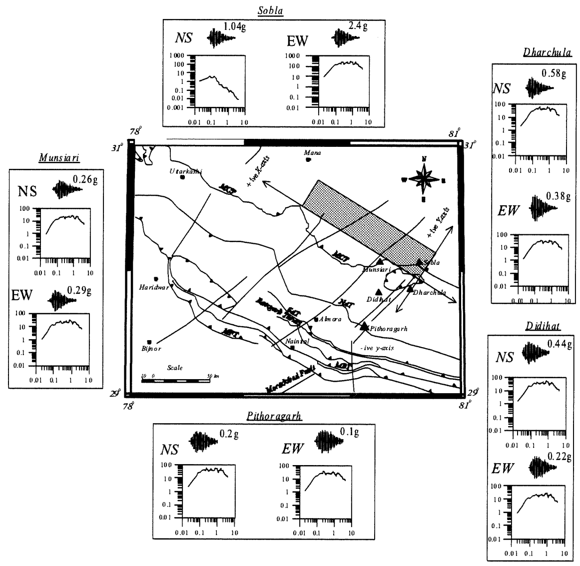

Figure 4 (a) NS (b) EW component of acceleration record. The response spectra prepared from(c) NS and (d) EW component of acceleration record for the Sobla, Dharchula, Didihat, Pithoragarh and Munsiari stations in Uttarakhand Himalaya.

Acknowledgements:

Authors sincerely acknowledge the data collected by Kyoshin network maintained by NIED, Japan. The work presented in this paper is outcome of DST project no. DST/23 (483)/SU/2004. Authors also thanks Indian Institute of

Technology Roorkee, Roorkee, India and Institute of Seismological Research, Ahemadabad, India for support needed for this research work.

References

Abrahamson, N.A. and Litehiser, J.J., 1989, Attenuation of Vertical Peak Acceleration, *Bull. Seism. Soc. Am,,* **79**, 549-580.

Bardet, J.P., 2004, Preliminary Observations of the Niigata-ken Chuetsu, Japan, Earthquake of October 23, 2004, *A preliminary report for the EERI-GEER earthquake engineering reconnaissance team.*

Boore, D.M., 1983, Stochastic Simulation of High Frequency Ground Motion Based on Seismological Models of Radiated Spectra, *Bull. Seism. Soc. Am.* **73,** 1865-1894.

Honda, R., Aoi, S., Sekiguchi, H., Morikawa, N., Kunugi, T., Fujiwara, H., 2004, Ground Motion and Rupture Process of the 2004 Mid Niigata Prefecture Earthquake Obtained from Strong Motion Data of K-NET and KiK-net (from website www.k-net.bosai.go.jp/k-net).

Irikura, K., 1983, Semi Empirical Estimation of Strong Ground Motion During Large Earthquakes, *Bulletin of Disaster Prevention Research Institute (Kyoto Univ.)* **33**, 63-104.

Irikura, K., T. Kagawa, H. Sekiguchi, 1997, Revision of the empirical Green's function method by Irikura, 1986, Programme and Abstracts, *The Seismological Society of Japan* **2**, B25.

Joshi, A., 1997, Modelling of peak ground acceleration for Uttarkashi earthquake of 20th October 1991, *Bull. Ind. Soc. Earth. Tech.* **34,** 75-96.

Joshi, A., Singh S. and Kavita G., 2001, The simulation of ground motions using envelope summations, *Pure Appl. Geophys* **158**, 877-901.

Joshi A., 2004, A simplified technique for simulating wide band strong ground motion for two recent Himalayan earthquakes, *Pure Appl. Geophys (PAGEOPH)* **8**, 161.

Joshi A., and S. Midorikawa, 2004, A simplified method for simulation of strong ground motion using rupture model of the earthquake source, *Jour. Seismol.* **8**, 467-484.

Joshi, A. and Midorikawa, S., 2005, Attenuation characteristics of ground motion intensity from earthquakes with intermediate depth, *Journal of Seismology.* **9**, 23-37.

Kanamori, H. and Anderson, D.L., 1975, Theoretical basis of some empirical relations in seismology, *Bull. Seism. Soc. Am.* **65**, 1073-1095.

Khattri, K.N. (1987). Great earthquakes, seismicity gaps and potential for earthquake disaster along Himalayan plate boundary,*Tectonophysics*, **38**, 79-92.

iyono, J., 1992, Identification and synthesis of seismic ground motion in structural response analysis, *Ph. D. Thesis, Department of Civil Engineering Kyoto University*.

Midorikawa, S., 1993, Semi Empirical Estimation of Peak Ground Acceleration From Large Earthquakes, *Tectonophysics* **218,** 287-295.

Nakamura, Y., 1988, Inference of seismic response of surficial layer based on microtremor measurement, *Quaterly report on railroad research* 4, Railway Technical Railway Institute, 18-27 (In Japanese).

Yu, G, Khattri, K.N., Anderson, J.G., Brune, J.N. and Zeng, Y., 1995, Strong Ground Motion from the Uttarkashi earthquake, Himalaya, India, Earthquake: Comparison of Observations with Synthetics Using the Composite Source Model, *Bull. Seism. Soc. Am.* **85**, 31-50.

Fifth International Conference on Urban Earthquake Engineering
March 4-5, 2008, Tokyo Institute of Technology, Tokyo, Japan

COMPLEX FAULTING PROCESS AND PREDICTION OF STRONG GROUND MOTION FROM CRUSTAL DEFORMATION

Satoshi Kurita[1)]

1) Professor, Department of Architecture, Faculty of Engineering Tokyo University of Science Japan
kurita@rs.kagu.tusac.jp

Abstract: This paper demonstrates the complex faulting process of an earthquake from observation data and proposes a prediction method of strong ground motions. The high-frequency radiation process of the 1994 Sanriku-Haruka-Oki earthquake is estimated from observed acceleration records. The accumulated tectonic stresses on the fault are calculated from a static analysis with the finite element method. The relationships between the radiation process of high-frequency wave and the distribution of accumulated tectonic stress are examined. The results suggest that the spatial distribution of the acceleration radiation intensity is related to the accumulated tectonic stress. For taking account of the accumulated tectonic stresses of a fault, a prediction method of strong ground motion is developed by using FEM. The method calculates the accumulated stresses before earthquake by compressing the FEM model of the crust including the fault with the crustal movement. The initial rupture of the fault is nucleated numerically on the base of the accumulated stresses, and induces spontaneous rupture propagation on the fault in the method. Numerical simulations of a fault are performed. The results of the simulations show that the slip velocity becomes larger in the area with high rupture resistance, and the slip velocity relates to the breakdown time.

1. INTRODUCTION

Aki (1984) pointed out that spatial and temporal irregularity of slip motions on earthquake fault affects the strong ground motion especially in case of large earthquakes. Papageorgiou and Aki (1983) called the irregularity as inhomogeneity of fault. The various simulation methods of the strong motion taking the inhomogeneity of fault into account have been proposed. From analyses of recent large earthquakes, the inhomogeneity of fault is recognized to be more important than before. Evaluation of the inhomogeneity of fault becomes more necessarily for the prediction of the strong ground motion in future large earthquake.

This paper presents an inhomogeneous rupture process with observation records and proposes a prediction method of the strong ground motion from crustal deformation. Applying an inversion method to the acceleration seismograms recorded at the 1994 Sanriku-Haruka-Oki earthquake occurred in Japan, the high-frequency radiation process on the fault is estimated. The accumulated tectonic stress on the fault is calculated numerically with the finite element method. By comparing the distributions of the slip, the high-frequency radiation intensity, and the accumulated tectonic stress, the complex rupture process is examined. On the results, a prediction method of strong ground motions is developed using the dynamic fault model of FEM. The method creates the initial rupture of a fault from the accumulated stress before earthquake calculated from the static finite element analysis of the crust model compressed bye the crustal movement, and propagates the spontaneous rupture. By generating a heterogeneous rupture resistance distribution and producing a spontaneous rupture over the fault with the method, the relationships among rupture resistance, slip velocity, and breakdown time are examined.

2. ESTIMATION OF COMPLEX FAULTING PROCESS

The acceleration radiation intensities and the rupture times of the 1994 Sanriku-Haruka-Oki earthquake are estimated by the envelope inversion method developed by Kakehi and Irikura (1996). The fault plane of Nakayama and Takeo (1997) is adapted to the inversion. Figure 1 shows the location and geometry of the fault plane. The acceleration seismograms used for the inversion were recorded at a station in the campus of HIT (Hachinohe institute of technology). The location of the station is plotted in Figure 1. Figure 2 shows the acceleration radiation intensities estimated by the inversion. The comparison of the results and the slip distribution obtained by Nakayama and Takeo (1997) is shown in Figure 3. The areas, I, II, and III with strong radiation intensity of high-frequency waves does not correspond with the large slip areas, but lie in the vicinity of the large slip area A and B or at the edges of the fault plane.

The accumulated tectonic stresses on the fault plane for the period from the 1968 Tokachi-Oki earthquake to the 1994 Sanriku-Haruka-Oki earthquake are evaluated by a viscoelastic analysis with 2D-FEM. The numerical modeling of the analysis is illustrated in Figure 4. This modeling is same as Sato (1987). He introduced the seismic coupling between the Pacific Plate and the Northeast Japan Marc Plate in the modeling, evaluated relative displacements on the plate boundary with a seismic coupling factor, and performed the numerical calculation by imposing the relative displacement on the plate boundary. Figure 5 shows the distribution of maximum shear stress on the boundary of the Pacific Plate obtained by the calculation. The horizontal axis indicates horizontal distance from the Japan Trench axis. The thick line (case-a) represents the result of uniform seismic coupling case. The other line (case-b) represents the result of nonuniform seismic coupling. The distributions of the maximum acceleration radiation intensity are also plotted in Figure 5. The accumulated shear stress in the distance range from 150 km to 200 km increases as the distance becomes longer. In the distance range, the variations of acceleration radiation and accumulated shear stress are similar. This distance range corresponds to the landward fault plane shown in Figure 1. From the above results, it is considered that the acceleration radiation intensity in the landward fault plane is related to the accumulated tectonic stress.

3. PREDICTION OF STRONG GROUND MOTION

3.1 Method

For taking account of the accumulated tectonic stresses on a fault plane into prediction of strong ground motions, an earthquake simulation method is proposed by using finite element techniques. The method evaluates the accumulated tectonic stresses before earthquake by the finite element model of the crust including the fault compressed with the crustal movement, and creates the initial rupture and spontaneous rupture propagation on the fault plane. The crust and the fault plane are discretized into finite elements for linear elastic body and modified joint elements,

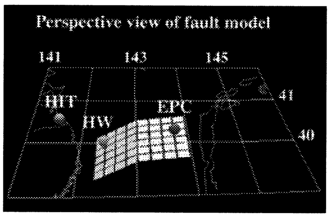

Figure 1 Fault model for the envelope inversion

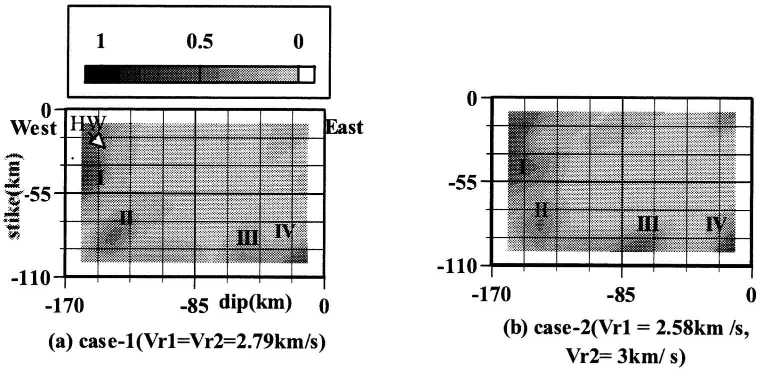

Figure 2 Distribution of acceleration radiation intensity on the fault plane

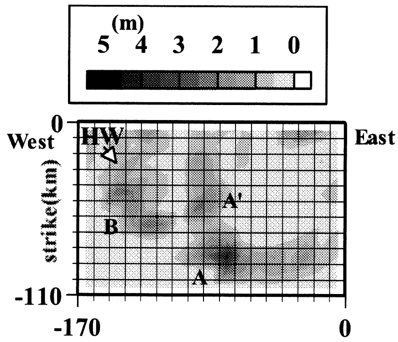

Figure 3 Slip distribution (Nakayama and Takeo (1997)

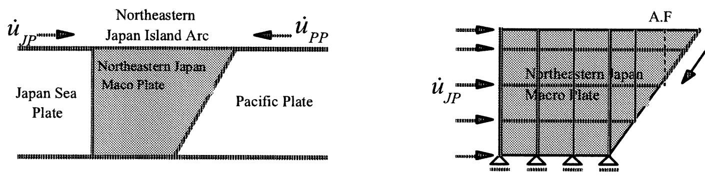

Figure 4 Modeling of the accumulated tectonic stress analysis using FEM

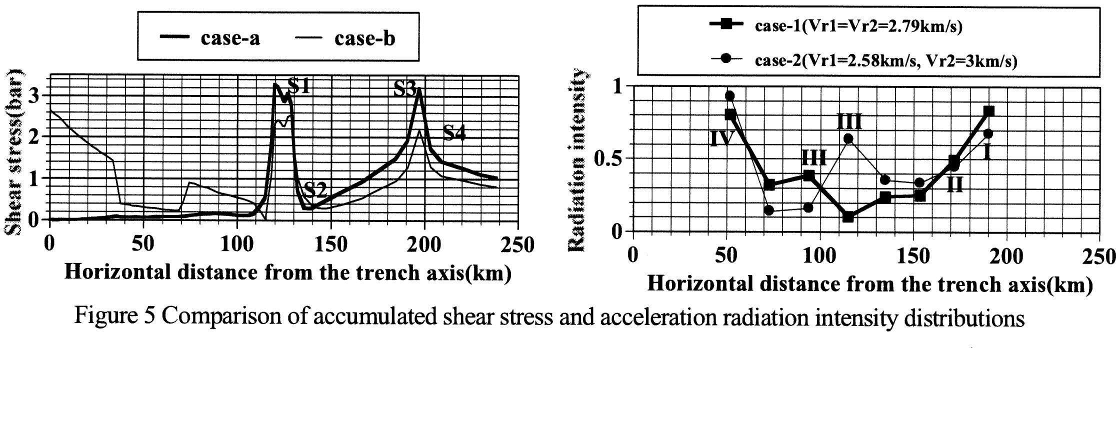

Figure 5 Comparison of accumulated shear stress and acceleration radiation intensity distributions

respectively. The constitutive law of shear shown in Figure 7 is employed for expressing slip weakening shear stress on the fault during earthquake. The method generates an earthquake by imposing the horizontal crustal displacements on both sides of the model and give rise to the slip of the fault plane. The computational procedure consists of three stages described below.

The first stage (stage 1) is the computation of a spatial distribution of shear stress over the fault plane just before a rupture nucleates on the fault. This computation is performed with the model shown in Figure 6-(a). The increments of the accumulated shear stresses on the fault are calculated by imposing a horizontal crustal displacement per year on both sides of the model. Supposing that the increments of the accumulated crustal stresses are linear with the imposed horizontal displacement, the method evaluates the shear stress distribution over the fault plane at the time when the shear stress of a point on the fault reaches a peak shear stress (yield shear stress, breakdown strength).

The second stage (stage 2) is the nucleation of an initial rupture that induces spontaneous rupture propagation on the fault. This nucleation is carried out with the finite element model shown in Figure 6-(b). Small horizontal crustal displacements are applied to both sides of the model on the condition that the linear relationship between shear stress and slip displacement is held after the first stage. The applied crustal displacements produce the unbalanced shear stresses in the vicinity of the point where the stress reached the peak shear stress at the first stage. The unbalanced shear stress means $\Delta\tau_2$ illustrated in Figure 8. This unbalanced stress is used to give rise to the spontaneous rupture propagation. The region where the shear stress is greater than the peak shear

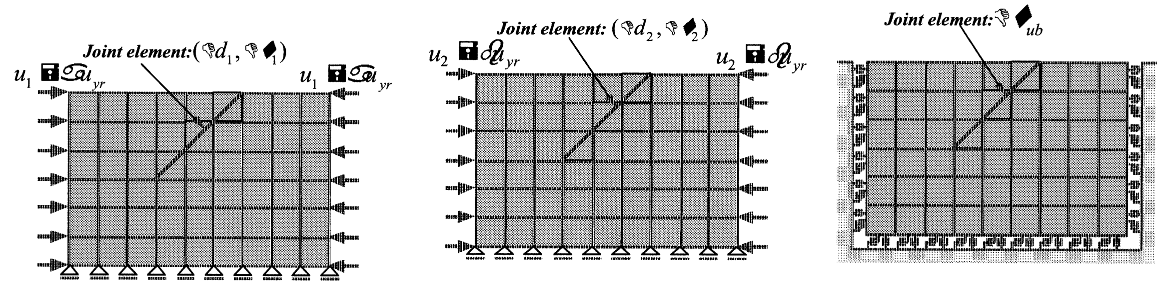

(a) state 1 (b) stage 2 (c) stage 3

Figure 6 Schematics of the prediction method from horizontal crust deformation

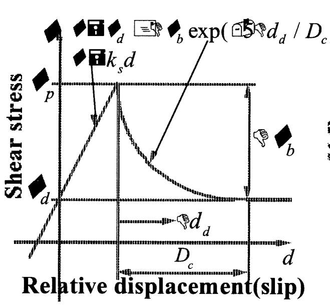

Figure 7 Constitutive law of shear stress

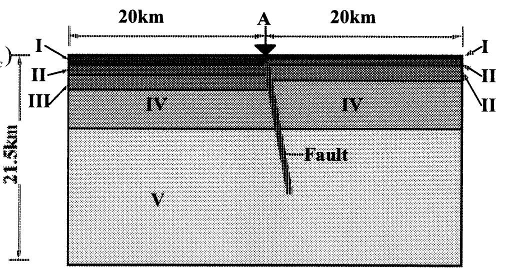

Figure 9 Fault model

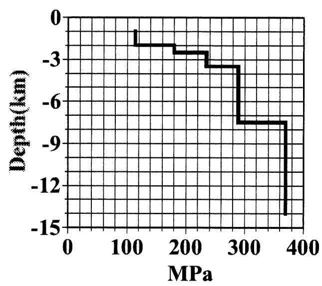

Figure 11 Shear stiffness

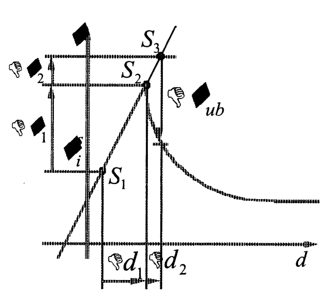

Figure 8 Unbalanced shear stress in stage 2

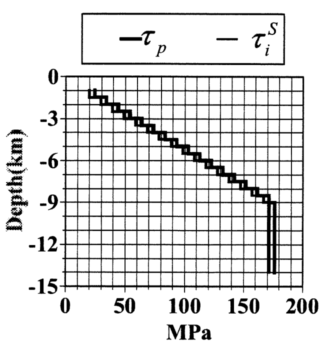

Figure 10 Peak shear stress and initial stress at the stage 1

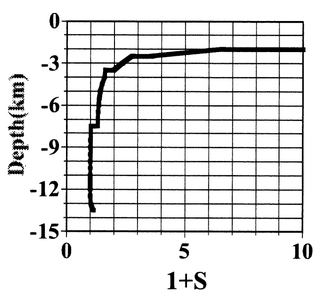

Figure 12 Rupture resistance

stress is considered as an initial rupture zone.

The equivalent nodal forces obtained from the unbalanced shear stresses are applied on the initial rupture zone of the dynamic model shown in Figure 6-(c), in order to satisfy the equilibrium-of-force of the model. The equivalent nodal force is called a driving force in this paper. This driving force induces an unstable dynamic rupture, and the rupture propagates spontaneously. The numerical analysis of the dynamic rupture propagation is the last stage (stage 3). This dynamic model is the same as that of the first stage except the boundary conditions. Viscous dampers are attached on both sides and the bottom of the dynamic model in order to absorb reflected waves at these ends of the model. The magnitude of the driving force depends on the size of the initial rupture zone, as you can find the description of the second stage.

3.2 Simulation

A numerical simulation of plain strain problem is performed with the proposed method. Figure 9 shows the geometry and structure of the model used in the simulation. This model is the same as that of Tsuboi and Miura (1996). The fault extends from 1 km to 14 km in depth. The dip angle of the fault is 80 degree. Figure 10 shows the distributions of peak shear stress and initial shear stress on the fault of the model used in the analysis of the first stage. Figure 11 shows the distribution of shear stiffness over the fault plane, which relates the static slip to the accumulated crustal shear stress in the state before rupture. The dynamic shear stress drops are uniformly distributed over the fault. The value of the stress drop is 47 bars. The analysis of the first stage is carried out with a horizontal crust displacement of 0.35 cm par year. This value of the crustal displacement is determined from the GPS observation of the Geographical Survey Institute of Japan. To nucleate the initial rupture, the crustal displacements for 1407 years are imposed on the model in the analysis of the first stage. The rupture resistances, 1+S, are calculated from the shear stresses on the fault obtained by the analysis of the first stage. The symbol S denotes a non-dimensional parameter called by Das and Aki (1977). If the shear stress equals the peak shear stress, 1+S becomes one. 1+S= 0 means no rupture resistance. The large value of 1+S means that the resistance to rupture is high. The distribution of the rupture resistances is shown in Figure 12. In the region in the depth range from 9 km to 12 km, the shear stress almost reaches the peak shear stress. The high rupture resistance lies near the upper edge of the fault. In the computation of the second stage, the horizontal crustal displacements for 3.2 years are imposed on each side of the model. Using the driving force obtained from the second stage, the dynamic analysis of the last stage is performed.

The results for the rupture time are shown in Figure 13. The initial rupture zone lies in the depth region from 10 km to 12 km. The rupture propagates bilaterally from the initial rupture zone. The distributions of the maximum slips and maximum slip velocities are shown in Figure 14. The slip and its velocity vary smoothly with depth. This means that the scheme of the initial rupture nucleation makes no artificial variations in those distributions. The slip velocity

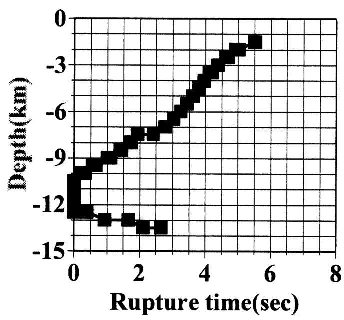

Figure 13 Distribution of rupture time

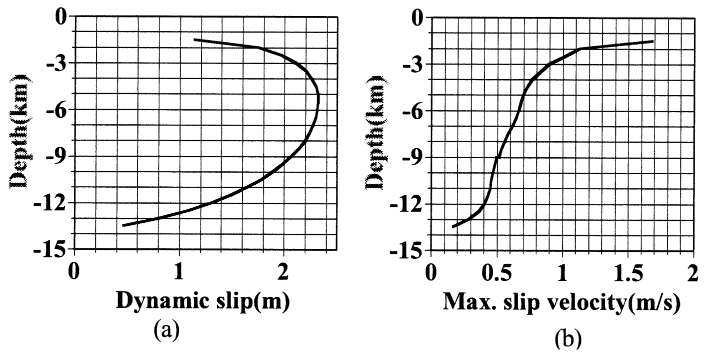

Figure 14 Distributions of maximum slip

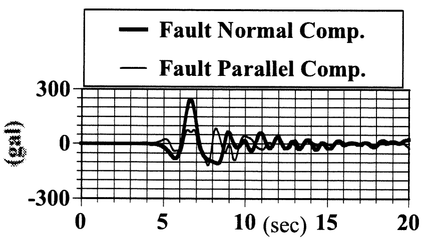

Figure 15 Time history of Acceleration at point A

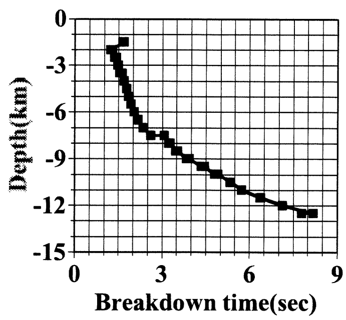

Figure 16 Distribution of breakdown time

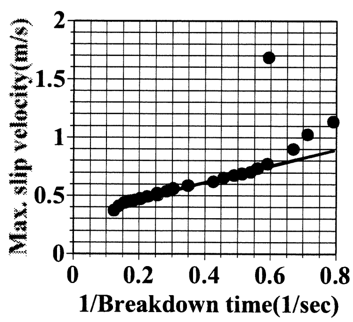

Figure 17 Relationship between breakdown time and maximum slip velocity

increases as the rupture approaches the upper edge of the fault. The large slip velocities distribute in the region near the upper edge of the fault where the rupture resistance is high. This result means that the ruptures in the region generate the strong seismic waves. Figure 15 shows the acceleration wave at point A obtained by the analysis of the state 3. The location of point A is plotted in Figure 9. The strong seismic waves radiated from the near upper edge of the fault produce the large amplitudes of the acceleration waves of the ground. Figure 16 shows the results for the breakdown time. The breakdown time (Ohnaka and Yamashita (1989)) is defined as the time that the local shear stress takes for dropping from the peak shear stress to the residual friction stress level. The breakdown time decreases with the depth of rupture location. Figure 17 shows the relationship between the maximum slip velocity and the reciprocal number of breakdown time. The maximum slip velocity is almost linear with the reciprocal number. Ohnaka and Yamashita (1989) observed this linear relationship from the stick-slip experiments of rock and the theoretical model. The numerical results of the proposed method agree with their results.

4. CONCLUSIONS

The high-frequency wave radiation process of the 1994 Sanriku-Haruka-Oki earthquake has been estimated by using the inversion method, and then the accumulated tectonic stress on the fault have been calculated using finite element method. The results indicate that the spatial distribution of the acceleration radiation intensities over the fault is related to the accumulated crustal stresses on the fault.

The earthquake simulation method using finite element techniques was proposed, which accounts the accumulated crustal stresses on a fault plane just before earthquake in prediction of strong ground motions. The method evaluates simultaneously the size of initial rupture zone and the magnitude of driving force producing spontaneous rupture propagation on the base of the physical model. The numerical simulation of the fault was carried out with the method. The results of the simulation indicate that the slip velocity becomes larger in the area of high rupture resistance, and the slip velocity relates to the breakdown time.

References:

Aki, K. (1984), "Asperities, barriers, characteristic earthquakes and strong motion prediction", J. Geohys. Res., 89, B7, 5867-5872.

Kakehi, Y. and K. Irikura. (1996), "Estimation of high frequency wave radiation area on the fault plane by the envelope inversion of acceleration seismograms.", Geohys. J. Int., 125, 892-900.

Madariaga, R., K. Olsen, and R. Archuleta. (1998), "Modeling dynamic rupture in a 3D earthquake fault model", Bull. Seismol. Soc. Am., 88, 1182-1197.

Nakayama, W. and M., Takeo. (1997), "Slip History of the 1994 Sanriku-Haruka-Oki, Japan, Earthquake Deduced from strong-motion Data", Bull. Seismol. Soc. Am., 87, 918-931.

Sato, K. (1987), "Stress and displacement fields in the northeastern Japan Island Arc as evaluated with three-dimensional finite element method and their tectonic interpretations", Doctor Thesis, Tohoku University.

Tsuboi, T. and F., Miura. (1996), "Simulation of rupture process of the reverse fault by a nonlinear finite element method", Proc. of the 1st symposium on mitigation of urban disasters by near-field earthquake, Kyoto: 53-56. (in Japanese)

Ohnaka, M. and T., Yamashita. (1989), "A cohesive zone model for dynamic shear faulting based on experimentally inferred constitutive relation and strong motion source parameters", J. Geophys. Res., 94: 4089-4104.

Papageorgiou, A. and K. Aki. (1983), "A specific barrier model for quantitative description of inhomogeneous faulting and the prediction of strong ground motion, I, Description of the model", Bull. Seismol. Soc. Am., 73: 693-722.

Fifth International Conference on Urban Earthquake Engineering
March 4-5, 2008, Tokyo Institute of Technology, Tokyo, Japan

DETAILED STUDY ON GROUND STRUCTURE AROUND HSINCHU CITY, TAIWAN UNSING GRAVITY AND MICROTREMOR SURVEYS

H. Morikawa[1], H.-T. Chen[2], C. Takahashi[3], H. Kawatsure[3], and M. Komazawa[4]

1) Associate Professor, Department of Built Environment, Tokyo Institute of Technology, Japan
2) Associate Professor, Department of Civil Engineering, National Central University, Taiwan
3) Graduate Student, Department of Built Environment, Tokyo Institute of Technology, Japan
4) Senior Researcher, Geological Survey of Japan, AIST, Japan
morika@enveng.titech.ac.jp, chenhtofpadau@seed.net.tw, kawatsure.h.aa@m.titech.ac.jp,
tchika@enveng.titech.ac.jp, komazawa-m@aist.go.jp

Abstract: To obtain a detailed model of the three-dimensional ground structure, the gravity and microtoremor surveys have been carried out around Hsinchu area, Taiwan. Observations of gravity at 393 sites was done and the structure with some different scales are found from the Bouguer anomaly. The trend of the Bouguer anomaly is independent of the topography and some localized structures are observed. Furthermore, shallow structures were estimated from microtoremor data of array observation at 10 sites.

1. INTRODUCTION

To estimate the earthquake ground motions, it is very important to know the ground structure, especially, deep and three-dimensional structure, because the ground motions excited by a large earthquake predominate components with long period which relates to the deep structure. For this purpose, we have many kinds of technique for the geological survey, though some of them may be costly. The microtremor and gravity survey are easy to conduct the survey and not so expensive techniques. Thus, for estimating the three-dimensional ground structure over a large area, these techniques are useful and provide good information without much cost. Especially, the gravity survey is suitable for the survey of very large area and can provide detailed configuration of bedrock, because of the easy operation by means of the automatic gravimeter and GPS (global positioning system).

However, since the Bouguer anomaly depends on the density structure, it is difficult sometimes to determine the velocity structure from it. To obtain the velocity structure, we can use information from the microtremor survey, because phase velocities obtained from microtremor array observation reflect the velocity strcuture directly.

The geological setting of Taiwan is really complicated because there is the boundary between the Eurasia and Philippine plates and we can find so many active faults in the Taiwan island. This means that the seismic activity is very high in Taiwan. Under this circumstance, we focus the target for our survey on Hsinchu city, Taiwan, where many industrial factories, especially for IT, computer, semiconductor companies are located. We, therefore, may say that Hsinchu area should be key for the Taiwanese economy.

From this, it is very important to know the ground structure and to estimate some strong ground motions in this area. As a first step to estimate earthquake ground motion for earthquake disaster mitigation, we will try to make a preliminary model of three-dimensional shape of the surface for the bedrock which is defined, hereafter, as hard rock.

2. GEOLOGICAL SETTINGS AROUND HSINCHU CITY, TAIWAN

Hsinchu city is located at the north-western area of Taiwan as shown in Figure 1. The altitude of north-western part is very low and the south-eastern part is very high such as more than 1000m. The topographical map is shown in Figure 2. Furthermore, we can find many faults around Hsinchu city as shown in Figure 3. In the southern part of Hsinchu city, anticline and syncline, whose directions are north-eastern to south-western, are found and the fault is recognized between them. The Hsincheng fault is considered as an active fault and it is key issue to consider mitigation of the earthquake disaster. Furthermore, we can see the similar structure in the northern part of Hsinchu city, which includes the anti- and syncline structure with Hsinchu fault.

As shown in the previous section, a part of Hsinchu city is called "science park" and there are many companies and research centers for high technology in this area. From this, Hsinchu city is called "Silicon Valley of Taiwan" and

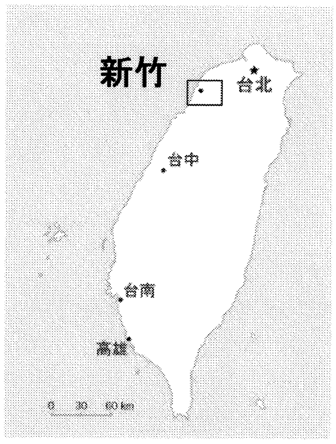

Figure 1 Location of Hsinchu city

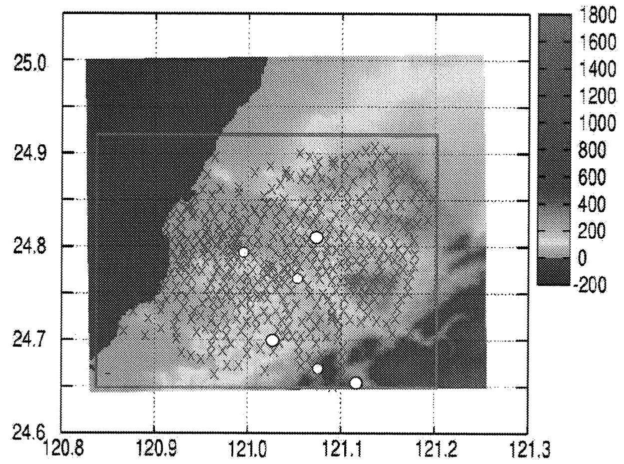

Figure 2 Topographical map around Hsinchu city. Horizontal and vertical coordinates show the longitude and latitude, respectively. In this map, × stands for the observation sites of gravity, ○ for the control points which are used for the calculation of the gravity basement, the rectangular frame for the area of the analysis.

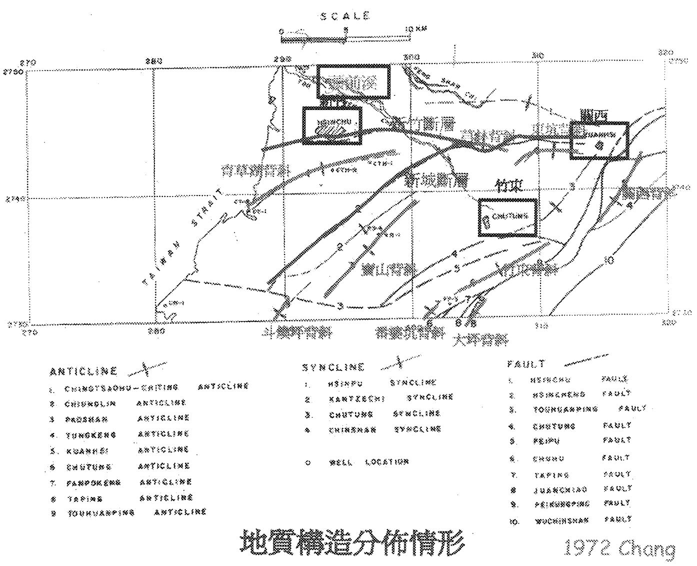

Figure 3 Faults and geological system around Hsinchu city

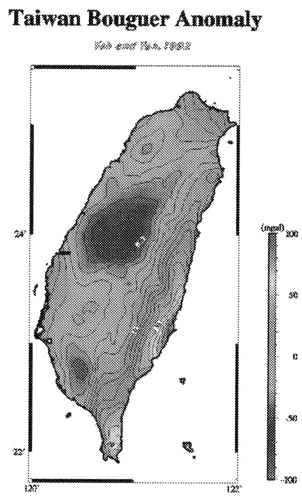

Figure 4 Bouguer anomaly map of Taiwan [1]

very important city of the Taiwanese economy. We hope the basic observation and research for the estimation of earthquake ground motion will help the provision against the future earthquake.

Some pioneering studies are available for the ground structure around Hsinchu from the geological points of view. These studies are summarized as "report on the ground structure of Hsinchu district" by Shu-Fan et al.[1], however the authors could not follow the detailed references and original sources. Thus, we introduce some important points from the report by Shu-Fan et al.

Gravity survey in Taiwan has been carried out, and especially, dense and accurate observations are done in the last decade. Thus, the the reliable Bouguer anomaly map is available as shown in Figure 4 by Yeh and Yen (1992). The details around Hsinchu city is shown in Figure 5. Furthermore, using the information of the gravity anomaly, the density structure is proposed as shown in Figure 6.

From these figures, the peculiar low anomaly of gravity is found in the southern part of Hsinchu city. They consider existence of the oil around this low anomaly area, and carried out many kinds of survey to know the ground structure including the deep borehole and dense gravity survey. Unfortunately, in this area, there is no oil, but we can see the geological profiles along some lines. Figures 7 and 8 are examples. Although these maps might be made by considering the gravity anomaly, the authors have no information about the detailed processes to make the profiles.

Many kinds of survey have been carried out, however,

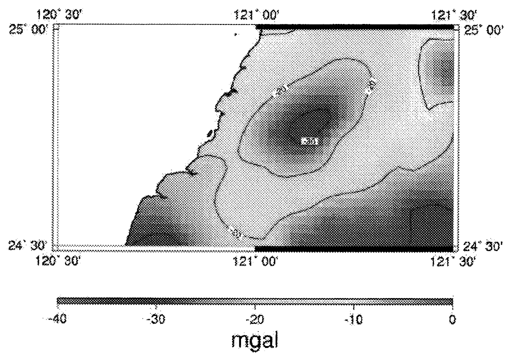

Figure 5 Bouguer anomaly map around Hsinchu city [1]

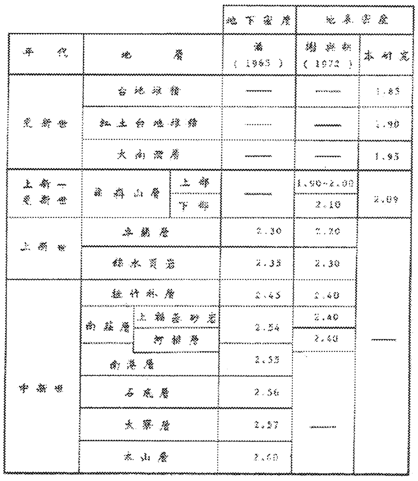

年代	地層		地下密度 蕭 (1965)	地表密度 謝尚新 (1972)	本研究
更新世	台地礫層		——	——	1.85
	紅土台地礫層		——	——	1.90
	大南灣層		——	——	1.95
上新—更新世	頭嵙山層	上部	——	1.90~2.00	2.09
		下部		2.10	
上新世	卓蘭層		2.30	2.20	
	錦水頁岩		2.33	2.30	
中新世	桂竹林層		2.45	2.40	
	南莊層	上福基砂岩	2.54	2.40	——
		東坑層		2.40	
	南港層		2.55		
	石底層		2.56		
	大寮層		2.57	——	
	木山層		2.60		

Figure 6 Examples of the available density structure [1]. The right column is obtained by the results of a research in 1975.

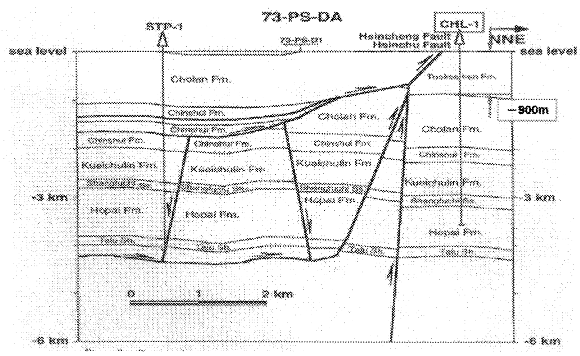

Figure 7 The SSW–NNE section of Hsinchu and location of control point (CHL1) (adding some information to the figure of Shu-Fan [1]).

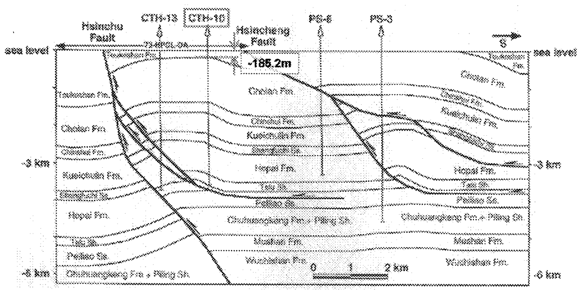

Figure 8 The S–N section of Hsinchu and location of control point (CHL10) (adding some information to the figure of Shu-Fan [1]).

the detailed information of the available geological data is not so clear. This means that they cannot provide enough information to make the model of ground structure for the estimation of earthquake ground motions. Of course, we use the available information at a maximum, but we carry out the gravity survey to be suitable for our objective.

3. OBSERVATIONS AND RESULTS

3.1 Gravity Survey

To obtain the three-dimensional ground structure at Hsinchu city accurately, we have carried out the measurements of gravity around the surrounding area, which includes many towns in Hsinchu County: 24°39′N – 24°55′N x 120°50′E – 121°12′E; 30 km NS x 40 km EW. We observed gravity at 393 sites during 20 days of September 7th to 28th, 2006. The averaged distances among close sites are about 1 km. The location of observation sites are shown in Figure 2.

For the observation, we used the Burris automatic gravity meter by ZLS Corporation and Type G Gravimeter by LaCoste & Romberg and applied the technique of relative observation. To determine the position of the observation site accurately, the differential survey using the GPS (Global Positioning System) is performed. As a result, the error of the position is less than 1m. The observation system are shown in Figure 9.

To apply the technique of relative observation, firstly, we set a reference site with absolute gravity value in Hsinchu city through the comparison between our reference site and the official gravity base site in Hsinchu area. Then, using the reference site, we carried out the relative observations of gravity and the absolute values of the gravity were determined at each site.

3.2 Bouguer Anomaly

We analyze the data with the existent gravity data, which were obtained at more than 60 sites in this area. We apply the data at 453 sites to calculate the Bouguer anomaly except for a few inaccurate data.

After some data correction such as corrections for height of the instrument, tide, drift, terrain, free-air, and Bouguer correction, the Bouguer anomaly can be obtained. For the Bouguer correction, we have to give a value of the assumed density ρ. For this purpose, some

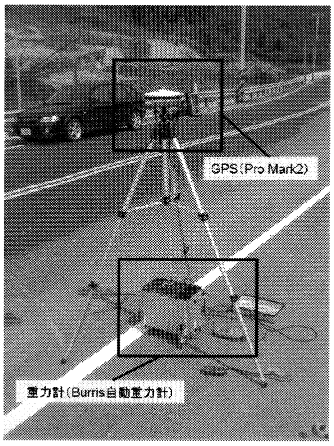

Figure 9 Observation system for the gravity. GPS receiver and its antenna on the tripod, and Burris automatic gravity meter below them.

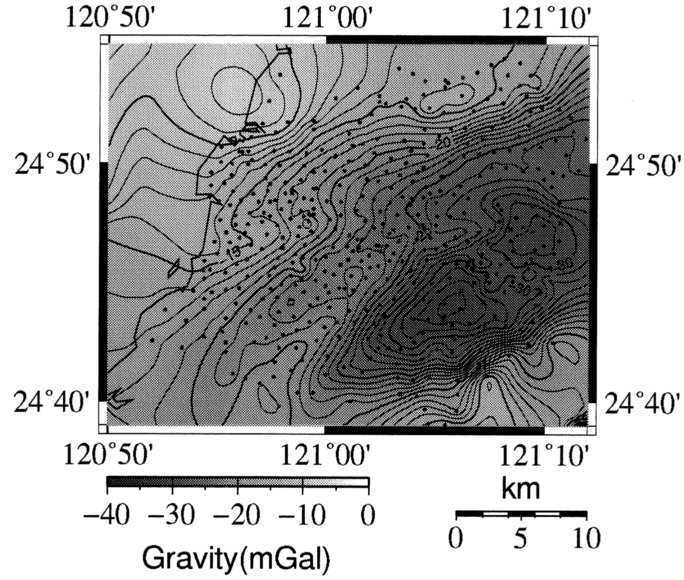

Figure 10 Bouguer anomaly map (assumed density: 2.1 t/m^3)

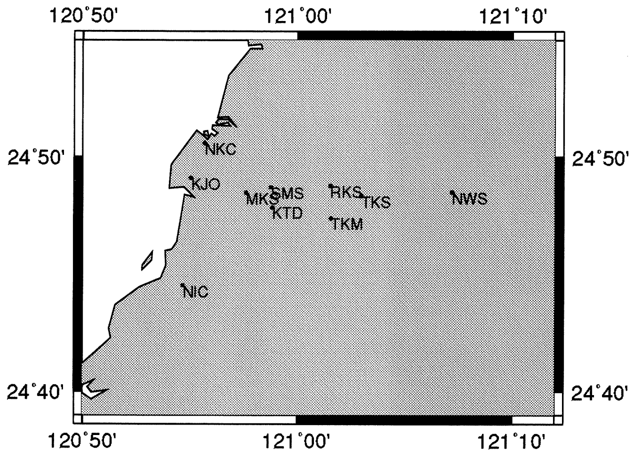

Figure 11 Sites for the array observation of microtremors.

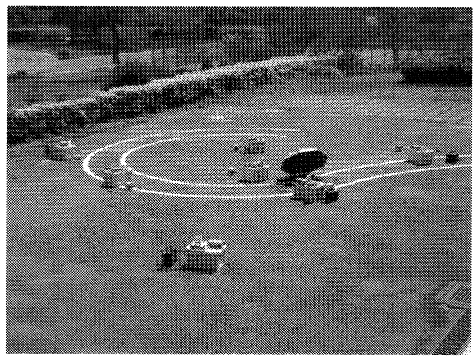

Figure 12 An example of sensor layout for array observation and system.

methods are proposed such as the G-H correlation method [2], and a method to check the correlation between the Bouguer anomaly map and topography [2]. We apply the latter technique and determine ρ as 2.3 t/m^3.

The obtained Bouguer anomaly map is shown in Figure 10. From this figure, we can say the follows:

- The Bouguer anomaly in the target area is negative and the negative anomaly increases from north-west to south-east. This trend is independent of the topography of the hilly area. However, this trend agrees with the peculiar low anomaly as shown in Figure 5.
- Around the south-eastern area of the Hsinchu city, minimum value of the Bouguer anomaly is found. This minimum value seems to correspond to the local minimum which is shown in the Bouguer anomaly map for whole Taiwan island of Figure 4.
- For most parts of south-eastern area, steep change of Bouguer anomaly is observed. This suggests that the existence of steep slope of the bedrock in this area.

3.3 Microtremor Survey

To determine the velocity structure, we carried out array observations of microtremors at 10 sites around Hsinchu city, where are shown in Figure 11. For this observation, we used Force-balanced-type accelerometers and digital recorder with 24-bit resolution $\Delta\Sigma$ A/D converter, which include an analog gained filter and GPS clock system. The time is synchronized by this clock and data is recorded by sampling rate 800 cps after passing the low pass filter with cut off frequency of 30 Hz.

The setting of the sensors and the observation system are shown in Figure 12. Radii of the arrays are 3 m to 800 m and the radii depend on the sites. Unfortunately, the response sensitivities of the sensors are not enough to observe the microtremors in long period range. We ap-

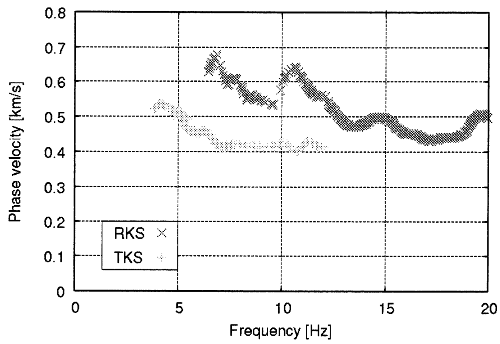

Figure 13 Examples of estimated phase velocities. Array radii are 6, 19, and 38 m at RKS and 17 and 35 m at TKS.

plied the spatial auto-correlation (SPAC) method [3] and estimated the phase velocities. Figure 13 shows a part of the results.

4. DISCUSSION

4.1 Comparison with the Known Structure

We can discuss the shallow structure with the residual gravity map. Thus, we show the residual gravity with the anti- and syncline in the target area as shown in Figure 14. From this figure it can be recognized the good correspondence of the geological structure and the residual anomaly. This means that the obtained gravity anomaly can explain the geological sytem.

4.2 Gravity Basement

Using the technique by Komazawa [4], we estimate a 3-D gravity basement under the assumption that the ground consists of two layers, which are homogeneous sediment and basement with density of 2.1 and 2.4 t/m^3, respectively.

To obtain a realistic model of gravity basement, we consider the follows: to remove the contribution for the Bouguer anomaly from the deep structure such as upper mantle and to constrain the depth to the basement using some other information. For the former, a band-pass filter (50 to 5000 m) is applied to the Bouguer anomaly. For the latter, we give some control points in Figure 2: that is, deep borehole sites CHL-1, STP-1, CTH-10, FP-3, and R-1 of Figure 3, which reach to the basement. The basement appear on the surface at the south control point in Figure 2. The boundary of sediments and basement is set at the surface of Kueichulin Form on the basis of Figure 6.

The 3-D shape of the gravity basement is shown in Figure 15. From Figure 15, depth of the gravity basement reaches to about 3000 m in the south-eastern area and about 1500m around the downtown of Hsinchu City. Steep slopes of the gravity basement are observed around the southern area of Hsinchu City, whose location corresponds to the known fault; Hsinchu and Hsincheng faults. However, the depth to basement around downtown of Hsinchu City is too deep compareing some available shallow borehole data.

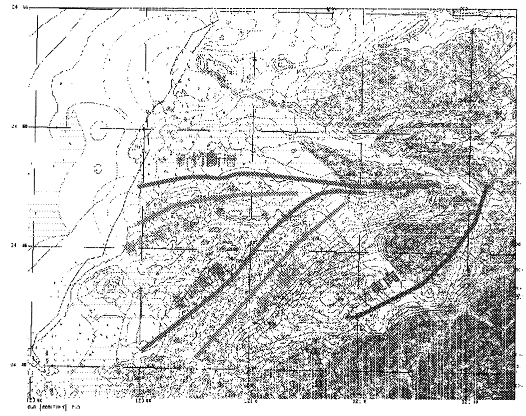

Figure 14 Residual gravity map (blued contour line represents positive and red negative anomaly).

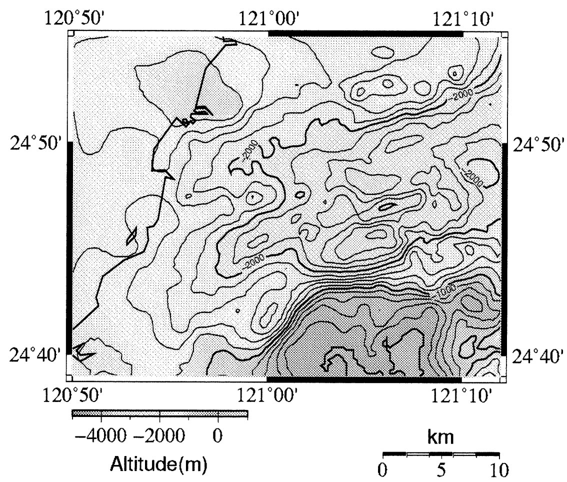

Figure 15 Altitude of the gravity basement (density of basement: 2.4 t/m^3, density of sediment: 2.1 t/m^3, unit of the altitude: m)

Thus, we consider another layer with slightly lower density than basement. The density of this added layer is set as 2.25 t/m^3 and it corresponds to Chinshui and Cholan Form. To obtain three-layered model, we apply the technique by Takahashi [5] and give the control points which are same as the two-layerd case. In this case, the boundaries of the layer are assumed as the surfaces of Cholan and Kueichulin Form.

Obtained density model is shown in Figure 16, where the upper panel shows the upper boundary of Cholan Form with density of 2.25 t/m^3 and lower panel is the upper boundary of basement (Kueichunlin Form with 2.4 t/m^3). From this figure, depth to the middle layer is very shallow around western coast and downtown of Hsinchu city. On the other hand, the depth to the basement is very deeper than two-layerd model around the low anomaly area of south-eastern part.

4.3 Velocity Structure

In this time, it is very difficult to discuss the deep velocity structure because of less information of phase veloc-

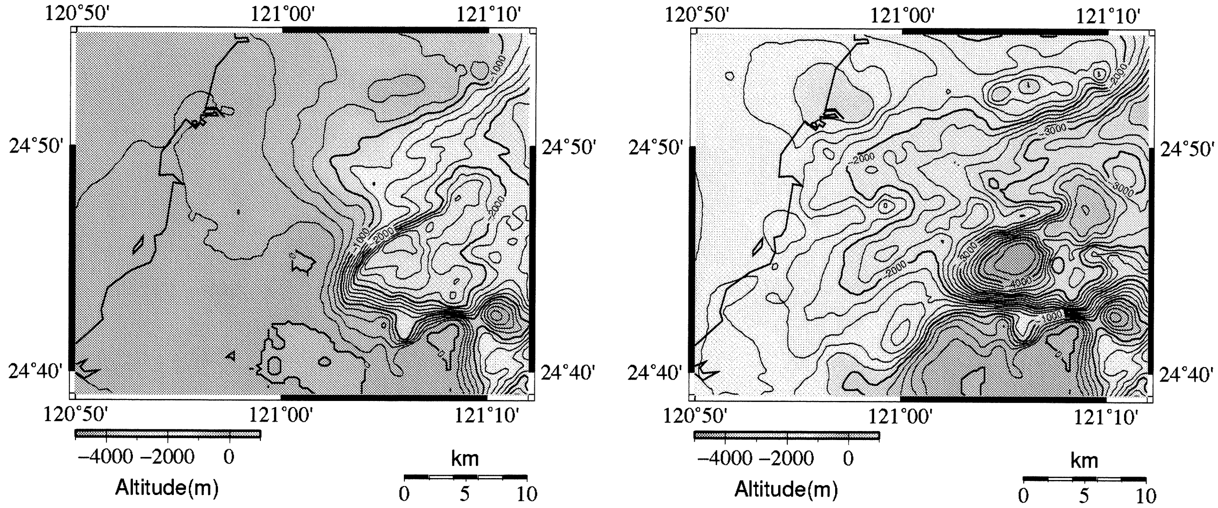

(a) Altitude of upper surface of middle layer. (b) Altitude of upper surface of basement.

Figure 16 Altitude of the upper surface of middle layer with density of 2.25 t/m^3 and basement with 2.4 t/m^3.

ity in long period range. However, it is observed that the phase velocities around lower gravity anomaly are slower than ones around heigher gravity anomaly. In the future development, we will discuss the relationships between the velocity and density structure in this area.

5. CONCLUSIONS

We have carried out the gravity observation at 393 sites and array observation of microtremor at 10 sites around Hsinchu area, Taiwan. Using this data, we estimated the Bouguer anomaly and phase velocities. Furthermore we estimate the gravity basement around this area. From this, we can say that the three-dimensional structure is very complicated: some different scales of structure are found. The results from this research is listed as follows:

- The density around Hsinchu area is estimated as 2.4 t/m^3 for basement and 2.1 t/m^3 and 2.25 t/m^3 for sediment.
- Negative Bouguer anomaly is found and the absolute value of anomaly increases from north-west to south-east. This trend can be seen in the shape of the gravity basement.
- To explain the very low Bouguer anomaly around south-eastern area, we introduce three-layerd density model. As a result, the depth to the middle layer is very shallow around the downtown of Hsinchu city.
- The depth to the middle layer is 200 m around Hsinchu city and 1200 m in the south-eastern area. The shape of the gravity basement is very complicated but it corresponds to the geological information such as anti- and syncline and some known faults.

Acknowledgments:

The authors wish to express their gratitude for the support of gravity data in Taiwan from Professor Chein-way Hwang of department of civil engineering, National Chiao Tung University, Taiwan and Ministry of Interior, Taiwan, Republic of China. Furthermore, we gratefully acknowledge helpful discussions and valuable comments with Profs. K.-L. Wen and H.-Y. Yen of Institute of Geophysics, National Central University, Taiwan, Republic of China. The following students of graduate school of civil engineering, National Central University, Taiwan are also gratefully acknowledged for their kind supports for the gravity observation in Hsinchu area: Mr. Dong-Ching Lin, Mr. Rey-Yung Chen, Mr. Jen-Jei Wu, Mr. Shan-Ming Hwang, and Mr. Wen-Shi Hwang.

References:

[1] Shu-Fan, Report on the ground structure around Hsinchu district, through the personal communication with Prof. Yen of National Central University, Taiwan.

[2] Komazawa, M., Gravity survey, *Handbook of Exploration Geophysics*, Vol.4, Society of Exploration Geophysicists of Japan, pp.433–468, 1998.

[3] Matsushima, T. and H. Okada, Determination of Deep Geological Structures under Urban Areas using Long-Period Microtremors, *Butsuri-Tansa*, Vol. 43, pp.21–33, 1990.

[4] Komazawa, M., Gravimetric Analysis of Aso Volcano and its Interpretation, *J. Geod. Soc. Japan*, Vol. 41, pp.17–45,1995.

[5] Takahashi, C., A Method to Detect a Vertical Boundary of Density Structure using Gravity and Magnetic Data, *Master Thesis*, Department of Built Environment, Tokyo Institute of Technology, 2008.

Fifth International Conference on Urban Earthquake Engineering
March 4-5, 2008, Tokyo Institute of Technology, Tokyo, Japan

EXPLORATION OF UNDERGROUND STRUCTURE FOR ESTIMATION OF GROUND MOTION IN FUKUOKA AREA AND PRACTICAL USE TO THE EARTH SCIENCE EDUCATION

Nobuyuki Yamada

Fukuoka University of Education, Japan
nyamada@fukuoka-edu.ac.jp

Abstract: Fukuoka city of the eighth population in Japan was damaged three years ago by the 2005 west off Fukuoka Prefecture Earthquake. There are some 3D underground structure velocity models around this area in previous study for estimation of the strong ground motion during some earthquakes. Ground motion FD simulation reproduced better result during a small earthquake using 3D model data. However, it has some uncertainty in the model, and it is difficult to repair for the model data. Therefore, I explored the underground structure of deep part by microtremor array measurement and shallow part by seismic refraction method. The latter was performed with students and teachers for earth science education, although the work didn't bring to us the structure elucidation. The maximum depth of the basin bottom around Fukuoka city is about 0.8km. And the cooperation with school is to be cue of an interest in science by these explorations.

1. INTRODUCTION

The 2005 west off Fukuoka Prefecture Earthquake (M_J7.0) had heavy damaged in Fukuoka city near the source fault. The earthquake struck a mega city more than one million population since 1995 Hyogoken Nanbu Earthquake. Although the 2005 disaster was not so severe than the 1995 one except for Genkai Island, many people was very surprised by the 2005 earthquake because of low seismicity in the northern part of Kyusyu Island in long term until then. Now, three years has passed since the 2005 earthquake occurred, and the damage area has almost revived as usual. Therefore, it is a possible that many people are forgetting the memories of the disaster. The duties of us are the progress of earthquake disaster prevention science and keeping the earthquake disaster memories or knowledge through an earth science education in school.

This article is described about 3D model in the Fukuoka area and ground motion simulation using the model. And the result of exploration underground structure in the area, besides the practical use to the education of the exploration work is described.

2. 3D VELOCITY MODEL IN FUKUOKA AREA

Fukuoka area locates at the northern part of Kyushu Island, faces the Hakata bay. The location is shown by Figure 1. The sedimentary basin size of Fukuoka area is small and deep in comparison with Kanto basin and Osaka basin. There are some 3D models in the area (*e.g.* Mori *et al.*, 2007). A digital 3D model data used in this study of the deep part to the basement of S-wave velocity (Vs) 3.1km/s layer is made by Fujiwara (personal letter). The model has 2 velocity layers of the Vs 0.6 and 2.1km/s. Figure 2 shows the boundaries depth distribution between 0.6 and 2.1km/s, 2.1 and 3.1km/s. A maximum depth is 0.12 and 1.60km respectively, and the point locates below at Meinohama near the central Fukuoka city and Hakata bay. Although one of the features of this model is the layer depth data each about 1km mesh, the original information of underground structure survey of the model has some uncertainties. Because there are a few explorations of the deep sedimentary structure around the northern part of Kyushu Island (*e.g.* Morijiri *et al.*, 2002), many space interpolations have in the 3D model in my guess. Even if there are some reports about the underground structure, almost the data or information is explored for mining coal around Fukuoka coalfield and Tikuhou coalfield away from the target basin area. However, these fields have been closed. Therefore, it is not too much to say that this area is a lack of underground information for ground motion estimation of the deep part, although more than one million people live in the area of Fukuoka city.

The other, the shallow sedimentary exploration data by boring exist at many sites, there is a detail shallow part 3D model. Figure 3 shows a one of the thickness contour map of Quaternary sediment by Satoh and Kawase (2006). The maximum depth of surface sediment of under Vs 0.3km/s has about 50m around north-eastern part of Kego fault. Naturally, there is not only the layer but also some low velocity layers less than 0.3km/s. For example, the velocity structure at FKO006 by K-NET observation in Figure 1 and 3 has the Vs 0.10, 0.13, 0.15, 0.18 and 0.32km/s layers, the depth of the bottom of Vs 0.32km/s correspond to the top of the Vs 0.60km/s in the contour map of Figure 3.

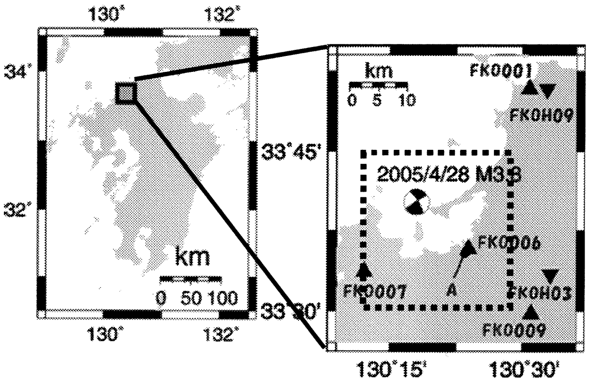

Figure 1. Map of the target area around Fukuoka. Dot square is ground motion simulation model area and black triangles show the location of K-NET and Kik-net observations in left figure.

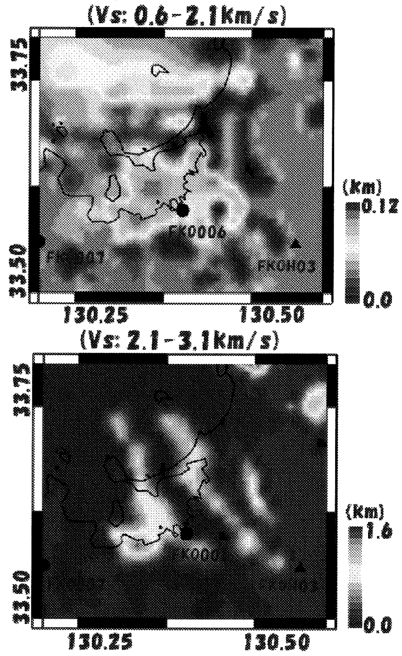

Figure 2. Boundary depth distribution by used 3D model data.

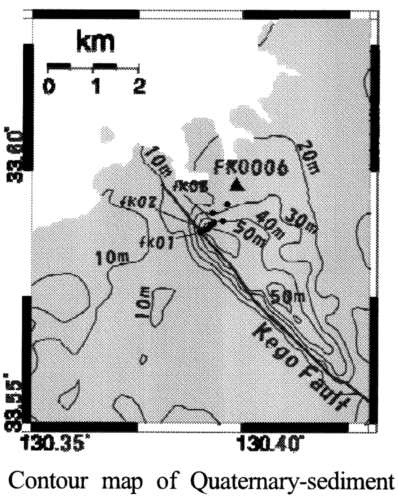

Figure 3. Contour map of Quaternary-sediment thickness touched in figure by Satoh and Kawase (2006). Dots show the location of aftershock observations of the 2005 west off Fukuoka Prefecture Earthquake by Yamanaka *et al.* (2005).

3. GROUND MOTION SIMULATION

To check a performance of the sedimentary 3D basin model data by Fujiwara (personal letter), ground motion during one of the aftershocks of the 2005 Fukuoka earthquake simulated with finite difference method (FDM). The analysis region about 30km width shows in Figure 1 (right). The model has 7 velocity layers as Table 1 with physical parameters. The first surface layer of Vs 0.4km/s referring to Satoh and Kawase (2006) is set in the 3D model, although 1st layer depth is 30m because of the simulation restriction of free surface condition and grid size of FD model. The flat boundaries from the 5th to 7th layer of referring to Asano and Iwata (2006) are set the model.

Simulation parameters for FDM and the source parameter show in the Table 2 and 3 respectively. The minimum FD grid space uses 60m with rectangular grids for z-direction. The lower period set 0.8s from the relation between minimum velocity and grid space. A target earthquake is M3.8 event at the 28 April 2005. The source model is assumed to be simple point source of smoothed source time function with duration of 1.0sec at the location of drown the source mechanism in Figure 1.

Figure 4 shows observed and synthesized ground motion waveforms resulting from the earthquake, as recorded by the aftershock observation array of the 2005 west off Fukuoka Prefecture Earthquake (M7.0) by Yamanaka *et al.* (2005). The location of the observation array points of fk01, fk02, fk08 and FKO006 shown by Figure 3 on a symbol 'A' in Figure 1. The stations array located across the surface layer step made by the Kego fault. The horizontal components velocity waveforms of band-pass filtered of period range from 0.8 to 5.0sec shown by Figure 4. A comparison with observed and synthesized waveforms indicate better reproduction in generally, although this simulation result is got from simplified point source model, and which the tuning of the model by simulations never done. However, there are some problems in the synthesized waveform by the detail comparison. The travel time of synthesized S-wave is earlier than the observed one at each observation. The cause looks like the problem of the deep structure in the 3D model. Otherwise, the amplitude of synthesized have about a half of observed in the each component at the fk02 and fk08. The small feature indicates inadequate for a lack of the reality of the 3D model, the shallower part particularly. In spite of these observations locate on the slop in the first layer, minimum FD grid space size has 30m at only surface grid, and there is not enough resolution for the configuration.

These results suggest that the differences between the real underground 3D structure and the modeled one for FD simulation exist. It is an inevitable to occur that the thing for using a 3D model made by limited underground information in the Fukuoka area. Therefore, we need more the information for accurate 3D basin model, and should explore the basin structure in the area. And besides, it needs the reconstruction of a new 3D model and the recheck one by ground motion simulation.

Table 1. Physical parameters of rock density, Vp, Vs and the boundary depth for each layers of simulation.

No.	ρ (g/cm^3)	Vp(km/s)	Vs(km/s)	Depth(km)
1	1.80	1.70	0.40	variable
2	1.90	2.00	0.60	variable
3	2.40	4.00	2.10	variable
4	2.50	5.00	2.70	variable
5	2.60	5.50	3.10	5.0km
6	2.70	6.00	3.46	18.0km
7	2.80	6.70	3.87	∞

Table 2. Simulation parameters for FDM.

Model dimension	$369\times386\times83^*$
dx	0.06km, 0.25km*
Vs min	0.4km/s
T min	0.8s

*Rectanguler Grid

Table 3. Source information and parameters.

date	2005/4/28
time	3h43m17.67s
epicenter	(33.67° , 130.30°)
depth	h=8.0km
	Mo =1.61*10^{14} N·m
strike, dip, rake	(328, 77, 4)

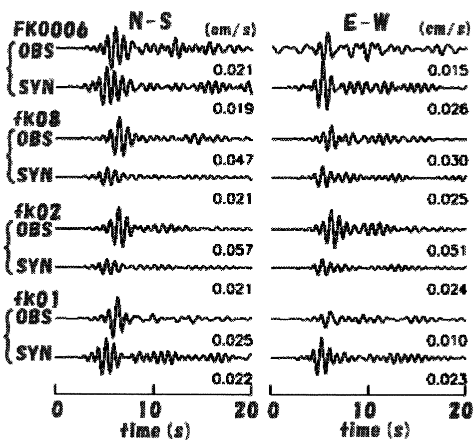

Figure 4. Comparison with observed and synthesized velocity waveform of the period range from 0.8 to 5.0sec.

4. Microtremor Array Exploration

For increasing underground data, our group conducted microtremor array explorations in the Fukuoka area to estimate 1D S-wave velocity profiles of deep sedimentary layers over the basement with a Vs about 3km/s. Recently, the exploration in the area came to be curry out by the other group of Dr. Kawase and Dr. Nishijima in Kyushu University, the underground structure information increases.

Figure 5 shows the locations of the finished or planned site of microtremor array measurement, from No. 1 to 5 have already done it. No .1 (Hakata: HKT), No. 2 (Tenjin: TJN) and No. 3 (Tojinmachi: TJM) have analyzed 1D profile. The details of the observation and analysis were described and discussed previous some papers (*e.g.* Yamanaka *et al.*, 2005). At each site, 2 arrays with different array size were deployed by installing 7 seismometers with station spacing of 0.1 to 0.8km. We can record 7 waveforms and estimate Rayleigh wave phase velocity from the f-k spectral analysis. The Rayleigh wave phase velocities observed in this study are shown Figure 6. The phase velocities at period range of 0.5 to 1.5sec are a little difference indicating variation of subsurface structure. The observed phase velocities are imagined the thing which the basin size is not so large, comparison with Kanto and Osaka basin. The phase velocity estimated at each site is inverted to an S-wave velocity profile by GA. In the inversion of all the phase velocities, I estimated a 3-layers model from previous study models, for example used 3D model data in this study. A 1D S-wave profile is determined with the GA inversion of phase velocity. Figure 7 shows the inverted S-wave profile and the comparison with a result of Mori *et al.* (2007) at the black square in Figure 5. The top of the basement depth Vs about 2.5km/s changes from 0.5 to 0.8km, with from west to east, although the surface layer bottom depth of Vs 0.8km/s is not so change. Our results and Mori *et al.* (2007) are comparable.

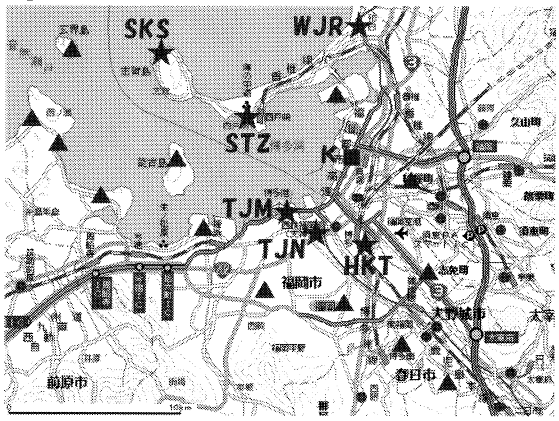

Figure 5. Location map of microtremor array observation, stars show finished site and triangles show planned sites.

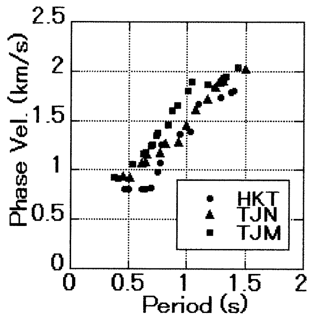

Figure 6. Observed Rayleigh wave phase velocities.

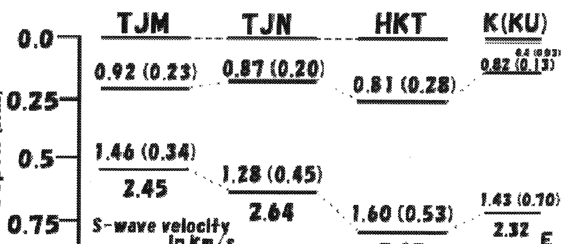

Figure 7. Vs profiles and a result of Mori *et al.* (2007).

Table 4. List of practice of cooperation with school education

No.	year	region	school name or object	class form	contents	etc
1	2006	Munakata city	5th attached high school with Tokai Univ.	L, E	ground environment	SPP: 4 times
2	2007	Kasuga city	Kasuga nishi JH	L, E	earthquake disaster	
3	2007	Onojo city	Hirano JH	L, E	ground motion	
4	2007	Fukuoka Pref.	Teachers	L	general earth science	
5	2007	Fukuoka Pref.	Teachers	L, E	earthquake	open school
6	2007	Onojo city	Oono E	E	electric importance	
7	2007	Kasuga city	Kasuga nishi JH	L	ground environment	SPP
8	2007	Kasuga city	Kasuga nishi JH	E	microtremor	SPP
9	2008	Kitakyushu city	Teachers	L, E	earthquake & volcano	

H: High School
JH: Junior High School
E: Elementary School

L: Lecture
E: Experiment or experience

SPP: Science Partnership Project

5. Cooperation with School Education

Japanese educational policy will be changed from April 2009 by Japan Ministry of Education, Culture, Sport, Science, and Technology (MEXT). One of the examples of the change which is the number of school hour unit of 'science education' will be increased from 350 to 405 in elementary education and from 290 to 385 in secondary one. And the contents of science subject will be increased, also. The other topic of the change is from the alternatively content of earthquake or volcano to the required contents both them in elementary education. It is natural to change the high school science education. Therefore, Japanese science education is crisis now, although the curriculum just only reverts to the past system.

By the way, some projects of cooperation between schools and university prevail, recently. Table 4 shows a list of only my practices to cooperate with school in a year. Although main object is school students, the opportunity for teachers of elementary and secondary school increases. These things look like to represent an importance for many teachers in primary education. They are conscious of poor the knowledge for science and the skill for science education, they are perplexed in my guess. Whether that some projects of cooperation as in Table 4 and others can help or not for the teachers, I have to evaluate the results.

In the before section, all the site of microtremor array exploration locate in or very near the public school as a part of practicing use to the earth science educations. However, because the array explorations are difficult for educational application, these results of basin structure should be used for leading of the cooperation between the schools and ours, and for estimating of ground motion. In my idea, the cooperation suit for the shallow part exploration by refraction examination. Fortunately, the exploration was realized by No. 1 in Table 4 by the grace of eager teachers. Although, it is difficult to carry out the cooperation, because many teachers are very busy and there is not leeway in school timetable. We need to observe whether these projects hard to practice or not by the educational policy changes. At any rate we have to continue the earth science and engineering education to children and their parents for prevention earthquake disaster.

6. CONCLUSIONS

In this article, an existent 3D model, a model performance of ground motion simulation used by it in the Fukuoka area and the results of the sedimentary basin explorations by microtremor array measurements describes. The 3D model performance and 1D S-wave velocity structures indicates in the Fukuoka. Besides, the case of practical use to the earth science education is introduced. These things are progressing to increase the number of the case of the exploration site and the practice for the research and education. I will report them regularly.

Acknowledgements:

I would like to special thank Prof. Hiroaki Yamanaka of Tokyo Institute of Technology for supports of exploration instruments and appropriate advices. The exploration works were cooperated with 11 students in my laboratory of Fukuoka University of Education. The educational practices were cooperated with the schools and teachers in Table 4 and were supported by Science Partnership Project (SPP) of Japan Science and Technology Agency (JST). And this study was supported by Grant-in-Aid for Young Scientists (B) 19700618 of MEXT.

References:

Asano, K. and Iwata, T. (2006), "Source process and near-source ground motions of the 2005 West Off Fukuoka Prefecture earthquake", *Earth Planets Space*, **58**, 93-98.

Mori, S., Kawase, H. and Umeda, N. (2007), "Re-construction of the deep underground structure in Fukuoka and application to estimate strong motion for a future earthquake", Summaries of Technical Papers of Annual Meeting AIJ, 421.

Morijiri, R., Hiroshima, T., Komazawa, M., Makino, M., Murata, Y., Nawa, K., Nishijima, J. and Mogi, T. (2002), "Bouguer gravity anomalies in the Fukuoka area, Kyushu, Japan", *Bull. Geol. Surv. Japan,* 53, 573-594.

Satoh, T. and Kawase, H. (2006), "Simulation of strong motions in Fukuoka City during the 2005 West Off Fukuoka Prefecture Earthquake with special reference to thick Quaternary sediments around the Kego fault, *Earth Planets Space,* **58**, 105-110.

Yamanaka, H., Motoki, K., Seo, K. and Kawase, H. (2005), "Observation of aftershocks of the 2005 west off Fukuoka prefecture earthquake in Tenjin area of Fukuoka city", Abstract of Seismological Society of Japan 2005, Fall meeting, B075.

Yamanaka, H., Komaba, N. and Yamada, N. (2005), "Estimation of 3D S-wave velocity model of the Kanto basin, Japan, for prediction of long-period strong ground motion", Second International Conference on Urban Earthquake Engineering, 227-232.

Fifth International Conference on Urban Earthquake Engineering
March 4-5, 2008, Tokyo Institute of Technology, Tokyo, Japan

WAVEFORM INVERSION OF SHALLOW SEISMIC REFRACTION DATA USING HYBRID HEURISTIC SEARCH METHOD

Hiroaki YAMANAKA[1], and Mika TAKEKOSHI[2]

1) Associate Professor, Dept. of Environmental Science and Tech., Tokyo Institute of Technology, Japan
yamanaka@depe.titech.ac.jp
2) Graduate Student, Dept. of Environmental Science and Tech., Tokyo Institute of Technology, Japan

Abstract: We proposed a waveform inversion method of SH-wave data obtained in a shallow seismic refraction survey to determine a 2D inhomogeneous S-wave profile of shallow soils. In this method, finite difference computation of the 2.5D equation for SH-wave propagation in a 2D media is used as the forward modeling. The misfit defined using differences of calculated and observed waveforms is minimized with a hybrid heuristic search method. We parameterize a 2D subsurface structural model with the boundary depth shapes and S-wave velocity of each block. Numerical experiments were conducted using synthetic SH-wave data with a white noise for a model having a blind layer and irregular interfaces. We could reconstruct the complex structure with reasonable computation time from surface seismic refraction data.

1. INTRODUCTION

Local site amplification is one of the important factors to characterize earthquake ground motion at a site with soft soils. It is therefore required a detailed data for subsurface structure to predict strong ground motion in such a site during an earthquake. In particular lateral variation of subsurface S-wave velocity must be known to understand spatial distribution of earthquake ground motion. Seismic refraction exploration using SH-waves generated with plank hammering is one of the most popular methods for profiling a two-dimensional shallow S-wave velocity structure of soft soils (e.g., Kramer, 1996). SH-waves are recorded with seismometers deployed in a surveying line on the surface. Travel times of initial phases of the SH-wave observed are used to deduce an S-wave velocity model from the surface down to a depth of several-ten meters. Although field operation and analysis in the shallow refraction method is easy and simple, an obtained S-wave profile is often too simple with a single surface layer over a firm soil with constant velocities. We sometimes have difficulties to determine a proper soil model from travel time data in a complex structure having a blind layer, a velocity inverse layer and so on. The existence of these layers can not be detected in the conventional travel time analysis of refracted initial phases (e.g., Burger, 1992). Furthermore, the travel time data are more or less contaminated with ambient noises, because the initial phases are often small in amplitude as compared with later phases. This also makes it difficult to reconstruct a proper model. Recently, surface waves in the refraction data are used in shallow S-wave profiling from dispersion analysis (e.g., Hayashi and Suzuki, 2004). Since travel times of initial S-wave are not used in the surface wave method, it is easily applied in noisy urban area. Although a two-dimensional image of S-wave velocity can be derived from the surface wave method, it is required to prepare many observed stations for detailed imaging. Furthermore separation of surface wave modes must be done before the dispersion analysis, when higher mode surface waves have larger or similar amplitudes to the fundamental modes.

In this study, we proposed a waveform inversion of shallow seismic refraction data to a 2D inhomogeneous S-wave profile using a hybrid heuristic algorithm. We used a 2.5D finite difference calculation to generate synthetic SH-wave data that are used in numerical experiments. After validation of the method using synthetic data for a simple model, application to a complex inhomogeneous structure is examined.

2. METHOD

2.1 Forward Modeling

In the waveform inversion it is required to use calculation of forward modeling which can generate synthetic SH-seismograms with true amplitudes in a 2D inhomogeneous soil model from a point source. Since effects of three-dimensional geometrical spreading must be included in calculation of wave field in 2D media, we used a 2.5D equation of motion of SH-waves

$$\rho\frac{\partial\dot{v}}{\partial t}=\frac{2}{r}\tau_r+\frac{\partial\tau_r}{\partial r}+\frac{\partial\tau_z}{\partial z} \tag{1}$$

$$\begin{cases} \dfrac{\partial \tau_r}{\partial t} = \mu\left(\dfrac{\partial \dot{v}}{\partial r} - \dfrac{\dot{v}}{r}\right) \\ \dfrac{\partial \tau_z}{\partial t} = \mu \dfrac{\partial \dot{v}}{\partial z} \end{cases} \tag{2}$$

with expression using stress and velocity for the forward modeling. The 2.5D equation of motion due to SH-waves is numerical solved with 4th-order and 2nd-order central finite difference approximation in space and time. The staggered finite difference grid is used in the approximation. The absorbing and sponge buffer conditions are subjected in the non-physical boundaries in the bottom, left and right sides of a finite difference grid model. The free surface condition is applied in the upper boundary of the model.

2.2 Parameterization

Subsurface structure is often parameterized with many cells in tomographic inversions. Since we are interested in waveform inversions of conventional refraction data with several to 10 observation data from one or two shots at the two ends of a surveying line. Tomographic image, such as Figure 1a, is difficult to be reconstructed from such a small number of observed data. On the other hand, parameterization with a stack of homogeneous layers having irregular shapes of interfaces in Figure 1b is not so difficult to invert the small number of data. However, lateral variation of S-wave velocity can not be included in the homogeneous-layer model. We therefore use a combined parameterization with the tomographic-cell and homogeneous-layer models as can be seen in Figure 1a.

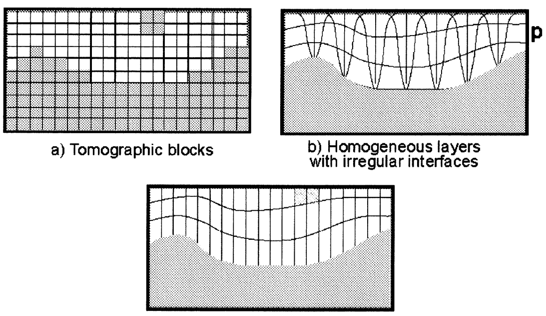

Figure 1. Model parameterization

A soil model consists of surface layers over a basement having a constant S-wave velocity that is one of the unknown parameters in the waveform inversion. The surface layers are divided into layers separated by the interfaces. For example, the model in Figure 1c has three surface layers. The depth shape of each interface is described with basis functions by Aoi et al. (1995). Using linear combination of a basis function ck(x) and a coefficient pk, the interface depth d(x) at location x is written as

$$d(x) = \sum_{k}^{L} p_k c_k(x) \tag{3}$$

where L is number of basis function. The basis function is defined as

$$c_k(x) = \begin{cases} 1/2 + 1/2\cos(\pi/\Delta(x - x_k)) & x_{k-1} \le x \le x_{k+1} \\ 0 & otherwise \end{cases} \tag{4}$$

where Δ and x_k are constant given in advance. The interface depth parameters are defined for each interface of a multi-layered model. The unknown parameters to be determined on the waveform inversion are the coefficients p_k in the equation (3) with respect to the interface shape. In order to model lateral variation of S-wave velocity in surface layers, it is divided into blocks as can be seen in Figure 1c. S-wave velocity for each block is also one of the parameters in the inversion. In order to stabilize the inversion we used smoothing of the S-wave velocity of the blocks in each layer with a weighted 3-points smoothing operation.

The unknown parameters to be determined in the inversion are P_k, S-wave velocities of all the blocks in surface layers and S-wave velocity of the basement. For example, total number of the unknown parameters for the model in Figure 1c are 61 (10*3P_k, 20*3+1 S-wave velocities).

The above-mentions parameterization of the subsurface structure can allow to model soils layers separated by geologically discontinuous interfaces with S-wave variations. We therefore assume small variations of S-wave velocities in the blocks that belong to the same layer in the inversion. This can be implemented with making narrow search limits of the S-waves for the blocks.

2.3 Definition of misfit

The misfit function to be minimized in the inversion is defined using observed and theoretical traces to determine the model parameters. The misfit, E, is calculated from

$$E = \frac{1}{N} \frac{\sum\left[s^c(t) - s^o(t)\right]^2}{\sum\left[s^c(t)\right]^2} \tag{5}$$

where $s^o(t)$ and $s^c(t)$ are the observed and calculated SH-waves. N is the number of stations along the surveying line. In the following numerical experiments, we assumed that source wavelet is known before the inversion. Probably deconvolution processing using a reference station must be applied to the observed and synthetic data before calculating the above misfit.

2.4 Inversion algorithm

It is expected that the misfit function has a complex multi-model shape. An appropriate initial model is required in the least-squared inversions, because of the local search characteristics. However, we often have no a priori knowledge on subsurface structure, especially for shallow near-surface soils. We therefore applied global search algorithms to minimize the misfit function in this study.

Heuristic approaches are one of the global search algorithms used in various kinds of geophysical inversions, such as GA and SA (e.g., Yamanaka, 2005). Since the heuristic inversion methods require many numbers of forward calculations, the heuristic approaches are not so often applied in inversions with relatively heavy forward computations. We however used the hybrid heuristic method proposed by Yamanaka (2007), because the method is capable to find the optimal model with less computational efforts than those for the conventional heuristic algorithms.

The computational flow is shown in Figure 2. The main part of the operations is based on the generic algorithm by Yamanaka and Ishida (1996) with three genetic operations of crossover, selection, and mutation. However, a generation-dependent probability for choosing new models from current models (X) and offspring models (Y') in the crossover operation is introduced in the hybrid method. The difference between the misfits of the offspring and current models

$$\Delta E = E(\mathbf{Y}') - E(\mathbf{X}) \qquad (6)$$

is calculated. We principally select either the parent model or the offspring model with smaller misfit than the other. If the difference of the two misfits is negative, the offspring model survives in the next generation. However, when ΔE is positive, the offspring model with a large misfit is still selected in the next generation with an acceptable probability defined as

$$P = \exp(-\Delta E / T_k) \qquad (7)$$

where T_k is temperature. The temperature is high in the early stage of the computation and becomes gradually small with increasing generations. The temperature T_k at the k-th iteration of temperature is calculated to decrease with the similar manner to the SA by Yamanaka (2005). According to the decrease of the temperature, the acceptable probability works differently in the early and late stages of the search. In the early stage, offspring models with large errors between observed and calculated waveforms can be frequently selected in the next generation, while such models are hard to survive in the later part of the iterations. Therefore, only the offspring models with smaller misfits than the parent models can be chosen in the final stages of the calculation. As similar to the SA, it is expected that the algorithm can search model space globally and locally because of the generation-dependent acceptable probability. It is also noted that the hybrid method with infinite temperature works as similar to the conventional GAs. In this study, we also include the elite selection rule by Yamanaka and Ishida (1996) in the hybrid method. The above-mentioned genetic operations are repeated with decreasing the temperature until the number of the iterations reach to a given value. In addition to this operation, we used a real-number coding of the parameters in the proposed hybrid method.

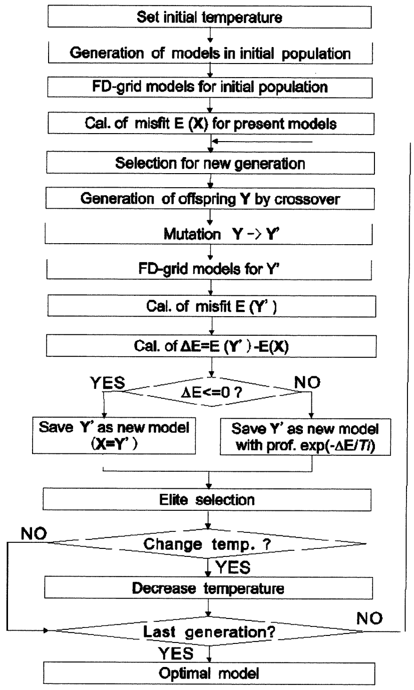

Figure 2. Computational flow of hybrid heuristic inversion

3. MODEL AND SYNTHETIC DATA

The model used in the numerical test has two surface layers over the basement with an S-wave velocity of 400m/s as shown in Figure 3. The thickness of the second surface layers is 1m. This layer can not be detected with conventional travel time analysis of initial phases, because the layer is too thin and no refracted waves propagating in the top of the second layer arrive at sites on the surface as initial phases. This kind of thin layer is known as a blind layer in refraction seismology. In additional to the blind layer, this model has a slope of the interfaces in the central part.

The synthetic SH-waves are calculated at the 10 stations located on the surface of the model using forward calculation. The locations of the stations are shown by triangles in the figure. We assumed an explosive point source at the surface. The source time function is assumed to be Ricker wavelet. In the inversion the source wavelet is given in advance. The grid space of the FD model is 0.1m in the calculation of forward modeling. Since this grid interval is sufficiently larger than the minimum requirements for the stable computation criteria, accuracy of calculated wave field is enough in the later phases that might be contaminated by the numerical dispersion. The computed waves are shown in Figure 4. This synthetic data is included theoretical SH-waves from the forward modeling and white noises whose amplitudes are 10% of the maximum value of each SH-wave.

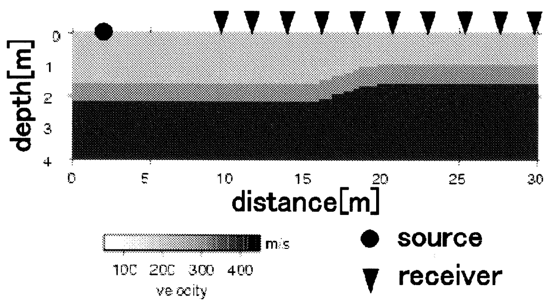

Figure 3. Two-dimensional S-wave velocity model used in numerical test. A circle and triangles indicate the source and stations

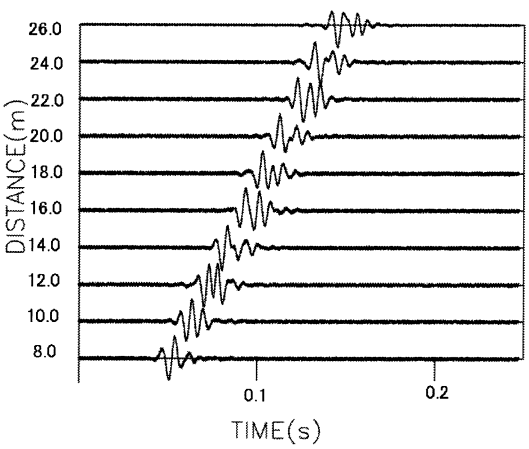

Figure 4. Synthetic waveform data calculated at the stations at the surface of the model used in numerical test. Random noises are included in the synthetic data

4. INVERSION RESULTS

The heuristic waveform inversion is applied to the synthetic data. We first conducted a tuning of the parameters of the algorithm, such as population size, probabilities of crossover and mutation and so on. The appropriate combination of the parameters was decided from trial runs of the program with several generations. They are as follows; population size 20, crossover probabilities 0.7, mutation probability 0.01 and initial temperature 10. The upper and lower limits of the search spaces for the parameters are tabulated in Table. 1

The average and minimum misfits among the 30 models in each generation is show in Figure 5 together with temperature decrease scheduled. The averaged misfit starts to decrease after the 40th generation, and becomes similar value to the 60th generation. This indicates that the many models in each generation concentrate around the minimum value because of the local search ability of the hybrid method. The variations of the S-wave velocities of some of the blocks in the first and second layers are shown in Figure 6. As expected from the average misfit variations in Figure 5, the S-wave velocities are converging to the true values at more than 60th generation.

Since many random numbers are used in the heuristic search methods including the hybrid method used in this study, the above-mentioned variations of the misfits and parameters are more or less dependent of the random numbers used in each execution of the program. We therefore conducted 10 inversions with different initial values of random number generator used in the program. The minimum misfits derived in the 10 inversions are shown in Figure 7 with their averaged values. The variation of the standard deviation of the minimum misfits is also shown in Figure 8. The standard deviation becomes small at the 50th generation indicating the stability of the inverted results with regardless of the initial values of the random number generator.

The model parameters for the minimum models estimated in the 10 inversions are averaged to determine the final inverted results. According to the idea of the acceptable solutions (Yamanaka, **) all the models with misfits of less than a threshold value are used in the averaging. We used 1.5 times larger misfits than that of the minimum misfit among the all misfits examined in the 10 inversions. The final model is depicted in Figure 9. The blind layer and the irregular part of the interfaces could be well reconstructed in the inverted model. The thickness to the basement becomes shallower than the true model near the source. This is due to low sensitivity of the structure near the source, because the observed motions are obtained at the stations with epicentral distance more than 10 meters. The standard deviations of the S-wave velocities for the blocks in the acceptable solutions are shown in Figure 10. Since most of the standard deviation for the S-wave velocities is less than 1%, they are well convergent to the true values. The synthetic seismograms for the inverted model are compared with those for the synthetic observed data in Figure 11. The synthetic seismograms are almost identical with the data.

Table 1 Search limits in inversion

Layer	Vs (m/s)	P_k (m)
1	150-250	0.1-2.0
2	250-350	0.1-1.5
3	350-450	

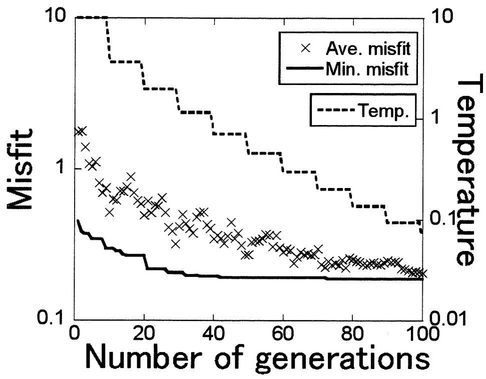

Figure 5. Variations of the minimum and average misfits of waveform inversion of synthetic data in Figure 3 with increasing generation. Temperature decrease is also shown

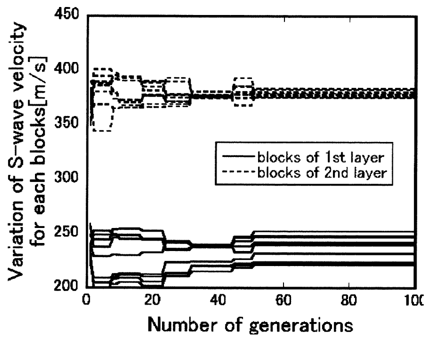

Figure 6. Variation of S-wave velocities of the blocks in the first and second layers in the waveform inversion of the synthetic data in Figure 3

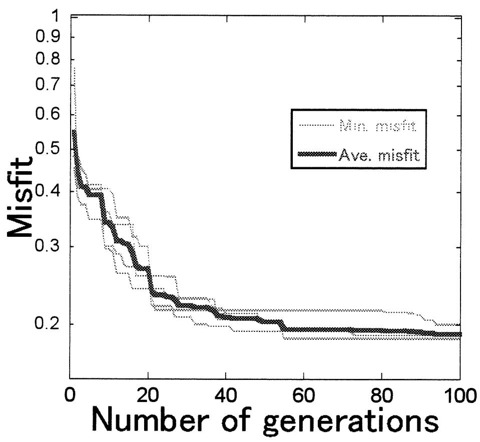

Figure 7. Variation of average of the minimum misfits for 10 inversions of the synthetic data in Figure 3 with different initial values of random number generator used in the program

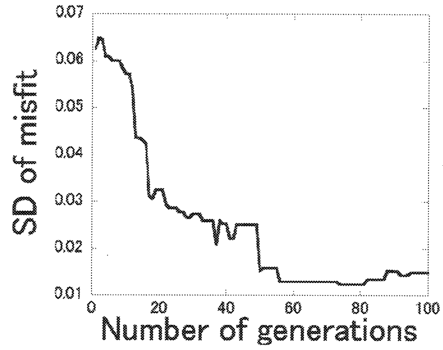

Figure 8. Variation of standard deviation of the minimum misfits for 10 inversions of the synthetic data in Figure 3 with different initial values of random number generator

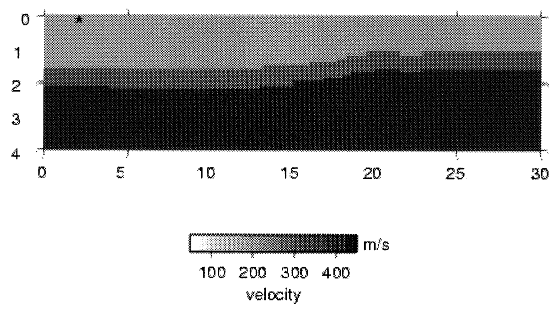

Figure 9. S-wave velocity model from waveform inversion of the synthetic data in Figure 3. The S-wave velocities and interface depth coefficients are derived from averaging the results of acceptable models

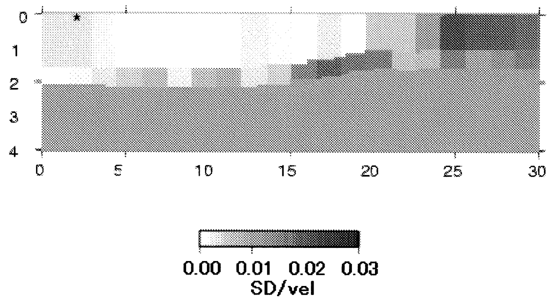

Figure 10. Distribution of standard deviation of the S-wave velocities of the blocks for the acceptable models

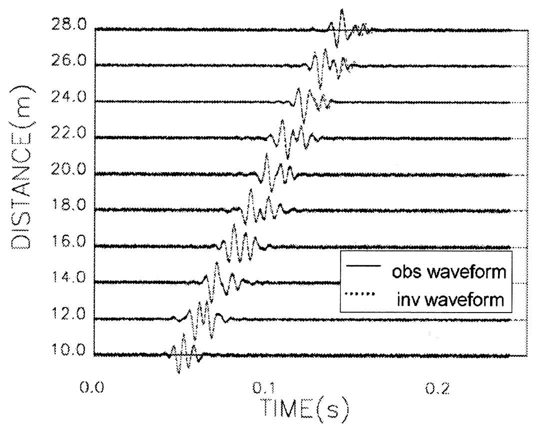

Figure 11. Comparison of calculated SH-waves for the inverted model in Figure 9 with synthetic observed data

5. CONCLUSIONS

The hybrid heuristic waveform inversion method is proposed to retrieve a two-dimensional S-wave velocity profile from shallow seismic refraction data. The subsurface structure is parameterized with irregular shape of interfaces of the surface layers which contained lateral S-wave velocity variations. The interface depth is expressed with linear summation of the basis functions. The inhomogeneity of the S-wave velocity in each layer is modeled with introducing blocks having different S-wave velocities. The effectiveness of the method was demonstrated from inversion of synthetic waveform data of SH-waves observed at the surface of the two-dimensional shallow soil model having a blind layer over the basement. The true model could be well reconstructed by the waveform inversion.

Acknowledgements:
The authors acknowledge support from Japan Ministry of Education, Culture, Sport, Science, and Technology (MEXT).

References:

Aoi S., T. Iwata, K. Irikura, and F. J. Sanchez-Sesma (1995), "Waveform Inversion for Determining the Boundary Shape of a Basin Structure," *Bulletin of the Seismological Society of America*, **85**, 1445-1455.

Burger, H.R. (1992),"Exploration geophysics of the shallow subsurface," Prentice-Hall Inc., 95-101.

Hayashi, K. and H. Suzuki (2004), "CMP cross-correlation analysis of multi-channel surface-wave data," *Exploration Geophysics*, 35, 7 – 13.

Kramer, S.L. (1996), "Geotechnical Earthquake Engineering," Prentice-Hall Inc.

Yamanaka, H. and H. Ishida (1996), "Application of genetic algorithms to an inversion of surface-wave dispersion data," *Bulletin of the Seismological Society of America*, 86, 436-444.

Yamanaka, H (2005), "Comparison of performance of heuristic search methods for phase velocity inversion in shallow surface wave methods," *Journal of Environmental and Engineering Geophysics*, 10, 163-173.

Yamanaka H. (2007), "Inversion of surface-wave phase velocity using hybrid heuristic search method," *Geophysical Exploration (Butsuri Tansa)*, **60**, 265-275 (in Japanese).

Fifth International Conference on Urban Earthquake Engineering
March 4-5, 2008, Tokyo Institute of Technology, Tokyo, Japan

STRONG MOTION SIMULATION AND MODELING OF THE 2001 GEIYO (MJ6.7), JAPAN, EARTHQUAKE, USING THE EMPIRICAL GREEN'S FUNCTION METHOD

Michihiro Ohori[1), 2)]

1) Researcher, Center for Urban Earthquake Engineering, Tokyo Institute of Technology, Japan
2) Researcher, DONET, Marine Technology Center, Japan Agency for Marine-Science Technology, Japan
ohorim@jamstec.go.jp

Abstract: In this study, I carried out source parameter estimation and strong motion simulation of the 2001 Geiyo earthquake (M_J6.7), Japan. Data obtained at 10 KiK-net stations located at 19 to 66 km in epicentral distance is used. To focus on the source modeling without consideration about nonlinearity of soft surface layers, borehole records are targeted. First, to derive rough estimates of basic source parameters, I inverted spectral amplitude from the S-wave main portion of the mainshock and 12 aftershocks (M_J3.5 to 5.0). The moment magnitude, the corner frequency and the stress drop for the mainshock were estimated to be 6.3, 0.5 Hz and 377 bar, respectively. Next, using data from the largest aftershock as the empirical Green's function, I estimated the relative moment release distribution on the fault plane and simulated the strong motion records targeting the mainshock in a range of 0.3 to 10 Hz. Waveform matching between synthesis and observed data is satisfactory. The maximum amplitudes of observed horizontal components from 10 stations were in a range of 24 to 123 gal in acceleration and 1.6 to 8.5 kine in velocity. At most of the stations, the observed maximum amplitudes were simulated within a factor of 2.0.

1. INTRODUCTION

The 2001 Geiyo earthquake (M_J6.7) ruptured in the Philippine Sea slab beneath the Seto Inland Sea of Japan at a depth (51 km) on March 24, 2001. The source mechanism of the event was normal faulting. This earthquake released high frequency energy to the southwest Japan and caused 2 deaths and injured 288 people. 70 houses were collapsed and 774 houses were damaged (Cabinet Office, 2001). The study on the source modeling and strong motion simulation for the earthquake is considered to be significant from both seismological and engineering points of views.

In this study, I carried out source parameter estimation and strong motion simulation with use of the empirical Green's function method. Fortunately, the KiK-net, one of the strong motion networks operated by the National Research Institute of Earth Science and Disaster Prevention (NIED), has been just started since August, 2000, seven months before the event. I targeted 10 KiK-net stations located at 19 to 66 km in epicentral distance. To focus on the source modeling without any consideration about nonlinear behavior of soft surface layers at many sites reported in previous studies [e.g. Kanno and Miura (2005)], borehole records were used.

First, I inverted spectral amplitude of the S-wave main portion from mainshock and 12 aftershocks (M_J 3.5 to 5.1) and derived rough estimates of basic source parameters characterizing the omega-square source spectrum by Brune (1970). Second, I carried out strong motion simulation based on the empirical Green's function method. A simple fault plane of 30 by 18 km^2 with strike of 180 deg. and dip of 60 deg. was assumed with reference of source models in previous studies [e.g. Kikuchi and Yamanaka (2001), Sekiguchi and Iwata (2001), Nozu (2001) and Kakehi (2004)]. Using data from the largest aftershock as the empirical Green's function, I estimated the relative moment release distribution on the fault plane and simulated the strong motion records from the mainshock.

2. Events and Stations

In Figure 1, locations of the mainshock (M_J6.7, labeled as Event 1) and 12 aftershocks (M_J3.5 to 5.0, Events 2-13) of the Geiyo earthquake are shown. The focal mechanism solutions of events determined by the F-net are inserted. Also, 10 KiK-net stations, which was used in Koketsu and Furumura (2002), are plotted with up-side-down solid triangles. These stations are surrounding the rupture area of the mainshock and their recordings are carried out not only at the surface but also at the borehole. They are located at 19 km to 66 km in epicentral distance for the mainshock, and the S-wave velocity at their boreholes (Vs_{max}) are ranging from 2000 m/s to 2900 m/s, except for two stations, HRSH07, EHMH04 with the Vs_{max} of 1200 m/s and 700 m/s, respectively. As for the mainshock, the nonlinear behavior of soft surface layers are pointed out [e.g. Kamino and Miura (2005)]. On the other hand, the data recorded at close distance from the source is considered to be rich in source characteristics. Therefore, to focus on the source modeling without any consideration about nonlinearity of surface layers, I used borehole data instead of surface data .

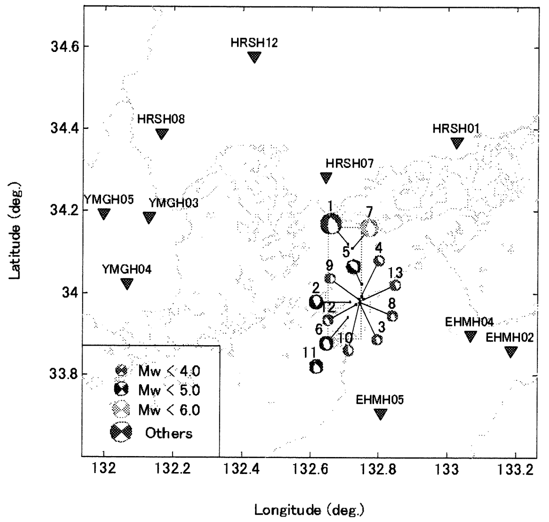

Figure 1 Map showing location of epicenters and stations targeted in this study. Focal mechanism solutions determined by the F-net are also inserted. Note that a rectangle surrounding the rupture area denotes a fault plane used for the simulation based on the empirical Green's function method with 30 km in length and 18 km in width. The strike and dip are set to 180 deg. and 60 deg.

3. Inversion of Spectral Amplitude

3.1 Data Processing

To have rough estimates for the source parameters, the spectral amplitude inversion was carried out. I took 20 second time window for the S-wave portions from the NS and EW components. The beginning and the end of the window were tapered with 1 second cosine taper. Then, I calculate the Fourier transform from a complex signal x(t)+iy(t), where x(t) and y(t) denote two orthogonal horizontal components. The amplitude spectrum was smoothed by a Parzen window with a width having frequency dependence: given by 0.1f with the minimum of 0.1 Hz and the maximum of 1.0 Hz. The spectral amplitude between 0.1 and 20 Hz was targeted in the spectrum inversion.

3.2 Analytical Method

Analytical procedure of the spectrum inversion employed in this study was almost the same as the method by Iwata and Irikura (1986), except that Q_s -value (quality factor of the S-wave) along the propagation path was given a priori after preliminary analyses.

Let us consider the spectral expression of the ground motion. The spectral amplitudes at the j-th station from the i-th event, $O_{ij}(f)$ can be given by

$$O_{ij}(f) = S_i(f) G_j(f) \frac{1}{R_{ij}} \exp\left(\frac{-\pi f R_{ij}}{Q_s(f) V_s}\right) \qquad (1)$$

where $S_i(f)$, $G_j(f)$ and $Q_s(f)$ represent the source spectrum, the site amplification, and quality factor along the path from source to station. Also, R_{ij} and V_s represent the corresponding hypocentral distance and the average S-wave velocity from source and station. V_s was assumed to be 3.8 km/s.

The equation (1) can be rewritten as

$$\overline{O}_{ij}(f) = S_i(f) G_j(f) \qquad (2)$$

where $\overline{O}_{ij}(f)$ is the path-effect corrected spectral amplitude given by

$$\overline{O}_{ij}(f) = R_{ij} O_{ij}(f) \exp\left(\frac{\pi f R_{ij}}{Q_s(f) V_s}\right) \qquad (3)$$

We take the logarithm of the equation (2) and derive the following expression:

$$\log_{10} \overline{O}_{ij}(f) = \log_{10} S_i(f) + \log_{10} G_j(f) \qquad (4)$$

The unknowns to be solved in the above equation are $S_i(f)$, $G_j(f)$ and $Q_s(f)$. As previously mentioned, in this study, $Q_s(f)$ was treated to be given. I tested several $Q_s(f)$ models in preliminary analyses and examined the spectrum matching between the synthesized spectrum and observed ones. As a result, $Q_s(f) = 81 f^{0.85}$ was seemed to be appropriate in this study. Therefore unknowns were reduced to two parameters, $S_i(f)$ and $G_j(f)$. Considering M events and N stations in total, M by N simultaneous equations are constructed for each frequency. These equations can be solved with the nonnegative least square method by Lawson and Hansen (1974). To solve the equations with a constraint of $G_j(f) \geq 2$, $G_j(f)$ was substituted by $2G'_j(f)(= G_j(f))$ because in solving the logarithmic solution, the nonnegative constraint of $\log_{10} G'_j(f) \geq 0$ corresponds to $G'_j(f) \geq 1$. Moreover, the equation (1) was normalized by the minimum amplitude of $\overline{O}_{ij}(f)$ for each frequency.

3.3 Results

In Figures 2a and 2b, the inverted source spectra for 13 events are shown with bold lines. In Figure 2c, the spectral ratios between the mainshock and each aftershock are shown.

In order to determine basic source parameters [the moment magnitude M_W (or the seismic moment), the corner frequency, the stress drop], I fit the theoretical source acceleration spectrum with inverted one. The source acceleration spectrum used here is the omega-square model by Brune (1970) combined with a high frequency cut-off filter, given by

$$S(f) = \frac{r_s M_0}{4\pi\rho\beta^3 R} \frac{(2\pi f)^2}{1+\left(\frac{f}{f_c}\right)^2} \frac{1}{1+\left(\frac{f}{f_{max}}\right)^n} \qquad (5)$$

where r_s is the average radiation pattern for the S-wave,

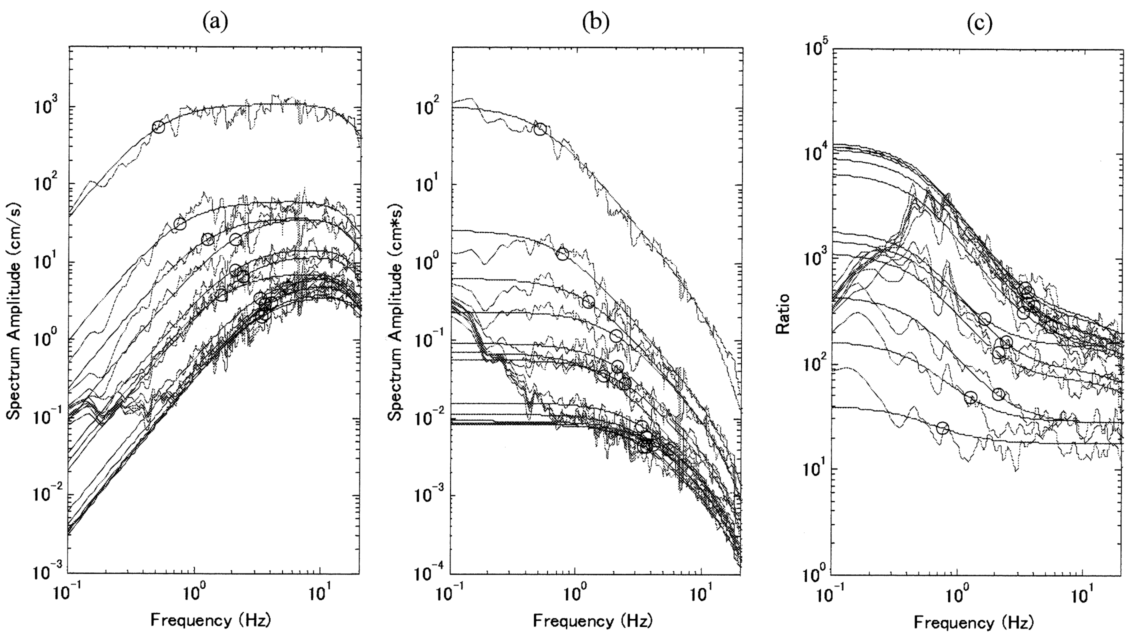

Figure 2 Source spectra obtained from the spectrum inversion. The source acceleration spectrum (a) and source displacement spectrum (b) are adjusted at 1 km in hypocentral distance. The spectral ratio (c) is calculated between the mainshock and the aftershocks. In each diagram, results from the spectrum inversion are denoted by thick (jagged) lines and those from the theoretical model are done by thin (smooth) lines.

Table 1 Source parameters of targeted events and results of spectral amplitude inversion.

Event	JMA				F-net	Spectrum Inversion		
	Date (y:m:d)	Clock (h:m:s)	Depth (km)	M_J	M_W	M_W	f_c (Hz)	$\Delta\sigma$ (bar)
1	2001:03:24	15:27:54.1	51.4	6.7	6.8	6.3	0.5	377
2	2001:03:24	22:37:33.6	46.9	4.1	4.1	4.2	1.6	8
3	2001:03:25	02:19:52.3	49.5	3.8	3.6	3.8	3.3	16
4	2001:03:25	09:10:54.1	50.1	3.8	3.5	3.6	5.4	35
5	2001:03:25	19:19:11.4	51.3	4.4	4.4	4.5	2.1	54
6	2001:03:26	02:16:00.3	47.6	3.9	4.1	4.3	2.1	22
7	2001:03:26	05:40:53.2	49.3	5.0	5.1	5.2	0.8	32
8	2001:03:26	18:59:23.3	49.4	3.9	3.5	3.6	4.1	16
9	2001:06:30	17:13:19.9	47.3	4.0	3.6	3.7	3.6	14
10	2001:08:24	21:44:32.5	47.8	4.3	4.0	4.1	2.4	21
11	2002:03:25	22:58:17.2	46.2	4.7	4.7	4.8	1.2	32
12	2002:12:20	03:48:58.2	46.0	3.8	3.6	3.6	3.6	11
13	2004:03:10	04:56:37.4	42.5	3.6	3.6	3.6	3.4	9

R is the hypocentral distance. ρ and β denote the density and the S-wave velocity in the source layer. f_{max} and n denote parameters for a high frequency cut-off filter. M_0 and f_c represent the seismic moment and the corner frequency. The stress drop is given by

$$\Delta\sigma_s = \left(\frac{f_c}{4.9\times10^6\beta}\right)^3 M_0 \qquad (6)$$

where R_s, R, ρ and β were assumed to be 0.63, 1 km, 3.1g/cm^3 and 4.62 km/s, respectively. M_0 and f_c were determined by fitting the inverted source spectrum with the model. n was assumed to be 1 and f_{max} was determined in a range of 14 to 24 Hz by eye inspection.

In Figures 2a, 2b, and 2c, the model source spectra were plotted with thin solid lines. The corner frequency for each event was plotted with an open circle. The model spectra agree well with the inverted ones so that the scaling law based on the omega-square model was considered to be valid among targeted events in this study.

In Table 1, the estimated results of source parameters are summarized. The moment magnitude (M_W), the corner frequency, and the stress drop were estimated to be 6.3, 0.5 Hz, and 377 bar for the maishock, and 5.2, 0.8 Hz, and 32 bar for the largest aftershock (Event 7 in Figure 1).

4. Simulation of the Mainshock

4.1 Fault Plane Discretization

Referring to the focal mechanism solutions, aftershock distribution, and waveform inversion results in previous studies [e.g. Kikuchi and Yamanaka (2001), Sekiguchi and Iwata (2001), Nozu (2001), and Kakehi (2005)] , I assumed simple rectangular fault plane with 30 km in length and 18 km in width, on which the mainshock hypocenter was located as a rupture point. See Figure 1. The strike and dip of the fault plane was set to 180 deg. and 60 deg., respectively. The depth of the fault plane is 45 km at top and 60 km at bottom.

To express rupture propagation from the hypocenter to the whole fault plane, it was divided into 10 by 6 subfaults with the size of 3 km by 3 km. Rupture velocity of 3.0 km/s was selected after comparison of the results with rupture velocity between 2.5 km/s and 3.5 km/s.

4.2 Method and Analytical Condition

Since a pioneering work by Hartzell (1978), the empirical Green's function method has been recognized as a useful technique to synthesize strong ground motion and extended in various ways by various researchers. Among them, I selected the method proposed by Dan and Sato (1998), because theirs can easily incorporate the variable-slip rupture model with the empirical Green's function method to simulate the broadband strong ground motion.

In this study, I used the data from the largest aftershock as the empirical Green's function. Note that the mainshock and aftershock have difference in the moment magnitude (or the seismic moment), the corner frequency, and the stress drop, as summarized in Table 1. Also, the rupture area of the aftershock was evaluated to be 2.2 km in radius whereas the equivalent radius of each subfault modeled here was about 1.7 km. The Dan and Sato's method can compensate such differences in frequency domain and provide the element wave from each subfault. Considering difference in timing and geometrical spreading between each subfault and the station, every element wave can be summed as the strong ground motion from the whole fault plane.

From a quick look at Figure 2c, the source spectrum ratio between the mainshock and the largest aftershock seemed to obey the scaling law based on the omega-square model [Brune (1970)]at a frequency higher than 0.3 Hz. Also, as mentioned in previous chapter, $f_{\max}$ is at least higher than 10 Hz, although it varies from event to event. In the following simulation, the data from the both mainshock and aftershock events was band-pass filtered between 0.3 and 1 Hz in waveform inversion and between 0.3 and 10 Hz in forward modeling.

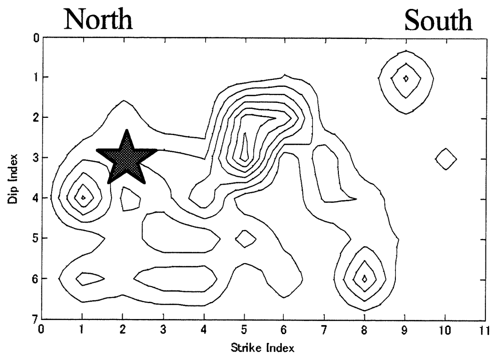

Figure 3 Relative moment release distribution on the fault plane for the mainshock. Contour lines are plotted with an unit step corresponding to the seismic moment of the largest aftershock (Event 7). A solid star inserted represents a rupture starting point (the mainshock hypocenter)

4.3 Results

Firstly, prior to the waveform simulation. I carried out waveform inversion to derive the rupture model using the element wave from each subfault as the empirical Green's function. The acceleration data was twice integrated into displacement with a bandpass-filter ranging from 0.3 to 1Hz. Simple inversion allowing each subfault to rupture once was carried out using the nonnegative least square method by Lawson and Hansen (1974). In Figure 3, the relative moment release on the fault plane is shown. This result means relative strength against the largest aftershock. On the basis that the Event 7 is an earthquake of M_W5.2, the mainshock can be evaluated to be M_W6.5. Note that the relative moment release distribution in Fugure 3 is similar with the result from more detailed analysis [Figure 7 in Kakehi (2004)].

Next, using the relative moment release model in Figure. 3, the strong ground motion for the mainshock was synthesized in a frequency range from 0.3 to 10 Hz. Waveforms for selected stations are shown in Figure 4 as examples. Also, in Figure 5, the maximum amplitudes for the mainshock are compared between the synthesis and data in acceleration (a), velocity (b), and displacement (c). On the whole, waveform matching between synthesis and observed data is satisfactory. The maximum amplitudes of observed horizontal components from 10 stations were in a range of 24 to 123 gal in acceleration and 1.6 to 8.5 kine in velocity. Present simulation reproduced most of the observed maximum amplitudes within a factor of 2.0. At two stations, HRSH01 and HRSH07, the simulation underestimated the observed data in most of the components. It may be partially attributed to isolated later phases appearing in the observed waveforms at these stations. Similar result was found in Sekiguchi and Iwata (2001). They suggested that the more complex rupture history was required for the simulation of the stations located in the northern direction from the rupture area.

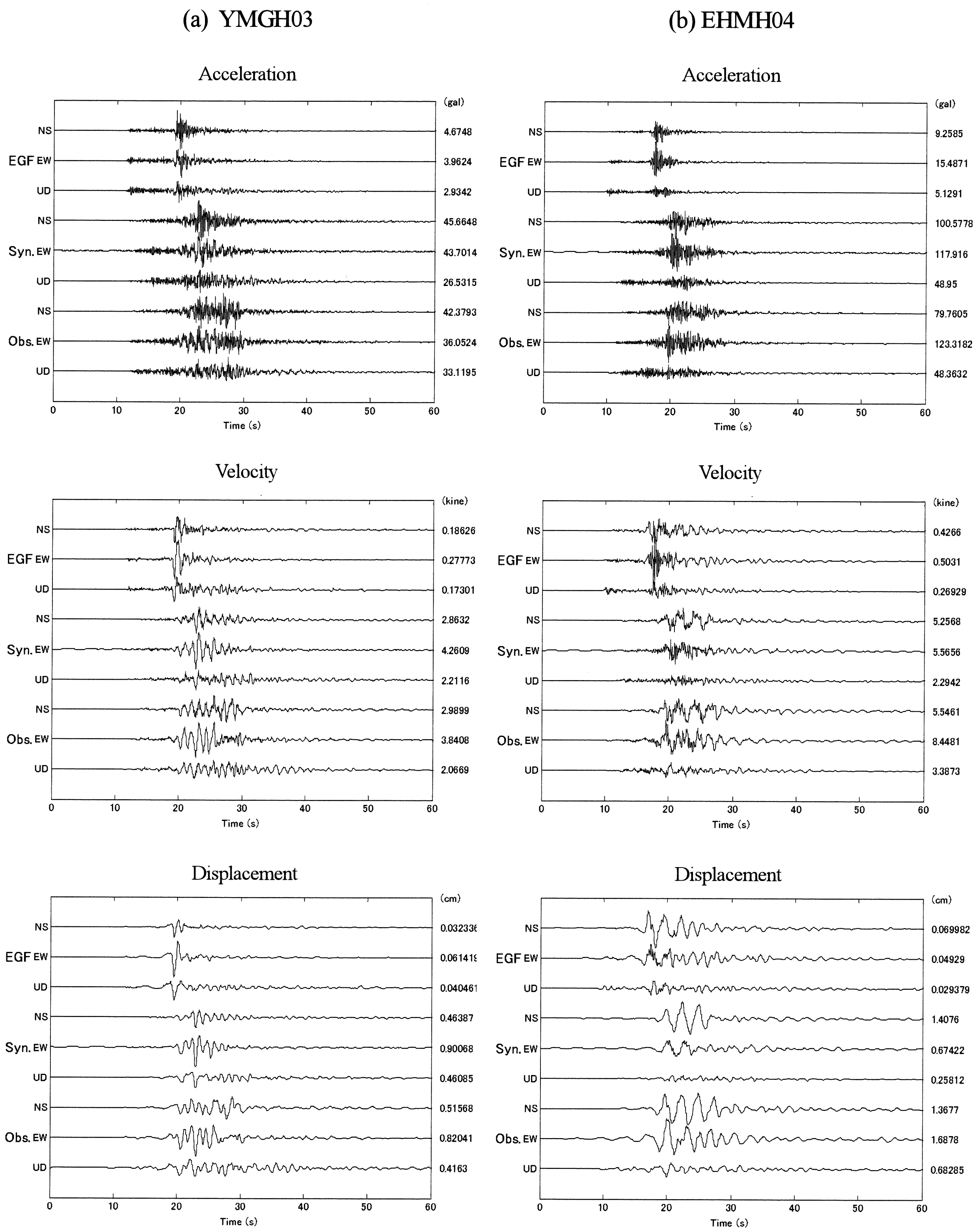

Figure 4 Comparison of synthesized waveforms and observed data. As example results, acceleration, velocity, and displacement waveforms are plotted for YMGH03 (a) and EHMH04 (b). In each diagram, nine traces are drawn: top three traces are the observed data for the Event 7 (EGF), middle three are the synthesized ones (Syn.), and others are the observed data for the mainshock (Obs.). Every three traces are aligned in the order of NS-, EW-, and UD-components. Numerals at the end of traces are absolute maximum amplitudes.

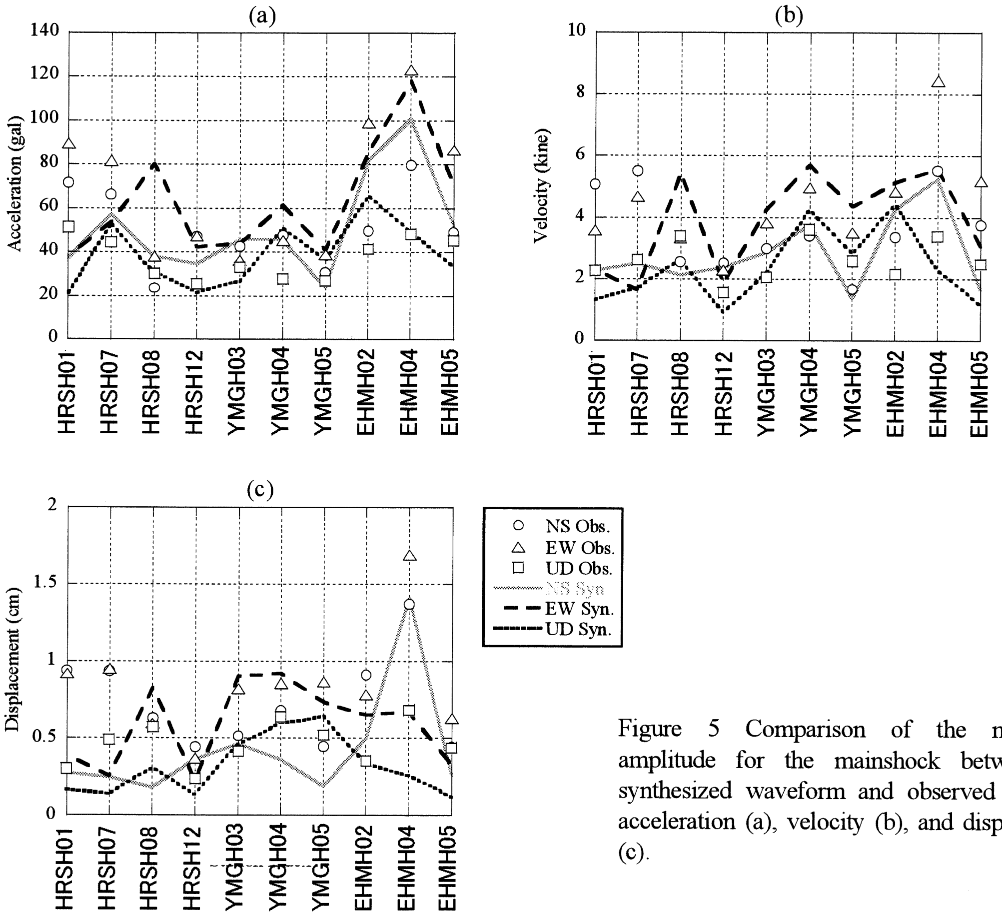

Figure 5 Comparison of the maximum amplitude for the mainshock between the synthesized waveform and observed data for acceleration (a), velocity (b), and displacement (c).

5. CONCLUSIONS

The source parameters of the 2001 Geiyo earthquake (M_J6.7) was estimated by the spectrum inversion using the KiK-net borehole data. The moment magnitude, the corner frequency, and the stress drop were estimated to be 6.3, 0.5 Hz, and 377 bar for the maishock, and 5.2, 0.8 Hz, and 32 bar for the largest aftershock. Next, based on the obtained source parameters, the empirical Green's function method was applied to simulate the strong ground motion for the mainshock. Element waves evaluated from the largest aftershock data were used for the waveform inversion and the strong motion simulation. Comparison of synthesized waveforms and observed data shows a good agreement.

Acknowledgements:

In this study, I used the strong motion data of the KiK-net and the source parameter information of the F-net, operated by the National Research Institute for Earth Science and Disaster Prevention. My sincere gratitude is given to whom it may concern.

References:

Brune, J. N. (1970), "Tectonic Stress and the Spectra of Seismic Shear Waves from Earthquakes", J. Geophys. Res, **81**, 4997-5009.

Cabinet Office, Government of Japan (2001), http://www.buosai.go.jp/kinkyu/akinada/akinada0919.pdf.

Dan, K. and Sato,T. (1998), "Strong-Motion Prediction by Semi-Empirical Method based on Variable-Slip Rupture Model of Earthquake Fault", J. Struct. Constr. Eng., Architecture Insitute of Japan, **509**, 49-60.

F-net (Broadband Seismograph Network) operated by National Research Institute for Earth Science and Disaster Prevention, http://www.fnet.bosai.go.jp/freesia/index.html.

Hartzell, S. H., (1978), "Earthquake aftershocks as Green's functions", Geophys. Res. Lett., **5**, 1-4.

Iwata, T. and Irikura, K. (1986), "Sparation of Source, Propagation and Site Effects from Observed S-waves", Zisin 2, **39**, 579-593.

Kakehi, Y. (2004), "Analysis of the 2001 Geiyo, Japan, Earthquake using High-density Strong Motion Data: Detailed Rupture Process of a Slab Earthquake in a Medium with a Large Velocity Contrast", Journal of Geophysical Research, **109**, B08306, doi:10.1029/2004JB002980.

Kanno, T., and Miura, K. (2005), "Evaluation of Site Effects during the 2001 Geiyo Earthquake in Hiroshima Prefectrure", J. Struct. Constr. Eng., Architecture Insitute of Japan, **597**, 151-157.

KiK-net (Digital Strong-Motion Seismograph Network) operated by National Research Institute for Earth Science and Disaster Prevention, http://www.kik.bosai.go.jp/kik/.

Kikuchi, M. and Yamanaka, K. (2001), http://wwweic.eri.u-tokyo.ac.jp/EIC/EIC_News/010324.html.

Koketsu, K. and Furumura, T. (2002), "The Distribution of Strong Motion from the 2001 Geiyo Earthquake and the Deep Underground Structure", Zisin 2, **55**, 97-105.

Lawson, C. L. and Hanson, D. J. (1974), "Solving least squares problems", Prentice-Hall Inc., Englewood Cliffs, New Jersey, 337 pp.

Nozu,A. (2001), http://www.pari.go.jp/information/news/h13d/jisin/geiyo/geiyo2/geiyo2.htm.

Sekiguchi, H. and Iwata, T. (2001), http://sms.dpri.kyoto-u.ac.jp/iwata/zisin/geiyo-e/html.

Fifth International Conference on Urban Earthquake Engineering
March 4-5, 2008, Tokyo Institute of Technology, Tokyo, Japan

AN ESTIMATION OF STRONG MOTIONS IN THE DAMAGED AREAS FOR THE NOTO HANTO EARTHQUAKE IN 2007 USING GROUND MOTION DATA FROM AFTERSHOCK OBSERVATIONS

Kentaro Motoki[1), Hiroaki Yamanaka[2)] and Kazuoh Seo[3)]

1) Assistant Professor, Dept. of Built Environment, Tokyo Institute of Technology, Japan
2) Associate Professor, Dept. of Environmental Science and Technology, Tokyo Institute of Technology, Japan
3) Professor, Dept. of Built Environment, Tokyo Institute of Technology, Japan
kmoto@enveng.titech.ac.jp, yamanaka@depe.titech.ac.jp, seo@enveng.titech.ac.jp

Abstract: The strong motion data on Monzen-machi Town, where is the one of the most severely damaged area, could not be obtained during the Noto Hanto Earthquake in 2007. This area is located near the Hakka-gawa River and the surface geology can be considered. We performed the aftershock observation densely, in order to evluate the site effect experimentally. We found that the site effect on damaged area was recognized higher than that on the non-damaged area and the effects were successfully evaluated quantitatively. In this paper, we estimated the strong motions during the main shock using aftershock motions. The source model for this estimation was calculated with empirical Green's function technique and GA using the data of the aftershock and the main shock provided by K-NET. The estimated motions are significantly high in the short period range, because the non-linear effect was not be considered in this estimation.

1. INTRODUCTION

The Noto Hanto Earthquake in 2007 with an M_{JMA} of 6.8 caused disastrous damage in buildings and civil engineering structures. For example, more than 684 of wooden houses were completely collapsed (Fire and Disaster Management Agency, 2007). Most of the damage was observed in Wajima City and especially the damage on Monzen-machi Town was severed. The seismic intensity at the Monzen Branch Office is 6.4 in the JMA scale, the highest for this earthquake. But strong motions could not be obtained in this area. Some part of surface geology in this area can be classified as soft soil because the Hakka-gawa River flow the through this area. It can be considered that the site amplification expand the damage area. Arai et. al. (2008) said that the site amplification can explain the damage distribution. We performed the aftershock observation densely, in order to evaluate the site effect experimentally. We found that the site effect of damaged area was recognized higher than that on the non-damaged area.

Irikura (1986) said that the strong mtions for the main shock can be synthesized using aftershock motions as empirical Green's function. The strong motions on the damaged area of the 1995 Kobe earthquake were sucessfully reproduced using aftershock motions (Kamae and Irikura, 1997).

In this study, we estimated the strong motions for the main shock of the Noto Hanto Earthquake in 2007 using the ground motion data of the aftershocks.

2. AFTERSHOCK OBSERVATION

Figure 1 shows the staion of the aftershock observation and the epicenters using as the element earthquake. Table 1 shows the specification of these events including the main shock. These information was evaluated by F-net. The event A is the largest event in the appropriate earthquakes which occured near the expected source region of the main shock. The event B occured before the installation and the data could not be obtained. Nevertheless the data of this event are also used for this estimation and to make an inversion to the source model, which will be mentioned below.

Each station was installed in Monzen area and across the Hakka-gawa River and the distances from the other are a couple of hundred meters. Figure 2 shows the velocity waveforms bandpass filtered between 0.5 - 20Hz of the event A. We could not record the earthquake motions of this event at some stations The predominant periods are evaluated between 0.3 and 1.0 second. The amplitudes at the alluvial sites, where are the L02, L03, L05, L06 and L07, are higher than the hilly sites, where are the L01 and L04, and the later phases at the alluvial sites observed for long duration. This difference of the waveforms implies

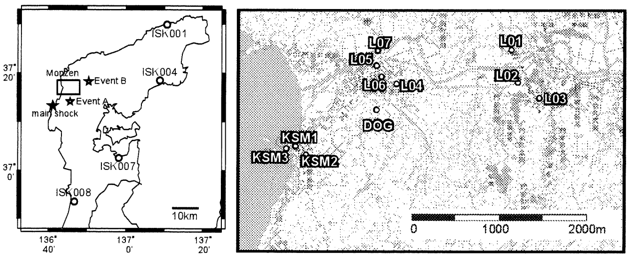

Figure 1 Distribution of Strong Motion Station and Epicenters of the main shock and aftershocks(left), Location of the Aftershock Observation(right)

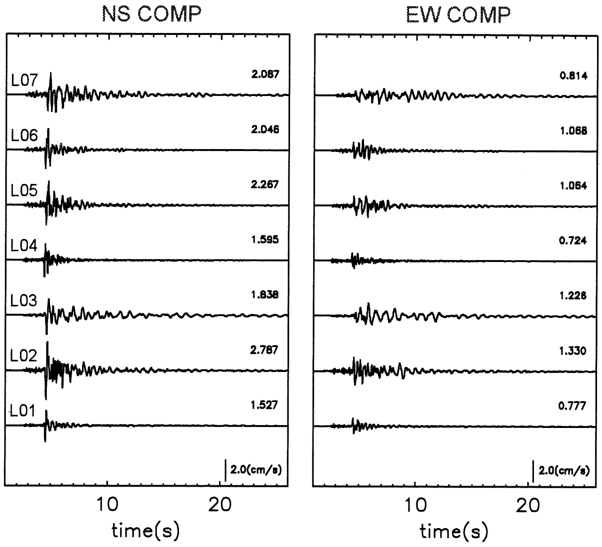

Figure 2 Velocity Waveforms obtained in Monzen Area of Event A

Table 1 List of the earthquakes Studied and Source Scaling Parameters

Event	Date	Depth(km)	Mw(M0[Nm])	C	N
A	2007/3/31 8:09	13.5	3.8 (5.83E+14)	0.89	5
B	2007/3/25 18:11	13.4	5.2 (6.22E+16)		
main shock	2007/3/25 9:42	10.7	6.7 (1.36E+19)	0.9	6

the difference of the effects of the surface geology. The damage near the site whose predominant period is long is severe.

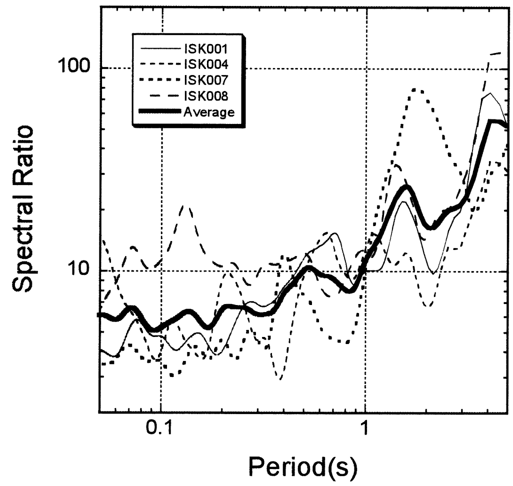

Figure 3 Spectral Ratios of the main shock to the event B.

3. INVERSION FOR SOURCE MODEL

The source model is necessary to estimate the strong motions of the main shock near the source region with the aftershock motions. We used the data of the main shock and aftershocks distributed by the K-NET to make an inversion for the source model. The stations we used for the inversion is shown in Figure 1 and are about 50 km distant from the source region. The data were resampled at 50Hz. The aftershock motions are used as the empirical Green's function and we adopted the filter function which multiplies in synthesization proposed by Irikura *et. al.* (1997). For this technique, the scaling parameters C and N is estimated from the constant levels of accelaration and displacement amplitude spectra of the events with the following the equation

$$N=\left(\frac{U_0}{u_0}\right)^{0.5}\left(\frac{a_0}{A_0}\right)^{0.5} \qquad C=\left(\frac{u_0}{U_0}\right)^{0.5}\left(\frac{A_0}{a_0}\right)^{1.5}$$

Where, U_0 and u_0 show the constant levels of the amplitude of the displacement spectra for the large and small events, respectively. A_0 and a_0 indicate the constant levels of the acceleration spectra. Namely, U_0/u_0 and A_0/a_0 mean the constant level of the spectral ratio in the longer period range and the shorter period range, respectively. Figure 3 shows the spectral ratio of the main shock to the event B. The thick line indicate the average of the spectra. In the shorter period range, the flat level can be easily detect but in the longer period range, it is difficult to find it. The seismic moment evaluated by F-net is used for the displacement flat level which means flat level in spectral ratio in the longer period range. The evaluated scaling factor is listed on Table 1. It is difficult to the synthetic

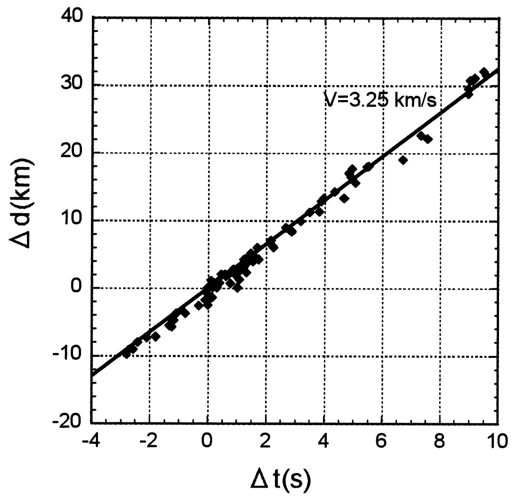

Figure 4 S-wave arrival time and hypocentral distance

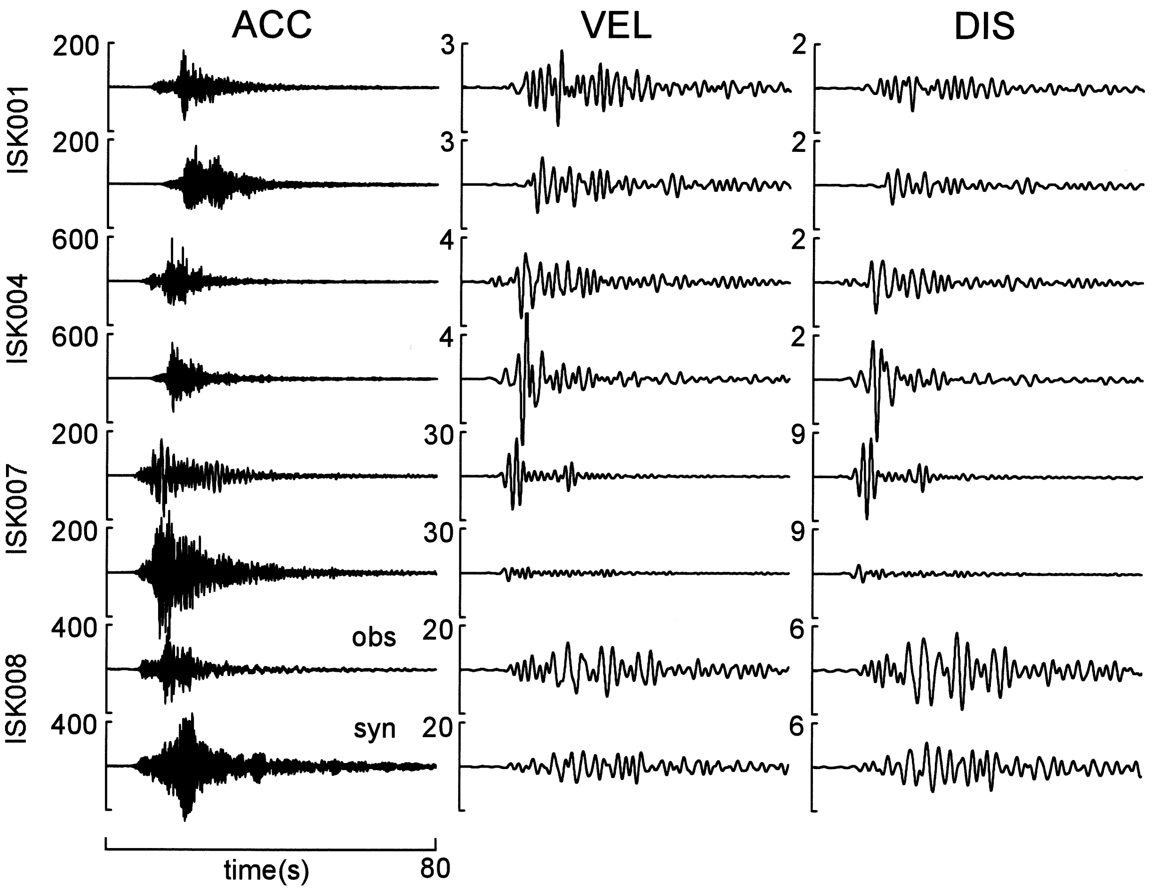

Figure 5 Comparison between waveforms synthesized from event B and observed waveforms of the main shock

the earthquake motions of the main shock from that of the event A, because the difference of the magnitude is large. Therefore, 2 steps are required to estimate the main shock from the event A through the event B.

Since the location of the hypocenter is different from each other, the travel time from the hypocenter is also different. Therefore the time shifting is needed to move the hypocenter. The S-wave arrival time of the aftershocks was picked up to evaluate the apparent velocity to calculate time shifting. Figure 4 shows the relation of the time difference and distance. We evaluate as 3.25 km/s the apparent velocity.

We used Genetic Algorithm (GA) to invert the location of the strong motion generation area (SMGA) proposed by Miyake *et. al.* (2003). In this inversion, unknown parameters representing the location, the trigger point, the size and the rise time were estimated to minimize the residuals of the velocity waveforms filtered 0.2 - 5.0Hz and the acceleration envelop. To take the heterogeniety of the source which cannot be express into account, we tried to invert with 2 SMGAs. To conserve the scaling law, the different scaling factor is required to set, but only the release energy of SMGA is changed in this paper.

Figure 5 shows comparison of waveforms between synthetic and observed for the main shock. These synthetic waveforms seem to give a good fit to observed in accelerations, velocities and displaecements except for velocity and displacement at ISK007. The synthetic waveforms of the event B estimated with those of the event A is also good fitting. The inverted SMGA area is consistent with the source model reported by the previous research (Aoi and Sekiguchi, 2007)

4. ESTIMATION OF GROUND MOTION ON DAMAGED AREA

The sources model derived in the previous section are userd for the estimation of the strong motion in Monzen area. The waveforms of the main shock were calculated with the waveforms of the event B synthesized with the observed waveforms of the event A. The estimated velocity waveforms are shown in Figure 6. The amplitudes of strong motions at some points are estimated larger than 200 cm/s and the amplitude at the L03 site is the highest. Figure 7 shows the pseudo velocity response spectra with 5% damping of these synthetic motions. The response is reached to 1000 cm/s and the predominant period can be evaluated to 0.8 second quite similar to those of aftershock motions. The spectral shape is similar to that at the Ojiya station for the Mid Niigata earthquake. The estimated motions are larger in the short period range. From this result, it is easy to understand that the damage in this area was quite severe because the responses are comparable to that at the Ojiya station.

This result is not considered the non-linear effect of the subsurface soil because the amplitudes of the data we used are significantly low comparing to the estimated motions. Therefore, the estimated amplitudes can be considered to be overestimated and the predominant period to be shorter. Nevertheless this result will be a material for the precise estimation taking into account the plastic behavior and the soil information.

5. CONCLUSIONS

We estimated the strong motion of the main shock around the damaged area during the Noto Hanto Earthquake. The responses of these motions are comparable to that during the Kobe earthquake. In the near future, we will evaluate the spatial distribution of the main shock with the microtremors we measured and the non-linear effect with the soil condition.

Ackknowledgements:

We thank the K-NET and F-net of the National Research Institute of Earth Science and Disaster Prevention for providing the strong motion data and the seismic information.

References:

Irikura, K., (1986) "Prediction of Strong Acceleration Motions Using Empirical Green's Function," *Proceedings of the 7th Japan Earthquake Engineering Symposium*, 151-156

Irikura, K., Kagawa, T. and Sekiguchi, H. (1997) "Revision of the empirical Green's function method by Irikura (1986)," Program and Abstracts of the Seismological Society of Japan, **2**, B25

Arai, H., *et. al.* (2008), "Peak Ground Velocity and Cause of Damage to Wooden Houses Estimated in Near-Source Area During the 2007 Noto Hanto Earthquake," *Jounal of Structural and Constraction Engineering*, Architectural Institute of Japan, **624**, 227-234

Motoki K. *et. al.* (2008), "Aftershock Observation and Microtremor Measurements in Monzen Town, the severely damaged area during the Noto Hanto Earthquake in 2007," *Summaries of Technical Papers of Annual Meeting*, Architectural Institute of Japan, B-2, 175-176

Fire and Disaster Management Agency (2008), "The 48th Report of the Noto Hanto Earthquake in 2007," http://www.fdma.go.jp/data/010711281355102977.pdf

Miyake, H., Iwata, T. and Irikura, K. (2003), "Source Characterization ofr Broadband Ground-Motion Simulation: Kinematic Heterogeneous Source Model and Strong Ground Motion Area," *Bulletin of the Seismological Society of America*, **93**(6), 2531-2545

Kamae, K. and Irikura, K. (1997), "A Fault Model of the 1995 Hyogo-ken Nanbu Earthquake and Simulation of Strong Ground Motion in Near-Source Area," *Jounal of Structural and Constraction Engineering*, Architectural Institute of Japan, **500**, 29-36

Aoi, S. and Sekiguchi, H. (2007), "The Source Inversion of the Noto Hanto Earthquake Using Near-Field Motions,", http://wwwold.k-net.bosai.go.jp/k-net/topics/noto070325/

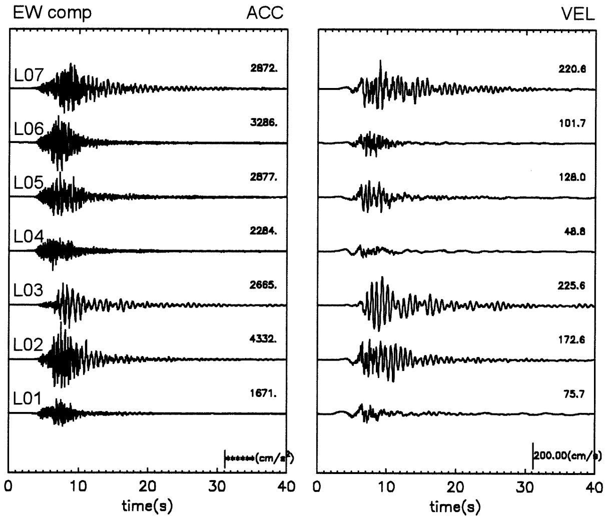

Figure 6 Synthetic Waveforms in Monzen area

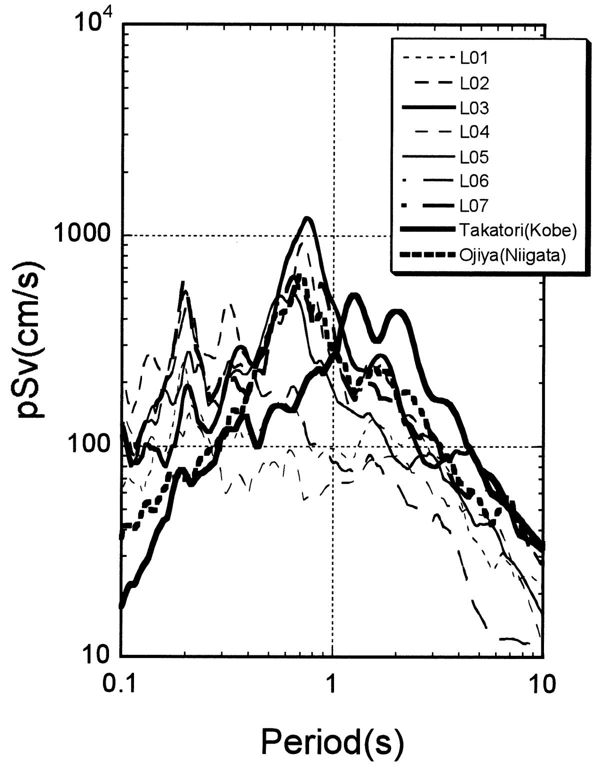

Figure 7 Pseudo Velocity Response Spectra

Fifth International Conference on Urban Earthquake Engineering
March 4-5, 2008, Tokyo Institute of Technology, Tokyo, Japan

A STUDY ON EVALUATION OF THE PHASE SPECTRA FROM SMALL EARTHQUAKE RECORDS

K. Shirai[1) and T. Ohmachi[2)

1) Research Fellowship of the Japan Society for the Japan for the Promotion of Science for Young Scientists, Graduate Student, Department of Built Environment, Tokyo Institute of Technology, Japan
2) Professor, Department of Built Environment, Tokyo Institute of Technology, Japan
kshirai@enveng.titech.ac.jp, ohmachi@enveng.titech.ac.jp

Abstract: Inversion technique is often used to evaluate stress drop of source mechanism, Q value of path characteristics and so on. It is well known that Fourier amplitude spectra have clear information such as source intensity, path attenuation and site amplification, in contrast with Fourier phase spectra (phase spectra). In this paper, inversion technique is applied to phase spectra of the small earthquake motions to decompose them into source and path characteristics. As a result, it is found that phase spectra are obtained as a frequency-dependent and non-linear function with respect to frequency.

1. INTRODUCTION

To design input earthquake ground motions, response spectra are often used in frequency domain. When time histories are needed, we must set both Fourier amplitude and phase spectra. Many studies have made it clear what Fourier amplitude spectra of earthquake records inform, and how they are theoretically formulated. However, as for Fourier phase spectra, those of the past records, for example the 1940 EL Centro, the 1952 Taft, the 1968 Hachinohe and so on, have been used because we do not know well about phase characteristics in general.

In signal analyses (e.g. Papoulis 1962, Papoulis 1977, Oppenheim and Schafer 1989), it is known that causal time functions such as earthquake records are decomposed into minimum phase shift and all pass functions. Regarding the minimum phase shift functions, their Fourier phase and amplitude are related to each other. Meanwhile, the all pass functions have Fourier phase only and their group delay time roughly indicates arrival time of the signal.

Izumi et al. (1990) applied the theory to earthquake records and pointed out that a minimum phase shift function is a transfer function of the ground and an all pass function includes information of travel time of direct S-wave from source to station. Sato et al. (1999) formulated characteristics of source, pass and ground by means of the group delay time of the minimum phase shift function. Sato (2005) used the all pass function as a receiver function to estimate P-SP time. These studies showed that an all pass function seems to be linear and a group delay time expresses arrival time of a direct S-wave from a source. However, the all pass function calculated from the earthquake records usually shows non linearity (Shirai and Ohmachi 2005) because the all pass function may include arrival times of not only direct S-wave but also direct P-wave, reflected and refracted body waves and surface waves. If an all pass function is theoretically formulated, Fourier phase spectra will be modeled because Fourier phase spectra of the minimum phase shift are determined from its Fourier phase in terms of Hilbert Transforms (Papoulis 1962, Papoulis 1977).

This paper describes a fundamental modeling of phase spectra of earthquake motion observed on firm ground by means of inversion technique and regression analysis.

2. CHARACTERISTICS OF MINIMUM PHASE SHIFT AND ALL PASS FUNCTIONS

2.1 De-convolution of a Causal Time Function

A time function is called to be causal if it equals zero for negative time:

$$x(t) = 0 \qquad for \qquad t < 0 \quad (1)$$

A causal time function can be decomposed into two functions. One is a minimum phase shift function and the other is an all pass function. A causal time function $x(t)$ is written by convolution of minimum phase shift $x_M(t)$ and all pass $x_A(t)$, as shown in Eq.(2)

$$x(t) = x_M(t) * x_A(t) \qquad (2)$$

where the subscripts M and A denote minimum phase shift function and all pass function, respectively. The decomposition is often introduced as factorization of a causal time function in signal analysis (Papoulis 1977). $x_M(t)$ and $x_A(t)$ satisfy the following.

$$x_M(t) = 0 \qquad for \qquad t < 0 \tag{3}$$
$$x_A(t) = 0 \qquad for \qquad t < 0 \tag{4}$$

In the meantime, Fourier transform $F(\omega)$ is defined by

$$x(t) \Leftrightarrow F(\omega) = |F(\omega)| e^{i\phi(\omega)} \tag{5}$$

where ω is angular frequency, the absolute $|F(\omega)|$ Fourier amplitude and $\phi(\omega)$ its phase.

When the Fourier transform is applied to Eq.(2), Eq.(6) is obtained.

$$F(\omega) = F_M(\omega) F_A(\omega) \tag{6}$$

Both minimum phase shift and all pass functions have the Fourier amplitude and phase as

$$F_M(\omega) = |F_M(\omega)| e^{i\phi_M(\omega)} \tag{7}$$

$$F_A(\omega) = |F_A(\omega)| e^{i\phi_A(\omega)} \tag{8}$$

Here, the Fourier amplitude of all pass function is unity:

$$|F_A(\omega)| = 1 \tag{9}$$

The Fourier transform $F(\omega)$ of $x(t)$ can be written in terms of minimum phase shift and all pass functions as,

$$F(\omega) = |F_M(\omega)| e^{i(\phi_M(\omega) + \phi_A(\omega))} \tag{10}$$

Therefore the Fourier amplitude $|F(\omega)|$ is equal to $|F_M(\omega)|$ and the Fourier phase of $x(t)$ is the sum of minimum phase shift and all pass phases.

$$|F(\omega)| = |F_M(\omega)| \tag{11}$$

$$\phi(\omega) = \phi_M(\omega) + \phi_A(\omega) \tag{12}$$

The Fourier amplitude and phase of minimum phase shift satisfy the following equations:

$$\phi_M(\omega) = \frac{1}{\pi} \int_{-\infty}^{\infty} \frac{\log|F_M(y)|}{\omega - y} dy \tag{13}$$

$$\log|F_M(\omega)| = -\frac{1}{\pi} \int_{-\infty}^{\infty} \frac{\phi_M(y)}{\omega - y} dy \tag{14}$$

Eq.(13) and Eq.(14) are known as the Hilbert transforms. Methods to calculate minimum phase shift and all pass functions are found elsewhere (e.g. Izumi et al 1988, Katsukura et al. 1989).

2.1 KiK-net Data Sets Used in this Study

Earthquake data are opened on internet supported by NIED, Japan. We have chosen small motions in Niigata-ken Chuetsu area recorded at three stations (Muika, Tadami and Hinoemata), because small earthquake events were simple and effective for characterization of site, path and source effects. In Figure 1 and Table 1, a location map of seismic events and stations is shown. Every station is located 25～45km distant from the epicenters.

3. RESULT OF INVERSION OF PHASE SPECTRA

Table 1 Detailed information of two events and three stations.

	KiK-net MUKA (Vs 1.5km/sec) Epicenter (km)	KiK-net TADAMI (Vs 1.6km/sec) Epicenter (km)	K-net HINOEMAT (Vs 2.6km/sec) Epicenter (km)
Event 1 2004/10/29, M3.2, Depth11km	27km	30km	40km
Event 2 2005/1/26, M3.0, Depth9km	25km	31km	46km

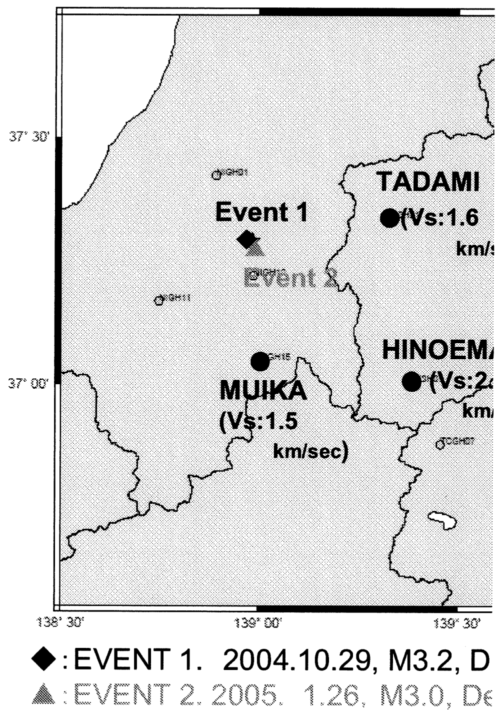

Figure 1 Map of epicenters in events and locations of stations.

3.1 Preparations of Inversion of Phase Spectra

In this study, we try an inversion of phase spectra of small earthquake motions, using the Morre-Penrose's inversion formula applied to phase spectra of source and path characteristics. Three stations are located on the firm ground where we can neglect site amplification.

The phase spectra recorded at three stations, Tadami, Muika and Hinoemata, are denoted as $\phi^{Tadami\ 1or2}(f)$, $\phi^{Muika\ 1\ or\ 2}(f)$ and $\phi^{Hinoemata\ 1\ or\ 2}(f)$, where f means frequency. Subscripts express station name, and event number 1 or 2.

The station phase spectra are made up of phase spectra at two source phase spectra $\phi^{Source\ 1}(f)$ or $\phi^{Source\ 2}(f)$, and phase spectra of path characteristics from source to each site, $\phi^{path\ Tadami}(f)$, $\phi^{Path2\ Muika}(f)$ and $\phi^{Path3\ Hinoemata}(f)$.

Thus, the station spectra are expressed as,

$$\begin{pmatrix} \phi^{Tadami1} \\ \phi^{Muika1} \\ \phi^{Hinoemata1} \\ \phi^{Tadami2} \\ \phi^{Muika2} \\ \phi^{Hinoemata2} \end{pmatrix} = \begin{pmatrix} 1 & 0 & 1 & 0 & 0 \\ 1 & 0 & 0 & 1 & 0 \\ 1 & 0 & 0 & 0 & 1 \\ 0 & 1 & 1 & 0 & 0 \\ 0 & 1 & 0 & 1 & 0 \\ 0 & 1 & 0 & 0 & 1 \end{pmatrix} \cdot \begin{pmatrix} \phi^{Source1} \\ \phi^{Source2} \\ \phi^{Path\ Tadami} \\ \phi^{Path\ Muika} \\ \phi^{Path\ Hinoemata} \end{pmatrix} \quad (15)$$

In Eq. (15), the left side vector is known because every parameter is observed. Meanwhile, right side vector is un-known. Solving Eq. (15) by using he Morre-Penrose's inversion formula, we can obtain the un-known phases on the right hand side of Eq. (15).

3.2 Regression of the Estimated Phase Spectra

Figure 2 shows results of the inversion regression. The un-known phases are shown by solid lines and their regression curves by dotted lines, respectively.

Time histories have been calculated by using regressed phase spectra shown in Figure 2 and recorded minimum phase shift functions which are given from Fourier amplitude spectra of the original records. The simulated and original time histories observed at three stations in two small earthquakes are compared in Figure 3 (a) and (b).

In Figure 3, simulated time histories are similar to the observations except for P wave motions. But, as for S wave motions, waveforms are simulated well, indicating good regression of the phase spectra.

4. CONCLUSIONS

Based on the theory of the factorization and causality widely used in signal analyses, this study has focused on phase spectra inversion of observed small earthquake motions, with findings like the followings:

1. Phase spectra of all pass functions of source and path characteristics are non-linear with respect to frequency.
2. Regressed phase spectra are expressed as, $\phi_A(\omega) = -c \cdot \omega^n$

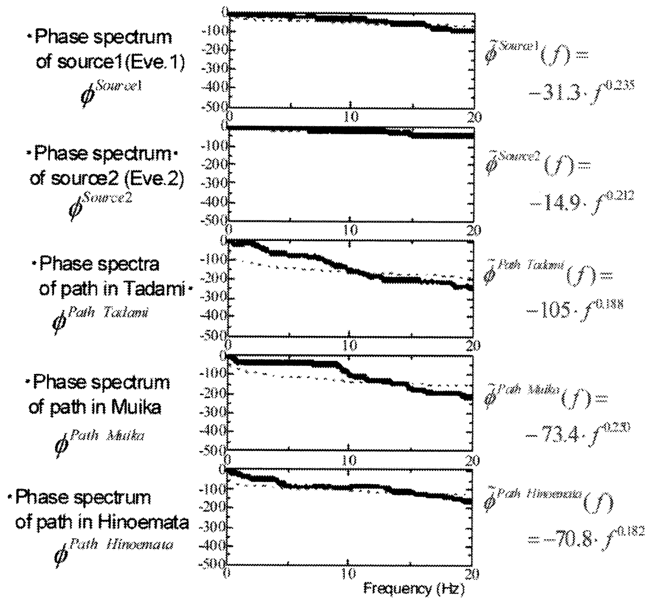

Figure 2 Inversed phase spectra, from upper side, 1st one is phase spectra of source1 in events1, 2nd of source2 in events2, middle shows phase spectra of path characteristic for Tadami, 4th phase spectra for Muika and the lowest for Hinoemata.

3. Using regression curves of phase spectra and recorded minimum phase shift functions, the time histories are well reproduced.

Acknowledgment:

This study was supported by the scholarship from Japan Society and Promotion Science, JAPAN. We had many useful comments and advises from Dr. M. OHORI, Yokohama Institute, JAMSTEC, JAPAN. We used data from KiK-net, NIED, JAPAN. We would like to appreciate all of them described above.

References:

Papoulis, A. (1962), "Fourier Integral and its Applications," McGraw-Hill.

Papoulis, A. (1977), "Signal Analysis," McGraw-Hill.

Oppenheim, A. V. and Schafer, R. W. (1981). "Discrete-Time Signal Processing," Prentice-Hall.

Izumi, M., Kurita, S., Endo, Y., Tobita, J. and Hanzawa, T. (1990), "Study on Causality of Transfer Functions and Components of Causal Transfer Functions in Systems of Seismic Wave Propagation in Soil", *Journal of Structural and Construction Engineering, Architectural Institute of Japan,* **412**, 31-41.

Sato. T., Murono. Y. and Nishimura. A. (1999). "Modeling of phase characteristics of strong earthquake motion," Japan Society of Civil Engineers, Journal of Structural and Earthquake Engineering, **612**/I-46, 201-213.

Sato, T. (2005), "Detection method of P-to-S converted Waves From Seismic Bedrock Using All-Pass function Deconvolved from Receiver Function," *Journal of Structural and Construction Engineering, Architectural Institute of Japan,* **592**, 67-74.

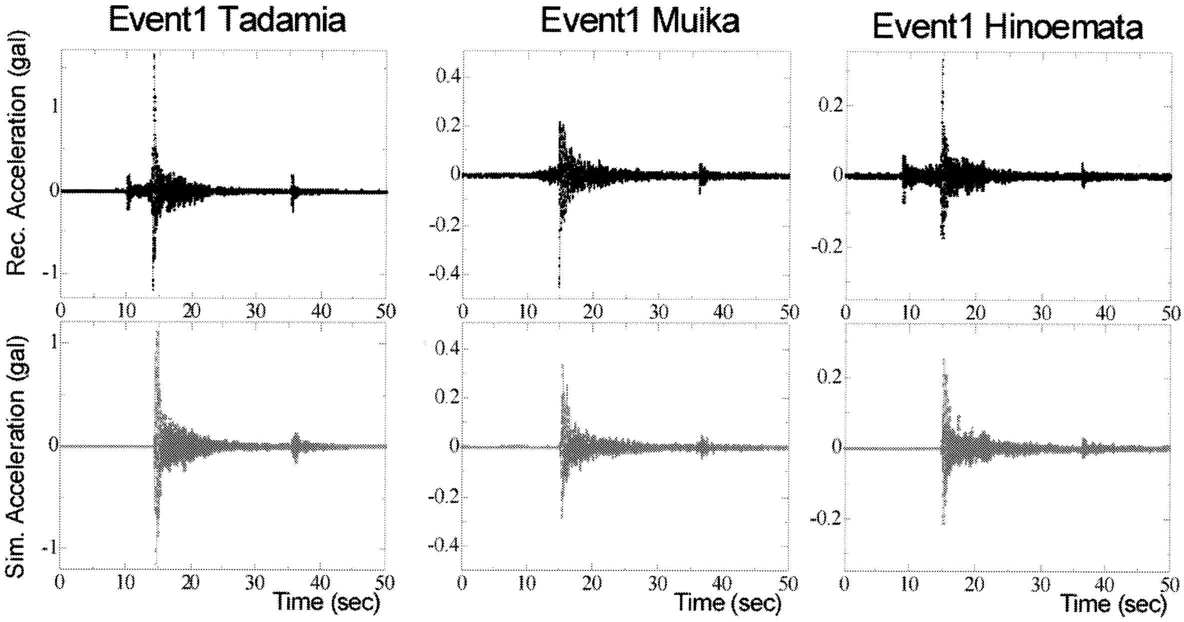

Figure 3(a) Recorded (Upper) and simulated (Lower) time histories at three stations in the event 1

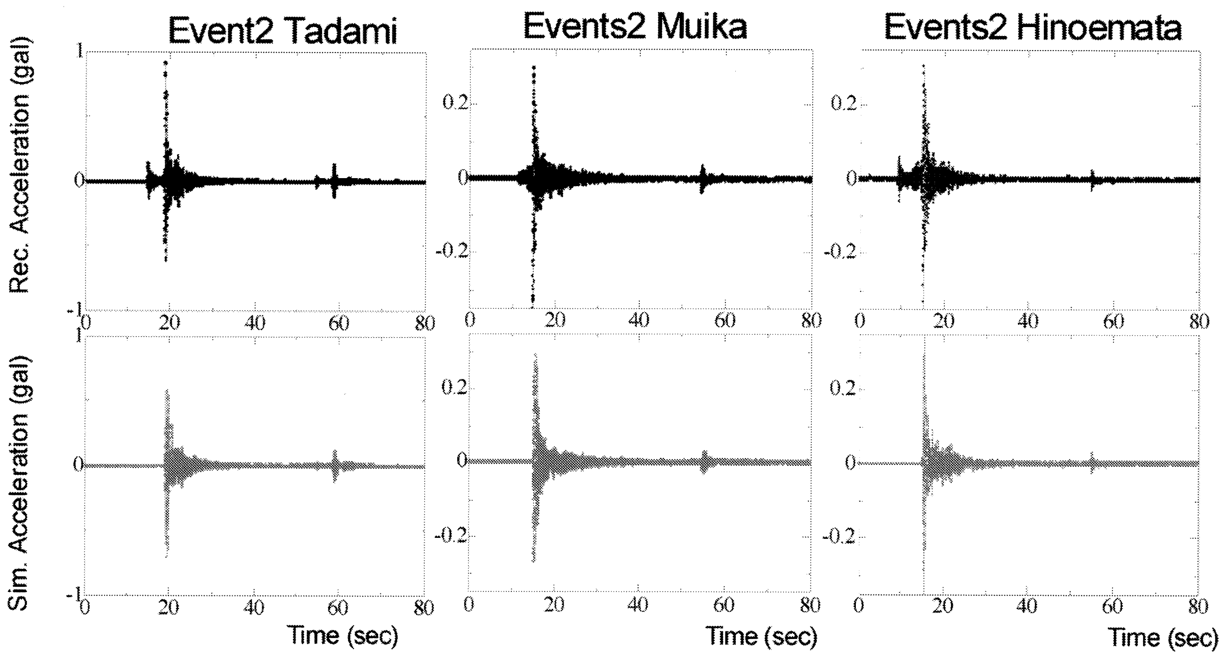

Figure 3(b) Recorded (Upper) and simulated (Lower) time histories at three stations in the event 2

Shirai, K. and Ohmachi, T. (2005), "Correlation Between Horizontal and Vertical Components of Near-Field Strong Motions", *Proceedings of the 2nd International Conference on Urban Earthquake Engineering, Center for Urban Earthquake Engineering, Tokyo Institute of Technology*, 295-300.

Izumi, M., Katsukura, H. and Ohno, S. (1988), " A Study on Deconvolution on Seismic Waves," *Journal of Structural and Construction Engineering, Architectural Institute of Japan*, **390**, pp27-33.

Katsukura, H., Ohno, S. and Izumi, M. (1989), "Symmetrical FFT Technique and Its Applications to Earthquake Engineering", *Earthquake Engineering and Structural Dynamics*, **18**, 717-725.

Fifth International Conference on Urban Earthquake Engineering
March 4-5, 2008, Tokyo Institute of Technology, Tokyo, Japan

CHARACTERISTICS OF HIGH RESOLUTION SATELLITE IMAGE AT DIFFERENT LAND USE UNITS FOR DETAILED GEOMORPHOLOGIC CLASSIFICATION MAPPING

Kazunori Ishii[1)], Saburoh Midorikawa[2)] and Hiroyuki Miura[3)]

1) Graduate Student, Department of Built Environment, Tokyo Institute of Technology, Japan
2) Professor, Department of Built Environment, Tokyo Institute of Technology, Japan
3) Assistant Professor, Department of Built Environment, Tokyo Institute of Technology, Japan
kazishii@enveng.titech.ac.jp, smidorik@enveng.titech.ac.jp, hmiura@enveng.titech.ac.jp

Abstract: As a preliminary study for detailed mapping of geomorphologic classification, the characteristics of high-resolution satellite image at different land use is examined to evaluate the effect of mixed pixel (mixel) to land use pattern. The QuickBird image whose spatial resolution is 0.7m is used. The mean value and its standard deviation of digital number and NDVI (Normalized difference vegetation index) of the image are computed from 10m-mesh for each land use unit. The heterogeneity degree is also calculated from the standard deviations of the meshes for the land use unit. The result shows that the mean values and the heterogeneity degrees are different for the different land use.

1. INTRODUCTION

In order to obtain ground shake map due to a scenario earthquake, distribution of site amplification factors is indispensable. The geomorphologic classification map whose mesh size is 1km has been used to compute the distribution of site amplification factors for the national seismic hazard map for Japan. The Central Disaster Prevention Council of Japan is encouraging detailed ground shake mapping with mesh size of 50m as an incentive to citizens' disaster mitigation actions such as seismic retrofit of their own houses.

The detailed mapping requires a high-resolution digital map of soil information such as geomorphologic classification. It is, however, a time and labor consuming task to create such a digital map from the existing analog maps. There would be some correlation between geomorphology and land use pattern. The land use pattern would be closely related with land cover information estimated from satellite images. Therefore, the characteristics of the satellite image (ASTER) as well as the digital elevation model were examined at different site geomorphology and the primary detailed mapping was conducted by using the simple classification rules based on the characteristics of the remote sensing data [Ishii *et al.*, 2007].

In the study, the digital numbers of the ASTER images whose mesh sizes are 15m or 30m are analyzed. Most of the meshes of such images are covered with multiple features because the scales of the features are usually larger than the mesh size. As shown in Fig. 1, a mixed pixel (mixel) is defined as a pixel which is covered with multiple features such as vegetation and building, while a pure pixel is defined as a pixel which is covered with a single feature [e.g., Kitamoto and Takagi, 1996].

Since there would be some correlation between the degree of the mixture and the land use pattern, it might be possible to improve the estimation accuracy of the land use by quantitatively evaluating the degree of the mixture for each land use unit using high-resolution satellite images, such as QuickBird images. Therefore, the examination of the relationship between the degree of the mixture and the land use pattern would sophisticate the detailed mapping of the geomorphologic classification. In this study, the relationship between the high-resolution satellite image and the land use pattern is examined by analyzing the characteristics of the digital numbers of the image and evaluating the effect of the mixels to the land use pattern.

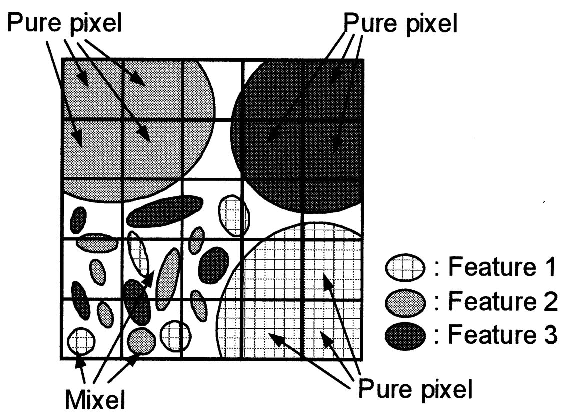

Figure 1 Schematic Diagram of Pure Pixel and Mixed Pixel (Mixel)

2. TARGET AREA AND DATA

Figure 2(a) shows the 50m-mesh geomorphologic classification map in Tsurumi ward, Yokohama, Japan. The northern part of Tsurumi ward is selected as the target area, extending 1.25km in NS direction by 2.5km in EW direction. In the area, various geomorphologic units are distributed such as terrace covered with volcanic ash soil, valley bottom lowland, natural levee, back marsh, abandoned river channel, delta and coastal lowland, marine sand and gravel bars, and river bed. The geomorphologic classification map in the area is shown Fig. 2(b).

Figure 2(c) shows the land use map in the area. The data was constructed in 2000 by Geographical Survey Institute (2007). The spatial resolution of the data is 10m. Totally 13 land use units are distributed in the area.

Figure 2(d) shows the QuickBird image used in this study. The image was observed in May 8, 2007. The spatial resolution of the image is 0.7m. The image consists of 4 bands. The band 1, 2 and 3 indicate blue, green and red band, respectively. The band 4 indicates near infrared band. To evaluate vegetation activity in a pixel, NDVI (Normalized difference of vegetation index) is computed from the image by the Eq. (1).

$$NDVI = \frac{DN_{NIR} - DN_{Red}}{DN_{NIR} + DN_{Red}} \tag{1}$$

Here, DN_{NIR} and DN_{Red} represent the digital number in the near infrared band and the red band image, respectively. NDVI is related to the amount of biomass within a pixel and yields a number from -1 to +1. A higher NDVI indicates a higher density of green leaves.

3. RELATIONSHIP BETWEEN GEOMORPHOLOGY AND LAND USE

In order to examine the relationship between the geomorphology and the land use, the number of meshes at

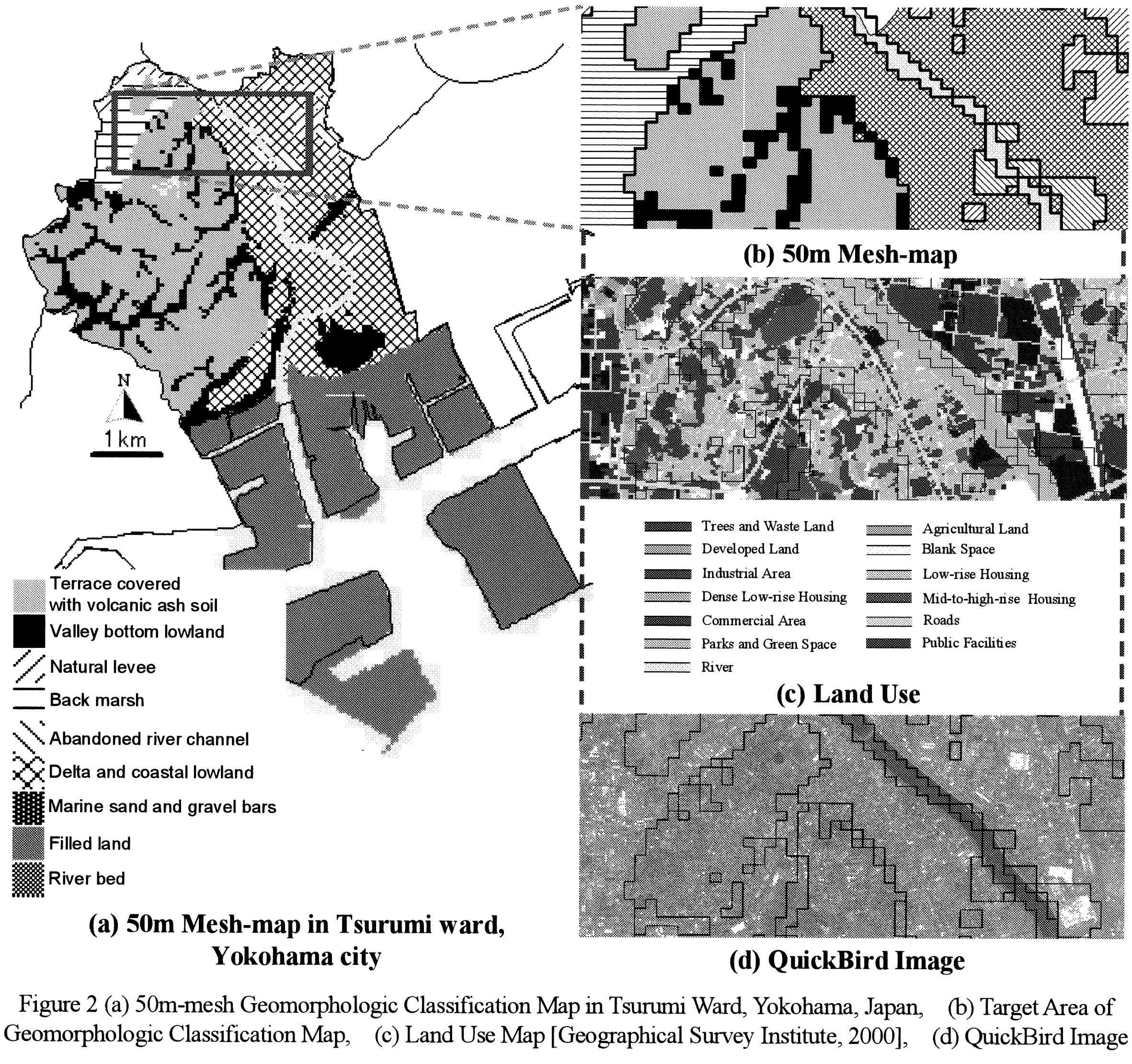

Figure 2 (a) 50m-mesh Geomorphologic Classification Map in Tsurumi Ward, Yokohama, Japan, (b) Target Area of Geomorphologic Classification Map, (c) Land Use Map [Geographical Survey Institute, 2000], (d) QuickBird Image

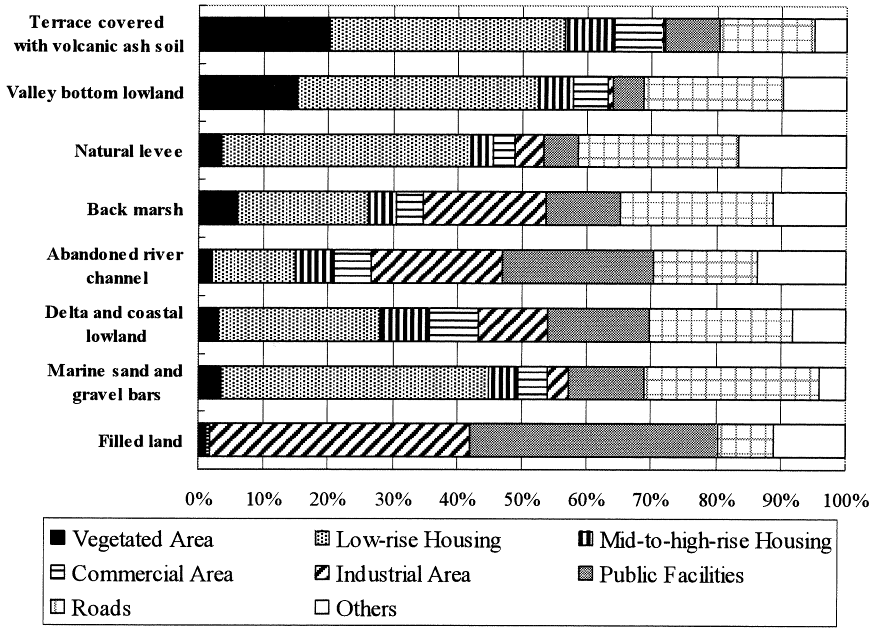

Figure 3 Area Proportions of Land Use for Each Geomorphology

each land use units is aggregated for each geomorphologic unit. Figure 3 shows the area proportions of the land uses for each geomorphologic unit. The vegetated area indicates trees/wasteland, parks/green space and agricultural area.

In the terrace area such as the terrace covered with volcanic as soil and the valley bottom lowland, the residential areas such as the low-rise housing and the mid-to-high-rise housing accounts for about 40% and the vegetated area accounts for 15-20%. The vegetated areas are mainly distributed in the boundary between the terrace and the lowland. Since the terrain of the boundary is steep slope and it is difficult to develop built-up area to the slope, the vegetations such as trees are remained in the boundary.

In the lowland area such as the natural levee, abandoned river channel and the delta and coastal land, the area proportion of the vegetated areas is less than 5% because the built-up areas is mainly developed in the lowlands. In the natural levee, the area proportion of the low-rise housing is about 40%. It suggests that the low-rise buildings are densely distributed in the area. In the back marsh and the abandoned river channel, the area proportions of the commercial and the public facilities areas is 30-50%. Because the back marsh and the abandoned river channel had been easily inundated by floods, the residential areas have not been significantly developed in these geomorphologies.

The delta and coastal lowland is covered with multiple land use units not only the low-rise housing but also the commercial and the industrial areas. In the marine sand and gravel bars, the area proportions of the low-rise housing and the roads are 40% and 25%, respectively. Since the filled land is newly developed area, the area proportions of the industrial and the public facilities areas are about 80%.

The results indicate that the characteristics of the land use pattern are different at different site geomorphology. It suggests that there would be some correlation between the geomorphology and satellite images because the land use pattern would be closely related with satellite images. In the next chapter, the relationship between the high-resolution satellite image and the land use is examined.

4. RELATIONSHIP BETWEEN LAND USE AND HIGH-RESOLUTION SATELLITE IMAGE

In order to compare the satellite image with the land use map, the mesh map whose size is 10m is constructed. Using the digital number (p_i) of a pixel (i) in the QuickBird image, the average (a_j) and the standard deviation (σ_j) of the digital numbers are computed in each 10m-mesh (j) as shown in the Eq. (2a) and (2b).

$$a_j = \frac{1}{m}\sum_{i=1}^{m} p_i \tag{2a}$$

$$\sigma_j = \sqrt{\frac{1}{m}\sum_{i-1}^{m}(p_i - a_j)^2} \tag{2b}$$

Here, m means the number of pixels included in a 10m-mesh. The σ_j value would be larger in a mesh in which many features are included such as a mixel, and smaller in a pure pixel (see Fig. 1).

By aggregating the a_j values of the 10m-meshes for each land use unit (L), the mean value (A_L) and the standard deviation (D_L) are calculated for each land use unit by the Eq.

(3a) and (3b).

$$A_L = \frac{1}{n}\sum_{j=1}^{n} a_j \qquad (3b)$$

$$D_L = \sqrt{\frac{1}{n}\sum_{j=1}^{n}(a_j - A_L)^2} \qquad (3b)$$

Here, n means the number of the 10m-meshes included in a land use unit. In order to evaluate the stochastic characteristics of the mixels, heterogeneity degree (H_L) defined as the Eq. (4a) and (4b) is computed from the σ_j values for each land use unit (L).

$$\overline{\sigma_L} = \frac{1}{n}\sum_{j=1}^{n}\sigma_j \qquad (4a)$$

$$\mathrm{H_L} = \sqrt{\frac{1}{n}\sum_{j=1}^{n}(\sigma_j - \overline{\sigma_L})^2} \qquad (4b)$$

Figure 4 shows the schematic diagrams of the heterogeneity degree. Higher H_L value indicates that the meshes whose σ_j value is large and the meshes whose σ_j value is small are mixed (see Fig. 4(a)). Lower H_L value indicates that the meshes whose σ_j value is large or small are concentrated (see Fig. 4(b) and (c)).

Figure 5 shows the A_L values, the D_L values and the H_L values of the band 1, 3 and NDVI for each land use unit. The figures for the band 2 and 4 are omitted because the results of the band 2 and 4 are similar to those of the band 1 and NDVI, respectively. The horizontal axis indicates the land use unit and the vertical axis indicates the digital number or NDVI. The error bars of the figure indicate the D_L values. The land use units are broadly classified into three categories such as vegetated area, built-up area and water area.

4.1 Characteristics in Vegetated Area

The A_L values of NDVI in the vegetated areas are higher than those in the other areas, while the A_L values of band 1 and 3 are relatively low. This is because NDVI strongly reflects the vegetations as trees and grasses compared with the other bands.

In the trees/wasteland, the A_L values of NDVI are higher than those in the parks/green space and the agricultural land. The H_L values of NDVI in the trees/wasteland are low. They suggest that the vegetations are densely distributed and the number of the mixels would be small in the trees/wasteland.

In the parks/green space, the A_L value of NDVI is also relatively high. It indicates that the vegetations are mainly distributed in the area. The H_L values of NDVI are higher than the other vegetated areas. It would come from that various vegetations such as trees and grasses are distributed since the vegetation activity is different between the kinds of vegetations.

In the agricultural land, the A_L value of NDVI is relatively low, while the A_L value of the band 3 is high. The H_L values of the band 1 and 3 are higher than the other vegetated areas. This is because not only the vegetation but also a lot of soils on fields are observed in the agricultural land. These mixels would produce the large H_L value.

4.2 Characteristics in Built-up Area

The A_L values of the band 1 and 3 in the industrial area

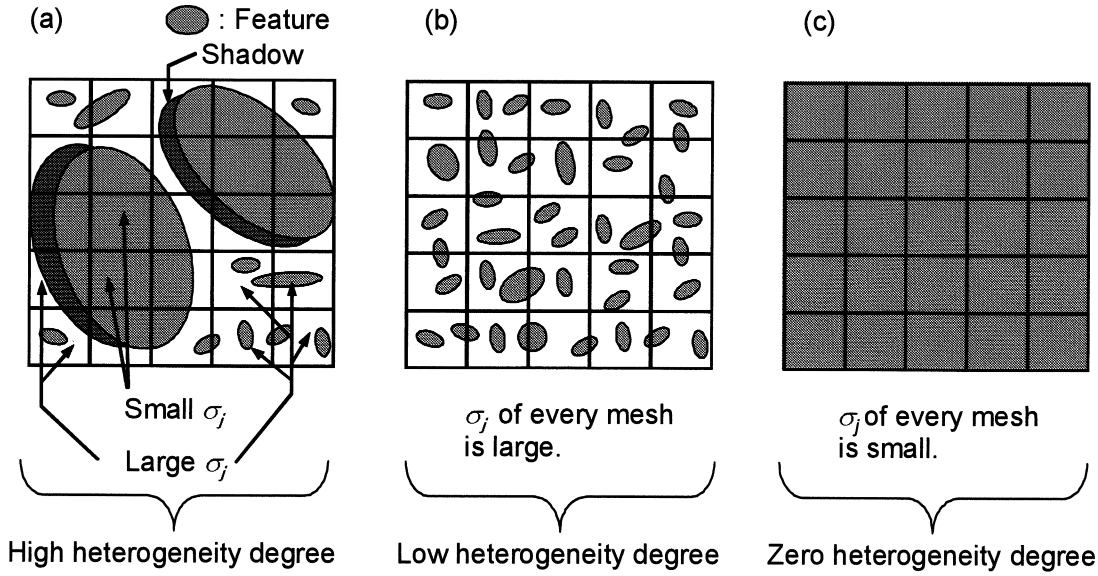

Figure 4 Schematic Diagram of Standard Deviation (σ_j) of Digital Number and Heterogeneity Degree (H_L)

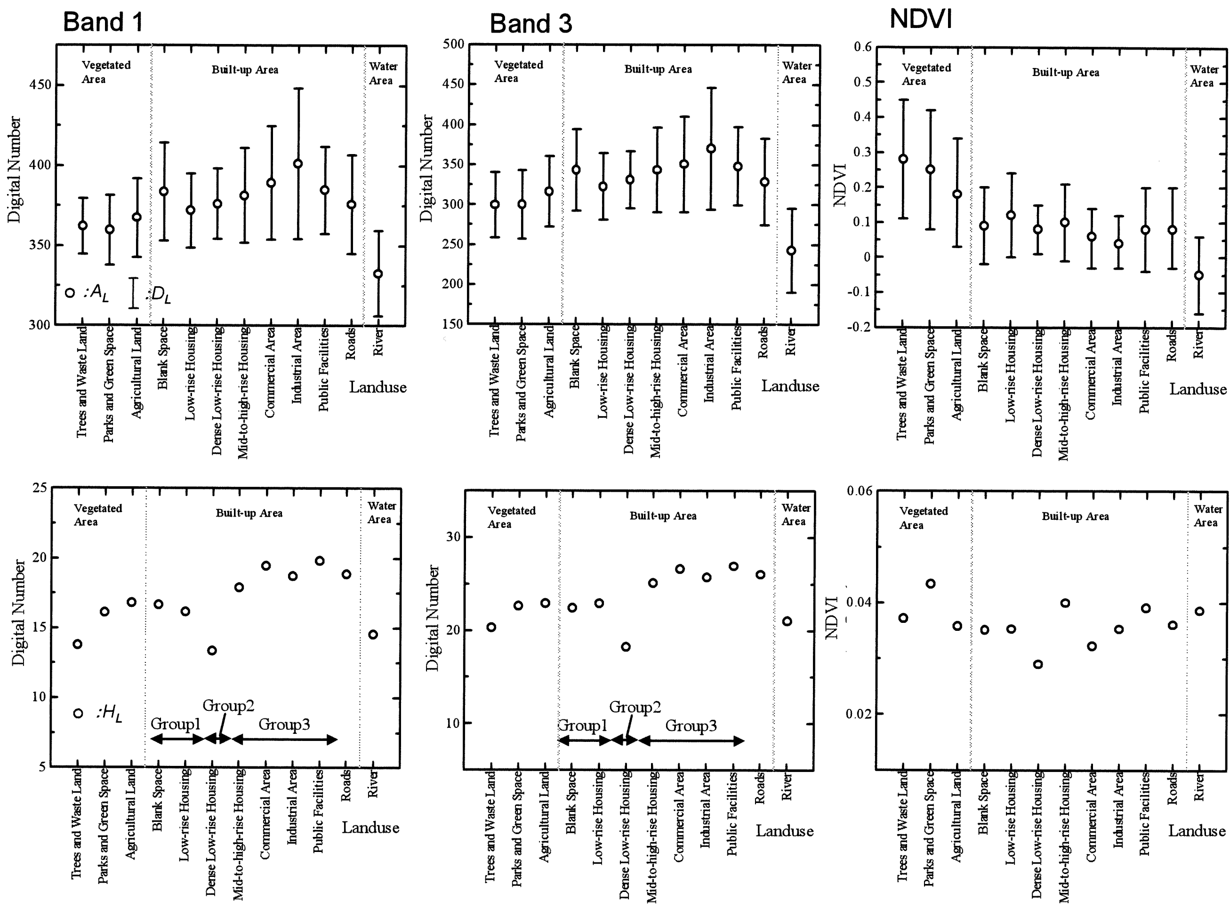

Figure 5 Mean Values (A_L), Standard Deviation (D_L) and Heterogeneity Degree (H_L) of Digital Number of QuickBird Image for Each Land Use Unit

are highest in the built-up area, while the A_L values in the low-rise housing area are lower than those of the other built-up areas. The trend of the A_L values shows that the larger the size of building is, the higher the A_L value is. This would come from the difference of the brightness of building roofs. The brightness of roofs of large buildings such as reinforced concrete (RC) building is relatively high. On the other hand, most of the low-rise buildings are wooden houses. The brightness of the roofs of such houses is generally dark because the color of the roof tile is mostly black or gray.

From the characteristics of the H_L values of the band 1 and 3, the built-up area is broadly classified into three groups as shown in Fig. 5. The Group 1 and 2 indicate the low-rise housing areas. The Group 3 indicates larger building areas such as mid-to-high-rise buildings and industrial buildings. The H_L values in the Group 1 and 2 are low especially in the dense low-rise housing area, while the H_L values in the Group 3 are higher. Because the size of the low-rise buildings is mostly 10 to 20m, homogeneous pixels would be concentrated in a 10m-mesh especially in the Group 2 such as the dense low-rise housing area.

In the Group 3, the number of pure pixels would be large because the size of the buildings is larger than the mesh size of 10m. The σ_j values would be small in these pure pixels. The meshes, however, also cover the mixels that include not only the buildings but also the associating features such as shadows as illustrated in Fig. 4(a). Because the contrast of the RC building roofs and the shadows is large, the σ_j values would be large in these mixels. Therefore, the H_L values are higher in the Group 3.

4.3 Characteristics in Water Area

In the river area, the A_L values of all the bands are significantly small. The H_L values are also low. These are because that the reflectance of water is low and the pure pixels of water are concentrated in the water area.

5. CONCLUSIONS

As a preliminary study for detailed mapping of the geomorphologic classification, the stochastic characteristics of the high-resolution satellite image at different land use is examined mainly to evaluate the effect of the mixels to the land use pattern. The QuickBird image whose spatial resolution is 0.7m is used. The mean value and its standard deviation of digital number and NDVI of the image are computed from 10m-mesh for each land use unit. The heterogeneity degree is also calculated from the standard deviations of the meshes for the land use unit. The result shows that the characteristics of the mean values and the heterogeneity degrees are different for the different land use.

Acknowledgment

This study was done as a part of "Development of Integrated Geophysical and Geological Information Database" supported by Special Coordination Funds Promoting Science and Technology of the Japanese Ministry of Education, Culture, Sports, Science and Technology.

References:

Geographical Survey Institute (2007), "Digital Map 5000 (Land Use) Metropolitan Area 2000" (in Japanese).

Ishii, K. Midorikawa, S. Miura, H. (2007), "Detailed Mapping of Engineering Geomorphologic Classification Using Digital Elevation Model and Satellite Image", *Journal of Social Safety Science*, No.9, 121-129 (in Japanese with English Abstract).

Kitamoto, A. and Takagi, M. (1996), "A Stochastic Model of Mixels and Image Classification", *Proc. 13th International Conference on Pattern Recognition*, B, 745-749.

RECOGNITION OF NONLINEAR SITE RESPONSE APPLYING THE MOVING WINDOW SPECTRAL RATIO METHOD

Chih-Wei Chang[1), Kuo-Liang Wen[2), and Che-Min Lin[3)

1) MSc student, Institute of Geophysics, National Central University, Taoyuan, Taiwan
2) Professor, Institute of Geophysics, National Central University, Taoyuan, Taiwan
3) PhD student, Institute of Geophysics, National Central University, Taoyuan, Taiwan n
956202015@cc.ncu.edu.tw, wenkl@earth.ncu.edu.tw

Abstract: The predominant frequency decrease and de-amplification of strong motion spectra at a soil site are recognized as occurring nonlinear site effects. In this study, the strong and weak motion events recorded by the LSST borehole array in Taiwan are analyzed by the moving window spectral ratio method. The spectral ratios of surface to borehole sites are calculated to analyze the predominant frequency variations with time. Based on the analysis of the strong motion record, it shows the predominant frequency varies with time from 3 Hz to 2 Hz, and it finally back to about 3 Hz. Therefore, the nonlinear soil response of strong motion can be recognized according to the variation of predominant frequency with time using the moving window spectral ratio method.

1. INTRODUCTION

In Taiwan, several large earthquakes were recorded by vertical arrays recently. Using the spectral ratio method in borehole data already provide direct evidence of the significance of nonlinear site effects in different parts of the world. Wen et al. (1986) demonstrated strong motion records of LSST array in Taiwan.

Spectral ratio of a two-station pair involves analyzing the near-surface amplification and predominant frequency, calculated from data records of surface and borehole instruments. The amplification function is controlled by the wave velocity and damping in the soil layer between the two stations. The predominant frequency becoming difference between weak and strong motions is an indication of nonlinearity (EPRI 1993 ; Beresnev and Wen 1996).

In this study, the moving window spectral ratio method for an event is introduced to identify the variation of predominant frequency with time and then to determine the soil response is linear or nonlinear.

2. DATA AND METHOD

The locations of LSST array on the surface is shown in Figure 1a, and there is a 1/4 scale model structure in the center. The two borehole arrays, designated as DHA and DHB, were located on the northern arm approximately 3.2 and 46.7 meters from the 1/4 model with accelerometers at depth of 6, 11, 17, and 47 meters, respectively, as shown in Figure 1b.

(a)
(b)
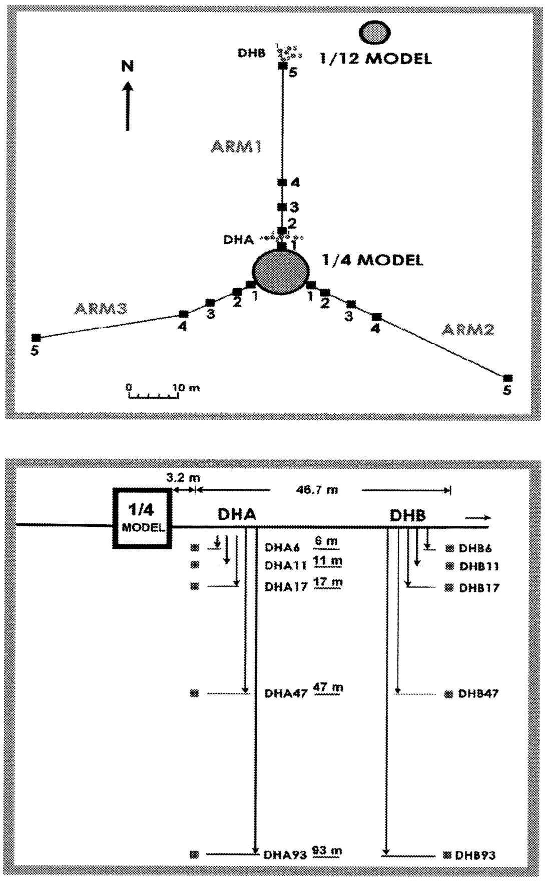

Figure 1 (a)The surface stations of the LSST array. (b) The configuration of borehole stations of the vertical array (derived from Institute of Earth Sciences, Academia Sinica, Taiwan).

Table 1 (Wen et al., 1995) gives the LSST array data from 1986 to 1988, including 6 weak motion events with peak ground acceleration (PGA) less than 60 gal and 3 strong motion events with PGA greater than 150 gal were selected. (Wen et al., 1995) showed that these three strong motion events recorded had nonlinear soil response.

Table 1 Selected LSST events. (Web et al., 1995)

Event	Date	Depth (km)	M_L	Δ (km)	PGA(gal)
Weak motion					
6	08/04/86	11	5.4	31	35.4
8	20/05/86	22	6.2	69	35.0
14	30/07/86	2	4.9	5	57.5
20	10/12/86	98	5.8	42	23.8
21	06/01/87	28	6.2	77	31.8
22	04/02/87	70	5.8	16	43.4
Strong motion					
7	20/05/86	16	6.5	66	223.6
12	30/07/86	2	6.2	5	186.7
16	14/11/86	7	7.0	78	167.2

Note : Δ is the epicenter distance.

We propose the moving window spectral ratio method to analyze the soil response, and there are some main steps in this study :

1. We set the time series window length (5.12 or 10.24 seconds) and moving length (1.28 seconds) of the events.
2. Add cosine taper to every time window and do Fourier transform to frequency series.
3. And we calculate the spectral ratios between surface and 11-m depth borehole stations.
4. Then, the spectral ratios of each window will be normalized (multiplying by the maximum ratio) respectively.
5. Each regulative ratio was then smoothed 5 times using the 3-point average method for weightings of 1/4, 1/2, and 1/4.

Finally, we will get the variation of predominant frequency with time and we can identify the soil response is linear or nonlinear on week or strong motion events.

3. RESULTS

In this work, the predominant frequency at the window before the strong motion part is 3 Hz shown in Figure 2 which is the same as the weak motion response shown in Figure 3 and it shows linear soil response at these time periods. During the strong shaking parts, the predominant frequency of the shear wave is decrease to 2 Hz and shows nonlinear soil response occurred at this time window (Figure 2). After the strong shear wave, the predominant frequency returns to 2.5-3 Hz immediately and it means soil response back to linear at this time period (Figure2).

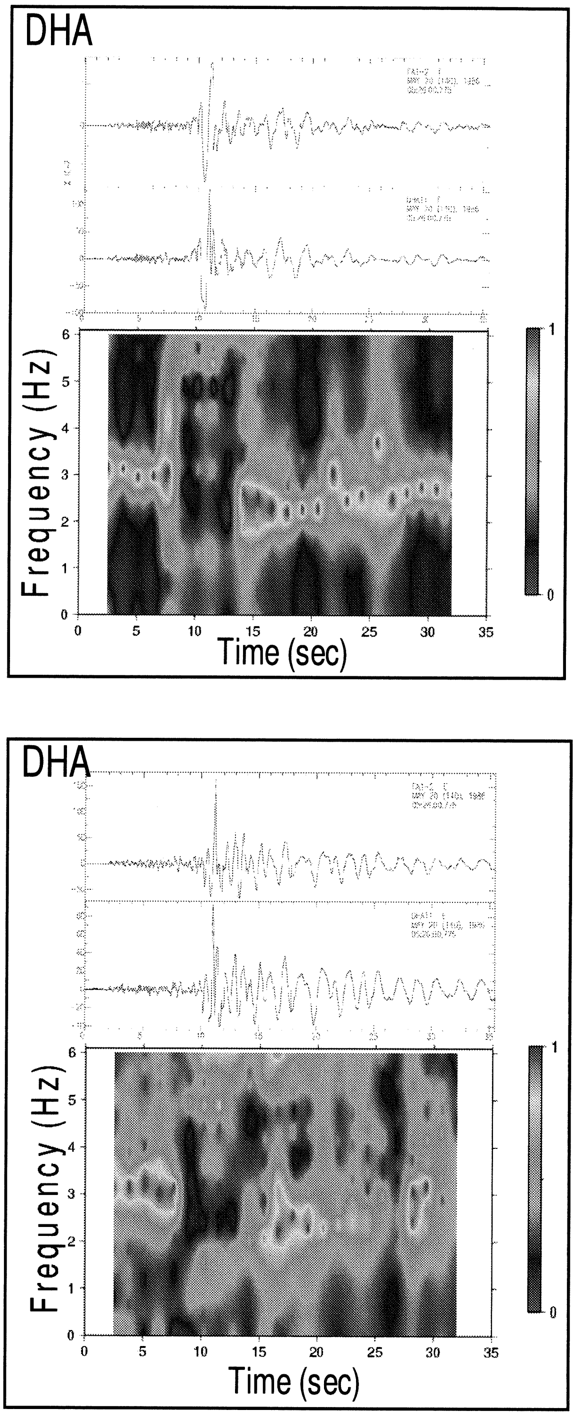

(a)

Figure 2(a) Spectral ratios with time of surface to 11-m deep borehole station for a strong motion event of the 20 May 1986 recorded by the LSST's DHA borehole array. The upper part is EW component, and the lower part is NS component. The color figures represent variation of predominant frequency with time. The color bar represents normalized amplification, and the color is shallower, the amplification is greater.

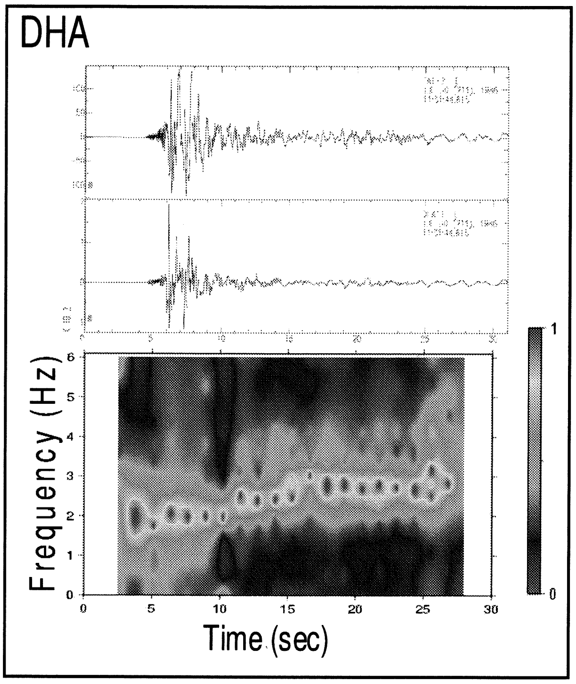

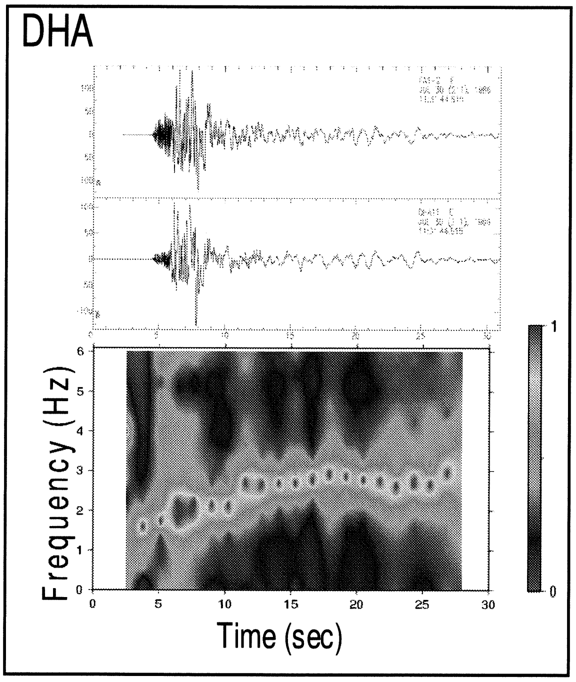

(b)

Figure 2(b) Spectral ratios with time of surface to 11-m deep borehole station for a strong motion event of the 30 July 1986 recorded by the LSST's DHA borehole array. The upper part is EW component, and the lower part is NS component. The color figures represent variation of predominant frequency with time. The color bar represents normalized amplification, and the color is shallower, the amplification is greater.

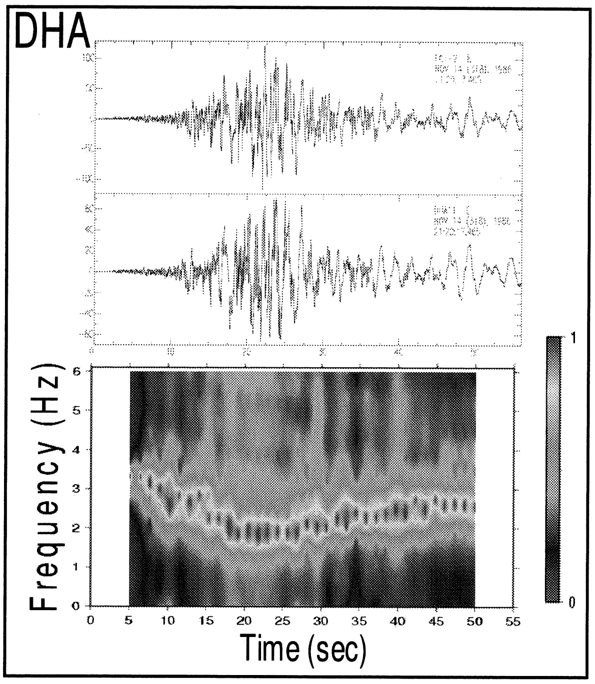

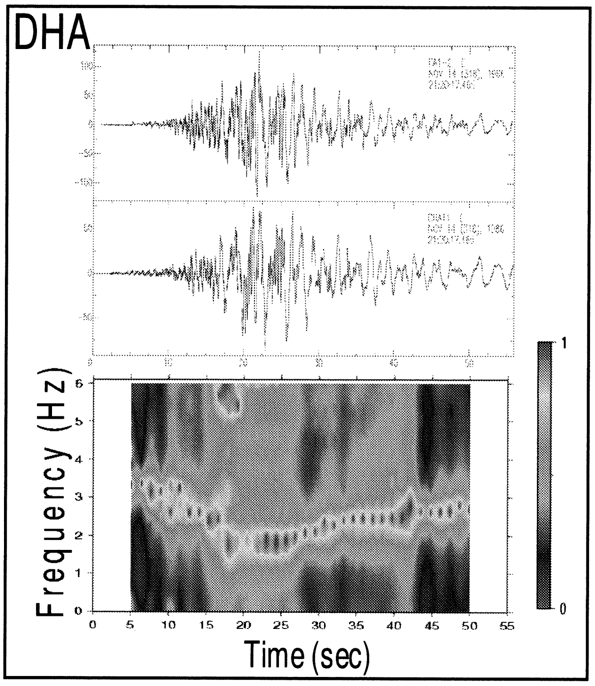

(c)

Figure 2(c) Spectral ratios with time of surface to 11-m deep borehole station for a strong motion event of the 14 Nov. 1986 recorded by the LSST's DHA borehole array. The upper part is EW component, and the lower part is NS component. The color figures represent variation of predominant frequency with time. The color bar represents normalized amplification, and the color is shallower, the amplification is greater.

The results reflected in Figure 2(a) indicate that there are some modes on shear wave part, and the predominant frequency of the first mode is 1-2 Hz during this part indistinctly shown soil nonlinear response. One point is worth making about Figure 2(b). That is the data is zero before the P wave coming, so the spectral ratio reflects lower frequency is illusory. Then, the Figure 2(c) is a representative result in this study, and indicates the variations of predominant frequency with time during the 14 Nov. 1986 strong motion.

On the other weak motion events, the predominant frequency keeps about 3 Hz shown in Figure 3, and does not varies with time from beginning to end of the motions using the same method and it demonstrated that the soil response is linear on the weak motion.

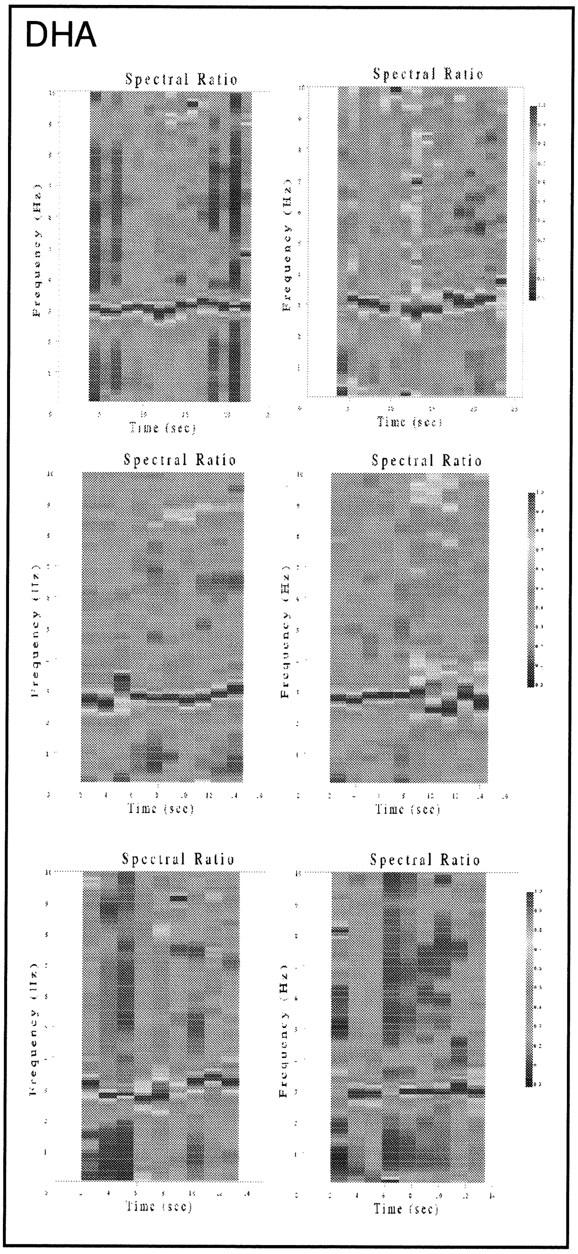

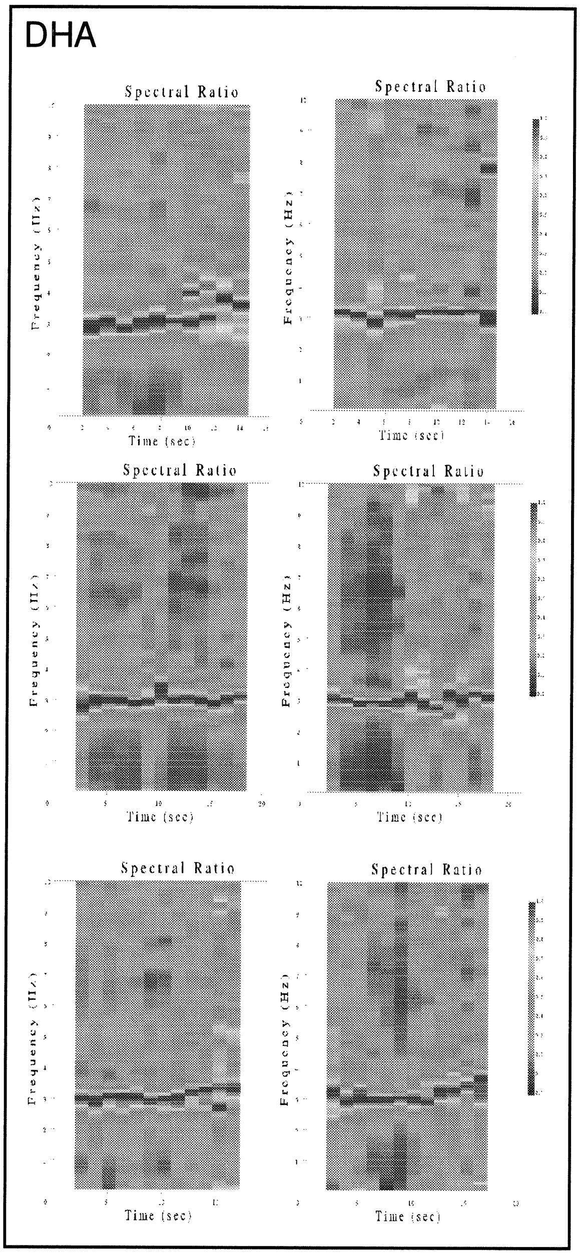

Figure 3 There are 6 weak motion events recorded by the LSST's DHA borehole array. The left hand is EW component, and the right hand is NS component. The color figures represent variation of predominant frequency with time. The color bar represents normalized amplification, and the color is deeper, the amplification is greater.

4. DISCUSSIONS AND CONCLUSIONS

In this paper, the moving window spectral ratio method was introduced to recognize nonlinear site response. The data from LSST borehole arrays, already shown to have nonlinear site response by previous spectral ratio analyses between surface and borehole stations (Wen et al., 2006) are here used to show the applicability of this method for nonlinear site response identification.

These results are entirely consistent with those reported for the soil nonlinear response in previous studies. In this work, during the shear wave of strong motion parts, the predominant frequency of the shear wave is decrease to 2 Hz and it shows nonlinear soil response. After the shear wave, the predominant frequency returns to 2.5-3 Hz immediately and it means soil response back to linear at this time period. But on weak motion events, the predominant frequency keeps about 3 Hz and there are not variations with time from beginning to end of the event using the same method and it identifies that the soil response is linear on the weak motion.

This study demonstrates that the moving window spectral ratio method can be used to recognize the soil nonlinear response of strong motion event through the variation of predominant frequency with time. Much remains to be done, then, but we anticipate that the same results will generate the horizontal-to-vertical (H/V) spectral ratio in this method. The method is subject to constant revision and changes in order to be improved.

Acknowledgements:
The earthquake data were provided from Institute of Earth Sciences, Academia Sinica, Taiwan. This study was supported by the National Science Council under grant no. NSC95-2745-M-008-003 and NSC96-2119-M-008-007.

References:

Beresnev, I. A., and Wen, K. L. (1996), "Nonlinear ground response – a reality ? (A Review)," *Bulletin of the Seismological Society of America*, **86**, 1964-1978

Electric Power Research Institute (EPRI) (1993), "Guidelines for determining design basis ground motions : method and guidelines for estimating earthquake ground motion in Eastern North America," *Report EPTI TR-102293*, V.1, Palo Alto, CA.

Wen, K. L., Yeh, Y. T., and Liu, C. C. (1986), "The observation system and data processing of the LSST array," *Institute of Earth Sciences, Academia Sinica*, ASIES-CR8602. (in Chinese)

Wen, K. L., Beresnev, I. A., and Yeh, Y. T. (1995) "Investigation of nonlinear site amplification at two downhole strong ground motion arrays in Taiwan," *Earthq. Eng. Struct. Dyn.*, **24**, 31324.

Wen, K. L., Chang, T. M., Lin, C. M., and Chiang, H. J. (2006) "Identification of nonlinear site response using the H/V spectral ratio method," *Terr. Atmos. Ocean. Sci.*, **17**, 533-546

Fifth International Conference on Urban Earthquake Engineering
March 4-5, 2008, Tokyo Institute of Technology, Tokyo, Japan

A NEW SPECTRAL REPRESENTATION OF STRONG MOTION EARTHQUAKE DATA: HILBERT SPECTRAL ANALYSIS OF TAIPOWER BUILDING STATION, 1994~2006

Sheng-Chung Su[1], Norden E.Huang[2], and Kuo-Liang Wen[3]

1) PhD student, Institute of Geophysics, National Central University, Taiwan
Junior Technical Specialist, Seismological Center, Central Weather Bureau, Taiwan
2) Director, Research Center for Adaptive Data Analysis, National Central University, Taiwan
3) Professor, Institute of Geophysics, National Central University, Taiwan
scsu0514@scman.cwb.gov.tw, Norden@ncu.edu.tw, wenkl@earth.ncu.edu.tw

Abstract: In this article, we use latest HHT method within newly developed Ensemble skills to analyze the records from Taipower Building Strong-motion station from 1994~2006. The station was designed in 1979 using ASD steel code that limiting the building shaking only in elastic range under small to moderate earthquakes. The station consists of 2 buildings, a main building - 27 floors and lower building - 12 floors. For earthquake hazard mitigation purpose, some buildings and bridges were equipped with sensors by Central Weather Bureau. This station was equipped by CWB in 1994 and has already triggered by 63 earthquakes until the end of 2006. Integrated earthquake catalogue shows the acceleration relationships between basement 3rd slab and 27th slab aren't proportional.

HHT results show the nonlinear and non-stationary characteristics in time-frequency domain. We define some new observational parameters for wave-propagating magnitude, structure dominant frequency, and structure coherence frequency characteristics. In the end of the article, we choose a typical event from the catalogue and show the nonlinear and non-stationary phenomena. The new data-processing methodology can help us understand the real world complexity and help us explore information and physical behaviors from real records without presetting any model.

1. INTRODUCTION

Former scientists and engineers made fundamental models for real objects to simplify physical complexities. There are serious complicated behaviors for the objects exposed in the nature environments. For example, structures suffered from floods, typhoons, earthquakes, and thermal effects. Besides, Human are ambitious to new engineering plans, there are high-rise buildings in the downtown, long-span bridges on the rivers, high-speed vehicles and airplanes travelling everywhere. When the design safe margin was narrowed by performance demands or by economic reasons, basic and traditional models were found to be rough and imprecise.

Empirical skills and methods are introduced in real business, but the theory from fundamental model remains the same. For instance, a building was built from engineer's drawings. That's the calculation results of basic physical and mechanical models. However, the actual properties weren't precisely as the design drawings. The main errors are from setting the fundamental linear and stationary models.

A new strategy was already made to correct the errors. Real records those from existing structures are ready to be analyzed. Exploring with useful tools from records and concluding the nonlinear and non-stationary intra characteristics will help us improve the model or create new evolutionary model. Then, use new model to predict future outcome.

In the beginning of the strategy, we find Hilbert-Huang Transform (HHT) is a useful and powerful tool. Now, let's start exploring.

2. HILBERT-HUANG TRANSFORM

The HHT consists of two parts: the adaptive Empirical Mode Decomposition (EMD) method and the instantaneous frequency in the Hilbert spectral analysis. This method was first introduced by Huang et al. (1998). The critical new concepts introduced are the adaptively defined basis and a way to compute a stable and physically meaningful instantaneous frequency through the Hilbert transform. A brief summary of the method is given below:

2.1 The Hilbert transform

For an arbitrary time series, $X(t)$, we can calculate its Hilbert Transform, $Y(t)$, as discussed above. The real advantage of the Hilbert transform only became obvious after Huang et al (1998) introduced the Empirical Mode Decomposition method.

2.2 The Empirical Mode Decomposition Method or the

Sifting Process:

Contrary to almost all the previous methods, this new method is intuitive, direct, *a* posteriori, and adaptive, with the basis of the decomposition based on and derived from the data. Each of the oscillatory modes produced is represented by an Intrinsic Mode Function (IMF) with the following definitions:

1. in the whole data set, the number of extreme and the number of zero-crossings must either equal or differ at most by one, and.
2. at any point, the mean value of the envelope defined by the local maxima and the envelope defined by the local minima is zero.

With the definition, one can decompose any function as follows: Identify all the local extreme, then connect all the local maxima by a cubic spline line as the upper envelope. Repeat the procedure for the local minima to produce the lower envelope. The upper and lower envelopes should cover all the data between them. Their mean is designated as $\boldsymbol{m_1}$, and the difference between the data and $\boldsymbol{m_1}$ is the first component, $\boldsymbol{h_1}$, i.e.,

$$X(t) - m_1 = h_1 \ . \tag{1}$$

Ideally, $\boldsymbol{h_1}$ should be an IMF, for the construction of $\boldsymbol{h_1}$ described above should have made it so as to satisfy all the requirements of IMF. Yet, even if the fitting is perfect, a gentle hump on a slope can be amplified to become a local extreme in changing the local zero from a rectangular to a curvilinear coordinate system. After the first round of sifting, the hump may become a local maximum. New extreme generated in this way actually recover the proper modes lost in the initial examination. In fact, the sifting process can recover signals representing low amplitude riding waves with repeated siftings. In the subsequent sifting process, $\boldsymbol{h_1}$ is treated as the data, then

$$h_1 - m_{11} = h_{11} \ . \tag{2}$$

After repeated sifting, up to k times say, $\boldsymbol{h_{1k}}$ becomes an IMF, that is

$$h_{1(k-1)} - m_{1k} = h_{1k} \ ; \tag{3}$$

then, it is designated as the first IMF component from the data.

$$c_1 = h_{1k} \ , \tag{4}$$

Overall, $\boldsymbol{c_1}$ should contain the finest scale or the shortest period component of the signal. We can separate $\boldsymbol{c_1}$ from the rest of the data by

$$X(t) - c_1 = r_1 \ . \tag{5}$$

Since the residue, $\boldsymbol{r_1}$, still contains longer period components, it is treated as the new data and subjected to the same sifting process as described above. This procedure can be repeated to all the subsequent $\boldsymbol{r_j}$'s, and the result is

$$\begin{aligned} r_1 - c_2 &= r_2 \ , \\ &\cdots\cdots \\ r_{n-1} - c_n &= r_n \end{aligned} \tag{6}$$

The sifting process can be stopped finally by any of the following predetermined criteria: either when the component, $\boldsymbol{c_n}$, or the residue, $\boldsymbol{r_n}$, becomes so small that it is less than the predetermined value of substantial consequence, or when the residue, $\boldsymbol{r_n}$, becomes a monotonic function from which no more IMF can be extracted. Even for data with zero mean, the final residue still can be different from zero. If the data have a trend, the final residue should be that trend. By summing up Equations (5) and (6), we finally obtain

$$X(t) = (\sum_{j=1}^{n} c_j) + r_n \ . \tag{7}$$

Thus, we achieve a decomposition of the data into n empirical modes, and a residue, $\boldsymbol{r_n}$, which can be either the mean trend or a constant.

2.3 The Hilbert Spectral Analysis

Having obtained the IMF components, the Hilbert Transform can be applied to each IMF component and the instantaneous frequency can be computed. After performing the Hilbert transform on each IMF component, the original data can be expressed as the real part, RP, in the following form:

$$X(t) = RP \sum_{j=1}^{n} a_j(t)\, e^{i\int \omega_j(t)\,dt} \ . \tag{8}$$

Here we have left out the residue, $\boldsymbol{r_n}$, on purpose, for it is either a monotonic function or a constant. Equation (14) gives both amplitude and frequency of each component as functions of time. The same data if expanded in Fourier representation would be

$$X(t) = RP \sum_{j=1}^{\infty} a_j\, e^{i\omega_j t} \ , \tag{9}$$

with both $\boldsymbol{a_j}$ and $\boldsymbol{\omega_j}$ constants. The contrast between Equations (14) and (15) is clear: The IMF represents a generalized Fourier expansion. The variable amplitude and the instantaneous frequency have not only greatly improved the efficiency of the expansion, but also enabled the expansion to accommodate nonlinear and non-stationary data. With IMF expansion, the amplitude and the frequency modulations are also clearly separated. Thus, we have broken through the restriction of the constant amplitude and fixed frequency Fourier expansion, and arrived at a variable amplitude and frequency representation. This frequency-time distribution of the amplitude is designated as the Hilbert Amplitude Spectrum, $H(\omega, t)$, or simply Hilbert Spectrum. If amplitude squared is preferred to represent energy density, then the squared values of amplitude can be substituted to produce the Hilbert Energy Spectrum instead.

2.4 The Ensemble Skills of HHT

There are two signal processing skills used here:

1. Ensemble EMD: One of the major drawbacks of the original EMD is the frequent appearance of mode mixing, which is defined as a single Intrinsic Mode Function (IMF) either consisting of signals of widely disparate scales, or a signal of a similar scale residing in different IMF components. The Ensemble EMD (EEMD), which defines the true IMF components as the mean of an ensemble of trials, each consisting of the signal plus a white noise of finite amplitude.
2. Ensemble HSP: A similar skill is used to Ensemble the HSP results. The skill is more applicable when the sampling frequency is several times higher than the dominant frequency of the object. The raw strong-motion acceleration record data is 200 Hz, so it's highest Nyquist frequency limit is 100 Hz. The object we want to analyze is a building, the highest frequency limit may not exceed 20 Hz. So we down-sample the raw data into 5 parts. Taking each part as an independent event and proceeding with EEMD, then we take the mean of 5 HSP and let it be the EHSP result. This skill also helps the added noise be cancelled and makes the result of EHSP more clear and more precise.

3. TAIPOWER BUILDING RECORD ANALYSIS

The station was designed in 1979 containing 2 buildings, 27 floors and 12 floors. The accelerometer instrument plan is shown in Figure 1.

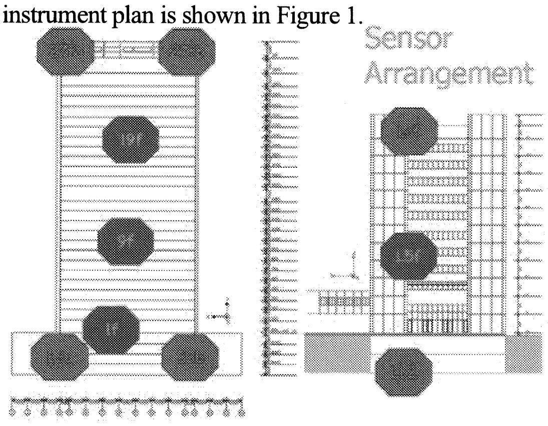

Figure 1 Taipower Building Station Instrument Plan.

In the beginning, we integrated all the records and made earthquake catalogue. The data was arranged in CH1 magnitude order, CH1 was the sensor installed in b3 floor in vertical direction. The catalogue is shown in Table 1, Table 2, and Figure 2.

Table 1 Earthquake Catalogue part 1:No.1~32

CWB Taipower Building EQ catalogue,TAPBA4,1994~2006,part1/2

編號	長度(sec)	年	月日	時分	秒	緯度	經度	深度	芮氏規模	震央距離	震源距離
No.	length(sec)	EarthQuake Time				Latitude	Longitude	Depth	Magnitude	EPicenter	HYPOcenter
unit	(sec)	Year	M.D	time	sec	(Degree)	(Degree)	(km)	ML	(km)	(km)
1	61.44	2006	415	2240	55	22.86	121.30	17.90	6.04	241.73	242.39
2	62.72	1994	606	857	24	24.43	121.95	3.45	5.06	80.12	80.20
3	62.72	1995	502	2248	21	23.83	121.97	23.93	5.24	140.60	142.62
4	61.44	1995	730	1800	53	25.17	121.58	5.23	3.06	17.45	18.22
5	102.40	2006	1226	1226	21	21.69	120.56	44.11	6.96	385.85	388.36
6	64.00	2005	430	1448	17	24.04	121.62	8.45	5.62	109.74	110.06
7	67.72	2005	1005	1616	35	24.84	121.64	73.35	4.84	22.63	76.76
8	89.60	2006	401	1002	20	22.88	121.08	7.20	6.23	242.51	242.61
9	102.40	1994	916	620	16	22.43	118.47	19.06	6.43	446.16	446.56
10	83.20	2006	1012	1446	29	23.96	122.65	25.26	5.80	170.59	172.45
11	69.12	2000	728	2028	8	23.41	120.93	7.35	6.10	190.60	190.74
12	122.88	2006	1226	1234	15	21.97	120.42	50.22	6.99	360.69	364.17
13	72.96	2004	1111	216	45	24.31	122.16	27.26	6.09	105.04	108.52
14	87.04	1996	305	1732	9	23.90	122.30	10.81	5.96	151.22	151.61
15	98.56	1994	1028	2351	10	24.64	122.27	2.00	5.66	92.54	92.56
16	75.52	1999	222	1348	58	23.98	122.65	4.21	5.90	170.50	170.55
17	84.48	1998	1117	2227	33	22.83	120.79	16.49	5.51	256.55	257.08
18	87.04	1995	714	1652	46	24.32	121.85	8.79	5.80	85.34	85.79
19	71.68	2005	906	116	0	23.96	122.28	16.76	6.00	144.55	145.51
20	107.52	2003	1210	438	14	23.07	121.40	17.73	6.42	217.43	218.15
21	78.08	1995	403	1154	40	23.94	122.43	14.55	5.88	156.61	157.28
22	101.12	2006	728	740	10	23.97	122.66	27.97	6.02	171.45	173.72
23	61.44	2002	907	2259	33	24.45	121.69	41.36	5.26	65.77	77.69
24	72.96	2002	916	3	31	25.10	122.39	175.67	6.80	95.79	200.09
25	84.48	1994	1005	113	24	23.16	121.72	31.28	5.83	208.04	210.38
26	96.00	2002	528	1645	15	23.91	122.40	15.23	6.20	156.12	156.86
27	101.12	1999	920	2146	38	23.58	120.86	8.57	6.59	176.04	176.25
28	81.92	2003	610	840	32	23.50	121.70	32.31	6.48	169.38	172.44
29	97.28	1999	922	49	43	23.76	121.03	17.38	6.20	149.95	150.95
30	120.32	1999	920	1816	18	23.86	121.04	12.53	6.66	139.59	140.15
31	61.44	2003	811	1630	14	24.59	121.56	58.49	5.38	47.37	75.27
32	61.44	1996	122	1922	58	24.93	121.72	66.86	5.11	23.69	70.93

Table 2 Earthquake Catalogue part 2:No.33~63

CWB Taipower Building EQ catalogue,TAPBA4,1994~2006,part2/2

編號	長度(sec)	年	月日	時分	秒	緯度	經度	深度	芮氏規模	震央距離	震源距離
No.	length(sec)	EarthQuake Time				Latitude	Longitude	Depth	Magnitude	EPicenter	HYPOcenter
unit	(sec)	Year	M.D	time	sec	(Degree)	(Degree)	(km)	ML	(km)	(km)
33	64.00	1995	1201	317	5	24.61	121.64	45.07	5.72	47.44	65.43
34	94.72	2005	601	1620	6	24.64	122.07	64.78	6.00	73.13	97.70
35	66.56	1994	1012	908	22	24.81	122.02	73.68	5.67	59.07	94.43
36	65.28	1999	507	103	24	24.74	121.89	4.17	5.44	50.80	50.97
37	99.84	1999	920	1757	16	23.91	121.04	7.68	6.44	134.31	134.53
38	103.68	1999	922	14	41	23.83	121.05	15.59	6.80	142.95	143.80
39	122.88	2000	610	1823	29	23.90	121.11	16.21	6.70	132.69	133.67
40	61.44	1997	624	1637	13	25.12	121.58	8.55	3.70	12.63	15.25
41	121.60	1999	920	1811	54	23.86	121.07	12.49	6.70	138.13	138.69
42	85.76	1996	729	2020	54	24.49	122.35	65.68	6.14	108.20	126.57
43	96.00	2005	1015	1551	4	25.10	123.81	190.85	7.02	253.40	317.23
44	62.72	1995	424	1004	1	24.65	121.62	63.07	5.28	41.95	75.75
45	61.44	2005	1129	2241	50	24.75	122.03	68.04	5.51	63.24	92.89
46	160.00	1995	223	519	3	24.20	121.69	21.69	5.77	92.16	94.68
47	83.20	2003	609	152	51	24.37	122.02	23.22	5.72	90.48	93.41
48	92.16	1995	324	413	51	24.64	121.86	76.00	5.64	55.96	94.38
49	74.24	2001	613	1317	54	24.38	122.61	64.41	6.25	139.04	153.23
50	121.60	2004	1108	1554	56	23.79	122.76	10.00	6.58	192.87	193.13
51	97.28	2000	910	854	47	24.09	121.58	17.74	6.20	103.83	105.33
52	121.60	1996	308	1452	27	23.93	122.36	6.00	6.40	152.20	152.32
53	62.72	2002	1110	7	5	24.89	121.84	110.27	5.42	37.56	116.49
54	115.20	2004	1015	408	50	24.46	122.85	91.08	7.10	159.39	183.55
55	121.60	2002	515	346	6	24.65	121.87	8.52	6.20	55.72	56.36
56	171.52	2005	305	1908	0	24.65	121.80	6.95	5.96	50.26	50.74
57	111.48	2001	614	235	26	24.42	121.93	17.29	6.30	79.93	81.78
58	102.40	1994	605	109	30	24.46	121.84	5.30	6.50	70.57	70.77
59	122.88	1995	625	659	7	24.61	121.67	39.88	6.50	48.26	62.60
60	62.72	2004	1023	1404	28	25.01	121.56	9.49	3.73	3.77	10.21
61	62.72	2005	1205	1015	30	25.00	121.58	10.68	3.68	5.30	11.92
62	213.76	1999	920	1747	16	23.85	120.82	8.00	7.30	151.98	152.19
63	122.88	2002	331	652	50	24.14	122.19	13.81	6.80	122.20	122.98

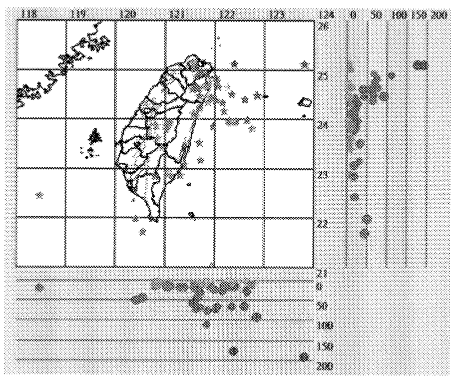

Figure 2 Earthquake Hypocenter Location:No.1~63

The following comparisons and analysis are made:

3.1 Time Domain Comparison: Acceleration Range and Amplification Value

Using raw record values, we compute the maximum and minimum and total oscillation range of each event for every channel. Because the shaking was amplified gradually through basement upward to upstairs, so we calculate the amplification value A.F. For instance, the amplification value of 27th floor "27a" point:

$$A.F_{27a} = \frac{AccRange_{27a}}{SourceAccRange} = \frac{AccRange(27a)}{AccRange(b3f)} \qquad (10)$$

The results of A.F value are shown in Figures 3 and 4. X-dir result reveals highly-nonlinear, Z-dir result reveals slightly-nonlinear.

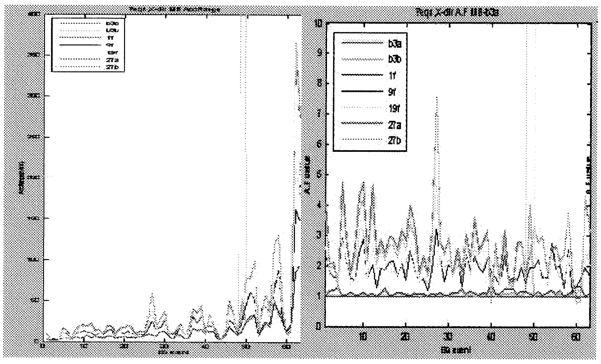

Figure 3 X-dir. Acc. range and amplification value.

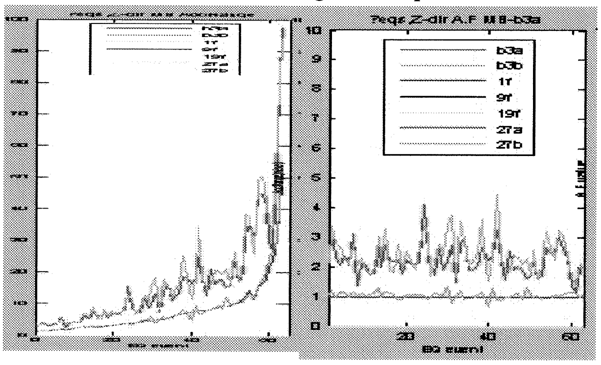

Figure 4 Z-dir. Acc. range and amplification value.

3.2 HHT Analysis:

For an arbitrary earthquake acceleration time series, ***X(t)***, we can calculate its Hilbert Spectrum within aforementioned EEMD & EHSP skills. The result is expressed as H{***X(t)***}, it shows the acceleration energy distribution in the time-frequency domain. Besides those equations of HHT, we will introduce two-station method and use its' concept everywhere. Then define 3 equations in HHT analysis.

1. Finding amplification: Two-station method

The earthquake energy is coming from hypocenter tectonic collisions, passing through underground geographic media, focusing on the specific site conditions, impacting the bottom of the structures and upward propagating to the top of the building. Some researchers (Borcheret, 1970) find the equations to explains the whole process in frequency domain as the following Equation (11). Aforementioned factors are included in the independent terms, $So(f)$ means source influence factor, $Pa(f)$ means path influence factor and $Si(f)$ means site influence factor. We can abbreviate (11) to (12), $F.F(So,Pa,Si)$ means free-field earthquake response influenced by source, path, and site factors. Then we use the same concept to introduce the response on the structures in Equation (13).

$$R_{b3f}(f) = So(f) * Pa(f) * Si(f) \qquad (11)$$

$$R_{b3f}(f) = F.F(So,Pa,Si) \qquad (12)$$

$$R_{27f}(f) = F.F(So,Pa,Si) * Str(f) \qquad (13)$$

Then we using (12) and (13) to form (14), (14) help us to focus on the influence of structure characteristics. Because in Equation (14) there is nothing about source, path, and site.

$$A.F = R_{27f}(f) / R_{b3f}(f) = Str(f) \qquad (14)$$

However, although some terms was erased in (14) but their influence still existing. Researchers should be careful about the hiding terms those consisting the earthquake frequency content.

2. Magnitude of wave propagation:

we use the same concept of "two-station method" to find out the amplification relationship between "source and destination" in time-frequency domain. Define Equation (15) as follows:

$$A.F_{27a,M} = \frac{HSP(27a)}{HSP(b3a)} = \frac{H\{X(t)_{27a}\}}{H\{X(t)_{b3a}\}} \qquad (15)$$

Equation (15) shows the amplification values in the time-frequency domain of wave propagating characteristics from b3 floor to 27th floor. Because earthquake records can be easily separated into 4 parts: Quiet section, P-wave section, S-wave section, and the Coda section. Total energy magnitude value of each section is extremely different. The result of (15) shows the characteristic only in P-wave section and S-wave section. The propagating characteristic values of the other two sections are too small to show on the same figure. To find out characteristics of structure under earthquake force, we define (16).

3. Characteristic of wave propagation:

$$A.F_{27a,F} = N.S[A.F_{27a,M}] \qquad (16)$$

Equation (16) shows the amplification characteristics (dominant frequency values) of the structure in the time-frequency domain of 27th floor. The N.S. means normalize the maximum value to 1 with respect to every time moment and smooth the spectrum in frequency domain for 5 times with a 5-point smooth method. Making such a calculation means we changing the topic from wave propagating characteristics to dominant frequency values of the structure. By definition, the figure only shows the characteristic of structure modal frequency, the total energy of this figure is meaningless.

4. Characteristic of structure coherence:

$$A.F_{27a,C} = \frac{N.S[HSP(27a)]}{N.S[HSP(b3a)]} \qquad (17)$$

Equation (17) shows the structure coherence characteristics between any two positions (b3f to 27f) in the time-frequency domain. Taking N.S. calculation shows characteristics to dominant frequency values of each position. The ratio means to find out the coherence between two different points.

3.3 HHT Results:

There are 63 events on the Catalogue. After inspections to the HHT result, a preliminary conclusion is made as follows:

The dynamic behavior was firstly explained by Single-Degree-of-Freedom linear model. The SDOF structure should have maximum response when it was driven under its dominant frequency. Engineers simulated real buildings as Lump-mass Multi-Degree-of-Freedom linear model and solved it with Modal Superposition Method. After modal superposition method the structure can be treated as a combination of several SDOF linear models. There are a lot of modal dominant frequencies in a high-raise building. The first modal dominant frequency is usually within the largest energy and the second dominant frequency is within lower energy under common condition.

The HHT results of 63 events showed: 16 events vibrated with the highest modal energy in first modal dominant frequency, 17 events vibrated with the highest modal energy in second modal dominant frequency, 25 events vibrated with the highest modal energy in first modal dominant frequency in one horizontal direction and vibrated with the highest modal energy in second modal dominant frequency in another horizontal direction, 5 events vibrated without the first dominant modal frequency. The modal energy distribution is quiet different with old concept. This is the preliminary result, maybe need more investigations. We just use "Signal-processing skills" to explore the data, we haven't use any physical model. The preliminary result maybe shows the true nature.

We will show a "typical type phenomena" in the following:

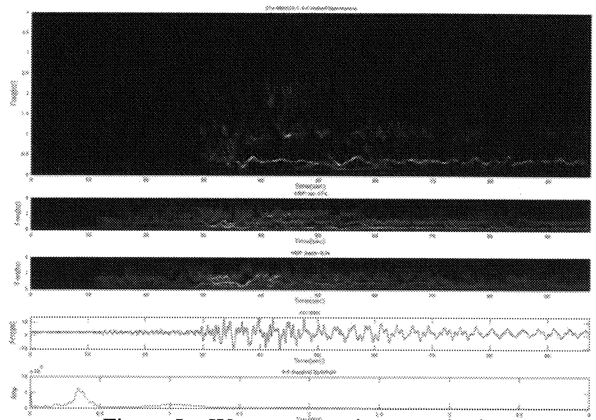

Figure 5 Wave propagating magnitude.

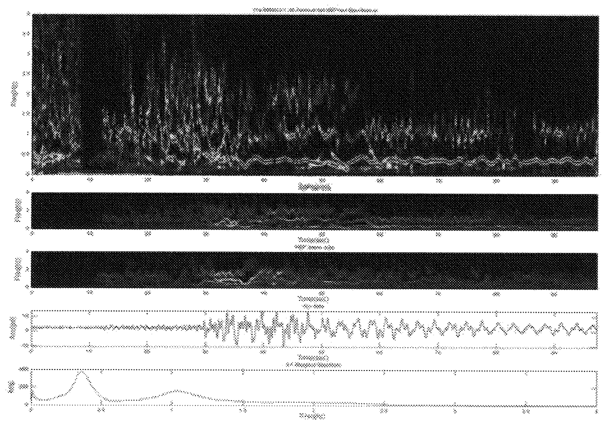

Figure 6 Wave propagating characteristic of 27F.

We can observe real dynamic behavior of Taipower building in Figures 5 and 6. The two figures show the modal energy distribution of the 27f. First, look at the upper chart of both figures. The third dominant modal frequency is about 2.09 Hz, it only existing in the strongest S-wave section. The second dominant modal frequency is about 1.04 Hz, it only existing in the S-wave section. The first (fundamental) dominant modal frequency is about 0.36 Hz, it keeps to the end of the record. The three dominant modal frequency keeping in perturbation in the figure, we think that's the phenomena of nonlinear and non-stationary characteristic of building. On the lowest chart of Figure 5, the energy-frequency relationship for magnitude, there are three dominant modal frequency existing during the whole record.

Figure 6 shows the structure modal energy characteristic of 27^{th} floor. We can see the energy distribution in the quiet section and P-wave section and total frequency band changing scenario in the whole data.

After we observe the magnitude and characteristic of dominant modal frequency, we start to find the coherence of structure in different floor records.

The following Figures 7~9 shows the structure coherence of modal characteristic of the 27f, 19f, 9f (all with respect to b3f). We can see the difference in different location. After further investigation in the future, we hope this figure can help us find out the damage position after earthquake.

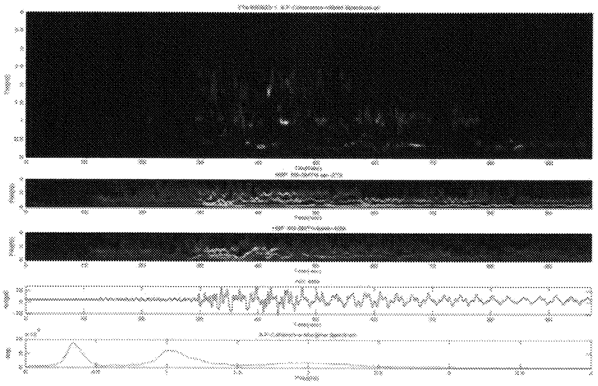

Figure 7 Structure coherence characteristic of 27F.

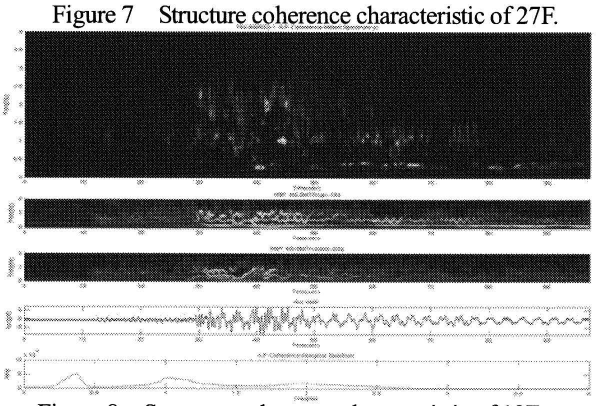

Figure 8 Structure coherence characteristic of 19F.

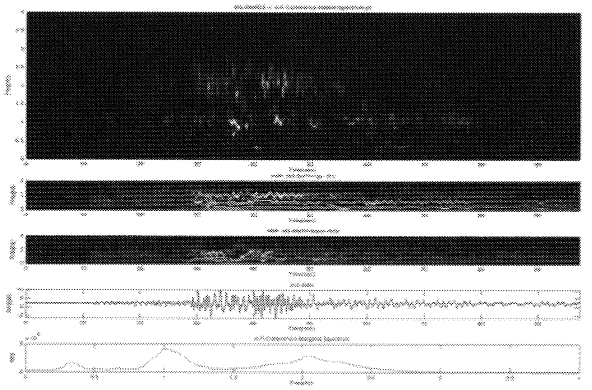

Figure 9 Structure coherence characteristic of 9F.

4. CONCLUSIONS AND DISCUSSIONS

We find out there is a bad senor in the 49^{th} event, it makes anomalous peaks in yellow line on Figure 3. Comparisons of modal dominant frequency between different methodologies are made by us. Loh (1998) used ARX identification method, Wang (2002) used Kalman Filter and Genetic Algorithm identification method. The values are very close, it seems new HHT method having the same performance with the old methods. The HHT analysis we use total record to calculate the modal dominant frequency in this paper, it means we calculated the average value of the whole record. Actually, we should focus on S-wave section only. The second and third modal dominant frequencies only exist in S-wave section.

After Observations from Figures 5 and 6, the four sections: Quiet section contains surroundings noise nature of the station, sometimes it's fulfilled with tiny P-wave excitation for long-distance earthquakes. P-wave section contains pressure wave which always behaves in higher frequency band than the S-wave section, but the amplitude is relative smaller than the S-wave. The S-wave section is the most important part; it carries destructive force in low frequency range and within the largest amplitude. The Coda section always contains two kinds of information. The excitation force of earthquake-surface-wave and the free-vibration characteristic of the building. In the future researches, the four segments should be discussed separately.

HHT results are not only in time domain but also in frequency domain, so we need to discuss the parameter of time in the future. In this paper, the earthquake arrival time between different positions is taken as the same.

Good presentations of structure intra characteristics are showed by HHT, only by Signal-processing skills. Detail behaviors are shown on these figures, nonlinear and non-stationary parameters are all available, so fundamental model can be adjusted or be reset by new parameters.

Acknowledgements:

The article used data from TSMIP-BA system of the Central Weather Bureau(CWB). The staff in the CWB have contributed to the planning, design, maintenance and other affairs and operating the system so well. We thank CWB for those contributions.

References:

Huang, N. E., Shen, Z., Long, S. R., Wu, M. C., Shih, S. H., Zheng, Q., Tung, C. C., and Liu, H. H. (1998), "The empirical mode decomposition method and the Hilbert spectrum for non-stationary time series analysis," Proc. Roy. Soc. London, A454, 903-995.

Wu, Z. and Huang, N. E. (2004), "A study of the characteristics of white noise using the empirical mode decomposition method," Proc. Roy. Soc. London, 460, 1597-1611.

Flandrin, P., Rilling, G., and Gonçalves, P. (2005), "EMD Equivalent Filter Banks, from interpretation to applications. Hilbert-Huang Transform and Its Applications," 57-74, Ed. N. E. Huang and S. S. Shen, World Scientific, Singapore.

Borcheret, R. D., (1970), "Effect of local geology on ground motion near San Francisco Bay", Bull. Seism. Soc. Am., 60, 29-61.

Wen, K. L., H. Y. Peng, Y. B. Tsai, and K. C. Chen (2001), "Why 1 g was recorded at TCU129 site during the 1999 Chi-Chi, Taiwan earthquake? " ,Bull. Seis. Soc. Am., 91, 5, 1255-1266, 2001. (SCI)

Loh, C. H. S. H. Hsieh, B.Y. Yang, S. T. Mau (1997),"Development of Automatic MIMO System Identification Program to Analyze the Seismic Response Data from Taiwan Building." Technical report Vol.19, No: MOTC-CWB-86-E-11,1997

Lin, W.C , Wang, G.S. (2001), "Application of Kalman Filter to Structural Dynamic Parameter Identification. " ,Master Thesis 2001,CYUT,Taiwan.

Lin, H.H , Wang, G.S. (2002), "Application of Genetic Algorithm to Structural Dynamic Parameter Identification", Master Thesis 2002,CYUT,Taiwan.

Fifth International Conference on Urban Earthquake Engineering
March 4-5, 2008, Tokyo Institute of Technology, Tokyo, Japan

TIME DOMAIN BEM ANALYSIS OF A CYLINDER EMBEDDED IN SOIL WITH ANISOTROPY

Alan Tan[1], and Sohichi Hirose[2]

1) Postdoctoral Researcher, Center for Urban Earthquake Engineering, Tokyo Institute of Technology, Japan
2) Professor, Dept. of Mech. and Environmental Informatics, Tokyo Institute of Technology, Japan
tan.a.aa@m.titech.ac.jp, shirose@cv.titech.ac.jp

Abstract: 2D time domain BEM for anisotropic elastic solids is used to study the dynamic response of a cylinder embedded in anisotropic soil. The scattering of waves by the cylindrical inclusion is studied. The cylinder embedded is either bonded or partially debonded. Debonded regions are considered as interface cracks with traction free surface. Also, the crack opening displacements of the debonded areas are considered. In this regard, the 2D BEM used here is based on the displacement boundary integral equations Tan et al. (2005) and the fundamental solutions are the ones derived by Wang and Achenbach in Wang *et al.* (1994). Synthetic seismic waves are incident to the cylinder and the displacements are considered. Different soil materials are also discussed and the differences in material velocities are shown. Further development for the applying the stick-slip type of boundary conditions is also discussed.

1. INTRODUCTION

Soil and rock formations are naturally anisotropic or with weak anisotropy. The purpose of this research is to see the effects of the waves as it propagates along an anisotropic soil with a cylindrical inclusion. The cylindrical inclusion is modeled using a circle in two dimensional media. The effect of the anisotropy on the displacement of a fully bonded cylinder as well as partially debonded cylinder is being studied here. The aim of this paper is to further analyze the interaction of seismic waves on inclusions. The 2D boundary element method (BEM) of anisotropic solids in previous works by the authors (Tan et al., 2005) is used for this study. The dynamic response of an embedded object is of interest for earthquake engineering and usually the assumption of perfect bonding between the material and the soil is carried out. But for practical problems, partial debonding or slipping occurs and this would severely change the response of the solid to vibration and seismic waves. Feng et al., (2003) studied the interface having contact but slipping. Currently, this paper shows only partial debonding. But further plan is to apply the slip and stick type boundary conditions to an embedded solid and to see the effect of anisotropy in the said problem.

2. PROBLEM STATEMENT

Consider a homogeneous anisotropic linearly elastic media with an inclusion as shown in Figure 1. Assume that the inclusion is embedded in an infinite region and an incident wave is propagated along the media. Without body forces, the solids must satisfy the equations of motion and Hooke's law (Zhang et al., 2002) as follows:

$$\sigma_{i\beta,\beta} = \rho \ddot{u}_i , \tag{1}$$

$$\sigma_{i\beta} = C_{i\beta k\lambda} u_{k,\lambda} , \tag{2}$$

where u_i denote the displacement components, $\sigma_{i\beta}$ are the stress components, ρ denotes the mass density, and C is the elasticity tensor. The equations follow the index notation where small roman numerals denote 1, 2 and 3 while the Greek subscripts denote 1 and 2 only. A comma denotes partial derivative while dot denotes derivative with respect to time. Repeated indices denote summation. u^{in}, shown in Figure 1, is the incident wave. The figure also shows a part of the boundary of the cylinder debonded from the outer matrix. In the figure the surrounding soil is considered as domain 1 while the embedded cylinder is called domain 2.

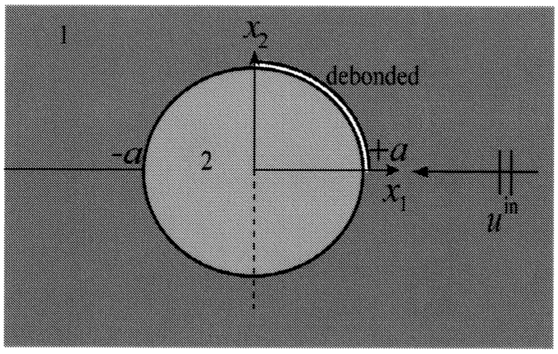

Figure 1 Cylindrical inclusion in 2D soil

As mentioned and shown, there are two regions with different boundary conditions. One is debonded while the other is the stick type or fully bonded region. Local coordinates are shown in Figure 2 and the boundary conditions are given in local coordinates. For the stick regions, the interface stresses are continuous as well as the displacements. These conditions may be written as

$$\begin{aligned} u_t^{(1)} &= -u_t^{(2)} \\ u_n^{(1)} &= -u_n^{(2)}, \end{aligned} \quad (3)$$

$$\begin{aligned} \sigma_t^{(1)} &= \sigma_t^{(2)} \\ \sigma_n^{(1)} &= \sigma_n^{(2)}, \end{aligned} \quad (4)$$

where t and n means normal and tangent to the surface, respectively. (1) and (2) here denotes the domain number. n is the unit normal vector while $\boldsymbol{\tau}$ is the unit tangential vector as shown in Figure 2. For the fully debonded region, the region will be considered to be traction free and the displacements are different in the two regions. The conditions are written as

$$\begin{aligned} u_t^{(1)} &\neq -u_t^{(2)} \\ u_n^{(1)} &\neq -u_n^{(2)}, \end{aligned} \quad (5)$$

$$\begin{aligned} \sigma_t^{(1)} &= \sigma_t^{(2)} = 0 \\ \sigma_n^{(1)} &= \sigma_n^{(2)} = 0 \end{aligned}. \quad (6)$$

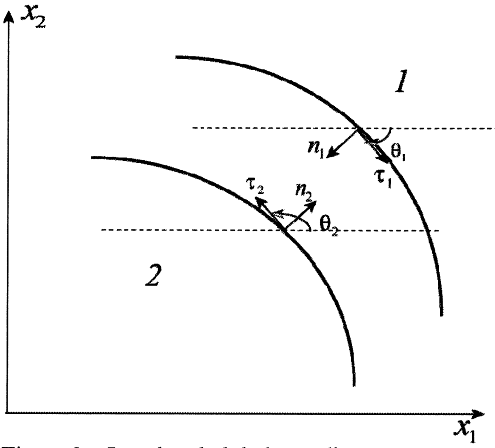

Figure 2 Local and global coordinate systems

3. BOUNDARY ELEMENT METHOD

The formulation of the general boundary integral equations for elastodynamic problems can be written using the Betti-Rayleigh reciprocal theorem. The system is assumed to be at rest at t < 0. The governing boundary integral equations for both regions may be written as

$$\begin{aligned} & u_k^{in}(\boldsymbol{y},t) - \int_S h_{ik}\left[(\boldsymbol{x}-\boldsymbol{y}),e(\boldsymbol{x});t\right] * u_i(\boldsymbol{x},t)d\boldsymbol{x} \\ & + \int_S g_{ik}\left[(\boldsymbol{x}-\boldsymbol{y}),e(\boldsymbol{x});t\right] * t_i(\boldsymbol{x},t)d\boldsymbol{x} \\ & = \begin{cases} u_k(\boldsymbol{y},t) & \boldsymbol{y}\in \boldsymbol{D} \\ u_k(\boldsymbol{y},t)/2 & \boldsymbol{y}\in \boldsymbol{S} \\ 0 & \text{otherwise} \end{cases} \end{aligned} \quad (7)$$

where S is either S_1 or S_2, surfaces in either domains, g_{ik} and h_{ik} are the displacement and traction fundamental solutions at time t. '*' denotes time convolution. D denotes the domain (either D_1 or D_2). t_i here denote tractions. It should be noted that u^{in} becomes zero for domain 2 if the incident wave is considered to be applied from domain 1 and vice versa. **x** and **y** are the source and observation points, respectively,. h_{ik}, the time-domain elastodynamic stress fundamental solutions are defined by

$$h_{ik}\left[(\boldsymbol{x}-\boldsymbol{y}),e(\boldsymbol{x});t\right] = C_{i\alpha j\beta}e_\alpha g_{jk,\beta}\left[(\boldsymbol{x}-\boldsymbol{y});t\right], \quad (8)$$

where e is a unit normal vector. For brevity, the time domain fundamental solutions for 2D anisotropic solids as derived by Wang et al. (1994) are given as follows,

$$\begin{aligned} g_{ij}^S(\boldsymbol{x}) &= -\frac{1}{4\pi^2}\int_{|n|=1}\sum_{l=1}^{L}\frac{P_{ij}^l}{\rho c_l^2}\log|\boldsymbol{n}\cdot\boldsymbol{x}|d\boldsymbol{n} \\ g_{ij}^R(\boldsymbol{x},t) &= \frac{H(t)}{4\pi^2}\int_{|n|=1}\sum_{l=1}^{L}\frac{P_{ij}^l}{\rho c_l^2}\log|c_l t+\boldsymbol{n}\cdot\boldsymbol{x}|d\boldsymbol{n} \end{aligned} \quad (9)$$

where $P_{ij}^l = E_{il}E_{jl}$ and

$$\left\{\Gamma_{pi}(n_1,n_2)-\rho c_l\delta_{pi}\right\}E_{il} = 0,(l=1,\ldots,L), \quad (10)$$

superscripts R and S denotes static (singular) parts and the dynamic (regular) parts.

4. NUMERICAL RESULTS

Consider a circular cylinder embedded in an infinite soil subjected to a P wave given by:

$$\begin{aligned} u_i^{in} &= u_0 D_i \sin\left\{\frac{\pi}{2a}\left[c_n t-(x_1+a)\sin\theta - x_2\cos\theta\right]\right\} \\ &\times H\left[c_n t-(x_1+a)\sin\theta - x_2\cos\theta\right] \end{aligned} \quad (11)$$

where θ is the angle of the incident wave (measured clockwise from negative x_2-axis, u_0 is the amplitude and H[ ] is the Heaviside function. D_i depend on the material properties and for isotropic materials, D_1 is sin θ and D_2 is cos θ . c_n denotes material velocity, 1 is for P-wave or quasi

P-wave or longitudinal wave speed and 2 for S-wave or quasi S-wave or transverse wave speed. Table 1 gives the material constants for the cylinder and the surrounding isotropic soil as used by Feng et al. (2003) and it also includes material properties for concrete and other soil types specifically Berea sandstone and coarse sand. Table 2 provides the material constants for transversely isotropic solids and the formations are for Austin chalk and Cotton valley shale (from Sinha et al. (2006)). A Transversely isotropic (TI) anisotropy can be expressed in terms of a 6x6 matrix as

$$C_{ij}=\begin{bmatrix} C_{11} & C_{12} & C_{13} & 0 & 0 & 0 \\ & C_{11} & C_{13} & 0 & 0 & 0 \\ & & C_{33} & 0 & 0 & 0 \\ & & & C_{44} & 0 & 0 \\ & & & & C_{44} & 0 \\ & & & & & C_{66} \end{bmatrix}, \tag{12}$$

where $C_{66}=(C_{11}-C_{12})/2$. As can be seen here, the material properties of the surrounding soil vary a lot and the anisotropy could in fact provide different conditions. For the given cylinder, the P-wave velocity is 1010 m/s and S-wave velocity of 583 m/s. The material properties for the cylinder were used by Feng et al. (2003). But if concrete is used for the cylinder, the P-wave would reach as high as 3737m/s while the S-wave would be 2282 m/s.

Table 1 Material constants of the cylinder and surrounding isotropic soil (Feng et al. (2003) and concrete and other soil types.

	Mass density ($x10^3$ kg/m^3)	Shear modulus ($x10^8$ Pa)	Poisson ratio
Cylinder	2.5	8.5	0.25
Soil (Feng)	2.0	1.8	0.25
Concrete	2.4	125	0.20
Rock (Berea sandstone)	2.458	60	0.20
Coarse sand	1.884	0.98	0.30

For the soil (Feng), the P-wave is a slow 519m/s and S-wave of 300m/s. The P and S-waves for Berea sandstone are 2551m/s and 1562m/s, respectively. For coarse sands, the waves are much slower, 425m/s and 228m/s. Amazingly, for the transversely isotropic materials (taken from Sinha), the wave speeds are much faster (because the soils are deeper and denser – are somewhat rocks). Austin chalk has a quasi P-wave of 3162m/s and SH- and SV-waves of 1187m/s and 1044m/s while Cotton valley shale has 5320m/s, 3370m/s and 2890m/s.

Two models are considered here, one is as shown in Figure 1 where the wave is incident from domain 1 and with direction to the negative x_1 axis. Quadrant I contains the debonded region. The second model is where all the elements are perfectly bonded. The radius of the circle (cylinder) is a=1.5m. In the calculations, the interface is subdivided into 80 elements.

Table 2 Material constants of the surrounding anisotropic soil (Sinha et al. (2006))

Formation	Rho kg/m^3	C11 ($x10^8$ Pa)	C12 ($x10^8$ Pa)	C13 ($x10^8$ Pa)	C33 ($x10^8$ Pa)	C44 ($x10^8$ Pa)
Austin chalk	2.2	220	158	120	140	24
Cotton valley shale	2.64	747.3	147.5	252.9	588.4	220.5

Only calculations for the isotropic soil (from Feng) with cylinder, soil (Feng) with concrete cylinder, Coarse sand with concrete cylinder and shale with concrete cylinder are shown. Figures 3-6 plots the displacements on the soil at $\pi/3$. The cylinder in Figure 3 uses a very low shear modulus as compared to the concrete cylinder and thus the displacements are much larger because of its ability to resist deformation. Comparing Figure 4 and 5, the displacements show a lot of similarities although the amplitudes differ. Finally, the shale, a TI anisotropic solid, shows a big difference with larger displacement and very different forms.

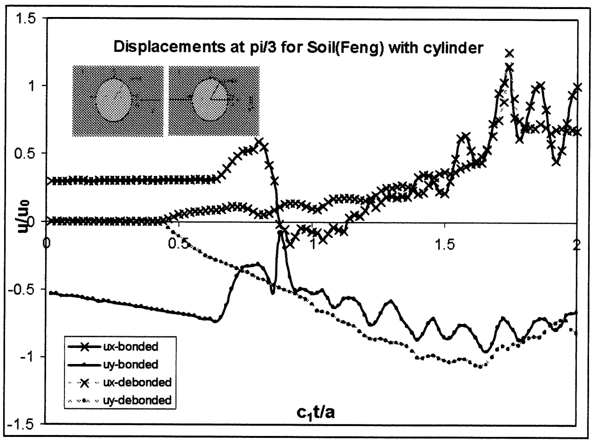

Figure 3 Displacements at $\pi/3$ for isotropic soil with cylinder for both bonded and debonded models

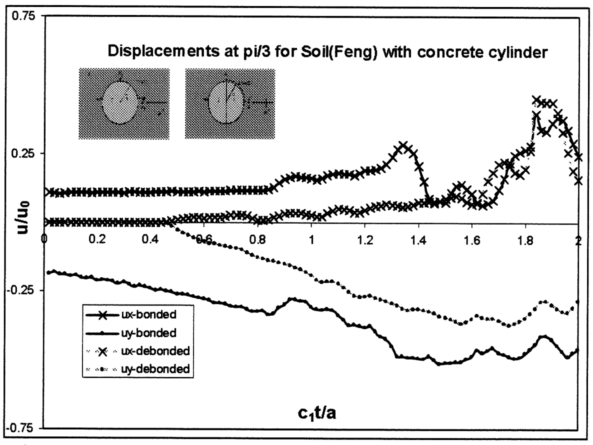

Figure 4 Displacements at $\pi/3$ for isotropic soil with concrete cylinder for both bonded and debonded models

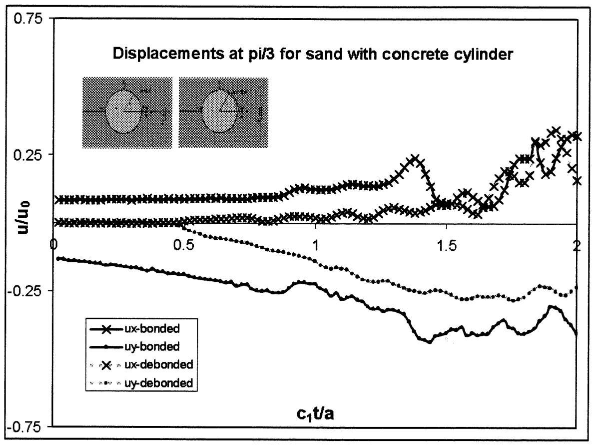

Figure 5 Displacements at $\pi/3$ for isotropic soil with concrete cylinder for both bonded and debonded models

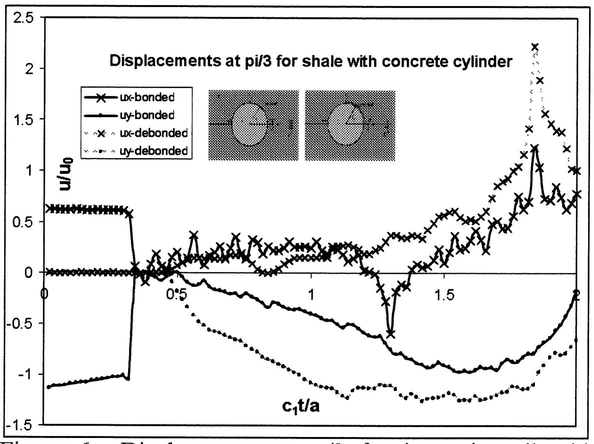

Figure 6 Displacements at $\pi/3$ for isotropic soil with concrete cylinder for both bonded and debonded models

5. CONCLUSIONS

The 2D BEM for anisotropic solids was implemented for two types of boundary conditions, perfectly bonded and partially debonded. Synthetic waves are used as incident waves. Calculations for the displacements and stresses are shown here. Further simulations are to be done for the slip-stick boundary conditions.

6. SLIP-STICK BOUNDARY CONDITIONS

For future work, the slip-stick boundary conditions will be applied and this section introduces the difference from the previous discussions. As discussed by Feng et al. (2003), a cylinder of infinite length embedded in an infinite solid has two possible boundary regions. Although we can argue that it should have another third possible boundary region where the interface is totally debonded. But local separation is to be ignored by assuming a confining pressure that will be applied to the interface. The stresses are again assumed to be continuous and the two different conditions are to be given.

For slip regions, the domains are assumed to be in contact with Coulumb friction. The boundary conditions for the slip regions are given as

$$\begin{aligned} u_t^{(1)} &\neq -u_t^{(2)} \\ u_n^{(1)} &= -u_n^{(2)}, \end{aligned} \tag{13}$$

$$\begin{aligned} \sigma_n^{(1)} &= \sigma_n^{(2)} \\ \left|\sigma_t^{(1)}\right| &= \left|\sigma_t^{(2)}\right| = f\left|\sigma_n^{(1)}\right|, \end{aligned} \tag{14}$$

where f is the coefficient of friction. Slipping occurs when the tangential stress exceeds the static friction stress but in this case we take it to be equal to the kinetic value. Thus only f is used for both conditions. The boundary conditions for the stick regions are given in eqns. (3) and (4). It should be noted that the type of boundary conditions for each elements may change depending values of the stresses per time step. Thus the type of boundary conditions are to be determined using an iterative method.

Acknowledgements:

The authors acknowledge support from Japan Ministry of Education, Culture, Sport, Science, and Technology (MEXT) for establishing the Center for Urban Earthquake Engineering (CUEE) in Tokyo Institute of Technology. The support has made possible this international conference, as well as international joint research projects and exchange programs with foreign universities.

References:

Tan, A., Hirose, S., Zhang, Ch., and Wang, C.-Y. (2005),"A 2D Time-domain BEM for Transient Wave Scattering Analysis by a Crack in Anisotropic Solids," *Engineering Analysis with Boundary Elements*, **28**, 610-623.

Zhang, Ch. and Zhu, H. (2002), "Transient Dynamic Analysis of an Antiplane Interface Crack in Anisotropic Solids," *Electronic Journal of Boundary Elements, Vol. BETEQ2001*, **2**, 179-186.

Wang C-Y and Achenbach, JD. (1994), "Elastodynamic fundamental solutions for anisotropic solids," *Geophys J Int*, **118**, , 384-392.

Feng, Y., Wang, Y., and Zhang, Z. (2003), "Time domain BEM analysis of dynamic response of a cylinder embedded in soil with frictional slip at the interface", *Soil Dynamics and Earthquake Engineering*, **23**, 303-311.

Feng, Y., Wang, Y., and Zhang, Z. (2003), "Transient scattering of SH waves from an inclusion with a unilateral frictional interface-a 2D time domain boundary element analysis", *Commun. Numer. Meth. Engg*, **19**, 25-36.

Sinha, B., Simsek, E., Liu, Q. (2006), "Elastic-wave propagation in deviated wells in anisotropic formation", *Geophysics*, 71, no. 6, D191-D202.

Fifth International Conference on Urban Earthquake Engineering
March 4-5, 2008, Tokyo Institute of Technology, Tokyo, Japan

EFFECT OF ACTIVE CONFINEMENT ON SHEAR BEHAVIORS OF HIGH-STRENGTH CONCRETE COLUMNS PRESTRESSED LATERALLY

Yasuji Shinohara [1)]

1) Associate Professor, Structural Engineering Research Center, Tokyo Institute of Technology, Japan
shinohara.y.ab@m.titech.ac.jp

Abstract: Experiments and 3-D FEM analyses were performed on high-strength concrete columns laterally prestressed by high-strength shear reinforcement in order to study the influence of active confinement on the shear strength and crack behaviors. Lateral prestress was introduced in proportion to the concrete strength, and the width of every crack near the transverse reinforcement was measured by a digital microscope. By increasing the lateral prestress as mentioned above, the shear crack strength and ultimate shear strength increased, but the effectiveness of active confinement was weakened as the axial force ratio decreased. FEM analyses can be used to evaluate the shear crack strength and the ultimate shear strength, and to explain the effect of active confinement on shear behaviors because FEM analyses evaluates the intensity of confinement in a tri-axial state of stress with minor principal stress as well as the degree of damage for compressive failures.

1. INTRODUCTION

Prestressing concrete structures is generally performed to control flexural cracks because prestressing arranges the tendons in the axial direction of a given member. On the other hand, in an attempt to delay the onset of shear cracking and to reduce the crack width, experimental studies have been conducted on reinforced concrete (RC) columns, which have been laterally prestressed by high-strength shear reinforcement [Watanabe et al. 2004]. The results of these flexure-shear tests have indicated that transverse prestressing increases the shear capacity at the first diagonal cracking (shear crack strength) and remarkably decreases the width of shear cracks, especially their residual openings. This reduction of the crack opening improves durability as well as earthquake resistance.

The main objectives of the present study are (1) to investigate how transverse prestressing in high-strength concrete columns affects the shear behavior with respect to the propagation of cracks and the triaxial state of stress, and (2) to quantitatively estimate the effect of active confinement on shear behaviors based on the triaxial state of stress in the concrete by 3D FEM analyses.

2. OVERVIEW OF TEST AND ANALYSIS

2.1 Test Specimens and Analytical Models

Figure 1 shows the details of the test specimen and the finite element model. Table 1 summarizes the specifications of the specimens. The compressive strength of the concrete used in the present study was aimed to be 45 and 90 N/mm^2 (Fc45 and Fc90). The ratio of the axial load to axial strength for Fc90 was limited to 0.15 due to the capacity of equipment, while that for Fc45 was set to 0.15 and 0.3 in order to investigate the effect of axial load on shear crack behaviors. Flexure-shear tests were performed on RC columns that were laterally prestressed (LPRC) and not prestressed (RC). Test designation was expressed by LPRC or RC, compressive strength, and the ratio of axial load to axial strength. The test specimens had a square cross section of 340 mm x 340 mm and a height of 900 mm. The specimens were designed to reach shear failure before the longitudinal reinforcement yield, in accordance with the design guidelines of the Architectural Institute of Japan (1999). For this reason, high-strength steel bars (D22, in Fig.

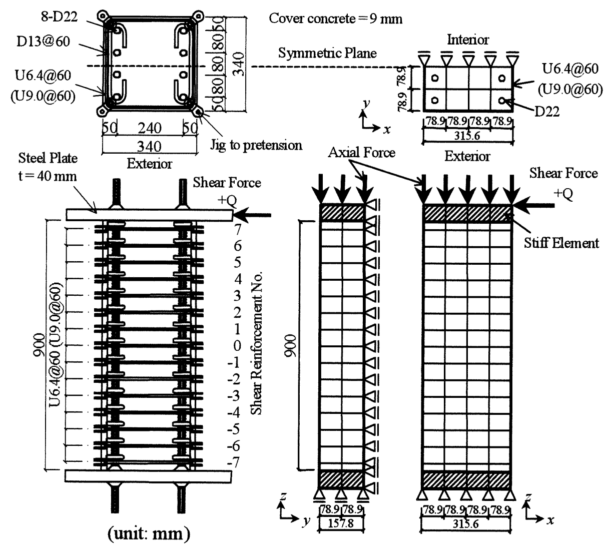

Figure 1 Details of Test Specimen and Finite Element Model

1, σ_y=1187 N/mm^2) were used for longitudinal reinforcement. Moreover, additional rebars (D13 in Fig. 1) were arranged to prevent columns from splitting due to bond failure. The lateral prestress, σ_L, which is proportional to the strength of the concrete, σ_B, (σ_L/σ_B≈0.03) was introduced into concrete as follows: (1) high-strength transverse hoops (U6.4, U9.0 in Fig. 1) were pretensioned to approximately 30% of the yield stress using rigid steel molds and special jigs, which are shown in Fig. 1, (2) concrete was placed vertically into the molds and cured until the strength of the concrete increased sufficiently, (3) the core concrete was laterally prestressed by removing the steel molds. The product of the ratio, p_w, and the stress, σ_{wp}, of the pretensioned transverse reinforcement was defined as the average lateral prestress, σ_L (=$p_w\sigma_{wp}$), to indicate the intensity of lateral prestress. Table 2 provides the mix proportion of concrete used in the test specimens. The coarse aggregate used in the mix is natural round sea gravel with a maximum aggregate size of 25 mm. The mechanical properties of the concrete and reinforcement are shown in Figs. 2 and 3 along with their idealizations in FEM analysis.

Table 1 List of Test Specimens

Test Designation	σ_B (N/mm^2)	σ_0/σ_B	p_w (%)	σ_{wp} (N/mm^2)	σ_L (N/mm^2)	σ_L/σ_B
RC-45-0.15	44.2	0.15	0.29	0	0	0
LPRC-45-0.15	46.2			513	1.5	0.032
RC-90-0.15	91.9	0.15	0.63	0	0	0
LPRC-90-0.15	93.0			428	2.7	0.029
RC-45-0.30	50.8	0.30	0.29	0	0	0
LPRC-45-0.30	46.5			536	1.6	0.034

σ_B=compressive strength of concrete,σ_0=axial stress of column, p_w=ratio of transverse hoop, σ_{wp}=introduced prestress in transverse hoop, σ_L=lateral prestress (=$p_w\,\sigma_{wp}$), RC-45-0.30 and LPRC-45-0.30 after Shinohara (2005)

Table 2 Mix Proportion (Unit: kg/m^3)

Nominal Strength	W / C	Water	Cement	Sand	Aggregate	Super-plasticizer
Fc45	0.50	184	373	762	945	0.93
Fc90	0.30	155	517	857	861	3.88

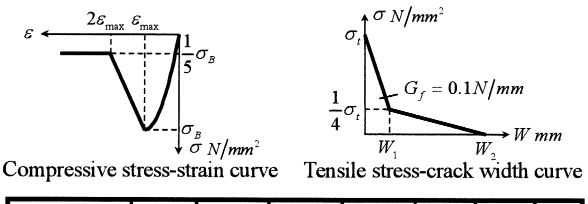

Test series	σ_B N/mm^2	ε_{max}	E_c N/mm^2	σ_t N/mm^2	W_1 mm	W_2 mm	ν
RC-45-0.15	44.2	-0.002	3.34E+4	2.6	0.034	0.17	0.2
LPRC-45-0.15	46.2	-0.002	3.41E+4	2.7	0.033	0.16	0.2
RC-90-0.15	91.9	-0.0026	4.21E+4	5.3	0.017	0.083	0.2
LPRC-90-0.15	93.0	-0.0026	4.30E+4	5.3	0.017	0.083	0.2
RC-45-0.30	50.8	-0.002	3.51E+4	2.9	0.031	0.15	0.2
LPRC-45-0.30	46.5	-0.002	3.45E+4	2.9	0.031	0.15	0.2

Figure 2 Mechanical Properties and Analytical Model for Concrete

Type	σ_y (N/mm^2)	σ_{max} (N/mm^2)	E_s (N/mm^2)
D22	1187	1298	1.96E+5
U6.4	1471	1506	2.05E+5
U9.0	1405	1466	2.05E+5

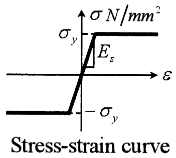

Figure 3 Mechanical Properties and Analytical Model for Reinforcement

2.2 Loading and Measuring Methods in Tests

Figure 4 shows the loading apparatus. The vertical force on the test specimen was supplied by a 2 MN hydraulic jack, and the ratio of axial load to axial strength was maintained constant at 0.15 or 0.3 during the test. The horizontal force was supplied by two hydraulic jacks with a capacity of 500 kN and 1000 kN, and the horizontal force was controlled in displacement. The cyclic horizontal load was applied to produce an antisymmetric moment in the column. The horizontal load was reduced when the rotation angle of a column, R, reached ±1/400, ±1/200, ±1/100, ±1/67, and ±1/50, until it reached the peak load. Two digital microscopes, which each had a resolution of 0.01 mm, were used to measure the width of each shear crack near the shear reinforcement three times for each loading cycle and twice for each unloading cycle. The crack width used in the present study was defined as the distance normal to the direction of the crack, which is illustrated in Fig. 5. Three strain gauges, locations, and designations, which are shown in Fig. 5, were attached to each leg of the transverse hoops.

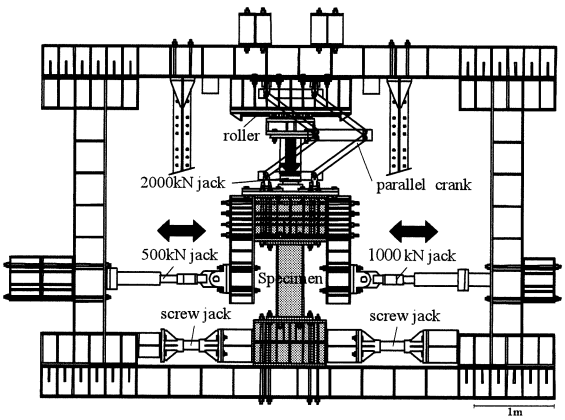

Figure 4 Loading Apparatus

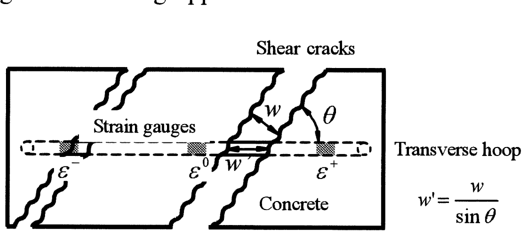

Figure 5 Definition of Crack Width and Designation of Strain Gauges

2.3 Assumptions and Procedures in Analyses

Figure 1 shows the finite element mesh and boundary conditions. Due to symmetry, only half of the column was analyzed. The stiff elements were attached at the top and bottom of a column to idealize the steel stubs. The top nodes were constrained to move uniformly in the vertical direction and to prevent rotation of the upper stiff elements, so that a column was deformed in an antisymmetric mode. Concrete was modeled by a twenty-node isoparametric solid brick element, and longitudinal reinforcement was embedded in the concrete elements to add stiffness. The shear reinforcement was modeled by a two-node numerically integrated truss element because the effect of bending was negligible. The bond-slip between the concrete and reinforcement was not considered in the analyses because an additional reinforcement was installed to avoid a bond splitting failure. The prescribed prestress was introduced into the shear reinforcement, then an axial load was applied with load control in ten steps up to the designated axial load ratio, and finally the shear load was applied with displacement control and a step of 0.01 mm. The maximum-tensile-stress criterion of Rankine was adopted as the failure criterion in the tension zone of concrete. According to this criterion, a crack arises when the maximum principal stress exceeds the tensile strength, regardless of the normal or shearing stresses that occur on other planes. Smeared cracking and bi-linear tension softening, which are shown in Fig. 2, were adopted in the analyses. The shear stiffness of cracked concrete generally depends on the crack width. This phenomenon is taken into account by decreasing the shear stiffness as the normal crack strain increases.

2.4 Mechanical Properties of Confined Concrete

Drucker-Prager criterion was used as the failure criterion in the compressive zone of concrete. The formulation is given by

$$f(I_1, J_2) = \alpha I_1 + \sqrt{J_2} - k = 0 \tag{1}$$

$$\alpha = \frac{2\sin\phi}{\sqrt{3}(3-\sin\phi)} \tag{2}$$

$$k = \frac{6\cos\phi}{\sqrt{3}(3-\sin\phi)}c \tag{3}$$

$$I_1 = \sigma_1 + \sigma_2 + \sigma_3 \tag{4}$$

$$J_2 = \left[(\sigma_1-\sigma_2)^2 + (\sigma_2-\sigma_3)^2 + (\sigma_3-\sigma_1)^2\right]/6 \tag{5}$$

where ϕ is the internal-friction angle, c is the cohesion, σ_1, σ_2, and σ_3 are the principal stresses. The internal-friction angle of confined concrete has often been estimated as 37.5° based on the experimental results performed on concrete cylinders with uniform lateral pressure by Richart (1928). According to Richart, the strength of concrete confined by lateral pressure increases to (σ_B+4.1σ), regardless of the intensity of σ, where σ_B is the uniaxial compressive strength of concrete and σ is the lateral pressure. Takamori et al. (1996, see Fig. 6) studied the effects of lateral confinement using concrete cylinders with different concrete strengths and hoop spacing. According to their test results, the strength of concrete confined by hoops similar to our specimen increases approximately to (σ_B+2.0σ), and the effect of confinement decreases as the strength of the concrete and the spacing of hoops increase. An increasing rate to σ of 2.0 is less than half of 4.1, which was proposed by Richart (1928) due to the partial confinement by the hoops. This internal-friction angle was estimated as 20°. From these results, the internal-friction angle is assumed as to be 20° for Fc45 and 15° for Fc90. Consequently, Drucker-Prager criterion is as follows:

$$f(I_1, J_2) = 0.15 I_1 + \sqrt{J_2} - 19.3 = 0 \qquad \text{for } Fc45 \tag{6}$$

$$f(I_1, J_2) = 0.11 I_1 + \sqrt{J_2} - 42.1 = 0 \qquad \text{for } Fc90 \tag{7}$$

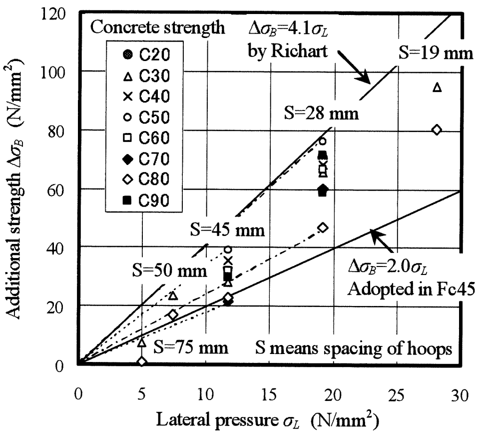

Figure 6 Relationships between Lateral Pressure and Additional Strength (Takamori et al. 1996)

3. SHEAR BEHAVIORS BY EXPERIMENT

3.1 Shear Load-Rotation Angle Curves

Figure 7 shows the shear load Q-rotation angle R curves obtained from the tests and compares them to the results of FEM analyses. A typical crack behavior observed during the tests was that flexural cracks initially appeared and then extended into flexural shear cracks near both ends of the specimen. Finally, shear cracks occurred as the shear load increased. The shear loads for both RC and LPRC were gradually reduced without reinforcement yielding because the concrete was crushed in the compressive zone at the top and bottom ends. Table 3 presents the shear crack strength and ultimate shear strength obtained from experiments and FEM analyses as well as the calculation results reported by Watanabe (2004), which consider the lateral prestress. The shear crack strength of analysis is defined as the shear load that causes the strain in the shear reinforcement to increase rapidly. The maximum shear load for the LPRC90-0.15 column was assumed to be 1048 kN when R = -1/50 because the welding of a longitudinal rebar was ruptured in loading to R=1/33. When the ratio of axial load for Fc45 series decreased from 0.30 to 0.15, the shear crack strength was reduced by 33% for the RC column and 22% for the LPRC column, and the ultimate shear strength was reduced by 4% for the RC column and 14% for the LPRC column, whereas the rotation angles at the peak load for both columns redoubled. As shown in Table 3, both FEM analyses and the calculations predict with a fair degree of precision the difference between the shear strength of the RC and LPRC columns. The relationship between shear crack stress, ${}_{exp}\tau_{sc}$

($=_{exp}Q_{sc}/bD$), and lateral prestress, and that between ultimate shear stress, $_{exp}\tau_{su}$ ($=_{exp}Q_{su}/bD$), and lateral prestress are plotted in Fig. 8, where the axis of abscissas indicates the ratio of lateral prestress, σ_L, to compressive strength, σ_B. The shear crack strength and the maximum shear strength increased with the same rate when the same ratio of σ_L/σ_B was introduced. Due to an increase in shear crack strength with increasing axial load, the effect of lateral prestress on the shear crack strength decreased as the axial load increased. On the other hand, for the maximum shear strength, the effect of lateral prestress was weakened as the ratio of the axial load to axial strength decreased, which is probably due to the triaxial state of stress in the core concrete and is investigated by FEM analyses in the next section.

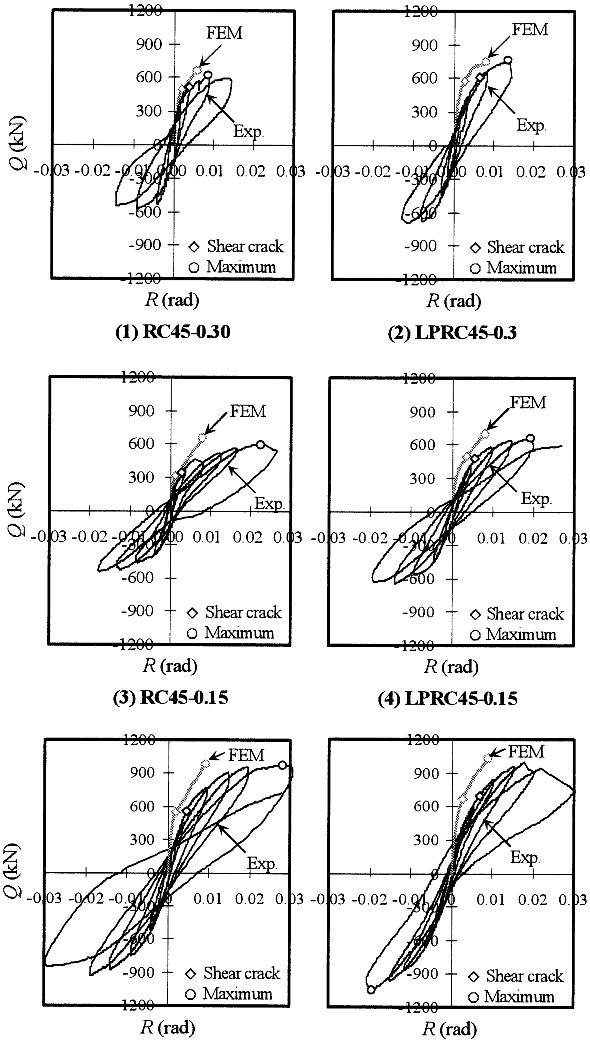

Figure 7 Comparisons between Analytical and Experimental Q-R Curves

Table 3 Shear Crack Strength and Ultimate Shear Strength

Test Designation	$_{exp}Q_{sc}$ (kN)	$_{exp}Q_{su}$ (kN)	$_{FEM}Q_{sc}$ (kN)	$_{FEM}Q_{su}$ (kN)	$_{cal}Q_{sc}$ (kN)	$_{cal}Q_{su}$ (kN)
RC45-0.15	343	595	316	646	339	484
LPRC45-0.15	475	658	498	699	450	—
RC90-0.15	562	973	551	983	564	820
LPRC90-0.15	780	1048	669	1027	774	—
RC45-0.30	515	617	495	655	496	591
LPRC45-0.30	611	762	577	747	606	—

$_{exp}Q_{sc}$ =shear crack strength by experiment, $_{exp}Q_{su}$ =ultimate shear strength by experiment
$_{FEM}Q_{sc}$ =shear crack strength by FEM, $_{FEM}Q_{su}$ =ultimate shear strength by FEM
$_{cal}Q_{sc}$ =shear crack strength by ref.(1), $_{cal}Q_{su}$ =ultimate shear strength by modified Arakawa

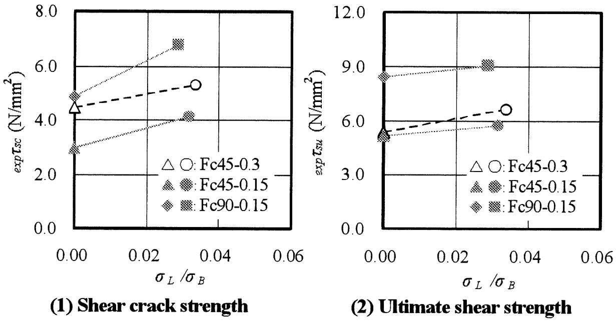

Figure 8 Increase in Shear Strength due to Lateral Prestress

3.2 Shear Crack Patterns

Figure 9 compares the shear cracks in the front of RC and LPRC specimens at maximum shear loads. Moreover, the figure shows the location with the maximum crack width and the inclination of the primary shear crack. The crack patterns in the front and back of the specimens were similar. The lateral confinement in the LPRC specimen greatly restrained the shear cracks from propagating so that the final crack pattern of the LPRC drastically differs from that of the RC. Shear cracks developed extensively in the upper and lower sides of the LPRC specimen, but they developed intensively in the center of the RC specimen. The spacing and width of the scattered cracks in the LPRC specimen were smaller than those of the localized cracks in the RC specimen. Because the ability to transmit shear force across a rough crack is exponentially reduced as crack width increases (Shinohara et al. 1999), a scattered crack with a smaller width can, to some extent, reduce the decrease in shear stiffness of a column. This small crack spacing in the LPRC specimen is probably due to an increase in both bond strength and tensile stress, which were generated by introducing lateral prestress.

Figure 10 shows the relationship between shear load and maximum crack width marked by ■ in Fig. 9. In the Fc45 series, the crack width of RC series rapidly increased immediately after cracking and exceeded 1 mm at the maximum load, but the crack width of LPRC series was approximately 0.5 mm at the peak load and 0.2 mm when unloaded. The crack width tended to increase as the axial load decreased. The increase in the shear load of the RC45-0.30 specimen was only 100 kN after cracking, whereas the shear load of the LPRC45-0.30 specimen increased by 150 kN after cracking. The transverse prestressing reduced the width values of shear cracks, especially their residual opening, and increased the shear stiffness after shear cracking. Consequently, this prestressing improved durability as well as earthquake resistance for the

RC structures. In the Fc90 series, the effect of the lateral prestress was not prominent due to the close confinement by the redoubled shear reinforcement.

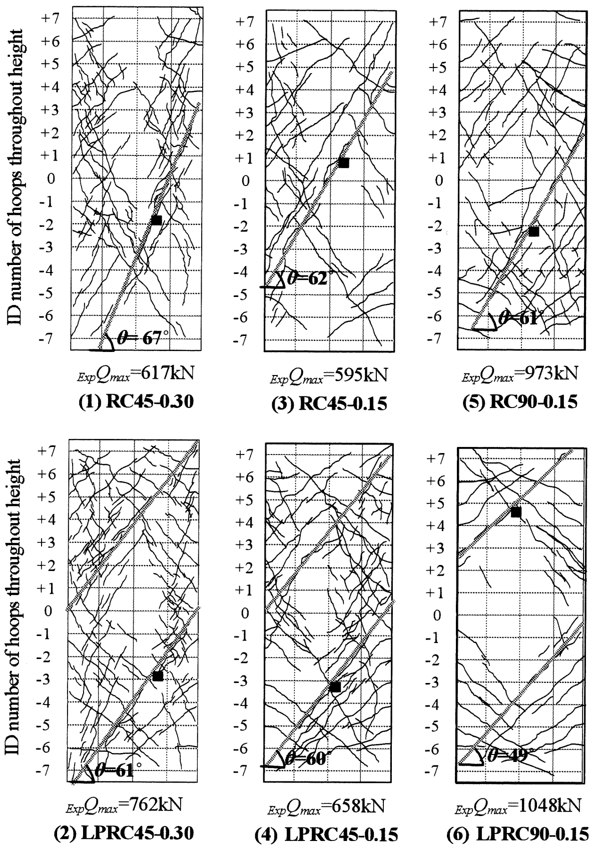

Figure 9 Crack Patterns at Maximum Shear Loads

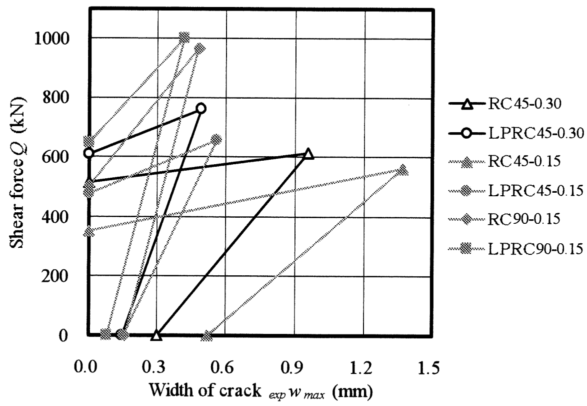

Figure 10 Relationships between Shear Force and Maximum Crack Width

4. TRIAXIAL STATE OF STRESS BY ANALYSES

The effect of the lateral confinement on the shear behavior was evaluated based on the triaxial state of stress in the concrete from 3D finite element analyses performed on the RC and LPRC specimens. Figure 11 shows the distributions of the minor principal stress in the center of the RC and LPRC specimens at the maximum loads. The analyses were also performed on the Fc90-0.15 specimens with a diameter of 6.4 mm for shear reinforcement (U6.4) in order to exclude the effect of its quantity. For the specimens with an axial load ratio of 0.3, introducing lateral prestress broadened the width of the compressive strut formed by a large compressive stress at the maximum load. Consequently, the ultimate shear strength became higher than the RC specimen. This difference is probably due to the crack patterns of the RC and LPRC specimens described above. On the other hand for the LPRC45-0.15 specimen, the width of the strut did not increase much because the smaller axial load lessened the confining effect from the triaxial state of compressive stress. For the specimens with a diameter of 9.0 mm for the shear reinforcement (U9.0), a relatively broad strut was formed due to the distributed crack pattern, and a substantial increase in the width of the strut did not occur in the LPRC specimen. For the LPRC90-0.15 specimen with U6.4, the strut width and the maximum shear load were approximately the same as the RC specimen because the shear reinforcement yielded around the peak load.

The degree of damage for compressive failures and the equivalent confining pressure were introduced as gauges to quantitatively evaluate the effect of active confinement on the stress state in the core concrete, as shown in Fig. 12. The degree of damage for compressive failures was defined using the deviated part of the stress state in principal stress

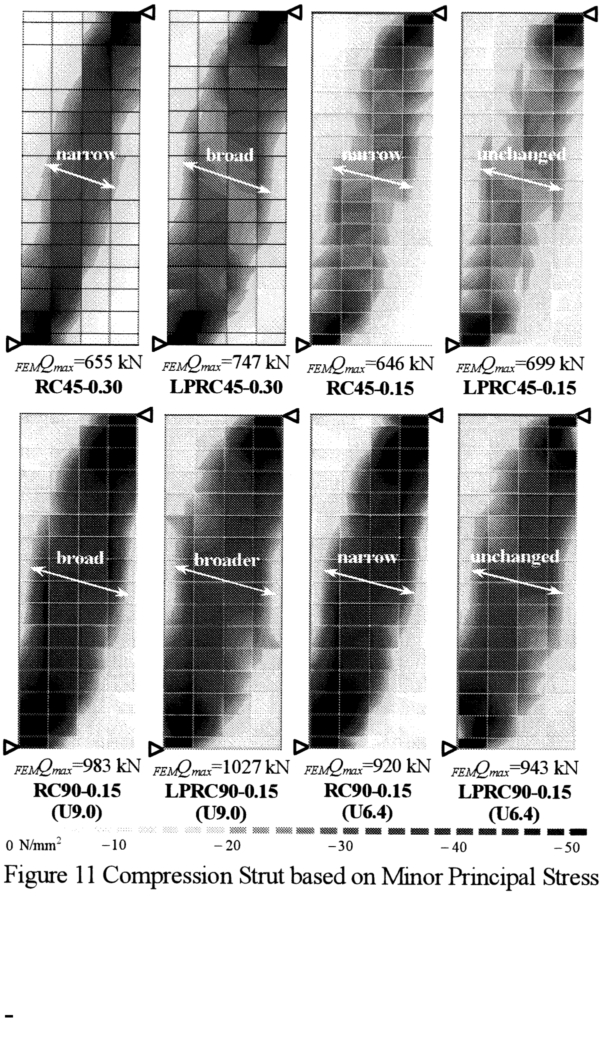

Figure 11 Compression Strut based on Minor Principal Stress

space. Figure 13 shows the degree of damage for compressive failures in the surface of the RC and LPRC specimens at the maximum shear loads. Figures 11 and 13 show that the distributions of the degree of damage correspond roughly to those of the minor principal stress. The degree of damage in the LPRC specimen compares favorably with that in the RC specimen at the same shear load due to active confinement (Shinohara et al. 2005). The red parts dotted with a white dot at the top and bottom ends (Fig. 13) represent the post-peak softening zone of concrete. Thus, the failure mode of analyses is quite similar to that of experiment. In a similar way to the width of the compressive strut, introducing lateral prestress enlarged post-peak softening zone, but the effect of the lateral prestress was weakened as the axial load decreased. Compared to the Fc45 specimen, the softening zone in the Fc90 specimen is limited to a small area in the corner, and the effect of the lateral prestress is lessened despite the diameter of shear reinforcement. Furthermore, the degree of damage in the Fc90 specimen is, on the whole, less than that in the Fc45 specimen. This indicates that the collapse of high-strength concrete is chiefly caused by a localized fracture process zone even if most portions are not damaged much, and that high-strength concrete is sensitive to the scale effect. Therefore, it is important for high-strength concrete to have a number of shear reinforcements and to improve resistance to the localized fracture by a substantial confinement.

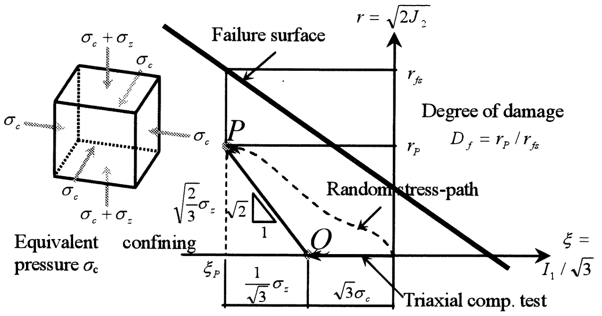

Figure 12 Degree of Damage and Equivalent Confining Pressure for Triaxial State of Stress in Meridian Plane of Drucker-Prager Criterion

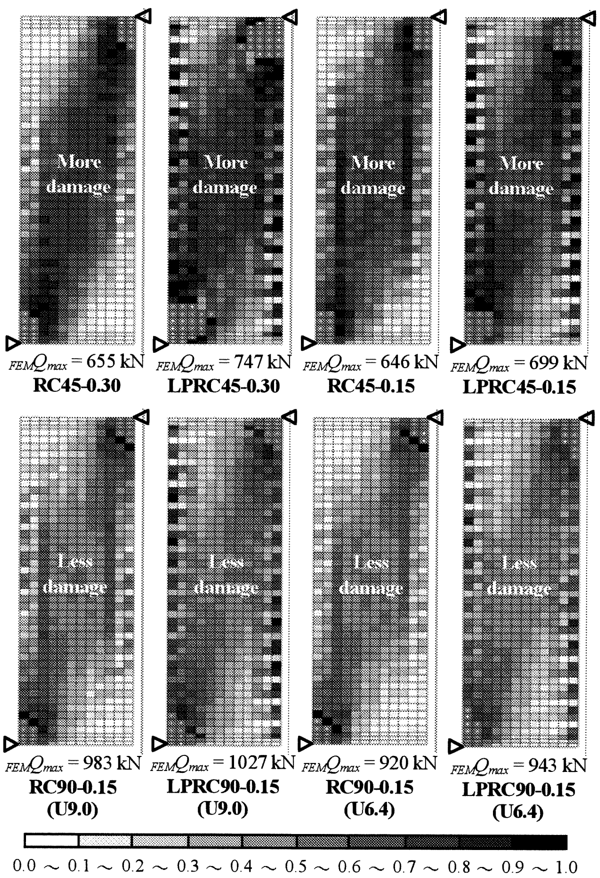

Figure 13 Comparison of Damage in Compression Zone

5. CONCLUSIONS

The experiments and 3-D FEM analyses on high-strength RC columns prestressed laterally were used to investigate the effects of active confinement on shear behaviors. The results led to the following conclusions:

1) The shear crack strength and maximum shear strength increase at the same rate upon introducing the same ratio of lateral prestress to compressive strength.
2) Although the ultimate shear strength increases with lateral prestress, the effect of active confinement by the lateral prestress is weakened as the axial load decreases.
3) The effect of the lateral prestress is concealed as the shear reinforcement increases because a distributed crack pattern similar to a LPRC specimen is formed.
4) High-strength concrete is sensitive to the scale effect because the collapse of high-strength concrete is mainly caused by a localized fracture process zone even if most portions are not damaged much.
5) Although the shear stiffness after shear cracking declines for specimen with smaller shear reinforcement, introducing lateral prestress improves considerably.

References:

Watanabe, H. et al. (2004). "Shear crack control by lateral prestress on reinforced concrete column and evaluation of shear strength." *J. Struct. Const. Eng.*, AIJ, No.577, pp.109-116 (in Japanese)

Architectural Institute of Japan (1999). "Design Guidelines for Earthquake Resistant Reinforced Concrete Buildings Based on Inelastic Displacement Concept." (in Japanese)

Shinohara, Y. et al. (2005). "Active confining effect and shear crack behavior for R/C columns prestressed laterally." *J. Struct. Const. Eng.*, AIJ, No.587, pp.147-153 (in Japanese)

Richart, F.E., Brandtzaeg, A. and Brown, R. L. (1928), "A Study of the Failure of Concrete under Combined Compressive Stresses", Univ. of Illinois, Engineering Experiment Station, Bulletin, No.185

Takamori, N., Benny Benni Assa, Nishiyama, M. and Watanabe, F. (1996), "Idealization of Stress-Strain Relationship of Confined Concrete", *Proceedings of the Japan Concrete Institute*, Vol.18, No.2, pp.395-400

Shinohara, Y. and Kaneko, M. (1999). "Compressive shear behavior in fracture process zone of concrete." *Journal of Structural and Construction Engineering*, AIJ, No.525, pp.1-6 (in Japanese)

Fifth International Conference on Urban Earthquake Engineering
March 4-5, 2008, Tokyo Institute of Technology, Tokyo, Japan

EVALUATION OF EARTHQUAKE DAMAGE OF REINFORCED CONCRETE BUILDINGS IN NIIGATA PREFECTURE

Daisuke Kato[1)], Tetsuo Nagahashi[2)], Takuya Kokubo[3)], and Yukiko Nakamura[4)]

1) Professor, Department of Civil Engineering and Architecture, Faculty of Engineering, Niigata University, Japan
2) SU Design Office, Niigata, Japan
3) Graduate Student, Department of Civil Engineering and Architecture, Faculty of Engineering, Niigata University, Japan
4) Lecturer, Department of Civil Engineering and Architecture, Faculty of Engineering, Niigata University, Japan
dkato@eng.niigata-u.ac.jp

Abstract: The objective building has suffered a great deal of damage during both the 2004 Chuetsu Earthquake and the 2007 Chuetsu Offing Earthquake. The damage of the first and the second floor during Chuetsu Earthquake was light although that by Chuetsu Offing Earthquake was moderate. This report introduces the properties of the earthquakes and the evaluated performance of the building. The result of a seismic response analysis is also reported. Moreover, the difference of failure modes between observation and calculation is also discussed.

1. INTRODUCTION

The Chuetsu Earthquake generated with the epicenter depth of 13km near Ojiya city of the Niigata Chuetsu district at 17:56 on October 23, 2004. An earthquake scale was M6.8 and the maximum seismic intensity was 7 on the Japanese scale in Kawaguchi town, Niigata. The Niigata Chuetsu Offing Earthquake generated with the epicenter depth of 17km of the Niigata upper Chuetsu Offing at 10:13 on July 16, 2007. An earthquake scale was M6.8 and the maximum seismic intensity recorded upper 6 on the Japanese intensity scale in Nagaoka city, etc.

Table 1 Properties of 2004 Chuetsu Earthquake and 2007 Chuetsu Offing Earthquake

JMA(Oguni Housaka)	2004 Chuetsu		2007 Chuetsu Offshore	
	EW	NS	EW	NS
max. ground acceleration PGA(gal)	692	395	613	504
max. ground velocity PGV (kine)	64.5	35.0	80.1 (composition of 3 directions)	

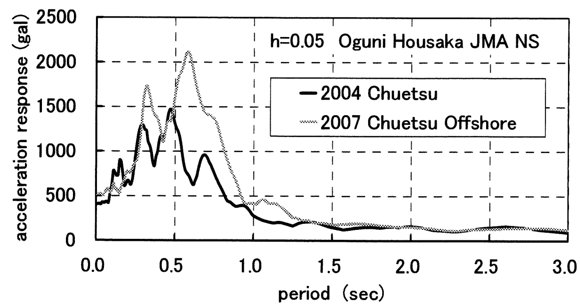

Figure 1 Acceleration response of 2004 Chuetsu Earthquake and 2007 Chuetsu Offing Earthquake(NS component)

2. DAMAGE OF THE BUILDING

The seismograph of Housaka, Oguni town, a nearest JMA seismograph, was located in about 3km of the directions of southwest of the building, and observed upper 6 on the Japanese intensity scale on the both sides of Chuetsu and the Chuetsu Offing Earthquake. Table 1 shows the maximum ground acceleration and velocity. Calculated acceleration response spectrum of NS direction, which is the parallel direction to the long direction of the building, is illustrated in Figure 1, showing that the response by the Chuetsu Offing Earthquake is larger that that by Chuetsu

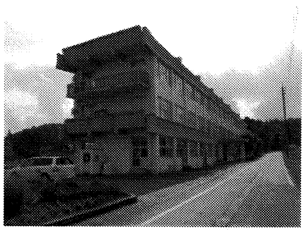

Photo 1 North view of S school building

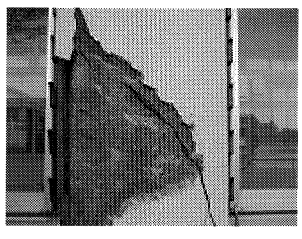

Photo 2 Shear failure of 1st floor column

Photo 3 Shear failure of 2nd floor column

Photo 4 Shear failure of shear wall

Earthquake in this direction.

The objective building is S elementary school classroom building in Oguni town of Nagaoka city, Niigata. This building was built in 1963. The photographs of the building and damaged members are shown in Photos 1-4.

3. FAILURE MODE OF COLUMNS

The seismic performance of the S building was evaluated. A list of the F value, which represents the deformation capacity, of 1st floor columns is shown in Figure 2. Although almost all columns failed in shear during the earthquake, the calculated results show those columns failed in flexure. This is a big problem when evaluating the earthquake resistance of a building.

In order to discuss the reason why those columns failed in shear although almost all columns were evaluated as flexural failing columns, the parametric study was conducted, paying attention to three parameters, strength of concrete, a hoop cross-section area and axial force. Figure 3(a) shows a case where strength of concrete is changed. Figure 3(b) shows a case where a hoop cross-section area is changed. Figure 3(c) shows a case where axial force is changed.

Those figures show that the effects of strength of concrete and a hoop cross-section area are very small and the real phenomenon can be explained when the subjected axial load was assumed to be very high, which could be caused by transverse and up-down earthquake motions.

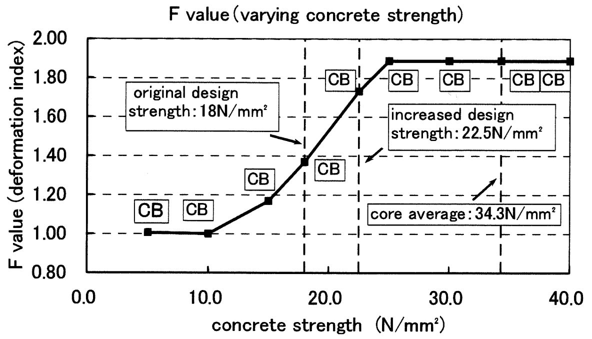

(a)Effects of concrete strength

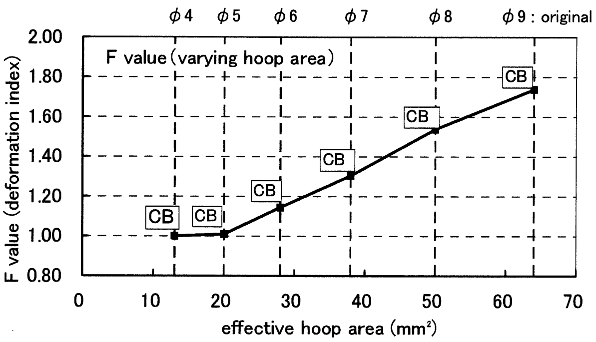

(b)Effects of hoop area

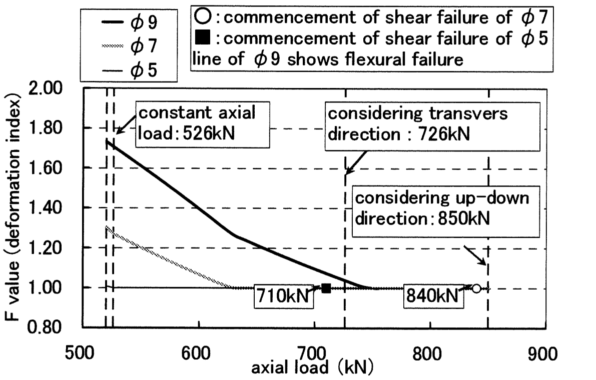

(c)Effects of axial load

Figure 3 Effects on calculated failure mode of column A-12

4. EARTHQUAKE RESPONSE ANALYSIS

Figure 4 shows a seismic-response-analysis result. The response by the Chuetsu Offing Earthquake is larger than that by the Chuetsu Earthquake, which can roughly explain the real damage. But the estimated damage is smaller than the real damage. It needs a future clarification because it is important to evaluate the action of the building which suffered a series of earthquake motions.

References:

Standard for Evaluation of Seismic Capacity of Existing reinforced Concrete Buildings, The Japan Building Disaster Prevention Association, 1990(in Japanese)

Standard for Judgment of Damage Level of Buildings Suffered from Earthquake, The Japan Building Disaster Prevention Association, 2001(in Japanese)

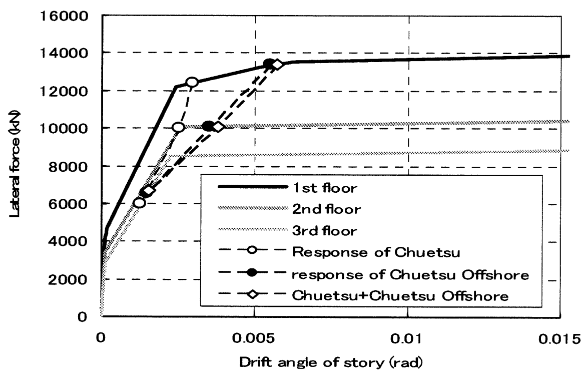

Figure 4 Calculated story response by Chuetsu and Chuetsu Offing earthquake

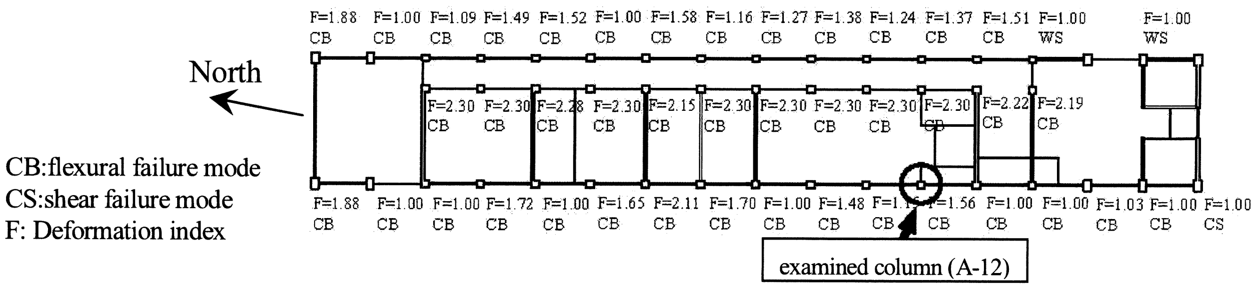

Figure 2 Evaluated failure mode of 1st floor columns and F value(deformation index) by Standard(1990)

Fifth International Conference on Urban Earthquake Engineering
March 4-5, 2008, Tokyo Institute of Technology, Tokyo, Japan

PERFORMANCE OF HYBRID SYSTEM WITH CORRUGATED STEEL SHEAR PANEL INSTALLED IN RC FRAMES

Susumu Kono[1], Yukako Ichioka[2], Yasuhiko Kashiwai[3], Yoshihiro Ota[4], and Fumio Watanabe[5]

1) Associate Professor, Dept. of Architecture and Architectural Engineering, Kyoto University, Japan
2) Ph. D. Candidate, Dept. of Architecture and Architectural Engineering, Kyoto University, Japan
3) Structural Engineer, NTT Facilities Inc., Nagoya, Japan
4) Research Fellow, Takenaka Research and Development Institute, Japan
5) Professor, Dept. of Architecture and Architectural Engineering, Kyoto University, Japan
kono@archi.kyoto-u.ac.jp, rc-ichioka@archi.kyoto-u.ac.jp, ohta.yoshihiro@takenaka.co.jp, kashiw30@ntt-f.co.jp

Abstract: This research aims to propose an economical seismic damage controlling system of RC frames using corrugated steel shear panels. This hybrid system was originally proposed by Mo and Perng in 2000. Their experimental results showed the poor seismic performance due to large relative displacement at the interface between surrounding RC members and a corrugated steel shear panel, and hence the obtained pinched hysteresis loops dissipated small amount of energy. Their test results made this hybrid system inappropriate to use in practical building design although great potential of the system was demonstrated. In this study, the hybrid system was revised to prove the excellence in controlling seismic damage. In an experimental phase a stud-type anchorage often used in bridge box girders was employed in four half-scale specimens to fix the corrugated shear panels, and then static cyclic loading was applied to the specimens. All hybrid frames showed more than 30% increase in lateral load carrying capacity. The degradation of lateral load carrying capacity after the peak load was small compared to reinforced concrete shear walls due to stable manner of yielding and buckling of corrugated steel shear panels. The final failure mode of the hybrid system was caused by tearing of the corrugated steel shear panel and forming a collapse mechanism of the surrounding reinforced concrete frame. In an analytical phase, a nonlinear frame analysis was conducted to evaluate the effect of corrugated steel shear panel on the performance of the reinforced concrete frame. The analysis simulated the behavior of the specimen with sufficient fixity of the shear panel but the specimens with insufficient anchorage had some room for improvement.

1. INTRODUCTION

It is a common practice to use reinforced concrete shear walls in high rise building structures to maintain high lateral load carrying capacity and stiffness. However, RC shear walls often increases the required lateral load carrying capacity in design because of its brittle ultimate failure mode. In order to improve the ductility of reinforced concrete shear walls, some efforts have been made by using low yield strength reinforcement or introducing slits but the ductility has not enhanced very much.

Steel shear walls have been used for some decades to increase ductility. In 1973, Takahashi et al. [1] studied the characteristics of load-deflection relations of steel shear walls obtained experimentally and reported the effects of configuration, width-thickness ratio, stiffeners' stiffness, etc. on the load-deflection relations. Studies on steel shear walls have been continued since then [2][3]. However, flat steel shear panels need stiffeners to prevent plate buckling, resulting in increase of self-weight and cost. In order to solve these problems, corrugated steel shear panels have been used in bridge structures since 1990s. They weigh less and decease prestressing loss due to their negligible axial stiffness compared to flat steel shear panels reinforced with stiffeners. Corrugated steel shear panels also have larger buckling strength than the flat panel due to its configuration. In 2000, Mo and Perng [1] reported the experimental work on corrugated steel shear panels as a main lateral load carrying component of building structures. They proved that corrugated steel shear panels are effective to delay buckling of shear panels. However, bolt anchorage fastening the shear panel to the surrounding RC frame was not very effective and a large slip took place at the interface. The resulting hysteresis loops were pinched and dissipated small energy. Their test results provided interesting information on the potential use of corrugated steel shear panels but shear panels have not been used in practice as a main lateral load carrying component as far as authors knows.

This paper re-examines use of corrugated steel shear panels as structural walls from the experimental work on RC portal frames with corrugated steel shear panels. The stud-type anchorage was employed to fully utilize the shear capacity and stiffness. The corrugated shear panels dissipate large energy after the peak load compared to RC shear walls.

Employing them as a main lateral load carrying component in building structures makes it possible to assign vertical load to columns and shear load to corrugated steel shear panels, resulting in a clear design philosophy. In addition, the ductility after shear yielding or even after buckling is excellent and the required lateral load carrying capacity may be decreased by considering the equal energy dissipation theory.

2. EXPERIMENTAL SETUP

Specimens were made of reinforced concrete portal frame with different anchorage configurations of corrugated steel shear panels [5]. Dimensions of four RC frames are identical as shown in Figure 1 and test variables are shown in Table 1. All shear panels had flange at all sides and two vertical stiffeners as shown in Figure 2. Thickness of vertical flange of Specimen C and four sides of Specimen D was 9 mm whereas other flange and stiffeners were 4.5mm. Mechanical properties of materials are listed in Table 2.

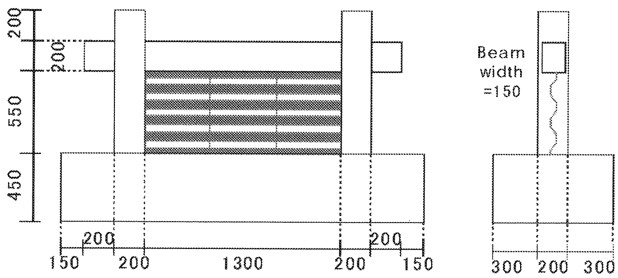

(a) Specimen dimensions

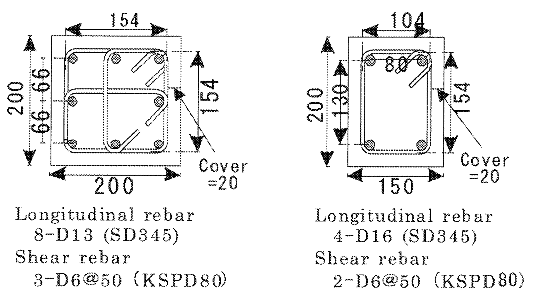

(b) Column reinforcement (c) Beam reinforcement

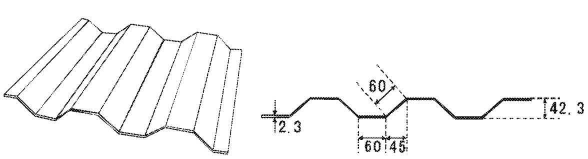

(d) Dimensions of the corrugated steel shear panel

Figure 1. Dimensions and reinforcement arrangement of specimens (Unit:mm)

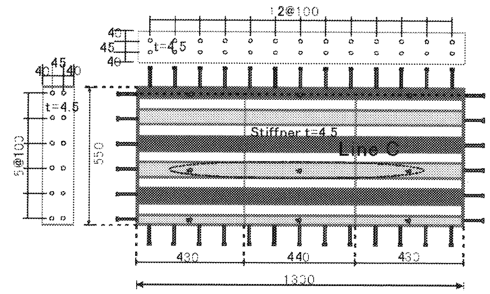

(a) Specimen A (Double studs)

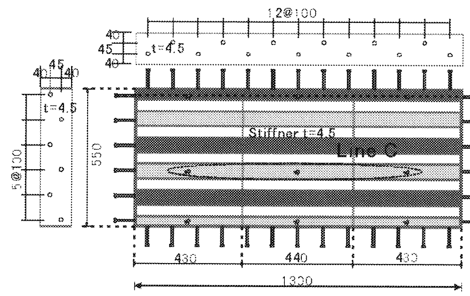

(b) Specimen B (Staggered studs)

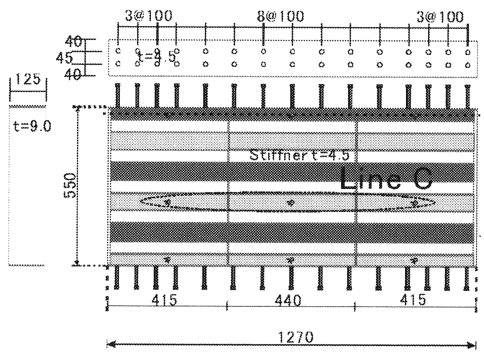

(c) Specimen C (Double studs on two sides)

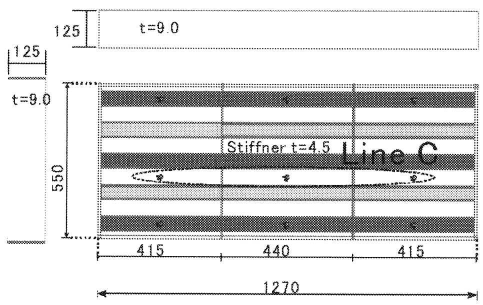

(d) Specimen D (No studs)

Figure 2. Dimensions of shear panels (Unit:mm. Each stud had a 9mm-diameter bolt with a head)

Table 1: Test variables

Specimen	Anchorage of the corrugated shear panel to the surrounding frame	Arrangement of studs	
		Horizontal joints (No. of studs)	Vertical joints (No. of studs)
A	studs	ϕ9 double@100 (26)	ϕ9 double@100 (12)
B	studs	ϕ9 staggered@100 (13)	ϕ9 staggered@100 (6)
C	studs	ϕ9 double@100 (30)*	None
D	grout mortar	None	None

* $\phi 9$ double@67.5 was used at the end region.

Table 2: Mechanical properties of materials

(a) Concrete

	Compressive strength (MPa)	Tensile strength (MPa)	Young's modulus (GPa)
Concrete	62.0	3.93	29.3
Mortar	63.4	–	–

(b) Steel

Type	Yield strength (MPa)	Tensile strength (MPa)	Young's modulus (GPa)
D6	1099	1207	196
D13	391	551	186
D16	391	569	180
Corrugated panel	264	362	191
Flange plate	282	438	200
Stud	479	512	208

The number of studs of Specimen A was determined based on the following equation[6][7].

$$(p/p_a)^{5/3} + (q/q_a)^{5/3} \leq 1.0 \qquad (1)$$

where p is the design tension force, q is the design shear force, p_a is the tensile strength when the stud experiences tension only, q_a is the shear strength when the stud experiences shear force only. The tensile strength, p_a, is the minimum value of 1) tensile strength due to a cone failure of surrounding concrete, 2) tensile strength due to tensile yielding of the stud, and 3) tensile strength due to bearing failure of concrete. The shear strength, q_a, is the minimum value of 1) shear strength due to bearing failure of concrete, and 2) shear strength due to shear yielding of the stud. The design tensile force, p, and the design shear force, q, was obtained from elastic FEM analysis as shown in Figure 3. In an analytical model, two columns and a beam consisted of cubic solid elements and corrugated shear panel and other steel plates consisted of shell elements. When the shear panel reached the yielding strength, the maximum normal stress was 31.5 N/mm^2 and the average shear stress was 160 N/mm^2 at the upper edge of the shear panel, which were substituted in p and q. Using of double studs of $\phi 9$ at 100 mm spacing, the left side of Eq. (1) became 0.99 and the equation was just satisfied. This determined the number of studs at the upper horizontal joint of Specimen A. The other interfaces were similarly computed. The number of studs was halved in Specimen B. The number of studs at the horizontal joints in Specimen C was basically the same with Specimen A but the number was increased so that the spacing was 67.5 mm instead of 100 mm at the end portion to prevent the local failure of studs as shown in Figure 2(c). Specimen D had no stud anchorage but the peripheral spacing was filled with high-strength grout mortal.

Figure 4 shows the loading system. Constant axial load of 365 kN (Axial load level 0.15) was introduced to each column. Equal magnitude of lateral load was applied to the both ends of the beam by two 1000 kN hydraulic jacks. Two cycles of lateral load was applied at ±150 kN and ±250 kN. Then two cycles of preselected drift angle was enforced at ±0.1%, ±0.2%, ±0.4%, ±0.6%, ±0.8%, ±1.0%, ±2.0%, ±4.0%. After 4.0%, drift was monotonically increased to +10 % which was limited by the loading system.

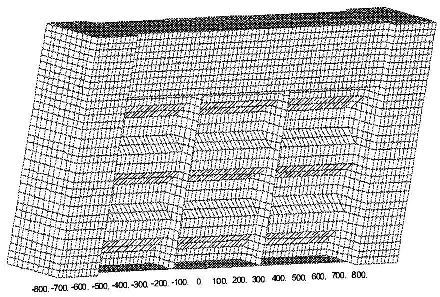

Figure 3. FEM analytical model to find the stresses at the interface between the shear panel and concrete.

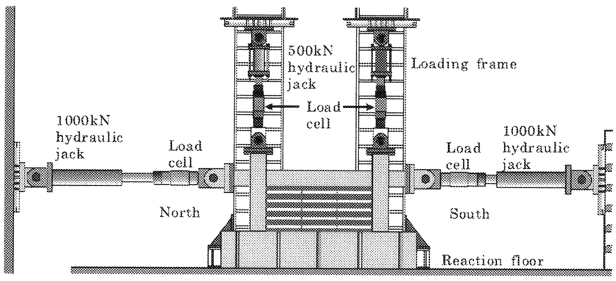

Figure 4. Loading system

3. EXPERIMENTAL RESULTS

3.1 Lateral load– drift relations

Figure 5 shows the lateral load – drift relations up to R=4.0%. Specimens A, B, and C showed similarly fat hysteresis loops up to the peak load at which buckling took place. Even after the buckling, the degradation of load carrying capacity was not drastic as RC shear walls failing in shear and reasonable amount of energy was dissipated. The degradation of load carrying capacity was severe in the order of Specimen C, B, A. Specimen D showed less peak load and hysteresis loops were pinched, and necessitated large drift angle to reach the peak load and the post-peak degradation of load carrying capacity was smaller than other three specimens. This is because Specimen D experienced openings at the interface between steel flange and joint mortar near the corner at R=±0.2% leading to the slip-type hysteresis loops afterward.

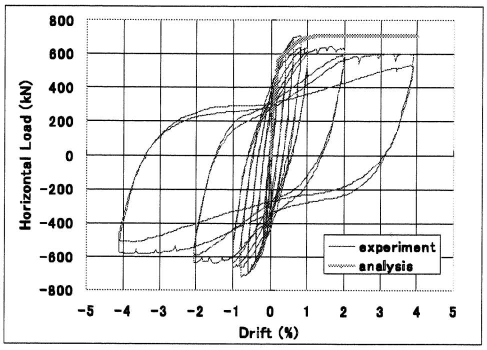

(a) Specimen A

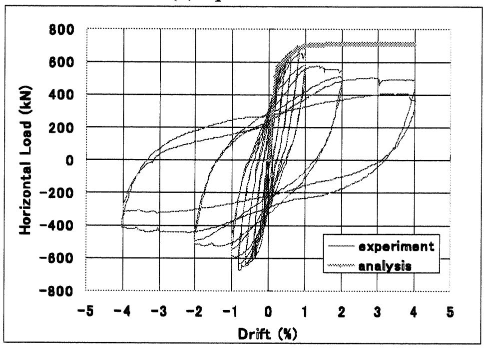

(b) Specimen B

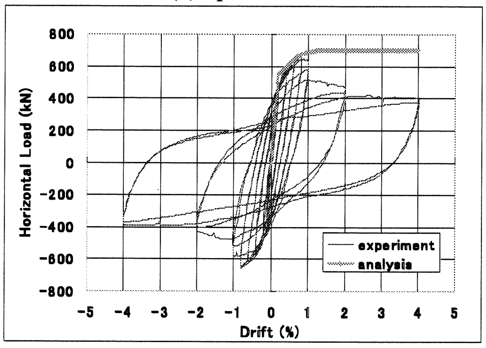

(c) Specimen C

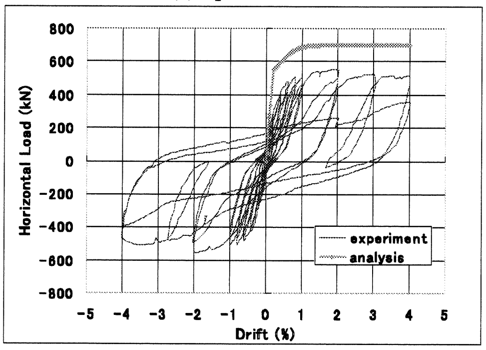

(d) Specimen D

Figure 5. Lateral load - drift angle relations and results of pushover analysis

The yielding lateral loads, lateral load carrying capacities and the initial stiffnesses are summarized in Table 3. The maximum lateral load capacity, Q_{max}, caused by buckling of the shear panel are larger n the order of Specimen A, B, C, and D and reflects the number of studs. However, the yielding lateral load, Q_y, was similar for all specimens although Q_y of Specimen B is slightly higher than the others. Drift angles at yielding, R_y, of Specimen A was the smallest and that of Specimen D was largest. Drift angle at yielding reflects the number of studs but it should be noted that the initial stiffness does not necessarily reflects the number of studs. Drift angle at the maximum capacity were similar for Specimen A, B, and C but that is much larger for Specimen D because of the slip at the interface. Specimens A, B, and C did not show any brittle failure until R=10%. The shear panel of Specimen D showed the out-of-plane deformation at R=5.0% and loading was terminated. It can be seen that behavior of the hybrid system is greatly affected by the amount of studs.

Table 3: Test results

Specimen	Yielding lateral load		Maximum lateral load capacity				Initial stiffness (10^5 kN/rad)
			Positive direction		Negative direction		
	Ry (%)	Qy (kN)	R (%)	Qmax (kN)	R (%)	Qmax (kN)	
A	+0.222	546	0.801	716	-0.759	-720	5.55
B	+0.359	614	0.797	702	-0.803	-676	4.10
C	+0.337	549	0.803	667	-0.733	-655	3.44
D	+1.338	544	1.97	556	-1.94	-555	4.56

3.2 Lateral load carried by shear panel

Lateral load carried by the shear panel is plotted in Figure 6(a). Shear force of the shear panel increased rapidly for Specimen A but with slower rate for the other specimens. As the number of studs increased, the shear panel became stiffer and the buckling initiated earlier. The ratio of lateral load carried by the shear panel to the total load is plotted in

Figure 6 (b) up to R=1.0%. The shear force carried by shear panel was computed from three Rosetta strain gages on Line C in Figure 2 assuming the plane stress condition and elastic-perfectly plastic yield condition with the von Mises yield criteria. It is seen that the shear panel carried 60% to 70% of the lateral load from the very beginning of the loading till buckling took place at R=1.0%. The computed contribution was 64% at the ultimate condition by considering the story shear force at the formation of collapse mechanism of the surrounding RC frame and the shear force of the shear panel at yielding.

3.3 Lateral load carried by shear panel

Equivalent viscous damping ratio (EVDR), H_{eq}, is shown in

Figure 7. EVDR of specimens with studs (Specimens A, B and C) increased rapidly from R=0.4% at which the shear panel yielded, and large amount of energy dissipated even after the buckling. Specimen A had largest EVDR and Specimen B had the second largest EVDR until yielding. Even after R=1.0%, a large amount of energy was dissipated in Specimen A, B, and C. The shear panel of Specimen D

did not follow the deformation of the RC frame and the yielding of the shear panel was delayed leading much smaller energy dissipation and EVDR.

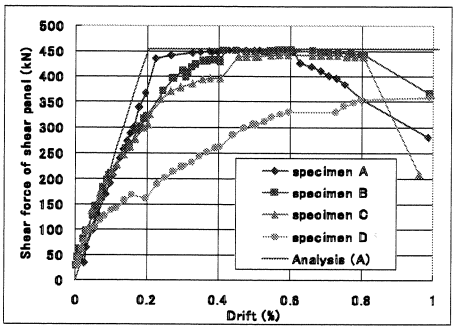

(a) Shear force of shear panel

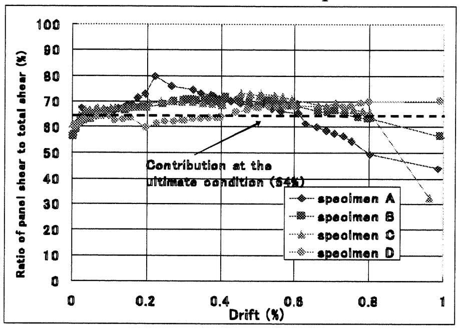

(b) Ratio of lateral load carried by the shear panel

Figure 6. Lateral load carried by the corrugated shear panel

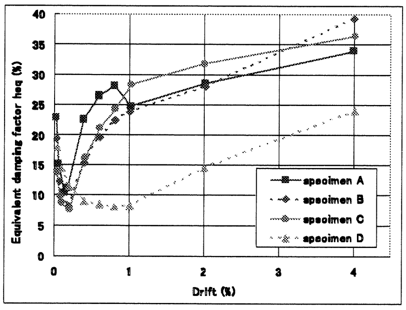

Figure 7. Equivalent viscous damping ratio, H_{eq}

4. ANALYTICAL MODELING

4.1 Numerical model with a frame analysis program

Behavior of the RC frame with the corrugated shear panel was simulated using a frame analysis program. The analytical model is shown in

Figure 8(a). Two columns and a beam were modeled as a single beam-column element with nonlinear rotational springs at both ends. Since the shear panel had shear stiffness without neither axial nor flexural stiffness, it was replaced with a nonlinear spring with an equivalent stiffness in the horizontal direction to the shear stiffness of the shear panel as shown in

Figure 8 (c). The nonlinear springs at the end of a beam and columns followed the trilinear curve defined in the design guidelines [8] and their moment-rotation relation is shown in

Figure 8 (b).

4.2 Analytical results

Results of pushover analysis are shown in Figure 5. A single analytical result assuming a perfect bond between the shear panel and concrete frame was plotted in all four figures. Analytical results well simulated the envelop curves for Specimens A, B, and C up to the peak although the analytical peak load became higher than the experimental load as the number of studs decreased. Analytical results of Specimen D overshot the experiment since the slip and opening behavior of shear panel is neglected.

Figure 6 (a) compares analytical shear force – drift relations of the shear panel in Specimen A to the experimental results. It is seen that the stiffness of the equivalent nonlinear spring is stiffer than the shear panel. Especially Specimen D did not reach the yield capacity even at R=1%.

Figure 9(a) shows the simulation of Specimen A up to R=2%. It also shows that the hysteresis loops were well simulated until R=1.0% at which buckling took place. After buckling, experimental loops became pinched but the analysis does not show this degradation.

Figure 9(b) separately shows the contribution of the shear panel and surrounding RC frame in the analysis.

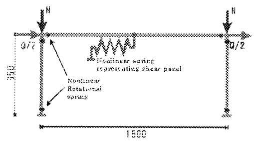

(a) Model

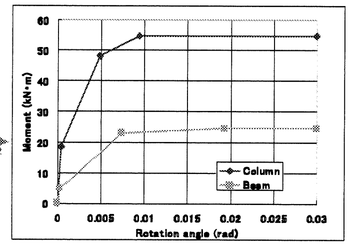

(b) Columns and beam

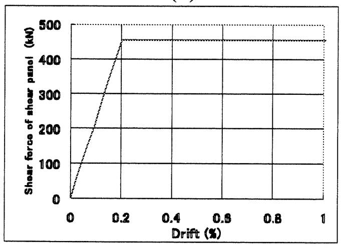

(c) Corrugated steel plate

Figure 8. Analytical model (Unit: mm)

5. CONCLUSIONS

A study was conducted on four RC frames reinforced with corrugated steel shear panel by varying the number of anchorage studs.

- The revised hybrid system with corrugated steel shear panels excellently behaved to control the seismic damage with large shear stiffness and shear capacity. In addition, the system showed some increase in shear force after yielding until buckling. The behavior after buckling was ductile and degradation in lateral load carrying capacity was about 20% even at R=5%. The behavior was stable if the number of studs satisfied the Japanese design guidelines (Specimen A). However, even specimens with half number of studs (Specimens B and C) showed the similar behavior although the stiffness and lateral load carrying capacity was lower.
- Lateral load carrying capacity at the peak was greater and the post-peak degradation of lateral load carrying capacity was greater for specimens with the larger number of studs. Specimen D, which had no stud anchorage, had smaller lateral load carrying capacity.
- Corrugated shear panel dissipated large amount of energy after yielding and the dissipation continued even after buckling of shear panel. Specimen D had inferior behavior on energy dissipation because of slip and opening at the interface.
- Analytical model well simulated the behavior of Specimen A but did not simulate the behavior of Specimens B, C, and D since the model assumed the complete anchorage.

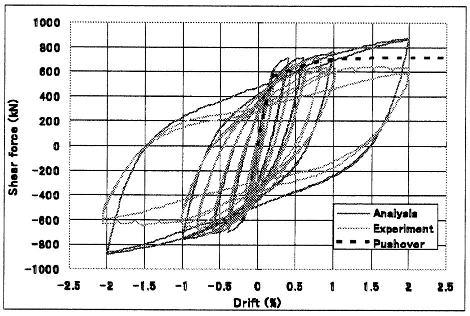

(a) Cyclic and pushover Analysis

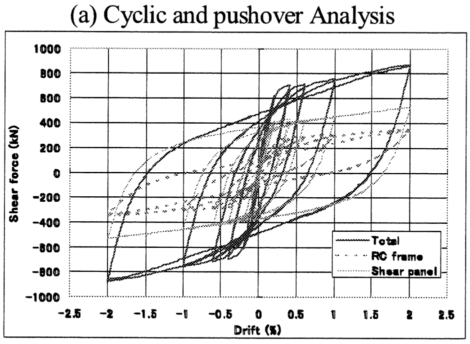

(b) Contribution of the RC frame and shear panel

Figure 9. Shear force - drift angle relations for Specimen A

ACKNOWLEDGEMENTS:

A part of this research was made possible by joint research project with Prof. Shizuo Hayashi in the Center for Urban Earthquake Engineering (CUEE) in Tokyo Institute of Technology. The research was financially supported by Japanese Ministry of Land, Infrastructure and Transport (PI, F. Watanabe), Japan Science and Technology Agency in Research for Promoting Technological Seeds (PI, S. Kono). The authors acknowledge Mr. K. Chosa, a former student at Kyoto University.

REFERENCES:

[1] Takahashi, Y., Takeda, T., Takemoto, Y. and Takagi, M., "Experimental Study on Thin Steel shear Walls Particular Steel Bracings under Alternative Horizontal Load," Preliminary Report of IABSE Symposium, Lisbon, 1973.

[2] Gaccese, V., Elgaaly, M. and Chen, R., "Experimental Study on Thin Steel-Plate Shear Walls under Cyclic Load," Journal of Structural Engineering, ASCE, Vol. 119(2), pp. 588-605, 1993.

[3] Driver, R G., Kulak, G L., Kennedy, L. and Elwi, A., "Cyclic Test of Four-Story Steel Plate Shear Wall," Journal of Structural Engineering, ASCE, Vol. 124(2), pp. 112-120, 1998.

[4] Mo, Y. L. and Perng, S. F., "Hybrid RC Frame-Steel Wall Systems," Composite and Hybrid Systems, ACI, SP-196, Ed. R. S. Aboutaha and J. M. Bracci, pp. 189 – 213, 2000.

[5] Chosa, K., Y. Kashiwai, Kono, S. and Watanabe, F., "Fundamental Study on Corrugated Steel Webs Used as Shear Walls," ***Summaries of Technical Papers of Annual Meeting,*** Architectural Institute of Japan, VOL.C2 , pp.721-722, 2006.

[6] Architectural Institute of Japan, Design Guidelines for Composite Structures, 1985.

[7] Japan Building Disaster Prevention Association, Design Guidelines for Seismic Retrofit of Existing Reinforced Concrete Building Structures, 2001.

[8] Architectural Institute of Japan, Design guidelines for Earthquake Resistant Reinforced Concrete Buildings Based on Inelastic Displacement Concept, 1999.

Fifth International Conference on Urban Earthquake Engineering
March 4-5, 2008, Tokyo Institute of Technology, Tokyo, Japan

A CONVENIENT SEISMIC RETROFIT TECHNIQUE OF SOFT STORY RC BUILDINGS

Tetsuo YAMAKAWA[1] and Pasha JAVADI[2]

1) Professor, Department of Civil Engineering and Architecture, University of the Ryukyus, Okinawa, Japan
2) PhD Candidate, Graduate School of Engineering and Science, University of the Ryukyus, Okinawa, Japan
yamakawa@tec.u-ryukyu.ac.jp, pasha_javadi@yahoo.com

Abstract: During the past earthquakes, it was observed that the buildings with a soft story were severely damaged by developing concentrated deformation in the soft story. In this paper, two techniques including application of thick hybrid wall (strength-ductility type method) and utilization of PC bars (ductility type method) have been proposed to retrofit RC columns. In the first method, application of thick hybrid wall, steel plates jacket the column and form a formwork to cast the additional concrete. In addition, PC bars are inserted through the holes punched on the steel plates into the body of the additional concrete to provide the shear sliding resisting force between the additional concrete and the steel plates. In the second method, utilization of PC bars, steel blocks are installed at the four corners of the column and connected by means of PC bars. The PC bars can also be subjected to tensile stress to enhance the confinement effect and, therefore, increase the shear strength. To assess the seismic performance of a soft-first-story building during earthquakes, nonlinear dynamic analyses were implemented for an existing soft-first-story building. The obtained results proved the applicability and efficiency of the proposed techniques on improvement in the seismic performance of soft-first-story buildings.

1. INTRODUCTION

A great number of RC structures were severely damaged during the past earthquakes such as Kobe 1995 in Japan. One of the common features of the failures is the soft story mechanism that develops due to low strength and stiffness of a story in comparison with its adjacent stories in any level of the building. In this category of failure mechanism, soft-first-story (i.e., pilotis story) mechanism is the most common (see Figure 1). This type of construction often results from a functional desire to open the lowest level to the maximum extent possible for retail shopping or parking requirements in urban areas. The provided opening space in the first story gives rise to a discontinuity in the lateral-force-resisting system.

Based on the simple concept of the capacity design philosophy proposed by Paulay (1979), base shear capacity of a soft-first-story building is governed by the lateral strength of its first story. Besides, according to equal-energy principle discussed by Newmark et al. (1971), a building with low strength requires high displacement ductility to dissipate the energy demand during earthquakes. Since, in soft-first-story buildings, the lateral strength of the first story is relatively low, a high ductility capacity is required. By contrast, the increase in the lateral displacement of the first story enhances the additional overturning moment due to the P-Δ effect, and, consequently, the probability of the collapse mechanism. However, to prevent the possible large displacement in the first story, it is essential to increase the lateral strength of this story to an adequate value.

In this paper, two retrofit techniques including application of thick hybrid wall (strength-ductility type method) and utilization of PC bars (ductility type method) are presented. Moreover, to assess the seismic performance of soft-first-story buildings during earthquakes, nonlinear dynamic analyses have been implemented for an existing soft-first-story building. The obtained results proved the applicability and efficiency of the proposed retrofit techniques on improvement in the seismic performance of soft-first-story buildings.

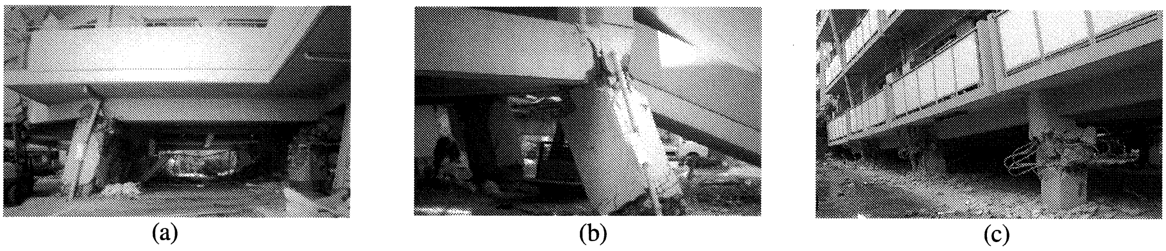

(a) (b) (c)

Figure 1 Damage of soft-first-story RC buildings. (a), (b) Hyogoken-nanbu Earthquake (M=7.2), Kobe, Japan, 1995, and (c) Geiyo Earthquake (M = 6.7), Hiroshima, Japan, 2001

2. PROPOSITION AND INVESTIGATION OF THICK HYBRID WALL

Strengthening soft-story buildings by thin panel-walls is a conventional retrofit method in Japan. In this technique, a thin panel-wall is cast inside the frame and connected to surrounding beams and columns by means of stud dowels (see Figure 2). The disadvantage of the conventional method is that the boundary columns and thin panel-wall behave as a shear critical member with a low ductility capacity. On the other hand, although the thin panel-wall increases the strength of the soft frame, the global performance of the boundary columns and panel-wall shows a brittle behavior. Considering this fact, it is necessary to propose a retrofit technique that provides superior performance, considerable ease in construction, and efficiency in economy. The early research by Yamakawa et al. (2006) demonstrated that the seismic performance of shear critical one-sided wing-wall RC columns could be improved by converting the thin wing-wall into thick hybrid wall with the additional concrete sandwiched by steel plates and PC bar prestressing. The proposed method has two major advantages in comparison with conventional method: (a) the geometric dimensions of the additional wing-wall can be readily designed to provide the demand of lateral strength, and, (b) the retrofitted column has a ductile behavior. Applicability of the thick hybrid wall at different locations of the first story is shown in Figure 3.

2.1 One-bay One-story Test Specimens

Following the conducted research on retrofitting shear critical one-sided wing-wall RC column, the applied technique has been used in the case of one-bay one-story test specimens (Yamakawa et al. 2006, Rahman et al. 2007). In this paper, for the sake of limited space, some of the test specimens are represented. The test specimens including one shear critical non-retrofitted standard bare frame and two retrofitted specimens (one opening-type wing-walls and one non-opening-type panel-wall) were tested under combination of simultaneous reversed cyclic horizontal force and constant vertical load. The scale factor of the test specimens was about 1/4-1/3, to model a low-rise school building designed according to the pre-1971 Japanese design code. The shear span to depth ratio of columns (M/(VD)) were 2.5. The details and experimental results of one-bay one-story test specimens are provided in Table 1.

The test specimen R05P-P0 is a non-retrofitted standard one. In this specimen, the longitudinal rebars of the columns started yielding at about R=0.67%. By progressing the loading test, the shear cracks were generated, and, finally, the right side column collapsed due to the shear failure at about

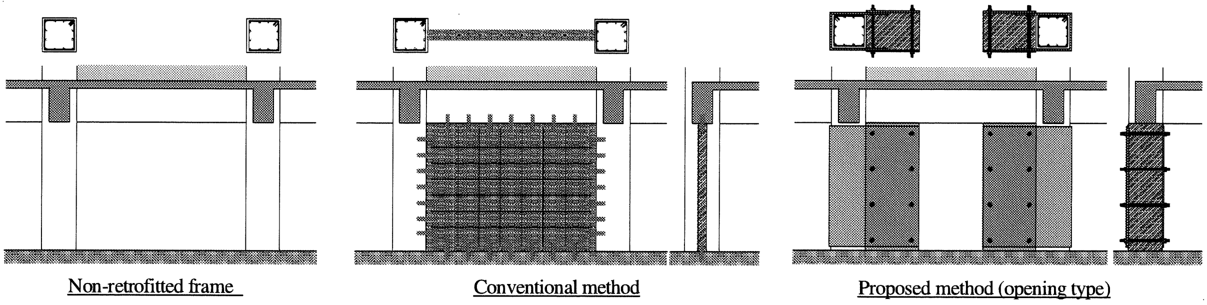

Figure 2 Features of conventional and proposed retrofit methods

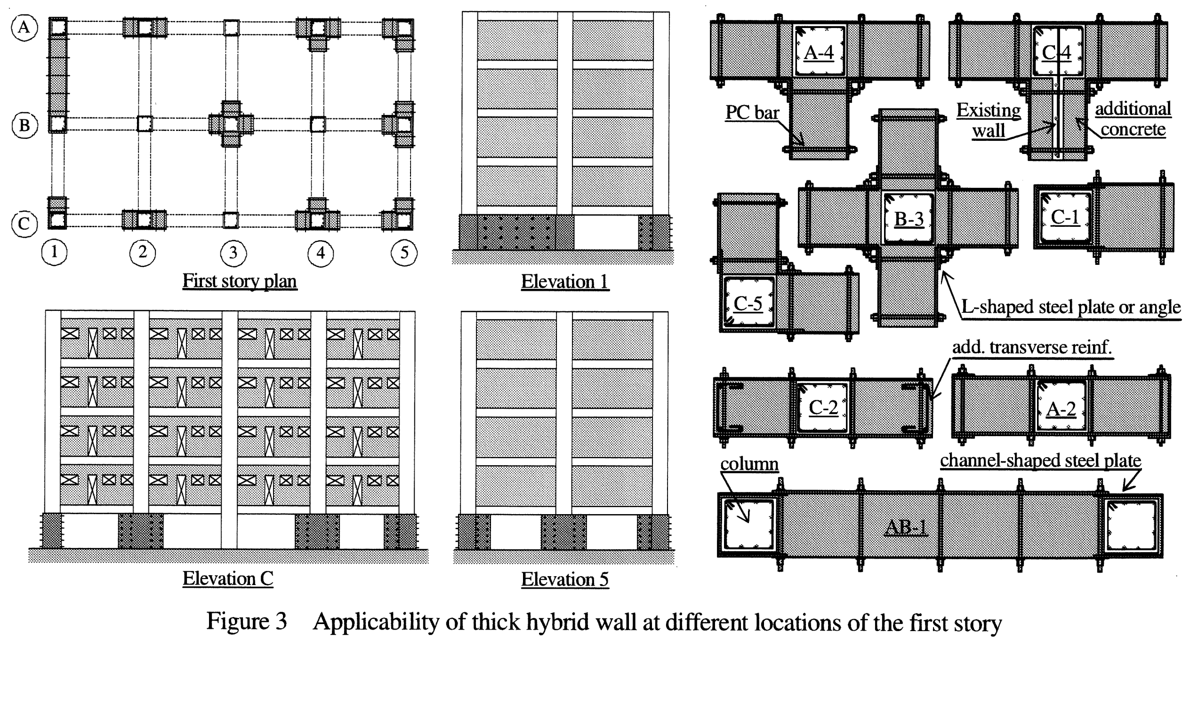

Figure 3 Applicability of thick hybrid wall at different locations of the first story

Table 1 Details and experimental results of one-bay one-story test specimens

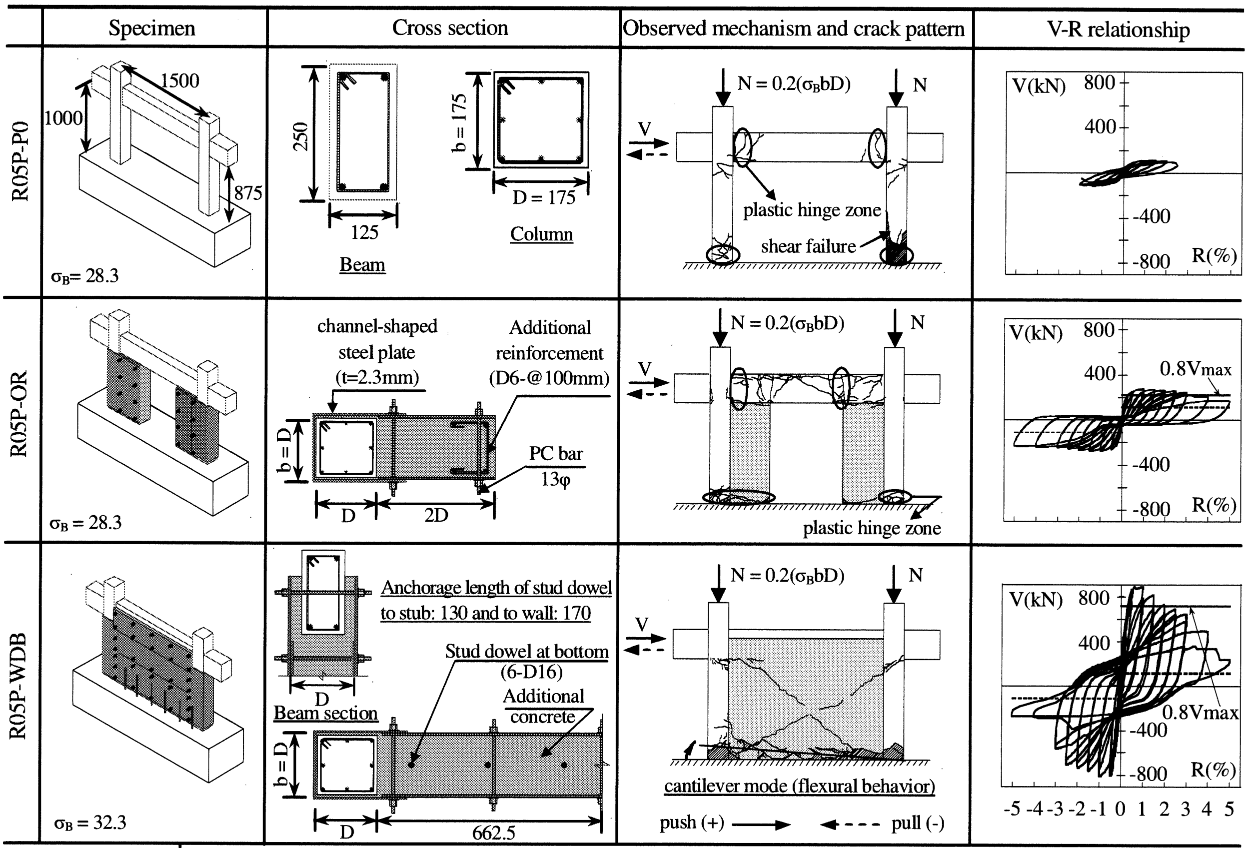

Identical details	Ratio of axial load, $N/(bD\sigma_B) = 0.2$ (per column); add. concrete strength, $\sigma_{B(add.)} = 32.3$; Reinf. in column: longitudinal reinf.: 8-D10 (ρ_g = 1.85 %), hoop: 3.7φ-@105 (ρ_w = 0.12 %); Reinf. in beam: longitudinal reinf.: 4-D13 (ρ_g = 1.63 %), stirrup: D6-@120 (ρ_w = 0.43 %); unit: N, mm

Notes: Dotted line in V-R diagrams is experimental lateral force capacity of non-retrofitted bare frame. The observed mechanisms result from push loading only. The crack patterns show the cracks at the final step of loading as a result of both push and pull directions.

R=2.5%.

The test specimen R05P-OR was retrofitted with cast-in-site wing-wall with opening inside the frame. In this retrofit technique, the main square columns were jacketed with a channel-shaped steel plate (thickness=2.3mm) and the other steel plates were connected to that channel using PC bars (diameter=13mm) to form a formwork for the wing-wall or panel-wall with a width equal to that of the column. After hardening of the post-cast concrete and before the cyclic loading test, initial tension forces were applied to the PC bars that were previously inserted across the wall. To prevent the spalling of concrete on the exposed face of the wing-wall of this specimen, additional reinforcements were provided inside the wing-wall. In this specimen the plastic hinges formed in the beam and at the bottom of the wing-wall columns. The experimental lateral force capacity was almost maintained until about R=3%, after which it decreased gradually due to tensile breakage of the longitudinal reinforcement in the outer row at the bottom of the column. Here, the experimental lateral force capacity increased to about 2.5 times of the non-retrofitted bare frame.

R05P-WDB was retrofitted with cast-in-site panel-wall without opening inside the frame. In this specimen, dowels were provided at the bottom of the panel-wall, and the top beam panel-wall connection was strengthened by casting additional concrete sandwiched by steel plates with PC bar prestressing up to the beam. During this retrofitting, holes were made in the beam to insert the PC bars, which were used to fix the steel plate to the beam. The experimental results show that the lateral resisting force reached to a maximum value of about 7 times of non-retrofitted bare frame, and then gradually decreased due to the crushing of concrete at the bottom of columns and panel-wall as a result of expanding the steel plates in those regions. Since the high tensile forces were generated in the boundary columns, in practical design, it is strongly recommended to take into account the uplift of foundation.

2.2 One-bay Two-story Test Specimens

In soft-first-story RC buildings, the second story usually contains spandrel walls or shear walls which increase the strength and stiffness of the top beams of the first story. To verify the influence of stiff-second story on the mechanism of soft-first story, a series of tests including one-bay two-story specimens were conducted. The details and experimental results of one-bay two-story test specimens are provided in Table 2.

The specimen R07P-P0 is a non-retrofitted standard test

Table 2 Details and experimental results of one-bay two-story test specimens

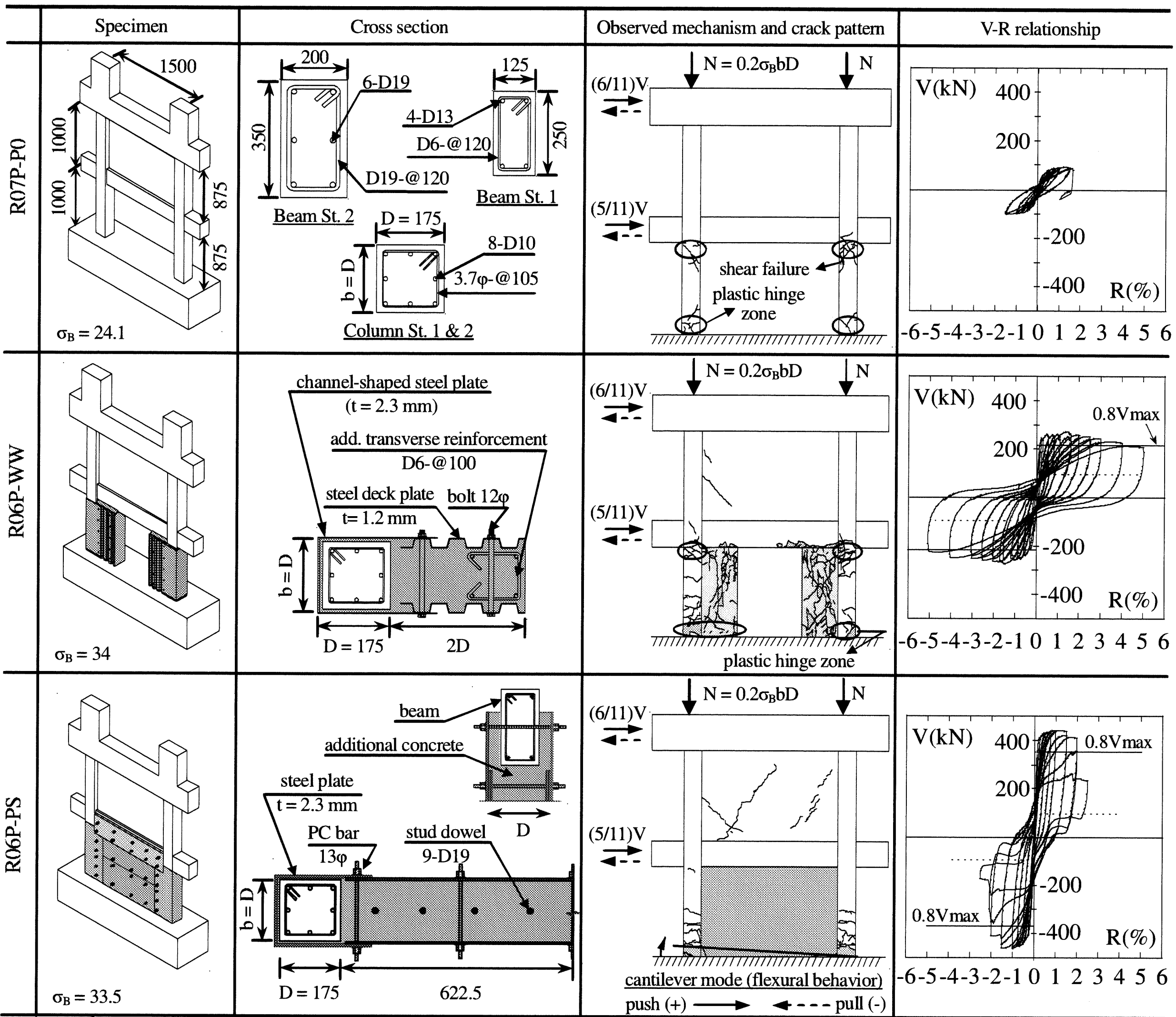

Identical details	Ratio of axial load, N/(bDσ_B) = 0.2 (per column); add. concrete strength, $\sigma_{B(add.)}$ of R06P-WW = 30.4, $\sigma_{B(add.)}$ of R06P-PS = 20.7; Reinf. in column (first and second stories): longitudinal reinf.: 8-D10 (ρ_g = 1.85 %), hoop: 3.7φ-@105 (ρ_w = 0.12 %); Reinf. in beam (first story): longitudinal reinf.: 4-D13 (ρ_g = 1.63 %), stirrup: D6-@120 (ρ_w = 0.43 %); Reinf. in beam (second story): longitudinal reinf.: 6-D19 (ρ_g = 2.46 %), stirrup: D10-@120 (ρ_w = 0.59 %); Reinf. in shear wall: 3.7φ-@60 (ρ_w = 0.30 %) in both vertical and horizontal directions. unit: N, mm

Notes: In V-R diagrams, R denotes drift angle response of first story and dotted line is experimental lateral force capacity of non-retrofitted bare frame. The observed mechanisms result from push loading only. The crack patterns show the cracks at the final step of loading as a result of both push and pull directions.

specimen with shear critical columns. In this specimen, the longitudinal rebars of the columns started yielding at about R=0.75%. By progressing the loading test , the shear cracks were appeared at both ends of first story columns, and, finally, the right side column collapsed due to the shear failure at about R=2.0%. No obvious crack was observed in the second story during the test.

In specimen R06P-WW, the retrofit procedure was similar to one-bay one-story specimen R05P-OR except the deck steel plates that was used instead of plain steel plates. The lateral strength of this specimen reached to a value about 2.8 times of the non-retrofitted specimen. It is noticeable that the experimental lateral force was almost maintained until R=5%. The damage in the second story was not significant.

Specimen R06P-PS was retrofitted with cast-in-site panel-wall without opening inside the frame. In this specimen, the process of retrofitting was the same as one-bay one-story specimen R05P-WDB. The experimental lateral force increased to a value about 4.5 times of the non-retrofitted specimen, and, after R=2.0 %, suddenly decreased as a result of rupturing of longitudinal rebars of the column.

3. EXPERIMENTAL INVESTIGATION ON FULL-SCALE COLUMNS RETROFITTED BY PC BARS

Application of PC bars (high strength steel bars) to retrofit shear critical RC columns was first proposed by Yamakawa et al. (1999). The main purpose of this method is

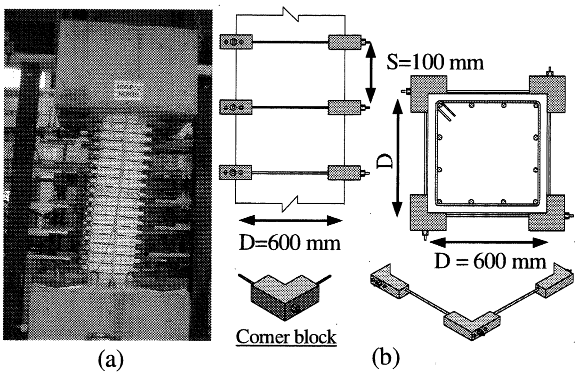

Figure 4 (a) specimen R06-PC2 at final drift angle, and (b) details of PC bar

Table 3 Details and properties of full-scale columns

Specimen	R06-BM	R06-PC2	R06-PC3
σ_B (MPa)	23.5	23.5	23.5
PC bar	-	9.2φ-@100 (ρ_P = 0.22 %)	9.2φ-@100 (ρ_P = 0.22 %)
Pretension strain level	-	2450 μ (490 MPa)	0 μ (0 MPa)
Identical details	M/(VD) = 1.5, axial force ratio = 0.3, Long. reinf: 12-D25 (ρ_g = 1.69 %), Trans. reinf: D10-@250 (ρ_w = 0.09 %)		

Table 4 Observed results of full-scale columns

	Specimen	Crack pattern	V-R relationship
R06-BM	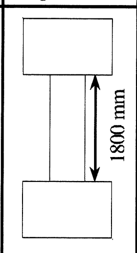	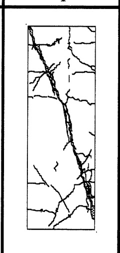	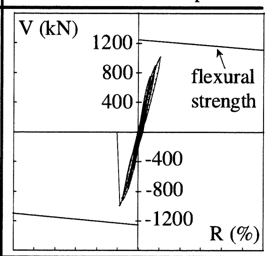
R06-PC2 (Prestressing)	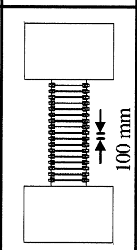	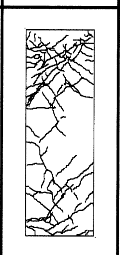	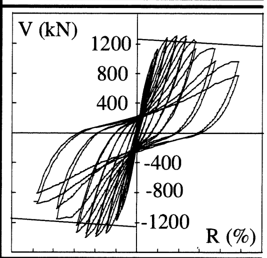
R06-PC3 (Non-prestressing)	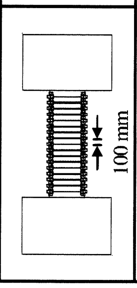	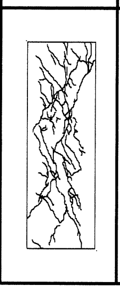	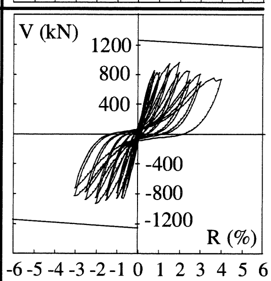

to convert the brittle shear failure mode of the shear critical RC column to ductile flexural one. In retrofit procedure (see Figure 4), steel blocks are installed at the four corners of the column and connected by means of PC bars. The PC bars can be subjected to tensile stress to enhance the confinement effect and, therefore, increase the shear strength. Three specimens were tested under axial force ratio of ($N/bD\sigma_B$)=0.3 and horizontal cyclic loading. During the loading tests, the top stub was always kept parallel to bottom one (Ken-Ken type loading). The details and properties of full-scale columns are shown in Table 3.

As shown in Table 4, R06-BM is non-retrofitted benchmark specimen that failed in shear at R= -1%. Specimen R06-PC2 was retrofitted with PC bars which were subjected to tensile strain of about 2450 μ. The experimental result shows that the lateral capacity of column reached to its flexural strength, and its ductility improved significantly. Specimen R06-PC3 was retrofitted with PC bars, but the PC bars were not subjected to tensile strain. In this specimen, at first, shear failure happened due to yielding of the transverse reinforcements at R=1%, and, then, the PC bars acted as an external hoops, and maintained the lateral strength until R=4%. The comparison between the experimental results of R06-PC2 and R06-PC3 points out the effectiveness of prestressing of the PC bars.

4. NONLINEAR DYNAMIC ANALYSIS OF AN EXISTING SOFT-FIRST-STORY BUILDING

To verify dynamic response of soft-first-story buildings, an existing soft-first-story building in the Ryukyu Islands,

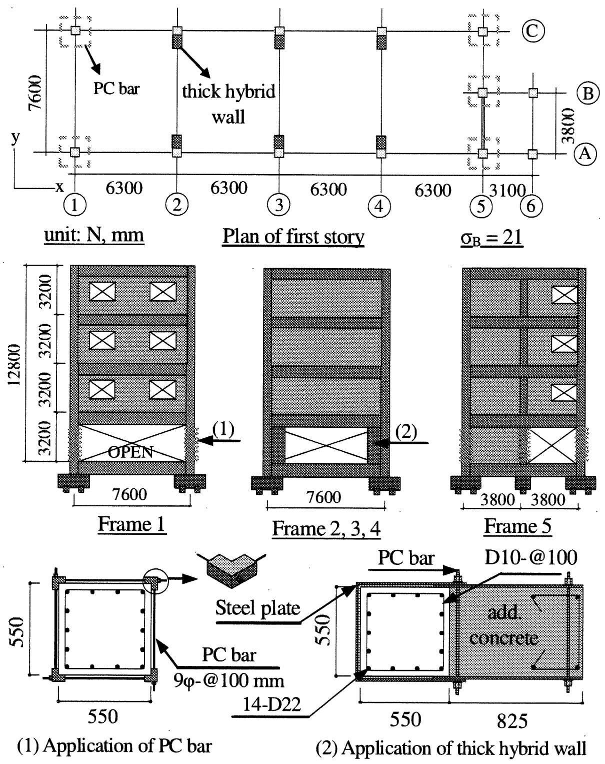

Figure 5 Details of retrofitted pilotis RC building

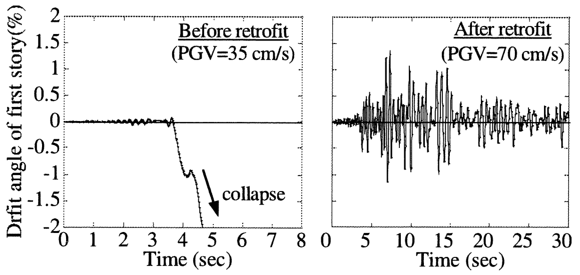

Figure 6 Time history of first story due to Taft earthquake

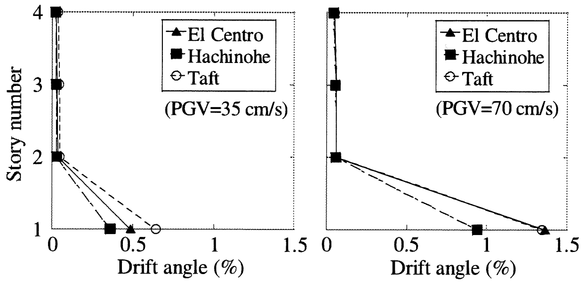

Figure 7 Drift angle responses of stories after retrofit

Okinawa, Japan has been modeled. The main purpose of this assessment is to exhibit the applicability of the proposed retrofit methods in the case of an actual building. The soft-first-story building was modeled in computer program RUAUMOKO for nonlinear dynamic analysis. The dynamic analyses were implemented before and after retrofitting of the vulnerable building due to three earthquakes namely, El Centro NS (1940), Taft EW (1952) and Hachinohe EW (1968). The input motions consist of two series of input waves, in which the first series was scaled according to the peak ground velocity (PGV) of 35cm/s, related to the local seismic hazard coefficient, and the second one was scaled according to the peak ground velocity of 70 cm/s, to assess the seismic performance of the building due to relatively strong ground motion. Since the shear strength of non-retrofitted columns was slightly more than their flexural strength, it was conservatively assumed that the columns failed in shear. The retrofit strategy of the vulnerable soft-first-story building was decided in such way that the columns of the frames 2, 3 and 4 were retrofitted by thick hybrid wall to increase the lateral strength and ductility, and the columns of the frames 1 and 5 were retrofitted by PC bar prestressing to prevent likely shear failure (see Figure 5). As suggested by Javadi et al. (2007), the columns retrofitted by thick hybrid wall are modeled by SINA hysteretic rule and the columns retrofitted by PC bars are modeled by Takeda hysteretic rule. As illustrated in Figure 6, after retrofitting, the drift angle of the first story shows a stable response. In Figure 7, the obtained results demonstrate that although the lateral deformation of the building is concentrated in the first story, the drift angle response of the first story falls within the rational range due to three basis earthquakes.

5. CONCLUSIONS

A retrofit technique using non-reinforced thick hybrid wing-walls or panel-walls increases the lateral strength, stiffness, and ductility of soft-story RC buildings. The length of additional wing-wall can be readily designed to obtain the demand strength, but, in the case of non-opening panel-wall, the uplift of the foundation must be taken into account. The proposed retrofit technique provides superior performance, considerable ease in construction, and efficiency in economy in comparison with conventional method.

The utilization of PC bar prestressing converts the brittle shear failure mode of shear critical RC column to ductile flexural one. Prestressing of PC bars plays an important role in increasing the shear strength of the column.

In the case of real soft-first-story building, it was found that the combination of ductility type retrofit (utilizing PC bars only) and strength-ductility type retrofit (using opening type thick hybrid wall) obtained a good seismic performance.

Acknowledgements:

The experimental investigations of full-scale columns were carried out possible by the joint research in National Center for Research on Earthquake Engineering (NCREE) under the supervision of Dr Keh-Chyuan Tsai, Prof. of National Taiwan University, and director of NCREE. The authors would like to express the deepest gratitude to Dr A. J. Carr, Prof. of the University of Canterbury, New Zealand, for his valuable guidance during stay in the university of the Ryukyus, Japan. The investigation reported herein was supported by a financial support of the Grant-in-aid for the Scientific Research (B), (17360272), 2007, by Japan Society for the Promotion of Science (JSPS). Other research grants for Construction Technology, Research and Development were provided by the Ministry of Land, Infrastructure and Transport, Japan.

References:

Paulay, T. (1979), "Capacity Design of Earthquake Resisting Ductile Multistory Reinforced Concrete Frames," *Proceedings of the 3rd Canadian Conference on Earthquake Engineering*, **2**, 917-948.

Newmark, NM., Rosenblueth, E. (1971), "Fundamentals of Earthquake Engineering," Prentice-Hall Inc.

Yamakawa, T., Rahman, MN., and Morishita, Y. (2006), "Experimental Investigation and Analysis Approach for Seismic Retrofit of RC Column with Wing-wall," *Journal of Structure and Construction Engineering*, Architectural Institute of Japan, **608**, 109-117.

Yamakawa, T., Rahman, MN., Nakada, K., and Morishita, Y. (2006), "Experimental and Analytical Investigation of Seismic Retrofit Technique For a Bare Frame Utilizing Thick Hybrid Walls," *Journal of Structural and Construction Engineering*, Architectural Institute of Japan, **610,** 131-138.

Rahman, MN., and Yamakwa, T. (2007), "Investigation of a Hybrid Technique for Seismic Retrofitting of Bare Frames," *Journal of Advanced Concrete Technology*, Japan Concrete Institute, **5**(2), 209-222.

Yamakawa, T., Kamongwa, S., and Kurashinge, M. (1999), "An Experimental Study on the Seismic Retrofit Technique for RC Columns Confined with PC Bar Prestressing as External Hoops," *Journal of Structural and Construction Engineering*, Architectural Institute of Japan, **526**, 141-145. (in Japanese)

Javadi, P., Takara, S., Yamakawa, T., Rahman, MN., and Carr, A, J. (2007), "Nonlinear Dynamic Analysis of Soft-first-story Building Before and After Retrofitting," Proceedings of 8th Pacific Conference on Earthquake Engineering, Paper No. 257.

Fifth International Conference on Urban Earthquake Engineering
March 4-5, 2008, Tokyo Institute of Technology, Tokyo, Japan

DYNAMICS AND CONTROL OF BUILDING STRUCTURES BY CONSTRAINTS

Hee-Chang Eun[1], Min-Su Lee[2], and Heon-Soo Chung[3]

1) Professor, Architectural Engineering, Kangwon National University,Korea
2)PhD Candidate, Dept. of Architectural Engineering, Kangwon National University, Korea
3) Professor, Department of Architectural Engineering, Chung-Ang University,Korea
heechang@kangwon.ac.kr, narasec@chol.com, chunghs@cau.ac.kr

Abstract: The dynamic problem of structural building or mechanical systems subjected to certain external excitation such as earthquake is sometimes established by a mathematical system consisting of dynamic equations and prescribed constraint conditions. The constrained behavior depends on the exact calculation of constraint forces required for satisfying the constraints and the dynamic responses are controlled by the control forces. This study considers the dynamic control that dynamic systems subjected to external excitation are controlled beyond the limit of linearly elastic behavior of dynamic systems.

1. INTRODUCTION

External excitations like earthquake must be a main cause to give the loss of property and life. It is desirable to accommodate the structural design method for alleviating the structural damage on seismic or wind load. And it is sometimes necessary to control dynamic responses by installing active or passive control devices in structures. The control devices influence on the dynamic characteristics of structures and provide the control forces calculated by proper control algorithms. Many control systems have been utilized in the structures to control the dynamic responses.

The control forces executed by active control systems are calculated from the quadratic form of state space and control force. If the dynamic responses are restricted by some given trajectories, the state space term is deleted in the quadratic form and the responses are obtained by minimizing the quadratic function of control force only with respect to the control force. The control force that the dynamic responses are controlled by given trajectories is interpreted as the constraint force to provide the structure for satisfying the given paths. The constraint forces act on the structure by control systems like passive devices or actuators. However, it is not easy to determine the constraint forces. There have been many attempts to explicitly describe the constrained responses of structures after Lagrange in 1797.

Gibbs (1879) and Appell (1911) provided an analytical method through a felicitous choice of quasi-coordinates. This approach is usually amenable to problem-specific situations and is likewise difficult to use, when dealing with systems having several tens of freedom. Kane (1983) introduced a method for constrained systems based on the development of Lagrange equations from D'Alembert's Principle.

Based on Gauss's principle (Gauss, 1829) and fundamental linear algebra (Graybill, 1983), Udwadia and Kalaba (1992) derived the generalized inverse method, which does not require the numerical determination of undetermined multipliers like Lagrange multipliers. Udwadia, Kalaba and Eun (1997) presented an extended D'Alembert's principle and proved the generalized inverse method. In spite of such effort, it is necessary that the validity and uniqueness of the method will be investigated.

There have been few papers to consider the dynamic control of structures with constraints. Gurgoze and Muller (1992) presented a method to determine the optimal positioning of the dampers, actuators and sensors for a linear conservative mechanical system on the basis of an energy criterion. Boutin, Misra and Modi (1999) presented a method to obtain the equations governing the constrained dynamics of the entire systems from equations of motion for individual sub-structures by eliminating the non-working constraint forces.

Starting from a function of the variation in kinetic energy at unconstrained and constrained states, and minimizing it with respect to the velocity variation, this study derives the equation of constrained motion. The constraints must satisfy within and beyond the linearly elastic range. The constrained control beyond the linearly elastic range requires the displacement control as well as the force control to satisfy the elastic and inelastic load-displacement relation. In order to verify the applicability of the generalized inverse method for inelastic nonlinear systems, this study considers the constrained dynamic behavior of inelastic systems based on the generalized inverse method and illustrated its applicability.

2. DYNAMIC CONTROL

The control system based on a quadratic performance index may be defined by

$$\dot{\mathbf{q}} = \mathbf{Dq} + \mathbf{Ef} \tag{1}$$

where $\mathbf{q}$: $n \times 1$ state vector
$\mathbf{f}$: $r \times 1$ control vector, $r < n$
$\mathbf{D}$: $n \times n$ constant matrix
$\mathbf{E}$: $n \times r$ constant matrix

The performance index is given by

$$J = \int_0^\infty \left(\mathbf{q}^{\mathbf{T}}\mathbf{Qq} + \mathbf{f}^{\mathbf{T}}\mathbf{Rf}\right)dt \tag{2}$$

where $\mathbf{Q}$ is a positive-definite Hermitian or real symmetric matrix, $\mathbf{R}$ is a positive-definite Hermitian or real symmetric matrix, and $\mathbf{f}$ is unconstrained.

Based on the second method of Liapunov, the optimal control system is derived by minimizing the performance index, and the control forces are determined. The control algorithm yields the minimum values of the state vector and the control forces at the unconstrained state.

If the dynamic responses of the system are restricted by constraints, the optimal control algorithm given by equation (2) should be modified because the constrained paths themselves follow the dynamic responses to minimize the performance index. Replacing the control vector $\mathbf{f}$ by the constraint force vector $\mathbf{F^c}$, the performance index can be written as

$$J = \int_0^\infty \left(\mathbf{F^c}^{\mathbf{T}}\mathbf{RF^c}\right)dt \tag{3}$$

Minimizing the performance index given by equation (3), the constraint force vector may be derived. This formulation is exactly the same as Gauss's principle. The Gauss's principle is as follows. Assuming that the configuration, $\mathbf{q}(t) = [q_1 \ \ q_2 \ \ \cdots \ \ q_n]^T$, and the velocity, $\dot{\mathbf{q}}(t) = [\dot{q}_1 \ \ \dot{q}_2 \ \ \cdots \ \ \dot{q}_n]^T$, of a constrained system at time t are prescribed, the acceleration of the unconstrained systems, $\mathbf{a}(\mathbf{q}, \dot{\mathbf{q}}, t)$, is known. Then the Gauss's principle informs us that the accelerations, $\ddot{\mathbf{q}}(t)$, are such that the Gaussian function, G, defined as

$$G = [\ddot{\mathbf{q}} - \mathbf{a}]^T \mathbf{M} [\ddot{\mathbf{q}} - \mathbf{a}] \tag{4}$$

is minimized over all $\ddot{\mathbf{q}}$ which satisfy the constraints.

The equation of motion at time t of the constrained system can be expressed as

$$\mathbf{M}\ddot{\mathbf{q}} = \mathbf{F}(\mathbf{q}, \dot{\mathbf{q}}, t) + \mathbf{F^c}(\mathbf{q}, \dot{\mathbf{q}}, t) \tag{5}$$

where $\mathbf{M}$ is an $n \times n$ mass matrix. Substituting equation (5) into equation (4), the Gaussian function is modified as

$$G = \mathbf{F^c}^{\mathbf{T}}\mathbf{M}^{-1}\mathbf{F^c} \tag{6}$$

It can be observed that the Gaussian function G is utilized as the same meaning as the performance index of equation (3). However, comparing two equations (3) and (6), it is indicated that the weighting matrix $\mathbf{R}$ in equation (3) must be the matrix $\mathbf{M}^{-1}$ based on the Gauss's principle. Thus, determining the constraint forces based on the minimization of the performance index of equation (3) or the Gaussian function (6), the constrained dynamic responses and control forces can be explicitly calculated.

3. EQUATIONS OF MOTION FOR CONSTRAINED SYSTEMS

The description of constrained responses depends on the determination of the constraint forces. Minimizing a function of the variation in kinetic energy at unconstrained and constrained states with respect to the velocity variation, the constraint forces and equation of motion for constrained structures are derived.

The kinetic energy of unconstrained structure to be described by a velocity vector $\dot{\tilde{\mathbf{u}}} = [\dot{\tilde{u}}_1 \ \ \dot{\tilde{u}}_2 \ \ \cdots \ \ \dot{\tilde{u}}_n]^T$ can be written as

$$\tilde{\mathrm{T}} = \frac{1}{2}\dot{\tilde{\mathbf{u}}}^{\mathbf{T}}\mathbf{M}\dot{\tilde{\mathbf{u}}} \tag{7}$$

where $\tilde{\mathrm{T}}$ denotes the kinetic energy of unconstrained structure and $\mathbf{M}$ is the $n \times n$ positive definite mass matrix.

Assume that the structure is subjected to m displacement constraints

$$f_i(\mathbf{u}) = r(t), \quad i = 1, \ 2, \ \cdots, \ m, \ m < n \tag{8}$$

where $\mathbf{u} = [u_1 \ \ u_2 \ \ \cdots \ \ u_n]^T$ denotes the actual displacements deviated from unconstrained state. Differentiating once the constraints with respect to time t, the constraints can be written in matrix form of

$$\mathbf{A}\dot{\mathbf{u}}(t) = \mathbf{b_1}(t) \tag{9}$$

where $\mathbf{A}$ is a real matrix of $m \times n$ and $\mathbf{b_1}(t)$ is an $m \times 1$ vector. The actual kinetic energy of the structure due to the existence of the constraints is also expressed by

$$\mathrm{T} = \frac{1}{2}\dot{\mathbf{u}}^{\mathbf{T}}\mathbf{M}\dot{\mathbf{u}} \tag{10}$$

Utilizing the velocity variation, $\delta\dot{\mathbf{u}}$, due to the constraints, the following relation between $\dot{\mathbf{u}}$ and $\dot{\tilde{\mathbf{u}}}$ is established that

$$\dot{\mathbf{u}} = \dot{\tilde{\mathbf{u}}} + \delta\dot{\mathbf{u}} \tag{11}$$

Also, let us $\tilde{\dot{\mathbf{u}}} = \mathbf{R}(\delta\tilde{\dot{\mathbf{u}}})$, where $\mathbf{R}$ is a positive definite matrix. Substituting equation (11) into equations (7) and (10), and finding the difference of the results, the variation in the kinetic energy can be expressed as

$$\delta T = T - \tilde{T} = \frac{1}{2}[\delta\dot{\mathbf{u}} + \mathbf{R}(\delta\dot{\mathbf{u}})]^T \mathbf{M}[\delta\dot{\mathbf{u}} + \mathbf{R}(\delta\dot{\mathbf{u}})] - \frac{1}{2}\tilde{\dot{\mathbf{u}}}^T \mathbf{M}\tilde{\dot{\mathbf{u}}}$$

$$= \frac{1}{2}\left[\mathbf{M}^{1/2}\delta\dot{\mathbf{u}} + \mathbf{M}^{1/2}\mathbf{R}(\delta\dot{\mathbf{u}})\right]^T \left[\mathbf{M}^{1/2}\delta\dot{\mathbf{u}} + \mathbf{M}^{1/2}\mathbf{R}(\delta\dot{\mathbf{u}})\right]$$

$$- \frac{1}{2}\left[\mathbf{M}^{1/2}\mathbf{R}(\delta\dot{\mathbf{u}})\right]^T \left[\mathbf{M}^{1/2}\mathbf{R}(\delta\dot{\mathbf{u}})\right] \tag{12}$$

Extremizing equation (12) with respect to the variation $\delta\dot{\mathbf{u}}$, the result yields

$$\frac{\delta T}{\delta\dot{\mathbf{u}}} = \mathbf{M}^{1/2}\delta\dot{\mathbf{u}} = 0 \tag{13}$$

Utilization of equation (11) into equation (9) yields

$$\mathbf{A}\left(\tilde{\dot{\mathbf{u}}} + \delta\dot{\mathbf{u}}\right) = \mathbf{b}_1(t) \tag{14}$$

In order to use equation (14) into equation (13), equation (14) is modified as

$$\mathbf{A}\mathbf{M}^{-1/2}\mathbf{M}^{1/2}\left(\tilde{\dot{\mathbf{u}}} + \delta\dot{\mathbf{u}}\right) = \mathbf{b}_1(t) \tag{15}$$

Utilizing the fundamental properties[1] of generalized inverse matrix, the general solution of equation (15) can be derived as

$$\mathbf{M}^{1/2}\left(\tilde{\dot{\mathbf{u}}} + \delta\dot{\mathbf{u}}\right) = \mathbf{Q}^+\mathbf{b}_1 + \left[\mathbf{I} - \mathbf{Q}^+\mathbf{Q}\right]\mathbf{y} \tag{16}$$

where $\mathbf{Q} = \mathbf{A}\mathbf{M}^{-1/2}$, the vector $\mathbf{y}$ is an arbitrary vector and '+' denotes the generalized inverse matrix.

Utilizing equation (13) into equation (16) and the fundamental relation of $\mathbf{Q}\mathbf{Q}^+\mathbf{Q} = \mathbf{Q}$, and solving the result with respect to the vector **y**, we obtain the equation

$$\mathbf{y} = \left[\mathbf{I} - \mathbf{Q}^+\mathbf{Q}\right]\left(\mathbf{M}^{1/2}\tilde{\dot{\mathbf{u}}} - \mathbf{Q}^+\mathbf{b}_1\right) + \left[\mathbf{I} - \mathbf{Q}^+\mathbf{Q}\right]\mathbf{z} \tag{17}$$

where $\mathbf{z}$ is another arbitrary vector.

Substituting equation (17) into equation (16) and arranging the result, it follows that

$$\mathbf{M}^{1/2}\delta\dot{\mathbf{u}} = \left(\mathbf{A}\mathbf{M}^{-1/2}\right)^+\left(\mathbf{b}_1 - \mathbf{A}\tilde{\dot{\mathbf{u}}}\right) \tag{18}$$

Finally, substituting equation (18) into equation (11) and differentiating the result once with respect to time, the equation of motion for constrained structure is written as

$$\ddot{\mathbf{u}} = \tilde{\ddot{\mathbf{u}}} + \mathbf{M}^{-1/2}\left(\mathbf{A}\mathbf{M}^{-1/2}\right)^+\left(\mathbf{b} - \mathbf{A}\tilde{\ddot{\mathbf{u}}}\right) \tag{19}$$

where $\tilde{\ddot{\mathbf{u}}}$ denotes the acceleration at the unconstrained state and $\mathbf{b} = \dot{\mathbf{b}}_1$. From equation (19), it is understood that the variation of acceleration due to the constraints and the constraint forces are expressed, respectively, by

$$\delta\ddot{\mathbf{u}} = \mathbf{M}^{-1/2}\left(\mathbf{A}\mathbf{M}^{-1/2}\right)^+\left(\mathbf{b} - \mathbf{A}\tilde{\ddot{\mathbf{u}}}\right) \tag{20a}$$

$$\mathbf{F}^c = \mathbf{M}^{1/2}\left(\mathbf{A}\mathbf{M}^{-1/2}\right)^+\left(\mathbf{b} - \mathbf{A}\tilde{\ddot{\mathbf{u}}}\right) \tag{20b}$$

It is shown that the derived equations coincide with the generalized inverse method proposed by Udwadia and Kalaba (1992). The dynamic responses of constrained structures are explicitly described by equation (19) and the constraint forces are calculated by equation (20b). Thus, it is expected that the proper selection of constraints will obtain desirable responses of structures.

4. APPLICATION

The dynamic system subjected to large external loads would exhibit the responses forloading, unloading and reloading beyond the linearly elastic range as shown in Figure 1. The constrained responses for the perfectly plastic behavior must satisfy the constraints themselves as well as the load-deformation relation. Assuming the elastoplastic deformation of Figure 2, the constrained responses require the determination of the stiffness for elastic or inelastic systems. The second-order differential equations for constrained inelastic systems are numerically solved by numerical methods like central difference method, Runge-Kutta method, and Newmark's method, etc., with the determination of the elastic or inelastic stiffness. Although the stiffness matrix in the constrained dynamic equation is not utilized as the weighting matrix in equation (19), the stiffness matrix should be explicitly determined because it is

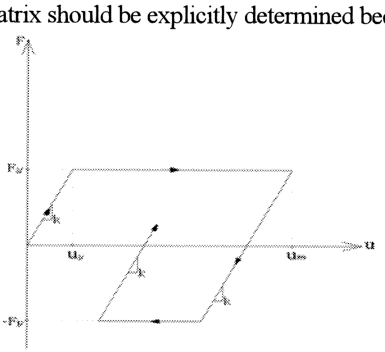

Figure 1 Responses for loading, unloading and reloading

[1] The generalized solution of $\mathbf{A}\mathbf{x} = \mathbf{b}$, where $\mathbf{A}$ is $m \times n$ matrix, $\mathbf{x}$ and $\mathbf{b}$ are $n \times 1$ and $m \times 1$ vectors, respectively, can be written as

$$\mathbf{x} = \mathbf{A}^+\mathbf{b} + \left[\mathbf{I} - \mathbf{A}^+\mathbf{A}\right]\mathbf{d},$$

where $\mathbf{I}$ is $n \times n$ identity matrix and $\mathbf{d}$ is $n \times 1$ arbitrary vector.

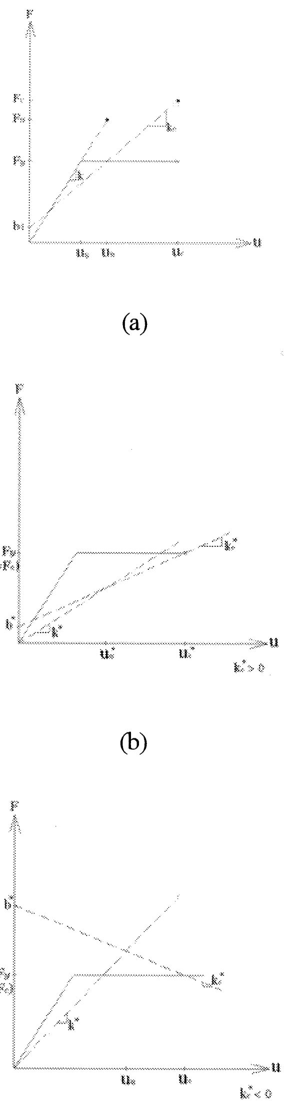

(a)

(b)

(c)

Figure 2 Load-deformation relation:
(a) elastic-perfectly plastic relation, (b) $\mathbf{K}_c^* > 0$, (c) $\mathbf{K}_c^* < 0$

deeply related to the displacement constraint. The central difference method and the Newmark's method of the second-order differential equations for constrained nonlinear system can not be applied because the stiffness matrix is rank deficiency. Thus, the stiffness beyond the linearly elastic limit is established.

Consider a dynamic system described by a displacement vector $\mathbf{y} = \begin{bmatrix} y_1 & y_2 & y_3 \end{bmatrix}^T$ as shown in Figure 3. The unconstrained equation of motion for the inelastic system can be written by

$$\mathbf{M\ddot{y}} + \mathbf{C\dot{y}} + \mathbf{F}(\mathbf{y},\dot{\mathbf{y}}) = \mathbf{P}(t) \tag{21}$$

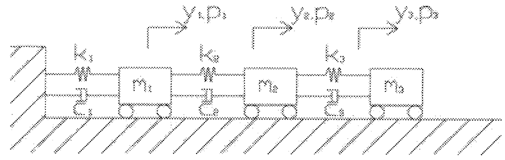

Figure 3 A three degrees of freedom system

where $\mathbf{M}$ and $\mathbf{C}$ denote the mass and damping matrices, respectively, $\mathbf{F}(\mathbf{y},\dot{\mathbf{y}})$ is the restoring forces corresponding to the force-deformation relation, and $\mathbf{P}(t)$ represents an external force vector. For deformation $y_i (i = 1,2,3)$ at time t, the restoring force depends on the prior history of motion of the system and whether the deformation is currently increasing ($\dot{y}_i > 0$) or decreasing ($\dot{y}_i < 0$).

Assume that the responses are restricted by a constraint

$$y_1 - 2y_2 + y_3 = 3e^{-\omega t} \sin \omega t \tag{22}$$

The constraint must satisfy the dynamic responses within and beyond the elastic limit. Differentiating Eqn. (36) twice with respect to time, it can be derived in the form of Eqn. (24) expressed as

$$\begin{bmatrix} 1 & -2 & 1 \end{bmatrix} \begin{bmatrix} \ddot{y}_1 \\ \ddot{y}_2 \\ \ddot{y}_3 \end{bmatrix} = -6\omega^2 e^{-\omega t} \cos \omega t \tag{23}$$

For the numerical application, the following nondimensional values were utilized.

$$k_1 = 1500,\ k_2 = 1200,\ k_3 = 1000,$$
$$u_{y1} = u_{y2} = u_{y3} = 2.0$$
$$m_1 = m_2 = 30,\ m_3 = 40,\ c_1 = c_2 = c_3 = 3.0 \tag{24}$$

Let us assume that the system is excited by the following external forces and the initial conditions to satisfy the constraint were selected.

$$\mathbf{P}_{(t)} = \begin{bmatrix} 300\cos 3t + 500\sin 6t \\ 250\sin 8t - 400\cos 7t \\ 450\sin 5t \end{bmatrix}$$

$$y_1(0) = 2,\quad y_2(0) = 1,\quad y_3(0) = \dot{y}_1(0) = \dot{y}_3(0) = 0,\quad \dot{y}_2(0) = -1.5\omega \tag{25}$$

Utilizing equations. (21) and (23) into equation (19), we can obtain the dynamic equations for the given system and the dynamic responses can be calculated by any numerical integration scheme.

Figure 4 compares the constrained responses in the

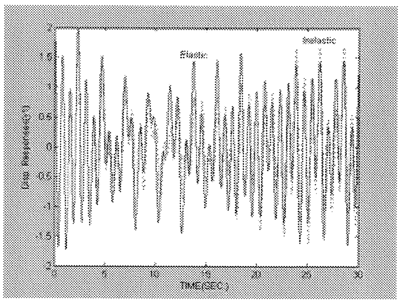

(a)

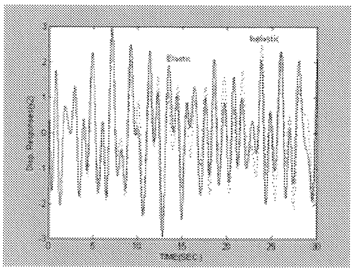

(b)

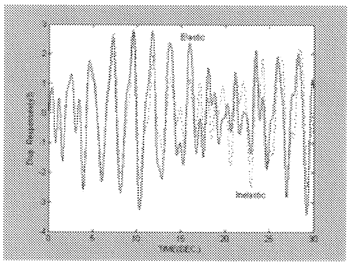

(c)

Figure 4 Displacement responses: (a) y_1, (b) y_2, (c) y_3, The solid and dashed lines denote elastic and inelastic responses, respectively.

elastic and inelastic states. Taking the displacements at yielding as $u_{y1} = u_{y2} = u_{y3} = 2.0$, it can be observed that the system is behaved beyond linearly elastic limit. The dynamic responses beyond linearly elastic limit exhibited higher than the responses in elastic limit due to the reduced effective stiffness k_c^*.

Figure 5 shows the constraint forces or control forces to act on the system for satisfying the constraint. It is illustrated that the control forces for the perfectly plastic range are explicitly and easily calculated. Comparing the constraint forces to act on the elastic and inelastic systems, their force difference was small because the stiffness as a function of weighting matrix represents a little difference.

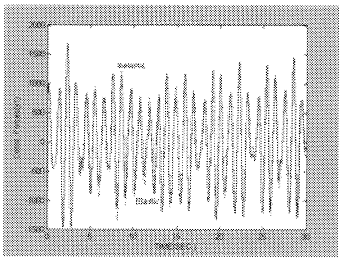

(a)

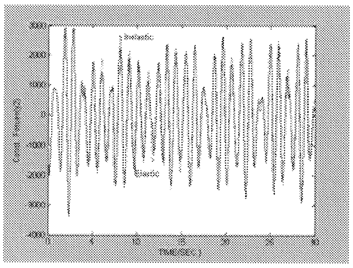

(b)

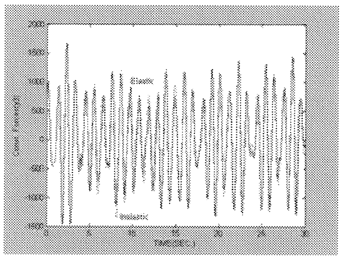

(c)

Figure 5 Constraint forces: (a) y_1, (b) y_2, (c) y_3 The solid and dashed lines denote elastic and inelastic responses, respectively

However, if the inelastic effects are neglected, the constraint control must be improperly taken and the dynamic system should be damaged by the improper forces. The validity of the proposed method is evaluated by the satisfying degree of the constraint.

The numerical results must follow the constrained trajectory and the validity of the solution depends on the satisfaction of the constraint. Figure 6 exhibit the error in the satisfaction of the constraint defined as

$$error1 = y_1 - 2y_2 + y_3 - 3e^{-\alpha t} \sin \omega t$$
$$error2 = \dot{y}_1 - 2\dot{y}_2 + \dot{y}_3 + 3\alpha e^{-\alpha t} \sin \omega t - 3\omega e^{-\alpha t} \cos \omega t \qquad (26)$$

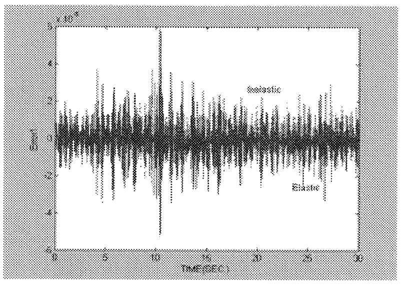

(a)

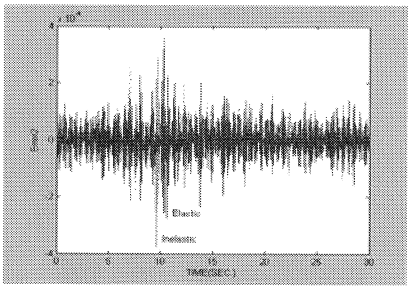

(b)

Figure 6; Errors in the satisfaction of constraints: (a) error1, (b) error2, The solid and dashed lines denote elastic and inelastic responses, respectively.

The plots represent that the dynamic responses satisfy the constraint even beyond the linearly elastic range. From the derivation and applications, it is observed that the dynamic control of inelastic systems require the satisfaction of constraints and load-deformation relation. The errors in the satisfaction of the constraint are caused by the neglect of the constraint itself and its first derivative with respect to time in the second-order differential equation (Eun et al., 2004).

5. Conclusions

Based on the generalized inverse method to describe the constrained responses, this study considered the constrained dynamic behavior beyond the linearly elastic range due to large deformation. The effective stiffness beyond the linearly elastic range should be obtained such that the constraints as well as the load-deformation by the displacement and force control are satisfied. In other words, the effective stiffness needs to define the weighting matrix for the constrained equilibrium equation and to satisfy the constraints for the constrained dynamic systems. Starting from the constrained equilibrium equation and based on the generalized inverse method with the effective stiffness, it was illustrated that the static and dynamic behavior for the nonlinear systems is explicitly described by applications.

References:

Appell, P. (1911), "Example De Mouvement D'un Point Assujetti A Une Liaison Exprimee Par Une Relation Non Lineaire Entre Les Composantes De La Vitesse," *Rend. Circ. Matem. Palermo*, **32**, 48-50.

Eun, H.C., Park, S.Y. and Lee, E.T., (2004), "An Analytical Approach for Structural Synthesis of Substructures," *KSME International Journal*, **18**(9), 1529-1536.

Eun, H.C., Park S.Y., Lee E.T. and Chung H.S. (2004), "Analytical Method for Constrained Mechanical and Structural Systems," *KSME International Journal*, **18**(10), 1691-1699.

Felippa, C.A., Park, K.C. and Filho, R.J. (1998), "The construction of free-free flexibility matrices as generalized stiffness inverses," *Computers and Structures*, **68**, 411-418.

Gauss, C.F. (1829) "Uber ein Neues Allgemeines Grundgesetz der Mechanik," *J. ine und Angawandte Mathematik*, 232-235.

Gibbs, J.W. (1879) "On the Fundamental Formulae of Dynamics," *American Journal of Mathematics*, **2**: 563-564.

Graybill, F. (1983), Matrices and applications to statistics. *Wadsworth Belmont California*.

Guyan, R.J. (1965), "Reduction of stiffness and mass matrices," *AIAA Journal*, **3**, 380.

Kane, T.R. (1983) "Formulation of Dynamical Equations of Motion," *Am., J. Phys*, **51**, 974-977.

Park. K.C. (2000), "Partitioned solution of reduced-integrated finite element equations," *Computers and Structures*, **74**, 281-292.

Park, K.C., Justino, Jr. M.R. and Felippa, C.A. (1997), "An algebraically partitioned FETI method for parallel structural analysis: algorithm description," *International Journal of Numerical Methods in Engineering*, **40**, 2717-37.

Udwadia, F.E. and Kalaba, R.E. (1992) "A New Perspective on Constrained Motion," *Proceedings of the Royal Society of London*, **439**, 407-410.

Udwadia, F.E., Kalaba, R.E. & Eun, H.C. (1997) "The extended D'Alembert's principle and equations of motion for constrained mechanical systems," *Quarterly of Applied Mathematics*, **55**: 321-331.

Fifth International Conference on Urban Earthquake Engineering
March 4-5, 2008, Tokyo Institute of Technology, Tokyo, Japan

COLLECTION AND ANALYSIS OF DENSE EXPERIMENTAL TEST DATA

Daniel Kuchma[1), Shaoyun Sun[2), Heui Hwang Lee[3)

1) Associate Professor, Department of Civil and Environmental Engineering, University of Illinois at Urbana-Champaign
2) Structural Engineer, Parsons, Chicago, Illinois
3) PhD Candidate, Department of Civil and Environmental Engineering, University of Illinois at Urbana-Champaign
kuchma@uiuc.edu; ssun@uiuc.edu; heuilee@uiuc.edu

Abstract: Barriers to the development of suitably-comprehensive and quantitatively-reliable computational tools include a lack of dense experimental test data, tools for the visualization, analysis, and comparison of data from tests with computational predictions, and formal methods for the calibration and validation of numerical models. Recent advancements in instrumentation technology now make it possible to collect an unprecedented level of detailed information about the response of test structures. New tools and procedures for the visualization, analysis, and use of this test data for the development of improved computational models are demonstrating great potential. As a research community, we are entering a new era where the value of our experiments will be judged by the level and organization of the collected test data, was well as the value of this data for the advancement of numerical models that support design and analysis practice. Advancements and challenges in instrumentation, data-visualization, and model validation are explored in this paper.

1. INTRODUCTION

Recent advances in measurement techniques make it possible to accurately measure the detailed response of test structures. These measurement systems can provide the point-wise displacements and strains at thousands of locations as well as full-field surface damage and deformation assessments. This is a particularly important advancement for understanding the behavior of concrete structures in which there is a highly complex and non-linear distribution of deformations that is controlled by concrete cracking, spalling, and local crushing, reinforcement yielding, buckling, and slip, and many other complex and poorly understood and modeled phenomena. This level of detail in experimental measurements is now beginning to approach the level of detail that finite element methods predict about structural behavior.

Such volumes of data and the multiplicity of measurement sources overwhelm traditional methods of data analysis; spreadsheets and other somewhat more advanced vector-based analysis tools. A major obstacle for complete data analysis has been the difficulty and tremendous effort required to examine all experimental data, to correlate data from large number of channels and different sources, and to understand the relevance of measurements in the context of where they are in the structure and its loading history. A significant need thereby exists for data analysis environments in which researchers can visualize, synthesize, and explore the measured data from multiple arrays of data and images sources within the coordinate space of the physical test structure. These types of visualization and analysis tools enable a greatly improved exploration and understanding of the measured behavior of the test structure and the discovery of new phenomena. This allows for the development, calibration and validation of more comprehensive and quantifiably-accurate non-linear finite element analysis tools (Gallagher, 1995).

Structural Engineers are justifiably cautious or reluctant to use present-day non-linear computation tools in design and analysis practice due to the uncertainties in the accuracy (reliability) of these tools for predicting all aspects of behavior including force and deformation capacity, modes of failure, and performance under all load levels. If the profession of structural engineering is to advance beyond its primary reliance on linear elastic analysis tools and the relationships and guidance in codes-of-practice, then a path forward is needed to support the development and use of suitably reliable non-linear computational models. This path forward must include archives of dense experimental test data, methods for model calibration and validation, and support for the use of non-linear analysis methods in professional practice.

This paper will present a summary of recent advancements in instrumentation, data-visualization, data-analysis, and the validation of computation tools. Two case studies are used in this discussion to demonstrate the potential of these advancements. This paper will conclude by presenting opportunities for the validation and use of non-linear computational tools in codes-of-practice.

2. INSTRUMENTATION METHODS

Over the last two decades there have been significant advancements in instrumentation technologies that now enable the collection of an unprecedented level and accuracy of experimental test data. Three of the key advancements have been in the collection of comprehensive displacements and strains as well as image analysis methods as summarized below.

2.1 Dynamic Coordinate Measurement Machines (CMMs)

Researchers have principally relied upon the use of displacement transducers for tracking the overall movements and relative displacements within test structures. Due to the cost, effort-requirement, and size of displacement transducers, it has not been possible to collect dense information about the response of structures. A more complete record of structural deformation can now be made through the use of Dynamic CMMs that can track the movement of hundreds and thousands of points in three dimensional space to accuracies down to a hundred of a millimeter and at up to thousands of readings per second. The underlying technology for these devices involve the tracking the movements of Light-Emitting Diodes (LEDs) along linear Charged Coupling Devices (CCDs), the analysis of dense high-definition digital images for identifying the position of reflective or high-contrast targets, and the use of laser-based technologies. These instruments all provide a complete x, y, z displacement time histories for all selected target points. These instruments are now in use in many structural engineering research laboratories.

2.2 Full-Field Displacement and Strain Measurements

Two methods for collecting comprehensive information on the surface straining of a structure are Digital Photoelastic Methods and Digital Image Correlation (DIC). In the former, a transparent coating is allied to the surface of the structure that is then subjected to a polarized light source. The birefringence properties of this coating are used in the reflected light so to measure the biaxial state of surface strains to an accuracy of about .5% of the selected range of measurements. In DIC, a random speckle pattern is sprayed onto the surface of the structure under study and then high-definition cameras are used to monitor the moving or deforming pattern of this speckle pattern. From this, both full-field strains and deformations can be obtained with accuracies down to around 100 microstrain and at measurement rates of up to 50 Hz.

2.3 Customized Image Analysis Technologies

Digital image analysis tools enable users to use photographic images to detect and characterize regions of damage including the location, width and slip along cracks, as well as regions of spalling and any other visual features of a structures response.

2.4 Example Implementations

The authors have used many of these technologies in their research for more fully understanding the behavior of tested concrete structures. For example, the Metris/Krypton Coordinate Measurement Machine was used to track the surface deformations the web faces of large prestressed concrete girders as shown in Figure 1. As another, the principles of close-range digital photogrammetry (Mikhail, 2001) were applied to the images from high-resolution cameras to evaluate the position and development of cracking throughout the loading history on these same prestressed girders as shown in Figure 2 (Russ, 1992).

Figure 1 Light-Emitting Diode Targets Spacing on 125-mm Grid on Test Girder

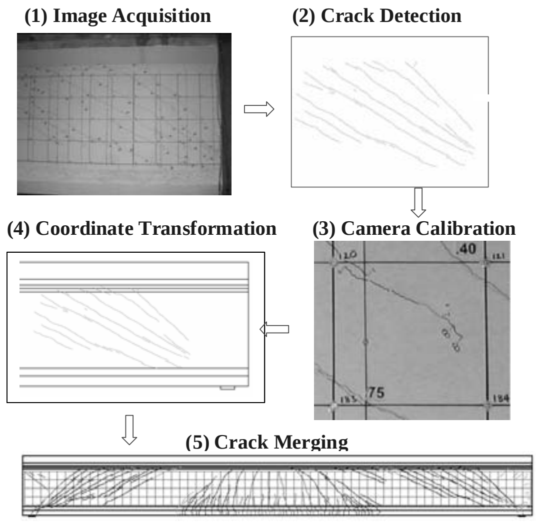

Figure 2 Evaluation of Accurate Crack Maps Using Image Processing and Photogrammetry Techniques

3. DATA VISUALIZATION AND ANALYSIS

While powerful tools have been developed for the visualization and analysis of numerical simulation data, researchers have principally relied upon the use of simple plotting tools for exploring the results from tests. While this approach may be suitable when only dozens of individual measurements are being examined, it is completely inadequate when more comprehensive data has been collected such as of the types described above. What has been needed is a data-visualization and analysis environment that can bring together the measured experimental data from all sources and combine this with the geometry and material properties of the complete test setup. A prototype program, named ExVis for Experimental Visualization was developed for this purpose.

3.1 ExVis Overview

ExVis is an object oriented program (Booch 1991, 1993) that was written for understanding the response of planar concrete structures whose response was captured by vector strain and displacement data and high-resolution still images. The available objects within the ExVis environment consist of the full geometry of the test structure, material properties, all instrumentation, and interpreted photographic data. All objects have as needed both temporal and spacial data in which two-way linked lists in a relational database system are used to correlate and use information with other ExVis functions. Examples of objects that can be individually identified in ExVis include all sections of the concrete structure as well as each reinforcing bar, loading device, support, strain gage, displacement transducer, Krypton LEDs, and crack. ExVis was written in Visual C++ and uses traditional MS window features for scrolling, zooming, and selecting objects.

3.2 ExVis Data-Visualization and Exploration

With ExVis, users may select a combination of measurements to view simultaneously. As an illustration, consider the ExVis screen shot that is shown in Figure 3 and in which the user has selected to zoom in on a section of the girder near the left-hand side support and to display the measured cracking pattern, location of selected instruments and strain in a particular strain gage 2-1.

Figure 4 presents a segment of a screen shot that displays the pattern of straining in a stirrup as measured by four gages along the length of this stirrup. The length of the horizontal line at each gage on the selected reinforcing bar is proportional to its magnitude. The pattern of cracking is also shown and illustrates that the strains in the stirrup are highest near the locations at cracking at this point in the loading history. Through this, ExVis enables the quantification of bond performance and tension stiffening relationships within the context of a realistically complex state of stress.

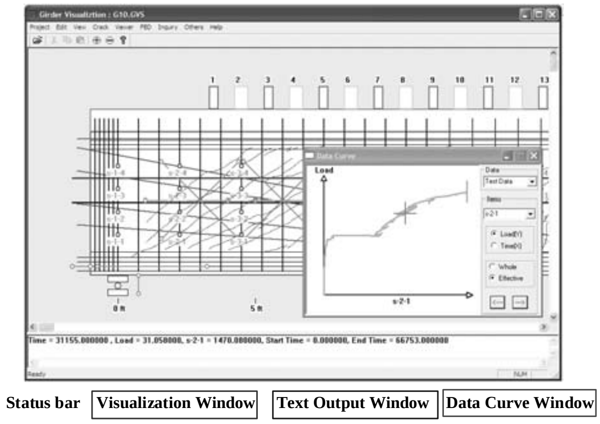

Figure 3 Screen Shot of ExVis Environment

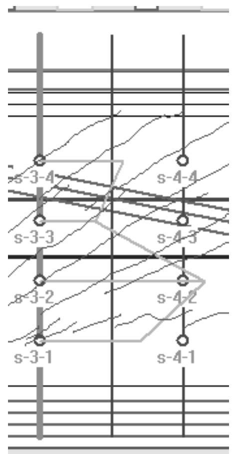

Figure 4 Distribution of Strain Along a Stirrup Based on Four Strain Gages with Crack-Pattern Overlay

3.3 ExVis Advanced Structural Analysis

In addition to being able to simultaneously view multiple aspects of structural response, tools such as ExVis need to enable more complete structural assessments. An an example of this extended functionality, ExVis enables the user to create Crack-Based Free Body Diagrams (FBD) in which the FBD diagram is automatically built and acting forces are automatically evaluated along all boundaries. See Figure 5. With this FBD and using the measured strains in the stirrups that cross the selected crack, the constitutive properties of the reinforcement, and the forces in the vertical loading jacks, the contribution of both stirrups and of the concrete to shear resistance over the loading history can be automatically calculated as shown in Figure 6 for one girder. This type of functionality made it possible to evaluate the load share for more than 300 crack-based FBD in this girder testing program. This is but one example of the type of needed advanced functionalities.

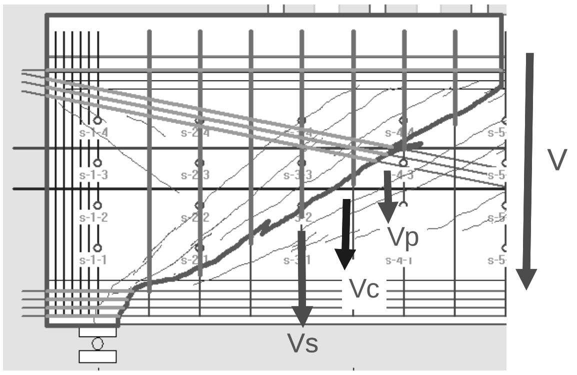

Figure 5 Crack-Based Free Body Diagram for Evaluation for Evaluation of Components of Resistance

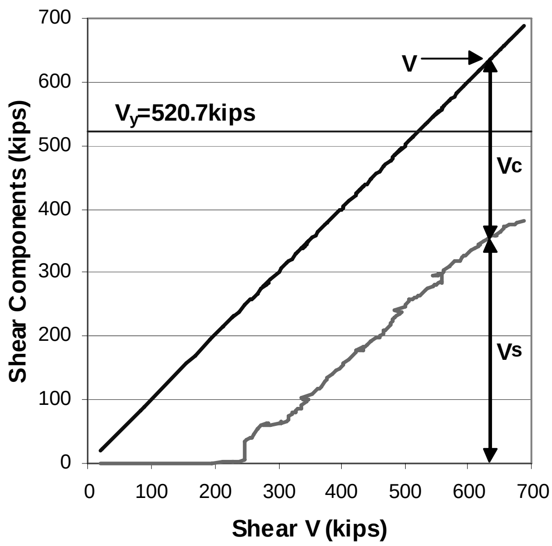

Figure 6 Measured Components of Shear Resistance (1 kip = 4.4482 kN)

4. MODEL VALIDATION

The common means of assessing the accuracy of a computational tool has been to compare the overall load-deformation responses by the computational tool with those measured by selected laboratory test structures. While this may be an effective approach when a narrow range of structures is being examined and when the mode of failure is well understood, it does not provide for a comprehensive evaluation of the computational tool. With advances in instrumentation technology, coupled with the development of data-visualization and analysis environments such as ExVis, it is now possible to make more complete assessments of computational tools with respect to their ability to predict all aspects of performance.

4.1 Developments in Model Validation

With the development and use of computational models across a spectrum of engineering disciplines and sciences, there have now been significant efforts in some fields to develop formal validation procedures (e.g. AIAA 1998; Department of Defense 2006; Oberkampf et al. 2003). One of these efforts is through the American Society of Mechanical Engineering committee on Verification and Validation in Computational Solid Mechanics (VnVCSM). This group has published a number of noteworthy white papers and guidelines that provide a useful framework and procedures that are applicable to the fields of structural and earthquake engineering (ASME 2006). They use the Sargent Circle (Schlesinger et al. 1979) to describe the interrelationships of the components of the VnV process as shown in Figure 7. There are three entities in this circle; the Reality of Interest (Structure or System), the Conceptual Model (Underlying Behavioral Models and Failure Theories), and the Computational Model (Computational Tool/Finite Element Analysis Package). A formal evaluation of the effectiveness of an analytical tool requires that verification and validation activities be carried out between these entities. The selected conceptual model for all portions of the structure or system under examination must be appropriate for the types of phenomena and aspects of performance being investigated. These conceptual models must be properly implemented within the computational model such that the sensitivity of the predicted behavior to all assumptions is well understood and compensated for. Finally, the predictions of the computational model for all aspects of the performance under examination must be fully assessed. Guidelines for the use and validation of linear and non-linear computational tools for the design and analysis of concrete structures are being published by the federation international du beton (*fib*).

As part of any model validation exercise, it is essential that the user starts by defining the goals for the use of the computational model so that the types of comparisons and sensitivity studies to be made can be properly selected. To the extent possible, the results of comparisons should be quantitative and with defined levels of certainty. However, given limitations in most analytical models and available test data, in some cases only qualitative comparisons are possible.

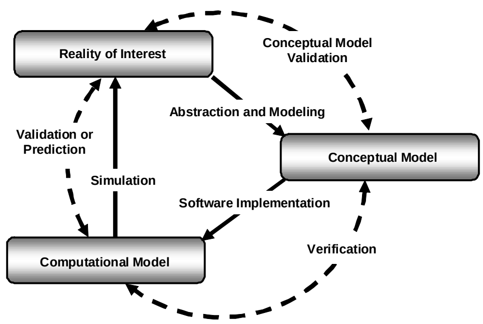

Figure 7 Sargent Circle

4.2 Validation Example

A validation exercise was completed for the use of a particular computational tool for predicting the shear behavior of 20 large prestressed concrete girder tests that were conducted at the University of Illinois and that made use of advanced measurement system and the ExVis program. The specific computational tool examined was program VecTor2 (Wong and Vecchio 2002) that employs the conceptual model of the Modified Compression Field Theory (Vecchio and Collins 1986). This validation exercise assessed the ability of the computational tool to predict the cracking strengths and ultimate capacity, the stiffness of the overall response, the shear response of the webs, cracking patterns and widths, and modes of failure. Since qualitative assessments are less common, two examples are now used to illustrate their value and current necessity.

In Figure 8, a comparison is made between the predicted and measured state of cracking in a test girder. As shown, VecTor2 predicted well the extent, angle, and widths of the cracking throughout this structure. Note that the lines within the elements of the VecTor2 prediction indicate whether or not cracking is expected within the region of each element rather than showing the location of a discrete crack. Figure 9 compares the VecTor2 predicted state of compressive stress in the right end region of a girder in the last converged load step versus the pictorially observed condition of the girder just prior to an explosive failure. Figure 9a provides the ratio of the principal compressive stress in each element to the principal compressive stress capacity; the image indicates that the mode of failure is expected to be due to diagonal crushing above the support. This mode of failure is visually confirmed in Figure 9b.

The results of this full model validation exercise provided a quantitative and qualitative assessment of a computational tool's predictive capabilities and thereby illustrated that this tool could be effectively used with calculable levels of reliability to predict many aspects of the performance of prestressed concrete girders.

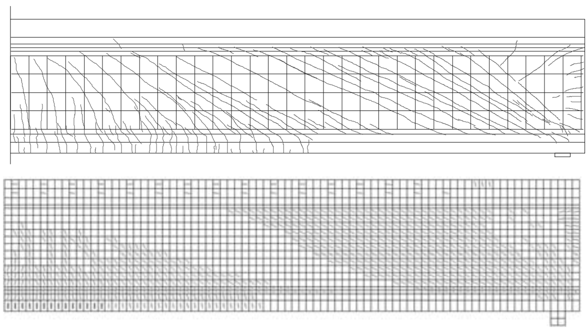

Figure 8 Predicted and Measured State of Cracking in Tested Prestressed Girder

4.3 Ongoing Validation-Focused Projects

As described above, advanced instrumentation devices, data-visualization and analysis methods, and model validation procedures were used in a recent girder testing project. These methods are being used and expanded upon in an ongoing NEES research project being led by researchers at the University of Washington, Illinois, and UCLA. The experimental research program is being conducted in the Newmark Structural Engineering Laboratory on the design and behavior of complex structural walls. In this program, component tests are being conducted on the bottom three stories of structural walls that are part of high-rise structures. The actions at this third storey level of axial load, moment, and shear are based on the performance of the full height wall and are being imposed on the test structures using the Loading and Boundary Condition Boxes at the Illinois NEES facility as shown in Figure 10. Some of the instrumentation, data-visualization, and model validation extensions in this testing program are:

- use of close-range photogrammetic system for measuring point-wise displacements
- development of much-more extensive crack mappings
- using as-built layout of reinforcement and gage locations
- formatting of all data for ingestion in a community (NEES) repository

These activities are central to the objectives of the NEES program and overall NSF digital archive initiatives to archive complete information from conducted research projects in a form that is more broadly useful to the national and international communities.

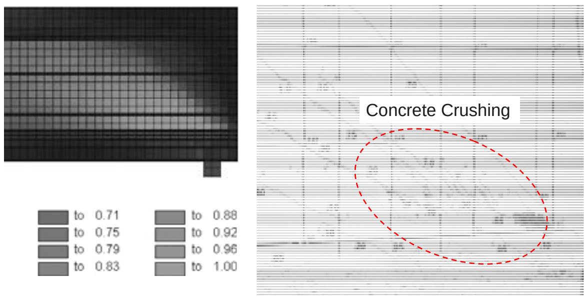

(a) Predicted Ratio of Compressive Stress to Compressive Strength in Each Element by VecTor2

(b) Observed Response of Lower Web Near Right Support

Figure 9 Comparison of Predicted and Observed Mode of Failure

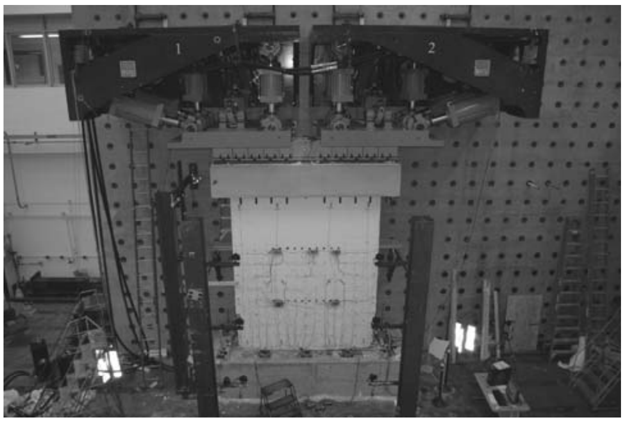

Figure 10 Component Test on Bottom Three Stories of Structural Wall

5. CONCLUSIONS AND FUTURE NEEDS

In order for the structural engineering profession to advance beyond a primary reliance on linear-elastic analysis methods and empirical codes-of-practice to an integrated non-linear analysis and design environment, computational tools are needed that have quantifiable levels of accuracy for all aspects of performance for which structures need be designed. This will require that experiments and research program have well-defined numerical model validation and development objectives.

Recent advancements in instrumentation technologies as well as experimental data-visualization and analysis techniques provide the tools for conducting more complete model-validation exercises and can produce quantifiably accurate non-linear computational tools for use in integrated non-linear design and analysis practice. To achieve this goal, the following is needed:

1.) More extensive use of advanced instrumentation methods in experimental research studies.

2.) Improved and more complete assessments of material properties.

3.) More complete consideration of previous conducted research in the design of experimental testing programs.

4.) Data-visualization tools for the more comprehensive examination of experimental test data and for direct comparison of test data with the predictions of computational methods.

5.) Improved archival and structuring of test data for its examination with visualization tools and for use in model validation activities.

6.) The establishment of formal procedures for validating models for all aspects of critical structural performance.

7.) The selection by code-of-practice committees of benchmark tests to use for model validation activities.

Many of the key ideas expressed throughout this paper are summarized in the video that is available at:
http://dankuchma.com/ExVis/ExVis.avi

Acknowledgements:

The authors wish to acknowledge the support of the US National Cooperative Highway Research Program, the Precast/Prestressed Concrete Institute, and the National Sciences Foundation Network for Earthquake Engineering program.

References:

Gallagher, R. S. (1995). “Computer visualization: graphics techniques for scientific and engineering analysis,” CRC, Boca Raton, Florida.

Mikhail, E.M., Bethel, J.S., and McGlone, J.C. (2001), “Introduction to Modern Photogrammetry,” Wiley, New York.

Russ, J. C. (1992), “The Image Processing Handbook,” CRC Press, Boca Raton, Florida.

Booch, G. (1991), “Object-Oriented Design with Applications,” Benjamin/Cummings Publishing, Redwood City, Calififornia.

Booch, G. (1993), “Object-Oriented Analysis and Design with Applications,” Benjamin/Cummings Publishing, Redwood City, California.

Oberkampf, W. L., Trucano, T. G., and Hirsch, C. (2003). "Verification, Validation, and Predictive Capability in Computational Engineering and Physics." Sandia National Laboratories (Albuquerque).

AIAA. (1998). “Guide for the Verification and Validation of Computational Fluid Dynamics Simulations,” American Institute of Aeronautics and astronautics, Reston, VA.

Department of Defense. (1994). "DoD Directive No. 5000.59: Modeling and Simulation (M&S) Management." Defense Modeling and Simulation Office, Office of the Director of Defense Research and Engineering <www.dmso.mil/docslib>

ASME PTC 60 Committee. (2006). "Guide for Verification and Validation in Computational Solid Mechanics." American Society of Mechanical Engineers, New York.

Schlesinger, S. (1979). "Terminology for model credibility." *Simulation*, **32**(3), 103-104.

Wong, P. S., and Vecchio, F. J. (2002). “Vector2 and Formworks User's Manual,” Toronto.

Vecchio, F. J., and Collins, M. P. (1986). "The Modified Compression-Field Theory for Reinforced-Concrete Elements Subjected to Shear." *Journal of The American Concrete Institute*, American Concrete Institute, **83**(2), 219-231.

SEISMIC RETROFIT OF GRAVITY-LOAD-DESIGNED CONCRETE STRUCTURES

Kiang Hwee Tan[1)]

1) Associate Professor, Dept. of Civil Engineering, National University of Singapore, Singapore
cvetankh@nus.edu.sg

Abstract: In this study, the use of externally bonded fiber-reinforced polymer (FRP) systems in retrofitting reinforced concrete shear walls, frames and beam-column joints in gravity-load-designed (GLD) buildings to resist lateral forces due to seismic action is presented. Pushover and cyclic tests were carried out on and 1/5-scale shear walls, 1/2-scale sub-frames and prototype joints. For the un-retrofitted shear wall, sudden failure was observed at the base of the side walls due to shear. Failure of the retrofitted wall was however more ductile with FRP debonding, followed by concrete crushing and FRP rupture at the compressive base of the side wall. The ultimate load capacity and lateral displacement of the retrofitted wall increased respectively by 45 and 66 percent. For the frames, test results revealed a strong-column–weak-beam failure mechanism. The retrofitted frame was 30 percent higher in ultimate strength but 12 percent lesser in ultimate drift ratio compared to the un-retrofitted frame. For the beam-column joints, the ductility was significantly increased with the application of externally bonded FRP systems although the ultimate load capacity increased only marginally. In addition, the provision of FRP systems at the joint core regions is effective in enhancing the performance under reversal cyclic loading.

1. INTRODUCTION

In general, buildings in Singapore are designed primarily for gravity loads as Singapore is sited on a stable part of the Eurasian Plate. However, some buildings are subjected to minor tremors due to earthquakes occurring some 400 to 700 kilometers away in Sumatra as a result of the amplifying effect of soft soils on low-frequency, long-distance waves (Balendra et al. 1990). Studies are being carried out at the National University of Singapore (Aripin 2006, Kong 2003, Li 2006, Shao 1999), which focus on the seismic vulnerability of existing reinforced concrete (RC) buildings in Singapore, and examine appropriate retrofitting measures where necessary.

This paper presents some of the experimental studies on reinforced concrete shear walls, frames and beam-column joints that are typically found in residential buildings in Singapore, with focus on the use of fiber-reinforced polymer (FRP) systems in enhancing the structural performance under lateral forces due to seismic action.

2. RETROFIT OF SHEAR WALLS

2.1 Test Specimens

Two 1/5-scale models of a shear wall, representing the lower 2.6 stories of a 25-story building, as shown in Figure 1, were fabricated. The I-shaped walls had a height of 1036 mm, with a built-up height of 1314 mm after attaching the loading beams at the top of the wall. The side wall components had a length of 657 mm, the center wall component has a length of 957 mm, and the wall thickness was 45 mm throughout.

One wall was not retrofitted while the other wall was retrofitted using glass FRP system. The average concrete cube compressive strength at 28 days was 31 and 25 MPa respectively. The internal reinforcement, consisting of $\phi 6$, $\phi 8$ and $\phi 10$ steel bars, had yield strengths of 350, 482 and 525 MPa, respectively. For the FRP retrofitted wall, a layer of unidirectional glass FRP fabric (with properties as shown in Table 1) was used to wrap the I-shaped wall in the horizontal direction. Fiber bolts were placed at the joint area between the side and center walls, at an average spacing of 85 mm, to provide continuity in the FRP reinforcement around each component wall.

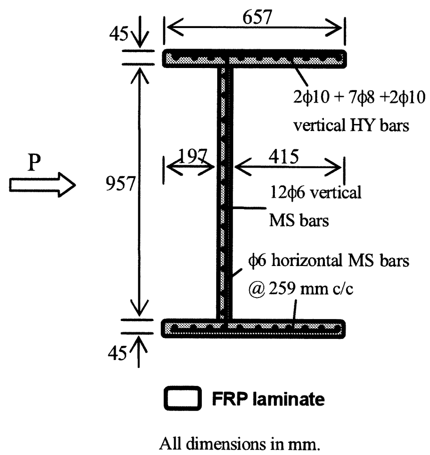

Figure 1 Cross-Section of Shear Wall

Table 1 Properties of Glass FRP System

Density	915 g/m^2
Thickness	0.353 mm/layer
Fibre orientation	Uni-directional
Young's modulus	69.7 GPa
Ultimate tensile strength	1670 MPa
Ultimate tensile strain	0.02

An axial load was applied on the wall specimen to simulate loadings from upper stories. This was done by using post-tensioning tendons which produced an average axial compression ratio of 0.24. A lateral point load was transferred to the wall through the loading beams. The wall was pushed at a rate of 0.006 mm/s until failure. To prevent out-of-plane bending of the side wall components during the tests, lateral supports were placed at two-third height.

2.2 Test results and discussion

Figure 2 compares the lateral force versus top lateral displacement characteristics of the two wall specimens. Initially, both walls showed approximately the same response. At a load of 90 kN, the force-displacement curve of the un-retrofitted wall deviated from that of the retrofitted wall due to initiation of inclined shear cracks, leading to a lower wall stiffness. First yielding of steel reinforcement occurred at about 130 kN.

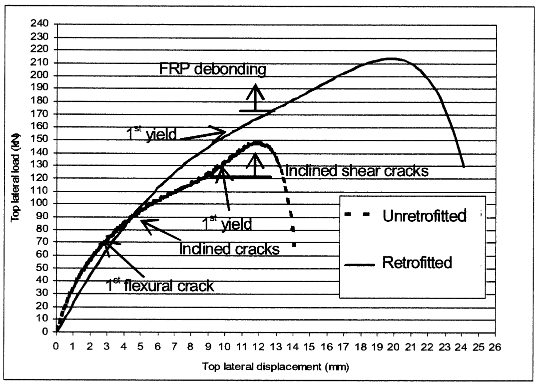

Figure 2 Load-Deflection Characteristics of Shear Walls

At the ultimate load of 148.4 kN, a 5-mm wide diagonal shear tension crack was observed to originate from the compression bottom edge of the side wall to the 2nd story level in the un-retrofitted wall specimen, as shown in Figure 3(a). The ductility of the wall measured by the ductility index, defined as the ratio of the displacement at ultimate to that at first yield of steel reinforcement, was 1.09.

For the FRP-retrofitted wall, failure was more ductile with FRP debonding, followed by concrete crushing and FRP rupture at the compressive base of side wall, as shown in Figure 3(b), at the ultimate load of 214.7 kN. First yielding in steel reinforcement occurred at a load of about 61 % of the ultimate load, and the ductility index was 1.4.

Thus, although the retrofitted wall did not exhibit increase in stiffness, the ultimate load capacity was increased 1.45 times while the ultimate lateral displacement was increased 1.66 times. Correspondingly, the ductility of the wall was increased 1.28 times.

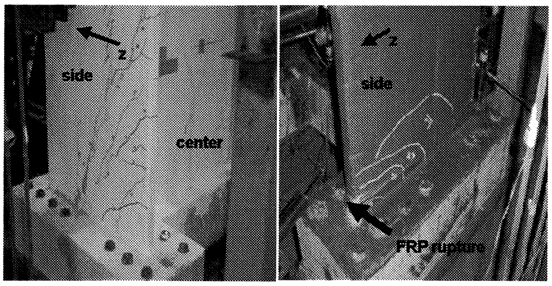

(a) (b)

Figure 3 Failure Characteristics of Shear Walls: (a) Un-Retrofitted Wall and (b) Retrofitted Wall

3. RETROFIT OF RC FRAMES

3.1 Test frames

Two half-scale, one-and-a-half bay, two-story sub-frames, representing the critical lower stories of a four-story frame, were fabricated. One of the frames was un-retrofitted and the other retrofitted using glass fiber-reinforced polymer (FRP) system as shown in Figures 4 and 5.

The average cube compressive strength and Young's modulus of concrete at the time of testing the frames were about 20.8 MPa and 18.7 GPa, respectively. Four types of longitudinal bars were used: 10 mm deformed bars, 8 mm, and 7 mm round bars, which corresponded to T20 mm, T16 mm and T13 mm bars in the actual structure. These steel bars had average yield strengths of 500, 527, and 555 MPa respectively. For the links, 6 mm round bars with a yield strength of 260 MPa were used. The properties of the glass FRP system are as shown in Table 1.

The total vertical load on the prototype frame was taken as the dead load plus 40% of the live load. Unit weight of reinforced concrete was taken as 25 kN/m^3, and the dead load included those due to partition walls and floor finishes of 1.0 and 1.2 kN/m^2 respectively. The live load was 1.5 kN/m^2. Pre-stressing load was applied at the top of the columns in the test frames to simulate the gravity load from the beams including those from the upper stories. The prestressing forces, were 60 and 80 kN for the external and internal columns respectively. They were applied using two ϕ9 mm prestressing wires for each column.

Each test frame was subjected to pushover loading, with 39% of the total lateral load on the first story and the remaining on the second story at the beam level, until one of these following conditions occurred: (a) a collapse mechanism due to the formation of sufficient plastic hinges; (b) a 20% reduction in the base shear capacity of the frame; or (c) the maximum drift has exceeded 2% of frame height.

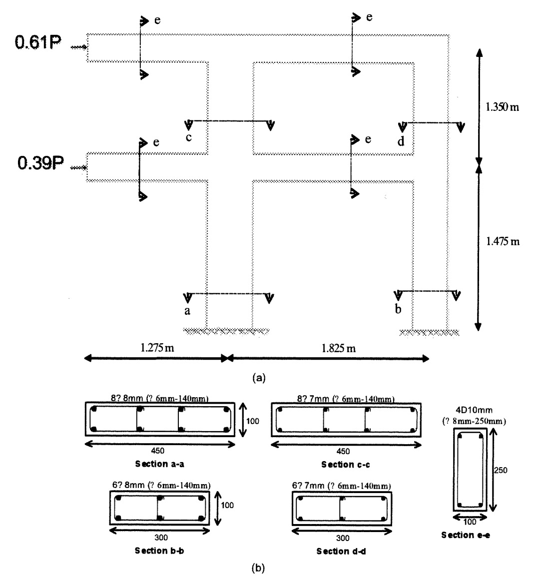

Figure 4 Un-retrofitted RC Frame: (a) Elevation, and (b) Section Details

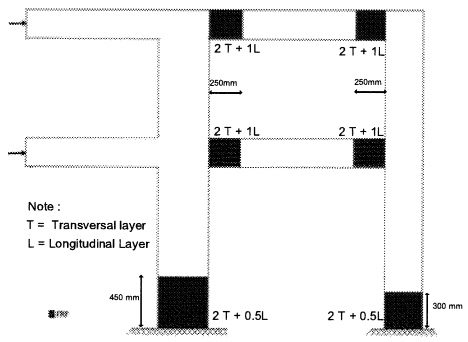

Figure 5 FRP Configuration for Retrofitted Frame

3.2 Test Results and Discussion

Figure 6 shows the pushover curves for the test frames. The lateral force is the total load on the frame while the drift ratio is the lateral displacement at the second story level divided by the height of the frame up to the second story level. Although the retrofitted frame exhibited a similar stiffness of about 12600 kN/m in the initial stage as the un-retrofitted frame, it had an ultimate strength of 101 kN compared to 79 kN and ultimate drift ratio of 1.75% versus 2% for the un-retrofitted frame. That is, the retrofitted frame exhibited both a higher yield and ultimate load but a lower ultimate drift ratio.

The cracking characteristics of the frames are shown in Figure 7. Flexural cracks first appeared in the retrofitted frame at location 1 at a later stage than in the un-retrofitted frame due to the presence of the glass FRP system. These cracks subsequently developed in an inclined direction, and were accompanied by shear cracks in the internal column and in the first floor beam. The order of appearance of cracks is indicated by the numbers in Figure 7. The cracks further propagated with increasing loads.

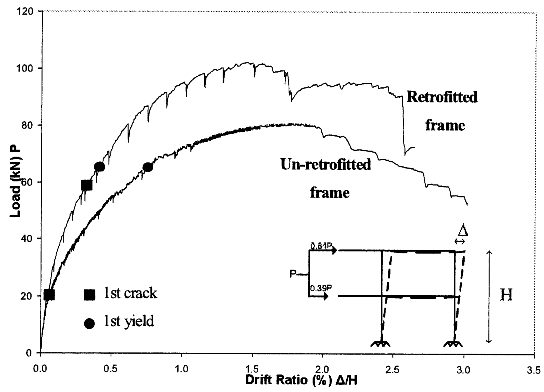

Figure 6 Load-Drift Ratio Relations of RC Frames

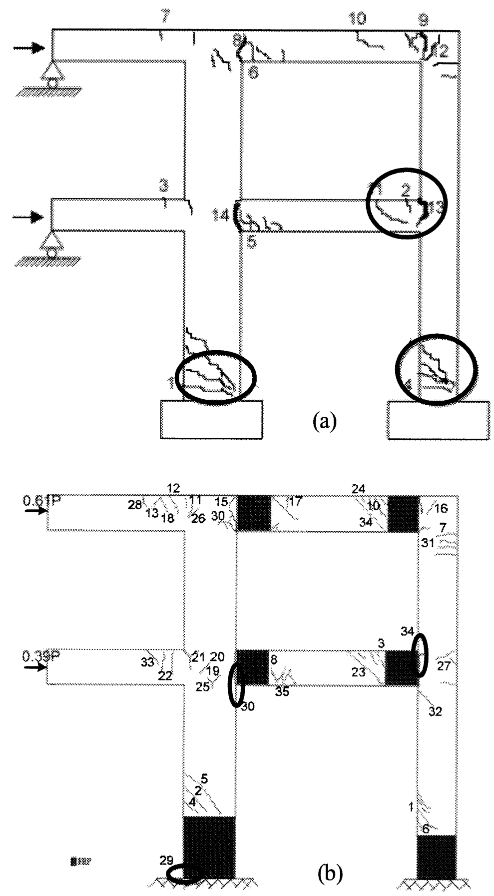

Figure 7 Cracking Characteristics of Test Frames: (a) Un-Retrofitted Frame, and (b) Retrofitted Frame

For the retrofitted frame, the cracks at locations 29, 30, and 34 became increasingly wider compared to other locations near the ultimate load. The lateral force reached the peak value at a displacement of 41 mm. When the lateral displacement was increased further to 52 mm, the cracks at location 30 has widened to the extent that the longitudinal FRP sheets had ruptured, resulting in a dramatic drop in the applied force.

From the strain gauge readings, the internal steel reinforcement was first observed to yield at the bottom of the internal column, at a load of 69.5 kN and a corresponding lateral displacement of about 11 mm. This was followed by the yielding of the reinforcing bars at the external column at a load of 75 kN and a displacement of 12.8 mm. First yielding of reinforcing steel in the beams was observed at a load of 85 kN with a displacement of 16.4 mm.

Most of the cracks occurred in the beams and near the base of the columns, with minor cracks in the joint area and elsewhere; thus the retrofitted frame remained a strong-column-weak-beam structure under lateral action.

4. RETROFIT OF BEAM-COLUMN JOINTS

4.1 Test Joints

Six beam-column joints were tested. The dimensions and the internal steel reinforcement are shown in Figure 8(a). The concrete had an average cube compressive strength of between 30 and 43 MPa. The average yield strength of T10 and T13 steel deformed bars were 490 and 470 MPa respectively. Two types of FRP systems were used, one with glass fibre sheets (with a tensile strength, elastic modulus, and ultimate strain of 580 MPa, 22.5 GPa, and 2%, respectively) that are pre-saturated in a specially formulated epoxy and the other consisting of unidirectional carbon fibre composite sheets (with a tensile strength, elastic modulus, and ultimate strain of 3550 MPa, 235 GPa, and 1.5%, respectively) with a two-part epoxy resin.

The specimens, designated CON, GLO, CLO, CLU, CLX and GLU, had different configuration of external FRP systems, as shown in Figure 8(b). Specimen CON was not bonded with external FRP sheets, and served as the reference specimen. Specimens GLO and GLU were bonded with glass fibre sheets while CLO, CLU and CLX with carbon fibre sheets. Specimens GLO and CLO each had two plies of "L-shaped" fibre sheets placed at each beam-column interface. CLU and GLU had, in addition to the "L-shaped" sheets, two plies of "U-shaped" fibre sheets at the joint core region. Specimen CLX was bonded with two plies of "X-shaped" carbon fibre sheets at the core region in addition to the "L-shaped" sheets. All the fibre sheets were anchored at their ends using transverse sheets.

Each specimen was mounted in a vertical plane on a test frame with the column component spanning horizontally over two steel bracket supports and the beam standing vertically. A cyclic load was applied using a 20-ton capacity hydraulic actuator with a ±75mm stroke by pushing and pulling laterally on the top of the beam component.

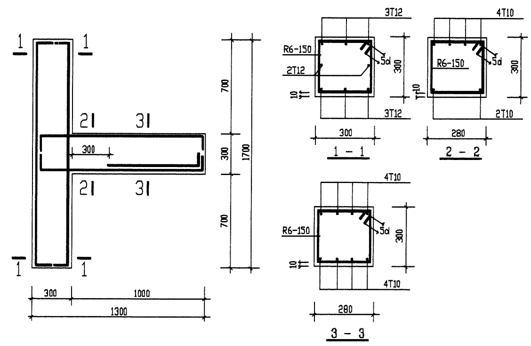

(a)

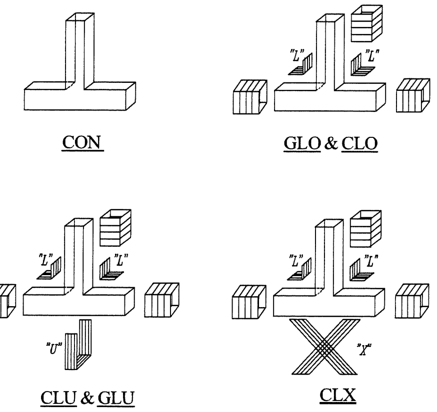

(b)

Figure 8 Details of Beam-Column Joints: (a) Cross-Section Properties, and (b) FRP Configurations

The loading history was as follows. First, the beam component was pulled (negative bending), such that the side with the heavier steel reinforcement (4T10) was subjected to tension. The loading cycle was repeated three times in each direction with the maximum deflection equal to that at which yielding of tensile reinforcement first occurred in the beam. This was followed by three cycles each to deflections equal to twice, thrice, and four times the deflection at first yield of tensile reinforcement until the specimen failed or until the actuator reached its stroke capacity.

4.2 Test Results and Discussion

In the un-retrofitted specimen CON, cracks first occurred in the beam component under both negative and positive bending at a load of around 12 kN. After four loading cycles, the steel reinforcement on both sides of the beam began to yield. After another two cycles, the concrete started to crush and the applied load decreased in magnitude. The peak loads were 38.0 kN, and 22.3 kN for negative and positive bending, respectively. In the eighth cycle under positive bending, the applied load reduced to less than 50% of the peak value and the loading process was stopped as the tensile steel reinforcement ruptured due to excessive deformation.

For Specimens CON, GLO and CLO, failure occurred at the interface of the beam and column components. For the other three specimens, failure occurred beyond the FRP-retrofitted region in the beam. That is, the presence of FRP systems at the joint core region in CLU, CLX and GLU shifted the plastic hinges away from the beam-column interface to the section beyond the confined region in the beam component, thus resulting in slightly increased strength of the specimens. Specimens CON, GLO and CLO were observed to fail on both faces, while CLU, CLX and GLU failed at the weak face (with 2T10 as tensile reinforcement).

The ultimate loads of the six specimens varied within a narrow range. For the strong face (that is, under negative bending), the maximum load ranged from 36.4 to 41.1 kN, while for the weak face (positive bending), the maximum load ranged between 20.0 to 23.2 kN.

The hysteresis curves for the six specimens are shown in Figure 9. Specimen CON sustained the least number of cycles (five cycles), while Specimens CLU and CLX sustained the most number of cycles (eleven cycles) before failure. Although the six specimens shared similar ultimate loads, specimens with FRP systems at the core regions, such as Specimens CLU, CLX and GLU, had a higher deformation capacity, that is, greater ductility at the ultimate state.

Comparing Specimens CLU and CLX, it is noted that the hysteresis curves of specimen CLU enclose a larger area than those of specimens CLX and GLU, especially in the last few cycles. Therefore, it is reasonable to deduce that the "U-shaped" FRP systems are more effective than the "X-shaped" systems and the carbon FRP systems are more effective than their glass counterpart in confining the joint core region, contributing to the better performance of the beam-column joints.

To compare the ductility of the specimens, two parameters were used. First, the displacement ductility index, μ, is defined as

$$\mu = \frac{\Delta_{0.8u}}{\Delta_y} \qquad (1)$$

where $\Delta_{0.8u}$ is the beam end deflection when the applied load has dropped to 80% of the peak value, and Δ_y is the beam end deflection at which the steel reinforcement first yielded.

Second, the cumulative ductility factor, CDF, is defined as (Kaku and Asakusa 1991)

$$CDF = \sum_{i=1}^{n} (i \times \delta_i) / \delta_1 \qquad (2)$$

where n is the number of cycle to failure, δ_i is the total lateral deflection during the i-th cycle, and δ_1 is the total lateral deflection in the first cycle.

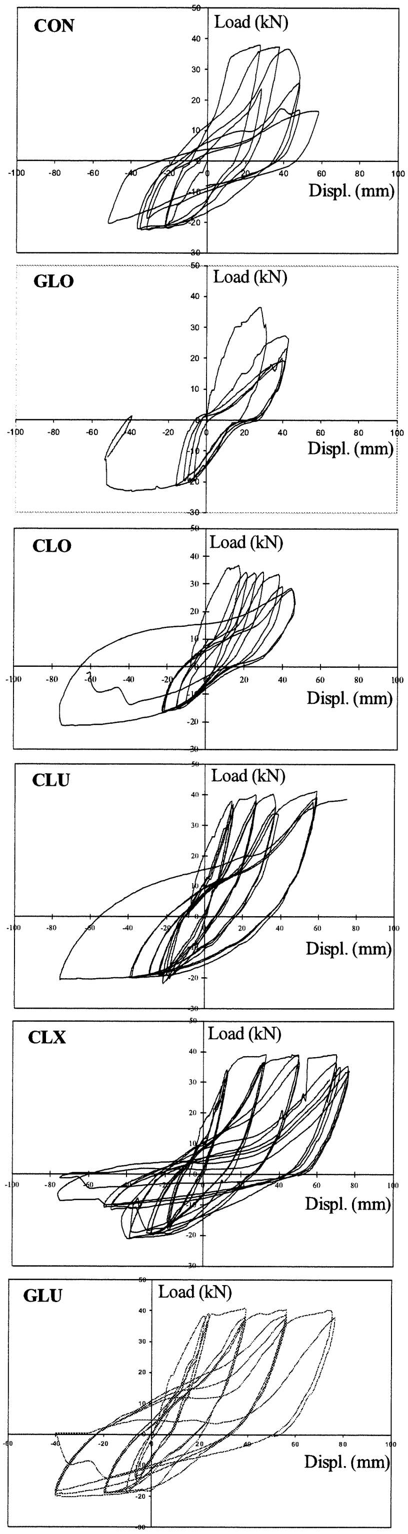

Figure 9 Hysteresis Curves of Joints

The values of μ and *CDF* are shown in Table 2 for the test specimens. Compared with the un-retrofitted specimen CON, the retrofitted specimens exhibited higher ductility. The displacement ductility indices of GLO and CLO were 6.3 and 6.9, with the cumulative ductility factors being 9.0 and 13, respectively. Specimens CLU, CLX and GLU, with the joint core region confined with the FRP system, showed even better performance. The ductility indices were more than 8 while the cumulative ductility factors were above 20.

Table 2 Ductility Indices and Cumulative Ductility Factors

Joint	f_c' (MPa)	μ	*CDF*
CON	43.0	3.7	5
GLO	32.7	6.3	9
CLO	30.4	6.9	13
CLU	31.2	>8	30
CLX	35.3	>8	26
GLU	29.5	>8	20

5. CONCLUDING REMARKS

The use of externally bonded glass FRP systems in retrofitting shear walls, frames and beam-column joints in gravity-load-designed RC buildings, to resist lateral forces was examined. Tests carried out on scaled specimens indicated that the retrofitting method resulted in improved behavior of shear walls and framed structures, in terms of delay in first cracking and first yield of steel reinforcement, as well as in the increase in ultimate strength, ultimate displacement and ductility of the structure. The failure characteristics were found to change from a brittle type to a more ductile type due to the application of the FRP system.

Test results also showed that the performance of beam-column joints under reversal cyclic loading in terms of ductility could be improved by bonding FRP systems. The application of FRP systems at the joint core regions was found to be effective in further enhancing the structural performance under reversal cyclic loading.

Acknowledgements:

The tests were carried out by Dr Kong S.K., Dr Li Z.J., Mr Shao Y.T. and Mr Aripin W. in the course of their graduate programs.

References:

Aripin, W. (2006), "Gravity-Load-Designed Reinforced Concrete Frame under Far-Field Earthquake Action," M.Eng. Thesis, National University of Singapore, 132 pp.

Balendra, T., Tan, T.S., and Lee, S.L. (1990), "An analytical model for far-field response spectra with soil amplification effects," *Engineering Structures*, **12**(4), 263-268.

Kaku, T. and Asakusa, H. (1991), "Ductility Estimation of Exterior Beam-Column sub-Assemblages in Reinforced Concrete Frames," *ACI Special Publication*, SP-123, pp. 167-185.

Kong, K.H. (2003), "Overstrength and Ductility of Reinforced Concrete Shear-Wall Frame Buildings Not Designed for Seismic Loads," PhD Thesis, National University of Singapore, 271 pp.

Li, Z.J. (2006), "Seismic Vulnerability of Reinforced Concrete Frame and Shear Wall Structures in Singapore," PhD Thesis, National University of Singapore, 313 pp.

Shao, Y.T. (1999), "Seismic Response of Beam-Column Connections Confined with External FRP Systems." M.Eng. Thesis, National University of Singapore, 125 pp.

Fifth International Conference on Urban Earthquake Engineering
March 4-5, 2008, Tokyo Institute of Technology, Tokyo, Japan

SIZE EFFECT ON THE SHEAR STRENGTH OF RC DEEP BEAMS

Kenji Kosa[1], Satoshi Uchida[2], Hiroshi Kobayashi[3], and Tsutomu Nishioka

1) Professor, Dept. of Civil Engineering, Kyushu Institute of Technology, Japan
2) Graduate Student, Dept. of Civil Engineering, Kyushu Institute of Technology, Japan
3) Senior Engineer, Hanshin Expressway Company, Japan
4) Senior Engineer, Hanshin Expressway Company, Japan

kosa@civil.kyutech.ac.jp

Abstract: To investigate the size effect on reinforced concrete (RC) deep beams with a shear span ratio (a/d) of 1.5, an experiment was conducted using the effective depth (300～1400mm) of a beam as the parameter. Strains in the specimens were measured using dummy reinforcements and acryl bars. From the experiment, it was confirmed that the relative shear strength decreased as the specimen size became larger due to a relative reduction in the strut width.

1. INTRODUCTION

As to the ordinary RC beams with a shear span ratio (a/d) of 2.5 or more, the size effect which decreases the shear strength as the member size increases has already been confirmed. And, the size effect is duly considered in the shear strength equation based on the loading test results.

As to the RC deep beams with an a/d of less than 2.5, Walraven et al. (1994) conducted an experiment using beams with a/d=1.0 and changing their effective depth (d) from 160mm to 930mm. They found that crack propagation became faster as the specimen size became larger. However, they did not treat the internal stress, with no measurement of it using a strain gage or by other means. Deep beams with a/d=around 1.5, which is the size frequently used for actual structures and whose damage pattern varies, has been studied very little. Therefore, we conducted an experiment using deep beam specimens with a/d=1.5 and by changing their effective depth (d) in the range of 300～1,400 mm (close to a real beam size). Using the measurement results such as strains of reinforcement and concrete, the size effect of deep beams was evaluated.

2. EXPERIMENTAL PROGRAM

2.1 Specimens

Table 1 shows the attributes of specimens and the results of a compression test. In this experiment, a total of 25 specimens with various parameters, such as a/d (0.5, 1.0. 1.5), shear reinforcement ratio Pw (0.0, 0.4, 0.8%), effective depth d (300～1,400 mm), were tested. However, only 19 of them with a/d = 1.5 were used for this analysis to evaluate the size effect.

Fig. 1 shows the reinforcement arrangement and the sectional configuration. The left side of the figure shows a typical reinforcement arrangement for Pw=0.0% and the right side for Pw=0.4 and 0.8%. For the specimens of Pw=0.0% with no arrangement of shear reinforcement, dummy reinforcement (Pw=less than 0.05%) was arranged within the shear span to enable measurement of strains in the vertical direction. The sectional configuration was made identical in all specimens, as shown in Fig. 1(b). Therefore, the main reinforcement ratio (about 2.0%) and the maximum aggregate size (Dmax=20 mm) were the same in all specimens. Also, to eliminate the effect of loading plate width and bearing plate width (**r**), **r/d** were made to 0.25 in all specimens.

2.2 Loading Method and Measurement Items

Using a 30,000 kN loading machine installed at the Public Works Research Institute (PWRI) and a 2000 kN loading machine installed at the Kyushu Institute of Technology, monotonic loads were applied at two symmetrical positions on the specimen. Typical measurement items were five: displacement of a specimen (vertical direction at the bottom of the specimen or at the loading plate, and horizontal direction), strain of reinforcement (main reinforcement, shear reinforcement, dummy reinforcement), strain of an acryl bar, shear displacement, and crack width measured by image analysis.

Fig. 2 shows typical installation positions of strain gages and LVTs. Strain gages on the main reinforcement were used to measure tensile strain in the horizontal direction caused by flexural deformation. Strain gages on the shear reinforcement and dummy reinforcement

Table.1 Attributes of specimens

Specimen No.	Shear span ratio a/d	Effective depth d (mm)	Shear reinforcement ratio P_w(%)	Main reinforcement ratio P_t (%)	Compressive strength fc (N/mm^2)	Maximum aggregate size D_{max} (mm)
B-2	0.5	400	0.0	2.02	36.2	20
B-3			0.4	2.02	36.2	
B-4			0.8	2.02	31.3	
B-6	1.0		0.0	2.02	31.3	
B-7			0.4	2.02	31.3	
B-8			0.8	2.02	37.8	
B-10.1	1.5	300	0.0	2.02	37.0	
B-10.1R				2.02	42.3	
B-10		400		2.02	29.2	
B-10R※				2.02	23.0	
B-10R2				2.02	37.0	
B-10.2		500		2.02	37.0	
B-10.2R				2.02	42.3	
B-10.3		600		2.11	37.8	
B-10.3R※				2.11	31.2	
B-10.3R2				2.11	37.0	
B-13※		800		2.07	31.6	
B-13R※				2.07	24.0	
B-14※		1000		1.99	31.0	
B-15※		1200		1.99	27.0	
B-16※		1400		2.05	27.3	
B-11		400	0.4	2.02	23.0	
B-17※		1000		1.99	28.7	
B-18※		1400		2.05	23.5	
B-12		400	0.8	2.02	31.3	

※ Taken from experiments at PWRI

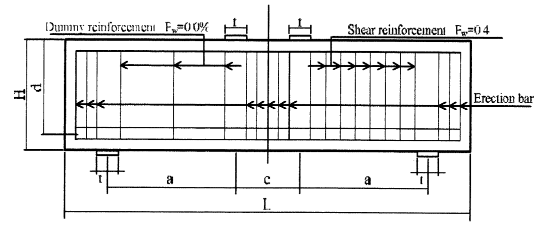

(a) Example of reinforcement arrangement

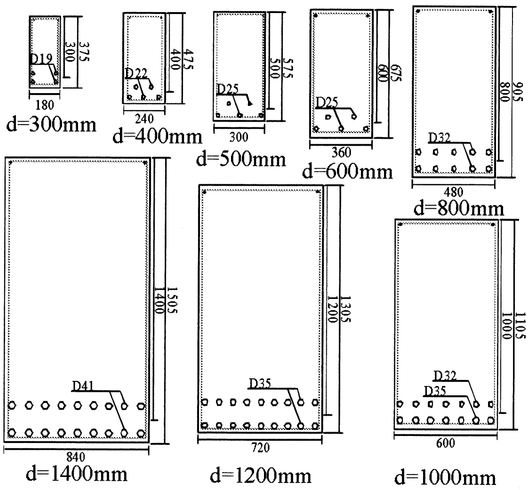

(b) Configuration of section

Fig.1 Configuration of specimens

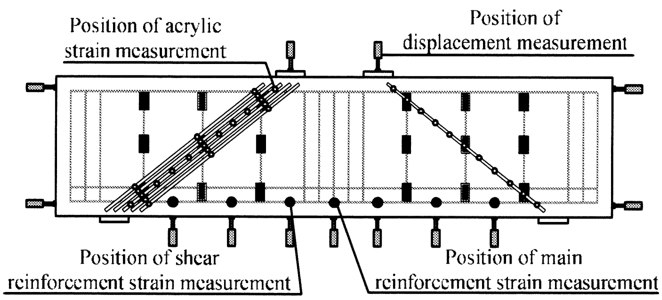

Fig.2 Positions of strain meters and displacement meters

were used to measure tensile strain in the vertical direction mainly around the strut area. Also, two LVTs were installed on the specimen surface at diagonal positions within the shear span to measure shear deformation.

2.3 Measurement of Diagonal Cracks

The width of diagonal cracks within the shear span was measured in the 200x300 mm range at the positions of loading plate, strut center, and bearing plate, using a digital camera (600M pixels). Using image analysis software, the crack width was measured at two crack profile-matching points along the crack line by comparing with a 5x5 mm mesh placed on the specimen in advance. Such measurements were made at five positions (interval: 10 mm) at each of the abovementioned three measurement positions and their average values were taken.

3. EXPERIMENTAL RESULTS

3.1 Failure of Specimens (a/d= 1.5)

From the loading test of specimens with a/d=1.5, two failure patterns were found: Pattern 1 – crushing failure occurred immediately below the loading plate; Pattern 2 – failure occurred as a result of propagation of a new split crack which started from below the loading plate.

(1) Failure pattern 1 (Specimen B-10R2)

Fig. 3(a) shows an example of crack propagation of failure pattern 1. In this specimen, shear cracking began under loading of 325kN and propagated up to the stop position shown in the figure. After that, the crack width widened and dummy reinforcement yielded at the position shown in the figure at 775kN. The specimen failed by compression at the position below the loading plate when the load was 781kN. The crack width widened to 1.70mm.

(2) Failure pattern 2 (Specimen B-10.3)

Fig. 3(b) shows an example of crack propagation of failure pattern 2. In this specimen, shear cracking started under loading of 650kN and propagated up to the stop position shown in the figure, just like failure pattern 1. After that, the crack width widened. The dummy reinforcement yielded at the position shown in the figure. Then, split cracking which started from beneath the loading plate at

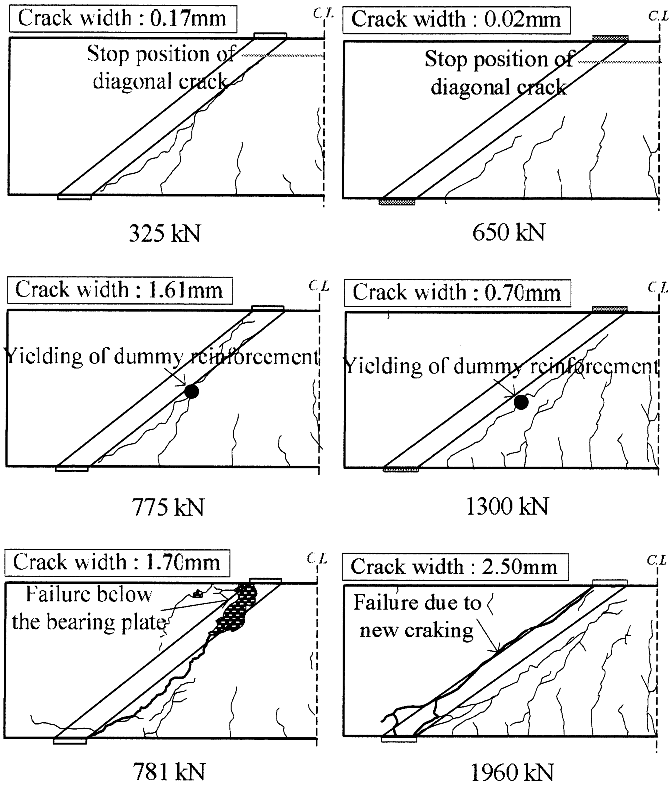

(a) Failure pattern 1 (B-10R2) (b) Failure pattern 2 (B-10.3)

Fig.3 Propagation of cracks

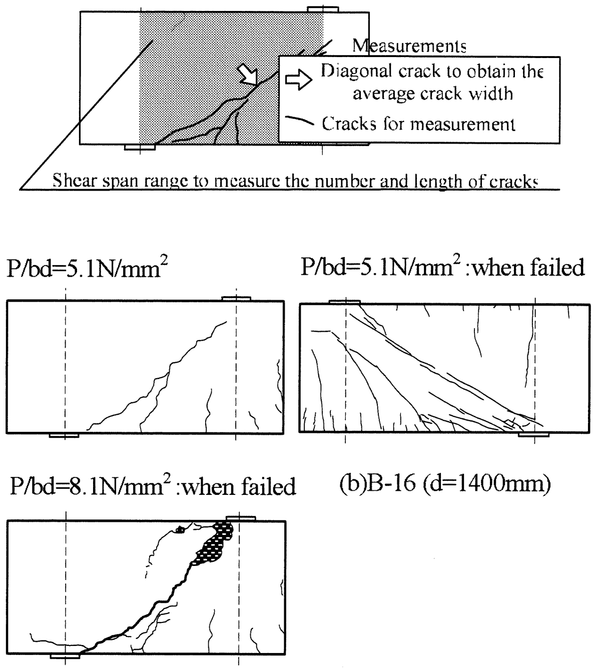

(a) B-10R2 (d=400mm)

Fig.4 Comparison of crack propagation

1960kN expanded within the compressive strut and ended in failure. When it failed, the crack width was as large as 2.50 mm.

3.2 Comparison of Crack Propagation

To find differences in failure pattern by beam size, crack propagation was compared between a large specimen with d=1400mm (Specimen B-16) and a small specimen with d=400 mm (Specimen B-10R2). The results of comparison are shown in Fig. 4. Comparison was made under the same mean shear stress which was obtained by dividing the load by **bd** (width x depth). The number, length, and width of cracks were measured within the shear span indicated by gray color in the figure. As the number of cracks, those that started from the bottom of a specimen were counted. To eliminate the effect of specimen size, the length and width of cracks are expressed using the length ratio by dividing the length and width by **d**.

For example, when the two specimens (B-16, B-10R2) were compared under P/bd=5.1N/mm^2 which was the maximum shear stress of B-16, crack length/d was 12.17 and 5.90 and the number of cracks 22 and 7, respectively, indicating that crack propagation of B-16 is faster. Specimen B-10R2 (small specimen) failed under the shear stress of P/bd=8.1N/mm^2 and the total crack length/d became 11.75, which was close to that under the maximum loading of B-16 (large specimen). Although the ultimate failure behavior of the specimens was identical because their relative crack length at the ultimate stage was identical, it can be said that crack propagation of a large specimen is faster than that of a small specimen.

3.3 Comparison of Strain Propagation

In the case of specimens with a/d=1.5, the position immediately below the loading plate failed in the end. Therefore, the distributions of strains below the loading plate was compared under the same mean shear stress, P/bd=6.2N/mm^2, which was the shear stress when Specimen B-14 failed.

Fig. 5 shows the distribution of strains below the loading plate. The average acryl bar strain of a large specimen was -1050.4μ and that of a small specimen -359.2μ. From this, it can be said that propagation of acryl bar strain is also faster in a large specimen than in a small specimen, just like the rate of crack propagation.

3.4 Mean Shear Stress

To confirm the presence/absence of the size effect in deep beams with a/d=1.5, the mean shear stress was calculated. Fig. 6 shows the comparison of mean shear stress **τ'** which was obtained by dividing the maximum load by the cross section **bd** (width x depth) of a member.

From the figure, it is known that the failure pattern differs in some case even though the effective depth is the

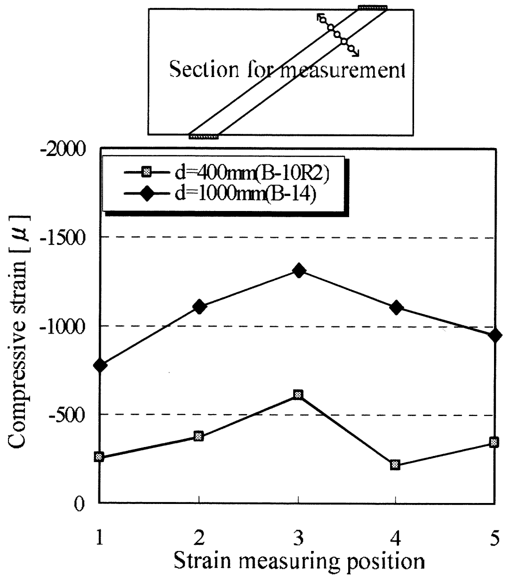

Fig.5 Comparison of strain propagations

same. This is because when a force acts locally due to unevenness of a loading plate or a difference in concrete strength, the resulting localized failure becomes the pattern 1 type. It is known that the strength of failure pattern 1 type beams is smaller than that of failure pattern 2 type. If attention is paid to each failure pattern, it is known that the size effect of $d^{-2/3}$ and $d^{-1/2}$ occurred for failure patterns 1 and 2, respectively. As to the entire specimen, the size effect of $d^{-1/3}$ occurred. The comparison of shear strength at P/bd took into account the effect of the member size, but a difference in the compressive concrete strength of specimen might still influence. Therefore, the effect of concrete strength was corrected using the ratio of the design strength **f'cd** to the compressive strength **f'ck**, expressed as Equation (1).

$$\tau^* = P/bd\left(\frac{f'_{ck}}{f'_{cd}}\right)^{\frac{1}{3}} \qquad (1)$$

where, **τ*** : mean shear stress with correction for the effect of compressive strength of concrete.

Fig. 7 shows the plot of corrected mean shear stress **τ***. It is known from the plot that, just like **τ'** (mean shear stress without correction), the corrected mean shear stress **τ*** decreased by $d^{-1/3}$ as the effective depth increased, although some differences existed. Therefore, it is considered that when a/d=1.5, the size effect that decreases the shear stress exists.

4. DISCUSSIONS

It was found in the previous section that when a/d=1.5, diagonal cracks propagate and end in failure due to the fracture below the loading plate, and that cracks and strains propagate faster as the member size becomes larger.

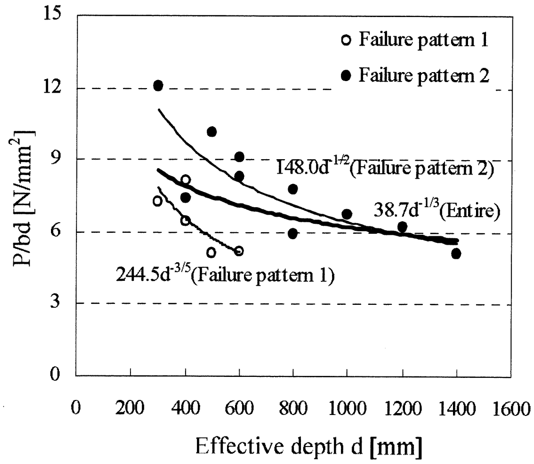

Fig.6 Comparison of shear strength

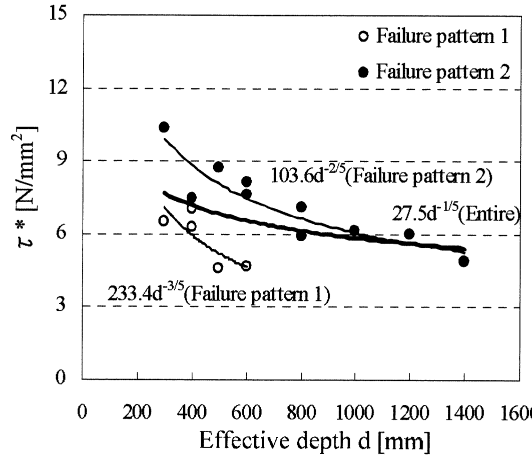

Fig.7 Shear strength with correction for the effect of concrete

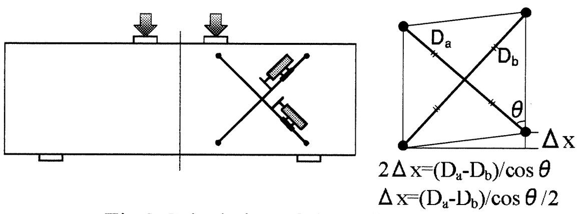

Fig.8 Calculation of shear displacement

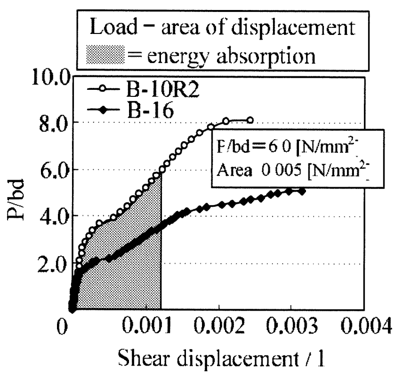

Fig.9 Calculation of energy

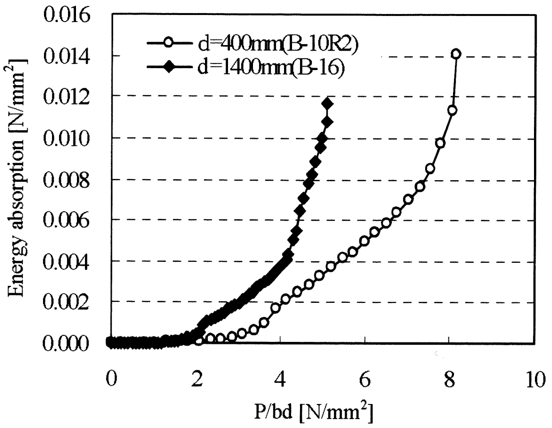

Fig.10 Development of energy absorption

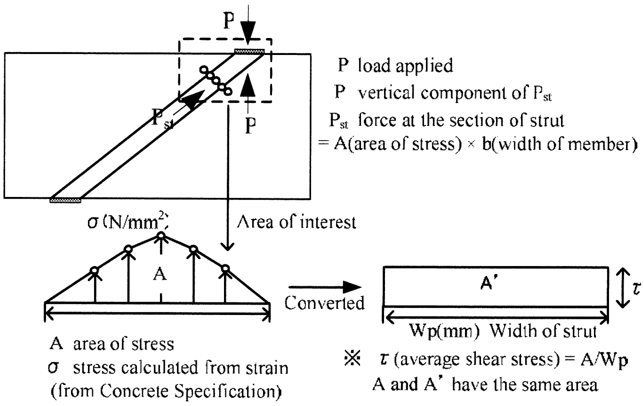

Fig.11 Calculation of P'

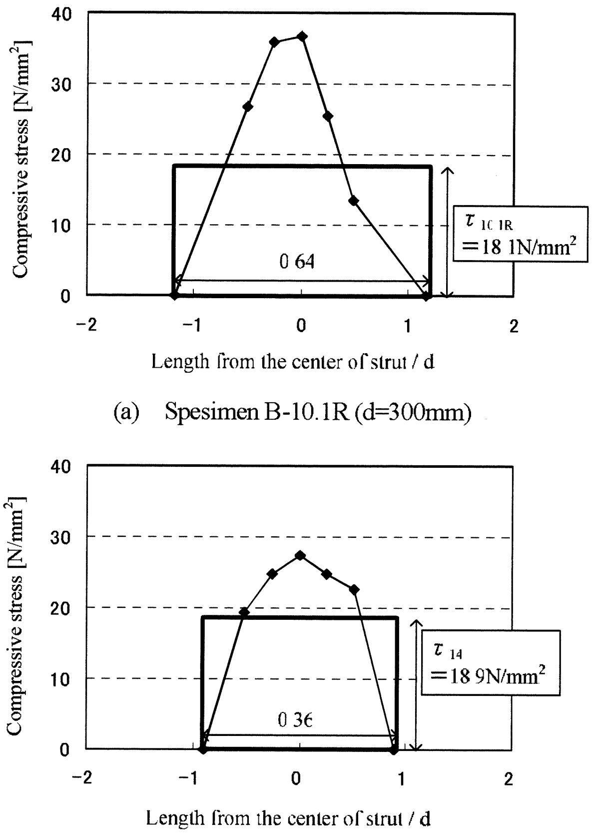

(a) Spesimen B-10.1R (d=300mm)

(b) Spesimen B-14 (d=1000mm)

Fig.12 Distribution of compressive stress

Therefore, in this section, discussions will be made on 1) rate of crack propagation; 2) failure below the loading plate that occurs eventually.

4.1 Rate of Crack Propagation

The energy consumption during the propagation of cracks was calculated. It was calculated from the shear displacement because propagation of shear cracks is largely dependent on shear deformation. First, shear displacement was obtained using the method in Fig. 8, and then, energy consumption was obtained from the relationship of mean shear stress (P/bd) vs. shear displacement/l. This process is shown in Fig. 9. For example, energy absorption of P/bd=6.0N/mm^2 of Specimen B-10R2 is the area depicted by gray color and its area is 0.005N/mm^2. In this way, energy consumption under each shear stress was calculated.

Fig. 10 shows the energy consumption of Specimen B-10R2 (small specimen) and B-16 (large specimen). It is known from the figure that energy absorption of B-16 is always larger than that of B-10R2 at the time of the same mean shear stress. Because of this, crack propagation is always faster in large specimens than in small specimens.

4.2 Failure below the Loading Plate

In our separate research (2005), we found that the vertical component **P'** of compressive force acting on the strut and the applied load **P** were approximately the same when a/d=1.5, as shown in Fig. 11. **P'** is influenced by the area of compressive stress distribution (A) shown in the figure, and **A** is determined by the compressive stress and the strut width **Wp**.

Therefore, we focused on the acting stress and **Wp**. The strut width which is necessary for the calculation of **Vc** (shear force carried by concrete) was obtained from the shape of compressive strain of an acryl bar at the time of 0.95Pmax which is close to the ultimate state.

To compare the acting stresses at the time of failure, the acting shear stress **τ** of large and small specimens wascalculated. As shown in Fig. 11, the stress distribution area A was divided by Wp to average the stress distribution. Figures 12(a) and 12(b) show the stress distribution of Specimen B-10.1R (d=300mm) and Specimen B-14 (d=1000mm), respectively. To make it dimensionless for comparison, Wp was divided by the loading width **d** and showed as the dimensionless length ratio in the figure. It is known from the figure that the maximum shear stress ($\tau_{10.1R}$) of Specimen B-10.1R was 18.1N/mm^2, and that the maximum shear stress (τ_{14}) of Specimen B-14 was 18.9N/mm^2. As seen, the acting shear stress was roughly the same when specimens failed,, indicating that Wp has a significant influence on the size effect. Figure 13 shows the results of comparison. It is seen that as the relative depth become larger, the apparent strut width decreased by $d^{-1/2}$ for failure pattern 1, $d^{-2/3}$ for failure pattern 2 and $d^{-1/3}$ for the

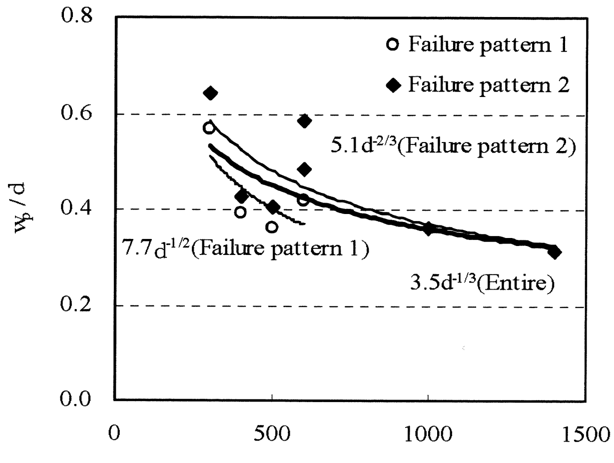

Fig.13 Comparison by making W_p dimensionless

entire specimen. It can be said that failure becomes localized as the specimen size becomes larger.

4.3 Effect on Shear Resistance

From the above investigation, it was confirmed that the propagation of cracks is faster and the failure is localized as the specimen size becomes larger in the case of specimens with a/d=1.5. To investigate if this nature has an effect on the shear strength of a deep beam, the authors proposed a shear resistance model for beams with a/d=1.5, which is shown in Fig.14. According to this model, the shear resistance during the propagation of cracks is primarily provided by the combination of **Va** (resistance by interlock of aggregates) and **Vc**. However, in the ultimate state, **Va** becomes smaller as the crack width widens and the shear resistance is primarily provided by **Vc**.

If this concept is applied, resistance **Va** of a large specimen becomes smaller than that of a small specimen relatively, because crack propagation is faster in the former specimen, as shown in Fig. 14(b). Similarly, resistance by **Vc** is also small in the ultimate state because a failure occurs locally. Because of a combination of these two phenomena which decrease the shear resistance, the shear strength of a specimen with a/d=1.5 becomes relatively small as the specimen size becomes larger.

5. CONCLUSIONS

The following conclusions were drawn from the study on the size effect which influences the shear strength of a deep beam with a/d=1.5.

(1) When the failure behaviors of a large specimen (B-16: d=400) and a small specimen (B-10R2: d=400mm) were compared under the same mean shear stress (ex.

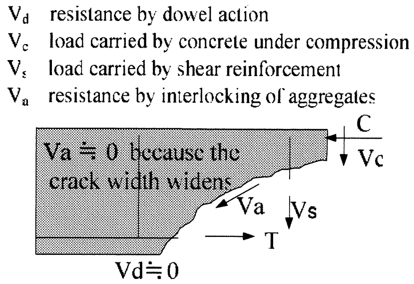

(a) Components of shear resistance for a/d = 1.5

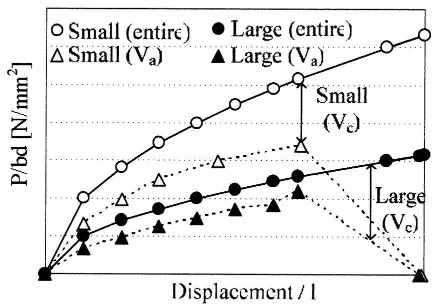

(b) Estimation of shear resistance

Fig.14 Schematic of shear resistance for the case of a/d = 1.5

P/bd=5.1N/mm²), the crack length /d became 12.17 and 5.90, respectively, indicating that crack propagation is faster in large specimens than in small specimens.

(2) From the analysis of the size effect, two types of failure patterns were found. As a whole, the size effect which decreased the shear stress by $\mathbf{d^{-1/3}}$ was found.

(3) From the investigation of the strut width of specimens with d=300~1400mm, it was found that the apparent strut width decreased by $\mathbf{d^{-1/3}}$ as the member size increased, and that the relative shear strength decreased due to a resulting localized failure.

REFERENCES:

Walraven, J. et al. (1994), Size Effects in Short Beams Loaded in Shear, *ACI Structural Journal (Sept-Oct)*, 585-593.

Wakiyama, T., Kosa, K., Nishioka, T., and Kobayashi, H. (2005), Effect on the Failure Behavior of Deep Beams, *Proc. of JCI*, 26 (2), 1015-1020 (in Japanese).

Kosa, K., Umemoto, Y., Nishioka, T., and Kobayashi, H. (2005), Experimental Study on the Damage Patterns of Deep Beams, *Proc. of Structural Engineering*, 51A, 1283-1290 (in Japanese).

Noguchi, H. and Ochiai, M (1980), Study of Shear Resistance Mechanism of Reinforced Concrete Beams, *Proc. of JCI*, 1, 441-444 (in Japanese).

Fifth International Conference on Urban Earthquake Engineering
March 4-5, 2008, Tokyo Institute of Technology, Tokyo, Japan

GRAVITY LOAD COLLAPSE OF REINFORCED CONCRETE COLUMNS

Manabu Yoshimura[1)]

1) Professor, Graduate School of Architecture and Building Engineering, Tokyo Metropolitan University, Japan
myoshim@arch.metro-u.ac.jp

Abstract: RC buildings designed by the Japanese codes older than 1971 are in danger of suffering heavy damages or even collapse during severe earthquakes. To evaluate seismic performance of those buildings, it is necessary to grasp post-peak behavior of old columns. Half-scale model specimens representing old columns that were designed to fail in shear or flexural yielding were tested until they came to be unable to sustain gravity load. Based on test results, post-peak behavior of old columns until gravity load collapse was examined.

1. INTRODUCTION

AS for ductile structures, various methods including the pushover analysis and nonlinear time history analysis are available and obtained results are also deemed reliable. However, as for brittle structures such as those constructed before 1971, these analyses, even if applied, are not expected to produce reliable results, because post-peak behavior of brittle columns is not well known. Therefore, the Standard for Seismic Evaluation of Existing RC Buildings (Evaluation Standard, 2001) is currently the only way that can be used to evaluate the seismic performance of old structures.

Under such a situation, it is intended in this study to experimentally examine post-peak behavior of old columns until gravity load collapse. Discussions are focused on the evaluation of lateral drift vs. lateral load relations and lateral drift vs. axial deformation relations until collapse.

2. COLLAPSE BEHAVIOR

2.1 Outline of Tests

Old columns, although in most cases fail in shear, may occasionally fail in flexure when their height is long. Therefore, half-scale model specimens with both failure types, twenty six in total number, were fabricated and tested (Yoshimura et al. 2005). Hereafter, shear-failing type is referred to as S-mode while flexural-yielding type as F-mode. However, note all specimens including the F-mode were designed to be classified as “Shear Column” in the Evaluation Standard (classified so when computed shear strength was smaller than computed flexural strength). Test variables were, transverse bar ratio (p_w), axial stress ratio (η), longitudinal bar ratio (p_g) and clear height ratio (h_0/D).

Test apparatus is shown in Fig.1, where the pantograph was placed so that the loading beam at the column top might not rotate (double curvature deformation might be realized). A loading method was as follows. The specimens were loaded to the lateral direction under constant axial load. The vertical actuator was controlled by load while the lateral actuator was by displacement. And the test was terminated by the limiter of the vertical actuator that was set to operate just when collapse occurred and column axial shortening reached 50mm.

A ratio of computed shear strength to computed flexural strength, strength ratio, is often used as an index to assess column deformability. The relations between strength ratio and observed collapse drift (lateral drift at collapse) are shown in Fig.2. The border of the two modes lies near the strength ratio of 0.7, considerably smaller than unity. It is because of the safety factor included in the computed shear strength. One can see the amplitudes of collapse drift range very widely for both modes.

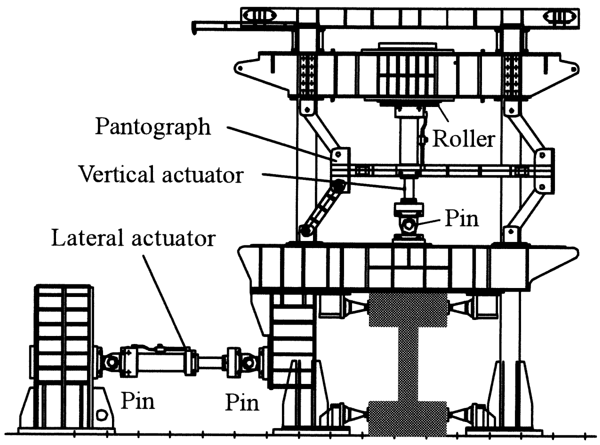

Fig.1 Test apparatus

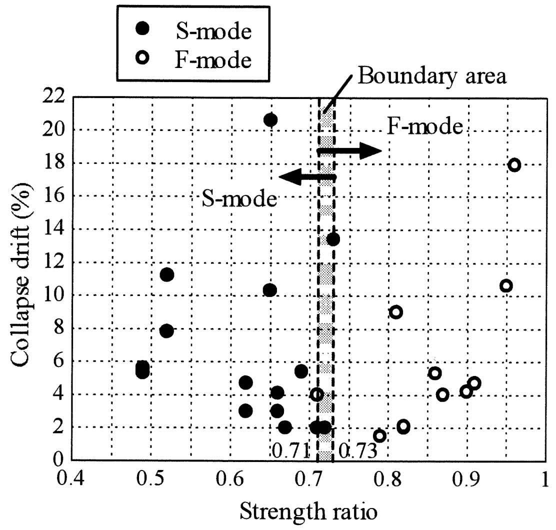

Fig.2 Strength ratio vs. collapse drift relations

2.2 Collapse of S-mode Specimens

The results of an S-mode specimen are shown in Fig.3. The occurrence of collapse was not soon later than shear failure but was when the main shear crack widened and lateral load decreased to nearly zero. The collapse accompanied the buckling of longitudinal bars. All S-mode specimens exhibited similar collapse behavior. The reason of bar buckling was, 1) the increase of axial compression carried by longitudinal bars resulting from the widening of the main shear crack, and 2) the decrease of compression capacity of these bars due to the local flexural deformation near the crack. In short, the reason of collapse for S-mode specimens was the failure of longitudinal bars.

2.3 Collapse of F-mode Specimens

The results of an F-mode specimen are shown in Fig.4. The collapse that occurred very suddenly without any symptom, accompanied the severe crushing of concrete at the column bottom. All F-mode specimens exhibited similar collapse behavior. The reason of collapse for F-mode specimens was the failure of concrete.

3. Evaluation of Collapse Drift and Drift vs. Load Relations

It was attempted to evaluate collapse drift based on the test results. The strength ratio is often used to evaluate column deformability, for example, lateral drift associated

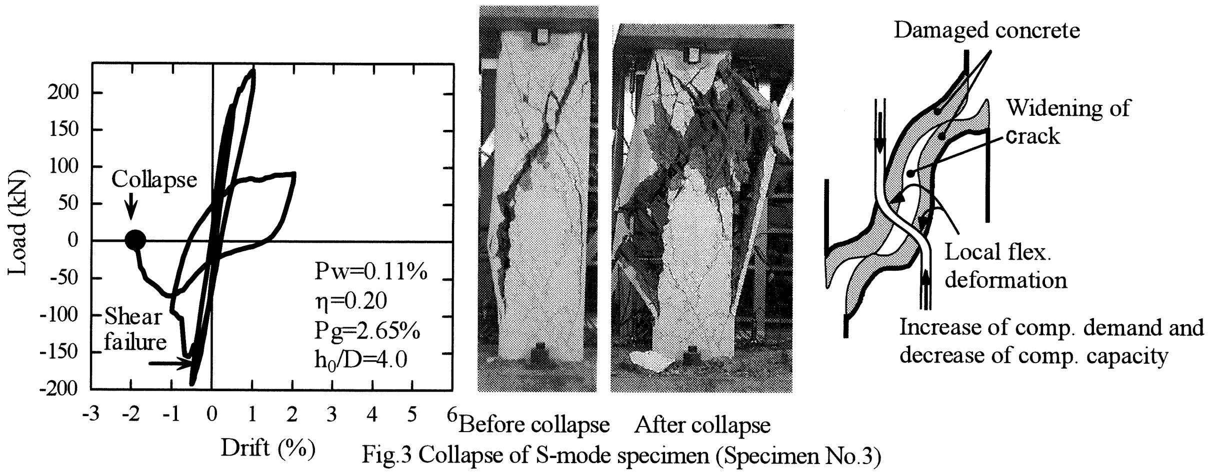

Fig.3 Collapse of S-mode specimen (Specimen No.3)

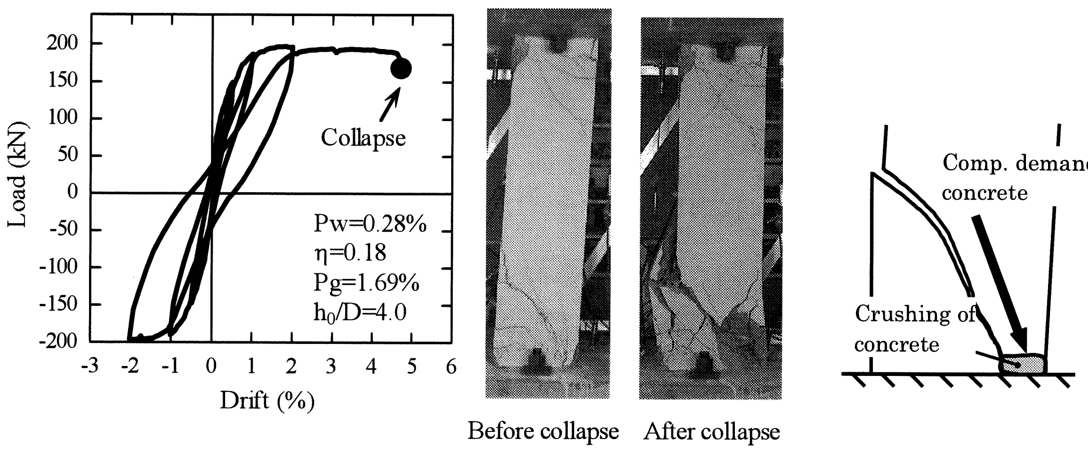

Fig.4 Collapse of F-mode specimen (Specimen Y28L)

with maximum load. However, one can not read from Fig.2 the trend that collapse drift becomes larger as the strength ratio is greater, indicating this ratio is not proper to evaluate collapse drift.

Thus, the effect of main test variables, transverse bar ratio, axial stress ratio and longitudinal bar ratio on collapse drift was studied. As for transverse bar ratio and axial stress ratio, collapse drift became larger as the former was larger and as the latter was smaller. It held true for both modes. These results were natural.

However, as for longitudinal bar ratio, collapse drift of the S-mode became larger as it was larger while that of the F-mode did larger as it was smaller (Fig.5). In other words, the effect of longitudinal bar ratio was opposite for both modes. It is apparent that such results are related to the above- mentioned reason of collapse. For the S-mode large amount of longitudinal bars is advantageous because collapse is controlled by longitudinal bars while for the F-mode small amount of them is advantageous because collapse is controlled by concrete. See Fig. 2 again. One can read the trend that for the S-mode collapse drift became larger except for two plots with drift more than 12% (only both cases showed bond-splitting failure after shear failure) as the strength ratio was smaller, or flexural strength was larger, or amount of longitudinal bars was larger, and the opposite trend for the F-mode.

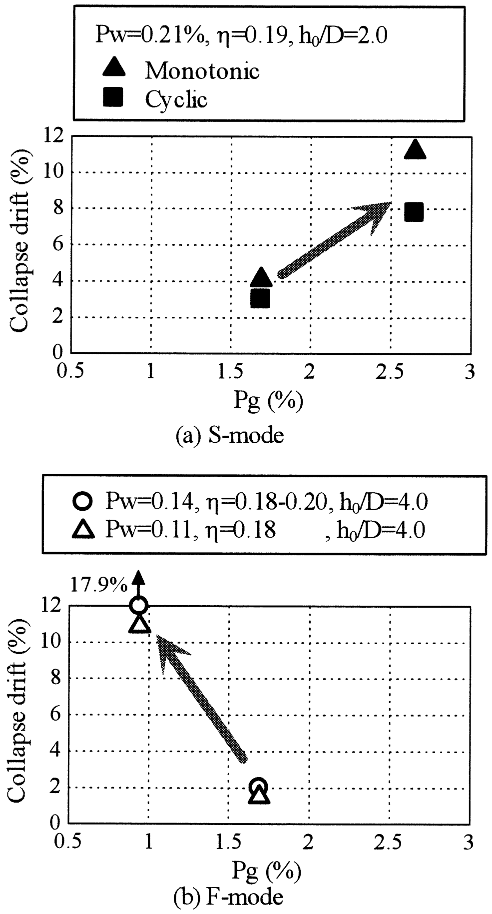

Fig.5 Longitudinal bar ratio vs. collapse drift relations

Moehle et al. proposed based on their tests the equation to predict collapse drift using shear-friction model, and reported the good agreement with the tests (Moehle et al. 2002). Note their specimens were mostly of the F-mode according to our definition. However, considering there are two types of collapse that are different depending on the failure mode, it is deemed difficult to express collapse by a single model. Then, it was attempted to form an empirical equation for each mode. The amplitude of collapse drift was assumed to be expressed as a linear combination of the amplitudes of the three main variables, and coefficients were determined by the least square method. The best fitted equations giving collapse drift (R_u) are as follows, where R_u, p_w and p_g are in %.

For the S-mode,

$$R_u = 62.2 \cdot p_w - 51.9 \cdot \eta + 6.07 \cdot p_g - 9.91 \geqq 1.5 \quad (1)$$

And for the F-mode,

$$R_u = 28.0 \cdot p_w - 42.3 \cdot \eta - 8.60 \cdot p_g + 20.6 \geqq 1.5 \quad (2)$$

Note the coefficients on longitudinal bar ratio are positive and negative, respectively for the S-mode and F-mode (the reason of this was stated earlier). The observed and evaluated values are compared in Fig.6.

Skeleton curves of drift vs. load relations, idealized as quadrilinear system, were proposed based on the evaluated collapse drift. Examples of evaluated skeleton curves are shown in Fig.7. It was assumed that strength decay was large for the S-mode (zero load at collapse) while small for the F-mode.

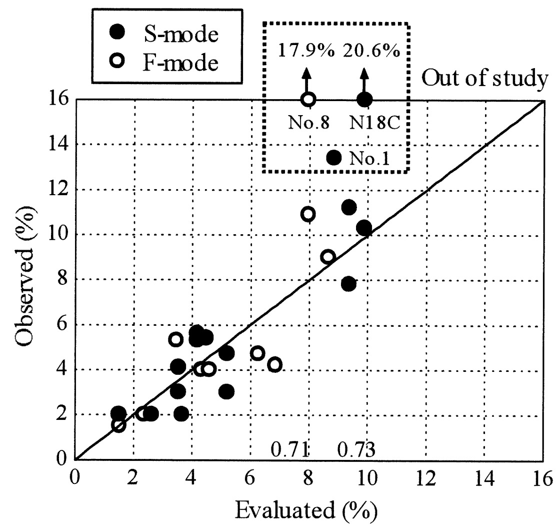

Fig.6 Comparison of collapse drift

4. Evaluation of Axial Deformation for S-Mode

Lateral drift vs. axial deformation relations for an S-mode specimen are shown in Fig.8. And the slope of these relations, defined as a ratio of axial deformation increment to lateral drift increment, is shown in Fig.9. In both figures,

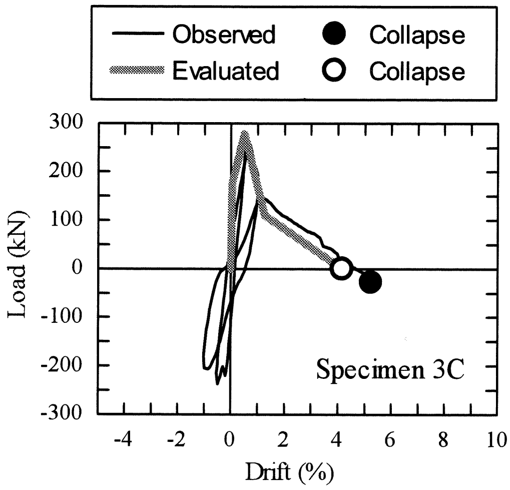

(a) S-mode

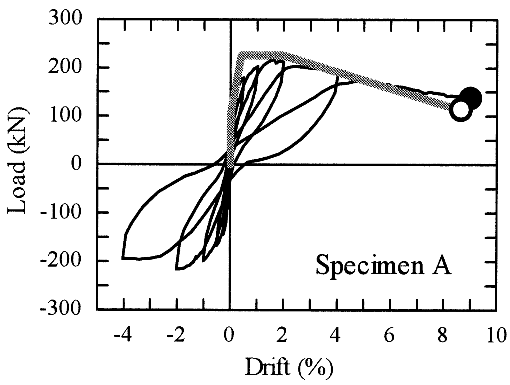

(b) F-mode

Fig.7 Lateral drift vs. lateral load relations

"Approximated" denotes the case where lateral drift vs. axial deformation relations were smoothed by using a cubic equation. The Slope after shear failure tends to increase with the increase of lateral drift, or the decrease of lateral load.

The reason why the Slope increases as the loading proceeds is discussed below (Nakamura et al. 2002). Figure 10(b) shows a conceptual sketch of lateral load – axial load interaction curve (failure surface). The initial failure surface that corresponds to the state of maximum load, is assumed as represented by a quadratic equation. Note the points of initial axial compression strength and initial axial tension strength lie on it. The failure progress that occurs after the maximum load is believed to accompany the deterioration of concrete, resulting in the reduction of axial compression strength as well as lateral (shear) strength. But axial tension strength is considered to keep an initial value because it is not affected by the deterioration of concrete. The contracted failure surface in the figure is determined by considering the above and assuming its shape is similar to that of the initial failure surface. By the way, one knows from the flow rule in plastic theory that the direction of incremental plastic deformation, n is normal to the failure surface. And the Slope coincides with this direction. Though exactly speaking the Slope has to be evaluated using plastic deformation (actually evaluated using total deformation), it is not a problem because elastic deformation is very small. As is shown in the figure, the Slope, n increases as the loading proceeds (failure surface is contracted), which agrees with the observations (Fig.9).

Based on the above discussions, lateral drift vs. axial deformation relations were formulated (Fig.10). The procedures are as follows. Firstly lateral drift, R vs. lateral load, P relations are determined from the idealized skeleton curve (Fig.7). Accordingly, P is expressed as a function of R. Secondly the Slope, n is expressed by a function of P. Therefore, the Slope, n is expressed by a function of R. Then by integrating n with respect to R, one can get lateral drift vs. axial deformation relations. An example of the evaluation is shown in Fig.11. The agreement with the observations is fairly good.

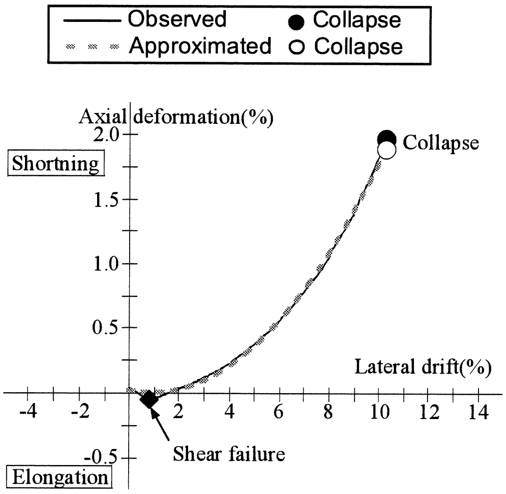

Fig.8 Lateral drift vs. axial deformation relations (Specimen N18M)

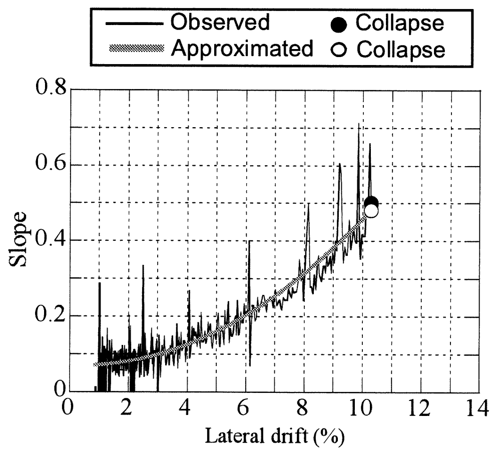

Fig.9 Lateral drift vs. slope relations (Specimen N18M)

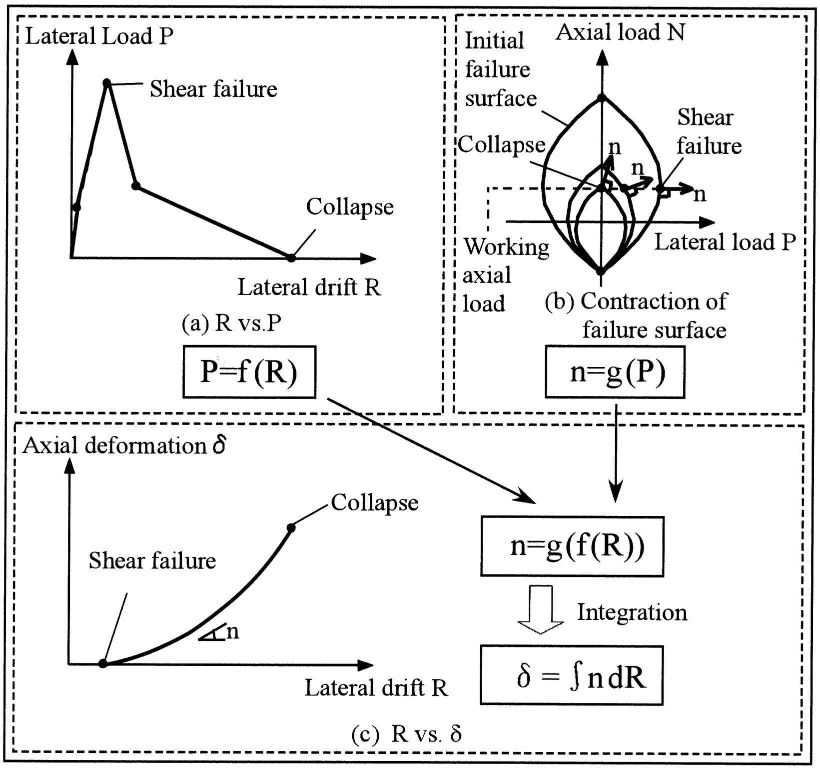

Fig.10 Evaluation of axial deformation

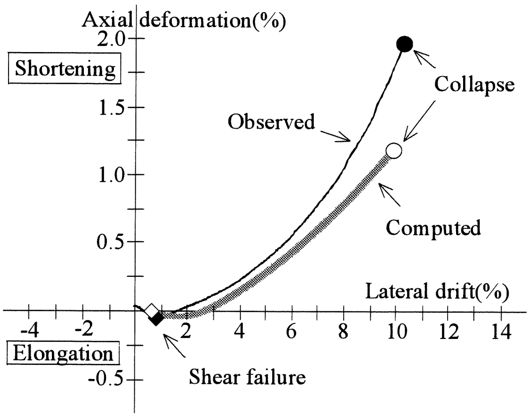

Fig.11 Comparison of lateral drift vs. axial deformation relations (Specimen N18M)

5. Conclusions

It was attempted to experimentally examine post-peak behavior of old columns until gravity load collapse. The major findings from the study are as follows.

(1) For the S-mode, collapse occurs when lateral load decreases to nearly zero. The reason of collapse is the failure of longitudinal bars, resulting collapse drift becomes larger as longitudinal bar ratio is greater.

(2) For the M-mode, collapse occurs very suddenly without showing significant strength decay. The reason of collapse is the failure of concrete, resulting collapse drift becomes larger as longitudinal bar ratio is smaller.

(3) The equation giving the skeleton of load-deflection relations until collapse was proposed for each mode.

(4) The method to evaluate axial deformation for the S-mode was proposed, where the contraction of failure surface and flow rule were used.

Acknowledgements:

The author expresses his special gratitude to Drs. Takaya Nakamura and Yoshikazu Takaine, who assisted him in studying in this text.

References:

Japan Association for Building Disaster Prevention (2001), "Standard for Seismic Evaluation of Existing RC Buildings." (in Japanese)

Yoshimura, M. and Takaine, Y. (2005), "Formulation of Post-Peak Behavior of Reinforced Concrete Columns Including Collapse Drift," Journal of Construction Engineering, Architectural Institute of Japan, No.587, 163-171. (in Japanese)

Moehle, J. P., Elwood, K. J., and Sezen, H. (2002), "Gravity Load Collapse of Building Frames during Earthquakes, " ACI SP-197, Behavior and Design of Concrete Structures for Seismic Performance, American Concrete Institute, 215-238.

Nakamura, T. and Yoshimura, M. (2002), "Gravity Load Collapse of Reinforced Concrete Columns with Brittle Failure Mode," Journal of Asian Architecture and Building Engineering, Architectural Institute of Japan, vol.1 no.1, 21-27.

Fifth International Conference on Urban Earthquake Engineering
March 4-5, 2008, Tokyo Institute of Technology, Tokyo, Japan

AN ANALYTICAL STUDY ON SEISMIC BEHAVIOR OF MULTI-STORY RC FRAMES WITH SHEAR-FAILURE TYPE PARTIAL WALLS

Hisato Hotta[1), Atsuko Yoshizaki[2), and Takafumi Asano[3)

1) Assoc.Prof., Graduate School of Science and Engineering, Tokyo Institute of Technology, Dr.Eng.
2) The Building Center of Japan.
3) Graduate Student, Graduate School of Science and Engineering, Tokyo Institute of Technology

Abstract: This study investigates the influences of shear-mode partial walls on the performance of RC rigid-frames. To express shear-axial coupled motion occurred with shear failure of walls, shear-axial softening behavior was modeled using the theory of plasticity and the concept of failure surface contraction. Push-over analysis was then conducted to RC frames that have various combinations of column over-design factors and wall breadths to simulate response to the seismic load and collapse mechanism. Some frames with low column over-design factor showed story collapse after shear failure of walls, while others showed more ductile mechanism. The results revealed how shear-mode partial walls can affect the performance of RC frames with different configurations.

1. INTRODUCTION

"Partial walls" in this paper are the walls connected to the upper and the lower beams, however, apart from the both side columns. In multi-story buildings, those walls are generally installed continuously at every story, and very popular as exterior walls in apartment houses in Japan. Generally they have not been regarded as structural elements because of a lack of requirement for bearing walls, and their presence has been ignored in structural calculation in Japanese Building Code. However, more accurate and sophisticated modeling of structures becomes important in recent years under performance based design, and it is necessary to grasp accurate behavior of structural systems including non-structural elements such as the walls dealt in this paper.

In the previous papers presented in the first and the third international conference conducted by CUEE(Hotta, 2004, 2006), we reported the influence of the flexural yield type partial walls and shear failure type ones on seismic behavior of the structural system examined empirically, and indicated that there is some probability of story collapse due to brittle failure of a wall at a certain story.

The objective of this paper is to grasp how shear failing of the walls affect seismic behavior of multi-story structural system through some numerical analyses.

2. ANALYTICAL MODERING OF RC FREMES AND PARTIAL WALLS

As shown in Fig.1, an RC frame consist of columns and beams with partial walls is modeled to several series springs as members and joints having a rigid region to a face of members. The beams are modeled to an elastic member with elasto-plastic end rotation springs at both the ends. In the elastic member, flexural and axial deformations are considered, however, shear one is not in consideration. Hysteretic rules for the end rotation springs is degrading stiffness tri-linear model proposed by Takeda(1970.) The columns are modeled to an elastic member with fiber springs at both the ends in which axial and flexural interaction is considered. The elastic member is similar to the one above mentioned. In the fiber spring, elasto-plastic moment and axial force versus end rotation and axial elongation interacting relationship is obtained by means of a hinge length equivalent to depth of the member and moment vs. curvature, axial force vs. axial strain, and their interacting relationship obtained by traditional section analysis. As for a model for the partial walls, a shear spring

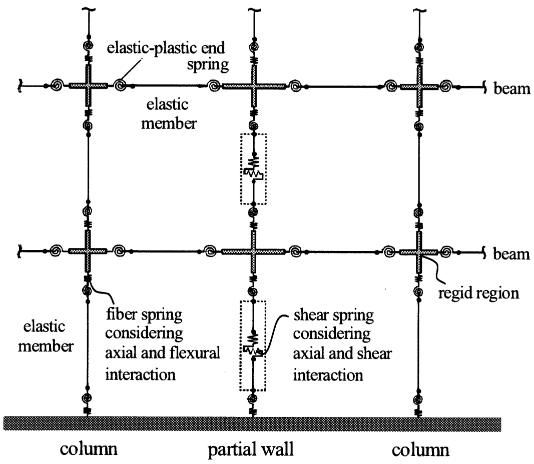

Figure 1 Analytical Model

in which shear softening behavior with axial and shear interaction can be considered is added to the model for the columns.

The property of the shear spring in the model for the partial walls is assumed to obey a flow rule and softening rule in the plastic theory. Initial failure surface is assumed an ellipse determined by Nc: compressive strength, Nt: tensile strength, and Q_0: shear strength when N=0 as shown in Fig.2(a.) Increase of plastic deformation of the spring can be written as

$$\begin{Bmatrix} du^P \\ dv^P \end{Bmatrix} = d\lambda \begin{Bmatrix} n_Q \\ n_N \end{Bmatrix} \quad \cdots\cdots\cdots\cdots\cdots (1)$$

by the flow rule, where (n_Q, n_N)is normal vector of the failure surface. Increase of internal force of the spring can be expressed using stiffness matrix [Ke] as

$$\begin{Bmatrix} dQ \\ dN \end{Bmatrix} = [K_e] \cdot \left(\begin{Bmatrix} du \\ dv \end{Bmatrix} - \begin{Bmatrix} du^P \\ dv^P \end{Bmatrix} \right) \quad \cdots\cdots\cdots\cdots (2)$$

and substituting eq.(1) into eq.(2), we get

$$\begin{Bmatrix} dQ \\ dN \end{Bmatrix} = [K_e] \cdot \left(\begin{Bmatrix} du \\ dv \end{Bmatrix} - d\lambda \begin{Bmatrix} n_Q \\ n_N \end{Bmatrix} \right) \quad \cdots\cdots\cdots (3)$$

Isotropic softening is assumed in this model, therefore undetermined non-negative scholar $d\lambda$ can be written using softening parameter h as

$$d\lambda = \frac{1}{h + \begin{Bmatrix} n_Q \\ n_N \end{Bmatrix} [K_e] \begin{Bmatrix} n_Q \\ n_N \end{Bmatrix}} \cdot \begin{Bmatrix} n_Q \\ n_N \end{Bmatrix} [K_e] \begin{Bmatrix} du \\ dv \end{Bmatrix} \quad \cdots\cdots (4)$$

The softening parameter h is determined by assuming bi-linear shear force versus shear deformation relationship as shown in Fig.2(b). Member angle due to shear deformation at complete collapse point Ru is from the previous research (Yoshimura 2005) as follows.

$$R_u = 62.2 \cdot p_w - 51.9 \cdot \eta + 6.07 \cdot p_g - 9.91 \geq 1.5 \quad \cdot\cdot (5)$$

where p_w: ratio of web reinforcement, η: ratio of axial force, and p_g : ratio of longitudinal reinforcement, respectively. Substituting eq.(4) into eq.(3), eventually we get the following stiffness matrix in which the shear and axial interaction is taken in account.

$$\begin{Bmatrix} dQ \\ dN \end{Bmatrix} = \left([K_e] - \frac{[K_e] \begin{Bmatrix} n_Q \\ n_N \end{Bmatrix} \cdot \begin{Bmatrix} n_Q \\ n_N \end{Bmatrix} [K_e]}{h + \begin{Bmatrix} n_Q \\ n_N \end{Bmatrix} [K_e] \begin{Bmatrix} n_Q \\ n_N \end{Bmatrix}} \right) \begin{Bmatrix} du \\ dv \end{Bmatrix} \quad \cdots (6)$$

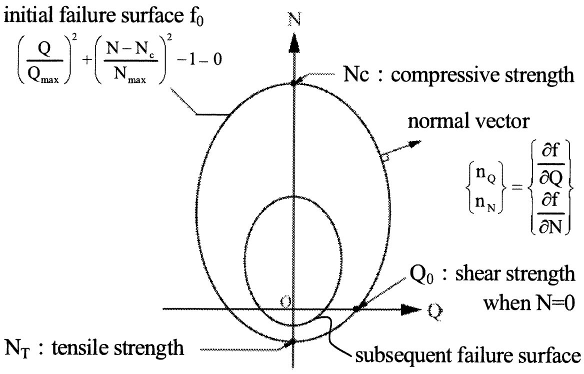

(a) Failure Surface

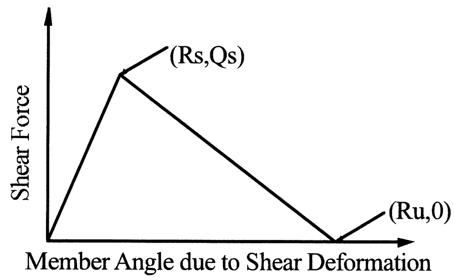

(b) Shear Force-Shear Deformation Relationship

Figure 2 Axial-Shear Interacton and Softening Characteristic of Shear Spring

In the softening region, where h becomes negative, the stiffness matrix in eq.(6) is not applicable for a static analysis because of numerical stability. In the case h<0, provisional balanced point is once solved as assuming the shear spring has perfect plastic property (h=0), and unbalanced force between the provisional and the true restoring force of the spring at the balanced point is reduced by traditional iterative routine.

3. COMPARISON OF NUMERICAL SIMULATION FOR 2 STORY RC FRAME WITH THE ONE DEALT IN THE PREVIOUS EMPIRICAL INVESTIGATION

A specimen provided for a static test in the previous study (Hotta 2006) is illustrated in Fig.3. That is about 1/8 scale model of actual frames and it has span length of 80cm and story height of 40cm. It has also 12 cm wide and 3 cm thick partial wall at mid-span at every story. As for the detail of other dimensions, properties of the material used and so on, refer to our previous paper (Hotta 2006.) In the static test, cyclic lateral force was applied at the center depth of the upper beam, controlling an axial force keeps constant (0.15bdsB.) as shown in Fig.3, however, loading was monotonic in the analysis. In the experiment, elongation of the partial walls were controlled to be same as the average of the ones of both columns by an equipment, which was a rectangular steel pipe with sufficient stiffness, as illustrated

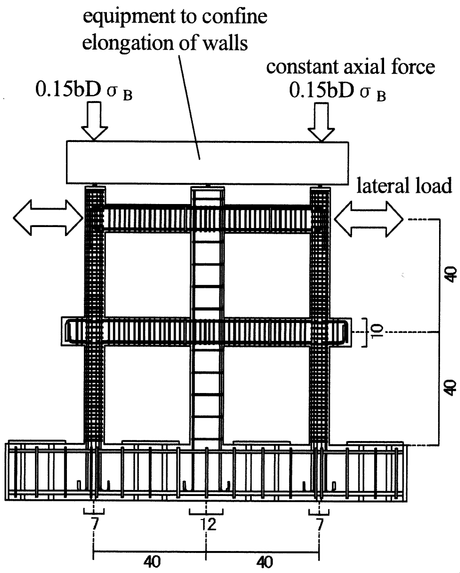

Figure 3 A Two-Story Specimen

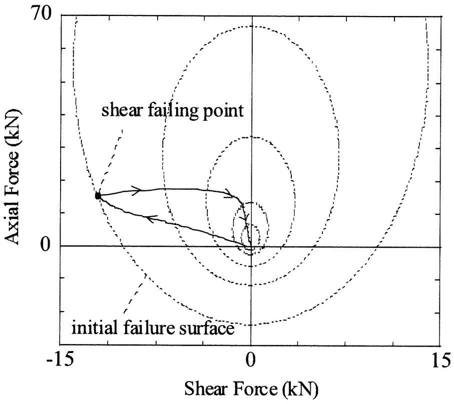

Figure 4 Axial and Shear Force Hysteresis of Shear-Failed Wall

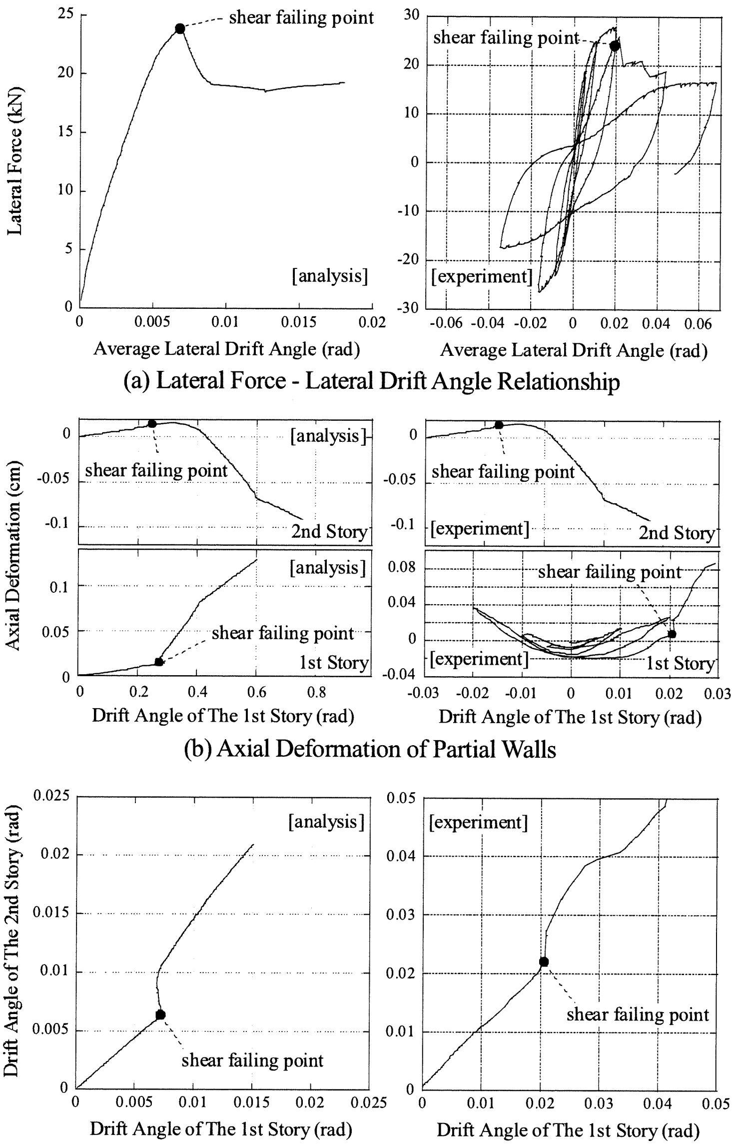

Figure 5 The Results of Analysis and Experiment

in Fig.3. Similar to the experiment, vertical displacement at the top of the partial wall was controlled in the analysis.

Figure 4 stands for a relationship between the axial and the shear force of the partial wall failed due to shear in the analysis. The axial force was ascent in proportion to the shear force in the ascending branch of the shear force, and after the shear failure, the wall kept the almost maximum axial force until the shear force was reduced to about 1/10 of the maximum shear force.

Lateral load versus story drift angle relationship, axial deformation of the walls versus story drift angle relationship and the one between the upper and the lower story drift angle were compared with each other in Fig.5. Except for the absolute value of the story drift angle, shear strength and shear degrading behavior in strength were similar between the analysis and the experiment. The main reason of the deference of the story drift angle is considered that the member joint was assumed rigid in the analysis. The axial behavior of the walls after shear failing of the wall was also similar. The wall failed due to shear shrank, by contrast, the remaining sound one expanded. The change of the relationship between both story drift angles was also similar between the analysis and the experiment.

4. PUSH-OVER ANALYSYS FOR 6 STORY RC FRAMES WITH PARTIAL WALLS

4.1 Analytical Object

Push-over analysis was carried out for 6 story RC frames with partial walls at mid-span as shown in Fig.6. Analytical parameters were breath of partial walls (100, 115, and 130 cm) and column over-design factor, which was determined as ratio of flexural strength of column section to

Table 1 Specifications of The Bench Mark Frame

Story	Column			Beam		Compressive Strength of Concrete (MPa)	Reinforcement Strength (MPa)	Column-to-Beam Strength Ratio
	B (cm) x D (cm)	Longitudinal Reinforcement Ratio (%)	Axial Compression Ratio	B (cm) x D (cm)	Tension Reinforcement Ratio (%)			
1	85×85	2.24	0.14	50×95	0.64	24	345	3.0
2	80×80	2.53	0.13	50×95	0.64			2.8
3	80×80	2.53	0.10	45×90	0.63			3.0
4	75×75	2.16	0.09	45×85	0.56			3.3
5	75×75	2.16	0.06	40×80	0.63			4.2
6	70×70	2.48	0.03	35×70	0.83			1.7

Table 2 Column Over-design Factors

Story	Column-to-Beam Strength Ratio				
	Column +5cm	Column ±0cm	Column -5cm	Column -10cm	Column -15cm
1	3.5	3.0	2.5	2.0	1.6
2	3.3	2.8	2.3	1.9	1.5
3	3.6	3.0	2.4	2.0	1.6
4	4.0	3.3	2.6	2.3	1.7
5	5.2	4.2	3.3	3.0	2.2
6	2.0	1.7	1.3	1.1	0.9
	3.5	**3.0**	**2.5**	**2.0**	**1.5**

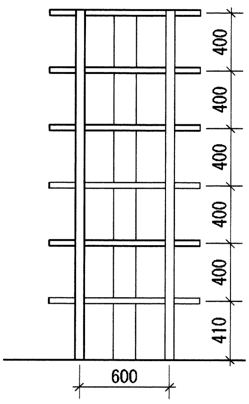

Figure 6 Analytical Object

Table 3 Specification of Partial Walls

	B (cm) x D (cm)	Longitudinal Reinforcement Ratio (%)	Web Reinforcement Ratio (%)
Partial Wall-100	100×15	1.18	0.48
Partial Wall-115	115×15	1.55	
Partial Wall-130	130×15	1.98	

beam section. An RC frame consist of beams and columns listed in Table 1 which were from a design example shown in "Guide line for evaluating performance of reinforced concrete structures" (2000) was placed as a bench mark, and frames with 5 kinds of column over-design factor as listed in Table 2 were made and analyzed in numerical space by changing sectional dimension of the columns. As a result, the column over-design factor ranged from 1.5 to 3.5. Specifications of partial walls are listed in Table 3.

Distribution of the external force in the push-over analysis was determined assuming Ai distribution of the seismic coefficient. All frames without any partial walls show complete collapse mechanism based on strong column-weak beam concept.

4.2 Analytical Result

Base shear versus story drift angle relationships are shown in Fig.7 for all cases of varying the parameters. Dashed lines in the figures stand for the relationships for the frames with no partial walls. As for the frames with partial walls, the walls located at the second or the third story failed due to shear at first, and then the shear failure of the walls extended to adjacent story successively in the case the frames had sufficiently high column over-design factor, however, the failure of the wall did not extend in the case of the frames with relatively low column over-design factor.

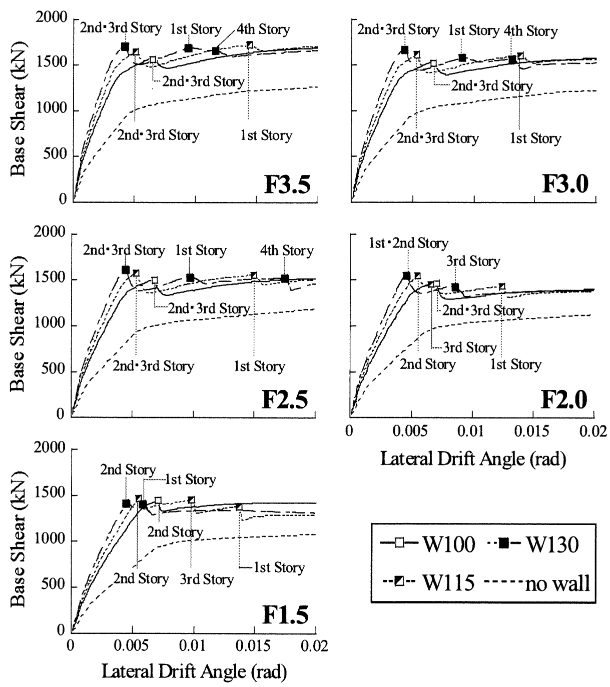

Figure 7 Base Shear - Lateral Drift Angle Relationship

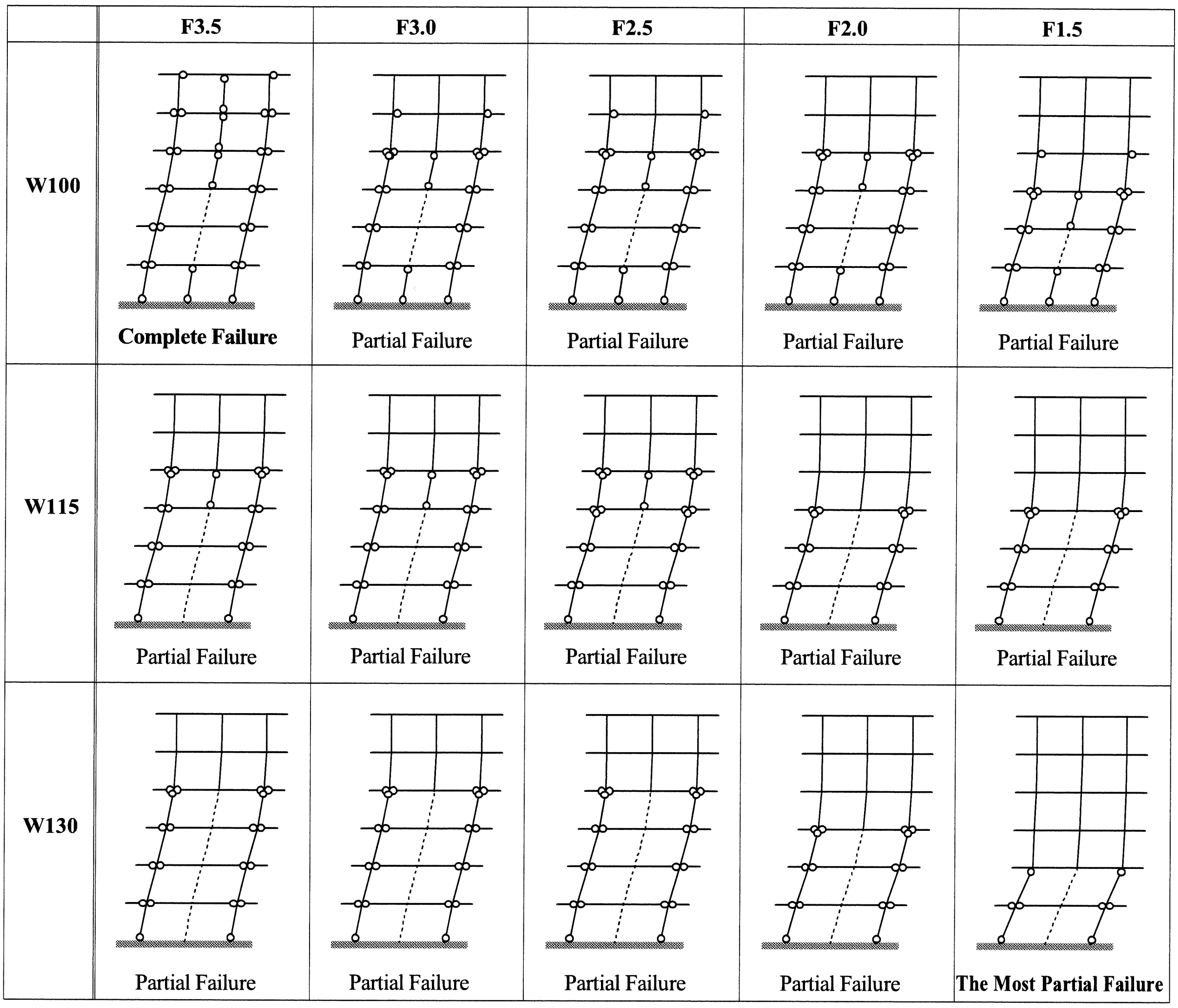

Figure 8 Collapse Modes

The shear strength was higher than the one for the frames without the walls.

Collapse modes are illustrated in Fig.8 for all the frames. Only one frame with 100 cm wide walls and column over-design factor of 3.5 showed complete mechanism, however all other frames showed partial mechanism even when they had the column over-design factor of 3.0 that is considered sufficiently high in general. Less column over-design factor and wider walls cause the partial mechanism at smaller part. The frame with 130 cm wide walls and column over-design factor of 1.5 showed the most partial mechanism where collapse occurred at the lowest 2 stories.

As for F3.5-W100 which showed the complete mechanism and F1.5-W130 which showed the most partial mechanism, moment diagram and axial force of the column and the wall are illustrated in Fig.9. Figure 9(a) shows the initial distribution of the axial force, and in Figs.9(b) and (c), two distributions just before and after the first failure of the partial wall are shown, respectively. The numerical values in the figure stand for axial force ratios. The axial force ratio of the columns was reduced from the initial value because of the axial force of the wall due to the axial confinement before the first wall was failed for both frames, especially, as for F1.5-W130, the axial force was reduced to almost half of the initial value. The walls at two stories were failed almost coincidently for both frames in the analysis. After the first failure of the walls, the moment at the top and the bottom ends of the columns of the stories where the walls were failed became higher. That is considered the main reason of the partial mechanism of the frames.

The distribution of the story drift angle for F3.5-W100, which showed the complete mechanism, is compared with that for F3.5-no walls in Fig.10. The story drift angle was large at the stories where the walls were failed compared with the other stories, and the distribution for F3.5-W100 is obviously different from the one for the frame without the walls in spite that the both showed the complete mechanism.

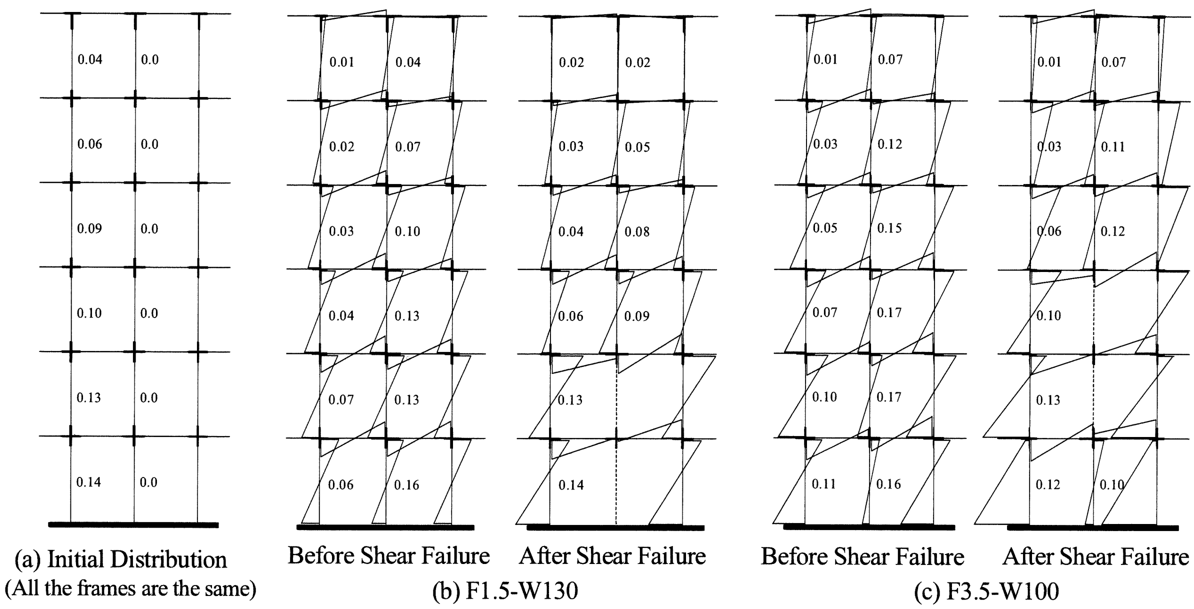

Figure 9 Moment Diagram and Axial Force of The Columns and The Walls

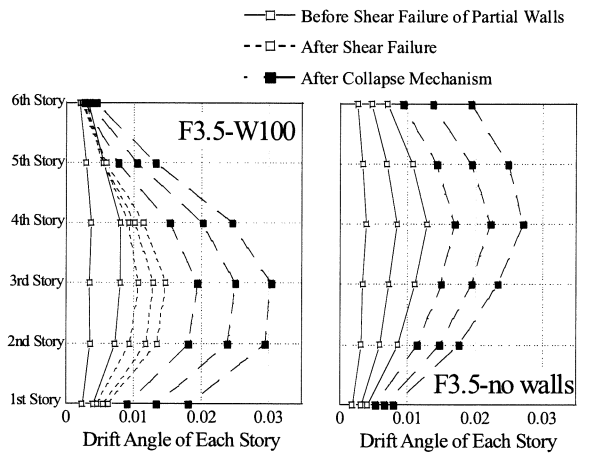

Figure 10 Transition of Distribution of The Drift Angle

5. CONCLUSIONS

As for 6 story RC frames with shear failure type partial walls, the influence of the walls on the strength and the collapse mechanism of the frames is investigated by a numerical analysis. Knowledge obtained by this study can be summarized as follows.

(1) There is a case that the collapse mechanism changes to partial one due to the presence of the walls, even when the frame have the column over-design factor of 3.0 that is considered sufficiently high in general.

(2) Partial walls strengthen the ultimate lateral strength of frames, even when the frame shows the partial mechanism.

(3) Story drift angle becomes large at the stories where walls are failed compared with the other stories, and its distribution in height direction becomes considerably different from the one for the frame without the walls, even when the frames has sufficient column over-design factor to avoid partial collapse mechanism.

References:

Takeda, T. , Sozen, M. A., and Nielsen, N. N. (1970), "Reinforced concrete response to simulated earthquakes," *Journal of the Structure Division*, ASCE, ST12, pp. 2557-2573.

"Guide Line for Evaluating Performance of Reinforced Concrete Structures," Gihoudou-Shuppan, 2000. (in Japanese)

Hotta, H. and Tsunoda, T. (2004), "An experimental study on influence of mullion-type wall of predominant bending failure in reinforced concrete frame," *Proc. of the 1st international conference on urban earthquake engineering*, Yokohama, Japan, 105-111.

Yoshimura, M. and Takaine, Y. (2005), "Evaluation of vertical deformation for R/C columns with shear mode based on concept of failure surface contraction," *Journal of Structural and Construction Engineering (Transaction of Architectural Institute of Japan)*, 592, 167-175. (in Japanese)

Hotta, H. and Nakajima, T. (2006), "A shaking table test of 2 story R/C frames with partial walls independent from columns," *Proc. of the 3rd international conference on urban earthquake engineering*, Tokyo, Japan, 577-584.

Fifth International Conference on Urban Earthquake Engineering
March 4-5, 2008, Tokyo Institute of Technology, Tokyo, Japan

COLLAPSE SIMULATION OF REINFORCED CONCRETE STRUCTURE UNDER SEISMIC EXCITATION

Chung-Yue Wang[1), Ren-Zuo Wang[2)

1) Professor, Department of Civil Engineering, National Central University, Chungli, Taiwan
2) Associate Research Fellow, National Center for Research on Earthquake Engineering, Taipei, Taiwan.
cywang@cc.nuc.edu.tw, rzwang@ncree.org.tw

Abstract: In this paper, nonlinear collapse analysis of reinforced concrete structures is developed by applying a new concept of computational mechanics, named as the vector form intrinsic finite element (VFIFE or V-5) method. The V-5 method models the analyzed domain to be composed of a finite number of particles and the Newton's second law is applied to describe each particle's motion. By tracing the motions of all the mass particles in the space, it can simulate the large geometrical and material nonlinear changes during the motion of structure without using geometrical stiffness matrix and iterations. The analysis procedure is vastly simple, accurate, and versatile. The formulation of VFIFE type frame element includes a new description of the kinematics that can handle large rotation and large deformation, and includes a set of deformation coordinates for each time increment used to describe the shape functions and internal nodal forces. A convected material frame and an explicit time integration scheme for the solution procedures are also adopted. In order to simulate the progressive collapse behaviors of the reinforced concrete structure, the material nonlinearity and associated damage criteria were considered into the fracture analysis of the frame elements. Contact detection and analysis algorithm for space frame are also developed for the collapse simulation. Numerical examples are presented to demonstrate capabilities and accuracy of the V-5 method on the nonlinear, dynamic, failure analysis on the collapse of RC structure under seismic excitation.

1. INTRODUCTION

To prevent the immeasurable losses of human lives and social properties due to earthquakes and terrorist attacks, the resistance evaluation and retrofitting of civil infrastructures becomes an emerged issue of many countries in the world. Intensive attention has been focused on a type of failure known as progressive collapse since the Ronan Point apartment collapse in London in 1986 (Griffiths et al. 1986). In recent year, however, terrorist attacks against the Alfred P. Murrah Building in Oklahoma City in 1995, and the World Trade Center could not withstand the fires from terrorist attacks that induce progressive collapse of structures at the New York in 2001. The 27 May 2006 earthquake hit the Provinces of Yogyakarta and Central Java, and leads to RC and brick building collapsed. Besides experimental and theoretical studies, the numerical simulation is another way to assist engineers to understand the nonlinear dynamic failure behavior of structure under the earthquake excitation. Nonlinear analysis methods developed since last century are used to study the behavior of structures with material and geometrical nonlinearities. Gallagher and Padlog (1963) first introduce the geometrical stiffness matrix into the nonlinear analysis of structure by considering the nonlinear strain terms in the formulation. Argyris et al. (1978) and Elias (1986) have tried to modify the definition of bending moment to derive a modified geometrical stiffness matrix to satisfy the equilibrium requirement at each deformed state. Yang and Kuo (1994) proposed a method to decompose the displacement of structural element into rigid body displacement and natural deformation displacement in each incremental step of the computation and this kind of decomposition can lead the geometrical stiffness matrix pass the rigid body motion test. It is well known that the core idea of the nonlinear analysis of structure is how to clearly identify the rigid body component and the deformation component in the motion.

Recently, a novel computation method called as the vector form intrinsic finite element (VFIFE, simply called V-5) method was proposed by Ting et al. (2004a, 2004b) and Shi et al. (2004). The VFIFE method has been successfully applied to the nonlinear motion analysis of 2D frame (Wu et al. 2006) and the dynamic stability analysis of space truss structure (Wang et al. 2005a, 2005b, Wang et al. 2006). Due to some special characters of the VFIFE method, it is very easy to be applied to study the highly nonlinear dynamic behavior of a structure system from continuous to discontinuous states. In this paper, the theory of space frame element in VFIFE (Wang, 2005) is briefly introduced. In order to model the nonlinear behavior of reinforced concrete under cyclic excitation and during collapse, material models and contact analysis for the frame elements are also addressed in this paper.

2. FUNDAMENTALS OF THE 3D FRAME IN VEFIFE

A novel computational method so called the Vector Form Intrinsic Finite Element is developed by Ting et al. (2004 a, b) to handle engineering problems with the following characters: (1) containing multiple deformable bodies and mutual interactions, (2) material non-linearity and discontinuity, (3) large deformation and arbitrary rigid body motions of deformable body. Since the conventional FEM based on variational method requires the total virtual work to be zero but does not require the balance of forces at nodes. These unbalanced residual forces will do some non-zero work under virtual rigid body motion and cause the inaccuracy and un-convergence of the calculation results. The computation procedure and some concepts of this VFIFE method are similar to the FEM. But the major difference is that the VFIFE does not apply the variational principle on the stress expressed equilibrium equations in its formulation. Instead, VFIFE maintains the intrinsic nature of the finite element method and makes strong form of equilibrium at nodes, the connections of members.

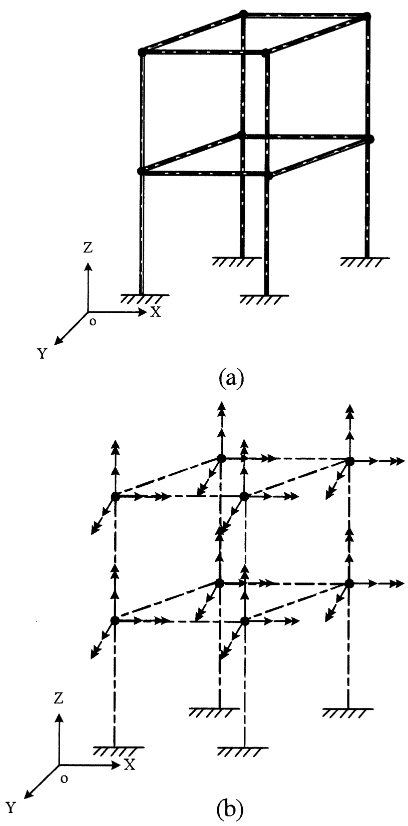

Figure 1 (a) A space frame structure, (b) Discrete particles modeling of space frame structure system by the VFIFE method.

In other words, the continuous bodies are represented by a set of mass points through lumped mass technique as shown in Fig. 1. Each mass point satisfies the law of mechanics, i.e. the conservation of linear and angular momentums. Since there are large translations and rotations in the motion of collapsing structure, the outstanding characters of the VFIFE method cause it be selected to conduct this nonlinear, dynamic and discontinuous deformation analysis. Similar to other well-developed VFIFE elements, a convected material frame and explicit time integration for the solution procedures are also adopted in the formulation of 3D frame element. The description of kinematics to discrete rigid body and deformation displacements, and a set of deformation coordinate for each time increment to describe deformation and internal nodal forces can be found in the thesis of Wang (2005).

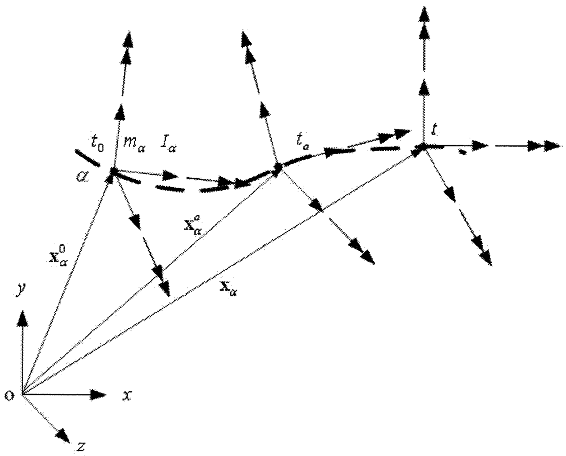

Figure 2. Motion trajectory of a particle α of frame structure with 6 degree of freedoms in space.

The basic modeling assumptions for the VFIFE method for 3D frame structures are essentially the same as those in classical structural analysis. A frame is constructed by means of prismatic members and joints. Members are subjected to forces and moments as shown in Fig. 2. Joints have work equivalent masses and mass moment of inertias, and can be modeled as discrete rigid bodies. Motions of the joints can be described by the principles of virtual work or equations of motion for particles. Members have no mass, and are thus in static equilibrium. The corresponding internal forces $\hat{\mathbf{f}}^* = (\hat{f}_{2x}, \hat{m}_{1y}, \hat{m}_{1z}, \hat{m}_{2x}, \hat{m}_{2y}, \hat{m}_{2z})^T$ of the frame element in the deformation coordinate system can be derived by the principle of virtual work. From the static equilibrium equations, all the internal forces at the two nodes of the frame element can be calculated. All the internal forces at those two nodes of a frame element in the deformation coordinate system at time t are expressed by a vector $\hat{\mathbf{f}}^{\text{int}}$ as

$$\hat{\mathbf{f}}^{\text{int}} = \{\hat{f}_{1x}, \hat{f}_{1y}, \hat{f}_{1z}, \hat{m}_{1x}, \hat{m}_{1y}, \hat{m}_{1z}, \hat{f}_{2x}, \hat{f}_{2y}, \hat{f}_{2z}, \hat{m}_{2x}, \hat{m}_{2y}, \hat{m}_{2z}\} \tag{1}$$

Since all the calculation is within the global coordinates, the internal forces $\hat{\mathbf{f}}^{\text{int}}$ obtained in the local deformation coordinates of each frame element have to be transformed to $\mathbf{f}^{\text{int}}$ in the global coordinate system. After calculating all the internal forces of element nodes, one can sum over all internal forces $-\mathbf{F}_{\beta}^{\text{int}}$ and external forces $\mathbf{F}_{\beta}^{ext}$ applied on a rigid body particle β and obtain the following equation of motion without damping effect:

$$\mathbf{M}_{\beta}\ddot{\mathbf{d}}_{\beta} = \mathbf{F}_{\beta}^{ext} - \mathbf{F}_{\beta}^{\text{int}} \tag{2}$$

Where $\mathbf{M}_{\beta}$ is the general mass matrix and $\ddot{\mathbf{d}}_{\beta}$ is the general displacement vector of the particle β. In the present analysis, the explicit time integration technique is used to solve Eq. (2). Since the VFIFE method uses the motion and relative displacements of particles to identify the internal forces among them. This feature allows users to do the displacement control type excitation. In the seismic analysis, variations of the displacements and rotations of the element nodes connected to ground can be assigned according to the history of ground motion.

3. MODELING OF REINFORCED CONCRETE FRAME UNDER CYCLIC EXCITATION

To model the global nonlinear behavior of a reinforced concrete frame under cyclic excitation, a three-parameter material model characterized by the stiffness degrading factor (S_1), the strength deterioration factor (S_2), and pinching factor (S_3) for the moment-curvature relation as shown in Fig. 3 is adopted into the VFIFE method. A famous and widely used damage index proposed by Park and Ang index (1985) is applied to evaluate the damage state of the frame in the failure analysis. This damage index has implemented in the original release of IDARC (Kunnath et al., 1992). Moments and curvatures data of the frame are used to determine its damage index by Eq. (4).

$$D = \frac{K_m - K}{K_u - K} + \beta_e \frac{\int dE}{M_y K_u} \tag{3}$$

Where

K_m = maximum curvature attained during load history

K_u = ultimate curvature capacity of section

K = recoverable curvature at unloading

β_e = strength degrading parameter

M_y = yield moment of section

$\int dE$ = dissipated hysteretic energy

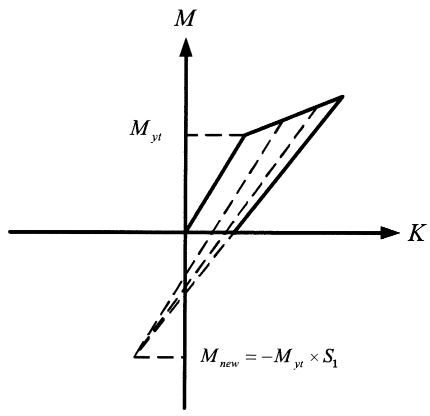

(a) Stiffness Degrading Factor S_1

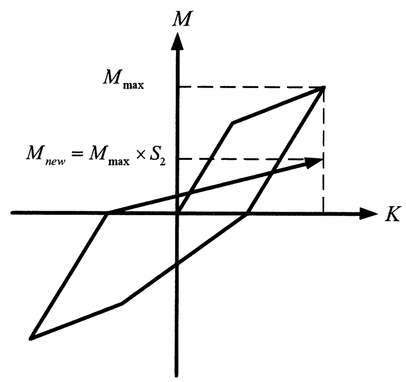

(b) Strength Deterioration Factor S_2

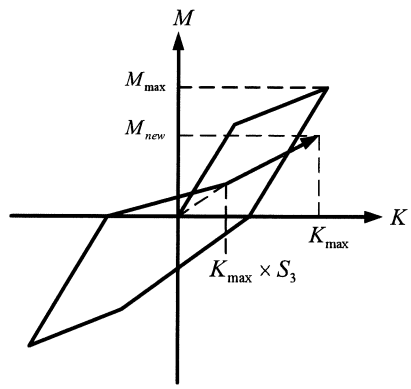

(c) Pinching Factor S_3

Figure 3. A three-parameter moment-curvature model for frame under cyclic excitation.

In the presented analysis, if the damage index of reinforced concrete frame arrive at D=0.77, we define the RC frame element is fractured. New node is added to the fracture interface to release the connectivity. The mass distribution, internal forces, external forces, nodal displacements and boundary conditions are updated for the fractured element in the presented mode.

A simple module to calculate the nonlinear moment-curvature relation for a composite section as shown in Fig. 4 is developed by the fiber section method. Nonlinear stress-strain relation of each material used in the composite section is considered to build up the load-deformation relation. The Mirza and Macgeror model is adopted for the stress-strain relationship of steel reinforcement. For the concrete material confined effect, the Kent and Park model (1971) is used for the calculation of sectional moment-curvature relation. In this model, we have:

$$\sigma_c = \sigma_{cc}[(\frac{2\varepsilon_c}{\varepsilon_{cc}}) - (\frac{\varepsilon_c}{\varepsilon_{cc}})^2] \qquad 0 < \varepsilon_c < \varepsilon_{cc} \qquad (4)$$

$$\sigma_c = \sigma_{cc}[1 - Z(\varepsilon_c - \varepsilon_{cc})] \qquad \varepsilon_{cc} < \varepsilon_c < \varepsilon_{20u} \qquad (5)$$

$$\sigma_c = 0.2\sigma_{cc} \qquad \varepsilon_{20u} < \varepsilon_c < \varepsilon_{cu} \qquad (6)$$

Where $\varepsilon_{20u} = \frac{0.8}{Z} + 0.002$ (7)

$$Z = \frac{0.5}{\varepsilon_{50u} + \varepsilon_{50h} - 0.002} \qquad (8)$$

$$\varepsilon_{50u} = \frac{0.21111 + 0.002 f'_c}{f'_c - 70.37014} \qquad (9)$$

$$\varepsilon_{50h} = \frac{3}{4}\rho_s\sqrt{\frac{b''}{s_h}} \qquad (10)$$

$$\varepsilon_{cu} = 0.004 + 0.9\rho_s\frac{f_{yh}}{3000} \qquad (11)$$

and

E_c : initial elastic modulus of concrete defined as

$15000\sqrt{f'_c}$ (kgf/cm^2),

σ_c : stress of concrete,

ε_c : strain of concrete,

f'_c : compression strength of concrete (kgf/cm^2),

σ_{cc} : maximum stress of concrete,

ε_{cc} : strain corresponding to the maximum stress,

ε_{cu} : ultimate strain of concrete 0.004

ε_{50u} : strain for concrete when stress reduces to 0.5 f'_c,

ε_{50h} : strain due the action of steel stirrup for concrete when stress reduces to 0.5 f'_c,

b'' : width of the core concrete surrounded by the stirrup,

s_h : interval between steel stirrups,

f_{yh} : yielding stress of steel stirrup (kgf/cm^2)

ρ_s : volume ratio of the steel stirrup and core concrete.

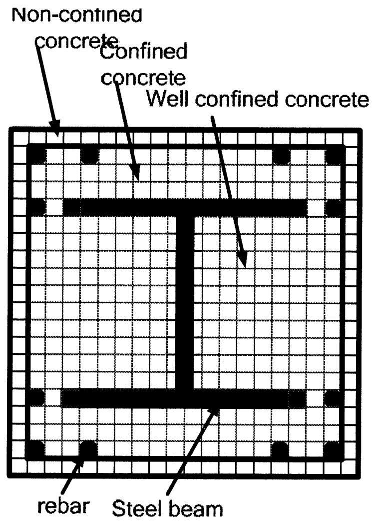

Figure 4. A typical cross section of a reinforced concrete frame.

4. CONTACT ANALYSIS OF SPACE FRAMES

In the collapse analysis of structure, contact detection scheme of discrete members is also a critical part of the simulation process. For each pair of frame elements in the spatial-temporal space, the contact detection is conducted to check whether the minimum distance between the centerlines of elements is satisfied the following criteria:

$$gap = d_{\min} - (r_1 + r_2) \qquad (12)$$

Where r_1 and r_2 are the maximum cross sectional radius from center line of frame elements in contact, respectively. If the value of *gap* is less than 0, it represents the two frame elements are in contact. Contact force calculated by the penalty method is applied to the point in contact with a direction same as the direction connecting the two points in contact.

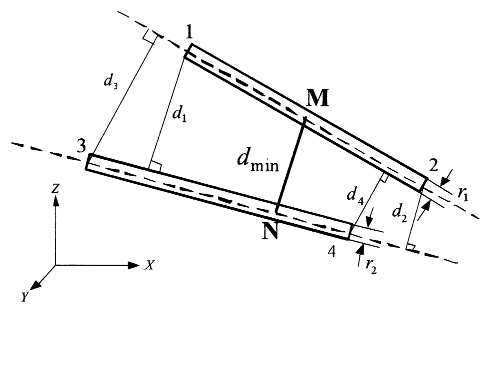

Figure 5. Contact detection of frames are not parallel in space.

As shown in Fig. 4, the minimum distance between two not parallel lines in space can be calculated by the following equation.

$$d_{\min} = abs[\overrightarrow{13} \bullet \frac{\overrightarrow{12} \times \overrightarrow{34}}{\left|\overrightarrow{12} \times \overrightarrow{34}\right|}] \tag{13}$$

Where

$\overrightarrow{ij}$ represents a vector connecting from node i to node j.

The coordinates of the two contact points M and N can be determined also. If the contact points M, N are not in the domain of elements, then the minimum distance among d_i ($i=1, 4$) is used for the contact detection.

5. NUMERICAL EXAMPLES

Example 1: Verification of the Moment-Curvature Relation

To verify the accuracy of the moment-curvature calculated by the presented method, the Response 2000 code is used to calculate the moment –curvature relation for a same frame section. Figure 6 shows the moment-curvature relations calculated by these two codes for a rectangular RC frame section of *width 30 cm x depth 50 cm* with the following data:
compression strength of concrete $f_c' = 210\ kgf/cm^2$, yielding stress of steel $f_y = 4200 kgf/cm^2$, tensile steels are located at *43 cm* from the top surface of the frame section, while the compression steel is located *7 cm* from the top. The discrepancy shown at the later part of those two curves is due to the consideration of strain hardening effect in the presented code.

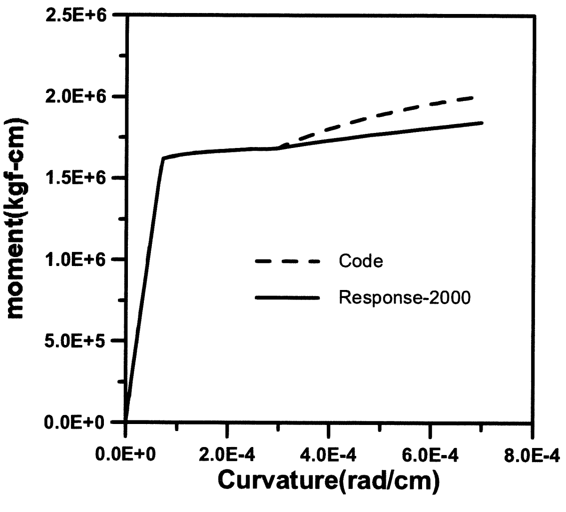

Figure 6 Comparison of the moment- curvature relation of a frame section calculated by the presented code and the Response-2000

Example 2 Collapse of RC Structure under Seismic Excitation

A five floors frame structure is excited by earthquake loading. The frames cross sectional data and material properties of reinforcements are shown in Table 1. The maximum compressive stress of concrete is $f_c' = 317.92\ kgf/cm^2$. The three parameters for the frame section under the action of cyclic loading are : the stiffness degrading factor $S_1 = 1.2$, the strength deterioration factor $S_2 = 0.98$, and the pinching factor $S_3 = 0.9$. The equivalent loading applied on the structure is obtained by the acceleration of earthquake. Once the damage index reaching to the critical value D=0.77, the element is fractured. From Fig. 7, one can find that the failure of the structure started from the bottom of the frame. The fractured component moved downward by the gravity force. The contact detection and analysis algorithm have been included in this study.

Table 1. Material properties and arrangement of steel reinforcements inside a RC frame

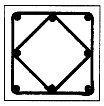	Width × Height	36 cm × 36 cm
Main reinforcement	Steel	8-19φ
	Yielding Stress	5190 kgf/cm^2
Steel Stirrup	Steel	6φ@20 cm
	Yielding Stress	6700 kgf/cm^2

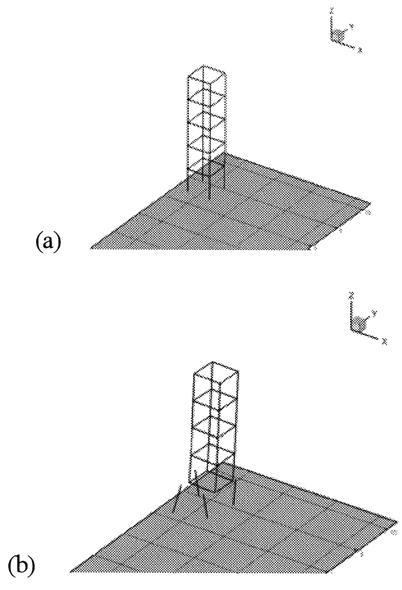

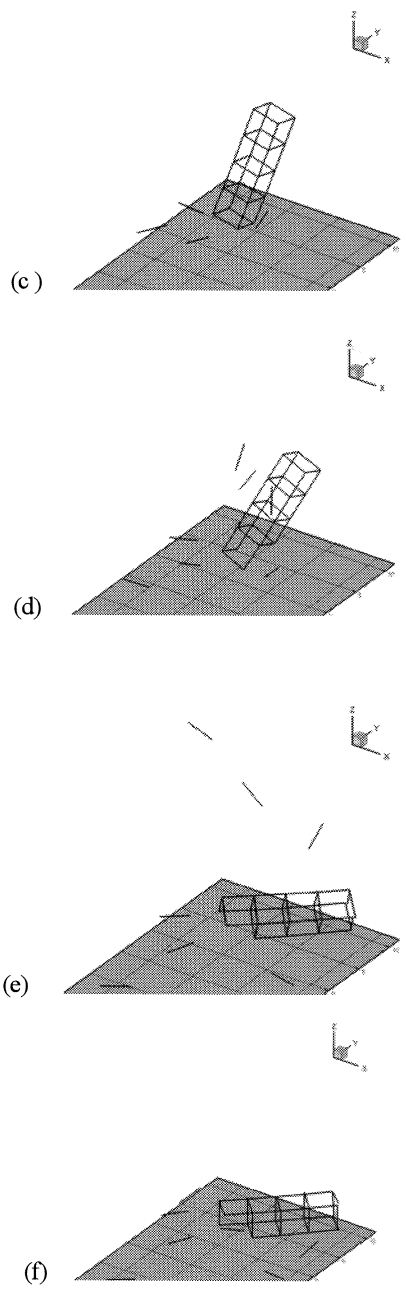

Figure 7 Progressive failure of a space RC frame structure under seismic excitation.

6. CONCLUSIONS

A novel numerical method called the Vector Form Intrinsic Finite Element (VFIFE) method for the motion analysis of space frame structure is presented. Due to some special features of VFIFE, it can conduct simulations of the progressive failure and collapse of structures relatively easy compared with conventional matrix type structural analysis methods. The effects from floors and walls will be included into the analysis in the future. It is believed that the further development of VFIFE method on the nonlinear analysis of reinforced concrete structures can provide engineers as an effective and friendly tool to analyze very complicated engineering problems.

References:

Argyris, J. H., Dunne, P. C., Scharpf, D. W., (1978). "On large displacement-small strain analysis of structures with rotational degree of freedom", *Computer Methods in Applied Mechanics Engineering*, Vol. 14, pp. 401-451.

Elias, Z. M., (1986). *Theory and Methods of Structural Analysis*, John Wiley & Sons, New York, N.Y.

Goldberg, J. E., Richard, R. M., (1963). "Analysis of nonlinear structures", *Journal of Structural Division, ASCE*, Vol. 89, No.4, pp. 333-351.

Griffiths, H., Pugsley, A., Saunders, O. (1986). *Report of the inquiry into the collapse of flats at Ronan Point*, Canning Town, Her Majesty's Stationary Office. London, England.

Kent, D. C. and R. Park, (1971). "Flexural Members with Concreted Concrete." *Journal of the Structural Division, ASCE*, Vol. 97, pp. 1969-1990.

Kunnath, S. K., Reinhorn, A. M., Lobo, R. F., (1992). "IDARC version 3.0: a program for the inelastic damage analysis of reinforced concrete structure structures", *Technical Report NCEER-92-0022*, National Center for Earthquake Engineering Research, State University of New York, Buffalo NY.

Park, R. and Ang, A. H. S., (1985). "Mechanistic seismic damage model for reinforced concrete buildings", *Journal of structural Engineering, ASCE*, Vol. 111, No. 4, pp. 740-757.

Park, Y. J., Reinhorn, A. M., Kunnath, S. K., (1987). "IDARC: Inelastic damage analysis of RC frame-shear wall structures", *Technical Report NCEER-87-0008*, National Center for Earthquake Engineering Research, State University of New York, Buffalo NY.

Shih, C., Wang, Y. K., Ting, E. C., (2004). "Fundamentals of a vector form intrinsic finite element: Part III. Convected material frame and examples", *Journal of Mechanics*, Vol. 20, No.2, pp. 133-143.

Ting, E. C., Shih, C., Wang, Y. K., (2004a). "Fundamentals of a vector form intrinsic finite element: Part I. basic procedure and a plane frame element", *Journal of Mechanics*, Vol. 20, No.2, pp. 113-122.

Ting, E. C., Shih, C., Wang, Y. K., (2004b). "Fundamentals of a vector form intrinsic finite element: Part II. plane solid elements," *Journal of Mechanics*, Vol. 20, No.2, pp. 123-132.

Wang, C. Y., Wang, R. Z., Chuang, C. C., Wu, T. Y., (2006). "Nonlinear Dynamic Analysis of Reticulated Space Truss Structure", *Journal of Mechanics*, Vol. 22, No.3, pp. 235-248.

Wang, R. Z. (2005), *Vector Form Motion Analysis of Structure,* Ph. D. Thesis, Department of Civil Engineering, National Central University, Taiwan (in Chinese).

Wang, R. Z., Chuang, C. C., Wu, T. Y., Wang, C. Y., (2005a). "Vector form analysis of space truss structure in large elastic-plastic deformation", *Journal of the Chinese Institute of Civil & Hydraulic Engineering*, Vol. 17, No.4, pp. 633-646.

Wang, R. Z., Kang, L. C., Wu, S. Y., Wang, C. Y., (2005b). "Numerical Simulation of the Whipping Problem of High Pressure Pipe", *Chinese Society of Structural Engineering*, Vol. 20, No.4, pp. 120-143 (in Chinese).

Wu, T. Y., Wang, R. Z., Wang, C. Y., (2006). "Large deflection analysis of flexible planar frames", *Journal of the Chinese Institute of Engineers*, Vol. 29, No.4, pp. 593-606.

Yang, Y. B., Kuo, S. R., (1994). *Theory & Analysis of Nonlinear Framed Structures*, Prentice-Hall.

Fifth International Conference on Urban Earthquake Engineering
March 4-5, 2008, Tokyo Institute of Technology, Tokyo, Japan

EVALUATION ON RESIDUAL LOAD CARRYING CAPACITY OF CORRODED RC BEAMS BY 3D LATTICE MODEL ANALYSIS

T. Miki[1] and J. Niwa[2]

1) Associate Professor, Department of Civil Engineering, Kobe University, Japan
2) Professor, Department of Civil Engineering, Tokyo Institute of Technology, Japan
mikitomo@port.kobe-u.ac.jp, jniwa@cv.titech.ac.jp

Abstract: This paper presents an evaluation of the residual structural performance of RC members damaged due to steel corrosion. A lattice model is focused on and developed to evaluate the shear resisting mechanism of corroded RC beams. An interface element is modeled for the bond behavior between corroded steel and concrete and is incorporated into the lattice model. The target is set on landing piers that were removed at 2004 because of deteriorations in service for about 40 years. The lattice model is extended to a three dimension to consider corrosion conditions of steels which varied spatially in the analysis. The analysis shows that the 3D lattice model can reasonably evaluate the yielding and maximum loads of RC structural members with corrosion-damaged steels.

1. INTRODUCTION

An appropriate method for the maintenance of existing RC structures has been required to keep the structures being the initial required performance. Deteriorations such as steel corrosion due to the permeation of chloride ions should be considered as one of the durability problem regarding RC structures. When steel corrosion in RC structures progresses, cracks, induced by the expansion pressure of corrosion products, occur in the cover concrete. The previous study (Kato et al. 2004) has shown that flexural capacities of RC beams decreased due to the deterioration of bond properties between a reinforcing bar and concrete. The decrease in the flexural capacity is much larger than that in the capacity which is estimated from the cross-sectional loss of a reinforcing bar.

For the deteriorated RC structures, it is required to evaluate the residual performance of the structures in the maintenance system, and the analytical tool to evaluate the performance is keenly needed. The aim of this study is to establish the method to evaluate the residual performance of RC structures using given information on the deterioration such as steel corrosion.

In the lattice model (Niwa et al. 1995, Miki and Niwa 2004), a RC member is discretized into truss elements. This is objective and simple modeling which can be used to explain the shear resisting mechanism of RC structural members. Suzuki et al. (2006) have considered the cross-sectional loss of reinforcing bars due to steel corrosion, and introduced interface elements modeled by using shear springs and vertical springs in the lattice model. The interface elements were able to express the deterioration of bond properties due to corrosion. Their research clarified that the updated lattice model was able to evaluate the structural performance of RC beams with corrosion-damaged steels. These analytical investigations were performed using the 2D lattice model in their study. In addition, the targets of the analysis were RC beams with corrosion-damaged steels by means of electric acceleration method. Concerning this reproduction method, Morinaga (1996) has pointed out that the electric corrosion condition was distributed more uniformly than that in the actual RC structures. When the steel corrosion spatially distributed among the actual structures, it is difficult to evaluate the response of such structures appropriately by using 2D analysis.

This study aims to evaluate the residual performance of RC structural members using the 3D lattice model. In the model, the corrosion condition spatially distributed in the actual structures is considered.

2. ANALYTICAL MODEL

2.1 Outlines of Lattice Model

The lattice model consists of concrete members and reinforcement members, as shown in Figure 1. In a RC beam, the concrete is modeled into flexural compression members, flexural tension members, diagonal compression members, diagonal tension members, horizontal members and an arch member. The longitudinal and transverse reinforcing bars are modeled into horizontal and vertical members, respectively. The diagonal members are arranged at regular intervals with inclined angles of 45 and 135 degrees with respect to the longitudinal axis of a beam. The arch member connecting the nodes at the opposite diagonal corners between the

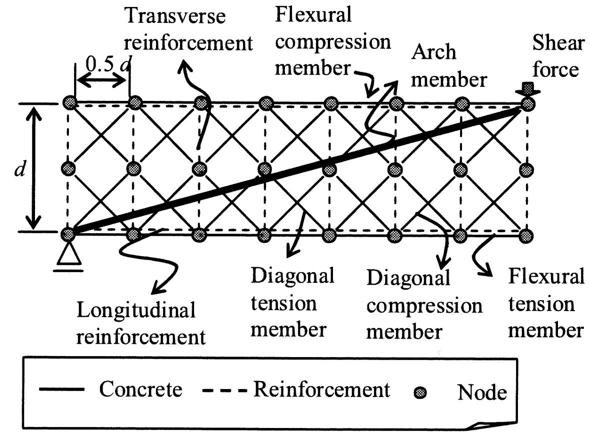

Figure 1 Schematic diagram of lattice model in side view

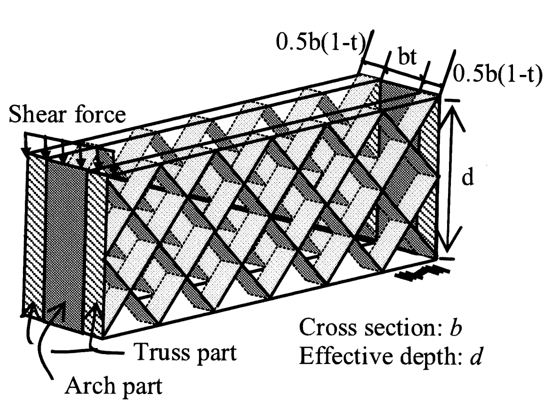

Figure 2 Cross-section of RC beam modeled by lattice model

loading point and a support in the beam is arranged according to the direction of the internal flow of compressive stresses.

Figure 2 illustrates a schematic diagram of cross-section of a RC beam modeled by the lattice model. The concrete is divided into truss and arch parts. When the value of t is defined as a ratio of the width of an arch part to the width of cross-section, the widths of an arch part and a truss part are given as bt and $b(1\text{-}t)$, respectively, where t ranges from 0 to 1. The value of t is determined based on the theorem of the minimization of the total potential energy for the lattice model with the initial elastic stiffness. The total potential energy is obtained from the difference between the summation of the strain energy in each element and the external work. The pre-analysis using the lattice model is carried out to determine the value of t according to the minimum total potential energy.

2.2 Material Constitutive Model

a) Concrete model

For a cracked concrete, the compressive softening behavior of concrete proposed by Vecchio and Collins (1986) is considered. The ability of cracked concrete to resist the compressive stress decreases as increase in the transverse tensile strain. For the flexural compression members, the stress-strain relationship proposed by Maekawa and Fukuura (1999) is used. As for the flexural tension members, which are provided around reinforcing bars, the tension-stiffening model (Okamura and Maekawa 1991) is applied in order to consider the bond effect between the concrete and reinforcing bars. On the other hand, when interface elements that will be mentioned later on are installed in the model, the 1/4 tension softening model (Uchida and Rokugo 1991) is applied as brittle behavior of plan concrete.

For the diagonal tension members, the 1/4 tension softening model (Uchida and Rokugo 1991) is applied. The stress-strain relationships proposed by Naganuma and Ohkubo (2000) are used, for the cyclic behavior of concrete under both compression and tension.

b) Reinforcing bar model

The envelope curve for the stress-strain relationship in tension of reinforcing bars is modeled as the average behavior in concrete by Maekawa and Fukuura (1999). As for the stress-strain relationship in compression, bi-linear model in which the tangential stiffness after yielding is set as 0.01 E_s, where E_s denotes the Young's modulus of a reinforcing bar, is used.

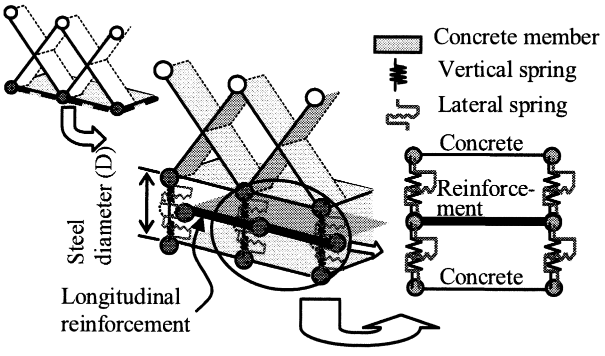

Figure 3 Outlines of interface elements

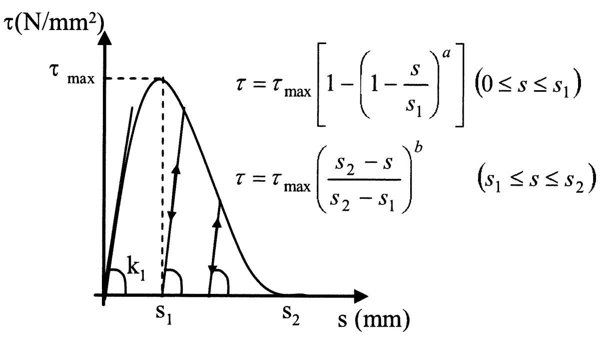

Figure 4 Bond property in the shear spring

2.3 Interface Elements Between Reinforcing Bar and Concrete

Figure 3 shows the outlines of the interface elements. The nodes are arranged such that the nodes of steel are located between the adjacent nodes of concrete. The thickness of the interface element is assumed to be as same as the diameter of a reinforcing bar (D). These nodes are connected with vertical springs transmitting the vertical stress and lateral springs transmitting the shear stress. The vertical spring is modeled as a linear elastic spring in which the tangential stiffness is as same as the Young's modulus of concrete, E_c. As for the lateral spring, it is assumed that the bond stress is uniformly distributed on the surface of the longitudinal reinforcing bar and the bond force on the surface is calculated by the bond stress being multiplied by the steel surface. In this study, τ (bond stress)-s (slip between steel and concrete) relationship as shown in Figure 4 is applied to the lateral spring. The parameters of this model are the maximum bond stress τ_{max}, the slip displacement at τ_{max}, s_1, the slip displacement at $\tau = 0$, s_2 and the exponential coefficients, a and b. Here, the exponents of a and b in the equations are determined based on the extensive parametric analysis. These are assumed to be constants; $a = 1$ and $b = 4$ in this study.

Based on Kato's study (2003), which is related with the ratio of the cross-sectional loss of a reinforcing bar to the degree of bond deterioration between a reinforcing bar and concrete, s_1 and s_2 are set as values of 0.1 mm and 0.2 mm, respectively. Figure 6 shows results in axial test and the analysis using appropriate parameters for the bond-slip behavior of the lateral spring. From the parametric analysis, it can be assumed that τ_{max} is determined by Eq. (1) using a ratio of cross-sectional loss of a reinforcing bar, x (%).

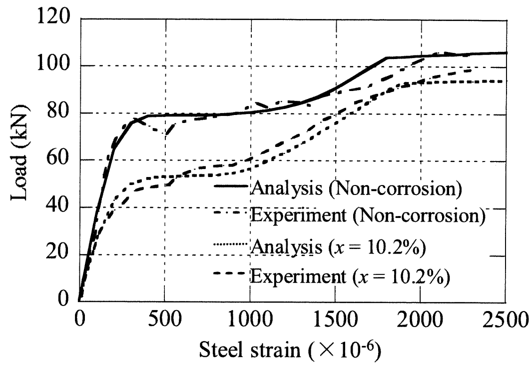

Figure 5 Load-steel strain relationship of RC members in the axial tension test and the lattice model analysis

$$\tau_{max} = -0.16x + 4.0 \quad (1)$$

3. RESIDUAL PERFORMANCE OF RC MEMBERS WITH CORROSION-DAMAGED STEELS

3.1 Analytical Target

In this study, the experimental tests conducted by Kato et al. (2006) are used as a target of the analysis. The specimens were six rectangular RC beams taken out from two slabs of the pier which had been in service for about 40 years. The pier was removed in 2004 because of serious deterioration such as cracks and spalling of cover concrete. Table 1 shows the dimension of the specimens.

The material tests of reinforcing bars and core concrete which were taken from the beams after bending tests were

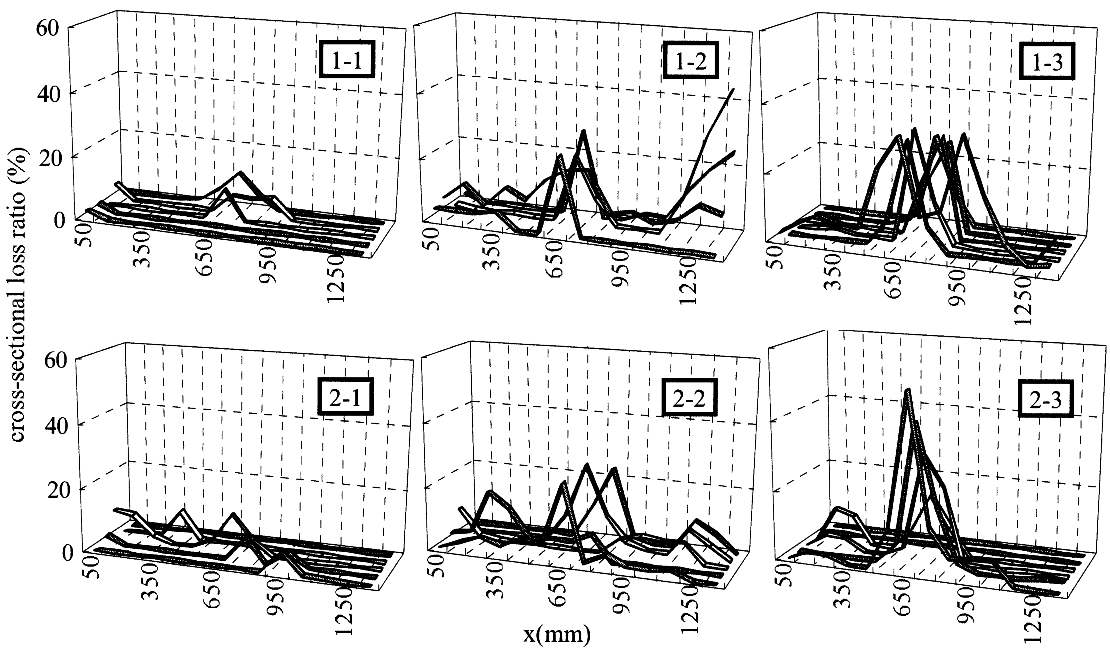

Figure 6 Cross-sectional loss distribution of lower reinforcing bars

Table 1 Dimension of specimens

Name	Series 1			Series 2		
	1-1	1-2	1-3	2-1	2-2	2-3
Width b(mm)*1	699	535	798	732	569	812
Depth h(mm)*1	300	300	300	310	310	310
N_u *2,*3	3	4	3	3	3	3
N_l *2,*4	5	4	6	5	5	6

*1 : mean, *2 : round bar of 13mm diameter
*3 : number of upper reinforcing bars
*4 : number of lower reinforcing bars

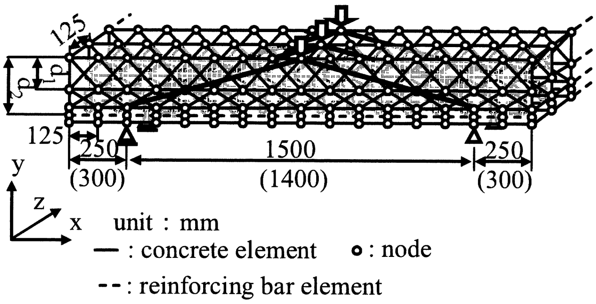

Figure 7 Configuration of 3D lattice model

conducted. The average yield strength and the average Young's modulus of reinforcing bars among the beams were 358 N/mm^2 and 218 kN/mm^2, respectively. The average compression strength and the average Young's modulus of concrete were 38.6 N/mm^2 and 29.1 kN/mm^2, respectively. Here, the ratio of cross-sectional loss of reinforcing bar is defined as a ratio of the weight-loss of corroded reinforcing bar from its initial weight to that of original reinforcing bar. Lower reinforcing bars were taken from RC beams within the bending span after bending tests, and all reinforcing bars were divided into 14 samples with the length of 100 mm. The ratios of cross-sectional loss were measured for each sample, and the distributions of the ratios of cross-sectional loss of lower reinforcing bars were calculated as shown in Figure 6. The figure clearly shows that the corrosion conditions of each reinforcing bar varied spatially. In these specimens, the ratios of cross-sectional loss tend to be highest in the center part of the bending span. In the specimen 2-3, although one reinforcing bar shows the maximum loss ratio 51 %, the other shows no corrosion in the center part of the bending span. Remarkable variation of the maximum loss of reinforcing bars can be confirmed for all beams taken from one slab. It seems likely that the causes of these variations of corrosion condition are initial defects such as unfilled concrete in the concrete cover.

Figure 7 shows the configuration of the 3D lattice model for these specimens. In this model, the 2D lattice models are arranged at the location of reinforcing bar in the z direction, and each 2D model is connected by the truss members in the x-z and y-z planes. To reflect effective depth

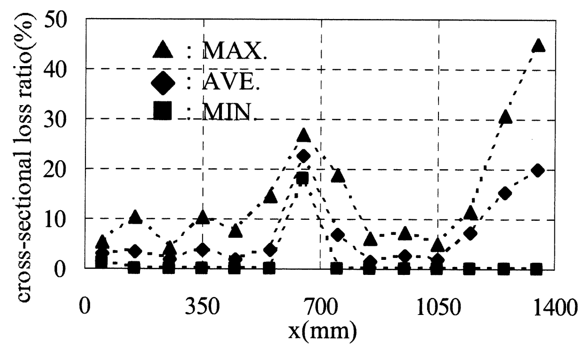

Figure 8 Distribution of the ratio of cross-sectional loss of reinforcing bars (specimen 1-2)

of upper and lower reinforcing bars, the nodes of the reinforcing bar elements are arranged at the location of reinforcing bars (d_1 and d_2) in the y direction. In the Series 1, d_1 and d_2 are 140 and 250 mm, respectively, and in the Series 2, d_1 and d_2 are 150 and 260 mm, respectively.

The cross-sectional loss of the reinforcing bar elements and τ_{max} of the shear spring elements are determined by using Eq. (1) substituted the ratio of cross-sectional loss measured within the bending span. These values express the influence of deterioration of bond properties in the analysis. Because the ratio of cross-sectional loss of reinforcing bars except between the supports are not measured, these ratios in the region from the support to the beam end are assumed to the constant values that are measured at the support.

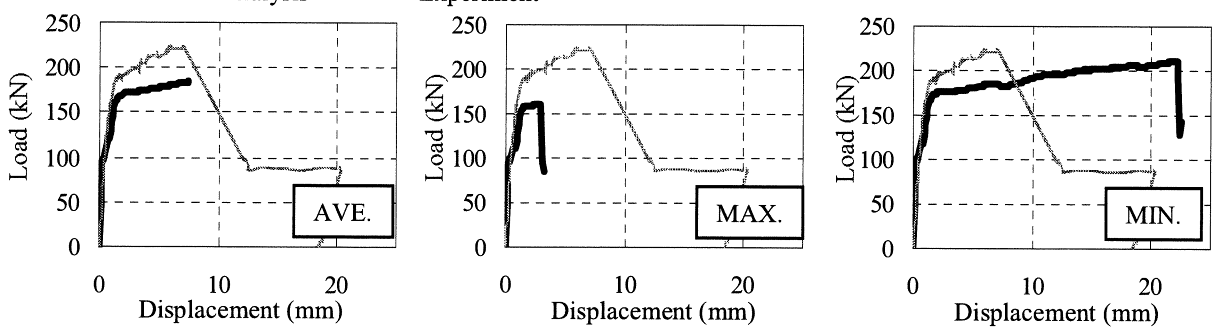

Figure 9 Load-displacement relationship of specimen 1-2 (2D lattice model)

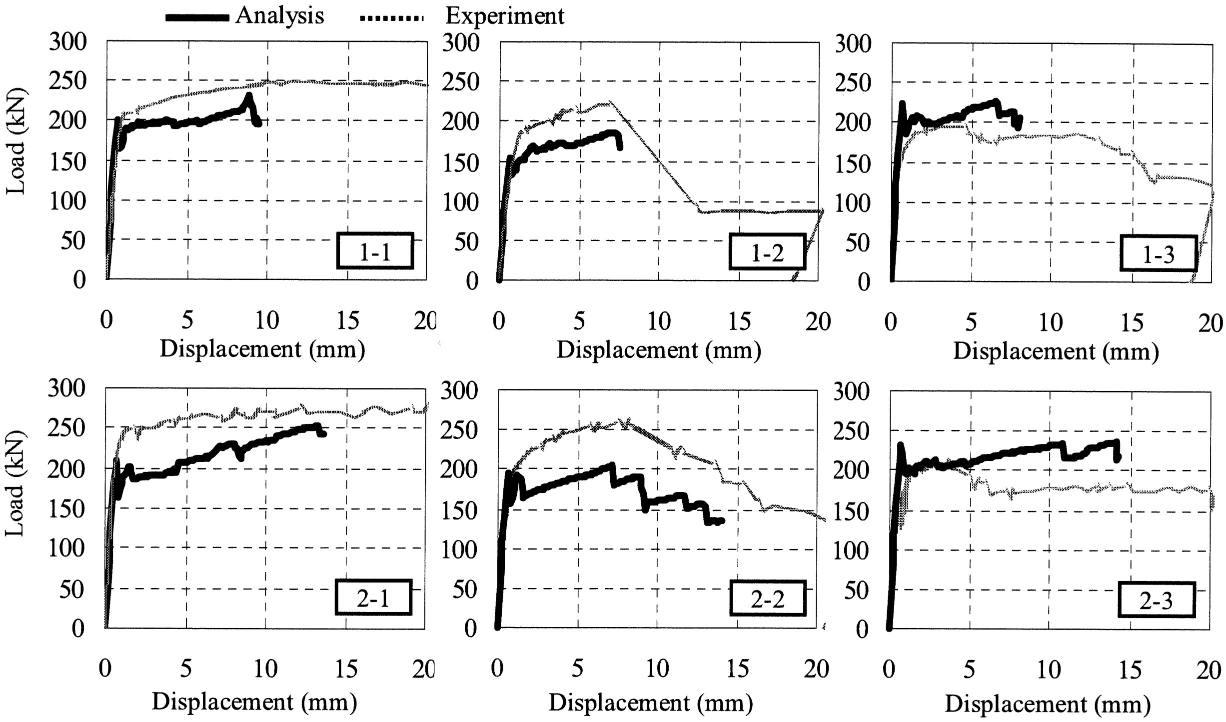

Figure 10 Load-displacement relationships computed by 3D lattice model

3.2 Applicability of the 2D Lattice Model

The structural performances of RC beams with corrosion-damaged steels are evaluated by using the 2D lattice model. The 2D lattice model cannot explain directly the actual corrosion conditions which varied spatially for each reinforcing bar. Herein, the maximum, the average and the minimum ratios of the cross-sectional loss for each reinforcing bar averaged along in the z direction are used as an input data. The results of the analysis for the specimen 1-2 were shown in the following section for an example.

Figure 8 shows the distributions of the ratios on cross-sectional loss of reinforcing bars measured in the specimen 1-2, and Figure 9 shows the load-displacement relationships obtained from the analysis and the experiment for the specimen 1-2. This specimen has the large ratio of cross-sectional loss at mid span and near a support. We can see that these values depicted in Figure 8 are highly variable along with the beam axis. For example, one reinforcing bar shows the maximum loss ratio 45 % at a support, and the other reinforcing bar shows no corrosion in the specimen 1-2. The analysis indicates that the flexural capacity and the deformation capacity of RC beam are remarkably depending upon the distributions of cross-sectional loss ratios of reinforcing bars (see Figure 9).

In the actual structure in which the corrosion condition varies spatially, the maximum, the average and the minimum ratios of cross-sectional loss of reinforcing bars that are input in the analysis have a significant dispersion. Consequently, the 2D lattice model analysis predicts the variability in the flexural and deformation capacities.

If the target of analysis is a structural member which has been deteriorated in the actual condition, the corrosion conditions vary spatially, so it is difficult to reflect its influence in the 2D analysis. Therefore, these problems should be solved by using the 3D analysis.

3.3 Extension to the 3D Lattice Model Analysis

Figure 10 shows the load-displacement relationship obtained from the analysis and the experiments. In addition, Figure 11 shows the cracking load, the yielding load and the maximum load in RC beams as the comparison between the analysis and the experiment.

As can be seen in Figure 10, the initial stiffness of RC beams obtained from the experiment, which indicates the stiffness before load-induced cracking of the beam, shows good agreement with that predicted in the analysis. However, the predictions of the cracking load are remarkably higher than those of the experiment in all beams. The stiffness after cracking obtained from the analysis is also different from those of the experimental results. On the other hand, as shown in Figures 11 (b) and 11 (c), the ratios of the analytical results to the experimental results range from 0.77 to 1.13 for the yielding load, 0.79 to 1.15 for the maximum load. As for the deformation capacity, even though the analysis predicted slightly smaller than the experiments, the analysis for all beams captured the experimental behavior approximately.

The cracking loads obtained from the analysis are higher than those of the experiments in all beams. The cause of overestimations is no consideration in the analysis for the

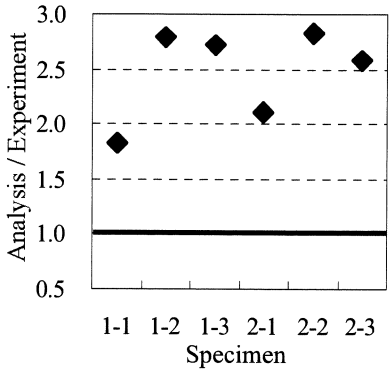

(a) Cracking load

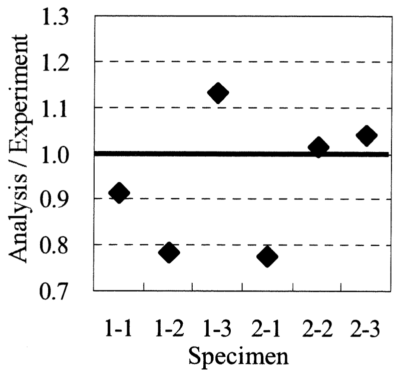

(b) Yielding load

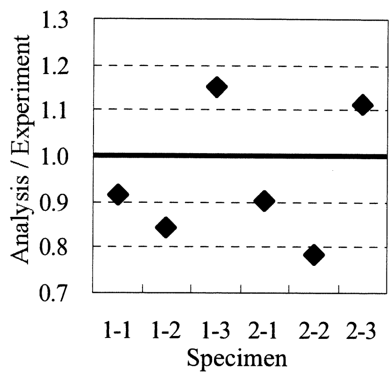

(c) Maximum load

Figure 11 Comparisons between the experiment and the analysis using 3D lattice model

reduction of concrete cross-sectional due to the initial defects such as unfilled concrete in the concrete cover and the corrosion cracking.

The discussion on Eq. (1) which expresses the maximum bond stress between a reinforcing bar and concrete is also required. This relationship is based on the experiment in which the maximum ratio of cross-sectional loss of a reinforcing bar measured is about 10 %. However, all specimens selected as the targets in this study show more than 10 % of the maximum ratios of cross-sectional loss of reinforcing bars, and the largest ratio is 51 %. To evaluate the residual performance of the structures with further accuracy, it is required to confirm the applicability of Eq. (1) to use in the analysis of actual RC structures having severely corroded reinforcing bars.

4. CONCLUSIONS

In this study, the RC structural members deteriorated in actual condition are selected as targets of the analysis. The residual performance of RC structural members is evaluated by using the 3D lattice model. In the model, the interface elements considering the bond deterioration between concrete and reinforcing bars are introduced. The conclusions obtained from this research are shown as follows:

1) In the case of the RC structural members with actual corrosion conditions in a reinforcing bar, it is difficult to evaluate the behavior of these members by 2D analysis. This is because the corrosion conditions of a reinforcing bar indicates the spatial dispersion in structural members and the corrosion condition cannot be averaged into the two-dimension properly.
2) The 3D lattice model analysis can appropriately evaluate the residual structural performance of RC structural members with corrosion-damaged steels, especially for the yielding and maximum loads.

References:

Kato, E., Iwanami, M., Yokota, H., Ito, H. and Sato, F. (2003), Bond Behavior between Corroded Rebar and Concrete, *Technical Note of the Port and Airport Research Institute*, **1044**.

Kato, E., Iwanami, M., Yokota, H., Nakamura, K. and Ito, H. (2004), Influence of Rebar Corrosion on Structural Performance of RC Beams Subject to Reversed Cyclic Loading, *Technical Note of the Port and Airport Research Institute*, **1079**.

Kato, E., Iwanami, M., Yamaji, T. and Yokota, H. (2006), Structural Performance and Deterioration due to Chloride Attack of Reinforced Concrete Deck of Existing Piers, *Technical Note of the Port and Airport Research Institute*, **1140**.

Maekawa, K. and Fukuura, N. (1999), Re-formulation of Spatially Averaged RC Constitutive Model with Quasi-orthogonal Bi-directional Cracking, *Journal of Materials, Concrete Structures and Pavements*, **634**(45), 157-176.

Miki, T. and Niwa, J. (2004), Nonlinear Analysis of RC Structural Members Using 3D Lattice Model, *Journal of Advanced Concrete Technology*, **2**(3), 343-358.

Morinaga, S. (1996), Remaining Life of Reinforced Concrete Structures after Corrosion Cracking, *Durability of Building Materials and Components*, 127-137.

Naganuma, K. and Ohkubo, M. (2000), An Analytical Model for Reinforced Concrete Panels under Cyclic Stresses, *Journal of Structural and Construction Engineering*, **536**, 135-142.

Niwa, J., Choi, I.C. and Tanabe, T. (1995), Analytical Study for Shear Resisting Mechanism Using Lattice Model, *Concrete Library International*, **26**, 95-109.

Okamura, H. and Maekawa, K. (1991), Nonlinear Analysis and Constitutive Models of Reinforced Concrete, Gihodo-Shuppan.

Suzuki, N., Miki, T. and Niwa, J. (2006), Lattice Model Analysis for Evaluation of Shear Loading Capacity of Damaged RC Beams, *Proceedings of the Japan Concrete Institute*, **28**(2), 235-240.

Uchida, Y. and Rokugo, K. (1991), Determination of Tension Softening Diagrams of Concrete by Means of Bending Tests, *Journal of Materials, Concrete Structures and Pavements*, **426**(14), 203-212.

Vecchio, F. J. and Collins, M. P. (1986), The Modified Compression Field Theory for Reinforced Concrete Elements Subjected to Shear, *ACI Journal*, **83**(2), 219-231.

Fifth International Conference on Urban Earthquake Engineering
March 4-5, 2008, Tokyo Institute of Technology, Tokyo, Japan

THE EXPERIMENTAL RESEARCH OF DUCTILITY AND ENERGY DISSIPATION OF STEEL FIBER REINFORCED CONCRETE SHEAR WALL

Jun Zhao[1],Xingliang Du[2],Danying Gao[1]

1) Professor,Department of civil engineering,Zhengzhou University,Zhengzhou China
2) Engineer,Department of engineering management,Henan College of Finance & Taxation ,Zhengzhou China
zhaoj71@hotmail.com, duxingliang521@126.com, gdy@zzu.edu.cn

Abstract: With the low frequency cyclic load test, the experimental research is carried out on the seismic behavior of steel fiber reinforced concrete shear wall. 6 shear walls with and without steel fibers are tested. The ductility, hysteretic capacity, energy dissipation of shear walls affected by the volume fraction of steel fiber and concrete strength are analyzed.It is shown that the ductility, energy dissipation of steel fiber reinforced concrete shear walls are improved obviously compared with ordinary R.C. shear wall.The steel fiber reinforced concrete shear walls have good seismic resistant property.

1. INTRODUCTION

Reinforced concrete shear wall is one of the main lateral force resistant elements in high rise building, the superiority of seismic resistance behavior of which has been accepted widely all over the world. The reasonable shear wall structures have the significant features of high bearing capacity,big stiffness,good ductility, and good energy dissipation. But the height of shear wall is more higher with the height of high building increased constantly, so mechanical properties of shear wall are required higher and higher. Especially, the strength grade of concrete has been extended to high grades in *Code For Design Of Concrete Structures* (GB50010-2002). The problems of seismic behavior of shear wall become increasingly apparent and important with the decrease of cross section and increase of concrete strength. And ordinary shear wall structures have the problems of crack, poor ductility,relatively lower carrying capacity, so it need more reinforcements to solve above problems. But these problems can not be effectively solved by using more reinforcements, and construction conditions are become poorer. In recent years, domestic and foreign researchers have been pursuing a way to raise bearing capacity,energy dissipation and seismic property at the same time.Relative measures are suggested for improvement by experimental researches and theoretical analysis.Comparing to ordinary reinforced concrete, steel fiber reinforced concrete has such significant advantages as high tensile strength and good deformation capacity, steel fiber reinforced concrete shear walls become an effective approach to improve energy dissipation and bearing capacity at same time.

2. RESEARCH PURPOSE

As shown in the work by Wang et al.(1985), the ductility and energy dissipation of shear wall affected by reinforcement ratio, reinforcement strength, concrete strength, shear-span ratio, boundary structure, axial compression ratio and load patterns. The main purpose of the experimental research is to study ductility, hysteretic capacity, energy dissipation of shear wall affected by the volume fractions of steel fiber and concrete strength. So other parameters and load patterns of specimens are the same except for volume fractions of steel fiber and concrete strength. Based on the researches of steel fiber reinforced concrete shear walls with different volume fractions of steel fiber and concrete strength, hysteretic curve of specimens are drawn, the rules of ductility and energy dissipation affected by volume fractions of steel fiber and concrete strength of shear walls are concluded.

3. TEST SURVEY

3.1 Specimen design

According to theoretical calculation and structure requirements of shear walls in *Technical specification for concrete structures of tall building* (JGJ3-2002*)*. Performances of 6 steel fiber reinforced concrete shear walls are analyzed in this thesis, namely, SW-00-40, SW-05-40,SW-10-40,SW-15-40,SW-20-40,SW-10-30. For example, "SW-05-40" is termed "a specimen of reinforced concrete shear wall with 0.5% volume fraction of steel fibers and concrete strength grade of C40".

Height-width ratio of specimen is 1:1, thickness and height are 200mm and 900mm respectively.In order to simulate rigid foundation and fix the specimen on platform of structural laboratory, high rigid foundation is designed in the bottom of specimen.And in order to simulate the constraint to shear wall and bear lateral load and vertical load, a loading beam is designed at the top of specimen.

These walls are divided into the following two series. In the first series, they are different volume fractions of steel fiber with same concrete strength.And in the second series,they are different concrete strength with the same volume fraction of steel fiber. In this test, all walls have been designed with same cross area dimension and same reinforcement, which is illustrated in figure 1.

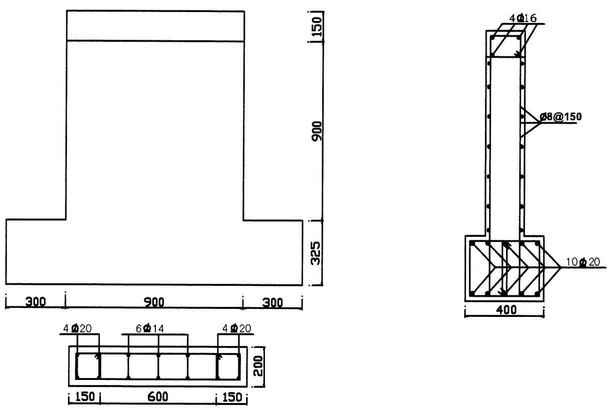

Figure 1 Design details of specimens

3.2 Test device

In this thesis, the experimental study is carried out with the low frequency cyclic load, the lateral load is applied to two side of specimen, the direction of it coincide with unchanged during test. There are proper rollers between synchronous cylinder and reaction beam in order to keep the top of specimen to move freely. The foundation is fixed with anchor bolt. centroidal axis of load beam. Vertical Load is applied to scheduled load by 2-3 times, and remained constantly.

3.3 Load scheme

The low frequency cyclic load is applied to scheduled load controlled by load and deformation, and divided into two stages as follows:

(1) Load controlling stage: the low frequency cyclic load is controlled by load before yielding, and each class load cycles once.

(2)Deformation controlling stage: the low frequency cyclic loading is controlled by multiple of horizontal displacement of top when yield, and each class load cycles 3 times.

4. THE HYSTERESIS CURVE

Relationship between load and deformation forms one hysteretic loop during each class load, the hysteretic curve were drawn by several cycles. The hysteretic curves were illustrated in figure2-7.

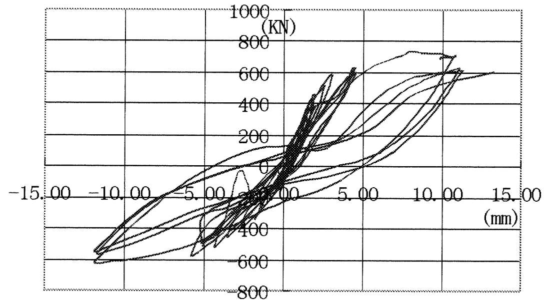

Figure 2 hysteretic curves of SW-10-30

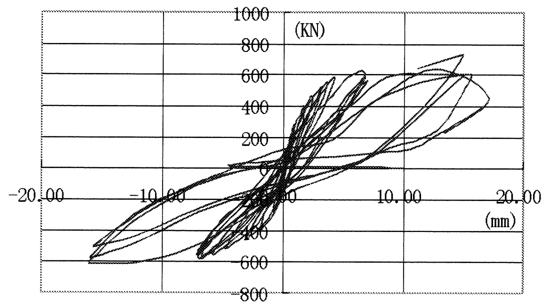

Figure 3 hysteretic curves of SW-00-40

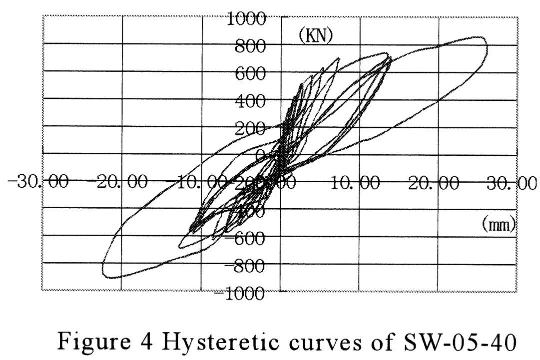

Figure 4 Hysteretic curves of SW-05-40

4.1 Characteristics of the hysteretic Curve

According to the curves, there are such characteristics as following:

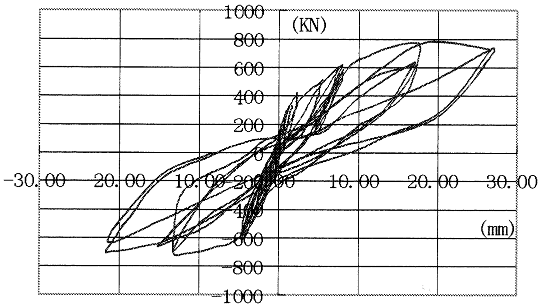

Figure 5 Hysteretic curves of SW-10-40

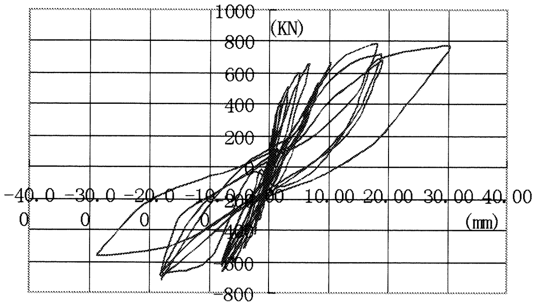

Figure 6 Hysteretic curves of SW-15-40

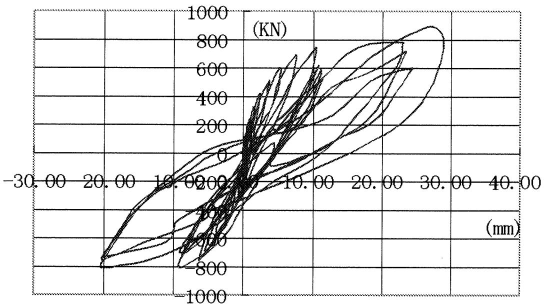

Figure 7 Hysteretic curves of SW-20-40

(1) The hysteretic curve approximate linear before crack, the area of hysteretic loop was small, the shape of hysteretic loop was long and thin, this phenomenon shows that there were no obvious change in stiffness and deformation, and the specimen keeps elastic stage. With continuous load, cracks appeared in bottom of shear wall, the shape of hysteretic loop was approximate reverse shape of "S", and inclined to displacement axis. The area of hysteretic loop increased gradually.The displacement of shear wall was not zero when lateral loading was zero,that is to say, there was residual deformation.

(2)The hysteretic curve was fundamental symmetric on positive and negative direction at initial crack stage.When the load increased,the elasticity of shear wall gradually decreased, the plasticity developed non-uniformly, cracks did not completely closed, shear wall start to keep elastic-plastic stage,deformation difference on positive and negative direction is more and more obvious.So the hysteretic curve shows asymmetry.

(3)After reinforcement yielded, the displacement of wall increased gradually in horizontal direction, crack width increased gradually. The stiffness of wall decreased gradually, the phenomenon was more obvious with continuous load,that is to say,stiffness began to degenerate obviously. But bearing capacity continued to increase, bearing capacity began to decrease after ultimate load. The plastic deformation of wall weaken gradually until to failure.

(4)All hysteretic loops of shear wall showed significant pinch phenomenon,this phenomenon was improved with the addition of steel fibers.The declined tendency of the hysteretic curve slowed down, which showed that steel fiber obviously constraint the development of crack, and he stiffness degenerated slowly.

(5)With the low frequency cyclic load,because of structural damage accumulated, bearing capacity and stiffness in two direction gradually became equal after yielded,the stiffness showed equivalent degradation in hysteretic loops.

4.2 Analysis of hysteretic capacity

According to curves of all shear walls, there were such conclusions as following:

(1) According to the hysteretic curves of the shear walls which were named with the symbols of (SW-00-40,SW-05-40,SW-10-40,SW-15-40,SW-20-40), comparing to ordinary shear wall, steel fiber reinforced concrete shear walls showed good ductility and energy dissipation, the ductility and energy dissipation increased with increasing of volume fractions of steel fibers.

(2)According to the hysteretic curves of the second series shear walls (SW-1.0-30、SW-1.0-40), comparing to ordinary shear wall, with the same volume fraction of steel fiber but different concrete strength,ultimate bearing capacity increased significantly,energy dissipation enhanced in some extent, ductility decreased slightly.

(3)In elastic stage, there were obvious difference of hysteretic curves. But when shear wall yielded, comparing to such walls as SW-10-30 and SW-00-40,the failure phenomena showed obvious shear failure features ; failure phenomena of SW-20-40 and SW-15-40 showed obvious flexural failure features, and the pinch phenomena of hysteretic curves were not significant. This phenomenon was due to the relative slipp between yielded reinforcement and concrete.When longitudinal steels of bended walls yielded, horizontal reinforcing steels had a long way to yield.

5. SKELETON CURVES

Skeleton curves were drawn from maximum points on load-displacement curve in every cycle, which were enveloping diagram of hysteretic curves. It was comprehensive reflection of relationship between stress and deformation, and seismic behavior of structure. The skeleton curves of specimens were illustrated in figure 8-13.

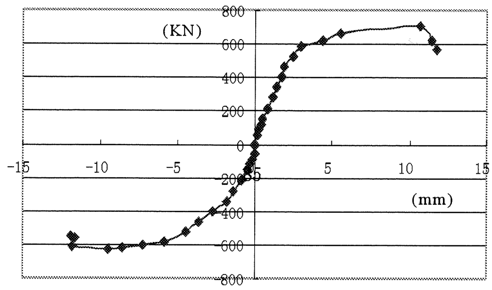

Figure 8 Skeleton curves of SW-10-30

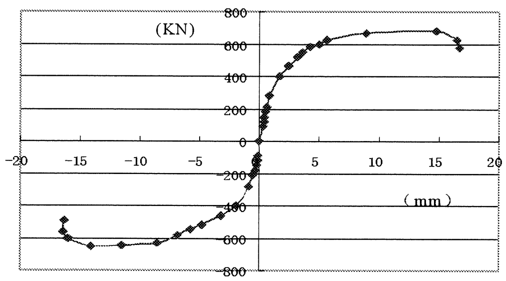

Figure 9 Skeleton curves of SW-00-40

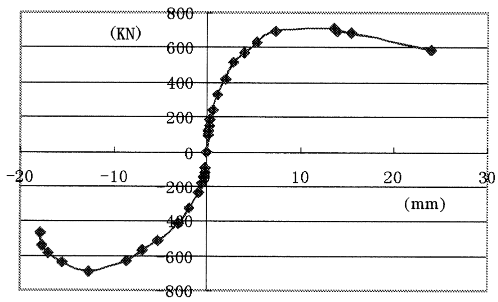

Figure 10 Skeleton curves of SW-05-40

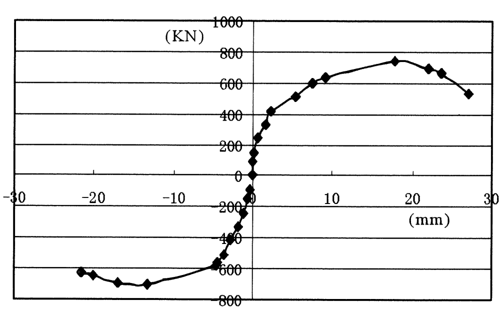

Figure 11 Skeleton curves of SW-10-40

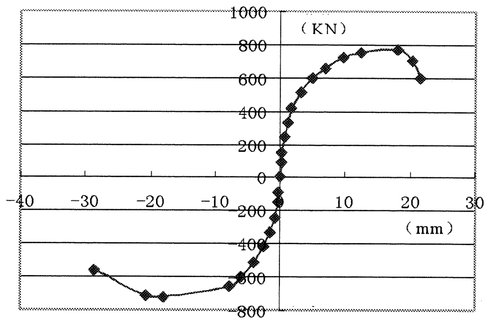

Figure 12 Skeleton curves of SW-15-40

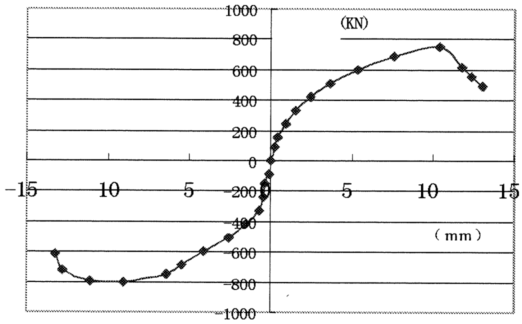

Figure 13 Skeleton curves of SW-20-40

6. DUCTILITY

Ductility is a important characteristic of seismic behavior of structure, and is measured with ductility factor. In this test, it was measured with displacement ductility factor. Displacement ductility factor included ultimate displacement (δu) and yielding displacement (δy):

6.1 Yielding displacement (δy)

During the test, according to monitor the yield of reinforcement, the yield of reinforcements was one by one.There were no obvious inflexion point on skeleton curves.So these components had no obvious yielding states. There were many methods to calculate yielding strength of these components .Among those *Graphical method*, *Park method* and *Equal Energy method* were important. In this test, graphical method as shown in the work by Shen et al.(1996) was used to calculate yielding strength, which was illustrated in figure 14. Point “D” was defined as yielding point.

6.2 Ultimate displacement (δu)

According to *Specification of Testing Methods for Earthquake Resistant Building* (JGJ101-96), during research bearing capacity and failure phenomena, the specimens were loaded to decreasing value, the decreasing value is taken as

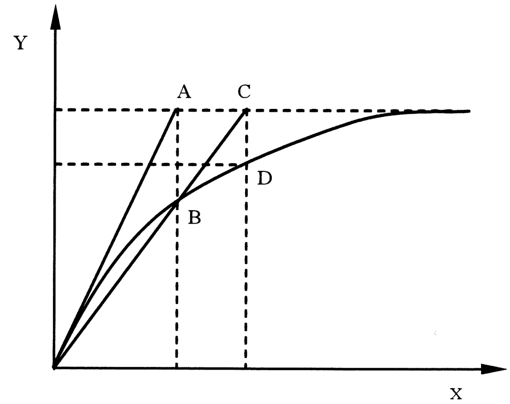

Figure 14 Graphical method

85 percent of ultimate loading for reinforced concrete specimens. So, ultimate displacement was taken as the displacement corresponding to 85 percent of ultimate loading at decreasing stage of skeleton curve.

6.3 Analysis of ductility

Based on skeleton curves of shear walls , ductility factors of shear walls are calculated ,and the research on ductility affected by the volume fraction of steel fiber and concrete strength is carried out.

6.3.1 Influence on ductility by volume fraction of steel fiber

According to calculating results, the relationship of ductility factor and volume fraction of steel fiber was illustrated in figure 15.

From figure 15, it was obviously that the ductility of shear wall was improved significantly with steel fiber, and ductility factors increased with increasing of volume fraction of steel fiber. Comparing to ordinary shear wall, ductility factors of steel fiber reinforced concrete shear walls were increased by 11.5%, 36.5%, 34.0% and 66.7%,respectively,corresponding to 0.5%, 1.0%,

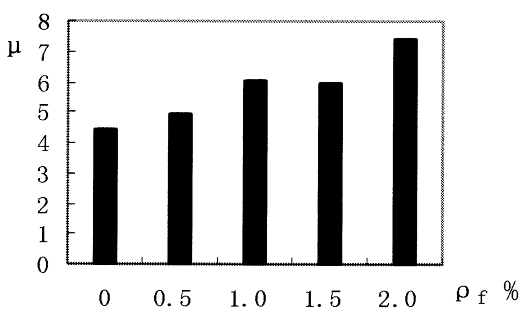

Figure 15 Comparison of ductility coefficient with volume fraction

1.5% and 2.0% for volume fraction of steel fiber. It could be explained that the steel fiber crossing cracks prevent crack developing significantly after crack, and improved the deformation capacity of shear wall. Preventing crack and improving deformation capacity by steel fiber were more obvious with load increase and crack developing, especially to deformation capacity in later stage.

6.3.2 Influence on ductility by concrete strength

According to calculating results, the relationship of ductility factor and concrete strength is illustrated in figure 16.

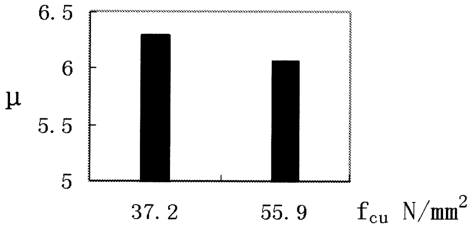

Figure 16 Comparison of ductility coefficient with concrete strength

According to figure 16, the ductility of shear wall affected by concrete strength in some extent. Comparing to shear wall with compressive strength of 55.9Mpa, the ductility of shear wall with compressive strength of 37.2Mpa was higher, it was seen that the ductility of steel fiber reinforced concrete shear wall decreased with the increase of concrete strength.

7. ANALYSIS OF ENERGY DISSIPATION

According to *Specification of Testing Methods for Earthquake Resistant Building* (JGJ101-96), energy dissipation coefficient of shear wall was measured with the area bounded by hysteretic curve, which was illustrated in figure 17.Energy

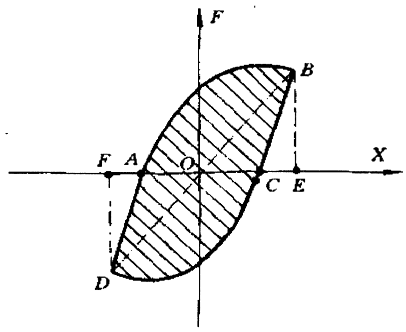

Figure 17 Calculation of energy dissipation

dissipation coefficient can be calculated with formula (1).

$$E = \frac{S(\Delta ABC + \Delta CDA)}{S(\Delta OBE + \Delta ODF)} \tag{1}$$

According to hysteretic curves of all walls, energy dissipation coefficient was calculated and illustrated in figure 18 and 19. Energy dissipation of shear wall affected by the volume fraction of steel fiber and concrete strength were studied respectively .

7.1 Influence on energy dissipation by the volume fraction of steel fiber

From figure 18, it was seen that energy dissipation coefficient of steel fiber reinforced concrete shear wall was higher than ordinary shear wall, and increased with the increase of volume fraction of steel fiber, the maximum increment of coefficient was 19%. So, energy dissipations of steel fiber reinforced concrete shear wall were significantly improved. The reason was the failure phenomena of steel fiber reinforced concrete

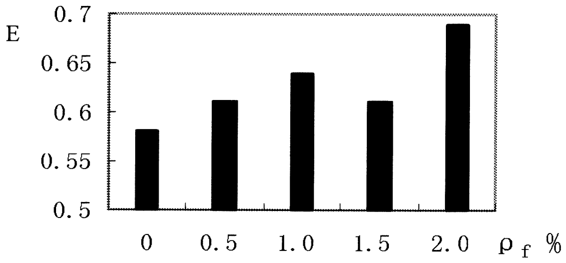

Figure 18 Comparison of energy dissipation coefficient

always lied in the pull out of steel fibers in many test. Because there were good bond force between concrete and steel fiber, and elastic modulus of steel fiber was higher, so energy dissipation of steel fiber reinforced concrete shear walls were closely related to energy dissipation of steel fiber when pulled out. In this test, crackes of shear walls developed more fully, deformationes of walls developed completely, energy dissipations of steel fibers were higher, so energy dissipation of steel fiber reinforced concrete shear walls was higher significantly too.

7.2 Influence on energy dissipation by concrete strength

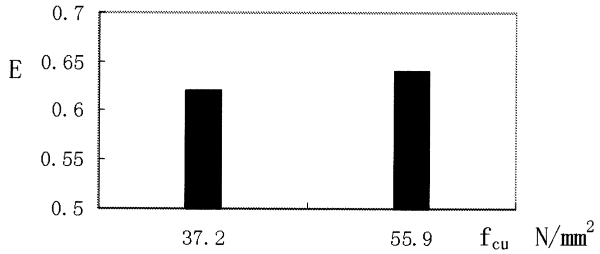

Figure 19 Comparison of energy dissipation coefficient

From figure 19, it was seen that energy dissipation coefficients of steel fiber reinforced concrete shear walls slightly increased with compressive strength, the energy dissipation coefficients of shear walls increased from 0.62 to 0.64 with compressive strength from 37.2Mpa to 55.9Mpa

8. CONCLUSION

From the analysis in this thesis, the conclusion were as follows.

(1) Comparing to ordinary reinforced concrete shear wall, the hysteretic curve of steel fiber reinforced concrete shear wall changed to be plumpy gradually, the decreasing stage of hysteretic curve dropped gently.It expressed good ductility and energy dissipation of shear walls. Ultimate bearing capacity increased obviously with the increase of concrete strength, but the ductility and energy dissipation had no obvious change.

(2)Ductility and energy dissipation of reinforced concrete shear walls were improved significantly with steel fibers, and ductility factor and energy dissipation increased with the increase of volume fraction of steel fibers. Steel fibers could prevent cracking and improv deformation capacity obviously with the increase of load , especially for deformation capacity in later stage.

(3)When the volume fraction of steel fiber kept constant, ductility decreased with the increase of concrete strength, but energy dissipation increased slightly .

Acknowledgements:
The authors acknowledge support from China national natural science foundation(50408008) and henan outstanding youth science foundation in China(0612002300).

REFERENCE:

China national standard. (2002). *Code For Design Of Concrete Structures* (GB50010-2002). China Construction Press, China.

Chuanzhi Wang,Zhiming Teng. *Theory Of Reinforced Concrete Structures*. China Construction Press, Beijing. 1985

China professional standard. (2002). *Technical specification for concrete structures of tall building* (JGJ3-2002). China Construction Press, China.

Zaikang Shen . *Application Asionalnd Comment Of New Standard Of Testing Methods Of Concrete Structures*. China Construction Press, Beijing. 1996.26-262

China professional standard. (1997). *Specification of Testing Methods for Earthquake Resistant Building* (JGJ101-96) China Construction Press, China.

Fifth International Conference on Urban Earthquake Engineering
March 4-5, 2008, Tokyo Institute of Technology, Tokyo, Japan

DYNAMIC COLLAPSE TESTS OF MINIATURE REINFORCED CONCRETE FRAMES UNDER HIGH-GRAVITY FIELD USING LARGE CENTRIFUGE

Rei Okada[1], Hiroyasu Sakata[2], Akira Wada[3], Hiroyuki Kubota[4], Hideo Katsumata[5], Hirofumi Okuda[5], and Shuichi Higuchi[5]

1) COE Researcher, CUEE, Tokyo Institute of Technology, Japan
2) Associate Professor, Structural Engineering Research Center, Tokyo Institute of Technology, Japan
3) Professor, Structural Engineering Research Center, Tokyo Institute of Technology, Japan
4) Graduate Student, Tokyo Institute of Technology, Japan
5) Researcher, Technical Research Institute, Obayashi Corporation, Japan
rokada@serc.titech.ac.jp, hsakata@serc.titech.ac.jp, wada@serc.titech.ac.jp, kubota.h.ab@m.titech.ac.jp, katsumata.hideo@obayashi.co.jp, okuda.hirofumi@obayashi.co.jp, higuchi.shunichi@obayashi.co.jp,

Abstract: In this paper, the results of the vibration tests concerning the scale model of Reinforced Concrete (RC) columns under high gravity field are shown. Due to many difficulties of shaking tests for full scale structure, there have been few experiments about the collapse behavior of structure under seismic excitation. On the other hand, in the scale model test, it is difficult to reproduce the stress field on the scale model. In this test, the appropriate stress field on the scale model is generated by the high gravity field using the centrifugal force. This experimental system is used, for the first time, to analyze the seismic behaviors of superstructures, although it has been used to verify the phenomena about soil and underground structures. The structural model is set on the shaking table located in the large centrifuge. In this test, the behaviors of two-storied structural model are simulated successfully. The outlines of the large centrifuge and the specimen are presented. And the experimental results are shown.

1. INTRODUCTION

It is important to clarify the collapse mechanism of structures in safety under the strong seismic motion. The most accurate experimental method to verify the collapse of structure would be the shaking table test using full-scale structural models. However, due to several problems (i.e. performance limitation of shaking table, costs and safety of experiments), it is not easy to shake the structure to the level of complete collapse. Meanwhile, there are many shaking table tests using the scale model. In 1[G] field, the vertical stress field on the model is underestimated by scale effect. In fact, in case of $1/N$ scale model (N: scale ratio), scale of area and that of weight become $1/N^2$ and $1/N^3$, respectively. So the scale of stress becomes $1/N$. In many dynamic tests using miniature specimen, the masses are added to the specimen to adjust the stress distribution such as the compressive stress of the column.

In this study, as another approach for verifying the collapse mechanism of the superstructure, the shaking table tests in the high gravity force field are carried out. The gravity force field is actualized by the large centrifuge. In the civil engineering field, this experimental system has not been used for verifying the seismic behaviors of superstructures, although it has been used for the phenomena about ground (i.e. the liquefaction of ground and the lateral flow of ground) and underground structures (i.e. the pile group). The aim of this study is to establish the experimental method for miniature structural models using the large centrifuge. In the dynamic test using 1/N scale model in N [G] (1G=9.8m/s^2) gravity force field, the stress field in the real scale are replicated. Tablel shows the similarity law in N [G] force field.

For the last several years, the experiments for steel structures (1. The weak column strong beam type mechanism: 3-storied structure, 2. The weak beam strong column type mechanism: 12-storied and 30-storied structures) were carried out.

In this paper, the results of the pilot experiment of two-storied Reinforced Concrete structural model are shown. The assumed collapse mode of this model is the story collapse at the 1st floor column.

Table 1 Similarity Law for Scale Model

Quantity	Reduction Scale in N [G]
Length	1/N
Cross Section	1/N^2
Weight	1/N^3
Stress	1
Strain	1
Velocity	1
Acceleration	N
Time	1/N
Frequency	N

2. EXPERIMENTAL OVERVIEW

2.1 Outline of Centrifuge Model Experiment

The dynamic tests under high-gravity field (Centrifuge model experiment) are carried out using the large centrifuge machine owned by OBAYASHI CORPORATION. The concept drawing of the Centrifuge model experiment is shown in Fig.1. The apparatus for the centrifuge model experiment consists of the revolving arm, the data measuring device, counter weight, and the shaking table as shown in this Figure.

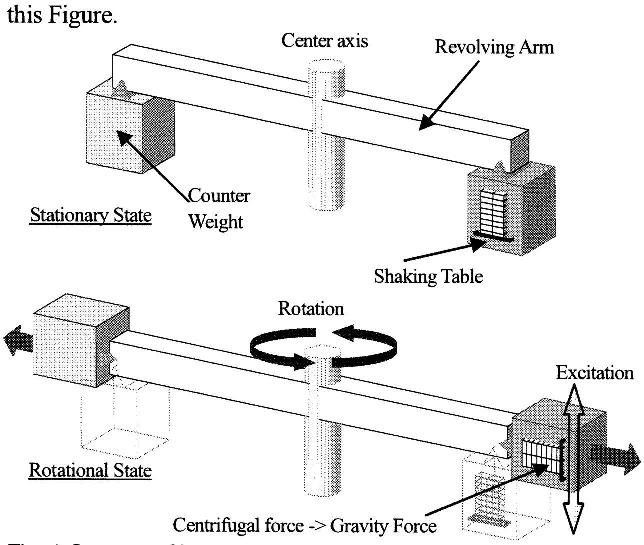

Fig. 1 Concept of Large Centrifuge Machine with Shaking Table

The experimental model is set in the stationary state. In the rotational state, the centrifugal force is acting on the structural model as gravity field. The gravity field is adjusted by the rotational speed. So the dynamic test in the high gravity force field is realized using this experimental apparatus.

2.2 Test Specimen

The test Specimen is 2-storied RC Frame. The collapse mode is the story mechanism. Therefore beams are rigid and the deformations of the beams are negligible. The plan and the elevations of the RC frame and the section of the column are shown in Fig. 2. The cross sections of beams of 2F and RF are 100mm*100mm. The sections of footing beams are 150mm (width) *100mm (depth).

The specimen consists of two planes of structure. Both are connected by the steel plates as shown in Fig. 2(a) and (b). These steel plates also work as the additional weight to adjust the axial force ratio of columns at the 1st floor. The reduced scale is 1/20.

2.3 Cross Section of the Column

The cross section of the column is 35mm (Vibration direction: X axis) * 40mm (Orthogonal direction: Y axis) to avoid the deformation of the orthogonal direction as shown in Fig. 3. The height of the column is 140mm. So the shear span to depth ratio is 2.0. The bar arrangement drawing is shown in Fig. 3.

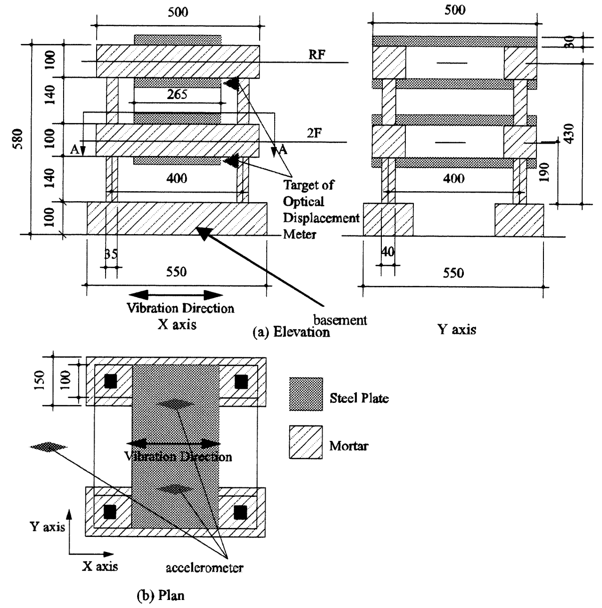

Fig. 2 Configurations of Specimen (Dimensions in mm)

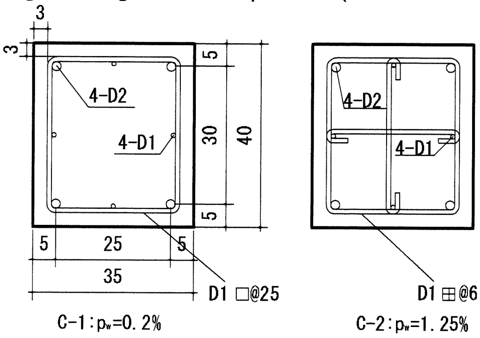

Fig. 3 Bar Arrangement Drawing of Column (Dimensions in mm)

The reinforcement ratio of the column (4-D1, 4-D2) is 1.44% and the tension reinforcement ratio of the column (p_t) (1-D1, 2-D2) is 0.65%. D1 deformed bars are used as the shear reinforcement. The thickness of cover concrete is 3mm. The bar-arrangement status of column is shown in Fig. 4 and the kinematical properties of reinforcement bars and mortar are shown in Table 2.

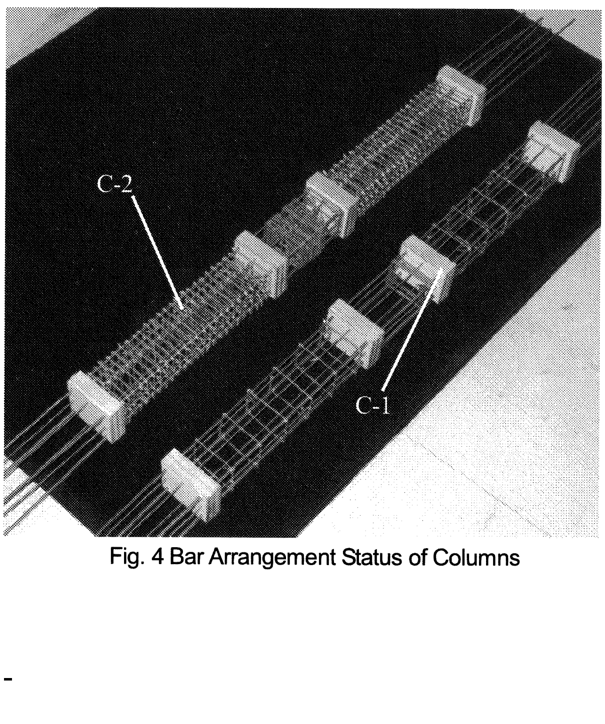

Fig. 4 Bar Arrangement Status of Columns

Table 2 Kinematical Properties

	Sectional Area[mm^2]	Yield Strength [MPa]	Tensile Strength [MPa]	Compressive Strength [MPa]
D1	1.003	325.1	399.8	–
D2	4.047	465.4	495.7	–
Mortar	–	–	–	37.0

The elastic 1st natural frequency based on the eigenvalue analysis is 55.2Hz. The decreasing ratio of the stiffness (α_y) is 0.26 which is calculated based on the Eq. (1). So the 1st natural frequency adjusted by the stiffness degradation is 28.1Hz.

$$\alpha_y = \left(0.043 + 1.64 n\, p_t + 0.043\frac{a}{D} + 0.33\eta_0\right)\left(\frac{d}{D}\right)^2 \qquad (1)$$

Where, n : ratio of Young's modulus, a :shear-span length, D : depth of column, d : effective depth of column, η_0 :axial force ratio.

2.4 Test Parameter

The parameter of this experiment is the shear reinforcement ratio (p_w). The value is 0.20% (Specimen: C-1) and 1.25% (Specimen: C-2). The shear force at the flexural yield (Q_{my}) and the ultimate strength in shear ($Q_{u\min}$) of C-1 and C-2 are shown in Table 3. These values are calculated based on Eqs. (3) and (4) using the data of the material testing carried out before the dynamic test.

Table 3 Comparing Strength of Specimens

M_y[kN*mm] Eq.(2)	Q_{my}[kN] Eq.(3)	Q_{umin}[kN] Eq.(4)	
		C-1	C-2
241.50	**3.22**	**2.46**	**3.52**

$$M_y = 0.8 a_t \sigma_y D_c + 0.5 N D_c\left(1 - \frac{N}{B_c D_c F_c}\right) \qquad (2)$$

$$[N \le 0.4 bDF_c]$$

$$Q_{my} = 2M_y / h \qquad (3)$$

$$Q_{u\min} = {}_c\tau_{su\min} bj = \left({}_b\tau_{su\min} + 0.1\sigma_0\right)B_c j_c$$
$$= \left\{k_u \cdot k_p(180+\sigma_B)\frac{0.115}{\frac{M}{Qd_c}+0.12} + 2.7\sqrt{p_w \cdot {}_w\sigma_y} + 0.1\frac{N}{B_c \cdot D_c}\right\}B_c j_c \qquad (4)$$

Where, M_y: bending yield moment, a_t: section area of tension reinforcement, σ_y: yielding stress, D_c: effective depth, N: axial force, B_c: effective breadth, F_c: compressive strength of mortar, h: height of column, ${}_c\tau_{su\ min}$: ultimate stress in shear, σ_0: axial stress, j_c: distance between tension and compression resultants, k_u: correction coefficients of shape, k_p: correction coefficients of tension reinforcement ratio, σ_b: compressive stress of mortar, M/Qd_c: shear span to depth ratio, p_w: hoop reinforcement ratio, ${}_w\sigma_y$: yielding stress of shear reinforcement.

In case of C-1, Q_{umin} is less than Q_{my}. So C-1 is the predominant shear yield type. In case of C-2, Q_{umin} is more than Q_{my}. So C-2 is the predominant flexural yield type. Those two types of specimen are simulated in this experiment. The ultimate base shear coefficients of C-1 and C-2 are 0.31 and 0.37.

2.5 Axial Force Ratio of 1st Storied Column

The design-time axial force ratio at the 1st columns is 0.20 (= 6.2MPa). The assumed compressive strength is 30.0MPa. This value is equivalent to 60% of the allowable stress for sustained loading. However, the compressive strength of the mortar is 37.0MPa. So the axial force ratio is 0.17 when the experiments using large centrifuge are carried out.

2.6 Measuring Equipment

As shown in Fig. 2, the accelerations (◀▶) using acceleration meters at the ground, the 2nd, and the roof floor are measured. The absolute displacements (▲) are measured using optical displacement meters at the 2nd floor and the R floor. The dynamic behaviors of structural model are taped by the CCD camera (3ch) and High-Speed Camera (1ch).

3. DYNAMIC TEST UNDER HIGH-GRAVITY FIELD

3.1 Outline of Dynamic Tests using Centrifuge Machine

Fig. 5 shows the picture of the experimental setup in the large centrifuge machine. In this present experiment, C-1 and C-2 are set in the centrifuge machine simultaneously to simulate the experimental models by the same input wave.

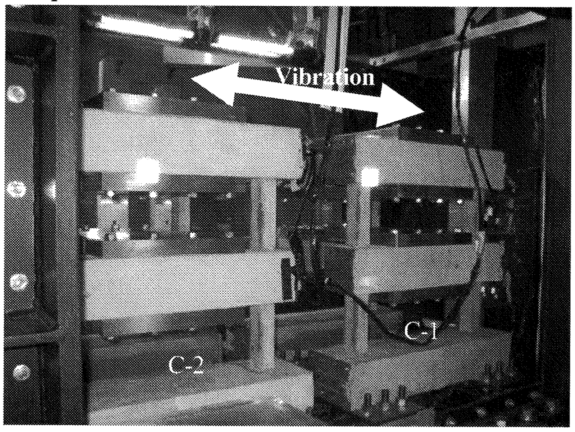

Fig. 5 Experimental Setup

3.2 Outline of Experimental Progression

The experiments are carried out in 20[G] gravity force field because the reduced scale of the length is 20. Ojiya wave EW component by K-net is used as the original input wave. The time history and the frequency characteristics of acceleration are shown in Fig.6. Outline of Experimental Progression is shown in Table 4.

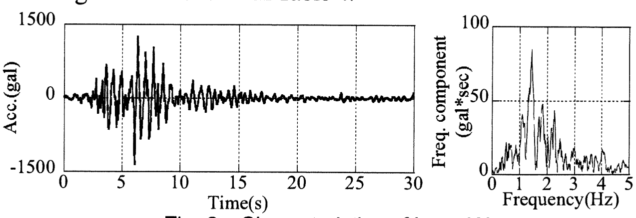

Fig. 6 Characteristics of Input Wave

Table 4 Outline of Experimental Progression

C-1	START	Seismic Wave Input (a_{max}=789~23000gal) low level white noise input and seismic wave act on the structural model alternately	Collapse	–		END
C-2				Sinusoidal Wave Input (a_{max}=1280～18190gal) low level white noise input and sinusoidal wave act on the structural model alternately	Collapse	

Where, a_{max} is the maximum acceleration of input wave.

As shown in Table 4, C-1 and C-2 are set in the shaking table. At first, the seismic wave input acts on the structural models. a_{max} is changed from 789gal to 23000gal. The incremental acceleration is around 700gal. The low level white noise inputs and excitations (seismic and sinusoidal wave) act on the structural model alternately to calculate the transfer function of the C-1 and C-2 using input acceleration and response acceleration at 2F level by Eq. (5).

$$H_{u,\ddot{u}_g}(j\omega) = \int_{-\infty}^{\infty} \ddot{u}(t) e^{-j2\pi\omega t} df \;/\; \int_{-\infty}^{\infty} \ddot{u}_g(t) e^{-j2\pi\omega t} df \qquad (5)$$

Where, $\ddot{u}$:Response acceleration $\ddot{u}_g$: Input acceleration, ω : circular frequency, $j = \sqrt{-1}$.

When a_{max} is 23000gal, the shear failures occur at the 1st floor columns of C-1.

After the shear failure occurs, the centrifuge stops and C-1 is removed then the centrifuge starts again. And the sinusoidal waves act on the C-2. The frequency of the sinusoidal wave is 20Hz which is assumed the latest natural frequency of C-2 based on the relations between displacement and input force at the 2nd floor. Then, a_{max} approaches the limit performance of shaking table, so the dominant frequency of sinusoidal wave changes to 25Hz. Finally, when a_{max} is 18190gal, the story collapse occurs at the columns of C-2 and the experiment is finished.

3.3 Transition of Dynamic Properties of C-1 and C-2

The initial transfer functions of C-1 and C-2 are shown in Fig. 7. These transfer functions are calculated by the input and output accelerations by the first white noise input using Eq(5).

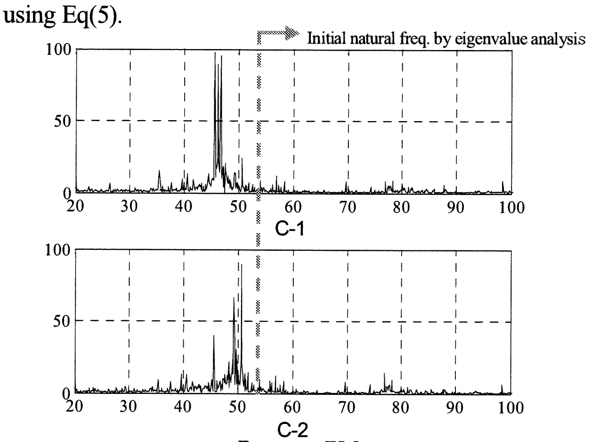

Fig. 7 Initial Transfer Functions

The dominant frequency of the initial transfer functions has almost the same values as initial natural frequency by eigenvalue analysis. In Fig. 8, the transitions of natural frequencies of C-1 and C-2 calculated by low level all white noise shakings are shown.

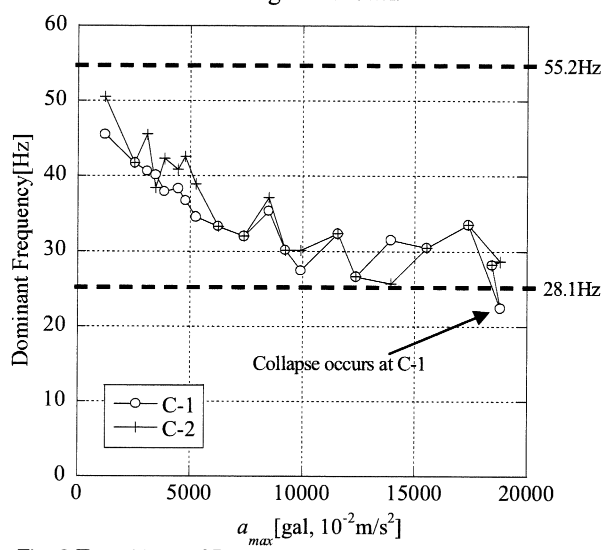

Fig. 8 Transitions of Dominant Frequency against a_{max}

In this figure, initial natural frequency by eigenvalue analysis (55.2 Hz) and the natural frequency considering the stiffness degradation by Eq. (1) (28.1Hz) are exhibited. The dominant frequency shifts during these frequencies.

Fig. 9 shows the relationship between the story deformation angle and the input force.

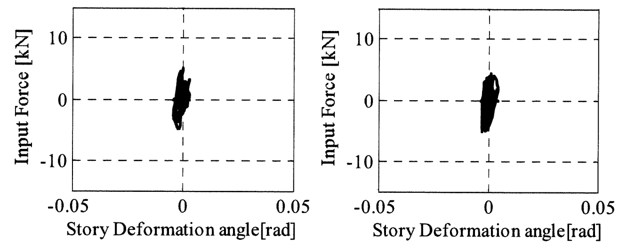

(a)around original Input Level of Ojiya Wave (1211gal)

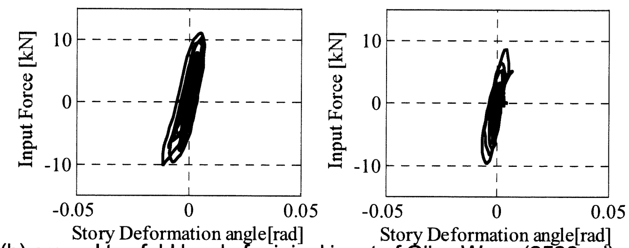

(b) around twofold level of original input of Ojiya Wave (2526gal)

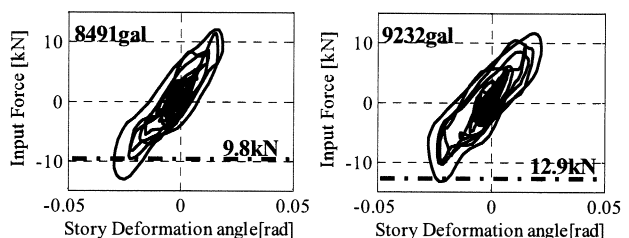

(c) Input force indicates the maximum value

C-1 C-2

Fig. 9 Relationships between Input Force and a_{max}

Fig. 9(a) and (b) show the relationships when the maximum input acceleration is around original wave (1211 gal) and around twofold level of original wave (2526gal). Fig. 9(c) shows the relationships when the input force indicates the maximum value (C-1: a_{max}=8491gal, C-2: a_{max}=9232gal). In Fig. 9(c), the strength of C-1(9.8kN) and C-2(12.9kN) based on Table 2 are also displayed. As shown in Fig. 8 and Fig. 9, the assumed properties of C-1 and C-2 about the dominant frequency and the strength are reproduced by the centrifuge model experiment.

3.4 Collapse Behaviors of Test Specimen

As written in section 3.2, C-1 is collapsed by the earthquake wave input, and C-2 is collapsed by the sinusoidal wave input. In this section, 'time histories of story deformation angles', 'relationships between input force and story deformation angle', and 'failure status when the collapses occur' are shown.

3.4.1 Collapse behavior of C-1

Time histories of story deformation angle of the 1st floor column of C-1 and C-2 are shown in Fig. 10.

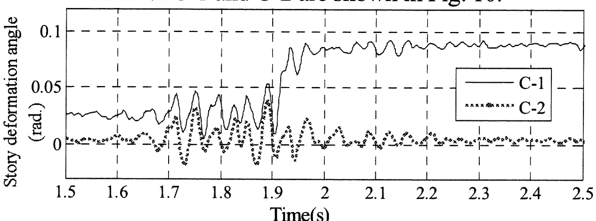

Fig.10 Time Histories of Story Deformation Angle

The story deformation angle of C-2 remains at around the origin after the shaking. Meanwhile the story deformation angle of C-1 has the residual story deformation angle because of the shear failure by the shaking. Before the shear failure occurs, there are no significant damages. The relations between the input force and the story deformation angle are shown in Fig. 11. This relation of C-2 shows the stable status with a central focus on the origin.

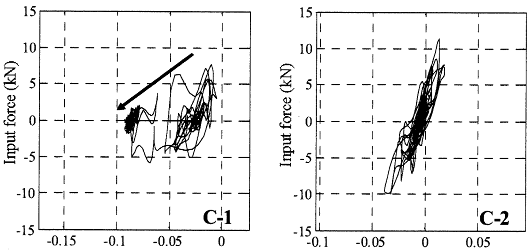

Fig. 11 Characteristics of Input Wave

The damages of C-1 concentrate on the columns at the 1st floor. After this shear failure occurs, there is no damage in the columns at the 2nd floor. Fig.12 shows the final collapse status of the whole structure of C-1 and Fig. 13 shows the final collapse status of 4 columns at the 1st floor.

As shown in Fig13, except the column <2>, the obvious shear failure occurs at the top or at the bottom of the column. Especially the crushing of mortar occurs in conjunction with the gravity force at bottom of column <3>. The 2nd floor of C-1 falls limply to one side as shown in Fig. 12.

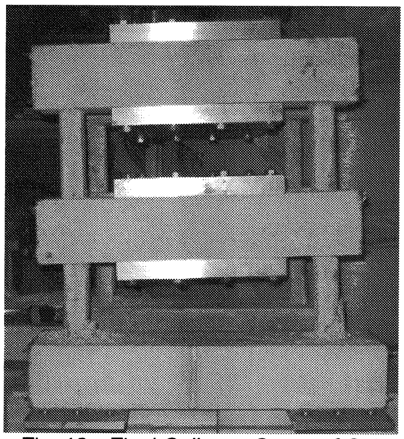

Fig. 12 Final Collapse Status of C-1

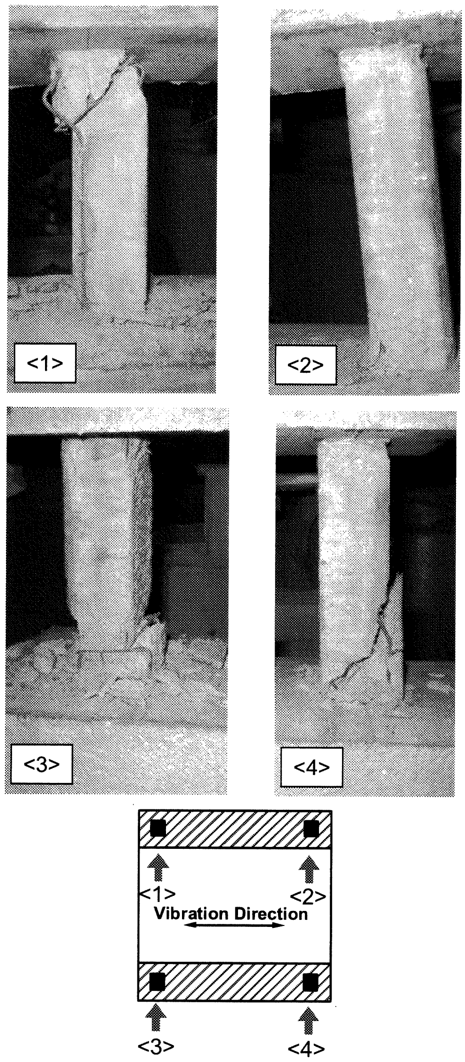

Fig. 13 Final Collapse Status of Columns of C-1 at 1st Floor

Meanwhile, the obvious damage does not appear except of C-2 at the top of the column at the 1st floor as shown in Fig. 14.

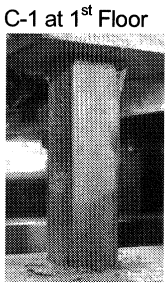

Fig. 14 Delamination Failure at Top of the 1st -Story Column of C-2

3.4.2 Collapse behavior of C-2

Fig. 15 shows the time histories of the story deformation angle of the 1st and the 2nd floor of C-2.

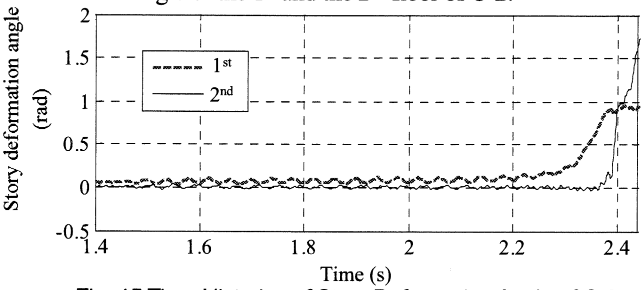

Fig. 15 Time Histories of Story Deformation Angle of C-2

The story deformation angle of the 1st floor increases at around 2.3 second. As the story deformation angle approaches around 1.0 rad at 2.4 second, the story deformation angle of the 2nd floor increases rapidly. This means that by the story collapse at the 1st story, the impact of the collision between the beams at the 2nd floor and the basement acts as the trigger of the story collapse at the 2nd floor.

This procedure can be observed in the movie captured by the CCD camera and the high-speed camera. Fig. 16 shows the time-lapse photography of the movie. The picture <1> is the C-2 before the shaking. The picture <2> is the C-2 when the story collapse at the 1st story begins. The picture <3> is the C-2 when the story collapse at the 2nd story occurs. The picture <4> is the C-2 after the shaking. Fig. 17 shows the final collapse status of the whole structure of C-2.

The ductility of C-2 is higher than that of C-1. As the story deformation angle increases, the story collapse occurs by the effect of the gravity force.

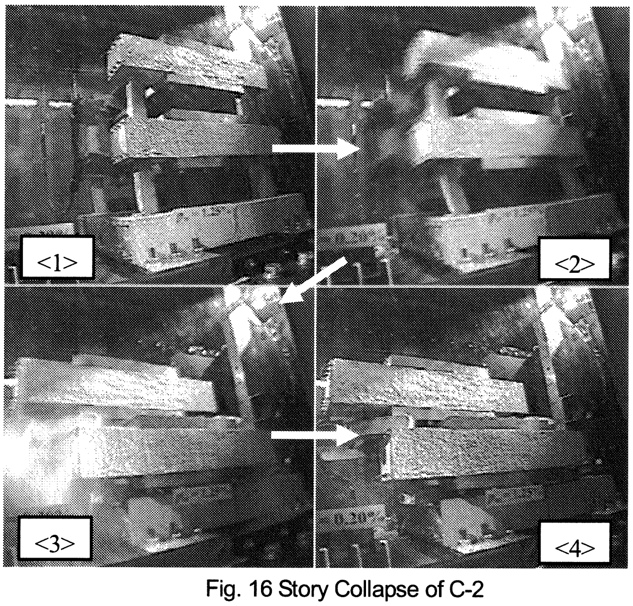

Fig. 16 Story Collapse of C-2

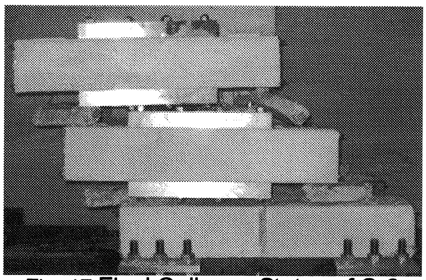

Fig. 17 Final Collapse Status of C-2

4 Conclusions

As one experimental approach to simulate the collapse behaviors using the miniature model of superstructure, the outline and the results of dynamic tests for the reinforced concrete frames under high-gravity force field generated by the large centrifuge machine are presented in this paper.

The test specimen is 2-storied RC Frame. The assumed collapse mode is the story mechanism. The parameter of the experiment is the shear reinforcement ratio. In C-1 and C-2, the specimen collapse in assumed mode.

Before the shear failure occurs, there are no significant damage. The damages of C-1 are concentrated in the columns at the 1st floor. After this shear failure occurs, there is no damage in the columns at the 2nd floor. The relation between the input force and the story deformation angle of C-2 shows the stable status with a central focus on the origin. The obvious damage does not appear when the shear failure occurs in C-1.

The story collapse occurs at the 1st story. The impact of the collision between the 2nd floor and the basement due to the story collapse at the 1st story acts as the trigger of the story collapse of the 2nd floor.

The ductility of C-2 is higher than the ductility of C-1, so the story deformation angle increases, and then the story collapse occurs by the effect of the gravity force.

Acknowledgment

On the procedure of the experiment, we were given the considerable contribution from Mr. Kenichi Ikeda and Isamu Akama, Obayashi Corporation.

Their contributions would be deeply appreciated.

References:

AIJ (1999), Standard for Structural Calculation of Reinforced Concrete Structures -Based on Allowable Stress Concept-

Rei Okada, Akira Wada, Satoshi Yamada, Masayoshi Takazawa, Matsutaro Seki, Hideo Katsumata, Shunichi Higuchi, and Hirofumi Okuda (2007), "Collapse Test of Steel Structural Model under High Gravity Force Field", Fourth International Conference on Urban Earthquake Engineering

Shunichi Higuchi, Hideo Katsumata, Matsutaro Seki, Masayoshi Takazawa, Akira Wada (2006), "Earthquake Collapse tests of Miniature Steel Frame Model using Large Centrifuge Machine", 8th U.S. National Conference on Earthquake Engineering.

Susumu Iai (1989),"Similitude for shaking table tests on soil-structure-fluid model in 1g gravitational field", Soils and Foundations Vol. 29, No. 1, 105-118

Xilin Lu1, Yun Zou1, Wensheng Lu1, and Bin Zhao1 (2007), Shaking table model test on Shanghai World Financial Center Tower, Journal of Earthquake Engineering Structural Dynamics; 36, 439-457

Fifth International Conference on Urban Earthquake Engineering
March 4-5, 2008, Tokyo Institute of Technology, Tokyo, Japan

EXPERIMENTAL AND NUMERICAL STUDIES ON THE DAMAGE OF CONCRETE COLUMN UNDER IMPULSIVE LOADING

Nobuaki Kawai[1], Satoshi Misawa[2], and Shizuo Hayashi[3]

1) Postdoctoral fellow, Center for Urban Earthquake Engineering, Tokyo Institute of Technology, Japan
2) Student, Dept. of Environmental Science and Technology, Tokyo Institute of Technology, Japan
3) Professor, Secure Materials Center, Tokyo Institute of Technology, Japan
kawai.n.ab@m.titech.ac.jp, misawa.s.aa@m.titech.ac.jp, hayashi.s.ac@m.titech.ac.jp

Abstract: This paper presents the results of numerical and experimental study on damage of concrete structure subjected to impulsive loading. In numerical study, the response of concrete structure to a vertical impulsive loading is simulated. The results show that concentration of tensile stress occurred at corner of beam-column joint caused by changing of accelerative direction. In experimental study, high velocity impact experiments are performed to investigate damage behavior of concrete column against impulsive loading. The results show that external stress field such as axial force has a great effect on suppression of crack development from damaged surface to inside column although damage of impact surface is predominated by local stress field induced by projectile impact.

1. INTRODUCTION

Recently, impact and explosion accidents associated with natural and man-made disasters generate serious damages. In case of such incidents, structures are secondarily damaged by fragment-impact of damaged structure in addition to primary damage by impulsive loading. In order to evaluate the safety of structures and facilities against impulsive loading and fragment impact, it is necessary to establish a method to predict structural failure under impulsive and impact loading. To predict structural failure, we usually employ two types of method. First one is scaled experiment, and another one is numerical simulation. In this paper, we present the results of numerical and scaled experimental study on damage of concrete structure subjected to impulsive loading.

2. NUMERICAL STUDY

Earthquake is one of the largest scale phenomena for dynamic loading. Failure of concrete structure by earthquake is mainly caused by horizontal loading. However, some researches (Beppu et al. 1997, Harada et al. 1999, Harada et al. 2000) suggest that failure of concrete structure is induced even by vertical earthquake shock. Although the damage mechanism for horizontal loading is fully investigated, the one for vertical loading is not fully understood. In this study, the response of concrete structure to vertical shock is investigated by numerical simulation.

2.1 Analutical Method

A multiple solver type finite difference hydrocode: AUTODYN (Birnbaum et al. 1987) is used for numerical simulation. In the code, we can make use of the Lagrangian, the Eulerian, the Arbitrary Lagrangian-Eulerian (ALE), the Smoothed Particle Hydrodynamics (SPH), the shell and the beam solvers. Moreover, interactions among these solvers can be taken into account.

Material model in AUTODYN consists of two parts: (1) the equation of state (EOS) describes the relationship among pressure (p), density (ρ) and internal energy (e), and (2) the material strength model simulates the constitutive relation including the failure model, as many hydrocodes do.

2.2 Numerical Modeling

In this study, we modeled three-layered beam-column joint as a part of concrete structure. Two-dimensional planar symmetric model was used in the numerical analysis. The dimension of calculation model is shown in Figure 1. The parts of concrete material were modeled by the Lagrangian frame of reference. The element size is 50 mm square. Reinforcement was neglected in this study. As a boundary condition, impulsive vertical velocity was applied at the bottom of structure. Figure 2 show impulsive vertical velocity profiles applied to the calculations. Velocity profile, amplitude of acceleration and maximum velocity are assumed as simple triangle shape, 1000 cm/s^2 and 50 cm/s, respectively. To examine the effect of velocity direction to structural response, velocity profile consists of upward and downward motion.

2.3 Material Modeling

In order to represent the material nonlinearity of the

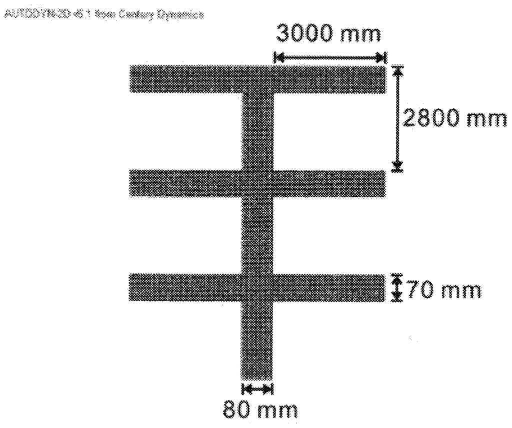

Figure 1 The Dimension of Calculation Model

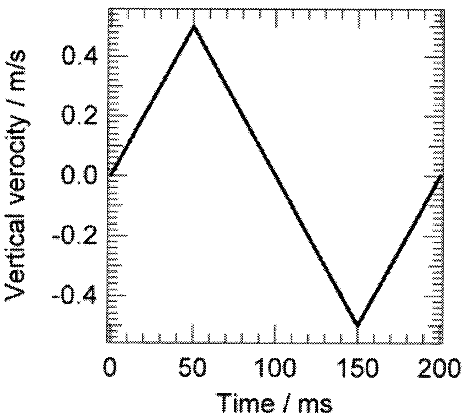

Figure 2 Vertical Velocity Profile Applied to Caluculation

concrete, we adopted the RHT model (Riedel et al. 1999) which has the following specific features like pressure hardening, strain hardening, strain hardening, strain rate hardening and damage with tensile crack softening. The material properties calibrated with the compression strength of 35 MPa were taken from the material library of AUTODYN.

Width of beam is usually smaller than that of column at beam-column joint. However, the width of beam and column in this calculation model are same because two-dimensional planar symmetric model was used. To reflect differences of width between beam and column in numerical analysis, strength and density of concrete beam were decreased by width ratio which is assumed as 0.75 in this study.

2.4 Numerical Results

Figure 3 shows the simulated results of damage evolution of concrete. In this figure, "Bulk Fail" means that the numerical element reaches failure criterion and is considered to be failed area that loses strength. At 60 ms, failed areas were observed at lower corner of beam-column joint part. The failed area of beam-column joint on the third

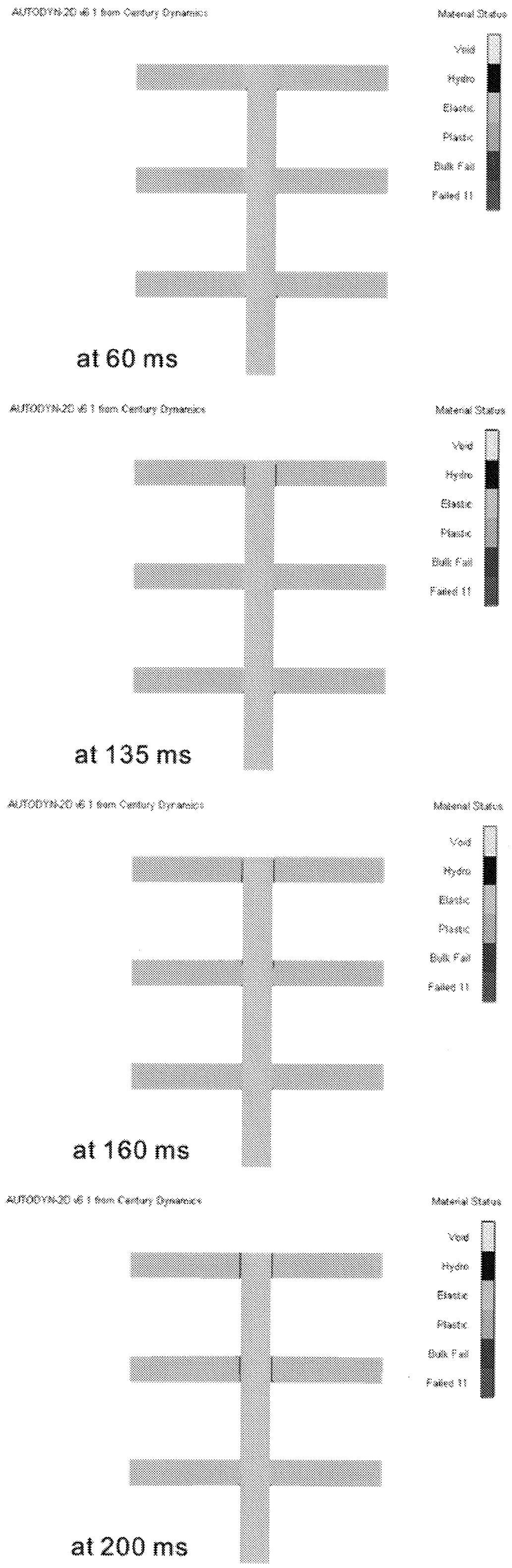

Figure 3 Dmage Evolution of Concrete Structure Subjected to Vertical Impulsive Loading

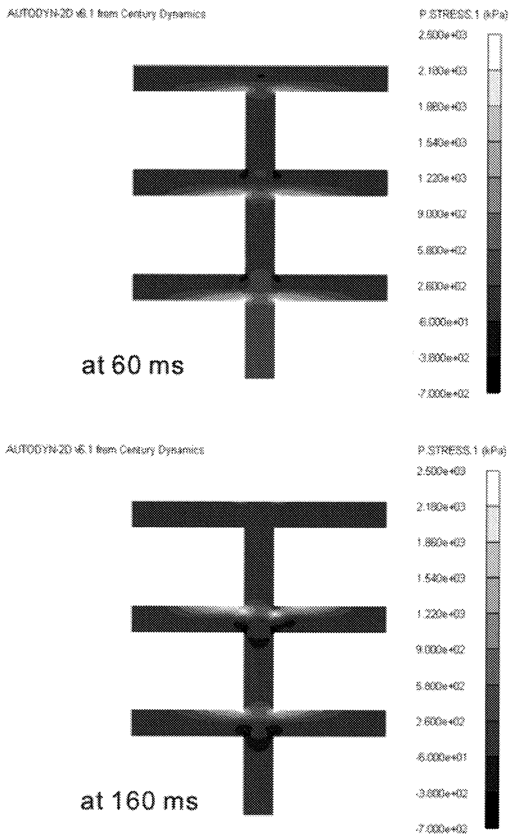

Figure 4 Principal Stress Distribution of Concrete Structure Subjected to Vertical Impulsive Loading

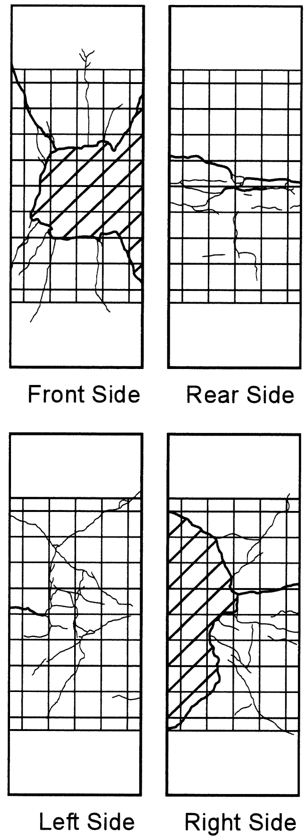

Figure 5 Typical Image of Impact-induced Damage on Concrete Column: Axial Force 0, Impact Velocity 700 m/s, Projectile Weight 8 g

layer was extended upward at 135 ms. At 160 ms, new failed areas were initiated at upper corner of beam-column joint part. These failed areas were extended downward.

To investigate the mechanism of damage initiation and propagation, we calculated the stress distribution just time the damage was observed. Figure 4 shows the principal stress distribution at 60 and 160 ms. At 60 ms, tensile stress concentrated on lower corner of beam-column joint. In contrast, concentration of tensile stress was observed at upper corner of beam-column joint at 160 ms. In both cases, direction of vertical acceleration applied to column just changed to opposite direction after reaching maximum or minimum vertical velocity. This column motion generates large gradient of vertical velocity in beam parts. The velocity gradient induces bending moment in beam. This could cause the severe tensile stress at the corner of beam-corner joint that resulted in fail of concrete. Direction of damage initiation and propagation are considered to depend on changing of accelerative direction.

2.5 Conclusion of Numerical study

Response of concrete structure to vertical shock is investigated by numerical simulation. The damage initiation and propagation were clearly observed at corners of beam-column joint. Numerical results also showed that concentration of tensile stress occurred at corner of beam-column joint caused by changing of accelerative direction. The damages were initiated and by propagated by that stress field. We can conclude that the dynamic behavior of concrete structure on a vertical impulsive loading was simulated quantitatively by the hydrocode AUTODYN and the mechanism to introduce the vertical damage at concrete beam-column joint was theoretically studied. Although this study is primitive one and a lot of improvements of simulation, such as three-dimensional calculation and modeling of reinforcement, are needed, this method has great possibility to become a useful tool to design the safety structure even in severe earth quake.

3. EXPERIMENTAL STUDY

Recent impact and explosive accidents as typified by train impact accident of JR-West Fukuchiyama Line and explosive accident of hot-spring facility at Shibuya in Tokyo, show the importance of a reliable method for protective design against impulsive loading and fragment impact. Against such background, some experiments (Ohkubo et al. 2007, Beppu et al. 2007) have been performed to investigate the damage mechanism of concrete structure subjected to impact and explosive loading. Such experiments have been

Table 1 Conditions for Impact Experiment of Concrete Column

Axial Froth Ratio	0	0.1	0.3	0
Projectile Weight (g)	8.5			17
Projectile Velocity (m/s)	300, 500, 700, 1000			300, 500

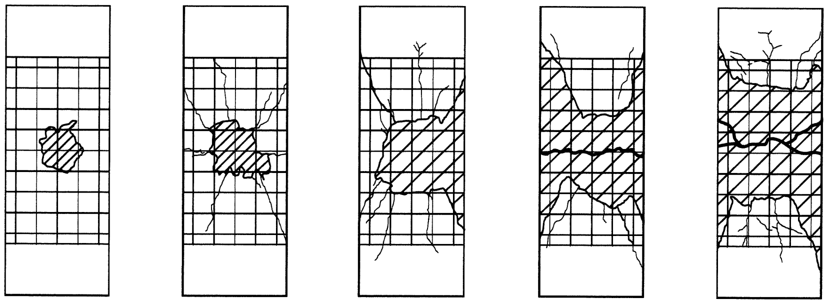

Projectile weight:	8.5 g	17 g	8.5 g	17 g	8.5 g
Projectile Velocity:	513 m/s	305 m/s	764 m/s	474 m/s	1048 m/s
Momentum:	4.36 N•s	5.19 N•s	6.49 N•s	8.06 N•s	8.91 N•s
Kinetic Energy:	1120 J	790 J	2480 J	1910 J	4670 J

Figure 6 Comparison of Impact-induced Damage on Several Experimental Conditions

mainly performed on concrete slab and not performed on column. In this study, high velocity impact experiments were performed to investigate damage behavior of concrete column against impact loading.

3.1 Experimental Setup

The overall dimension of concrete column was 100 mm square and 180 mm height, which was 1/10 scaled model of concrete column for piloti floor. The static compression strength of concrete was 55 MPa. Aggregate size was less than 5 mm.

Impact experiments were performed with a powder gun, which can accelerate a projectile up to 1500 m/s by using expansion of combustion gas. The projectile consists of impact plate made of SUS 304 alloy and plastic sabot made of high-density polyethylene. The diameter of projectile was 20 mm. The weight of projectile was varied by thickness of impact metal plate. The thicknesses of metal plate used in this study were 1 mm and 4.5mm, corresponding projectile weights were 8.5 g and 17 g respectively.

Experimental conditions were listed in Table 1. At first, impact experiments were performed to examine the effect of momentum and kinetic energy of projectile on damage of concrete column by using light and heavy projectiles. After that, the effect of axial force on damage by projectile impact was examined.

Penetration depth, damaged aria on impact surface and crack width were measured to evaluate the damage property of concrete column in each experiment.

3.2 Experimental Results

Figure 5 shows typical image of impact-induced damage on concrete column. The experimental condition is as follows. Projectile weight is 8.5 g. Projectile velocity is 700 m/s. Axial force ratio is 0. A lot of cracks extended to radial direction from center of impact surface. Crater was formed at center part of impact surface by projectile impact. Horizontal cracks were formed at center of rear surface. These features were observed on every column.

Figure 6 shows comparison of impact-induced damage on several experimental conditions. Columns are sorted by damage area from left to right. This result clearly shows that there is clear correlation between degree of damage and momentum of projectile, and kinetic energy of projectile does not correlate with degree of damage.

Figure 7 show impact velocity dependences of penetration depth, damaged area on impact surface and maximum horizontal crack width on rear surface, respectively. In the case of penetration depth and damaged are on impact surface, the effect of axial force was not observed. These results indicate that damage of impact surface is affected by external stress field such as axial force, but affected by localized stress field induced by projectile impact. In contrast, maximum horizontal crack width on rear surface was dramatically suppressed by axial force. In the case of none axial force, complete splitting fracture of concrete column occurred with expanding of the horizontal crack under 1000 m/s impact. In the case of axial force ratio 0.1 and 0.3, splitting fracture did not occur under 1000 m/s impact. In addition, column was completely sustaining axal force even after impact. This result indicates that axial force has a great effect on suppression of crack development from damaged surface to inside column.

3.3 Conclusion of Experimental Study

In this chapter, we presented the results of high velocity impact experiments which were performed to investigate damage behavior of concrete column against impact loading. The summary of the results observed in this study is as follows. Degree of damage induced by high velocity impact on concrete column has clear correlation with momentum of projectile. External stress field such as axial force has a great effect on suppression of crack development from damaged surface to inside although damage of impact surface is predominated by local stress field induced by projectile impact. These results are very important for fundamental understanding of damage behavior for concrete structure subjected to impact loading. For further understanding, we plan to investigate the effect of reinforcement, distribution of aggregate size and compression strength of concrete on damage induced by impulsive loading.

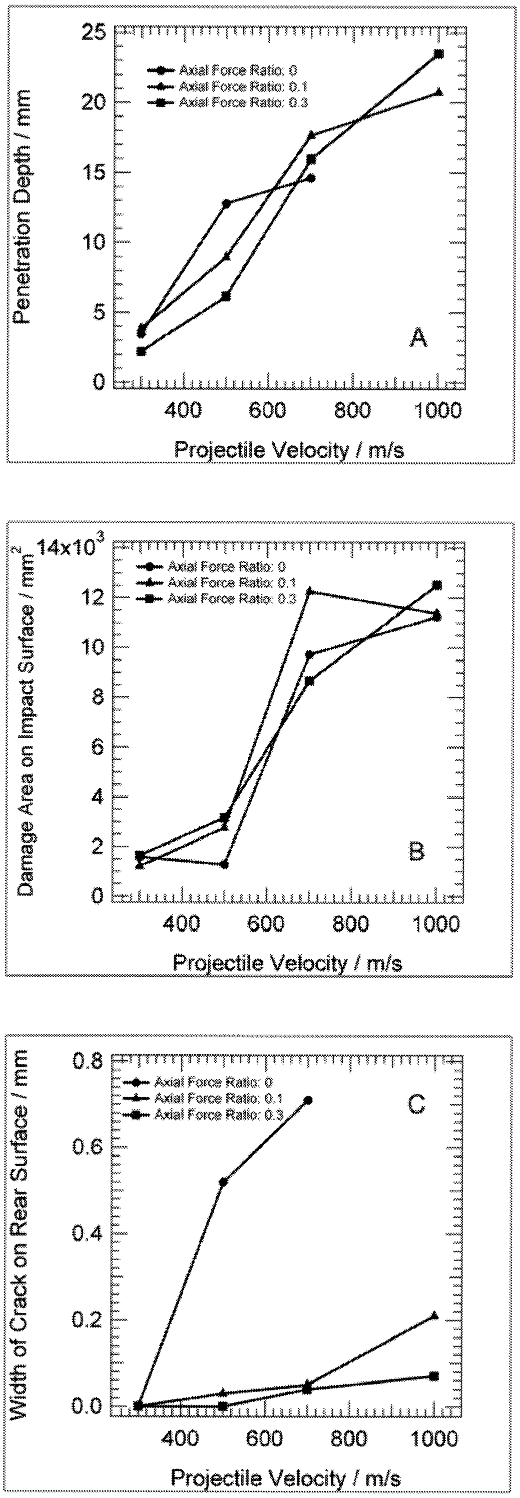

Figure 7 Impact Velocity Dependences of Damage Properties A: Penetration Depth B: Damaged Area on Impact Surface C: Maximum Horizontal Crack Width on Rear Surface

Acknowledgements:

The authors thank H. Ishii, K. Kawashima, Y. Kyahata and H. Hasegawa of Materials and Structures laboratory, Tokyo Institute of Technology for their assistance in constructing the experimental set up. The authors acknowledge support from Neturen Co. Ltd., Taiheiyo Cement Co. Ltd. and BASF Pozzolith Ltd for performance of this study. This work was supported by Center for Urban Earthquake Engineering and Grant-in-Aid for Young Scientists (B) No. 19760487.

References:

Beppu, M., Katsuki, S., Ishikawa, N. and Miyamoto A. (1997), "An Experimental Study on Circumferential Crack of RC Pier Model by Push-up Impact Text" *Journal of Structural Mechanics and Earthquake Engineering*, Japan Society of Civil Engineering, **577**(I-41), 165-180 (in Japanese).

Harada, K., Ishikawa, N., Katsuki, S. and Ohta, T. (1999), "Experimental Study on The Horizontal Crack of The Large Scale RC Column Model under Vertical Shock" *Journal of Japan Concrete Institute*, **21**(3), 1237-1242 (in Japanese).

Harada, K., Ishikawa, N., Katsuki, S., Ohta, T. and Hino, S. (2000), "An Experimental Study on The Transient Response from Propagation Field to Vibration Field of RC Column under Vertical Earthquake Shock" *Journal of Structural Mechanics and Earthquake Engineering*, Japan Society of Civil Engineering, **662**(V-49), 135-148 (in Japanese).

Brinbaum, N. K., Cowler, M. S., Itoh, M., Katayama, M. and Obata, H. (1987), "AUTODYN - An Interactive Non-liner Dynamic Analysis Program for Microcomputer through Supercomputer" *Transactions of the Ninth Structural Mechanics in Reactor Technology*, Vol. B, 401-406.

Riedel, W., Thoma, K., Hiermaier, S. and Schmolinske, E. (1999), "Penetration of Rainforced Concrete by BETA-B-500 Numerical Analysis using a New Macroscopic Concrete Model for Hydrocodes" *Ninth International Symposium, Interaction of the Effect of Munitions with Structures*.

Ohkubo, K., Ohyama, H., Beppu, M., Ohno, T. and Katayama, M. (2007), "Fundamental Study on the Local Damage of Concrete Plate due to the Contact and Closed-in Explosion by C4 Explosive" *Journal of Structural Engineering*, Japan Society of Civil Engineering, **53A**, 1273-1283 (in Japanese).

Beppu, M., Miwa, K., Ito, M., Katayama, M. and Ohno, T. (2007), "A Numerical Study on Mechanism of the Local Damage of Concrete Plate Subjected to Impact by Rigid Projectile" *Journal of Structural Engineering*, Japan Society of Civil Engineering, **53A**, 1293-1304.

Fifth International Conference on Urban Earthquake Engineering
March 4-5, 2008, Tokyo Institute of Technology, Tokyo, Japan

SHEAR FAILURE OF SHORT CANTILEVER RC COLUMNS UNDER CYCLIC LOADING: EXPERIMENT AND ANALYSIS

Ionut O. Toma[1], Toshihide Kimura[2], Ken Watanabe[3] and Junichiro Niwa[4]

1) Post Doctoral Fellow, Department of Civil Engineering, Tokyo Institute of Technology, Japan
2) Graduate Student, Department of Civil Engineering, Tokyo Institute of Technology, Japan
3) Assistant Professor, Department of Civil Engineering, Tokyo Institute of Technology, Japan
4) Professor, Department of Civil Engineering, Tokyo Institute of Technology, Japan
iotoma@cv.titech.ac.jp, tkimura@cv.titech.ac.jp, ken@cv.titech.ac.jp, jniwa@cv.titech.ac.jp

Abstract: A series of three short RC columns containing conventional reinforcement and 1% steel fibers were subjected to cyclic loading until shear failure. The columns had different shear reinforcement ratios in order to account for its effect on the behavior of RC columns subjected to cyclic loading. A 2D nonlinear FEM analysis was also performed to model the behavior of the tested specimens. The increase in the shear reinforcement ratio results in a slight increase in the resisted peak load and in a larger energy dissipation. The FEM analysis can predict the resisting peak load with good accuracy.

1. INTRODUCTION

During recent seismic events, it was observed that the failure of reinforced concrete structures was closely related to the occurrence of the shear failure of columns. The types of columns that are more susceptible to shear failure are short columns. Even though, recently, the construction of such columns in seismically active areas has been avoided, there are still a large number of buildings that have short columns as a part of their structure.

Columns built following the old codes have been designed to resist mainly flexure. However, there were cases when an abrupt non-ductile failure of short columns occurred before their flexural strength was reached. Brittle shear failure reduces the energy dissipating capacity of the columns compared to a more ductile flexural failure. Because of that design codes specify shear reinforcement placing methods in order to prevent such brittle failure. However, densely placed reinforcement might make pouring of concrete very difficult and possibly result in large gaps inside the concrete members.

The addition of steel fibers can significantly improve the engineering properties of concrete, notably the shear strength, as reported by Swamy et al. (1993). It also increases the fatigue strength and the resistance to cracking. Even in already damaged concrete members, the presence of steel fibers can improve the structural behavior of such members compared to conventionally reinforced concrete structural members, Toma et al. (2007).

Recently, the numerical simulations of the experimental procedures have shown an increasing trend. The necessity of having good FEM models that can match the experimental results is of paramount importance. The benefits of using FEM analysis are manifold: shorter time until the results are obtained, the parameters can be easily changed in order to assess their influence on the behavior of analyzed structural members, etc.

The present study focuses on the shear carrying capacity and shear behavior of short reinforced concrete columns containing both conventional reinforcement and steel fibers, subjected to lateral cyclic loading. The increase of the shear reinforcement ratio r_w, results in an increase in the peak resisting load and in the energy dissipation capacity of the columns. The numerical simulations give reasonable agreement with the experimental results in terms of peak resisting load. However, the ductile post peak behavior of the columns could not be captured by the non-linear FEM analysis with sufficient accuracy.

2. MATERIALS

2.1 Concrete

For this study, a concrete with a design compressive strength of 30 N/mm^2, obtained from uniaxial compression tests at 7 days according to JIS A 1108, was considered. The compressive strength of each batch cast using the concrete mix proportion shown in Table 1 was measured at the day of testing.

2.2 Reinforcement

The longitudinal reinforcement used in this study was

Table 1 Concrete mix proportion

Concrete Mix	W/C (%)	s/a (%)	W[*1] (kg/m^3)	C[*2] (kg/m^3)	S[*3] (kg/m^3)	G[*4] (kg/m^3)	Admixture[*5] (%)
F10R00							
F10R21	55	47	172	314	838	950	0.3
F10R42							

*1 Water; *2 High early strength Portland Cement, specific gravity = 3.14; *3 Sand; *4 Coarse aggregate, G_{max} = 20 mm; *5 Air entraining and water reducing admixture, percentage of the cement mass.

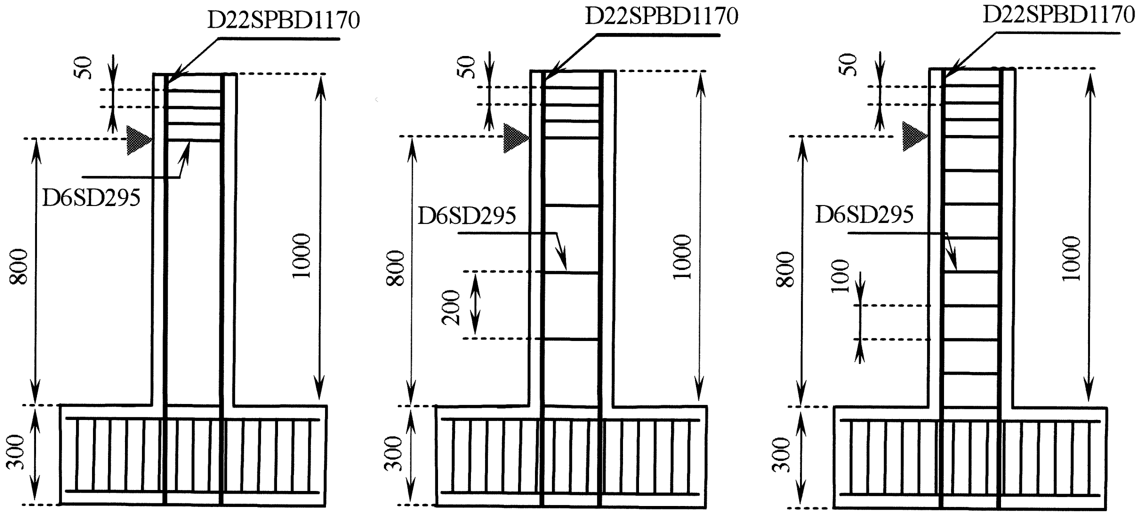

(a) F10R00 (b) F10R21 (c) F10R42

Figure 1 Specimen geometry and reinforcement layout (unit: mm)

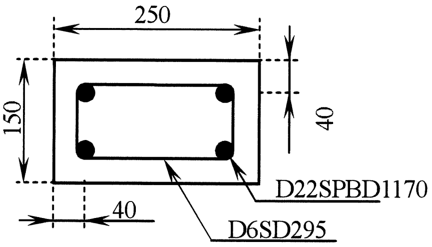

Figure 2 Cross sectional dimensions (unit: mm)

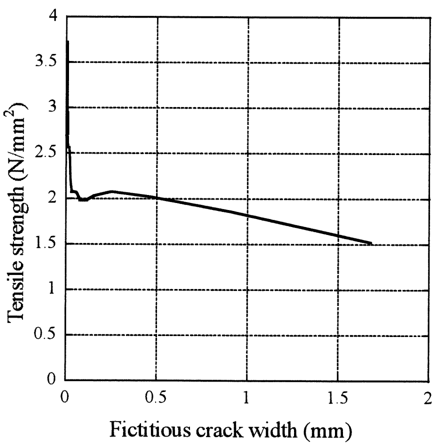

Figure 3 Tension softening curve

of deformed type, D22 SPBD1170, with the area of the bar equal to A_s = 387.1 mm^2. The yield strength of the longitudinal reinforcement was measured and the value was

Table 2 Material properties of concrete

Concrete Mix	Compressive Strength[*1] N/mm^2	Tensile Strength[*2] N/mm^2	Elastic Modulus N/mm^2
F10R00	36.1	3.5	28600
F10R21	36.6	3.2	28100
F10R42	38.7	3.2	28100

*1 Measured according to JIS A 1108 *2 Measured according to JIS A 1113

Table 3 Material properties of conventional reinforcement

Reinforcement name	Type	Yield Strength N/mm^2
Transverse	D6 SD295	350
Longitudinal	D22 SPBD1170	1198

f_y = 1198 N/mm^2.

The shear reinforcement was also of deformed type, D6 SD295, with the area of the bar equal to A_s = 31.67 mm^2. The yield strength of the shear reinforcement was also measured and the value was f_y = 350 N/mm^2.

2.3 Steel fibers

The steel fibers used in this study were with crimped ends. The length is L_f = 30 mm and the diameter is d_f = 0.6 mm, giving an aspect ratio of L_f/d_f = 50. The ultimate tensile strength f_u is 1000 N/mm^2 and the elastic modulus E is 2.1×10^5 N/mm^2.

3. TEST PROGRAM

3.1 Experimental procedure

The specimens presented in this paper are a part of a larger experimental program on short RC columns with various percentages of steel fibers, subjected to lateral cyclic loading. They were selected in order to assess the influence of the shear reinforcement ratio, r_w, on the behavior of the columns.

The reinforcement layouts of the test specimens are presented in Figures 1(a), 1(b) and 1(c). Figure 2 shows the cross section of the columns. For all the specimens, the shear span by the effective depth ratio, *a/d*, was 3.08. The longitudinal reinforcement ratio, p_w, was also kept constant for all the columns and the value was set to 2.49%. The high value for p_w was chosen to ensure the occurrence of shear failure. The specimens were denoted according to the contained percentage of steel fiber and their shear reinforcement ratio. Hence, F10R21 means that the column has 1.0% steel fibers and the shear reinforcement ratio is 0.21%.

3.2 FEM analysis

A two dimensional nonlinear FEM analysis was conducted by means of DIANA program. The columns and the footings were modeled using 4-node plane stress elements, based on linear interpolation and Gauss integration.

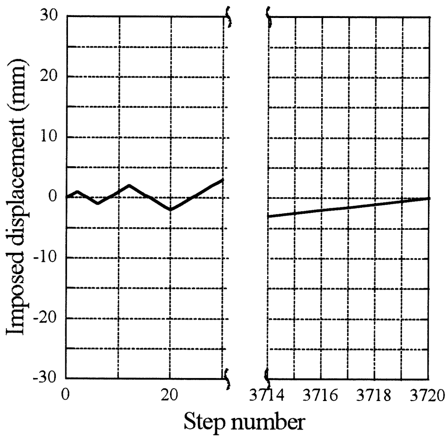

Figure 4 Loading diagram for the FEM analysis

The reinforcement was modeled by means of embedded reinforcement elements. The values of the material properties for the concrete and the conventional reinforcement were obtained experimentally and are summarized in Tables 2 and 3, respectively.

The concrete was modeled using Thorenfeldt model (Thorenfeldt et al. 1987) for the compression region. For the tensile regime, the tension-softening curve shown in Figure 3 was used (Odera 2004). The shear retention function was adopted according to Maekawa et al. 2003. The function is based on the contact density model that defines a nonlinear relationship between the normalized shear strain and the crack shear stress. The governing equation has various parameters and is different for loading and unloading/reloading, depending on the value of the normalized shear strain. The latter depends on the crack shear strain and the crack opening.

The closing of the formed cracks on the unloading stages was also considered. This means that the gradual increases in stresses at the faces of the cracks are taken into account in the finite element analysis.

The models were loaded by using imposed displacements according to the diagram shown in Figure 4. The displacement increment was 0.5 mm. The specimens were loaded until the maximum displacement of 30 mm obtained in the experiment was reached. The iteration procedure was controlled in terms of relative energy variation with a tolerance of 10^{-5}. The loading diagram presented in Figure 4 was similar to the actual loading steps used in the experimental procedure.

4. RESULTS AND DISCUSSIONS

4.1 Cracking and load-displacement curves

Figure 5 presents the load-displacement diagrams for the tested columns with the data obtained from the loading tests. From the envelope curves (the bold lines joining the values of the load corresponding to the maximum displacement according to each loading step), it can be observed that there are no sudden drops in the load even in the post peak region. This is due to the fact that steel fibers were used in the mix proportion.

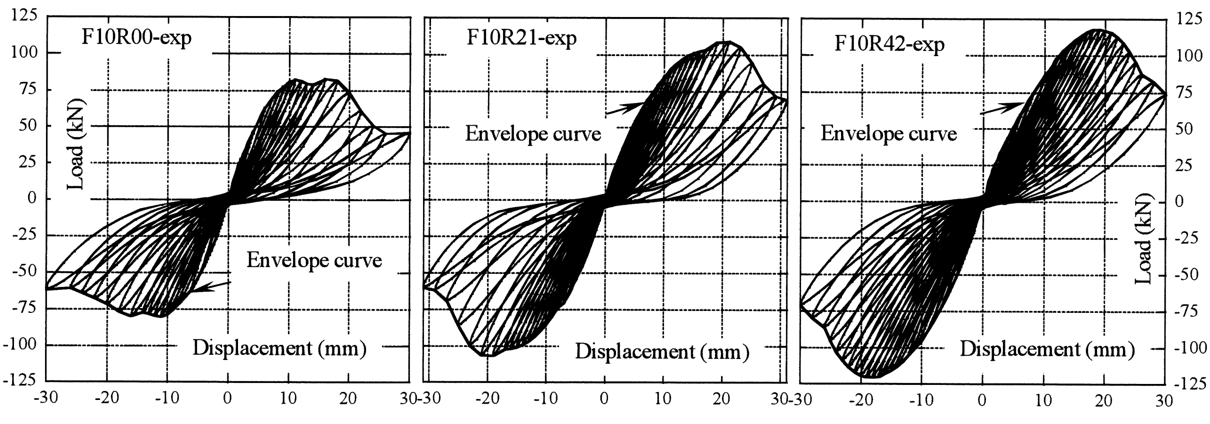

Figure 5 Load-displacement diagrams for the tested specimens (experimental results)

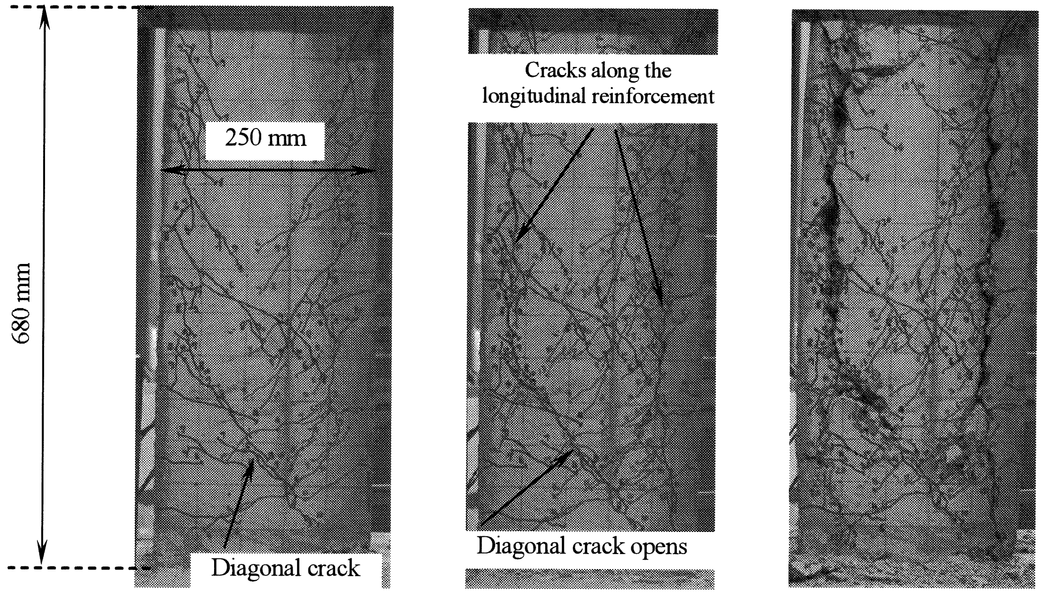

(a) Formation of the diagonal crack (b) Diagonal crack opening (c) Failure of the specimen

Figure 6 Failure stages of specimen F10R00

Specimen F10R00 exhibited a first peak at a displacement of ±10 mm that was consistent with the complete formation of the first diagonal crack, Figure 6(a). By the time the displacement reached ±16 mm a second peak was recorded, corresponding to the opening of the existing diagonal crack and to the full propagation of the cracks along the longitudinal reinforcement, Figure 6(b). From this point on, the load decreased continuously until the complete failure is reached at a displacement of ±30 mm, Figure 6(c).

In this study, the load corresponding to the failure of the columns was considered to be 0.6 $\times P_{max}$, in the post-peak region. It should be noted that even though the specimen was heavily damaged with large crack openings and debonding of the longitudinal reinforcement, the cover concrete did not spall. The benefit from adding steel fibers can be easily observed. This would be of great importance for structures located in areas where severe earthquakes could occur.

Figure 7 shows the comparison between the location of the diagonal crack obtained from the experiment and the analysis. It can be seen that the FEM analysis can predict the location and the shape of the shear crack with sufficient accuracy. Due to the space limitation, only the comparison results for the ±10 mm displacement (complete formation of the first diagonal crack) are shown in this paper.

Looking at Figure 5 it can be noticed that the other two specimens did show a slightly different behavior. They both reached their peak loads at a displacement of around ±20 mm. At the same, the peak load increased from 82.97 kN for F10R00 to 109.15 kN and 118 kN for the specimens F10R21 and F10R42, respectively. This can be explained by the confining effect of the shear reinforcement on the concrete core of the column. At the same time, it prevents the excessive deformation of the longitudinal reinforcement at large lateral displacements, as reported by Woods et al. 2007.

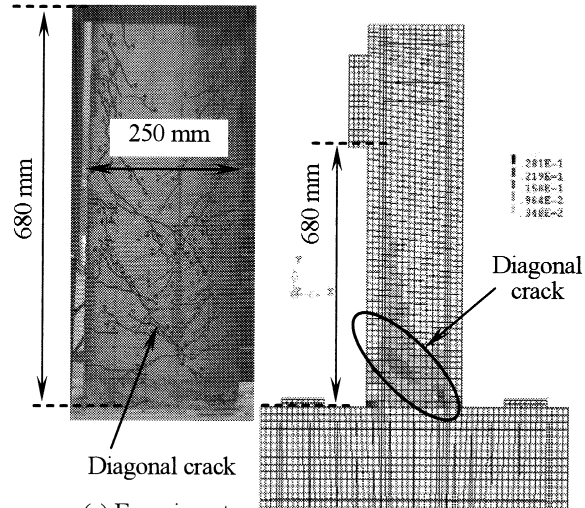

(a) Experiment

(b) Principal tensile strains (FEM analysis)

Figure 7 First diagonal crack for F10R00 (experiment and analysis) at ±10 mm displacement

However, increasing the shear reinforcement ratio from 0.21% to 0.42% has little effect in terms of the peak resisting load or in terms of the maximum displacement for which 0.6 $\times P_{max}$ is reached.

On the other hand, the presence of the shear reinforcement has a more significant effect on the dissipated hysteretic energy, as it will be shown in the subsequent section.

Figure 8 presents the load-displacement curves obtained from the FEM analysis. All analyzed cases exhibit slightly increased initial stiffness compared to the tested specimens. The post-peak behavior however shows a sudden drop in the load followed by an almost horizontal region.

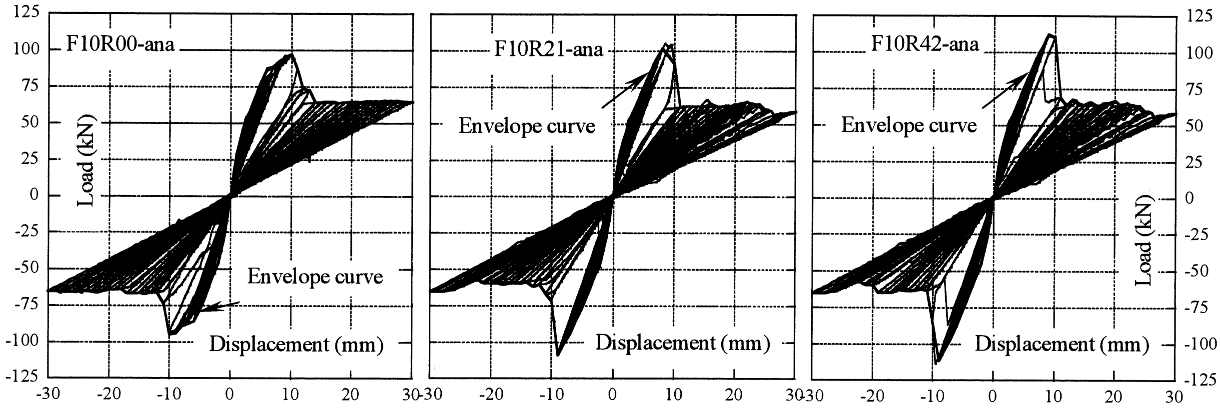

Figure 8 Load displacement curves for the tested specimens (analytical results)

Table 4 Experimental results vs. analytical results

Specimen	P_{max}^{exp} (kN)	P_{max}^{ana} (kN)	P_{min}^{exp} (kN)	P_{min}^{ana} (kN)	$P_{max}^{exp} / P_{max}^{ana}$	$P_{min}^{exp} / P_{min}^{ana}$
F10R00	82.97	97.4	-80.3	-95.06	0.85	0.84
F10R21	109.15	105.2	-106.8	-108.8	1.04	0.98
F10R42	118	112.5	-120.2	-113.6	1.05	1.06

Table 5 Dissipated hysteretic energy

Specimen	E_{hyst}^{exp} (kN×mm)	E_{hyst}^{ana} (kN×mm)
F10R00	4.45×10^3	2.21×10^3
F10R21	6.75×10^3	2.54×10^3
F10R42	7.75×10^3	2.63×10^3

Table 6 Ductility factor

Specimen	Ductility factor μ	
	Experiment	Analysis
F10R00	1.63	1.9
F10R21	1.55	2.0
F10R42	1.58	1.2

Such a different behavior could be explained by the material models that were used in this study. Because steel fiber reinforced concrete is a rather new material and has been in use only in a rather small number of cases for the past decade, there is only a limited number of data available. The tension-softening behavior shown in Figure 3 even though it was obtained from a limited number of experimental results showed good agreement with the results obtained from subsequent tests. However, the compressive behavior of the steel fiber reinforced concrete (SFRC) has not been studied so extensively. Further study in this particular field should be conducted in order to improve the FEM analysis results when it comes to SFRC.

4.2 Peak load and dissipated hysteretic energy

Table 4 summarizes the peak resisting loads of the specimens tested in this study. It can be seen that the FEM analysis provides good agreement with the experimentally obtained results in both sides of the hysteretic loop.

Similar to the experiment, the analytical results show a significant improvement in the peak load when transverse reinforcement is used. However, increasing the shear reinforcement ratio has little influence on the peak load: doubling the value of r_w from 0.21% to 0.42% results only in a 1.1% increase in the peak load for the experimental results and in a 1.07% increase for the results obtained using FEM analysis.

The improvement becomes clearer if the dissipated hysteretic energy is taken into account. The higher the dissipated energy for a structural member is, the better it behaves during a seismic excitation. The energy dissipation capacity is an important parameter in the design of short-period structures and structures subjected to long-duration earthquakes. The energy dissipation capacity also accounts for the history of loadings in addition to the maximum displacement attained.

The dissipated energy was calculated according to the following equation:

$$E_{hyst} = \sum_{i=1}^{n} E_i \qquad (1)$$

where n is the number of cycles (in this case 30) and E_i is the energy (kN×mm) dissipated in each cycle i. E_i can be computed as the area between the loading curve and the unloading curve for both positive and negative ranges.

The calculated results are summarized in Table 5. Indeed, a closer look at the values of E_{hyst} obtained from the experiment confirms the influence of the shear reinforcement on the dissipated hysteretic energy. The results are in agreement with the load-displacement diagrams shown in Figure 5. Specimens F10R21 and F10R42 exhibit higher peak load than F10R00. On the other hand, the post peak behavior of F10R42 shows a slower decrease in the load compared to F10R21. Since all specimens contain steel fibers, the benefit comes from the confining effect of shear reinforcement on the core concrete of the columns.

On the other hand the results obtained from FEM analysis show only slight difference between the specimens with or without shear reinforcement. Looking at Figure 8 it can be observed that the unloading path is almost similar to the loading curve. Consequently, the area between these curves is very small and so is the energy dissipated during a single loading cycle.

4.3 Ductility factor

The response of columns to seismic excitations can be also quantified in terms of the ductility factor. In the seismic design the elastic deformations are generally quantified by ductility parameters and by energy dissipation capacity.

In this paper, the ductility factor is defined as:

$$\mu = \frac{\Delta_u}{\Delta_p} \tag{2}$$

in which Δ_p is the displacement corresponding to the peak load (mm) and Δ_u is the displacement (mm) corresponding to the ultimate resisting load. As previously mentioned, Section 4.1, the column is considered to have failed when the lateral load reaches a value equal to $0.6 \times P_{max}$.

An alternate definition of the ductility factor is in terms of the displacement corresponding to the yielding of the longitudinal reinforcement, Δ_{yl}, and Δ_u. Since one of the objectives of this research was to study the shear behavior of RC columns subjected to lateral cyclic loading, high grade steel was chosen for the longitudinal reinforcement and a large value of the longitudinal reinforcement ratio p_w was set.

The calculated values of the ductility factor, according to Eq.(2), are summarized in Table 6 both for the experiment and the analysis.

According to Eq.(2), a very ductile structural member would reach the peak load at a very small displacement. The curve in the post peak region would have to have a very lean slope to allow for a very large value of Δ_u.

Looking at the values presented in Table 6 for the experiment, it can be seen that F10R00 has the highest ductility factor, reaching the peak load at a displacement of ±16 mm and $0.6 \times P_{max}$ at a displacement of ±26 mm. The other two specimens, F10R21 and F10R42 have comparable values of the ductility factor. They both reached the peak load at a displacement $\Delta_p \simeq \pm 20$ mm. This was mainly due to the increased stiffness of the columns caused by the presence of shear reinforcement. It can also be observed that increasing the value of r_w has only a slight effect on the ductility factor as compared to its effect on the dissipated hysteretic energy.

A similar tendency could be observed for the analytical results, as well. According to the calculated values of μ for the specimen F10R00 is more ductile than F10R42. When it comes to the specimen F10R21, the value of the ductility factor is on a par with the value obtained for F10R00 and largely overestimating the experimental result. The cause of this spurious result is believed to be the lack of accurate material models for simulating the behavior of fiber reinforced concrete. Further study should be conducted in the particular field to develop reliable numerical simulations that would ultimately help in better understanding the behavior of short RC columns with various percentages of fibers.

5. CONCLUSIONS

Using steel fibers led to an improved performance of short reinforced concrete columns under lateral cyclic loading. Even the specimen without stirrups in the shear span showed a large value of the dissipated energy. On the other hand, the specimen exhibits a ductile post peak behavior. Short steel fiber can be a good counter-measure against brittle failure of short columns located in seismically active areas.

In addition to fibers, shear reinforcement ratio plays also an important role on the overall behavior of concrete columns. Due to the confining effect on the core concrete, columns with a higher shear reinforcement ratio can withstand larger lateral displacements. Moreover, stirrups act towards a limitation of the longitudinal reinforcement deformation. However, increasing the amount of shear reinforcement ratio has little influence on the peak resisting loads of the specimens tested in this study.

FEM analysis is also employed in the present research work. The analytical results show good agreement with the experimental values in terms of peak resisting loads and cracking condition. On the other hand, the post peak behavior of the columns observed during the experiments could not be captured by means of FEM analysis. Further studies should be conducted in order to obtain more accurate models for the steel fiber reinforced concrete that can be used in conjunction with FEM programs.

References:

Swamy, R.N., Jones, R. and Chiam, A.T.P. (1993): "Influence of steel fibers on the shear resistance of lightweight concrete T-Beams", *ACI Structural Journal*, **90**(1), 103-114.

Toma, I.O., Miki, T. and Niwa, J. (2007): "Influence of random cracks on the behavior of reinforced concrete beams containing steel fibers", *Doboku Gakkai Ronbunshuu E*, **63**(1), 66-78.

Thorenfeldt, W., Tomaszewicz, A. and Jensen, J.J. (1987): "Mechanical properties of high-strength concrete and applications in design", *Proceedings of the Symposium on the Utilization of High-Strength Concrete*, Stavanger, Norway, 1987.

Odera, I. (2004): "Mechanical properties of hybrid short fiber reinforced concrete using steel and synthetic fibers", *Master thesis*, *Department of Civil Engineering*, Tokyo Institute of Technology.

Maekawa, K., Pimanmas, A. and Okamura, H. (2003): "Nonlinear Mechanics of Reinforced Concrete", SPON Press (Lonon).

Woods, J.M., Kiousis, P.D., Ehsani, M.R., Saadatmanesh, H. and Fritz, W. (2007): "Bending ductility of rectangular high strength concrete columns", *Engineering Structures*, **29**, 1783-1790.

Fifth International Conference on Urban Earthquake Engineering
March 4-5, 2008, Tokyo Institute of Technology, Tokyo, Japan

THE INFLUENCE OF SEGMENTAL LENGTH ON THE SHEAR BEHAVIOR OF SEGMENTAL CONCRETE MEMBERS

Chunyakom SIVALEEPUNTH[1], Ken WATANABE[2], Tomohiro MIKI[3] and Junichiro NIWA[4]

1) PhD. Candidate, Department of Civil Engineering, Tokyo Institute of Technology, Japan
2) Assistant Professor, Department of Civil Engineering, Tokyo Institute of Technology, Japan
3) Associate Professor, Department of Civil Engineering, Kobe University, Japan
4) Professor, Department of Civil Engineering, Tokyo Institute of Technology, Japan
chunyakom@cv.titech.ac.jp, ken@cv.titech.ac.jp, mikitomo@port.kobe-u.ac.jp, jniwa@cv.titech.ac.jp

Abstract: This paper describes the results of an experimental study and nonlinear finite element method in order to examine the shear failure mechanism of segmental prestressed concrete beams by varying the segmental length. The parametric study on the influence of loading position on the shear transfer of segmental beams is performed. It is found that the segmental length and loading position have less significant effect in shear carrying capacity of segmental beams. The experimental results are also compared with the simplified truss model and M_{cr} method for shear carrying capacity. It is found that the results from the simplified truss model agree well with the experimental results.

1. INTRODUCTION

By taking the advantages of prestressing force, the prestressed concrete members can be perfectly utilized to respond the requirements of high shear resistance and reduction of dead load to the substructures. When the earthquake occurred, it is necessary to confirm that the shear failure of prestressed concrete superstructures does not take place before the development of hinge in the columns as illustrated in Figure 1. Recently, prefabricated segmental concrete bridges with external prestressing are associated with a span-by-span construction technique that is thought to be the fastest and simplest among this type of construction process. For the construction of each of the spans, the segments are placed one next to the other with epoxy joint, suspended from an erection girder, and are post-tensioned with external tendons. Due to the popularity of external tendons in prestressed concrete structures, an examination of the design and analysis for shear carrying capacity of such structures is required.

The prediction of shear carrying capacity of externally prestressed monolithic concrete beams by the simplified truss model has already been presented in Sivaleepunth et al. (2007). For evaluating the shear carrying capacity of slender prestressed concrete beams (shear span to effective depth ratio, *a/d*, is greater than or equal to 2.5.), which are predicted to fail in the shear compressive mode of failure, Sivaleepunth et al. (2007) conducted the parametric study by using the nonlinear finite element method (FEM). The influential parameters, such as lower fiber stress, upper fiber stress, etc., were found to have a significant effect on the change of the inclination of concentrated stress flow in a web, which is a key to solve the problem of shear compression failure mode. The simplified truss model was found to be able to predict the several experimental results of externally prestressed concrete monolithic beams very well. However, due to the discontinuity of segmental concrete beams, the simplified truss model may not be able to predict the shear carrying capacity, especially in the cases when the segmental joints open. The shear transfer across opened joints is more complex.

The objectives of this study were (a) to investigate the shear failure mechanism of segmental concrete beams prestressed with external tendons by varying the segmental length, (b) to examine the influence of loading position, in order to simulate the practical loading condition, on the shear transfer in segmental concrete beams, (c) to check the accuracy of the simplified truss model (Sivaleepunth et al. (2007)) and M_{cr} Method (Ito et al. (1992)) for evaluating the shear carrying capacity and (d) to investigate the accuracy in the prediction of critical crack from the simplified truss model.

2. LITERATURE REVIEWS

Due to the comprehensive explanation for the failure mechanism of prestressed concrete beams, the simplified truss model (Sivaleepunth et al. (2007)) is adopted in this study. The schematic diagram of the simplified truss model for analyzing the shear carrying capacity of externally prestressed concrete beams is illustrated in Figure 2. The parameter m is used in the model to represent the inverse of slope of concentrated stress flow, where m = cotθ and θ is

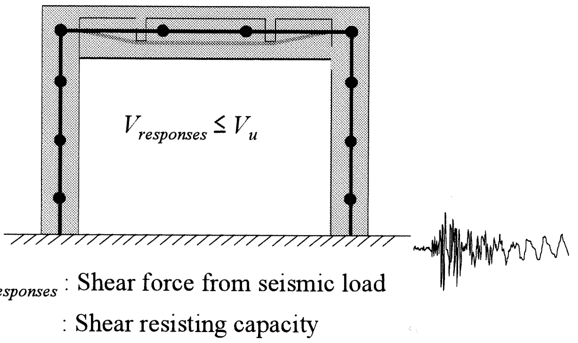

Figure 1 Seismic performance of externally prestressed concrete girder

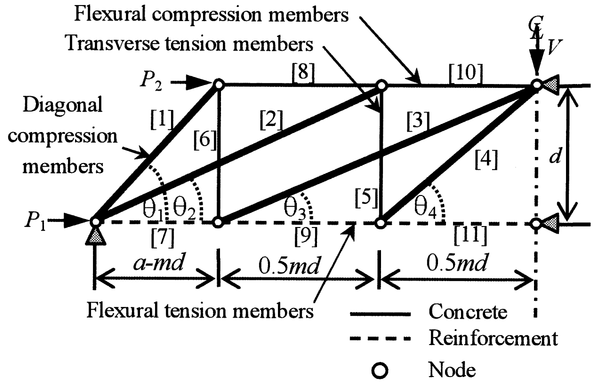

Figure 2 Schematic diagram of the simplified truss model (half of the beam)

the angle of the concentrated stress flow. From the parametric study of the externally prestressed concrete beams, the equation for estimating the value of m can be expressed as the following:

$$m = 1.3\left[\left(1 + 0.2\frac{\sigma_u}{\sigma_u + \sigma_l}\right)\frac{\sigma_l}{k}\right]^{-\frac{2}{3}}\left(\frac{a}{d}\right)^{\frac{2}{5}}\left(\frac{f_c'}{k}\right)^{\frac{1}{3}} \quad (1)$$

where, k is a constant equal to 1 N/mm^2; σ_u is the upper extreme fiber stress (N/mm^2); σ_l is the lower extreme fiber stress (N/mm^2); f_c' is the compressive strength of concrete (N/mm^2).

By considering the effects of bearing plates and effective depth, the values of the horizontal thickness in the vicinity area of a loading point, t_l, and support, t_s, are expressed in Eqs. (2) and (3).

$$t_s = (w_l + 0.1d)\left(\frac{b_f}{b_w}\right)^{\frac{1}{5}}\left(1 + \sqrt{\frac{A_s}{b_w d}}\right)\left(1 + \left(\frac{A_{sv}}{b_w s}\right)^{\frac{1}{4}}\right) \quad (2)$$

$$t_s = 2(w_s + 0.1d)\left(\frac{b_f}{b_w}\right)^{\frac{1}{5}}\left(1 + \sqrt{\frac{A_s}{b_w d}}\right)\left(1 + \left(\frac{A_{sv}}{b_w s}\right)^{\frac{1}{4}}\right) \quad (3)$$

where, w_l is the loading plate width; w_s is the support plate width; b_f is the width of flange; b_w is the width of web; A_s is the cross sectional area of longitudinal bonded tensile reinforcement; A_{sv} is the cross sectional area of stirrup; s is the spacing of stirrups. In the model, the members [1] – [2], and members [3] – [4] in Figure 2 are considered to be affected by support and loading plates, respectively. The cross sectional area of each strut member can be computed as the values of t_l or t_s multiplied with b_w and its inclination.

The resistance capacity of each diagonal compression member, R_i, can be obtained from f_c' incorporating the concrete softening parameter, η, the cross sectional area, A_i, and the inclination of each member (according to the result from Eq. (1)) as following expression.

$$R_i = \eta f_c' A_i \sin\theta_i \quad (4)$$

In order to calculate the shear carrying capacity of externally prestressed concrete beams, the equivalent elastic analysis is applied. That is, after computing the value of m (Eq. (1)), each member force, F_i, caused by the externally applied shear force, V, can be determined by employing the Castigliano's second theorem. After obtaining the member force, F_i, the shear carrying capacity can be estimated by comparing F_i with R_i, when one of struts becomes critical that is F_i/R_i becomes greatest and equal to 1.0.

Although the simplified truss model (Sivaleepunth et al. (2007)) is proven to provide simplicity and high accuracy in the prediction on the shear carrying capacity of externally prestressed concrete beams, it is not checked to extend this model to the segmental concrete beams. Because of the discontinuity of segmental concrete beams, the behavior of stress flow or shear transfer inside segmental concrete beams may different with externally prestressed concrete monolithic beams. This may lead to the shortcoming of the simplified truss model, which based on the stress flow concept.

3. EXPERIMENTAL PROCEDURES

The test specimens consisted of two segmental concrete beams prestressed with external tendons, with the same total length at 3.5 m, cross section dimensions and reinforcement details as shown in Figure 3. The specimens were named as H40 and H80 as tabulated in Table 1. The main parameter was the segmental length. The design effective prestress in terms of the lower extreme fiber stress, σ_l, was set to 19 N/mm^2. For the actual values of effective prestress are shown in Table 1.

Table 1 Details of test beams

Beams	Segmental length (mm)	Upper fiber stress, σ_u (N/mm^2)	Lower fiber stress, σ_l (N/mm^2)	Compressive strength of concrete, f_c', batch A (N/mm^2)	Compressive strength of concrete, f_c', batch B (N/mm^2)	Tensile strength of concrete, f_t, batch A (N/mm^2)	Tensile strength of concrete, f_t, batch B (N/mm^2)
H40	400	0.1	18.5	69.7	65.5	4.3	4.2
H80	800	0.0	19.6	61.8	69.7	4.1	4.4

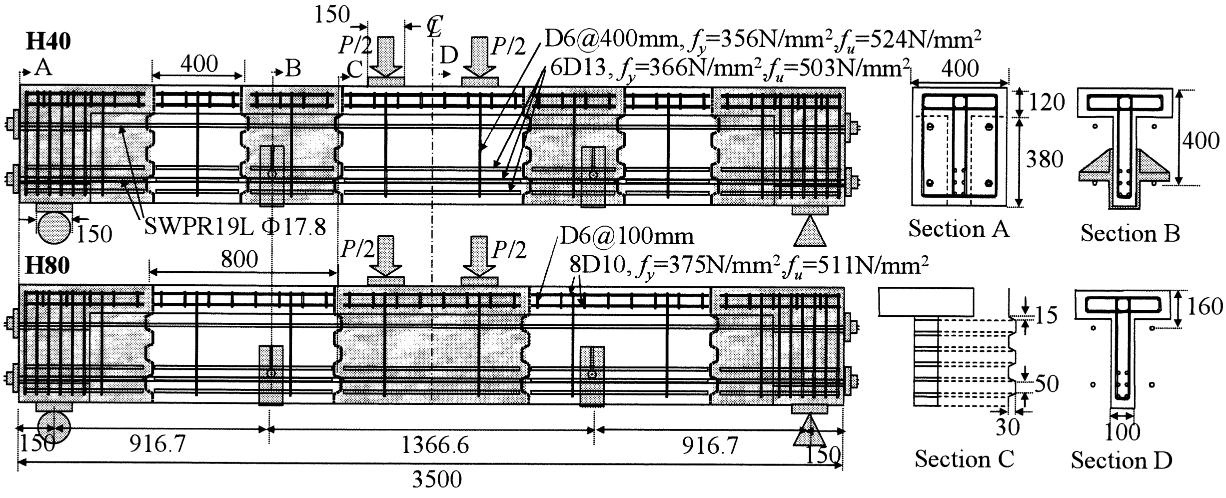

Figure 3 Dimension and steel layout

3.1 Materials

In all specimens, the internal longitudinal tensile reinforcement consisted of six deformed steel bars with nominal diameter of 13 mm (A_s = 126.7 mm^2), eight deformed steel bars are for longitudinal compressive reinforcement with nominal diameter of 10 mm (A_s' = 71.33 mm^2). Transverse reinforcement with a nominal diameter of 6 mm (A_v = 63.34 mm^2) was provided in web and flange throughout the length of beams with the spacing, s, of 400 mm and 100 mm, respectively. Their average yield strength, f_y, average tensile strength, f_u, modulus of elasticity, E_s, are illustrated in Figure 3. For external tendons, two straight 19-wire prestressing tendons with a nominal diameter of 17.8 mm (A_{ps} = 208.4 mm^2) were prepared at the bottom and top layers as external tendons. The yield strength, f_{py}, the tensile strength, f_{pu}, and the modulus of elasticity of external tendons, E_{ps}, were 1680 N/mm^2, 1900 N/mm^2 and 191.3 kN/mm^2, respectively.

The match-cast technique was utilized in this study; therefore, the concrete was cast for two times in each segmental beam. Firstly, the batch A, shaded area in Figure 3, was cast. After hardening of batch A, the formwork was removed and prepared for batch B, unshaded area. The actual compressive and tensile strengths of concrete in each batch were measured on the day of testing, and tabulated in Table 1. The compressive and tensile strengths of epoxy, which was used at segmental joints, were more than 60 N/mm^2 and 12.5 N/mm^2, respectively.

3.2 Experimental Setup

Before testing, the beam specimens were prestressed using symmetrically arranged external tendons on both sides of the section deviated at 916.7 mm from the supports by two deviators and anchored at the ends of beams. The strain of the prestressing tendon was taken as its average value of three electrical strain gauges, placed on the tendons at the midspan. All beams had straight tendon profiles, with an effective depth of 400 mm at the midspan for the bottom layer, and 160 mm for the top layer. The tendons were stressed as indicated by σ_u and σ_l in Table 1.

Deflections at the midspan and deviators, crack width, joint opening, prestressing force in external tendons, and strains of concrete, steel and tendon were measured and monitored in each beam. The beams were simply supported over a span of 3.2 m and four-point symmetrical loading with a distance between loading points of 400 mm was provided. The shear span was set as 1.4 m, and the effective depth was 400 mm (i.e. shear span to effective depth ratio, a/d, was 3.5). The 150 mm width of loading and support plates were used in the test.

4. FEM ANALYSIS

The nonlinear FEM using DIANA system has been conducted to examine the shear failure mechanism of segmental prestressed concrete beams. Four-node quadrilateral isoparametric plane stress elements in a two dimensional configuration were adopted for concrete as illustrated in Figure 4. The interface elements used at the deviators and at the end anchorages are also shown in Figure 4. The friction between the tendons and the deviators is

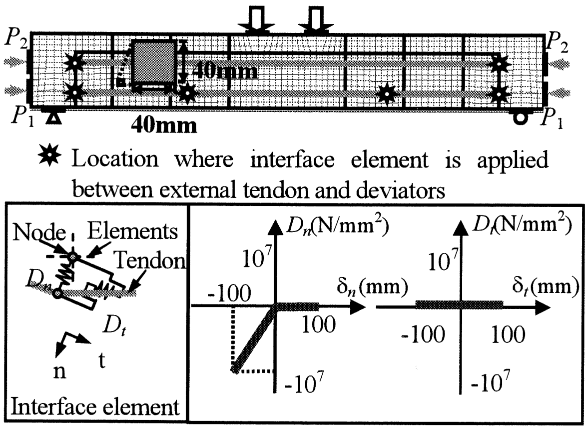

Figure 4 Finite element analytical model and interface element at deviator and end anchorage

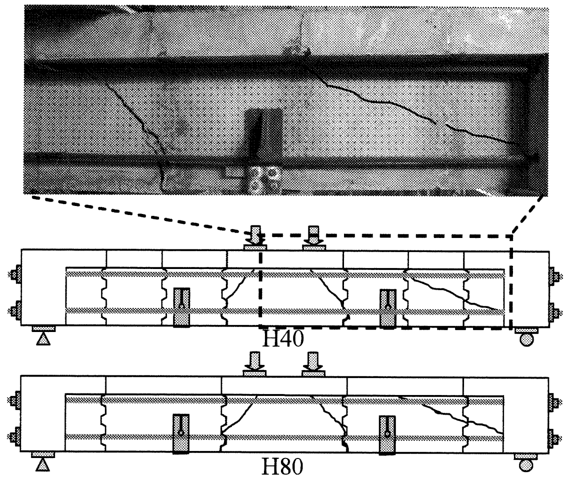

Figure 5 Crack patterns

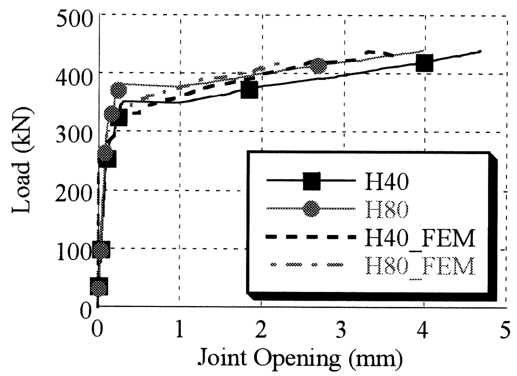

Figure 6 Load-joint opening response

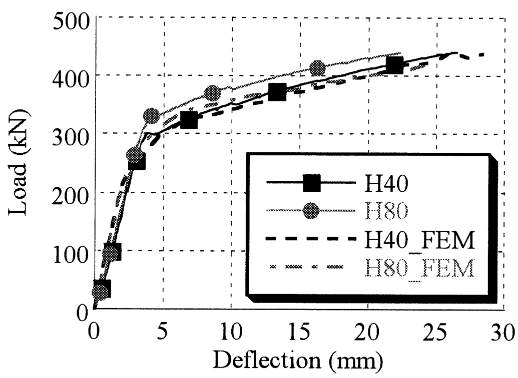

Figure 7 Load-deflection response

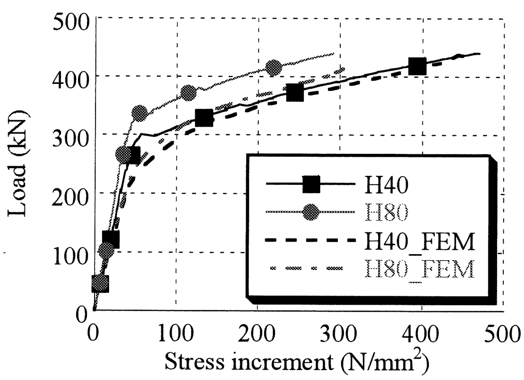

Figure 8 Load-stress increment response

neglected. The stiffness in n-axis, D_n, is set to be zero for tension due to the opening between the tendons and the deviators. For compression, due to the closing between the tendons and the deviators, the extremely large stiffness is applied as shown in Figure 4. For t-axis, the stiffness, D_t, is set to be zero due to the assumption of no friction between the deviators and tendons. Because of its applicability and simplicity, the flat joint model as proposed in Turmo et al. (2006) is applied at the segmental joints. The flat joint model is composed of two-node interface elements, with different constitutive laws depending on the real geometry of shear key that the elements were reproducing. The constitutive equation of the flat joint model is adopted from Turmo et al. (2006) due to the similar dimension of shear keys. Since the cracking observed in the experiment corresponded to the development of one single crack that accumulates all the deformations, a discrete crack model is selected as for interface elements in segmental joints. The elastic stiffness matrix, D_n and D_t, had a sufficiently high values as 10^7 N/mm^3 in order to model the continuous geometry (i.e. before joint opening). The tensile strength of the concrete, f_t, was obtained from the experiment. The value of fracture energy, G_F, was found by considering the average compressive strength of concrete and the maximum size of the aggregate, i.e. G_{max} = 20 mm, as recommended from JSCE specification (2002).

In the analysis, the smeared crack model is adopted as the crack model to concrete elements. For the constitutive model in compression, Thorenfeldt's model (Thorenfeld et al. (1987)) is applied. After cracking, the tension softening model proposed by Hordijk (1991) is utilized as the concrete constitutive model under tension. Two-node truss elements are applied for the tendon elements. These truss elements are connected to the concrete only at the deviators and end anchorages by means of using the interface element as shown in Figure 4. The bilinear elasto-plastic model of steel is adopted for the longitudinal reinforcement and prestressing tendons. During the analysis, the prestressing force is applied by using the incorporated prestressing command in DIANA system at the first step. After the first

Table 2 Summary of experimental results

Beams	Joint opening (mm)	P_{joint} *1 (kN)	P_u *2 (kN)	δ_u *3 (mm)	f_{ps} *4 (N/mm^2)	d_{pu} *5 (mm)
H40	4.7	298	439	27	1341	388
H80	4.0	329	440	28	1204	389

Note: *1 Loading resistance at joint opening
*2 Loading resistance at peak
*3 Midspan deformation at peak
*4 Tendon stress at peak
*5 Bottom tendon level from upper fiber

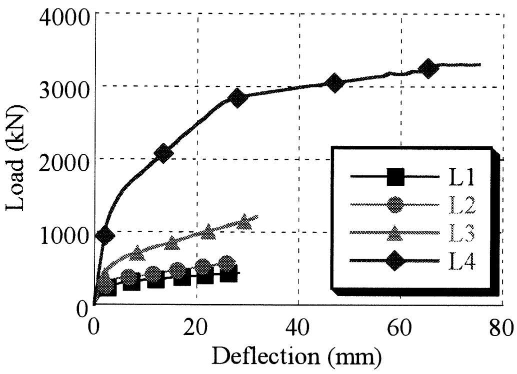

Figure 10 Load-deflection response

step, the displacement control and the Quasi-Newton method (secant method) is used for the iteration.

5. RESULTS AND DISCUSSION

5.1 Crack Patterns and Joint Opening

The crack patterns are depicted in Figure 5. There was no flexural crack that could be observed. However, the vertical crack in the shear span near to the segmental joints, where is next to the loading points, could be observed after the diagonal cracks occurred from the loading points to the segmental joints as shown in Figure 5. As the load increased, the vertical crack next to the segmental joints, where is next to the loading points, opened (joint opening). This joint opening were measured at the lower extreme fiber of the beams between each segments during the test, and plotted as illustrated in Figure 6. After the joint opening, the only two joints at the midspan increase significantly in width and propagate upward along the diagonal crack to the top flange of the beams. The load is suddenly dropped due to the second diagonal crack near to the support.

5.2 Load-Deflection and Stress Increment

Figures 7 and 8 illustrated the responses of applied load versus deflection and load versus stress increment of beams, respectively. The summary of measured data, which includes the load at joint opening, the peak load, the midspan deflection, the stress in external tendons at the peak and tendon depth at the peak, is tabulated in Table 2. At the beginning, the beams behaved as the linear elastic body. The increase in deflection and stress increment in external tendon were very small, until the sudden diagonal cracks can be observed at the middle segment near to the loading points. The load was slightly dropped, and the vertical crack near to the segmental joints, which was close to the loading points, opened and the stiffness of the beams was reduced. After that the deflection increased with the small increase in load until the peak load resulting also in significant increase of stress increment in external tendons. At the peak load the second sudden diagonal crack occurred near to the support, causing the sudden failure of the beams. From Figures 7 and 8, it can be observed that specimens H40 and H80 have almost the same loading resistance. Therefore, from this experimental study, it can be said that the segmental length has less significant effect to the shear carrying capacity.

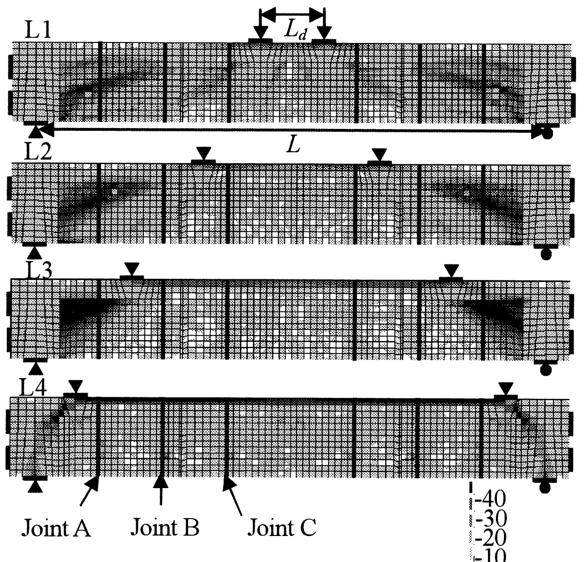

Figure 9 Principal stress at peak load

Table 3 Joint opening from FEM

Beams	Joint opening (mm) refer to Figure 9		
	Joint A	Joint B	Joint C
L1	0.0	0.0	3.7
L2	0.0	0.3	4.9
L3	0.5	2.2	5.4
L4	5.9	8.1	12.3

The validation of nonlinear FEM is made by comparing the analytical results with the experimental results as illustrated in Figures 6, 7 and 8. It can be observed that the nonlinear FEM can predict the load-deflection, load-stress increment and the load-joint opening responses of segmental prestressed concrete beams very well.

6. INFLUENCE OF LOADING POSITION ON SHEAR CARRYING CAPACITY

The nonlinear FEM is applied in order to investigate the influence of loading position on the compression stress

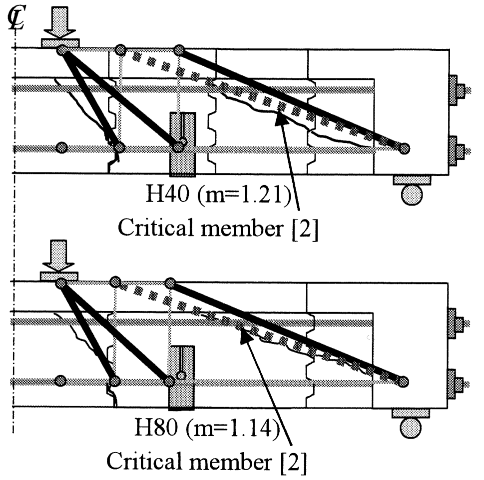

Figure 11 Critical members and crack patterns

flow and shear carrying capacity in segmental prestressed concrete beams. The main parameter is the ratio of loading distance to span length, L_d/L, for 4 cases. Those are L1 (same as specimen H40), L2, L3 and L4, having L_d/L equal to 0.13, 0.34, 0.63 and 0.84, respectively. The dimensions and reinforcement layouts are the same with specimen H40 in Figure 3.

Figure 9 shows the principal compressive stress at the peak load for those beams (L1, L2, L3 and L4) and Figure 10 and Table 3 show the response between load and deflection and the joint opening in each segmental joint at the peak load, respectively. It is found that when the loading point moves near to the support, the compressive stress flow transfers directly to the support; therefore, the beams can resist more shear force as illustrated in Figure 10. Please note that when the load moved to the support, it leads to the change of *a/d*, which affects on the shear carrying capacity of concrete beams. From FEM analysis, it results that the joints located within the flexural span open significantly as shown in Table 3. On the other hand, the segmental joints in shear span remain nearly in contact, which can transfer the compressive stress to the support. Therefore, it is proven from this result that by moving the loads toward the supports, the compressive stress can still transfer to the supports.

7. COMPARISON WITH THE PREDICTION EQUATIONS

In this study, the shear carrying capacity of two beams from the experiment is used to confirm the applicability of the simplified truss model (Sivaleepunth et al. (2007)) and M_{cr} method (Ito et al. (1992)). In calculation of the simplified truss model, four diagonal compression members are considered. The number of diagonal compression member is demonstrated in Figure 2. The typical crack patterns from the experiments at the ultimate stage are utilized to compare with the critical members in the simplified truss model as illustrated in Figure 11. The bold dashed line in Figure 11 represents the critical member of each case. From these comparison results, it is proven that the simplified truss model is applicable for predicting the location of the critical crack of segmental prestressed concrete beams. Moreover, the comparisons for shear carrying capacity of the experimental results with the calculated results show that the simplified truss model yields the reasonable accuracy and reliability in prediction with an average value (AVE.) of P_u/P_{CAL} of 1.20, while the AVE. of P_u/P_{CAL} of M_{cr} method is 1.32.

8. CONCLUSIONS

(1) The segmental length has less significant effect to the shear carrying capacity of the beams according to the experimental and analytical results in this study.
(2) The analytical model of nonlinear FEM is applicable to examine the shear failure mechanism of segmental concrete beams, such as load-deflection, load-joint opening and load-stress increment responses.
(3) The loading position has less influence to the compressive stress flow in segmental concrete beams. As long as the segmental joints in shear span remain in contact, the compressive stress can transfer to the supports.
(4) The simplified truss model can provide the good agreement with the experimental results according to this study.

Acknowledgements:

Sincere gratitude is expressed to Mr. Tsuyoshi Hasegawa and Dr. Yuzuru Hamada, research engineers from DPS Bridge Works, Co., Ltd., and Mr. Dinh Hung Nguyen, graduated student from Tokyo Institute of Technology for their assistance in conducting the experiment. The authors also would like to express their gratitude to the COE program for providing financial support to accomplish this research.

References:

Sivaleepunth, C., Niwa, J., Bui, K.D., Tamura, S. and Hamada, Y. (2007), "Simplified Truss Model for Externally Prestressed Concrete Beams," JSCE Journal of Materials, Concrete Structures and Pavements, Vol. 63 No.4, pp. 562-574.

Ito, T., Yamaguchi, T. and Ikeda, S. (1992), "Flexural Shear Behavior of Precast Segmental PC Beam," Proceedings of the JCI, Vol. 16, No.2, pp. 967-972. (in Japanese)

Turmo, J., Ramos, G. and Aparicio, A.C. (2006), "FEM Modeling of Unbonded Post-tensioned Segmental Beams with Dry Joints," Engineering Structures, Vol. 28, pp. 1852-1863.

Japan Society of Civil Engineers (JSCE) (2002), "Standard Specification for Concrete Structures" (Structural Performance Verification).

Thorenfeldt, E., Tomaszewicz, A. and Jensen, J. J. (1987), "Mechanical Properties of High-strength Concrete and Applications in Design," Symposium Proceedings of Utilization of High-strength Concrete, Norway.

Hordijk, D. A. (1991), "Local Approach to Fatigue of Concrete," PhD thesis, Delft University of Technology.

Fifth International Conference on Urban Earthquake Engineering
March 4-5, 2008, Tokyo Institute of Technology, Tokyo, Japan

EVALUATION OF THE LOCAL BEHAVIOR OF RECYCLED CONCRETE UNDER CYCLIC LOADING BY USING IMAGE ANALYSIS

Yasutaka Noma[1], Ken Watanabe[2], Tomohiro Miki[3] and Junichiro Niwa[4]

1) Ph.D. candidate, Department of Civil Engineering, Tokyo Institute of Technology, Japan
2) Assistant professor, Department of Civil Engineering, Tokyo Institute of Technology, Japan
3) Associate professor, Department of Civil Engineering, Kobe University, Japan
4) Professor, Department of Civil Engineering, Tokyo Institute of Technology, Japan
ynoma@cv.titech.ac.jp, ken@cv.titech.ac.jp, mikitomo@port.kobe-u.ac.jp, jniwa@cv.titech.ac.jp

Abstract: The strength and the softening behavior of high strength concrete with a large amount of recycled aggregate under uniaxial compressive cyclic loading were investigated. The compressive behavior was different depending upon the quantity of recycled aggregate. The effect of the lateral displacement and the lateral local strain on the compressive behaviors were clarified by using a π–shaped displacement gage and the lattice method by using image analysis.

1. INTRODUCTION

In recent years, many recycled materials have been developed to reduce environmental burdens. Broad use of recycled materials as a substitute for traditional construction materials is expected to be encouraged with continued increases in environmental awareness. Recycled aggregate made from concrete mass obtained from demolished concrete structures can be included. The production of high-quality recycled aggregate has become possible by reducing residual mortar adhering to aggregate using treatment equipment (Hayakawa et al. 2003). Much research has been performed relating to mechanical properties and durability of concrete using recycled aggregate (recycled concrete). However, the fracture mechanisms of recycled concrete under static and dynamic (seismic) loading have not been clarified.

By standard practice, it is rare to take into account the quantity of coarse aggregate as an influence factor affecting compressive strength. Meanwhile, the effect of the variance of the quantity of coarse aggregate on compressive strength has been studied. Noguchi et al. (1993) reported compressive strength increases as the quantity of coarse aggregate increases in high strength concrete. Liu (2007) clarified the mechanical properties of high strength concrete with the quantity of coarse aggregate increasing up to the limit of the percentage of solid volume under the condition of W/C constant and normal crushed stone. It is shown that the relationship between the quantity of coarse aggregate and the compressive strength. It also showed that the compressive strength became maximum when the quantity of coarse aggregate was 500 ℓ. The compressive strength decreased when the quantity of coarse aggregate was 600 ℓ. Many cracks were generated and propagated at the interfaces between coarse aggregate and mortar phases in the case of the quantity of coarse aggregate equal to 600 ℓ (Liu 2007). In this research, the effect of the quantity of coarse aggregate of recycled concrete on the compressive strength was investigated. The fracture mechanisms of this concrete were studied in terms of the deformation characteristics of each phase such as coarse aggregate and mortar phases (Local behavior).

This research is aimed at investigating the fracture mechanisms of concrete using a large quantity of recycled aggregate under cyclic loading. Firstly, the uniaxial compressive cyclic loading was conducted. The effect of the quantity of coarse aggregate on the compressive strength and the compressive softening behavior is described. The lateral displacement was measured by using a π–shaped displacement gage. Furthermore, the lattice method by using image analysis (Matsuo et al. 2004) was conducted to measure the strain on the surface of specimens. Finally, the effect of the variance of the quantity of coarse aggregate on the compressive behavior under cyclic loading is clarified by using the lateral displacement and the lateral local strain.

2. TEST DESCRIPTION

2.1 Employed Materials

Table 1 shows the properties and ingredients of cement, aggregate and admixture. Normal crushed stone (CS) and high quality recycled aggregate (RH) were employed. The high quality recycled aggregate was made from the concrete mass produced when a concrete structure that had been in-service, had been demolished. The screw triturator (Hayakawa et al. 2003) was used to reduce mortar adhering to the aggregate. The high quality recycled aggregate in this

Table 1 Materials

Materials		Properties
Cement (C)	Ecocement	Density 3.17 g/cm^3, Specific surface area 4310 cm^2/g
Fine aggregate (S)	Land sand	Density in SSD condition 2.66 g/cm^3, Absorption 0.93 %
Coarse aggregate (G)	Normal crushed stone (CS)	Density in SSD condition 2.62 g/cm^3, Absorption 0.65 %, Maximum aggregate size 20 mm
	High quality recycled aggregate (RH)	Density in SSD condition 2.53 g/cm^3, Absorption 2.97 %, Maximum aggregate size 20 mm
Admixture	Super plasticizer	Polycarboxylic acid type, Density 1.10 g/cm^3
	Air entraining agent	Alkyl ether type, Density 1.025 g/cm^3

Table 2 Mix proportion

Name	Coarse aggregate	Quantity of Coarse aggregate (ℓ/m^3)	W/C (%)	s/a (%)	Unit weight (kg/m^3)				Super plasticizer (g/m^3)	Air entraining agent (g/m^3)
					Water	C	S	G		
CS-400	CS	400	30	37.7	150	500	644	1048	170	113
CS-500		500		22.2			378	1310	195	169
CS-600		600		6.6			112	1572	280	263
RH-400	RH	400		37.7			644	1032	170	120
RH-500		500		22.2			378	1290	195	165
RH-600		600		6.6			112	1548	333	315

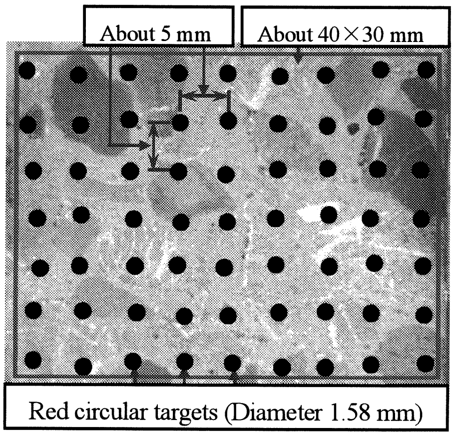

Figure 1 The side for calculating the strain

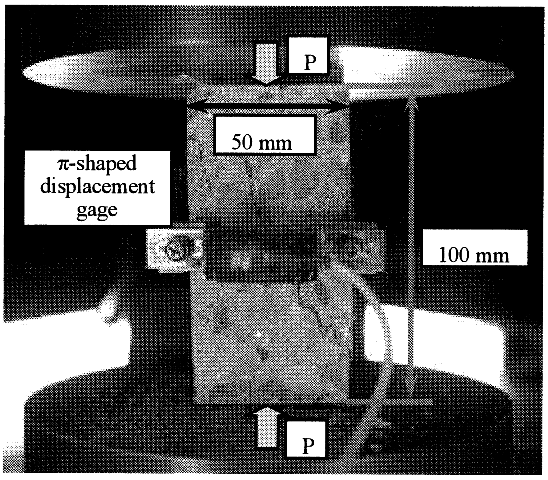

Figure 2 Lateral side

research satisfies JIS A 5021 [Recycled aggregate for concrete - class H].

2.2 Mix Proportion

The mix proportions used in the experiments are shown in Table 2. The water content of 150 kg/m^3 and W/C=30 % were constant in all mix proportions. Slump and air content were adjusted by using super plasticizer and air entraining agent to obtain the values of 20.0±3.0 cm and 4.0±2.0 %, respectively. Specimens cured for 14 days in water prior to performing tests. To compare with the concrete using normal crushed stone, CS-400, CS-500 and CS-600 were used as shown in Table 2.

2.3 Experimental Procedure

Three specimens were made for each case and test. The following tests were conducted.

Compressive strength was measured according to JIS A 1108. A rectangular concrete specimen was cast with a size of 100×100×400 mm. After 14 days, the size of specimen was reduced to 50×50×100 mm by using concrete cutter. Red circular targets with the diameter of 1.58 mm were arranged at about 5 mm intervals on the surface of the specimen as shown in Figure 1. During uniaxial compressive cyclic loading tests, several photos were taken for each loading step (10 kN) by using a high resolution digital camera (4368×2912 pixels) during the tests. The displacement in both the loading direction and lateral direction were measured. The displacement in the lateral direction was measured by using a π-shaped displacement gage as shown in Figure 2. The coordinates of target centers were calculated by image processing software. The displacement and the strain in each element were interpolated by using shape functions for a nine-node isoparametric element.

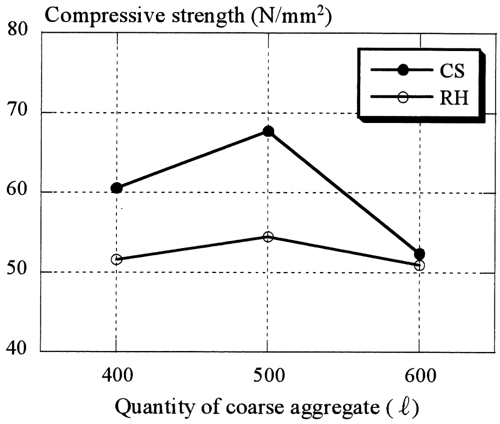

Figure 3 The relationship between the quantity of coarse aggregate and the compressive strength

3. Experimental results

Compressive strengths are shown in the average value. The result of the typical specimen is shown as a representative value in the case of the uniaxial compressive stress-strain relationship and the lateral local strain distribution.

3.1 Compressive strength

Figure 3 shows the relationship between the quantity of coarse aggregate and the compressive strength. The result is similar to the result obtained by Liu (2007) using normal crushed stone. That is, the compressive strength of CS-500 increases compared to that of CS-400, and decreases in the case of CS-600. In the case of using RH, the compressive strength slightly increases in the case of RH-500. The variance of the compressive strength when using RH is less than that of CS. The compressive strengths of CS-400 and CS-500 are higher than that of RH-400 and RH-500. However, the compressive strength of CS-600 and RH-600 are almost the same. Liu (2007) reported that the brittle behavior of the interface between the coarse aggregate and the mortar may become the critical structural defect by a large amount of bleeding in certain cases. The decrease of the compressive strength of CS-600 is caused by this defect. The effect of the quantity of coarse aggregate on the compressive strength becomes smaller in the case of using RH comparing to the case of using CS. There is a possibility that the brittle behavior of mortar residue and the old interfaces in RH becomes the structural defect.

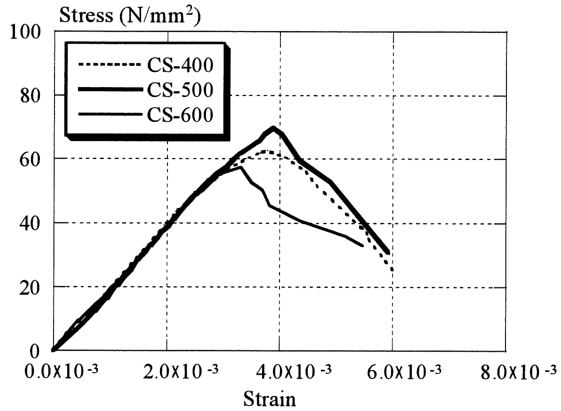

Figure 4 Uniaxial compressive stress-strain relationship (CS)

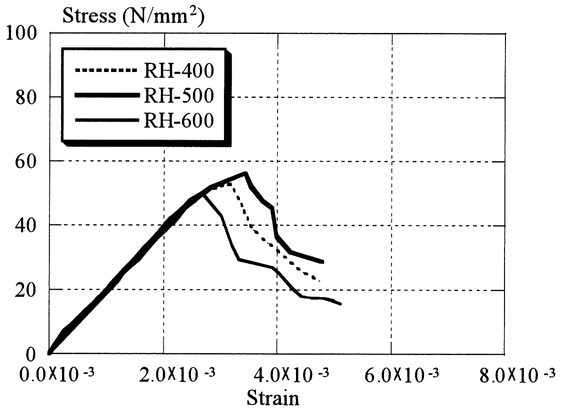

Figure 5 Uniaxial compressive stress-strain relationship (RH)

3.2 Compressive softening behavior

The stress was obtained by dividing the load by the cross sectional area of specimen. The strain was also obtained by dividing the displacement in the loading direction by the initial length of the specimen. Figures 4 and 5 show the uniaxial compressive stress-strain relationship for each specimen. In addition, these uniaxial compressive stress-strain relationships represent envelopes of hysteresis curves obtained in the uniaxial compressive cyclic loadings.

No significant difference is observed in the initial stiffness of each specimen. However, the compressive softening behavior is different depending on the types of coarse aggregate and the quantity of coarse aggregate. These differences are clearly visible just before and after the peak (Figures 4 and 5). The compressive strength of concrete using RH is lower than that of concrete using CS. The softening slope of concrete using RH is steeper than that of concrete using CS. This slope does not depend on the quantity of coarse aggregate in the case of both CS and RH.

The compressive strength and the transmitted stress in the post peak region were observed to be maximum for both CS and RH under the uniaxial compressive cyclic loading. These results indicate that the seismic performances can be improved by increasing the quantity of coarse aggregate up to 500 ℓ for both types of course aggregate material.

3.3 Lateral local strain distribution

Figure 6 shows the uniaxial compressive stress –lateral displacement relationship obtained during the experiments. The lateral displacement was measured using a π–shaped displacement gage. These are data measured from the beginning of the test to the beginning of the second

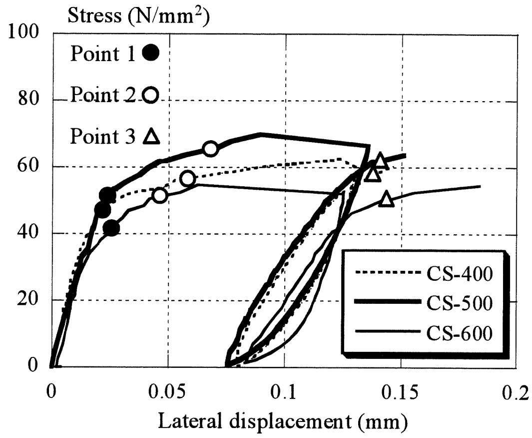

Figure 6 Uniaxial compressive stress -lateral displacement relationship (CS)

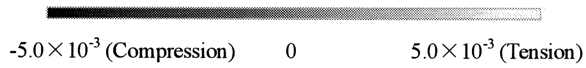

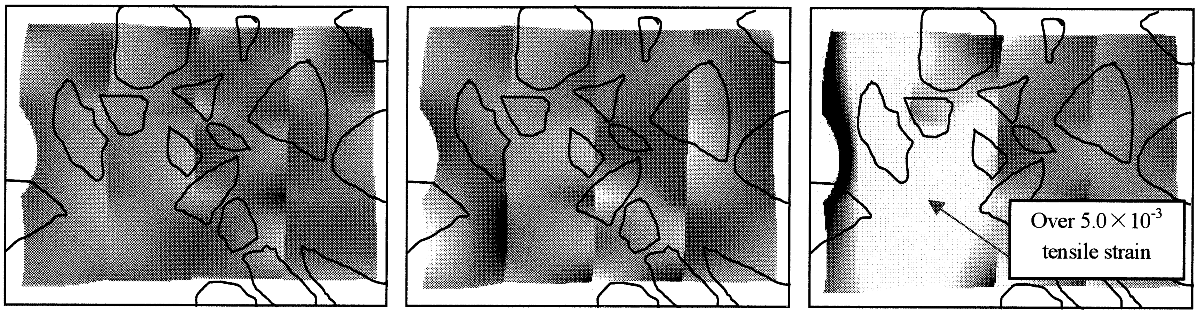

(a) Point 1 (b) Point 2 (c) Point 3

Figure 7 Lateral local strain distribution (CS-400)

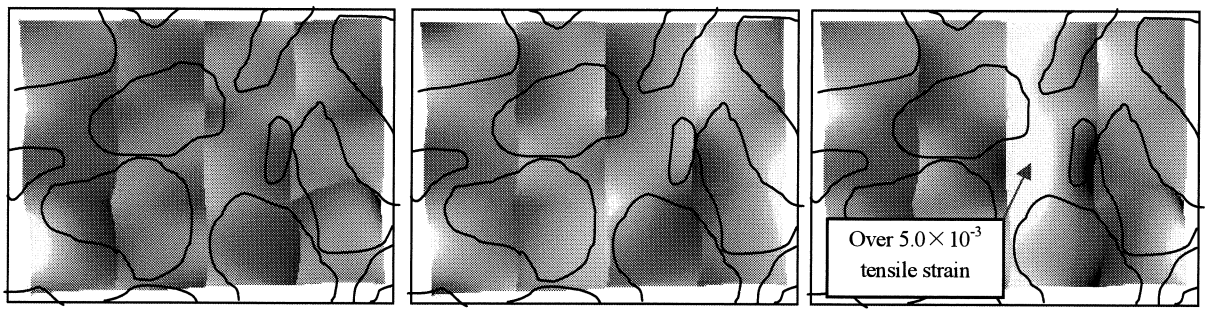

(a) Point 1 (b) Point 2 (c) Point 3

Figure 8 Lateral local strain distribution (CS-500)

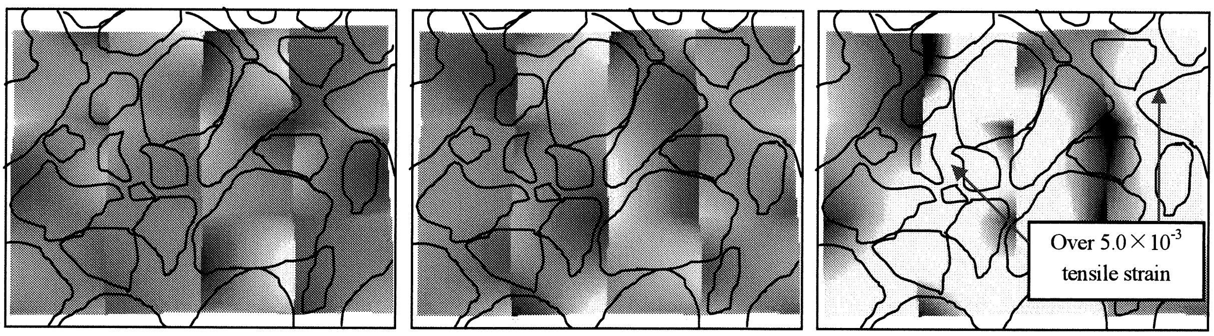

(a) Point 1 (b) Point 2 (c) Point 3

Figure 9 Lateral local strain distribution (CS-600) unloading. These relationships show almost linear between 0 and 30 N/mm². The increasing rate of stress diminishes when the stress approaches the first peak. This tendency can also be observed from the beginning of the first reloading to the beginning of the second unloading.

The lateral displacement of CS-500 becomes smaller than that of CS-400 and CS-600. Therefore, it shows the lateral deformation is small under the compressive stress in the loading direction. It can be considered that this tendency is related to the compressive strength and the compressive softening behavior of CS-500. The lateral displacement of CS-600 is large at about 50 N/mm². It may also be considered that this tendency is related to the compressive

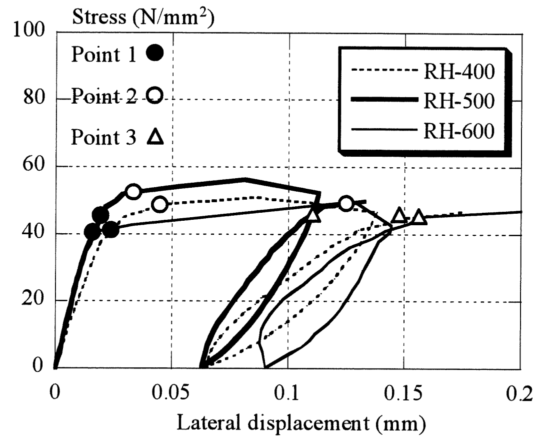

Figure 10 Uniaxial compressive stress -lateral displacement relationship (RH)

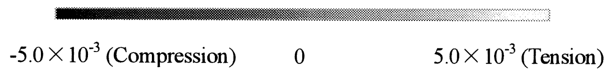

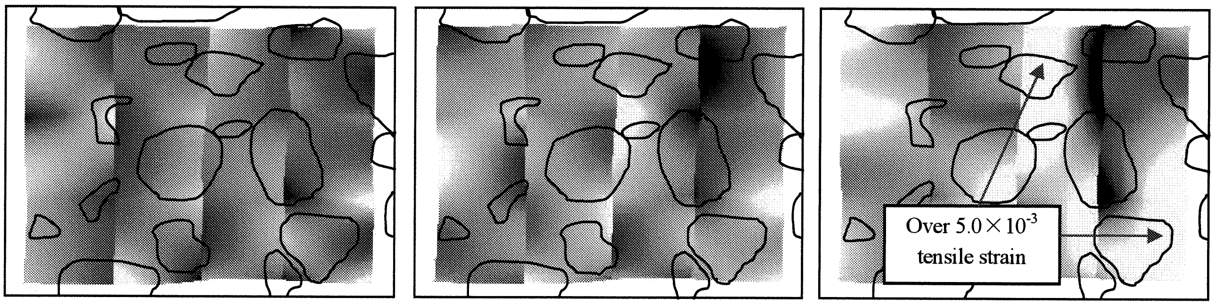

(a) Point 1 (b) Point 2 (c) Point 3

Figure 11 Lateral local strain distribution (RH-400)

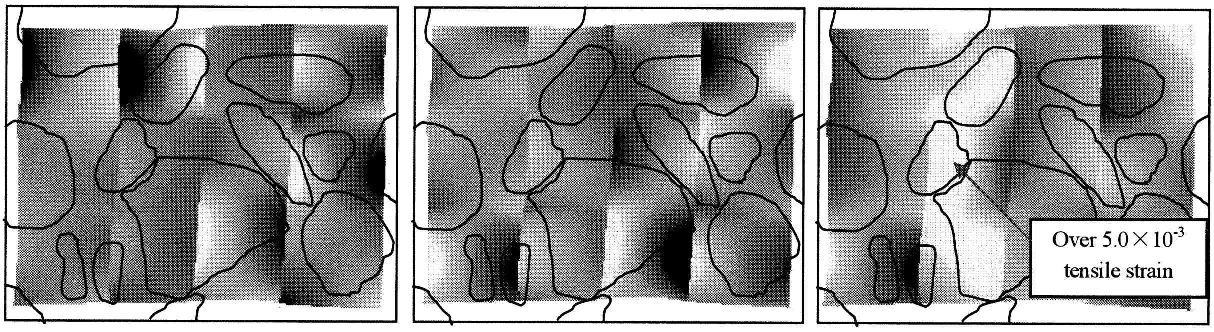

(a) Point 1 (b) Point 2 (c) Point 3

Figure 12 Lateral local strain distribution (RH -500)

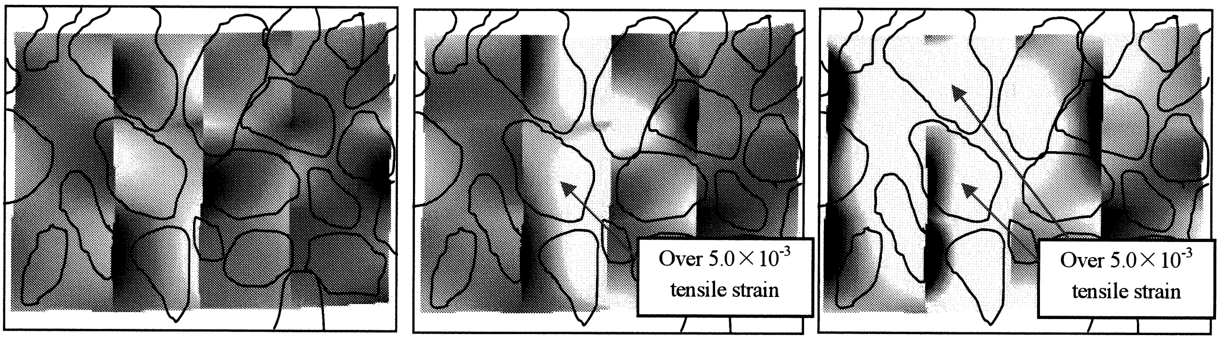

(a) Point 1 (b) Point 2 (c) Point 3

Figure 13 Lateral local strain distribution (RH -600) strength and the compressive softening behavior of CS-600.

Figures 7, 8 and 9 show the lateral local strain distribution on the surface of specimens in uniaxial compressive cyclic loadings obtained from the lattice method by using image analysis. These displacements and strains link to points 1, 2 and 3 in Figure 6. The coarse aggregate distribution observed from the surface of the specimen is also shown.

Both compressive and tensile strains can be seen, and local and large strain concentration can not be seen at points 1 and 2. In particular, tensile strain concentration cannot be observed although applied stress is more than 60 N /mm^2 in the case of CS-500. However, the region of tensile strain is expanded as the lateral displacement becomes large. Tensile strains of more than 5.0×10^{-3} are present in all cases at point 3. These strains can be observed after the first peak load.

From Figure 6, the lateral displacements for each case are almost the same. However, the region of tensile strain of CS-500 is narrower than that of CS-400 and CS-600. This shows the strain is locally located in the case of CS-500 (Figure 8 (c)).

Cracks generated in mortar phase can be approximately predicted, since the tensile strain in the lateral direction is large in the mortar phase outside the coarse aggregate phase, at point 3 in the case of CS-400 and CS-500, as shown in Figures 7 (c) and 8 (c). However, the tensile strain is concentrated in the region where there are many coarse aggregates, in the case of CS-600, as shown in Figure 9 (c). Liu (2007) reported the tendency that many cracks are generated and propagated at the interfaces between coarse aggregate phase and mortar phase. In this research, cracks generated and propagated at the interfaces are predicted since the strain concentration near the coarse aggregate phases (high quality recycled aggregate (RH)) can be observed.

Figure 10 shows uniaxial compressive stress –lateral displacement relationship. The lateral displacement of RH-600 is large at 50 N/mm^2 comparing with that of RH-400 and RH-500. The lateral displacements of RH-400, RH-500 and RH-600 are large at 50 N/mm^2 comparing with the results observed for CS as shown in Figure 6.

Figures 11, 12 and 13 show the lateral local strain distribution on the surface of specimens in uniaxial compressive cyclic loadings obtained from image analysis by using the lattice method. These displacements and strains link to points 1, 2 and 3 in Figure 10.

Local and large strain concentration cannot be seen at point 1, similar to the case of using CS. Tensile strain concentration cannot be observed, although applied stress is more than 50 N/mm^2 in the case of RH-500. The region of tensile strain of RH-500 is narrower than that of RH-400 and RH-600 at point 3. These tendencies are same as those of using CS.

The strain concentration, crack generation and propagation in RH can be predicted, since lateral tensile strain is concentrated in coarse aggregate at point 3 in the case of RH-400, RH-500 and RH-600 as shown in Figures 11 (c), 12 (c) and 13 (c).

4. CONCLUSIONS

In this research, the compressive behaviors of high strength concrete with a large amount of coarse aggregate were clarified. Furthermore, the local behaviors under cyclic loading were investigated by using image analysis. The following summarizes the obtained results.

1) The quantity of coarse aggregate affects the compressive behavior of high strength concrete with a large amount of recycled aggregate. When the quantity of coarse aggregate is 500 ℓ, the compressive strength and the transmitted stress after peak become the largest under the uniaxial compressive cyclic loadings. Hence, the seismic performance can be improved by increasing the quantity of coarse aggregate up to 500 ℓ. However, this tendency is not significant comparing to those of using normal crushed stone.
2) It can be considered that the lateral displacement and lateral local strain affect the compressive strength and the compressive softening behavior of concrete. The influence of these parameters is small when the compressive strength is high and becomes large when the compressive strength is low.
3) The lateral local strain distribution can be identified by using image analysis. It can approximately predict the strain concentration locations such as coarse aggregate and mortar phase. Analysis indicates that strain concentrated outside aggregates in concrete using CS and inside aggregates in concrete using RH.

Acknowledgements:

Sincere gratitude is expressed to Taiheiyo Cement Corporation and Central Research Institute of Electric Power Industry for their cooperation. The authors also would like to express their gratitude to the COE program for providing financial support to accomplish this research. This study is also partially supported by Grants-in-Aid for Scientific Research, by the Ministry of Education, Science and Culture (A, No.19206050).

References:

Hayakawa, M. et al. (2003), "Mix Design and Properties of Concrete with Recycled Aggregates Produced with Different Systems," *Proceedings of the Japan Concrete Institute*, Japan Concrete Institute, **25**(1), 1247-1252. (in Japanese)

Noguchi, T. (1993), "Effect of Coarse Aggregate on Compressive Strength of High-Strength Concrete" *JCA Proceedings of Cement and Concrete*, Japan Cement Association, **47**, 684-689. (in Japanese)

Liu, Y. (2007), "Mechanical Properties of High Strength Concrete with Variance of Coarse Aggregate Quantity" *Master thesis in Tokyo Institute of Technology*, 18-22.

Matsuo, T. et al. (2004), "An Experimental Study on Shear Resisting Mechanism of RC Beams with Corroded Reinforcement," *Concrete Research and Technology*, Japan Concrete Institute, **15**(2), 69-77. (in Japanese)

Fifth International Conference on Urban Earthquake Engineering
March 4-5, 2008, Tokyo Institute of Technology, Tokyo, Japan

GENERALIZED SCALING RELATIONS FOR DYNAMIC LEVEL GROUND RESPONSE

Tetsuo Tobita [1], Susumu Iai [2] and Saki Noda [3]

1) Assistant Professor, Disaster Prevention Research Institute, Kyoto University, Japan
2) Professor, Disaster Prevention Research Institute, Kyoto University, Japan
3) Student, Department of Civil and Earth Resources Engineering, Kyoto University, Japan
tobita@geotech.dpri.kyoto-u.ac.jp, iai@geotech.dpri.kyoto-u.ac.jp, noda@geotech.dpri.kyoto-u.ac.jp

Abstract: To investigate the generalized scaling relation in centrifuge modeling, a prototype is scaled down to 1/100 with 9 combinations of scaling factors of virtual 1 G and centrifugal field. The model ground is flat and made of a homogeneous sand layer. Five accelerometers are employed in various depths. Dynamic input motions are scaled accordingly. In prototype scale, the applicability of the scaling relation is evaluated by examining the identity of dynamic responses obtained from 9 cases. Results show that shear wave velocities are approximately the same value and, therefore, the generalized scaling relation of shear wave velocity is confirmed. For the scaling relation of acceleration, when the ground response is nearly elastic, the scaling law is confirmed for a range of centrifugal acceleration applied in this study.

1. INTRODUCTION

The size of physical model is increasing with demands from earthquake engineering community for rigorous investigation on structure's ultimate state. For example, the world largest shaking table of 20 × 15 m has been built in the E-defense, Japan. It can shake a real scale 6-story reinforced concrete building (1,000 t) (Chen et al. 2006), or 2 wooden Japanese houses simultaneously (Suzuki et al. 2006). However, even with such a large shaking table, when dynamic behavior of a whole structure including its foundation buried into the ground is examined, a prototype has to be scaled down due to limitations of shaking table's capacity (Tokimatsu et al. 2007).

In centrifuge modeling, geometrical scale of a model can be theoretically decreased by increasing the centrifugal acceleration. However, with decreasing model scale, the problem of scaling effects, i.e., dependence of model behavior on a relative size of structure and granular material, becomes more and more apparent (e.g., Honda and Towhata 2006). Other problems for dynamic testing under larger centrifugal acceleration are the requirements of more powerful actuator and its precise control (Chazelas et al. 2006).

To overcome these deficiency in centrifuge tests and increase the efficiency of small to medium size geotechnical centrifuges, two stage scaling relationship called generalized scaling relationship for centrifuge tests was proposed by Iai et al. (2005) (Figure 1). In this scaling relation, recorded physical model parameters are converted to those in the virtual 1G field with scaling factor for centrifuge model tests, η [Fig. 1(a)], then the parameters are further converted to prototype with scaling factor for 1G tests, μ [Fig. 1(b)] (Iai 1989). By using this scaling relationship, model tests with scaling factor (prototype/physical model) of 100 or much higher may be possible.

Tobita and Iai (2007) studied the applicability of the scaling law with pile foundations. However, they encountered some difficulties concerned with precise control of shake table required for rigorous investigations. In the present study, a newly equipped shake table is employed. In the experiments, a prototype is scaled down to 1/100 with 9 combinations of scaling factors of virtual 1 G and centrifugal field. Input motions are also scaled accordingly. Then the generalized scaling relation is examined by comparing dynamic responses in the prototype scale. If the generalized scaling law is valid, those responses are identical regardless of scaling factors. In the present paper, only 4 out of 9 cases, and cases of the smallest input motion are mainly discussed.

2. GENERALIZED SCALING RELATIONSHIP

This section briefly reviews the derivation of generalized scaling relationship (Iai et al. 2005) of physical model tests based on the fundamental physical laws, for example, stress equilibrium, definition of strains, and a constitutive relation.

Stress equilibrium:

$$\partial\sigma_{ij,j} + X_i = \rho\ddot{u}_i \tag{1}$$

Definition of strain:

$$\varepsilon_{ij} = \left(u_{i,j} + u_{j,i}\right)/2 \tag{2}$$

Constitutive relation:

$$\sigma_{ij} = C_{ijkl}\varepsilon_{kl} \tag{3}$$

where σ_{ij} is stress tensor, x_i is coordinate system, ρ is density, $\ddot{u}_i$ is acceleration and dots mean temporal

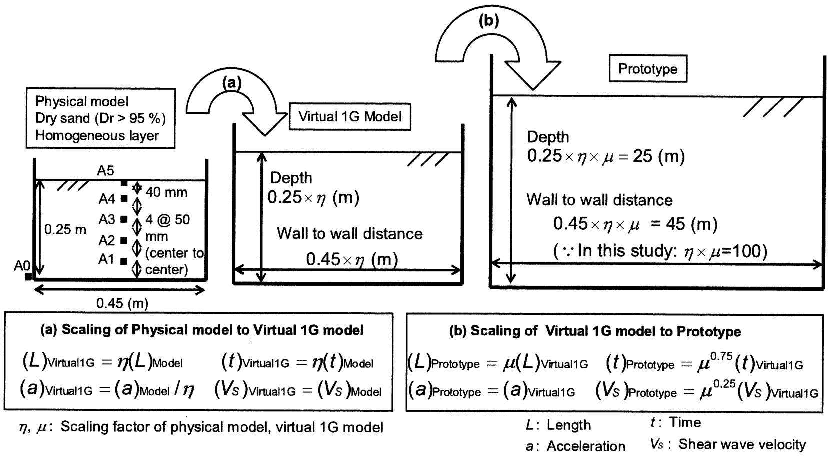

Figure 1. Physical model setup and concept of the two stage scaling with associated scaling relationship: (a) scaling relations for centrifugal field and (b) scaling relations for 1G field.

differentiation and $X_i = (0, -\rho g, 0)$, g is acceleration due to gravity, ε_{ij} is strain tensor and C_{ijkl} is tangential stiffness modulus. Here, the summation rule is supposed.

The scaling relations for centrifuge model tests are derived by introducing scaling factors for variables appearing in equations (1) - (3) as follows and by demanding that these variables must satisfy both the equations for prototype and the model.

$$(x_i)_p = \lambda (x_i)_m, \ (\sigma_{ij})_p = \lambda_\sigma (\sigma_{ij})_m, \ (u_i)_p = \lambda_u (u_i)_m,$$
$$(\rho)_p = \lambda_\rho (\rho)_m, \ (g)_p = \lambda_g (g)_m, \ (\varepsilon_{ij})_p = \lambda_\varepsilon (\varepsilon_{ij})_m,$$
$$(t)_p = \lambda_t (t)_m, \ (C_{ijkl})_p = \lambda_C (\varepsilon_{ijkl})_m$$

where subscripts "p" and "m" mean, respectively, "prototype" and "model." By substituting variables for prototype into Eq. (1),

$$(\sigma_{ij,j})_p + (X_i)_p = (\rho)_p (\ddot{u}_{ij})_p \tag{4}$$

Then introducing scaling relations into Eq. (4),

$$\lambda_\sigma / \lambda (\sigma_{ij,j})_m + \lambda_\rho \lambda_g (X_i)_m = \lambda_\rho \lambda_u / \lambda_t^2 (\rho)_m (\ddot{u}_{ij})_m \tag{5}$$

Since variables for model also satisfy Eq. (1), then all the coefficients of Eq. (5) must be equal as follows,

$$\lambda_\sigma / \lambda = \lambda_\rho \lambda_g = \lambda_\rho \lambda_u / \lambda_t^2 \tag{6}$$

Table 1. Generalized scaling factors for centrifuge model tests ($\mu_\varepsilon = \mu^{0.5}$) (Iai et al. 2005)

	Partitioned		Generalised
	Centrifugal field	Virtual 1G field	
	η=Prototype /physical model	μ=Prototype /virtual model	Prototype /physical model
Length	η	μ	$\mu\eta$
Density	1	1	1
Time	η	$\mu^{0.75}$	$\mu^{0.75}\eta$
Stress	1	μ	μ
Pore water pressure	1	μ	μ
Displacement	η	$\mu^{1.5}$	$\mu^{1.5}\eta$
Particle velocity	1	$\mu^{0.75}$	$\mu^{0.75}$
Shear wave velocity	1	$\mu^{0.25}$	$\mu^{0.25}$
Acceleration	$1/\eta$	1	$1/\eta$
Strain	1	$\mu^{0.5}$	$\mu^{0.5}$
Bending moment	$\eta^{3.0}$	$\mu^{4.0}$	$\mu^{4.0}\eta^{3.0}$
Flexial rigidity	$\eta^{4.0}$	$\mu^{4.5}$	$\mu^{4.5}\eta^{4.0}$

Now, from the left hand side of Eq. (6), the scaling relation of stress is written as,

$$\lambda_\sigma = \lambda \lambda_\rho \lambda_g \tag{7}$$

From Eq. (2), (3) and (6) in the same way, the scaling relation of time, displacement and stiffness are given by,

$$\lambda_t = \left(\lambda \lambda_\varepsilon / \lambda_g\right)^{0.5}, \ \lambda_u = \lambda \lambda_\varepsilon, \ \lambda_C = \lambda \lambda_\rho \lambda_g / \lambda_\varepsilon \tag{8}$$

Now let us partition the scaling factors for length, density, acceleration, and strain as follows,

$$\lambda = \eta\mu, \ \lambda_\rho = \eta_\rho \mu_\rho, \ \lambda_g = \eta_g \mu_g, \ \lambda_\varepsilon = \eta_\varepsilon \mu_\varepsilon \tag{9}$$

where η and μ denote respectively the scaling factor of length for centrifuge and 1 g model tests. The value of the scaling factor for acceleration due to gravity in 1 g field is unity ($\mu_\sigma = 1$) and that for centrifugal field is $\eta_g = 1/\eta$. The scaling factor for density and strain in centrifugal field are $\eta_\sigma = \mu_\varepsilon = 1$. Substituting these into the above relations yields the generalized scaling relationship,

$$\lambda = \eta\mu, \ \lambda_\rho = \mu_\rho, \ \lambda_g = 1/\eta, \ \lambda_\varepsilon = \mu_\varepsilon \tag{10}$$

In general, scaling relation of shear wave velocity can be derived as follows by using the shear wave velocity of the model ground, $(V_s)_m$, and that of the prototype ground, $(V_s)_p$. Shear modulus at small strain, of the model ground $(G_0)_m$ and the prototype ground $(G_0)_p$ are expressed,

$$(G_0)_m = (\rho)_m (V_S)_m^2 \tag{11}$$

$$(G_0)_p = (\rho)_p (V_S)_p^2 \tag{12}$$

Table 2. Scaling factors applied in the present study

	Scaling factor		
	Centrifugal field	Virtual 1G field	Prototype
Case	η	μ	$\mu\eta$
1G	1	100	
8G	8	12.5	
10G	10	10	
20G	20	5	
30G	30	3.33	100
40G	40	2.5	
50G	50	2	
60G	60	1.67	
70G	70	1.43	

These moduli give the scaling factor for the tangent modulus of soil as,

$$\begin{aligned}\lambda_C &= [(\rho)_p (V_S)_p^2]/[(\rho)_m (V_S)_m^2] \\ &= \lambda_\rho [(V_S)_p/(V_S)_m]^2\end{aligned} \quad (13)$$

whereas the similitude of shear modulus is $\lambda_C = \lambda\lambda_\rho\lambda_g/\lambda_\varepsilon$ (Eq. 8). Consequently, the scaling factor for the strain is given by,

$$\lambda_\varepsilon = \lambda\lambda_g/[(V_s)_p/(V_s)_m]^2 \quad (14)$$

Therefore, the scaling relation of shear wave velocity is given by,

$$\begin{aligned}\lambda_{Vs} &= (V_s)_p/(V_s)_m = \sqrt{\lambda\lambda_g/\lambda_\varepsilon} \\ &= \sqrt{(\eta\mu)(\eta_g\mu_g)/\mu^{1-N}} = \sqrt{(\eta\mu)(1/\eta)/\mu^{1-N}} = \mu^{N/2}\end{aligned} \quad (15)$$

where the scaling factor of strain is assumed to be $\mu_\varepsilon=\mu^{1-N}$. The generalized scaling relationships are summarized in Table 1 with the scaling factor of density and strain $\mu_\rho=1$ and $\mu_\varepsilon=\mu^{0.5}$ (i.e., N=0.5) in 1 g field (Iai 1989). Note that the scaling factor of particle velocity, $\mu^{0.75}$ is different from that of shear wave velocity, $\mu^{0.25}$ in 1g field.

3. CENTRIFUGE MODEL TESTS AND INVESTIGATION OF THE GENERALIZED SCALING LAW

The experiments were conducted in a rigid wall container mounted on 2.5 m radius geotechnical centrifuge at the Disaster Prevention Research Institute, Kyoto University (DPRI-KU). Overall dimensions of the rigid container are 450 × 150 × 300 mm in length, width, and height, respectively. Dynamic excitation was given in the direction parallel to the cross-section shown in Figure 1 by a shake table mounted on a platform. The shake table was controlled by displacement signals. An accelerometer was attached to the base plate of the shake table to measure input motion. Five accelerometers were installed in the model ground of compacted dry silica sand (e_{max}=1.19, e_{min}=0.71, and D_{50}=0.15 mm) with relative density more than 95% (Figure 1). To obtain firm model ground, dry tamping method was employed.

As shown in Table 2, total 9 cases with various scaling factors of length, η and μ were considered. Since the model ground was well compacted, the experiments were consecutively carried out from small to large centrifugal acceleration. The scaling factors of centrifugal field, η, correspond to the centrifugal acceleration, while the scaling factors of the virtual 1 G field, μ are selected so that the scaling factor of prototype, $\eta \times \mu$, is equal to 100. Other scaling factors, time, shear wave velocity, displacement and acceleration for each centrifugal acceleration are given in Figure 2 together with the scaling factor of length whose value is constant, i.e., $\eta \times \mu$=100. As shown in Fig. 2(b), the scaling factor of shear wave velocity is rather insensitive to centrifugal acceleration (it varies from 1 to 3 for a range of 1 G to 70 G), while that of acceleration and displacement are sensitive to centrifugal acceleration. Scaling factor of acceleration varies from 1 to 0.014 in a range of centrifugal acceleration of 1 G to 70 G, and that of displacement from 1000 to 120 in the same range of centrifugal acceleration.

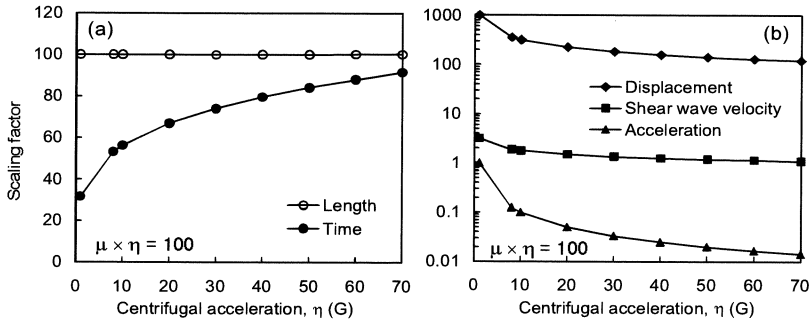

Figure 2. Scaling factors of length and time (a), displacement, shear wave velocity and acceleration (b) for model tests conducted in the present study.

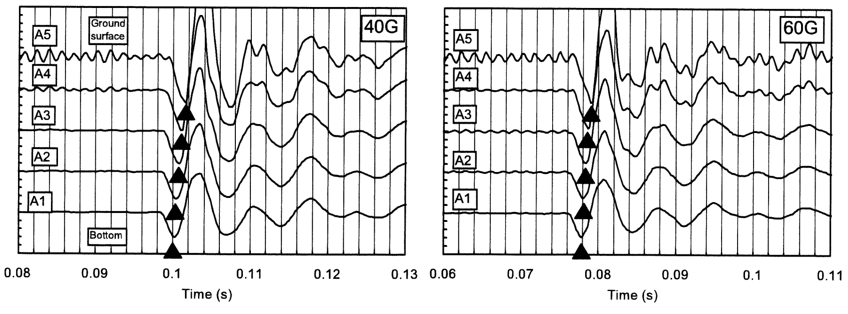

Figure 3. Time histories of response acceleration against impulsive input motion and arrival time of the 1st peak specified with solid triangle for Cases 40 G and 60 G (in model scale).

The scaling factor of time varies from 31 to 91 in a range of 1 G to 70 G.

To evaluate scaling relationship of the shear wave velocity, travel time of impulsive input motion (single sin wave with 250 Hz in model scale) was measured. The travel time in this study was taken as the arrival of the 1st peak due to a difficulty encountered to specify exact arrival time of signals. Based on the time histories of acceleration, such as shown in Fig. 3 for cases 40 G and 60 G, shear wave velocities in the model scale were derived [Fig. 4(a)], then, by using scaling factors shown in Fig. 2(b), they were converted to the prototype scale [Fig. 4(b)]. Shear wave velocities with different markers shown in Fig. 4 are derived by the difference of distance and travel time between sensors A3 to A5 and A1. Travel time of A2 was not used because time difference between A1 and A2 was too small to be captured by the sampling frequency employed in the tests (5 kHz). In model scale, shear wave velocities tend to increase as centrifugal acceleration increase [Fig. 4(a)], while, in prototype scale [Fig. 4(b)], shear wave velocity becomes more or less constant, about 230 m/s on average.

Next, to investigate the scaling law of acceleration, the

Table 3. Input frequencies for sinusoidal waves

Case	Frequency (Hz) Centrifugal field	Prototype
1G	20.6	
8G	34.6	
10G	36.6	
20G	43.5	
30G	48.1	0.65
40G	51.7	
50G	54.7	
60G	57.3	
70G	59.5	

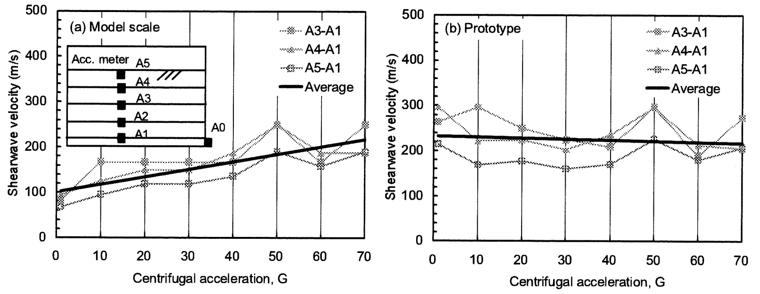

Figure 4. Shear wave velocities in model scale (a), and prototype (b)

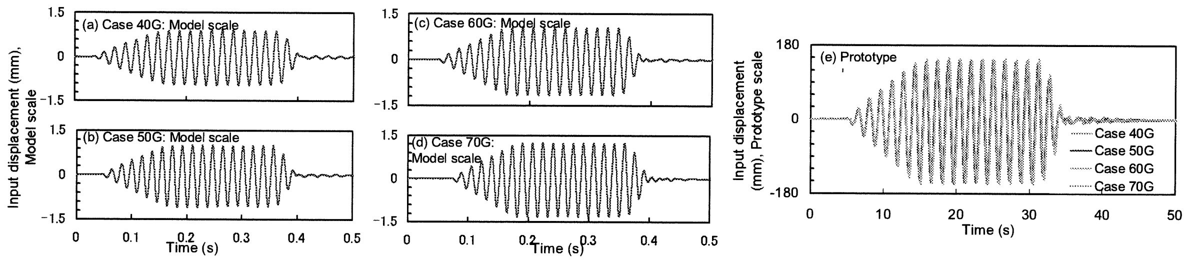

Figure 5. Time histories of input displacements of Case 40G (a), 50G (b), 60G (c), and 70G (d) in model scale, and all cases combined in prototype scale (e).

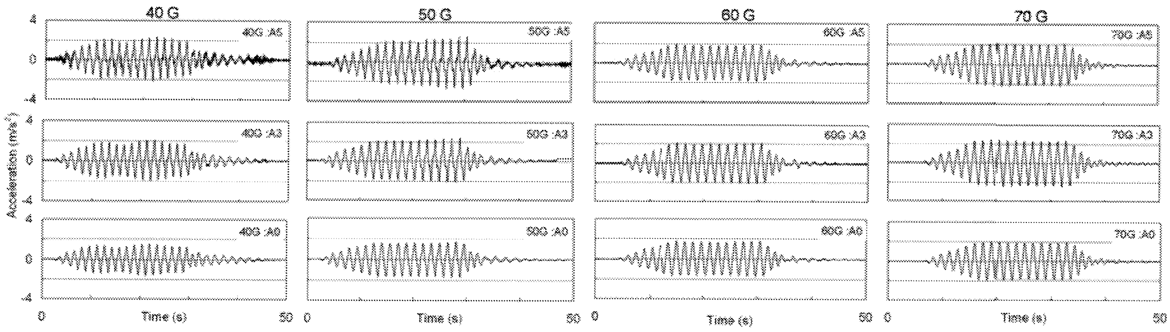

Figure 6. Time histories of input (A0) and response (A3 and A5) acceleration of Cases 40 G to 70G.

model was excited by sinusoidal input motions (0.65 Hz, duration 35 s in prototype scale) (Table 3). Figures 5(a) to (d) are the time histories of input displacements in model scale and Fig. 5(e) is the converted time history in prototype scale. A range of displacement amplitude is from 0.9 mm to 1.2 mm in model scale. After conversion, the amplitude becomes 150 mm in prototype scale. As shown in Fig. 5(e), similar input motions were employed in all cases. Time histories of acceleration recorded at the base (A0), in the middle layer (A3), and at the ground surface (A5) for Cases 40 G to 70 G are plotted in Fig. 6. These are all in prototype scale. As seen in Fig. 6, all the input and response acceleration amplitude except for Case 40 G are about 2 m/s^2 indicating the response may be in a linear elastic range. In this range, the generalized scaling law of acceleration under the centrifugal acceleration of 50 G up to 70 G is validated. For Case 40 G, input acceleration amplitude is reduced to about 1 m/s^2. This might be due to the mechanical resonance of the centrifuge equipment used in the present study as seen in Fig. 6 (Case 40 G) with lasting vibration after the end of shaking. The other possibility is the sensitivity of scaling factor of acceleration to centrifugal acceleration shown in Fig. 2(b). Considering other tests cases with lower centrifugal acceleration, the applicability of the generalized scaling relation is largely confirmed.

4. CONCLUSION

Applicability of the generalized scaling law for centrifuge modeling is investigated. In the present study, a prototype is scaled down to 1/100 with 9 combinations of scaling factors of virtual 1 G and centrifugal field. Input motions are also scaled accordingly. Four out of 9 cases with the smallest input motions are mainly discussed. The generalized scaling relation is investigated by comparing responses in the prototype scale. Prototype shear wave velocities were close each other and the generalized scaling law of shear wave velocity was confirmed. For the scaling law of acceleration, when the ground response was nearly linear elastic, the scaling law was confirmed with centrifugal acceleration of 50 G up to 70G. Considering other tests cases with lower centrifugal acceleration, the applicability of the generalized scaling relation is largely confirmed.

Acknowledgements:

The financial support for this research is provided by the Japan Ministry of Education, Culture, Sport, Science, and Technology (MEXT), Scientific Research (B) under Grant No. 18360228.

References:

Chazelas, J. L., Derkx, F., Thorel, L., Escoffier, S., Rault, G., Buttigieg, S., Cottineau, L. M., and Garnier, J. (2006). "Physical modelling of earthquakes in the LCPC centrifuge." 1st European Conference on Earthquake Engineering and Seismology, 3-8 September, Geneva, Switzerland., ID 1064.

Chen, S., Kabeyasawa, T., and Kabeyasawa, T. (2006). "Analytical research of full-scale reinforced concrete structure test on E-Defense." Proceedings of the 100th Anniversary Earthquake Conference, San Francisco, California, USA, April 18-22, 8NCEE-000666.

Honda, T., and Towhata, I. (2006). "Study of similarity rules in centrifuge model tests on embankment during liquefaction." The 41 st Japan National Conference on Geotechnical Engineering, Kagoshima, Japan, No. 928.

Iai, S. (1989). "Similitude for shaking table tests on soil-structure-fluid model in 1g gravitational field." Soils and Foundations, 29(1), 105-118.

Iai, S., Tobita, T., and Nakahara, T. (2005). "Generalized scaling relations for dynamic centrifuge tests." Géotechnique, 55(5), 355-362.

Suzuki, Y., Saito, Y., Okuda, T., Ogasawara, M., and Suda, T. (2006). "Large-scale shaking table tests of Kyoto's traditional wood houses." The Annual Conference of Disaster Prevention Research Institute, Kyoto University, E-07.

Tobita, T., and Iai, S. (2007). "Verification of generalized scaling relations for dynamic centrifuge experiments." 4th International Conference on Urban Earthquake Engineering, Tokyo Institute of Technology, 755-762.

Tokimatsu, K., Suzuki, H., Sato, M., and tabata, K. (2007). "Soil-pile-structure interaction during multi-dimensional shaking through physical model tests using E-Defense facility." The Fourth International Conference on Urban Earthquake Engineering 841-848.

Fifth International Conference on Urban Earthquake Engineering
March 4-5, 2008, Tokyo Institute of Technology, Tokyo, Japan

EXPERIMENTAL EVALUATION OF STRESS STATE AROUND PILE GROUP DURING LATERAL FLOW OF LIQUEFIED SOIL

Ramin Motamed[1], Ikuo Towhata[2], and Mitsutoshi Yoshimine[3], Ngo Tuan Anh [4]

1) JSPS Postdoctoral Fellow, Department of Civil Engineering, Tokyo Institute of Technology, Japan
2) Professor, Department of Civil Engineering, The University of Tokyo, Japan
3) Associate Professor, Department of Civil Engineering, Tokyo Metropolitan University, Japan
4) Graduate Student, Institute of Industrial Science, The University of Tokyo, Japan.
motamed@cv.titech.ac.jp, towhata@geot.t.u-tokyo.ac.jp, yoshimine-mitsutoshi@c.metro-u.ac.jp, ngo1982@iis.u-tokyo.ac.jp

Abstract: This paper presents the results of a series of 1-g shaking table model tests conducted on a 3×3 pile group subjected to liquefaction-induced large ground deformation. The stress state of soil around the pile group was assessed experimentally using two different methods. In the first approach, excess pore water pressure records were utilized. In the second technique, vane shear test data performed before and after shaking were employed. The results from both approaches consistently confirmed the compression stress state in front of pile group (up-slope) and extension stress condition in back side of pile group (down-slope).

1. INTRODUCTION

Pile foundations located in liquefiable sloping ground or near waterfront structures are susceptible to kinematic force caused by liquefaction-induced lateral spreading. Several case histories have been reported from the 1964 Niigata, 1964 Alaska, 1983 Nihonkai-Chubu, and 1995 Kobe earthquakes (Hamada et al. 1986, Bartlett and Youd 1992, Tokimatsu and Asaka 1998). The significant damages to the piles revealed that in addition to inertial force of structure, the kinematic force of liquefied soil during large lateral displacement also should be properly considered in design procedure. Although some design codes, e.g. JRA2002, have already initiated applying the lateral force of the liquefied soil, the mechanism of this lateral force is not completely clear yet.

Tokimatsu and Suzuki (2004) investigated the pore water pressure response on the subgrade reaction of pile during liquefaction through large shaking table tests on soil-pile-structure systems. They found that relative displacement between soil and pile during liquefaction alternatively creates extension stress state on one side and compression stress state on the other side of the other side of the pile. Their experimental results showed that pore pressure and earth pressure on the extension side decrease significantly, while those on the compression side maintain almost constant or increase slightly. However, they mainly focused on the cyclic behavior of soil-pile-structure system; while, it is believed that the large monotonically increasing shear strain in soil becomes dominant during lateral spreading.

Goh and O'Rourke (1999) presented an analytical model and design procedure for foundation piles subjected to large lateral ground deformation triggered by liquefaction using *p-y* method. They considered the stress conditions around pile to characterize a proper *p-y* curve and used the triaxial extension test as the most appropriate analogue for the loading condition.

This paper aims to evaluate the stress state around a pile group when subjected to liquefaction-induced large ground displacement. Experimental program includes a series of 1-g shaking table model tests a 3×3 pile group in which piles were subjected to liquefaction-induced large ground displacement. Two different approaches were employed in this study to investigate the stress state. In the first method, pore water pressure records were utilized; while, in the second technique, vane shear apparatus was used to distinguish the stress conditions around the pile group.

2. 1-G SHAKING TABLE MODEL TESTS

A series of 1-g shaking table model tests was conducted on a 3×3 pile group in a sloping ground in the Geotechnical Engineering Laboratory, The University of Tokyo. Schematic cross section and plane view of the tests are illustrated in Figure 1. As can be seen, configuration of the model was a gently sloping ground with the inclination of 5%. Piles were fixed at the bottom against any rotation or displacement, being free at top (see Table 1 for material properties). Spacing between piles was 2.8D (D is the pile diameter, D=3.2 cm). The model ground consisted of a liquefiable soil layer made of Toyoura sand (see Table 2 for properties) mainly with the relative density of 30% which were prepared using water sedimentation method. Table 3 provides the specifications of these experiments. The main objective of this series of experiments was to study the behavior of pile group subjected to liquefaction-induced large ground deformation. As a result, in order to reproduce the in-situ stress-strain behavior of the liquefied soil, model ground was prepared with much lower density in 1-g shaking table models than the prototype density (Towhata, 2008). The models were densely instrumented with various sensors such as accelerometers, pore water pressure (PWP) transducers, inclinometers, laser-displacement transducer, and a shapeware. Shapeware is a fiber optic based sensor originally developed for biomedical studies to capture human body's movement; however, it was employed in this research to record the lateral soil displacement between piles inside the group. In addition, many strain gauges were pasted on the piles to measure bending strain. Thus, the time histories of numerous parameters were recorded during shaking and some results are presented in this paper. Furthermore, it should be noted that since the main objective of this study concerns the kinematically induced-lateral force of liquefied soil, the monotonic components of some of the recorded parameters (e.g. displacement and bending moment) were focused on after filtering out the cyclic component. Sign convention in this study is as follows: horizontal ground displacement, and lateral soil pressure were considered positive in the down-slope direction, while acceleration was assumed to be positive in the up-slope direction. Further details of the model preparation, materials, and instrumentations can be found in Motamed (2007).

Figure 2 shows an example of input motion which was applied to the model in the direction parallel to the slope of ground. As can be seen, the input motion was gradually increased during the first fifteen seconds, then kept constant for ten seconds, and finally was gradually decreased within ten seconds.

Table 1 Material properties of pile foundation

Material	Polycarbonate
Height (cm)	53
Outer/Inner diameter (cm)	3.2/2.7
E (N/cm^2)	2.7×10^5
I (cm^4)	2.5385

Table 2 Basic geotechnical properties of Toyoura sand

Specific gravity (g/cm^3)	2.651
Maximum void ration, e_{max}	0.971
Minimum void ration, e_{min}	0.615
Mean grain size, D_{50}	0.204
Coefficient of uniformity, U_c	1.233

Table 3 Experimental program of 1-g shaking table model tests

Test no.	Relative density (%)	Frequency (Hz)	Amplitude (Gal)
Test 1	30%	10	300
Test 2	30%	5	300
Test 3	30%	3	300
Test 4	18%	10	500
Test 5	30%	10	500
Test 6	30%	10	150

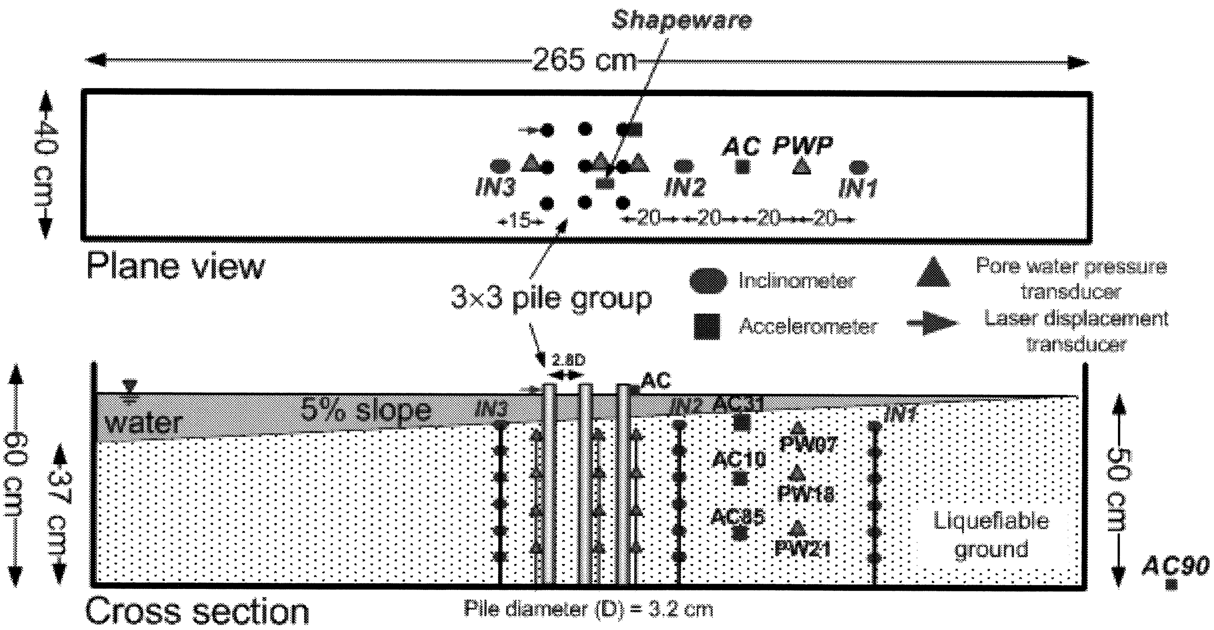

Figure 1 Configuration of 3×3 pile group in sloping ground model

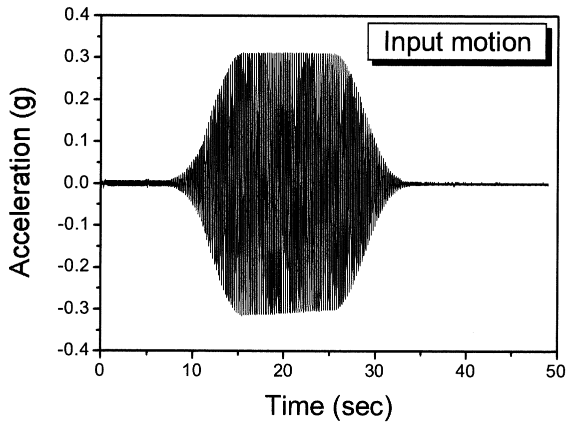

Figure 2 Time history of input motion – Test 2 (300 Gal, 5 Hz)

3. SOIL AND PILE LATERAL DISPLACEMENT

The lateral soil displacement was measured by three inclinometers and a shapeware. As is shown in Figure 1, soil displacement was measured at four points: far from pile group in up-slope, in front of pile group in up-slope, between piles inside group, and back side of pile group in down-slope. These instruments were able to provide the time history of lateral soil displacement at different depths. In addition, colored sand and small tags were employed to record the residual ground deformation. Small tags were put on the ground surface at different predetermined points to understand the deformation pattern of the liquefied sand during lateral spreading.

Reliability and accuracy of each method has been thoroughly investigated by the direct observation after each experiment which results can be found in Motamed (2007). Results from this evaluation indicated that the inclinometers can provide a sound estimation of the lateral soil displacement, and the shapeware sensor can also supply a valuable information of soil displacement with an acceptable resolution specially in cases in which no inclinometer can be utilized (e.g. between piles inside group). The deflection of pile was obtained through two approaches. In the first method, deflection at pile head was recorded by a laser sensor which was fixed to measure the pile deflection at top. While in the second technique, the deflection along the pile was back calculated from bending strain data. Due to the page limitation, this back calculation is not explained in this paper, and further information can be found in Motamed (2007). An example of both soil and pile displacements are given in Figure 3. This figure includes the time histories of monotonic component of soil displacement at four aforementioned points, and the curves illustrate that the soil deformation at back side of pile group in down-slope was the largest; while, the soil movement inside the pile group was the smallest. The soil lateral displacement showed a steady increase throughout the shaking, approaching a residual values at the end of shaking.

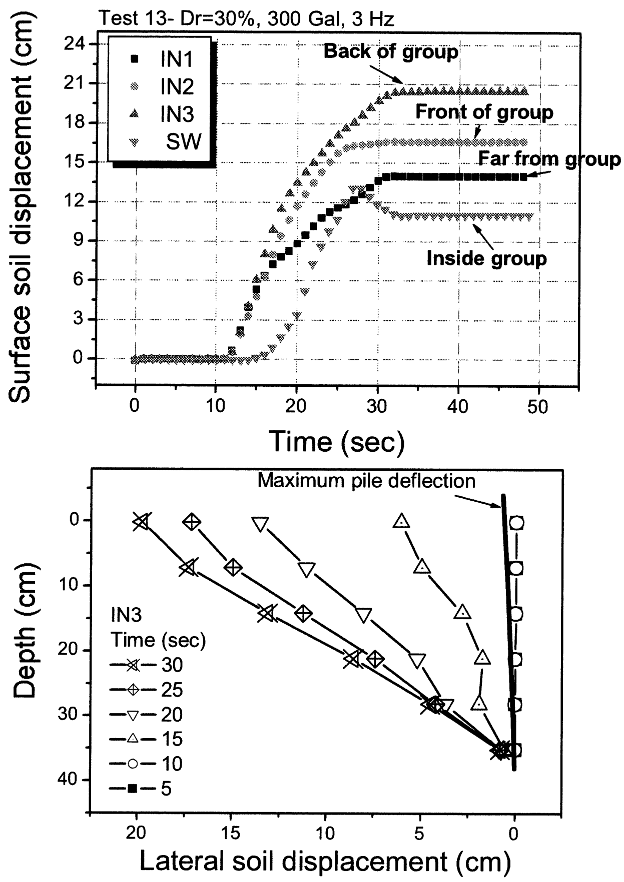

Figure 3 (a) time histories of soil displacement at ground surface, (b) profile of soil deformation at back side of pile group in down-slope and maximum pile deflection

Furthermore, the profile of soil lateral displacement is displayed in Figure 3 at different time steps. As is shown, the maximum soil deformation occurred at the ground surface. For comparison, the maximum pile deflection is also included in this figure, and it is apparent that the soil lateral flow is much larger than the maximum pile deflection.

4. EXCESS PORE WATER PRESSURE

Generation of excess pore water pressure during shaking was recorded by several pore water pressure sensors at different positions: far from group in up-slope, in front of group in up-slope, between piles inside group, and back side of group in down-slope (Figure 1). At each point, the sensors were put at different depths of ground. For instance, Figure 4 displays the recorded pressure data in front of pile group in up-slope at different levels. As can be seen, high excess pore water pressure developed just at the early stage of shaking and maintained throughout the test. The results in this section confirmed that the liquefaction state was achieved successfully in these experiments.

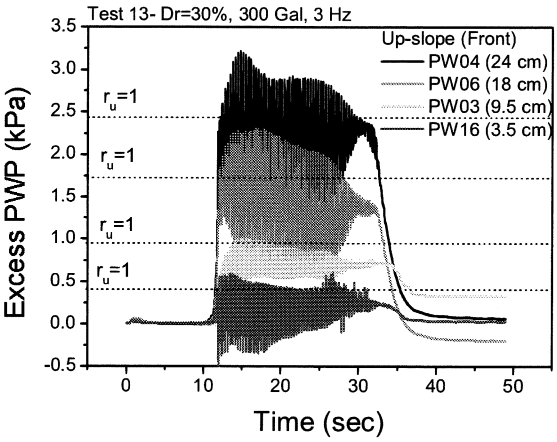

Figure 4 Time histories of excess pore water pressure in front of pile group (up-slope)

In order to investigate the stress state around the pile group, a numerous number of pore water transducers were installed on the piles, providing valuable information of stress state in soil. Figure 5 schematically illustrates the suspected stress conditions and the position of PWP sensors in the model. It is worthy to note again that the lateral soil displacement was far larger than the pile deflection, being similar to a monotonic lateral force of liquefied soil on the piles. An example of recorded PWP data at both front and back sides of pile group is given in Figure 6. As can be seen, although they had a similar amplitude, record in back side showed a significant drop which would be as a result of the extension stress condition in back side of pile group in down-slope. This apparent drop diminished when the lateral flow stopped,; however, PWP still maintained a high value due to liquefaction state.

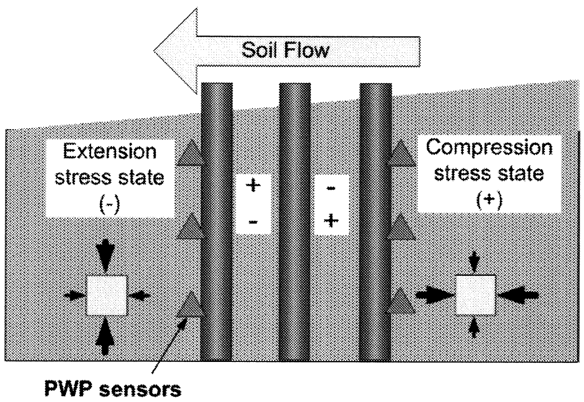

Figure 5 Stress state around a pile group in sloping ground and position of PWP sensors

Furthermore, it was observed that the PWP records in front and back sides of the pile group are out of phase, since they were located in opposite sides of the piles, i.e. up-slope and down-slope.

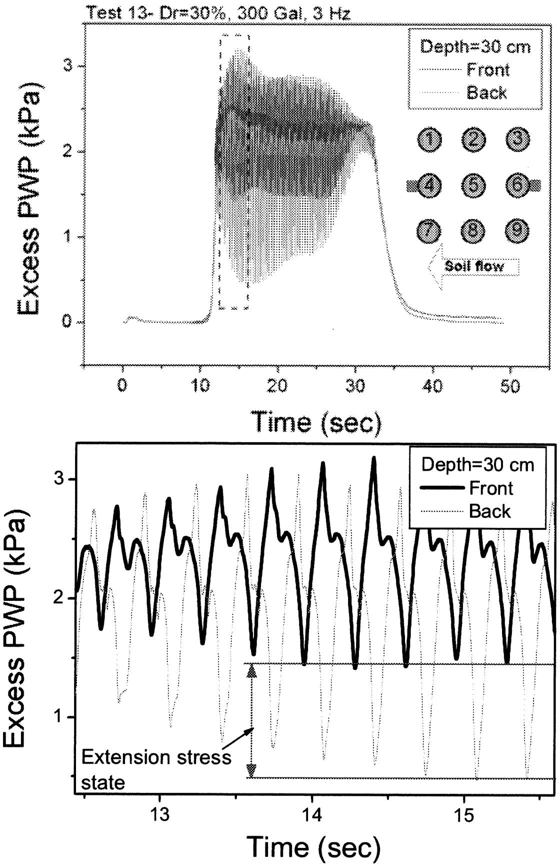

Figure 6 Excess pore water pressure records in front and back sides of pile group (a) whole records (b) close up

5. VANE SHEAR TEST

The second technique to determine the stress state in the soil around the pile group was to use a vane shear apparatus (Figure 7). This small apparatus was employed to measure the undrained shear strength of the loose saturated soil. The measurements were conducted at several positions and different depths (10cm, 15cm, and 20cm). The data presented in this paper are limited to the measurements which were carried out at three points: far from the pile group, in front of the pile group in up-slope, and back side of the pile group in down-slope. According to the illustration in Figure 5, the data in front of pile group supposed to represent the compression stress state, while those recorded in the back side display the extension stress condition. In addition, the data of the point far from the pile group could be perceived as a neutral condition or isotropic state.

To evaluate the stress conditions, the vane shear measurements were performed at each point two times: before and after the shaking, and the results are given in Figure 8. In this figure, the vertical axis demonstrates the data of vane shear test after the shaking, while the horizontal axis reveals the vane shear values before experiment. Hence, slope of the fitted linear curve represents extend of the contraction in the soil due to shaking. According to the results, the slope of fitted curves in the compression stress state increased in comparison with the isotropic stress condition; while, it decreased in the extension stress circumstance. Furthermore, the ratio of vane shear test data after and before experiments was calculated for different depths and the average of results are illustrated in Figure 9. This figure expresses the stress conditions around pile group in another way. As can be seen, the ratio is the largest in all depths in the front side of pile group in up-slope demonstrating compression stress state, while is the smallest in the back side of pile group in down-slope revealing extension stress conditions. The data which correspond to the isotropic stress state (far from pile group) also locates between these two extreme states.

It should be mentioned here that the increment in the recorded vane shear data after the shaking includes the effect of reconsolidation after the liquefaction too. Since this effect would be identical for all points, the results could clearly illustrate the stress conditions.

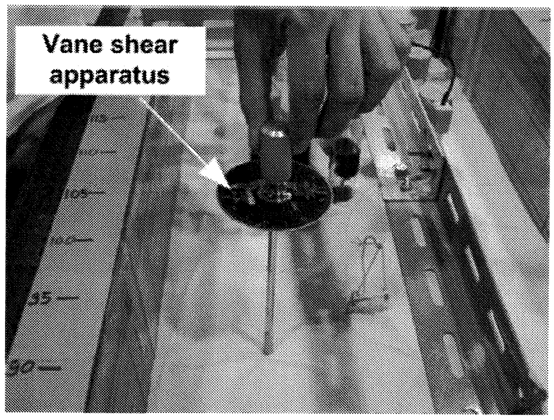

Figure 7 Vane shear apparatus used in this study (blade was penetrated into soil)

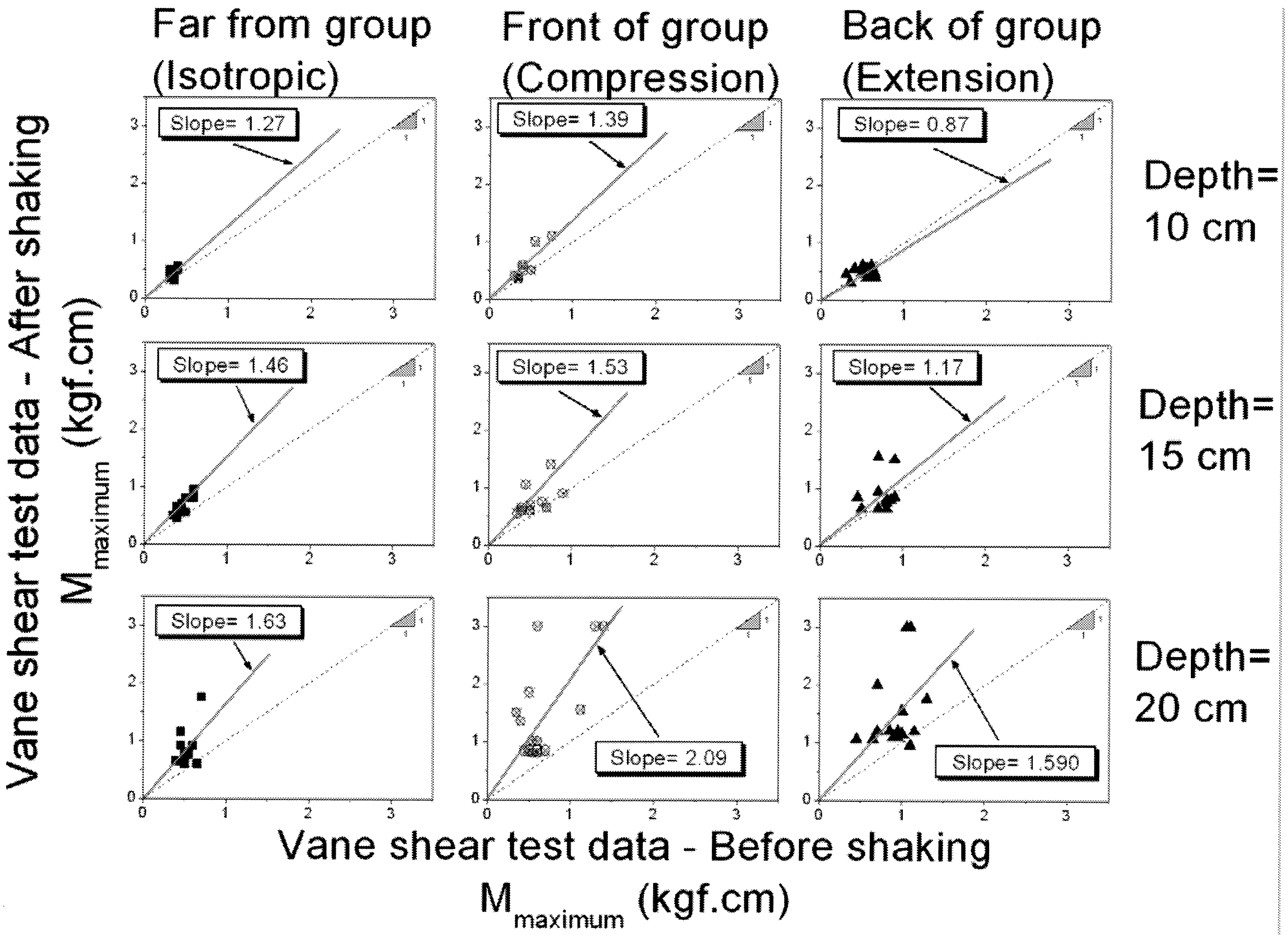

Figure 8 Vane shear test data measured before and after shaking at different depths

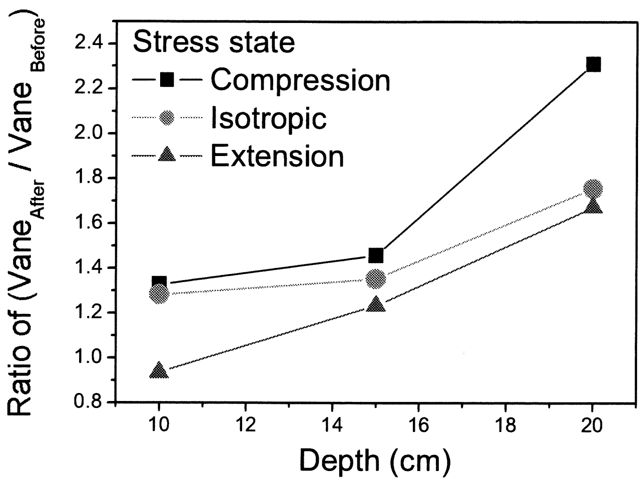

Figure 9 Ratio of vane shear data before and after shaking (average)

6. CONCLUSIONS

The stress condition around a pile group during the liquefaction-induced large ground displacement was investigated using two different approaches. The results from the experiments lead to the following conclusions:

1. Excess pore water pressure data which were recorded at front of pile group in up-slope side showed steady higher lever illustrating the compression stress state. The fluctuations in the PWP data were because of soil-pile interaction.
2. The significant drops in the PWP data which were recorded at back side of pile group in down-slope revealed the extension stress state
3. The comparison between vane shear test data measured at different positions also confirmed the aforementioned stress conditions around pile group. The ratio of vane shear test data after shaking to those measured before shaking was obtained, and the results showed that the largest ratio belonged to the data in front of pile group (up-slope), indicating compression stress state. The smallest ratios also were observed for the data at the back of pile group in down-slope; while, the data measured at far from pile group located in between, indicating the isotropic stress state.

References:

Bartlett, S.F., and Youd, T.L. (1992) "Case histories of lateral spread caused by the 1964 Alaska earthquake" *Case Studies of Liquefaction and Lifeline Performance During Past Earthquakes*, Vol. 2, United States Case Studies, Technical Report NCEER-92-0002, NCEER, Buffalo, NY.

Goh, S.H., and O'Rourke, T.D. (1999) "Limit state model for soil-pile interaction during lateral spread" *Proceedings of 7th US-Japan Workshop on Earthquake Resistance Design of Lifeline Facilities and Countermeasures Against Soil Liquefaction*, Seattle, WA, August 15-17, 237-260.

Hamada, H., Yasuda, S., Isoyama, R., and Emoto, K. (1986) "Study on Liquefaction Induced Permanent Ground Displacements" Research Report, Association for the Development of Earthquake Prediction, Japan.

Motamed, R. (2007) "Shaking Table Tests on Pile Groups Subjected to Liquefaction-Induced Large Ground Deformation" PhD Dissertation, Department of Civil Engineering, The University of Tokyo, Tokyo, Japan, September 2007.

Tokimatsu, K. and Asaka, Y. (1998) "Effects of Liquefaction-Induced Ground Displacements on Pile Performance in the 1995 Hyogoken-Nambu Earthquake" *Special Issue of Soils and Foundations*, pages 163–177.

Tokimatsu, K., and Suzuki, H. (2004) "Pore water pressure response around pile and its effects on p-y behavior during soil liquefaction" *Soils and Foundations*, Vol. 44, No. 6, 101-110.

Towhata, I. (2008) "Earthquake Geotechnical Engineering" Chapter 23, to be published by Springer Verlag

GEOTECHNICAL CENTRIFUGE TESTS ON THE LATERAL RESPONSE OF DOUBLE-PILE GROUP SUBJECTED TO LATERALLY SPREADING LIQUEFIED SAND

Jonathan R. Dungca[1)], Jun Izawa[2)], Sakae Seki[3)], and Jiro Kuwano[4)]

1) Associate Professor, Dept. of Civil Engineering, De La Salle University, Philippines
2) Assistant Professor, Dept. of Civil and Environmental Engineering, Tokyo Institute of Technology, Japan
3) Technician, Dept. of Civil and Environmental Engineering, Tokyo Institute of Technology, Japan
4) Professor, Geosphere Research Institute of Saitama University, Japan
rivernathan@gmail.com, jizawa@cv.titech.ac.jp, seki@cv.titech.ac.jp, jkuwano@mail.saitama-u.ac.jp

Abstract: This paper presents an experimental study on the lateral resistance of a double-pile group subjected to liquefaction-induced lateral spreading. A series of geotechnical centrifuge tests were conducted with different pile spacing. This study focuses on the effect of the liquefied ground on the lateral resistances of the two piles. The differences in the lateral resistances between the two piles for different pile spacing were also studied. Test results show that there is a bigger difference in the lateral resistance between the two piles if they are spaced closed to each other. It was also observed that the excess pore water pressure between the two piles plays an important role in the differences of the lateral resistances of the piles.

1. INTRODUCTION

Recent large-scale earthquakes like the Hyogo-ken Nambu Earthquake of 1995 have shown that pile foundations are susceptible to earthquake-induced damage due to the reduction of stiffness of surrounding liquefied soils during earthquake shaking as well as due to the lateral spreading of ground induced by soil liquefaction. These damages were observed in sites where large lateral movement of liquefied soil overlaid a non-liquefied soil.

The objectives of this study are, (1) to determine the effect of laterally spreading liquefied ground on the lateral resistance of double piles; (2) to determine the spacing of double piles where each individual pile can be treated as a single pile; and (3) to check the effect of relative density, on the lateral resistance of double piles. To achieve this objectives, a series of geotechnical centrifuge tests with different pile spacing were conducted

The piles considered in this study are in line with each other. The center to center distances between the piles were varied. The different spacing of piles considered will be discussed in the succeeding section. If the liquefied ground is moving in the leftward direction, as shown in Figure 1, the pile in the front will be referred in this study as the "leading pile", while the pile at the back will be called as the "trailing pile". The spacing of the piles will be referred as "s" throughout the course of this study.

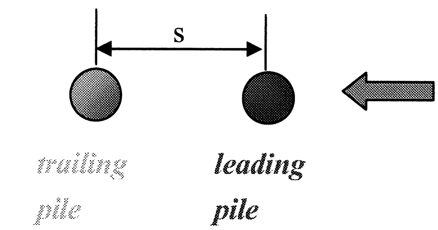

Figure 1 Leading and trailing piles

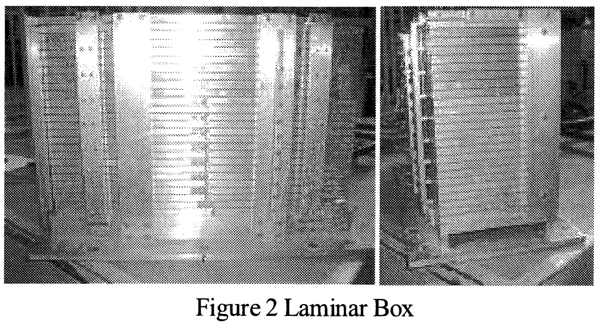

Figure 2 Laminar Box

2. METHODOLOGY

2.1 Model Layout

2.1.1 Laminar Box

Centrifuge experiments were conducted using the rectangular, flexible wall laminar box as shown in Figure 2. The interior dimensions of the box are 440mm in width, 150mm in breadth, and 265mm in height. This box is composed of 26 aluminum alloy rectangular rings separated by linear roller bearings, arranged to permit relative movement between rings with minimal friction. To model a

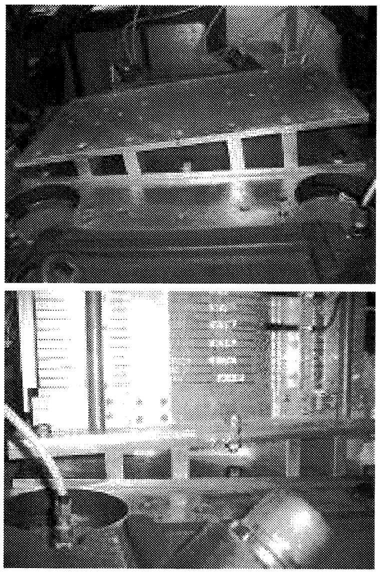

Figure 3 Spacer

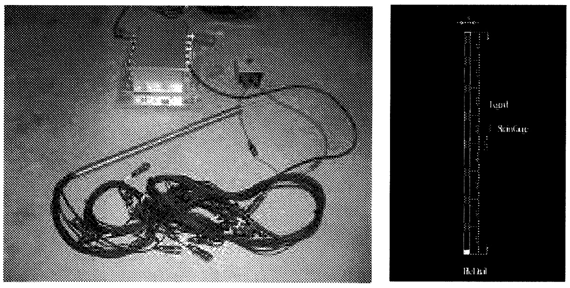

Figure 4 Model pile

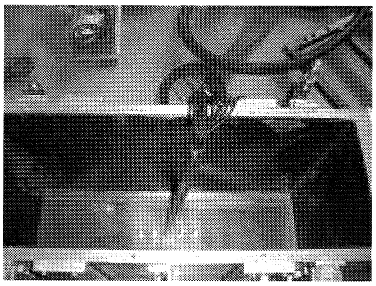

Figure 5 Pile connection

liquefaction-induced lateral spreading, the laminar box was tilted at an angle equivalent to 5 degrees using a spacer as shown in Figure 3. This spacer was attached to the bottom of the laminar box and the mechanical shaker.

2.1.2 Soil Properties

To model the seismically induced lateral spreading, a combination of Toyoura sand with methyl-cellulose solution was used in this study. The physical properties of the Toyoura sand were the following: specific gravity, Gs=2.65, mean particle diameter D_{50}=0.20mm, maximum void ratio e_{max}=0.98, minimum void ratio e_{min}=0.60 and relative density Dr=80%.

2.1.3 Model pile

A model stainless steel pile with an outside diameter of

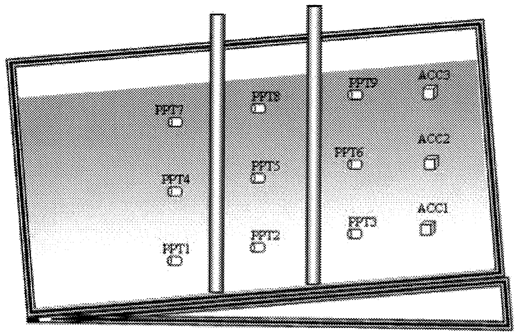

Figure 6 Schematic layout of the model and instrumentations

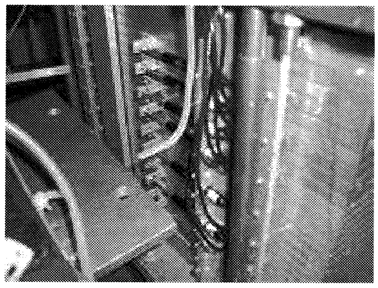

Figure 7 Linear variable displacement transducers (LVDT)

15 millimeters (the prototype outside diameter is 750 millimeters at 50G), inside diameter of 13 millimeters (650 millimeters in the prototype at 50G) a length of 320 millimeters (16 meters in the prototype) and a modulus of elasticity of 200 GPa was used in this test. The model pile was instrumented with 16 strain gauges, placed at 8 levels inside the pile, as shown in Figure 4, to measure the bending moment. In order to fix the pile at the bottom of the laminar box, wedge screw threads were provided at the end of the pile and holes with wedge screw threads were provided on the bottom of the laminar box (Figure 5).

2.1.4 Description of the model and model layout

The model layout is presented in Figure 6. It consists of 220 mm high (11 meter high in the prototype) Toyoura sand layer, which is placed at different relative densities in a laminar box. It is fully saturated with methyl-cellulose solution, inclined at 5 degrees to the horizontal, spun at centrifuge acceleration of 50g. The input acceleration time history at the base of the box consists of 20 cycles of a 100 Hz sinusoidal input, with variable amplitude. For the 50g centrifuge acceleration, this corresponds to a frequency of 2Hz in the prototype.

An accelerometer was installed at the mechanical shaker to measure the input acceleration. Three accelerometers were installed in the saturated ground model at 34mm, 114mm, and 184mm from the bottom, to measure the accelerations of the soil at different elevations.

To measure the excess pore water pressures at different locations, 9 pore pressure transducers were placed in the model ground, three of which on the downstream side of the pile, three in between the piles and the other three were placed at the upstream side.

As shown in Figure 7, six linear variable displacement

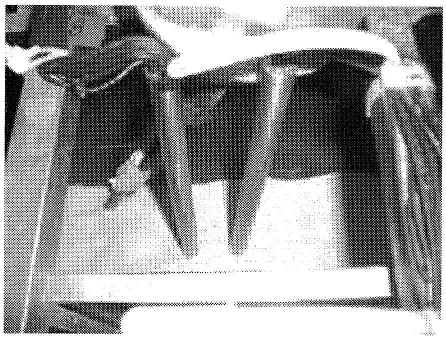

Figure 8 Pile connections in the box

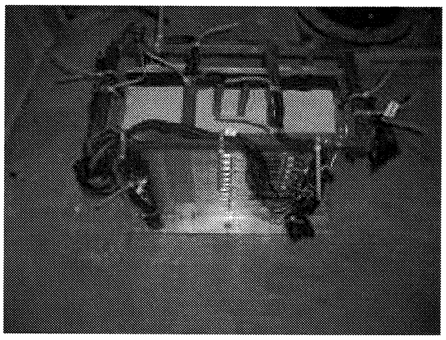

Figure 9 Desired depth of the model ground

transducers (LVDT) were installed on the laminar box rings at various levels to measure the displacement of the rings induced by the movement of the liquefied ground inside the laminar box.

2.1.5 Model preparation

The model piles were fixed at bottom of the laminar box. Sand was set into the laminar box by dry pluviation method, as shown in Figure 8, through a funnel. The funnel was manually moved back and forth along the longer dimension of the box and the free falling distance was controlled to provide the desired relative density. Pore pressure transducers and accelerometers were placed at their designated positions simultaneous with the sand pluviation. The model ground was set to a desired a depth of 220 millimeters (Figure 9), corresponding to a depth of 11 meters in the prototype scale.

A black latex rubber membrane (the black material that can be seen on the walls of the laminar box in Figure 8) was installed on the inside walls of the laminar box to prevent leakage of the contents. The methyl-cellulose solution was prepared separately and was vacuumed and stirred for about 12 hours until all the bubbles in the solution were gone. The equipment used is shown in Figure 10.

When the preparation of the model ground has been completed, the laminar box was placed inside a vacuum tank (Figure 11) and was vacuumed for about two hours. The de-aired methyl-cellulose solution was then introduced to the soil through the inlet tubes installed at the top of the laminar box and saturated the soil for about 48 hours. As soon as the water level rose above the surface of the sand layer, the supply of the methyl cellulose solution was halted and the vacuum was released.

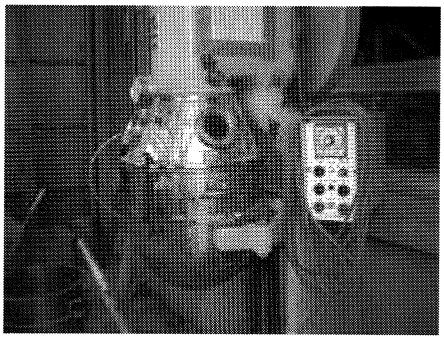

Figure 10 Methyl-cellulose preparation

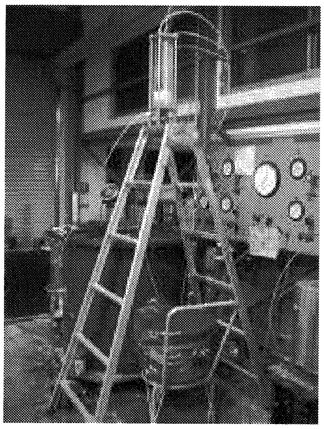

Figure 11 Saturation of the model ground

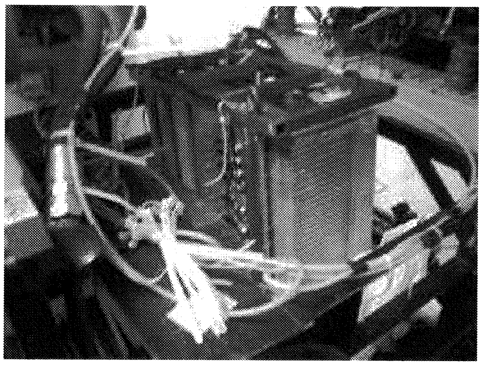

Figure 12 Laminar box on the shaker and centrifuge

2.1.6 Model testing and data acquisition

When the preparation and saturation of the model ground are finished, the box was moved onto the centrifuge arm and placed over the slip table of the shaker, as shown in Figure 12. The centrifuge acceleration was increased gradually from 0 to 50g. Transducer measurements were recorded at 10g increments. When the centrifugal acceleration of 50g has been reached at the mid-depth of the sand layer, the acceleration was maintained for 2 minutes, and the shaking was applied to the model.

Transducer excitation and signal conditioning was performed on the centrifuge arm, and the signals were then passed through the slip rings to the recording system located in the control room. The signal was amplified, filtered, and

Table 1 Test Conditions

Case	Pile Spacing	Relative Density (%)
3D_LDR	3D	56
3D_HDR	3D	83
4.5D_LDR	4.5D	56
4.5D_HDR	4.5D	82
6D_LDR	6D	55
6D_HDR	6D	80

finally digitized in real time using an array of PC-type digitizing boards. The data were then recorded on a disk for later processing. A video camera was also installed to observe the model while spinning.

3. DATA ANALYSIS

3.1 Test Conditions

The test conditions in this study are shown in Table 1. To check the effect of pile spacing on the lateral resistance of double piles, three spacings were used in this study; 3D (the spacing is three times the pile diameter), 4.5D and 6D. To determine the effect of the relative density on the lateral resistance, a relative density of about 55% was used to represent the low relative density and about 80% that will represent the high relative density.

3.2 Calculations of the lateral resistances of the piles

The lateral resistance of the pile will be presented in this study in terms of *p-y* behavior, where p is the lateral resistance of the pile at a given depth and y is the lateral displacement of the pile relative to the free-field soil profile at the same depth.

The *p-y* behavior was calculated using the computed bending moment distribution M(z) along the pile using the *simple beam theory* according to the following equations (Wilson, et al., 2000).

$$p = \frac{d^2}{dz^2} M(z) \qquad (1)$$

$$\frac{d^2}{dz^2} y = \frac{M}{EI} \qquad (2)$$

Where p is the lateral resistance of the pile; y is the absolute lateral displacement of the pile; EI is the flexural rigidity of the model pile (EI = 1.35383×10^6 kN-m^2); and z is the depth below the ground surface.

The moment distribution on the pile was derived from the 16 strain gauge measurements installed inside the model piles using the formula,

$$M(z) = \frac{EI}{r_i} (\varepsilon_l - \varepsilon_r) \qquad (3)$$

Where:

$M(z)$ = Bending Moment of the Pile
E = Modulus of elasticity of the pile (200GPa)

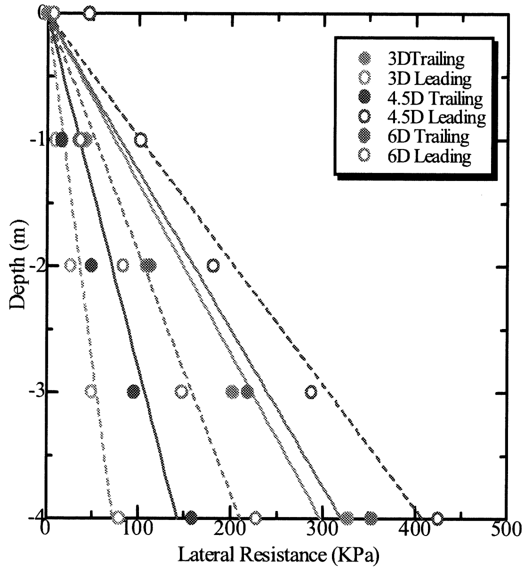

Figure 13 Lateral Resistance of the piles (kPa) from depth 0 to depth 4m

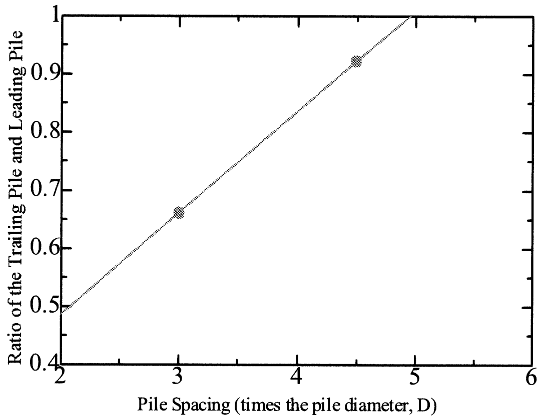

Figure 14 Lateral Resistance of the piles (kPa) from depth 0 to depth 4m

I = Centroidal moment of inertia of the pile (6.76915×10^4 m^4)
r_i = inner radius of the pile (0.375m)
ε_l = Strain at the left of the pile
ε_r = Strain at the right of the pile

3.3 Results

Figures 13 show the graph of the lateral resistances of the trailing pile and leading pile for the three pile spacings. We can observe from this graph that the difference in lateral resistance between the two piles is greater at pile spacing of 3D and 4.5D than 6D. The ratio of lateral resistances of the trailing pile with the leading pile was graphed in Figure 14. One could observe from this graph that as the pile spacing becomes larger the ratio of the lateral resistances between the trailing pile and leading pile becomes bigger. One could also observe that the unity, where the lateral resistance of the trailing pile is equal to the leading pile is at spacing of 5D. This indicates that for an in-line double pile group, there is no double pile effect if the spacing of the piles is 5D or greater. Both the leading and trailing piles will have the same lateral resistance and they will behave like a single pile.

The lateral resistance of a pile subjected to laterally spreading liquefied ground is the sum of the forces at the front of the pile and at the back of the pile induced by the combined effects of negative pore water pressure and the increased stiffness of soil induced by the increase in effective stress (or the decrease in the pore pressure). The force on the compression side plays a more affecting role in the lateral resistance of a pile. In the case of trailing pile, with smaller spacing, the force on the compression side can not be mobilized effectively due to the presence of the leading pile as the deformation of the soil in between the two piles is limited. The deformation of the soil is the source of the decrease in the pore pressure, thereby, an increase in the stiffness of the soil. When the pile spacing is much bigger, the soil between the piles can deform more freely, thus will give bigger lateral resistance on the trailing pile. Since the force on the compression side of a pile plays an important role in the lateral resistance of a pile, as mentioned earlier, the leading pile has a lesser dependency on the trailing pile, thus, lesser dependency on the spacing. However, the lateral resistance of the trailing pile is much affected by the presence of the leading pile.

4. CONCLUSIONS

The lateral resistance of an in-line double pile group was studied by conducting a series of centrifuge experiments. Three different pile spacings, 3D, 4.5D and 6D were used. Preliminary results indicate that the leading pile has greater lateral resistance than the trailing pile. The ratio of the trailing and leading piles increases as the pile spacing becomes bigger. The spacing at unity was found out at 5D spacing.

The force on the compression side plays a more affecting role in the lateral resistance of a pile. In the case of trailing pile, with smaller spacing, the force on the compression side can not be mobilized effectively due to the presence of the leading pile as the deformation of the soil in between the two piles is limited. The deformation of the soil is the source of the decrease in the pore pressure, thereby, an increase in the stiffness of the soil. When the pile spacing is much bigger, the soil between the piles can deform more freely, thus will give bigger lateral resistance on the trailing pile. Since the force on the compression side of a pile plays an important role in the lateral resistance of a pile, as mentioned earlier, the leading pile has a lesser dependency on the trailing pile, thus, lesser dependency on the spacing. However, the lateral resistance of the trailing pile is much affected by the presence of the leading pile.

Acknowledgements:

The authors would like to express their sincere gratitude for the financial support given by Heiwa-Nakajima Foundation for this research project.

References:

Abdoun, A. & Dobry, R. 1998. "Seismically induced lateral spreading of two-layer sand deposit and its effect on pile foundations," Proc. of the Int'l Conf. Centrifuge 98, Vol.1, 321-328.

Fujii, S., Isemoto, N., Satou, Y., Kaneko, O., Funahara, H., Arai, T. & Tokimatsu, K. 1998, "Investigation and analysis of a pile foundation damaged by liquefaction during the 1995 Hyogoken-Nambu Earthquake," Soils and Foundations, Special Issue on Geotechnical Aspects of the Jan. 17 1995 Hyogoken-Nambu Earthquake, No.2, 179-192.

Horikoshi, K., Tateishi, A. & Fujiwara, T. 1998, "Centrifuge modeling of a single pile subjected to liquefaction-induced lateral spreading," Soils and Foundations, Special Issue on Geotechnical Aspects of the Jan. 17 1995 Hyogoken-Nambu Earthquake, No.2, 193-208.

Matsui, T. & Oda, K. 1996, "Foundation damage of structures," Soils and Foundations, Special Issue on Geotechnical Aspects of the Jan. 17 1995 Hyogoken-Nambu Earthquake, No.1, 189-200.

Satoh, H., Ohbo, N. & Yoshizako, K. 1998, "Dynamic test on behavior of pile during lateral ground," Proc. of the Int'l Conf. Centrifuge 98, Vol.1, 327-332.

Takahashi, A., Takemura, J., Kawaguchi, Y., Kusakabe, O. & Kawabata, N. 1998, "Stability of piled pier subjected to lateral flow of soils during earthquake," Proc. of the Int'l Conf. Centrifuge 98, Vol.1, 365-370.

Takemura, J., Kimura, T. & Suemasa, N. 1989, "Development of earthquake simulators at Tokyo Institute of Technology," Technical Report of Dept. of Civil Eng., Tokyo Inst. of Tech., No.40, 41-68.

Towhata, I., Vargas-Mongem W., Orense, R.P. & Yao, M. 1999, "Shaking table tests on subgrade reaction of pipe embedded in sandy liquefied subsoil, Soil Dynamics and Earthquake Engineering, Vol.18, No.5, 347-361.

Yasuda, S., Terauchi, T., Morimoto, H., Erken, A. & Yoshida, N. 1998, "Post liquefaction behavior of several sands," Proc. of 11th European Conf. on Earthquake Eng.

Fifth International Conference on Urban Earthquake Engineering
March 4-5, 2008, Tokyo Institute of Technology, Tokyo, Japan

OBSERVED AIRPORT FACILITIES PERFORMANCE DURING LIQUEFACTION BY CONTROLLED BLAST IN ISHIKARI BAY NEW PORT, HOKKAIDO

Yasuo Kasugai [1), Ryuichiro Ushijima [2), Junichi Mizukami [3), Yukitomo Tsubokawa [4), Kentarou Asayama [5), Hiroshi Nakazawa [6) and Takahiro Sugano [7)

1) Director, International Affairs Office for Airport Construction Div., Aerodrome Dept., Ministry of Land, Infrastructure, Transport and Tourism (MLIT), Japan
2) Managing Director for Research Affairs, Port and Airport Research Institute, Japan
3) Head, Airport Facilities Division, National Institute for Land and Infrastructure Management, MLIT, Japan
4) Senior Researcher, Airport Facilities Division, National Institute for Land and Infrastructure Management, MLIT, Japan
5) Senior Planning Officer for Airport Safety Engineering, Construction Div., Aerodrome Dept. MLIT, Japan
6) Researcher, Structural Dynamics Division, Port and Airport Research Institute, Japan
7) Head, Structural Dynamics Division, Port and Airport Research Institute, Japan
kasugai-y87t2@mlit.go.jp, ushijima-r29e@pari.go.jp, mizukami-j83ab@ysk.nilim.go.jp, tsubokawa-y92y2@ysk.nilim.go.jp
asayama-k238@mlit.go.jp, nakazawa@pari.go.jp, sugano@pari.go.jp

Abstract: Full-scale experiment using controlled blasting was conducted in the Ishikari Bay New Port (Ishikariwan-shinko) in Hokkaido Island, Japan, to assess the performance of airport facilities subjected to the liquefaction. Airport facilities in this study included runway pavement with full specifications for B747 aircraft and apron pavement with/without countermeasures for liquefaction, air traffic control facilities such as the Glide Slope Antenna, the Localizer Antenna, drainage conduit and etc. This paper presents some of the test results while the measurement and investigation are progressing now.

1. INTRODUCTION

A full-scale liquefaction experiment was carried out on October 27, 2007 at Ishikari Bay New Port (Ishikariwan-shinko) in Hokkaido Island, Japan. Port and Airport Research Institute (PARI) organized the project associated with Ministry of Land, Infrastructure, Transport and Tourism (MLIT) and National Institute for Land and Infrastructure Management, MLIT. The primary objective of the experiment was to assess the performance of airport facilities during liquefaction. To investigate damage mechanism and effect of countermeasures for liquefaction, the runway pavement of 50m in length and 60m in width was constructed.

The experimental site was reclaimed with dredged fine sand. The thickness of liquefiable layer was about 7m, and the total experimental area was 1.65ha (16,500m^2).

Controlled blast technique was used to induce liquefaction, total 1,750kg of explosives were divided in 583 pieces at GL-4.5m and GL-9m in depths and 6.5m horizontal grid spacing in the experimental area.

Various structures such as runway, apron, embankment, drainage conduit, air traffic control glide slope antenna, localizer antenna and countermeasures for liquefaction were installed in the experimental area and installed about 500 measurement devices. Several new non-invasive health monitoring devices, such as laser profiler, ground radar and Falling Weight Deflectmeter were also adopted.

Forty one organizations such as universities, construction companies and research institutes, participated in this project as a collaborative research organization as shown in Table 1.

2. OUTLINE OF THE EXPERIMENT

2.1 Role of Airport after an Earthquake

The occurrence of a large earthquake may be a rare event, however, its societal and economic impact can be so divesting that it is a matter of national interest. Predicted probability of occurrence within 30 years of major earthquakes (M>8), such as Tokai, Tounankai and Nankai Earthquakes are over 50% probability, which will severely damage our city and facilities.

We cannot prevent an earthquake to happen, yet we can minimize its damage simply by becoming aware of potential hazards and taking some basic precautions.

The earthquake of magnitude 6.8 JMA occurred in 13 km in depth of the Chuetsu district, Niigata Prefecture at 5:56p.m., October 23, 2004. The Joetsu Shinkansen train derailed while in service. Eight out of ten cars of the TOKI 325 train derailed in Yamato, the Joetsu Shinkansen re-opened on December 28, 2004 (Hokuriku Regional

Table 1 Collaborative Research Organizations

	Category	Collaborative Organization	Proposed project
1	Sounding	Kanto Gakuin Univ. /KOWA Co., Ltd.	Subsurface investigation and soil properties evaluation before and after liquefaction.
2		OYO Corporation	Evaluation of airport facilities damage due to liquefaction using geotechnical sounding techniques.
3		National Research Institute for Earth Science and Disaster Protection	Subsurface investigation and soil properties evaluation before and after liquefaction.
4		DIA Consultants Co., Ltd. / Kawasaki Geological Eng. Co., Ltd. / Masuda Giken Co., Ltd.	Applicability investigation of pressure meter with five pressure cells.
5	Pavement Management	Nippon Koei Co., Ltd.	Evaluation of runway pavement serviceability after liquefaction Vibration observation in neighboring area of explosion.
6		Nippon Road Co., Ltd.	Damage observation of runway pavement after liquefaction.
7		Toa Road Co., Ltd. /Tokyo Sokki Kenkyujo Co., Ltd.	Bearing capacity and subsidence investigation of runway pavement./Measurement of strain distribution in pavement.
8		Nippo Co., Ltd.	Evaluation of runway pavement surface after liquefaction
9		Taisei Rotec Co., Ltd.	Investigation of runway surface roughness after liquefaction
10		Gaeart T.K Co., Ltd. / GEOSTR Co., Ltd.	Applicability investigation of high strength precast RC pavement.
11		NTT InfraNet Co.,Ltd. /AIREC Engineering Co., Ltd.	Applicability investigation of optical fiber for health monitoring of runway pavement/Damage investigation of runway subbase course and subgrade using ground probing radar.
12		NEWJEC Inc.	Evaluation of runway pavement serviceability after liquefaction using geotechnical sounding techniques.
13		Sealam Engineering Co., Ltd. / Maintec Co., Ltd.	Damage investigation of runway subbase course and subgrade using ground probing radar.
14		Oregon State Univ. / U.S. Geological Survey	Evaluation of runway surface roughness after liquefaction using the Laser Imaging Detection and Ranging technique
15		Service Center of Port Engineering	Design and construction management of runway pavement and apron pavement.
16	Countermeasures for Liquefaction	Compacting Grouting Society of Japan	Performance and B/C analysis of compacting grouting method (CPG).
17		Study group of Permeable Grouting Method	Performance and B/C analysis of permeation grouting method.
18		Multiple-Permeation Grouting Method Group	Performance and B/C analysis of multiple-permeation grouting method.
19		Institute of Technology, Shimizu Co., Ltd. / Study Group of Thixotropic Gel Compction Grouting Method / Kato Construction Co., Ltd.	Verification of thixotropic gel compaction grouting improvement effect.
20		X-jet Association	Evaluation of soil improvement performance using a cross jet grouting with its columns in a grid pattern.
21		Musashi Institute of Technology / Sato Kogyo Co., Ltd. / Advanced Industrial Science and Technology	Evaluation of microbubbles effect on countermeasures for liquefaction.
22		Chemical Grouting Co., Ltd.	Evaluation of soil improvement performance using high pressure jet grouting.
23	Underground installation	High Stiffness Polyethylene Pipes Association	Investigation into behavior of buried polyethylene pipe during liquefaction
24		Nihon Suido Consultants Co., Ltd.	Evaluation of manhole uplift prevented manhole during liquefaction
25	Monitoring	Kyowa Electronic Instruments Co., Ltd.	Observation of airport facilities behavior during liquefaction using several sensors.
26		Akebono Brake Industry Co., Ltd. / GEO design Inc.	Observation of airport facilities behavior during liquefaction using several sensors.
27		Geosurf Co., Ltd.	Observation of airport facilities behavior during liquefaction using RTD GPS
28	Reinforced Embankment	Okasan Livic Co., Ltd. / Eternal Preserve Co., Ltd.	Evaluation of reinforced soil embankment using High-strength Geosynthetic
29	Underground shopping street	Construction Burau, City of Sapporo / Nihon Suido Consultants Co., Ltd. / Hokkaido Univ. / Hirosaki Univ.	Evaluation of flexible joint performance between under ground shopping street and building during liquefaction

Development Bureau, 2004). Also, East Nippon Expressway Co. closed all expressways in Niigata prefecture. The most severe damaged segment between Nagaoka interchange and Koide interchange re-opened on November 5, 2004 (Hokuriku Regional Development Bureau, 2004). We had no ground traffic access just after the earthquake.

Niigata Airport, which suspended flights shortly after the earthquake, resumed service after finding no damage. To help emergency medical services (EMS), recovery activities, reach out to the refugees and long-distance travelers, All Nippon Airways and Japan Airlines each added a round-trip flight from Tokyo/Osaka to Niigata airport from October 24, 2004 to November 14, 2004(Hokuriku Regional Development Bureau, 2004).

The Civil Aviation Bureau, MLIT organized technical advisory committee which concerned with seismic performance of airports in Japan. The committee report said,

A) Starting special operation for transporting living necessities for sufferers' daily life immediately (within one day) after the earthquake.

B) Restarting commercial logistic operation with 50% of service level, within three days after the earthquake.

The concept A) is the policy to support these sufferers' minimum standard of living including EMS. Just after the strong earthquake, many people lose their food, clothing and shelter. Almost all the land routes are cut off, and so the air routes can transport relief goods. Airports are the entrance where prompt transportation to the earthquake-stricken area. Also, sea ports are the entrance where mass transportation to the earthquake-stricken area.

The concept B) is the policy to support the activities of the enterprises located around the airport. If the airport cannot restart functioning logistic operation within three days, the enterprises around the airport lose their way for transportation to support their activity.

2.2 Experimental Site Conditions and Layout

The Ishikari Bay New Port is located in Otaru city, within very close range of Sapporo, 15km, 40mins by car, from the city center of Sapporo, Hokkaido.

The site is located in the coastal line of Ishikari Bay which consists of gentle slope of sea bed surface reclaimed with dredged sands and sand dunes. The typical soil profile was shown in Figure 1. The particle size distribution of the soil is shown in Figure 2, as can be seen most of the soil samples are rather uniform particle diameter and which within 'possibility of liquefaction zone' (MLIT, 2007).

As shown in Figure 3, lots of airport facilities were installed in the experimental site. The runway pavement area were divided three parts as shown in Figure 4, as following,

a) Left top area was improved by Compaction Grouting method,

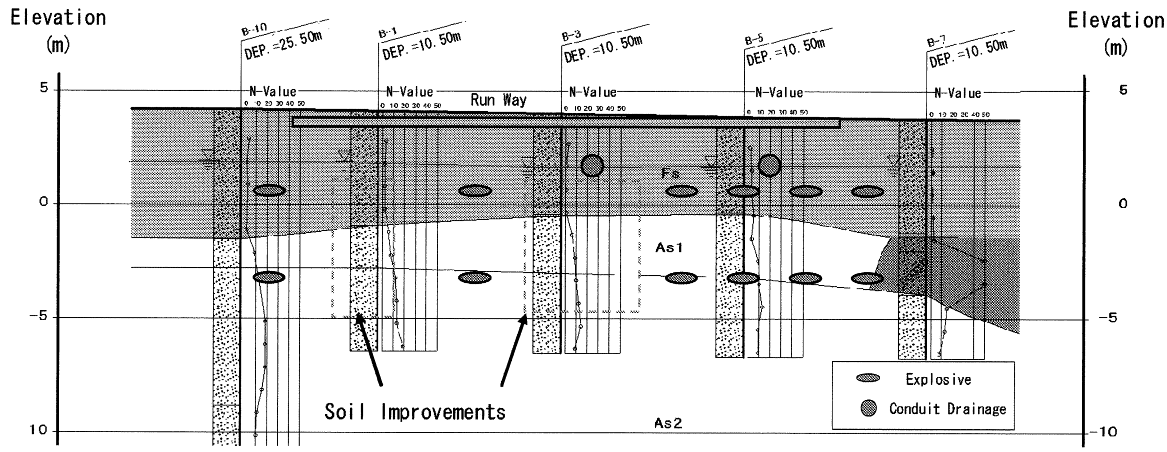

Figure 1 Soil Profile of the Runway Area

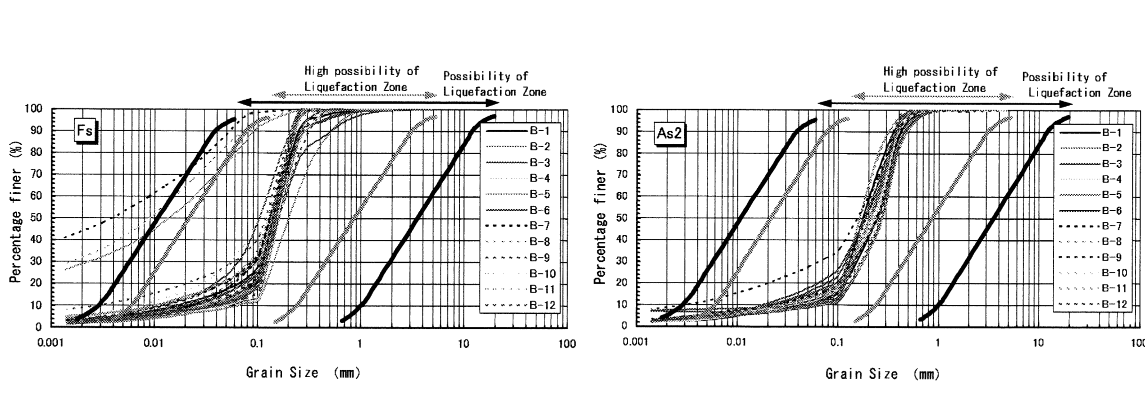

Figure 2 Grain Size Distribution of Soils Tested before Blasting

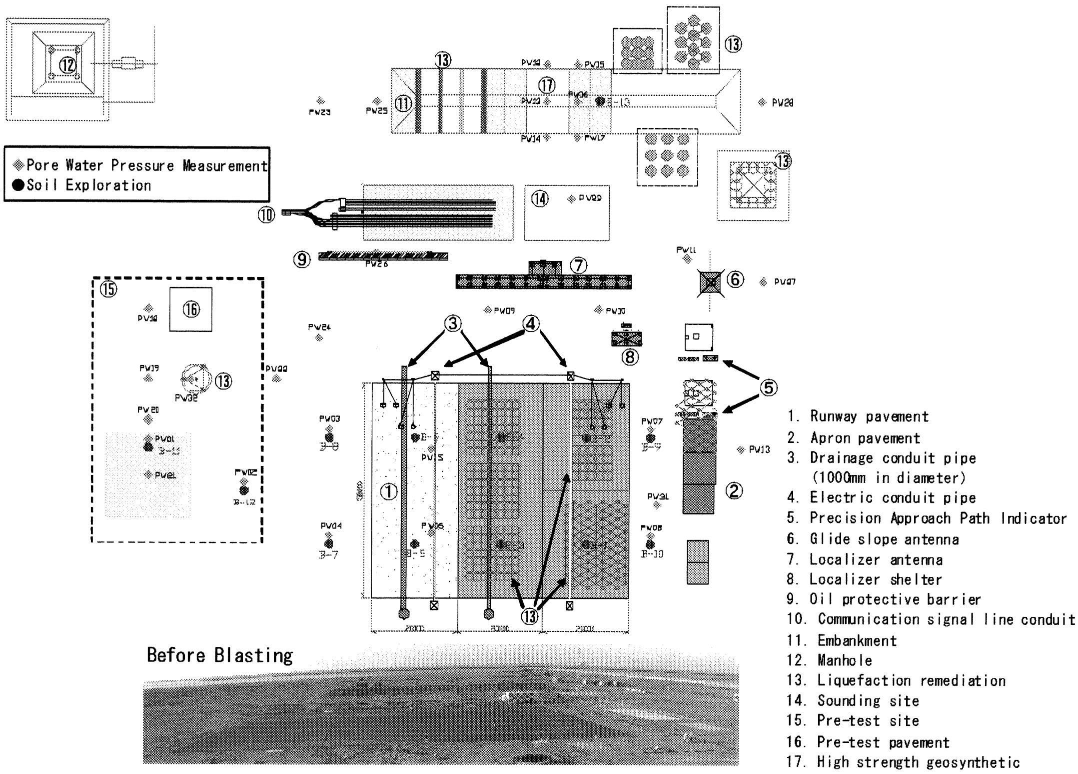

Figure 3 Plan View of Experimental Site

b) Left bottom area was improved by Multi-Permeation Grouting method

c) Middle area was improved by Permeable Grouting method, and

d) Right area was unimproved area.

All of the improvement methods were installed with cost reduction design specification compared with present design procedures.

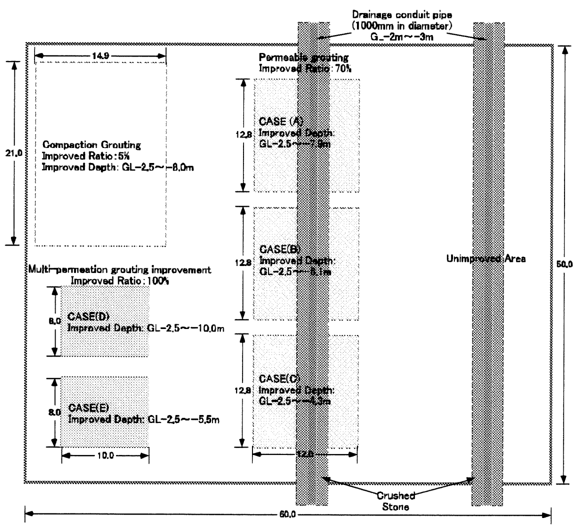

Figure 4 Plan View of Runway Pavement Area

2.3 Controlled Blast Sequence

Three sets of data can be used to investigate the mechanism of damages during an earthquake;

1) Strong motion record nearby the damaged facility,

2) Geotechnical data (e.g. boring log, soil test results), design conditions (e.g. design drawings, design documents) and damage data (e.g. residual deformation), and,

3) Numerical simulation or model test results.

However, an important piece of information as 'behavior of full-scale structure' during an earthquake is not available explicitly. In this project, we focused on the behavior of full-scale airport facilities during liquefaction state using controlled blast technique.

Generally, the vertical boreholes were charged with 4kg explosive at GL-9m, 2kg explosive at GL-4.5m depth as shown in Figure 5(a). Figure 5(b) show, the under path boreholes of pavement used horizontal directional drilling machine were also charged with 4kg explosive at GL-9m, 2kg explosive at GL-4.5m in depth (Photograph 1). Each charged explosive was ignited domino toppling manner with 200ms time interval. It took about 139 seconds to complete the blasting of 538 explosives.

From the pretest results, the effective range for fully liquefaction was about 3m in radius.

The typical mechanism of liquefaction during an earthquake is as following,

a) shear wave progressing into the sandy soil layer,

b) subjected to shear deformation,

c) negative dilation occurred, and,

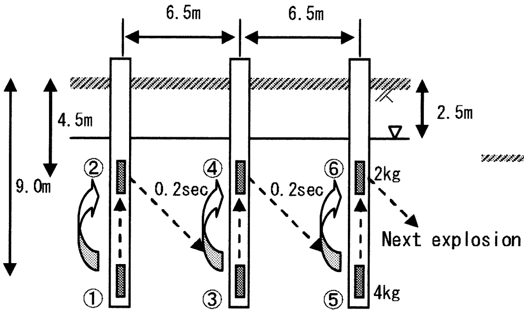

(a) Vertical boreholes

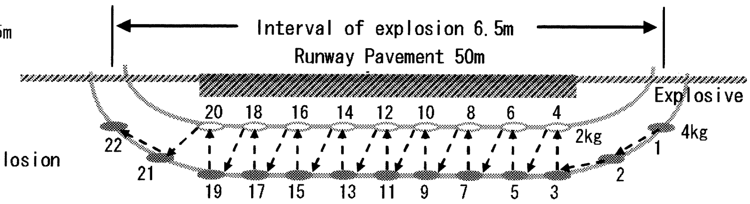

(b) Horizontal directional drilling boreholes

Figure 5 Outline of Controlled Blast Sequence

Photograph 1 Charge Process of explosive

Ptotograph 2 Bird's-eye View of Experimental Site

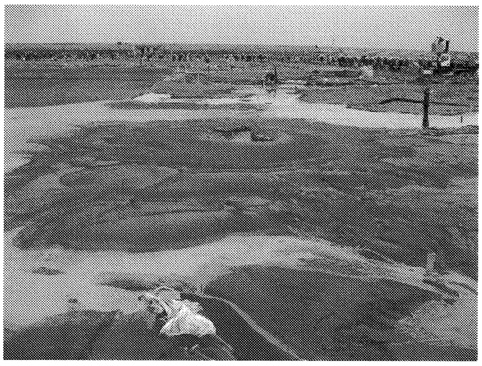

Photograph 3 Observed Sand Boil around ManholeInstalled in Unimproved Soil Region

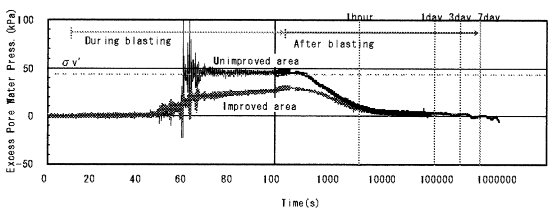

Figure 6 Comparison of Excess Pore Water Pressure Measured at GL-3.5m between Compaction Grouting Area and Unimproved area

(Unit mm)

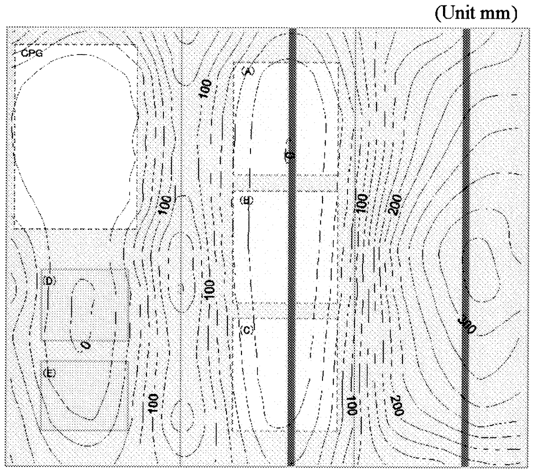

Figure 7 Subsidence Contour Chart after One Hour of Blasting

d) generated excess pore water pressure.

On the other hand, the mechanism of controlled blast induced liquefaction is as following,

a) blast, then, the sand particle structure brake,

b) re-location of sand particles (densification), and,

c) generated excess pore water pressure.

In case of controlled blasting, it is possible to reproduce excess pore water pressure built up to overburden pressure like earthquake induced liquefaction, however, it is impossible to reproduce acceleration and cyclic loading conditions.

2.4 Situation after the Blasting

Photograph 2 shows the bird's-eye view of experimental site. We can see the sand boil and water due to the blast induced liquefaction. Most extreme sand boil was observed at manhole with unimproved soil region as shown in Photograph 3.

Figure 6 shows time history of excess pore water pressure in Compaction Grouting improved region and unimproved region. The black line (unimproved region) reached overburden pressure and the crest of blue line indicates about 50% of overburden pressure. The generated excess pore water pressure dissipated within one day.

The subsidence contour chart after one hour of blasting (Figure 7), expressing the situation of countermeasures for liquefaction (i.e. Compaction Grouting, Permeable grouting, and Multi-permeation grouting improvement) area and unimproved area.

3. SUMMARY AS OF PRESENT

A lot of valuable knowledge was obtained through the blast experiment. Especially, from aspect of the subsidence of runway, it is confirmed that tried countermeasures for liquefaction with cost reduction deign specification are effective. However, we have to examine the relation between the aircraft load and the runway support system during liquefaction and excess pore water pressure dissipation states.

Many kinds of challenges to investigate seismic performance of airport facilities are conducting in collaboration with 42 organizations (including PARI). The site observation and analysis works are presently continuing by individual organization participated in this project. The result will be presented in the future.

Acknowledgements:

The authors acknowledge support from Hokkaido Regional Development Bureau, MLIT and Ishikari Bay New Port Authority. The support has made possible this unprecedented project.

References:

Hokuriku Regional Development Bureau, MLIT (ed.) (2004), “Report of Damage and Restoration Situation due to 2004 Niigata Chuetsu Earthquake”, **2**. (in Japanese)

Ministry of Land, Infrastructure, Transport and Tourism, Japan (ed.) (2007) “Technical Standards for Ports and Harbour Facilities and Commentaries”, Japan Port and Harbour Association, P.384 (in Japanese)

Fifth International Conference on Urban Earthquake Engineering
March 4-5, 2008, Tokyo Institute of Technology, Tokyo, Japan

CENTRIFUGE MODEL TESTS ON SOIL DE-SATURATION AS A LIQUEFACTION COUNTERMEASURE

Jiro Takemura[1], Reina Igarashi [2], Jun Izawa[3], and Mitsu Okamura[4]

1) Associate Professor, Dept. Civil and Environmental Engineering, Tokyo Institute of Technology, Japan
2) Graduate Student, Dept. Civil and Environmental Engineering, Tokyo Institute of Technology, Japan
3) Assistant Professor, Dept. Civil and Environmental Engineering, Tokyo Institute of Technology, Japan
4) Associate Professor, Dept. Civil Engineering, Ehime University, Japan
jtakemur@cv.titech.ac.jp, reina@cv.titech.ac.jp, jizawa@cv.titech.ac.jp, okamura@dpc.ehime-u.ac.jp

Abstract: In this study a series of centrifuge model test has been conducted to investigate the mechanical behavior of the submerged but partially saturated sand during earthquake. In the centrifuge tests, an attempt was made to prepare partially saturated model sand by lowering and regaining ground water table under 50g centrifugal acceleration. The process of de-saturation were monitored by Time Domain Reflect meter (TDR) and pore pressure transducers (PPT). A shaking test of the model was then conducted for the de-saturated sand with a gravity type structure on the top to study the applicability of soil de-saturation as a liquefaction countermeasure.

1. INTRODUCTION

Effect of degree of saturation, S_r, on liquefaction of sand has been mostly studied through laboratory tests. In early research works, the negative effects of incompleteness of the saturation were investigated to avoid the undesirable unsaturated condition which resulted in overestimation of the liquefaction resistance (e.g., Martin et al., 1978). Recently the positive effects of partial saturation on the liquefaction resistance have been investigated to discuss the applicability of soil de-saturation as a liquefaction countermeasure by many researchers using laboratory tests and field tests (e.g., Yoshimi et al, 1989; Tsukamoto et al., 2002; Okamura and Soga, 2006). Okamura and Soga (2006) found a unique relationship between the liquefaction resistance ratio "R_u/R_s", where R_u and R_s are liquefaction resistance of unsaturated and saturated soils respectively and the potential volumetric strain ε_v^* defined by the following equation.

$$\varepsilon_v^* = \frac{\sigma_c'}{p_0 + \sigma_c'}(1 - S_r)\frac{e}{1+e} \qquad (1)$$

where σ_c', p_0 and e are denote the effective confining pressure, the absolute pressure of the fluid and the void ratio of soil respectively.

Centrifuge modeling has been used as a useful approach in the study of soil liquefaction, especially for verification of countermeasures against liquefaction (e.g., Kimura et al, 1997). Eq. (1) implies that the effect of the degree of saturation cannot be well represented in small scale models at 1g but centrifuge models. Furthermore, the capillary rise can be well scaled in the centrifuge model, which is crucial in the simulation of lowering the ground water table, one of the methods of soil de-saturation as shown in Figure 1.

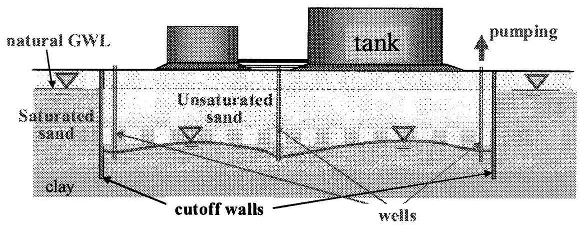

Figure1 De-saturation of liquefiable soils by groundwater

In the centrifuge model test of this study, an attempt was made to prepare partially saturated model sand but ground water table at the ground surface with gravity type footing. A shaking test of the model was then conducted to study the applicability of soil de-saturation as a liquefaction countermeasure.

2. CENTRIFUGE MODEL TESTS

2.1 Soils used for tests

Two types of silica sand with properties shown in Table 1 were used for the tests. In centrifuge modeling, viscous liquids are often used as pore-fluid to overcome mismatch in the similitude concerning seepage and dynamic events. However, to avoid uncertainty in the mechanical behavior of unsaturated sand with such viscous liquids, fine silica sand (No.8) and coarse sand (No.3) were used as the materials for the liquefiable sand and bottom drainage layer respectively with water as the pore-fluid in this study. In the centrifugal field of 50g, the permeability coefficients of the two silica

Table 1 Properties of silica sands used

	No.8	No.3
Specific gravity: G_s	2.65	2.56
Mean particle size: D_{50} (mm)	0.100	1.47
Particle size: D_{10} (mm)	0.041	1.21
Coefficient of uniformity: U_c	2.93	1.26
Max. void ratio: e_{max}	1.333	0.971
Min. void ratio: e_{min}	0.703	0.702
Permeability coef.: k (m/sec)	2.0×10^{-5}	4.6×10^{-3}
(k in prototype scale with 50g)	(1.0×10^{-3})	(2.3×10^{-1})

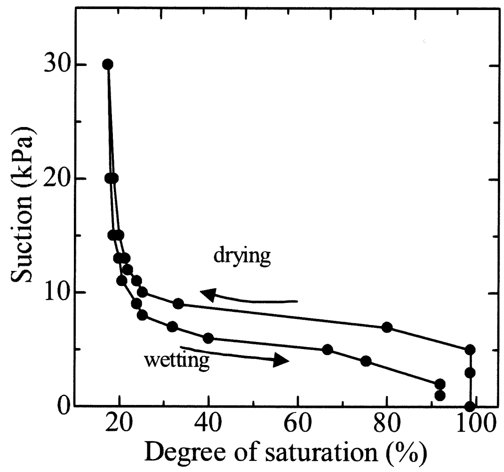

Figure2 Capillary pressure and degree of saturation curve (Silica sand No.8)

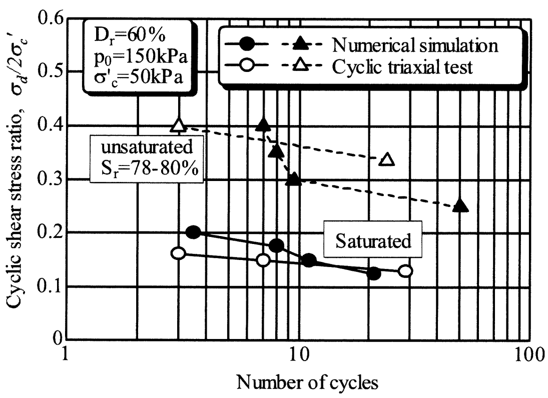

Figure 3 Relationship between cyclic stress ration and number of cycles: Silica sand No.8

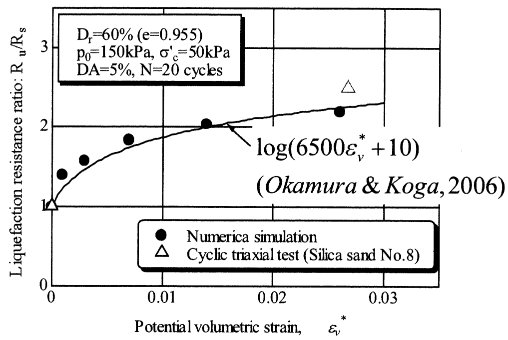

Figure 4 Relationship between potential volumetric stain and liquefaction resistance ratio: Silica sand No.8

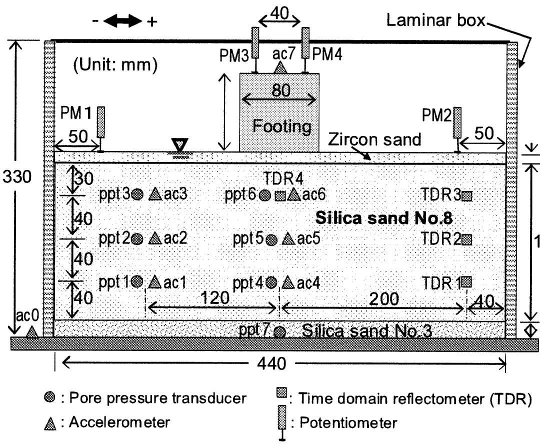

(a) Test setup and location of sensors in the model

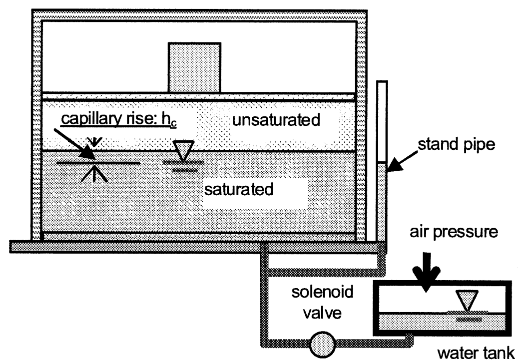

(b) Control of ground water level in the model

Figure 5 Test setup

sands in prototype scale are 50 times those in 1g as shown in Table 1. Capillary pressure - Sr curve of Silica sand No.8 is Figure 2. Air entry value of the silica sand is about 10kPa.

In Figure 3 liquefaction curves obtained from cyclic triaxial tests on Silica sand No.8 with Dr=60% are shown together with the curves obtained from FEM code LIQCA (Oka et al., 1994). Figure 4 depicts the relationship between the potential volumetric strain and the liquefaction resistance. In the figure, relationship proposed by Okamura and Soga (2006) are also shown. Liquefaction resistance for 80% saturation is about 2.5 times greater than that for full saturation.

Table 2 Test condition

Test code	S10	U15	U10
Relative density Dr (%)	62	2.65	2.56
Degree of saturation* (%)	100	93	92
Input acceleration	10	13	10

*: evaluated from the water remained in the water tank

2.2 Model preparation and test procedures

A shear box made of aluminum with inner sizes of 440mm in width, 150mm in breadth and 310mm in height was used for the tests. Silica sand No.3 was first place as the bottom drainage layer by compacting with a wooden rod and a dry

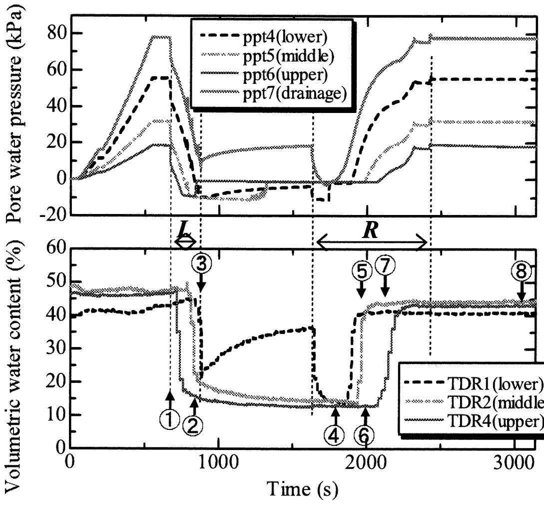

Figure 6 Variation of pore pressure and volumetric water

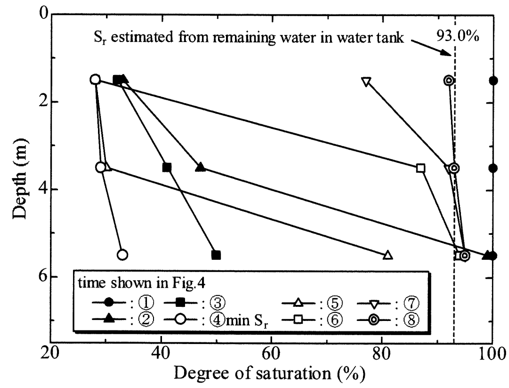

Figure 7 Depth profile of degree of saturation in de-saturation process: U15

layer of Silica sand No.8 was made by air pluviation with Dr=60%. 10mm thick Zircon sand was laid on the surface of the silica sand to give the surcharge pressure of 10kPa in 50g. During the sand preparation, various sensors were placed at the location shown in Figure 5(a). The model ground was saturated in a vacuum tank by introducing de-aired water from the bottom of the box. After saturating the sand, a model footing made of solid aluminum with the dimensions of 80mm in width, 80mm in height and 150mm in breadth was placed on the center of the ground surface carefully. The mass of the footing is 2.5kg, giving the base contact pressure, p_f=100kPa in 50g. The model was then taken to Tokyo Tech Mark III Centrifuge and mounted on the shaker (Takemura et al. 2002). Potentiometers were installed at the position shown in Figure 5(a) and centrifugal acceleration was increased up to 50g.

After confirming the equilibrium condition in the model, the water was drained from the bottom to the water tack by opening the solenoid valve (Figure 5(b)). The valve was closed when the ground water level (GWL) in the standpipe lowered to the bottom of the sand layer. Achieving stationary reading of TDR sensor, the water was recharged from the bottom by applying air pressure to the water tank and opening the valve.

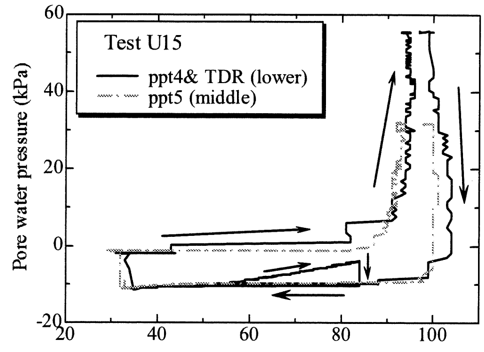

Figure 8 Variation of pore water pressure with S_r

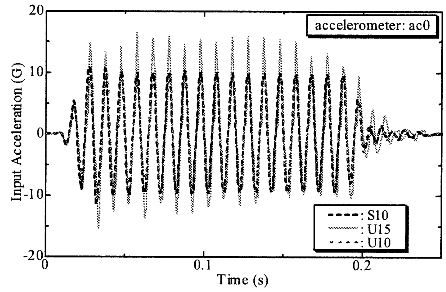

Figure 9 Base input acceleration measured by acc0

Confirming no change in the reading of TDR sensors and PPTs after the water table recovered to the original level, horizontal sinusoidal waves with frequency of 100Hz were applied to the model for 0.2 sec. Three tests were conducted in this study with the condition shown in Table2.

3. TEST RESULTS AND DISCUSSIONS

In the following discussion, test results are given in prototype scales except of Figures 6 and 9.

3.1 De-saturation process

Figure 6 shows the pore water pressures and volumetric water contents observed with PPT and TDR sensors during the de-saturation process in U15. The variation of depth profile of S_r is depicted at various stages shown in Figure 7. S_rs. in the de-saturation process were calculated from the water volumetric content assuming full saturation before lowering the water table. By lowering the GWL, S_r decreased to about 30% and recovered to 93% at the original GWT. S_r obtained in U10 was 92%. The potential volumetric strain for these S_rs with the same conditions shown in Figure 3 is 0.0086 and R_u/R_s estimated by the equation given in Figure 4 is 1.8. The variations of pore pressure with S_r are shown in Figure 8. From this figure, capillary rise in the sand is about 1m, which indicates that the same size of 1g model could be fully saturated by the capillary rise if the GWL is at the bottom of the sand. The sudden increase of pore water pressure is due to the limitation of capacity of PPT in measuring the suction.

3.2 Shaking tests

Input base accelerations measured by acc0 (Figure 5(a)) are shown in Figure 9.

(1) Acceleration response

Horizontal accelerations observed by the vertical array of accelerometers at the center of model are compared for S10 and U10 in Figure 10. Clear attenuation was observed just beneath the footing in the saturated case (S10) but not in the unsaturated case (U92), while that of the footing is vice versa. It is hard to find the clear effect of partial saturation in the acceleration response. Complicated motion of footing might occur, which could not be captured by one accelerometer at the top.

(2) Pore water pressure behavior

Observed excess pore water pressures (EPEP) during shaking are compared in Figure 11(a). Figure 11(b) shows observed excess pore pressure during and after shaking. In the figure effective vertical stress, σ'_{v0}, is shown. At the free field, EPWP reached to σ'_{v0} in early stage of motion at all depths for U10, implying the clear liquefaction. While for U10 and U15, generation of EPWP was more gradual, confirming the effect of partial saturation on the liquefaction resistance. It should be noted that the locations of PPT might be different from those targeted, which is considered as a reason of higher EPWP greater than σ'_{v0}. Large cyclic variation of EPWP in the free field is attributed to the cyclic load from the footing. Although the direct comparison is not possible between the free field and the portion underneath the footing because of different stress condition, similar positive effect of the partial saturation is also observed in EPWP underneath the footing as in the free field. The difference between saturated case and partially saturated cases is more eminent at the shallow portion, which is explained the effect of absolute fluid pressure, p_0, on the potential volumetric strain in Eq. (1).

(3) Settlement behavior

Observed settlements of the footing during shaking tests are shown in Figure 12. The settlement of U10 is about one third of that S10 and the settlement of U15 with input motion 50% greater than S10 and U10 is about one second of S10. Although the settlement rate is very different between the cases, it was slightly decreasing with time in S10 but gradually increasing with time in S10, which can be attributed to the delayed decrease of effective stress for U10. Clear effect of partial saturation on the differential settlement could not be confirmed in the tests. The settlement of the footing and free field during and after shaking are shown in Figure 13. In Figure 14 total settlement of the footing and free field are compared with fraction of those during and after shaking. Majority of the footing settlement took place during shaking, while the free field showed long term settlement after shaking. The ratio of the settlements after shaking to that during shaking in the free field is larger for the saturated case than the partially saturated cases and

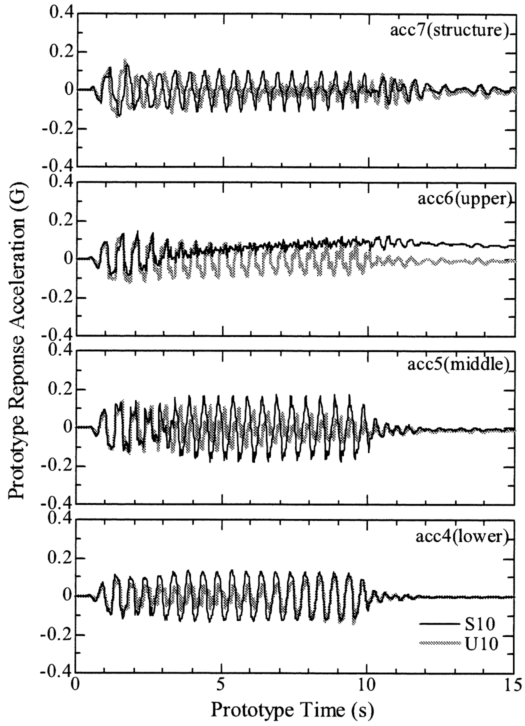

Figure 10 Observed acceleration beneath the footing

larger for U15 than U10. From these comparisons, it can be said that the extent of liquefaction highly influences the settlement after shaking in the free field.

4. CONCLUSIONS

The following conclusions can be drawn in this study.

1) Centrifuge modeling is a useful tool to simulate the de-saturation process by lowering and recovering ground water table in sandy ground. With the conditions adopted in the study, residual degree of saturation was about 92-93%.
2) Pore water generation can be effectively sustained both at free field and underneath structure by de-saturation process even with relatively high S_r given in above. The efficiency is more apparent in shallower depth than the deep one.
3) Settlements of structure on partially saturated sand are much smaller than that of the saturated sand.

5. Remarks

Although centrifuge is very useful for the study in saturated and unsaturated sand, it is still a lot of limitation, e.g., inconsistency of similitude about Bond number in micro scale. To verify the applicability of centrifuge and quantify the effect of de-saturation, further tests with various conditions is recommended.

Acknowledgements:

The authors acknowledge the support by the DaiDaiToku project I from the Ministry of Education, Culture, Sport, Science, and Technology (MEXT).

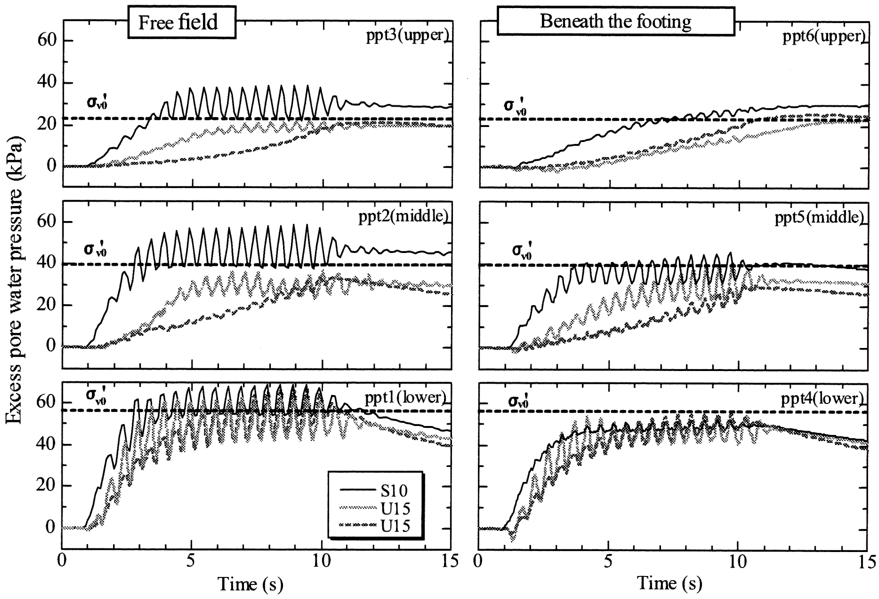

Figure 11 (a) Variation of excess pore pressure in the model ground during shaking with $t_P(=Nt_m)$

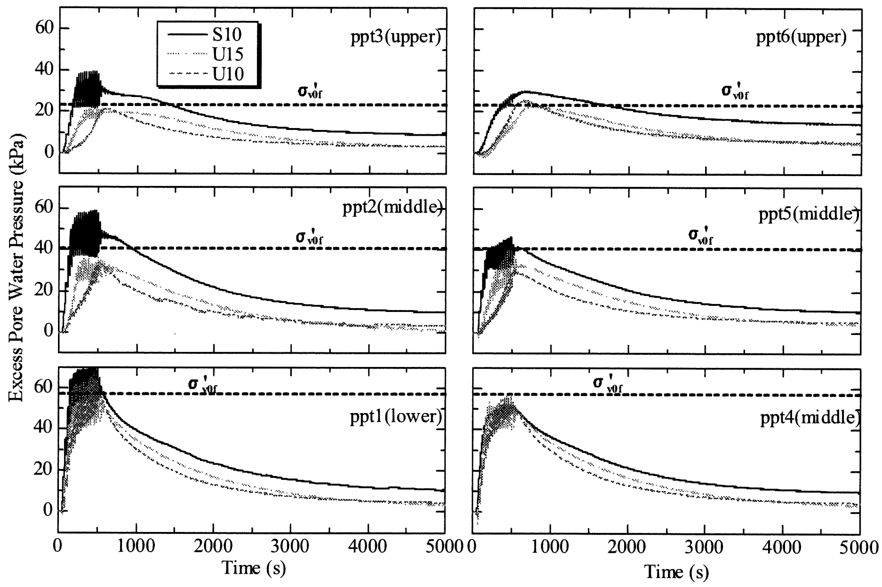

Figure 11 (b) Variation of excess pore pressure in the model ground during and after shaking with $t_P(=N^2t_m)$

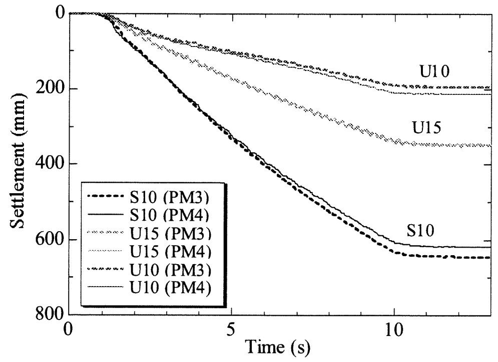

Figure 12 Variation of settlements of the footing during shaking with $t_P(=Nt_m)$

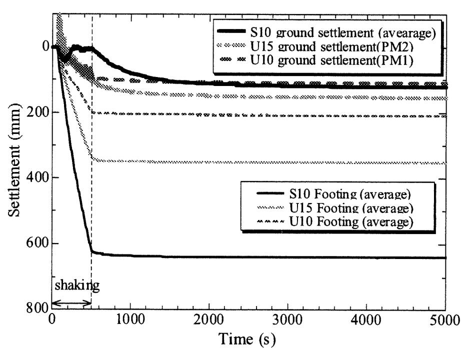

Figure 13 Variation of settlements of the footing during and after shaking with $t_P(=N^2t_m)$

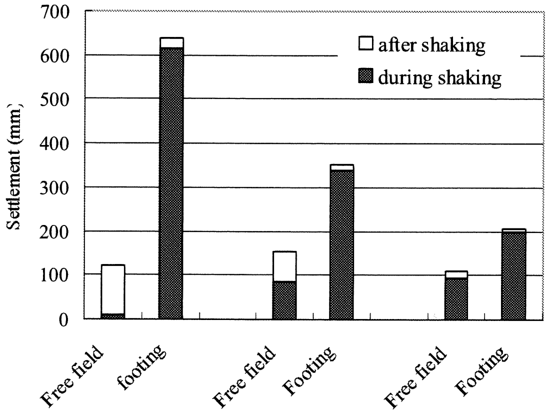

Figure 14 Settlements of the footing and free field

References:

Kimura, T., Takemura, J., HiroOka, H. and Okamura, M., 1997, Countermeasures against liquefaction of sand deposits with structures, *Proc. Intn. Conf. Earthquake Geotechnical Engineering, IS Tokyo 95*, Vol.3, 1203-1224.

Martin , G. R., Finn, W.D. L, and Seed, H. B., 1978, Effects of system compliance on liquefaction tests, *J. Geotech. Engrg. Div., ASCE,* 104(4), 463-479.

Oka, F., Yashima, A., Shibata, T., Kato, M., and Uzuoka, R., 1994, FEM-FDM coupled liquefaction analysis of a porous soil using an elasto-plastic model, *Applied Scientific Research*, Vol.52, 209-245.

Okamura, M. and Soga, Y., 2006, Effects of pore fluid compression on liquefaction resistance of partially saturated sand, *Soils and Foundations*, 46(5), 695-700.

Takemura, J., Takahashi, A. and Aoki,T., 2002, Development of horizontal-vertical 2D shaker in a centrifuge." *Proc. of ICPMG '02*, St John's, Balkema, 163-168.

Tsukamoto, Y., Ishihara, K. Nakazawa, H., Kamada, K. and Huang, Y., 2002, Resistance of partially saturated sand to liquefaction with reference to longitudinal and shear wave velocities, *Soils and Foundations*, 42(6), 93-104.

Yoshimi, Y., Tanaka, K. and Tokimatsu, K., 1989, Liquefaction resistance of a partially saturated sand, *Soils and Foundations*, 29(3), 157-162.

Fifth International Conference on Urban Earthquake Engineering
March 4-5, 2008, Tokyo Institute of Technology, Tokyo, Japan

SIMPLE SHEAR TESTS ON SAND IMPROVED BY CEMENT IN GRID PATTERN

Akihiro Takahashi[1), Hideki Sugita[2), Masanori Ishihara[3), and Shunsuke Tanimoto[2)

1) Associate Professor, Dept. of Civil and Environmental Engineering, Tokyo Institute of Technology, Japan
(Formerly, Public Works Research Institute, Japan)
2) Public Works Research Institute, Japan
3) Shikoku Regional Development Bureau, Ministry of Land, Infrastructure and Transport, Japan
takihiro@cv.titech.ac.jp, sugita@pwri.go.jp, isihara@skr.mlit.go.jp, s-tanomo@pwri.go.jp

Abstract: To mitigate liquefaction-induced settlement of levees, improvement of liquefiable foundation ground by cement is often adopted. In this study, mechanical properties of sand improved by cement in grid pattern were examined by means of the simple shear tests on the improved sand. Test results reveal that the unimproved sand in grids prevents out-of-plane deformation of improved soil walls arranged in grid pattern and makes the shearing resistance of the overall improved zone larger. It is also found that the stress–strain relations of the sand improved in grid pattern can be a unique line when they are normalised by the unconfined compression strength of the cement-treated sand and improvement ratio.

1. INTRODUCTION

Large settlement of levees in the past earthquakes was primarily induced by liquefaction of foundation soils (TCCRFE, 1996). The liquefied soil beneath a levee laterally spreads away from the levee, resulting in the large settlement of the levee. Such deformation mode of the levee is also observed in physical model tests (e.g., Koga & Matsuo, 1990; Okamura & Matsuo, 2002).

To mitigate the levee settlement induced by the lateral spreading of the liquefied foundation soils, remedial measures are often adopted to the foundation near toes of a levee and many types of remedial measures have been proposed. Among others solidification of the liquefiable foundation near the toes is widely used in practice. To create such solidified blocks in the liquefiable ground, the deep mixing method is often adopted. As the replacement ratio is connected directly with the construction costs, the smaller the replacement ratio is better. Thus the ground improvement in grid pattern is proposed and is widely used as a remedial measure for levees. This type of ground improvement not only restrains the lateral spreading of the liquefied foundation soils when it is used for levees but also prevents liquefaction of the soils surrounded by the soil cement walls by restraining the shear deformation of soils during an earthquake. The latter is examined physically and numerically (e.g., Namikawa *et al.*, 2005).

In the design practice of such ground improvement, internal as well as external stability of the solidified zones is examined. For the internal stability of the solidified zone, no failure is expected as such soil cement is regarded as a brittle material. Tanimoto *et al.* (2007) performed a series of centrifuge model tests to assess seismic performance of levees with the ground improvement near the toes in strong earthquakes. In their tests, the ground improvement in grid pattern was adopted. Their test results reveal that even if the soil cement walls are cracked and permanent deformation occurs in the improved zones, the seismic performance of the levee, i.e., amount of the levee settlement, is comparable to the case without such a failure in the improved zones.

This suggests that a certain level of the seismic performance of levees can be achieved even if the permanent deformation of the improved zones occurs. To allow such a permanent deformation in the ground improvement, ductility of the improved ground has to be examined. In this study the simple shear tests on the improved soils in grid pattern were performed to study the ductility of the composite material that consists of the untreated and cement-treated soils.

2. SOIL TESTED AND TEST PROCEDURES

Typical plan view of the ground improvement by cement in grid pattern is shown in Fig. 1. In this study one unit of the grid (clipped by the dashed line in the figure) was modelled. Figure 2 illustrates a simplified unit of the ground improvement in grid pattern. In the tests, the specimen shown in the figure was sheared in the simple shear mode. The specimen is a 100mm-cube. Thicknesses of the soil cement walls (t_1 & t_2) and the strength of the soil cement were changed in the tests.

The simple shear box used is illustrated in Fig. 3. The metal plates encloses the specimen have blades to secure the better contact between the specimen and plate. The planes parallel to the shearing direction are confined by acrylic plates so that the shearing can be done under the plain strain condition and observation of the specimen during shearing can be made. When a specimen is sheared in the simple shear mode, volume change of the specimen should not occur. However, as

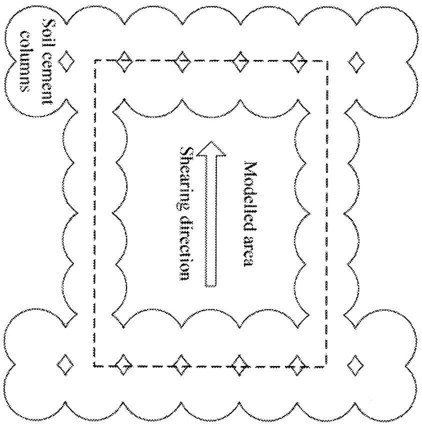

Figure 1 Plan view of ground improvement in grid pattern.

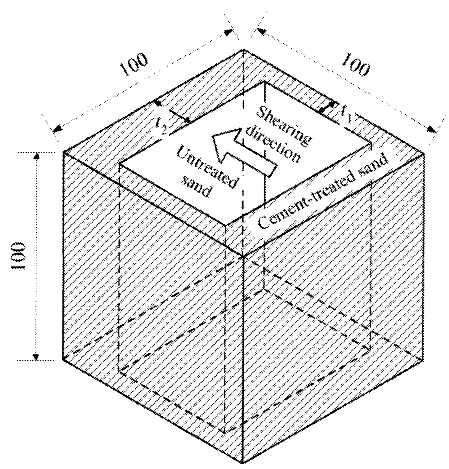

Figure 2 Bird's eye view of specimen used. (Unit: mm)

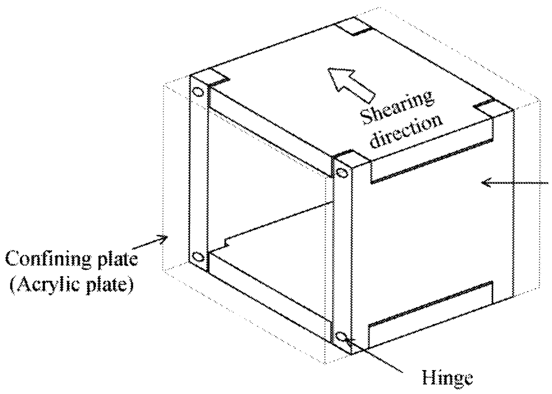

Figure 3 Simple shear box used.

the four metal plates that surrounds the specimen are connected by hinge each other in this study, small volume change of the specimen occurred when relatively large shear strain was imposed; volume change of the specimen ε_v=0.045% when nominal shear strain γ=3%, ε_v=0.18% when γ=6%, and ε_v=0.40% when γ=9%.

The sand used was Edosaki sand (ρ_s=2.72Mg/m^3, D_{50}=0.26mm, F_C=8.6%, U_C=3.4, w_{opt}=16%). The sample preparation procedures are as follows: Firstly the shear box was filled with the cement-treated sand. The sand mixed with the Portland cement (the cement-treated sand) with a near-optimum water content was compacted in layers to a dry density of 1.26Mg/m^3, corresponding to a relative compaction of 80%. Then the middle of the specimen was bored (white portion in Fig. 2) to make the untreated portion in the specimen. This untreated sand in the specimen is referred to as infilling sand in connection with this sample preparation procedure. The infilling sand (untreated sand) was compacted to a dry density of 1.34Mg/m^3, corresponding to a relative compaction of 85%, with the similar method used in the cement-treated sand preparation. After completion of a specimen, the lid (upper metal plate) was attached to the shear box and it was cured for one day in air and for six days under water. The specimens were then sheared at a nominal shear strain rate of 0.3%/min in the direction indicated by the arrow in Figs. 2 & 3 using a hydraulic actuator.

Test conditions are summarised in Table 1. Thicknesses of the soil cement walls (t_1 & t_2) and the strength of the soil cement were changed in the tests (Cases 01–07). Cement contents of 6% and 12% were used in the tests. Table 2 summarises the unconfined compressive strengths of cement-treated sand. In Case 05, instead of the infilling sand, a dummy block was placed in the soil cement walls so that it can prevent out of plane deformation of the soil cement walls parallel to the shearing direction. In this case, since the dummy block has no shearing resistance in the shearing direction, contribution of the infilling sand to overall resistance of the specimen can be examined by comparing with Cases 03 & 04. Apart from the cases mentioned above, the test on the untreated sand only (Case 08) and the tests on the cement-treated sand only (Cases 09–10) were also performed.

Table 1 Test conditions.

Case	Cement content, C	Infilling sand	Replacement ratio, a_c	t_1	t_2
01	6%	w/o	52%	10mm	20mm
02	6%	w/	52%	10mm	20mm
03	12%	w/o	52%	10mm	20mm
04	12%	w/	52%	10mm	20mm
05	12%	w/o*1	52%	10mm	20mm
06	12%	w/o	64%	20mm	20mm
07	12%	w/	64%	20mm	20mm
08	0%	w/*2	0%	0mm	0mm
09	6%	w/o*3	100%	50mm	50mm
10	12%	w/o*3	100%	50mm	50mm

*1: Instead of infilling sand, a dummy block is placed to prevent out of plane deformation of soil cement walls parallel to shearing direction.
*2: Untreated sand only. *3: Treated sand only.

Table 2 Unconfined compressive strength of cement-treated sand.

Cement content, C	Average of q_u	Coefficient of variation
6%	408kPa	9.0%
12%	1010kPa	12%

3. TEST RESULTS AND DISCUSSION

3.1 Contribution of Untreated Sand in Soil Cement Walls to Overall Shearing Resistance of Improved Ground

Figure 4 shows the nominal shear stress–strain relations for Cases 01–07. Here the nominal shear stress is defined by the horizontal load applied to the upper metal plate divided by the projected area (100×100mm^2) and the nominal shear strain is defined by the horizontal displacement of the upper metal plate divided by the specimen height (100mm). Irrespective of the replacement ratio or cement content, τ–γ curves for the cases without the infilling are located below those for the case with the infilling sand, showing the strain softening after reaching the peak. For the smaller replacement ratio cases without the infilling sand (Cases 01 & 03, t_1=10mm, a_c=52%) the difference between the peak and residual strength is not so large, while the difference is relatively large for the case with the larger replacement ratio (Case 06, t_1=20mm, a_c=64%). The cases with the infilling sand (Cases 02, 04 & 07) show no strain softening and the shearing resistance is larger than those without the infilling sand.

These results indicate that the remaining sand, i.e., untreated sand, in the soil cement walls makes the shearing resistance of the overall improved ground larger and provides ductility to the improved ground. The simplistic thinking may draw a conclusion that the shearing resistance of the untreated sand makes the shearing resistance of the overall improved ground larger. However the shearing resistance of the untreated sand may not be comparable to that of the cement-treated sand, as the expected pressure confining the untreated sand is small in this series of tests. To examine how the infilling sand contributes to the better performance of the improved ground, the test on the untreated sand only (Case 08) and the test with the dummy block in place of the infilling sand (Case 05) were performed.

Figure 5 plots the stress path and nominal shear stress–strain relation for untreated sand (Case 08). Since the vertical stress cannot be controlled with the shear box used in this study, in Case 08 the untreated sand specimen was prepared following exactly the same procedures mentioned above and the vertical stress change was measured by four earth pressure cells attached on the upper metal plate. Representative vertical stress of the specimen was calculated by averaging the four pressure cell readings. The initial vertical stress before shearing was 27kPa in Case 08. In the other cases, measurement of the vertical stress distribution was also attempt. However reliable readings could not be obtained due to (1) the large stiffness difference between the treated and untreated sands and (2) difficulties in having good contact between the pressure cell and treated soil. Since the stiffness of the untreated sand is much smaller than that of the cement-treated sand, in the other cases with the cement-treated sand the vertical stress of the untreated sand may have been less or equal to the value observed in Case 08. As seen in the figure, the shearing resistance of the untreated sand is remarkably smaller than that of the treated sand and the stress path goes for the origin. These suggest that the expected shearing resistance of the untreated sand in the soil cement walls was very small in this study. Thus, it can be concluded that the direct contribution of the shearing resistance of the untreated sand to the overall shearing resistance of the improved soil was small.

Cracks observed on the surface of the soil cement wall parallel to the shearing direction at γ=9% are illustrated in Fig. 6 for Cases 01–04. The dashed lines in the figure indicate the location of the inside surface of

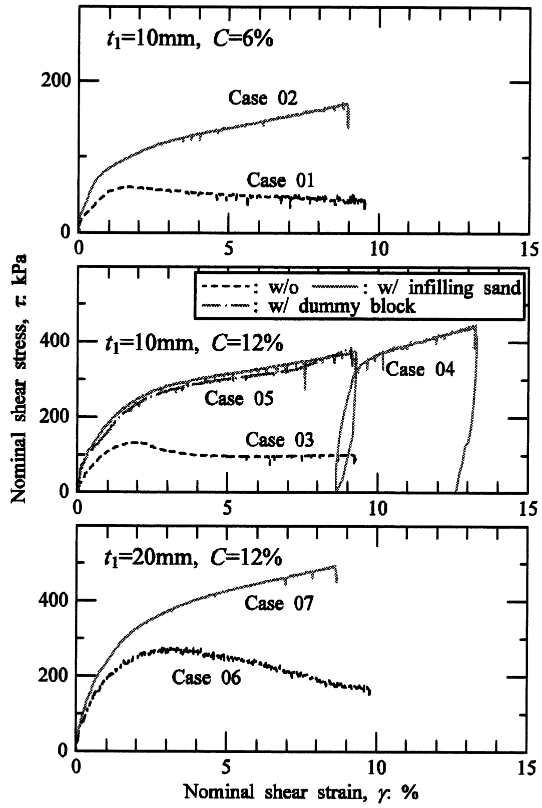

Figure 4 Nominal shear stress–strain relations (Cases 01–07).

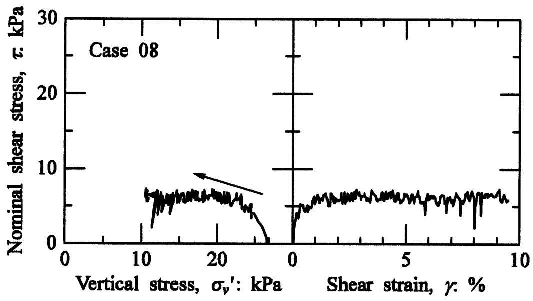

Figure 5 Stress path and nominal shear stress–strain relation for untreated sand (Case 08).

the soil cement wall normal to the shearing direction. In the cases with the infilling sand (Cases 02 & 04 and Case 07 (no drawing here)), no major crack was observed. (Although no drawing for Case 07 is shown here due to limitations of space, it is similar to Cases 02 & 04.) In the tests for the cement-treated sand only (Cases 09–10), no visible crack was observed, while potential diagonal cracks were found in the post-mortem examination of the specimens. On the other hand, in the cases without infilling sand (Cases 01 & 03 and Case 06 (no drawing here)), just after reaching peak in the stress–strain relation, the major cracks appeared in the soil cement walls parallel to the shearing direction, resulting in the diagonal (Case 03) or vertical major cracks (Cases 01 & 06). In these cases, the soil cement walls parallel to the shearing direction showed out-of-plane deformation during sharing and parts of the wall fell in the walls arranged in grid pattern.

As mentioned above, considering the fact that the expected shearing resistance of the untreated sand is

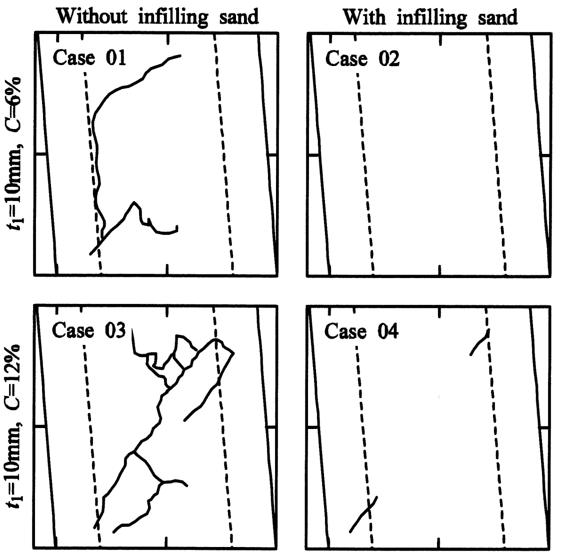

Figure 6 Cracks observed on surface of soil cement wall parallel to shearing direction at γ=9% (Cases 01–04).

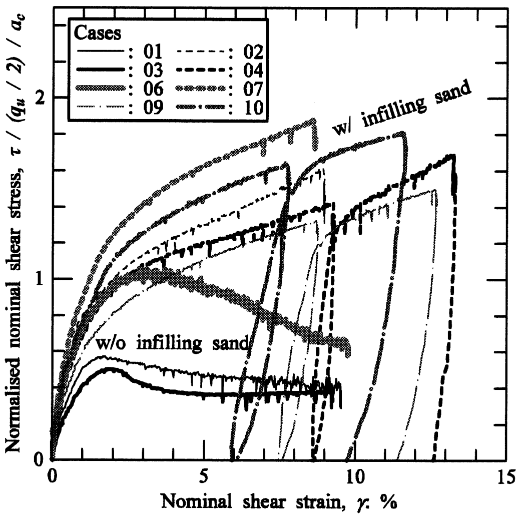

Figure 7 Normalised nominal shear stress–strain relations for all cases but Cases 05 & 08.

small, the major function of the untreated sand in the soil cement walls may be to prevent out-of-plane deformation of the soil cement walls parallel to the shearing direction during sharing. To confirm this, the test without the infilling sand but the dummy block that prevents out of plane deformation of the soil cement walls parallel to the shearing direction was conducted (Case 05). The plot for Case 05 is shown in Fig. 4. As seen in the figure, τ–γ curve for Case 05 is comparable to that for Case 04 (the case with the infilling sand). This confirms that the major function of the untreated sand in the soil cement walls is to prevent out-of-plane deformation of the soil cement walls parallel to the shearing direction, resulting in the larger shearing resistance and ductile behaviour of the improved ground.

3.2 Normalisation of Shearing Resistance of Improved Ground by Unconfined Compressive Strength and Replacement Ratio

Figure 7 plots the normalised nominal shear stress–strain relations for the all cases but Cases 05 & 08. In the figure, the nominal shear stress is normalised by the unconfined compressive strength of the cement-treated sand and replacement ratio. As the strength of the cement-treated sand varies rather widely as shown in Table 2, in the strict sense, the normalised τ–γ curves are not unique.

However, as a whole, it seems that (1) the τ–γ curves for the cases with the infilling sand seem can be normalised by the unconfined compressive strength of the treated sand and replacement ratio and (2) the residual strength for the cases without infilling sand. When the untreated sand remains in the soil cement walls arranged in grid pattern, the shear stress at yield τ_{yield} / (q_u / 2) / $a_c \approx 1$ within the experimental conditions.

On the other hand, when the there is no untreated sand in the soil cement walls arranged in grid pattern, even though the shear stress at yield seems to depend on the thickness of the soil cement walls parallel to the shearing direction (t_1) and unconfined compressive strength of the treated sand (q_u), the residual shear strength τ_{res} / (q_u / 2) / $a_c \approx 0.4$ within the experimental conditions.

4. SUMMARY

To mitigate the levee settlement induced by the lateral spreading of the liquefied foundation soils, remedial measures are often adopted to the foundation near toes of a levee and solidification of the liquefiable foundation is widely used in practice. In this study the simple shear tests on the improved soils in grid pattern were performed to study the ductility of the composite material that consists of the untreated and cement-treated soils.

Test results reveal that the unimproved sand in grids prevents out-of-plane deformation of improved soil walls arranged in grid pattern and makes the shearing resistance of the overall improved zone larger. It is also found that the stress–strain relations of the sand improved in grid pattern can be a unique line as a whole when they are normalised by the unconfined compressive strength of the cement-treated sand and replacement ratio.

References:

Koga, Y. & Matsuo, O. (1990), "Shaking table tests of embankments on liquefiable sandy ground", *Soils and Foundations*, Vol.30, No.4, 162-174.

Namikawa, T., Suzuki, Y. & Koseki, J. (2005), "Seismic response analysis of lattice-shaped ground improvement", *Proc. Deep Mixing '05*, 263-271.

Okamura, M. & Matsuo, O. (2002), "Effects of remedial measures for mitigating embankment settlement due to foundation liquefaction", *Int'l J. Physical Modelling in Geotechnics*, Vol.2, No.2, 1-12.

Tanimoto, S., Sugita, H. & Takahashi, A. (2007), "Dynamic centrifuge model tests on levees with ground improvement by soil cement walls in grid pattern", *Proc. 42nd Japan National Conf. of Geotechnical Engineering*, 1731-1732 (in Japanese).

Technical Committee on Countermeasures for River Facilities against Earthquake (1996), Interim Report (in Japanese).

Fifth International Conference on Urban Earthquake Engineering
March 4-5, 2008, Tokyo Institute of Technology, Tokyo, Japan

NUMERICAL SIMULATION OF LIQUEFACTION PROCESS OF UNSATURATED SOIL

Ryosuke Uzuoka[1], Tatsuhiro Shoji[2], Noriaki Sento[3], Motoki Kazama[4] and Toshiyasu Unno[5]

1) Associate Professor, Dept. of Civil Engineering, Tohoku University, Japan
2) Graduate Student, Dept. of Civil Engineering, Tohoku University, Japan
3) Assistant Professor, Dept. of Civil Engineering, Tohoku University, Japan
4) Professor, Dept. of Civil Engineering, Tohoku University, Japan
5) Postdoctoral fellow, The National Institute for Rural Engineering, Japan
uzuoka@civil.tohoku.ac.jp, shoji.t@soil1.civil.tohoku.ac.jp, nsento@civil.tohoku.ac.jp, motoki_kazam@civil.tohoku.ac.jp, tunno@affrc.go.jp

Abstract: Numerical simulations of the unsaturated triaxial tests were performed using the porous media theory and simplified elasto-plastic constitutive model for sand. In the tests, cyclic shear strain was applied to fine clean sand with the same dry density but different initial suction states under the undrained condition. The zero effective stress state (i.e. liquefaction) for unsaturated sand was found to have been established when both the pore air and water pressures build up to the point where it is equal to the initial total pressure. Therefore, the consideration of pore air pressure is necessary for simulation of liquefaction of unsaturated sand. In this paper, the behavior of three phases with soil skeleton, pore water and pore air were considered based on porous media theory. The simplified elasto-plastic constitutive model is based on the non-associated flow rule and nonlinear kinematic hardening rule. The simulations well reproduced the triaxial test results in the cases with higher degree of saturation than about 70%. The simulations, however, overestimated the pore water and air pressures in the cases with lower degree of saturation than about 70%.

1. INTRODUCTION

Artificial residential or rural grounds and soil structures such as road embankments etc. have been severely damaged during earthquakes. Particularly artificial grounds located on a old valley largely deformed due to liquefaction because the ground water level was high after rainfall. Moreover the capillary zone in an artificial ground with a volcanic soil with high water retention is usually thick; therefore it possibly liquefies during earthquake (Uzuoka et al. 2005).

Cyclic triaxial tests with unsaturated soil have been performed by many researchers (e.g. Yoshimi et al. 1989, Tsukamoto et al. 2002, Selim and Burak 2006). It is well known that the liquefaction strength of unsaturated sand is larger than that of saturated sand with the same dry density. These studies mainly focused on the cyclic behavior of unsaturated soil from macroscopic view. Recently liquefaction mechanism of unsaturated soil has been discussed (e.g. Okamura and Soga 2006) and it is suggested that the behavior of pore air plays an important role during liquefaction of unsaturated soil.

Liquefaction analyses of unsaturated ground have been performed using porous media theory (e.g. Meroi and Schrefler 1995). Most liquefaction analyses, however, assumed that pore air pressure was zero and the behavior of pore air was not directly treated.

In this study, the behavior of three phases with soil skeleton, pore water and pore air are considered based on porous media theory. Numerical simulations of the unsaturated triaxial tests (Unno et al. 2008) are performed using the porous media theory and simplified elasto-plastic constitutive model for sand. The simplified elasto-plastic constitutive model is based on the non-associated flow rule and nonlinear kinematic hardening rule. The applicability of the numerical method is discussed through the simulations.

2. CYCLIC TRIAXIAL TESTS OF UNSATURATED SAND

Cyclic triaxial tests which continuously measured pore air and water pressure were performed. A glass fiber filter and ceramic disk with an AEV of 200 kPa air were installed at the top and bottom of specimen respectively. The volume change of the whole specimen was measured directly from the differential pressure meter between the inner cell and outer water head. Continuous measurements of the pore water and air pressure were taken to obtain the soil suction.

The specimen was made of Toyoura sand by air pluviation method. The relative densities of the specimens were about 26 % and 60 %. The degree of water saturation was set to be from 20 % to 100 % by controlling air pressure during the isotropic consolidation process. The physical and stress conditions of the specimens after the consolidation are shown in Table 1. Table 1 shows the only cases for the simulations in this study. The pore water pressure was

Table 1 Physical and stress conditions of specimens

After consolidation

Case No.	c-1	c-3	c-6	c-7	c-9	c-10
Void ratio	0.74	0.74	0.73	0.74	0.72	0.74
Water saturation	100.0	94.8	64.8	51.6	20.2	0.0
Mean total stress	20.5	21.4	24.1	23.7	30.0	20.0
Pore water pressure	0.0	0.0	0.0	0.0	0.0	-
Pore air pressure	0.0	3.2	3.9	5.3	10.9	-
Suction	0.0	3.2	3.9	5.3	10.9	-
Net stress	20.5	18.2	20.2	18.4	19.1	-
MASS	20.5	21.2	22.7	21.1	21.3	20.0

After cyclic loading

Case No.	c-1	c-3	c-6	c-7	c-9	c-10
Void ratio	0.74	0.74	0.70	0.69	0.71	0.65
Water saturation	100.0	94.6	68.6	54.8	20.6	0.0

almost zero after the consolidation and the pore air pressure increased with the decrease in water saturation. The MASS, mean average skeleton stress (e.g. Gallipoli et al. 2003), which means the mean effective stress of unsaturated soil, was about 20 kPa through all cases.

The cyclic shear was applied to the specimen under undrained air and water conditions. The input axial strain was the sinusoidal wave with multi step amplitudes whose single amplitudes were 0.2, 0.4, 0.8, 1.2, 1.6, and 2.0 with every ten cycles. The frequency of the sinusoidal wave was 0.005 Hz. This loading rate is slow enough to achieve an equilibrium condition between air and water pressure. The test results are shown later with the simulation results.

3. CYCLIC TRIAXIAL TESTS OF UNSATURATED SAND

3.1 Balance and constitutive equations

Firstly the basic equations are derived based on porous media theory (e.g. de Boer 2000, Schrefler 2002). The partial densities of soil skeleton, pore water and air are defined as follows,

$$
\begin{aligned}
\rho^s &= n^s\rho^{sR} = (1-n)\rho^{sR} \\
\rho^w &= n^w\rho^{wR} = ns^w\rho^{wR} \\
\rho^a &= n^a\rho^{aR} = ns^a\rho^{aR} = n(1-s^w)\rho^{aR}
\end{aligned}
\tag{1}
$$

where ρ^s, ρ^w and ρ^a are the partial densities of soil skeleton, pore water and air phase respectively. ρ^{sR}, ρ^{wR} and ρ^{aR} are the real densities of each phase, n^s, n^w and n^a are the volume fraction of each phase. n is the porosity, s^w is the degree of water saturation and s^a is the degree of air saturation.

Mass balance equation for α phase ($\alpha = s, w, a$) is

$$
\frac{D^\alpha\rho^\alpha}{Dt} + \rho^\alpha \operatorname{div}\mathbf{v}^\alpha = 0 \tag{2}
$$

where $D^\alpha\square/Dt$ is the material time derivative with respect to α phase, $\mathbf{v}^\alpha$ is the velocity of α phase. The mass exchange among three phases is ignored. The linear momentum balance equation of α phase is

$$
\rho^\alpha\frac{D^\alpha\mathbf{v}^\alpha}{Dt} = \operatorname{div}\boldsymbol{\sigma}^\alpha + \rho^\alpha\mathbf{b} + \hat{\mathbf{p}}^\alpha \tag{3}
$$

where $\boldsymbol{\sigma}^\alpha$ is the Cauchy stress tensor of α phase, $\mathbf{b}$ is the body force vector, $\hat{\mathbf{p}}^\alpha$ is the interaction vector against other phases. Although $\hat{\mathbf{p}}^\alpha$ is related to the relative velocity between phases, this term is not necessary for the simulation of undrained triaxial tests assuming that stress and strain in the specimen are homogeneous.

Constitutive equations are the followings. The partial Cauchy stress of each phase is defined as

$$
\begin{aligned}
\boldsymbol{\sigma}^s &= \boldsymbol{\sigma}' - (1-n)(s^w p^w + s^a p^a)\mathbf{I} \\
\boldsymbol{\sigma}^w &= -ns^w p^w\mathbf{I} \\
\boldsymbol{\sigma}^a &= -ns^a p^a\mathbf{I}
\end{aligned}
\tag{4}
$$

where $\boldsymbol{\sigma}'$ is the average skeleton stress tensor (e.g. Gallipoli et al. 2003), p^w is the pore water pressure and p^a is the pore air pressure. These pressures are defined as positive in compression. The compressibility of pore water under an isothermal condition is assumed as

$$
\frac{D^s\rho^{wR}}{Dt} = \frac{\rho^{wR}}{K^w}\frac{D^s p^w}{Dt} \tag{5}
$$

where K^w is the bulk modulus of pore water. The compressibility of pore air under an isothermal condition assumed as

$$
\frac{D^s\rho^{aR}}{Dt} = \frac{1}{\Theta\bar{R}}\frac{D^s p^a}{Dt} \tag{6}
$$

where Θ is the absolute temperature, $\bar{R}$ is the specific gas constant of air. The constitutive relation between water saturation and suction is assumed as

$$
\frac{D^s s^w}{Dt} = c\frac{D^s p^c}{Dt} = c\frac{D^s(p^a - p^w)}{Dt} \tag{7}
$$

where c is the specific water capacity. The function of this soil water characteristic curve (SWCC) based on VG model (van Genuchten, 1980) is assumed as

$$
s^w = \beta_{vg}\left\{1 + (\alpha_{vg}p^c)^{n_{vg}}\right\}^{-m_{vg}} \tag{8}
$$

where the coefficients are assumed as

$$
\begin{aligned}
&\beta_{vg} = s_0^w\left\{1 + (\alpha_{vg}p_0^c)^{n_{vg}}\right\}^{m_{vg}} \\
&\alpha_{vg} = \alpha'_{vg}/s_0^w \\
&n_{vg} = s_0^w \quad m_{vg} = m'_{vg}/s_0^w
\end{aligned}
\tag{9}
$$

where the subscript 0 shows the initial value before cyclic shear. α'_{vg} and m'_{vg} are the material constants.

3.2 Simplified constitutive equation for soil skeleton

A simplified constitutive equation for soil skeleton is used in order to discuss the applicability of porous media theory. Assuming that plastic deformation occur only when the deviatoric stress ratio changes, the yield function is assumed as

$$
f = \|\boldsymbol{\eta} - \boldsymbol{\alpha}\| - k = \|\mathbf{s}/p' - \boldsymbol{\alpha}\| - k = 0 \tag{10}
$$

where $p' = -\mathrm{tr}\,\boldsymbol{\sigma}'/3$ is the mean average skeleton stress, $\mathbf{s}$ is the deviatoric stress tensor, k is the material parameter which defines the elastic region. $\boldsymbol{\alpha}$ is the kinematic hardening parameter and its nonlinear evolution rule (Armstrong and Frederick 1966) is assumed as

$$\dot{\boldsymbol{\alpha}} = a\left(b\dot{\mathbf{e}}^p - \boldsymbol{\alpha}\dot{\varepsilon}_s^p\right)$$
$$\dot{\varepsilon}_s^p = \left\|\dot{\mathbf{e}}^p\right\| \tag{11}$$

where a, b are the material parameters, $\dot{\mathbf{e}}^p$ is the plastic deviatoric strain rate tensor. Assuming non-associated flow rule, the plastic potential function is assumed as

$$g = \|\boldsymbol{\eta} - \boldsymbol{\alpha}\| + M_m \ln\left(p'/p'_a\right) = 0 \tag{12}$$

where M_m is the material parameter which defines the critical state ratio, p'_a is p' when $\|\boldsymbol{\eta} - \boldsymbol{\alpha}\| = 0$. Finally the elastic module are assumed as

$$K^e = K^* p' \quad G^e = G^* p' \tag{13}$$

where K^e is the elastic bulk modulus, G^e is the elastic shear modulus, K^* and G^* are the dimensionless elastic module respectively.

3.3 Governing equations for simulation of triaxial test

A right-handed coordinate system is adopted and the z-direction is the vertical axial direction of triaxial specimen. With equations (4), (7) and the boundary condition that the lateral total stresses are constant, the followings are obtained.

$$\dot{\sigma}'_x = \dot{p}^w(s^w - cp^w + cp^a) + \dot{p}^a(s^a + cp^w - cp^a) = \dot{\sigma}'_y$$
$$\dot{\sigma}'_z = \dot{\sigma}_z + \dot{p}^w(s^w - cp^w + cp^a) + \dot{p}^a(s^a + cp^w - cp^a) \tag{14}$$

With equations (1), (2), (5), (6), (7) and undrained conditions for pore water and air, the continuity equations of pore water and air with respect to soil skeleton are obtained as

$$n\left(\frac{s^w}{K^w} - c\right)\dot{p}^w + nc\dot{p}^a + s^w\dot{\varepsilon}_v^s = 0$$
$$n\left(\frac{s^a}{\rho^{aR}\Theta\bar{R}} - c\right)\dot{p}^a + nc\dot{p}^w + s^a\dot{\varepsilon}_v^s = 0 \tag{15}$$

where $\dot{\varepsilon}_v^s$ is the volumetric strain rate of soil skeleton. With equations (14), (15) and the rate form of constitutive equation of soil skeleton, the unknown variables (the lateral strain rate $\dot{\varepsilon}_x^s = \dot{\varepsilon}_y^s$, the vertical total stress rate $\dot{\sigma}_z$, pore water pressure rate $\dot{p}^w$ and pore air pressure rate $\dot{p}^a$) can be calculated from the input axial strain rate $\dot{\varepsilon}_z^s$.

4. NUMERICAL CONDITIONS AND RESULTS

4.1 Calibration of material parameters

The material parameters of constitutive equation of soil skeleton are calibrated with the test results in the cases "c-1" (saturated sand) and "c-10" (dry sand) in Table 1. The constitutive model with the calibrated material parameters reproduced the time histories of void ratio in "c-10" and excess pore water pressure in "c-1". Table 2 shows the calibrated material parameters of the constitutive model. The SWCC parameters in equation (9) were determined to reproduce the change in the water saturation of the specimen during cyclic loading. The SWCC parameters and physical parameters of pore water and air also are shown in Table 2.

Table 2 Material parameters in simulations

Elasto-plastic model parameters		VG model paramters	
Dimensionless shear modulus, Ge	873	α'_{vg}	0.01
Dimensionless bulk modulus, Ke	582	m'_{vg}	0.3
Nonlinear hardening paramter, a	1.2/0.8	Phisical paramters of water and air	
Nonlinear hardening paramter, b	5000	K^w (kPa)	1.00E+06
Critical state stress ratio, Mm	1.2/0.8	$1/(R\Theta)$ (s^2/m^2)	1.21E-05
Yield function parameter, k	0.001	ρ^{aR} (Mg/m^3)	1.23E-03

4.2 Test and simulation results in unsaturated cases

The time histories of pore water pressure, pore air pressure, suction, mean average skeleton stress and void ratio from tests and simulations in "c-3", "c-6", "c-7" and "c-9" are shown in Figure 1, 2, 3 and 4 respectively. In the test results (denoted "Test" in the figures), the pore water and air pressure increase during cyclic shear under undrained condition of water and air. In the case "c-3" and "c-6" with higher water saturation, the pore water and air pressure attain the mean total stress and the suction becomes almost zero. At the same time the mean average skeleton stress also become almost zero and the unsaturated specimen liquefies completely. Although this behavior is similar to liquefaction of saturated sand, the void ratio of unsaturated sand deceases unlike saturated sand. This volumetric change in unsaturated specimen is due to negative dilatancy and high compressibility of pore air. On the other hand, in the case "c-7" and "c-9" with lower water saturation, the suction and the mean average skeleton stress do not attain zero although the pore water and air pressure increase during cyclic loading.

In the simulated results (denoted "Model" in the figures), the model well reproduces the test results in the case "c-3" and "c-6" with higher water saturation. Therefore, the simplified constitutive equation of soil skeleton is applicable to predict liquefaction of unsaturated sand in the framework of three-phase porous media theory. On the other hand, in the case "c-7" and "c-9" with lower water saturation, the model overestimates the pore and air pressure of test results. In particular, the error is very large in the case "c-9" and the simplified constitutive is not applicable to this case. The modification of the constitutive equation is necessary in the case with low initial water saturation.

5. CONCLUSIONS

Numerical simulations of the unsaturated triaxial tests were performed using the three-phase porous media theory and simplified elasto-plastic constitutive model for sand. The simulations well reproduced the triaxial test results in the cases with higher degree of saturation than about 70%. The simplified constitutive equation of soil skeleton is applicable to predict liquefaction of unsaturated Toyoura sand in the framework of three-phase porous media theory. The simulation, however, overestimated the pore water and air pressures in the cases with lower degree of saturation than about 70%.

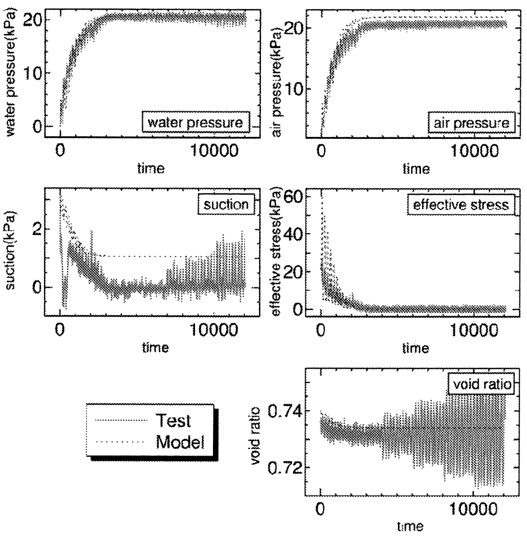

Figure 1 Test and simulation in "c-3"

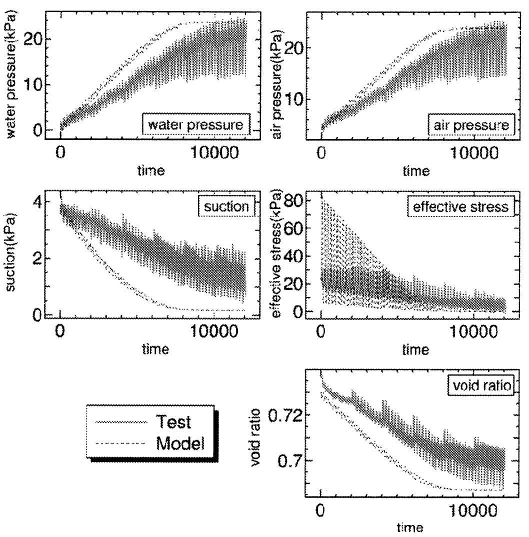

Figure 2 Test and simulation in "c-6"

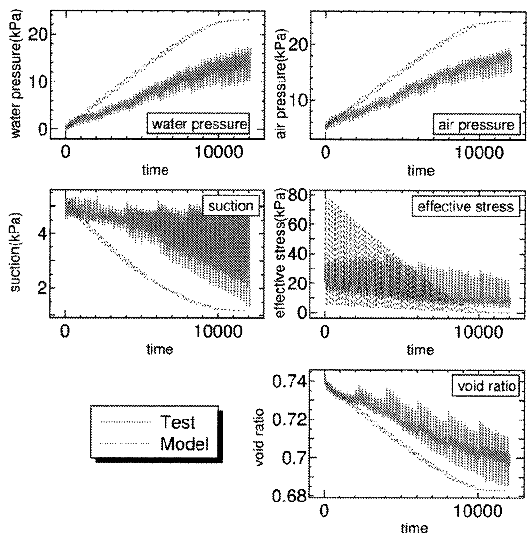

Figure 3 Test and simulation in "c-7"

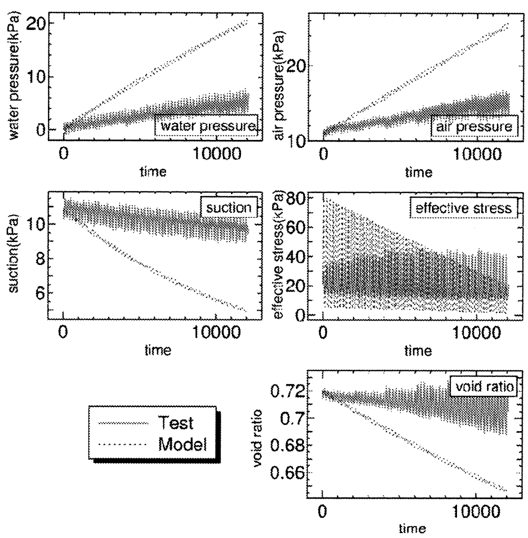

Figure 4 Test and simulation in "c-9"

References:

Armstrong, P.J. and Frederick, C.O. (1966), "A mathematical representation of the multiaxial Bauschinger effect," C.E.G.B. Report RD/B/N731, Berkeley Nuclear Laboratories, Berkeley, UK.

de Boer, R. (2000), "Contemporary progress in porous media theory," *Applied Mechanics Reviews*, **53**(12), 323-369.

Gallipoli, D., Gens, A., Sharma, R. and Vaunat, J. (2003), "An elasto-plastic model for unsaturated soil incorporating the effects of suction and degree of saturation on mechanical behaviour," *Geotechnique*, **53**(1), 123-135.

van Genuchten, R. (1980), "A Closed-form Equation for Predicting the Hydraulic Conductivity of Unsaturated Soils," *Soil Science Society of America Journal*, **44**, 892-898.

Meroi, E.A. and Schrefler, B.A. (1995), "Large strain static and dynamic semisaturated soil behavior," *Int. J. for Numerical and Analytical Methods in Geomechanics*, **19**(8), 1-106.

Okamura, M. and Soga, Y. (2006), "Effects of pore fluid compressibility on liquefaction resistance of partially saturated sand," *Soils and Foundations*, **46**(5), 93-104.

Schrefler, B.A. (2002), "Mechanics and thermodynamics of saturated/unsaturated porous materials and quantitative solutions," *Applied Mechanics Reviews*, **55**(4), 351-388.

Selim, A., A. Burak, G. (2006), "Cyclic stress-strain behavior of partially saturated soils," *Proc. of 3rd Int. Conf. on Unsaturated Soils*, 497-507.

Tsukamoto, Y., Ishihara, K., Nakazawa, H., Kamada, K. and Huang, Y. (2002), "Resistance of partly saturated sand to liquefaction with reference to longitudinal and shear wave velocities," *Soils and Foundations*, **42**(6), 93-104.

Unno, T., Kazama, M., Uzuoka, R. and Sento, N. (2008), "Liquefaction of unsaturated sand considering the pore air pressure and volume compressibility of the soil particle skeleton," *Soils and Foundations*. (in press)

Uzuoka, R., Sento, N., Kazama, M. and Unno, T. (2005), "Landslides during the earthquake on May 26 and July 26, 2003 in Miyagi, Japan," *Soils and Foundations*, **45**(4), 149-163.

Yoshimi, Y., Tanaka, K. and Tokimatsu, K. (1989), "Liquefaction resistance of a partially saturated sand," *Soils and Foundations*, **29**(3), 157-162.

Fifth International Conference on Urban Earthquake Engineering
March 4-5, 2008, Tokyo Institute of Technology, Tokyo, Japan

EVALUATION OF PERFORMANCE OF EXISTING PILE FOUNDATION AGAINST SEISMIC SOIL DISPLACEMENTS

Shinichiro Mori[1)] and Ryoma Yamazaki[2)]

1) Associate Professor, Department of Civil and Environmental Engineering, Ehime University, Japan
2) Undergraduate Student, Department of Civil and Environmental Engineering, Ehime University, Japan
mori@dpc.ehime-u.ac.jp

Abstract: Pile foundations for structures are subjected to seismic lateral displacements from their surrounding ground. Provisions with regard to such seismic soil displacements have been newly introduced into design codes as seismic actions in design of pile foundations. However, there are no efficient tools for vulnerability evaluation of pile foundations against such newly introduced seismic actions for prioritizing and screening an inventory of existing structures. The objectives of this paper are to propose a new concept of evaluation chart on the basis of performance-based design and to demonstrate the developed evaluation charts with actual application. It is concluded that the proposed concept of developing evaluation charts for existing pile foundation against seismic lateral displacement is effective for prioritizing and screening an inventory of pile foundations of many kinds of structures from the theoretical and practical viewpoints.

1. INTRODUCTION

Pile foundations for structures are subjected to seismic lateral displacements from their surrounding ground. The seismic lateral soil displacements are due to spreading of ground during and after liquefaction and the horizontal vibration of the ground. Damages to the subsurface portions of piles were repetitively reported in past earthquakes including the 1995 Kobe earthquake. It has been found that this kind of damage is mainly caused by the above mentioned seismic soil displacements. For measurement against such a seismic risk, provisions on consideration of the seismic soil displacements as newly introduced seismic actions in design of pile foundations has recently emerged in some revised design codes in Japan and newly developed International Standard ISO23469.

The performance of pile foundations agaisnt the seismic soil displacements can be evaluated by numerical methods varying from simplified equivalent static to detailed dynamic analyses. Thus, designers can choose an appropriate method in the seismic design of newly constructed structures. On the other hand, many of such various analysis methods are not efficient for vulnerability evaluation of pile foundations against such newly introduced seismic actions for prioritizing and screening an inventory of existing structures. Because the evaluation by numerical analyses, even the simplified methods, requires geotechnical engineers and lots of their work time. For this reason, it is necessary to develop simple evaluation techniques for civil and building engineers for quick prioritizing and screening.

The objectives of this paper are to propose a new concept of evaluation chart on the basis of performance-based design, to demonstrate the developed evaluation charts with actual application, and to discuss the perspective of the charts to be elaborated.

2. CONCEPT OF EVALUATION CHARTS

Concept of evaluation chart for seismic performance of piles is described in this section. Figure 1 shows two kinds of seismic actions for design of a pile foundation; inertial forces from the superstructure and footing, and seismic soil displacements along the depth from its surrounding ground.

Evaluation charts to be developed are required to be theoretically rational and easy for the use by practicing civil and building engineers. Moreover, the charts should be easy to develop for various given conditions in terms of type,

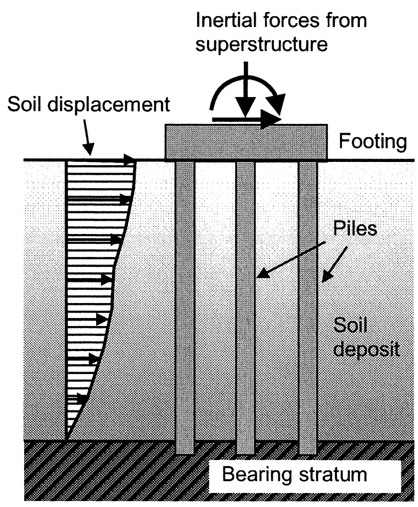

Figure 1 Seismic Actions on a Pile Foundation

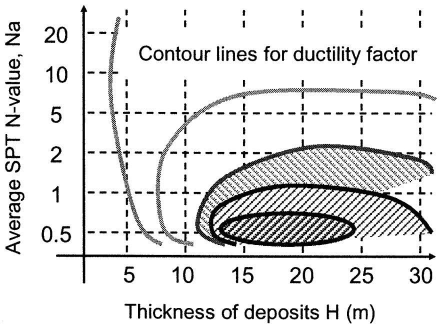

Figure 2 Conceptual Chart for Pile Evaluation

diameter and length of pile, stratification of ground, and design input earthquake motion in existing pile foundations.

The concept of the evaluation charts is realized by the diagrams of contour lines of ductility factor of pile drawn in two parameter space. The contour lines are drawn based on the interpolation of the results of parametric calculations by numerical seismic analysis for systematically combined couples of the two parameters, such as the thickness of a soil deposit and the average of a characteristic value of the soil deposit. Figure 2 illustrates a schematic diagram of ductility factor estimation for the evaluation chart.

3. ASSUMPTIONS FOR DEVELOPMENT

3.1 Seismic Performance Criterion of Pile

Ductility factor of pile is adopted as a seismic performance criterion of pile. The ductility factor of pile, m is defined by the ratio of response curvature of pile, φ to curvature of pile at yielding, φ_y, as in equation (1). Allowable ductility factor for structural safety depends on a relevant seismic design code to be used. Thus, actual values of m for existing pile foundations of interest need to be evaluated by referring the design code used in the design of the pile foundations.

Here, we assume that the existing pile foundations have been appropriately designed against inertial forces from superstructure as per a relevant design code in time. In this research, it is roughly assumed that m is equal to 1.0, based on the consideration on performance of pile foundations designed according to Design Specifications issued by Japan Road Association (JRA) in 1980 through 1996 in terms of specifications and actual practice.

$$m=\varphi/\varphi_y \tag{1}$$

3.2 Input Earthquake Motion

Input earthquake motion for evaluation is given. However, this may not be identical to the input motion used in the design of the existing structures. In this study, expected earthquake motion provided by Central Disaster Management Council (CDMC) of Japan in the Nankai earthquake, which is due to hit pacific coast of southern Japan in near future, is used for site response analyses and evaluation of amplitude of seismic soil displacement. Figure 3 shows the time history of acceleration at bedrock of site of interest.

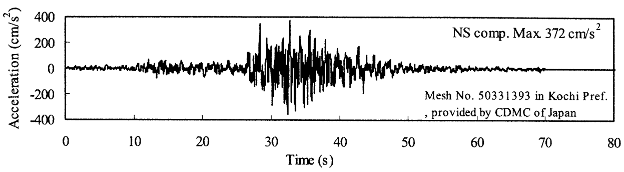

Figure 3 Input Earthquake Motion for Evaluation

3.3 Model of Ground

In general, ground for pile foundation is assumed to be a soil deposit. This is characterized by stratification, type of soil, rigidity of soil, and the existence and the depth of boundaries of layers with high contrast of soil rigidity. For end bearing pile, the boundary with highest contrast may be the top of bearing stratum. Hence, a two-layer model consisting of homogeneous soil deposit overlying the bearing stratum is adopted as a standard model for evaluation (see Figure 4 (a)). The soil deposit is characterized by thickness of the soil deposit, H, and an average of SPT N-values in the deposit, N_a.

The ground for pile foundation may also be featured by soil deposit with soft clayey or silty layer overlying relatively dense sandy layer. The boundary between such two layers may have the second highest contrast. Hence, a three-layer model consisting of soil deposit with soft upper layer overlying relatively firm layer underlain by bearing stratum is also adopted as another standard model (see Figure 4 (b)). In this model, thickness of upper and lower layer in the soil deposit are H_1 and H_2, respectively, and averages of N-values in those two layers are N_1 and N_2, respectively. The following equations are used for parameter conversion of between two- and three- layer models.

$$H_1+H_2=H \tag{2}$$

$$(N_1H_1+N_2H_2)/H= N_a \tag{3}$$

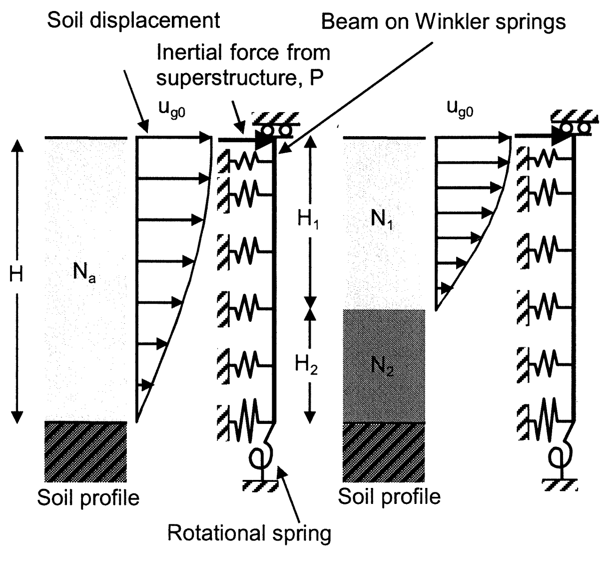

(a) Two Layer Model (b) Three Layer Model

Figure 4 Models of Ground, Seismic Displacement and a Pile Foundation for Numerical Analysis

In this study, it is assumed that H_1=10 m, N_2=20, for representing the typical feature of deposits in area of interest.

3.4 Model of Pile

A pile foundation can be modeled to a single pile under some assumptions. Only horizontal inertial force is considered neglecting the effects of vertical force and overturning moment from superstructure. In this study, end bearing pile without side friction along the length of pile is assumed. In addition, the length of pile, L is assumed to be identical to the thickness H for simplification of the problem. The embedded length into bearing stratum is assumed to be equal to the pile diameter.

3.5 Dynamic Property of Soil

Natural period of soil deposit under small strain level, T_g is dominated by average of shear wave velocity, V_{sa}, and it can be estimated by equation (4). In this study, shear wave velocity, V_s is estimated by equations (5) as recommended in the JRA Specification for seismic design, using SPT N-value, N. Grounds in the area of interest in this study are predominant of clayey and silty soil. Thus, the equation (5a) is used.

$$T_g=(H/V_{sa})/4 \qquad (4)$$

$$V_s=100N^{1/3} \quad \text{(for clayey and silty soils)} \qquad (5a)$$

$$V_s=80N^{1/3} \quad \text{(for sandy soils)} \qquad (5b)$$

Subgrade reaction coefficient k_h is estimated by a JRA recommended equation using N-value. The value of N of the bearing stratum is assumed to be 50.

3.6 Seismic Soil Displacement

The distributions along the depth z of seismic soil displacement due to oscillation of ground, u_g are assumed to be cosine function as shown in equations (6a) and (6b), where u_0 is displacement at the surface.

$$u_g(z)=u_0\cos(\pi z/(2H)) \quad \text{(two layer model)} \qquad (6a)$$

$$u_g(z)=u_0\cos(\pi z/(2H_1)) \quad \text{(three layer model)} \qquad (6b)$$

The amplitude of displacement at the surface tends to be larger with the increase of T_g. In this study, the surface displacement amplitude in centimeter is modeled as equation (7), referring the estimation equation in the code of geotechnical design for railway facilities in Japan.

$$u_0=85.6\ T_g^{1.7} \qquad (7)$$

3.7 Phase Difference of Two Seismic Actions

The timings of action between the inertial force and the seismic soil displacement may different because of interaction between soil and structure having each different natural period. Herein, both the same and the reversal phases are considered in numerical analyses, and then larger response would be adopted in making the charts.

3.8 Numerical Analysis

A pile is modeled as a beam supported by Winkler type springs that transfer the seismic soil displacement to pile. The pile cap is restrained in terms of rotation and is free from horizontal displacement. The resistance of embedded portion of the end bearing pile is modeled by horizontal and rotational springs.

3.9 Nonlinearity of Soil

Nonlinearity of soil is preferable to be considered in both the evaluation of seismic displacement and the modeling of subgrade reaction springs. In this study, the former is considered but the latter is neglected by modeling as linear elastic springs.

3.10 Pile Nonlinearity and Estimation of Ductility Factor

Although constitutive pile model of numerical analysis is linear elastic, the ductility factor of pile as an expected nonlinear response is estimated based on equal energy assumption. Constitutional pile model for evaluation is bilinear type which is characterized both the moment and the curvature at yielding, M_y, φ_y and those at ultimate point, M_u, φ_u are given. The inclination of the first skeleton line up to the yielding point is $K_1=M_y/\varphi_y$ and that of the second skeleton line between the yielding and ultimate points is $K_2=M_u/\varphi_u$, then the ratio of K_1/K_2 is defined as a constant of a. Figure 5 shows a skeleton of bilinear model with

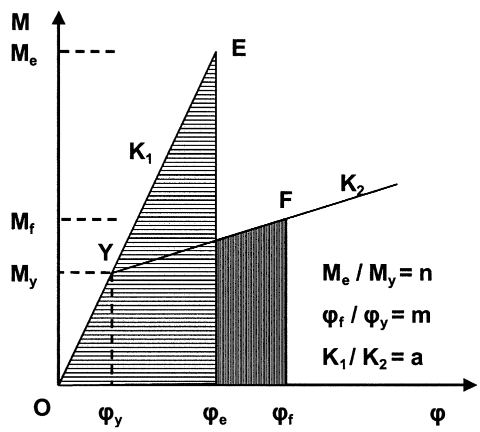

Figure 5 Skeleton of Bilinear Model with Characteristic Values and Equal Energy Assumption

characteristic values.

Bending moment and curvature of responses of linear elastic pile, M_e, φ_e can be summarized into multiplication factor n, which is defined as the ratio of M_e/M_y. The ductility factor of pile, m is easily obtained by equations (8a) and (8b) based on equal energy assumption. If the flexural rigidity of pile is same as assumed pile, piles with different amount of reinforcement can also be able to be evaluated by using these equations.

$$m = 1 + (a^2 + (n^2 - 1)a)^{1/2} - a \qquad (K_2>0) \qquad (8a)$$

$$m = (n^2 + 1) / 2 = 1 + (n^2 - 1) / 2 \qquad (K_2=0) \qquad (8b)$$

Mori and Hirata (2002) studied the equal energy approximation concept, which was proposed for nonlinear dynamic response of SDOF system by Newmark and Rosenblueth (1971), in the estimation of pile deformation obtained by nonlinear dynamic analysis with structure-pile-soil coupled system. Their case study shows that the values of curvature estimated by equal energy assumption vary from 50 % to 120 % of the results of nonlinear analyses and the average ratio is about 70 %.

3.11 Inversion of Design Lateral Force on Pile Heads

Existing pile foundations are assumed to have n=1 as mentioned before, so the design lateral force acting on the pile heads can be inversely calculated easily. Once the curvature φ_0 when a lateral force P_0 is applied onto the pile head of model is obtained by numerical calculation, the design lateral force is back calculated by equation (9).

$$P = \varphi_y/\varphi_0 \times P_0 \tag{9}$$

4. DEMONSTRATION OF EVALUATION CHARTS

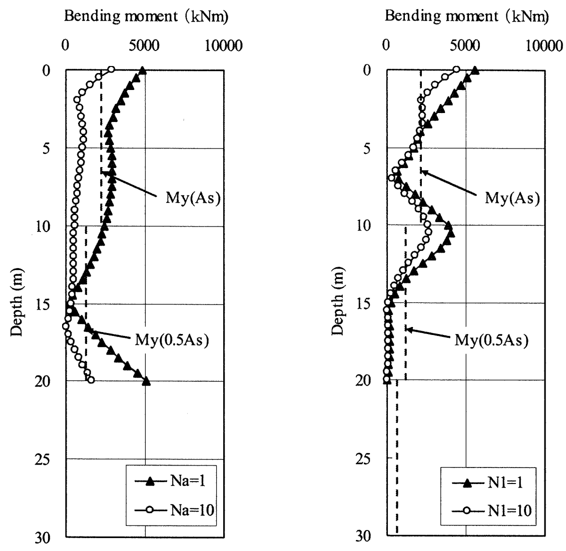

(a) Two Layer Model (b) Three Layer Model

Figure 6 Bending Moment Distributions in Both Models

4.1 Basic Information on Development of Charts

Evaluation charts based on the proposed concept are developed and demonstrated in this section.

For the development, we assume cast-in-place concrete pile with a diameter of 1.2 m, which represents most common type and size of pile used in bridge pier in express highways in Shikoku, the fourth largest island in Japan. Table 1 shows the characteristic parameters of skeleton of R/C piles.

Along the express highway of interest, soft clayey grounds are predominant. The thickness of soil deposit H increases from 10 to 30 m in 5 m increments in any case of the average N-values N_a of 0.5, 1, 2, 5, 10, and 20 in systematically parametric calculations. The number of combination of two parameters for numerical analysis is 30. These 30 cases of numerical calculation for both two- and three- layer models has been performed for development of charts for various portions of piles with various amount of reinforcement.

Table 1 Characteristic Parameters of Skeleton of Piles

Reinforcement	Yielding		Ultimate	
	My (kNm)	φy (1/m)	Mu (kNm)	φu (1/m)
As	2169	1.3×10^{-4}	3368	2.5×10^{-2}
0.5×As	1204	2.4×10^{-3}	1798	1.9×10^{-2}

4.2 Bending Moment in Two Models

Figure 6 shows bending moment distributions in both models for 20 m long piles in deposits with N values of 1 and 10. In two-layer model, the values of bending moment at pile head and at pile end are predominant. The moments at pile head are larger than those at pile end in ground models with smaller N_a. However, the moments at pile end are larger than those at pile head in firmer deposits.

In three layer model having an upper sub-layer with constant thickness of 10 m and a lower sub-layer with constant SPT N-value, N_2 of 20, the values of bending moment at pile head and near the layer boundary, above which seismic displacements are distributed along the depth in the upper layer, are predominant.

At the bottom of deposit in two layer models and at the bottom of the upper layer of the deposits, the predominant moments are produced. In both cases, it can be indicated that reinforcement reduction leads more vulnerable situations below a depth of 10 m.

4.3 Evaluation Charts by Two Layer Models

Figure 7 shows contour diagrams of multiplication factor of bending moment n by 2 layer models. The smaller N_a is, the greater n is both at the pile head and pile end. On the other hand, the larger H is, the greater n is at the pile head but the smaller n is at the pile head. The increase of n with the reduction of reinforcement at the pile end is clearly demonstrated.

Figure 8 shows charts for estimation of ductility factor of pile, m under three conditions. The tendencies of the changes of m in these three charts are proportionally similar to those of the change of parameter n. The pile heads are almost safe except extremely soft soils. Even the same amount of reinforcement at pile head may not secure the integrity of pile at pile ends in very soft and deeper deposits. Furthermore, the reduced amount of reinforcement according to practical manner as per a standard design code may increase vulnerability against seismic soil displacements in terms of an ultimate ductility factor of 8 from the standpoint of capacity.

4.4 Evaluation Charts by Three Layer Models

Figure 9 shows contour diagrams of n by 3 layer models. The smaller N_a is, and the larger H is, the greater n is both at the pile head and at the boundary between 2 sub-layers of deposits. The shapes of distributions of

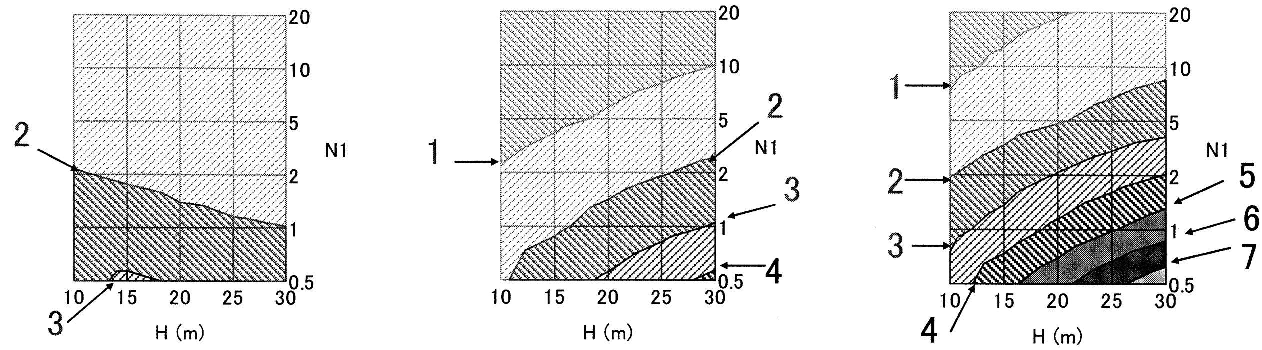

(a) Pile Head (b) Pile End (Without Rebar Reduction) (c) Pile End (With Rebar Reduction)

Figure 7 Contour Diagrams of Multiplication Factor of Bending Moment, n of Pile by Two Layer Models

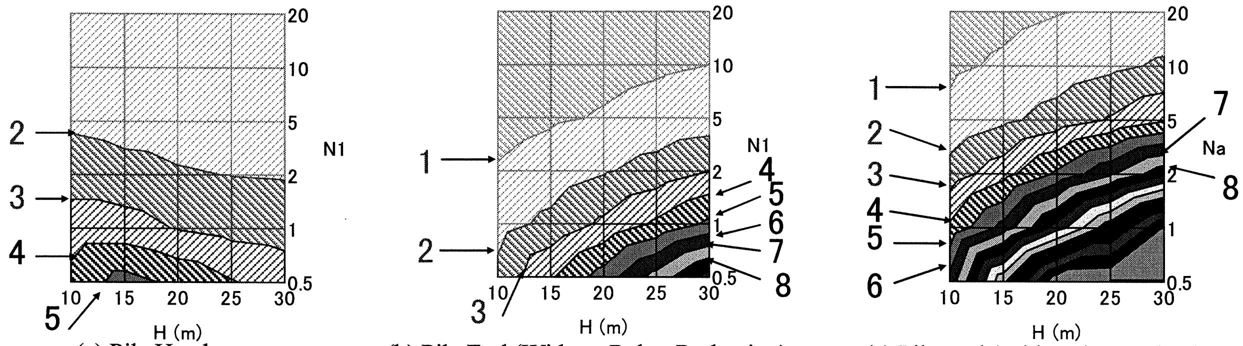

(a) Pile Head (b) Pile End (Without Rebar Reduction) (c) Pile End (With Rebar Reduction)

Figure 8 Charts for Estimation of Ductility Factor m of Pile by Two Layer Models

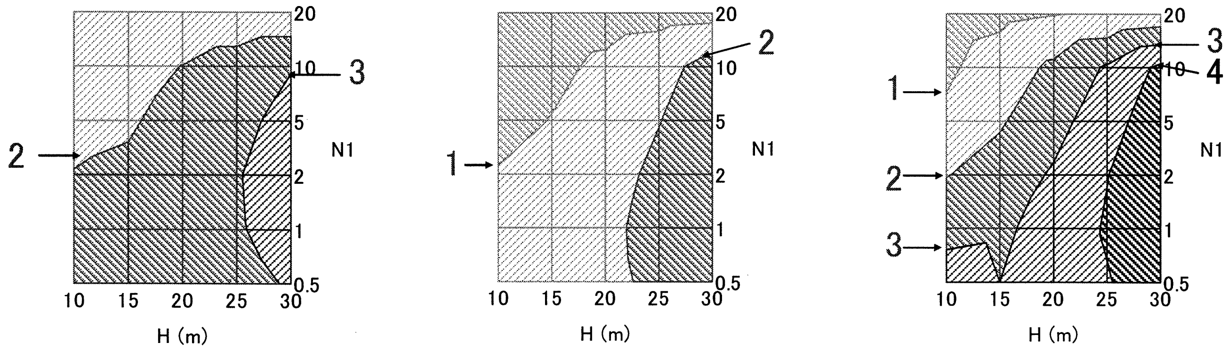

(a) Pile Head (b) Near Boundary (Without Rebar Reduction) (c) Near Boundary (With Rebar Reduction)

Figure 9 Contour Diagrams of Multiplication Factor of Bending Moment, n of Pile by Three Layer Models

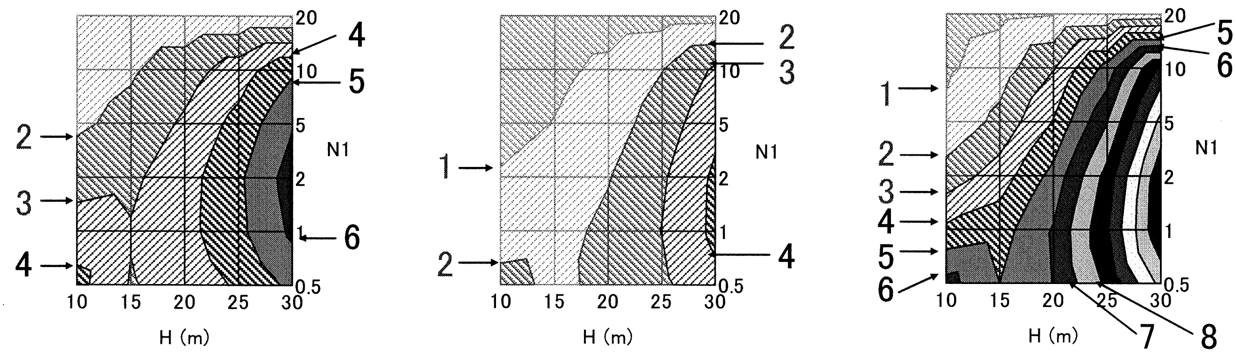

(a) Pile Head (b) Near Boundary (Without Rebar Reduction) (c) Near Boundary (With Rebar Reduction)

Figure 10 Charts for Estimation of Ductility Factor m of Pile by Three Layer Models

contours have similar tendencies of having possible peaks around the point having a N_1 value of 2 and a depth of 30 m.

This suggests that they depend on both the function of seismic displacement in terms of natural period of ground and the degree of discontinuity of soil rigidity at the boundary. On the other hand, the greater n is at the pile head but the smaller n is at the pile head. Comparing with the results by two-layer models, the values of n are relatively

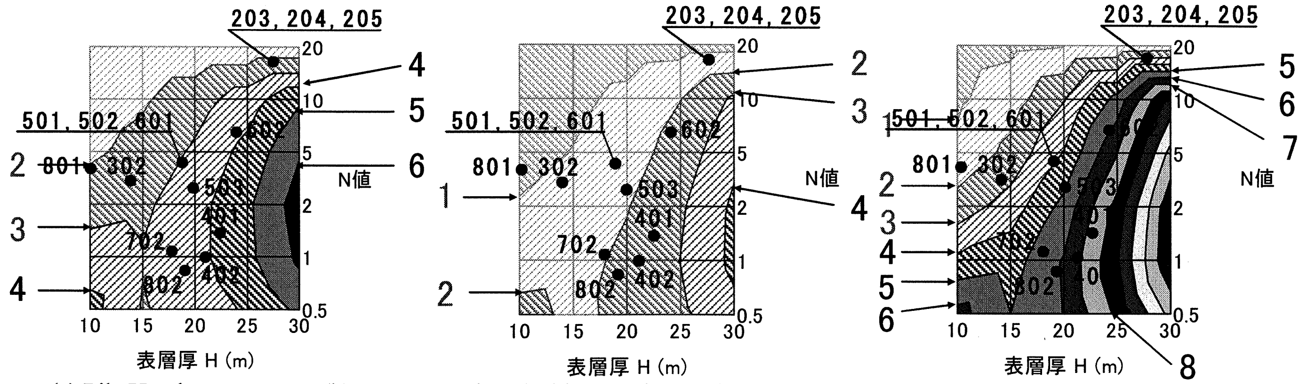

(a) Pile Head (b) Near Boundary (Without Rebar Reduction) (c) Near Boundary (With Rebar Reduction)

Figure 11 Results of Application of Evaluation Charts for Expressway Bridge Piles by Three Layer Models

small. This seems have been derived by the mitigation of the contrast between two layers at their boundary.

Figure 10 shows charts for estimation of m under three conditions based on three-layer models. The tendencies of the change of contour of the factor m in these three conditions are proportionally similar to those of the change of parameter n. The values of m at the pile head by three-layer models are relatively high, compared to those by two-layer models. As a result, even the integrity of pile heads may not be secured in soft and deep deposits. At the boundaries of two sub-layers of deposits, the piles with the same amount of reinforcement as the pile heads would be almost safe. In contrast, many of the piles with reduced reinforcement by half as practical design are expected to be highly vulnerable due to plastic deformation at the boundaries.

5. APPLICATION OF CHARTS

The authors had an opportunity to apply the proposed chart system to actual bridge pile foundations of an expressway in a committee on seismic evaluation of existing expressway facilities. The objectives of the application is prioritizing and screening an inventory of the bridge foundations based on a rough evaluation of the vulnerability against potential seismic soil displacements.

Figure 11 shows the results of the application of charts by three-layer models to bridge pile foundations of an expressway. The dots in these charts correspond to specific pile foundations with the numbers denoting the three digit codes for management of foundations.

Almost all the pile foundations are evaluated safe at the pile heads. At the boundaries of two sub-layers of deposits, almost half of the piles with reduced reinforcement are evaluated as unsafe, and if the piles have the same amount of reinforcement as the pile heads would be. These results well demonstrate that the avoidance of the reduction of reinforcement at deeper portions of pile is an effective measure against seismic lateral displacement from the viewpoint of foundation engineering practice. Moreover, the application of these charts is effective to newly designed foundation as well, especially for the judgment of the necessity of detailed analysis on this seismic vulnerability.

It took several days for a bridge engineer to evaluate the vulnerability of 34 bridges using the charts including determination of parameters. The result seemed to be appropriate for all the committee members. Therefore, the proposed concept of developing evaluation charts for existing pile foundation against seismic lateral displacement is effective for prioritizing and screening an inventory of pile foundations of many kinds of structures from the theoretical and practical viewpoints.

6. CONCLUSIONS

(1) A new concept of evaluation chart for existing pile foundations against seismic lateral displacements on the basis of performance-based design was proposed and the charts were developed.

(2) The proposed concept was validated by the development of evaluation charts that successfully demonstrated vulnerable combination of thickness of soil deposits and average SPT N-value in given conditions.

(3) The avoidance of reinforcement reduction of concrete pile in depth can be an effective measure for improvement of seismic performance.

(4) Application to actual pile foundations of highway bridge demonstrated practical efficiency for prioritizing and screening an inventory of pile foundations of many kinds of structures from the theoretical and practical viewpoints.

Acknowledgements:

The authors acknowledge the opportunity of application of their developed charts in Seismic Evaluation Project in Shikoku Branch of West Nippon Expressway Company (NEXCO) and the advices from members of committee on the project.

References:

Japan Road Association (1996), "Design Specification of Highway Bridge, Part V Seismic Design."

Mori, S. (2007), "Perspective on quick assessment of seismic vulnerability of existing pile foundation considering effect of ground displacement," *Proceedings of Annual Conference of Shikoku Branch of Japan Geotechnical Society*, Japan Geotechnical Society, **12**, 65-66, (in Japanese).

Mori, S. and Hirata, A. (2002), "Evaluation of nonlinear seismic response of pile by constant energy rule," *Proceedings of 37th Annual Conference of Japan Geotechnical Society*, Japan Geotechnical Society, 1495-1496, (in Japanese).

Newmark, N.M. and Rosenblueth, E. (1971), "Fundamentals of Earthquake Engineering," Prentice-Hall Inc.

Railway Technical Research Institute (1999), "Structure Design Standard (Seismic Design)," Maruzen Inc., (in Japanese).

Fifth International Conference on Urban Earthquake Engineering
March 4-5, 2008, Tokyo Institute of Technology, Tokyo, Japan

DYNAMIC SOIL BEHAVIOR AND ROCK OUTCROP MOTION BACK-CALCULATED FROM DOWNHOLE ARRAY RECORDS AT KASHIWAZAKI-KARIWA NUCLEAR POWER PLANT IN THE 2007 NIIGATA-KEN CHUETSU-OKI EARTHQUAKES

Kohji Tokimasu[1] and Hiroshi Arai[2]

1) Professor, Dept. of Architecture and Building Engineering, Tokyo Institute of Technology, Japan
2) Research Engineer, Nat'l Res. Inst. for Earth Science and Disaster Prevention, Japan
kohji@o.cc.titech.ac.jp, arai.h@bosai.go.jp

Abstract: Nonlinear soil behavior and rock outcrop motion are back-calculated using strong motion downhole array records at the Service Hall of the Kashiwazaki-Kariwa nuclear power plant during the 2007 Niigata-ken Chuetsu-oki earthquakes. A technique used for this inversion is genetic algorithm coupled with a one dimensional equivalent linear response analysis in which damping ratios vary with Fourier amplitude of shear strain in the frequency domain. The Holocene and Pleistocene dune sands with V_s = 200-350 m/s at depths smaller than 70 m showed strong nonlinear behavior with shear modulus ratios of about 0.01-0.8 and damping ratios of about 20-35 % at maximum shear stains of about $2x10^{-3}$ - $3x10^{-2}$. The reduction in shear modulus ratio is consistent with previous laboratory test results for sand consolidated under similar confining pressures but the corresponding damping ratio seems to be slightly higher than that of the previous studies. The mudstone with V_s =500 m/s located at depths greater than 70 m did not show any strong nonlinearity during the main shock, with shear modulus ratios of about 1.0 and damping ratios of up to 5 % at maximum shear strains up to about $5x10^{-4}$ - $2x10^{-3}$. The peak acceleration and velocity of the back-calculated rock outcrop motion at a depth of 250 m are 12 m/s^2 and 0.76 m/s.

1. INTRODUCTION

The Niigata-ken Chuetsu-oki earthquake (M_j=6.8) that occurred at 10:13 hrs on July 16, 2007, with an epicenter off the Niigata Prefecture, affected the coastal areas of the southwestern Niigata prefecture including Kashiwazaki city and Kariwa village as well as the Kashiwazaki-Kariwa nuclear power plant of Tokyo Electric Power Company (TEPCO). The earthquake claimed a death toll of eleven, with almost two thousand injuries. More than thirty-five thousand residential houses were either totally collapsed or were partially damaged.

Both ground shaking and ground failure problems affected residential houses in the area. Most of the houses affected by ground shaking were very old, built with traditional Japanese construction technique and with large opening along the street, and thus constituted a soft first story prone to deformation parallel to the street. Many houses on reclaimed alluvial sandy deposits and slopes of sand dunes suffered from ground failure problems involving soil liquefaction. Ground failure problems also affected many infrastructures such as railways, highways, roads, bridges, embankments and lifelines (Kayen et al, 2007).

A matter of utmost concern is the performance of the Kashiwazaki-Kariwa nuclear power plant during and after the earthquake. A fire broke out around a house electric transformer and many less critical structures as well as incidental components such as pipes and ducts were damaged; however, three reactors in full operation as well as one in a start-up state during the quake were automatically shutdown and all the critical structures including reactor and turbine buildings seemed to be in good condition.

A total of 97 accelerometers of old and new systems were installed at the site (TEPCO, 2007a). The old system includes 36 stations in the reactor and turbine buildings, 2 for the main exhaust stacks, and 29 on and in the ground, while the new system includes 28 in the reactor and turbine buildings, and 2 on the ground surface at Units 1 and 5. The strong motions at 33 locations were recorded for the main shock, but unfortunately, the recordings obtained at the other 63 locations from the old system as well as one from the new system, including three free-field downhole arrays close to the reactor buildings, were lost, with the exception of the peak values of the old system. The recovered 33 recordings included all of the new system except one in the Unit 3 turbine building, and one 4-depth free-field downhole array at the Service Hall of the old system (TEPCO, 2007a, 2007b).

The downhole array records at the Service Hall, the only ones that included "within" ground motions at the site, seem to be particularly important not only to determine the input rock outcrop motions for analytically reviewing dynamic behavior of the critical buildings but also to estimate nonlinear dynamic soil properties at the site under high confining pressures that are difficult to observe in the conventional laboratory test but definitely required for the analysis. The objective of this paper is to estimate nonlinear soil properties and rock outcrop motion of the site based on an inverse analysis of the downhole array records using genetic algorithms combined with a one-dimensional equivalent linear response analysis.

2. SITE CONDITIONS AND OBSERVED RECORDS AT SERVICE HALL DOWNHOLE ARRAY STATION

The Kashiwazaki-Kariwa nuclear power plant is located along the coast on the north of Kashiwazaki city, about 16 km from the epicenter. Figure 1 shows a map of the site. The plant is not only one of the largest nuclear power plants in the world, having seven generators (Units 1 through 7) with a total output capacity of 8.2 GW within an area of 4.2 km^2, but also the first one that experienced strong ground shaking. The Service Hall downhole array and its observation station are located on the east of the main gate, as indicted in Fig. 1.

Figure 2 shows the geological and geophysical logs

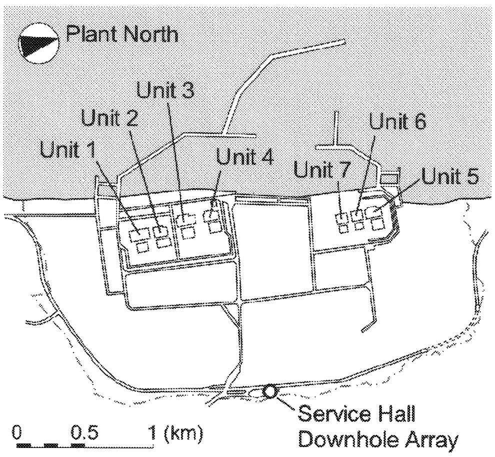

Figure 1. Map showing TEPCO's Kashiwazaki-Kariwa nuclear power plant

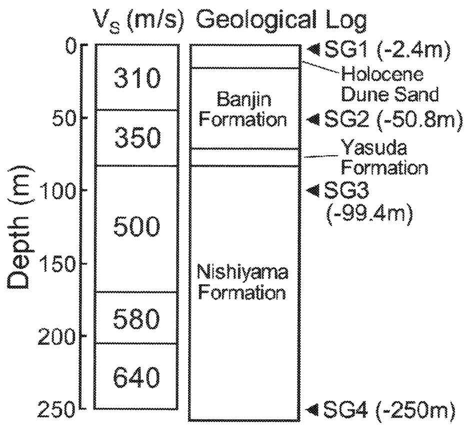

Figure 2. Geological and geophysical logs with accelerometer locations at Service Hall

along with the location of the downhole accelerometers. The elevation of the site is 67.5 m, which is 62.2 m or 55.2 m higher than those (5.3m or 12.3 m) of Units 1-4 or 5-7. The Holocene and Pleistocene sand dune deposits overlie the Pleistocene Yasuda Formation that in turn overlies the Pliocene Nishiyama Formation. The shear wave velocities, V_{so} of the Holocene sand dune (New sand dune), Pleistocene sand dune (Banjin Formation), Yasuda Formation, and Nishiyama Formation are 310, 310-350, 350, and 500-640 m/s, respectively. Their mass densities are estimated to be 1.65, 1.65-1.80, 1.80, and 1.65-1.75 Mg/m^3, respectively.

The Service Hall downhole array includes four three-component accelerometers installed at depths of 2.4 m, 50.8 m, 99.4m, and 250 m, as shown in Figure 2. The NS and EW directions of the accelerometers were set to the two principal axes of the plant buildings and thus were rotated clockwise 18.9 degrees from the true ones. The ground water table was located at a depth of about 35 m.

The 2007 Niigata-ken Chuetsu-oki earthquake caused a ground settlement of about 15 cm around the observation station at the Service Hall. No apparent sign of soil liquefaction was identified nearby.

Downhole array recordings for the main shock as well as six aftershocks are available (TEPCO, 2007a-2007c). The ground motions during the main shock dominate in the E-W direction, which is nearly perpendicular to the coastline. Figure 3 shows the EW acceleration time histories observed by the downhole array during the main shock. The peak accelerations were de-amplified from 7.3 m/s^2 at a depth of 250 m to 4.4 m/s^2 near the ground surface, losing their short period component, whereas the peak velocities were amplified from 0.46 m/s to 1.3 m/s.

Figure 4 shows the distributions of peak horizontal ground acceleration with depth for the main shock together with those for the two aftershocks that occurred at 15:37 hrs

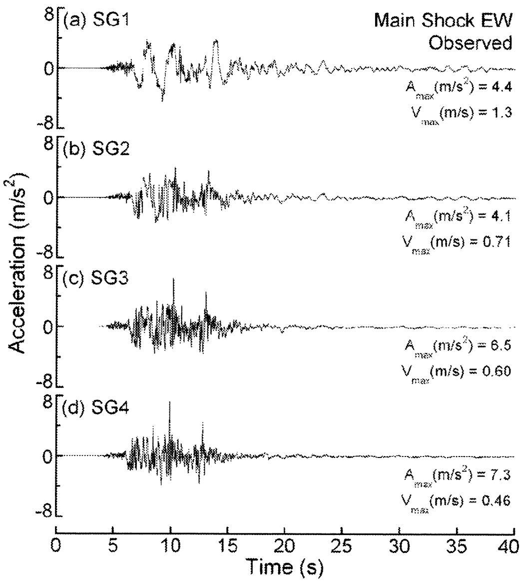

Figure 3. EW acceleration time histories observed by the downhole array during the main shock

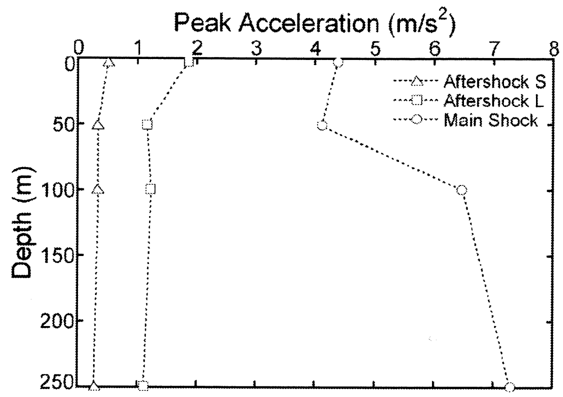

Figure 4. Distribution of peak acceleration with depth for three earthquakes

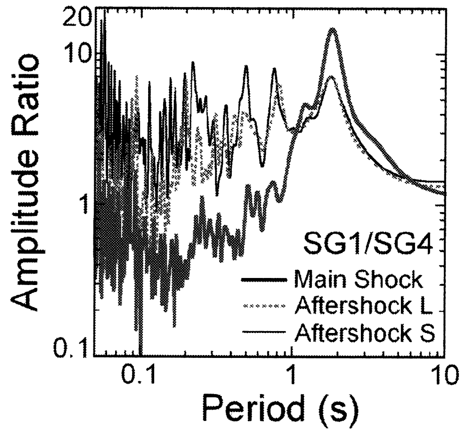

Figure 5. Comparison of amplitude ratios from different earthquakes

and 21:08 hrs on the same day, herein called aftershocks L and S. The de-amplification of acceleration towards the ground surface occurred only during the main shock.

Figure 5 compares the amplitude ratios between 2.4 m and 250 m depths for the main shock and two aftershocks. The amplitude ratios at periods less than 1 s are significantly lower in the main shock than in either of the two aftershocks.

The above findings in Figures 3 to 5 suggest that degradation of stiffness and/or increase in damping of the near-surface soil might have occurred and lowered the amplitude ratios in the short period range during the main shock, compared with those of the aftershocks.

3. INVERSE ANALYSIS OF STRONG MOTION ARRAY RECORDS USING GENETIC ALGORITHMS

Nonlinear soil characteristics are back-calculated for the deposit of the Service Hall at the Kashiwazaki-Kariwa nuclear power plant based on its strong motion downhole array records during the 2007 Niigata-ken Chuetsu-oki earthquakes. The goal of this inversion is to find a soil layer model that minimizes the misfit of observed and computed Fourier amplitude ratios between any of the two depths in the array (e. g., Kobayashi et al, 1999), defined as:

$$F = \sum_{i=1}^{I-1} \sum_{j=i+1}^{I} \sum_{k=k_{min}}^{k_{max}} w_k^2 (\log_{10} A_{m,ij}(f_k) - \log_{10} A_{C,ij}(f_k))^2 \qquad (1)$$

in which A_m and A_C are the observed and computed Fourier amplitude ratios between the i-th and j-th accelerometers in the array, I is the number of accelerometers, k_{min} and k_{max} are integers defined as f_{min}/T and f_{max}/T in which f_{min} and f_{max} are the minimum and maximum frequencies to be considered, T is the duration of the earthquake and w_k is a weighting factor defined as $1/f_k$.

It is assumed that A_C in the above equation be determined with a one-dimensional equivalent-linear response analysis of a deposit in which damping ratios are dependent on Fourier amplitude of shear strain in the frequency domain (e.g., Sugito et al, 1994), which is an extended version of SHAKE (Schnabel et al, 1972) to improve its deficit in over-damping in the short period range during strong shaking. It is also assumed that the target soil deposit consists of N sub-layers including the bottom half space, each characterized by the mass density, thickness, equivalent shear wave velocity, and damping ratio in the frequency domain defined as:

$$h(f) = h_{min} + (h_{max} - h_{min})(\gamma_{eff}(f)/\gamma_{ref}) / (1 + \gamma_{eff}(f)/\gamma_{ref}) \qquad (2)$$

$$\gamma_{eff}(f) = 0.8\gamma_{max} \cdot \Gamma(f) \qquad (3)$$

in which h_{min} and h_{max} are the minimum and maximum damping ratios; γ_{ref}, γ_{max}, $\gamma_{eff}(f)$, and $\Gamma(f)$ are the reference shear strain, maximum shear strain in the time domain, effective shear strain for a given frequency f, and normalized Fourier amplitude of shear strain at a given f with respect to the maximum Fourier amplitude of shear strain in the frequency domain, respectively. Thus, once knowing all the soil properties in the deposit, A_C in Eq. (1) can be determined by iterative procedure until $h(f)$ becomes compatible with Fourier amplitude of shear strain.

Adopted in the optimization using Eq. (1) are genetic algorithms (GA; Goldberg, 1989, Kobayashi et al., 1999) in which four parameters including the equivalent shear wave velocity, minimum and maximum damping ratios and reference shear strain of each sub-layer are sought with other parameters such as the thickness and mass density being predetermined and with N=15, I=4, T=81.92 s, f_{max}=25 Hz, and f_{min}=0.2 Hz.

In the GA space, an 8-bit Gray coded integer is used for each of the unknown parameters. This leads to a 480 (8x15x4)-bit integer (chromosome) for an individual soil layer model consisting of 15 sub-layers with four unknown parameters each.

An initial population of 200 soil layer models is generated randomly, covering the range of possible solutions, and the succeeding generation of the same population is reproduced until the 500th generation. The parameter search ranges are 0-5% for h_{min}, 15-40% for h_{max}, 10^{-4}-10^{-2} for γ_{ref} and $(0.05\text{-}0.5)V_{so}$-$(0.7\text{-}1.2)V_{so}$ for V_s. Roulette wheel

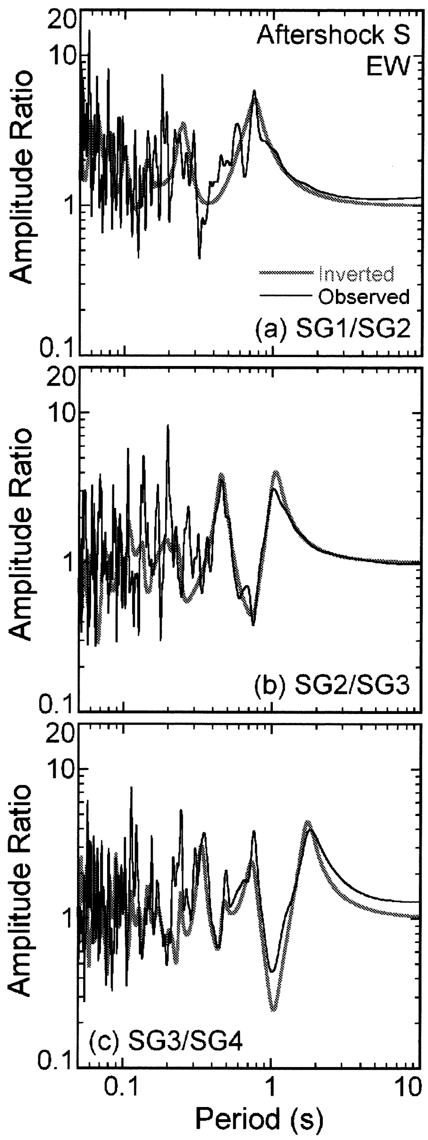

Figure 6. Comparison of observed and computed amplitude ratios for aftershock S

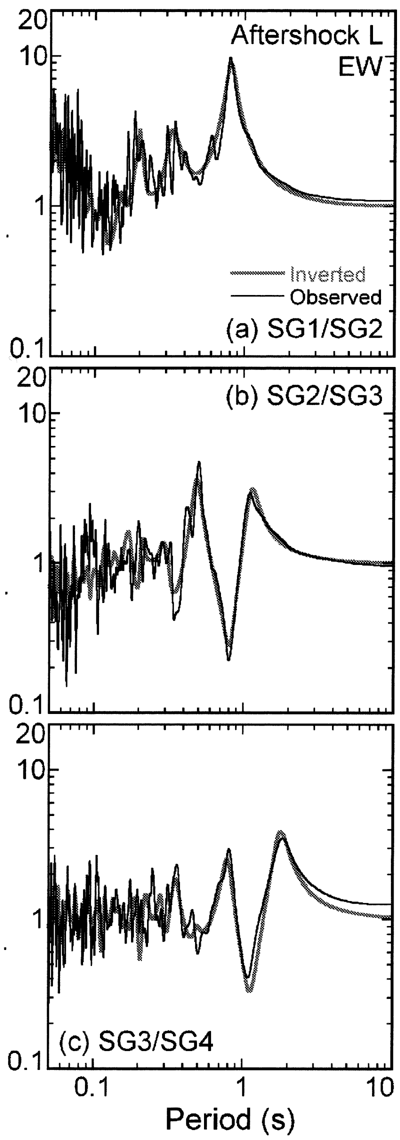

Figure 7. Comparison of observed and computed amplitude ratios for aftershock L

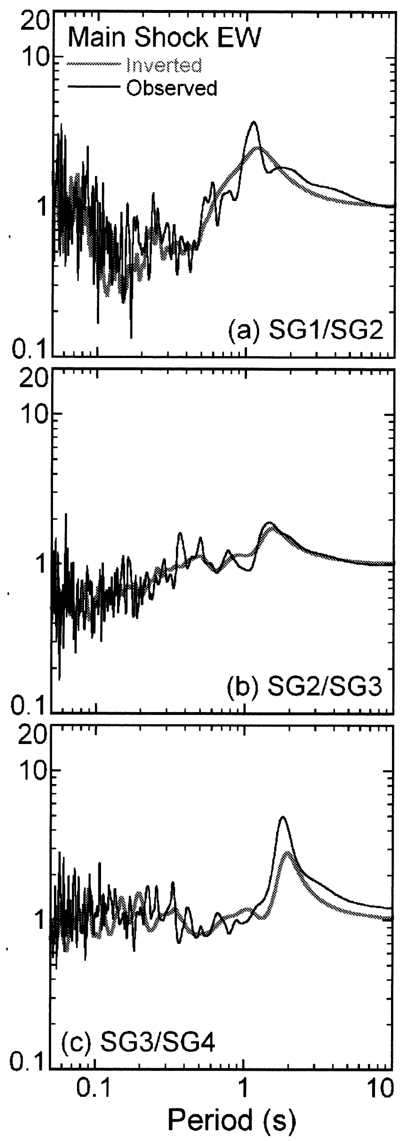

Figure 8. Comparison of observed and computed amplitude ratio for main shock

selection is used to choose and mate a pair for the new generation based on the fitness of each individual soil layer model defined by 1/F, with a crossover rate of 0.7 and a mutation rate of 0.02. The soil layer model having the best fitness in the final generation is assumed to be the solution for one trial. A total of ten trials are made for each set of the array data observed during the main shock and the two aftershocks L and S.

4. NONLINEAR SOIL PROPERTIES AND ROCK OUTCROP MOTION ESTIMATED FROM INVERSE ANALYSIS

Figures 6 to 8 compare the Fourier amplitude ratios computed for the back-calculated soil layer models having the best fitness with those of the observed records for the aftershocks S and L and the main shock. Good agreement exists between the observed and computed amplitude ratios for the three events, indicating that the back-calculated soil profiles are reasonably reliable.

Figure 9 shows the distribution of back-calculated equivalent shear wave velocity and maximum shear strain with depth for the three events compared with an available V_s profile determined by PS logging. The maximum shear strains during the main shock are either one or two orders of magnitude greater than those of the aftershock L or S. The estimated shear wave velocities at depths smaller than about 70 m are therefore significantly smaller in the main shock than in either of the two aftershocks. In contrast, those at deeper depths for the three events are almost identical. The back-calculated shear wave velocities at deeper depths are consistent with the available shear wave velocity profile, whereas those at the shallow depths even for the aftershock

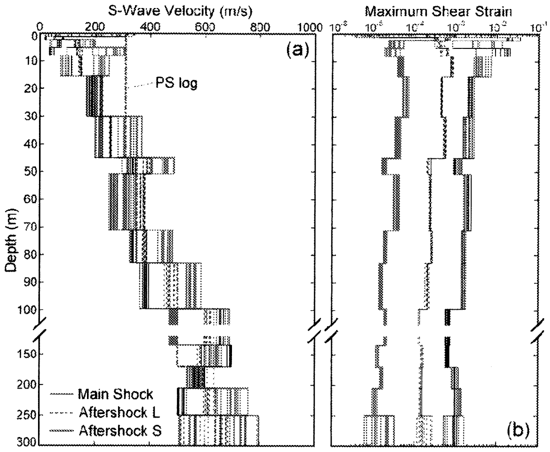

Figure 9. Back-calculated Vs profile and shear strain

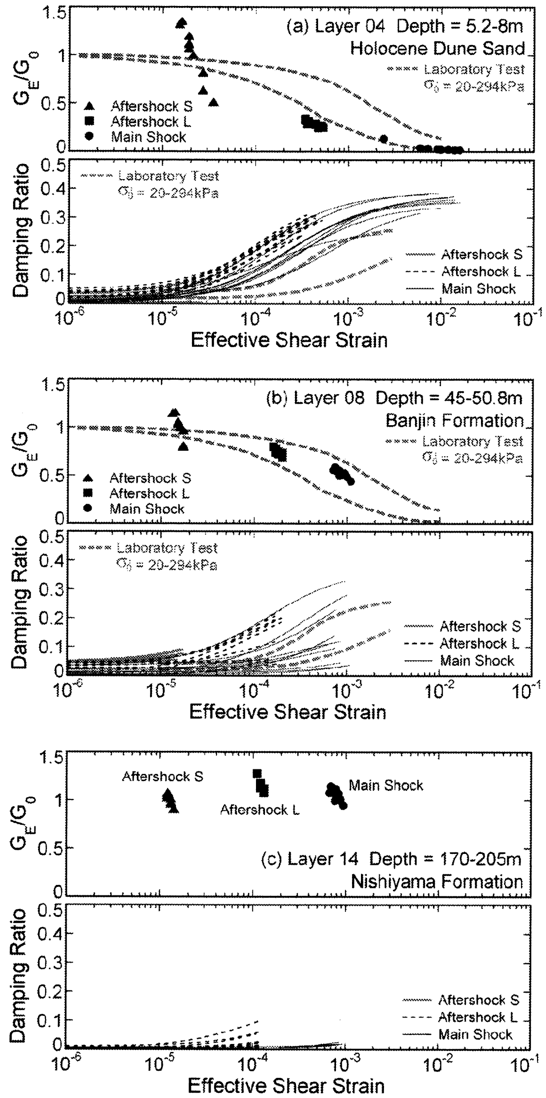

Figure 10. Back-calculated strain-dependent shear modulus and damping ratios

S are significantly smaller than the available V_s values. This poses a question about the accuracy of the available V_s profile at the shallow depths.

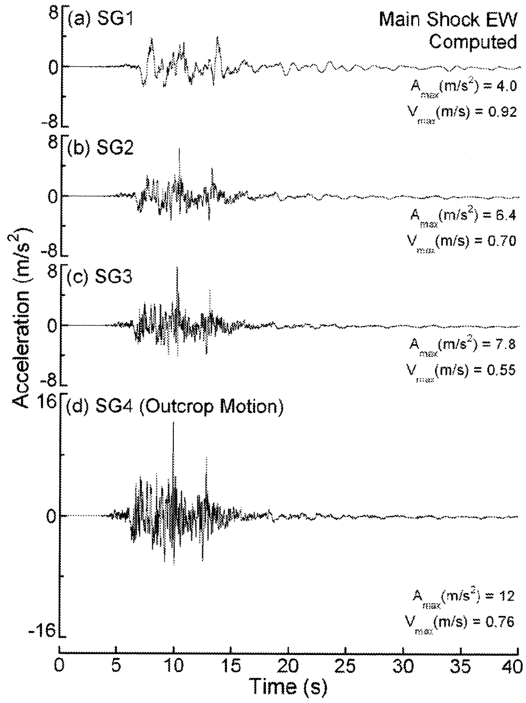

Figure 11. Back-calculated acceleration time histories for the main shock

Figure 10 shows the back-calculated strain-dependent shear modulus and damping ratios at three depths for the three earthquakes. The shear modulus has been normalized with respect to the elastic shear modulus estimated using $G_o = \rho V_s^2$ in which V_s is the average of the back-calculated values for the aftershock S. The shear modulus ratios in the sand dune deposits at depths smaller than about 70 m decrease to 0.01-0.8 and their damping ratios increase to about 20-35% with increasing shear strain up to $2x10^{-3}$ - $3x10^{-2}$ or with increasing ground shaking. Also shown in the figures are the laboratory test data for sand tested under confining pressures (Kokusho, 1980) similar to those of the dune sands. The back-calculated strain-dependent shear modulus ratios are consistent with those of the previous study but the back-calculated damping ratios are slightly higher than those of the previous study. The shear modulus and damping ratios at depths greater than 70 m are about 1.0 and less than 5% and do not show any significant change irrespective of shear strain amplitude that varies depending on ground shaking from $1x10^{-5}$ to $2x10^{-3}$.

Figure 11 shows the computed acceleration time histories at the three depths (SG1-SG3) as well as on the outcrop rock at a depth of 250 m (SG4) using the back-calculated soil layer model with the best fitness for the main event. Not only the waveforms but also the peak accelerations at the three depths (SG1-SG3) are consistent with the observed ones. The peak acceleration and velocity of the rock outcrop motion at a depth of 250 m are estimated to be 12 m/s^2 and 0.76 m/s. The fairly good agreements between the observed and computed accelerations at the three depths (SG1-SG3) suggest that not only the inverted soil profile but also the acceleration time history of the rock outcrop motion at a depth of 250 m is reasonably reliable.

5. CONCLUSIONS

The strain-dependent shear modulus and damping ratios as well as the rock outcrop motion have been estimated based on the inverse analysis of the strong motion downhole array records at the Service Hall of the Kashiwazaki-Kariwa nuclear power plant during the 2007 Niigata-ken Chuetsu-oki earthquakes. The following conclusions may tentatively be made:

1) The computed spectral ratios and acceleration time histories show a good agreement with the observed ones, indicating that the back-calculated nonlinear soil properties and rock outcrop motion are reasonably reliable.

2) The Holocene and Pleistocene dune sands with V_s = 200-350 m/s at depths smaller than about 70 m showed strong nonlinear behavior with shear modulus ratio of about 0.01-0.8 and damping ratios of about 20-35 % at maximum shear stains of about $2x10^{-3}$ - $3x10^{-2}$, during the main shock.

3) The back-calculated shear modulus ratios at depths smaller than 70 m during the main and aftershocks are consistent with previous laboratory test results for sand consolidated under similar confining pressures but the back-calculated damping ratios seem to be slightly higher than that of the previous studies.

4) The mudstone with V_s =500 m/s located at depths below 70 m did not show any strong nonlinearity during the main shock and aftershocks, with a shear modulus ratio of about 1.0 and a damping ratio of up to 5 % at a maximum shear strain up to about $5x10^{-4}$ - $2x10^{-3}$.

5) The peak acceleration and velocity of the back-calculated rock outcrop motion at a depth of 250 m are 12 m/s^2 and 0.76 m/s.

ACKNOWLEDGEMENTS:

The strong motion array records and geological and geophysical logs at the Service Hall of the Kashiwazaki-Kariwa nuclear power plant, used in this study, were provided by Tokyo Electric Power Company (TEPCO, 2007a and 2007b). The field investigation at the site was made possible through the courtesy of TEPCO.

REFERENCES:

Goldberg, D. E. (1989): Genetic Algorithms in Search, Optimization and Machine Learning, *Addison-Wesley Publishing Company, Inc.*, 412pp., 1989.

Kayen, R. et al (2007): Preliminary observations on the Niigata-Chuetsu Oki, Japan, Earthquake of July 16, 2007, EERI-GEER Web Report 2007-1 v.6.

Kobayashi, K., Kyuke, H., Uetake, T., Mashimo, M., and Kobayashi, H. (1999): Estimation of Q value for soil layers by simultaneous inversion of transfer functions at many sites Part 3, Summaries of Technical Papers of Annual meeting, Architectural institute of Japan, B-2, 255-256 (in Japanese).

Kokusho, T. (1980): cyclic triaxial test of dynamic soil properties for wide strain range, Soils and Foundations, Vol. 20, No. 2, 45-60.

Schnabel, P. B., Lysmer, J. and Seed, H. B. (1972): SHAKE-A Computer Program for Earthquake Response Analysis of Horizontally Layered Sites, EERC Report, No.72-12.

Sugito, M., Goda, H., Masuda, T. and Etsunada, K. (1993): Equi-linearlized method with frequency-dependent shear modulus and damping, *Proceedings of the 28th Japan National Conference on Soil Mechanics and Foundation Engineering*, 1129-1132 (in Japanese).

TEPCO (2007a): Report on analysis of observed records at Kashiwazaki-Kariwa Nuclear Power Plant during the Niigata-Chuetsu-Oki earthquake 2007.

TEPCO (2007b): Acceleration time histories at Kashiwazaki-Kariwa nuclear power plant during the 2007 Niigata-ken Chuetsu-oki earthquakes, Main shock at 10:13 a.m. on July 16, 2007, CD-ROM.

TEPCO (2007c): Acceleration time histories at Kashiwazaki-Kariwa nuclear power plant during the 2007 Niigata-ken Chuetsu-oki earthquakes, 6 aftershocks, CD-ROM.

Fifth International Conference on Urban Earthquake Engineering
March 4-5, 2008, Tokyo Institute of Technology, Tokyo, Japan

EFFECTS OF LOCAL SITE AMPLIFICATION ON DAMAGE TO WOODEN HOUSES IN NEAR-SOURCE REGION FOR THE 2007 NOTO HANTO EARTHQUAKE

Hiroshi Arai[1)], Takeshi Morii[2)], Masumi Yamada[3)], Hidemaru Shimizu[1)], and Yasuhiro Hayashi[4)]

1) Research Engineer, National Research Institute for Earth Science and Disaster Prevention, Japan
2) Assistant Professor, Dept. of Architecture and Architectural Engineering, Graduate School of Engineering, Kyoto University, Japan
3) Assistant Professor, Pioneering Research Unit for Next Generation, Kyoto University, Japan
4) Professor, Dept. of Architecture and Architectural Engineering, Graduate School of Engineering, Kyoto University, Japan
arai.h@bosai.go.jp, morii@archi.kyoto-u.ac.jp, masumi@eqh.dpri.kyoto-u.ac.jp, hidemaru@bosai.go.jp, hayashi@archi.kyoto-u.ac.jp

Abstract: Effects of local site amplification characteristics on strong ground motions and damage to wooden houses in Hashiride and Kuroshima districts of Monzen area, Wajima city, Japan, during the 2007 Noto Hanto earthquake, are examined based on damage survey and microtremor measurements. Using simplified analytical models of surface soils and wooden houses for the districts, response spectra of strong ground motions and maximum drift angles of wooden houses are simulated. Comparing the simulated results with the observed damage, it is revealed that the wooden-house responses are mainly controlled by strong ground motions with a period of about 1-3 s, at which the site amplification factors were significantly influenced by impedance ratios (V_S contrasts) and nonlinear properties of surface soils in the districts. It is thus indicated that the heavily damage to wooden houses could be due to low ground impedance ratio resulting in strong soil nonlinearity while the slightly ones could be due to high ground impedance ratio inducing weak soil nonlinearity.

1. INTRODUCTION

The Noto Hanto earthquake of March 25, 2007, destroyed over 600 residential buildings at the cities of Wajima and Anamizu in the northwest area of the Noto Peninsula, Ishikawa Prefecture, Japan. Within Hashiride and Kuroshima districts of Monzen area, Wajima city, in particular, a large number of two-storied wooden houses sustained either partial or complete collapse typically of a soft first story (see Photo 1 and Figure 1). To examine causes of the building damage during the 2007 earthquake, the effects of surface soil conditions on strong ground motion characteristics and wooden-house responses should be properly estimated in the districts.

The objective of this article is to evaluate the maximum drift angles of wooden houses considering local site effects in Hashiride and Kuroshima districts during the 2007 Noto Hanto earthquake based on dynamic response analyses of simplified single-degree-of-freedom (SDOF) building systems and surface soil models, which are resulted from inventory survey of building damage and microtremor measurements in the districts.

2. DAMAGE SURVEY OF WOODEN HOUSES IN HASHIRIDE AND KUROSHIMA

An inventory survey was conducted for all buildings in the central zones of Hashiride and Kuroshima districts. The survey zones are shown in Figure 1 as broken thick lines. These zones are hereinafter labeled as Aa-Ae in Hashiride and Ba-Bc, Ca-Cc, and Da-Dd in the northern, middle, and

Photo 1. Examples of damage to wooden houses in (a), (b) Hashiride and (c) Anamizu during main shock.

southern Kuroshima districts, respectively. Location, age, use, structural material and system, number of stories, and foundation of each building were investigated as well as observed damage level, which is classified into three grades: D0 (no damage), D1-D3 (slightly and moderately damaged), and D4-D5 (heavily damaged and collapsed including demolished) according to the studies by Okada and Takai (1999). Number of buildings investigated was totally 482 in the target zones, and all of them were one- or two-storied wooden houses which are traditional in the Noto Peninsula.

Figure 2 indicates the distribution of damage ratios for wooden houses investigated at zones Aa-Ae, Ba-Bc, Ca-Cc, and Da-Dd in Hashiride and Kuroshima districts. In Hashiride, the values of D4-D5 ratios are about 0.1-0.2 through zones Aa-Ae. In Kuroshima, however, the damage ratios of wooden houses at the northern and mid zones Ba-Bc and Ca-Cc are larger than those at the southern zone Da-Dd. In zones Ba-Bc and Ca-Cc, furthermore, the damage ratio varies at a maximum of about 0.3 depending on distance from the seashore, which is running in the

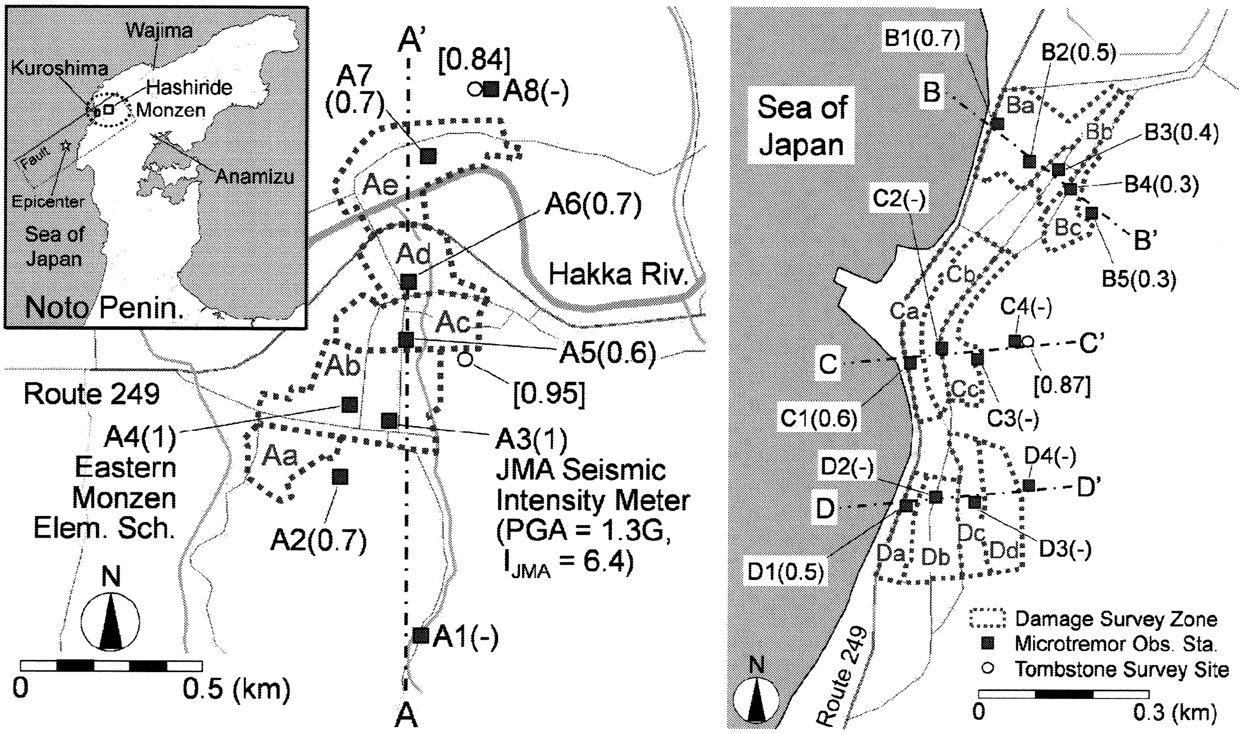

Figure 1. Maps showing zones for building inventory survey, locations of microtremor observation stations, and tombstone investigation sites in Hashiride (left) and Kuroshima (right). Values within ( ) and [ ] in the figure indicate H/V peak periods (in s) of microtremors and overturning ratios of tombstones, respectively. (-) means that microtremor H/V have no significant peak at the station.

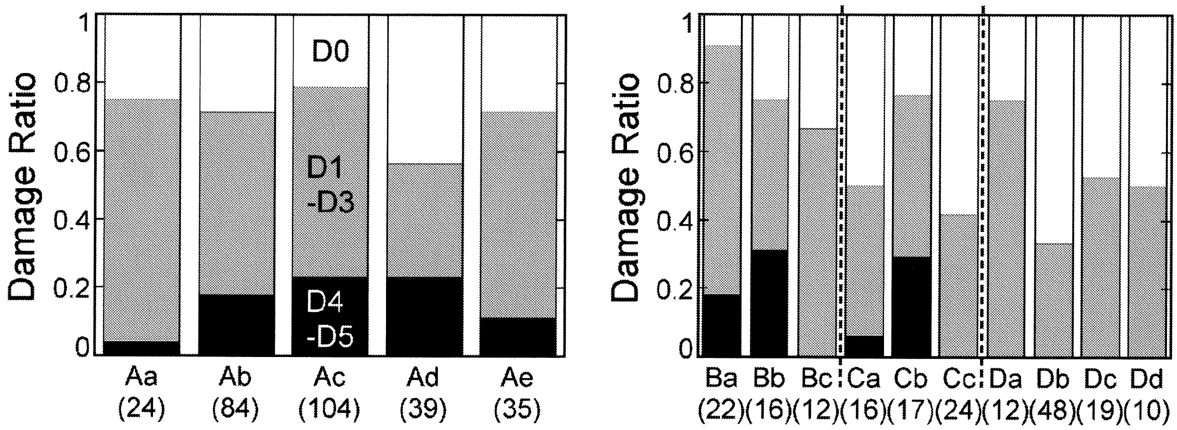

Figure 2. Distribution of damage ratios for wooden houses investigated at zones Aa-Ae in Hashiride (left) and Ba-Bc, Ca-Cc, and Da-Dd in Kuroshima (right). Numbers within ( ) in the figure express those of buildings surveyed.

north-south direction at the western side of Kuroshima. These indicate that the damage ratio of wooden houses within Kuroshima district changes drastically in both the north-south and east-west directions.

3. S-WAVE VELOCITY PROFILING OF SURFACE SOILS IN HASHIRIDE AND KUROSHIMA

To determine S-wave velocity (V_S) structures of surface soils for estimating local site effects in Hashiride and Kuroshima, single-station measurements of microtremors using a three-component sensor were performed at 21 sites shown in Figure 1 as solid squares. These observation stations are hereinafter called as A1-A8 in Hashiride and B1-B5, C1-C4, and D1-D4 in the northern, mid, and southern Kuroshima districts, respectively. In Hashiride, stations A2-A7 are located on an alluvial plain while stations A1 and A8 are on the southern and northern hills, where the building damage was slight.

Open circles in Figure 3 show horizontal-to-vertical (H/V) spectra of microtremors (Nakamura, 1989) observed at stations A1, A4, A6, A7, B1, B3, B5, C2, D1, and D3. At stations A1 located on the southern hill in Hashiride and C2, D1, and D3 in the mid and southern Kuroshima, the observed H/V spectra have no significant peaks. This suggests that the engineering bedrock outcrops at these stations. At stations A4, A6, and A7 located on the plain in Hashiride and B1, B3, and B5 in the northern Kuroshima, on the other hand, the observed H/V spectra have significant peaks. The H/V peak period varies in the ranges of 0.5-1 and 0.3-0.7 s in Hashiride and the north Kuroshima, respectively. The variation of H/V spectra suggests that the V_S profiles change drastically along the lines passing through stations A1-A8 in Hashiride and B1-B5 in the northern Kuroshima.

The inverse analyses of microtremor H/V spectra (Arai and Tokimatsu, 2004, 2005) are performed to determine the V_S structures for the 21 observation stations. In the inversion, the following assumptions are made: (1) the soil profile down to engineering bedrock at each station consists of a two-layered half-space, and (2) the V_S values of top and base layers (sediments and bedrock) at each station are assigned to those listed in Table 1, which are based on a borehole data at the eastern Monzen elementary school (station A4) in Hashiride, available geological information in the district (Monzen Town, Ishikawa Prefecture, 1970), and the spatial variation of H/V shapes observed in Kuroshima. This leaves only the thickness of sediments unknown in the inversion.

Figure 4 shows two-dimensional (2-D) V_S structures thus determined for lines A1-A8 in Hashiride and B1-B5, C1-C4, and D1-D4 in the northern, mid, and southern Kuroshima districts, respectively. Broken lines in Figure 3 are the H/V spectra of surface waves for the inverted V_S profiles. Good agreements between the observed and theoretical H/V spectra indicate that the inverted structures are reasonably reliable. In Figure 4, within Hashiride, it is estimated that the clayey sediments with a depth of about

Table 1. Two-layered analytical models of surface soils inferred in Hashiride and Kuroshima.

District	Soil Type	Sediment V_S (m/s) [1.8]	Bedrock V_S (m/s) [2.0]	Natural Site Period, T_0 (s)
Hashiride	Clayey	145	520	0.5, 0.7, 1
Northern Kuroshima	Sandy	145	380	0.3, 0.5, 0.7
Mid Kuroshima		215	380	0.3, 0.5
Southern Kuroshima		275	400	0, 0.3, 0.5

Values within [ ] in the table denote assumed densities (in Mg/m^3).

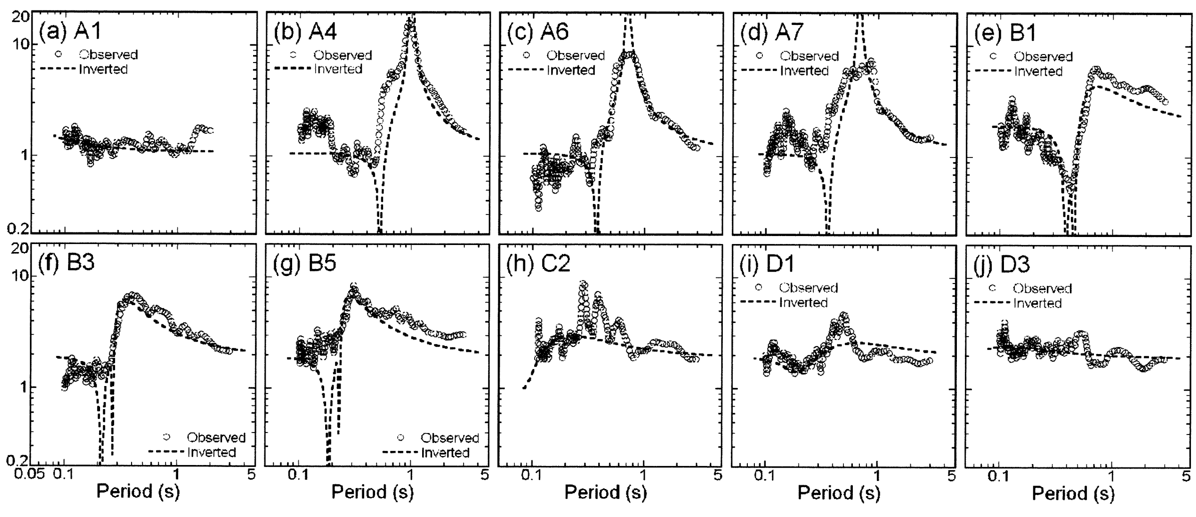

Figure 3. H/V spectra of microtremors (open circles) compared with those of surface waves (broken lines) for soil profiles inferred by H/V inversion at stations A1, A4, A6, and A7 in Hashiride, B1, B3, and B5 in northern Kuroshima, C2 in mid Kuroshima, and D1 and D3in southern Kuroshima.

20-40 m overlie the engineering bedrock in the plain while the bedrock outcrops on the northern and southern hills. In Kuroshima, on the other hand, the engineering bedrock is covered by sandy soils with a depth of about 10-25 m and slopes gradually seaward. Also indicated in the figure is that the impedance ratios between sediments and bedrock in Hashiride and the northern Kuroshima are about 0.3 or lower while those in the mid and southern Kuroshima are about 0.5 or higher. The spatial variation of ground impedance ratios is consonant with that of wooden-house damage ratios shown in Figure 2, suggesting that the impedance ratios of surface soils could have significant effect on the damage to wooden houses.

4. SIMULATION OF GROUND AND BUILDING RESPONSES IN HASHIRIDE AND KUROSHIMA

4.1 Outline of Method and Condition for Simulation

To estimate local site amplifications and wooden-house drift angles in Hashiride and Kuroshima during the main shock, a simplified analytical method proposed by Morii and Hayashi (2003) is employed in this study. In the simplified method, one-dimensional (1-D) nonlinear site amplification is approximately computed by using a response spectrum technique for two-layered ground model, and the maximum drift angle of wooden house is roughly calculated by using the equivalent-performance response spectrum of a SDOF building system (Hayashi, 2002). Details of the response analyses used are found in the studies by Hayashi (2002), Morii and Hayashi (2003), and Hayashi *et al.* (2007).

In the site amplification analyses, two-layered surface soil models listed in Table 1 are used for Hashiride and the northern, mid, and southern Kuroshima districts. In that table, natural site periods, T_0, are parametrically set, based on the V_S profiles estimated from microtremors in the districts (Figure 4), and the stress-strain relationships for clayey and sandy soils are inferred from the studies by Sun *et al.* (1988) and Kokusho (1980), respectively. Also required in the analyses is the acceleration response spectrum with a damping ratio of 0.05 for input bedrock motion, S_{aB}, which can be characterized by its predominant period, T_P, and maximum velocity, V_{max} (Architectural Institute of Japan, 1997). In this study, T_P and V_{max} of the bedrock motion are assigned as 1 s and 80 cm/s, respectively, based on the following two facts:

(1) T_P of strong ground motion records during the main shock, which were provided by K-NET and KiK-net observation systems of the National Research Institute for Earth Science and Disaster Prevention (NIED), Japan and the Japan Meteorological Agency (JMA), could be less than about 1 s at the observation stations with fault distance under about 100 km (Figure 5).

(2) The overturning ratios of tombstones observed at several sites in the districts were over about 0.8 (see Figure 1), suggesting that V_{max} could be larger than 80 cm/s when T_P is less than about 1 s (Kaneko and Hayashi, 2000).

In the building response analyses, the bi-linear model is used for the force-displacement relationship of SDOF system, and its dynamic properties are inferred from the results of inventory survey for wooden houses in Hashiride and Kuroshima and detailed ones in other districts in Japan (e.g., Shimizu *et al.*, 2005). The equivalent height and yield drift angle of SDOF system are predetermined as 4.5 m and 1/100, respectively. The yield base shear coefficient of the system, C_y, is parametrically set as 0.2, 0.4, and 0.6.

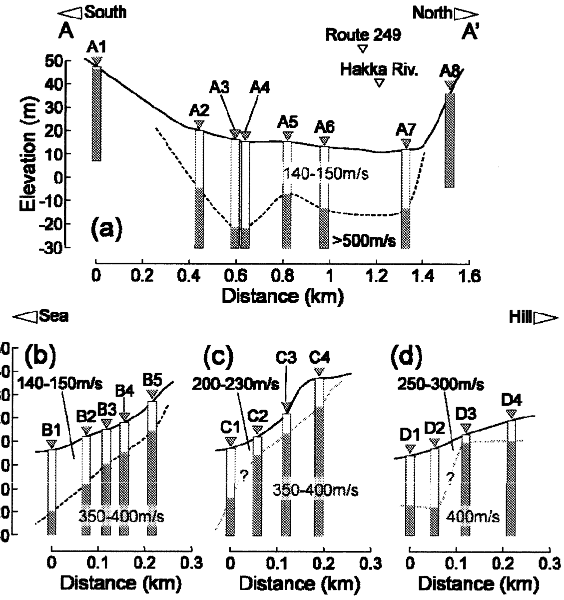

Figure 4. S-wave velocity structures estimated from microtremors in (a) Hashiride, (b) northern Kuroshima, (c) mid Kuroshima, and (d) southern Kuroshima.

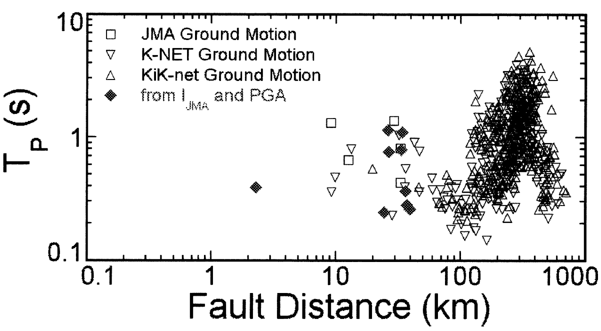

Figure 5. Relationship between predominant periods, T_P, of strong ground motion records and fault distances of observation stations during main shock.

4.2 Drift Angle and Damage Ratio of Wooden Houses

Solid, broken, and chained thick lines in Figure 6 indicate the acceleration response spectra of ground surface motions, S_{aS}, estimated from the site amplification analyses for each natural period T_0 set in Hashiride and the northern, mid, and southern Kuroshima districts. Chained thin lines in the figure are the acceleration response spectrum of the input bedrock motion, S_{aB}, inferred in the analyses. Also shown in

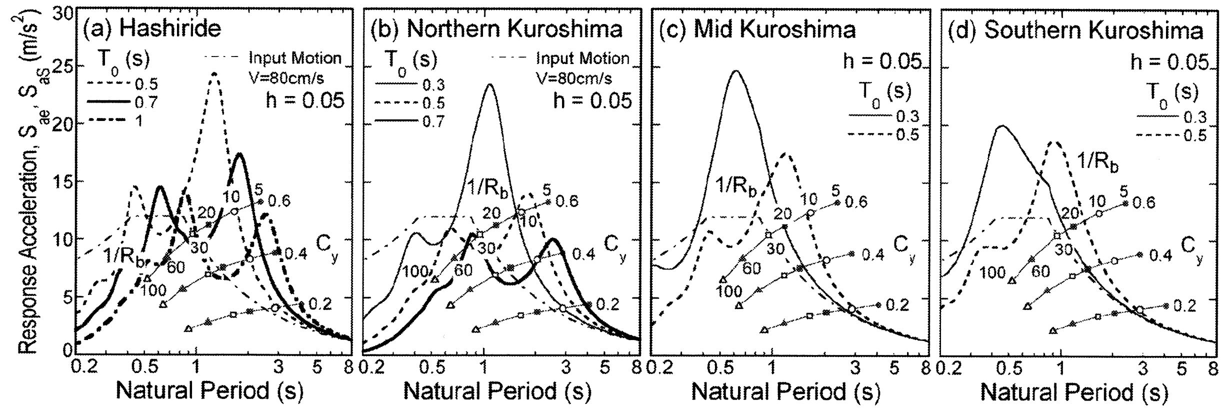

Figure 6. Comparison between equivalent-performance response spectra for wooden houses, S_{ae}, and acceleration response spectra of strong ground motions, S_{aS}, estimated in (a) Hashiride, (b) northern Kuroshima, (c) mid Kuroshima, and (d) southern Kuroshima.

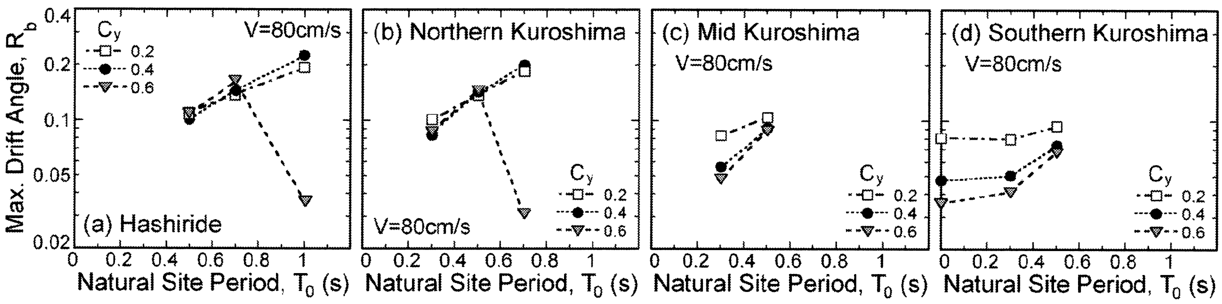

Figure 7. Variation of wooden-house drift angle R_b estimated for each yield base shear coefficient C_y with natural site period T_0 in (a) Hashiride, (b) northern Kuroshima, (c) mid Kuroshima, and (d) southern Kuroshima.

the figure as symbolized thin lines are the equivalent-performance response spectra of wooden houses, S_{ae}, derived from the building analyses for each yield base shear coefficient C_y. In Figure 6, the maximum drift angle, R_b, of a wooden house for C_y at a site with natural period T_0 can be determined from a crossing point between the response spectra S_{ae} and S_{aS} corresponding to C_y and T_0, respectively (Hayashi, 2002; Hayashi *et al.*, 2007). Figure 7 summarizes the variation of the wooden-house drift angle R_b evaluated for each yield base shear coefficient C_y with natural site period T_0 in the districts.

From Figure 7, the maximum drift angles R_b of wooden houses for C_y = 0.2 and 0.4 are over about 1/10 in Hashiride and the northern Kuroshima districts, where building damage was significant. In the other districts of Kuroshima, however, the values of R_b decrease southward and are less than about 1/15 in the southern Kuroshima, where the building damage was slight. Comparing Figures 4, 6, and 7, it is revealed that the maximum drift angles of wooden houses (R_b) could mainly be controlled by the response spectra of strong ground motions (S_{aS}) at a period of about 1-3 s. In Kuroshima, also indicated is that the strong ground motion with such a period is significantly amplified at the northern (heavily damaged) district due to low ground

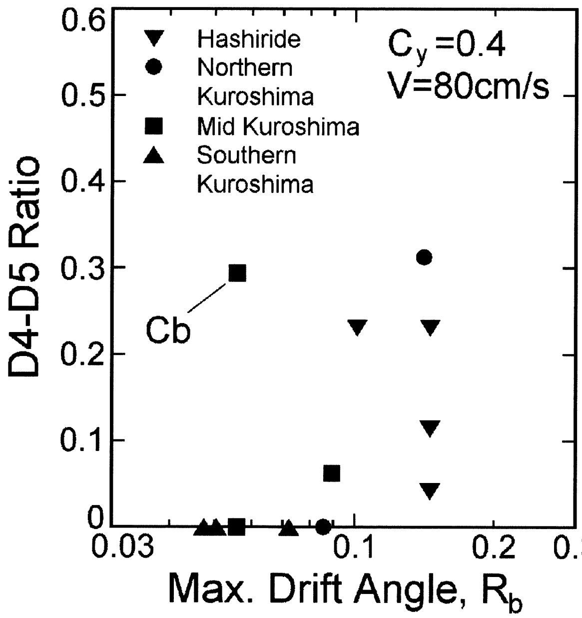

Figure 8. Relationship between estimated drift angles R_b of wooden houses with C_y = 0.4 and observed D4-D5 ratios in Hashiride and Kuroshima.

impedance ratio resulting in strong soil nonlinearity while it is not at the southern (slightly damaged) district due to high ground impedance ratio leading to weak soil nonlinearity.

Furthermore indicated from Figure 7 is that the maximum drift angles R_b of wooden houses for $C_y = 0.2$ and 0.4 increase with lengthening the natural site period T_0 in any district. In case of wooden house for $C_y = 0.6$, however, the values of R_b reduce drastically at sites with $T_0 = 1$ s in Hashiride and $T_0 = 0.7$ s in the northern Kuroshima. Based on Figures 6 and 7, it is considered that the R_b reduction in the districts are chiefly caused by increasing soil damping with lengthening T_0, and thus, the response spectra S_{as} of ground motions at sites with large T_0 values could get smaller than the equivalent-performance response spectra S_{ae} of wooden houses with high C_y values.

Figure 8 shows the relationship between the evaluated drift angles R_b of wooden houses with $C_y = 0.4$ and the observed D4-D5 ratios in Hashiride and Kuroshima districts. In the figure, the R_b data estimated at sites with $T_0 = 1$ s in Hashiride and $T_0 = 0.7$s in the northern Kuroshima are not involved because of the consideration stated previously. The figure suggests that the maximum drift angles R_b of wooden houses could be over 1/10 at sites where the D4-D5 ratios exceed about 0.1. Similar trends exist in cases of $C_y = 0.2$ and 0.6. These also indicate that the simulated drift angles R_b are reasonably reliable.

5. CONCLUSIONS

Effects of local site amplification characteristics on strong ground motions and damage to wooden houses in Hashiride and Kuroshima districts of Monzen area, Wajima city, Japan, during the 2007 Noto Hanto earthquake, are examined based on building inventory survey and microtremor single-station measurements. Using simplified analytical models of surface soils and wooden houses for the districts, response spectra of strong ground motions and maximum drift angles of wooden houses are simulated. Comparing the simulation results with the observed damage, the following conclusions are made:

1. The wooden-house responses during large earthquakes are mainly controlled by strong ground motions with a period of about 1-3 s.
2. The site amplification factors at a period of about 1-3 s were significantly influenced by impedance ratios (V_S contrasts) and nonlinear properties of surface soils in the districts.
3. The heavily damage to wooden houses could be due to low ground impedance ratio leading into strong soil non-linearity while the slightly ones could be due to high ground impedance ratio inducing weak soil nonlinearity.

Acknowledgements:

The authors would like to express their sincere thanks and appreciation to Prof. Dr. James Mori of the Disaster Prevention Research Institute (DPRI), Kyoto University, Japan, Dr. Sun-Cheon Park of the Korea Meteorological Administration (KMA), Korea, and Ms. Shoko Ida, Mr. Wataru Kudo, Mr. Michito Shoji, and Mr. Shugoro Miyaji, graduate students, Kyoto University, for their assistance in the field survey. The strong ground motion records used in this study were provided by the National Research Institute for Earth Science and Disaster Prevention (NIED), Japan and the Japan Meteorological Agency (JMA). We are also grateful to these organizations. Our gratitude and appreciation would be extended to a board of education, Wajima city, Japan, who provided the boring data at the eastern Monzen elementary school in Hashiride.

References:

Arai, H. and Tokimatsu, K. (2004), "S-Wave Velocity Profiling by Inversion of Microtremor H/V Spectrum," *Bull. Seism. Soc. Am.*, **94**(1), 53-63.

Arai, H. and Tokimatsu, K. (2005), "S-Wave Velocity Profiling by Joint Inversion of Microtremor Dispersion Curve and Horizontal-to-Vertical (H/V) Spectrum," *Bull. Seism. Soc. Am.*, **95**(5), 1766-1778.

Architectural Institute of Japan (1997), "Recommendations for Loads on Buildings," 406-409. (in Japanese)

Hayashi, Y. (2002), "Evaluation of Seismic Design Based on Equivalent-Performance Response Spectra," Proc., *11th Japan Earthquake Engineering Symposium*, 651-656. (in Japanese with English Abstract)

Hayashi, Y., Saratani, A., and Morii, T. (2007), "Seismic Risk Evaluation of Wood Houses Considering Aged Deterioration and Long-term Occurrence Probability of Earthquakes," Proc., *2nd Int'l Conf. on Urban Disaster Reduction*, Nov. 27-29, Taipei, Taiwan, CD-ROM, article 2-3-4.

Japan Meteorological Agency, http://www.seisvol.kishou.go.jp/eq/2007_03_25_noto/EVENT1/noto_kyosin.html (in Japanese)

Kaneko, M. and Hayashi, Y. (2000), "Proposal of A Curve to Describe Overturning Ratios of Rigid Bodies," *J. Struct. Constr. Eng., Architectural Institute of Japan*, **536**, 55-62. (in Japanese with English Abstract)

Kokusho, T. (1980), "Cyclic Triaxial Test of Dynamic Soil Properties for Wide Strain Range," *Soils and Foundations*, **20**(2), 45-60.

Monzen Town, Ishikawa Prefecture (1970), "A History of Monzen Town," 842pp. (in Japanese)

Morii, T. and Hayashi, Y. (2003), "Effect of Characteristics if Incident Ground Motion and Ground Motion Amplification in Surface Soil on Wood Houses Response," *J. Struct. Constr. Eng., Architectural Institute of Japan*, **568**, 75-82. (in Japanese with English Abstract)

Nakamura, Y. (1989), "A Method for Dynamic Characteristics Estimation of Subsurface Using Microtremor on The Ground Surface," *Q. Rep. Railway Tech. Res. Inst.*, **30**(1), 25-33.

National Research Institute for Earth Science and Disaster Prevention, K-NET, http://www.k-net.bosai.go.jp/

National Research Institute for Earth Science and Disaster Prevention, KiK-net, http://www.kik.bosai.go.jp/

Okada, S. and Takai, N. (1999), "Classifications of Structural Types and Damage Patterns of Buildings for Earthquake Field Investigation," *J. Struct. Constr. Eng., Architectural Institute of Japan*, **524**, 65-72. (in Japanese with English Abstract)

Shimizu, H., Hayashi, Y., Suzuki, Y., Saito, Y., and Goto, M.(2005), "Evaluation of Structural Characteristics and Seismic Performance of Damaged Wooden Houses by The Northern Miyagi Earthquakes of July 26, 2003," *J. Struct. Constr. Eng., Architectural Institute of Japan*, **598**, 43-49. (in Japanese with English Abstract)

Sun, J. I., Golesorkhi, R., and Seed, H. B. (1988), "Dynamic Moduli and Damping Ratios for Cohesive Soils," *EERC Report* 88-15.

Fifth International Conference on Urban Earthquake Engineering
March 4-5, 2008, Tokyo Institute of Technology, Tokyo, Japan

CENTRIFUGE MODELING OF ROCKING OF SHALLOW FOUNDATIONS FOR BRIDGES

José A. Ugalde[1], Bruce L. Kutter[2], Boris Jeremic[3], Sivapalan Gajan[4], Lijun Deng[5]

1) Graduate Student, Dept. of Civil & Environmental Engineering, University of California, Davis, CA, U. S. A.
2) Professor, Dept. of Civil & Environmental Engineering, University of California, Davis, CA, U. S. A.
3) Associate Professor, Dept of Civil & Environmental Engineering, University of California, Davis, CA, U. S. A.
4) Assistant Professor, Dept of Civil Engineering, North Dakota State University, Fargo, ND, U. S. A.
5) Graduate Student, Dept. of Civil & Environmental Engineering, University of California, Davis, CA, U. S. A.
jaugalde@ucdavis.edu, blkutter@ucdavis.edu, jeremic@ucdavis.edu, s.gajan@ucdavis.edu, ljdeng@ucdavis.edu

ABSTRACT: The capacity, energy dissipation, and self centering characteristics of shallow foundations have potentially important effects on the performance of a soil-foundation-bridge deck system. As the foundation width decreases, the energy dissipated by the foundation increases while permanent settlement and rotation increase and construction costs decrease. Centrifuge tests on rocking of bridge foundations show that square shallow foundations with dimensions significantly smaller than those designed according to current procedures used in California performed reasonably well. The rocking foundations displayed excellent ductility, relatively small permanent deformations, and they provide a self-centering mechanism. Furthermore, the moment capacity of rocking foundations can in most cases be accurately predicted. Considering these benefits, rocking foundations should be considered to be a practical tool for reducing demands on structural elements of a bridge and as a potential tool for dissipating energy through plastic deformation of the soil.

1. INTRODUCTION

A schematic diagram of a rocking bridge bent is shown in Figure 1(a). The important parameters are the masses of the deck and footing, the stiffness of the column, length of the footing (L=B), critical contact length (Lc) which is the length of foundation in contact with the soil when the bearing capacity is mobilized, the height to center of gravity of the deck mass (Hcg_{deck}), and the ground motion.

Housner (1963) pointed out that structures allowed to rock survived in several earthquakes while more modern stable structures were severely damaged. Housner (1963) showed that the dynamic characteristics of rocking systems on an elastic half space are much different than those of elastic fixed base systems. In practice there are currently two approaches used by the California Department of Transportation (Caltrans) to characterize rocking of bridge foundations. The first approach, typically used in new construction, allows for no rocking or uplift of the footing. This ensures that the failure mechanism is plastic hinging in the column (Alameddine and Imbsen 2002). Column yielding may be preferred because soil response is considered to be unreliable and column damage may be easily inspected following an earthquake.

The second approach is used in retrofit evaluations, in which case rocking of the footing is permitted. Estimates of the displacements of the foundation are calculated using an algorithm based on the concepts of Housner (1963) implemented in an algorithm formulated by Priestly et al (1996) and packaged by Caltrans in a program called Winrock (Alameddine and Imbsen 2002).

Based on the above, and more recent work (e.g., Mergos and Kawashima (2005), Gajan (2006)), some of the known effects of rocking are summarized below:

1. Peak moment demand in the column is limited by moment capacity of the foundation. In this respect the foundation can act like a mechanical fuse or isolation mechanism.
2. Uplift of a foundation stores gravitational potential energy. Closure of the gap upon unloading restores the footing toward it initial position.
3. Local bearing pressures increase causing plastic deformation of soil around the footing which is a source of hysteretic damping.
4. Rocking results in lengthening of the natural period which tends to reduce acceleration and force demands and increase displacement demands on the superstructure.
5. The magnitude of settlement caused by rocking depends on the number of cycles and amplitude of loading as well as the bearing capacity of the soil.

One goal of this paper is to help engineers to quantify the above factors so that rocking may be accounted for in the design process. If properly quantified, the benefits of rocking may be used to reduce construction costs without unduly sacrificing performance.

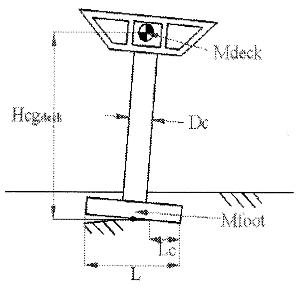

(a)

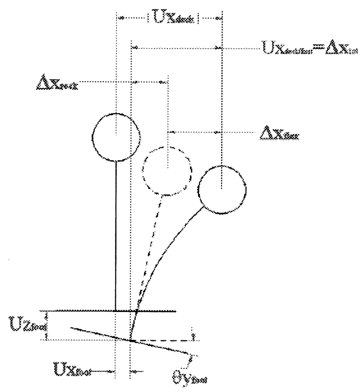

(b)

Figure 1(a) Schematic of problem and definition of some system parameters; Figure 1(b) Definition of coordinate system and displacements; x is horizontal and z is downward.

2. CENTRIFUGE EXPERIMENTS

2.1 General descriptions of the structure

Sakellaraki et al. (2005) performed experiments experimental and numerical analysis shaking experiments on a model bridge resting on a rubber foundation. Below we describe results of model bridge structures tested on sand in a geotechnical centrifuge. The basic centrifuge scaling laws can be derived by defining the length scale factor as $L^* = L_m/L_p$, by assuming that identical materials are used in model and prototype (hence material densities scale according to $\rho^* = \rho_m/\rho_m = 1$), and requiring that the stresses in the model should scale to be identical to those in the prototype; i.e., $\sigma^* = \sigma_m/\sigma_p = 1$. Because soil has nonlinear mechanical properties that are a function of confining stress, it is important that stresses scale one to one. Simple dimensional analysis shows that $\sigma^* = 1$ may be accomplished by increasing accelerations (including gravity) by a factor $a^* = 1/L^*$ and scaling time by $t^* = L^*$. In the present paper, $L^* = 1/44$ and $a^* = 44$.

Many test structures were placed into one model soil container. The structures were spaced so that they were an adequate distance from each other and the walls of the container. Each structure location was given a station name, Station A through Station G. Slow cyclic tests at Stations A and B were directly loaded with a hydraulic actuator (Fig. 2(b)) and Stations C through G (Fig 2(a)) were excited by ground motions applied to the base of the soil container.

The model tests were scaled from typical bridge configurations used by Caltrans. The prototype footings were square with widths of 3, 4, or 5 times the diameter of the column (Dc =1.83 m). The prototype scale mass and width of the footings at dynamic stations C, D, E, and F are (362 Mg, 9.1 m), (265 Mg, 7.3 m), (186 Mg, 5.5 m), and (265 Mg, 7.3 m) respectively. The mass of the deck at stations C, D, E, and F is 998 Mg. The fixed base natural period of these structures is 1.6 seconds. The total structure mass and footing width of structures at stations A and B are (1200 Mg, 9.1m) and (1080 Mg, 5.5m) respectively. Nevada Sand (mean grain size = 0.15 mm) was placed by dry pluviation in air to a uniform relative density of about 80% to create a 210 mm deep soil deposit in the 1.76 x 0.9 m (77.4 x 40 m prototype scale) model container. For this density, and for pressures appropriate to the footing loads, the friction angle is about 40° to 42° (Gajan 2006). The foundation soil contained accelerometers for measuring both vertical and horizontal accelerations.

The vertical bearing capacity of a shallow foundation on sand for bridge structures turns out to be quite large (F = 30 to 70 for the experiments described here). This is because the governing criteria for large footings on sand tend to be the allowable settlement and the required moment capacity; bearing capacity seldom governs the design. The footings are sized by allowable bearing pressures. The footings described herein had bearing pressures that ranged between 80% and 150% of the pressure that would be expected to cause 25 mm of settlement under the static vertical loads.

The prototype structure was a typical reinforced concrete single column bridge bent modeled as a "lollipop" structure with a deck mass and column connected to a shallow spread footing. Figures 2(a) depict the system modeled used in the centrifuge tests carried out at UC Davis. The deck was modeled by a steel block, the reinforced concrete column was modeled by an aluminum tube that had a bending stiffness, EI closely scaled to the calculated EI of the cracked section of the prototype concrete column. The footings were constructed of aluminum plate with sand glued to their bases to provide a rough concrete-like interface with the soil.

For slow cyclic tests, the vertical load on the footing was scaled, but the distribution of the mass and the stiffness of the structure were not considered important parameters. Therefore, essentially rigid steel plates were used to provide the desired mass and a vertical cantilever upon which lateral loads were applied by an hydraulic actuator acting horizontally at a height approximately equal to the elevation of the effective height of the prototype deck-footing system.

2.2 Loading and test setup sequence

At the time that the sand was placed, all seven model foundations were embedded to a depth of 40 mm (1.8 m prototype) at seven stations (A-G). Structures at one or two stations were tested during a given spin; the structures were bolted to their embedded foundation, then the centrifuge was spun and the loading events were applied. After stopping the centrifuge, the model structures were removed and new structure(s) were placed at other station(s) for testing in the next spin.

The sequence of testing involved in 5 different spins. Prior to the first spin, a rigid wall structure was attached to the square footing. Then an actuator was attached to the wall as depicted in Figure 2. Restraint on the sides of the wall was provided to prevent out of plane movement as described in detail by Gajan (2006). After spinning up to 44 g, slow cyclic lateral loading was applied by an actuator. The actuator was typically commanded to apply packets of 3 cycles of a sinusoidal displacement wave at a time. For Stations A and B, 8 to 12 packets of sine waves with amplitudes varying between 0.14% and 5.4% were applied to the structure. Results from the last three packets of sine waves with amplitudes 5.4%, 2.2%, and then 0.54% are shown in Figure 4.

Structures at Stations C-G were subject to dynamic loading using the shaking table mounted on the centrifuge to shake the entire model container. The ground motions imposed on the model container were scaled and filtered motions from recordings in the Tabas 1978 earthquake and a Los Gatos recording of the 1989 Loma Prieta earthquake. These motions come from the near field records posted at the SAC Steel Project (2006) website. Twelve to fifteen scaled motions were applied to each structure. The testing sequence for dynamic stations started with low amplitude step waves, followed by scaled down earthquake ground motions, then large amplitude earthquake ground motions and finally step waves similar to those applied before strong shaking. The peak ground accelerations ranged between 0.1 g and 0.8 g.

The instrumentation is briefly depicted in the drawings in Figure 2. For slow cyclic testing, each structure was instrumented with a load cell to measure the horizontal actuator load and four displacement transducers; any three of the four displacement sensors was sufficient to determine the rotation, settlement and sliding of the footing.

During dynamic loading, six accelerometers were placed on the foundation and six on the deck in order to resolve all six rotational and translational degrees of freedom for these relatively rigid bodies. Six displacement transducers were also used to determine the six displacement degrees of freedom of the footing.

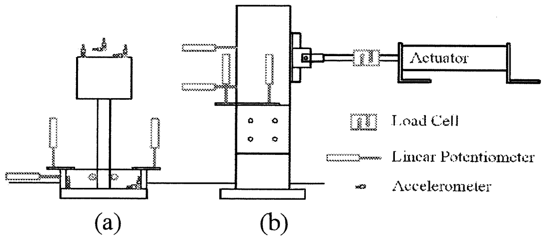

Figure 2 Side view of structures and instrumentation for: (a) a dynamic test and (b) a slow cyclic test

3. EXPERIMENTAL RESULTS

The coordinate system as well as definition of displacements is indicated in Figure 1(b). The data from all of the accelerometers and displacement transducers mounted at various points on the foundation and deck were combined and processed to provide the measurements of the translational and rotational accelerations and displacements at the center of gravity of the foundation and deck mass. The deck mass included attached instrumentation and half the column mass. The footing mass included the attached instrumentation, half of the column mass, as well as the plastic frame fixed to the foundation.

The rocking moment, M_y, and the horizontal sliding force, F_X ,computed at the base center point of the footing are calculated as follows:

$$\begin{aligned} M_y &= -(m * a_x * Hcg)_{deckcg} + (I * \alpha_y)_{deckcg} \\ &- (m * a_x * H_{cg})_{footingcg} + (I * \alpha_y)_{footingcg} \\ &+ (m * (1g + a_y) * U_{x_{deck/foot}})_{deckcg} \end{aligned} \qquad (1)$$

$$F_x = -(m * a_x)_{deckcg} - (m * a_x)_{footingcg} \qquad (2)$$

The five terms in equation (1) represent the moments due to lateral acceleration of the deck, the rotational acceleration of the deck, the lateral acceleration of the footing, the rotational acceleration of the footing, and the static and dynamic P-Δ moments. The greatest contributor to moment is the inertial force from the deck mass. At large rotations the P-Δ term becomes significant. The I*α terms of the deck mass and foundation are relatively small. But inclusion of these terms in the equation resulted in significantly improved data quality. Some "noise" that appeared in the data was eliminated by accounting for the moments due to the I*α terms. The inertia forces associated with added mass of the soil adjacent to the footing was neglected.

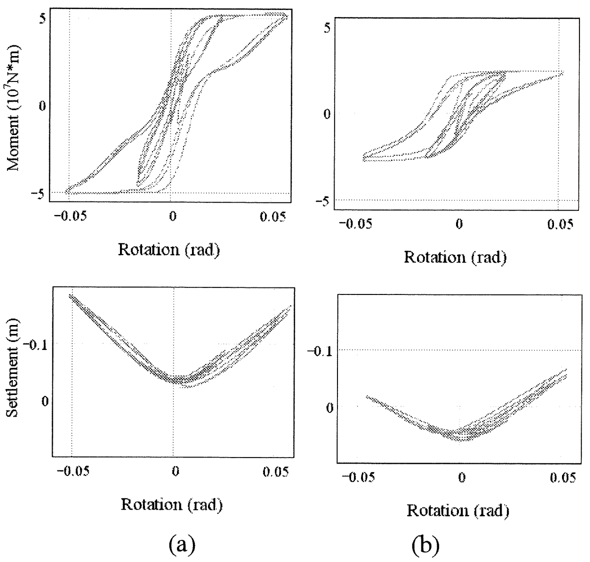

Figure 3 Slow cyclic load-deformation behavior of footing (a) B = 3 Dc. (b) B = 4 Dc

3.1 Slow Cyclic Tests

As seen in Figure 3, both the smallest (B = 3 Dc) and the largest (B = 5 Dc) foundations show large moment-rotation loops indicating significant energy dissipation. The moment capacity shows negligible degradation with the amplitude of rotation.

The footings show mobilization of their moment capacity at about 2% rotation. The smaller footing (B = 3 Dc) has about 3/5 of the moment capacity of the largest footing (B = 5 Dc), consistent with expectations for rotation about one edge of the footing. The theoretical moment capacity may be expressed as:

$$M_{capacity} = V(B - Bc)/2 \tag{3}$$

where V is the vertical load, B is the footing width, and Bc is the width of the footing required to support the vertical load V. The fact that the moment capacity for the small footing is slightly less than 3/5 of the capacity of the large footing is expected because the mass of the small footing is slightly less than that for the large footing (vertical load V is slightly smaller) and furthermore, for the small footing, Bc is a larger fraction of the total width, B.

The shape of the moment-rotation loops for the large foundation differs from the small foundation in that a larger percentage of the plastic rotation is recovered by the large foundation. Figure 4 shows a sudden recovery of rotation while unloading from about 2.5 to 1.5 x 10^7 Nm. The flag shape type hysteresis loop seen in the larger foundation is hypothesized to be caused by soil falling underneath the foundation during uplift. The gap around the edge of the footing, shown in Figure 3 appeared to develop by soil sloughing under the footing to fill gaps formed during rocking. For a given amplitude of rotation, the size of the gap is proportional to the footing size; because the gap is larger for a large footing, the sloughing of particles under the large footing may be more significant than it is for the small footing. Settlement rotation plots show that the larger foundation has a net uplift after the series of tests, while for the smaller footing, there is a net settlement. This is also consistent with the hypothesis that soil was falling into the gap under the large footing.

3.2 Dynamic Tests

Figure 4 shows the moment-rotation and settlement-rotation response of the two structures simultaneously loaded during a scaled version of the Los Gatos ground motion. These structures are identical except for their foundation widths. During dynamic shaking both footings show a net settlement. The amplitude of rotation is smaller for the larger footing, and the moment capacity is larger for the larger footing. The shapes of the moment-rotation curves are similar to those observed in the slow cyclic tests shown in Figure 4.

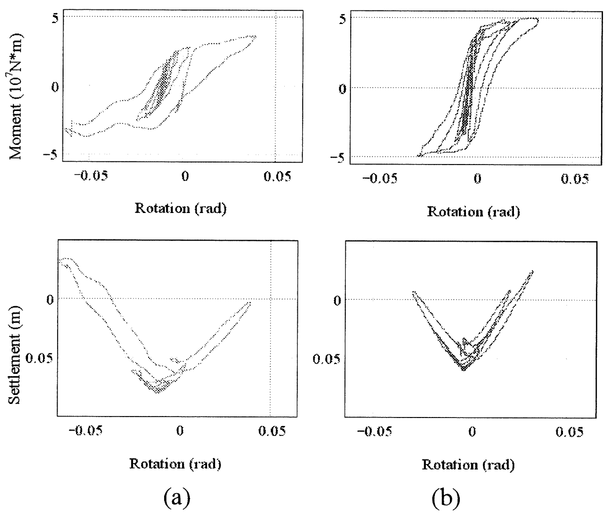

Figure 4 Moment rotation and settlement rotation loops for Los Gatos event scaled to pga of 0.55 g . (a) Station E (B=3 Dc). (b) Station F (B=4 Dc)

Figure 5 shows time histories of column moment, deck acceleration, and the footing settlement for Stations E and F. The column moment time histories show that the structure with B = 3 Dc has about 20% smaller moment demand in than the structure with B = 4 Dc. The acceleration along the shaking direction at the center of gravity of the deck mass is proportional to the largest term contributing to the moment (Equation 1). As such, it makes sense that the deck acceleration time history is very similar to the column moment time history. (The sign of the moment and acceleration time histories are opposite due to the sign convention.)

The dynamic testing showed that as footing size decreased, the permanent deformations increased and the moment demand on the column decreased. The B = 3 Dc footing settled about 30 mm per large shaking event while the structures on the larger foundations (B = 4 Dc or 5 Dc) settled about 15 mm per strong shaking event.

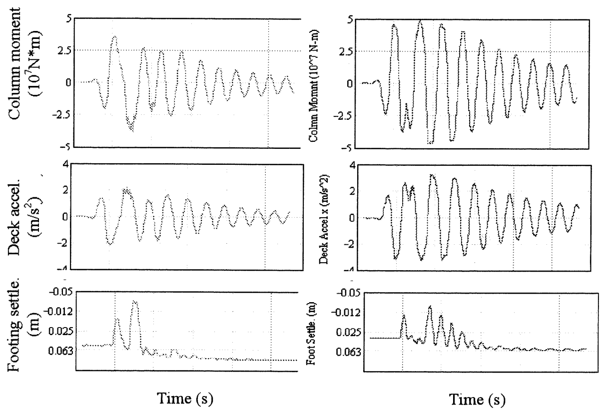

(a) (b)

Figure 5 Time histories for 0.55 g Los Gatos event. (a) (B = 3 Dc), (b) (B = 4 Dc)

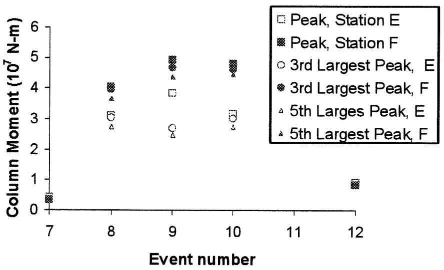

Figure 6 Peak moments in column during the strong shaking events in Spin 5

Figure 6 shows the largest amplitude peak, the 3rd largest amplitude peak, and the 5th largest amplitude peak column moments for a sequence of shaking events imposed on the structures with B = 3 Dc and B = 4 Dc, subject to the same shaking event. From this it is easily seen that during large shaking events the capacity of the foundation limits the moment demand on the column. The peak column moments are consistently larger for the larger footing.

4. DISCUSSION

4.1 Dynamic vs. Slow Cyclic

There were some differences in the load deformation behavior of the foundation under slow cyclic testing and dynamic testing. The amplitude of foundation rotations during dynamic testing tended to be smaller than those imposed during slow cyclic testing. The amplitude of rotation depends on the dynamics of the system and frequency content of the ground motion hence the amplitude of dynamic deck response also varied with footing size. Despite the fact that the amplitude of rotation tended to be smaller during the selected ground motions for dynamic tests, settlements were larger during dynamic loading than during slow cyclic loading. This was due partially to the settlement of the ground surface during shaking, but also may be associated with a reduction in bearing capacity caused by dynamic shaking of the soil combined with dynamic loading from the footing. In all cases, the magnitude of settlements were small enough that the performance may be judged to be satisfactory. For the smallest footing in the largest shaking event, the settlements were about 30 mm per shaking event.

4.2 Mechanisms for Yielding and Predicting Failure

In seismic resistant design of bridge structures, the designer ought to make a conscious decision regarding the capacity and demand that will be placed on various elements of the system. One design philosophy is to allow yielding but prevent collapse during extreme shaking events. If yielding is to be allowed, a decision should be made regarding which elements should yield and then to ensure that the yielding elements are ductile and that their capacity should not suffer drastic degradation.

Civil Engineers are trained that soil properties are heterogeneous and uncertain; hence they may develop the false impression that the moment capacity of a spread footing has a high uncertainty. On the contrary, with the exception of footings with low factors of safety with respect to bearing capacity, the moment capacity of a spread footing is largely controlled by the size of the footing and the vertical load on the footing and these key factors can be determined with good certainty and hence the moment capacity can be accurately calculated by equation (3). The present study (along with work of many previous researchers) shows that a rocking foundation has very ductile behavior with negligible loss of capacity. Rocking foundations also have significant damping capacity. The uplift of a shallow foundation provides a self-centering mechanism associated with gap closure upon unloading. This self centering upon unloading is not a typical characteristic of yielding reinforced concrete columns.

Assuming that yielding does occur during a large seismic event, the reparability of the yielded element should also be considered. Damage to concrete may be argued to be more dangerous that damage to soil. Damaged concrete columns are likely to crack, spall and crumble under extreme cyclic loading. Soil is already an assembly of tiny pieces of broken rock that are difficult to break into smaller pieces. Soils derive their strength from reliable friction as opposed to concrete cohesion that disappears upon cracking.

Practical procedures such as grouting are available that could be used to close up the gaps and restore full contact between the footing and soil. Considering the above factors, yielding of a rocking foundation has potential to serve as a repairable fuse to isolate columns from large seismic demands.

5. CONCLUSIONS

Centrifuge models of seismic shaking of a bridge bent supported on shallow foundations in sand is reported. The performance of a bridge bents a with smaller footing (B = 3 Dc) (Dc is the area of the column) is in some aspects preferable to the performance of systems supported on larger footings (B = 4 or 5 times Dc). Contrary to what many engineers may believe, the moment capacity of rocking shallow foundations on soil is often relatively straight forward to calculate with the necessary accuracy.

Consistent with findings of Mergos and Kawashima (2005), rocking of foundations can produce an isolation mechanism that reduces ductility demand on bridge columns. The present study shows that as the footing size decreases, maximum moment and ductility demands on the column as well as acceleration demands on the deck are expected to reduce, but displacement demands on the deck may increase.

Smaller footings do suffer greater permanent rotations and settlements than larger footings. The magnitude of settlements may be acceptable; permanent settlements were on the order of 30 mm (prototype scale) during large seismic events.

The moment rotation behavior is very ductile with no apparent loss of capacity with large amplitude cyclic loading. The hysteretic loops observed are significantly larger than that observed in the experiments by Sakellaraki et al. (2005). Because yielding associated with rocking of shallow foundation is ductile, repairable, and includes self centering due to closure of the gap associated with rocking, foundation rocking may be an acceptable mechanism of yielding; engineers should consider the option of allowing shallow foundations to rock as a method of dissipating energy and protecting the columns. The above conclusions are most applicable to shallow foundations on medium dense sandy soils. Additional testing may be required prior to application to other soil types.

Acknowledgements

Financial support for this research is provided by the California State Department of Transportation under a project titled "STAP 13: Design Guidelines for Foundation Rocking of Bridge Piers". The Caltrans project managers, Craig Whitten and Fadel Alamaddine, provided valuable guidance during the project, especially in regard to selection of realistic masses and dimensions for the foundation-structure systems. Steve Mahin, Andy Espinoza, Dan Wilson, and staff of the Center for Geotechnical Modeling provided significant contributions to this work.

References:

Alameddine F. and Imbsen R. (2002), "Rocking of Bridge Piers Under Earthquake Loading," *Proceedings of the Third National Seismic Conference & Workshop on Bridges and Highways.*

Gajan S. (2006), "Physical and Numerical Modeling of Nonlinear Cyclic Load-Deformation Behavior of Shallow Foundations Supporting Rocking Shear Walls," Ph.D. Thesis. University of California at Davis, College of Engineering.

Housner G. W. (1963), "The Behavior of Inverted Pendulum Structures During Earthquakes," *Bulletin of the Seismological Society of American*, **53**(2), 403-417.

Kutter B. L. (1995), "Recent Advances in Centrifuge Modeling of Seismic Shaking," *Proceedings of the Third International Conference on Recent Advances in Geotechnical Earthquake Engineering and Soil Dynamics*, Vol.**2**, 927-942.

Mergos, P.E., and Kawashima, K. (2005), "Rocking Isolation of a Typical Bridge Pier on Spread Foundation," J. Earthquake Engr., Vol. 9 Special Issue 2, 395-414.

Priestley N. M. J., Seible F. and Calvi G. M. (1996), "Seismic design and retrofit of bridges", John Wiley & Sons Inc.

SAC Steel Project (2006), "Impulsive Near-Field Earthquake Ground Motions, " http://nisee.berkeley.edu/data/strong_motion/sacsteel/motions/nearfault.html.

Sakellaraki, Watanabe, G. and Kawashima, K. (2005) "Experimental Rocking Response of Direct Foundations of Bridges, Second Int. Conf. on Urban Earthquake Engr., Tokyo, pp. 497-504.

Schofield, A. N. (1980), "Cambridge Geotechnical Centrifuge Operations," *Geotechnique*, **30**(3), 227-268.

Fifth International Conference on Urban Earthquake Engineering
March 4-5, 2008, Tokyo Institute of Technology, Tokyo, Japan

CYCLIC SOFTENING OF LOW-PLASTICITY CLAY AND ITS EFFECT ON SEISMIC FOUNDATION PERFORMANCE

Daniel B. Chu [1)], Jonathan P. Stewart [2)], P.S. Lin [3)], and R.W. Boulanger [4)]

1) Chief Geotechnical Engineer, Ninyo & Moore, Irvine CA. USA.
2) Professor and Vice Chair, UCLA, Civil & Environ. Engineering Dept., CA USA
3) Professor, National Chung-Hsing University, Taichung, Taiwan
4) Professor, University of California, Civil & Environmental Engineering Department, Davis, CA USA.
Daniel.chu@ninyoandmoore.com, jstewart@seas.ucla.edu, rwboulanger@ucdavis.edu

Abstract: We describe the results of field investigations and analyses of a region in Wufeng, Taiwan that exhibited a range of ground performance during the 1999 Chi Chi earthquake. The region is located along a line 350 m long with single story residential structures on the east end with no evidence of ground failure and 3-6 story reinforced concrete structures on the west end that underwent foundation failures. No free-field ground failure was observed. Surficial soils consist of low-plasticity silty clays. Analyses were performed of the potential for cyclic softening of the clays, which is related to the development of large cyclic shear strains. The resistance to cyclic softening is evaluated using monotonic and cyclic strength testing. Seismic demand on the soil is evaluated from analysis of free-field ground response and soil-structure interaction. Results indicate low factors of safety in foundation soils below the six-story buildings, which contributes to bearing capacity failures at the edges of the foundation. Similar analyses indicate high factors of safety in foundation soils below one-story buildings as well in the free field. Accordingly, analysis of the site within a framework that accounts for the clayey nature of the foundation soils successfully predicts the field performance.

1. INTRODUCTION

The 1999, Chi-Chi, Taiwan Earthquake caused extensive ground failure and structural damage in Wufeng, Taiwan. Liquefaction-induced ground failure occurred in the form of sand boils, lateral spreading, and ground settlement (Stewart, 2001). However, some of the most interesting examples of ground failure occurred in areas underlain by low plasticity clayey soils, in which ground failure was generally not manifest in the free-field nor beneath low-rise buildings, but only beneath relatively tall 3- to 6-story reinforced concrete frame structures with shallow foundations (mats and footings). As will be shown in this paper, these case histories push the limits of liquefaction analysis tools that form the current standard of practice. Accordingly, in this paper we analyze a well-documented case history using an alternative framework for ground failure in clayey soils.

This article presents a very brief overview of work presented in more detail by Chu (2006) and Chu et al. (2008).

2. WUFENG BUILDINGS

The subject of this paper is a region referred to as Site A located in the southern part of Wufeng. It consists of a series of buildings along an E-W trending line 350 m in length. The east end of the line is a residential area with single-story buildings, which sustained neither structural damage nor ground failure. This single-story housing community is located approximately 200 m from the fault rupture. The west end of the line consisted of 3-6 story reinforced concrete buildings that sustained not only heavy structural damage, but also underwent extensive foundation failures including differential settlement, foundation punching failures, and foundation bearing failures. Typical building damage involved column failure in the soft first floor level. These buildings also sustained settlement on the order of 10 to 30 cm. Many buildings also showed column footing punching failures with intermediate slab heaving.

3. FIELD AND LABORATORY EXPLORATION

In 2001 and 2002, we completed four rotary wash borings with SPT and in-situ vane shear tests, four back-hoe test pits for in-situ vane shear tests, and nine CPT soundings. Figure 1 presents an east-west cross section, which shows on the east side of Site A an approximately 3-10 m low plasticity silt and clay layer (plasticity index, PI= 0-13) and on the west side an approximately 8-12 m low plasticity (PI=1-16) silt and clay layer.

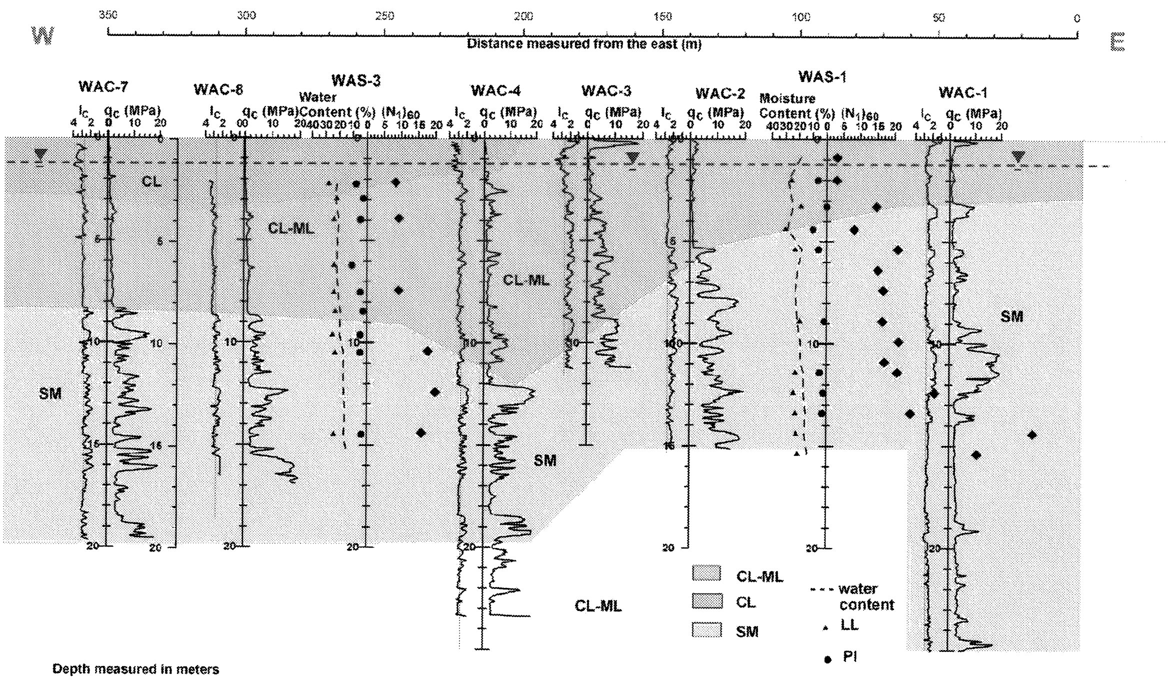

Figure 1. Cross section showing soil conditions at Wufeng site

The surficial silty clays have characteristics that are at the boundaries of what is often judged liquefiable by index-test-based criteria such as that proposed by Bray and Sancio (2006) and Boulanger and Idriss (2006). As shown by Chu et al. (2008), approximately 50% of the clays will be susceptible according to the Bray-Sancio criteria. Similar results are obtained using the Boulanger and Idriss (2006) criteria. However, a liquefaction analysis using common SPT and CPT based liquefaction correlations is unable to explain the observed field performance.

A suite of tests were performed including soil index tests, consolidation tests, isotropically consolidated undrained (ICU) monotonic triaxial compression tests, cyclic undrained triaxial tests, and post-cyclic monotonic triaxial compression tests Details of each laboratory test procedure and the results are described and presented by Chu (2006) and Chu et al. (2008). Summaries of the soil shear strength and stress profiles on the west side (3-6 story buildings) of the site are presented in Figure 2. Undrained strength ratios were evaluated using the SHANSEP technique (Ladd, 1991) using triaxial testing, with the results shown in Figure 3. Those results were used to estimate pre-earthquake shear strengths beneath the affected structures, with the results in Figure 2. Also shown in Figure 2 are undrained shear strengths (s_u) from in-situ vane shear tests and calibrated CPT correlations [using $N_k = (q_c-\sigma_v)/s_u = 20$]. The in-situ vane shear tests were used to evaluate both peak and residual shear strengths, and indicated a sensitivity ranging from 1.0 to 4.4 with an average sensitivity of approximately 2.1.

Cyclic triaxial testing was performed on selected specimens to evaluate the number of cycles of shaking required to achieve ±3% axial strain. Following the cyclic testing, post-cyclic undrained shear strengths were evaluated by monotonically shearing the specimens to failure. The post cyclic shear strengths were considerably less than the pre-cyclic strengths. The degradation ratio (ratio of pre-cyclic strength ratio divided by the post-cyclic strength ratio) is approximately 1.5 and 2.2 for over consolidation ratios (OCRs) of 2 and 3, respectively. The degradation ratio is generally slightly less than the sensitivity (2.1).

4. ANALYSIS OF CYCLIC SOFTENING OF CLAYS

The potential for cyclic softening of the on-site low-plasticity clay during earthquake shaking was analyzed by comparing the seismic demand in the form of a Cyclic Stress Ratio (*CSR*) and the cyclic resistance in the form of Cyclic Resistance Ratio (*CRR*). These comparisons provided insight into the potential for the clays to have experienced large cyclic strains during earthquake shaking, and were conducted using the general procedure described by Boulanger and Idriss (2007). For brevity, we do not present the details here, which are presented by Chu et al. (2007).

The results indicate that the foundation soils underlying 6-story structures would be expected to undergo cyclic failure (since *CRR*<*CSR*) from 2-3 m and 7-11 m depth. This result is generally consistent with ground failure observed around these tall buildings. In the free-field, *CRR* is greater than *CSR* from 2 to 7 m depth. This result is generally consistent with the lack of free-field ground failure. Although not shown here for brevity, Chu et al. (2008) show that on the east side, *CRR* > *CSR* over the full depth of the clay (0 to approximately 5.0 m) both beneath the one-story structures and in the free-field. This is consistent with field

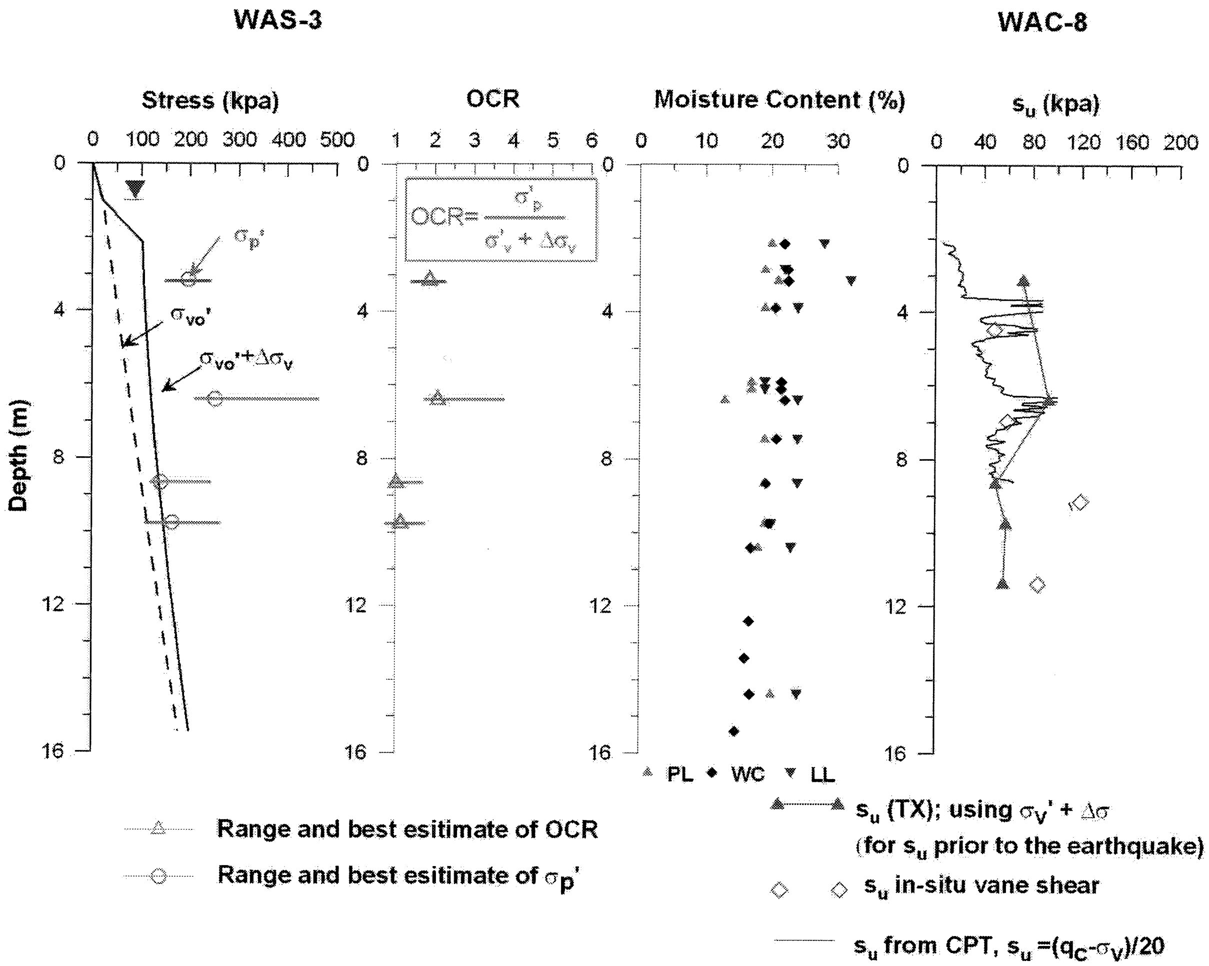

Figure 2. Results of shear strength and stress history tests at Wufeng site

observations of no ground failure in this area.

5. BEARING CAPACITY FAILURE POTENTIAL EVALUATION

Chu et al. (2008) evaluate the bearing capacity of the foundation soils beneath buildings on the west side of Site A (tall) and east side (single story) to investigate whether bearing capacity theory, when used with properly chosen undrained strength parameters, can successfully predict the observed performance. They examine three conditions. Two involve static bearing capacity, one pre-earthquake and one post-earthquake with shear strengths reduced by cyclically induced pore pressures. The third condition involves bearing capacity during strong earthquake shaking.

Without repeating the details of the analysis, it is noted here that the following considerations were taken into account in the seismic bearing capacity analysis: (1) effects of cyclic softening and loading rate on shear strength (reduces *resistance* relative to static case); (2) effects of anisotropy of shear strength, which reduces *resistance* relative to triaxial test results; (3) load inclination and inertial

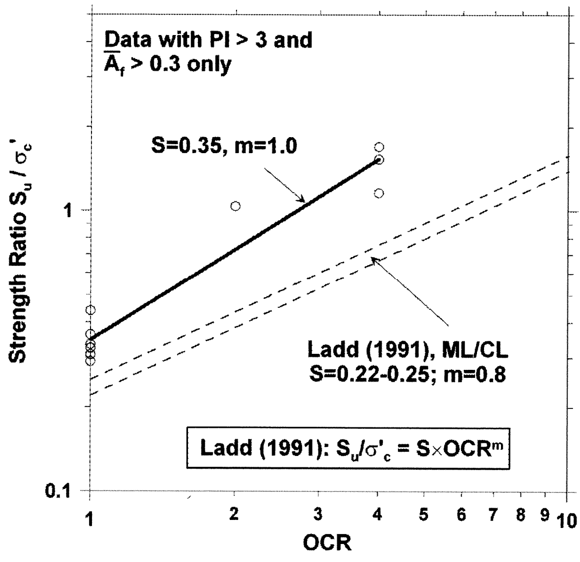

Figure 3. Shear strength ratio (normalized by the preconsolidation stress) versus OCR from ICU triaxial compression tests.

effects on bearing capacity factors (reduces *resistance*); and (4) the effects on foundation pressures of base moment developed in the nonlinear structure during earthquake shaking (increases *demand).* The results of the calculations were that the foundation was stable (factors of safety well over unity) for the pre-earthquake case and post-earthquake case, including softening effects. However, during the earthquake, factors of safety are expected to have temporarily dropped below unity during strong cycles of ground motion. This suggests that the observed foundation failures were in fact bearing failures that occurred due to both earthquake-induced strength reductions from pore pressure generation and large transient moment demands on the foundation.

6. SUMMARY AND CONCLUSIONS

The potential for cyclic softening was evaluated for three locations: (1) beneath footing and mat foundations of a six story building (where ground failure was observed); (2) beneath the foundation of a single-story building (no observed failure); and (3) in the free-field (no observed failure). Cyclic softening potential is evaluated by comparing the *CSR* and *CRR*. If $CRR > CSR$ at a given depth, cyclic softening is not expected, whereas cyclic softening is expected if $CRR < CSR$. Beneath footing foundations for the 6-story building, $CSR > CRR$ over two depth intervals (0-2 m and 7-10 m), indicating a potential for cyclic softening. Similar results were obtained for the mat foundation. Bearing capacity analyses using reduced strengths to account for cyclic softening indicate factors of safety against bearing capacity failure for the footings that are less than unity, which is consistent with the field performance.

Acknowledgements:

This project was sponsored by the Pacific Earthquake Engineering Research Center's Program of Applied Earthquake Engineering Research of Lifeline Systems supported by the State Energy Resources Conservation and Development Commission and the Pacific Gas and Electric Company. This work made use of Earthquake Engineering Research Centers Shared Facilities supported by the National Science Foundation under Award #EEC-9701568. In addition, the support of the California Department of Transportation's PEARL program is acknowledged.

References:

Boulanger, R. W., and Idriss, I. M. (2007). "Evaluation of cyclic softening in silts and clays" *J. Geotech. and Geoenv. Engrg*, ASCE, 133 (6), 641-652.

Boulanger, R. W., and Idriss, I. M. (2006). "Liquefaction susceptibility criteria for silts and clays" *J. Geotech. and Geoenv. Engrg*, ASCE, 132 (11), 1413-1426.

Bray, J.D., and Sancio, R.B. (2006). "Assessment of the liquefaction susceptibility of fine-grained soils," *J. Geotech. and Geoenv. Engrg*, ASCE, 132 (9), 1165-1177.

Chu, D.B. (2006). "Case studies of soil liquefaction of sands and cyclic softening of clays induced by the 1999 Taiwan Chi-Chi earthquake," *Ph.D. Dissertation*, Department of Civil and Environmental Engineering, University of California, Los Angeles.

Chu, D.B., Stewart, J.P. Boulanger, R.W., and Lin, P.-S. (2008). "Cyclic softening of low plasticity clay and its effect on seismic foundation performance," *J. Geotech. & Geoenv. Engrg.*, ASCE, accepted.

Ladd, C. C. (1991). "Stability evaluation during staged construction," *J. Geotech. Engrg.*, ASCE, 117 (4), 540-615.

Stewart, J.P.: coordinator (2001). Chapter 4: Soil liquefaction. Chi-Chi, Taiwan Earthquake of September 21, 1999 Reconnaissance Report, J. Uzarski and C. Arnold, eds., *Earthquake Spectra*, Supplement A to Vol. 17, 37-60.

Fifth International Conference on Urban Earthquake Engineering
March 4-5, 2008, Tokyo Institute of Technology, Tokyo, Japan

DEVELOPMENTS IN DYNAMIC CENTRIFUGE MODELLING: THE UK-NEES PROJECT

Gopal SP Madabhushi[1] and Stuart Haigh[2]

1) Reader in Geotechnical Engineering, Schofield Centre, University of Cambridge, UK
2) Senior Research Associate, Schofield Centre, University of Cambridge, UK
mspg1@cam.ac.uk, skh20@cam.ac.uk

Abstract: This paper will focus on two aspects of dynamic centrifuge modelling which is now widely accepted as 'the' experimental technique that can be used to understand complex behaviour of soil-structure systems subjected to earthquake loading. The first aspect of the paper will deal with dynamic centrifuge modelling at the Schofield Centre in Cambridge which has been active for more than 30 years in this area. The earthquake loading is simulated on the Cambridge centrifuge using simple mechanical actuators that produce sinusoidal shaking. While such input motions are simple and helpful in deciphering certain important aspects of soil behaviour particularly while assessing damaging effects of the earthquakes, the complex non-linear behaviour of soils requires more sophisticated earthquake actuators that can simulate multi-frequency nature of real earthquakes. The second aim of this paper is to discuss some of the exciting developments that are occurring in the modelling of earthquakes on the Cambridge centrifuge. The outline design of the 1-D and 2-D (horizontal and vertical) shakers being developed at Cambridge is presented. Similarly creation of distributed testing facilities that are networked within UK under the UK-NEES project that is linked to US-NEES, NZ-NEES and other similar networks opens up a new era of collaborative testing in earthquake engineering.

1. INTRODUCTION

Physical modelling in earthquake engineering with reduced scale experiments in the centrifuge is now widely considered as 'the' established experimental technique of obtaining data in controlled conditions to help engineers and researchers to understand the mechanisms involved in the response of soil – structure systems to seismic loading. This experimental approach recreates the stress state in soils which is a fundamental condition to observe realistic soil behaviour. Of course, as any other experimental method it has its limitations, among which the most evident is the boundary effect due to the fact that the soil model mounted in the centrifuge is necessarily of limited dimensions. The boundary effects are mitigated by using laminar or Equivalent Shear Beam (ESB) model containers, which allow the natural deformation of a soil column. Teymur and Madabhushi (2003) investigated the boundary effects in the ESB model container using in-flight CPT testing before and after earthquake loading. Another important limit is the choice and ability to impose a realistic input at the base of the soil model. Earthquakes generate a complex sequence of vibrations that can lead to 3D displacements with a broad frequency content of very variable duration. Firstly, it is difficult to build a 3D shaking table in the limited volume of the basket of a centrifuge. Secondly, it is difficult to generate independent time histories for each axis of shaking: it is of course simpler to generate harmonic inputs than to reproduce broad band records of real earthquakes. Note that these two problems apply as well to full scale shaking tables. The purpose of this paper is to present the current experimental facilities at Cambridge and discuss the implications on the choice of input motions. This will be followed by the use exciting new developments in the modelling of earthquake geotechnical engineering problems.

2. CURRENT FACILITIES

The success of earthquake geotechnical engineering at Cambridge depended to a large extent on the simple mechanical actuators that have been used for more than 30 years. First attempts of centrifuge shaking tables were mechanical 1D harmonic devices based on leaf spring device (Morris, 1979), bumpy road tracks (Kutter, 1982) or cams systems (Suzuki et al., 1991, Kimura et al, 1998). Other technologies have been tested – such as explosives (Zelikson et al., 1981), piezo-electric jacks (Arulanandan, 1982), electromagnetic shakers (Fuji, 1994) - but the majority of the existing devices are now electro-hydraulic (Ketcham et al., 1988, Van Laak et al. 1994) because of the ability of electric servo-valves to accept complex driving functions and the ability of hydraulic jacks to provide input motions with a rich frequency content. A few 2 D devices have been developed either with two horizontal shaking directions or one horizontal and one vertical notably at UC Davis (N-S and U-D directions), RPI, New York and HKUST in Hong Kong (N-S & E-W directions).

The current earthquake actuator at Cambridge relies on Stored Angular Momentum (SAM) to deliver powerful earthquakes at high gravities was developed and is in operation for 12 years, Madabhushi et al (1998). In Fig.1 a view of the 10 m diameter Turner beam centrifuge at Cambridge is presented. In Fig.2 the front view of the SAM actuator is shown while in Fig.3 a view of the SAM actuator loaded onto the end of the centrifuge is presented. The model seen in Fig.3 was from an investigation carried out by Haigh and Madabhushi (2002), on lateral spreading of liquefied ground past square and circular piles.

The SAM earthquake actuator is a mechanical device which stores the large amount of energy required for the model earthquake event in a set of flywheels. At the desired moment this energy is transferred to the soil model via a reciprocating rod and a fast acting clutch. When the clutch is closed through a high pressure system to start the earthquake, the clutch grabs the reciprocating rod and shakes with an amplitude of ± 2.5 mm. This is transferred to the soil model via a bell crank mechanism. The levering distance can be adjusted to vary the strength of the earthquake. The duration of the earthquake can be changed by determining the duration for which the clutch stays on. Earthquakes at different frequency tone bursts can be obtained by selecting the angular frequency of the flywheels.

Recent modifications to the SAM actuator were carried out to further enhance its capabilities and to improve the performance envelope. Early earthquakes using this device were non-symmetric as the clutch migrated downwards to an end stop once the centrifugal acceleration was applied. This meant that at the start of the earthquake the clutch body was hitting the end stop if it grabbed the reciprocating rod during its downward motion. This problem has been rectified by incorporating a pneumatic actuator that centralises the clutch prior to every earthquake. Logic controls automatically turn the air to the pneumatic actuator off once the earthquake is fired and the clutch starts to move with the reciprocating rod.

In its original conception the SAM actuator was mounted onto the end of the beam centrifuge and shook a package on the special swing, reminiscent of the Bumpy Road actuator, Kutter (1982). However this arrangement was modified and a self-contained swing platform was developed that could house the SAM actuator as shown in Fig. 5 following a research grant (No:GR/L90415/01) from EPSRC, UK. This has transformed the usage of the SAM actuator and since 1994 with 11 PhD students and 5 MPhil students utilised this facility and several industrial, EPSRC and EU projects were successfully completed using this actuator.

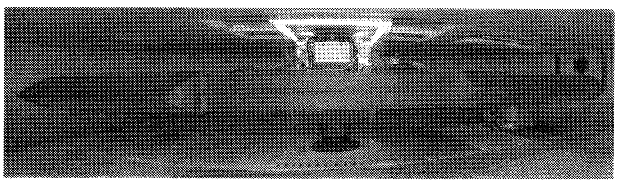

Figure 1 The 10m diameter Turner beam centrifuge

Table 1 Specifications of SAM actuator

Parameter	**Value**
Maximum g-level of operation	100 g
Dimension of the soil models	56 m (L) × 25 m (B) × 22 m (H) 80 m (L) × 25 m (B) × 40 m (H)
Earthquake strength of choice	Up to 0.4g of bed rock acceleration
Earthquake duration of choice	From 0 s to 150 s
Earthquake frequency of choice	From 0.5 Hz to 5 Hz Swept sine wave capability

Note: All parameters above are in prototype scale

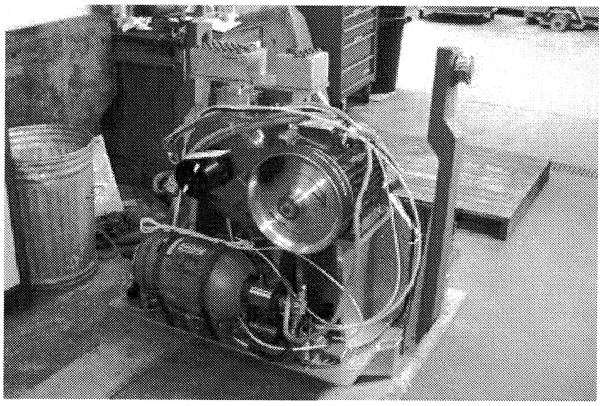

Figure 2 A view of the SAM earthquake actuator

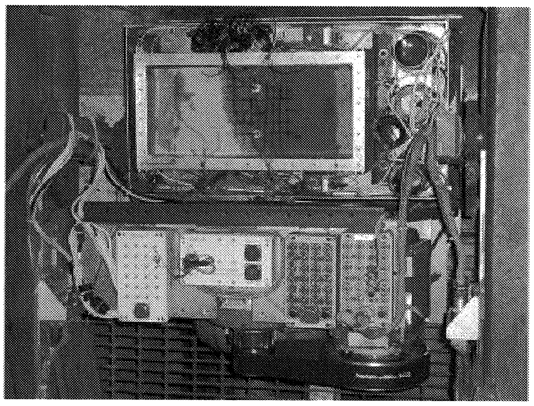

Figure 3 A centrifuge model of sloping ground with square and circular piles loaded on the end of the centrifuge

3. CHOICE OF INPUT MOTIONS

The earthquake input motion (applied at the bedrock level) that has simple, sinusoidal tone bursts at different frequency will lend itself to easy analysis of the response the soil and the superstructure. This is used extensively at Cambridge on a wide range of boundary value problems in which the key mechanisms of failure are eloquently deciphered. The choice of input motions, to some extent is independent of the actuators available with RPI centrifuge facility using sinusoidal inputs even though their servo-hydraulic shaker is capable of simulating realistic earthquakes. Similarly, use of a more realistic input motion from a previous earthquake such as Kobe motion or Northridge motion would be considered useful from the design of future structures point of view. Further, the role of multi-frequency input motion on the dynamic behaviour of soils is not fully understood.

It is generally argued that for soil liquefaction problems, use of simple input motions is sufficient. Recently, finite element analyses were carried out by Ghosh and Madabhushi (2003) and dynamic centrifuge modelling was carried out by Madabhushi et al (2006) to investigate the role of type of input motions in the generation of excess pore pressures. These investigations revealed that the amount of excess pore pressure generated in loose, saturated sands may be not be effected by sinusoidal input motions or more realistic input motions. However, the amount of lateral spreading of sloping ground that can occur may be quite different if sinusoidal motions are used as the dilation spikes that occur during strong shaking cycles are more pronounced compared to a more realistic input motion with only a few strong cycles of shaking.

3.1 Accelerations in lateral spreading of ground

As mentioned earlier the SAM actuator was used in the investigation of several boundary value problems. As an example of the input motions generated by the SAM actuator the following investigation of liquefaction induced lateral spreading problem is presented, Haigh et al (2000). The dynamic behaviour of a slope shown in Fig. 3 earlier was studied using miniature instrumentation for the measurement of pore-pressures and accelerations throughout the slope. Analysis of these signals has revealed interesting details about the response of these slopes to earthquake loading. The accelerometer time-histories in Fig.4 show the measured base (ACC 9082), mid layer acceleration (ACC 8076) and surface accelerations (ACC 8025) in one of the models. It can be seen that whilst the base motion is approximately constant from cycle to cycle, the surface response late in the earthquake shows alternate cycles having profoundly different behaviour.

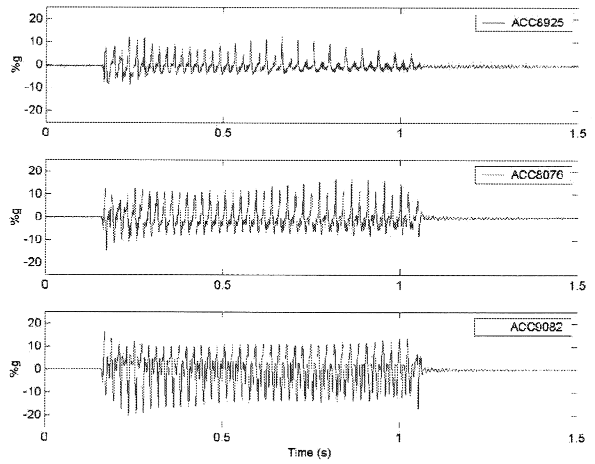

Figure 4 Acceleration-time histories in a sloping ground

This shows itself as an amplified frequency component at half of the fundamental earthquake frequency upon study of FFT's. Measurement of the phase lag of acceleration between base and surface of the models, as could be achieved from the time-histories shown in Fig.5 (indicated by red and blue lines), allows estimates of the shear wave velocity to be made at different times during the earthquake. From this data it can be shown that as the soil liquefies and softens, the shear wave velocity falls to such a point that the natural frequency of the soil column becomes approximately 25 Hz, half that of the earthquake excitation. It is thus postulated that the soil column is resonating at this natural frequency, hence giving the behaviour described above.

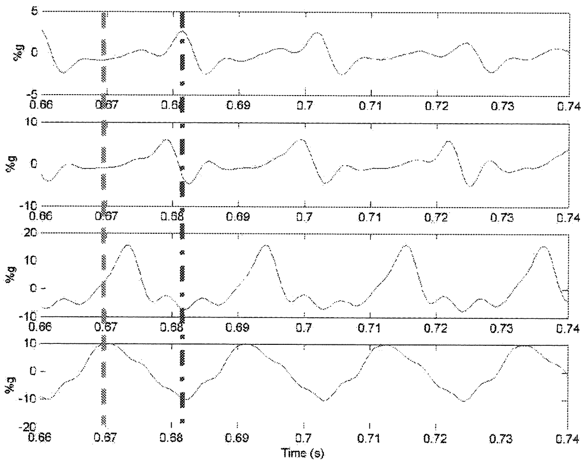

Figure 5 Upward propagation of S_h wave through the slope

3.2 Excess pore pressures during lateral spreading

It is also interesting to note the dilative response of the soil slope. All of the PPT's present in the model show significant dilative behaviour occurring with the generation of a "suction-spike" once per cycle. Examining the timing of these spikes with respect to depth illustrates that this suction pulse propagates vertically from the base of the model to the surface at the shear wave velocity. This behaviour is illustrated in Fig.6 (indicated by the red and blue lines). It is postulated that this is due to the dynamic shear stress applied by the wave, superimposed on the initial static shear stress causing the soil stress path to cross the characteristic state threshold and hence the soil to dilate. This pore-pressure behaviour will cause a slip-stick motion of the soil down the slope, with velocity and displacement being accumulated while the base is accelerating upslope and then locking up on the other half-cycle when dilation occurs.

As described earlier using a sinusoidal input motion may lead to an under-estimate of the amount of lateral spreading of sloping ground that can occur as strong cycles of shaking are applied throughout the model earthquake, making the liquefied soil to dilate in each half cycle and hence stopping the lateral displacement of the ground. If a more realistic earthquake motion such as the one recorded during the Kobe earthquake of 1995 is used in this centrifuge test, then the ground liquefies on the arrival of the first one or two strong cycles in the earthquake. It will then stay liquefied during the smaller cycles that follow allowing the ground to suffer much larger lateral displacement. In other words, the smaller cycles that follow the initial strong cycles do not cause sufficient dilation in the soil to stop it from moving down the slope. This will lead to a much more accumulated lateral spreading through the earthquake. This is one example where type of input motion can have a bearing on the output from the centrifuge test.

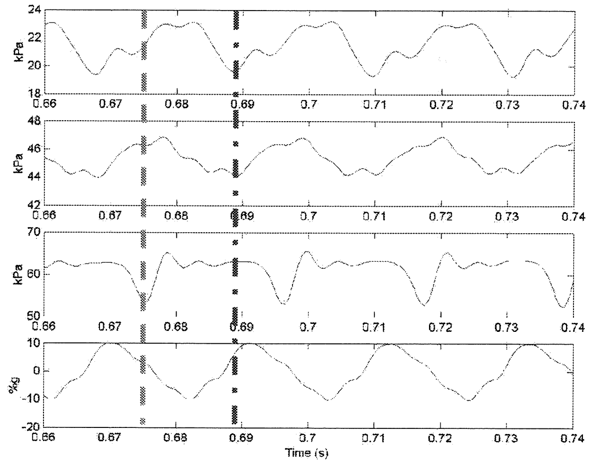

Figure 6 Upward propagation the suction spike through the slope

5. FUTURE DEVELOPMENTS IN EARTHQUAKE ACTUATION

Currently the SAM earthquake actuator at Cambridge is being complemented by a single axis servo-hydraulic earthquake actuator. This will be followed with the development of a 2-D earthquake actuator. The preliminary design of a new 1-D earthquake actuator has been recently completed. This will be followed by a 2-D actuator that will be able to shake the soil models both horizontally and vertically akin to the 2-D actuator recently established at UC Davis in the USA. The vertical ground accelerations can play an important role in the ultimate performance of a structure. Recent earthquakes have yielded many recordings of vertical accelerations which are quite large (in some cases up to 0.8g to 1.0g). Current design codes only allow for a fraction of these as vertical accelerations. Also the combination of vertical shaking followed by strong horizontal shaking can lead to unexpected and interesting failure mechanisms in a wide range of civil engineering structures. With this in view the Cambridge 2-D earthquake actuator project has been initiated and is currently at an early stage. A schematic diagram of the 2-D earthquake actuator assembly is presented in Fig.7 below. A Pro-Engineer CAD drawing is presented in Fig.8. The design of this 2-D actuator for the Cambridge centrifuge is quite demanding as the payload capacity of the Turner beam centrifuge is limited to 1 tonne. In addition there are severe space constraints. Further, the Turner beam centrifuge is used extensively for non-earthquake testing which means that the 2-D earthquake actuator needs to be loaded and unloaded on and off the centrifuge quite frequently. These bring in additional complexities such as breaks in high pressure hydraulic lines, contamination of the hydraulic fluid etc. Despite these difficulties the design of this 2-D actuator is progressing well and with suitable funding should be available for use in a few years time. This would become the only 2-D earthquake actuator to serve the European Community.

The specifications of the 2-D shaker in Table 2 were drawn taking to consideration the special requirements of the Turner beam centrifuge. Unlike the LCPC shaker and the C-CORE shakers which rely on counter-reacting masses to avoid large shaking forces on their centrifuges, Chazelas et al (2007), the entire centrifuge is used as the reaction mass as the swing platform on which the 2-D shaker is mounted is locked onto the centrifuge when the centrifuge is speeded up beyond 10g's. Also the use of the 2-D shaker is expected to complement the SAM earthquake actuator that can operate at high gravities and deliver powerful sinusoidal earthquakes. The 2-D shaker will be used at relatively lower g levels but with more realistic earthquake input motions in horizontal and vertical directions.

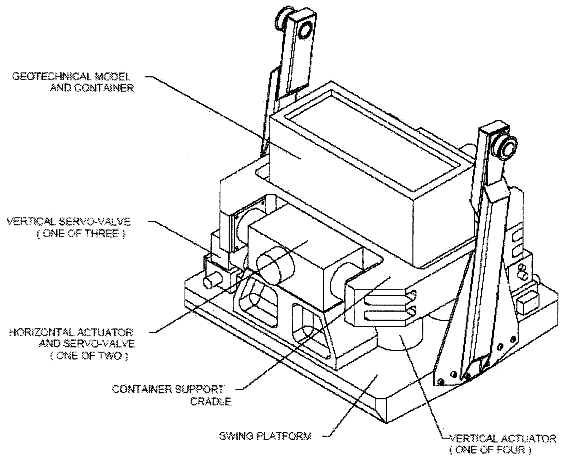

Figure 7 Schematic view of the 2-D actuator assembly

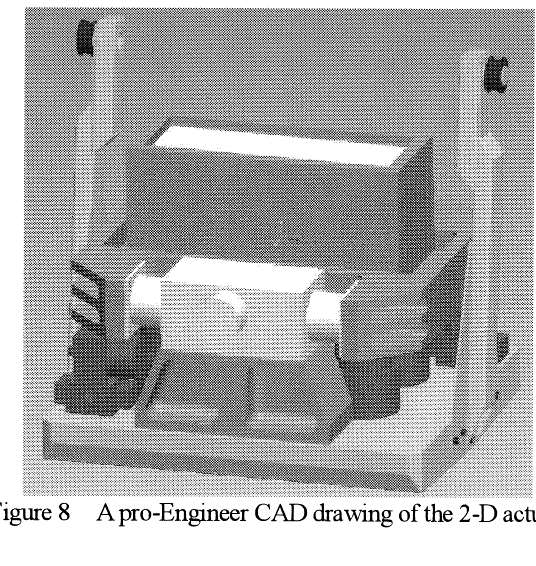

Figure 8 A pro-Engineer CAD drawing of the 2-D actuator

Table 2 Preliminary design specifications of the 2-D earthquake actuator

Parameter	Value
Maximum g-level of operation	50 g ~ 80 g
Dimension of the soil models	56 m (L) × 25 m (B) × 22 m (H)
	80 m (L) × 25 m (B) × 40 m (H)
Earthquake strength of choice: Horizontal	Up to 0.8g
Earthquake strength of choice: Vertical	Up to 0.6g
Earthquake duration of choice	From 0 s to 150 s
Earthquake frequency of choice	From 0.5 Hz to 5 Hz

Note: All parameters above are in prototype scale

6. THE UK-NEES PROJECT

Another exciting development in the field of earthquake engineering research is the NEES project in the USA that established the concept of distributed testing at geographically distributed sites. This concept is extremely useful for Europe given the expertise in earthquake engineering in Europe and the geographical distances between the centres of excellence. In addition the NEES style network will enable European research centres and universities to link up on collaborative projects with centres of excellence in earthquake engineering in Japan, Taiwan and Hong Kong. Having distributed experimental facilities that are linked to a dedicated network will enable research workers worldwide to not only access the experimental data but to actually have tele-observation and tele-participation capabilities. The USA-NEES project has been well set up and a similar network in Europe benefits from the technological advances already achieved in the USA. For example, network protocols for data sharing and data archiving are already available.

To complement the US-NEES, EPSRC funded a research project to develop a UK-NEES network among Cambridge, Oxford and Bristol universities. In this project an In-SORS based system that will allow real time exchange of data, audio and video information was established at all of the UK participants. This project is at an early stage and a further opportunity arose to collaborate with NZ-NEES program in New Zealand. In Fig.9 a snapshot of one of the meetings is presented which shows the teams from Cambridge, Oxford, Bristol and Auckland are taking part with the Auckland team making a Power point presentation. The In-SORS system can handle an unlimited number of parallel information ports (data, video, presentations etc). As part of the UK-NEES project two IP-Cameras are now installed on the Cambridge centrifuge that are available through a dedicated server on http://neespop.eng.cam.ac.uk/. Progress of centrifuge tests can be observed from anywhere in the world through this system.

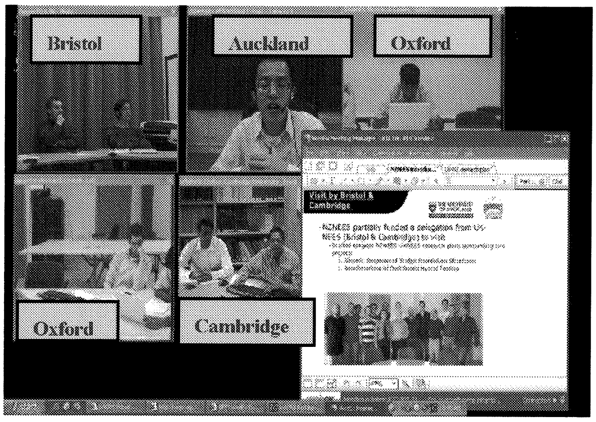

Figure 9 The UK-NEES INSORS Facility

As part of the UK-NEES project the distributed testing capabilities will be developed between University of Cambridge, Oxford and Bristol. This is explained based on the schematic diagram in Fig.10 that allows testing of a bridge structure. Distributed testing will enable centrifuge model testing to be carried out on foundations at Cambridge, while suitable part of the super-structure such as a pier support being tested at Bristol on their shaking table with the information on foundation behaviour being fed in real time from Cambridge. At Oxford a sub-structure testing facility will utilise the information from Bristol on the actual pieer structure response as a part of the system being tested at Bristol on the shaking table and numerically model other piers. The response of the whole structure will be evaluated partly by loading the sub-structure mechanically such as decks and bearings and partly carrying out numerical analyses. The combined response of the entire structure would therefore incorporate the foundation behaviour from Cambridge, dynamic response from shaking table at Bristol, the sub-structure response and the numerical model results from Oxford.

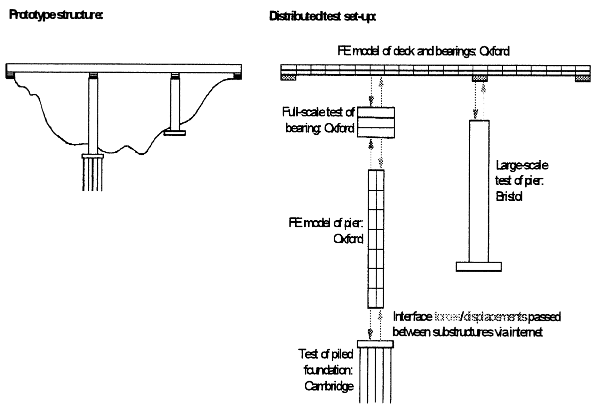

Figure 10 The concept of distributed testing of a bridge structure

The concept of such distributed testing is quite powerful and allows collaboration between research centres in different countries and even continents possible.

7. CONCLUSIONS

In this paper the focus has been on the use of dynamic centrifuge modelling for developing a sound understanding of the complex behaviour of soil-structure systems. The first aim of the paper was to highlight the facilities available at the Schofield Centre in terms of modelling of earthquake geotechnical engineering problems. The current capabilities in terms of SAM earthquake actuator are highlighted. Further the importance of carefully choosing the type of input motion is illustrated with the help of acceleration-time histories and excess pore pressure-time histories recorded in a laterally spreading ground. It was concluded that the amount of lateral spreading obtained by applying a simple, sinusoidal input motion may be an 'under-estimate' compared to the actual lateral spreading that can occur during a Kobe type realistic input motion with few strong cycles followed by many small cycles of shaking. This necessitates the development of new earthquake actuators at Cambridge using the servo-hydraulic systems currently available elsewhere. The paper then highlights the development of 1-D and 2-D servo-hydraulic shakers that are currently being designed at Cambridge along with the desired specifications.

Finally the paper explains the UK-NEES project in which distributed testing facilities are being developed to link the experimental facilities within the UK at Cambridge, Bristol and Oxford. Such networks of distributed testing are anticipated to promote greater collaboration both within Europe and also with USA, Japan, Taiwan and Hong Kong.

References:

Chazelas, J.L., Madabhushi, S.P.G. and Philips, R., (2007), "Reflections on the importance of the quality of the input motion in seismic centrifuge tests", Proc. IV International Conference on Soil Dynamics and Earthquake Engineering, Thessaloniki, Greece.

Fuji N, (1991), "Development of an electromagnetic centrifuge earthquake simulator", Ko H.Y., McLean F.G. (eds), Proc. Centrifuge 91 Balkema, Rotterdam, pp 351-354.

Ghosh, B. and Madabhushi, S.P.G., (2003), "A numerical investigation into single and multiple frequency earthquake input motions", Journal of Soil Dynamics and Earthquake Engineering, Vol. 23, pp 691-704.

Haigh, S.K., Madabhushi, S.P.G., Soga, K., Taji, Y. and Shamoto, Y., (2000), "Lateral spreading during centrifuge model earthquakes", Proc. Geo2000 Intl conference on Geotechnical Engineering, University of Sydney, Australia.

Haigh, S.K. and Madabhushi, S.P.G., (2002), "Dynamic Earth Pressures on Piles due to Lateral Spreading", Proc. International Conference on Physical Modelling in Geotechnics, St John's, Newfoundland, Canada, July, Balkema, Rotterdam.

Ketcham S.A., Ko H.Y., Sture S., (1988), "An electrohydraulic earthquake simulator for centrifuge testing", Corté J.F. (ed), Centrifuge 88, Proceedings of the international conference on geotechnical centrifuge modelling, Paris, France, April, Balkema, Rotterdam, pp 97-102.

Kutter, B. L., (1982), "Centrifugal modelling of the response of clay embankments to earthquakes", PhD thesis, Cambridge University, UK.

Kimura T, Takemura J., Saitoh K, (1988), "Development of a simple mechanical shaker using cam shaft", Corté J.F. (ed), Centrifuge 88, Proceedings of the international conference on geotechnical centrifuge modelling, Paris, France, Balkema, Rotterdam,, pp 107-110.

Madabhushi S.P.G., Schofield A.N., Lesley S., (1988), "A new strored angular momentum (SAM) based earthquake actuator", Kimura, Kusakabe & Takemura (eds), Centrifuge 98, Tokyo, Japan, Balkema, Rotterdam, pp 111-116.

Madabhushi S.P.G., Ghosh B., Kutter B. L., (2006), "Role of input motion in excess pore pressure generation in dynamic centrifuge modelling", International Journal of Physical Modelling in Goetechics., **3**, pp 25-34.

Morris, D.V., (1979), "The centrifuge modelling of dynamic behaviour", PhD Thesis, Cambridge University, UK.

Teymur, B and Madabhushi, S.P.G., (2003), "Experimental study of boundary effects in dynamic centrifuge modelling", Geotechnique, **53**, No.7, pp 655-663.

Van Laak P.A. , Elgamal A.W., Dobry R., (1994), "Design and performance of an electrohydraulic shaker for the RPI centrifuge", Leung CF, F.H. Lee, Tan T.S. (eds), Centrifuge 94, Singapore, Balkema, Rotterdam, pp 139-144.

Fifth International Conference on Urban Earthquake Engineering
March 4-5, 2008, Tokyo Institute of Technology, Tokyo, Japan

PHYSICAL MODELLING ON SEISMIC PERFORMANCE OF UNDERGROUND STRUCUTURES

Osamu Kusakabe[1), Jiro Takemura[2), Akihiro Takahashi[2), Jun Izawa[3) and Shuhei Shibayama[4)

1) Professor, Dept. of Civil and Environmental Engineering, Tokyo Institute of Technology, Japan
2) Associate Professor, Dept. of Civil and Environmental Engineering, Tokyo Institute of Technology, Japan
3) Assistant Professor, Dept. of Civil and Environmental Engineering, Tokyo Institute of Technology, Japan
4)Graduate Student, Dept. of Civil and Environmental Engineering, Tokyo Institute of Technology, Japan
kusakabe@cv.titech.ac.jp, jtakemur@cv.titech.ac.jp, takihiro@cv.titech.ac.jp, jizawa@cv.titech.ac.jp, sh4880@cv.titech.ac.jp

Abstract: In the framework of performance based design codes, numerical analysis and physical modelling are equally recommended to adopt for the verification of performance of designed structures. To establish the communication between numerical and physical modelling communities are of vital importance for verification of performance of geo-structures. This paper introduces the recent development of experimental seismic displacement method in a centrifuge and some applications to underground structures.

1. INTRODUCTION

It is widely accepted from past experiences that underground structures are generally stable, when the ground is stable because of confining effects from the surrounding ground. Underground structures are considered to follow the movement of the surrounding ground, since the effect of inertia force is relatively small, and also the oscillation of the underground structures rapidly ceases due to radial damping. Underground structures are, therefore, considered to have higher seismic stability. Past experiences suggest, however, the following cases where possible damage might occur as are illustrated in Figure 1 (Kusakabe et al., 2008).

On the other hand, Performance-based design framework has been introduced in geotechnical design. Although calculation methods are, in principle, to use for routine design practice, physical modelling and numerical analysis are equally recommended to adopt for the verification of performance of designed structures. In particular, physical modelling is highly recommended to adopt for cases where the level of uncertainties is high (JGS 4001-2004, 2006). In the physical modelling, new and unexpected phenomena are often discovered, whereas numerical simulation provides the results totally governed by the model used. To bridge between the numerical and physical modelling and to establish the communication between numerical and physical modelling communities are of vital importance for verification of performance of geo-structures.

This paper describes briefly the principle of seismic displacement method used in the structural analysis for underground structures and then introduces the recent development of experimental seismic displacement method

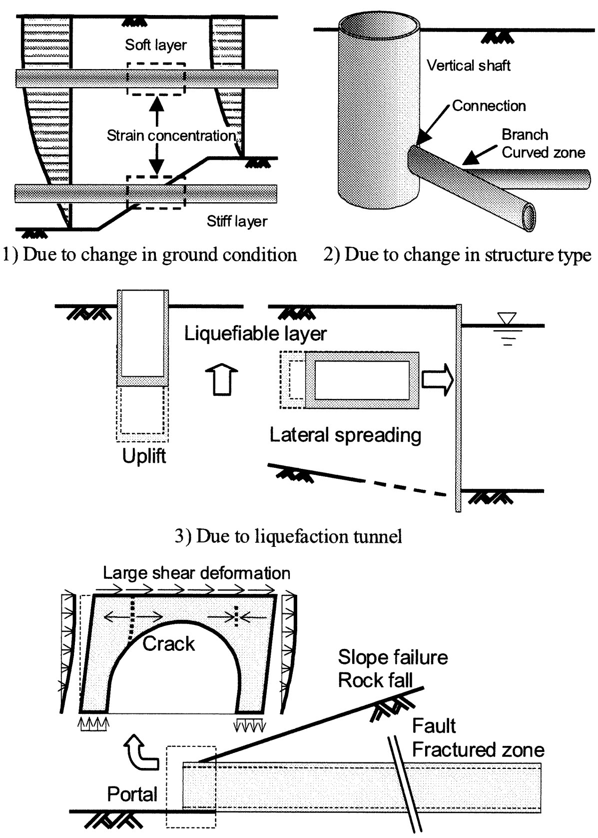

1) Due to change in ground condition 2) Due to change in structure type

3) Due to liquefaction tunnel

4) Possible damage in a mountain tunnel

Figure 1 Illustrations of possible damage of underground structures during earthquakes

Table 1 Specifications of the active type shear box

Max. operation centrifugal acceleration	100-g
Number	3 for laminar box 1 for pile head
Stroke	+/- 20 mm for laminar box +/- 40 mm for pile head
Force capacity at 20.5 MPa oil pressure	25.8 kN for outward 18.0 kN for inward
Peak velocity	133 mm/sec
Number of stacks	13
Inner size	W450*B200*H325mm
Flexural rigidity of plate spring: EI	0.14 N.m^2, 0.56 N.m^2

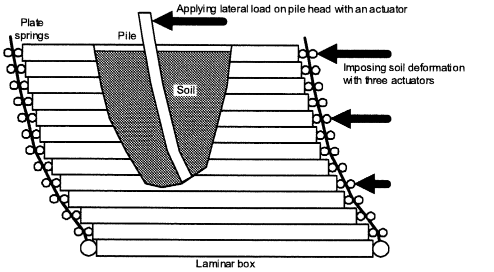

Figure 2 Schematic diagram of the active type shear box

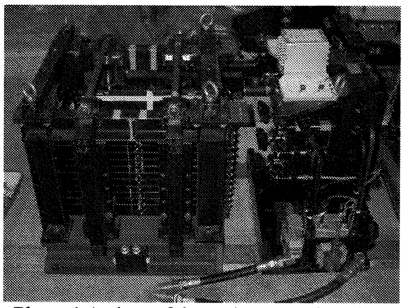
Photo 1 A view of the active type shear box

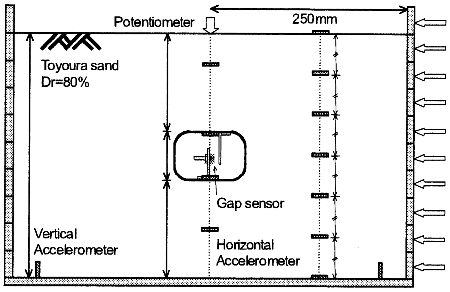

Figure 3 Model setup for D-test

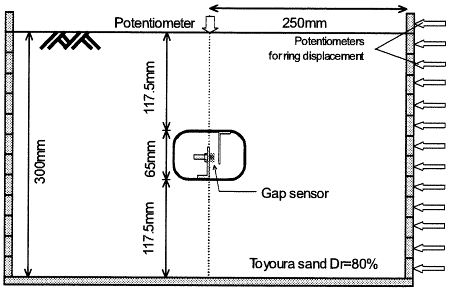

Figure 4 Model setup for S-test

in a centrifuge, followed by the verification of the experimental seismic displacement method by comparing the structural responses between the observations in dynamic centrifuge tests and the corresponding static centrifuge tests. Some applications of the experimental seismic displacement method to underground structured are also presented.

2. Experimental seismic displacement method

An active type shear box in a geotechnical centrifuge has been initially developed for investigating the behaviour of a pile subjected to a large soil movement (Takahashi et al., 2001). The shear box was designed to fit the Mark 3 centrifuge at Tokyo Institute of Technology (Takemura et al., 1999) to be operational under 100 G Schematic diagram and photograph are shown in Figure 2 and Photo 1 respectively. Specifications are summarized in Table 1.

It may be considered that static loading test using the active type shear box is an experimental version of the seismic displacement method, it is called, the experimental seismic displacement method. In this paper, a comparative study between dynamic shake table test and active type shear box test was carried out to verify the experimental seismic displacement method.

3. Applications to shallower tunnels

3. 1. Model and test description

Two types of 2-D centrifuge test: dynamic shake table test (termed as D-test hereafter) and pseudo-static active type shear box test (termed as S-test), were conducted for the same prototype configuration of 3.25m wide and 5.0m high rectangular tunnel with a cover of 5.875m embedded in dry dense sand under the same centrifugal acceleration of 50 G D-test was conducted in the centrifuge at Kajima Research Institute (Kajima Technical Research Institute). On the other hand, S-test was carried out in the Mark 3 centrifuge at the Tokyo Institute of Technology, using the active type shear box apparatus.

Dry Toyoura sand (G_s = 2.64, D_{50} = 0.19mm, U_c= 1.56, e_{max}= 0.978, e_{min}= 0.605) was used for preparing the model ground of 300 mm thick by air pluviation method to achieve a relative density of 80% (γ_d = 15.4kN/m3, ϕ= 42deg.). Each model setup is shown in Figures 3 and 4, respectively. A two dimensional rectangular model tunnel used in the two tests was made of aluminium with 2mm thickness. Surface conditions of the model tunnel were considered to be smooth. Figures 5 (a) and (b) show the schematic illustrations of the rectangular model tunnel, together with the locations of a set of strain gauges in D-test and S-test, respectively. Strain gauges were attached on both outer and inner sides of the model in pairs. It should be noted that the number of strain gauges differs for the two tests; 18 sets for D-test and 5 sets for S-test due to limitation of measurement channels. Horizontal and vertical relative displacements between upper and lower slabs were measured by gap sensors installed in the model tunnel as is illustrated in Figure 7.

It has been recognized that seismic stability of the flat cross section tunnel is lower than that of usual circular tunnel and needs some kind of countermeasures against earthquake. In addition, therefore, effectiveness of some

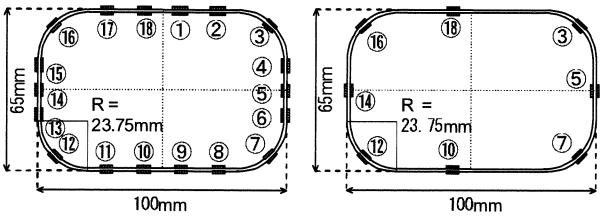

a) for D-test b) for S-test

Figure 5 Schematic illustrations of rectangular model tunnel and strain gauge arrangements

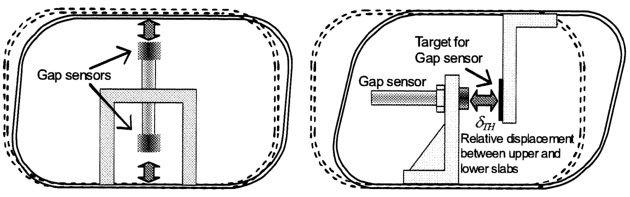

a) Vertical direction b) Horizontal direction

Figure 6 Arrangement of gap sensors

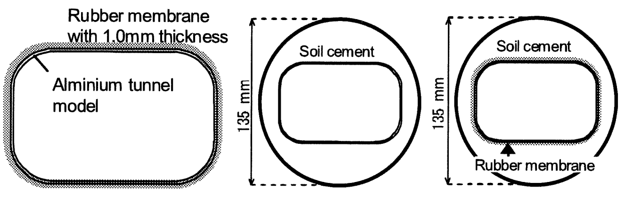

(a) Rubber membrane (RM) (b) Round shaped soil cement ground (SC) (c) Combination (RM+SC)

Figure 7 Countermeasures applied for the aluminium tunnel

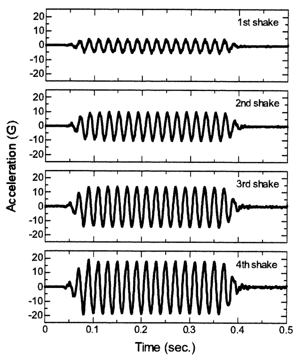

Figure 8 Examples of input waves

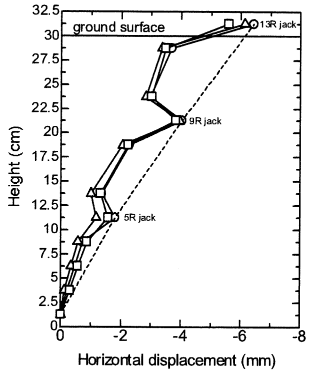

Figure 9 Distributions of lateral movement in S-test

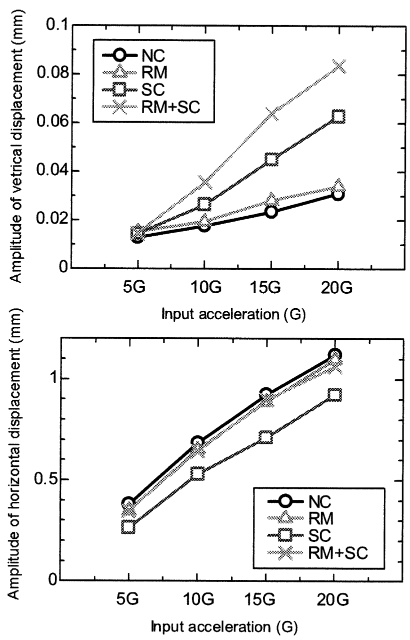

Figure 10 Amplitude of relative displacement between upper and lower slabs during dynamic loading

kind of countermeasures was investigated. In this research, three types of the following countermeasures are adopted as illustrated in Figure 7. (1) Rubber membrane was glued around the outer surface of the tunnel as a seismic isolation layer (hereafter, called as RM) (2) Round-shaped soil cement ground (q_u = 1.0MPa) was arranged surrounding tunnel as ground improvement (hereafter called SC), and (3) Combination of these (called RM+SC). The test without any countermeasures is termed as NC.

In D-test, four dynamic events were input with a peak horizontal acceleration of 5G, 10G, 15G and 20G, respectively. 20 sinusoidal waves with a frequency of 100Hz by a hydraulic dynamic actuator were applied to the model ground for each dynamic event. The acceleration time histories are given in Figure 8.

A sinusoidal wave with a frequency of 0.01Hz and half a cycle was applied to the shear box . Input distribution of the horizontal displacement at the jack locations was linearly decreasing with depth and the horizontal displacement at the top laminar ring was about 6mm, imposing a nominal shear strain of 2.0% to the model ground. Figure 9 shows the measured distribution of horizontal displacement measured by displacement transducers attached to each laminar ring. Detailed test procedures are summarized in Yamada et al. (2004) and Izawa et al. (2006).

3. 2. Results and discussion

Figure 10 plots the amplitude of relative vertical and horizontal displacements over one wave between two slabs during dynamic loading against input base acceleration. It is noticed that the displacements approximately increase linearly with the acceleration for both directions. The effect of countermeasures is seen in SC case for the horizontal direction and in SC and RM+SC for the vertical direction respectively, although the magnitude of relative vertical displacement is one order smaller compared to that of the horizontal displacement.

It is considered that the seismic isolation layer is effective in reducing the dynamic sectional forces to reduce the shear stress induced by seismic ground strain to the tunnel. Figure 11 shows the amplitude of bending moment and axial force for input acceleration levels of 20G. Differences in bending moment are limited among the 4 cases. On the other hand, an apparent difference is seen in the axial force distribution. That is, the axial forces in SC case at the side walls remarkably larger than those of the other cases. Furthermore, RM+SC case can ease such concentration of axial force at the corners.

Figure 12 shows the bending moment distributions in D-test and S-test with respect to the values at the same

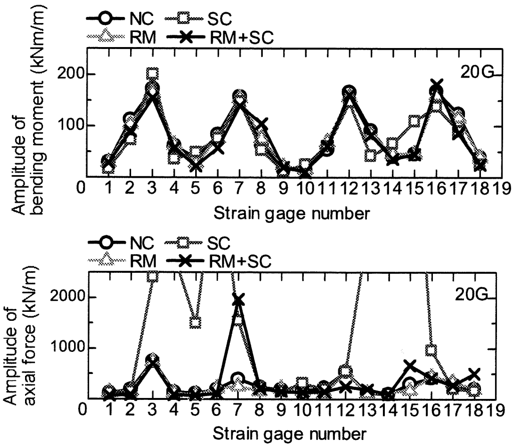

Figure 11 Amplitude of sectional forces during dynamic

horizontal relative displacement between upper and lower slabs, δ_{TH}, of the tunnel. Similarly Figure 12 compares the axial force distributions between D-test and S-test at the same value of the horizontal relative displacement. Positive axial force indicates the compressive axial force. Positive bending moment is defined as the case for the inner surface of the tunnel suffers tension force. Considering Figures 11 and 12 together, it can be said that both bending moment and axial force distributions are practically identical to each other, when the tunnel is subjected to the same magnitude of the horizontal relative displacement.

The horizontal relative displacement between upper and lower slabs, δ_{TH}, must be related to the ground movement. Then, δ_{TH}, measured in D-test as well as S-test are plotted against the values of relative horizontal displacement of the ground around the tunnel, δ_R in Figure 13. Here, the value of δ_R was determined from the relative horizontal displacement between two laminar rings, which were located near upper and lower slabs of the tunnel. The broken line in the figure is a skeleton curve of δ_{TH}-δ_R relations for D-test. It agrees well with the δ_{TH}-δ_R curves obtained from S-test. This provides strong experimental evidence, confirming that the δ_{TH}-δ_R relations shows almost one to one relation and D-test and S-test give a practically identical relationship regardless. Thus, if the same magnitude of horizontal relative displacement is imposed to the tunnel, the same stresses would generate in the tunnel lining, both in D-test and S-test. And, if the same horizontal displacement is applied to the ground, almost the same horizontal relative displacement between upper and lower slabs would take place regardless of the static and dynamic loading. This means that the experimental seismic displacement method is useful to evaluate the seismic performance of tunnel. Furthermore, effectiveness of countermeasures can be examined using experimental seismic displacement method.

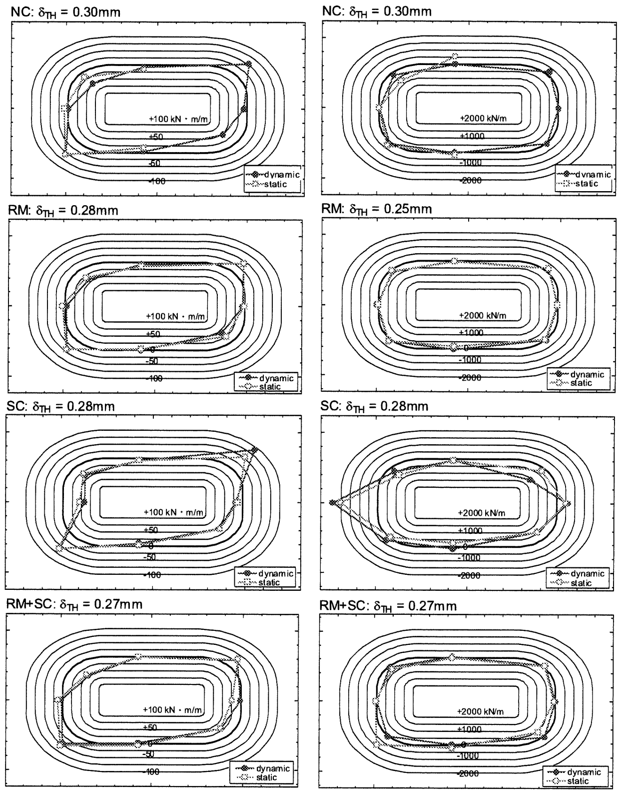

Figure 12 distributions of bending moment and axial force in D-test and S-test

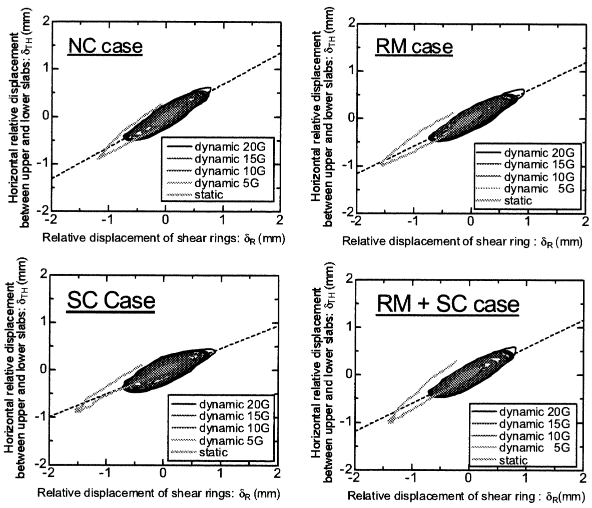

Figure 13 Relationships between δ_{TH} and δ_R in D-test and S-test of the tunnels with

4. Applications to deeper tunnels

4. 1. Modification of active type shear box

As the second stage of the present study, the pseudo-static shear test using the active type shear box was used for the study of earth pressure on deeper tunnel lining before and after earthquake. However, height of the original active type shear box was not sufficient for test of deeper tunnel, whose C/D ratio is about two at lowest. Therefore, in order to simulate the deeper tunnel, the active type shear box was modified especially in the depth (Takemura et al., 2005).

Photo 2 shows a view of the modified active type shear box. Major modifications of the new box are the height of the box and number of actuators. Number of laminae was increased from 13 to 21 and the height of the box from 325mm to 524mm. The increase in the height is equivalent to C/D ratio of two for the model tunnel with 100mm width. Removing the small actuator for the pile head loading, one

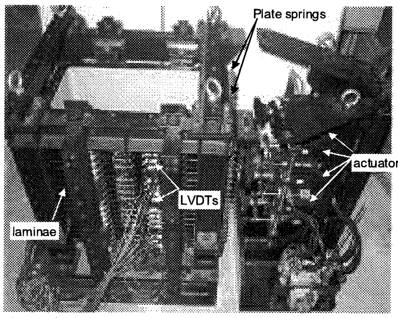

Photo 2 A view of the modified active type shear box for tests on deeper tunnels

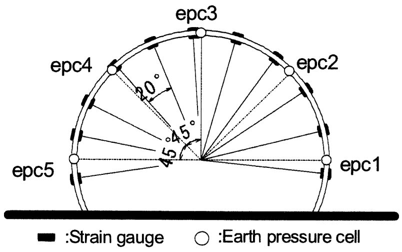

Figure 14 Positions of strain gauges and earth pressure cells

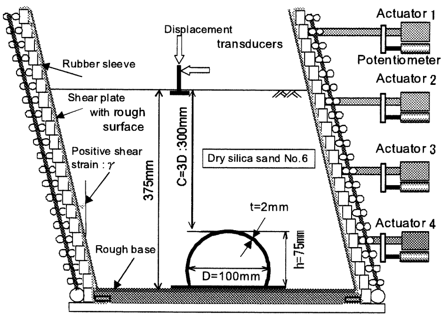

Figure 15 Test setup

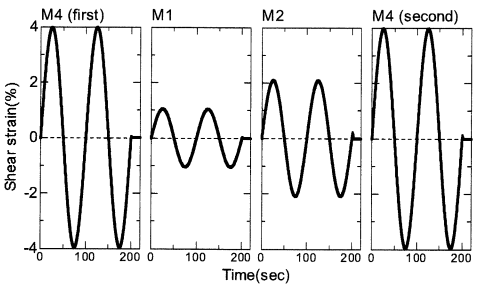

Figure 16 Input shear strain history

hydraulic actuator for displacing laminae was added to produce the continuous displacement of the laminae.

4. 2. Model and Test description

Assuming horseshoe-shaped mountain tunnel, a semi-circular aluminium model tunnel was used, in which only tunnel lining was modelled. It has a diameter of 100mm, a height of 75mm and a thickness of 2mm with smooth surface, which approximately corresponds to a 5m diameter tunnel with a RC lining of 300mm thickness in the prototype scale. The ends of the lining were rigidly fixed to a 5mm thick aluminium plate. 22 strain gauges were attached on both outer and inner sides of the model in pairs to obtain

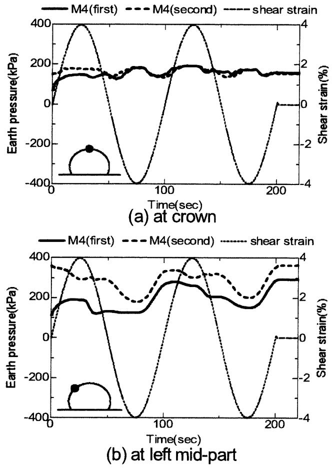

Figure 17 Measured earth pressure at crown and left mid-part

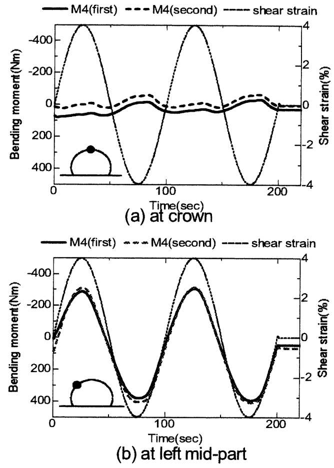

Figure 18 Measured bending moment at crown and left mid-part

bending moments of the tunnel lining. 5 earth pressure cells of 6.2mm diameter and 0.75mm thick were embedded to measure the distribution of the earth pressure acting on the lining on the outer surface of the tunnel at the tunnel crown, spring lines and the mid-parts between the crown and spring lines. Figure 14 illustrates the positions of the strain gauges and the earth pressure cells.

Dry silica sand No.6 ($G_s = 2.64$, $D_{50} = 0.51$mm, $U_c = 1.74$, $e_{max} = 0.922$, $e_{min} = 0.565$) was used for the model ground in the test. The model ground was constructed to achieve a relative density of 80% (γ_d= 15.8kN/m^3, ϕ= 41deg.). The height of the model ground was selected to be 375mm, creating the cover of 300mm, which corresponds to a C/D ratio of 3.0. The model setup is illustrated in Figure 15.

The input shear strain history is shown in Figure 16. The two cycles sinusoidal shear strains with 0.01 Hz, of which amplitudes were 4%, 1%, 2% and 4% respectively (termed as M4(first), M1, M2 and M4(second), respectively), were imposed to the model ground continuously.

4. 3. Results and Discussions

Figure 17 shows variations of earth pressure measured at the tunnel crown and the mid-part between crown and left spring line in the loading steps of M4(first) and M4(second) with shear strain, γ= 4%. Variations of bending moments near the two parts are also shown in Figure 18. The positive bending moment means that the inner surface of the tunnel suffers tension force. In the cycles of M4(first), the model was first sheared, while the cycles of M4(second) were applied after several shear strain cycles were applied to the model including M4(first). Earth pressures in the first cycle show a gradual increase during shearing as shown in Figure 17(a). Cyclic variation of earth pressure and bending moment at the crown is smaller than those at the mid-part. It is interesting to note that at the left mid-part the earth pressure varies randomly as shown in Figure 17(b), while Figure 18(b) clearly indicated that the bending moment varies in the same phase with the input shear strain.

Figures 19 and 20 show earth pressures and bending moments measured before and after cyclic shearing in M4(first) and M4(second) respectively. The terms ‘before’

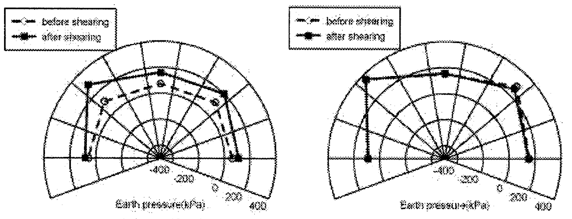

(a) M4(first) (b) M4(second)

Figure 19 Earth pressure measured before and after shearing

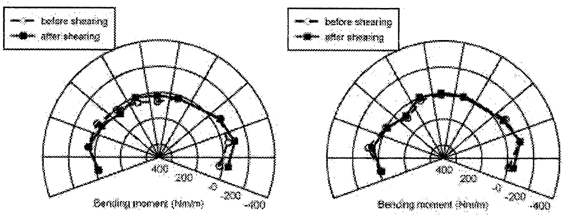

(a) M4(first) (b) M4(second)

Figure 20 Bending moment measured before and after shearing

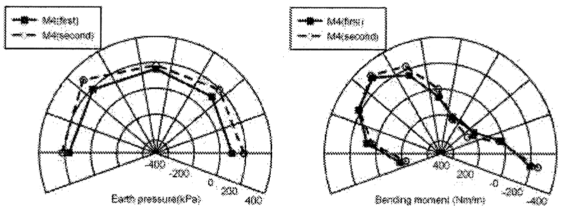

(a) Earth pressure (b) Bending moment

Figure 21 Earth pressure and bending moment at maximum shear strain, γ=4%

and 'after' in the figures correspond to the test elapsed time of 0 second and 200 seconds respectively in Figure 16. Figure 21(a) and (b) show earth pressures and bending moments measured when the positive maximum strain first applied in the M4(first) and M4(second) which corresponding to elapsed time of 25 seconds in Figure 16.

From Figure 19, two observations can be made. The first one is that the initial earth pressures before the first shearing indicated as M4(first) are much smaller, probably due to the formation of arch action during the period of increasing centrifugal acceleration up to 50G. The second one is that the earth pressures increase after the first shearing history, suggesting that deterioration of the arch action takes place. In Figure 19(b), the earth pressures before and after loading cycles are almost the same, because the ground has already been subjected to 4%, 1% and 2% shear strain cycles and arch action diminished by shearing. After applied several shear histories, the soil-tunnel interaction showed elastic behaviour with no change of earth pressures and bending moments before and after shearing as shown in Figures 19(b) and 20(b). It is interesting to note that bending moment distributions show no appreciable change before and after shearing even if a 4% shear strain cycle is imposed.

From the moment distribution at the maximum shear strain shown in Figure 21, it can be confirmed that the bending moment due to shear deformation of the ground becomes maximum at about 45^{o} from the tunnel crown, which were also found by Yamada et al. (2002) from the circular shield tunnel model in sand.

5. Concluding Remarks

This paper introduced the physical modelling technique for an experimental seismic displacement method and confirmed the usefulness of the method by comparing the structural responses between the observations in dynamic centrifuge tests and the corresponding static centrifuge tests. A few applications were presented to seismic stability problems of tunnels constructed both shallow and deeper depths. Further studies on the development of possible countermeasures against earthquakes for underground structures are expected using in this facility.

Acknowledgements

This research was partially supported by Grant-in-Aid for Scientific Research(A), 2005-2007, No. 17206050, "Seismic stability of the large cross-section urban tunnel with located in relatively shallow depth". The authors gratefully acknowledge the funding for this research from the 21st Century Centre of Excellence (COE) program entitled "Evolution of Urban Earthquake Engineering". The authors would like to thank Mr. Takemine Yamada, Dr. Hideki Nagatani and Dr. Naoto Ohbo, Kajima Technical Institute, for their cooperation.

References:

Izawa J., Kusakabe O., Nagatani H., Yamanda T. and Ohbo N. 2006. Centrifuge modelling on seismic behaviour of rectangular tunnels, Proceedings of Physical Modelling in Geotechnics, Proc. of 6th International Conf. on Physical Modelling in Geotechnics, pp. 1163-1169.

Japanese Geotechnical Society. 2006. Principles for Foundation Designs Grounded on a Performance-based Design Concept.

Kajima Technical Research Institute, Geotechnical Centrifuge, http://www.kajima.co.jp/tech/katri/leaf/pdf/2002-37.pdf

Kusakabe, O., Takemura, J., Takahashi, A., Izawa, J. and Shibayama, S., Physical modeling of seismic responses of underground structures, Keynote lecture, The 12th International Conference ofInternational Association for Computer Methods and Advances in Geomechanics, 2008.(now printing)

Takahashi A., Takemura A., Suzuki A., and Kusakabe O. 2001. Development and performance of an active type shear box in a centrifuge, International Journal of Physical Modelling in Geotechnics, Vol.1, No.2, 1-17.

Takemura J., Izawa J., Shibayama S. and Kusakabe O. 2006. Active type shear box and its application on a stability of shallow tunnel in a centrifuge, Proceedings of 3rd International Conference on Urban Earthquake Engineering, pp. 639-646.

Takemura J., Kondo M., Esaki T., Kouda M. and Kusakabe O, 1999, Centrifuge model tests on double propped wall excavation in soft clay, Soils and Foundations, Vol. 39, No. 3, pp. 75-87.

Yamada T., Nagatani H., Igarashi H. and Takahashi A. 2002. Centrifuge model tests on circular and rectangular tunnels subjected to large earthquake-induced deformation, Proceedings of Geotechnical Aspects of Underground Structures in Soft Ground, pp. 673-678.

Yamada T., Nagatani H., Ohbo N., Izawa J., Shigesada H. and Kusakabe O. 2004. Seismic performance of flat cross-sectional tunnel with countermeasures, Proceedings of 13th World Conference on Earthquake Engineering, paper No. 706.

Fifth International Conference on Urban Earthquake Engineering
March 4-5, 2008, Tokyo Institute of Technology, Tokyo, Japan

INFLUENCING PARAMETERS FOR THE BEHAVIOR OF MODERATELY BURIED HDPE PIPELINES SUBJECT TO SEISMIC GROUND FAULTING

Tarek H. Abdoun[1), Da Ha[2), and Michael J. O'Rourke[3)

1) Associate Professor, Department of Civil and Environmental Engineering, Rensselaer Polytechnic Institute, USA
2) Post-doc Research Associate, Department of Civil and Environmental Engineering, Rensselaer Polytechnic Institute, USA
3) Professor, Department of Civil and Environmental Engineering, Rensselaer Polytechnic Institute, USA
abdout@rpi.edu, had@rpi.edu, orourm@rpi.edu

Abstract: Seismic ground faulting is a severe hazard for continuous buried pipelines. Over the years, researchers have attempted to understand pipe behavior, most frequently via numerical modeling and simulation. However, there has been little, if any, physical modeling and tests to verify the numerical modeling approaches. This paper presents results of four pairs of centrifuge tests designed to investigate the influence of various factors on the behavior of buried HDPE pipelines subject to strike-slip faulting. Parameters considered are the initial fault-pipe orientation angle, fault offset rate and soil moisture content. The centrifuge tests results show that the behavior of moderately buried pipe, specifically pipe strain and pipe lateral forces are nominally not affected by the fault offset rate and soil moisture content when the pipe is subject to strike-slip faulting. On the other hand, the initial fault-pipe angle can have significant influence on the peak pipe axial strains.

1. INTRODUCTION

Over the past 30 years, researchers have tried to understand the complex behavior of buried pipelines subject to ground ruptures most often via numerical simulation. Unfortunately, there was a lack of laboratory tests, either full scale or small scale centrifuge tests, which are needed to validate and confirm numerical simulation assumption and results. Fortunately, a recent NEESR-SG grant (Grant Number: CMS-0421142) provided an opportunity for Rensselaer Polytechnic Institute and Cornell University to conduct a comprehensive laboratory investigation on the behavior of buried pipeline subject to ground faulting. The tests utilized state of the art testing equipment and cutting-edge sensing technologies. Both full-scale and centrifuge tests were conducted to simulate the situation of buried pipelines subject to ground faulting. Because of cost and other considerations more centrifuge tests were conducted than the full scale tests. Some centrifuge tests were used to directly compare with the full scale testing while others were used to study the influence of various parameters.

The response of continuous buried pipe to fault offset is a function of a number of parameters. Among the most important are the types of fault (e.g. normal faults, strike-slip faults) and for strike-slip faults, the orientation of the pipe with respect to the fault trace. In previous papers, researchers at Rensselaer Polytechnic Institute and Cornell University have addressed the influence of fault type (Ha et al. 2008), and the differences in the pipe behavior for strike-slip faulting which induces net axial tension and compression in the pipe (Ha et al. 2007a).

Herein, the influences of three potentially significant variables on the response of HDPE pipe subject to strike-slip faulting are studied. The variables are initial fault-pipe orientation angle, fault offset rate, and soil moisture content.

2. CENTRIFUGE MODELING OF HDPE PIPE RESPONSE TO SEISMIC GROUND FAULTING

2.1 Design and Setup of Centrifuge Tests

The centrifuge tests reported herein were designed to evaluate the influence of various parameters on the behavior of buried HDPE pipelines subjected to strike-slip faulting. Table 1 is a summary of the parameters for each of the four pairs of centrifuge tests. The parameters for each pair of tests were identical except for the type of instrumentation.

For one of the two tests in each pair, the HDPE pipe was instrumented with strain gages along the pipe springlines. They were used to measure the total longitudinal strain distribution on both the active and passive sides of the pipe. The longitudinal strains are due to a combination of axial and bending (flexural) strains. Axial strains were calculated as the average of the strain at opposite springlines. Bending strains were calculated as one-half the difference between the longitudinal strains at opposite springlines. For the other test in each pair, the pipe was instrumented with tactile pressure sensor sheets manufactured by TEKSCAN Inc. The sensor sheets were wrapped around the test pipes for a longitudinal distance of 0.25 m at model scale (3.0 m in prototype) on either side of the fault. The pressure sensor sheet measures the pressure at the soil-pipe interface, which is used to calculate the strength and stiffness of equivalent soil spring. The details about the tactile pressure sensor instrumentation and data interpretation were discussed in a separate paper (Ha et al. 2007b).

Table 1 Summary of Centrifuge Test Parameters (all dimensions in prototype scale)

Model Number	Instrumentation	Initial Pipe-Fault Angle (degrees)	W_c, %	Offset Rate (m/min)
T_1	Gage	-85	4.0 ~ 4.5	0.318
T_2	Tactile	-85	4.0 ~ 4.5	0.318
T_3	Gage	-63.5	4.0 ~ 4.5	0.318
T_4	Tactile	-63.5	4.0 ~ 4.5	0.318
T_9	Gage	-63.5	4.0 ~ 4.5	41.3
T_10	Tactile	-63.5	4.0 ~ 4.5	41.3
T_11	Gage	-63.5	0	0.318
T_12	Tactile	-63.5	0	0.318

In all the tests, the fault offset was simulated using a recently upgraded hydraulic servo-controlled split-box container (inside dimension: 1.14 m x 0.76 m x 0.45 m) shown in Figure 1. The container is capable of simulating both vertical and horizontal offset in flight, although only horizontal (strike-slip) offset were simulated in this series of test. Additional information about the split container was presented by Ha et al. (2006).

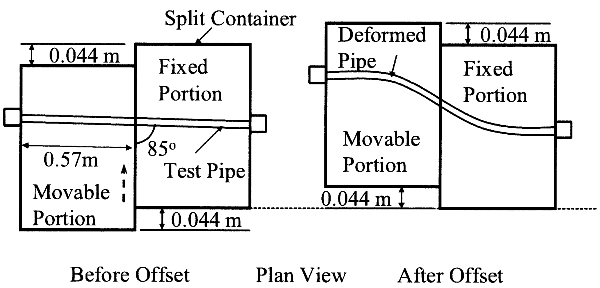

(a)

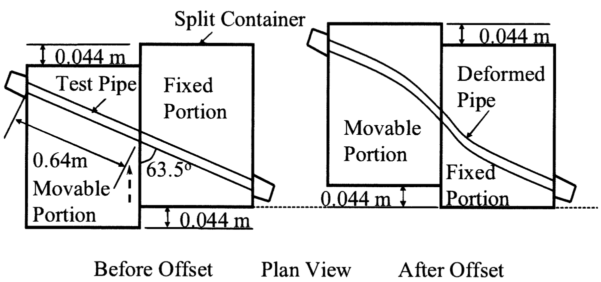

(b)

Figure 1 Configurations of the centrifuge model before and after offset (dimensions in model scale): (a) tests T_1 and T_2, and (b) tests T_3 through T_12

Figure 1 also shows the high density polyethylene (HDPE) experimental pipeline before and after fault offset. In all tests, the initial angle between the pipe and fault trace was 63.5°, and the right lateral offset results in net tension in the pipe. As shown in Figure 1, during the test the movable portion of the container was offset horizontally a total of 0.088 m in model scale and since all tests were conducted at a centrifugal gravity level of 12.2 g, this corresponding to a prototype offset of 1.06 m.

2.2 Effect of Initial Fault-Pipe Orientation Angle

Figure 2 shows the measured axial and bending strains in pipe models T_1 and T_3. At small offsets, where the pipe material is nearly linearly elastic, there is an approximately linear decrease in axial strain with distance from the fault. This is consistent with a constant longitudinal friction force per unit length at the soil-pipe interface. At large offsets, where the pipe material becomes highly nonlinear, the axial strain versus distance plot is more convex, with strain increasing at a more rapid rate near the fault trace. As shown in Figure 2, for a given offset, the bending strain distribution is consistent with double curvature bending, concave on one side of the fault and convex on the other. As shown in Figure 2, the axial strains are significantly different for the two models whereas the bending strains are quite similar.

Large surface cracks were observed on the passive (soil being pushed by the test pipe) side of the pipe. That is, in Figure 3 there is a ground crack far to the left of the pipe in the top portion of the photo and another crack far to the right of the pipe in the lower portion of the photo (cracks indicted by thinner dashed lines). The cracks appear to be the surface expressions of passive soil wedges. Additional cracks also appear between the outermost surface expression of the passive soil block and the trace of the pipeline, likely due to soil heaving during the soil wedge formation process. Note the shape of the deformed pipe is indicated in Figure 3 as a thicker dashed line. The deformation shape was determined by using the surface grid drawing to locate the center and the two ends of the test pipe and also taking the test pipe bending strains into consideration.

Because the tactile pressure sensor does not measure tangential traction (friction) and Coulomb friction was assumed, a constant friction coefficient, μ, must also be assumed to determine the total lateral force at the soil-pipe interface. A value of $\mu = 0.4$ was used as an expected value (corresponding to an HDPE-sand interface friction angle $\phi = 22°$ with full slip), which is also consistent with the friction coefficient measured and reported elsewhere for sand-HDPE interfaces (O'Rourke et al., 1990). Figure 4 show the resulting pipe lateral force per unit length. As expected, the pipe lateral force generally decreases with increasing distance from the fault, generally increases with offset. For a given offset and distance from the fault, the lateral force on the pipe is larger for $\alpha = -85°$ than for $\alpha = -63.5°$. For example, at 1.25 m from the fault, the pipe lateral force for $\mu = 0$ ranges from 10 kN/m to 41 kN/m for $\alpha = -85°$, while for $\alpha = -63.5°$ it ranges from 5 kN/m to 30 kN/m.

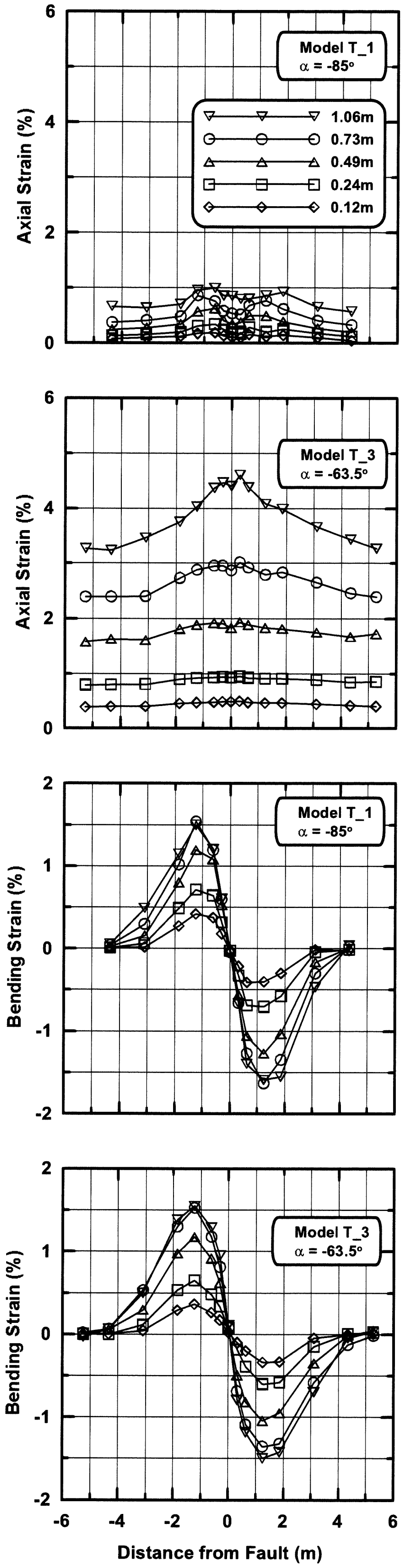

Figure 2 Axial and bending strains for two initial pipe-fault angles, plotted as functions of distance from fault (tests T_1 and T_3)

For high offsets, the lateral pipe force reaches a constant value at locations close to the fault, presumably due to passive soil wedge formation discussed previously. As an example, for $\mu = 0.4$, the peak lateral pipe force is about 70 kN/m for $\alpha = -85^{\circ}$ and 58 kN/m for $\alpha = -63.5^{\circ}$.

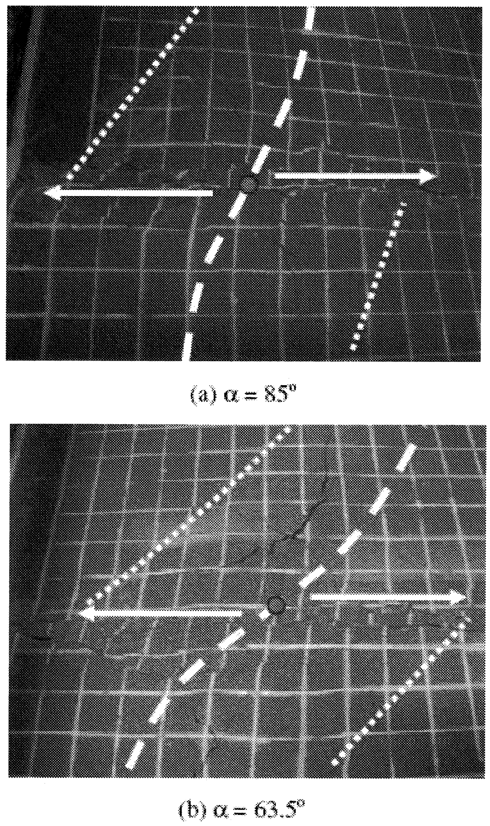

Figure 3 Post-test surface observations of the two test setups.

For design purposes, the ASCE Guidelines (1984) provide a bi-linear relationship for the transverse pipe-soil interaction force, based in part on the results from full scale two-dimensional tests on dry sand by Trautmann and O'Rourke (1985). The peak lateral force per unit length on the pipe, P_u:

$$P_u = N_{qh} \gamma H D \qquad (1)$$

where N_{qh} is the dimensionless maximum lateral force; γ is the effective unit weight of soil; H is the depth of soil from the surface to the center of the pipe; and D is the pipe outer diameter.

The parameter N_{qh} is a function of both the soil internal friction angle ϕ and the dimensionless pipe depth (H/D). For the tests shown in Figure 4, the soil internal friction angle $\phi = 40^{\circ}$, and $H/D = 2.8$ ($H = 1.12$ m and $D = 0.408$ m), for which the corresponding $N_{qh} = 8.5$ in the ASCE Guidelines for dry sand. Hence for an effective unit weight of the soil backfill $\gamma = 15.3$ kN/m^3, the peak transverse force as per the ASCE guideline (N_{qh} = 8.5) is 58.3 kN/m. Figure 4 shows the measured pipe lateral force along with the ASCE suggested values.

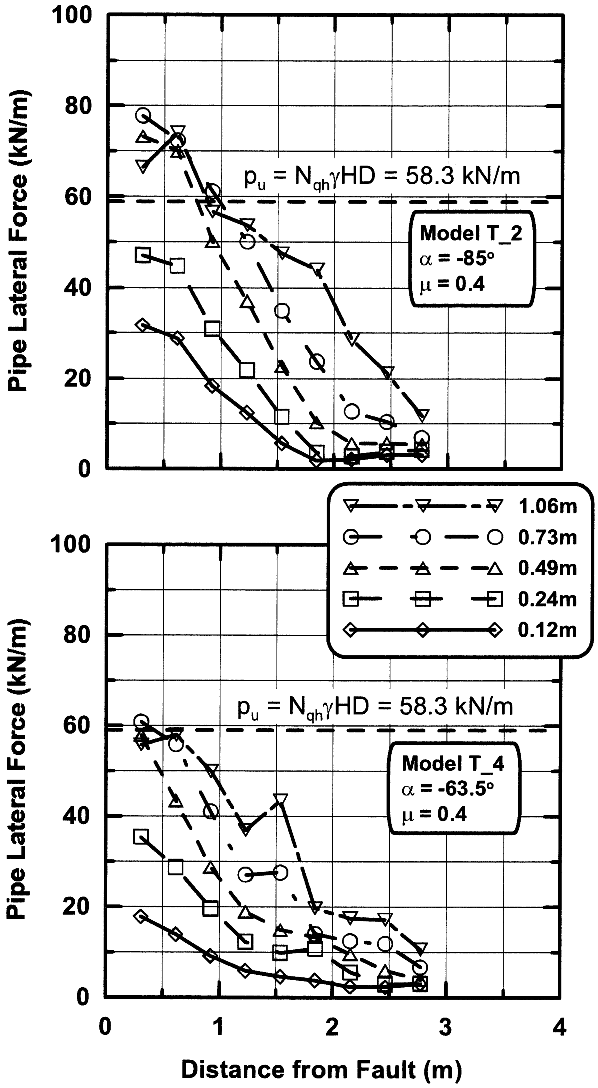

Figure 4 Lateral force distribution along the pipe for two initial pipe-fault angles (tests T_2 and T_4)

2.3 Effect of Fault Offset Rate

High Density Polyethylene (HDPE) pipe is becoming more widely used for buried pipelines due to its excellent ductility. However, the HDPE material is strain rate dependent (i.e. stiffener at higher strain rates) and centrifuge tests were undertaken to determine the influence of this parameter with respect to fault crossing behavior.

The offset rate used in most of the centrifuge tests was 0.32 m/min, which corresponds to a strain rate around 1%/min in the pure tension (no soil) tests. This offset rate for the centrifuge tests was chosen so that comparisons could be made with full-scale test measurements at Cornell University on the same HDPE pipe material in similar, partially saturated sand. However, an upper bound for the expected prototype (actual earthquake) offset rate is around 1 m/sec (60 m/min), which corresponds to a pure tension test strain rate around 190%/min. Hence, the offset rate used in the Cornell tests and a majority of the centrifuge tests was much smaller than the expected prototype offset rate by a factor of 190.

In this series of centrifuge tests, two test pairs were conducted at different strain rates (one pair at around 1%/min and another pair at around 190%/min) to investigate the effect of fault offset rate on the HDPE pipe response to PGD.

Measured pipe strains from fast offset test are presented in Figure 5.

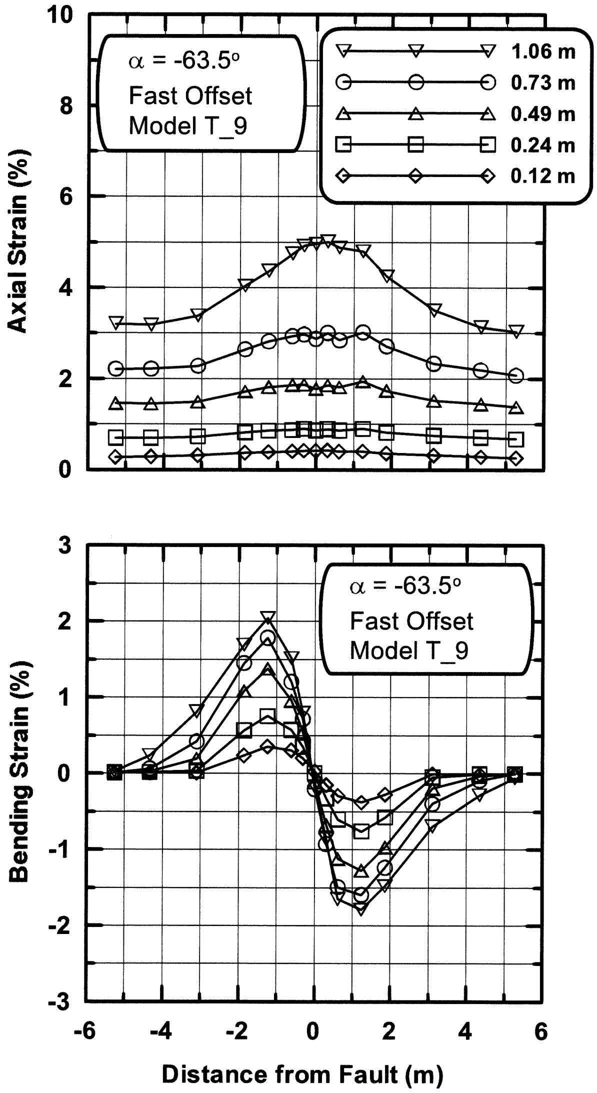

Figure 5 Pipe axial and bending strains for fast fault offset, plotted as functions of distance from the fault trace (test T_9)

Figure 6 shows the effect of fault offset rate upon the transverse soil-pipe interaction pressure. An increase in the fault offset rate by a factor of around 130 results in only about 10% increase in the peak soil-pipe interaction pressure. However, well away from the fault (i.e. points more than 1.5 m away from the fault) the soil-pipe interaction pressure for the fast offset rate test is higher than that for the slow offset rate test. This is generally consistent Figure 5, which shows an increase in pipe bending strain with increased offset rate. Note that the pressure sensors record normal pressure only.

As shown in Figure 6, the peak lateral force per unit length from the ASCE Guidelines (1984) (dash line without symbols) compares well with measured peak lateral force on the HDPE pipe at locations close to the fault.

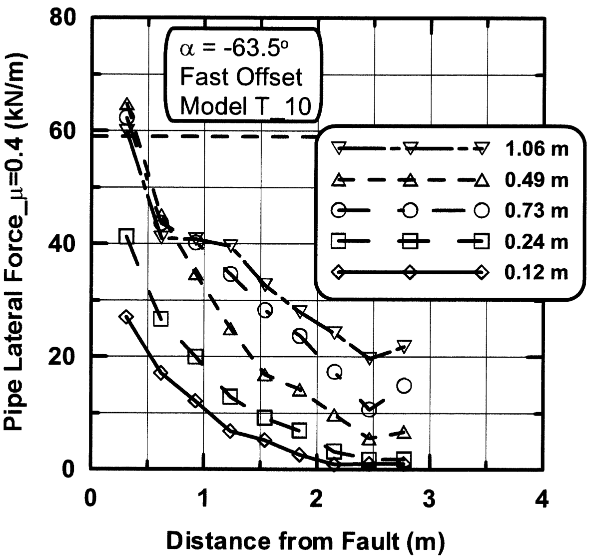

Figure 6 Lateral force distribution along the pipe for fast offset rate (test T_10)

2.4 Effect of Soil Moisture Centent

The effect of soil moisture content on the pipe strains is presented in Figure 7 and Figure 8. Using dry sand as the backfill material does not appreciably change either the axial or bending strains on the HDPE pipe, in comparison with moist sand backfill. As indicated by Figure 7, the peak axial strain on the pipe using dry sand backfill is only about 5% higher than the peak axial strain obtained in the moist sand test. At small offsets, the bending strain recorded in the dry sand test is slightly smaller than the bending strain recorded in the moist sand test. However, the peak bending strain recorded in the dry sand test is about 13% higher than that recorded in the moist sand test. The locations of the peak strains for both dry sand test and moist sand test are nominally the same.

Figure 8 shows the influence of soil moisture content on the transverse soil-pipe interaction pressure. The behavior is somewhat complex. At low offsets (less than 0.25 m) the trans-verse pressure at the fault in the moist soil test is some what larger than in the dry soil test. How-ever, for prototype offset of 0.49 m and larger the reverse is true. This is generally consistent with Figure 8(b) wherein at low offsets the flexural strains for moist sand test were larger, but not at large offsets. In the dry sand test, the peak soil-pipe interaction pressure for the entire pipe oc-curs when the fault offset reaches about 0.73 m. When the fault offset reaches 1.06 m the soil-pipe interaction pressure drops a little bit (less than 5%). In contrast, in the moist sand test, the soil-pipe interaction pressure keeps increasing until the fault offset reaches its maximum value of 1.06 m. Although the influence of moisture content is complicated, the overall effect in terms of changes in pipe strains is small.

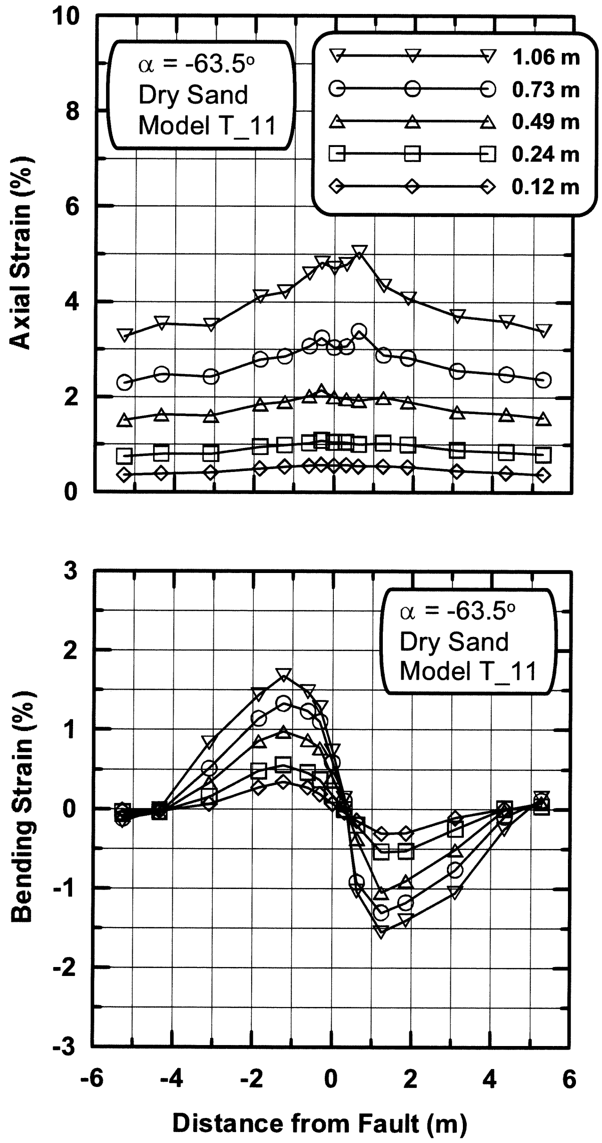

Figure 7 Pipe axial and bending strains for dry sand test, plotted as functions of distance from the fault trace (test T_11)

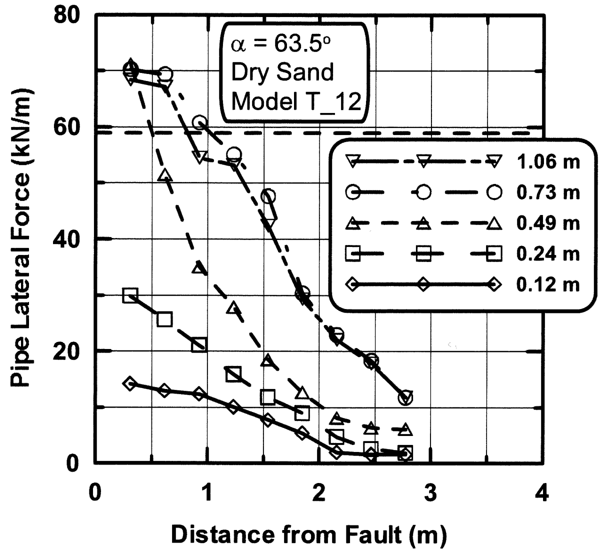

Figure 8 Lateral force distribution along the pipe for dry sand test (test T_12)

3. CONCLUSIONS

Eight centrifuge tests were carried out to investigate the behavior of buried pipelines systems subject to strike-slip faulting. Two tests with a slow fault offset rate, moist sand backfill and a pipe-fault angle of -63.5° were used as a standard. Tests with a different pipe-fault angle (α = -85°), a faster fault offset rate, and dry sand backfill were used respectively to investigate the influence of each individual parameter.

The test results show that fault offset rate and soil moisture content do not have significant influence on the amplitudes and locations of the peak strains, as well as the peak lateral forces on the pipe. The pipe-fault angle in the investigated range can significantly influence the amplitudes of the peak pipe axial strains, but does not have a significant influence on the pipe bending strain and lateral forces.

The measured peak lateral force from the tactile pressure sensor compared well with values suggested by the ASCE Guidelines (1984).

Acknowledgements:

This work is part of a collaborative project involving full-scale buried pipe tests at Cornell University and companion centrifuge tests at Rensselaer Polytechnic Institute. This work was supported primarily by the George E. Brown, Jr. Network for Earthquake Engineering Simulation (NEES) Program of the National Science Foundation under Grant Nos. CMS-0421142, CMS-0086555, and CMS-0217366. Any opinions, findings and conclusions or recommendations expressed in this material are those of the authors and do not necessarily reflect the views of the National Science Foundation.

References:

American Society of Civil Engineers. (1984). "Guidelines for the seismic design of oil and gas pipeline systems." Committee on Gas and Liquid Fuel Lifelines, *Technical Council on Lifeline Earthquake Engineering*, ASCE, New York.

Ha, D., Abdoun, T., O'Rourke, M., Van Laak, P., O'Rourke, T. and Stewart, H. (2006). "Split-containers for centrifuge modeling of permanent ground deformation effects on buried pipeline systems." *The Sixth International Conference on Physical Modeling in Geotechnics*, August 4-6, 2006, Hong Kong, China, pp. 729-734.

Ha D., Abdoun T., O'Rourke M., Symans M., O'Rourke T., Palmer M. & Stewart H. (2007a) "Earthquake Faulting Effect on Buried Pipelines- Case History and Centrifuge Study", *International Journal of Physical Modeling in Geotechnics* (Accepted).

Ha D., Abdoun T., O'Rourke M., Symans M., O'Rourke T., Palmer M. & Stewart H. (2007b) "Centrifuge Modeling of Permanent Ground Deformation Effect on Buried HDPE Pipelines", *ASCE Journal of Geotechnical and Geoenvironmental Engineering* (Accepted).

Ha D., Abdoun T., O'Rourke M., Symans M., O'Rourke T., Palmer M. & Stewart H. (2008) "Buried HDPE Pipelines Subjected to Normal Faulting - A Centrifuge Approach", *Canadian Geotechnical Journal* (under review).

Trautmann, C. H., and O'Rourke, T. D. (1985). "Lateral force displacement response of buried pipe." *J. Geotech. Eng.*, 111(9), 1077–1092.

Fifth International Conference on Urban Earthquake Engineering
March 4-5, 2008, Tokyo Institute of Technology, Tokyo, Japan

EFFECT OF EXCAVATION ON THE SEISMIC BEHAVIOR OF ADJACENT TUNNEL

Huei-Tsyr Chen[1], Jien-Chi. Liu [2] and Chung-Jung Lee[3]

1) Associate Professor, Department of Civil Engineering, National Central University, Taiwan
2)Engineer, Charn-Wan Construction Company, Taiwan
3) Professor, Department of Civil Engineering, National Central University, Taiwan

chenht@cc.ncu.edu.tw

Abstract: In this study a three-dimensional finite element procedure is adopted to analyze the displacement of a cut-and-cover tunnel due to near-by deep excavation and then for each excavation stage the effect of deep excavation on the seismic response of the tunnel is investigated. From the parametric studies, it is found that (1) the effect of deep excavation on the settlement and tilting of tunnel is less significant than that on the lateral displacement for both static and seismic analyses; (2) the seismic response of the tunnel increases as the depth of excavation increases; (3) to avoid the displacement exceeding the safety requirement, it is suggested that the displacement induced by the deep excavation by static analysis should not be very close to the specified limit.

1. INTRODUCTION

In urban area, due to scarcity of land, high-rise buildings become a feasible solution to meet the needs for office and inhabitation use. The construction of high-rise building usually requires deep excavation which will cause instability to the surrounding ground and/or structures. Over the last years a significant number of researches have been devoted to the study of deep excavation through either observation at the construction site or numerical modeling (Clough and Duncan 1969, Ghaboussi and Pecknold 1984; Chen and Li 1993).

As a result of urbanization, many high-rise buildings will be inevitably constructed near the existing subway tunnel. In the past there were some studies concerning the effect of deep excavation on the adjacent subway tunnel. Liu (1995), using the effective-stress based two-dimensional finite element method, found that deep excavation will cause the tunnel to tilt, and the degree of tilting increases with longer construction period, shallower burial of tunnel, closer to the excavation site and larger excavation width. Wang and Ji (1999) adopted finite difference approach to investigate the effect of deep excavation on the adjacent shield tunnel. They found that the embedment depth of diaphragm wall will have only slight effect on the lateral displacement of tunnel and it would be impractical to reduce the lateral displacement of tunnel by using larger embedment depth of wall.

Apparently, the deep excavation of high-rise building may have a pronounced damaging effect on the tunnel if the appropriate measure is not taken. In Taipei there was such an instance (Chang et al. 2001). That instance happened for the tunnel of Bannan line of Taipei Mass Rapid Transit (MRT) system, where the adjacent excavation inflicted the lateral displacement, the settlement and tilting to the tunnel and the cracks to the lining of the tunnel. Luckily, it occurred before its completion, but the MRT authority set up a rule for performing deep excavation adjacent MRT tunnel from then. In that rule, it requires that before construction the contractor must submit calculated results for review, showing that the excavation will not cause the tunnel to displace laterally more than 2.5 cm and the slope for the differential settlement to be less than 1/750. It should be noted that the calculation is based on static analysis only.

The analyses mentioned previously are static and two-dimensional. In reality, the interaction analysis for deep excavation and adjacent subway tunnel is a three-dimensional problem; furthermore, there is a possibility that during the deep excavation, the earthquake hits. Therefore, in this paper the seismic interaction analyses using nonlinear three-dimensional finite element method are performed to investigate the effect of each stage of deep excavation on the adjacent subway tunnel and to verify the adequateness of the static analysis.

2. METHOD AND PROCEDURE OF ANALYSIS

2.1 Method of Analysis

The static analysis is made using the program

NCUEXCA3D (Lien, 1993). In this program, the soil, buttress and diaphragm wall are modeled using the 8-node block element, while the truss element is employed to model the strut. The nonlinearity of soil is assumed to follow Mohr-Coulomb failure criterion; however, the diaphragm wall, buttress and strut are considered to behave elastically during the analysis. It also adopts infinite element to model the infinite lateral extent of soil stratum underlain by rigid bedrock.

The seismic analysis is performed using the program NCUDYNA3D which is modified from a previous program developed by Lin (1999). Except the modeling of lateral infinite extent of soil stratum, the main features of this program are the same as those described for the NCUEXCA3D. The lateral infinite extent of soil stratum is modeled using the viscous boundary proposed by Miura et al. (1989). The initial stiffness method as well as the Newmark β method are adopted for the solution of equation of motion.

A note should be mentioned about the excavated elements. In the static analysis the stiffnesses of the excavated elements are modified to have very small values so that the analysis for the following excavation step can be made without altering the mesh. This scheme does not cause any instability in the solution. However, in the seismic analysis, this scheme causes the numerical instability and thus a new mesh in line with each excavation stage has to be established. In such a situation, a care must be taken to ensure that the stresses of the elements from static analysis will be correctly transferred for the seismic analysis.

2.2 Procedure of Analysis

The steps for the analysis in this study are as follows:

1. Set up the finite element mesh for the static analysis and prepare the input data according to the site conditions and excavation procedure.
2. Perform the analysis for desired excavation step and store the computed stresses in the disk file for use in the seismic analysis..
3. Establish the finite element mesh corresponding to the excavation step for step 2 and prepare the necessary input data including the stress output from step 2.
4. Perform the seismic analysis and display the desired results.

3. RESULTS AND DISCUSSIONS

The tunnel considered in this study is a cut-and-cover tunnel. For the static analysis, the roller-type boundary is specified at a distance of 5 times excavation depth from the diaphragm wall, and the same domain size is used for the seismic analysis. Table 1 and Table 2 described the parametric values used for the static and seismic analyses, respectively. The parametric values of Table 1 are taken from the back analysis of a monitored construction site in Taipei (Liu, 2005). By comparing Table 1 and 2, one may find that the values of Young's modulus are different. This is due to the fact that in the static analysis the Young's modulus is obtained using the secant method, while in the seismic analysis the Young's modulus is obtained through G_{max}.

Table 1 Parametric Values for Static Analysis

Depth (m)	Soil Layer	N	γ_t (KN/m^3)	E (KN/m^2)	ν	C	ϕ	K_0
5.6	1	2-4	18.25	$350S_u$	0.49	30-0.3σ_v'	0	0.47
8.0	2	4-11	18.93	$100N$	0.3	0	31	0.48
33.0	3	2-5	18.15	$350S_u$	0.49	0.32 σ_v'	0	0.47
35.0	4	9-24	19.62	$100N$	0.3	0	31	0.48
37.5	5	9-11	19.13	$350S_u$	0.49	0.32 σ_v'	0	0.47
46.0	6	14-37	19.62	300000	0.3	0	32	0.48

S_u; undrained shear strength
σ_v : effective overburden stress
Parametric values for diaphragm wall:
Young's modulus(E_c)=10.6 x 10^6 kpa
Poisson ratio(ν)=0.2
Unit weight(γ_t)=$23KN/m^3$

Table 2 Parametric Values for Seismic Analysis

Depth (m)	Soil Layer	N	γ_t (KN/m^3)	E (KN/m^2)	ν	C	ϕ	K_0
5.6	1	2-4	18.25	Note 1	0.49	30-0.3σ_v'	0	0.47
8.0	2	4-11	18.93	Note 2	0.3	0	31	0.48
33.0	3	2-5	18.15	Note 1	0.49	0.32 σ_v'	0	0.47
35.0	4	9-24	19.62	Note 2	0.3	0	31	0.48
37.5	5	9-11	19.13	Note 1	0.49	0.32 σ_v'	0	0.47
46.0	6	14-37	19.62	Note 2	0.3	0	32	0.48
Rayleigh damping coefficient $\alpha =$ 0.16664, $\beta =$ 0.00240								
Note 1 : $E = 3500S_u$								
Note 2 : $V_s = 65.58\,N^{0.502}$								
$E = 2V_s^2\rho(1+\nu)$								

Table 3 Properties of Supports for Excavation

Support Type	Short Direction (kN/m/m)	Long Direction (kN/m/m)	Prestressed Force (kN/member)
Top Support	7488	6712	784.8
Low Support	31384	12255	1177
15cm-Thick RC Slab	77987	30452	NA

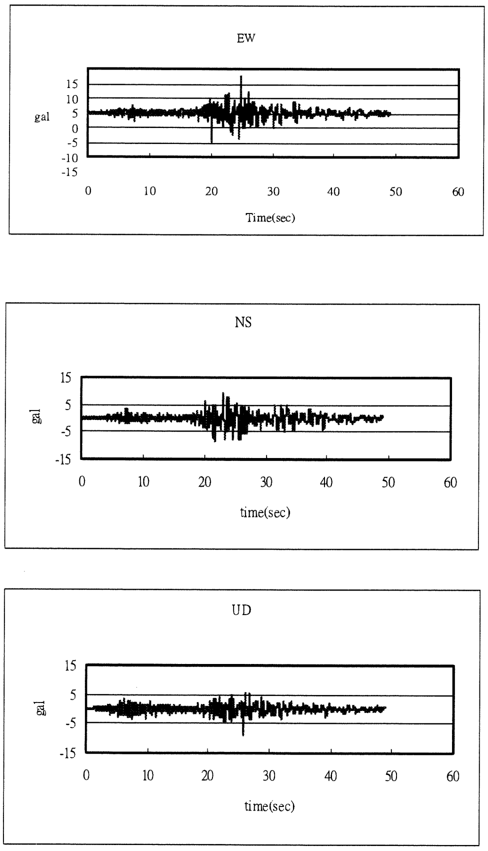

Figure 1 Time History at Jr-Nan Temple Station

The time history used for the analyses, as shown in Fig. 1, are the three components recorded at Jr-Nan Temple Station. During the analysis the largest peak acceleration of the three records is normalized to 0.02g, 0.1g and 0.2g, respectively, where g is the gravitational constant and the scaling factors are then applied to the other two records. This is done to investigate the effect of earthquake intensity.

In this study the lateral displacement, settlement and tilting of the tunnel are obtained (Liu, 2005); however, the instantaneous peak values and peak residual values for settlement and tilting are much less than the specified limits. Therefore, in the following discussions, only the results for the lateral displacements are presented and discussed.

Figure 2 and 3 are the plane view and side view for the cut-and-cover tunnel case, respectively. The excavation zone is assumed to have width of 30m, length of 60m and excavation depth of 19.7m. The thickness and embedment length of diaphragm wall are 70cm and 35m, respectively. To ensure that the wall deformation meets the requirements set by MRT authority, i.e. displacing laterally no more than 2.5 cm and the slope for the differential settlement being less than 1/750, three 6m-long buttress walls are installed below the final excavation surface. The excavation process is also shown in Figure 3. The tunnel, buried at a depth of 7.2m, has a rectangular cross section with 11m x 6.1m and thickness of 50cm.

Shown in Fig. 4 are the results for the instantaneous peak lateral displacement of tunnel. The depth 0 corresponds to free-field case. The results for static analysis show that the lateral displacements are less than 2.5

cm, satisfying the specified limit. At each stage of excavation, the displacement increases with increasing intensity of seismic motions. For a given seismic intensity, the displacements also increase with increasing excavation depth for first five stages and then remain almost a constant value for further increase in excavation depth. For the static and PGA 0.02g cases, the displacement meets the requirement. For the PGA=0.1g case, the lateral displacement will be larger than the specified limit after the excavation stage 3, while for the PGA=0.2g case, even in the free-field situation, the displacement will be larger than the specified limit.

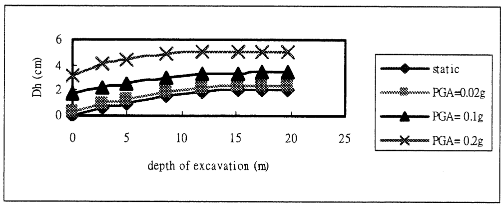

Figure 4 Peak Instantaneous Displacements for Different Stages of Excavation and Earthquake Intensities for Cut-And-Cover Tunnel

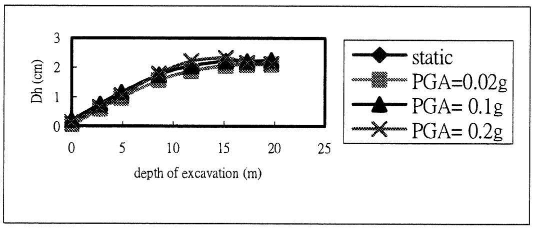

Figure 5 Residual Displacements for Different Stages of Excavation and Earthquake

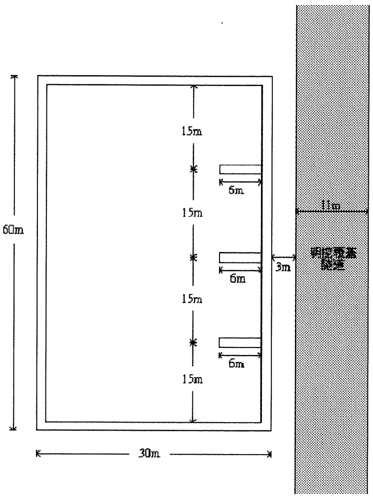

Figure 2 Plane View for Cut-And-Cover Tunnel Case

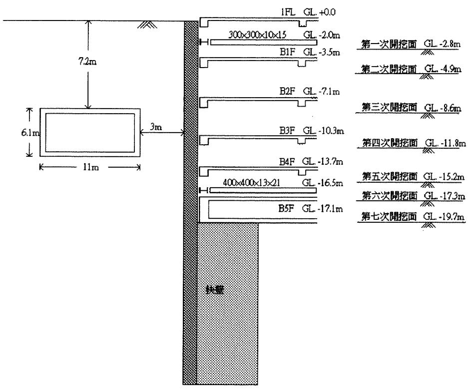

Figure 3 Side View for Cut-And-Cover Tunnel Case

Figure 5 illustrates the peak residual displacement after the cease in earthquake motion. For the static and PGA=0.02g cases, they are almost the same, while slightly larger values are observed for the cases of PGA=0.1g and PGA=0.2g for each stage of excavation which are 0.14cm and 0.22cm larger than the specified limit, respectively.

4. CONCLUSIONS

In this study a three-dimensional finite element procedure is adopted to analyze the displacement of a cut-and-cover tunnel due to near-by deep excavation and then for each excavation stage the effect of deep excavation on the seismic response of tunnel is investigated. From the parametric studies, it is found that (1) the effect of deep excavation on the settlement and tilting of tunnel is less significant than that on the lateral displacement in both static and seismic analyses; (2) the seismic response of the tunnel increases as the depth of excavation increases; (3) to avoid the displacement exceeding the safety requirement under seismic motions, it is suggested that the displacement induced by the deep excavation by static analysis should not be very close to the specified limit.

Acknowledgements:

The authors acknowledge support from National Science Council, Taiwan, under the grant no. NSC 93-2211-E-008-008.

References:

Chang, C.T., Sun, C.W., Duann, S.W., Hwang, R.N. (2001), "Response of a Taipei Rapid Transit System (TRTS) Tunnel to Adjacent Excavation," Tunneling and Underground Space Technology, **16**, 151-158.

Chen, H.T. and Li, C.C. (1993), "Sdudyt of Deep Excavation for MRT System," Research Report, Department of civil

Engineering, National Central University. (in Chinese)
Clough, G.W., and Duncan, J.M. (1969), "Finite Element Analysis of Port Allen and Old River Locks", Contract Report S-69-6, U.S. Army Engineering Waterways Experiment Station, Corps of Engineers, Vicksburg, Mississippi.
Ghaboussi, J., and Pecknold, D.A. (1984), "Incremental Finite Element Analysis of Geometrically Altered Structures," International Journal for Numerical Methods in Engineering, **20**,.2051-2064.
Lien, Y.W. (1993), "Nonlinear Three-Dimensional Analysis of Deep Excavation," Master Thesis, Department of Civil Engineering, National Central University. (in Chinese)
Lin, F.J. (1999), "Numerical Simulation of Ground Motion Induced by Pile-Driving," Master Thesis, Department of Civil Engineering, National Central University. (in Chinese)
Liu, J.C. (2005), "Three-Dimensional Seismic Interaction Analysis of Deep Excavation and Adjacent Subway Tunnel," Master Thesis, Department of Civil Engineering, National Central University. (in Chinese)
Liu, M.Y. (1995), "Preliminary Investigation on the Interaction between Deep Excavation and Adjacent Subway Tunnel," Master Thesis, Department of Civil Engineering, National Central University. (in Chinese)
Miura, F. and Okinaka, H. (1989), "Dynamic Analysis Method for 3-D Soil-Structure Interaction Systems with The Viscous Boundary Based on The Principle of Virtual Work," Journal of JSCE, **404** .
Wang, C.J. and Ji, S.Y. (1999), "Analysis of Displacement of Shield Tunnel Induced by Adjacent Deep Excavation," The 8th Conference on Current Researches in Geotechincal Engineering In Taiwan, 1369-1382. (in Chinese)

Fifth International Conference on Urban Earthquake Engineering
March 4-5, 2008, Tokyo Institute of Technology, Tokyo, Japan

EFFECTS OF LATERAL RESPONSE OF EMBEDDED FOOTING ON PILES DURING SOIL LIQUEFACTION

Shuji Tamura[1), Nobuhiro Maeda[2), Tadashi Sakamoto[2) and Takenori Hida[2)

1) Associate Professor, DPRI, Kyoto University, Japan
2) Graduate Student, Kyoto University, Japan
tamura@sds.dpri.kyoto-u.ac.jp

Abstract: Based on results of dynamic centrifuge tests, this study examines effects of the lateral response (earth pressure and sidewall friction) of an embedded footing on pile stress during soil liquefaction. Results suggest the following conclusions: (1) The lateral response of the footing supported by the piles with high flexural rigidity tends to be in phase with the superstructure inertia. (2) The lateral response of the footing supported by the piles with low flexural rigidity tends to be out of phase by 180 deg with the superstructure inertia. (3) Low flexural rigidity and high ductility capacity are important points to reduce pile stress during soil liquefaction.

1. INTRODUCTION

The extensive soil liquefaction that occurred on reclaimed land areas of Kobe during the 1995 Hyogoken-Nambu earthquake imparted serious damage to pile foundations. Several studies of the failure mechanism of piles have been conducted based on field investigations (Oh-Oka et al. 1998, Tokimatsu et al. 1998) and centrifuge tests (Sato et al. 1995, Horikoshi et al. 1998). Comparison of the numerical analysis results with the observed pile damage suggests that the lateral response, which comprises earth pressure and friction acting on the embedded footing, is out of phase by 180 deg with the superstructure inertia; it induces a smaller bending moment at the pile heads during soil liquefaction (Fujii et al. 1998). On the other hand, it is reported that the lateral response tends to be in phase with the superstructure inertia; it induces a larger bending moment at the pile heads during soil liquefaction based on large-scale shaking table tests (Tamura et al. 2002) and dynamic centrifuge tests (Tamura et al. 2007). The difference in the bending moment described above suggests that the phase difference between the lateral response of an embedded footing and the superstructure inertia is the key to evaluate pile stress. However, knowledge of the phase difference during soil liquefaction is limited.

This study is intended to examine the effects of piles' flexural rigidity on the phase difference between the lateral response of an embedded footing and the superstructure inertia during soil liquefaction. Dynamic centrifuge tests were conducted on piles with either high flexural rigidity or low flexural rigidity.

2. CENTRIFUGE TESTS PERFORMED

2.1 Model Preparation

Centrifuge tests were performed at 40 × *g* centrifugal acceleration using the geotechnical centrifuge at the Disaster Prevention Research Institute, Kyoto University. A pile-footing-superstructure model was prepared in a laminar shear box with inner dimensions of 450 mm (length) × 150 mm (width) × 200 mm (height). Two cases of the performed tests are presented in Fig. 1. The tests used 2 × 2 pile models. The piles had equal diameter of 8.0 mm, length of 176 mm but with different flexural rigidity, *EI*. The piles in Case 1, round stainless steel bars, had flexural rigidity of 3.85×10^{-2} kN·m^2. The piles in Case 2, aluminum pipes, had a thickness of 1.0 mm and flexural rigidity of 0.84×10^{-2} kN·m^2. A sketch and conditions of a pile-footing-superstructure model are depicted respectively in Fig. 2 and Table 1. The lid-shaped footing was modeled with rigid brass of 86 mm (shaking direction) × 64 mm (width) × 54 mm (height). The pile heads were linked rigidly to the upper plate of the footing; their

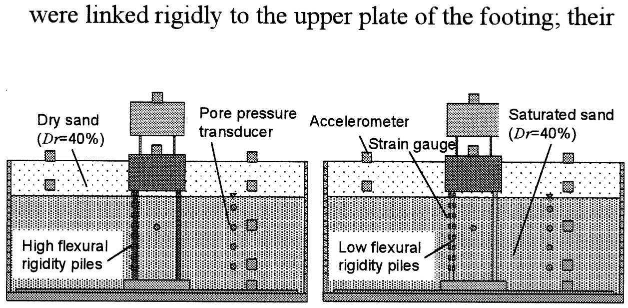

(a) Case 1 (b) Case 2

Figure1 Test cases

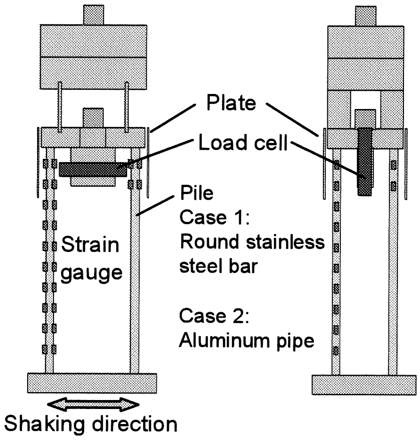

Figure 2 Piles-footing-superstructure model

Table 1 Conditions of piles-footing-superstructure system

		unit	Prototype	Model
Pile	Diameter	m	0.32	0.008
	EI (Case 1)	kNm^2	9.86×10^4	3.85×10^{-2}
	EI (Case 2)	kNm^2	0.22×10^4	0.84×10^{-2}
Footing	Mass	kg	50,560	0.79
	Length (L×B×H)	m	3.44×2.56×2.16	0.086×0.064×0.054
Structure	Mass	kg	128,000	2.00
	Natural frequency	Hz	2.63	105

tips were also linked rigidly to the laminar shear box. The strain gauges at the pile heads were not in contact with the soil. Four plates supported by load cells were set up on the active and passive sides and shearing sides of the footing to evaluate the earth pressure and sidewall friction. The load cells were available for measurement in two different directions.

The soil profile consists of a 54 mm layer of dry sand crust overlying a 146 mm layer of saturated sand deposit in both cases. The soil used for the sand deposits was Toyoura sand (D_{50}=0.21 mm) with relative density Dr=40%. The sand layers were prepared using pluviating dry sand. In the vacuum state, a viscous fluid, Metolose (Shin-Etsu Chemical Co. Ltd.), which has a viscosity that is 40 times that of water, was allowed to seep up from the base plate.

The footing model surface is smoother than that of the prototype. Therefore, Toyoura sand was pasted on the active/passive sides and shearing sides of the footing. The footing was embedded 44 mm into the dry sand crust. The superstructure was modeled with rigid brass. The superstructure mass was 2.00 kg; that of the footing was 0.79 kg. The natural frequency of the superstructure under the fixed footing condition was about 105 Hz. Excitation for all tests used Rinkai92, which is a synthesized ground motion for the Tokyo Bay area. All data presented in the following sections are of prototype scale.

2.2 Dynamic Response of the Soil-Pile-Superstructure System

Figures 3 and 4 show the acceleration time histories of the superstructure, footing and ground surface, as well as those of input accelerations, the total earth thrust defined by the difference between the active/passive sides earth pressure, and the sidewall friction defined by the sum of side shear of the footing, the footing and ground surface displacement, and the excess pore water pressure ratio at G.L. -3.2 m in Cases 1 and 2, respectively. The displacements were calculated according to the double integration of the accelerometer recordings. The excess pore water pressure began to increase at about 8 s and reached the effective confining pressure at about 20 s in both cases. The amplitudes of the ground surface, footing, and superstructure acceleration decrease at about 20 s in both cases because of soil liquefaction. Meanwhile, the amplitudes of the footing and ground surface displacement increase at about the same time in both cases. It is interesting to note that the amplitude of the total earth thrust and sidewall friction increase in Case 1 but decrease in Case 2 at about 20 s.

Figures 5 and 6 respectively depict the time histories of the superstructure footing inertia defined by the sum of the superstructure and footing inertia, the sum of shear force at the pile heads evaluated by the differentiation of the strain, and the bending moment at the pile heads. The amplitudes of shear force at the pile heads are less than that of superstructure footing inertia until 20 s in both cases. The amplitude of the shear force increases rapidly, becoming greater than that of the superstructure footing inertia at 20 s in Case 1. This tendency is typical shear force at pile heads during soil liquefaction (Tamura et al. 2007). On the other hand, the shear force amplitude remains less than that of superstructure footing inertia after 20 s in Case 2. The shear force amplitudes and the bending moment in Case 2 are much less than those in Case 1, indicating that the piles' flexural rigidity markedly affects pile stress.

3. EFFECTS OF EARTH PRESSURE AND SIDEWALL FRICTION ON PILE STRESS

3.1 Superstructure Footing Inertia, Lateral Response of the Footing, and Shear Force at Pile Head

To elucidate the differences in the shear force between Cases 1 and 2, Fig. 7 portrays: the time histories of the superstructure footing inertia; the lateral response, which comprises earth pressure and sidewall friction acting on the embedded footing; and the shear force at the pile heads for time t=10-40 s. In Case 1, the lateral re-

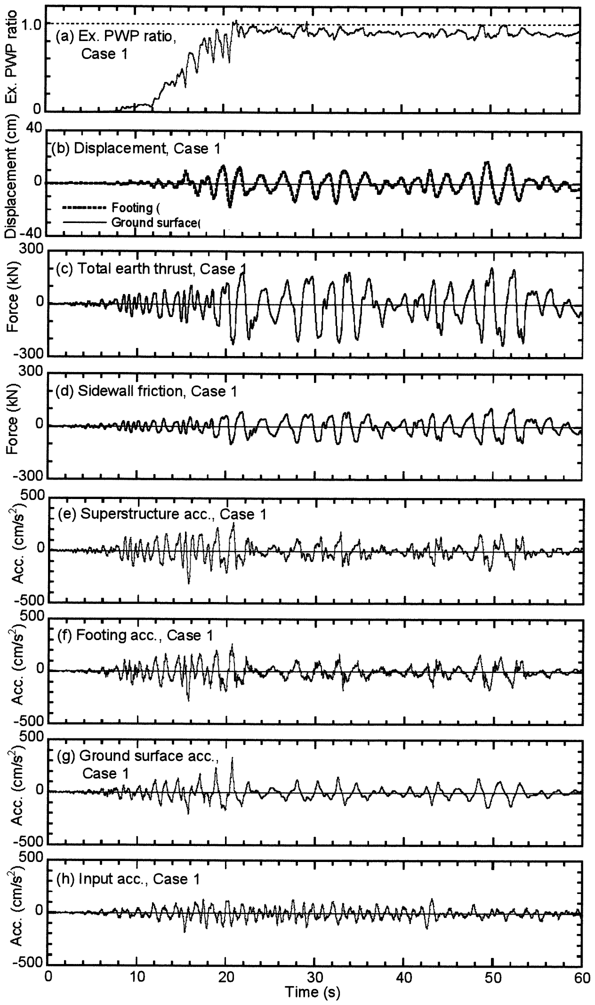

Figure 3 Time histories in shaking table tests in Case 1 (High flexural rigidity piles)

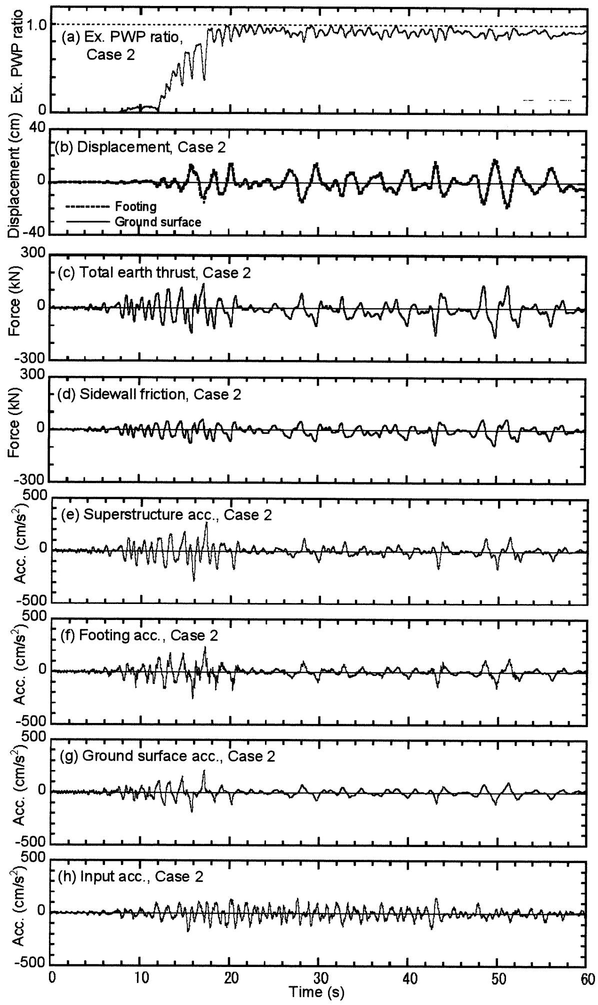

Figure 4 Time histories in shaking table tests in Case 2 (Low flexural rigidity piles)

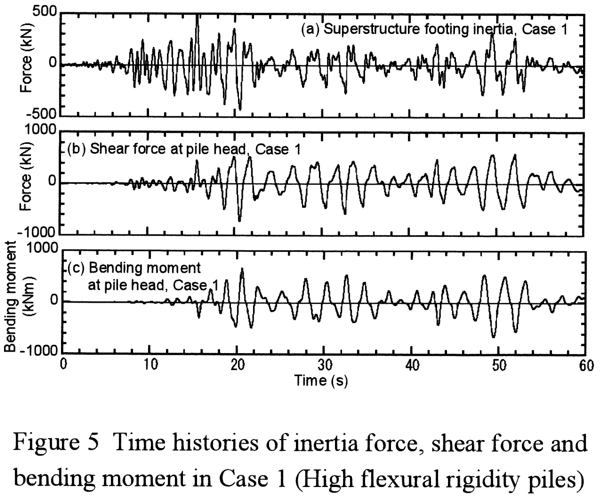

Figure 5 Time histories of inertia force, shear force and bending moment in Case 1 (High flexural rigidity piles)

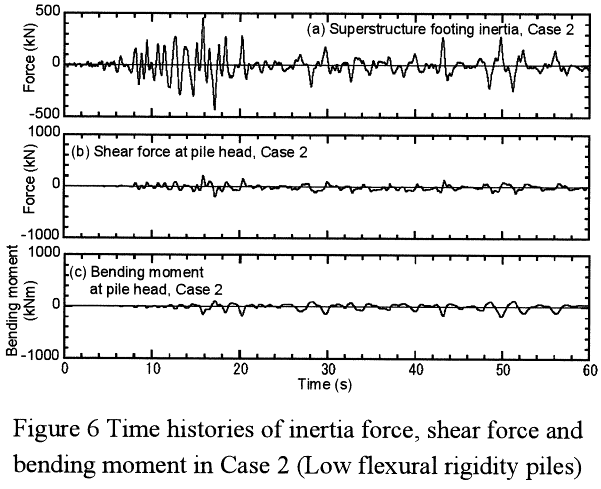

Figure 6 Time histories of inertia force, shear force and bending moment in Case 2 (Low flexural rigidity piles)

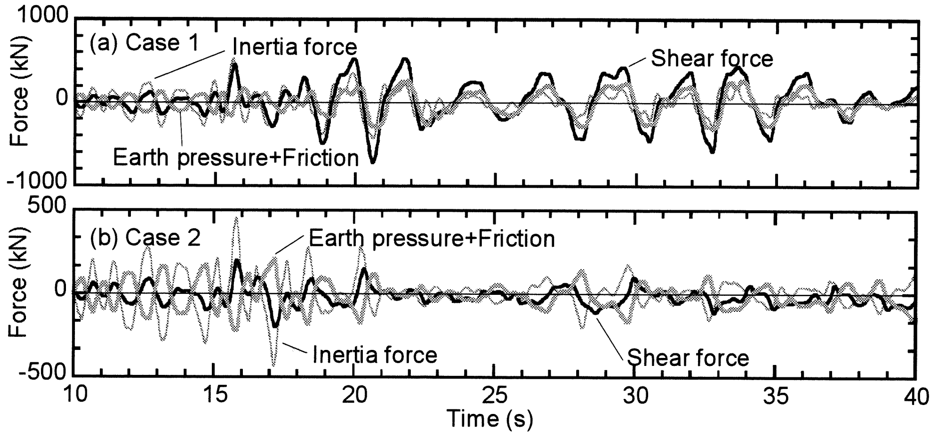

Figure 7 Time histories of the superstructure-footing inertia, lateral response, shear force at pile heads

sponse of the footing is out of phase by 180 deg with the superstructure footing inertia and has smaller amplitude than the superstructure footing inertia until about 20 s. Such tendencies show that the lateral response, which is generated as a reaction force of the superstructure footing inertia, counters the inertial force transmitted from the superstructure footing to the pile heads. Therefore, the shear force amplitude is less than the superstructure footing inertia amplitude. In contrast, the lateral response tends to be in phase with the superstructure footing inertia after 20 s. Consequently, the shear force amplitude increases.

In Case 2, the lateral response is out of phase by 180 deg with the superstructure footing inertia all the time. Therefore, the shear force amplitude is less than the superstructure footing inertia amplitude. That fact indicates that the phase difference between the inertia force and the lateral response of an embedded footing is an important point to evaluate pile stress.

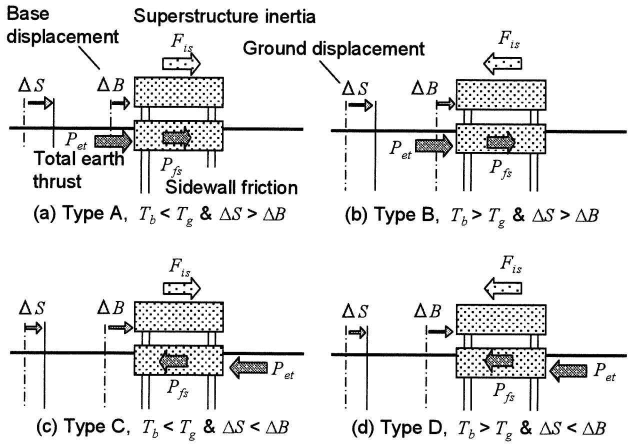

Figure 8 Phase between superstructure inertia and total earth pressure and sidewall friction

3.2 Phase between Superstructure Inertia and Lateral Response of Embedded Footing

A method for estimating the phase between superstructure inertia and total earth pressure has been proposed by Tamura et al. (2002) based on the natural period of the superstructure under the fixed footing condition T_b, the predominant period of the ground T_g, the soil displacement ΔS, and the footing displacement ΔB. Considering that the sidewall friction tends to be in phase with the total earth thrust, as shown in Figs. 3 and 4, the phase between the superstructure inertia and the lateral response of an embedded footing can be classified into the following four types.

a) The lateral response tends to be in phase with the superstructure inertia (Fig. 8(a)) if $T_b < T_g$ and $\Delta S > \Delta B$.

b) The lateral response tends to be out of phase by 180 deg with the superstructure inertia (Fig. 8(b)) if $T_b > T_g$ and $\Delta S > \Delta B$.

c) The lateral response tends to be out of phase by 180 deg with the superstructure inertia (Fig. 8(c)) if $T_b < T_g$ and $\Delta S < \Delta B$.

d) The lateral response tends to be in phase with the superstructure inertia (Fig. 8(d)) if $T_b > T_g$ and $\Delta S < \Delta B$.

Figure 9 shows the relation between the lateral response of the embedded footing and the superstructure inertia during soil liquefaction in Cases 1 and 2. The data in the first and third quadrants show that the lateral response tends to be in phase with the superstructure inertia, whereas those data in the second and fourth quadrants show that the lateral response tends to be out of phase by 180 deg with the soil inertia. A black line in the figure shows that the soil displacement ΔS is greater than the footing displacement ΔB; a blue line shows that ΔS is less than ΔB and a red line shows that ΔS is out of phase by 180 deg with ΔB.

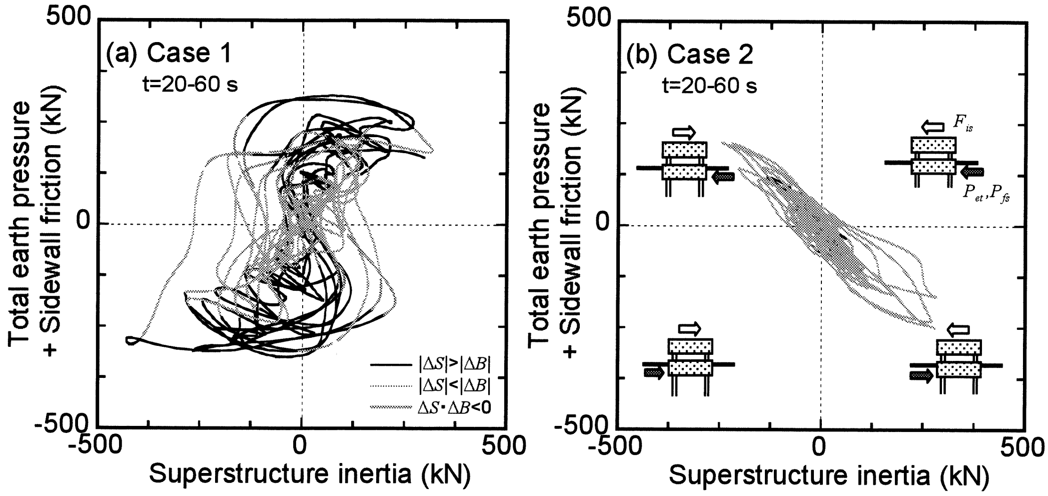

Figure 9 Relation between superstructure inertia and lateral response of the embedded footing

In Case 1, most test data are the first and third quadrants, indicating that the lateral response tends to be in phase with the superstructure inertia. For that reason, the shear force and bending moment increase rapidly after 8 s, as shown in Figs. 5(b) and 5(c). In addition, ΔS tends to be larger than ΔB when the total earth pressure reaches its peak. Moreover, T_b is shorter than T_g because of soil liquefaction. These conditions correspond to Type A in Fig. 8.

In Case 2, most test data are in the second and fourth quadrants, which indicates that the total earth pressure is out of phase with the superstructure inertia by 180 deg. Furthermore, ΔS tends to be smaller than ΔB when the total earth pressure reaches its peak. Considering that T_b is shorter than T_g, the conditions in Case 2 correspond to Type C in Fig. 8.

The difference in phase between Cases 1 and 2 described above depend on the amplitudes of the soil and footing displacement. The footing displacement amplitude tends to be less than the soil displacement in Case 1 because the footing was supported by the piles with high flexural rigidity. However, the footing displacement amplitude tends to be greater than the soil displacement in Case 2 because the footing was supported by piles with low flexural rigidity. These test results suggest that low flexural rigidity and high ductility capacity are important points to reduce pile stress in soil liquefaction.

4. CONCLUSIONS

This study investigated effects of the lateral response of an embedded footing consisting of earth pressure and sidewall friction on pile stress during soil liquefaction. Dynamic centrifuge tests were conducted on high bending rigidity and low bending rigidity piles. The following conclusions were drawn.

1. The lateral response of the embedded footing supported by the piles, with their high flexural rigidity, tends to be in phase with the superstructure inertia, thereby increasing the shear force and bending moment at the pile heads.
2. The lateral response of the embedded footing supported by the piles with low flexural rigidity tends to be out of phase by 180 deg with the superstructure inertia, thereby reducing the shear force and bending moment at the pile heads.
3. The centrifuge test results suggest that low flexural rigidity and high ductility capacity are important points to reduce pile stress during soil liquefaction.

Acknowledgements:

The authors are grateful for financial support from the Japan Iron and Steel Federation.

References:

Fujii, S., Isemoto, N., Satou, Y., Kaneko, O., Funahara, H., Arai, T. and Tokimatsu, K. (1998), "Investigation and analysis of a pile foundation damaged by liquefaction during the 1995 Hyogoken-Nambu earthquake," *Soils and Foundations, Special issue on Geotechnical Aspects of the 1995 Hyogoken Nambu Earthquake*, No. 2, 179-192.

Horikoshi, K., Tateishi, A., and Fujiwara, T. (1998), "Centrifuge Modeling of a Single Pile Subjected to Liquefaction-induced Lateral Spreading", *Soils and Foundations, Special issue on Geotechnical Aspects of the 1995 Hyogoken Nambu Earthquake*, No. 2, 193-208.

Oh-Oka, H., Fukui, M., Hatanaka, M., Ohara, J. and Honda, S. (1998), "Permanent deformation of steel pipe piles penetrating compacted fill at wharf on port Island", *Soils and Foundations, Special issue on Geotechnical Aspects of the 1995 Hyogoken Nambu Earthquake*, No. 2, 147-162.

Sato, M., Shamoto, Y. and Zhang, J. -M. (1995), "Soil Pile-structure during Liquefaction on Centrifuge," *Proc. 3rd*

International Conference on Recent Advances in Geotechnical Earthquake Engineering and Soil Dynamics, 1, 135-142.
Tamura, S., Tokimatsu, K., Uchida, A., Funahara, H. and Abe, A. (2002), "Relation between Seismic Earth Pressure Acting on Embedded Footing and Inertial Force Based on Liquefaction Test Using Large Scale Shear Box," *Journal of Struct. Constr. Engng.*, No. 559, 129-134. (in Japanese)
Tamura, S., Imayoshi, T. and Sakamoto, T. (2007), "Effects of seismic earth pressure and sidewall friction on pile stress during soil liquefaction," *4th International Conference on Earthquake Geotechnical Engineering,* Paper No. 1702, 2007. 7
Tokimatsu, K. and Asaka, Y. (1998), "Effects of liquefaction-induced ground displacements on pile performance in the 1995 Hyogoken-Nambu Earthquake," *Soils and Foundations, Special issue of Geotechnical Aspects of the 1995 Hyogoken Nambu Earthquake*, No. 2, 163-177.

Fifth International Conference on Urban Earthquake Engineering
March 4-5, 2008, Tokyo Institute of Technology, Tokyo, Japan

PRELIMINARY ANALYSIS ON SEISMIC RESPONSES OF QUAY WALL MODELED IN CENTRIFUGE SHAKING TABLE TESTS USING HILBERT-HUANG TRANSFORM

Chung-Jung Lee[1], Yu-Chen Wei[2], Huei-Tsyr Chen[3] and Jin-Hung Hwang[1]

1) Professor, Dept. of Civil Engineering, National Central University, Taiwan
2) Graduate student, Dept. of Civil Engineering, National Central University, Taiwan
3) Associate Professor, Dept. of Civil Engineering, National Central University, Taiwan
cjleeciv@cc.ncu.edu.tw, hwangjin@cc.ncu.edu.tw, chenht@cc.ncu.edu.tw, u0116000@cc.ncu.edu.tw

Abstract: In the paper, the empirical mode decomposition method combined with the Hilbert spectrum (HHT) is used to analyze the quay wall responses through the recording data set measured from the geotechnical centrifuge shaking table tests. The predominant frequencies identified by the three peaks on the amplification factor spectra are well consistent with the theoretical fundamental frequencies calculated from the corresponding measured shear wave velocities. The time histories of amplification factor and of instantaneous frequency prove that during earthquake shaking the higher the excess pore water pressure developed, the lower the soil stiffness becomes and the lower the instantaneous frequency of an embedded structure experiences.

1. INTRODUCTION

Site liquefaction or partial loss of soil strength during earthquakes will cause severe damages to geotechnical structure systems, i.e., settlements of buildings, lateral spreading of soils, and etc. Importance of liquefaction related damages to harbor facilities has been revealed during past earthquakes, from the 1995 Kobe earthquake and the 1999 Chi-Chi earthquake. Even after a close examination of the limited post-earthquake data provided by field investigation, it is still difficult to assess the response of the wall during earthquakes. Therefore, many researchers have experimentally conducted shaking table tests in geotechnical centrifuge as well as in 1g shaking table tests both with extensive instrumentation to investigate the effects of the large lateral soil movement, especially liquefaction-induced lateral spreading, on the failure and deformation of the quay wall. Extracting physically meaningful information as much as possible from the signals of the testing records of the shaking table test in geotechnical centrifuge is valuable to know well the response of a quay wall or of a sand deposit when backfills liquefied behind the wall during earthquakes.

A novel method, Hilbert-Huang-Transform (HHT), is a powerful tool for processing nonlinear and non-stationary signals (Huang et al. 1998). In earthquake engineering, the HHT has been successfully applied to analysis of earthquake ground motions, structure damage detection and health monitoring (Loh, et al. 2001). In the study characterization of quay wall response from the records measured with geotechnical centrifuge shaking tests with the aid of HHT data processing skill and analysis is performed and it will help understanding the behavior of quay wall during backfill liquefaction.

2. FUNDMENYAL OF HILBERT – HUANG TRANSFORM

A method of data processing (Huang et al., 1998), referred to as Hilbert-Huang-transform (HHT), has capability of analyzing non-stationary recordings for non-linearity characterization. The HHT method consists of two parts: empirical mode decomposition (EMD) and Hilbert spectral analysis (HSA). The purpose of EMD is to decompose a signal, $X(t)$, into a finite set of intrinsic mode functions (IMFs). The IMF is defined by the following two conditions:

(1). Over the entire time series, the number of extrema (either maxima or minima) and the number of zero-crossings must be equal or differ at most by one; and

(2). At any point, the mean value of the envelope defined by the local maxima and envelope defined by the local minima is zero.

An IMF represents a simple oscillatory mode similar to a component in the Fourier based simple harmonic function but more general. Any waveform can be decomposed as follows:

(1) Identify all the local extrema. Connect all the local maxima by a cubic spline function to produce the upper envelope, and repeat the same procedure for the local minima to produce the lower envelope.

(2) The mean of the upper and lower envelopes is a function of time. The difference between the data and the mean is the first IMF component, which contains the shortest period component of the wave. This process is called sifting process. The difference between the data and the mean after the first round sifting is treated as a new data set for the next round sifting process if the difference does not satisfy all the conditions set in the definition of an IMF. In practice, several iterative sifting processes are needed to single out the first true IMF component.

(3) One can then remove the first IMF component from the data to obtain the residue, which is treated as the new data and subjected to the same iterative sifting progress as describe previously. This process is repeated to obtain the all the IMF components. The sifting process is terminated if either the last IMF component or the residue is less than a predetermined value of consequence, or if the residue becomes a monotonic function from which no other IMF can be extracted.

By summing up all the calculated IMFs, we finally obtain

$$X(t)=\sum_{j=1}^{n}c_j(t)+r_n(t) \tag{1}$$

in which c_j is the j^{th} IMF component, n is typical around 10 for most earthquake ground motion records, and r_n is the residue. Each IMF component, c_j, admits a well behaved Hilbert Transform. Its Hilbert Transform is written as:

$$d_j(t)=\frac{1}{\pi}\int_{-\infty}^{+\infty}\frac{c_j(\tau)}{t-\tau}d\tau \tag{2}$$

and its analytic signal is defined as:

$$z_j(t)=c_j(t)+d_j(t)i=a_j(t)e^{i\theta_j(t)} \tag{3}$$

Then the instantaneous frequency, $\varpi_j(t)$, can be calculated:

$$\varpi_j(t)=\frac{d\theta_j(t)}{dt} \tag{4}$$

Both amplitude and frequency of each IMF are a function of time and can be represented as a function of time-frequency-amplitude in the three-dimensional space, which is named the Hilbert amplitude spectrum, $H(\varpi,t)$.

$$H(\varpi,t)=\sum_{j=1}^{n}a_j(t) \tag{5}$$

The predominant instantaneous frequency of a motion, $\tilde{\varpi}(t)$ is defined as the frequency with the largest amplitude in Hilbert amplitude spectra. That is:

$$\tilde{\varpi}(t)=\varpi\,|_{H(\varpi,t)=max(H(\varpi,t))} \tag{6}$$

In addition, the Hilbert marginal spectrum, $h(\varpi)$, which measures the total amplitude contribution from each frequency value, is defined as:

$$h(\varpi)=\int_0^T H(\varpi,t)dt \tag{7}$$

The Hilbert and marginal Hilbert amplitude spectra provide information similar to the Fourier amplitude spectrum which obtained from a short windowed Fourier transform. However, the shorter the window, the better the temporal localization of the Fourier amplitude spectrum, but the poorer the frequency resolution is.

3. GEOTECHNICAL CENTRIFUGE SHAKING TABLE TEST

A series of centrifuge modeling tests with an in-flight shaker were carried out in order to model both the deformation characteristics of backfill and the seismic responses of caisson-type walls embedded in soils. The dimensions of the test model as shown in Figure 1 are in centimeters, and the prototype dimensions in parentheses are in meters (Lee, 2005). The dimensions of the model walls are a height of 10 cm and a width of 8.33 cm; the wall was tested in a 120 g gravitation field, and hence represent prototype quay walls 12 m in height and 10 m in width sitting on a 6 m thick sand foundation, with a water table 1 m above the ground surface. Horizontal accelerometers (AH#) and vertical accelerometers (AV#) were installed in and on the quay wall and also embedded in the backfill at the positions shown in Figure 1.

A total of 6 accelerometers (2 vertical accelerometers on top of the wall, 2 horizontal accelerometers on the front face of the wall (on the sea side) at different elevations, and 2 accelerometers (1 vertical and 1 horizontal) embedded at the gravity center of the quay wall), were installed in or on the quay wall. The arrangement of the accelerometers on the wall was aimed at tracing the vibration modes of the wall. Three horizontal accelerometers (AH7, AH3, and AH9) were also embedded in the backfill, enabling the study of the responses of both the wall and the backfill. The horizontal displacement of the wall was monitored with a horizontal LVDT (LHT). Two vertical LVDTs (LV1 and LV2) recorded the vertical displacements on the two sides of the wall at the top of the wall; these measurements enabled the calculation of the time history of angular displacements of the wall during shaking. The vertical surface settlements of the backfill were recorded using two LVDTs (LV3 and LV4) as well.

The model quay wall has a unit weight of 19.6 kN/m^3. Six earth pressure cells (EPC), three of them mounted on the back face of each model wall (on the sand side) and the others mounted on the base, were used to measure the total contact pressures at various elevations and positions. Two pore water pressure transducers (PPTs) attached to the rear of wall (on the sand side) were located at the same elevations as the earth pressure cells, so as to be able to calculate the corresponding effective earth pressures on the wall. One PPT was installed at the center of the base of the wall. These three PPTs were used to record the time histories

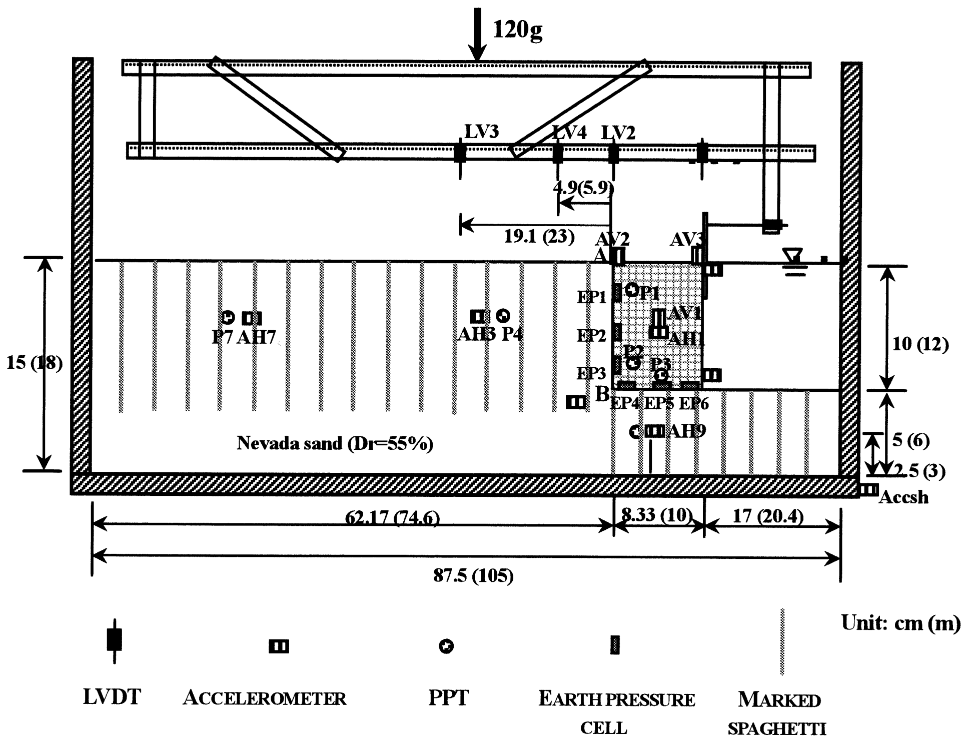

Figure 1 Set-up of model quay wall: model dimensions are in centimeters and prototype dimensions (in parentheses) are in meters

of pore water pressure on the wall. In addition, two PPTs (P4 and P7) were also embedded in the backfill to monitor the pore water pressure buildup in the free field. In an effort to quantify the rate of pore fluid dissipation within the model, pore fluids (Methocel cellulose ether dissolved in hot water) with viscosities higher than water was used. A total of four tests were conducted. The test conditions and the corresponding permeability and soil type in the prototype for each test are listed in Table1. We used these four models to characterize the responses of quay wall embedded in fine sand, coarse sand, fine gravel deposits, and in un-liquefied soils.

Table 1 Summary of test conditions

Test No.	Peak Acc. (g)	Viscosity of fluid	Prototype K, (m/s)	Soil types in prototype
QW TEST2	0.17	60 μ_{water}	3.3×10^{-3}	Coarse sand
QW TEST3	0.16	μ_{water}	6.6×10^{-3}	Coarse sand or fine gravel
QW TEST4	0.16	120 μ_{water}	5.5×10^{-5}	Fine sand or silty sand
QW TEST5	0.16	Dry sand	-	-

4. ANALYSIS OF TESTING RECORDINGS

To explore the effectiveness of the HHT on the analyzing the test results of the geotechnical centrifuge shaking table tests, the 3 acceleration recordings embedded in the three different permeabilities measured at AH7 (embedded depth of 6 m) from a distance of 47 m behind the quay wall (QWTEST2, QWTEST3, and QWTEST4) as shown in Figure 2 are first examined. The acceleration recording measured at AH3 from a distance of 9.6 m behind the quay wall (QWTEST5) is also shown in Figure 2 for comparison. These four recordings were located at the sites far enough from the wall, are equivalent to those of vibrations in free field. The measured amplitudes of acceleration for Model QWTEST2 and QWTEST4 decreases significantly after the 3rd cycle, but no obvious decrease was found in the magnitude for Model QWTEST3 and QWTEST5. The time histories of r_u ($\Delta u/\sigma'_v$) at the points (P7) in the vicinity of AH7 are shown in Figure 3 as well. Where Δu is the excess pore water pressure and σ'_v is the effective overburden pressure at the measured points. The values of r_u raised to 1.0 if the soil liquefied. The values of r_u oscillated between 1.0 and 0.84 throughout the shaking of Models QWTEST2 and QWTEST4, whereas on Model QWTEST3 they touched 1.0 (about at 3rd -6th cycle) and then oscillated but gradually returned to zero at the end of the shaking.

The backfill with lower permeability would experience slower dissipation of the excess pore water pressure (higher excess pore water pressure). After a comparison of Figure 2 and Figure 3, the decrease in the amplitude of acceleration is clearly related to the difficulty that shear waves have in traveling through liquefied soil due to significant reduction in stiffness and strength of the soil.

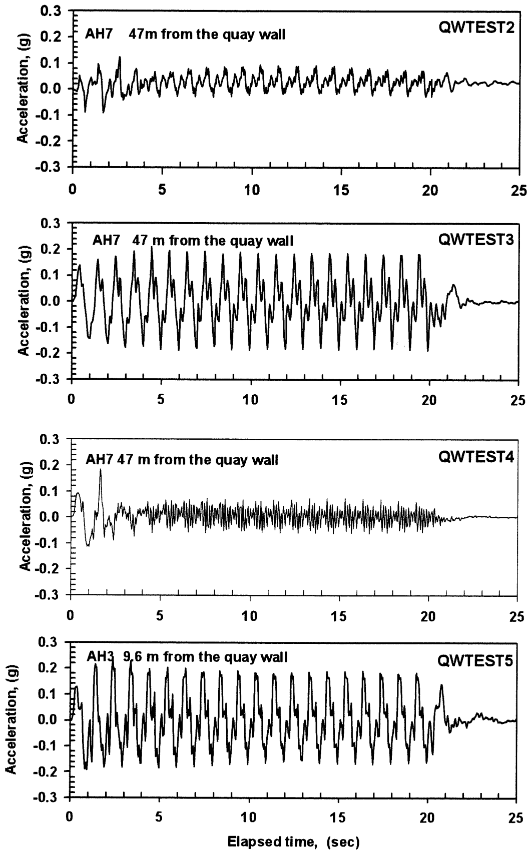

Figure 2 Acceleration time histories measured at AH7 and AH3

The average velocity, V_s, of shear waves propagated vertically in the backfill can be determined from the travel time required for the wave to traverse the distance between two accelerometers. The time histories obtained by the three accelerometers (AH3, AH7, and AH9) were used to determine the instants at which the waves arrival. Figure 4 displays the attenuations of the average shear wave velocities with the elapsed time. The characteristic site frequency, $f_s=V_s/4H$, which depends only on the thickness of soil deposit (H) and the shear wave velocity, provides a very useful indication of the frequency of vibration at which the most significant amplification can be expected. The thickness of the tested sand deposit is 18 m, therefore, the characteristic site frequencies with the elapsed time can be calculated with the measured shear wave velocity as shown in the right axis of Figure 4.

5. ANALYSIS OF MEASURED RECORDINGS USING HHT DATA ANALYSIS

Figure 5 demonstrates the time-frequency-amplitude distributions of Hilbert spectra of Accsh (input table motion) and AH7 (free field motion) for QWTEST4. The measured maximum amplitudes at Accsh maintained nearly a constant value throughout the entire test period, while those measured at AH7 declined significantly after the 2nd second due to occurrence of severe liquefaction as shown in Figure. 3 (r_u

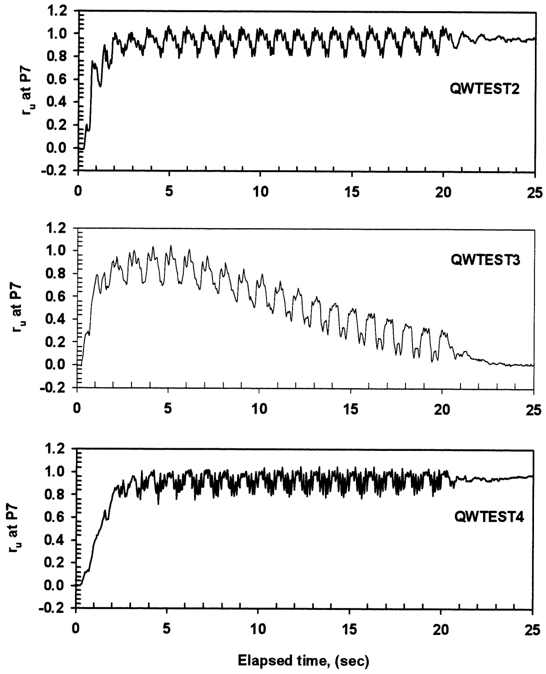

Figure 3 Time histories of r_u at P7

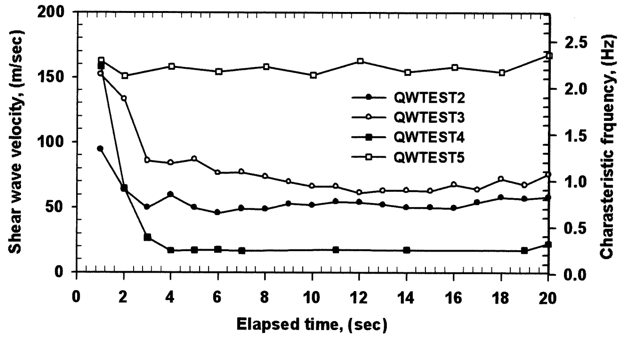

Figure 4 Time histories of shear wave velocity and characteristic frequency

raised to 1 and maintained 1 throughout the entire test period for QWTEST4). This demonstration has shown that the HHT can give much finer energy-time-frequency distribution properties comparing with the Fourier Transform. The HHT-based amplification factor in the study is defined as the ratio of marginal Hilbert amplitude spectra (the marginal Hilbert amplitude of AH7/ the marginal Hilbert amplitude of Accsh), which is similar to the ratio of Fourier amplitude spectra (the Fourier amplitude of AH7/ the Fourier amplitude of Accsh). Accsh is the input of base acceleration time history.

Figures 6(a) and 6(b) and Figures 7(a) and 7(b) show, respectively, the HHT-based amplification factor to the frequency and to the elapsed time for Accsh and AH7 in Model QWTEST4 and QWTEST3. Three frequencies at the peaks of the amplification factor spectra as shown in Figure 6(a) may determine the predominant frequency of the tested sand bed. Three frequencies are identified as 0.52,

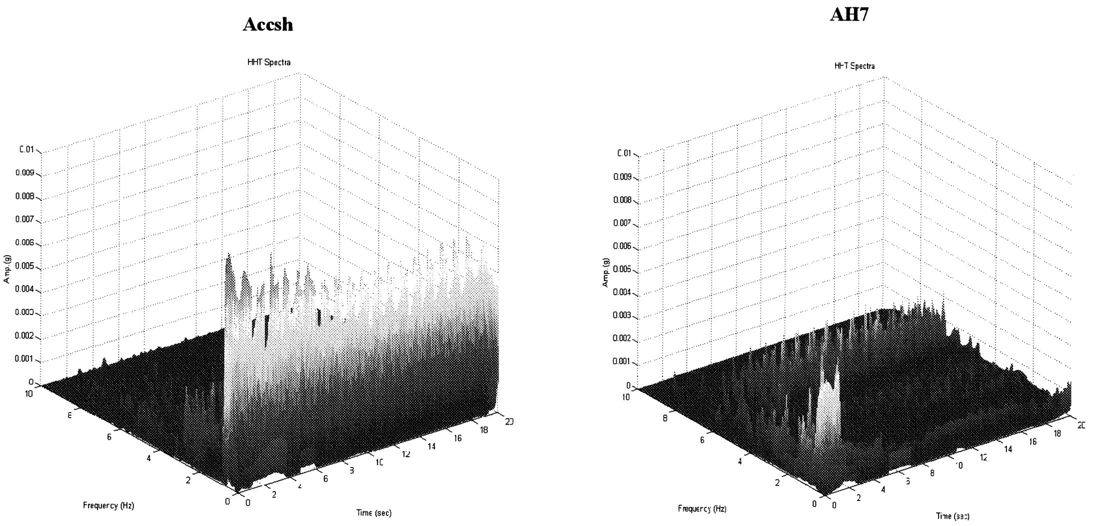

Figure 5 time-frequency-amplitude distributions of Hilbert spectra of Accsh and AH7 for QWTEST4

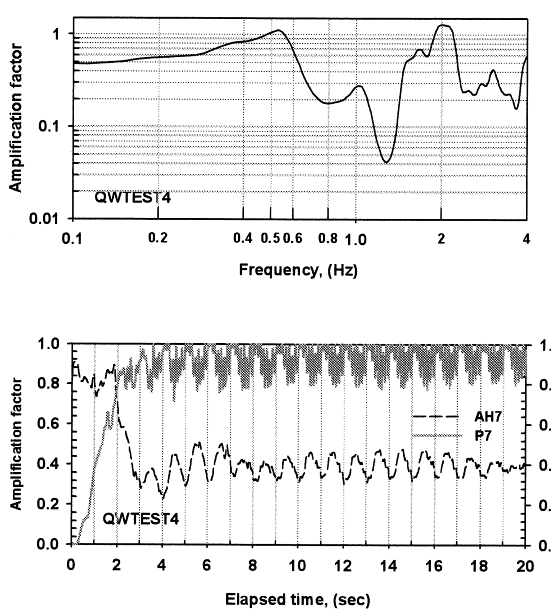

Figure 6 (a) HHT-based amplification factor for Accsh and AH7 (QWTEST4);
(b) HHT-based amplification factor and r_u to elapsed time (QWTEST4)

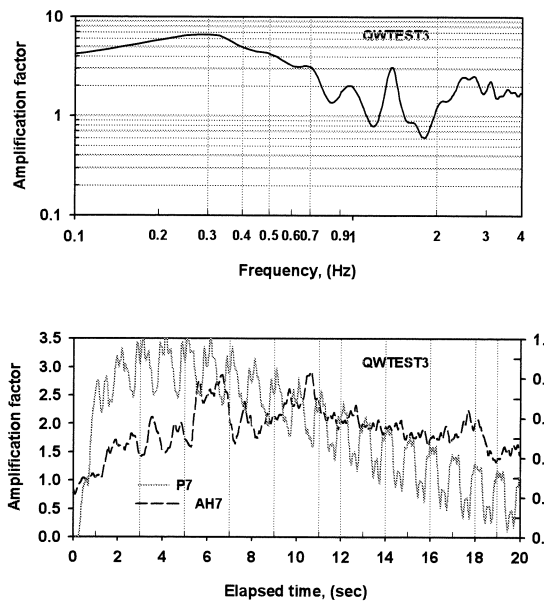

Figure 7 (a) HHT-based amplification factor for Accsh and AH7 (QWTEST3);
(b) HHT-based amplification factor and r_u to elapsed time (QWTEST3)

1.05, and 2 Hz, respectively. These predominant frequencies are close to the calculated characteristic frequencies (2.1, 1.0, and 0.3 Hz) at the beginning of, intermediate phase of, and final phase of shaking (shown in Figure 4). Figure 7(a) shows that the predominant frequencies are 0.94, 1.4, and 2.4 Hz as well. We can conclude that the excess pore water pressure ratio, r_u, dominates the response of the tested sand bed. Figure 6(b) demonstrates that once the value of r_u reached 0.8, the amplification factor declined significantly due to slower dissipation of the excess pore water pressure (higher excess pore water pressure) resulting in that shear waves have difficulty in traveling through liquefied soil due to significant reduction of soil in stiffness and strength (V_s=20~30 m/sec). Figure 7(b) demonstrates the time histories of the amplification factor measured in QWTEST3. It is very obvious that even the amplification factors at the beginning of shaking are nearly the same as those in QWTEST4, however, they continuously increase till the 8th second and then have a small decrease in the later shaking. The smallest measured shear wave velocities in QWTEST3 as shown in Figure 4 is about 80 m/sec (much larger than the shear wave velocity of 20 m/sec measured in QWTEST4) in the final phase of shaking. Moreover, the oscillation of the amplification factor with the time is opposite to the oscillation of r_u during the shaking in both Figure 6(b) and Figure 7(b). The peak amplification factor appears at the lowest value of r_u, , and vice versa, as shown obviously in both of Figures 6(b) and 7(b) due to dilation of sand during shearing. The time history of amplification factor can give one of cost-effective approaches for detecting occurrence of liquefaction in a soil deposit during earthquakes. In addition the HHT-based amplification factor may give an alternative way to evaluate the degradation of the dynamic soil properties during shaking, especially liquefaction occurring. Figure 8 is the FFT-based amplification factor at AH7 for QWTEST4. After a comparison of Figure 6(a) and Figure 8, we see that FFT-based amplification factor cannot identify the frequencies of 0.52, 1.05, and 2 Hz as those indicated in Figure 6(a). This distortion of frequency may result from that the Fourier amplitude spectrum defines harmonic components globally and thus yields average characteristic over the entire duration of the data. Figure 9 is the HHT-based amplification factor to the elapsed time for QWTEST5. The amplitude of amplification factor continuously oscillated in each cycle, however, when neglecting the part of fluctuation in the amplification factor no obvious changes is found due to none liquefaction occurrence during the shaking.

Figure. 10 shows the HHT-based instantaneous frequency to the elapsed time measured at the gravity center of Quay wall (AH1) for Model QWTEST4. The instantaneous frequency oscillated between 1.2 Hz and 0.6 Hz in the intermediate to final phase of shaking (the 6^{th} - 20^{th} second). The value of r_u oscillates correspondingly as well but with a phase difference of 180 degree. The peak instantaneous frequency appears at the instant when the lowest value of r_u appears, and vice versa. This may infer that soil stiffness changes with the magnitude of excess pore water pressure. In soil deposits the higher the excess pore water pressure developed, the lower the soil stiffness becomes and the lower the instantaneous frequency of a structure embedded in is expected. The HHT provides an opportunity for discerning the instantaneous frequency at any instant during shaking. We may be possible to take this advantage to evaluate the degradation of the soil dynamic properties during shaking.

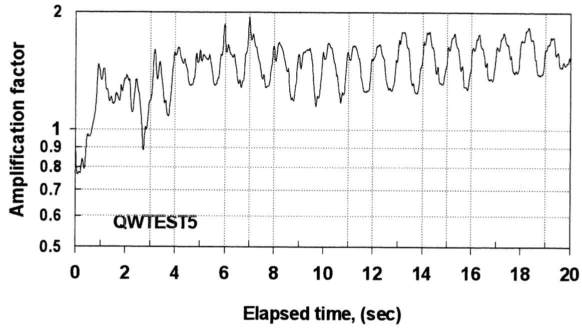

Figure 9 HHT-based amplification factor to elapsed time (QWTEST5)

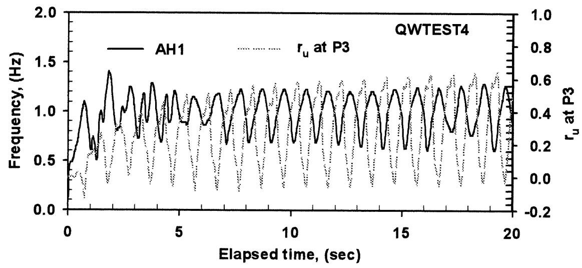

Figure 10 HHT-based instantaneous frequency to elapsed time

6. CONCLUSIONS

The HHT data processing procedure is successfully applied to characterize the quay wall response from the records measured with a series of geotechnical centrifuge shaking tests. The amplification factor is defined as the ratio of marginal Hilbert amplitude spectra for helping identifying the instant of backfill liquefaction during shaking. The predominant frequencies identified by the three peaks on the amplification factor spectra are well consistent with the theoretical frequencies calculated from the corresponding measured shear wave velocities. The time histories of amplification factor and of instantaneous frequency prove that the higher the excess pore water pressure developed, the lower the soil stiffness becomes and the lower the instantaneous frequencies of an embedded structure are.

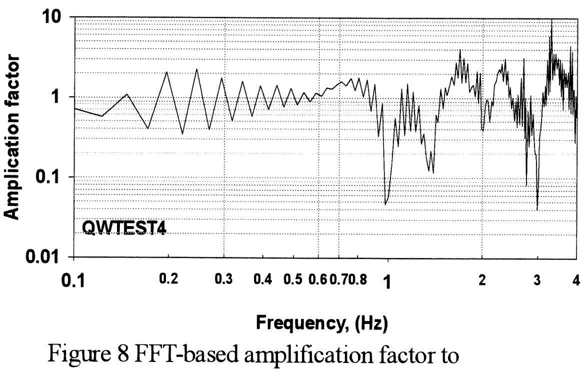

Figure 8 FFT-based amplification factor to frequency (QWTEST4)

References:

Huang, N.E., Shen, Z., Long, S.R., Wu, M.C., Shih, H.H. Zheng, Q., Yen, N.C., Tung C.C., and Liu, H.H. (1998), "The Empirical Mode Decomposition and the Hilbert Spectrum for Nonlinear and Non-stationary Time Series Analysis," *Proc. Royal Society London*, **454**, 903-995.

Loh, C.H., Wu, T.C., and Huang, N.E. (2001), "Application of the Empirical Mode Decomposition-Hilbert Spectrum Method to Identify Near-Fault Ground Motion Characteristics and Structure Response," *Bulletin of the Seismological Society of America*, **91**(5), 1339-1357.

Lee, C.J. (2005), "Centrifuge modeling on the behavior of caisson-type quay walls during earthquakes," *Soil Dynamics and Earthquake Engineering*, **25**, 117-131.

Fifth International Conference on Urban Earthquake Engineering
March 4-5, 2008, Tokyo Institute of Technology, Tokyo, Japan

EFFECTS OF SHEAR STRAIN INCREASE ON p-y SPRING FOR PILE FOUNDATIONS IN NON-LIQUEFIED GROUND

Hiroko Suzuki[1] and Kohji Tokimatsu[2]

1) Assistant Professor, Department of Architecture and Building Engineering, Tokyo Institute of Technology, Japan
2) Professor, Department of Architecture and Building Engineering, Tokyo Institute of Technology, Japan
hsuzuki@arch.titech.ac.jp, kohji@o.cc.titech.ac.jp

Abstract: Effects of shear strain increase on p-y spring for pile foundations are estimated through large shaking table tests conducted on a soil-pile-structure model. In the shaking table tests, degradation of soil stiffness occurs, accompanied by changes in the predominant period of soil. The shear modulus ratio G/G_0 computed from the predominant period of soil decreases to 0.2 at a shear strain of 1 %. To estimate changes in p-y spring with respect to the shear strain, the pseudo static analysis is conducted based on the test results. When the shear strain is smaller than 1 %, the scaling factor for p-y spring β is almost 1. When the shear strain reaches 1 %, β decreases to 0.5, which is twice as large as G/G_0.

1. INTRODUCTION

To establish reliable seismic design of pile foundations, it is important to clarify kinematic forces defined as p-y springs. It is known that the p-y spring changes due to soil liquefaction, and then many studies have been conducted to estimate the p-y spring in liquefied ground based on physical model tests (e.g., Boulanger et al. 2003 and Tokimatsu et al. 2002). In reality, an increase in shear strain occurs even in no-liquefied ground during strong ground shaking, which might have induced changes in the p-y spring for piles. Studies, which have dealt with the change in the p-y spring in non-liquefied ground, however are rare.

The object of this study is to estimate effects of shear strain increase on the p-y spring for pile foundations through large shaking table tests, which were conducted on a pile-structure model in a dry sand deposit. In the shaking table test, an increase in shear strain was induced due to strong ground shaking. Pseudo static analysis is conducted to investigate the change of p-y spring with respect to the shear strain.

2. LARGE SHAKING TABLE TESTS

2.1 Soil-pile-structure model in shaking table tests

Large shaking table tests were conducted using the shaking table facility at the National Research Institute for Earth Science and Disaster Prevention in Japan (Tokimatsu et al., 2005). Figure 1 shows a soil-pile-structure system on the shaking table used in the tests. The soil-pile-structure system was constructed in a laminar shear box with dimensions of 5.6 m x 12.0 m x 3.5 m on the shaking table.

A soil profile prepared in the laminar shear box was of homogeneous layer with a thickness of 4 m. The sand used was Nikko Sand (e_{max} = 0.98, e_{min} = 0.65, D_{50} = 0.42 mm). After constructing piles in the laminar box, dry sand was air-pluviated. The relative density of sand was about 70 %. A pile group consisted of 2x2 steel piles 4 m long. Each pile had a diameter of 165.2 mm with a 3.7 mm wall thickness. The tips of piles were connected to the base of the laminar shear box with pin joints and their heads were fixed to a steel foundation of 20.6 kN. The foundation carried a steel superstructure of 139 kN. The soil-pile-structure system was densely instrumented with accelerometers, displacement transducers, and strain gauges, as shown in Figure 1.

In the shaking table tests, an artificial ground motion called Rinkai having a maximum acceleration scaled to 0.3, 2.4 and 4.8 m/s^2 was used as an input motion. The shaking table tests are, hereafter, called AS30, AS240 and AS480, corresponding to the maximum acceleration of the input

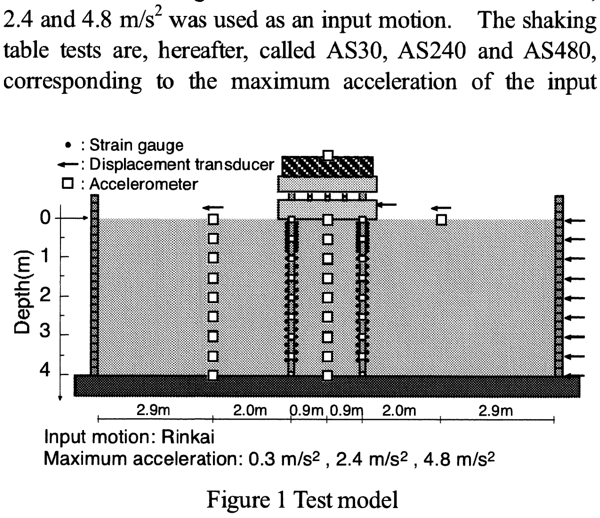

Figure 1 Test model

motion.

2.2. Bending strains in pile during shaking

Figures 2-4 show time histories of the bending strains at pile heads, displacement of ground surface and accelerations of superstructure and shaking table in AS30, AS240 and AS480. The higher the input motion, the larger the superstructure accelerations and the ground surface displacement (Figures 2-4(b)(c)). In particular, the ground surface displacement in AS480 is significantly larger than others. The bending strains at pile heads increase with increasing superstructure acceleration in all the tests (Figures 2-4(a)(c)). In AS480, the bending strain increases significantly at about 23 s and probably yields with an accumulated residual component (Figure 4(a)). In contrast, in AS30 and AS240, the piles remain elastic (Figures 2 and 3(a)).

Figures 5 and 6 show distributions of bending strains and displacements in AS30, AS240 and AS480 at instances, at which the bending strain takes a large value, i.e., 23 s for AS480. The magnitude of inertial force induced by the superstructure and foundation accelerations is also shown in Figure 5. The depth, at which the inflection point in bending strain occurs, increases with increasing input ground motion. This suggests that the inertial force from the superstructure and foundation is transmitted to the lower parts of the pile as the input ground motion increases. Considering that the magnitudes of the inertial force in AS240and AS480 are almost the same as shown in Figure 5, the ground displacement increase might have affected the difference in pile strains between the two tests. Figure 6 shows that the pile displacement is larger than ground displacement in the three tests, suggesting that the ground resists the pile deformation.

2.3 Change in soil stiffness

To estimate the ground displacement increase during strong ground shaking, Figure 7 shows the time histories of shear strain at four depths in AS480. The shear strain of soil is computed from the soil displacement given by the integration of the observed soil acceleration. The shear strains at all four depths take peaks/increase abruptly at about 15 s The value of shear strain reaches 1 % even at a depth of 3.5 m (Figure 7(d)), at which it is the smallest among the four depths. Figure 8 compares the shear strain at the middle of the soil layer (a depth of 2.0 m) in AS30, AS240 and AS480. The shear strain in AS30 is almost the same throughout shaking. The shear strain in AS240 increases abruptly in 15 s similarly to that in AS480; nonetheless, it is about 0.1 %.

To investigate the effects of shear strain increase on soil stiffness, Figure 9 shows changes in amplitudes of the ground surface acceleration with respect to the input motion in AS30, AS240 and AS480. The amplitude is presented in three time durations, i.e., 0-10 s, 20-30 s and 40-50 s. The predominant period in AS30 does not vary with time, whereas those in AS240 and AS480 vary significantly with time. Namely, the predominant periods in AS240 and AS480 are longer with smaller peaks in 20-30 s than those in 0-10 s. As shown in Figure 8 (b)(c), the shear strains in AS240 and AS480 increase abruptly in about 15 s and then

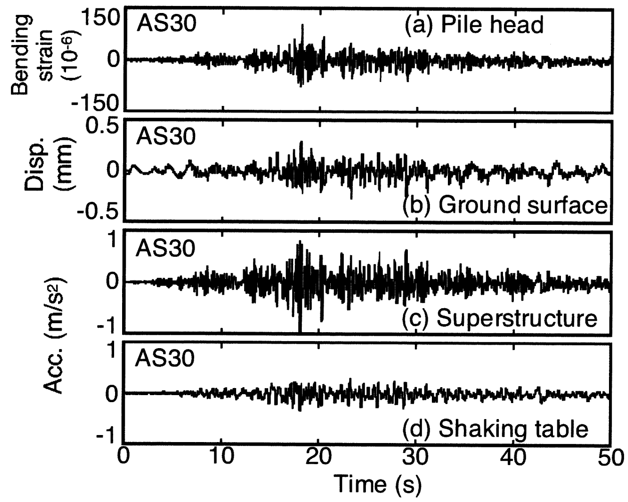

Figure 2 Time histories of major values in AS30

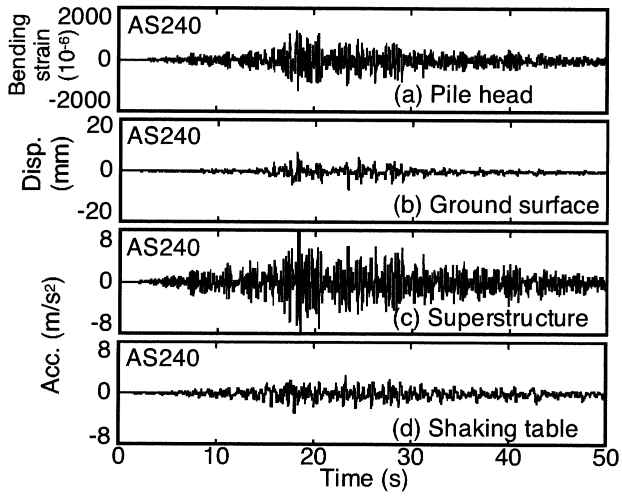

Figure 3 Time histories of major values in AS240

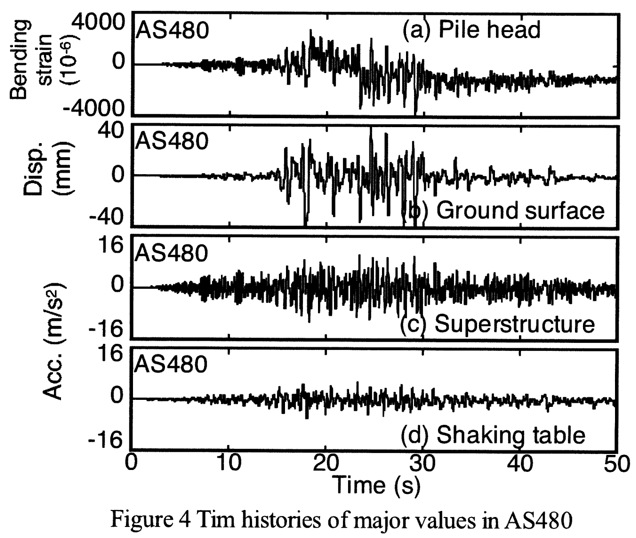

Figure 4 Tim histories of major values in AS480

the degradation in soil stiffness occurs. The difference in predominant periods between 0-10 s and 20-30 s is more significant in AS480 than in AS240, corresponding to the shear strain level. It is interesting to note that the predominant periods in 40-50 s of AS240 and AS480 are almost the same with those in 0-10 s of the same tests. This indicates that the soil stiffness recovers from the degradation to the original value when the shear strain decreases.

To estimate the degradation of soil stiffness, shear modulus ratios G/G_0 in five time durations of ten seconds, i.e., 0-10 s, 10-20 s, 20-30 s, 30-40 s and 40-50 s in AS30, AS240 and AS480 are computed based on the following equation:

$$\frac{G}{G_0} = \left(\frac{T_0}{T}\right)^2 \tag{1}$$

in which T is the predominant period in each time duration and T_0 is the predominant period under the small strain level.

Figure 10 shows the relation between modulus ratio and effective shear strain for the five time durations in the three tests. The effective strain is given as 0.65 times the maximum shear strain in the soil for the corresponding time duration. The lines drawn in the figures are typical laboratory test results for sands. The data from the shaking table tests falls within the area bounded by the two lines regardless of the input motion, indicating that the computed modulus ratio is appropriate. The computed modulus ratio decreases from 1.0 to 0.2 with increasing soil shear strain; i.e., it is 1.0 in AS30, 0.4 in AS240 and 0.2 in AS480. This confirms that the strong ground shaking induces the degradation in soil stiffness.

3 EFFECTS OF SOIL STIFFNESS DEGRADATION ON p-y SPRING IN PSEUDO STATIC ANALYSIS

To estimate effects of the degradation in soil stiffness on the p-y spring, pseudo static analysis is conducted on a soil-pile-structure model. Simplified pseudo static methods using the p-y spring are based on the following equations (Architectural Institute of Japan 1988, 2001 and Railway Technical Research Institute 1997):

$$EI\frac{d^4y}{dx^4} = -p \tag{2}$$

$$p = k_h B\left(y - y_g\right) \tag{3}$$

in which E and I are the Young's modulus and the moment of inertia of a pile, y and y_g are the horizontal displacement of a pile and ground, x is the depth, p is the subgrade reaction, k_h is a coefficient of horizontal subgrade reaction, and B is a pile diameter. The coefficient of subgrade reaction k_h is given by the following equation (Tokimatsu et

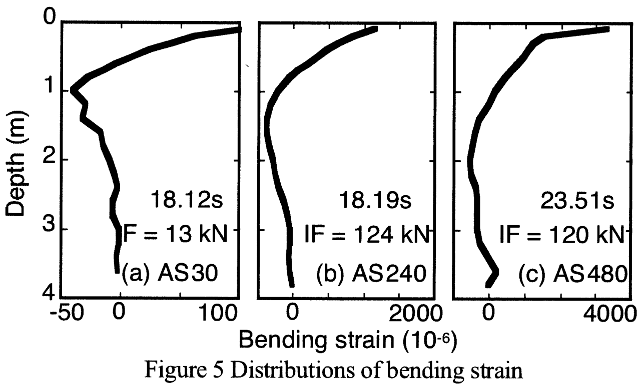

Figure 5 Distributions of bending strain

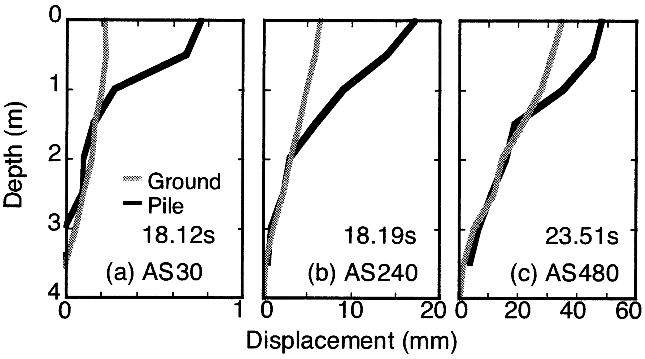

Figure 6 Distributions of pile and ground displacements

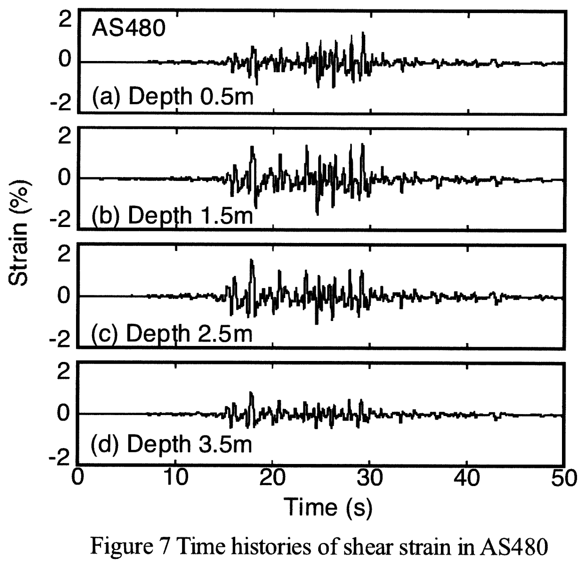

Figure 7 Time histories of shear strain in AS480

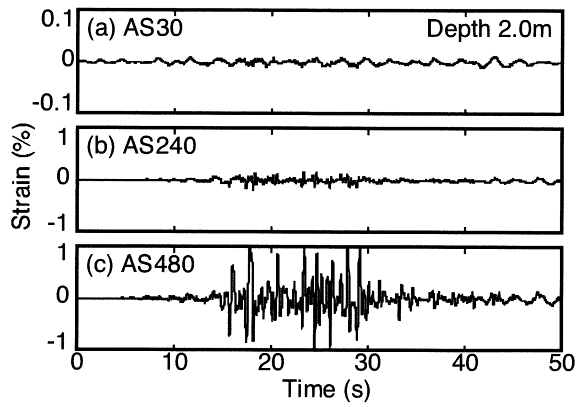

Figure 8 Time histories of shear strain

al. 2002):

$$k_h = k_{h1}\frac{2}{1+|y_r/y_1|}\beta \qquad (4)$$

in which k_{h1} is the reference value of k_h, defined as a function of N-value. y_1 is the reference value of y_r and β is a scaling parameter for a reduction in coefficient of subgrade reaction.

Figure 11 shows a soil-pile-structure model in the analysis. It is assumed that the inertial force and the ground displacement are equal to the observed values in the tests. k_{h1} is given by the N-value computed from the CPT-resistances measured prior to each shaking table tests and y_1 is one percent of a pile diameter. To take the degradation of soil stiffness into account, β is assumed to be equal to 1.0 in AS30, 0.4 in AS240 and 0.2 in AS480 based on G/G_0 in Figure 10.

Figure 12 compares the estimated and observed bending strains in AS30, AS240 and AS480. The estimated bending strain in AS30 is in good agreement with the observed one, whereas those in AS240 and AS480 are larger than the observed ones. This indicates that the p-y spring defined by the coefficient of subgrade reaction is probably softer in the analysis than in the tests.

Based on the abovementioned analysis results, β is assumed to be equal to 1.0 in AS240 and 0.5 or 1.0 in AS480. Figure 13 shows the estimated and observed bending strains in AS240 and AS480. In AS240, the estimated bending strain with β of 1.0 is in good agreement with the observed one. This suggests that the p-y spring does not change under the shear strain level of 0.1 %. In AS480, the estimated bending strain with β of 0.5 is in good agreement with the observed one. This indicates that the p-y spring decreases to 0.5 under the shear strain level of 1 % but that the scaling factor β is about twice the modulus ratio G/G_0.

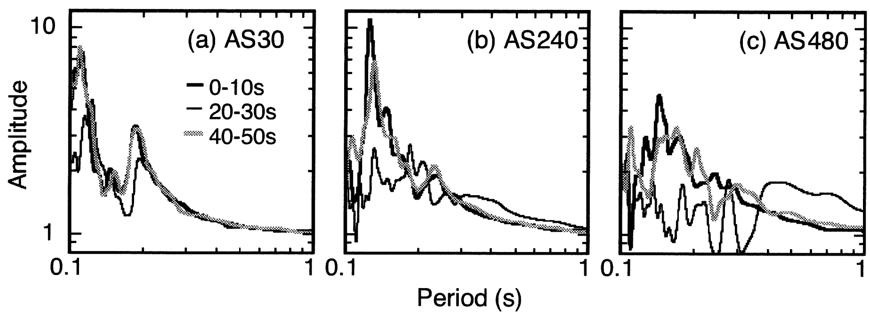

Figure 9 Amplitude of soil surface with respect to input motion

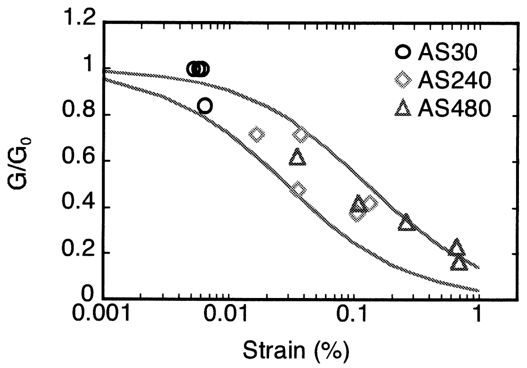

Figure 10 Relation of G/G_0 and shear strain

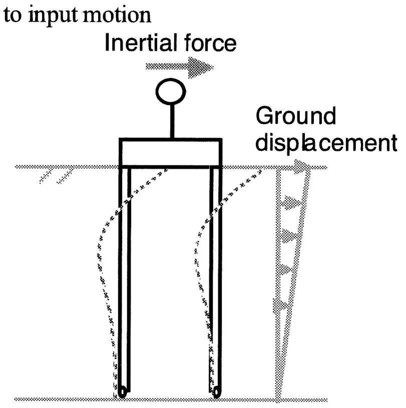

Figure 11 Soil-pile-structure model

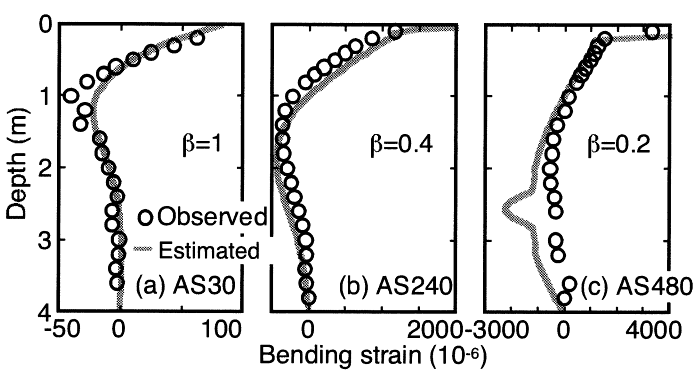

Figure 12 Comparison of estimated and observed bending strain

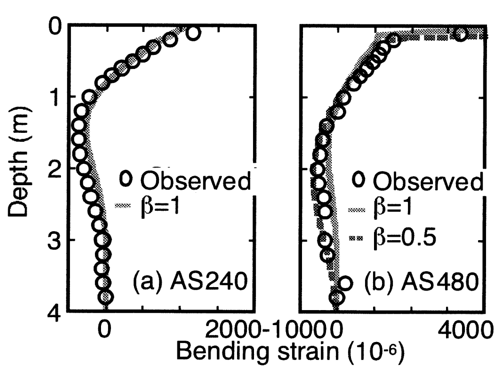

Figure 13 Comparison of estimated and observed bending strain in AS240 and AS480

4. CONCLUSIONS

The effects of shear strain increase on the p-y spring are estimated based on large shaking table tests and pseudo static analysis. The results have shown the following:

1) In the shaking table test, strong ground shaking induces a significant increase in shear strain of soil, accompanied by changes in the predominant period of soil. The relation of modulus ratio G/G_0, which is computed from the change in the predominant period of soil, with shear strain corresponds to that of typical laboratory test results for sands.

2) When the shear strain of soil is smaller than 1 %, the scaling factor for p-y spring β is almost 1. When the shear strain reaches 1 %, β decreases to 0.5, which is about twice the shear modulus ration G/G_0.

Acknowledgements:

The study described herein was made possible through Special Project for Earthquake Disaster Mitigation in Urban Areas, supported by the Ministry of Education, Culture, Sports, Science and Technology (MEXT). The authors express their sincere thanks to the above organization.

References:

Architectural Institute of Japan (1988, 2001), "Recommendations for design of building foundations" (in Japanese).

Boulanger, R. W., Kutter, B. L., Brandenberg, S. J., Singh, P. and Chang, D. (2003), "Pile foundations in liquefied and laterally spreading ground during earthquakes: Centrifuge experiments & analyses", Center for Geotechnical modeling, Department, of Civil Engineering, UC, Davis, Report No. UCD/CGM-03/01.

Railway Technical Research Institute (1997), "Foundation design codes for railway structures" (in Japanese).

Tokimatsu, K., Suzuki, H. and Saeki, E. (2002), "Modeling of horizontal subgrade reaction of pile during liquefaction based on large shaking table", *Journal of Structural and Construction Engineering*, AIJ, **559**, 135-141 (in Japanese).

Tokimatsu, K., Suzuki, H. and Sato, M. (2005), "Effects of dynamic soil-pile-structure interaction on pile stresses, *Journal of Structural and Construction Engineering"*, AIJ, **587**, 125-132 (in Japanese).

Fifth International Conference on Urban Earthquake Engineering
March 4-5, 2008, Tokyo Institute of Technology, Tokyo, Japan

MECHANICAL BEHAVIOR OF PILE-SHEET PILE COMBINED FOUNDATION SUBJECTED TO LATERAL AND MOMENT LOADING

Jun Izawa[1), Kazunobu Takahashi[2), Yoshirou Ishihama[3) and Jiro Takemura[4)

1) Assistant Professor, Department of Civil and Environmental Engineering, Tokyo Institute of Technology, Japan
2) Graduate student, Department of Civil and Environmental Engineering, Tokyo Institute of Technology, Japan
3) Steel R&D Laboratory, Nippon Steel Corporation
4) Associate Professor, Department of Civil and Environmental Engineering, Tokyo Institute of Technology, Japan
jizawa@cv.titech.ac.jp, k-takahashi@cv.titech.ac.jp, ishihama.yoshiroh@nsc.co.jp, jtakemur@cv.titech.ac.jp

Abstract: Pile-Sheet pile foundation has been developed to increase the horizontal bearing capacity of a usual pile foundation in this research. This paper describes mechanical behavior of the pile-sheet pile foundation. In order to discuss the effect of the sheet piles on the performance of small scale pile foundation subjected to horizontal and moment loading in cyclic manner, series of centrifuge model test has been conducted to study the effect of sheet piles. In the centrifuge tests, four types of foundations were modeled to compare the foundation type to study the effect of rigidity and number of sheet piles.

1. INTRODUCTION

In the design of foundation structures, various factors are considered, such as geotechnical conditions (soil profiles, strengths and stiffness, ground water, etc.), loading conditions (types of superstructure, dead weight, earthquake, wind, etc.), working conditions (space for construction, surrounding environment, etc.). According to these factors, a foundation type is selected to secure the safety and economical construction. Among various foundation types, such as slab foundation, caisson foundations, pile foundation, steel sheet pipe pile foundation, diaphragm wall foundation, the pile foundation has been the most commonly used, since it is applicable for various soil conditions and various types and sizes of superstructure.

Pile foundation should stand for the various external loading. The critical one is horizontal loading by earthquake, especially for the foundation of tall superstructures, such as, bridge pier, high rise building, transmission, tower. According to the seismic design of foundation of the Design Specifications of Highway Bridges (JRA, 2002), yielding of foundation is defined as the condition when the horizontal displacement of the points at which an inertial force from the super structure acts increases remarkably. The yielding is caused by either yielding of foundation materials, yielding of ground material, lifting of foundation or their combination. As the allowable displacement of foundation, the rotation or inclination of footing is only considered, 0.02 radian, which should be avoided as a result of yielding. For the pile foundation, the first two causes are considered as main possible reasons, i.e., failure of piles, and bearing failure at the pile tip. However, for the pile foundation with a small footing, which is the case with limited construction space for the small scale structure, it becomes difficult to secure the requirement about the rotation of the foundation, because the narrow spacing of the piles cannot have sufficient moment resistances (Figure 1).

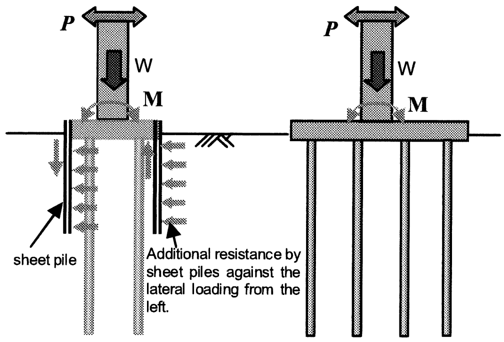

(a) Narrow foundation with sheet pile (combined foundation)
(b) Wide foundation having large resistance against moment load

Figure 1 Combined foundation showing the additional resistance by sheet piles

Combined foundations in which a flexible sheet piles surround the slab or footing have been developed to increase the bearing capacity of the existing foundation as a retrofitting method for satisfying a new design code or as a new type of foundation applicable to difficult design conditions (Koda, et al., 2003; Nishioka et al., 2004).

In this research a series of centrifuge model test has been conducted to study the effect of sheet piles on the performance of small scale pile foundation subjected to horizontal and moment loading in cyclic manner. From the test results, the failure mechanism and the effect of the sheet piles on the bearing behavior were discussed.

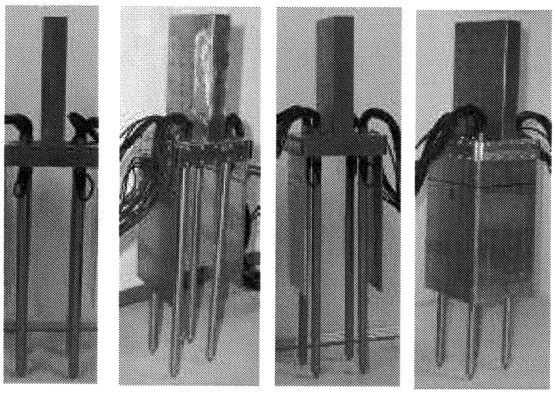

Photo 1 Model foundations used for the centrifuge tests

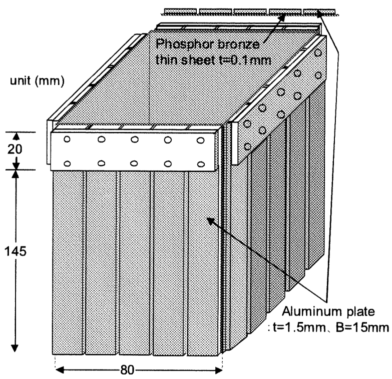

Figure 2 Model sheet piles used in CF-4SP

2. CENTRIFUGE MODEL TESTS

2. 1. Model foundations:

Four types of foundations were modeled as shown in Photo 1 and Figure 2.

1) PF: pile foundation;
2) CF-2P: pile foundation with thin aluminum plate at the two side of the square footing;
3) CF-2SP: pile foundation with model sheet piles at the two sides of the footing;
4) CF-4SP: pile foundation with the model sheet piles at four sides of the footing.

All four foundations have four identical piles made of stainless steel tube of 10mm outer diameter and 0.5mm thickness with square arrangement with 50mm in spacing. The four piles are rigidly fixed to a square footing with the dimension of 80mm*80mm*20mm. On top of the footing, fixed is a 120mm height stainless steel thick plate as a superstructure, to which horizontal load is applied at different heights. Mass of the footing and superstructure, which is the dead weight to the piles, is 2.2kg (110kg in 50g).

Two types of model sheet pile were used. One, used in CF-2P, is 1.5mm thick aluminum plates with the same flexural rigidity (EI) in the vertical and horizontal directions and the other, used in CF-2SP and CF-4P, 1.5mm thick aluminum strips attached to a thin phosphorus bronze sheet (t=0.1mm). The vertical EI of the latter is the same as the former, but the horizontal EI is less than one thousands of the former, which is similar to the real steel sheet piles used for the combined foundations. Specifications of the model pile and sheet piles are given in Table 1(a)~(c).

Table 1(a) Specifications of model pile

Material	Stainless steel
Diameter or width (D)	10 mm
Thickness (t)	0.5 mm
Flexural rigidity (EI)	33.8 Nm^2

Table 1(b) Specification of model sheet piles for CF-2P

Material	Aluminum
Width (W)	80 mm
Thickness (t)	1.5 mm
Flexural rigidity (EI_v=EI_h)	20.5Nm^2/m

Table 1(c) Specification of model sheet piles for CF-4P

Material	Aluminum and Phosphorus bronze
Width of PB sheet	80mm
Width of Al strip	15mm
Thickness (t)	1.5 mm
Vertical flexural rigidity (EI_v)	20.5 Nm^2/m
Horizontal flexural rigidity (EI_h)	~ 0.001 EI_v

Table 2 Physical properties of Toyoura sand

Specific gravity (G_s)	2.65
Mean particle diameter (D_{50})	0.19
Particle diameter D_{10}	0.14
Coefficient of uniformity (U_c)	1.56
Maximum void ratio (e_{max})	0.973
Minimum void ratio (e_{min})	0.609

2. 2. Soil used and sample preparation

Soil used for the tests is dry Toyoura sand with the physical properties given in Table 2.

Tokyo Tech Mark III Centrifuge was used for the tests. The model container is made of steel with inner dimension of 493mm in length, 300mm in breadth and 360mm in depth. Setup of the centrifuge model is shown in Figure 3. The sand sample was prepared by air pluviation with a target relative density of 80%. After making the sand layer with 50mm depth at the bottom of the container, the model foundation was set at the center of the container. Then further poured to have the embedment depth of pile with 220mm. A smaller sand hopper was used to fill the sand in the narrow portion beneath the model footing. To avoid interaction between footing and ground surface, and create a clear condition as a pile foundation, the model footing was set 20mm above the ground surface. Displacement of the model footing was measured by potentiometers (PMs) and lazar displacement transducers (LDTs). Bending moment and axial force of the pile were measured by strain gages. The locations of the instrumentations were shown in Figure 3.

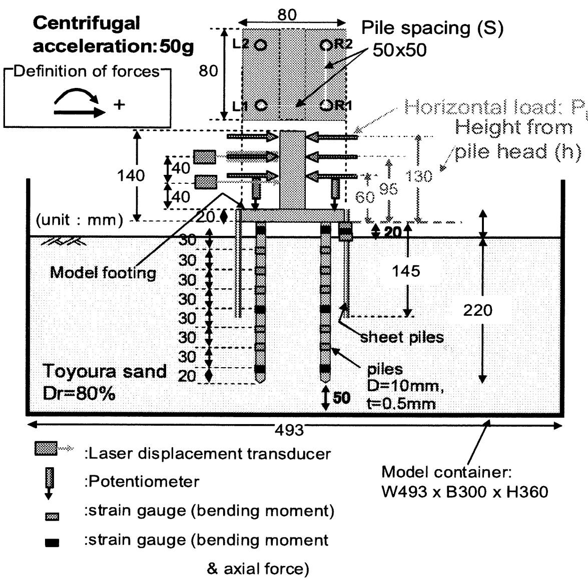

Figure 3 Model setup and locations of sensors

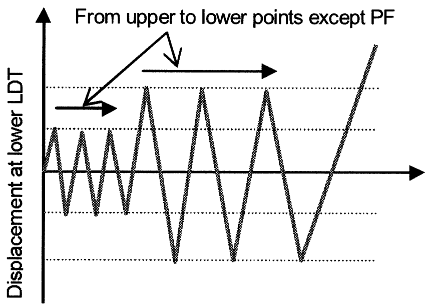

Figure 4 Sequence of loading in the test

2. 3. Test procedures

Having completed the model setup, it was mound on the centrifuge and then centrifugal acceleration was increased to 50g. Horizontal displacement was applied by the two way actuator from left side and then right side at three heights shown in Figure 4. Rightward horizontal load and displacement, and clockwise moment are taken positive in this study as shown in the figure. This loading cycle was repeated twice with displacement amplitudes of 1mm and 2mm at the location of lower LDT as shown in Figure 4. By the instrumentation shown in Figure 3, measured are the horizontal displacements at pile head, δ_{ph}, rotation of the footing, θ_F, and bending moment and axial force of the piles caused by the horizontal load, P_L, and moment on the center of footing base by the P_L, M_L.

3. TEST RESULTS AND DISCUSSIONS

3. 1. Horizontal load-displacement and moment-rotation curves

Relationships between the horizontal load, P_L, and the pile head displacement, δ_{hp}, and the moment load, M_L, and the footing rotation, θ_f, for the case with PF and CF-2P are shown in Figure 5 (a) and (b) respectively. The horizontal displacement was applied from the lower point to the upper in PF, which was different from other tests. In the first loading, the resistance was small compared to the subsequent loading, which is attributed to the densification of sand surrounding piles by first shearing. Regardless the height of loading points from the pile head h, P_L and M_L of CF-2P is larger than that of PF through the experiment. P_L-δ_{ph} relations are different for the cases with different h. The higher the loading location, i.e., the higher the relative

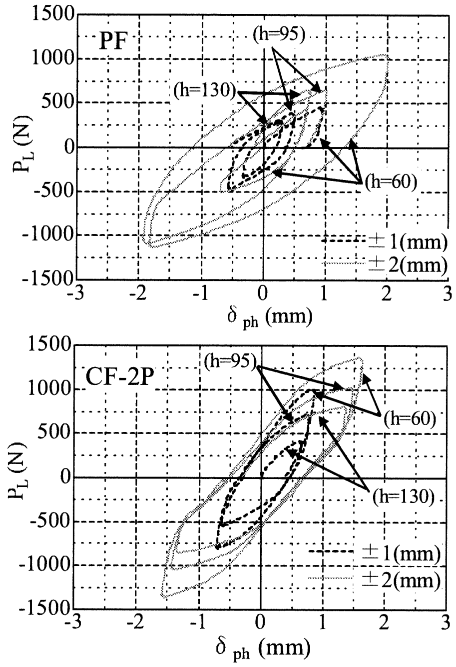

Figure 5 (a) Horizontal load – pile head displacement curves

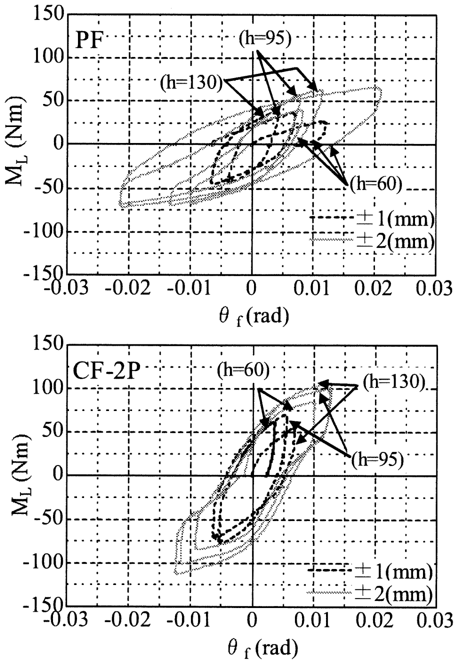

Figure 5(b) Moment load – footing rotation curve

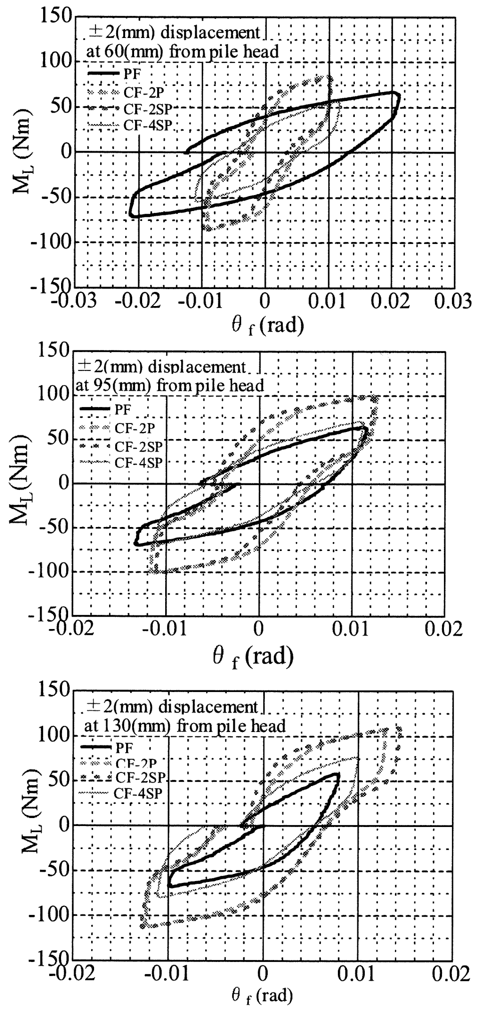

Figure 6 Comparison of M_L- θ_f relations of four different foundations

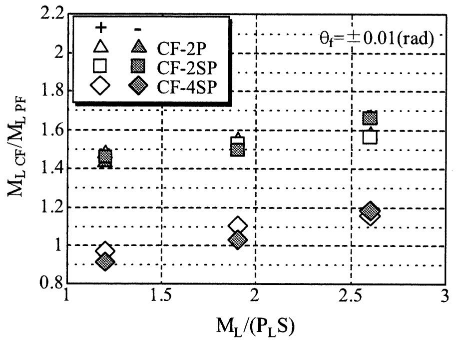

Figure 7 Variation of the ratio of M_L of combined foundation

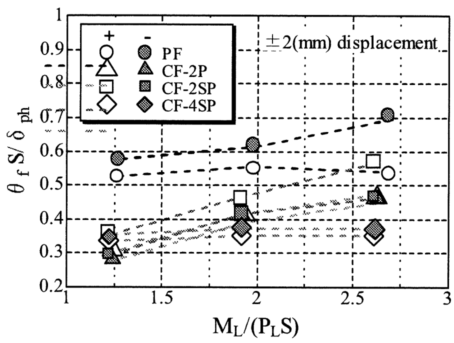

Figure 8 Variation of the ratio of $\theta_f S$ to δ_{ph} with M_L/P_LS

moment load to horizontal load is, the larger the horizontal load resistance at the same horizontal pile head displacement. On the other hand, the difference in M_L-δ_f relation for the different h is not so significant.

Figure 6 shows the comparison of M_L-θ_F relations observed in four different foundations for the loading conditions of ±2mm displacement amplitude at h = 60, 95 and 130mm. M_L-θ_F relations for CF-2P are similar to those for CF-2SP both in shape and magnitude. This means that horizontal flexural rigidity of sheet pile has no significant effect on the lateral resistance of the combined foundation with the sheet piles at the two side of the footing perpendicular to the loading direction. From this fact it can be inferred that vertical forces acting to the footing from the sheet piles, such as pullout and bearing resistances, play more significant roles than horizontal resistance. Although CF-4SP is expected to have the largest resistance among the four foundations, resistance of CF-4P was smaller than those of CF-2P and CF-2SP. The sand in the sheet piles wall was only poured from the small hole in the footing, while for the other cases the sand can be poured from the lateral side beneath the footing. The difficulty in pouring sand from the small hole made the density of the sand under the footing looser for CF-4SP than the other cases and caused the smaller resistance.

3. 2. Horizontal resistance and displacement behavior

Figure 7 shows relationship between the ratio of moment load of combined foundation to that of the pile foundation, $M_{L\_CF}/\ M_{L\_PF}$ at θ_F = ±0.01(rad) and the moment load normalized by the horizontal load and pile spacing, M_L/P_LS. Moment resistances of CF-2P and CF-2SP are about 1.4 -1.7 times larger than those of pile foundations. The ratio increases with increasing normalized moment load. Although the ratio of CF-4P is smaller than those of CF-2P and CF-2SP, the increase seems more apparent for the former than the latter. It can be confirmed from these finding that installing sheet piles at the perimeter of the footing can increase the moment resistance of the foundation significantly.

The ratios of $\theta_f S$ to δ_{ph} with are plotted against M_L/P_LS at the displacement amplitude of ±2mm in Figure 8. This ratio represents the horizontal displacement caused by the rotation of the footing relative to the horizontal pile head displacement. The relative rotations of the combined foundation are smaller than those of pile foundation, showing the efficiency in preventing the inclination of the superstructure. It can be seen from the figure that the relative rotation of CF-4SP is smaller than those of CF-2P and CF-2SP for the large relative moment.

3. 3. Deformation mechanism

Typical M_L and δ_F relation observed in CF-2P in the loading with displacement magnitude of ±2mm is given in

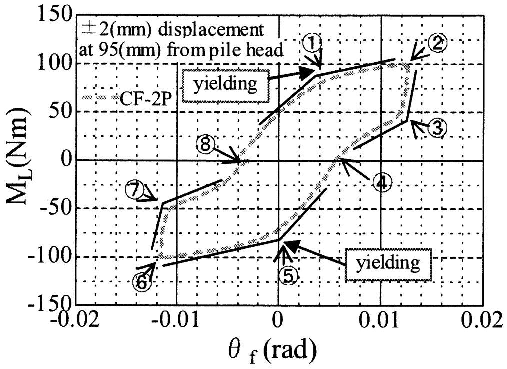

Figure 9 Typical M_L and θ_f relation observed in CF-2P and CF-2SP in the loading with ±2mm displacement

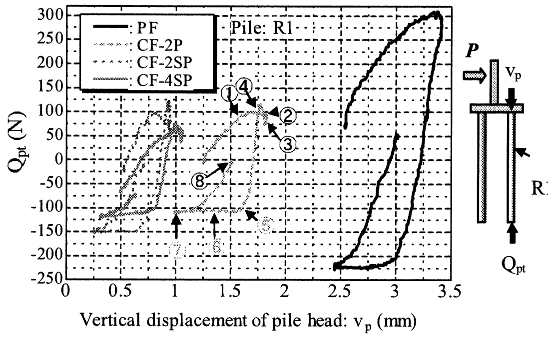

Figure 10 Variation of bearing stress of pile tip, Q_{pt}, with vertical displacement of pile head, v_p, observed in the loading cycle of ±2mm displacement magnitude

Figure 9. Clear yielding points (① and ⑤) and clear kinks(③ and ⑦) can been seen in the loading and unloading process respectively, which were also not apparent in PF and CF-4SP(Figure 6).

Variation of bearing stress of pile tip, Q_{pt}, with vertical displacement of pile head observed in the right pile R1(Figure 3) in the loading cycle with ± 2mm displacement magnitude is given in Figure 10. In the figure, the points corresponding to ① - ⑧ shown in Figure 6 are also indicated for CF-2P. The onset of pullout of the tension pile can be confirmed at the points where upward vertical displacement occurs at constant tip resistance, which is the tip resistance before lateral loading. The onset of pullout of the pile corresponds to the yielding point, ⑤. It is also noted that from the points ⑥ to ⑦, upward displacement occurred and the tip resistance was kept almost constant, although the moment load decreased from 100Nm to 50Nm. The upward displacement of tension pile after reaching pullout resistance is larger for CF-2P than PF, which can be attributed to the smaller downward vertical displacement of compression piles for the former than the latter. These differences are caused by the additional resistance from the sheet piles. From the above observation it can be said that pullout behavior of the tension pile is closely related to the typical M_L-δ_F relations observed in combined foundations with sheet piles at two side of the footing (Figure 9).

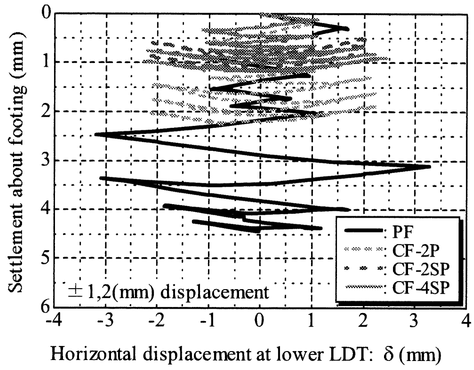

Figure 11 Observed settlements of the footing caused by cyclic loading.

3. 4. Settlement of combined foundations

Observed settlements are plotted against imposed horizontal displacement at the location of lower LDT in Figure 11. Although the imposed displacements of PF are different from the others, it can be confirmed that the settlements of combined foundations are much smaller than those of pile foundation.

3. 5. Bending moment of piles

Figure 12 shows bending moment profiles of Right1 pile observed at the specific points shown in Figure 9 in the loading cycle of ±2mm displacement amplitude and h=95mm. Maximum bending moment in compression side is larger than tension side. The location of the maximum bending moment is deeper for the combined foundation than pile foundation. The bending moment at the pile head does not show the maximum magnitude at the max moment load (②, ⑥) decreasing from yielding point ① to the point of the maximum moment load ② for PF, CF-2P and CF-2SP. While for CF-4SP, the pile head bending moment becomes the maximum magnitude at the point of the maximum moment load ②.

Relationship between the normalized moment load, M_L/P_LS, and the ratio of maximum bending moment of pile, $M_{p\max}$ to M_L for the loading of ±2mm displacement amplitude is depicted in Figure 13. The ratios of the combined foundation are much smaller than those of pile foundations, even for CF-4SP with relatively small density of sand in the sheet pile wall, especially for the case with larger normalized moment. It can be confirmed that sheet piles installed at the perimeter of the footing can reduce the moment deflection of the pile.

4. CONCLUSIONS

As for pile-sheet pile combined foundation, the following conclusions are derived from the centrifuge model tests done in this study:

1) Moment resistance of small scale pile foundation can be increased by reinforcement of sheet piles.
2) Rotation of the footing can be restrained effectively restrained by sheet piles. This effect becomes more

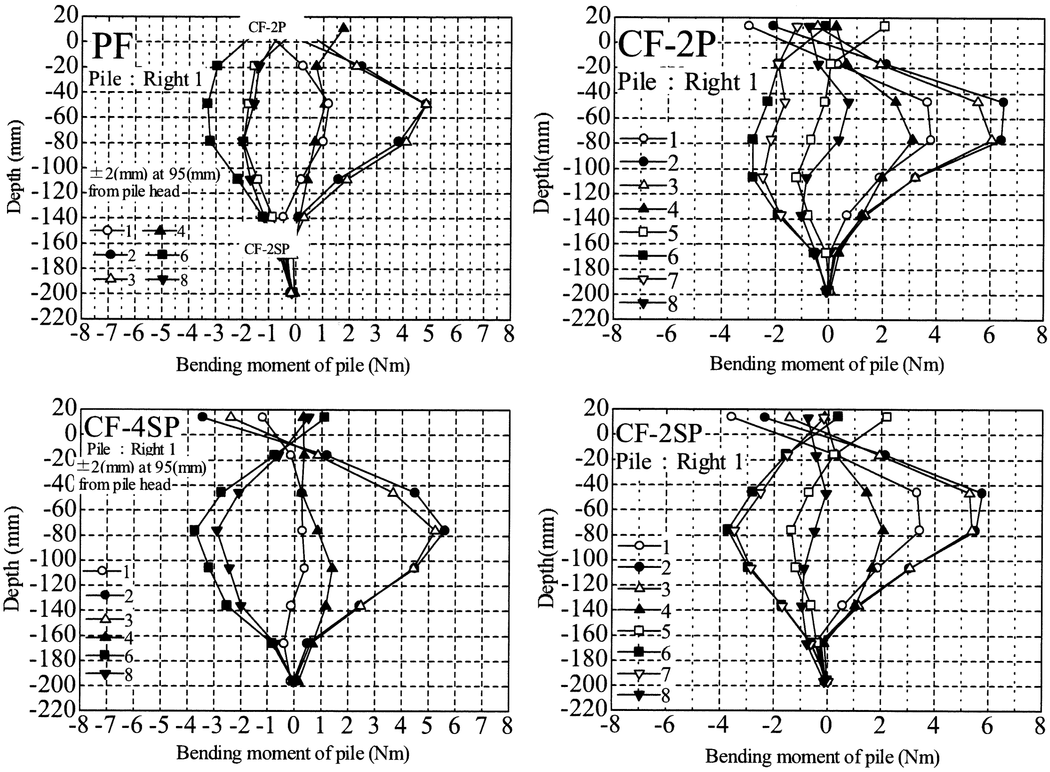

Figure 12 Variations of bending moment of piles during horizontal loading

significant by constraining the soil beneath the foundation with the sheet piles at all perimeter pf of the footing.

3) Sheet pile reinforcement can reduce the settlement of foundation and the maximum bending moment of the pile.
4) The horizontal flexural rigidity of sheet piles does not have an effect on the lateral resistance of the combined foundations.
5) Vertical forces imposed from the sheet piles to the footing more predominantly control the behavior of the combined foundation than the horizontal resistance of the sheet pile. As a result the pullout behavior of tension pile is closely related to relation between the moment load and rotation of foundation.

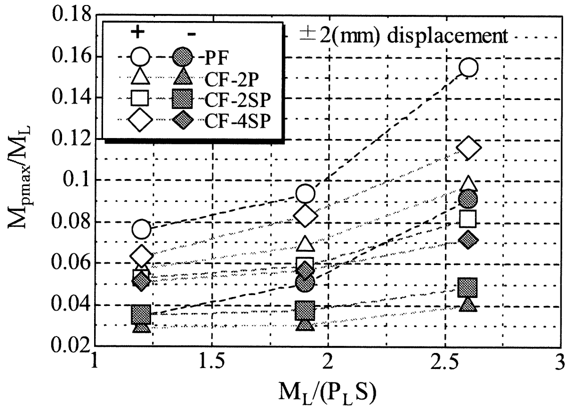

Figure 13 Relationship between M_L/P_LS and ratio maximum bending moment of pile, M_{pmax} to M_L for the loading of ±2mm displacement amplitude

References:

Japan Highway Association, 2002, Seismic design, Design Specification of Highway Bridge.

Koda, M. Murata, O., Nishioka, H., Punrattanasin, P. and Kusakabe, O., 2003; Proposal of slab foundation combined with sheet piles, Tsuchi-to-Kiso, JGS, Vol.51, No.11, pp.8-10.

Nishioka, H., Koda, M., Murata, O., Matsuda, T. and Hirao, J., 2004, Experimental study on the method to joint sheet fiples to a footing of sheet-pile foundation, Proc. Symposium on Geotechnical Engineering, JGS, pp.275-282.

Fifth International Conference on Urban Earthquake Engineering
March 4-5, 2008, Tokyo Institute of Technology, Tokyo, Japan

NONLINEAR STRESS-STRAIN RELATION OF SAND FOR EXPANDING DYNAMIC ANALYSIS

Hiroshi OHKAWA[1] and Jiro KUWANO[2]

1) Doctoral Student, Dept. of Civil and Environmental Engineering, Tokyo Institute of Technology, Japan
2) Professor, Geosphere Research Institute, Saitama University, Saitama City, Japan
bigriver@cv.tiech.ac.jp, jkuwano@mail.saitama-u.ac.jp

Abstract: It is very important to obtain precise and detail relationship of stress-strain for expanding numerical analysis either static or dynamic. In many conventional yield surface models, it has been assumed that the yield surface coincides with the state boundary surface, and the deformation behavior is assumed to be elastic within the yield surface. However, actual behavior of soil is non-linear even within the yield surface. To describe the soil behavior more precisely, Jardine (1992) proposed multiple yield surfaces model. It consists of three yield surfaces, Y_1, Y_2 and Y_3. The Y_3 yield surface is the same as the conventional yield surface. The Y_1 represents the linear elastic limit and the Y_2 represents the starting point of rapid development of the plastic strain. In this study, Jardine's model was applied to dense Toyoura sand and these three yield surfaces were identified in a p'-constant shear plane and their characteristics were studied experimentally by using hollow cylinder apparatus. At the same time, the characteristic of stiffness was carried out by conducting small cyclic loading test at some stress states.

1. INTRODUCTION

Failure of the ground has been a main concern in construction of structure. However, it has been recognized that we have to consider not only the failure of the ground but also the deformation of ground, because very large structures are made and buildings are constructed closer each other in the city. It is very important to evaluate the deformation of the ground even at very small strain level.

In many conventional yield surface models, which have been used for practice, it has been assumed that the yield surface defined at relatively large shear strain coincides with the state boundary surface, and the deformation behavior is assumed to be elastic within the yield surface. However, actual behavior of soil is non-linear even within the yield surface. Elastic behavior of sand is observed only at very small strain of the order of 0.001 %. The deformation behavior beyond this strain level is highly non-linear with rapid decrease in stiffness moduli, that is, the conventional yield surface model does not describe the behavior of sand accurately within yield surface.

To describe the behavior within conventional yield surface, Jardine (1992) proposed multiple yield surfaces model shown in p' (confining pressure) - q (shear stress) plane as Fig. 1. It consists of three yield surfaces Y_1, Y_2 and Y_3. The Y_3 yield surface represents the large-strain yield surface, which is the same as conventional yield surface. The Y_1 surface represents the linear elastic limit and the Y_2 surface represents the starting point of rapid development of plastic strain. The sub-yield surfaces Y_1 and Y_2 move with current stress point. In this study, Jardine's model was applied to Toyoura sand and these three yield surfaces were identified in p'-constant shear plane and their characteristics were studied experimentally.

Dense Toyoura sand (relative density Dr = 80 %) was sheared by using hollow cylinder apparatus. small unload-reload cycle tests were also carried out during shearing to observe quasi-elastic modulus characteristics and effect of cyclic loading on deformation of sand.

2. APPRARATUS

Hollow cylinder apparatus (HCA) was used. It gives an advantage over conventional triaxial apparatus as the torsional shear stress can be applied to the specimen in addition to the deviator shear stress (see Fig. 2). Also three normal stresses can be varied independently, unlike the conventional triaxial apparatus where two normal stresses in radial direction are always equal. Therefore, a general stress path of any kind can be applied to the specimen.

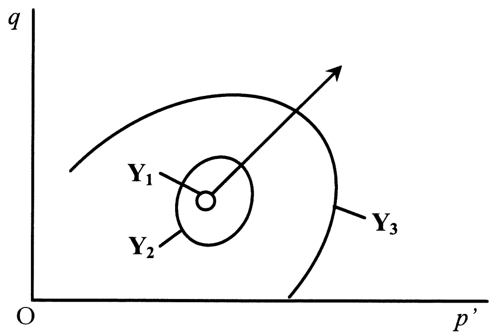

Fig. 1 Multiple yield surfaces model (Jardine, 1992)

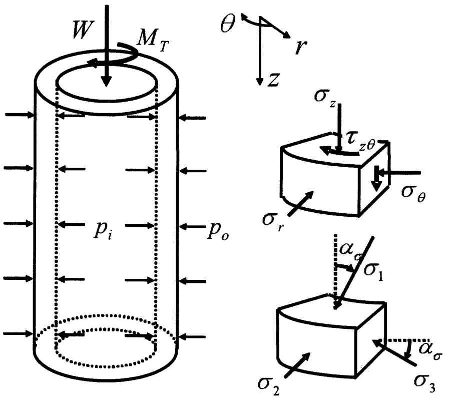

Fig. 2 Stress condition in HCA

The outline of hollow cylinder apparatus is given in Fig. 2. Vertical load, W, was controlled by air pressure. The torque, M_T, was controlled by oil pressure. Inner and outer cell pressures, P_i and P_o, were applied by air pressure controlled by E/P transducer. All the stress and strain measuring devices and control were connected to amplifier and then to a personal computer through a 16-bit A/D and D/A converter. It makes automatic measuring and system control possible.

From above four forces, we can calculate and get stress component and principle stress angle:

σ_1, σ_2, σ_3 : principal stresses

σ_z : vertical stress

σ_r : radial stress

σ_θ: circumferential stress

$\tau_{z\theta}$: torsional shear stress

α_σ: principal stress angle

3. TEST PROGRAM

3.1. Outline

Toyoura sand specimens were prepared by air pluviation method to achieve the relative density of 80 %. Specimens were saturated by vacuum method, then consolidated isotropically to p' = 98.1 kPa, then sheared in drained condition (see Fig. 3). Specimens were sheared on p' = 98.1 kPa constant plane. Soil deformation consists of two components, shear and volumetric strains. If p' is constant, only effects of shearing can be observed. During shearing, the parameter for intermediate principal stress, b - value, was kept at 0.5. Therefore, $\sigma_2 = \sigma_r$ was constant throughout the shearing.

At various maximum shear stresses, τ_{max}, during shearing, stress state was kept constant for more than 2 - 3 hours to stabilize a state of sand specimen. Then, small unload - reload cycles of $\Delta\sigma'_z$, $\Delta\sigma'_\theta$ and $\Delta\tau_{z\theta}$ whose magnitude was generally ± 2 kPa, ± 4 kPa and –6 kPa, were applied to measure quasi-elastic moduli and to observe effect

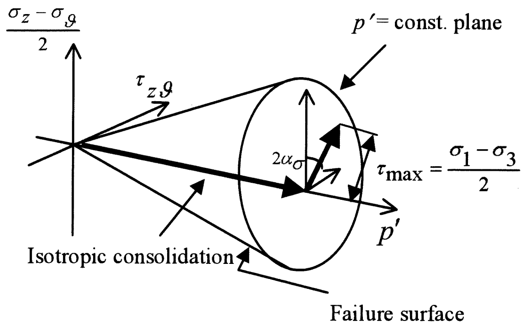

Fig. 3 Isotropic consolidation before shearing

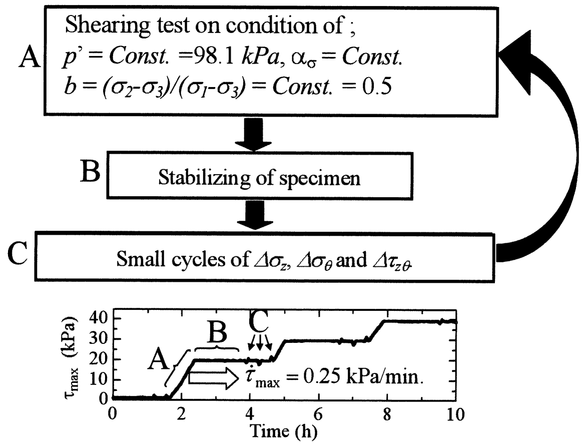

Fig. 4. Flow of experiment

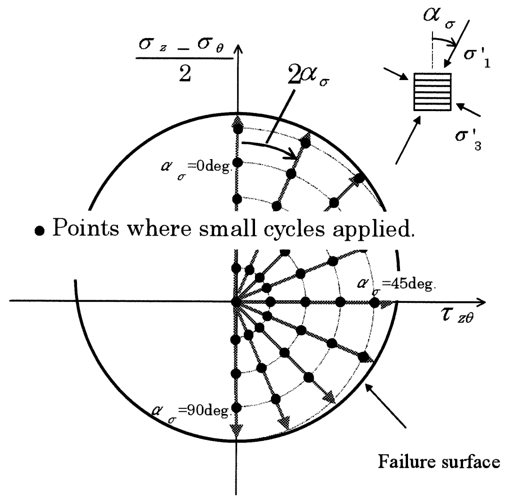

Fig. 5 Stress path for test series 1

of cyclic loading on deformation at various stress states. In this study, the test cycles of "A: Shear test → B: stabilizing → C: Small unload - reload cycle test" were repeated until the failure state. This flow is shown in Fig. 4.

3.2. Shearing stress path

In test series 1, nine specimens were isotropically consolidated to p' = 98.1 kPa. Then, they were sheared along various α_σ directions from isotropic stress state point as shown in Fig. 5. The radial shearing test to study the yield behavior around any stress point is called 'stress probing test'.

Fig. 6 shows test series 2 – 6. In test series 2, six specimens consolidated isotropically were pre-sheared α_σ = 22.5 deg. to τ_{max} = 30 kPa which is within Y_3 yield surface obtained from test series 1. Then stress probing tests from Point A1 were carried out along six directions. While, in test series 3, six specimens were sheared along α_σ = 67.5 deg. to τ_{max} = 20 kPa, then stress probing tests from B1 were carried out. In test series 4, six specimens consolidated isotropically were pre-sheared along α_σ = 22.5 deg. to τ_{max} = 39 kPa which is outside Y_3 yield surface obtained from test series 1. Then stress probing tests were carried out from A2. While, in test series 5, six specimens were sheared along α_σ = 67.5 deg. to τ_{max} = 30 kPa, then stress probing tests from B2 were carried out. And in test series 6, four specimens ware sheared along α_σ = 45.0 deg. to τ_{max} = 34 kPa, then stress probing tests from C1 ware carried out.

Finally, Fig. 7 illustrates test series 7 – 9. In test series 7, six specimens consolidated isotropically were pre-sheared along α_σ = 22.5 deg. to τ_{max} = 39 kPa which is outside initial Y_3 surface, then unloaded to τ_{max} = 30kPa along the same direction, and then stress probing tests from A3 were carried out. In test series 8, six specimens consolidated isotropically were pre-sheared along α_σ = 67.5 deg. to τ_{max} = 30 kPa, and unloaded to τ_{max} = 20 kPa then stress probing tests from B3 were carried out. And in test series 9, four specimens pre-sheared along α_σ = 45.0 deg. to τ_{max} = 34 kPa, then unloaded to τ_{max} = 27 kPa, and then stress probing tests from C2 were carried out.

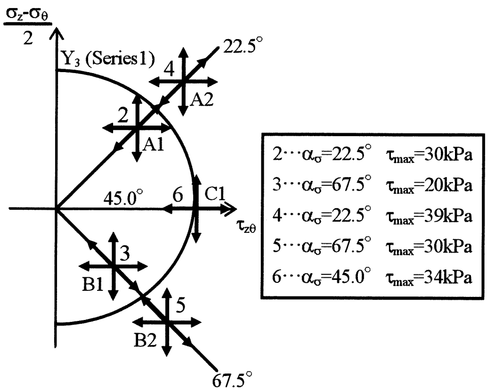

Fig. 6. Stress Path for Test Series 2 - 6

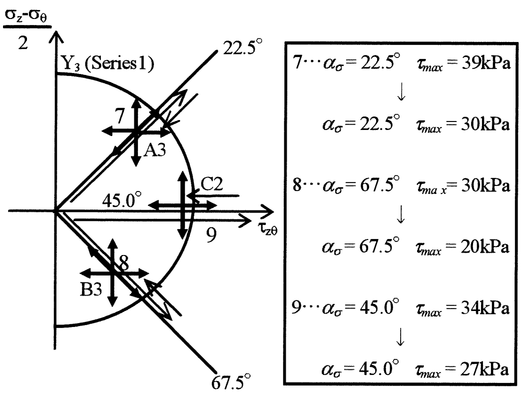

Fig. 7 Stress path for test series 7 - 9

5. TEST RESULTS

5.1. Definition of yield surfaces

The stress-strain curve at small strain level is shown in Fig. 9. It can be observed that the behavior is linear up to a shear strain of approximately 0.002 %. This point is designated as Y_1. (Where, γ_{max} is maximum shear strain.)

The total shear strain increment, $d\gamma_{max}$, against maximum shear strain, γ_{max}, relationship is given in Fig. 10. It can be seen that the total strain increment starts to develop rapidly at some point. This point is designated as Y_2. Jardine defined Y_2 as the point where plastic strain increment starts to develop rapidly. Even in this study, we have to accept this definition, but slightly higher scatter in result about plastic strain increment was obtained at Y_2 strain level. So, total strain increment was used in this study, because the development of plastic strain increment leads to that of total strain increment. Essentially, both are considered as the same. It can be seen that the range of shear strain at Y_2 yield point is 0.005 % - 0.01 %. It was also found that plastic volumetric strain started to develop at the strain level of Y_2 (e. g. Kuwano et al., 2003).

Plastic strain increment ratio, $d\gamma_{max}^P/d\gamma_{max}$, against γ_{max} relationship is given in Fig. 11. The plastic strain increment ratio $d\gamma_{max}^P/d\gamma_{max}$ shows the degree of plastic deformation. In Fig. 11, it can be observed that plastic strain increment ratio converged between 0.8 and 1.0. It represents that the sand

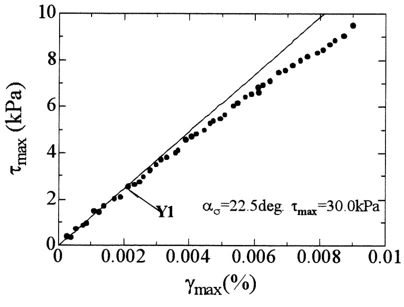

Fig. 8, Definition of yield point Y_1

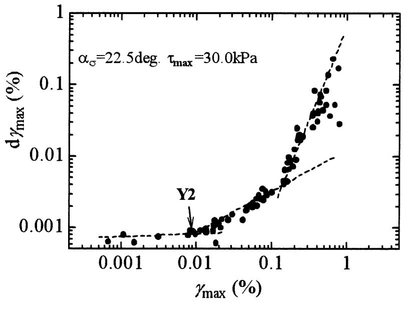

Fig. 9, Definition of yield point Y_2

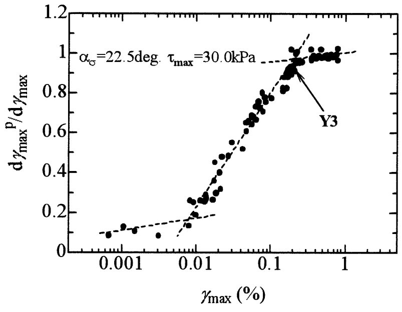

Fig. 10, Definition of yield point Y_3

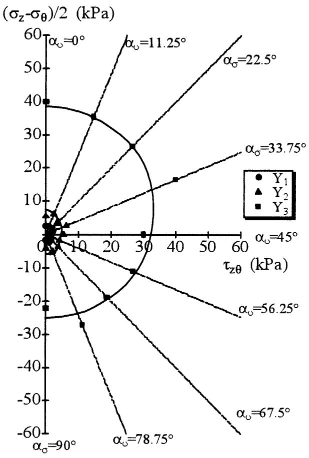

Fig. 11 Test series 1

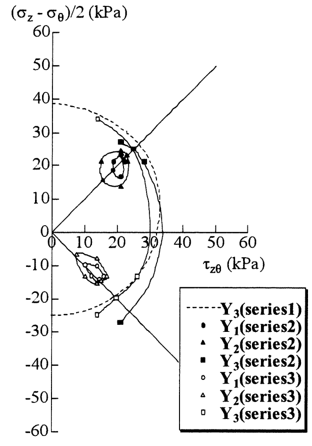

Fig. 12 Test series 2 and 3

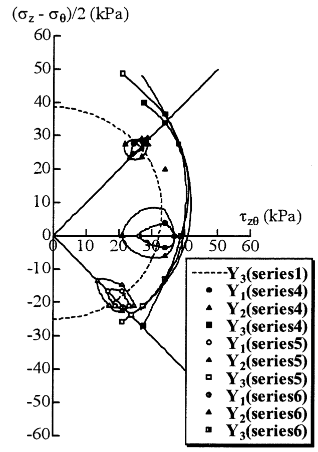

Fig. 13 Test series 4, 5 and 6

completely yielded and strain increment became almost plastic in this strain level. This point is designated as Y_3. It was obtained that the range of shear strain at Y_3 yield point is 0.05 % - 0.15 %.

5.2. Yielding characteristic

Yield points obtained from the former definitions are plotted in p'- constant plane in Figs. 11 - 14. The yielding character is taken from these figures.

The results from test series 1 are summarized in Fig. 11. In this test series, tests were not carried out in area of $\tau_{z\theta} < 0$, considering yielding character is symmetrical with respect to $(\sigma_z-\sigma_\theta)/2$ axis. It was observed that Y_1 and Y_2 loci were roughly circular in shape without one-side. It shows little anisotropy in Y_1 and Y_2. While, Y_3 surface was circular with the center shifted towards compression side ($(\sigma_z-\sigma_\theta)/2 > 0$), that is, Y_3 locus has anisotropy.

The plot of yield loci obtained from test series 2 and 3 are given in Fig. 12. In these test series, specimens were pre-sheared within initial Y_3 yield surface. The sub-yield loci Y_1 and Y_2 moved with current stress point and they were now elliptical in shape, compared to circular in test series 1. They tended to orient along the direction of shearing. It was observed that Y_3 yield loci was approximately at the same place as that from test series 1, that is, Y_3 locus does not move with current stress point within initial Y_3 surface.

The results from test series 4, 5 and 6 are shown in Fig. 13. The same tendency as former series was obtained about Y_1 and Y_2 loci, moving with current stress point and being elliptical in shape orienting along the direction of shearing. On the other hand, Y_3 has grown in size and moved outward from the initial Y_3 surface. This indicates that the Y_3 surface is modified when it is intersected by the current stress point, and is not affected when the stress point is within the initial Y_3 surface. This may be considered as hardening of conventional yield surface.

The results from test series 7, 8 and 9 are shown in Fig. 14. Like former series, Y_1 and Y_2 moved with current stress point and were elliptical in shape and oriented along the direction of shearing. Regarding the size, however, different

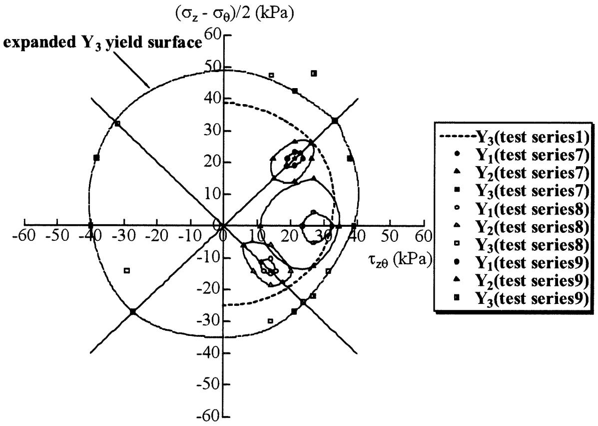

Fig. 14 Test series 7, 8 and 9

tendency was observed. Y_1 was almost the same in size as the other test series, while the size of Y_2 has grown by load-unload shear stress history. In these test series, the shearing was made up to $\tau_{z\theta} < 0$ region and Y_3 yield surface was drawn as closed curve. It can be seen that Y_3 locus was symmetric with respect to $(\sigma_z-\sigma_\theta)/2$ axis. Their sizes were approximately the same as extended Y_3 surface obtained in test series 4, 5 and 6. This indicates that Y_3 yield surface shows isotropic hardening by loading and not softening by unloading.

5.3. Small cyclic loading test

Fig. 15 demonstrates typical characteristic of non-linearity of stress-strain relationship. In these figure, a relation of torsional shear stress and torsional shear strain is plotted with respect to the test series 6. The figure (a) and (b) are at τ_{max} = 10 kPa and τ_{max} = 30 kPa, during loading. The figure (c) is at τ_{max} = 30 kPa, during unloading.

In these figures, it can be seen that hysteresis curve does not close at part of loading of (a) and (b). The $\Delta\tau_{max}$ = + 4 kPa part of (a) or (b) is the first time maximum load applied to specimen. Therefore, the relationship between

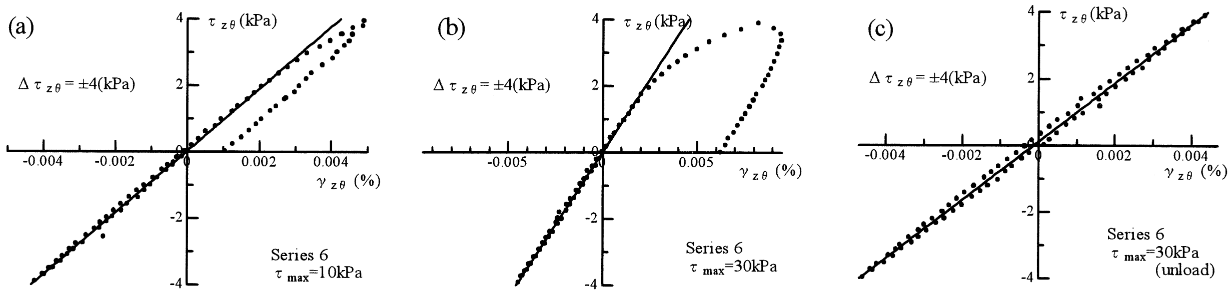

Fig. 15 Relationship of $\gamma_{z\theta}$ - $\tau_{z\theta}$ in series 6 at (a) τ_{max} = 10 kPa, (b) τ_{max} = 30 kPa and (c) τ_{max} = 30 kPa (unload)

stress and strain is highly nonlinear, especially at large shear level. This can be considered from the Fig. 8 which explains linear elastic limit at very small strain level. On the other hand, hysteresis curve of figure (c) completely closes and highly linear relation though shear stress level is the same as figure (b). The small cyclic loading test in this case was conducted when specimen had been subjected load-unload stress history.

When a dynamic analysis is used in a geotechnical problem like earthquake, it is usually employed a damping ratio. As shown in Fig. 16, the damping ratio is determined by a maximum stored energy, W, and an energy dissipation, ΔW. W is an elastic energy basically, but when the stress-strain relation is nonlinear, there are several ways to define it. ΔW represents the area enclosed by the hysteresis loop per one cycle. In this study, however, the same amplitude cyclic load was applied only once at some stress state. Therefore, it is difficult to obtain W or ΔW from Fig. 15 (a) and (b), and to obtain the effect of number of cyclic loading on deformation of specimen. Consequently, in further study, it is necessary to find out a proper method which can evaluate the damping ratio by single cyclic hysteresis, and to combine nonlinear deformation within conventional yield surface with dynamic analysis.

6. CONCLUSIONS

1) It is confirmed that the linear elastic range is very small strain level, that is, about 0.002%.
2) The yielding behavior of Toyoura sand was characterized by plastic strain increment.
3) The sub-yield surfaces, Y_1 and Y_2, move with current stress state and become elliptical shape along pre-shearing direction.
4) The Y_2 surface becomes slightly large by load-unload history.
5) The Y_3 surface does not move, but when the initial Y_3 is intersected by current stress point, it shows isotropic hardening by loading and no softening by unloading.
6) The nonlinearity of stress-strain relation of dense Toyoura sand was clearly observed by small cyclic loading test.
7) The nonlinearity appears in virgin loading even if the stress state is within conventional yield surface.

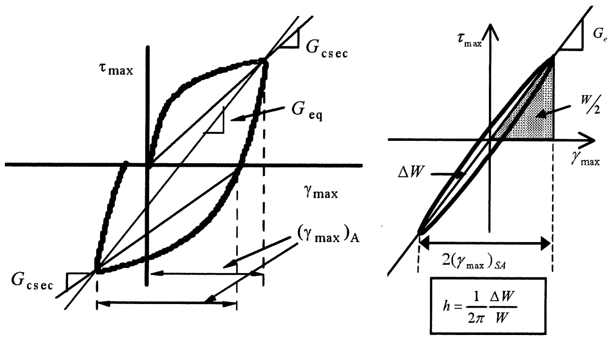

Fig. 16 Definition of secant and equivalent shear moduli, G_{csec} and G_{eq}, and concept of damping ratio, h.

8) It is necessary to create new method which can be applied to dynamic analysis with respect to nonlinear relation or hysteresis curve and it is considered that this first step is to employ the theory of the damping ratio.

References:

1. Chaudhary, S. K., Kuwano, J., Hashimoto, S., Hayano, Y. and Nakamura, Y. (2002): Effects of initial fabric and shearing direction on cyclic deformation characteristics of sand. *Soils and Foundations*, **42**(1), 147-157.
2. Chaudhary, S. K. and Kuwano, J. (2003): Anisotropic multiple yielding of dense Toyoura sand in p'-constant shear plane. *Soils and Foundations*, **43**(4), 59-69.
3. Ishihara, K. (1996): Soil Behaviour in Earthquake Geotechnics. *Oxford Science Publications.*
4. Jardine, R. J. (1992): Some observation on the kinematic nature of soil stiffness. *Soils and Foundations*, **32**(2), 111-124.
5. Kuwano, J., Hashimoto, S. and Chaudhary, S. K. (2001): Shear stress dependency of small-strain stiffness and creep of Toyoura sand. *Proc. of 15th ICSM and Geotechnical Engineering*, Istanbul, 179-182.
6. Kuwano, J. and Nakada, T. (2005): Effects of shear stress history on yielding of dense Toyoura sand in p'-constant shear plane. *Proc. of 16th ICSM and Geotechnical Engineering*, Osaka, 527-530.
7. Ohkawa, H., Kusakabe, O. and Kuwano, J. (2006): Effect of shear stress history on deformation properties of dense sand. *Proc. of SIDE 2006 and 5th RSID in Civil Engineering*, Philippines, **CD-ROM**, GEO-013.

Fifth International Conference on Urban Earthquake Engineering
March 4-5, 2008, Tokyo Institute of Technology, Tokyo, Japan

EFFECTS OF STRESS RELEASING OF GROUND ON SEISMIC STABILITY OF TUNNEL

Shuhei Shibayama[1), Jun Izawa[2), Jiro Takemura[3) and Osamu Kusakabe[4)

1) Doctoral student, Department of Civil Engineering, Tokyo Institute of Technology, Japan
2) Assistant Professor, Department of Civil Engineering, Tokyo Institute of Technology, Japan
3) Associate Professor, Department of Civil Engineering, Tokyo Institute of Technology, Japan
4) Professor, Department of Civil Engineering, Tokyo Institute of Technology, Japan
sh4880@cv.titech.ac.jp, jizawa@cv.titech.ac.jp, jtakemur@cv.titech.ac.jp, kusakabe@cv.titech.ac.jp

Abstract: In order to reduce construction cost of urban tunnel, mountain tunnels have extended its application to urban area. Because of unlined construction process of mountain tunnel, the stresses in a ground are released, which might create loosing area above tunnel. The lining sectional forces and deformation are affected by this complicated soil condition, which might be changed by the ground deformation due to earthquake. Underground structures were considered to have high seismic stability because of a confining effect from the ground. However, tunnel structures have experienced serious damages. Although the need for seismic performance of tunnels is emphasized in specification of tunnels, it is required to understand detailed mechanisms on the interaction between the structure and soil. Arch action of the ground is expected to occur in mountain tunnel and stress resultants of the tunnel lining is much smaller than that by shield tunneling method. It is hardly explained that how long the advantage, arch action, remains effectively during or after earthquakes. In this study, active type shear tests in a centrifuge was carried out to understand the effects of stress releasing of ground about seismic behavior of the tunnel.

1. INTRODUCTION

Recently, a number of constructions of urban tunnels have been increasing because intensive use of urban areas has inevitably promoted utilization of underground space.

In order to reduce construction cost of the urban tunnels, mountain tunnels have extended its application to urban area in cemented soft ground or non-consolidated geological formation at relatively shallow depth. Because of unlined construction process of the mountain tunnel, stresses in a ground are released, which might create loosing area above tunnel. The lining sectional forces and deformation are affected by this complicated soil condition, which might be changed by the ground deformation due to earthquake.

Underground structures were considered to have high seismic stability because of a confining effect from the ground. However, tunnel structures have experienced serious damages in 1995 Hyogoken-Nanbu Earthquake (Iida et al., 1996, Asakura and Sato, 1996), the design codes of tunnel have been revised especially for cut-and-cover tunnels and shield tunnels (JSCE, 1996). The revised specification recommends taking consideration on the soil-structure interactions by proper methods, such as seismic displacement methods and dynamic response analyses. The seismic displacement method is a kind of pseudo-static approach in which seismically induced ground motion is applied to the tunnel through soil springs. As the reaction from the soil to the tunnel is affected by many factors, e.g., stress conditions of soil, deformation, condition of tunnel surface, lining structures, there are many uncertainties in the application of seismic displacement method. As the effects of these factors on the tunnel behavior are not easy to be investigated from the performance of real tunnels, physical models can be employed for this purpose.

Although the need for seismic performance of urban tunnels is emphasized in JSCE standard specifications of tunnels, it is required to understand detailed mechanisms on the interaction between the structure and soil under various conditions of the ground and geometric constraints.

Arch action of the ground above a tunnel is expected to occur in mountain tunnel, i.e. loosening the ground is allowed, and the earth pressure acting on the tunnel lining is much smaller than that by shield tunneling method. It is hardly explained that how long the advantage, arch action, remains effectively during or after earthquakes. It is therefore said that these are the major problems to extend the wider applications of mountain tunnel.

In this study, active type shear tests in a centrifuge was carried out to understand the effects of stress releasing of ground about seismic behavior of the tunnel.

2. CENTRIGUGE MODEL TESTS

A seismic stability of an underground structure such as a tunnel is usually evaluated by means of the seismic displacement method. The method evaluates stress resultants of tunnel by applying the lateral movement of ground to the tunnel in a pseudo-static manner, because effects of inertia force acting to the underground structure can be neglected as compared with super structures. Photo. 1 shows an active type shear box used in this study. The seismic displacement method was replicated experimentally by using the shear box. Validity of this experimental seismic displacement method for a rectangular tunnel and its countermeasures in sand has been confirmed by previous studies (Izawa et al, 2004). In this study, seismic stability of tunnels was investigated by experimental simulating seismic displacement method using the active type shear box in a centrifuge.

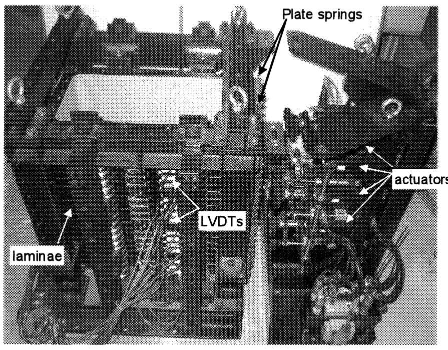

Photo. 1 A view of the active type shear box

2.1 Test setup

Figure 1 illustrates a schematic diagram of the model setup for the active type shear test. The shear box was consisted of two parts, a laminar box and actuators. The laminar box was consisted of 20 stacked 24mm lamina with the roller bearing support and one fixed lamina at the base of the box. The shear deformation of the box was produced by four hydraulic actuators connected to the four laminae at specific elevations. Lateral displacements of the other laminae were created by transmitting forces from the actuators to them through four linked sets of 0.6mm plate springs, and it was possible to apply forced lateral displacements to the model ground in the rings. A rectangular shape rubber sleeve was placed on the inner wall of the box to prevent the soil particles from getting into the gaps of the laminae. Thin stainless vertical sheets and a horizontal sheet of 0.2mm thickness with rough surface were fixed to both the end wall and the base respectively. These sheets are for mobilizing the shear stresses on the inner boundary when the box is sheared.

The input shear strain history is shown in Figure 2. The two cycles sinusoidal shear strains with 0.01 Hz, of which amplitudes were 1%, 2% and 4% respectively, were imposed to the model ground continuously.

2.2 Tunnel model

Assuming horseshoe-shaped mountain tunnel, a semi-circular aluminium model tunnel was used, in which only tunnel lining was modelled. It has a diameter of 100mm, a height of 75mm and a thickness of 2mm with smooth

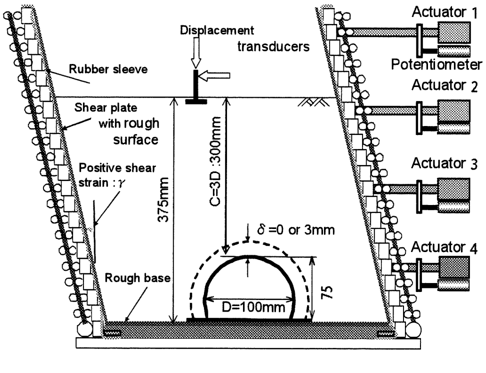

Figure 1 Test setup

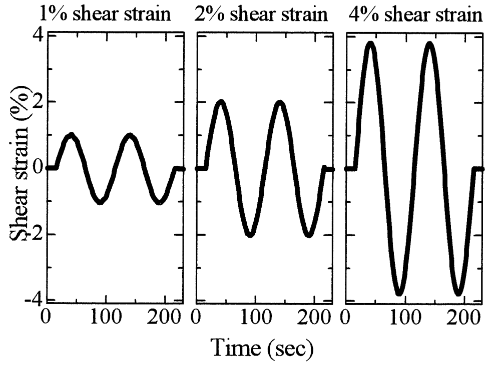

Figure 2 Input shear strain history

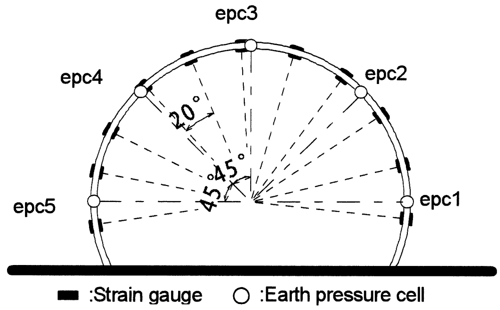

Figure 3 Positions of strain gauges and earth pressure cells

Table 1 Material properties of cemented sand

Unconfined compressive strength: q_u (kPa)	50~60
Secant modulus of elasticity: E_{50} (kPa)	2000~5000
Water content: w (%)	30
Unit waght: γ (kN/m^3)	18

surface, which approximately corresponds to a 5m diameter tunnel with a RC lining of 300mm thickness in the prototype scale. The both ends of the lining has a V shape of 90 degrees, which are placed in a 90 degree V shape notch of a 5mm thick steel plate fixed on the base of the laminae box.
22 strain gauges to obtain sectional forces (especially bending moment in this study) were attached on both outer and inner sides of the lining in pairs. 5 earth pressure cells to measure the earth pressure acting on the tunnel lining were placed on the outer surface of the tunnel at the tunnel crown, spring lines and the midpoints between the crown and spring lines. Figure 3 illustrates the positions of the strain gauges and the earth pressure cells.

2.3 Model ground

Assuming cemented soft ground, cemented sand was used as model ground in this study. Properties of the ground material are shown in Tables 1.

The model ground was formed with stress releasing to understand the effect on seismic behavior of the tunnel lining. Stress releasing was presented by allowed displacement of the tunnel surroundings δ in centrifugal stress field as shown in Figure 1. The value of the stress releasing δ in the test are 0mm and 3mm, which are in ratio to tunnel diameter (i.e. δ/D) 0% as the case of without stress releasing and 3% as the case of with stress releasing respectively.

In the model test of urban tunnel, tunnel cover-diameter ratio (C/D) is an important parameter, as the depth controls the stress condition of tunnel surrounding, including formation of arch action above the tunnel. Although the depth of urban tunnel is relatively shallow, it normally has the depth of a several times the tunnel width. Thus the tunnel cover depth in the test was adopted to be 300mm, which are 3 times larger than tunnel diameter D.

3. RESULTS AND DISCUSSION

In the tests, earth pressers could not be measured, hence only bending moments are discussed here.

Figure 4 shows variations of bending moment measured at tunnel crown, right spring line and mid-part between them in tests of with stress releasing and without stress releasing. The positive bending moment is defined as the case for the inner surface of the tunnel lining suffers tension force. In this Figure 4, solid and broken lines indicate case of with stress releasing and without stress releasing, respectively and dashed lines show input shear strain in the tests. Cyclic variations of the bending moment at the crown and right spring line are smaller than one at mid-part. At the crown and spring line, initial values of bending moment of the case of with stress releasing are close to zero and approach to the case of without stress releasing, during shearing.

Figure 5 shows the bending moments measured before and after cyclic 1% shear strain in the cases of with stress releasing and without stress releasing, and Figure 6 shows the bending moments measured before and after cyclic shearing 4% shear strain in the cases of without stress releasing and with stress releasing. The terms 'before' and 'after' in the figures correspond to the test elapsed time of 15 second and 215 seconds respectively in Figure 2. In the case of with stress releasing, the bending moments before the first shearing (1% shear strain) are much smaller than those after shearing, and the bending moments at near the crown increase and in side parts decrease after 1% shearing, as shown in Figure 5 (a). While in the case of without stress releasing, 1% shear strain, the moment distributions before and after shearing show almost no change (Figure 5 (b)). Probably, this can be explained by the formation of arch action of the cemented sand above the tunnel with stress

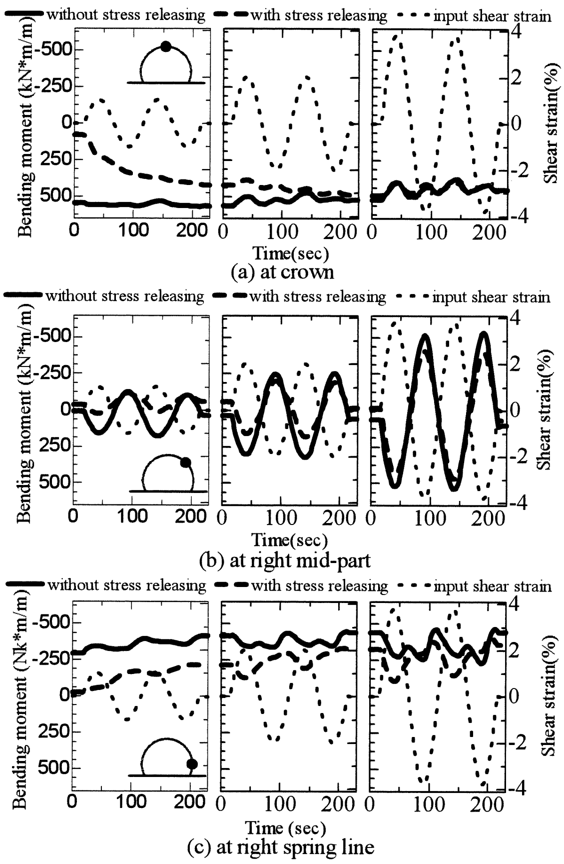

Figure 4 Variations of bending moment

releasing during centrifugal acceleration up to 50G, and deterioration of the arch action takes place due to shearing. In Figures 6 (a) and (b), distributions of bending moment before and after 4% shearing show no change in the both cases of with stress releasing and without stress releasing and distributions of the cases of with stress releasing and without stress releasing are almost the same, because the ground of the case with stress releasing has already been subjected to 1% and 2% shear strain cycles and arch action diminished by shearing. After applied several shear histories, the soil-tunnel interaction showed elastic behaviour with no change of bending moments before and after shearing as shown in Figure 6.

Figures 7 (a) and (b) show the bending moments measured when the maximum shear strain was first applied in cyclic shearing 1% and 4% in the cases of with stress releasing and without stress releasing which corresponding to elapsed time of 40 seconds in Figure 2. In Figure 7 (a) right hand side of the distributions of bending moment of the cases with stress releasing and without stress releasing are almost the same, but left hand side of the distributions of the both cases are different, because the arch action formed by stress releasing are still remain in right hand side. While, in Figure 7 (b) the distributions of the both cases are almost the same, because of the deterioration of arch action of the ground by several shear histories.

4. CONCLUSIONS

This paper presented some results of active type shear tests in a centrifuge by modeling a semi-circular aluminum tunnel in cemented sand ground to understand the effects of stress releasing on seismic stability of tunnel. According to the results, the following findings were obtained.

1) Stress releasing reduces bending moments in the tunnel lining close to zero due to the formation of the arch action of the ground before shearing.
2) The arch action formed by stress releasing deteriorated by shearing.
3) After several shearing, stress releasing dose not affect to the bending moment of the tunnel lining.

Acknowledgements:

This research was partially supported by Grant-in-Aid for Scientific Research (A), 2005-2007, No. 17206050, "Seismic stability of the large cross-section urban tunnel with located in relatively shallow depth". The authors gratefully acknowledge the funding for this research from the 21st Century Centre of Excellence (COE) program entitled "Evolution of Urban Earthquake Engineering".

References:

Iida, H., Hiroto, T., Yoshida, N., and Iwafuji, M. (1996). "Damage to Daikai Subway Station" *SPECIAL ISSUE on Geotechnical Aspects of the January 17 1995 Hyogoken-Nambu Earthquake, Soils and Foundations*, No. 1, 283- 300.

Asakura, T. and Sato, Y. (1996). "Damage to Mountain Tunnels in Hazard Area", *SPECIAL ISSUE on Geotechnical Aspects of the January 17 1995 Hyogoken-Nambu Earthquake, Soils and Foundations*, No. 1, 301-310.

Japan Society of Civil Engineers. (1996), "Specification of cut-and cover tunnels" (in Japaneese)

Japan Society of Civil Engineers. (1996), "Specification of shield tunnels"

Izawa, J., Kusakabe, O., Nagatani, H., Yamada, T. and Ohbo, N. (2006), "Centrifuge modelling on seismic behaviour of rectangular tunnels", *Physical Modelling in Geotechnics 6th ICPMG*, 1163-1169

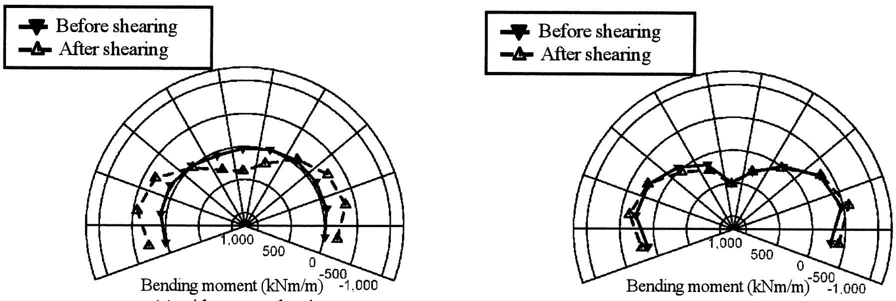

(a) with stress releasing (b) without stress releasing

Figure 5 Bending moments measured before and after 1% shearing

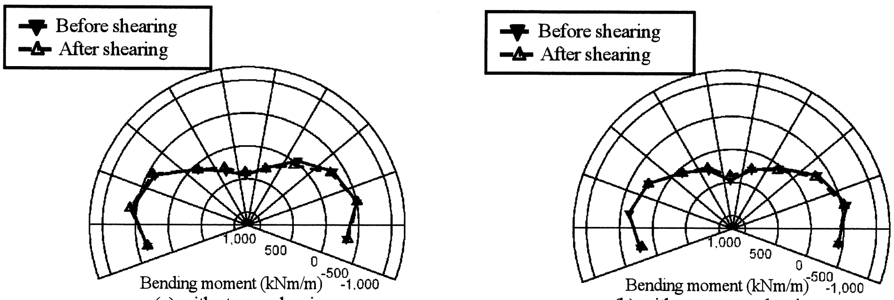

(a) with stress releasing (b) without stress releasing

Figure 6 Bending moments measured before and after 4% shearing

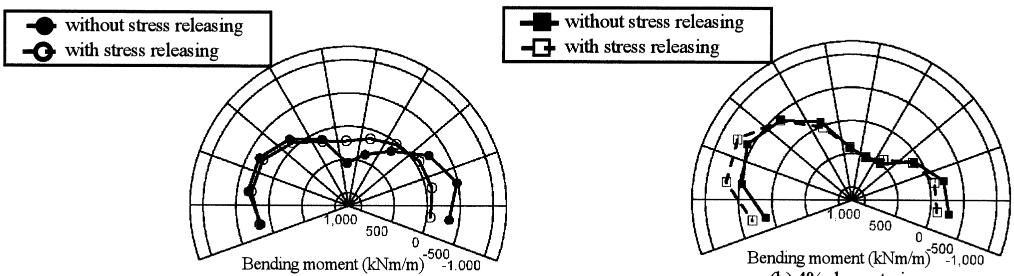

(a) 1% shear strain (b) 4% shear strain

Figure 7 Bending moments measured at maximum shear strain

MODEL TESTS ON BEHAVIOR OF TUNNELS UNDER DEFORMATION OF THE GROUND UPON EARTHQUAKE

Kazuhide Yashiro[1], Yoshiyuki Kojima[2], Masaichi Nonomura[3], Toshihiro Asakura[4] and Jiro Takemura[5]

1) Assistant Senior Researcher, Tunnel Engineering Laboratory, Railway Technical Research Institute, Japan
2) Laboratory Head, Tunnel Engineering Laboratory, Railway Technical Research Institute, Japan
3) Director, Design and Technology Department, Japan Railway Construction, Transport and Technology Agency, Japan
4) Professor, Department of Civil and Earth Resources Engineering, Kyoto University, Japan
5) Associate Professor, Department of Civil Engineering, Tokyo Institute of Technology, Japan
kyashiro@rtri.or.jp, ykojima@rtri.or.jp, m.nonomura@jrtt.go.jp, asakura2@kumst.kyoto-u.ac.jp, jtakemur@cv.titech.ac.jp

Abstract: Mountain tunnels are generally thought to be less susceptible to seismic damage. However, tunnels that have even a small overburden or that exist under poor ground conditions are often subjected to ground displacement, cracking, compressive failure or other damages depending on the magnitude of the earthquake and the distance from the epicenter. The authors performed model tests to clarify the mechanism of earthquake-related damage to tunnels as well as the aseismic performance of tunnel lining. The authors found that experiments using model tunnel loading test apparatus are possible to evaluate the deformation and fracture behavior of tunnels subjected to horizontal displacement in an earthquake, and countermeasures (inverts, a mixture of fibers and a buffer material) can reduce tunnel deformation, width of crack or bottom-heaving.

1. INTRODUCTION

Mountain tunnels are generally thought to be less susceptible to seismic damage. According to the available research results (Asakura et al. 2000) however, tunnels that have even a small overburden or that exist under poor ground conditions are often subjected to ground displacement, cracking, compressive failure or other damages depending on the magnitude of the earthquake and the distance from the epicenter. Indeed, a number of mountain tunnels were damaged in the 2004 Niigataken Chuetsu Earthquake.

The damage caused by earthquakes is broadly divided into the three patterns seen in tunnels that (1) have a small overburden, (2) are subjected to poor ground conditions, and (3) experience fault slippage. (Asakura et al. 2000) With a particular focus on damage pattern (2) above, the authors implemented a loading test on a tunnel in model ground to clarify the mechanism of earthquake-related damage to tunnels as well as the aseismic performance of tunnel lining. The authors also performed model tests on effect of countermeasures for newly constructed tunnels of placing invert, using fiber reinforced concrete and inserting a buffer material between the lining and the shotcrete.

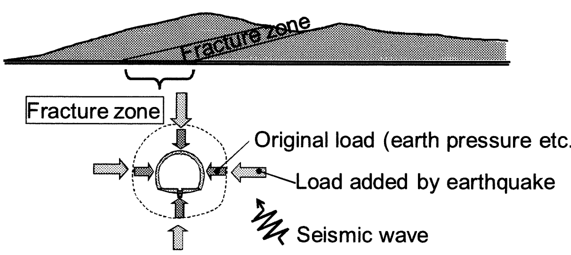

Figure 1 Mechanism by which Earthquake Damage Occurs in Tunnels under Poor Ground Conditions.

2. MECHANISM OF EARTHQUAKE-RELATED DAMAGE IN TUNNELS SUBJECTED TO POOR GROUND CONDITIONS

Figure 1 shows the mechanism by which earthquake damage occurs in tunnels under poor ground conditions. With tunnels in mountains that contain faults, fracture zones or other poor ground conditions, the lining can be exposed to earth pressure even before being hit by an earthquake. In addition, seismic displacement generally tends to be larger, as the ground is normally soft under such conditions. Such mountain tunnels are often damaged by earthquakes as a synergy of these effects. (Asakura et al. 2000)

When an earthquake causes additional displacement to a mountain tunnel with a large overburden, different deformation modes emerge in and around the tunnel depending on the angle of incidence of the seismic wave. In this study, however, the authors assumed a case where the tunnel is subjected to damage as a result of horizontal displacement (with the angle of incidence of the seismic

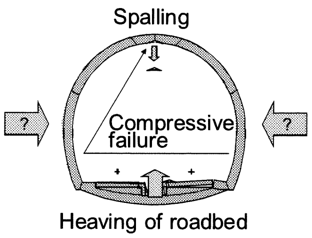

Figure 2 Damage to the Myoken Tunnel (Yashiro et al. 2007)

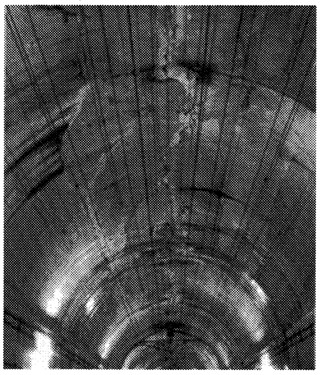

Photo 1 Damage to the Myoken Tunnel (Yashiro et al. 2007)

wave assumed as 45°) and applied a single-sided load horizontally from the left of the tunnel. Figure 2 and Photo 1 show damage to the Myoken Tunnel as an example of a case where damage is thought to have been caused by horizontal displacement.

3. TEST METHOD

For the test, the authors used the 1:50-scale model tunnel loading test apparatus (Figure 3 and Photo 2). The apparatus was composed of an earth tank (inner dimensions 600 × 600 mm, depth 300 mm), a reaction frame, two loading jacks (each 200 kN), load cells, loading plates, model ground and a model tunnel. The jacks were hydraulically controlled, and the displacement of the loading plate resulting from the force applied by them was transmitted to the model tunnel through the model ground. After completing the model ground, the authors placed a top cover on the earth tank and implemented the test while assuming a two-dimensional strain condition. At the location of the tunnel, there was a circular observation window through which the conditions of the tunnel lining were visually observed.

To reduce friction between the ground and the earth-tank wall, two layers of Teflon sheet applied with fluid paraffin were pasted. Hisatake et al.(1998) remark that, in order to transmit 80% or more of the loading pressure to the tunnel, the length (depth) of the earth tank must be the same as or larger than the thickness of the overburden. To satisfy this condition, therefore, the authors secured a length (depth) of 300 mm for the earth tank against a distance of 200 mm from the earth-tank wall to the tunnel wall.

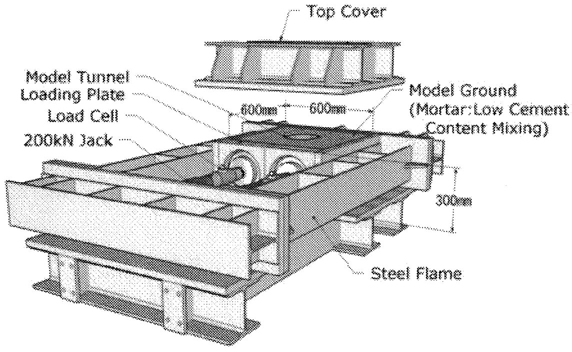

Figure 3 The Model Tunnel Loading Test Apparatus

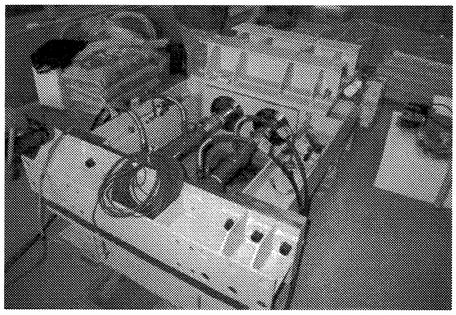

Photo 2 The Model Tunnel Loading Test Apparatus

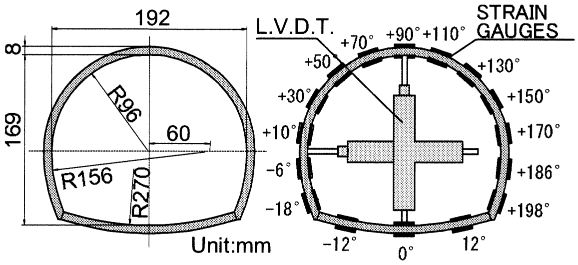

Figure 4 Outline of the Model Tunnel

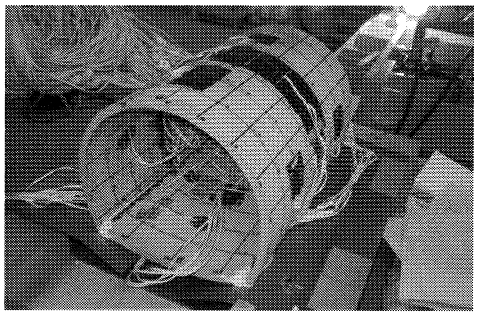

Photo 3 Appearance of the Model Tunnel

To simulate a standard section of Shinkansen tunnel (NATM), the authors prepared two types of 1:50-scale mortar-made tunnel models, three with an invert and one without.

To prepare the ones with an invert, the authors casted an arch section and an invert section separately and joined them with adhesive. Since the tensile strength of the adhesive was sufficiently small, the bending moment at the joint was not thought to be large. Shotcrete was not modeled for the test.

Table 1 Dimensions of the Model Ground and the Model Tunnel

Model Ground	Material	Mortar (Low cement content mixing)
	Fine aggregate	Silica
	W/C	3.5
	Strength	0.5MPa (7day)
	Young's modulus	100MPa
	Friction angle	9.5°
Model Tunnel	Material	Mortal
	Strength	26MPa (28day)
	Thickness	8mm
	Depth	300mm
	Joint	None
	Fiber	Polypropylene fiber, d=0.06mm, L=6mm, Vol.0.5%
	EPS	Density 0.12kN/m^3, Thickness 3mm

Table 2 Proportions Used in the Mortar of Low Cement Content Mixing

Material	Type		Unit content kg/m^3	Note
Water	W		649	W/C=3.5
Cement	C	Portland cement	185	
Fine aggregate	S	Silica	650	
Admixture mineral	B	Bentonite	64.9	0.1W
Chemical admixture	AD1	Water reducing admixture	17.1	0.092C
	AD2	Separation prevention admixture	0.278	0.015C

The authors set four displacement transducers in the tunnel to measure the convergence displacement, and pasted strain gauges on the inner and outer lining surfaces to measure the strain in the lining. See Figure 4 for an outline of the model tunnel and Photo 3 for its appearance.

Table 1 shows the dimensions of the model ground and the model tunnel. The ground was made of mortar of low cement content mixing to simulate soft rock ground. The W/C was adjusted to set the ground strength for the test (seven days after casting) at about 0.5 MPa.

Table 2 shows the proportions used in the mortar of low cement content mixing, which was similar to the one the authors had used for previous studies.(Kojima et al. 2003) It was mixed with bentonite and a separation prevention admixture, which ensured fluidity and a separation-free quality despite its lean proportion. It had an internal friction angle ϕ of 10° or less, with characteristics close to those of cohesive soil. The authors set the value of W/C at 3.5 for the test, though the basic W/C value of the said mortar is 3.0. Figure 5 shows the results of unconfined compression tests of the mortar. Its stress reaches a peak when the axial strain is about 1% and decreases thereafter.

For the test, the authors inserted a material with a low elastic coefficient between the shotcrete and the lining as a buffer to prevent earthquake damage, and investigated its effect. For this purpose, the authors used EPS as the low-elasticity material. Before the test, the authors assessed its deformation behavior through an unconfined compression test (see Figure 6 for the test results).

Figure 6 shows that the EPS plasticizes when strain exceeds 2% and hardens when it exceeds 60% as bubbles are compressed to the point of disappearance. The elastic

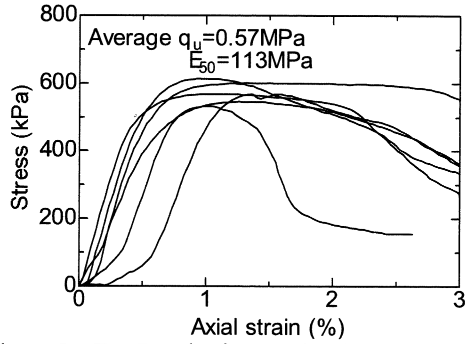

Figure 5 Test Result of Unconfined Compression Tests of the Mortar

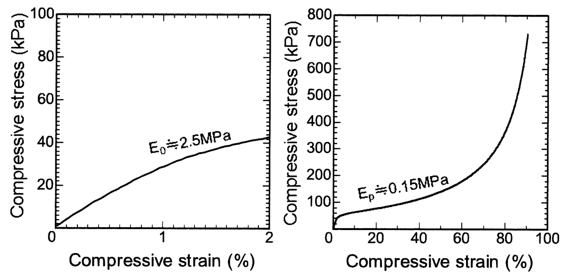

Figure 6 Test Result of Unconfined Compression Tests of the EPS

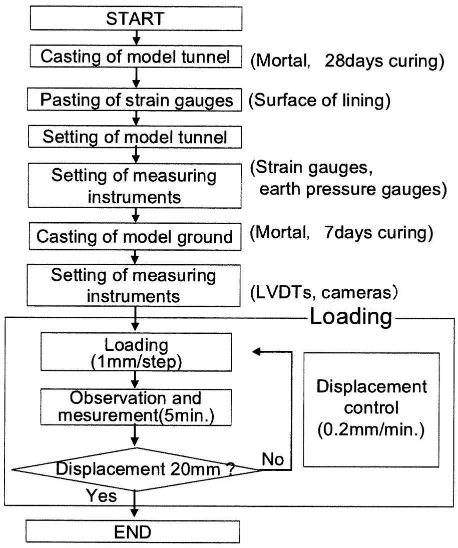

Figure 7 Loading Procedure

coefficient is approximately 2.5 MPa in the elastic region, and the tangential elastic coefficient is approximately 0.15 MPa in the plastic region.

4. TEST CONDITIONS

Figure 7 shows the loading procedure. While controlling the displacement of the loading plates, the authors repeated a process of load application for five minutes at 0.2 mm/min, then implemented observation and measurement for five minutes until the displacement of the

Table 3 Test Cases

No.	Mortar	Invert	Note
Case1	Plain	None	Without invert
Case2	Plain	Modeled	With invert
Case3	Fiber reinforced	Modeled	Fiber reinforced
Case4	Plain	Modeled	With EPS

Table 4 Test Cases

Case1	Case2	Case3	Case4
Plain mortar (Without invert)	Plain mortar Invert	Fiber reinforced mortal Invert	Plain mortar EPS Invert

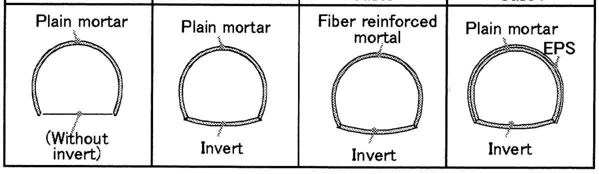

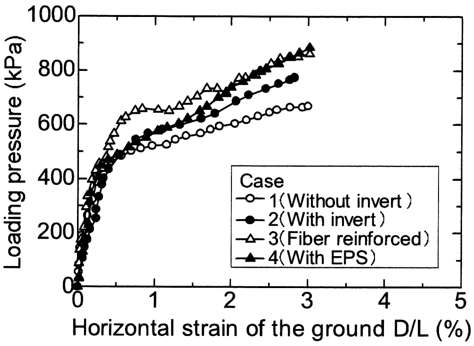

Figure 8 The Relationship between the Loading Plate Pressure and the Horizontal Strain of the Ground

loading plate reached 20 mm (equivalent to 3.3% of the horizontal strain of the ground).

Tables 3 and 4 summarize the following cases of lining examined in this test:

Case 1: A plain mortar lining without an invert (standard lining

Case 2: A lining with a modeled invert

Case 3: A lining made of mortar with polypropylene fibers added (vol. 0.5%)

Case 4: A lining with EPS (thickness 3 mm) pasted around the outer circumference

Case 2 is to examine the effect of lining with and without an invert. Case 3 is to investigate the effect of fiber-reinforced concrete, which has often been used in recent years as a method to reinforce linings. Case 4 studies the effect of a buffer inserted between the lining and the shotcrete as a countermeasure to prevent seismic damage.

5. TEST RESULTS

5.1 Loading Pressure and Horizontal Strain of the Ground

Figure 8 shows the relationship between the loading plate pressure applied by the jacks and the horizontal strain of the ground, or the displacement D of the loading plate divided by the length L of the earth tank. See Figure 9 for

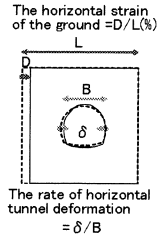

Figure 9 Definition of the Horizontal Strain of the Ground.

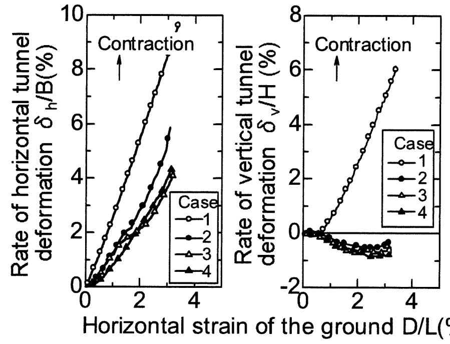

Figure 10 Relationship between the Horizontal Strain of the Ground and the Rate of Tunnel Deformation.

the definition of the horizontal strain of the ground.

The authors applied a load until the horizontal strain of the ground reached about 3%. Figure 8 indicates that the ground deformed elastically until the horizontal strain reached about 0.5% and yielded thereafter, thus reducing rigidity. The loading pressure was the largest in Case 3, followed in order by those in Cases 4 and 2, and was the smallest in Case 1. It is thought that the disparity in the loading pressure in different cases was caused partly in proportion to the difference in the compressive strength of the ground. However, the loading pressure in Case 1 (without invert) was thought to be the smallest because the tunnel bottom heaved, causing large-scale fracture (explained later) as the displacement of the loading plate increased.

5.2 Rate of Tunnel Deformation

The authors used the horizontal strain of the ground and the rate of tunnel deformation (the contraction δ divided by the width B of the convergence) as indices to summarize the tunnel deformation data. See Figure 9 for the definition of the rate of tunnel deformation. As Figure 8 indicates, the loading pressure varies with ground strength, although the difference is not great. To discuss the relationship between the input deformation and the deformation/fracture behavior of the tunnel, therefore, the authors evaluated the test results based on the horizontal strain of the ground and the rate of tunnel deformation.

Figure 10 shows the relationship between the horizontal strain of the ground and the rate of tunnel deformation. In the horizontal direction, the tunnel contracted as the load increased in all cases. In Case 1 (without invert), however, the rate of horizontal deformation was about twice that of Cases 2 to 4 (with invert). In the

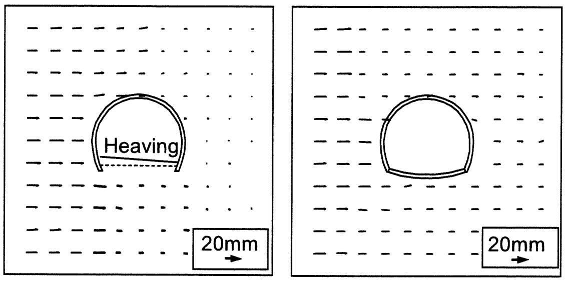

(a) Case1 (b) Case3

Figure 11 Displacement Vectors of the Ground (After Unloading)

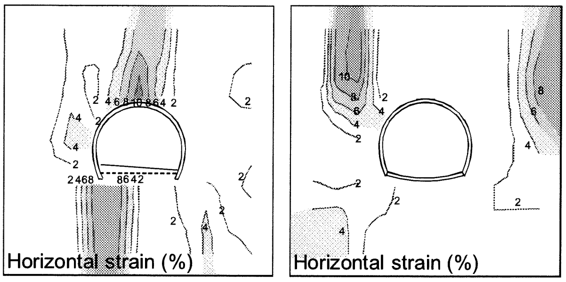

(a) Case1 (b) Case3

Figure 12 Distribution of Horizontal Strain in the Ground (After Unloading)

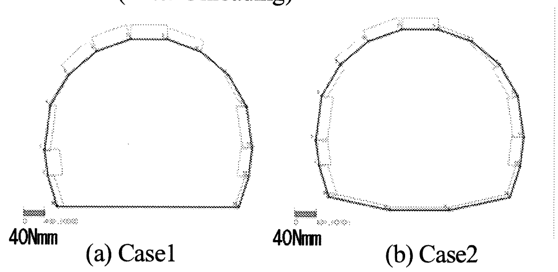

(a) Case1 (b) Case2

Figure 13 Moment Generated in the Lining before Cracking (Horizontal Strain of the Ground is 0.5%)

vertical direction on the other hand, the tunnel contracted in Case 1 and expanded in Cases 2 to 4. It is proved, therefore, that the convergence contracted to a large extent in the vertical direction in Case 1 (without invert). Figure 10 shows that the invert significantly suppresses tunnel deformation.

5.3 Displacement and Deformation of the Ground

After finishing the loading on the tunnel, the authors removed the top cover from the earth tank and read the displacement of the ground surface from the preset mark. Figure 11 shows the displacement vectors in Case 1 (without invert) and Case 3 of the fiber-reinforced lining (with invert). Figure 12 illustrates the distribution of horizontal strain in the ground thus obtained in these cases. Cases 2 and 4 (with invert) presented similar fracture behavior to that of Case 3.

In Case 1 (without invert), the ground at the tunnel bottom fractured and heaved, with large strain distributed at the top and bottom of the tunnel. In Case 3 of the fiber-reinforced lining (with invert), heaving did not occur at the tunnel bottom, with large strain distributed in areas

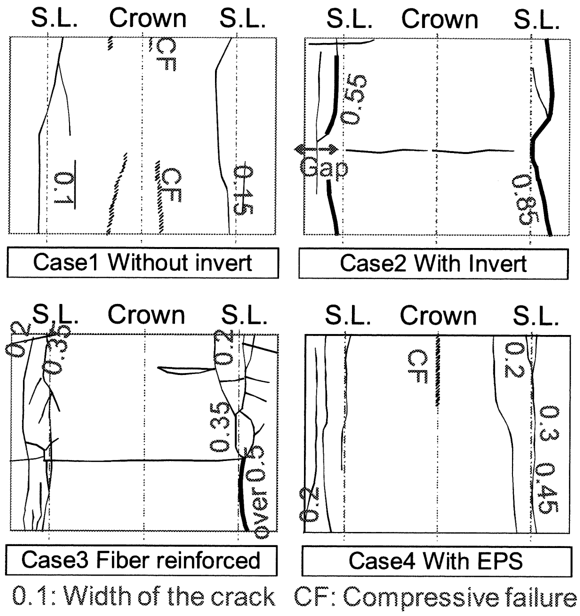

Figure 14 Cracks on the Lining (inside) (Horizontal Strain of the Ground is 3%)

distant from the tunnel. This proves that large strain does not occur in the ground around the tunnel (unlike in Case 1), presumably because the horizontal rigidity of the structure is not large if there is no invert. This pattern of deformation suggests that tunnels that do not have an invert deform more than those that do.

5.4 Section Force in the Lining

Similarly, Figure 13 shows the moment generated in the lining before cracking (when the horizontal strain of the ground was 0.5%) in Cases 1 and 3. As the lining was loaded in the horizontal direction, a positive moment emerged at the wall and a negative one at the crown. This corresponds to the fact that cracks occurred in these locations (as referred to later). As regards the bending moment, the maximum value at the crown was larger in Case 1 (with invert), and the range subjected to bending tended to be wider than in other cases.

5.5 Cracks on the Lining

Figure 14 shows the cracks on the lining (inside) when the horizontal strain of the ground was 3%. Tension cracks were generated at the side wall as the lining was subjected to horizontal loading. Tension cracks also occurred at the outside surface of the crown in all cases (not shown in Figure 14). Tension cracks were not observed on the invert, however.

As the load increased, compressive failure took place on the inside surface of the crown in Case 1 (without invert), but was not observed visually in Cases 2 or 3 (with invert). In Case 1, deformation (rotation) was concentrated at the crown where compressive failure occurred. Since the displacement of the side wall progressed due to the lack of invert in Case 1, the cracks of the side wall itself seemed to be smaller. In Case 2 (mortar lining), a large crack was

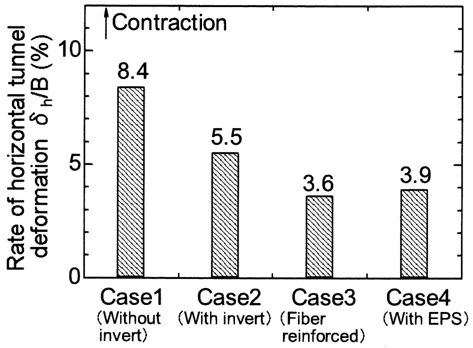

Figure 15 Rate of Horizontal Deformation of the Tunnel (Horizontal Strain of the Ground is 3%)

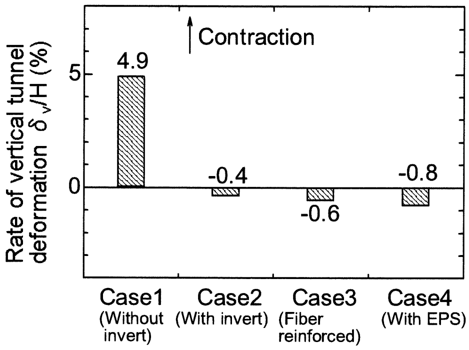

Figure 16 Rate of Vertical Deformation of the Tunnel (Horizontal Strain of the Ground is 3%)

generated at the side wall as loading progressed, but no other cracks emerged, with growth seen only in the width of the said crack. In Case 3 where the lining material was mixed with fibers, the number of cracks with smaller widths increased approximately where the single crack was seen in Case 2, presumably due to the effect of the performance of bending deformation that was improved by the mixed fibers. This is expected to improve resistance against flaking when a tunnel undergoes deformation.

In Case 4 where a buffer material was pasted on the outside lining surface, compressive failure was observed on the inner side of the crown, though the crack widths on the side wall were smaller. This was thought to have occurred because the ground reaction decreased at the crown, thus increasing deformation in the vertical direction, though deformation decreased in the horizontal direction due to the effects of the buffer material. This can also be confirmed in Figure 10.

5.6 Effect of Countermeasure

Figures 15 to 16 summarize the rate of horizontal and vertical deformation of the tunnel when the horizontal strain of the ground is 3%. These figures prove that deformation both in the horizontal and vertical directions can be suppressed by the adoption of an invert, fiber-reinforcement, and a buffer material.

6. CONCLUSIONS

Focusing on tunnel damage under poor ground conditions, the authors implemented a loading test on a tunnel in model ground to clarify the mechanism by which tunnels are damaged in earthquakes and the aseismic performance of lining. The authors also performed model tests on effect of countermeasures for newly constructed tunnels of placing invert, using fiber reinforced concrete and inserting a buffer material between the lining and the shotcrete. The conclusions obtained from the test are as follows:

(1) Experiments using model tunnel loading test apparatus proved that it is possible to evaluate the deformation and fracture behavior of tunnels subjected to horizontal displacement in an earthquake.

(2) Inverts can reduce tunnel deformation and bottom-heaving.

(3) A mixture of fibers can improve the ductility of lining, scatter cracks and reduce crack widths.

(4) The introduction of a buffer material potentially suppresses tunnel deformation.

The authors plan to continue discussions on the issues dealt with in this paper through numerical analysis and examine the effects of poor ground conditions distributed over a small range in the longitudinal direction.

The research introduced in this paper is part of a series of studies on the mechanism of seismic damage and improvement of the earthquake resistance of mountain tunnels, jointly conducted by Kyoto University, the Railway Technical Research Institute (RTRI) and the Japan Railway Construction, Transport and Technology Agency (JRTT) under "Program for Promoting Fundamental Transport Technology Research" from the Japan Railway Construction, Transport and Technology Agency (JRTT).

Acknowledgements:

The authors wish to express their sincere gratitude to Mr. Naoki Tachibana of RTRI and Mr. Yoshio Matsumoto of TESS Co., Ltd., who kindly extended cooperation in the testing performed for the promotion of this research.

References:

Asakura, T., Shiba, Y., Matsuoka, S., Oya, T. and Yashiro, K. (2000), "Damage to mountain tunnels by earthquake and its mechanism (in Japanese)," *Journals of the Japan society of civil engineers*, No.659, III-52, pp.27-38

Yashiro, K., Kojima, Y. and Shimizu, M. (2007), "Historical earthquake damage to tunnels in Japan and case studies of railway tunnels in the 2004 Niigataken-Chuetsu earthquake," *QR of RTRI*, Vol. 48, No. 3, pp.136-141

Hisatake, K. and Shibuya, S. (1998), "Design of tunnel model test device and considerations on initial stress generation (in Japanese)," *Proceedings of the 10th Japan symposium on rock mechanics*, pp.545-550

Kojima, Y., Yoshikawa, K., Yashiro, K., Noma, T., Asakura, T. and Tsuchiya, T. (2003), "Ground surface loading model test on deformation behavior of tunnel lining (in Japanese)," *Journals of the Japan society of civil engineers*, No.729, III-62, pp.73-86

Fifth International Conference on Urban Earthquake Engineering
March 4-5, 2008, Tokyo Institute of Technology, Tokyo, Japan

ECCENTRIC BUILDING POUNDING CONSIDERING EFFECTS OF UNDERLYING SOIL

Kabir Shakya[1], and Anil C. Wijeyewickrema[2]

1) Graduate Student, Department of Civil Engineering, Tokyo Institute of Technology, Japan
2) Associate Professor, Department of Civil Engineering, Tokyo Institute of Technology, Japan
shakya.k.aa@m.titech.ac.jp, wijeyewickrema.a.aa@m.titech.ac.jp

Abstract: In this paper an analysis of seismic pounding of eccentrically located reinforced concrete 6-story and 8-story buildings with non-equal story heights, including soil-structure interaction is presented. The foundation-soil interaction is included by using the discrete model and pounding between buildings is incorporated through impact elements which consist of a gap element and a Kelvin-Voigt element. Impact forces, interstory displacements and normalized story shear are used to evaluate the responses of the buildings for two near field and two far field earthquakes. The buildings under consideration experience the maximum impact forces and interstory displacements due to the near field earthquakes for both fixed foundation and flexible (soil) foundation cases. Upon consideration of underlying soil, significant reduction in interstory displacements is observed. The maximum interstory displacements occurred when there is no pounding. The buildings with fixed foundation experience higher normalized story shear.

1. INTRODUCTION

Adjacent buildings having different dynamic characteristics may vibrate out of phase and collide during earthquakes, if the separation between them is insufficient. In the past, especially in urban areas, many buildings were constructed even up to their property lines because of rapid increase in urban development and the associated increase in real-estate values. This may cause non-structural and structural damage to the buildings and may also lead to total collapse of buildings during seismic pounding. The characteristics of input ground motion, geometric configurations and dynamic characteristics of buildings, soil parameters and gap between the adjacent buildings highly influences the location and magnitude of impact. To avoid seismic pounding, some of the building codes such as IBC 2003 have provided a clause to make a provision of sufficient separation between adjacent buildings. However, this clause has not been included in IBC 2006. Due to constraints in availability of land and in order to fulfill functional requirements, adjacent buildings may also be constructed eccentrically, with different floor heights and this may give rise to eccentric and mid-column pounding. Most of the seismic pounding analyses are performed without considering the effects of underlying soil. The consideration of underlying soil leads to an increase in degrees of freedom at the foundation level and also allows energy dissipation. Hence, it is necessary to include effects of soil on the seismic pounding analysis of buildings. Five major types of poundings; mid column pounding, heavier adjacent building pounding, taller adjacent building pounding, eccentric building pounding and end building pounding have been reported by Jeng and Tzeng (2000).

Anagnostopoulos (1988) used the spring-damper element in order to simulate the earthquake induced pounding between adjacent structures representing damping constant in terms of the coefficient of restitution. Furthermore, non-linear viscoelastic model was implemented by Jankowski (2005) for more accurate simulation of structural pounding during earthquakes. The analysis results were compared with the results of experiments performed by van Mier et al. (1991) through which the characteristics of concrete-to-concrete impact and steel-to-steel impact were also obtained.

The parametric study on eccentric pounding of two symmetric buildings conducted by Leibovich et al. (1996) showed the amplification in the response of the buildings due to impact eccentricity and that the effect is not proportional to impact eccentricity. Rahman et al. (2001) highlighted the influence of soil flexibility effects on seismic pounding for adjacent multi-story buildings of differing total heights, by using 2-D structural analysis software, RUAUMOKO for which the discrete model proposed by Mullikan and Karabalis (1998) was used. In the present paper too, the soil-structure interaction is incorporated through the discrete model. The schematic diagram of the

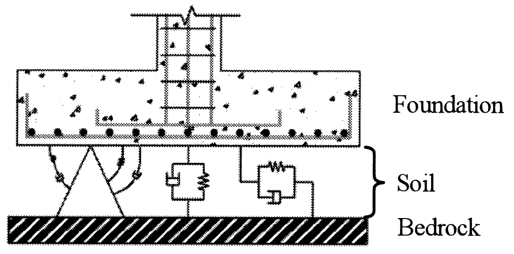

Figure 1 Discrete Model for Soil-Foundation Interaction

mass-spring-damper is shown in Figure 1. The mass-spring-damper properties are calculated using equations 2.42a ~ 2.44 and Table 2-4 of Wolf (1988) (pg 32-36).

The purpose of this paper is to investigate the effects of soil on mid-column seismic pounding of eccentrically located reinforced concrete buildings, for which the discrete model is used to incorporate foundation-soil interaction. The effects of soil are studied by comparing impact forces, interstory displacements and normalized story shear of the buildings.

2. POUNDING FORCE AND IMPACT ELEMENT

The pounding between adjacent structures are often modeled using elastic or viscoelastic impact elements but the linear spring-damper (Kelvin-Voigt model) element is mostly used to model impact between two colliding structures. The viscous component of the linear spring-damper element dissipates energy throughout the approach and restitution period but, in reality, most of energy dissipation takes place during the approach period and minor energy dissipation is observed during the restitution period. However, for simplicity, to simulate structural pounding the linear viscoelastic model has been widely used. The force in the linear viscoelastic model $F(t)$ during impact is given by

$$F(t) = k_L \delta(t) + c_L \dot{\delta}(t), \tag{1}$$

where, $\delta(t)$ is the relative displacement of colliding structural elements, $\dot{\delta}(t)$ is the relative velocity between colliding elements, k_L is the stiffness and c_L is the damping coefficient and is given by

$$c_L = -2 \ln e_r \sqrt{\frac{k_L m_1 m_2}{\left[\pi^2 + (\ln e_r)^2\right](m_1 + m_2)}}, \tag{2}$$

where, e_r is the coefficient of restitution, m_1 and m_2 are masses of structural members (Anagnostopoulos (1988)). The numerical simulation performed by Jankowski (2005) showed that for concrete-to-concrete impact, $k_L = 93{,}500$ kN/m and $e_r = 0.65$ provides good correlation between experimental results provided by van Mier et al. (1991) and theoretical results. Besides Anagnostopoulos (1988), Azevedo and Bento (1996), Mouzakis and Papadrakakis (2004) and Jankowski (2006) have also used $e_r = 0.65$ for concrete to concrete impact. In the present study also $k_L = 93{,}500$ kN/m and $e_r = 0.65$ are used.

The impact elements are inserted between buildings as shown in Figure 2(a) to simulate contact of buildings and pounding force. The link element shown in Figure 2(c) is created by combining the gap element shown in Figure 2(b) with Kelvin-Voigt model. The force transmits from one structure to another only when contact occurs. The force-deformation relationship of gap element is given by

$$f_G = \begin{cases} k_G[(u_i - u_j) - gap] & \text{if } u_i - u_j > gap, \\ 0 & \text{if } u_i - u_j < gap, \end{cases} \tag{3}$$

where, f_G is the force, k_G is the spring constant, u_i and u_j are the nodal displacements of nodes i and j and gap is the initial gap opening. The stiffness of gap element k_G is considered as $100\,k_L$ to avoid error in convergence and to ensure that it works nearly rigidly when the gap is closed.

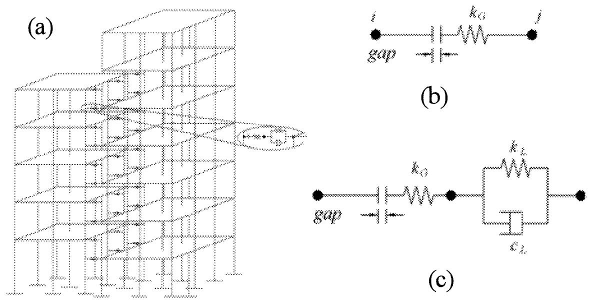

Figure 2 (a) Buildings Connected with Impact Elements; (b) Gap Element; and (c) Impact Element Composed of Gap Element and Kelvin-Voigt Element

3. DESCRIPTION OF BUILDINGS AND DESIGN

Two residential buildings, 6-story and 8-story, located eccentrically as shown in Figure 3, are considered for the analysis. The story height of the first floor of the 6-story building is 4.5 m while all other story heights of 6-story and 8-story buildings are 3.0 m, which gives rise to mid-column pounding. The software SAP2000 is used to analyze the buildings considering 5% damping ratio. For analysis and design, concrete with compressive strength $f_c' = 27$ N/mm^2, unit weight γ_c = 24 kN/mm^3, modulus of elasticity E_c =24,281 N/mm^2, and Poisson's ratio ν_c = 0.2 and reinforcing steel with yield strength f_y = 414 N/mm^2 are used. Considering live load of 2 kN/m^2, roof load of 1

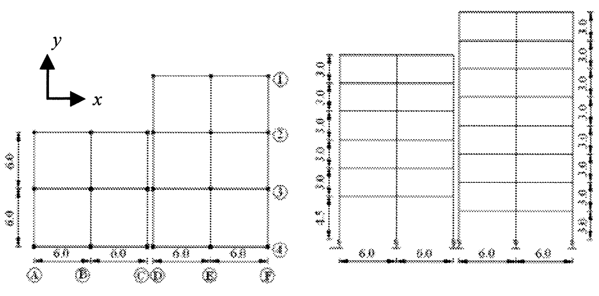

Figure 3 The 6-Story and 8-Story Buildings: (a) Plan; and (b) Elevation

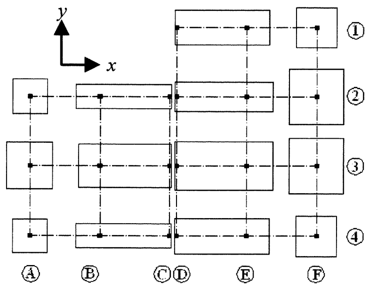

Figure 4 Foundation Arrangement Plan

kN/m^2 and partition wall load of 1 kN/m^2, the structural components including foundations of the buildings are designed to fulfill the code requirements of ACI 318-02 and IBC 2003. Site class D, seismic use group II and seismic design category A are considered in order to calculate the lateral loads. The buildings are provided with 180 mm thick floor slabs which are considered as rigid floor diaphragms and 300 mm x 500 mm beams. The column sizes and steel reinforcements and dimensions of footings are shown in Tables 1 and 2. The arrangement of footings is shown in Figure 4.

4. NUMERICAL ANALYSIS AND RESULTS

The coefficients of frequency independent mass-spring-dampers at each footing are calculated using the designed footing size with 1.5 m embedment and soil properties: density $\rho_s = 16.5$ kN/m^3 , Poisson's ratio $\nu = 1/3$ and shear modulus $G = 18.75$ N/mm^2 . For this analysis, the gaps between the buildings are considered as 50 mm. Two far field earthquakes, 1940 El Centro (Imperial Valley irrigation station, N-S component, PGA = 0.298g, M_w = 7.0) and 1968 Hachinohe (Hachinohe city station, N-S component, PGA = 0.229g, M_w = 7.9) and two near field earthquakes, 1994 Northridge (Sylmar county hospital parking lot station, N-S component, PGA = 0.843g, M_w = 6.7) and 1995 Kobe (0 KJMA station, N-S component, PGA = 0.821g, M_w = 6.9) are used as earthquake inputs along *x*-direction. Newmark method with $\beta = 0.25$, $\gamma = 0.5$ and time step $\Delta t = 0.002$ sec is adopted for time history analysis of buildings.

The fundamental time periods and fundamental frequencies of the buildings are shown in Table 3 , where an increase in fundamental time period of the buildings is observed when underlying soil is considered. From the Fourier spectrum of input ground motions, the dominant frequencies of El Centro, Hachinohe, Northridge and Kobe earthquakes are found to be 2.151 Hz, 0.361 Hz, 0.633 Hz and 1.417 Hz, respectively. The dominant frequency of Northridge earthquake is close to the fundamental frequency of 8-story building with flexible (soil) foundation and that of Kobe earthquake is close to the fundamental frequency of 6-story building with fixed foundation.

The impact force time history at roof level of 6-story building, column C3, is shown in Figure 5 where it can be

Table 1 Column size and Main Steel Reinforcement

Floor	Grid	A/C	B	D/F	E
1	1			C1 - 4-25Ø + 4-16Ø	C2 - 4-28Ø + 8-20Ø
2	1			C1 - 4-25Ø + 4-16Ø	C2 - 4-25Ø + 8-20Ø
3	1			C1 - 4-20Ø + 4-16Ø	C2 - 4-25Ø + 8-16Ø
4-8	1			C1 - 8-16Ø	16Ø
1	2	C1 - 8-16Ø	C2 - 4-25Ø + 8-16Ø	C2 - 8-25Ø + 4-20Ø	C4 - 8-28Ø + 4-20Ø
2	2	C1 - 8-16Ø	C2 - 12-16Ø	C2 - 4-25Ø + 8-20Ø	C4 - 4-28Ø + 8-20Ø
3	2	C1 - 8-16Ø	C2 - 12-16Ø	C2 - 4-20Ø + 8-16Ø	C4 - 12-20Ø
4-6	2	C1 - 8-16Ø	16Ø	C2 - 8-16Ø	20Ø
7-8	2			C2 - 8-16Ø	20Ø
1	3	C2 - 8-20Ø	C3 - 12-28Ø	C2 - 8-25Ø + 4-20Ø	C4 - 8-28Ø + 4-20Ø
2	3	C2 - 8-20Ø	C3 - 8-28Ø + 4-16Ø	C2 - 4-25Ø + 8-20Ø	C4 - 4-28Ø + 8-20Ø
3	3	C2 - 8-20Ø	C3 - 4-28Ø + 8-16Ø	C2 - 4-20Ø + 8-16Ø	C4 - 12-20Ø
4-6	3	C2 - 8-20Ø	16Ø	C2 - 8-16Ø	20Ø
7-8	3			C2 - 8-16Ø	20Ø
1	4	C1 - 8-16Ø	C2 - 4-25Ø + 8-16Ø	C1 - 4-25Ø + 4-16Ø	C2 - 4-28Ø + 8-20Ø
2	4	C1 - 8-16Ø	C2 - 12-16Ø	C1 - 4-25Ø + 4-16Ø	C2 - 4-25Ø + 8-20Ø
3	4	C1 - 8-16Ø	C2 - 12-16Ø	C1-25Ø + 4 16Ø	C2 - 4-25Ø + 8-16Ø
4-6	4	C1 - 8-16Ø	16Ø	C1 - 8-16Ø	16Ø
7-8	4			C1 - 8-16Ø	16Ø

C1: 360 mm x 360 mm
C2: 450 mm x 450 mm
C3: 500 mm x 500 mm

Table 2 Footing Details

Grid	A	B C	D E	F
1			8.15 x 3.00 x 0.50	3.50 x 3.50 x 0.45
2	3.00 x 3.00 x 0.40	8.20 x 2.10 x 0.40	8.45 x 4.20 x 0.60	4.75 x 4.75 x 0.60
3	4.00 x 4.00 x 0.50	8.00 x 3.70 x 0.60	8.45 x 4.20 x 0.60	4.75 x 4.75 x 0.60
4	3.00 x 3.00 x 0.40	8.20 x 2.10 x 0.40	8.15 x 3.00 x 0.50	3.50 x 3.50 x 0.45

(All dimensions are in m)

Table 3 Dynamic Characteristics of Buildings

Foundation Type	Fundamental Time Period (sec)		Natural Frequency (Hz)	
	6-Story	8-Story	6-Story	8-Story
Fixed	0.9693	1.0855	1.0317	0.9212
Flexible (Soil)	1.0198	1.1430	0.9806	0.8749

seen that the collision between buildings occurs at different times with different magnitudes. Kobe earthquake has the dominant effect on both fixed foundation case and flexible foundation case. The maximum impact forces due to Kobe and Hachinohe earthquakes are larger when underlying soil is considered. Higher magnitude of impact forces are observed in the case of near field earthquakes. On comparing the maximum impact forces at each floor level of 6-story building, column C3 (Figures 6), it is clearly seen that the impact forces have been reduced when a flexible foundation is considered, however, impact force at the 6th floor is significantly increased in the case of Kobe and Hachinohe earthquakes upon considering soil.

The responses of buildings are also expressed in terms of interstory displacements in Figure 7 for no pounding fixed foundation, fixed foundation pounding and flexible foundation pounding cases. Reduction in interstory displacement is observed while pounding between adjacent buildings occur. The interstory displacement is maximum when there is no pounding and is minimum when soil effects are considered. Northridge earthquake yielded maximum interstory displacement in 8-story building without pounding (Figure 7(a)), however, in rest of the cases Kobe earthquake contributed to the maximum interstory displacement. In this regard, it is clearly seen that near field earthquakes yield significant effect on interstory displacements for the given buildings.

Normalized story shear of the buildings are obtained after normalizing the story shear of the buildings due to pounding by the story shear for fixed foundation no pounding case and are shown in Figure 8. Except for Hachinohe earthquake, (Figures 8(c), (d)), the normalized story shear at each floor is higher for fixed foundation case, however, even for Hachinohe earthquake the maximum normalized story shear is observed in the case of fixed foundation. For 8-story building, the maximum normalized story shear for fixed foundation case is 1.676 due to Kobe earthquake and that for flexible foundation case is 1.108 due to Hachinohe earthquake. Similarly, for 6-story building, the maximum normalized story shear for fixed foundation case is 2.846 due to Kobe earthquake and that for flexible foundation case is 2.481 due to Hachinohe earthquake. The results show that in terms of normalized story shear, Kobe earthquake is dominant when foundation is fixed and Hachinohe earthquake is dominant when foundation is flexible.

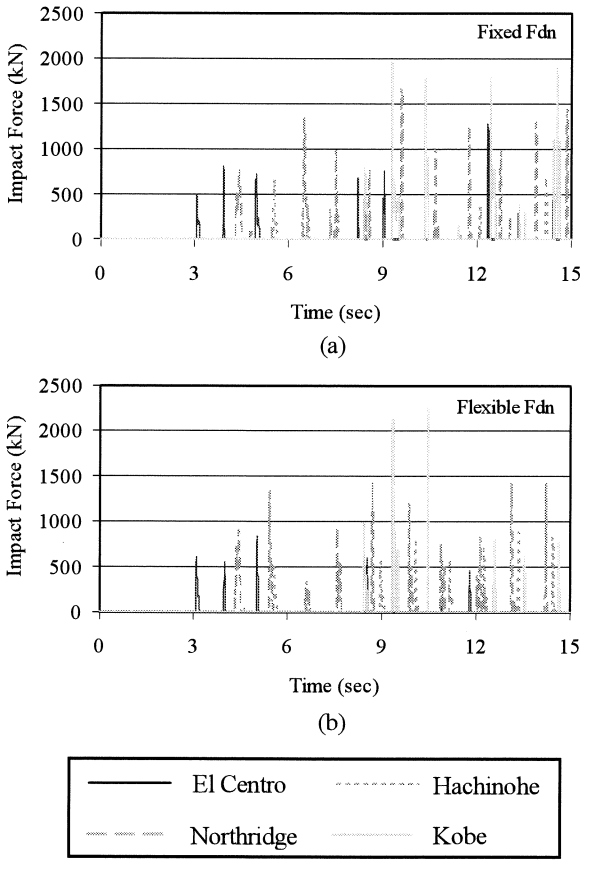

Figure 5 Impact Force Time History at Roof Level of 6-Story Building Column C3: (a) Fixed Foundation; and (b) Flexible Foundation

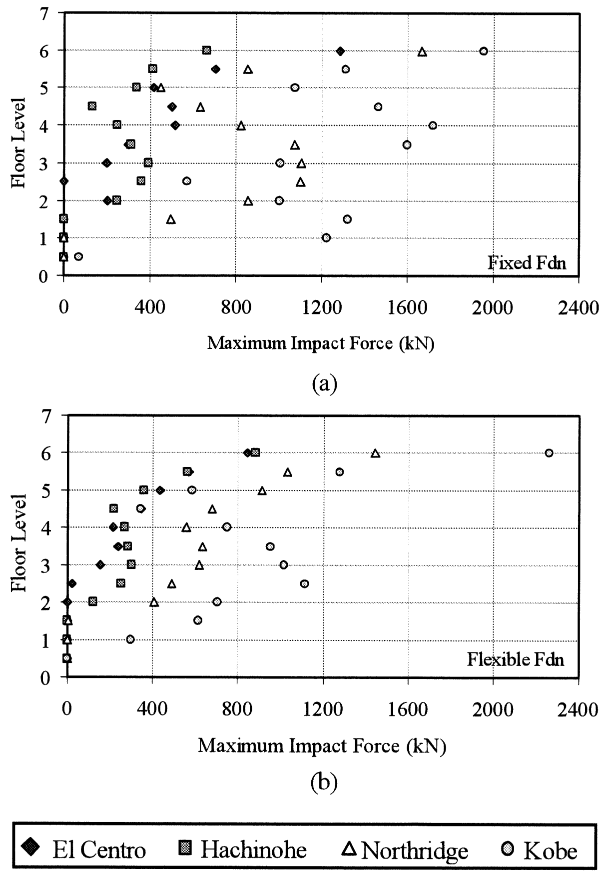

Figure 6 Maximum Impact Force at 6-Story Building Column C3: (a) Fixed Foundation; and (b) Flexible Foundation

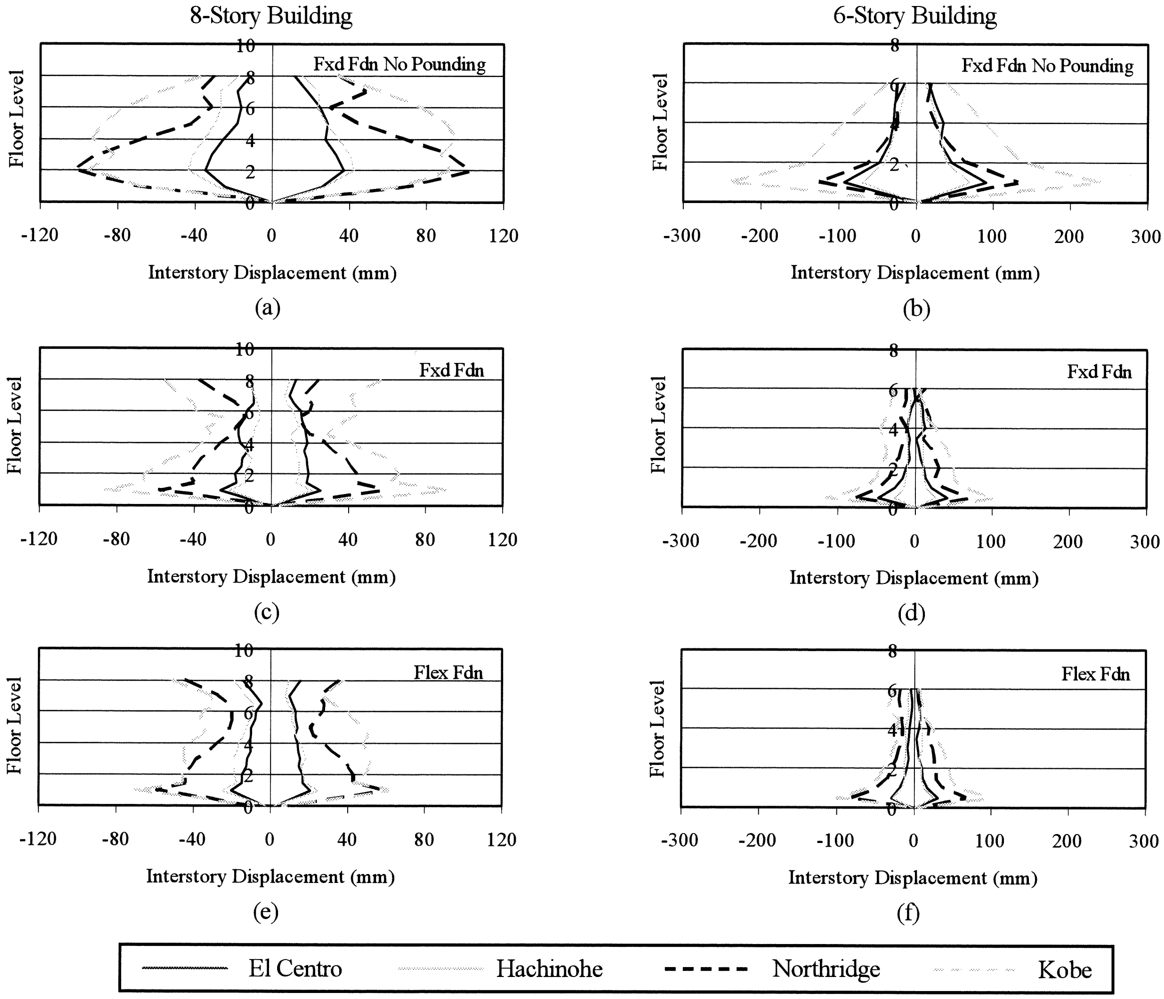

Figure 7 Maximum Interstory Displacement of Columns C3 and D3: (a) 8-Story Building, Fixed Foundation without Pounding; (b) 6-Story Building, Fixed Foundation without Pounding; (c) 8-Story Building, Fixed Foundation; (d) 6-Story Building, Fixed Foundation; (e) 8-Story Building, Flexible Foundation; and (f) 6-Story Building, Flexible Foundation

5. CONCLUSIONS

The importance of considering underlying soil on the study of seismic pounding is presented in this paper. Two eccentrically located buildings are subjected to two near field and two far field earthquakes which caused mid column pounding in the buildings. The building responses are expressed in terms of impact forces, interstory displacements and normalized story shear. The maximum interstory displacements are observed when there is no pounding. The results show the reduction in impact forces, interstory displacements and normalized story shear when soil effects are taken into account. In general, response of the buildings under consideration are more significant due to near field earthquakes and adopting soil effects for pounding analysis is beneficial.

Acknowledgements:

The first author gratefully acknowledges a Monbukagakhusho scholarship for master students from the Japanese government. The authors are very grateful to Prof. Tatsuo Ohmachi, COE Program Leader of Center for Urban Earthquake Engineering (CUEE), Tokyo Institute of Technology, and Prof. Kohji Tokimatsu, COE Program Sub-leader of CUEE, for their advice and support. Financial support from CUEE through the project "Development of Practical Urban Earthquake Engineering Research for Mitigation of the Metropolitan Great Earthquake Disaster", is gratefully acknowledged.

References:

American Concrete Institute (ACI) (2002), "Building Code Requirements for Structural Concrete" ACI 318-02, Farmington Hills, Michigan.

Anagnostopoulos, S. A. (1988), "Pounding of Buildings in Series During Earthquakes", *Earthquake Engineering and Structural Dynamics*, **16**, 443-456.

Azevedo, J. and Bento, R. (1996), "Equivalent Viscous Damping for Modeling Inelastic Impacts in Earthquake Pounding Problems", *Eleventh World Conference on Earthquake Engineering,* Acapulco, Mexico, Paper No. 1063.

International Building Code (IBC) (2003), International Code Council Inc., Country Club Hills, Illinois.

International Building Code (IBC) (2006), International Code Council Inc., Country Club Hills, Illinois.

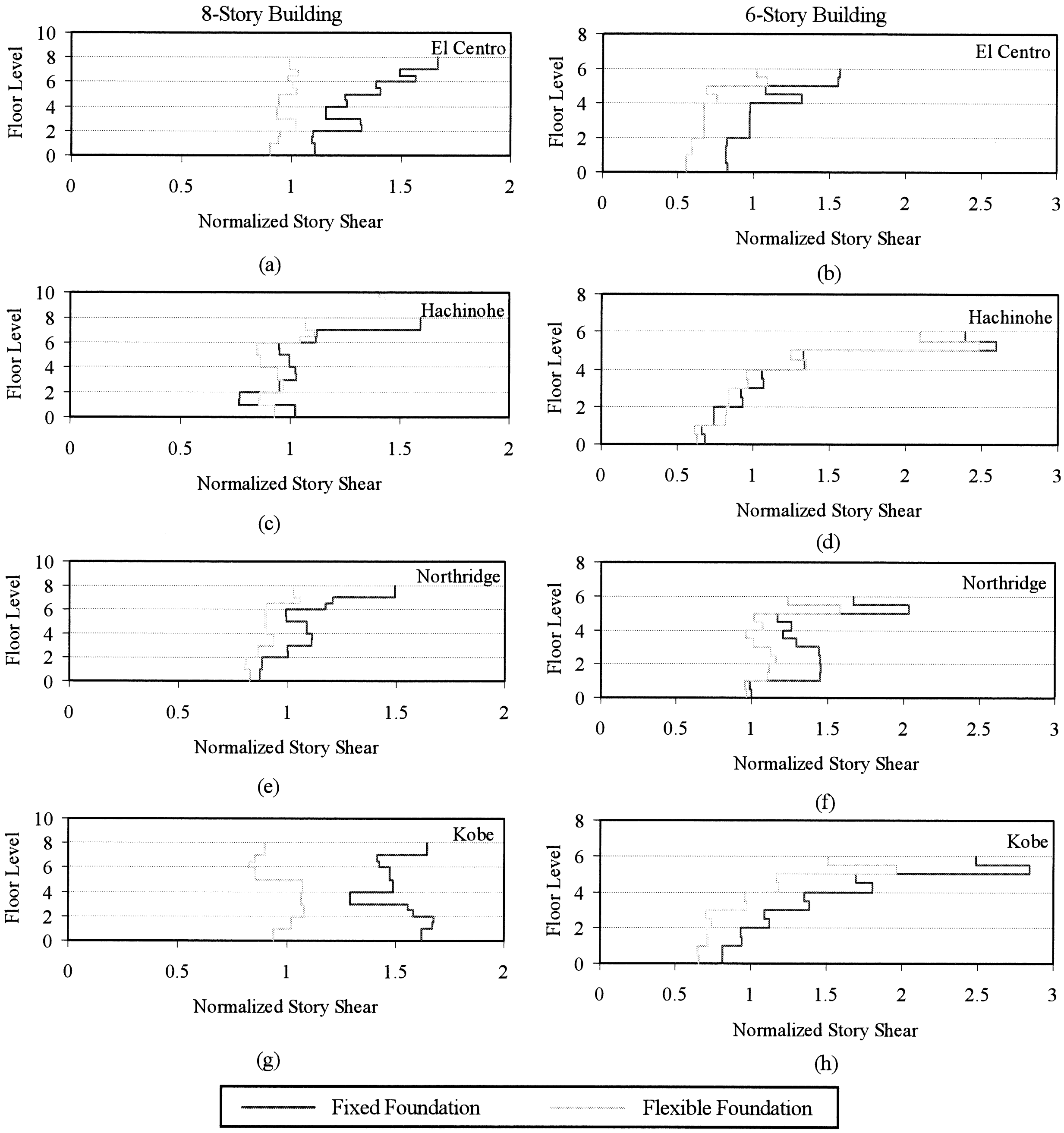

Figure 8 Normalized Story Shear: (a), (b) El Centro; (c), (d) Hachinohe; (e), (f) Northridge; and (g), (h) Kobe Earthquakes

Jankowski, R. (2005), "Non-linear Viscoelastic Modelling of Earthquake-Induced Structural Pounding", *Earthquake Engineering and Structural Dynamics*, **34**, 595-611.

Jankowski, R. (2006), "Pounding Force Response Spectrum Under Earthquake Excitation", *Engineering Structures*, **28**, 1149-1161.

Jeng, V. and Tzeng, W. L. (2000), "Assessment of Seismic Pounding Hazard for Taipei City", *Engineering Structures*, **22**, 459-471.

Leibovich, E., Rutenberg, A. and Yankelevsky, D. Z. (1996), "On Eccentric Seismic Pounding of Symmetric Buildings", *Earthquake Engineering and Structural Dynamics*, **25**, 219-223.

Mouzakis, H. P. and Papadrakakis M. (2004), "Three Dimensional Nonlinear Building Pounding with Friction During Earthquakes", *Journal of Earthquake Engineering*, **8**, 107-132.

Mullikan, J. S. and Karabalis, D. L. (1998), "Discrete Model for Dynamic Through-the-Soil Coupling of 3-D Foundations and Structures", *Earthquake Engineering and Structural Dynamics*, **27**, 687-710.

Rahman, A. M., Carr A. J. and Moss P. J. (2001), "Seismic Pounding of a Case of Adjacent Multiple-Storey Building of Differing Total Heights Considering Soil Flexibility Effects", *Bulletin of The New Zealand Society for Earthquake Engineering*, **34**(1), 40-59.

van Mier, J. G. M., Preuijssers, A. F., Reinhardt, H. W., and Monnier, T. (1991), "Load-Time Response of Colliding Concrete Bodies", *Journal of Structural Engineering*, **117**, 354-374.

Wolf, J. P. (1988), "Soil-Structure-Interaction Analysis in Time Domain", Prentice Hall Inc.

Fifth International Conference on Urban Earthquake Engineering
March 4-5, 2008, Tokyo Institute of Technology, Tokyo, Japan

PRACTICAL THREE-DIMENSIONAL EFFECTIVE STRESS ANALYSIS CONSIDERING CYCLIC MOBILITY BEHAVIOR

Hiroyuki Yoshida[1], Kohji Tokimatsu[2], Tatsuya Sugiyama[3], and Tadahiko Shiomi[4]

1) Researcher, Architectural & Structural Engineering Operation Center, Tokyo Electric Power Services Co., Ltd., Japan
2) Professor, Department of Architecture and Building Engineering, Tokyo Institute of Technology, Japan
3) Senior Researcher, Research & Development Center, Tokyo Electronic Power Company, Japan
4) Senior Manager, Research & Development Institute, Takenaka Corporation, Japan
yoshida@tepsco.co.jp, kohji@o.cc.titech.ac.jp, s.tatsuya@tepco.co.jp, shiomi.tadahiko@takenaka.co.jp

Abstract: A number of effective stress analysis methods have been developed; however, they are often complex, requiring a number of parameters that are not easy to determine in practice. A strong need, therefore, exists to develop a more practical method capable of simulating essential features of the soil subjected to strong shaking. In this paper, a practical three-dimensional effective stress analysis coupled with a three-dimensional stress-strain model of sand is presented which utilizes only soil properties obtained from a common field and laboratory test results. A key mechanism simulating liquefaction and cyclic mobility behavior is modeled based on the accumulated damage concept for pore pressure generation with a generalized hardening model for shear behavior.

1. INTRODUCTION

It is important to consider the effects of soil liquefaction and cyclic mobility in the design of structures to be constructed in liquefiable soils. For this purpose, a number of effective stress analysis methods have been developed; however, they are often complex, requiring a number of parameters that are not easy to determine in practice. A strong need, therefore, exists to develop a more practical method capable of simulating essential features of the soil subjected to strong shaking. In this paper, a practical three-dimensional effective stress analysis coupled with a three-dimensional stress-strain model of sand is presented in which only soil properties obtained from a common field and laboratory test results, i.e., geological and geophysical logs, strain-dependent elastic shear modulus and damping ratios, and liquefaction curve, are required as the input parameters.

2. COMPOSITION RULE

Figure 1 shows the example of the examination result. The behavior of sand is greatly different before and after generating cyclic mobility as shown in Figure 1. Then, it separates before and after generating cyclic mobility, and the behavior is evaluated.

In addition, the composition rule that has been constructed for a one-dimensional shear stress-strain relation is extended to three-dimensional problems.

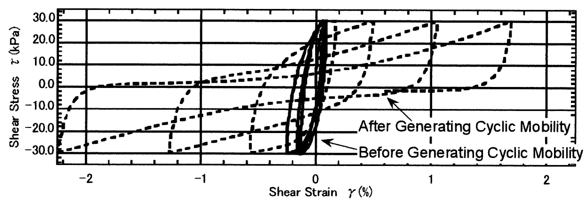

(a) Stress-Strain Curve

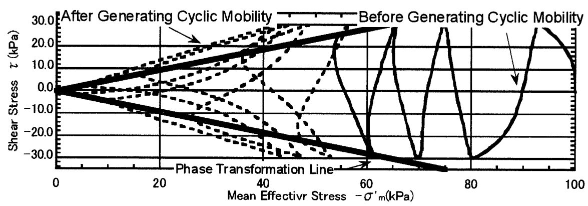

(b) Effective Stress Pass

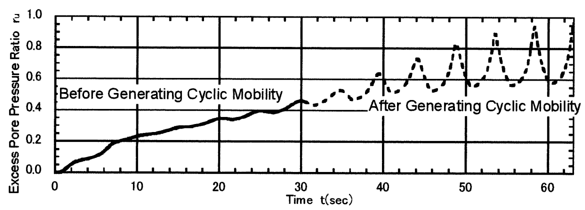

(c) Time History of Excess Pore Water Pressure Ratio

Figure 1 Example of Cyclic Loading Torsional Shear Test

2.1 Before Generating Cyclic Mobility

The nonlinearity of the soil is separated from the nonlinearity for the shear strain γ behavior and the one for the mean effective stress σ'_m behavior; the shear stress τ can be expressed by:

$$\tau = G_0 \cdot \mathrm{f}(\gamma) \cdot \mathrm{g}(\sigma'_m) \tag{1}$$

in which τ = shear stress of soil, G_0 = initial elastic shear modulus, $\mathrm{f}(\gamma)$ = strain dependent elastic shear modulus ratio, $\mathrm{g}(\sigma'_m)$ = mean stress dependent elastic shear modulus ratio. Moreover, elastic shear modulus G_{m0} and shear strength $\tau_{\max}$ can be expressed by:

$$G_{m0} = G_{ref} \cdot (\sigma'_m / \sigma'_{ref})^n \tag{2}$$

$$\tau_{\max} = \sigma'_m \cdot \tan \phi_f + c \tag{3}$$

in which G_{m0} = initial elastic shear modulus when mean stress equals σ'_m, G_{ref} = initial elastic shear modulus when mean stress equals σ'_{ref}, $\tau_{\max}$ = shear strength when mean stress equals σ'_m, σ'_m = mean stress, σ'_{ref} = reference mean stress, n = parameter, ϕ_f = friction angle, c = cohesion.

(1) Hardening Model for Shear Behavior

The nonlinearity of the soil for the shear strain γ behavior is often shown by the dynamic strain dependent characteristic, i.e., G/G_0-γ curve and h-γ curve. It is because the value can be examined directly by cyclic triaxial tests or cyclic torsional test. Moreover, it is considered that having often used an equivalent linear analysis SHAKE that uses this dynamic strain dependent characteristic also influences synergistic. A lot of research and proposals have been made for developing an analytical method that uses the dynamic strain dependent characteristic for a truly nonlinear analysis so far. The typical one is the hyperbolic model and Ramberg-Osgood model. However, these analytical methods need modeling for the skeleton curve where the dynamic strain dependent characteristic is shown by some analytical parameters. Therefore, the dynamic strain dependence characteristic is not able to show the strain levels. Engineering judgment is needed as to which strain level to show by the problem of targeting it.

Yoshida et al. (1990) proposed an analytical method that sets the skeleton curve directly as a partial linear function from the curve aiming to assume only soil properties obtained from a common field and laboratory test results to be an analytical parameter as shown in Figure 2. In addition, a fictitious skeleton curve is defined by the hyperbolic function so that the hysteresis damping obtained from the hysteresis curve per cycle and the one obtained from h-γ curve become equal. The stress-strain relationship at each cycle can be completely matched to the dynamic strain dependence characteristic by using this analytical method. This method was decided to be used as a hardening model for shear behavior in this proposal method.

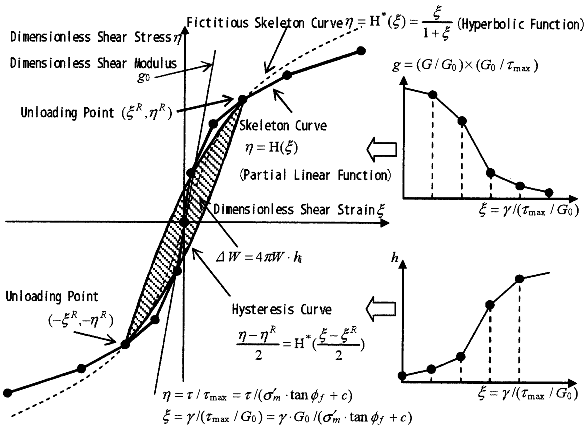

Figure 2 Modeling of Nonlinearity for Shear Strain Behavior

(2) Evaluation Method of Excess Pore Water Pressure Ratio

The easiness of the rise of excess pore water pressure ratio in sand that receives cyclic shear loading to do is often shown in the liquefaction strength curve. It is because the value can be examined directly by triaxial test or torsional test as well as the dynamic strain dependence characteristic. A lot of research and proposals have been made for developing an analytical method that uses the liquefaction strength curve for an effective stress analysis. The basic method is to construct the mathematical model to be able to simulate general behavior at liquefaction, and to set an analytical parameter where the liquefaction strength curve can be reproduced based on engineering judgment.

On the other hand, the authors have developed an analytical method CWELL to which behavior was able to be evaluated without needing an advanced engineering judgment, and assuming only the soil properties obtained from a common field and laboratory test results to be a direct input as an analytical parameter. First of all, the increment of the damage parameter $\Delta D_{(i)}$ by liquefaction is calculated from the maximum shear stress ratio $\tau_{\max(i)}/\sigma'_{m0}$ and the liquefaction strength curve in a half cycle of i turn as follows:

$$\Delta D_{(i)} = 1/2N_{f(i)} \tag{4}$$

in which $N_{f(i)}$ = a number of cycles where liquefaction is generated by shear stress ratio $\tau_{\max(i)}/\sigma'_{m0}$. As shown in Figure 3, the accumulated damage parameter obtained by this increment of the damage parameter $\Delta D_{(i)}$ accumulates to a half cycle of n turn is calculated as follows:

$$D_{(n)} = \sum_{i=1}^{n} \Delta D_{(i)} \tag{5}$$

in which $D_{(n)}$ = an accumulated damage parameter at n turn.

However, excess pore water pressure ratio changes in discontinuity in the CWELL method as understood from Figure 4. Then, an increase of excess pore water pressure ratio in a half cycle is continuously evaluated in this law as follows. The accumulation damage parameter at time t_{n+k} in the half cycle of n turn is defined by:

$$D_{n+k} = \sum_{i=1}^{n-1} \Delta D_{(i)} + \Delta D_{(n,k)} \tag{6}$$

in which $\Delta D_{(n,k)}$ = an increment of the damage parameter till time t_{n+k} in the half cycle of n turn.

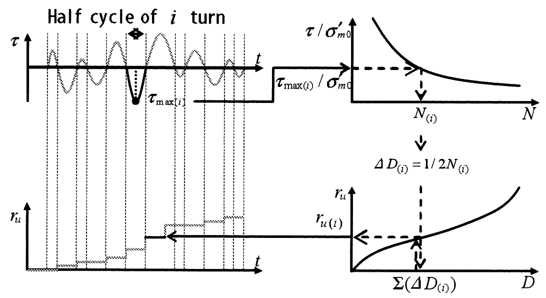

Figure 3 Evaluation Method of Excess Pore Water Pressure Ratio in CWELL Method

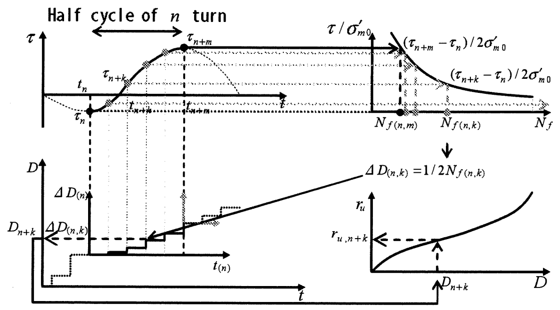

Figure 4 Evaluation Method of Excess Pore Water Pressure Ratio in Proposal Method

2.2 After Generating Cyclic Mobility

For behavior after generating cyclic mobility, it separates to the section from the phase transformation line to the unloading point and the one from the unloading point to the phase transformation line, and the nonlinearity is evaluated.

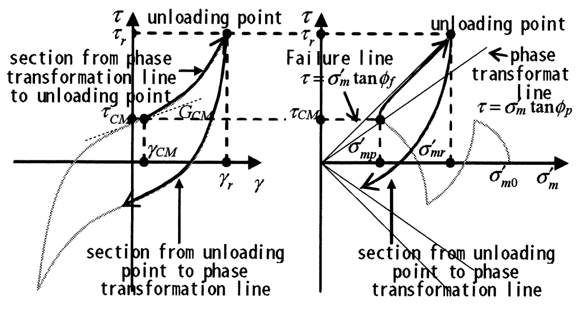

(a) Stress-Strain Curve (b) Effective Stress Path

Figure 5 Separation of Section after Generating Cyclic Mobility

(1) The Section from the Phase Transformation Line to the Unloading Point

For the section from the phase transformation line to the unloading point, the tangent elastic shear modulus G_T is calculated from mean effective stress σ'_m and the maximum shear strain $\gamma_{\max}$ experienced till then by using the empirical formula (7)-(10) obtained from the study of the laboratory test results.

$$G_T = G_{CM} + f_b \cdot \frac{\sigma'_m - \sigma'_{mp}}{\sigma'_{m0}} \cdot G_{m0} \tag{7}$$

$$G_{CM} = G_{m0} \cdot 10^{6(\sigma'_{mp}/\sigma'_{m0})^{0.15} - 6.6} \tag{8}$$

$$f_b = 5b \cdot \exp(-40 \cdot \gamma_{\max}) + b \tag{9}$$

$$b = 350 \cdot (G_{m0}/\sigma'_{m0})^{-1.4} + 0.045 \tag{10}$$

in which G_{CM} = a tangent elastic shear modulus when effective stress path crosses the phase transformation line, f_b = an increase rate of G_T, b = parameter.

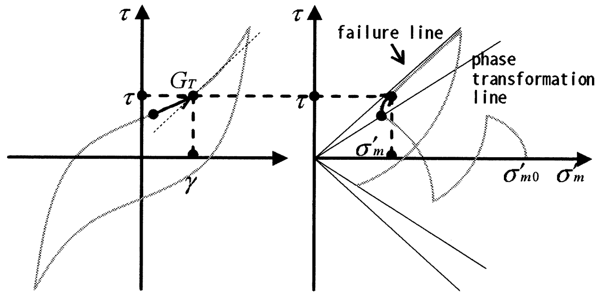

Figure 6 Tangent Elastic Shear Modulus G_T

It is considered that the stress point is asymptotic from the phase transformation line in the failure line according to an increase in the shear stress, and the mean effective stress is calculated by:

$$\sigma'_m = \frac{1}{\tan\phi_f} \cdot \frac{|\tau/\tau_{\max}| - M_0}{1 - M_0} \cdot \tau \tag{11}$$

in which σ'_m = mean effective stress, τ = shear stress, $\tau_{\max}$ = shear strength, $M_0 = \tan\phi_p / \tan\phi_f$, ϕ_f = friction angle, ϕ_p = phase transformation angle.

(2) The Section from the Unloading Point to the Phase Transformation Line

The initial elastic shear modulus is calculated by the same formulation (2) and (3) as before generating cyclic mobility. Moreover, mean effective stress is calculated from shear stress by using the effective stress path expressed by the empirical formula (12) obtained from the study of the laboratory test results.

$$\frac{\sigma'_m - \sigma'_{mr}}{\sigma'_{mp} - \sigma'_{mr}} = \sin\left\{ \frac{\pi}{2} \cdot \left(\frac{\tau - \tau_r}{\tau_p - \tau_r} \right)^{1.2} \right\} \tag{12}$$

in which σ'_{mr} , τ_r = a mean effective stress and shear stress at unloading point, σ'_{mp} , τ_p = a mean effective stress and shear stress effective stress path crosses the phase transformation line, σ'_m , τ = a current mean effective stress and shear stress.

2.3 Extension to Three-Dimensional Problems

The composition rule previously described is constructed for one dimensional problem. It is necessary to extend this composition rule to a three-dimensional problem. The relationship between shear stress τ and shear strain γ in the one-dimensional problem is given as the relationship between equivalent stress σ_e and equivalent strain e in a three-dimensional problem. Then, it follows Yoshida et al. (1993), and the nonlinearity is evaluated to the increment of equivalent stress from the unloading point in this composition rule as shown in

Figure 7, in which η_{ij} = a dimensionless equivalent stress $\sigma_e / \tau_{\max}$, $\eta_{ij,R}$ = a dimensionless equivalent stress at unloading point

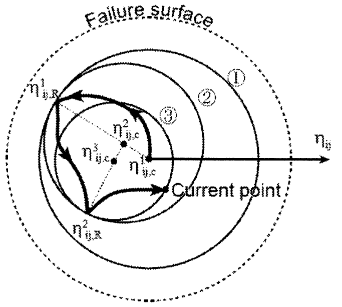

Figure 7 Increment of Equivalent Stress: Yoshida et al. (1995)

3. SIMULATION ANALYSIS

The records of vertical array observation were simulated aiming to confirm the effectiveness of the proposed composition rule. The result is shown as follows.

3.1 Record of Vertical Array Observation

The vertical array observation record that the examination targeted is a record in the 1993 Kushiro-oki Earthquake shown in Iai et al. (1995). The recording station is located at the central part of Kushiro Port as shown in Figure 8. The recorded time histories of acceleration are shown in Figure 9. A distinctive change can be observed in the ground surface motion after about 30 seconds in the N-S direction shown in Figure 9; most of high frequency motions are filtered out and instead 1.5 seconds overlain by spike at each peak of the motion.

3.2 Model Parameters for Numerical Simulation

Table1 shows the parameter used by Iai et al. (1995).

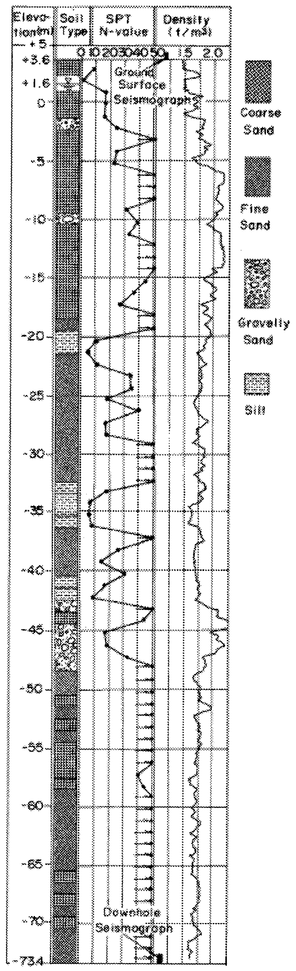

Figure 8 Boring log at the recording station: Iai et al. (1995)

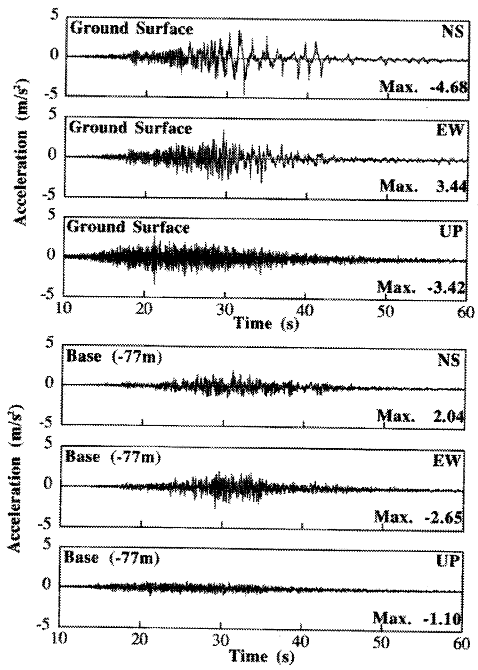

Figure 9 Recording Accelerations: Iai et al. (1995)

In this composition rule, dynamic strain dependent characteristics and the liquefaction strength curves are needed as an input parameter. However, they are not obtained by the laboratory test. Then, G/G_0-γ curve was set by obtaining the shear strength $\tau_{\max}$ from the reference effective confining pressure σ_{ma}, the elastic shear modulus G_{ma} and friction angle ϕ_f that Iai et al. (1995) used, and expressing skeleton curve by Hardin-Drnevich model. And, h-γ curve was set from the hysteretic damping factor h (=30%) that Iai et al. (1995) used by Hardin- Drnevich model. Moreover, the liquefaction strength curve was set to the one given by the element simulation by the composition rule and the parameters that Iai et al. (1995) used.

Table1 Model Parameters for Numerical Simulation: Iai et al. (1995)

Layer no.	H (m)	ρ (t/m³)	V_s (m/s)	G_{ma} (kPa)	$-\sigma_{ma}'$ (kPa)	ϕ_f (deg)	ϕ_p (deg)
1	2.0	1.54	249	106600	37	40	—
2	7.0	1.72	249	106600	37	40	28
3	14.0	1.98	326	210400	98	48	28
4	9.0	1.73	265	121500	164	37	—
5	4.0	1.76	341	204700	195	44	—
6	8.0	1.70	286	139100	224	44	—
7	8.0	2.00	302	182400	269	45	—
8	25.0	1.73	341	201200	354	44	—

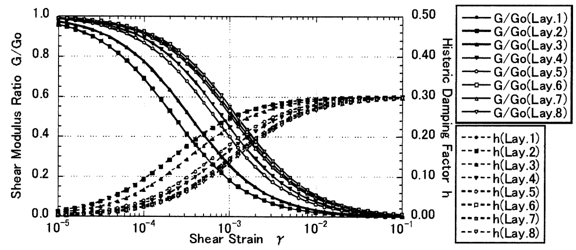

Figure 10 Dynamic Strain Dependent Characteristic

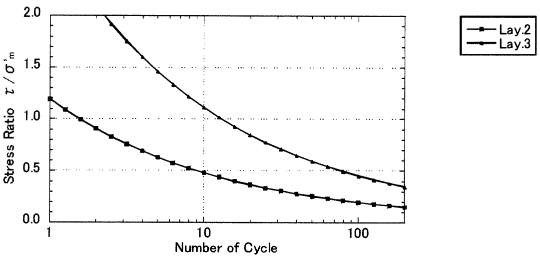

Figure 11 Liquefaction Strength Curve

3.3 Result of Numerical Simulation

Figure 12 shows the time histories of the acceleration at the ground surface of the numerical simulation results. The numerical simulation acceleration in the N-S direction captures essential features of the record acceleration that the cyclic motion becomes predominant with a period of about 1.5 seconds overlain by a spike after about 30 seconds. Liquefaction is generated at about 30 seconds, and the influence of cyclic mobility appears. This phenomenon

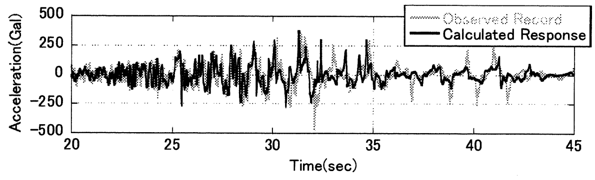

(a) N-S direction

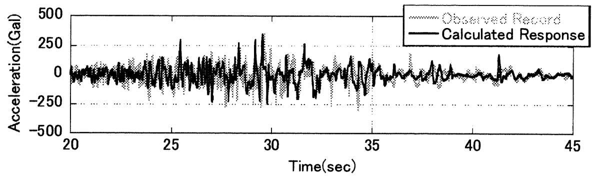

(b) E-W direction

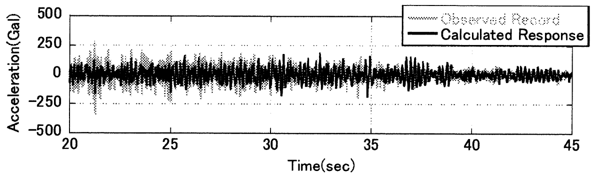

(c) U-D direction

Figure 12 Acceleration at G.L.0m

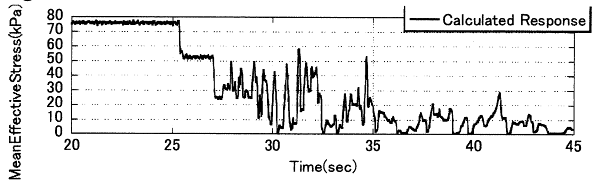

Figure 13 Mean Effective Stress at G.L.-8.5m

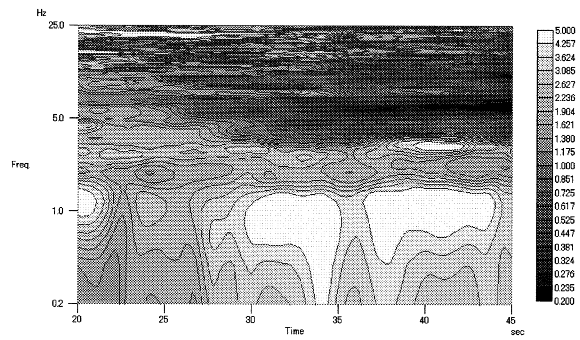

(a) Observed Record

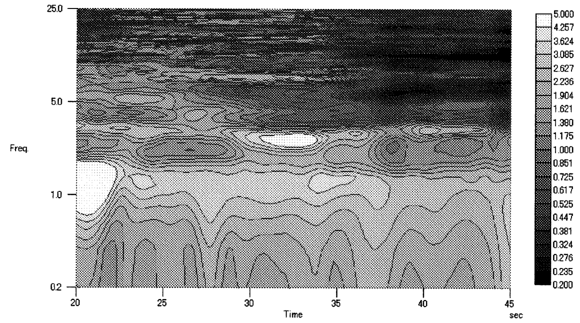

(b) Calculated Response

Figure 14 Running Spectra of Transfer Function (G.L.0.0m/-77.0m) can be confirmed from the mean stress time history shown in Figure 13. Moreover, the feature is captured in other directions.

Next, running spectra of the acceleration transfer function of G.L. 0m to G.L.-77m is shown in Figure 14. It can be confirmed that the amplification rate comes to fall below 1.0 in the high frequency region in observed record after about 30 seconds, and the response does not transmit by liquefaction. A similar tendency can be reproduced even by the calculated response.

4. CONCLUSIONS

In this paper, a practical three-dimensional effective stress analysis coupled with a three-dimensional stress-strain model of sand is presented in which only soil properties obtained from a common field and laboratory test results are required. To demonstrate the effectiveness of the proposed analysis, records of vertical array observation are simulated. The computed results are found to be in good agreement with observed records. The good agreement suggests that the proposed method, which requires soil parameters readily obtained from common filed and laboratory tests as input, is convenient and yet effective in practice.

Acknowledgements:

The authors acknowledge the support from Japan Ministry of Education, Culture, Sport, Science, and Technology (MEXT) for establishing the Center for Urban Earthquake Engineering (CUEE) in Tokyo Institute of Technology. The support has made possible this international conference, as well as international joint research projects and exchange programs with foreign universities.

References:

Yoshida,H., Tokimatsu,K., Hijikata,K., et al. (2006), "Study on practicable 3-dimensional effective stress analysis using the ground survey result," *Summaries of Technical Papers of Annual Meeting Architectural Institute of Japan*, **B-1**, 623-626.

Yoshida,H., Tokimatsu,K., Hijikata,K., et al. (2007), "Study on influence of multi-dimensional input by three-dimensional effective stress analysis," *Summaries of Technical Papers of Annual Meeting Architectural Institute of Japan*, **B-1**, 539-540.

Yoshida,H., Tokimatsu,K., and Sugiyama,T. (2007), "Simulation of full-scale model test by practicable, three-dimensional effective stress analysis," *Proceedings of the 5th Annual Meeting of Japan Association for Earthquake Engineering*, 176-177.

Yoshida,N., Tsujino,S., and Ishihara,K. (1990), "Stress-strain model for nonlinear analysis of horizontally layered deposit," *Summaries of Technical Papers of Annual Meeting Architectural Institute of Japan*, **B**, 1639-1640.

Shiomi,T., Tokimatsu,K., et al. (2005), "Equivalent linear analysis taking into account excess pore water pressure built-up due to liquefaction," *Journal of structural and construction engineering. Transactions of AIJ*, **No.598**, 93-100.

Yoshida,N., Tsujino,S., et al. (1993), "A simplified practical stress-strain model for the multi-dimensional analysis under repeated loading," *The 28th Japan National Conference on Soil Mechanics and Foundation Engeering*, 1221-1224.

Iai,S., Morita,T., Kameoka,.T, Matsunaga,Y. and Abiko,.K. (1995), "Response of a dense sand deposit during 1993 Kushiro-Oki Eartquake," *Soils and Foundation*, Japanese Society of Soil Mechanics and Foundation Engineering, **Vol.35**, 115-131.

Fifth International Conference on Urban Earthquake Engineering
March 4-5, 2008, Tokyo Institute of Technology, Tokyo, Japan

A STUDY ON DYNAMIC CHARACTERISTICS OF THE EDGE OF DILUVIAL TERRACE

Toru Sekiguchi[1)], Shoichi Nakai[2)] and Yoko Nagata[3)]

1) Assistant Professor, Dept. of Architecture and Urban Science, Chiba University, Japan
2) Professor, Dept. of Architecture and Urban Science, Chiba University, Japan
3) Graduate Student, Dept. of Human Environment Design and Science, Chiba University, Japan
tsekiguc@faculty.chiba-u.jp, nakai@faculty.chiba-u.jp, nagata-yoko@graduate.chiba-u.jp

Abstract: In order to examine the dynamic properties of the edge of diluvial terrace, boring exploration at the edge of terrace and simultaneous observations of seismic motions at the terrace and the edge are conducted. The transfer functions between the ground surface and the top of the bottom layer were also computed based on the one-dimensional linear analysis using the *Vs* logs. The peak ground accelerations of the seismic records on the edge of terrace are about two times larger than those on the terrace. It is shown that the surface soil and the topography of the edge of diluvial terrace affects on the dynamic properties.

1. INTRODUCTION

It is well known that earthquake disasters tend to occur at an irregular topography and a boundary between land forms. The dynamic properties of such landforms are, however, complicated and not well understood. It is said that many earthquake-induced failures have occurred at a top of steep slopes in particular. Shaking table tests with a large-scale slope model showed an increase in response accelerations at the upper part of the slope (Asano et al. 2003).

In the southern part of Kanto region, lowlands are complicated with terraces. Therefore there are many slopes at the boundary between lowlands and terraces. It was reported that many slopes collapsed at the edge of terraces during 1987 east off Chiba prefecture earthquake. It is important from the point of view of urban earthquake engineering to examine the dynamic properties of the edge of terraces.

Nagata et al. (2007) examined the dynamic properties of the edge of terrace in Chiba city using microtremor and seismic motion observations and 2-D finite element analyses. At a later time, boring exploration at the edge of terrace and simultaneous observations of seismic motions at the terrace and the edge were conducted. The objective of this paper is to examine the dynamic properties of the edge of terrace using the results of the exploration and the observations.

2. GEOLOGICAL SETTING

Figure 1 shows the geomorphological land classification map of the central part of Chiba city (Chiba Pref. Gov., 1980) and the investigation area. This area

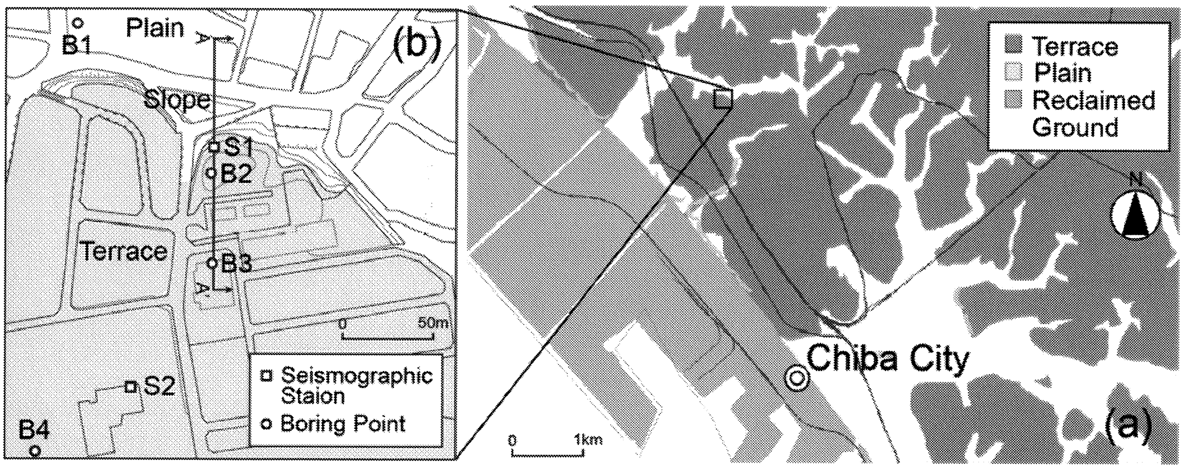

Figure 1 (a) Geomorphological land classification map of the central part of Chiba city and (b) investigation area

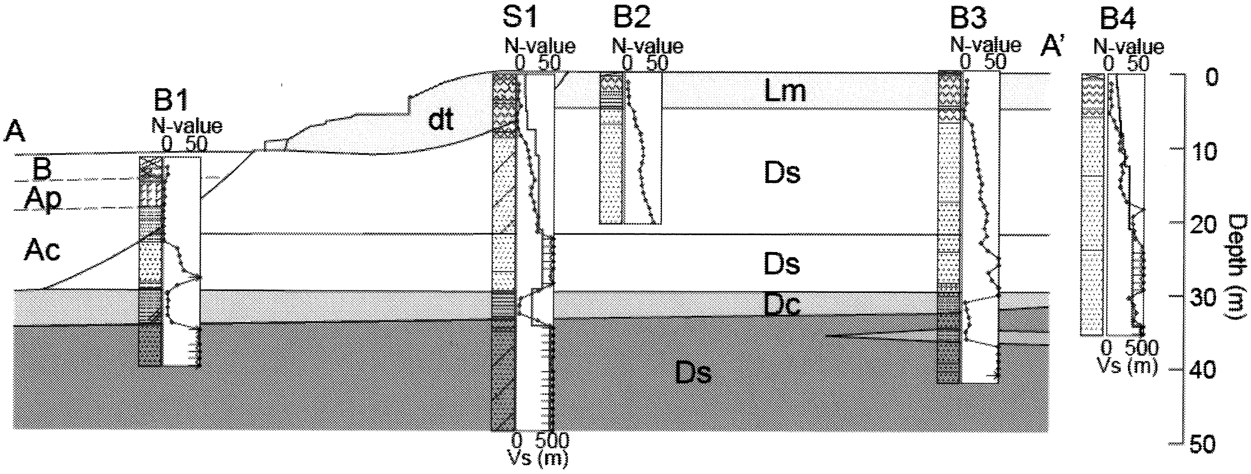

Figure 2 Geological and geographical logs and soil profile along line A-A' in Figure 1

consists of diluvial terrace and alluvial plain.

Figure 2 shows the boring and shear wave velocity logs and the geological cross section along line A-A' shown in Figure 1 including that of the edge of terrace. The shear wave velocity log at S1 is based on P-S logging and that at B4 is based on surface wave method. The cross section of the surface soil at the slope is based on the investigation of surface wave method.

Diluvial terrace is covered with a volcanic cohesive soil layer called Kanto loam with a thickness of about 5 m. Under the loam formation, there is a heap of diluvial sands called Narita formation of Shimousa group. At the edge of terrace, the surface soil to a depth of 8 m is soft detritus consisting of loam.

3. MICROTREMOR AND SEISMIC GROUND MOTION CHARACTERISTICS

Microtremor and seismic ground motion observations were conducted at two stations (S1, S2) in Figure 1. S1 is a site on the edge of terrace and S2 is a site on the terrace.

The H/V spectra (Arai and Tokimatsu, 2005) were calculated from the three component motions of microtremors at the two stations and are shown in Figure 3. The H/V spectra at S1 have a prominent peak at 5 Hz and those at S2 do not show a prominent peak. This indicates that S1 is a site with a high *Vs* contrast in surface soils and S2 is a site with a low *Vs* contrast in surface soils.

Seismic array observation was conducted at two stations to examine seismic ground motion characteristics of each site. Seismic ground motions of 5 earthquakes at the stations have been simultaneously recorded on August 18, 2007. Table 1 summaries the earthquakes with the major characteristics and peak ground accelerations recorded at the stations. The epicentral distances are from 33 to 39 km. The JMA magnitudes (*Mj*) are within 4.0 to 5.1. The peak ground accelerations at S1 station are about two times larger than those at S2 station for

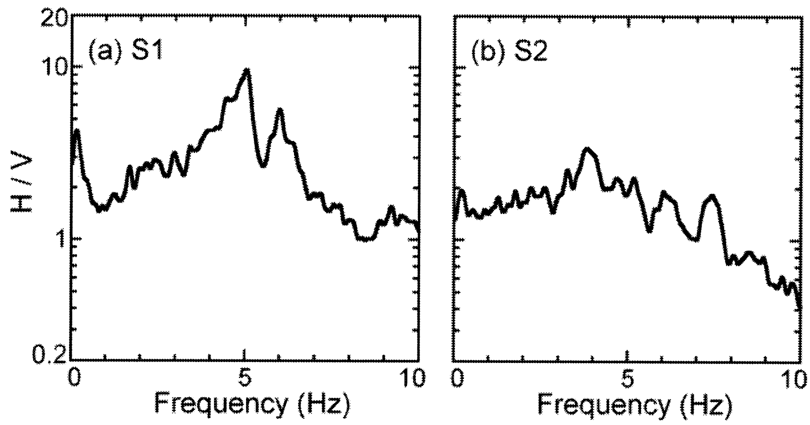

Figure 3 Microtremor H/V spectra

Table 1 List of earthquakes with PGA recorded at two stations

Date	Epicentral Region name	M_J	Focal Depth (km)	Epicentral Distance (km)	PGA (cm/s^2) S1 NS	S1 EW	S2 NS	S2 EW
2007/08/18 04:14	south part of Chiba Pref.	4.8	20	39	67.3	82.6	28.1	30.2
2007/08/18 13:36	northeast part of Chiba Pref.	4.6	30	39	22.0	29.0	10.1	12.2
2007/08/18 16:55	south part of Chiba Pref.	5.1	20	39	96.5	83.4	41.9	41.6
2007/08/18 17:07	northeast part of Chiba Pref.	4.0	30	39	27.5	15.5	9.7	8.6
2007/08/18 23:16	northeast part of Chiba Pref.	4.0	30	33	25.5	21.3	9.8	10.3

all the earthquakes.

Figure 4 compares acceleration time histories of NS components recorded at the stations during the earthquake of 16:55 August 18, 2007. Figure 5 compares Fourier spectra (smoothed by Parzen window with 0.2 Hz Band width) of two components of the same earthquake recorded at the stations. The spectral amplitudes at S1 station on the edge of terrace are larger than those at S2 station on the terrace in most of the frequency range from 1 to 10 Hz.

Figure 6 shows spectral ratios of two observed components at S1 station on the edge of terrace against S2 station on the terrace for all the earthquakes shown in Table 1. Regardless of the earthquakes, the spectra show stable characteristics and the spectral peak is found at 5Hz which is same as the H/V spectra at S1 station for both components. The spectral shape of the two components, however, is a little different.

The above findings indicate that the surface soil and the three-dimensional shape of the edge of terrace significantly affect the seismic ground motions.

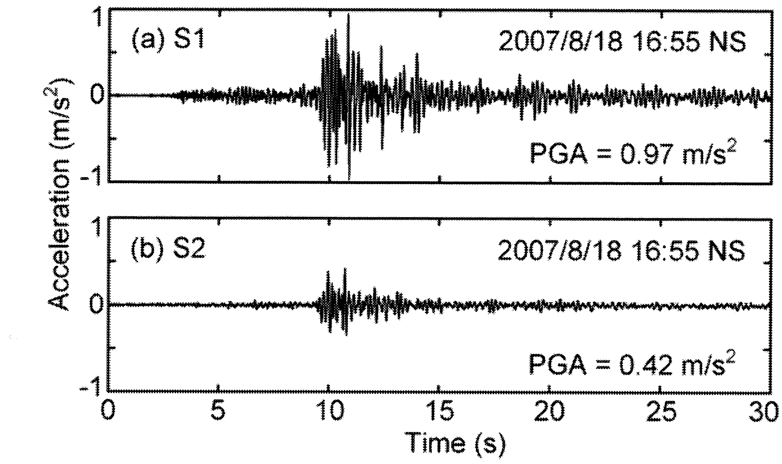

Figure 4 Acceleration time history

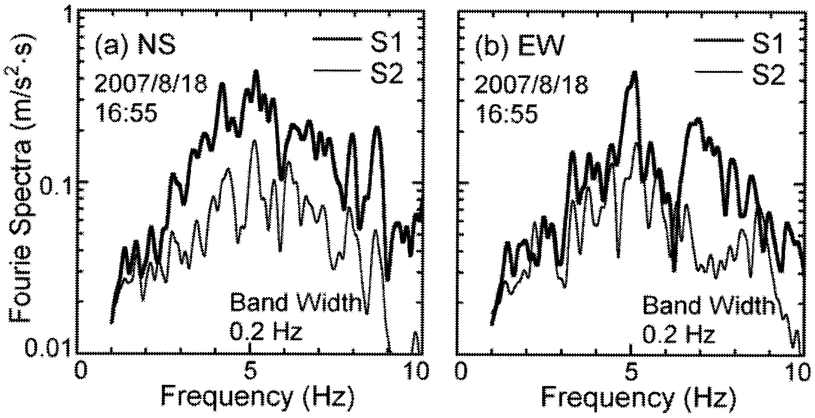

Figure 5 Fourier spectra recorded at two stations

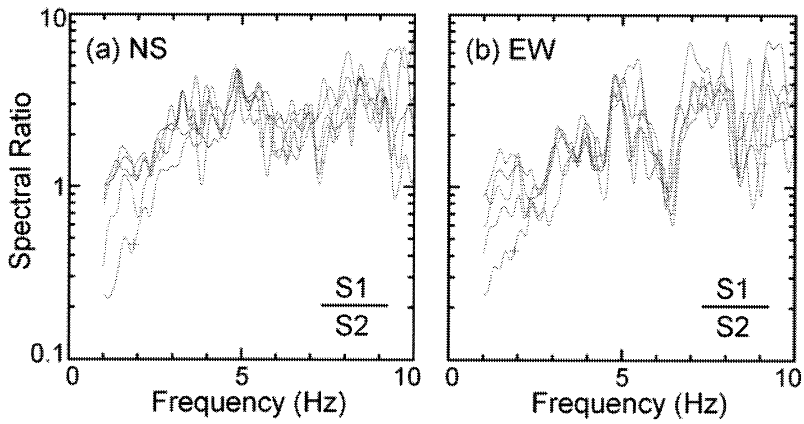

Figure 6 Spectral ratio between two stations

4. THEORETICAL TRANSFER FUNCTION

To evaluate the effect of the surface soil on the dynamic properties of the edge of terrace, the transfer functions, defined as the spectral ratio of incident S waves between the ground surface and the top of the bottom layer of the soil profile in Figure 2, were computed based on one-dimensional linear analysis (Schnabel et al., 1972) using the *Vs* logs of S1 and S2 stations. Figure 7 shows computed transfer functions of the two stations. The spectra at S1 have a prominent peak at 4.2 Hz and those at S2 do not show a prominent peak. The spectral peaks from the one-dimensional analysis show a fairly good agreement with those of the spectral ratio of the seismic records between the two stations and those of the microtremor H/V spectra at the two stations.

There is, however, a difference in the spectral ratios between NS and EW components in Figure 6. It seems that the irregular topography affects on the difference in the dynamic properties of the edge of terrace. The two or three dimensional dynamic response analysis, therefore, must be conducted using the detailed soil profiles of the edge of terrace hereafter.

5. CONCLUSIONS

The dynamic properties of the edge of terrace were examined based on field investigations and subsequent analyses. Base on the results and discussions, the following conclusions may be made:

1. The peak ground accelerations of the seismic records on the edge of terrace are about two times larger than those on the terrace.

2. The spectral ratios between the seismic records on the edge of terrace and those on the terrace show stable characteristics regardless of earthquakes. The spectral ratios of two components show different characteristics.

3. The natural site periods computed from one-dimensional analysis for two stations are generally consistent with the spectral peaks of the spectral ratio of the seismic records between the two stations and those of the microtremor H/V spectra at those stations.

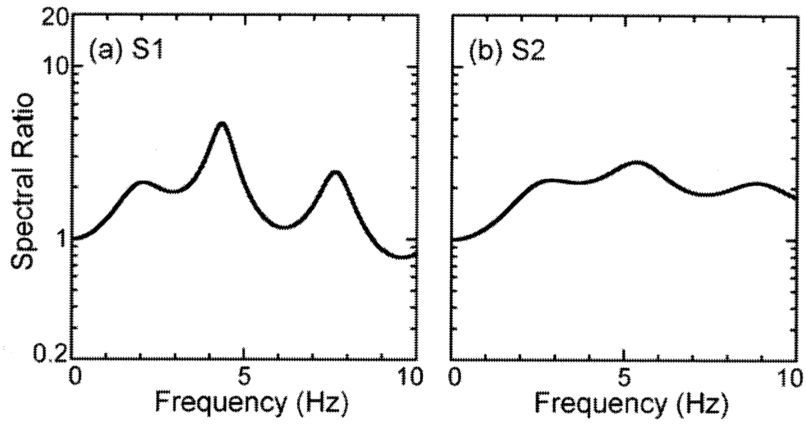

Figure 7 Transfer function between ground surface and top of bottom layer

References:

Arai, H. and Tokimatsu, K. (2005), "S-wave velocity profiling by joint inversion of microtremor dispersion curve and horizontal-to-vertical (H/V) spectrum," *Bulletin of the Seismological Society of America*, **95**(5), 1766-1778.

Chiba Prefecture Government (1980), *Fundamental Research on Landform classification Chiba.*

Nagata, Y., Nakai, S. and Tosauchi, Y. (2007), "Dynamic properties of the ground near the edge of diluvial terrace," *Proceedings of the Pacific Conference on Earthquake Engineering.*

Schnabel, P. B., Lysmer, J. and Seed, H. B. (1972), "SHAKE – A computer program for earthquake response analysis of horizontal layered sites," Report No. EERC 72-12, University of California, Berkeley.

Tsunami Hazard and Forecast Study in South China Sea

Philip L.-F. Liu[1,2], Xiaoming Wang[1], Andrew J. Salisbury[1]

1) School of Civil and Environmental Engineering, Cornell University, Ithaca, USA
2) Institute of Hydrological and Oceanic Sciences, Jhongli, Taiwan
pll3@cornell.edu, xw46@cornell.edu, ajs233@cornell.edu

Abstract: In this paper we discuss the potential tsunami hazard existing in the South China Sea region. A methodology is presented to demonstrate a tsunami early warning system for the region.

1. INTRODUCTION

Tsunami is one of the most devastating natural disasters that could inflict coastal regions. Most of significant tsunamis are generated by submarine earthquakes occurring along subduction zones. Tsunamis can also be triggered by volcano eruptions and large landslides. The prediction of an earthquake is still not satisfactory. However, when a tsunamigenic earthquake occurs, newly developed tsunami warning system makes it possible to provide an early warning of incoming tsunami, including the arrival time and the height of leading wave, for areas far away from the source region (Wei et al 2003).

The tsunami warning system is now operational in the Pacific Ocean and has proven its effectiveness and validity in recent tsunami events. If a similar early warning system had been available in the Indian Ocean, the 2004 Indian Ocean tsunami would have caused much less loss in property and human lives in Sri Lanka, India, Maldives and other coastal regions.

In the South China Sea (SCS), the Manila subduction zone has been identified as the most hazardous tsunamigenic earthquake source region. No earthquake larger than Mw 7.6 has been recorded in the past 100 years in this region, suggesting a high probability for larger earthquakes in the future. And more dangerously, there is no operational tsunami warning system available in this region. If a tsunamigenic earthquake occurs in this region, a tragedy similar to the 2004 Indian Ocean tsunami might repeat itself.

In this paper, the potential tsunami hazard in SCS region is studied and a conceptual tsunami early warning system is developed by using inverse method (Satake, 1987 and Titov et al, 2001). This system will be capable of releasing early warning information, including both tsunami arrival times and wave heights, to the surrounding countries for earthquakes along the Manila subduction zone. When using this information as input, inundation forecasts will also be possible by applying tsunami runup models in coastal regions of interest.

2. HAZARDOUS TSUNAMIGENIC ZONES IN SOUTH CHINA SEA

In the 2006 USGS Tsunami Source Workshop, three subduction zones, the Manila subduction zone, Ryukyu subduction zone and N. Sulawesi subduction zone, were identified as having high potentials to generate tsunamis capable of striking the coastal areas surrounding the South China Sea.

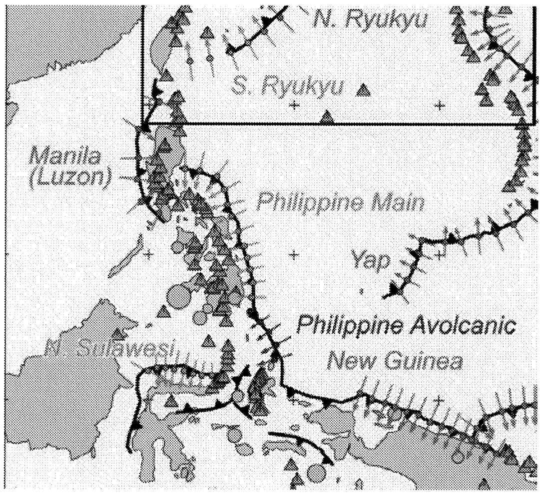

Figure 1 Subduction zones near/in South China Sea (source: Kirby et al., 2006 USGS workshop)

Preliminary numerical studies indicate that tsunamis generated from the Ryukyu subduction zone and N. Sulawesi subduction zone are not dangerous to South China Sea region. For tsunamis generated from the Ryukyu subduction zone, most of energy propagates into the Pacific Ocean due to the shielding of very shallow ridges between Taiwan and Luzon and the island northwest to Sulu Sea (Palawan, Philippine). For tsunamis generated from N. Sulawesi subduction zone, most of tsunami energy is trapped inside the Celebes Sea. Neither of them will have significant impacts on the surrounding regions of the South China Sea. Therefore, in this paper only the tsunamis generated from the Manila subduction zone will be investigated.

2.1 Source Region Parameters along Manila Trench

The Manila subduction zone, or so-called Manila

Trench, is where the Eurasian Plate subducts under the Philippine Sea Plate at a speed of 70mm/yr (Lin, 2000). Manila Trench, starting from the northern tip of Palawan, Philippine, evolves to the north along the west edge of Luzon, Philippine and ends in Taiwan, with a total length about 1,000 kilometers. Earthquake records show that the largest earthquake in this subduction zone in the past 100 years is about $M_w = 7.5$ (The 1999 Chi-Chi Earthquake was 7.6 and the 1934 earthquake offshore from the northern Luzon was 7.5), making this region the most hazardous in the future (Willie Lee, personal communication).

Along Manila Trench, six hypothetical fault segments were identified in USGS Tsunami Sources Workshop 2006 (Kirby et al., 2005), including their strike angle, dip angle and center position of each fault segment. In this study, six fault planes are constructed based on Kirby et al.'s suggestion. The fault line (e.g., the top edge of a fault plane) starts and ends at major cracks along Manila Trench. This also determines the length of a fault plane. The strike angle of a fault plane is determined by aligning the fault line of each segment parallel to the orientation of the trench locally and the epicenter of each fault plane is defined as the center of the top edge of a fault plane (as shown by the red crosses in Figure 2). The epicenters are slightly different from those recommended by Kirby et al. (2005) whose are shown by yellow crosses in Figure 2. The same dip angles, as indicated by Kirby et al., are adopted for each fault plane. The rake angle is assumed 90 degree for all the fault planes, which will make a maximum contribution to the seafloor deformation. The focal depth, defined as the distance from the seafloor to top edge of a fault plane, is assumed to be 15km, which is commonly observed in several major past earthquake events in this region. Now we have the following fault parameters available for each fault segment.

Table 1 Fault parameters

Fault	Lon	Lat	Length	Strike	Dip	Rake
E1	120.5°	20.2°	160km	10°	10°	90°
E2	119.8°	18.7°	180km	35°	20°	90°
E3	119.3°	17.0°	240km	359°	28°	90°
E4	119.2°	15.1°	170km	3°	30°	90°
E5	119.6°	13.7°	140km	320°	22°	90°
E6	120.5°	12.9°	100km	293°	26°	90°

The most difficult task is to determine the width of a fault plane, which in fact will never be known before an earthquake actually occurs. This parameter is inferred from past earthquake events in this region and empirical studies. By searching historical earthquakes in the database of National Earthquake Information Center (NEIC), several events which occurred in the Manila subduction zone are used to determine the width of fault plane.

On December 11 1999 a strong earthquake with magnitude $M_w = 7.30$ occurred. Its epicenter is marked by a yellow cross in Figure 3. Seven small aftershocks are indicated by white dots. By drawing a rectangular region enclosing the main shock and its aftershocks, the size of the

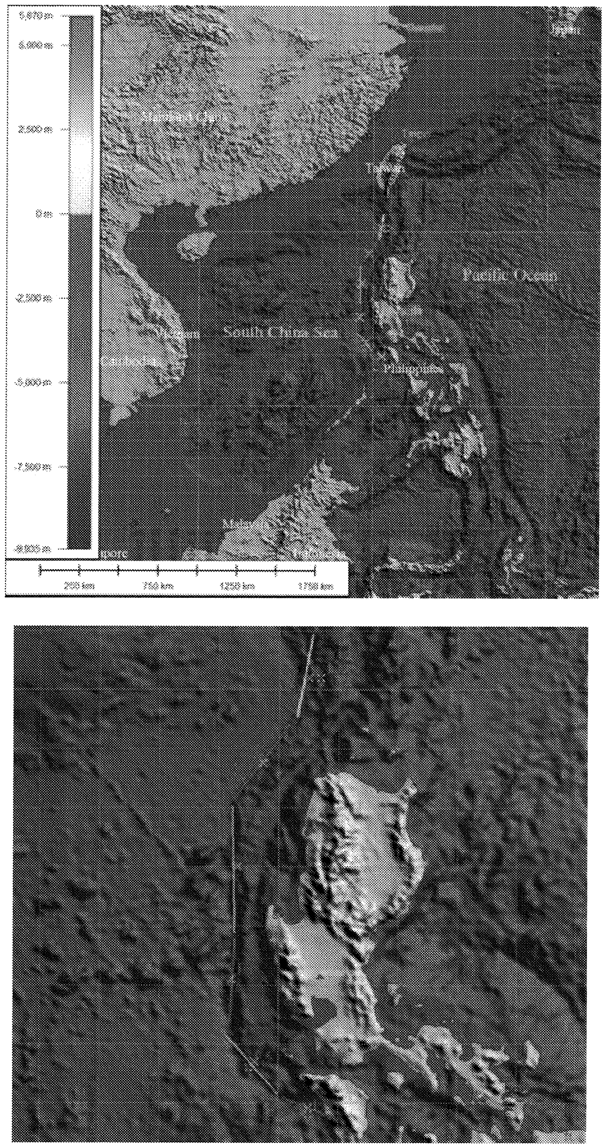

Figure 2 Hypothetical fault segments along Manila Trench

source area for this event is outlined and the width of the fault plane for this event is estimated to be 34 km (width of fault plane = measured width in Figure 3 divided by cos(dip angle) = 30km/cos(28°)).

Alternatively, the size of the ruptured area during an earthquake event may also be determined from empirical formulae. Wells and Coppersmith (1994) studied 421 historical earthquake events and among them, 244 earthquakes with relatively reliable fault parameters were statistically analyzed and established empirical relationship between earthquake's moment magnitude (M_w) and one of rupture length, rupture width and dislocation. The calculated width of each fault plane with Wells and Coppersmith's relationships is given in Table 2. In this table, "SRL" denotes surface rupture length and "RLD" sub-surface rupture length.

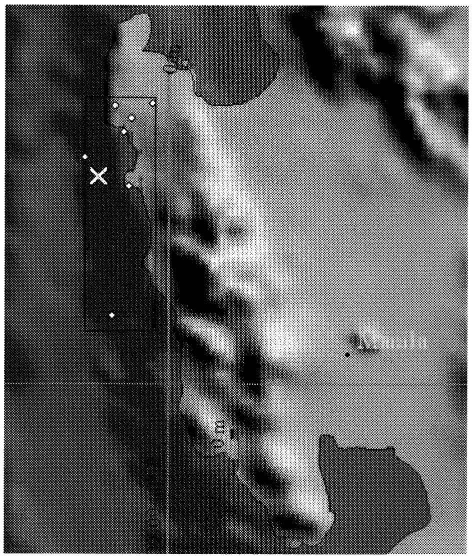

Figure 3 Identify width of source area by using the information from the December 11, 1999 earthquake. The black rectangular is outlined by enclosing the main shock and all its aftershocks.

If we use the length of our constructed fault plane as the surface rupture length in Wells and Coppersmith's study, the mean value of the estimated rupture is 35.1 km and if we use the length of our constructed fault plane as the surface rupture length in Wells and Coppersmith's study, the mean value of the estimated rupture is 38.2 km. Although, we could adopt different width for each fault plane, or even use Wells and Coppersmith's relationship to calculate the width based on earthquake magnitude, for simplicity, we choose one value as the width of all the fault planes. From the above analysis, we finally adopted 35.0 km as the width of a fault plane and applied it to all the fault segments. The fault parameters for these hypothetical fault planes are summarized in Table 3.

If we assume an earthquake with magnitude M_w 8.0, with the fault parameters listed in Table 3, the amount of slip motions can be computed via the following equations

$$M_0 = \mu DLW \tag{1}$$

$$M_w = \frac{2}{3}\log_{10} M_0 - 10.7 \tag{2}$$

where μ is the rigidity of earth mantle, D is the amount of slip motion (slip) and L is the length of the fault plane and W is the width of the fault plane, M_0 is the scalar moment of an earthquake and M_w is the moment magnitude of an earthquake. The rigidity, $\mu = 3.0 \times 10^{10}\ N/m$, is taken for all the calculations throughout this document. The calculated slip amount on each fault plane is shown in the last column in Table 3.

With all the fault parameters shown in the Table 3, the seafloor deformation over each fault segment can be computed via Okada's elastic fault model (Okada, 1985).

3. STUDY OF TSUNAMIS GENERATED ALONG MANILA TREANCH

With the constructed hypothetical fault planes, investigations on the hazards of these tsunami sources can be further studied via numerical simulations. In this section, we analyze tsunami arrival time, amplitude and energy distribution using a hypothetical earthquake of magnitude M_w = 8.0 and assuming that the earthquake ruptures the entire the fault plane. The numerical results will help to identify the most dangerous source areas for the surrounding countries/regions in the South China Sea. The arrival time analysis will be an especially important contribution to the determination of Bottom Pressure Recording (BPR) device (i.e., tsunami sensors) locations for tsunami measurements and forecast. This can be considered as preliminary work leading to the establishment of a tsunami forecast system in South China Sea.

We assume that the sea surface mimics the seafloor deformation instantly. This is reasonable since the duration of an earthquake is usually measured in seconds and the size of the rupture area is very large compared to the water depth. Therefore, there is no time for the water above the seafloor deformation to drain out. Tsunami propagation is simulated with a validated tsunami simulation model -- COMCOT, which adopts an explicit Leap-Frog finite difference scheme to solve Shallow Water Equations (Liu et al., 1994, 1995 and 1998). In this preliminary study, uniform 2-minute grid from ETOPO2, is implemented for all the simulations. The numerical domain ranges from 99°E to 133°E in longitude and 1°S to 33°N in latitude with a grid dimension 1021×1021. Vertical wall boundary is assumed along shorelines, where water depth is 5.0m.

Table 2 Rupture width estimated by Wells and Coppersmith's relationships (1994)

Segment	Length	Mw(SRL)	Mw(RLD)	Width (SRL)	Width (RLD)
E1	160km	7.69	7.77	34.9km	37.6km
E2	180km	7.75	7.85	36.9km	40.6km
E3	240km	7.90	8.04	42.6km	48.6km
E4	170km	7.72	7.81	35.9km	39.1km
E5	140km	7.62	7.69	32.7km	34.9km
E6	100km	7.44	7.47	27.6km	28.4km

Table 3 Hypothetical Fault Planes along Manila Trench

Fault	Lon	Lat	Length	Width	Strike	Dip	Rake	Slip
E1	120.5°	20.2°	160km	35km	10°	10°	90°	6.68m
E2	119.8°	18.7°	180km	35km	35°	20°	90°	5.94m
E3	119.3°	17.0°	240km	35km	359°	28°	90°	4.45m
E4	119.2°	15.1°	170km	35km	3°	30°	90°	6.29m
E5	119.6°	13.7°	140km	35km	320°	22°	90°	7.63m
E6	120.5°	12.9°	100km	35km	293°	26°	90°	10.69m

Note: the focal depth is chosen as 15.0km for all the fault planes.

3.1 Arrival time and Tsunami Amplitude Distribution

For a tsunami forecast and early warning system, two factors are very important. One is the arrival time and the other is the tsunami wave height. Based on numerical results, arrival time, tsunami wave height distribution and the maximum tsunami wave amplitudes along shorelines surrounding the South China Sea, including Taiwan, China, Vietnam, Philippine and Malaysia, are investigated to identify the source regions most dangerous to these countries/regions. This information will be used to determine the locations of tsunami sensors and finally lead to the prototype of a tsunami early warning system, which will be outlined in a later section.

In the following arrival time contour plots, the arrival time is defined as the time when the water surface starts to be elevated more than 1 cm above the mean sea level due to the arrival of the leading wave. For regions where waves are relatively high, this criterion works well. However, for regions far from the source area where tsunami wave amplitude is very small (close to 1 cm), especially when bathymetry is complicated as well (with islands, submarine features and etc), the criterion becomes unreliable.

Numerical results show that for an earthquake occurring in the hypothetical fault segment 1 which is closest to Taiwan, the generated tsunamis will impact the southern part of Taiwan in 20 minutes. Arrival time plots also indicate that for future earthquakes along Manila Trench, the generated tsunamis will attack coastal regions of Southeast China (Fujian province, Gudong province, Hong Kong, Macao and Hainan Island) in 2 to 3 hours. Vietnam will also be affected in 2 hours. Tsunamis generated in Manila subduction zone will strike Malaysia in 3 hours. The tsunami amplitude distribution plots indicate that for earthquakes occurring within hypothetical fault segment 1 and segment 2, the southern part of Taiwan will be greatly affected. For earthquakes occurring in other segments, the tsunami impacts on Taiwan will be relatively small. The plots also show that a major part of tsunami energy generated by earthquakes within fault segment 1, 2, 3 and 4 will travel to the west and northwest. As a result, the coastal regions of Southeast China will be threatened by these tsunami sources. For regions along Vietnamese coast, fault segment 4 and 5 can be considered as the most hazardous tsunami sources. For the coastal region of Malaysia, only tsunamis from fault segment 5 will exert serious impact. The hazardous tsunami source regions for surrounding countries/regions in the South China Sea are summarized in Table 4.

Table 4 Hazardous tsunami sources for different regions

Countries/regions	Hazardous tsunami sources	
	Fault segments	Latitude Range
Philippine	All segments	12.7°N to 21.2°N
Southeast China	1, 2, 3 and 4	14.2°N to 21.2°N
Taiwan	1, 2 and 3	15.9°N to 21.2°N
Vietnam	3 and 4	14.2°N to 18.0°N
Malaysia	5	13.1°N to 14.2°N

4. DEVELOPMENT OF A TSUNAMI FORECAST MODEL IN SOUTH CHINA SEA

4.1 General Procedures to Establish Tsunami Forecast System

The establishment of a tsunami early warning system involves the following stages:

- Deployment of Tsunami sensors

The locations of tsunami sensors in deep ocean are determined according to studies on source regions, tsunami arrival times and the regions to be protected.

- Construction of unit sources

The entire subduction zone is divided into small segments; each segment is treated as "unit" source for tsunami generation.

- Pre-Calculation

Tsunami wave field generated by each unit source is pre-calculated (thus we have a numerical Green's function corresponding to each unit source) and the free surface elevation and velocity everywhere inside the domain are stored into a database.

- Tsunami detection

Tsunami is detected by one or more sensors in deep ocean and the time history of measurements is made available for inverse calculation.

- Data assimilation and inverse calculation

The time history measurement at specific buoy is adopted (usually only leading wave) to inversely calculate the weighting factor of each unit source by best-fitting the measurement.

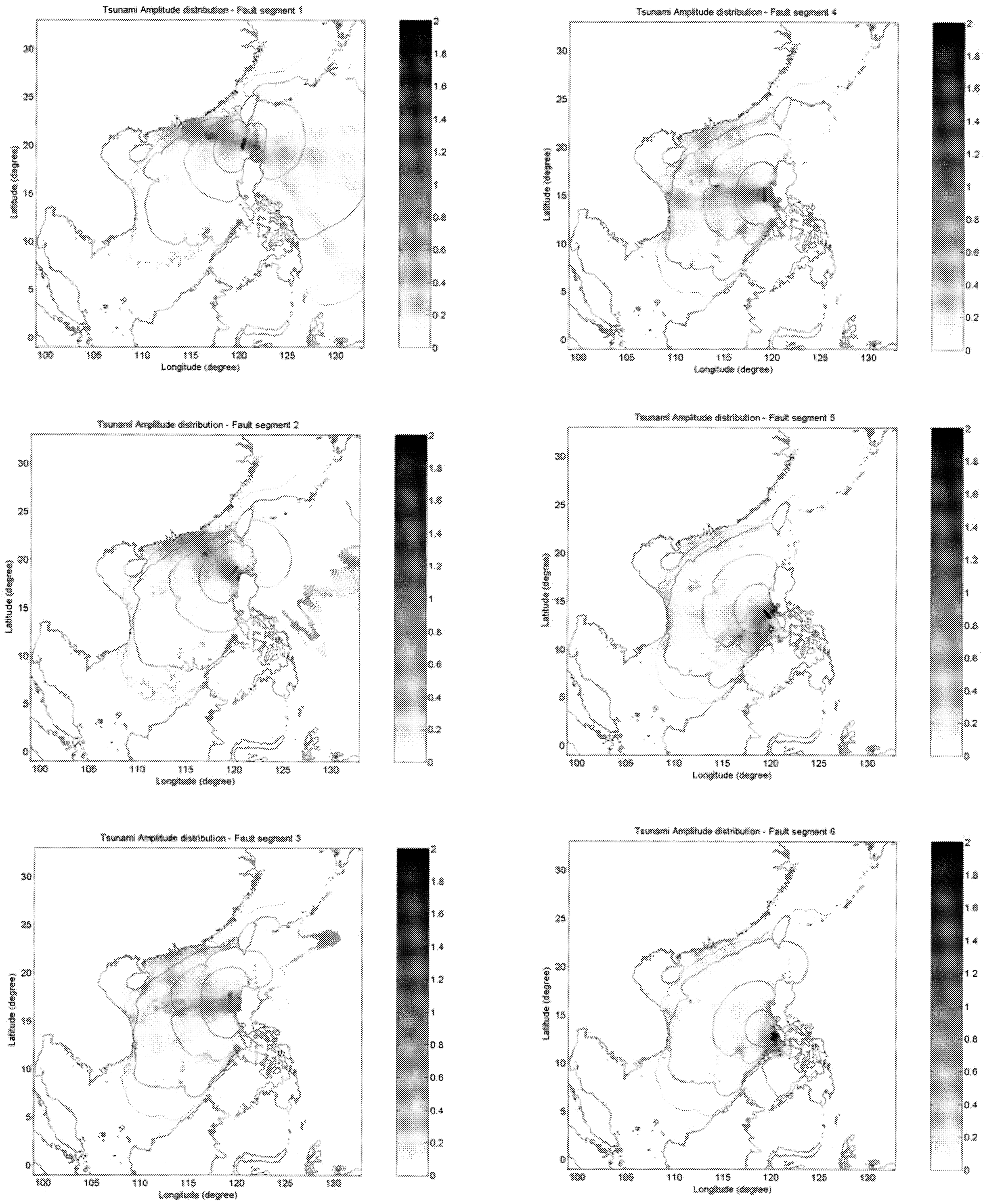

Figure 4 Arrival time contours and tsunami amplitude distributions (Mw = 8.0. Red line: 30-minute contour; Pink line: 1.0-hour contour; Blue line: 2.0-hour contour; Green line: 3.0-hour contour; Yellow line: 4.0-hour contour; and Gray color scale is in meters.)

- Tsunami forecast

Once the weighting factors of unit sources are obtained, tsunami amplitude can be obtained everywhere by linearly combining the pre-calculated result from each unit source with its weighting factor as the coefficient. Then, a forecast can be made available.

- Emergency responses

Based on predicted tsunami arrival time and amplitude, a decision for warning or evacuation will be made.

4.2 Tsunami Early Warning System in South China Sea

A prototype of tsunami early warning system is developed in this section for the South China Sea region.

4.2.1 Deployment of Tsunami Sensors

Basically, information for tsunami forecast comes from two origins: field measurements and numerical analysis. To have accurate measurements and make them useful for tsunami forecast in a timely manner, the locations where tsunami sensors are being deployed should be considered carefully. Also, due to the cost of maintenance, the number of sensors will be very limited. Thus, the locations chosen should allow sensors detecting tsunamis from as many sources as possible and still leaving enough time for forecast. In the South China Sea, at least two tsunami sensors are needed to detect the south and north portions of the Manila Trench. In case of failure, one more sensor is suggested. Totally 3 tsunami sensors will be deployed in our proposed system. Additionally, several factors have to be considered when determining sensor locations.

Firstly, sensors need to be deployed in flat, deep ocean to reduce the disturbances from complex bathymetry, coastal reflection and the trembling of source region. This requires that sensors should be far away from the source region. By examining the bathymetry map of South China Sea, two areas satisfy these requirements: southwest of Luzon and northwest of Luzon, where the sea floor is flat and water depth is around 3.0 – 4.0 km.

Secondly, tsunami forecast requires that sensors should be able to detect tsunamis as early as possible so that enough time can be left for forecast. This implies that the location of sensors should be close enough to the source regions. Also, to detect tsunamis as early as possible, the sensors should be deployed on the paths where tsunamis travel fastest (the fastest portion of the arrival time contours). By studying the arrival time contours, three fastest portions can be identified as the west of segment 1, west of joint between segment 2 and segment 3, and the southwest of the joint between segment 4 and segment 5. The three tsunami sensors will be deployed in regions corresponding to these portions.

From the preliminary analysis in the previous section (i.e., arrival time contours for each fault segment), tsunamis generated from segment 1 and segment 2 will arrive at Taiwan in 20 to 30 minutes. Considering the period of a tsunami will be up to 30 minutes, there is no time to send out early warnings via the above inverse procedure. To leave Taiwan at least 20 minutes for early warning and evacuation, segment 1 and segment 2 are out of consideration in determining locations of tsunami sensors. For segment 3, the generated tsunami will strike Taiwan in 1.0 hour. Therefore, the tsunami sensors should be deployed no more than 10 minutes away from the source region, which is equivalent to about 120km. This distance will allow more than 1.0 hour warning time for other regions. By considering the above requirements for buoy deployment, three possible locations can be identified, which are outlined by red circles in Figure 5.

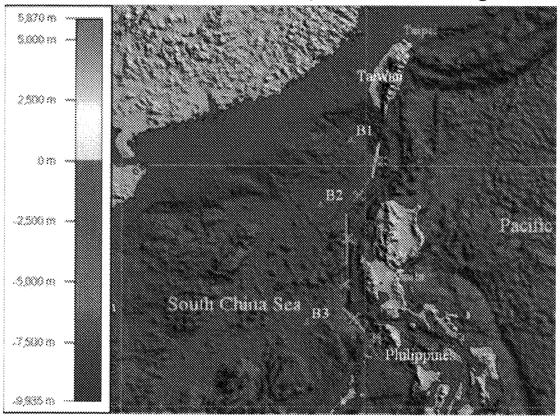

Figure 5 Locations of tsunami sensors

The following three locations are suggested to deploy the three tsunami sensor: B1 (119.40°E, 20.10°N), B2 (118.15°E, 18.40°N) and B3 (117.60°E, 13.50°N).

4.2.2 Construction of Unit Sources

The entire fault plane along Manila subduction zone is divided into small segments. Each segment contains a sub-fault plane of 70 km long and 35 km wide, which becomes the unit source for tsunami generation as shown in Figure 6. The detailed parameters for each unit source are given in Table 5.

4.2.3 Pre-Calculation

COMCOT is used to calculate the tsunami wave field generated by each of the 39 constructed unit sources and the results are stored in a database. The wave field from each unit source is denoted as $G_i(x,y,t)$, where G represents free surface elevation (or velocity) at location (*x,y*) at time t after the main shock; the subscript i presents the *i*-th unit source.

4.2.4 Data Assimilation and Inverse Calculation

During an earthquake event in the Manila subduction zone, once a tsunami is first detected at sensor *j* (sensor B1, B2 or B3), the time history of sea surface elevation measurement at this sensor will be made available for inverse calculation. Assume that the sensor is location at (x_o, y_o), the measurement at this sensor can be written as

$$Z(x_o, y_o, t_k)\ , k=1, N_t \qquad (3)$$

Table 5 Parameters of unit source

Fault #	Lat	Lon	Depth	Length	Width	Strike	Dip	Slip
1	12.63°	120.85°	15km	70km	35km	322°	26°	90°
2	13.00°	120.35°	15km	70km	35km	294°	26°	90°
3	13.38°	119.81°	15km	70km	35km	314°	22°	90°
4	13.89°	119.45°	15km	70km	35km	336°	22°	90°
5	14.50°	119.27°	15km	70km	35km	351°	26°	90°
6	15.13°	119.24°	15km	70km	35km	3.0°	30°	90°
7	15.80°	119.27°	15km	70km	35km	1.0°	30°	90°
8	16.44°	119.27°	15km	70km	35km	359°	28°	90°
9	17.10°	119.26°	15km	70km	35km	359°	28°	90°
10	17.75°	119.25°	15km	70km	35km	0.0°	24°	90°
11	18.37°	119.46°	15km	70km	35km	35°	20°	90°
12	18.91°	119.86°	15km	70km	35km	35°	20°	90°
13	19.45°	120.24°	15km	70km	35km	32°	15°	90°
14	20.07°	120.49°	15km	70km	35km	11°	10°	90°
15	20.73°	120.56°	15km	70km	35km	3°	10°	90°
16*	21.37	120.53	15km	70km	35km	355°	20°	90°
17*	13.79	120.34	15km	70km	35km	318°	22°	90°
18*	14.47	119.98	15km	70km	35km	347°	24°	90°
19	13.64	120.04	15km	70km	35km	317°	22°	90°
20	14.38	119.66	15km	70km	35km	347°	24°	90°
21	15.13	119.58	15km	70km	35km	3°	28°	90°
22	15.79	119.60	15km	70km	35km	1°	30°	90°
23	16.44	119.60	15km	70km	35km	359°	28°	90°
24	17.10	119.59	15km	70km	35km	359°	28°	90°
25	17.75	119.59	15km	70km	35km	6°	24°	90°
26	18.33	119.84	15km	70km	35km	35°	20°	90°
27	18.85	120.22	15km	70km	35km	35°	16°	90°
28	19.40	120.59	15km	70km	35km	29°	12°	90°
29	20.00	120.82	15km	70km	35km	12°	10°	90°
30	20.62	120.90	15km	70km	35km	3°	10°	90°
31	21.28	120.90	15km	70km	35km	358°	10°	90°
32	16.67	119.94	15km	70km	35km	359°	28°	90°
33	17.34	119.93	15km	70km	35km	0.0°	26°	90°
34	18.06	120.10	15km	70km	35km	30	22	90

35	18.64	120.48	15km	70km	35km	35°	20°	90°
36	19.20	120.86	15km	70km	35km	29	15	90
37	19.81	121.12	15km	70km	35km	16°	10°	90°
38	20.46	121.24	15km	70km	35km	5.0°	10°	90°
39	21.12	121.25	15km	70km	35km	358°	10°	90°

Note: the slip for each unit fault plane is assumed as 15.0m and the dip angle is from interpolation.

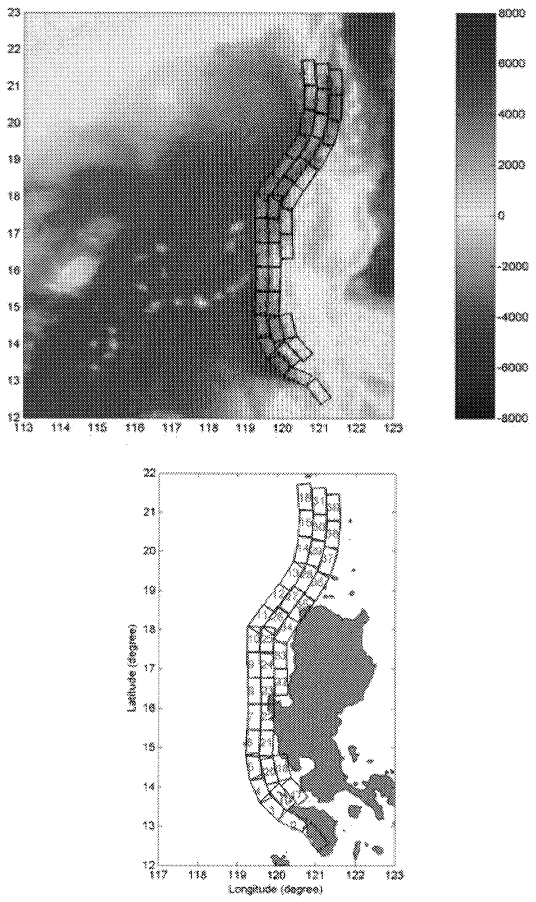

Figure 6 Fault planes of unit sources

where N_t represents total number of measurements within a given time duration, usually covering the entire leading wave. Once the complete form of leading wave is obtained, the inverse calculation starts immediately to determine the weighting factors of unit sources by solving

$$\min_c \|Ac - b\|_2 ,$$

subject to non-negative constraints and

$$A = \begin{Bmatrix} G_1(x_o, y_o, t_1) & \cdots & G_{N_s}(x_o, y_o, t_1) \\ \cdots & \ddots & \cdots \\ G_1(x_o, y_o, t_{N_t}) & \cdots & G_{N_s}(x_o, y_o, t_{N_t}) \end{Bmatrix}$$

$$c = \begin{Bmatrix} c_1 \\ \vdots \\ c_{N_s} \end{Bmatrix} \qquad b = \begin{Bmatrix} Z(x_o, y_o, t_1) \\ \vdots \\ Z(x_o, y_o, t_{N_t}) \end{Bmatrix} \tag{4}$$

where N_t represents the total number of measurements within a given time duration; *Ns* represents the total number of unit sources included in the inverse calculation (Wang and Liu, 2005). Since the above set of equations is over-determined (the number of measurements larger than the number of unit sources), the solution is unique.

If the seafloor deformation due to unit source i is represented by $F_i(x, y)$, the resultant seafloor deformation by the earthquake can also be determined as

$$F(x, y) = \sum_{i=1}^{N_s} c_i F_i(x, y), \tag{5}$$

and the moment magnitude of the earthquake can be derived from

$$M_w = \frac{2}{3}\log_{10}\left(\sum_{i-1}^{N_s} \mu D_i L_i W_i\right) - 10.7 . \tag{6}$$

4.2.4 Tsunami Forecast

With weighting factor, c_i, obtained for each unit source, the sea surface elevation at any location can be forecasted as

$$Z_f(x, y, t) = \sum_{i=1}^{N_s} c_i \cdot G_i(x, y, t) . \tag{7}$$

4.2.5 Example of Forecast calculation

To test the above developed forecast model, an earthquake with magnitude M_w=8.0 is assumed to occur at the fault segment 4 in Manila subduction zone and rupture the entire segment. Fault parameters are the same as those used in tsunami hazardous analysis for fault segment 4 in section 3. The epicenter of the earthquake is located at (119.2°E, 15.1°N).

Time histories of sea surface elevations are recorded at the sensors B1, B2, B3 and other pre-defined numerical tidal gage locations for inverse calculation and the validation of predictions. Since the sensor B3 is the closest to the source region, its measurement is adopted for inverse calculation to determine the weighting factors of unit sources. At 36 minutes after the earthquake, the first complete wave form is obtained and the inverse calculation starts immediately. The

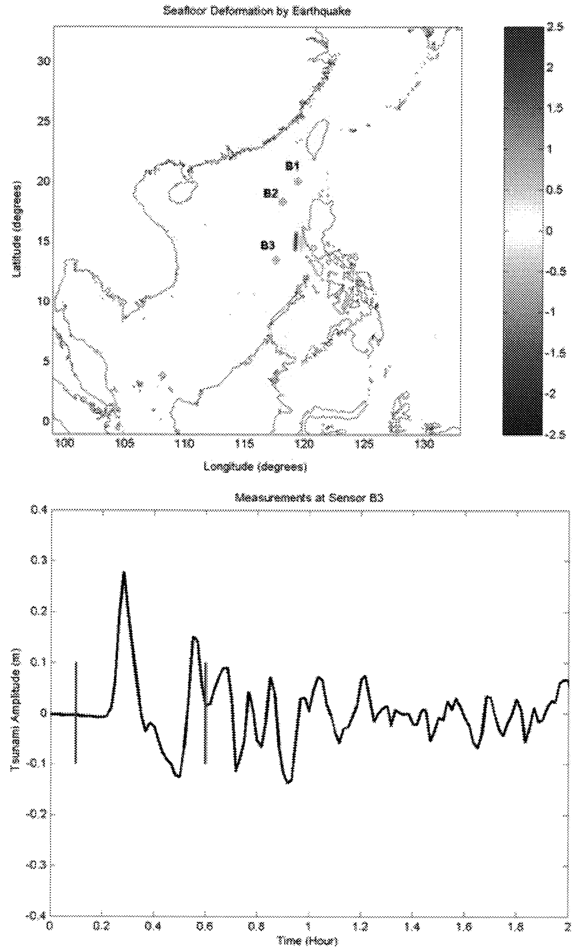

Figure 7 Seafloor deformation and the time history of measurement at sensor B3

time history records from t = 6 minutes to t = 36 minutes, 31 measurements in total, are adopted for inverse calculation to determine the weighting factors of the unit sources (records between blue lines in Figure 7).

However, the number of unit sources to be included in the reverse calculation should be considered carefully. Practically, it is not necessary to include all the unit sources. Especially when the total number of unit sources is larger than the number of measurement, the solution is no longer unique. Additionally, for the selected range of measurements, the waves generated by unit source very far away from the epicenter have not arrived at sensor B3, which will render the weighting factors for these unit sources less accurate. Therefore, we must limit the number of unit sources and only select those unit sources within a reasonable range to be included in the inverse calculation. This range is determined from the empirical relationship between the rupture length and moment magnitude of an earthquake derived by Wells and Coppersmith (1994), which has the form

$$L = 10^{\frac{M_w - 4.49}{1.49}} \tag{8}$$

where M_w is the moment magnitude of an earthquake and L is the subsurface rupture length by the earthquake (e.g., length of the fault plane).

Calculations on historical events show that Wells and Coppersmith's empirical estimates are very close to those from seismic wave analysis. For larger earthquakes, the empirical relationship slightly overestimates the rupture length. In our inverse calculation, we adopt the empirical rupture length, which is 300 km, to determine how many unit sources are included in the calculation. If the epicenter of any unit sources falls into a circular region, centered at the epicenter of the earthquake (119.2E, 15.1N) with a radius 300/2 km, it will be included in the inverse calculation. In this calculation, the unit sources included in the calculations are 4, 5, 6, 7, 18, 20, 21 and 22 (see Figure 6), covering an area of 280km by 105km, which is much larger than the source region (e.g., fault segment 4). And the weighting factors for these unit sources are 0.1600, 0.1597, 0.4739, 0.2609, 0.0143, 0.0000 and 0.1103, respectively.

The predicted and measured time histories are compared at the nearshore of cities around the rim of the South China Sea (Figure 8) and are shown in Figure 9.

We can see that the predictions match the measurements pretty well. Tsunami amplitude and arrival of leading wave and its following waves are matched quite satisfactorily. Additionally, the seafloor deformation synthetic from the weighting factors is also presented to compare with that of the earthquake (Figure 10).

The moment magnitude from the inverse solution is $M_w = 8.04$, which is very close to the earthquake magnitude $M_w = 8.0$ used for tsunami generation. Time history comparisons are also available at other locations in South China Sea. Besides the accuracy, during this hypothetical earthquake event, our model gives 30 minutes to Taiwan, 2.5 hours to China and Vietnam, and 2.0 hours to Malaysia for early warning and evacuation. In general, we could say our prototype of tsunami early warning system gives a very satisfactory performance.

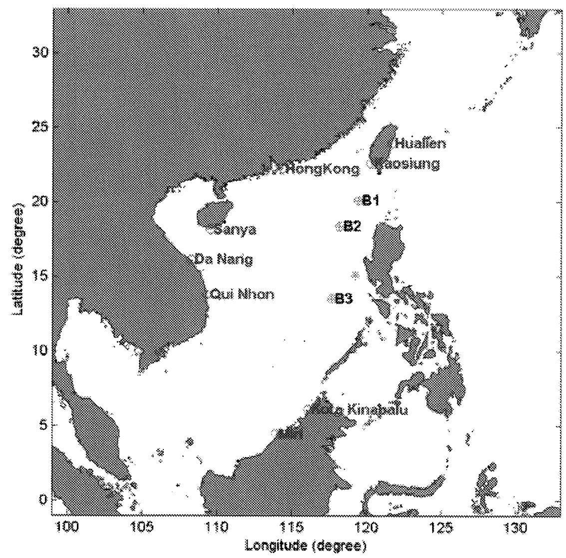

Figure 8 Epicenter of hypothetic earthquake (red star), Tsunami Sensors (B1, B2 and B3) and cities for comparison The predicted and measured time histories of sea surface elevations in surrounding cities are given in Figure 9.

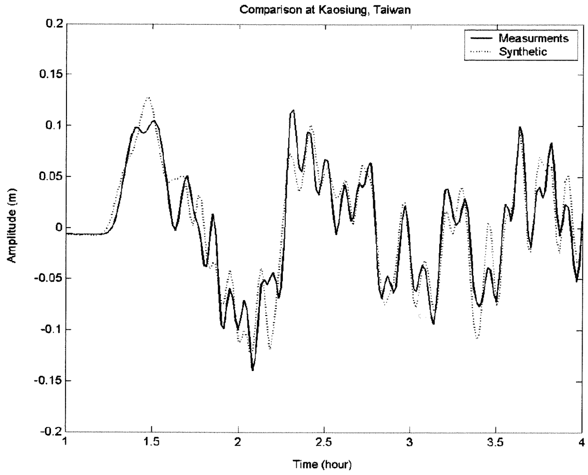
Comparison at Kaosiung, Taiwan
Measurments
Synthetic
Amplitude (m)
Time (hour)

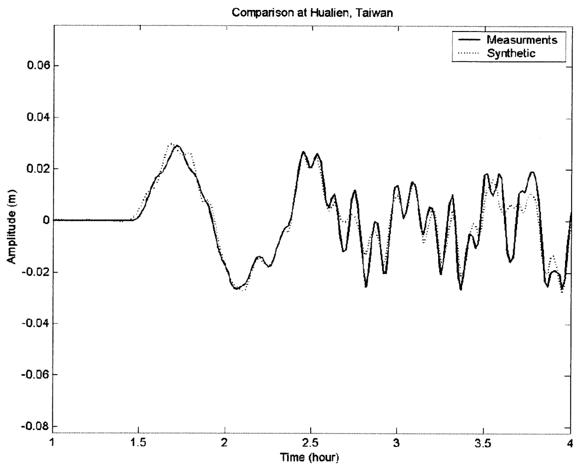
Comparison at Hualien, Taiwan
Measurments
Synthetic
Amplitude (m)
Time (hour)

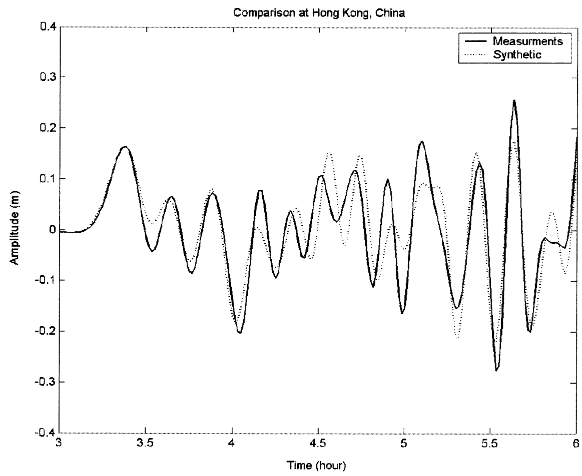
Comparison at Hong Kong, China
Measurments
Synthetic
Amplitude (m)
Time (hour)

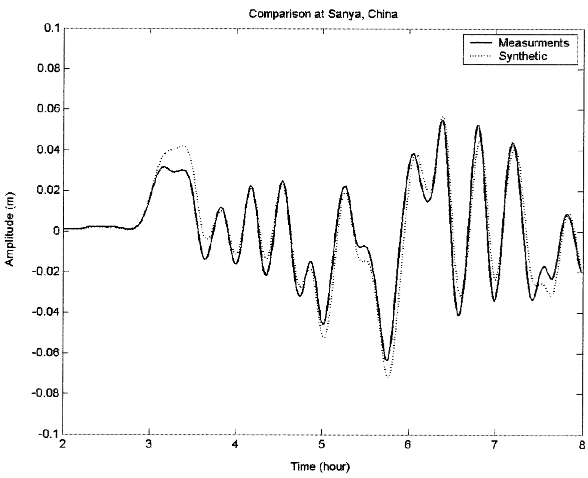
Comparison at Sanya, China
Measurments
Synthetic
Amplitude (m)
Time (hour)

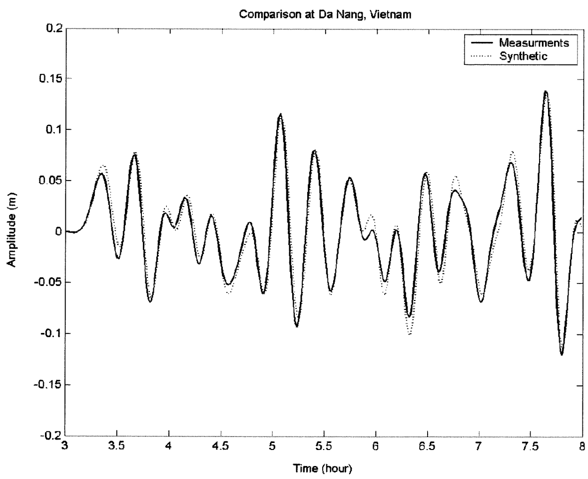
Comparison at Da Nang, Vietnam
Measurments
Synthetic
Amplitude (m)
Time (hour)

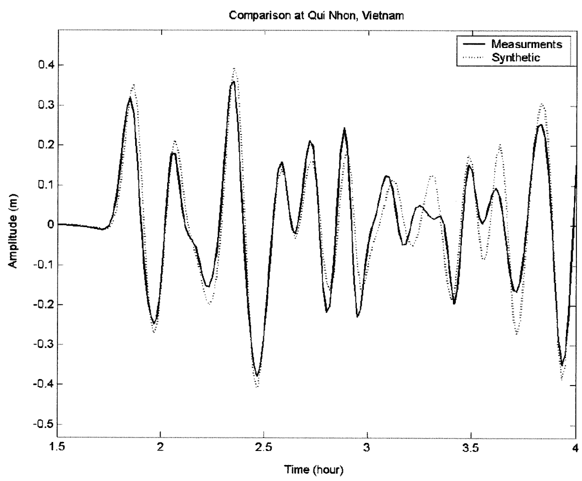
Comparison at Qui Nhon, Vietnam
Measurments
Synthetic
Amplitude (m)
Time (hour)

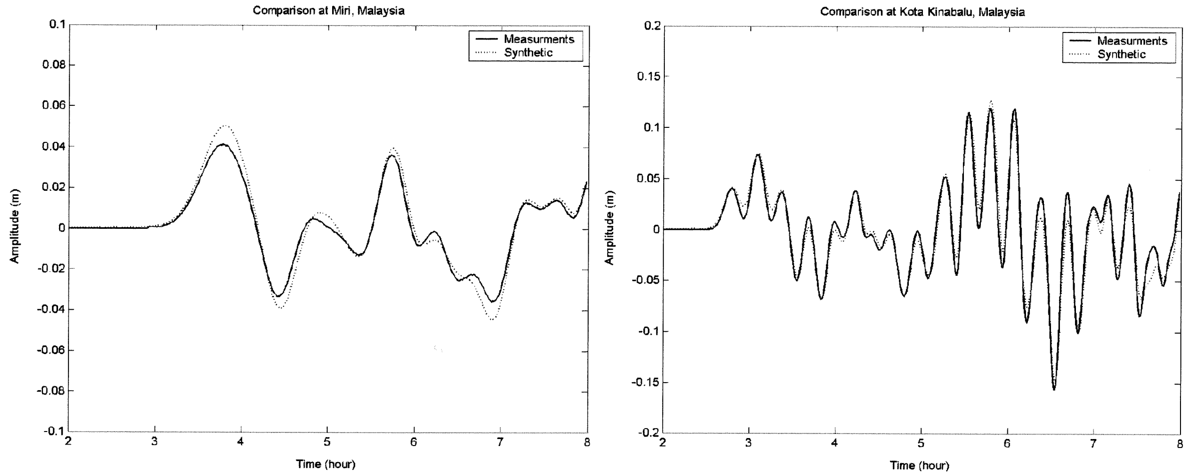

Figure 9 Comparisons between the predicted and measured time histories near coastal cities (see Figure 8)

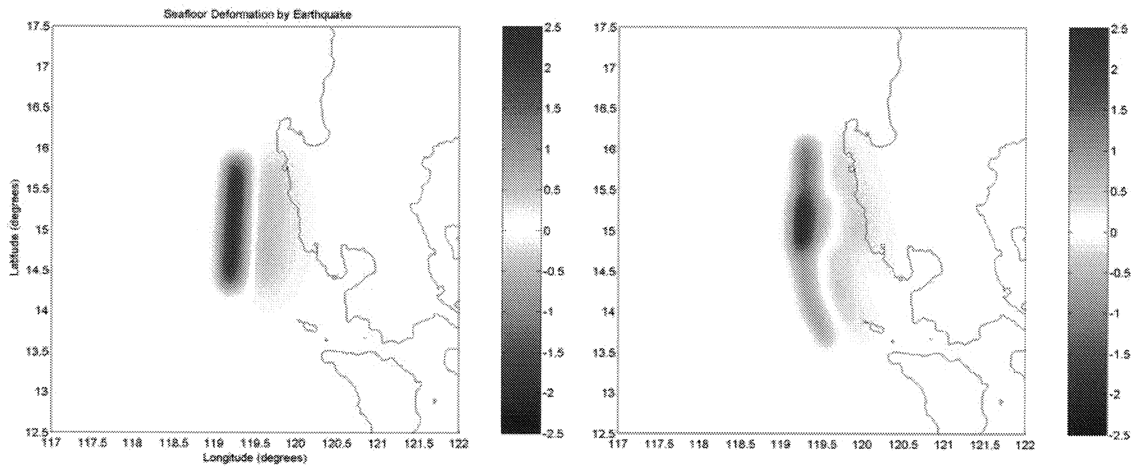

Figure 10 Comparison between earthquake-generated seafloor deformation and synthetic seafloor deformation

6. Concluding Remarks

In this study, fault parameters are identified for tsunami sources in Manila subduction zone and six potential source segments are constructed to analyze tsunami hazards to the surrounding countries/regions in the South China Sea. Arrival time and tsunami amplitude are both investigated, which are further used to determine the locations of tsunami sensors for early warning. A prototype of a tsunami early warning system is suggested in South China Sea by using an inverse method. With a hypothetical earthquake as a test case, the constructed unit sources make very good predictions throughout the South China Sea in comparison with the measurements. These efforts will be very useful to the establishment of the first operational warning system in this region.

References

Lin, Cheng-Horng (2000). Thermal modeling of continental subduction and exhumation constrained by heat flow and seismicity in Taiwan. Tectonophysics 324 (2000) 189-201.

Liu, P. L.-F., Cho, Y.-S., Yoon, S. B. and Seo, S. N., 1994. "Numerical simulations of the 1960 Chilean tsunami propagation and inundation at Hilo, Hawaii" in Recent Development in Tsunami Research, Edited by M. I. El-Sabh, Kluwer Academic Publishers.

Liu, P.L.-F., Cho, Y-S., Briggs, M.J., Synolakis, C.E., and Kanoglu, U., 1995 "Run-up of Solitary Waves on a Circular Island", J. Fluid Mechanics, 302, 259-285.

P. L.-F. Liu, S-B. Woo and Y-S. Cho (1998). Computer programs for tsunami propagation and inundation, Cornell University.

USGS Tsunami Sources Workshop 2006: Great earthquake tsunami sources: Empiricism & Beyond, April 21-22, 2006.

Satake, K. (1987). Inversion of tsunami waveforms for the estimation of a fault heterogeneity: method and numerical experiments. J. Phys. Earth, 35, 241-254, 1987.

Okada, M. (1985) "Surface deformation due to shear and tensile faults in a half-space." Bull. Seismol. Soc. Am., 75(4), 1135–1154.

Titov, V. V., Mofjeld, H. O., Gonzalez, F. I. and Newman, J. C. (2001) "Offshore forecasting of Alaskan tsunamis in Hawaii." In: G. T. Hebenstreit (ed.): Tsunami Research at the End of a Critical Decade. Birmingham, England: Kluwer Acad. Pub., Netherlands, pp. 75–90.

Wang, X. and Liu, P. L.-F. (2005) "A numerical investigation of Boumerdes-Zemmouri (Algeria) earthquake and tsunami". CMES, Vol.10, No.2, pp.171-184.

Wells, D. L. and Coppersmith, K. J. (1994) New empirical relationships among Magnitude, rupture length, rupture width, rupture area and surface displacement. Bulletin of the Seismological Society of America, Vol.84, No.4, pp. 974-1002.

Y. Wei, K. F. Cheung, G. D. Curtis and C. S. McCreery (2003). "Inverse Algorithm for Tsunami Forecasts." J. Waterway, Port, Coastal and Ocean Engineering. March/April 2003.

Fifth International Conference on Urban Earthquake Engineering
March 4-5, 2008, Tokyo Institute of Technology, Tokyo, Japan

CALIBRATION OF TSUNAMI LOADING ON A DAMAGED BUILDING

Panitan Lukkunaprasit[1), Chatpan Chintanapakdee[2), Nuttawut Thanasisathit[3)

1) Professor, Department of Civil Engineering, Chulalongkorn University, Thailand
2) Assistant Professor, Department of Civil Engineering, Chulalongkorn University, Thailand
3) Ph.D. Candidate, Department of Civil Engineering, Chulalongkorn University, Thailand
lpanitan@chula.ac.th, fceccn@eng.chula.ac.th, nutwut@gmail.com

Abstract: The survival of a large number of buildings with minor structural damage under 2-6 m inundation heights above the ground in the 2004 Indian Ocean Tsunami tragedy suggests that it is necessary to validate the formulas stipulated by FEMA-55 (2000) for computing tsunami loadings. In this study, the weather monitoring building of the Meteorological station at Takua Pa, Phang Nga is used as the case study. The building suffered only minor structural damage to the columns and girders. However, most of the non-structural members such as infill brick panels were damaged. The FEMA-55 loading is calibrated with the structural capacity evaluated using a nonlinear pushover analysis, and the actual building performance from a field load test.

1. INTRODUCTION

The unprecedented devastating Indian Ocean tsunami on December 26, 2004 was caused by an Mw of 9.2 mega-earthquake in the subduction zone off the west coast of Banda Aceh, North Sumatra Island, Indonesia. Tsunamis of about 5-12 m heights (some reported up to 20 m at a few locations) struck the western coast of southern Thailand, causing more than 8,000 deaths and missing, and heavy damage to buildings in the affected areas in Thailand. The lack of historical records of destruction by tsunamis on Thai coastlines made the public, and even most academics, to be unaware of the possibility of tsunamis occurring along the coasts of the country. Consequently, the country was not prepared for the hazard, leading to great catastrophe and economic losses of tens of thousands of Baht.

Besides lack of knowledge of tsunami phenomenon and lack of an early warning system, in flat terrains as in Bang Niang, Khao Lak and Ban Nam Kem, inundation penetrated more than 1 km, resulting in heavy fatalities, especially among the elderly, women and small children since they could not escape safely to high ground in time. However, the survival of many multi-story buildings even though they were not designed for tsunamis nor earthquakes indicates that it is possible to design buildings to withstand moderate tsunamis to serve as evacuation shelters, or to reduce damage of buildings for rapid restoration (Lukkunaprasit and Ruangrassamee 2008). Existing design standards, codes or guidelines have been based on laboratory investigations. This study attempts to calibrate the lateral tsunami loading stipulated by FEMA-55 (2000) with the lateral capacity of a building that has survived the 2004 Indian Ocean Tsunami with minor structural damage.

2. THE CASE STUDY BUILDING

The case study building is a weather monitoring building of the Meteorological station at Takua Pa, Phang Nga, Thailand in figure 1. The single story reinforced concrete (RC) building, whose details are shown in figure 2, has survived the 4.4 m wave height (above the ground) with only minor cracks in the structural beam - column frames. Most nonstructural infill brick panels were destroyed, except a few which are essentially perpendicular to the shoreline including one major brick wall which is 2.6 m wide and spans the full height as shown in figure 3. As in normal practice in southern Thailand, the building was not designed for earthquake nor tsunami. The specified material properties were 17.5 MPa compressive strength for concrete, and 240 MPa yield strength for reinforcing steel. The infill brick masonry is usually of low quality. The compressive strength was estimated to be 4.5 MPa or lower.

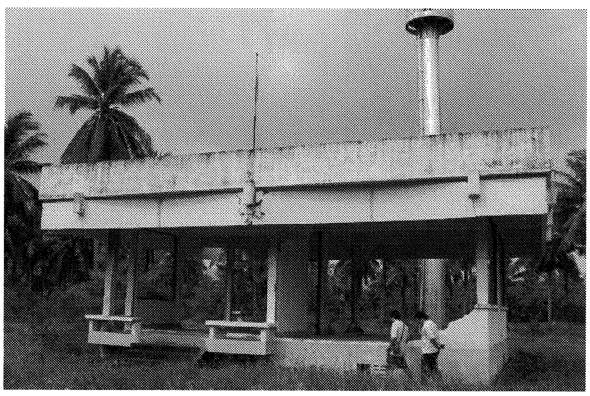

Fig. 1: Photograph of case study building (front view)

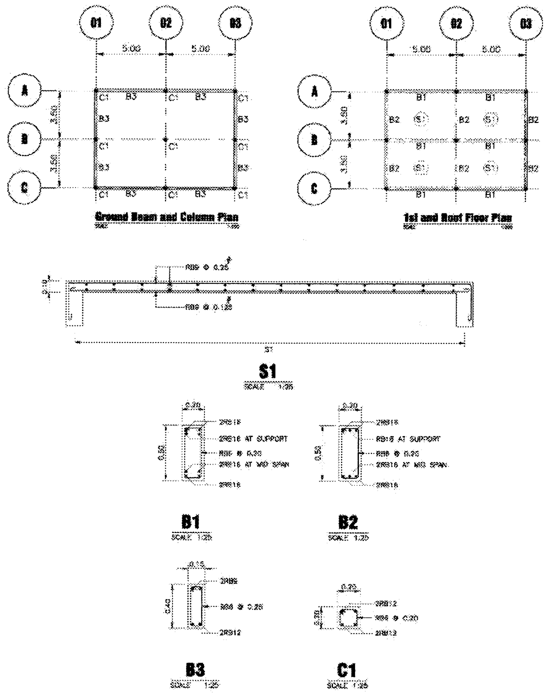

Fig. 2: Building details

Fig. 3:The interior view of the building showing the remaining brick wall

3. LATERAL LOAD DUE TO TSUNAMIS

The tsunami loading on vertical walls have been experimentally investigated by Fukui et al. (1963), Cross (1967), and Ramsden and Raichlen (1990). Cross also developed a simple theory to estimate the force exerted by a bore impinging on a vertical wall. Asakura et al. (2002) carried out hydraulic model tests on land structures in a 3-dimensional wave basin, considering both tsunamis with and without fissions. Yeh (2007) reviewed existing design guidelines and proposed a rational methodology for determining tsunami forces on land structures using inundation map information.

To compute tsunami surge force acting on vertical walls, the City and County of Honolulu building code, CCH (2000) and Okada et al. (2005) stipulate an equivalent linear pressure distribution over 3 times the indundation height with the pressure at the base being 3 times the hydrostatic value. This is applicable only when wall height is higher than three times the inundation height. The resultant surge force is $4.5\rho g h^2$, where ρ is mass density of fluid, g is acceleration due to gravity, and h is design still water flood depth.

FEMA-55 suggests that the lateral force due to tsunami can be computed by combining hydrostatic and hydrodynamic forces as follows:

$$F_{sta} = \frac{1}{2}\rho g h^2 w \tag{1}$$

$$F_{dyn} = \frac{1}{2}C_d \rho v^2 A \tag{2}$$

where w is width of structure, C_D is drag coefficient, v is flow velocity, and A is surface area of obstruction normal to flow.

It should be noted that the flow velocity of $2\sqrt{gh}$ is implied in surge force specified in the CCH code, whereas the FEMA-55 formula explicitly contains the flow velocity as a parameter. However, FEMA-55 recommends that the flow velocity of $2\sqrt{gh}$ be used in an extreme event like tsunami. Yeh (2007) suggested that this value was too high. By image processing of a video recording of the 2004 tsunami striking some beaches close to the site, the tsunami velocity has been estimated to be around $1.4\sqrt{gh}$. Obviously, if the actual flow velocity is over-estimated, then the computed tsunami loading can be significantly over-estimated. Therefore, the flow velocity is one of the most important parameters in computing tsunami-related forces.

Based on the FEMA-55 recommended flow velocity of $2\sqrt{gh}$, the total lateral force acting on the case study building computed according to the FEMA-55 specifications is 2072 kN.

4. NONLINEAR PUSHOVER ANALYSIS

A nonlinear static pushover procedure based on BSSC(1997) was performed to obtain the nonlinear response of the building under incremental lateral loading, using the software SAP 2000. Figure 4 shows the finite element model of the structure. The beams and columns of the structure were idealized using elements with end plastic hinge models. Solid un-reinforced masonry infill panels were modeled as equivalent diagonal compression struts.

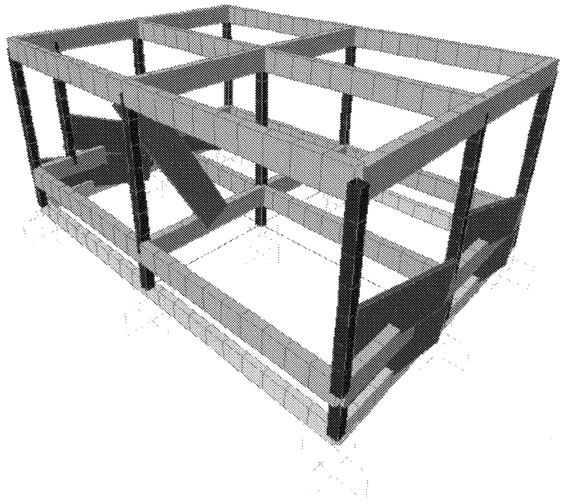

Fig. 4: Finite element model of the structure
(slabs not shown for clarity)

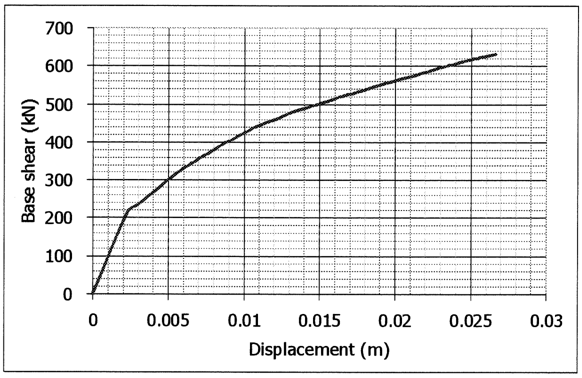

Fig. 5: Base shear vs. displacement from pushover analysis

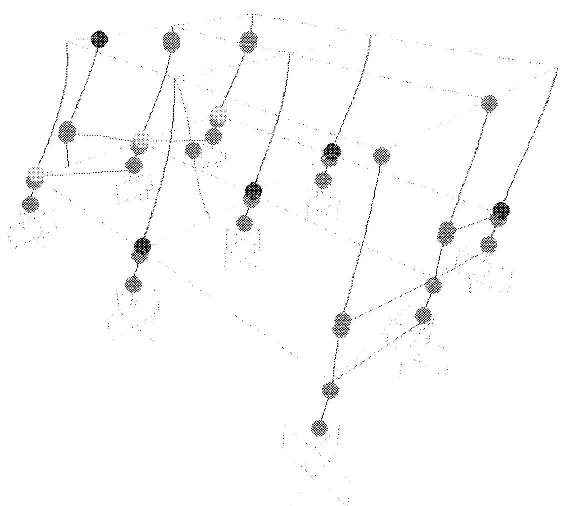

Fig. 6: Plastic hinges developed at final step
(Base shear = 635 kN)

Figure 5 depicts the total load – roof displacement relationship obtained from the nonlinear pushover analysis. The plastic hinges developed at the final step are shown in figure 6. The structural capacity evaluated by the analysis is seen to be only about 30% of the wave force computed in accordance with FEMA-55 using a tsunami velocity of $2\sqrt{gh}$. This indicates that the building should have collapsed if the FEMA-55 load actually acted on the building, in contradiction to the good condition of the survived building which is not at all near collapse. However, real structures may exhibit significant over-strength, and the actual capacity may be under-estimated. The best solution is to perform field load test of the building.

5. FIELD LOAD TEST

As depicted in figure 7, the loading that acted on the structure can be approximately determined by re-loading it past the state of the previous loading, which is reflected by the degree of damage in the building before it is re-loaded. The building was field-loaded until sufficiently more damage was observed in the structural columns as well as the main infill brick panel which has remained and served as a shear wall. At termination of the test, a major crack in the brick panel increased in width from the initial value of 0.45 mm to 2.5 mm. The corresponding total load acting on the building was about 655 kN, which corresponds to the FEMA-55 load based on a velocity of about $1.13\sqrt{gh}$. Details of the field load test appears in a companion paper (Ruangrassamee,et al. 2008).

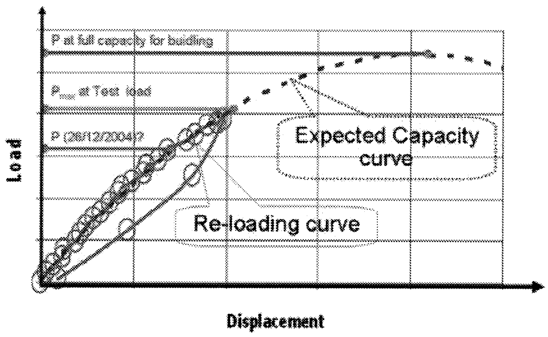

Fig. 7: Re-loading curve.

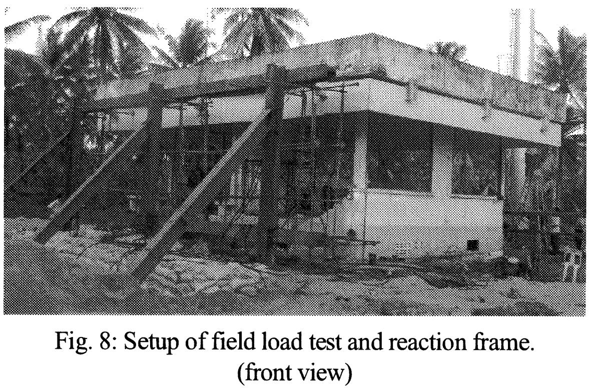

Fig. 8: Setup of field load test and reaction frame.
(front view)

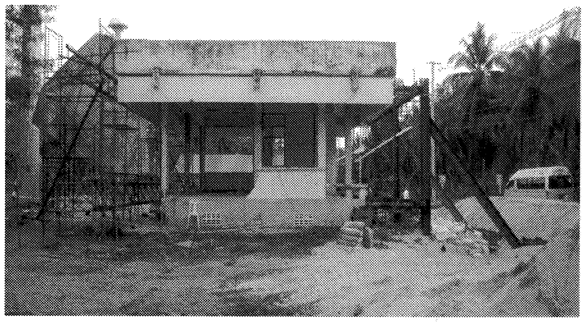

Fig. 9: Setup of field load test and reaction frame. (side view).

6. CONCLUSIONS

For the beach conditions in Southern Thailand, the tsunami load computed from FEMA 55 guidelines based on a velocity of $2\sqrt{gh}$ is excessively large, exceeding the theoretical capacity of the case study building, in contradiction to the excellent performance of the building observed.

The field load test of the Meteorological building in Phang Nga that has survived a 4.4 m. inundation height with minor cracks in the structural members confirms that the tsunami load that occurred would be in the order of FEMA-55 loading based on a velocity of $1.13\sqrt{gh}$

Upstream condition near the building of interest (e.g. density of vegetation, presence of obstruction to flow, etc.) certainly affects the flow velocity. Allowing 25% for uncertainties, for the upstream condition near the building, the tsunami load may be estimated using FEMA-55 guidelines based on a velocity of $1.4\sqrt{gh}$, provided that the waves have broken before hitting the structure.

Acknowledgements:

The funding from the Department of Public Works and Town and City Planning, Ministry of Interior and The Royal Golden Jubilee Project of the Thailand Research Fund are gratefully acknowledged. The support of Chulalongkorn University is highly appreciated. The authors greatly appreciate the valuable contributions of Asst. Prof. Anat Ruangrassamee. The assistance of Dr. Somboon Siangchin and Mr. Surakai Banchuen is also acknowledged.

References:

Asakura, R., Iwase, K., Ikeya, T., Takao, M., Kaneto, T., Fuji, N., and Ohmori, M. (2002), "The Tsunami Wave Force Acting on Land Structures," Proceedings of the 28th International Conference on Coastal Engineering, Vol. 1, pp. 1191-1202.

Building Seismic Safety Council (BSSC). (1997), "NEHRP Guidelines for the Seismic Rehabilitation of Buildings," FEMA-273, Federal Emergency Management Agency, Washington, D.C.

Cross, R.H. (1967), "Tsunami surge forces," Journal of the Waterways and Harbors Division, Proceedings of the American Society of Civil Engineers, Vol.93, No.WW4, 1967, pp. 201-231.

Department of Planning and Permitting of Honolulu Hawaii (2000), "City and county of Honolulu building code," Chapter 16 Article 11.

Federal Emergency Management Agency. (2000), "Coastal construction manual-demonstrates design and construction techniques for construction in coastal high hazard areas," FEMA-55.

Fukui, Y., Nakamura, M., Shiraishi, H., and Sasaki, Y. (1963), "Hydraulic Study on Tsunami," Coastal Engineering in Japan, The Japan Society of Civil Engineers, Tokyo, Vol.6, 1963, pp.67-82.

Lukkunaprasit, P. and Ruangrassamee, A. (2008), "Building damage in Thailand in 2004 Indian Ocean tsunami and clues for tsunami-resistant design," The Institution of Engineers Singapore Journal, Part A: Civil and Structural Engineering, Vol.1(1), 17–30.

Matsutomi, H., Takahashi, T., Matsuyama, M., Harada, K., Hiraishi, T., Suparatid, S. and Nakusakui, S. (2005), "The 2004 Off Sumatra Earthquake Tsunami and Damage at Khao Lak and Phuket Island in Thailand," Annual Journal of Coastal Engineering, JSCE, Vol.52, in printing, 2005.

Ramsden, J.D., and Raichlen, F. (1990), "Forces on Vertical Wall caused by Incident Bores," Journal of Waterway, Port, Coastal, and Ocean Engineering, ASCE, 116(5), pp. 592-613.

Ruangrassamee, A., Thanasisathit, N., Stitmannaithum, S., and Lukkunaprasit, S., "Behavior of a Reinforced-Concrete Building under Tsunami Loading Patterns by Full-Scale Pushover Test," Proceedings, 5th International Conference on Urban Earthquake Engineering, Center for Urban Earthquake Engineering (CUEE), Tokyo Institute of Technology, Japan, March 2008.

Okada, T., Sugano, T., Ishikawa, T, Ohgi, T., Takai, S, and Hamabe, C. (2005), "Structural design method of building for tsunami resistance (proposed)," Building Technology Research Institute, The Building Center of Japan.

Yeh, H. (2007), "Tsunami Load Determination for On-Shore Structures," Proceedings of the Fourth International Conference on Urban Earthquake Engineering, Tokyo Institute of Technology, pp.415-422.

Fifth International Conference on Urban Earthquake Engineering
March 4-5, 2008, Tokyo Institute of Technology, Tokyo, Japan

BEHAVIOR OF A REINFORCED-CONCRETE BUILDING UNDER TSUNAMI LOADING PATTERNS BY FULL-SCALE PUSHOVER TEST

Anat Ruangrassamee[1], Nuttawut Thanasisathit[2], Boonchai Stitmannaithum[3], and Panitan Lukkunaprasit[4]

1) Assistant Professor, Department of Civil Engineering, Chulalongkorn University, Thailand
2) Ph.D. Candidate, Department of Civil Engineering, Chulalongkorn University, Thailand
3) Associate Professor, Department of Civil Engineering, Chulalongkorn University, Thailand
4) Professor, Department of Civil Engineering, Chulalongkorn University, Thailand
fcearr@eng.chula.ac.th, nutwut@gmail.com, fcebst@eng.chula.ac.th, lpanitan@chula.ac.th

Abstract: The 2004 Indian Ocean tsunami caused human loss and devastating damage to civil engineering structures along the west coast of southern Thailand. People's lives could have been saved if they had evacuated in time. After the event, a study was conducted to develop the design guideline for evacuation buildings in low-lying areas. Tsunami forces are evaluated by a series of flume experiments to understand tsunami pressure on buildings. So far, the performance of reinforced concrete buildings under tsunami loading patterns has not been investigated. The full-scale pushover test was conducted on a reinforced concrete building slightly damaged by the tsunami. The response of the building is discussed in this paper.

1. INTRODUCTION

The 26 December 2004 Indian Ocean tsunami was generated by the M = 9.0+ earthquake off the shore of northwestern Sumatra. The first wave of the tsunami struck the coast of Thailand, Malaysia, and other countries in the Andaman Sea about two hours after the earthquake. The tsunami caused human loss and devastating damage to civil engineering structures along the west coast of southern Thailand (Ruangrassamee et al. 2006). To develop the design guideline for evacuation buildings, it is important to understand the response of existing buildings under tsunami loadings. In this study, a full-scale pushover test was conducted on a reinforced concrete building slightly damaged by the tsunami. The experiment becomes the first of its kind. The result will be used for calibration of mathematical models of the building subjected to tsunami loads.

2. TESTED BUILDING

The building tested in this study is the former office of Thai Meteorological Department in Phang-Nga Province. The building is located at 8° 41.444" N 98° 14.489" E in Khaolak, Phang-Nga. Khaolak is the hardest hit area in southern Thailand. Tsunami amplitudes reached 10 m above the mean sea level. Figure 1 shows the building slightly damaged the tsunami. The building is about 100 m from the shoreline and the building front faces the shoreline in the west. The inundation height at the building was about 4.4 m. Figure 2 shows the plan and elevation of the building. The building has one story with two bays. The floor is raised above the ground level by about 0.9 m. The building weighs about 70 ton. Beams, columns, and slabs are made of reinforced concrete and walls are of brick masonry. The building is supported by shallow foundation. The column size is 0.20 m x 0.20 m. Primary members except perimeter beams for architectural purposes suffered minor damage. Hairline cracks are observed in columns. Brick walls in the plane perpendicular to tsunami flow were swept away. The perimeter beams serving architectural purposes is placed at the front and back at about 4 m from the ground. The beams experienced lateral bending due to tsunami flow as seen in Figure 3.

Before the test, concrete samples were collected by coring floor beams at six points. Concrete strength is approximately 12 MPa.

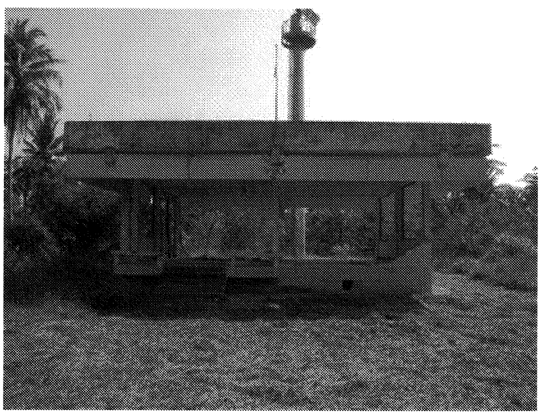

Figure 1 Building tested in this study

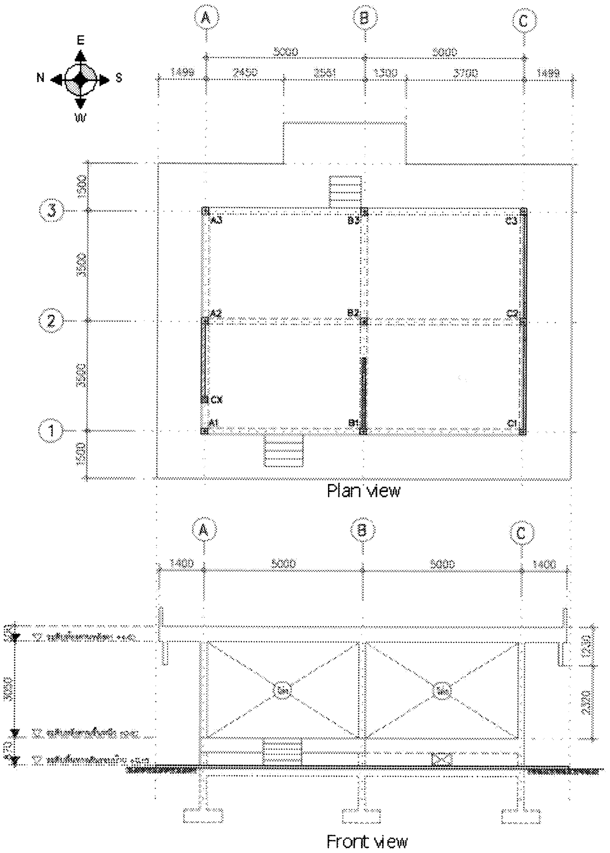

Figure 2 Plan and elevation of the building

3. TEST SETUP

Hydrodynamic forces from tsunami flow act laterally on the building. To simulate the condition, lateral loads generated by hydraulic jacks are applied at six beam-column joints at the building front. A reaction frame was constructed in the front of the building to counterbalance the forces applied by jacks as shown in Figure 4. Load cells are installed at the jacks to monitor loads.

Displacement transducers are installed on the back of the building to measure floor and roof displacements. The transducers are designated as shown in Figure 5. Strains at the base of the column A3 are monitored.

4. TSUNAMI LOADING PATTERNS

Two patterns of tsunami pressure acting on a building are considered in the study:

1) uniform pressure over the height representing a hydrodynamic effect on the building. The pressure is gradually increased.
2) FEMA-55 pattern which is the combination of hydrostatic pressure (triangularly distributed pressure) and uniform pressure from hydrodynamics as shown in Figure 6 (FEMA, 2000). The hydrostatic pressure is applied to the building first and then the uniform pressure is gradually increased.

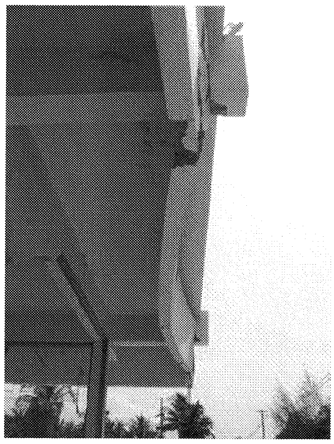
Figure 3 Lateral bending of architectural beams


Figure 4 Reaction frame and hydraulic jacks

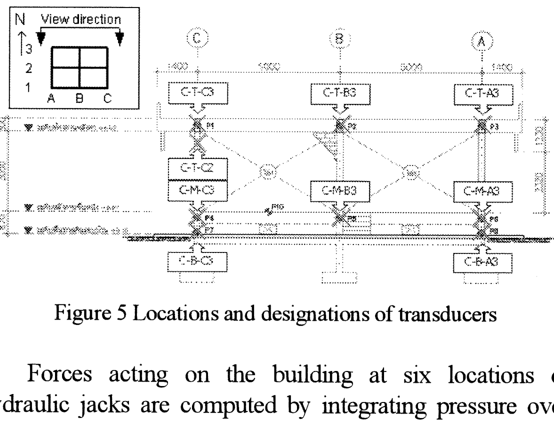

Figure 5 Locations and designations of transducers

Forces acting on the building at six locations of hydraulic jacks are computed by integrating pressure over tributary areas. The forces are applied using a force control scheme until the building experience slight nonlinear behavior. The response will be used in a subsequent study for correlation between analysis and experiment.

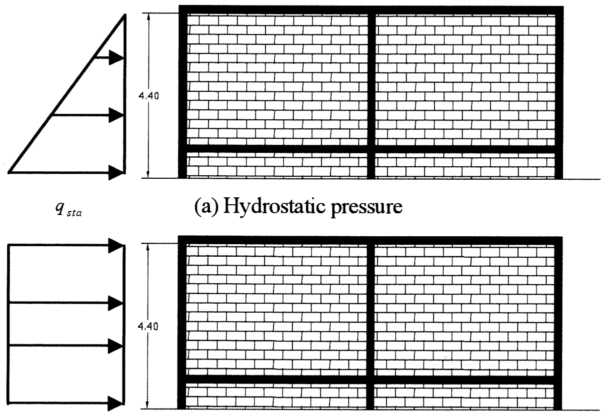

(a) Hydrostatic pressure

(b) Hydrodynamic pressure

Figure 6 Pressure according to FEMA-55

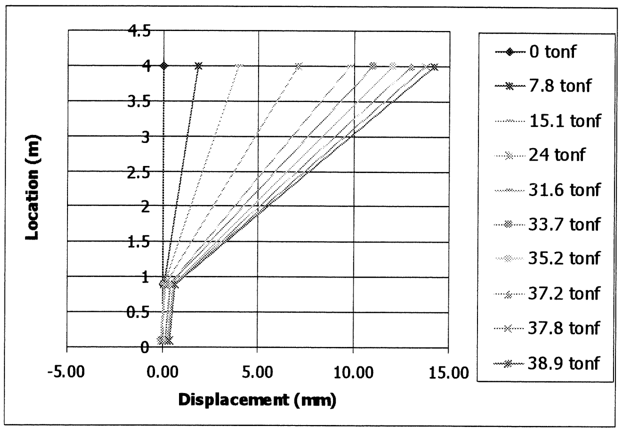

Figure 9 Displacement profiles of Frame A at different loads for the uniform pressure pattern

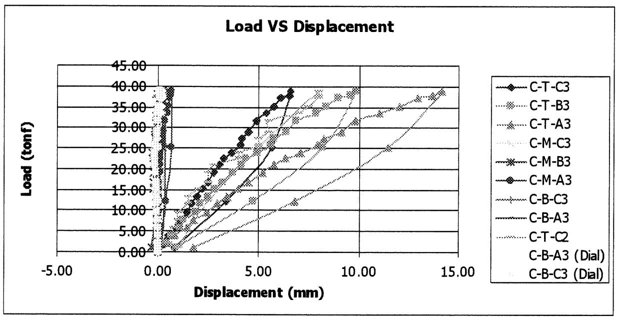

Figure 7 Lateral load vs. lateral displacement relation at the roof and floor levels of Frames A, B, and C for the uniform pressure pattern

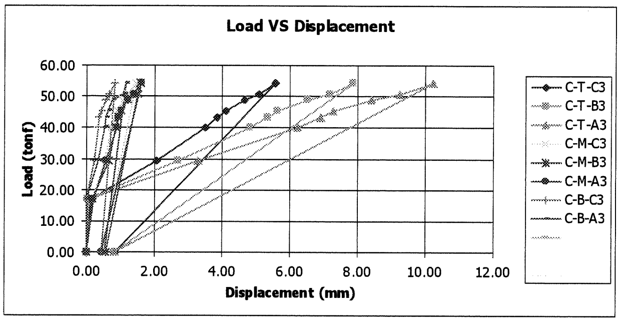

Figure 10 Lateral load vs. lateral displacement relation at the roof and floor levels of Frames A, B, and C for the FEMA-55 pattern

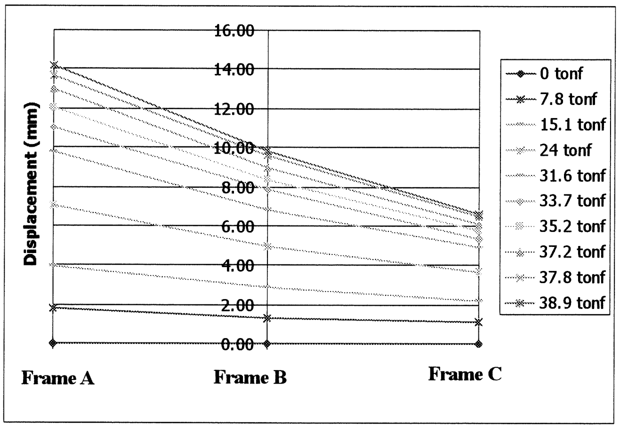

Figure 8 Roof displacement at different loads for the uniform pressure pattern

5. RESULTS AND DISCUSSIONS

5.1 Uniform Pressure Pattern

Figure 7 shows the lateral load vs. lateral displacement relation at the roof and floor levels of Frames A, B, and C. The relation exhibits slight nonlinearity when the load is above 30 ton. The building was unloaded at a load of 40 ton with the maximum roof displacement of about 14 mm. After unloading the residual displacement is about 2 mm. Since the floor displacement is very small, the residual displacement is mainly associated with inelasticity of columns and brick walls above the floor.

It is seen that the displacement is larger in Frames A and B. So, there is torsional rotation in the clockwise direction. In Frame C there are 1-meter-high brick walls resulting in the drift of the center of rotational stiffness toward Frame C. Figure 8 shows the roof displacement at different loads. The roof rotation is evident.

Figure 9 shows displacement profiles of Frame A at different loads. The displacement arises mainly at the roof. The maximum strain at the column A3 is about 500 $\mu\varepsilon$.

5.2 FEMA-55 Pattern

After the test with the uniform pressure pattern, the building was unloaded and reloaded using the FEMA-55 pattern. Figure 10 shows the lateral load vs. lateral displacement relation at the roof and floor levels of Frames A, B, and C. Since the hydrostatic pressure is applied first and the force due to uniform pressure is gradually increased, there is the change in slopes at a load of 18 ton. In this pattern, larger forces due to hydrostatic pressure result in a larger floor displacement when compared to Figure 7. The maximum roof displacement is about 10 mm at the load of

55 ton. Then, the building is unloaded. The residual displacement at the roof is about 1 mm and close to the residual displacement at the floor. The residual displacement arises from inelasticity of reinforced concrete members and brick walls beneath the floors.

From the test, it is seen that the building could withstand the lateral loads well. Further analysis will be conducted to correlate analytical results with these experimental results in order to gain insights in the response of buildings under tsunami loads.

6. CONCLUSIONS

The paper presents the result from full-scale pushover test of a reinforced concrete building subjected to tsunami loading patterns. This is the first pushover test of a building under tsunami loading patterns. The result will be used for validation of mathematical models of the building subjected to tsunami loads. It is found that brick walls help resist large forces, the model of brick walls need to be investigated in details.

Acknowledgements:

The authors acknowledge financial support from Department of Public Works and City Planning, Ministry of Interior. The members of Center of Excellence on Earthquake Engineering and Vibration, Chulalongkorn University had assisted the test since the beginning. Their contributions are highly appreciated.

References:

Federal Emergency Management Agency (2000), "Coastal Construction Manual - FEMA-55," USA.

Ruangrassamee, A., Yanagisawa, H., Foytong, P., Lukkunaprasit, P., Koshimura, S., and Imamura, F. (2006) "Investigation of Tsunami-Induced Damage and Fragility of Buildings in Thailand after the December 2004 Indian Ocean Tsunami," Earthquake Spectra, 22(S3), S377-S401.

Fifth International Conference on Urban Earthquake Engineering
March 4-5, 2008, Tokyo Institute of Technology, Tokyo, Japan

CHALLENGES FOR TSUNAMI DISASTER REDUCTION BY NATIONAL HIGHWAY ADMINISTRATORS

Kataoka Shojiro[1)]

1) Senior Researcher, Earthquake Disaster Prevention Division, National Institute for Land and Infrastructure Management, Japan
kataoka-s92rc@nilim.go.jp

Abstract: National highway administrators have been challenging to mitigate tsunami disaster more intensively than ever after the 2004 Indian Ocean tsunami. This manuscript summarizes those challenges of Sanriku National Highway Office and Kinan Office of River and National Highway. They have been working on improving publicity work, disaster information sharing, and disaster drills and reconstruction of road stations to be used as disaster measures bases.

1. INTRODUCTION

Great earthquakes often have occurred at the boundaries of continental and oceanic plates around Japan. These earthquakes generate not only ground shaking but also tsunami and hence have caused major disasters especially along the Pacific coast.

Roads are expected to support urgent activity such as evacuation, rescue, and restoration of lifelines after major earthquakes and tsunamis. In particular, national highways have often served as critical infrastructures for the urgent activity.

National highway administrators have been challenging to mitigate tsunami disaster more intensively than ever after the 2004 Indian Ocean tsunami. This manuscript summarizes those challenges of Sanriku National Highway Office and Kinan Office of River and National Highway (Sanriku Office and Kinan Office, respectively, from now on). Both these offices are located near the source area of past tsunamis as shown in Figure 1.

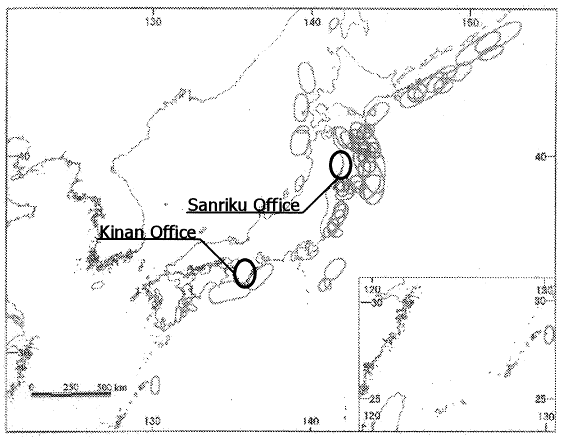

Figure 1 Source area of tsunami (1885-1994) around Japan (Earthquake Research Committee, 1997) and administration areas of Sanriku and Kinan Offices.

2. CHALLENGES FOR TSUNAMI DISASTER REDUCTION

2.1 Sanriku and Kinan Offices

Sanriku Office administers national highways R45 and R283 within Iwate Prefecture as shown in Figure 2. Since R45 runs along the Pacific coast, 36 sections of which total length is 36km are possible to be inundated by tsunamis of the 1886 off-Sanriku earthquake (M8.5), the 1933 off -Sanriku earthquake (M8.1), or a hypothetical off-Miyagi earthquake (M8.0).

Kinan Office administers most of national highway R42 within Wakayama Prefecture as shown in Figure 3. R42 also runs along the Pacific coast and 29% of its length under administration of Kinan Office are supposed to be

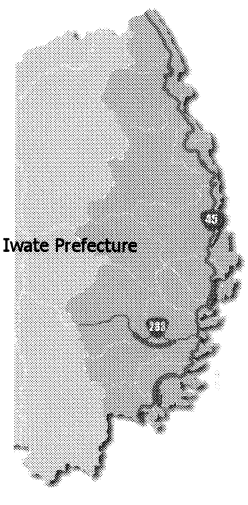

Figure 2 National highways R45 and R283 under administration of Sanriku Office.

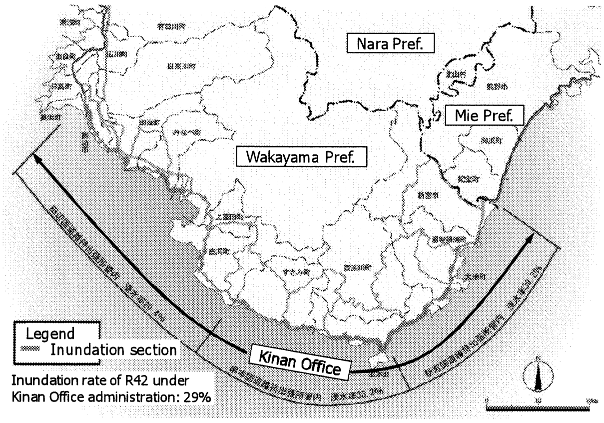

Figure 3 National highway R42 under administration of Kinan Office.

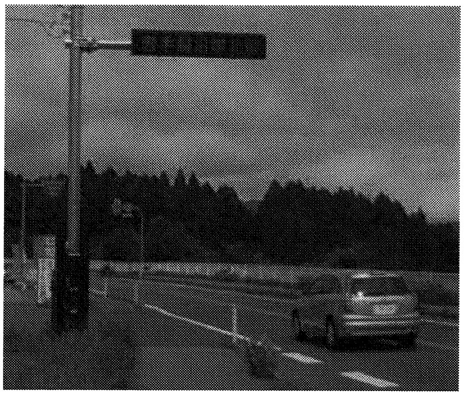

Photo 2 Road information sign that can show tsunami alert (Sanriku Office).

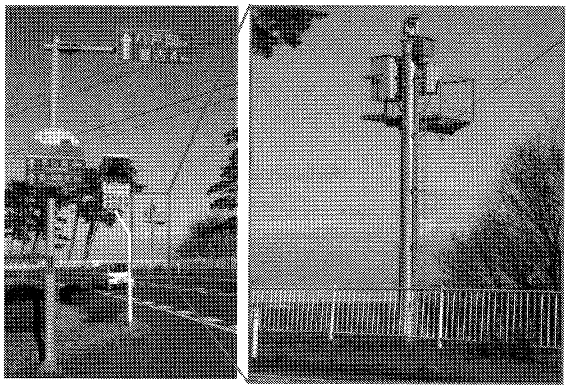

Photo 3 CCTV camera installed at R45 for prompt conformation of road conditions.

Photo 1 Road signs showing estimated tsunami inundation area. Top: Sanriku Office, Bottom: Kinan Office.

inundated due to the coupled Tokai-Tonankai-Nankai earthquake (M8.6).

2.2 Publicity Work

Sanriku and Kinan Offices have installed road signs to inform road users that they are entering or in the estimated tsunami inundation area as shown in Photo 1. Kinan Office uses blue lines on the safety fence to show the inundation area.

Sanriku Office has been installing 32 road information signs (Photo 2) and 34 CCTV cameras (Photo 3) during FY2004-2007. The guidance system for road information signs, which is developed by Tohoku Regional Development Bureau and has been operated since March 2007, helps them to show tsunami alert several minutes after the tsunami warning by Japan Meteorological Agency. It took more than an hour before the installation of the guidance system because the tsunami warning was faxed to the road administrators and then confirmed and input into the operation system. The guidance system made the procedure to be automatic. The CCTV cameras are expected to help the officers to confirm road conditions in real-time.

Kinan Office has been investigating real-time information service for earthquakes and tsunamis by means of Vehicle Information and Communication System (VICS). The use of VICS, however, has to be popularized far more than now to make the service effective.

Both Offices publishes leaflets to inform their local residents of the possible inundation areas and their measures against tsunami.

2.3 Disaster Information Shearing

Sanriku Office has held "Liaison Committee for Disaster Prevention of Roads and Others in Sanriku Coastal Region" once a year since 1998 with Iwate prefecture, cities, towns, police, lifeline companies, and so on. One of the results of the committee is real-time image sharing; images obtained by tsunami watching cameras are collected and

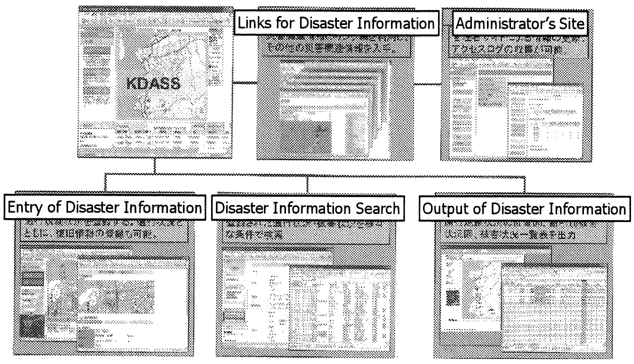

Figure 4 Screen images of KDASS.

Table 1 Users of the disaster measures base and how it is used.

Users	How to use
1. Road users left in the area isolated by tsunami inundation 2. Evacuee from Taro area by car 3. Evacuee looking for information and/or foods 4. Victims looking for light during blackout 5. Volunteers and workers for restoration	1. Temporary evacuation 2. Information collection and exchange 3. Food supply 4. Relay base for transport

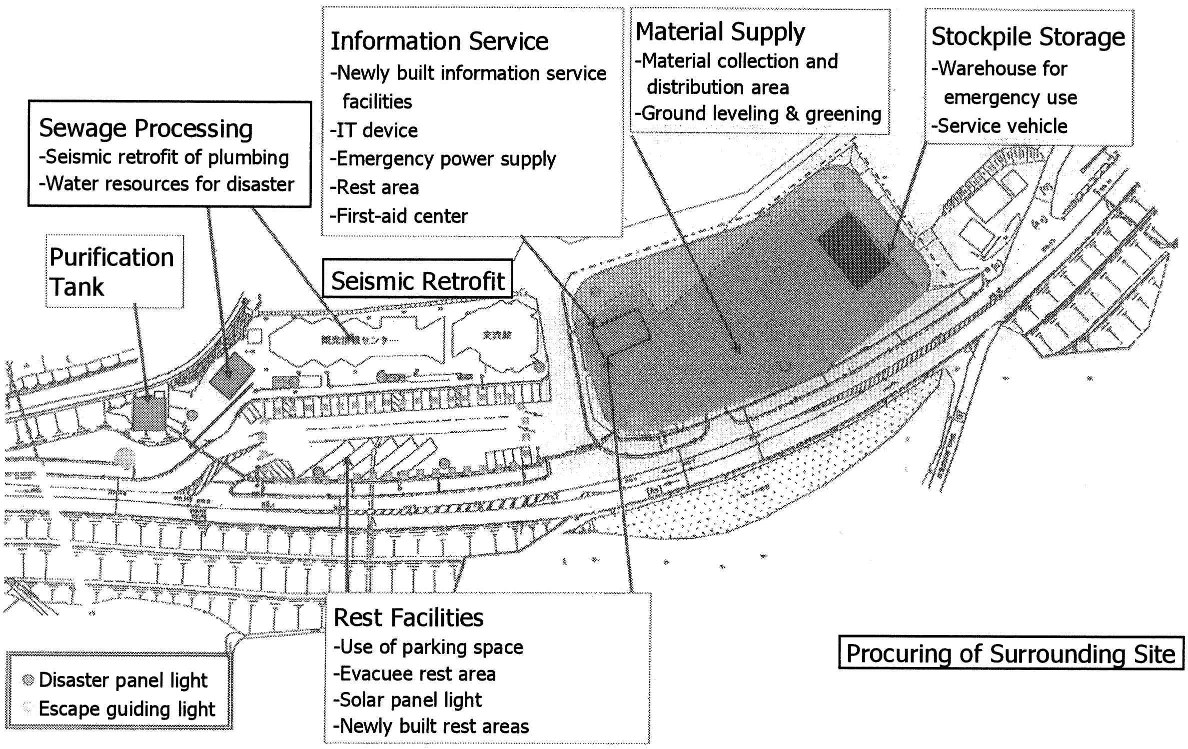

Figure 5 Reconstruction plan for the road station "Taro" to be used as a disaster measures base.

transmitted to Iwate prefectural office and Tohoku regional development bureau. It enables these organizations to be ready for the urgent activity promptly.

Kinan Office has held "Kinan Area Liaison Meeting" every year with 20 organizations including the public works office of Wakayama prefecture, cities, towns, and a highway company. KDASS, Kii area Disaster Antidote Support System, has been used for disaster information sharing among these organizations. Figure 4 shows the screen images and outline of KDASS. Road administrators input the road conditions such as damage to facilities and traffic control sections into KDASS and the information is opened to the other organizations without delay. The main server of KDASS is installed in Osaka where it can avoid the effects of major earthquakes and tsunamis.

2.4 Utilization of Road Stations

Road stations are service areas beside national highways and other arterial roads for road users to park and take a rest.

Road station "Taro" is located out of possible inundation sections of R45 and has been reconstructed to also function as a disaster measures base. The reconstruction, of which outline is shown in Figure 5, is planned taking account of various kinds of people who possibly use the base and how it is used after major disasters (Table 1).

Road station "Shihara-Kaigan" beside R42 is also under reconstruction to be used as a disaster measures base as shown in Figure 6. Publicity work for road users and the contents of the information service need further

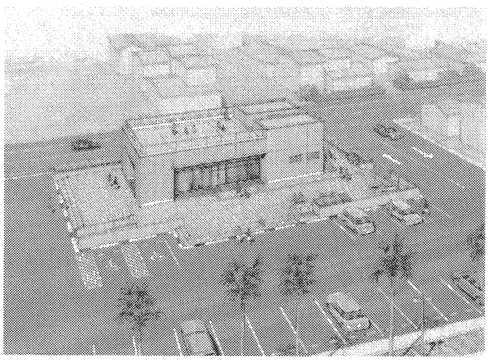

Reconstruction image of the road station "Shihara-Kaigan"

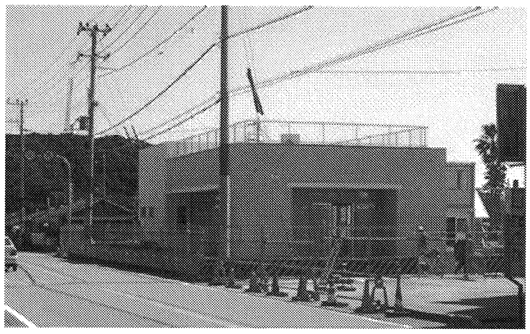

March 2007

Disaster scenario

Scenario earthquake and tsunami	-JMA Seismic Intensity: 6 upper -Tunami arrival: 12 min. after earthquake
Estimated damage	-Inundation above the floor level of the road station
Estimated number of users	-22 (road users in a peak hour)
Period to be used as the base	-One week (until lifeline recovery)

Provisions

Functions	Person in charge	Provisions
Resting	Road adminis -trator	-Rest facility for 22 people
Temporary evacuation		-Evacuation area for 22 people on rooftop -Simple washroom
Information service		-Terminal for road and weather information
Material storage	Local govern -ment	-Water and food for emergency -Blankets and tarpaulins
Volunteer center		-Existing restaurant to function as food providing center -Management of evacuation areas

Figure 6 Reconstruction plan for the road station "Shihara-Kaigan" to be used as a disaster measures center.

consideration. In addition, a heliport is under construction just beside Kinan Office; helicopters are expected to assist early confirmation of the road condition and transportation.

2.5 Disaster Drills

Sanriku Office conducts disaster drills three times a year. A comprehensive disaster drill was carried out in September 2007 assuming a hypothetical earthquake with JMA seismic intensity of 6 upper. The officers in charge of disaster measures gathered at a meeting room and carried out the drills such as installation of branch office for disaster measures, information transmission, inspection of facilities, and emergency restoration of damaged facilities.

Sanriku Office also conducts a tunnel disaster drill as a member of "Liaison Committee for Disaster Prevention of Roads and Others in Sanriku Coastal Region". The drill has been carried out every year since 1998 under the assumption of a traffic accident in a long tunnel. Report, traffic control, operation of disaster prevention equipment, fire control, rescue, first aid and emergency transport, helicopter transport, discussion for traffic control release, and car removal drills were carried out and these drills are considered effective in case of earthquakes and tsunamis.

Kinan Office had prepared an initial action manual in 1998 and distributed as pocket notebooks and pocket cards to the officers. Initial action drills are carried out in order to master and revise the manual. The manual has revised in 2001 and 2006 based on the lessons learned from the drills. Evacuation from tsunami is included in the drills in recent years. The exact day and time of the drills were not notified to the officers in some cases.

3. CLOSING REMARKS

Tosa National Highway Office and Kyushu Regional Development Bureau have been also investigating measures against tsunami disaster in cooperation with National Institute for Land and Infrastructure Management. A technique for developing earthquake-tsunami disaster scenarios (Kataoka, 2007) is utilized to find the best solution in each area. These results will be reported in the near future.

Acknowledgements:

I would like to thank Mr. Kanno (Sanriku National Highway Office), Mr. Yamada (Kinan Office of River and National Highway), Dr. Fujii (INA Corporation) and Mr. Usami.(National Institute for Land and Infrastructure Management) for their kind support to the investigations.

References:

Earthquake Research Committee, The Headquarters for Earthquake Research Promotion (1997): Seismic activity in Japan, http://www.hp1039.jishin.go.jp/eqchreng/eqchrfrm.htm

Kataoka, S. (2007): A scenario of earthquake-tsunami disaster and a policy of measures for road networks, *4th International Conference on Urban Earthquake Engineering*, pp. 467-474.

Fifth International Conference on Urban Earthquake Engineering
March 4-5, 2008, Tokyo Institute of Technology, Tokyo, Japan

APPLICATION OF GREENBELT TO MITIGATE TSUNAMI HAZARD

Tetsuya Hiraishi

Head, Wave Division, Port and Airport Research Institute, Japan
hiraishi@pari.go.jp

In 2004 Indian Ocean Tsunami, large coastal areas facing the Indian Ocean were heavily destroyed by tsunami wave attack. Several mitigation tools are under consideration in the areas to mitigate such tsunami hazards in the future. One of the most sustainable methods is the application of coastal forests (greenbelt). The paper describes the effect of greenbelt using a simple calculation method to propose an appropriate arrangement of greenbelt.

1. INTRODUCTION

The 2004 Indian Ocean Tsunami caused a catastrophic disaster in the coastal areas facing to the ocean. The break of residential areas was widely broadcasted and some field reports analyzed the tsunami run-up height distribution. The other characteristic of tsunami damage was the beach erosion and scouring at the foot of sea walls. The eroded volume became so large in the Banda Ache City, Indonesia that some coastal grounds disappeared after tsunami attack. Meanwhile several reports (Danielsen F. et al. (2005)) described the effect of coastal forests composed of tropical pains and coconuts trees or mangroves to reduce the tsunami force destroying the coastal villages. The importance of greenbelt (coastal forest or coastal vegetation) as barrier against tsunami had been demonstrated mainly in the model experiments. We investigated the effect of greenbelt to reduce the coastal erosion as well. In the following sessions, a simple numerical calculation for tsunami force variation by the coastal vegetation is carried out to find its appropriate density and width to protect the wooden houses widely employed in the South-East Asian and Pacific Ocean coasts. Secondary we discussed the practical effect of coastal vegetation according to the field survey on the tsunami hazard in 2007 Solomon Islands Earthquake generated on April 2, 2007.

2. NUMERICAL MODEL AND RESULTS

2.1 Estimation method of tsunami force reduction due to coastal vegetation

The field survey on the greenbelt effect demonstrated that the tsunami flow pressure was reduced by the dense greenbelt and the beach erosion depth became smaller in the beach with the greenbelt behind it than in the beach without. The reduction of tsunami flow pressure becomes important to prevent the washing out of village houses. In near future we have to establish the greenbelt tsunami prevention technique to reduce the human life and property. I conducted the numerical study to estimate the effect of greenbelt to reduce tsunami flow pressures. The drag and inertia resistance in a hydraulic model test has been already described (Hiraishi, T. et al. (2003)). The resistance force of greenbelt in a unit area is expressed in Eq.(1) and the drag C_D and inertia C_M coefficient is expressed in Eq.(2).

$$WF = \frac{1}{2} C_D \frac{\rho A_o u|u|}{\Delta s} + C_M \rho \frac{V_o}{D \Delta x V} \frac{\partial u}{\partial t} \tag{1}$$

$$\begin{aligned} C_D &= 8.4(V_1/V + V_2/V) + 0.66 \\ C_M &= 1.70 \end{aligned} \tag{2}$$

where, u : Tsunami flow velocity, A_o: Projection area of vegetation, V_o: Volume of vegetation, D: Inundation depth and V : Total volume under water. Projection area and volume of vegetation is determined in the number of trees per unit area and in the diameter of tree trunk D'. The number of tree N is accounted in a unit area Δs(10m x 10m=100m^2) and it is employed as the greenbelt density. Another dominant parameter is the total width of greenbelt B. The reduction effect due to coastal vegetation was employed to simulate the variation of tsunami profiles by non-linear long wave model.

Compared with the inertia resistance, the drag resistance is much larger. The simple computation of drag resistance variation indicates the approximate effect of greenbelt to reduce the tsunami acting force. Figure 1(1) shows the image of greenbelt effect. The greenbelt effect is determined in the density N, width B and trunk diameter D'. The vertical graph in the figure indicates the imaginary tsunami force obtained in the front and backside of greenbelt. The tsunami force is proportional to the square of flow velocity and it is mainly determined by the intensity of tsunami flow velocity. Figure 1(2) shows the mechanism of tsunami drag force reduction by coastal vegetation. In the design of coastal vegetation, several access roads to coasts are necessary for the daily fishing and beach activities. Such access roads may become the evacuation roots in the emergency time with tsunami warning.

The tsunami flow velocity in such gaps between neighboring coastal vegetation areas may become larger than the original tsunami flow velocity in plane coasts because some part of flows are disturbed in the dense vegetation. The evaluation of flow velocity in the gaps is needed to determine the safe evacuation roots in emergency time.

Figure 2 shows the image of determination of tsunami flow velocity in the gaps. We assume the flow flux ($=u_1W$) is reserved in a coast and total flux is the same in the front and backward of greenbelt. In the figure the reduction rate is determined as the ratio of reduced tsunami force in greenbelt to the initial tsunami force. The parameters in the figure are defined as follows;

W: Length of coastal vegetation along shore line
γ: Opening ratio of vegetation (Dimensionless width of gap)
u_1: Original tsunami flow velocity
u_2: Flow velocity in backward of vegetation area
u_3: Flow velocity in gap

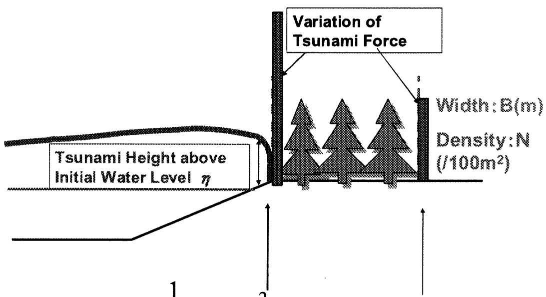

$$p_1(N/m)=\frac{1}{2}\rho C_D u_1^2 \eta_1$$

$$p_2(N/m)=\frac{1}{2}\rho C_D u_2^2 \eta_2$$

(1) Image of reduction mechanism

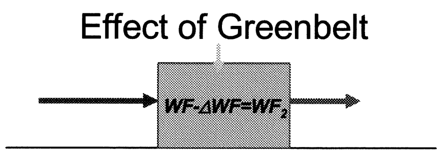

$$WF=\rho\eta u_1^2\Delta x\Delta y/2 \qquad WF_2=\rho\eta u_2^2\Delta x\Delta y/2$$

$$\Delta WF=\rho u_1^2 C_D' A_1/(\Delta x\Delta y)\Delta x\Delta y N_S/2$$

$$C_D'=(8.4\pi d_1^2(N/100)/4+0.66) \qquad A_1=\eta(d_1(N/100)\Delta x\Delta y)$$

Drag Term Resistance   Effective Projection Area

(2) Calculation method

Figure 1 Mechanism and calculation of reduction rate of tsunami force in coastal vegetation

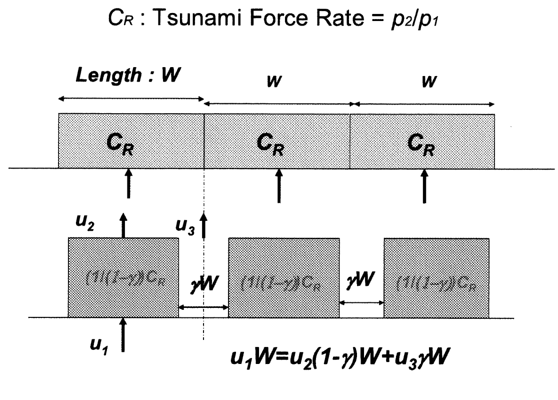

Figure 2 Sketch of tsunami flow velocity calculation

The total tsunami inundation volume is assumed to be constant and the velocity in backside of vegetation u_2 is calculated in the equations in Figure 2.

2.2 Predicted effect of coastal vegetation

Figure 3 shows the variation of the tsunami force reduction rate for each vegetation density N. The dimensionless tsunami force is estimated as the ratio of tsunami drag force behind the greenbelt (p_2) to that in front of greenbelt (p_1). The dimensionless tsunami force decreases as the density of greenbelt N and the width B increase. When the tsunami run-up height is 5m, the allowable force level for wooden house is 0.15 in the expression of the figure because a wooden house is easily damaged in the inundation level of 1.0m. For the wooden house safety, the greenbelt should become wider than 200m.

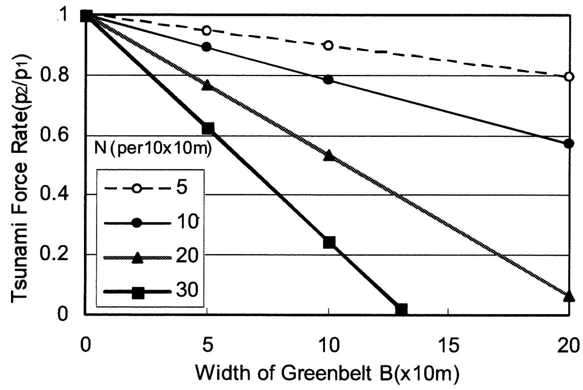

Figure 3 Variation of tsunami force for greenbelt width and density

Figure 4 shows the variation of tsunami force reduction rate for total tree number per 10m shore line. The total tree number per unit shore line length is calculated as the product of density and width of greenbelt. The reduction rate varies slightly according with the density and the figure shows the averaged reduction rate for the same total tree number with different density. The tsunami force at the backside of the greenbelt is reduced to 10% of the initial one as the total tree number becomes more than 400. The diameter of a tree is 0.3m in calculation.

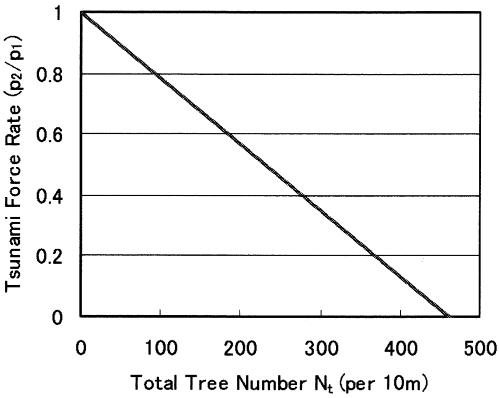

Figure 4 Variation of tsunami force for total density

The variation of velocity in the gaps is expressed in Figure 5. The flow velocity rate indicates the ratio of tsunami flow inside the gap to the incident tsunami flow velocity in front of greenbelt. The tsunami flow velocity in the gaps increases when the tsunami force ratio becomes small and the opening ratio becomes small. Therefore the narrow gap raises the flow velocity and the escape along the gap becomes dangerous.

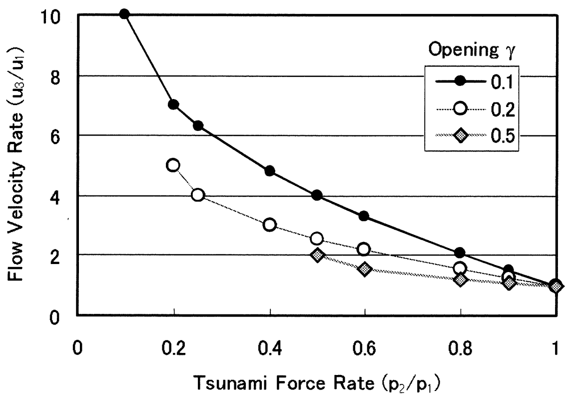

Figure 5 Variation of tsunami flow velocity in gap between greenbelt

3. FIELD SURVEY IN SOLOMON ISLAND

The Solomon island tsunami was generated on April 2, 2007. The location of epicenter was (S8.6°, E157.2°) and the moment magnitude 8.1. Figure 6 shows the tsunami inundation and run up height obtained by Prof. Fujima's survey. According to his survey the house damage was severe especially in the Gizo Island, West Solomon but several houses behind the tropical forest remained after the tsunami attack. We investigated the damages in the villages to reveal the effect of coastal forest for the remained houses. The target villages (Suva etc.) were located in Gizo Island and Figure 7 shows the location of field survey area.

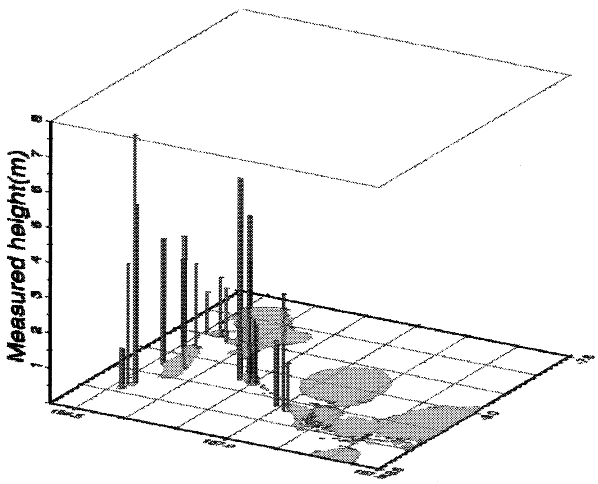

Figure 6 Tsunami height obtained in the survey by Prof. Fujima (National Defense Academy)

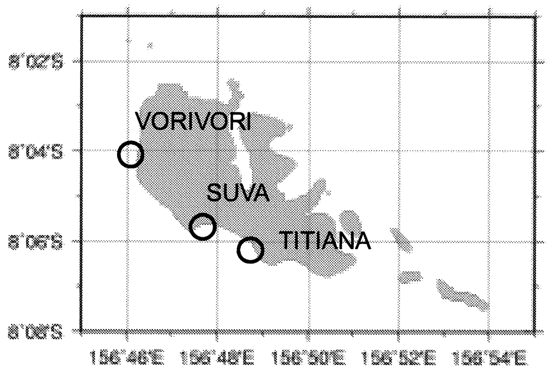

Figure 7 Location of field survey in Gizo Island

In our survey, we obtained the variation of ground level and the density of vegetation in Suva, Vorivori and Titiana villages in Gizo Island, Solomon Islands on 2007 June. An example in Suva is mainly represented here. Two lines are determined as the representative line in the area completely damaged by tsunami and in the area with remained houses. Figure 8 shows the situation in the devastated area (Line-1) and in the less damaged area (Line-2). Figure 9 shows the location of coastal trees. Photograph 1 shows the remained house on the Line-2 and tropical tree with a trunk diameter of about 1m.

The calculation of tsunami force reduction rate was done employing the method introduced in the session **2**. The calculation condition is shown in Table 1. In the table N_s shows the width of greenbelt (N_s x 10m). The density N is calculated as the averaged tree number included in a unit area (10m x 10m). The diameter D' is derived as the averaged value of the trees in the target area. The tsunami inundation height obtained in the field survey was 2m.

Figure 10 shows the calculated tsunami reduction rates in the target villages. The reduction rate (tsunami force rate) becomes 0.8 in Suva and the effect of coastal forest was the largest in Suva because of the relatively dense forest. Hiraishi et al. (2006) shows that the resistance by friction on the ground becomes the same order to those by the greenbelt resistance as the tsunami height is smaller than about 2m. Therefore we calculated the effect of ground friction as well as the drag force reduction by greenbelt. The white symbol in Figure 10 shows the reduction rate including the ground surface friction. Considering the ground friction the total reduction rate of tsunami force becomes about 0.6 in Suva. The wide ground and the dense forest situated in front of the house might mitigate the tsunami force acting the house and it might remain with comparable minor damages. The effect of coastal trees obtained in the field survey revealed the dense forest had effects to protect a wooden house in Gizo Island when the tsunami attacked the target island on April 2, 2007.

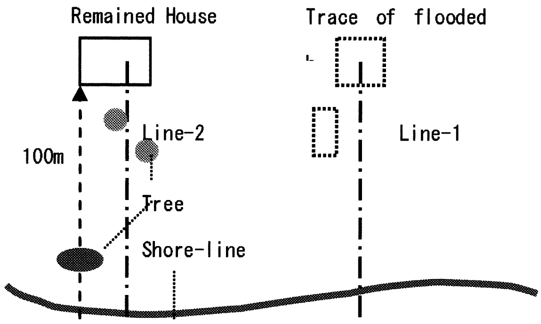

Figure 8 Situation of lines in devastated village

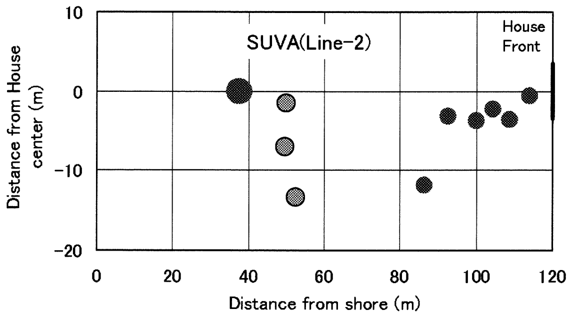

Figure 9 Location sketch of coastal tree and house

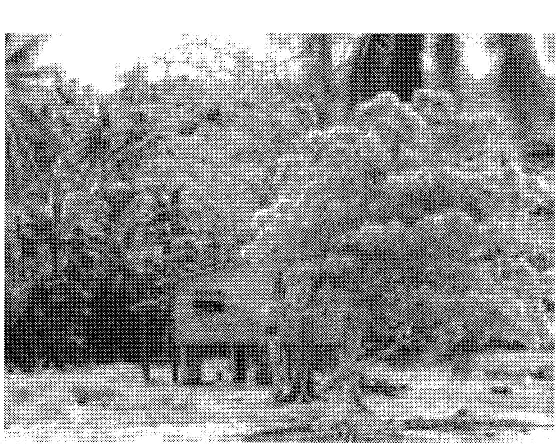

(1) Remained house behind coastal forest

(2) Situation of coastal tree (BUNI)

Photograph 1 Remaining house and tree on Line-2

Table 1 Greenbelt width and density in field

	N	Ns	D' (CM)
SUVA	2	8	76
VORIVORI	7	1	48
TITIANA	5	1	73

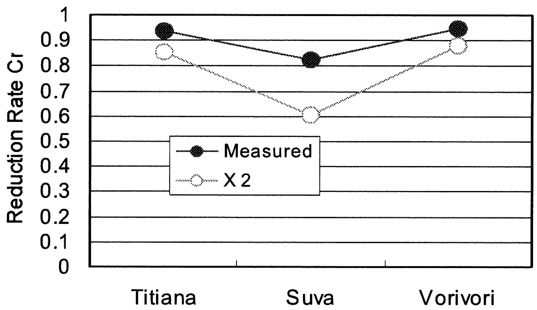

Figure 10 Variation of tsunami force reduction

4. CONCLUSIONS

1) A simple calculation for greenbelt effect derived that the tsunami force acting a house was reduced to 10% of the original as the total density of trees became 400 per 10m coast line.
2) The field survey results revealed that the tsunami force was mitigated behind the dense coastal forest.

References

Danielsen F. et al.(2005):The Asian Tsunami: A protective role for coastal vegetation, SCIENCE, Vol.310, p.643.

Hiraishi, T. and K. Harada(2003):Greenbelt tsunami prevention in South-Pacific region, Report of the Port and Airport Research Institute, Vol.42, No.2, pp.3-25.

Hiraishi T., Y. Minami and M. Tanaka (2006): Fundamental study on tsunami force reduction by greenbelt countermeasure, Technical Note of The Port and Airport Research Institute, No.1124, 17p.

Fifth International Conference on Urban Earthquake Engineering
March 4-5, 2008, Tokyo Institute of Technology, Tokyo, Japan

DEEP-SEA SURVEY FOR DEVELOPMENT OF OFFSHORE NETWORK OBSERVATORY OFF KII-PENINSULA

Hiroyuki Matsumoto[1), Katsuyoshi Kawaguchi[1), Eiichiro Araki[1), Atsushi Sakuma[1), Sho Kaneko[1), Shin'ichiro Kamiya[1), Hiroyasu Momma[1), Tohru Kodera[2), and Yoshiyuki Kaneda[1)

1) Japan Agency for Marine-Earth Science and Technology, Japan
2) Nippon Marine Enterprises Ltd., Japan
hmatsumoto@jamstec.go.jp

Abstract: A dense network observatory in the Nankai Trough for monitoring mega-thrust earthquakes, and followed by tsunamis will be established in four years. This project has launched since the fiscal year of 2006 as a project by the Japanese government. It consists of at least 20 seismic sensors as well as tsunami sensors, covering Tonankai seismogenic zone, where the probability of the future plate-boundary earthquake is estimated to be relatively high. In the first year, the location of the observatory has been determined. Then the deep-sea survey and other basic examination related to deployed sensors have been conducted by using JAMSTEC's research vessels and deep-sea vehicles. This report describes the results of the deep-sea survey carried out during this fiscal year.

1. INTRODUCTION

Japan has started installing the cabled observatories for disaster mitigation purposes since late 1970s. We have already developed seven cabled observatories around Japan, in particular along the Pacific Rim, and brought us invaluable information. For example, the 2003 Tokachi-oki earthquake of M8.0, seafloor phenomena such as a generation process of tsunami, seafloor uplifts, etc., were observed (Mikada et al., 2006). The 2004 off Kii peninsula earthquake of M7.4, the offshore observatory could detect the tsunami 20 minutes before its arrival at the nearest coast (Matsumoto and Mikada, 2005).

Since 2006, Japan Agency for Marine-Earth Science and Technology (JAMSTEC) has started to develop a new dense network system by using sub-marine cable off Kii-Peninsula, where the last Tonankai earthquake was took place in 1944 (e.g., Kaneda et al., 2007). The Headquarters for Earthquake Research Promotion in the Ministry of Education, Cultutre, Sports, Science and Technology (MEXT) has estimated that the probability of the next Tonankai mega-thrust earthquake is 60 % or more in the next 30 years, because the recurrent time of the plate boundary earthquake there is approximately 100 to 150 years. Thus, the offshore seismic monitoring system for the forthcoming Tonankai earthquake is urgently needed to mitigate future disasters from the earthquake and resulting tsunami. The system to be developed contains 20 seismometers, 20 tsunami meters and other geophysical observation sensors covering the expected Tonankai earthquake source region in order to monitor both long-term seismic activities and mega-thrust earthquakes and tsunamis. Our goals are postulated to accomplish high precision earthquake prediction modeling, to detect precursory prier to the mega-thrust earthquake, and to contribute to mitigate disaster caused by the earthquake and the tsunami by providing the information, in addition to develop the network system itself.

Natural events such as slumps, slides and turbidity currents on steep, sediment covered slopes, and earthquake events are risks to the network system in the deep-sea area in its lifetime. In the shallow area, on the other hand, the potential risks to the network system are from human related activities, specifically from bottom contact fisheries and large ships' anchors. There is also a smaller danger that dumping or dredging operations could harm a submarine cable. For the first step in the network system development, an in-situ survey and a risk assessment is necessary in order to find better observatory's sites and safer submarine cable route. In this article, preliminary results of the deep-sea survey used by JAMSTEC's vessels and deep-sea vehicles are reported.

2. DESKTOP STUDY AND SURVEY PLAN

2.1 Observatories Location

In the first fiscal year, the location of 20 observatories and the related cable route was examined with respect to the previous seismological study and the existing survey results such as topography maps, side scan sonar images, and sediment sampling. Existing cables are also taken in to

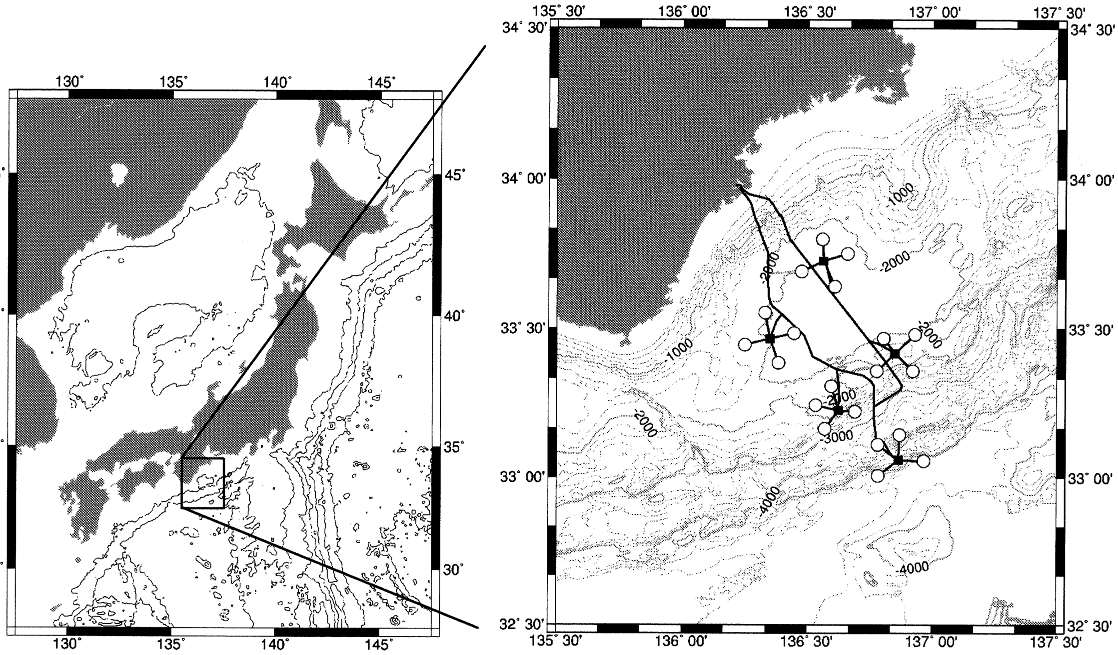

Figure 1 Map showing the deep-sea network system to be deployed off Kii-Peninsula. Circles and dots represent the observatories and the science nodes, respectively

Table 1 Time line of the JAMSTEC's research vessels and vehicles used in the fiscal year of 2007.

Research Vessel	Vehicle	Missions	FY2007
Kaiyo	*Deep Tow*	Bathymetric survey Route survey Sediment sampling	April to May ⟷ 34 days; August to September ⟷ 18 days
Yokosuka	*Deep Tow*	Obstacles removal	July ⟷ 7 days
Kairei	*Kaiko*	Bench marks' installation Sensors' recovering	November ⟷ 12 days
Natsushima	*Hyper Dolphin*	Sensors' installation/recovering	December ⟷ 9 days; February ⟷ 10 days

account for the future maintenances and replacement. Location of the observatories and cable route are shown in Fig. 1. The network system consists of 20 observatories at their interval of 10 kilometers, which are linked by 5 science nodes connecting approximately 300 kilometers backbone cable. As shown in Fig. 1, the backbone cable runs in water depth greater than 2,000 meters along the Kumano Trough, and then reaches the Nankai Trough, where water depth is greater than 4,000 meters. The network system will be designed as redundant, so that the backbone cable rings. Link cable is used between the each science node and the each sub-sea sensor that can extend up to 10 kilometers long for the each observatory. Link cable is more flexible than the backbone cable, because replacement or supplement of observatories is considered in advance. Landing site, which supplies electricity to the network system and compiles the dataset from the observatories will be located at Owase, Mie prefecture.

In order to find the safest possible environment for the permanent network system, a comprehensive in-situ survey should be conducted along the cable route. In the deep-sea area, greater than 1,000 meters, where the cable will be neither buried nor protected, the survey data should be able to identify features likely to cause cable suspensions and rocky areas that could cause cable chaffing if there are bottom currents.

2.2 Time Line of Research Vessels and Vehicles

Time line of the deep-sea survey is strongly depended on the ship's schedule. Research vessels (R/Vs) with

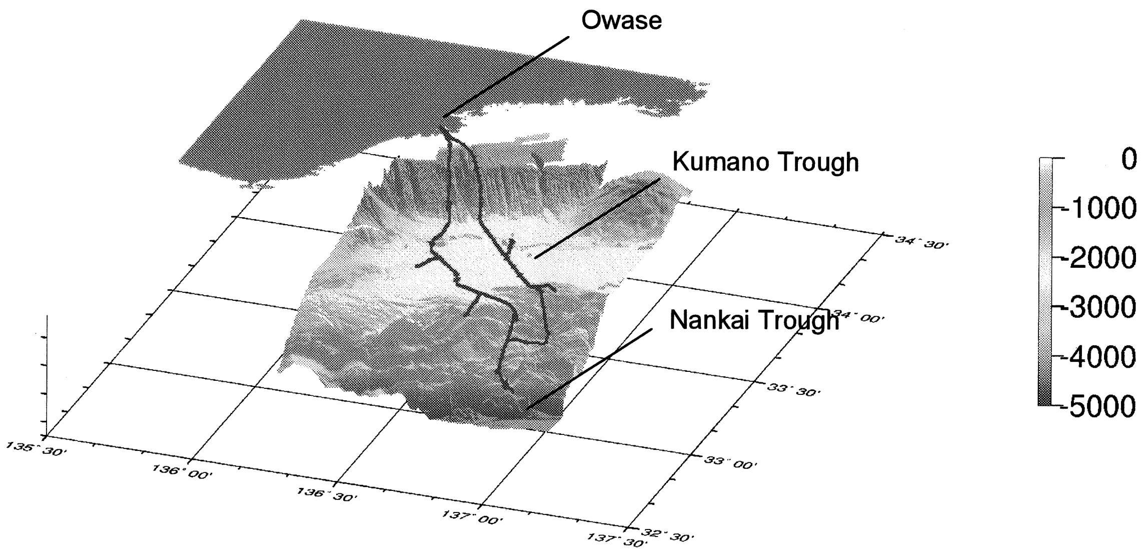

Figure 2 A whale's eye view of the bathymetry map off Kii-Peninsula obtained by *Kaiyo* drawing with the backbone cable. The upper and the lower basins are the Kumano Trough and the Nankai Trough, respectively.

adopted vehicles have been planned to employ as displayed in Table 1. R/Vs *Kaiyo*, *Kairei*, *Natsushima*, and *Yokosuka* have been used. Among them, the ship time of *Yokosuka* has been arranged ad hoc. All vessels can carry deep-sea survey system or remotely operated vehicles (ROVs).

Detailed bathymetric mapping survey and route survey were planned at first. Detailed bathymetric map is fundamental information to design both the backbone cable and the link cable in the desktop study. For selection of the most desirable cable route, a fairly detailed topographic chart must be prepared. Sediment sampling by piston corer has been also planned, because substrate at the observatories should be understood before deploying the sub-sea sensors. Then, the sensor's test were carried out by using ROVs.

Kaiyo is employed twice in the year. *Kaiyo* can support dives of the deep-sea survey system, *Deep Tow*, and conduct seafloor topography surveys. *Deep Tow* supported by *Kaiyo* or *Yokosuka* is a deep-sea survey system that can be outfitted with plural cameras and towed through the water at low speeds at the end of a cable measuring several thousand meters in length. Its major missions are as follows; 1) surveys of the deep-sea, ocean floor topography, geology, resources, and physical oceanography, 2) bathyal organism surveys, 3) preliminary surveys before manned or ROV submersible dive surveys, and 4) searches for man-made objects, installation of observational instruments. Route survey between the science node and the observatory, and the backbone cable running scarps and cliffs are carried out by *Deep Tow*. Obstacles in the deep-sea preventing ROV operation are also removed by *Deep Tow*.

Kaiko carried on *Kairei* is a 7,000 meters class ROV, that can survey deep-sea areas of the observatory. It recovered the Doppler current meters in the trough and observed the benchmark which is designed for the platform of the observatory.

Hyper Dolphin is a new ROV that is able to conduct surveys at a maximum depth of 3,000 meters. Difficult operations in the deep-sea can be done by the two manipulators (robot arms) on the vehicle. It is mainly used to install/recover the seismometers in the benchmark whole.

Thus, the four research vessels with one deep-sea survey system and two ROVs have been employed in the period. Almost 100 days in total were spent as a preliminary survey.

3. SURVEY RESULTS

3.1 Bathymetry Survey

The network system will lie on the continental slope above the subducting Pacific Plate. Interactions between plate boundaries result in major deformations on the seafloor. Subduction processes that may occur along the cable route could potentially threaten the safety of the cable. The cable may be at risk in areas where sediments are unstable, in particular in the vicinity of submarine canyons and across the continental slope, where turbidity currents, sediment slumps and slide may occur. The potential danger to a submarine cable in seismically active areas is not primarily form the immediate surface or ground shaking, but from the effects of loose sediments found on slopes (NEPTUNE, 2002).

Seafloor topography covering the network system has been obtained by the multi-narrow beam echo sounder during two *Kaiyo* cruises. Principal of multi-narrow beam echo sounder is simply described as follows. An acoustic beam is periodically transmitted to the seafloor from the bottom of the vessel. Hydrophone array will receive the acoustic beams reflected from the seafloor in order to determine the distance between the vessel and the seafloor. The seafloor topography is determined based on this data.

Detailed bathymetric map obtained by the present two *Kaiyo* cruises in addition to the previous cruses is compiled. A bird's eye view developed from the bathymetry dataset is

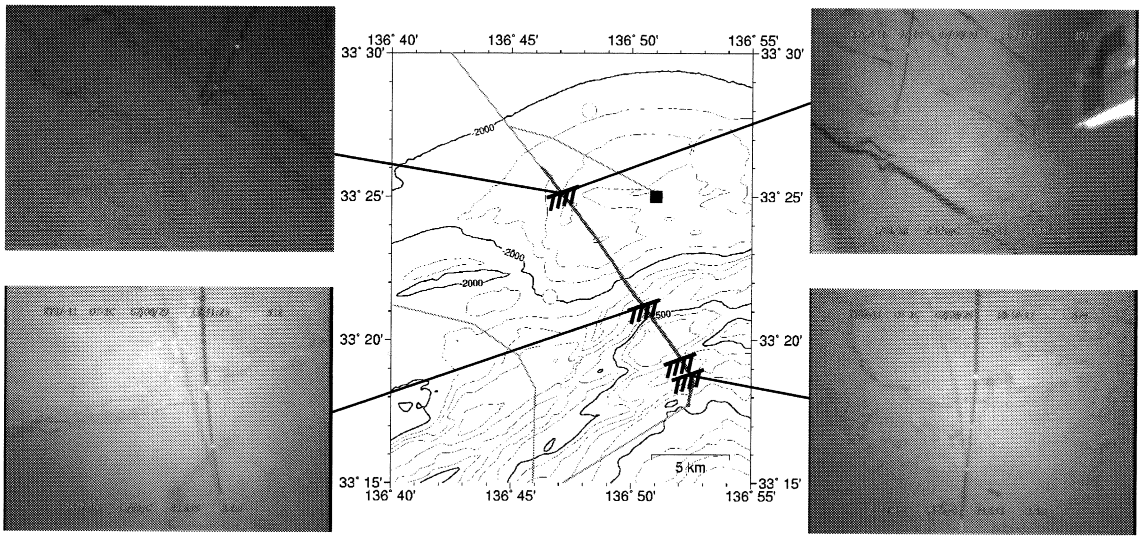

Figure 3 An example of the observing survey results along the backbone cable route close to the Nankai Trough. Blue line represets the dive track of *Deep Tow*, while gray line indicates the planned backbone cable route.

shown in Fig. 2, which is useful to understand the topography of concerned area.

The backbone cable inevitably runs through two narrow scarp zones divided by the Kumano Trough. Slope of the northern edge of the Kumano Trough shows about 1,000 meters, in which a lot of small canyons exist. The other complicated steep topography, i.e., a part of accretionary prism exists between the Kumano Trough and the Nankai Trough dropping from 2,000 to 4,000 meters, where the link cables also will be deployed in addition to the backbone cable. Both the backbone cable and the link cable routes have been designed based on the detailed bathymetric map.

3.2 Cable Route Survey

Cable route survey is carried out in order to obtain the necessary information for the selection of a cable landing site, cable route and observatory sites, and for designing the cable system such as cable type, and for planning cable laying and burial operations (Shirasaki et al., 2005). In deep waters, i.e., greater than 1,000 meters, the best protection against natural risk is generally achieved by running the cable into areas of smooth seafloor, away from known active faults (NEPTUNE, 2002). From the point of view of cable protection over the long term, the cable route must be selected by avoiding the rocky area and steep area. However, many routes of the scientific network systems cannot avoid such hazardous areas. A more detailed visual survey of the cable route and the observatory sites before installation are essential for maintaining correct cable installation and safe deployment of instruments.

As for the commercial telecommunication cable, observing survey by cameras in the deep-sea area is not always carried out before installation. In our project, however, the backbone cable is not expected any primary system failure in the operation lifetime. The expected risks to the backbone cable and the link cables would be reduced in advance.

Cable route surveys of the backbone cable and the link cable running through the potentially risky region have been done by using *Deep Tow* carried by *Kaiyo* in order to find safer route if necessary. As a result, local cliffs and scarps that may be risk to the cable have been found, which have not been recognized in the bathymetry map by multi-narrow beam echo sounder (Fig. 3). The cable route must be detoured from such potentially risky topographies. During the cable route survey, the Doppler current meters have been released at some points on the seafloor in order to measure daily bottom current. They were recovered by either *Kaiko* or *Hyper Dolphin* depending on the deployed water depth.

During the cable route surveys, unexpected behaviors of *Deep Tow* have been occurred a few times. These are because *Deep Tow* has been captured by something in the deep-sea. The obstacles in the deep-sea are usually from human activities. A lot of fishing equipments lie both on the seafloor and at the sea surface, because fisheries' activities seem relatively high at the Kumano Trough. Such equipments still remain even after finishing the fishing season. Buoy systems are also used, but they are often floated away by storm surges or damaged and apart from the bottom anchor by other ships. We have removed unused fishing equipments by *Deep Tow* carried by *Yokosuka* in order to keep safe for future ROV's operation in the area of the network system.

3.3 Recovery of Marine Sediment

Seismic sensors attached with the network system will be buried below the seafloor. The platform for the seismic sensors is designed as a borehole. We call the platform the bench mark. Although pelagic sediments such as mud or silt are predominant in the deep-sea area, we should evaluate how deep the bench mark can be deployed below the seafloor. Therefore, detailed sediment types are classified

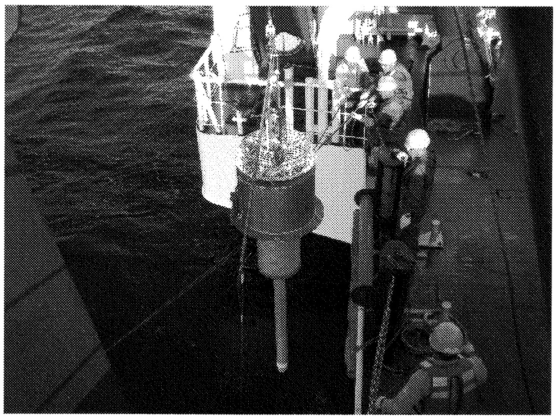

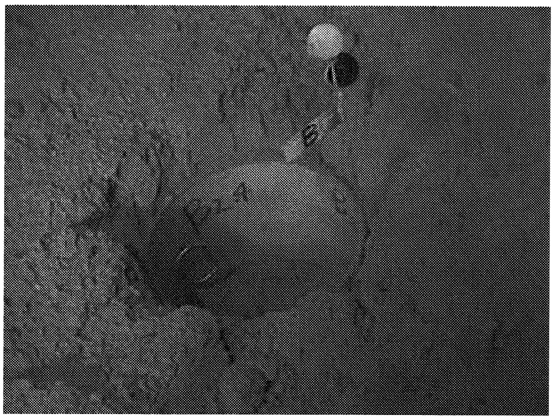

Figure 4 Installation of the bench mark attached with the piston corer from the vessel (left), and a view of the bench mark penetrated below the seafloor (right). A seismic sensor package would be installed into the borehole of the bench mark later.

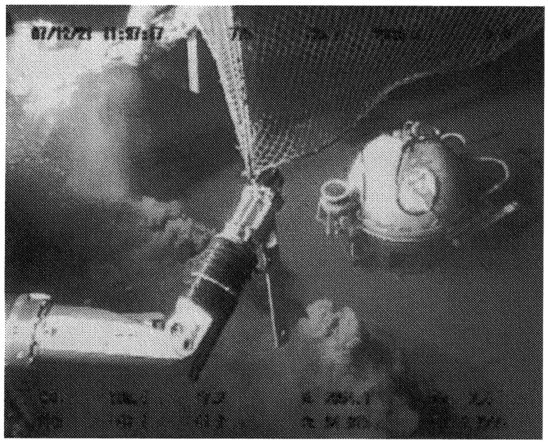

Figure 5 Installation of the broadband seismometer inside the bench mark (left), whose gap would be filled with the sand. The other broadband seismometer on a heavy flat anchor has been installed on the seafloor nearby (right). Two months continuous observations will be done.

by recovering marine sediment by using a piston corer.

A piston corer consists of a heavy weight and a long pipe to collect the sediment core samples. We used 6 meters pipe with 0.8 tons weight. Recovery of marine sediment could be done at 11 observatories by two cruises so far. All collected samples suggest that it is soft enough to deploy 4 meters bench mark at the observatory. Shear strength was also measured in terms of torque force.

Then, a couple of bench mark, with short and long pipes, have been deployed at the central Kumano Trough by using piston corer during *Kairei* cruise (Fig. 4). A procedure to deploy the bench mark below the seafloor is as follows. A piston corer covered with a bench mark pipe penetrates into sediment layer as usually done. After landing a piston corer at the seafloor, an outer bench mark pipe is released. And only a piston corer pipe is recovered with remaining the bench mark below the seafloor. Finally, the bench mark is simply deployed. In the same cruise, we observed the deployed bench mark by *Kaiko*. The bench mark is buried completely in the sediment layer (Fig. 4).

3.4 Sensors Installation

The network system aims to detect precursory associated with the mega-thrust earthquake. Therefore, target range of our observation by seismic sensors is very broad frequency as well as dynamic range. We are planning to develop a combined sensor system containing of broadband seismometer, strong motion accelerometer, and geophones. This approach is similar to those of land broadband seismic network in Japan. Various methods to install seismic sensors on the seafloor have been compared elsewhere (Araki et al., 2004; Kaneko et al., 2007), and their results suggest that burying contributes to reduce background noise in the low frequency range mainly due to the bottom current.

At the end of the present period, different deployed seismic sensors' observations have been compared. One broadband seismometer has been deployed inside the bench mark and another sensor on a heavy flat anchor has been deployed on the seafloor nearby by using *Hyper Dolphin* (Fig. 5). A Doppler current meter has been also deployed in order to estimate the bottom current effect on the sensors.

After two months continuous observations, both seismic sensors will be recovered by *Hyper Dolphin* again, and we will compare the obtained dataset.

4. FUTURE PLAN

Two years have passed since the project has been launched. We schedule to accomplish the network system at the end fiscal year of 2009. Both cable route survey and sediment sampling still remain for all observatories. They will be completed by the end of the first half of the fiscal year of 2008. After finishing cable route survey, the backbone cable design whether armed type or not will be processed.

Improvements of the ROV are required in order to install the link cable between the science node and the observatory. The long extension of the small diameter cable has been done by using *Deep Tow* before (Kawaguchi et al., 2002), but at this time, we will use *Hyper Dolphin* because of its durability, heavy-lift capability, and high available power. It is a big issue that some operations will be conducted in the deep water, greater than 3,000 meters, which means *Hyper Dolphin* cannot approach so far. Other technological devices such as a science node, wet-mate connectors also must be developed at the same time.

5. CONCLUDING REMARKS

This is the first challenge such a dense network system will be developed in the deep-sea area. Desktop study was conducted by compiling the previous studies and surveys as a first step. Based on the desktop study, an in-situ survey was planned. In this article, preliminary results of the deep-sea survey for the offshore network observatory have been described.

Detailed bathymetry mapping has been carried out by *Kaiyo*, which can be useful to efficiently manage the cable route design process. Observing survey by *Deep Tow* also has been done, which have revealed locally dangerous areas for the cable route. A few detours both of the backbone cable and the link cable are required after the observing survey.

A couple of bench mark that will be a platform of the observatory have been deployed at the central Kumano Trough. An in-situ examination of seismic sensors has been done. One seismic sensor has been deployed in the bench mark and the other has been deployed on a heavy plane on the seafloor nearby. Both of dataset will be compared after recovered, and we evaluate the most suitable installation method of the network system.

Technological development regarding ROV operation should be involved in the near future, e.g., to develop link cable extension system, and to modify to possibly operate in the deep water, greater than 3,000 meters.

Acknowledgements:

This project is funded by the Japan Ministry of Education, Culture, Sport, Science, and Technology (MEXT). The authors thank to the captains, Hitoshi Tanaka, Fusao Saito, and Eiko Ukekura, of R/Vs, *Kaiyo, Kairei*, *Yokosuka*, and *Natsushima*, and the crew of those vessels. Dr. Yuichi Shirasaki kindly advised us in the matter of the survey procedures. Technical staffs of Marine Works Japan Ltd. and Nippon Marine Enterprises Ltd. supported our work on board.

References:

Araki, E., Shinohara, M., Sacks, S., Linde, A., Kanazawa, T., Shiobara, H., Mikada, H., and Suyehiro, K. (2004), “Improvement of Seismic Observation in the Ocean by Use of Seafloor Boreholes”, *Bull. Seism. Soc. Am.*, **94**, 678-690.

Kaneda, Y., Kawaguch, K., Araki, E., Matsumoto, H., Nakamura, T., Kamiya, S., Hori, T., and Baba, T., “Precise Real-time Observatory and Simulating Phenomena of Earthquakes and Tsunamis around the Nankai Trough –Towards the Understanding of Mega Thrust Earthquekes-”, *Proc. International Workshop on Scientific Use of Submarine Cables and Related Technology 2007*, 299-300.

Kaneko, S., Araki, E., Kawaguchi, K., and Kaneda, Y. (2007), “Installation Qeruirements for Seismic Observation in the Seafloor”, *Proc. International Workshop on Marine Technology.*, SK068 (CD-ROM volume).

Kawaguchi, K, Hirata, K., Nishida, T., Obana, S., and Mikada, H. (2002), “A New Approach for Mobile and Expandable Real-time Deep Seafloor Observation -Adaptable Observation System”, *IEEE J. Ocean Eng.*, **27**, 182-192.

Matsumoto, H. and Mikada, H. (2005), “Fault Geometry of the 2004 Off the Kii Peninsula Earthquake Inferred from Offshore Pressure Waveforms”, *Earth Planets Space*, **57**, 161-166.

Mikada, H., Mitsuzawa, K., Matsumoto, H., Watanabe, T., Morita, S., Otsuka, R, Sugioka, H., Baba, T., Araki, E., and Suyehiro, K. (2006), “New Discoveries in Dynamics of an M8 Earthquake -Phenomena and their Implications from the 2003 Tokachi-oki Earthquake Using a Long Term Monitoring Cabled Observatory-”, *Tectonophysics*, **426**, 95-105.

NEPTUNE (2002), “Project NEPTUNE Desktop Study”, http://www.neptune.washington.edu/documents/ENGNRG/dts.pdf (online).

Shirasaki, Y., Kojima, J., and Kawaguchi, K. (2005), “Installation and Maintenace of Real-time Seafloor Cabled Observatories”, Proc. International Symposium on Marine Geosciences, 63-66.

Fifth International Conference on Urban Earthquake Engineering
March 4-5, 2008, Tokyo Institute of Technology, Tokyo, Japan

RECENT VERIFICATION OF THE DYNAMIC TSUNAMI SIMULATION

Tatsuo Ohmachi[1], and Shusaku Inoue[2]

1) Professor, Interdisciplinary Graduate School of Science and Engineering, Tokyo Institute of Technology, Japan
2) Research Associate, Ditto
ohmachi@enveng.titech.ac.jp, shusaku@enveng.titech.ac.jp

Abstract: Findings from the dynamic tsunami simulation are verified by actual data in near-field of the 2003 Tokochi-oki earthquake (M8.0) observed by the JAMSTEC offshore monitoring system. Contrast to conventional ones, the simulation takes into account both effects of dynamic displacement of the seabed resulting from seismic faulting and acoustic water pressure. Although this paper describes a kind of preliminary check only, the findings on tsunami generation seems to be consistent with the observation.

1. INTRODUCTION

Recently authors have developed a numerical technique for tsunami simulation in three dimension. It takes into account not only acoustic effects of water but also dynamic effects of seabed displacement resulting from seismic faulting, which is referred to as the dynamic tsunami simulation technique. In contrast to this, conventional tsunami simulation techniques that take into account only static (or residual) ground displacement by neglecting the dynamic effects is here referred to as static ones. The development of the dynamic technique aims to simulate processes of tsunamis as precisely as possible by using the state of the art of numerical technology and advanced knowledge on seismic faulting and tsunami generation.

As for the processes of tsunami generation followed by propagation in the ocean, the dynamic simulation technique has demonstrated to reproduce the processes to a satisfactory level of accuracy. Thus, the objective of the present study is to extend the ability of the technique such as run-up to the land and impact with coastal structures, and demonstrate its usefulness by comparing various related observation data.

2. OUTLINE OF THE DYNAMIC SIMULATION

2.1 General

In the 3-D dynamic simulation, weak-coupling is assumed between the seabed and the seawater, from which the motion of the seawater is influenced by that of the seabed, but the motion of the seabed is not influenced by that of the seawater. Based on this assumption, the present technique consists of a two-step simulation. The first is to simulate the dynamic seabed displacement resulting from a seismic faulting using the boundary element method (BEM), and the second is the dynamics of the seawater disturbance which includes tsunamis followed by their propagation, run-up and impacts with structures. The seawater disturbance which includes tsunamis, is simulated by solving the Navier-Stokes equation, using the finite difference method (FDM), imposing the velocity of the dynamic seabed displacement as an input to fluid domain at the seabed. The extended dynamic simulation technique will especially help us to predict the behavior of near-field tsunamis with high accuracy.

$$\begin{aligned}
&\frac{\partial u}{\partial t}+u\frac{\partial u}{\partial x}+v\frac{\partial u}{\partial y}+w\frac{\partial u}{\partial z}=-\frac{1}{\rho}\frac{\partial p}{\partial x}+\nu\left(\frac{\partial^2 u}{\partial x^2}+\frac{\partial^2 u}{\partial y^2}+\frac{\partial^2 u}{\partial z^2}\right)\\
&\frac{\partial v}{\partial t}+u\frac{\partial v}{\partial x}+v\frac{\partial v}{\partial y}+w\frac{\partial v}{\partial z}=-\frac{1}{\rho}\frac{\partial p}{\partial y}+\nu\left(\frac{\partial^2 v}{\partial x^2}+\frac{\partial^2 v}{\partial y^2}+\frac{\partial^2 v}{\partial z^2}\right)\\
&\frac{\partial w}{\partial t}+u\frac{\partial w}{\partial x}+v\frac{\partial w}{\partial y}+w\frac{\partial w}{\partial z}=g_z-\frac{1}{\rho}\frac{\partial p}{\partial z}+\nu\left(\frac{\partial^2 w}{\partial x^2}+\frac{\partial^2 w}{\partial y^2}+\frac{\partial^2 w}{\partial z^2}\right)
\end{aligned} \tag{1}$$

$$\frac{1}{a^2}\frac{\partial p}{\partial t}+\rho\left(\frac{\partial u}{\partial x}+\frac{\partial v}{\partial y}+\frac{\partial w}{\partial z}\right)=0 \tag{2}$$

2.2 Fluid Domain Analysis

In the fluid domain analysis, the Navier-Stokes equation in Eq. (1) and the mass conservation equation in Eq. (2) are used, where u, v and w are velocities of x, y and z directions, and p, ρ, a, ν and g are pressure, density, sound velocity of water, kinematic viscosity of the fluid and acceleration of gravity, respectively. Eq. (2) means that the fluid is regarded as locally compressible but globally incompressible.

As for the simulation algorithm, we applied the SOLA method (C. W. Hirt et al., 1975) with a height function for the free surface, because the function is easy to introduce in our 3-D program and efficient to reduce the computational time.

In recent years, it has become possible to simulate tsunami from generation to run-up onto a coastal area in three dimension, by introducing the so-called nesting technique (Kubo et al, 2006).

3. ANALYTICAL EXAMPLES

3.1 Tsunami Generation

A tsunami generated by a thrust faulting in an elastic half-space was simulated in two and three dimensions (Ohmachi et al, 2001a). For simplicity, 2-D simulation is shown below. As shown in Figure 1, the fault rupture is propagated from the bottom to top of the fault at a constant rupture velocity. Figures 2 and 3 show results of the dynamic tsunami simulation, for which parameters shown in Table 1 were used.

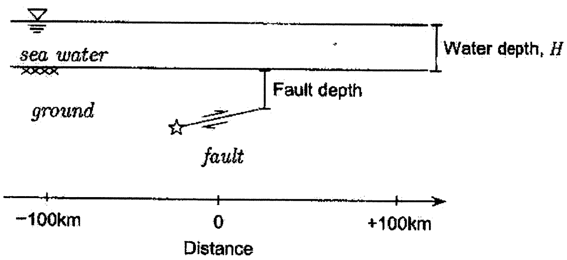

Figure 1 A 2-D simulation model

Width	30 km
Fault depth	5 km
Dip	30 degree
Dislocation	10 m
Rupture velocity	3.0 km/s
Rise time	2.0 s
P-wave velocity	7.0 km/s
S-wave velocity	4.0 km/s
Density of the ground	2.7 g/cm^3

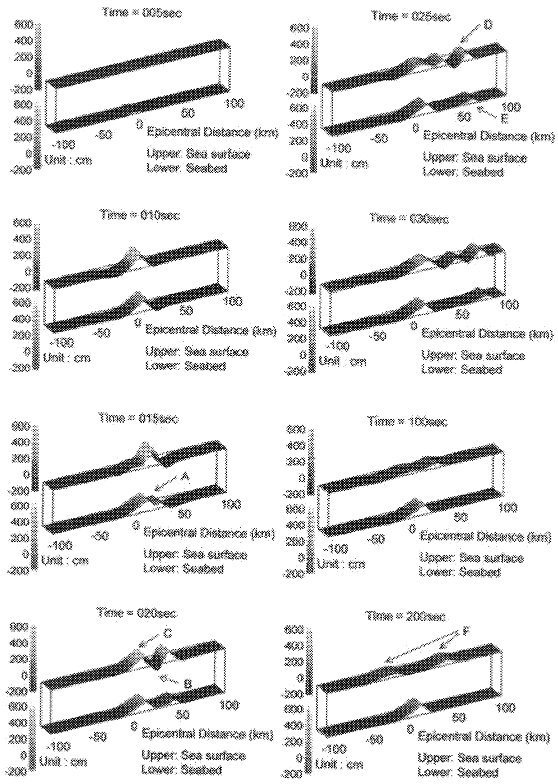

Table 1 Parameters of the Fault and the Ground

Figure 2 Snapshots of 2-D Dynamic Tsunami Simulation

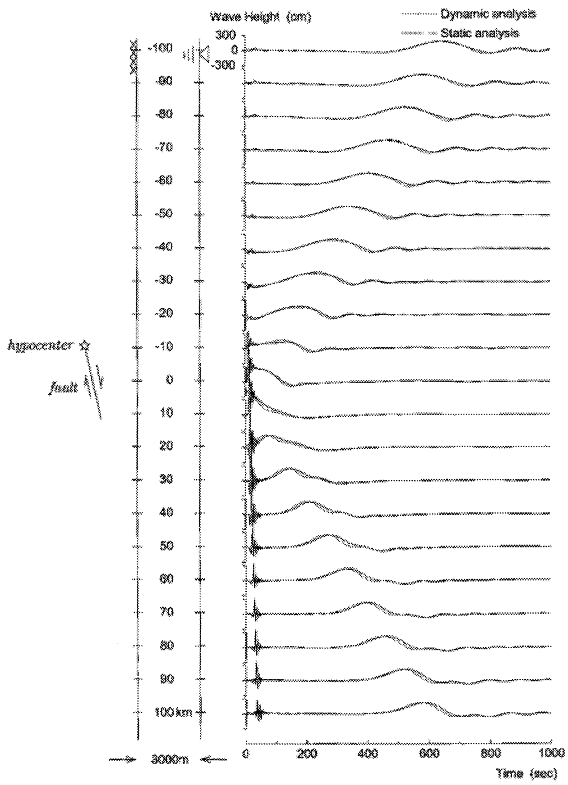

Figure 3 Time Histories of 2-D Tsunami Simulations

In Figure 2, the lower and upper surfaces represent the seabed and the sea surface, respectively. Findings from Figures 2 and 3 are, for example,

1. The dynamic sea bed displacement makes a remarkable contribution to increase water wave height, especially just above the seismic fault.
2. The increase is mainly caused by superposition of two types of water waves. One is the tsunami that travels as a long wave, and the other is the oceanic Rayleigh wave that travels much faster than the tsunami.
3. The oceanic Rayleigh wave is followed by several water waves of the similar period.
4. In the far-field, the water wave height from the dynamic and static analyses are almost the same.
5. Due to the local compressibility of water, water pressure change of very short period is obtained in the sea water, which does not induce the water level change on the sea surface (Ohmachi et al, 2001b).
6. Thanks to higher accuracy in the analyses of near-field tsunamis, the dynamic simulation can reduce the difference between fault models from tsunami data and those from seismic data.

4. TSUNAMI GENERATION PROCESS INFERRED FROM NEAR-FIELD OBASERVATION DATA

Some of the above-mentioned findings from the dynamic tsunami simulation were demonstrated by using observation data from a small earthquake (Ohmachi et al, 2001b). This paper describes another trial, which follows.

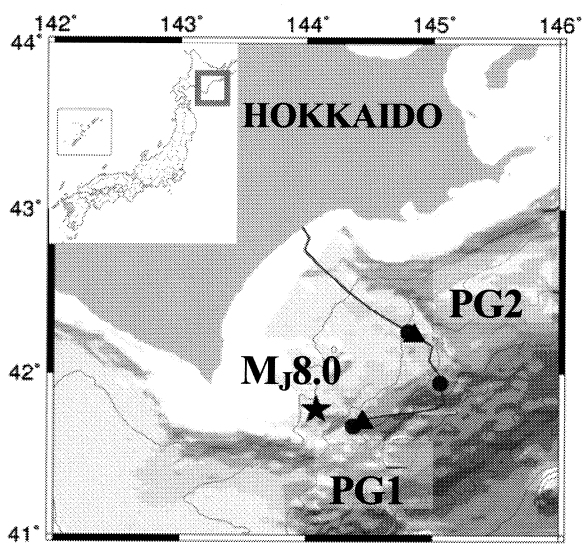

Figure 4 Location map of the 2003 Tokachi-oki earthquake and the JAMSTEC real-time monitoring system

Figure 4 shows a location map of the earthquake that occurred on September 25, 2003. Epicenter of the main shock M_J8.0 shown by a star in the figure. In the near-fault area, since 1999, a cabled-observation system has been installed on the seabed by JAMSTEC (Japan Agency for Marine-Earth Science and Technology), which includes 2 pressure gauges at PG1 and 2 shown by triangles and 3 seismometers at OBS1, 2 and 3 shown by circles (Watanabe et al, 2004). Reportedly, epicentral distance was about 30km for PG1 and OBS1, and about 80km for PG2 and OBS3, respectively.

Time histories of the water pressure at PG1 and seismic acceleration at OBS1 are shown in Figure 5. Sampling rates of the histories were 1Hz for the water pressure and 100Hz for the acceleration. As was pointed out (Watanabe et al, 2004), the water pressure record showed a remarkable base line shift amounting to about 40cm, as shown in Figure 6, which corresponds to the earthquake-induced permanent uplift of the sea bed.

Fourier spectra of the records shown in Figure 5 are shown in Figure 7. Among the spectral peaks in Figure 7, the peaks at 3 and 6 sec are commonly found in both spectra.

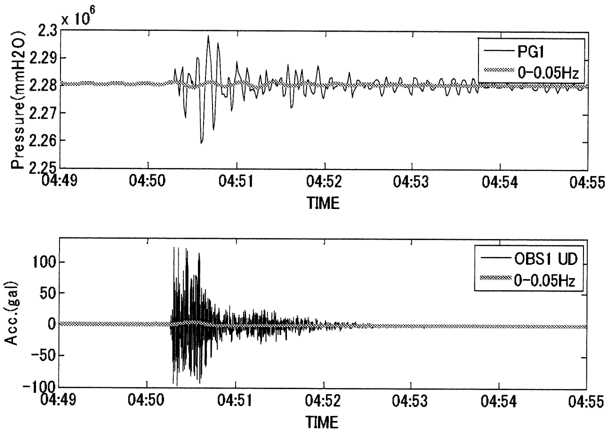

Figure 5 Water pressure (upper) and vertical acceleration (lower) observed at PG1and nearby point OBS1

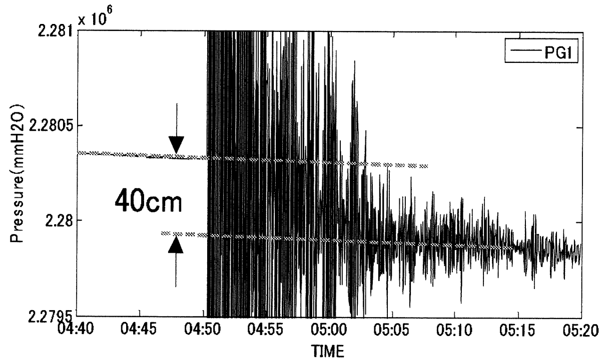

Figure 6 Baseline shift of the water pressure at PG1

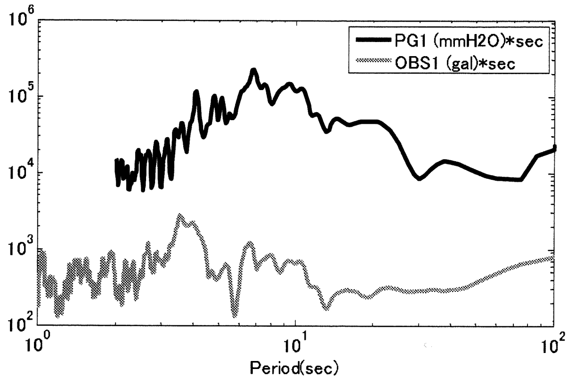

Figure 7 Fourier spectra of water pressure and seismic acceleration shown in Figure 5

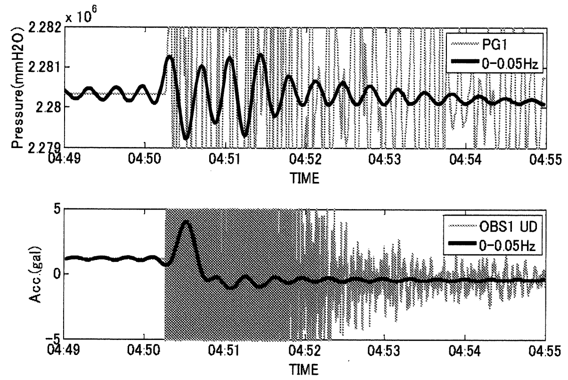

Figure 8 Long period components of the water pressure (upper) and seismic acceleration (lower)

The highest spectral peak at 6.5 sec in the water pressure is related to the first mode of elastic oscillations of sea water column (Matsumoto et al, 2005; Nosov et al, 2005). The natural periods of the oscillation is generally given by

$$T = 4H/c(1+2n) \tag{3}$$

where H, c and n are water depth, acoustic wave velocity of water and mode number, respectively. When H=2400m, c=1500m and n=0 are substituted, Eq. (3) gives the first mode period of 6.4 sec, which is very close to the observed period of 6.5 sec.

The period components longer than 20 sec are shown in Figure 8 by solid lines. Apparently, 20-25sec components are predominant in both time histories. While a single pulse is seen in the acceleration, at least 3 or 4 pulses are seen in the water pressure. Note that a series of pulses or a wave train is also seen in the snapshots of the sea surface shown in Figure 2, from which we could find causes and effects of the dynamic seabed displacement in detail. The amplitude (half of top-to-bottom) of the 3 or 4 pulses is about 1m in terms of the water height (or depth), which is almost double the static seabed displacement of 0.4m. Thus, it is different from tsunami, but is probably related to Rayleigh waves traveling along the seabed.

Several fault models have been presented for the 2003 Tokachi-oki earthquake. According to Koketsu et al (2004), the fault was 90x70km with a rupture velocity of Vr=4km/s, dipping at 20 deg to the northwest. A single asperity with a maximum slip of 8m is located in the middle of the fault., which may be related to the acceleration pulse in Figure 8. With these parameters or others, we are planning to simulate the tsunami generation process by the dynamic technique, and compare the result with the observation.

5. CONCLUSIONS

Records from the offshore monitoring system of the 2003 Tokachi-oki earthquake are very precious for not only understanding the tsunami generation process but to verify the dynamic tsunami simulation. Although, up until now, our verification is limited in a preliminary level yet, findings from the simulation such as water column oscillation and oceanic Rayleigh waves look consistent with the observation. But further study is needed to verify the usefulness of the simulation. For this purpose, we are planning a series of dynamic simulations of the 2003 earthquake-induced tsunami.

Acknowledgements:

The authors are grateful to JAMSTEC for providing them the observation data of the 2003 Tokachi-oki earthquake and tsunami from the offshore monitoring system.

References:

Hirt, C. W. Nichols, B. D., and Romero, N. C. (1975), "SOLA, A Numerical Solution Algorithm for Transient Fluid Flows," Los Alamos Scientific Laboratory Report, LA-5852.

Ohmachi, T, Tsukiyama, H., and Matsumoto, H. (2001a), "Simulation of Tsunami Induced by Dynamic Displacement of Seabed due ot Seismic Faulting," Bull. Seis. Soc. Am, Vol. 91, No.6, pp.1898-1909.

Ohmachi, T, Tsukiyama, H., and Matsumoto, H. (2001b), "Seawater Pressure induced by Seismic Ground Motions and Tsunamis," ITS 2001 Proceedings, Session 5, No.5-4, pp.595-609.

Watanabe, T., Matsumoto, H., Sugioka, H., and Suyehiro, K. (2004), " Offshore Monitoring System Records Recent Earthquake off Japan's Northernmost Island, Eos, Vol. 85, No.2, 13, January.

Matsumoto, H., Sugioka, H., and Mikata, H., (2005)"Tsunami Generation predicted by Acoustic wave of Water, Cho-onpa TECHNO, pp.13-17,

Nosov, M.A., Kolesov, S.V., Ostroukhova, A.V., Alekseev, A.B. (2005), "Elastic Oscillations of the Water Layer in a Tsunami Source, Doklady Earth Science, Vol.404, No.7, pp.1097-1100.

Koketsu, K., Hikima, K., Miyazaki, S. and Ide, S. (2004), " Joint Inversion of Strong Motion and Geodetic Data fro the Source Process of the 2003 Tokachi-oki, Kokkaido, Earthquake", Earth Planets Space, 56, No.3, pp.329-334.

Fifth International Conference on Urban Earthquake Engineering
March 4-5, 2008, Tokyo Institute of Technology, Tokyo, Japan

INFRASTRUCTURE SERVICES IN A TIME OF DISASTER: LESSONS FROM THE 2004 INDIAN OCEAN TSUNAMI IN BANDA ACEH, SUMATRA, INDONESIA

Ibnu Syabri

Associate Professor, Urban and Regional Infrastructure System Research Division, Bandung Institute of Technology, Indonesia
syabri@pl.itb.ac.id

Abstract: This exploratory research focuses on infrastructure services of Banda Aceh provided before, during, and two-year after the 2004 Indian Ocean earthquake in northern Sumatra, Indonesia on December 26, 2004. The objective of this research is to better understand typical infrastructure systems behavior of medium-size cities in Indonesia such as Banda Aceh, resilience, and recovery under critical conditions with the aim of generalizing policy formulation that lead to resilient infrastructure. This study explores pre-event infrastructure condition, service interruption, and infrastructure resiliency. The research includes an evaluation of the impacts on the water supply and sanitation, telecommunications, transportation, and power. Such lessons offer the broader impact of improved preparedness and response to future disaster.

1. INTRODUCTION

On December the 26th 2004, a series of events occurred that had catastrophic consequences for hundreds of thousands of people throughout much of South East Asia. A series of earthquakes, the largest recording 9.3 on the Richter Scale, rocked the province of Aceh on the island of Sumatera in Indonesia. This was immediately followed by a tsunami, with four waves reaching the height of 30 meters that has been described as the biggest natural disaster the world has ever faced in the last 60 years that caused massive loss of human life and devastated widespread areas of the province of Aceh in Indonesia (Pearce & Holmes, 2005). It is estimated that more than 150,000 people lost their lives, and no less than 500,000 people were internally displaced. The tsunami destroyed thousands of wooden and brick houses, damaged port and harbor facilities and caused massive damage to infrastructure, hospitals, schools, environment, and communities. As reported by BRR (the Governmentof Indonesia Executing Agency for Reconstruction of Aceh and Nias), the areas affected covers 800 kilometer coastal areas with total area damaged around 12,345 kilometers square. Sixteen out of 24 districts in Aceh and Nias were directly affected by Tsunami. The worst damage was in Banda Aceh, Aceh Jaya, and Aceh Besar (BRR, 2006).

The Indian Ocean tsunami impacted four major categories of critical infrastructure systems: water and sanitation; power lines; transportation networks; and communications. First, tsunamis had a catastrophic impact on power-generating stations and their support infrastructure (transmission networks and lines, water and sewerage systems, etc.). For example, in many parts of Aceh province, this led to interrupted electricity, and petroleum supply systems. Destruction of treatment facilities, storage areas, and pipe networks in turn affected water and sewerage provision. Second, the Indian Ocean tsunami caused significant devastation to coastal transportation networks and facilities. Roads covered with mud and debris typically became unusable while unpaved coastal road networks were often completely washed away. In addition, bridges located on low-lying coastal plains were destroyed, hampering relief work and the movement of goods and people. Facilities located directly on the coast such as harbor and port infrastructure (e.g. harbors, boats, fishing fleet stock) were among the first to be affected. Third, the Indian Ocean tsunami caused the loss of communications systems (including radio and telephone network systems) due to power losses and direct damage to buildings, cables, and transmission networks.

In this paper, the consequences of the tsunami disaster on civil infrastructure systems are explored, and a summary of performance is given for water supply and sanitation, electrical power, telecommunications, and transportation. The characteristics of damage and systems performance resulting from the tsunami disaster are examined. Lessons learned is drawn with respect to causes of damage, and factors that contribute to both the resiliency of the infrastructure to extreme events.

2. WATER SUPPLY AND SANITATION SERVICES

Aceh, especially, is one of Indonesia's already poorest and most troubled regions. Even before those events, Aceh's poverty levels stood at 28.5 percent, about twice the country's average (World Bank's APEA, 2006). Levels of poverty in Aceh had been increasing steadily since 1996, at which time it stood at just less than 15 percent. The financial crisis of 1997 and a prolonged political conflict had combined to raise the poverty levels in the province. In addition to the enormous loss of life, the tsunami drove another 325,000 into poverty, raising the poverty level to well over 30 percent. Before the earthquakes struck, Aceh and Nias had among the weakest capacity in Indonesia to respond to disasters. That capacity was further diminished by the tsunami and earthquakes (Bappenas, 2006).

Prior to the disaster of December 2004, access to formal water and sanitation services in Aceh was low by any standards. It is estimated that only 9% of households were formally connected to PDAM (Local Water Supply Enterprises) piped water supply (Burke and Afnan, 2006, p.29). The majority of the people obtained water directly from wells constructed either by households with their own funds, or by communities/villages with access to project financing, but many householders obtained water from military tankers. All urban and rural sanitation in Aceh was on-site â˜ mainly in the form of septic tanks and pit latrines, often constructed adjacent to wells. There was limited sludge collection, no wastewater treatment, and no urban sewerage in Aceh prior to the tsunami. This reflects low levels of sewage treatment typical of Indonesia in which an estimated 1% of the total population is currently connected to a sewerage system. Low water and sanitation coverage rates are a significant cause for concern in national planning, health and public works departments.

Since pre-tsunami, water supply and sanitation services has been chronically inadequate. The services are the responsibility of District Governments in Aceh. PDAMs (Local Water Supply Enterprises), as elsewhere, are legally mandated to function as autonomous water enterprises and normally managed and operated the urban water supply in the main cities as well as the smaller kecamatan (subdistrict) centers. In practice however the PDAMs served less than 50% of the residents of these centers, the network and facilities were poorly maintained, supply was intermittent and of poor quality, pressure was low and the system suffered high levels of unaccounted for water (estimates suggest 48% unaccounted-for-water in Banda Aceh). The existing water treatment plants had seen little maintenance for some years and were operated by only a few staff untrained in maintenance regimes. The Department of Public Works was responsible for human settlements, water supply and sanitation and at the District level would provide technical support to local government in relation to the planning implementation and operation of water supply and sanitation services.

Given the low service coverage provided by PDAMs, the majority of the population, particularly the rural population, has to rely on self-provision, community-based systems, and private small-scale water providers and vendors. Self-provision and community based systems are mainly based on dug wells and pumps (boreholes), which account for about 77% of water sources in Aceh Province, and about 57% in North Sumatra Province respectively.

Sanitation in urban and rural areas is provided by on-site facilities, mainly septic tanks and pit latrines. The sludge of septic tanks in urban areas is emptied by local government administration and, in some of the affected cities, disposed in septage treatment plants. Based on experience in other Indonesian cities, it can be assumed that the septage treatment plants are only partly operational. Only eight cities in Indonesia have partial sewerage systems; none of these cities is in the disaster-affected area.

In the post-tsunami situation, the relief effort immediately following the tsunami saw an unprecedented local, national and international humanitarian effort motivated to support the victims of the disaster. Basic needs were accommodated, including emergency water and sanitation services. Despite some gaps and ongoing problems of coordination, the massive contribution of a range of public, private, international and NGO actors prevented the predicted outbreak of water. The true extent of damage to the water and sanitation sector will probably never be accurately estimated. What was lacking before has now been completely wiped out in many rural areas. Reports indicate that damage and loss assessment estimated the total damage in Aceh at US$ 40 Million. In urban areas, damage to existing networks was significant in a number of cities. In Banda Aceh, the PDAMs lost about 65% of its physical operating assets to tsunami and ensuing theft, and customer connections reduced from 25,000 customers in December 2004 to only 8000 after the tsunami.

Overall it appears that PDAMs have managed to continue providing water at reduced capacity, which is supplemented by water provided by relief agencies and army from mobile treatment plants. Reports from relief agencies indicate, that due to these mobile water treatment plants, water supply poses fewer problems than sanitation issues during the relief phase. Information on damage to urban sanitation, including public toilets, vacuum trucks for emptying septic tanks, and septage treatment plants, is still limited.

3. TELECOMMUNICATIONS

PT Telkom is the sole provider of fixed line telephone services in Indonesia and is also now rolling out limited mobility CDMA services (TelkomFlexy) in cities including Banda Aceh. Through a majority-owned subsidiary (51% publicly owned), PT Telkomsel, it is also the largest GSM mobile operator. PT Indosat, which is now 85% privately owned, is developing a limited mobility domestic network, has the second largest GSM customer base. Both companies serve Aceh, but customer numbers are small and Telkom has just 15,000 and fixed line customers in Banda Aceh.

Telecommunications suffered moderately severe damage, primarily to the fixed connection services and to transceiver facilities for cellular phones. There was a heavy loss of connections in Banda Aceh and Meulaboh, amounting to 28,000 customers of 40% of connections. Total damage and losses are estimated at about Rp. 203 billion, comprising about Rp. 9 billion for postal services, Rp. 5 billion for universal service obligation (USO) connections and Rp. 162 billion for fixed connection services including cellular telephone (World Bank, 2005).

The tsunami caused significant damage to Telkom's fixed line network, and in particular the last mile of copper wire connection. There was also damage to exchanges, although repairs were made very quickly in many instances. Both Telkomsel and Indosat/Satelindo suffered damage to GSM base transceiver stations and associated facilities, most of which were reinstated quickly. However, MOC reported that all but eight of 111 lines provided to remote villages are damaged. Telkom and other operators were quick to mobilize VSAT and satellite communications equipment to support relief and recovery efforts.

4. TRANSPORTATION

The earthquake and tsunami caused extensive damage to large portions of the transport infrastructure, particularly along the west coast of Aceh. The road network, not in good condition prior to the disaster, became impassable in many places due to severe degradation of the surface, destruction of or damage to bridges, and change in topography. Logistics constraints severely hampered the transition from early recovery to full scale reconstruction.

Aceh province is served by six arterial road routes, totaling 1,587 kilometers length and 875 bridges. The four National roads, comprising 1,136 kilometers length and nearly 600 bridges, provide the major links along the northeast coast from Bandah Aceh to Lhoksumawe and to Medan in North Sumatra, and along the west coast from the capital to Meulaboh and Tapaktuan, connecting to Sidikalang in the southern part of North Sumatra province. All are asphalt-paved and in good/fair condition. Pre-disaster traffic volumes on these roads averaged 2,000-3,500 veh/day and up to 8,000 veh/day in the capitalâ€™s urban area. It is estimated that 316 kilometers or 19% of the road length was damaged and 46% of bridges, including about 120 bridges destroyed. The national road along the north-eastern coast (Banda Aceh to Langsa), sustained only minor damage and was passable after clean-up of surface debris. The north road from Banda Aceh to Krueng Raya lost five bridges. The national coastal road to Meulaboh in the south has been destroyed over 80 kilometers or 30% of its length and 110 or 60% of the bridges. That road was impassable over most of its length, which blocked relief efforts and made ground surveys impractical. No damage was reported in the south-eastern part of the Province (Bappenas, 2005).

5. ELECTRIC POWER SUPPLY

Indonesia's public electricity supply is provided by PT PLN, the state-owned electricity company. Aceh province accounts for a very small share of its total installed capacity, customers, and energy sales. Over 90% of Aceh customers are residential, and over 80% have very small capacity connections (up to 450VA). The capacity of primary and standby captive generation plant in the private sector is reportedly over 550MW, substantially exceeding PLNâ€™s installed power capacity. Most is located in Lhokseumawe, notably at the Arun LNG plant, and in Langsa on the east coast.

There has been severe damage to PLN's distribution networks in the Banda Aceh and Meulaboh regions, and to a lesser extent in the the Sigli and Bireun regions. PLN reported that the estimates damage in these four regions at 1,100 circuitkilometers of medium voltage line, 1,750 circuit-kilometers of low voltage line, 45 MVA distribution transformer capacity, and 90,000 household connections have been damaged. Total replacement cost is estimated at Rp. 323 billion. In practice, some transformers and other materials (including poles) will likely be salvageable and the actual cost may be lower.

6. LESSONS LEARNED

The tsunami disaster was an immense and complex event. Work is in progress to collect additional information that will lead to refinements in the databases and further clarification of the issues raised by the disaster. Lessons learned are summarized under the three subheadings that follow.

6.1 Water Supply and Sanitation

Although physical damage to water pipelines and sanitation, was confined principally to the area of debris and indunation impact around the damage areas, the temporary loss of these systems extended far beyond this perimeter. After the tsunami sept out the coastal areas as far as 10 Km from the soar line, damaged zones of the water supply and sanitation had to be isolated to preserve flow in undamaged sections. Because the extent of damage was unknown, conservative decisions were made about the size of the isolation zones. In extreme events, conservative decisions under emergency conditions are likely to result in a substantial zone of temporarily lost service. For planning purposes, significant system disruptions should be anticipated.

The tsunami damage to water supply and sanitation services was caused by direct impact from mud and debris. There is no direct evidence of damage caused by ground vibrations due to the earthquake prior to the tsunami. Virtually all damage of major consequence was the result of direct impact. Consequently, the areal extent of damage to critical water and power lines and telecommunications was confined principally to the zones of debris impact and inundation. This lesson is significant for establishing planning and emergency response scenarios. It indicates that the infrastructures damage along the coastal areas from the tsunami will likely be confined within the near vicinity of the damage areas.

6.2. Telecommunications

Redundant, dispersed facilities and the ability to rapidly by-pass damaged telecommunication nodes were important contributors to the performance of the telecommunications system (Zimmerman, 2001). The proximity of many telecommunication facilities was a distinct asset during response and recovery. These configurations may not be present in Banda Aceh, thereby prompting consideration of additional facilities and dispersion of facilities where loss of business and commercial activity can have severe regional and national consequences. Special consideration should be given to facilities that affect urban, state, and national programs.

Wireless e-mail proved to be a valuable asset after the Indian Ocean tsunami 2004. The use of handheld e-mail devices greatly facilitated communications and contributed to substantial improvements in emergency response efficiency.

In general, the telecommunication equipment performed very well. The successful performance of telecommunication equipment encourages continued testing and evaluation of critical facilities, guided by observations of performance during extreme events.

6.3 Transportation

Even while recovery and reconstruction have picked up pace in areas where access has improved with on-going emergency repairs and temporary bridges, many settlements in remote areas have remained under serviced. At the same time, the increased traffic of heavily loaded vehicles carrying construction materials keeps adding strain to the road conditions. The tonnage of materials and equipment that needs to be moved will be enormous.

Some immediate implications of transport-related damage include strategically reviewing the transport system to introduce some redundancy; providing alternative routes and access in the event of disruption; incorporating hazard risk assessment into the design and location of transport infrastructure, and the importance of re-assessing earthquake-damaged structures, e.g. bridge supports, culverts, transport-related buildings, to determine whether there is a need for repair or full replacement.

6.4 Electric Power Supply

Implications for rehabilitation and reconstruction from damage to the energy sector include (1) a focus on protecting the power distribution network and transformers from vulnerability; (2) identifying opportunities to salvage materials such as transformers, poles and household fittings in order to lower the cost of re-establishing the distribution network; (3) minimizing leakage from the oil depots and potential damage from cleaning out contaminated tanks at retail pump stations, and (4) incorporating energy conservation and renewable energy sources as planning considerations in revitalizing the sector.

Perhaps the most important observation from the Indian ocean tsunami disaster and other incidents described in this paper is that damage becomes most pervasive when it interferes with the electric power system. The electric power system is, in effect, the gateway for local damage to escalate or cascade into other systems. The effects of local damage appear to be influenced by the proximity of damage to an electrical substation. When damage affects a Mealulaboh substation, its potential for cascading consequences increases dramatically resulting no electricity for the whole city in five consecutive days.

The damage on Indian ocean tsunami 2004 was so extensive that disruption spread through all distribution networks along the coastal lines. Extensive isolation, repairs, and new feeder installation were required for power restoration for hospitals, houses, government offices and commercial centers in Banda Aceh. Rehabilitation on such a scale within the short time frame was only possible through extensive stockpiling of specialized parts and the availability of many trained, highly motivated, and well-equipped staff. System resilience depended on organizational resilience that was embedded in the planning and preparations that had been developed for emergency response.

7. CONCLUSIONS

The disaster in Aceh has presented an opportunity for the emergence of a more efficient and effective infrastructure services that meets the needs of the Acehnese people. It has resulted in the funds, space, momentum and enabling environment to establish coverage levels higher than any other province in the country.

Research on the Indian ocean tsunami 2004 disaster can help us to understand response and recovery in various disaster settings. While many aspects of this disaster were unique, it was a large-scale crisis event that had similarities to other disasters, including many natural disasters. This preliminary study was intended to increase our knowledge about infrastructure services in the damaged areas in a disaster setting and to offer suggestions for new directions in policy.

Acknowledgements:

This paper is based in part on work supported by two grants from the Bandung Institute Technology (ITB) Emergency Task Force for Aceh Rehabilitation and ITB Priority Research: the Reserch Division for Urban and regional Infrastructure System Cooperative Agreement No. 19/2006. Any opinions, findings, and conclusions or recommendations expressed in this document is those of the author and do not necessarily reflect the views of the Bandung Institute Technology Research Foundation.

References:

Bappenas and World Bank, 2005, Indonesia: Preliminary Damage and Loss Assessment, December 26, 2004 Natural Disaster.

Bappenas and the International Donor Community, 2006, Preliminary Damage and Loss Assessment.

BRR, 2006, Update Working MDTF Powerpoint Presentation given to the MDTF steering committee.

Burke, A and Afnan, 2006, Aceh: Reconstruction in a Conflict Environment Views from Civil Society, Donors and NGOs, Unpublished report.

Pearce, F. & Holmes, B. (2005) Tsunami: the impact will last for decades, New Scientist.

World Bank, 2005, Proposed NAD-Nias Settlement Rehabilitation and Reconstruction Program Appraisal Report.

Zimmerman, R., 2001, "Social Implications of Infrastructure Network Interactions," Journal of Urban Technology, Volume 8, No. 3, pp. 97-119.

MYSTERIOUS SMALL TSUNAMI IN TOYAMA BAY CAUSED BY THE 2007 NOTO HANTO EARTHQUAKE

Shusaku Inoue[1], Tatsuo Ohmachi[2], and Akane Takahashi[3]

1) Research Associate, Department of Built environment, Tokyo Institute of Technology, Japan
2) Professor, Department of Built environment, Tokyo Institute of Technology, Japan
3) Undergraduate student, Department of Civil and Environmental Engineering, Tokyo Institute of Technology, Japan
shusaku@enveng.titech.ac.jp, ohmachi@enveng.titech.ac.jp, takahashi.a.ah@m.titech.ac.jp

Abstract: An earthquake occurred off northwest of Noto Peninsula, Japan on March 25, 2007. Associated with this earthquake, a small tsunami was excited, and a mysterious early arrival tsunami was observed at Toyama. First we show observed wave height records and estimate the tsunami by considering only vertical displacement of fault movement. Then we assume the source region of the tsunami at Toyama from inverse propagation diagrams and finally attempt to simulate the mysterious early arrival tsunami there.

1. INTRODUCTION

At 09:41:58 March 25, 2007 (JST) (00:41:58 UTC) an earthquake occurred off northwest of Noto Peninsula, Japan (JMA, 2007). The epicenter was located at 37°13.2′ N, 136°41.1′ E with a focal depth of 11 km, and JMA magnitude was 6.9 (JMA, 2007). Strong 6 on the Japanese seismic scale was observed at Wajima, Nanao, Namizu in Ishikawa prefecture. One person was killed, about 350 people were injured, and about two thousand houses were collaped (JSCE and JGS report, 2007).

Associated with this earthquake, a small tsunami was excited off northwest of Noto. The maximum tsunami height was about 20 cm at Wajima. In the meanwhile, a mysterious tsunami was observed at Toyama off southeast of Noto Peninsula. This small tsunami arrived soon after the earthquake occurrence, and the wave height was about 10 cm. This arrival time could not be explained by considering tsunami propagation from the epicenter to Toyama bay via north of Noto Peninsula. In addition, an overturn of a pleasure boat was reported. According to our interview to the captain, the boat was capsized about 2 minutes after he had felt shaking on the boat.

A lot of tide gages and tsunami meters are installed around Japan. We could collect 11 wave height records provided by Port and Airport Research Institute (PARI), Japan Meteorological Agency (JMA), and Geographical Survey Institute (GSI). In this paper, we compile and exhibit these data in Section 2 and estimate the tsunami by considering only vertical displacement of fault movement in Section 3. In Section 4, we assume the tsunami source of southeast from inverse propagation diagrams and finally attempt to simulate the mysterious early arrival tsunami at Toyama.

2. WAVE HEIGHT RECORDS

Noto Peninsula is located on north of middle Japan and protrudes into Japan Sea. Figure 1 illustrates the epicenter and observation points. These colors (black, gray, and white circles) indicate the installed organization (PARI, JMA, and GSI).

Specifications such as latitude, longitude, depth, and sampling rate of these instruments are shown in Table 1. Toyama and Wajima each have two instruments of different organizations. An instrument of Fushiki Toyama provides 20 minutes record every 2 hours, but does not provide continuous records, then we do not use this data in this

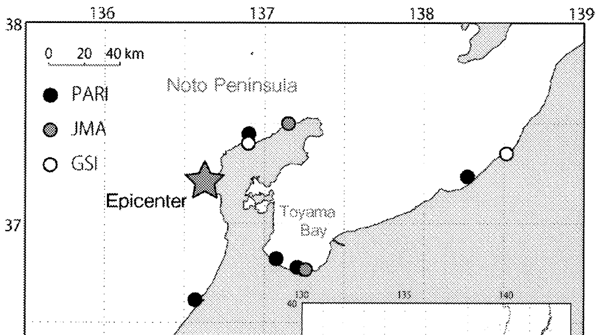

Figure 1 Locations of the epicenter and observation points.

Table 1 List of observation points.

No.	Org.	Place Name	North Latitude			East Longitude			Depth (m)	Sampling Rate (s)	Instrument Type
			deg.	min.	sec.	deg.	min.	sec.			
1	PARI*	Naoetsu	37	14	9	138	16	25	32.7	0.5	USDWM***
2	PARI	Toyama	36	46	40	137	12	18	20.0	0.5 or 5	USDWM
-**	PARI	Fushiki Toyama	36	49	15	137	4	29	0.0	0.5	Tide gage
3	PARI	Wajima	37	25	51	136	54	8	52.0	0.5	USDWM
4	PARI	Kanazawa	36	36	50	136	34	3	21.1	0.5	USDWM
5	PARI	Fukui	36	9	50	136	4	30	36.7	0.5	USDWM
6	JMA*	Toyama	36	46	-	137	14	-	0.0	15.0	Tide gage (Sonic wave)
7	JMA	Noto	37	30	-	137	9	-	0.0	15.0	Tsunami meter (Sonic wave)
8	GSI*	Kashiwazaki	37	21	-	138	31	-	0.0	30.0	Tide gage (Float)
9	GSI	Wajima	37	24	-	136	54	-	0.0	30.0	Tide gage (Float)
10	GSI	Mikuni	36	15	-	136	9	-	0.0	30.0	Tide gage (Float)

* PARI: Port and Airport Research Institute, JMA: Japan Meteorological Agency
GSI: Geographical Survey Institute
** No continuous records
*** USDWM: Ultra Sonic Directional Wave Meter

paper.

Instruments of PARI are part of NOWPHAS (Nationwide Ocean Wave information network for Ports and HArbourS) which has been operated since 1970 (Nagai et al. 2004). These are put on the sea-bed a few kilometers from the shore and are possible to measure water pressure, water level and 3 layer's current velocities at high sampling rate (0.5 s) (Hashimoto et al. 1996). It is reported by Nagai et al. (2007) that there instruments observed short period water pressures at this event. Tsunami meter of JMA is put on quayside and measure water level by reflection of sonic wave. Tide gage is a well connected to sea and water level of the well are measured instead of the sea level. Main differences between NOWPHAS and other instruments are set location and sampling rate.

Observed waveforms from 9:30 to 12:00 are plotted in Figure 2. No. 1-5, 6-7, 8-10 are PARI's, JMA's, and GSI's data. We conducted band-pass (200s to 10000s) filter to No. 1-5 because the raw data have very short period noises. Maximum wave height is about 40cm observed at Noto (JMA). However, we should notice that wave heights of offshore and shore are difference and the height of shore usually becomes larger. From No. 2 and No. 6 Toyama, we can find the early arrival tsunamis whose periods are shorter compared to other places.

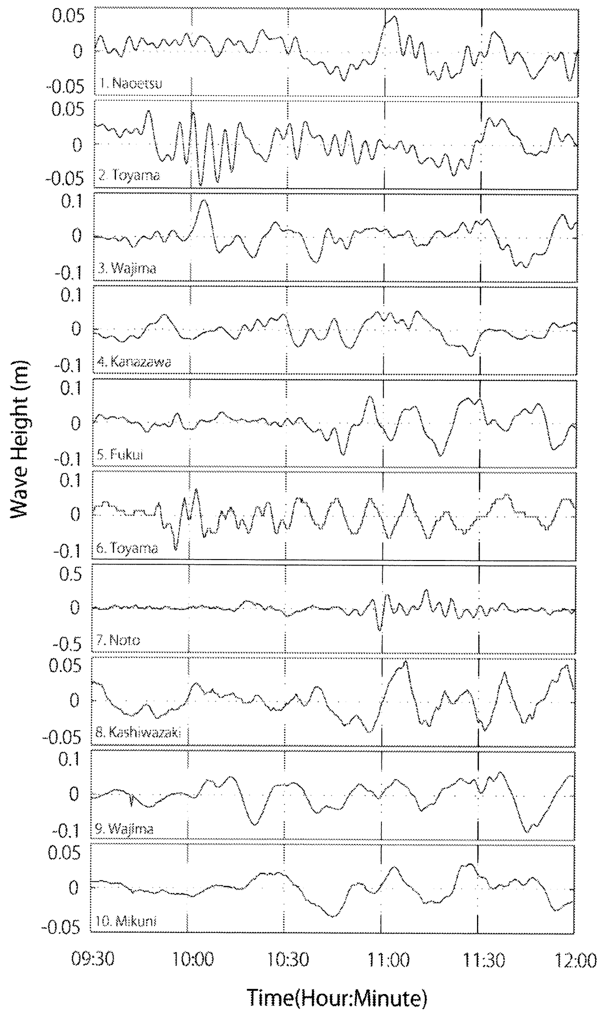

Figure 2 Observed wave height records

3. TSUNAMI SIMULATION

To estimate observed tsunami, we performed tsunami simulation. Figure 3 shows the simulation area covering 555 km by 533 km in N-S and E-W directions, and its

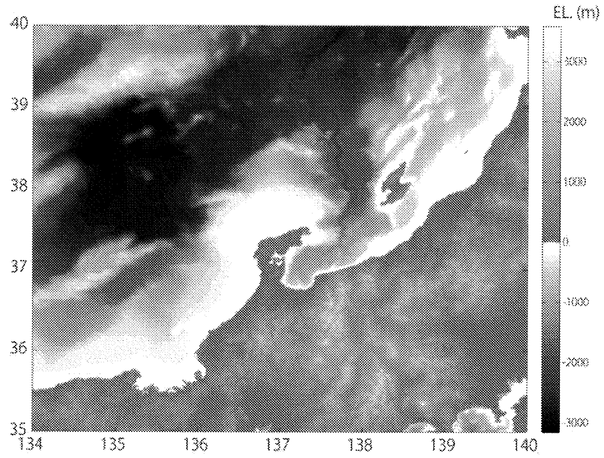

Figure 3 Calculation area and its topography

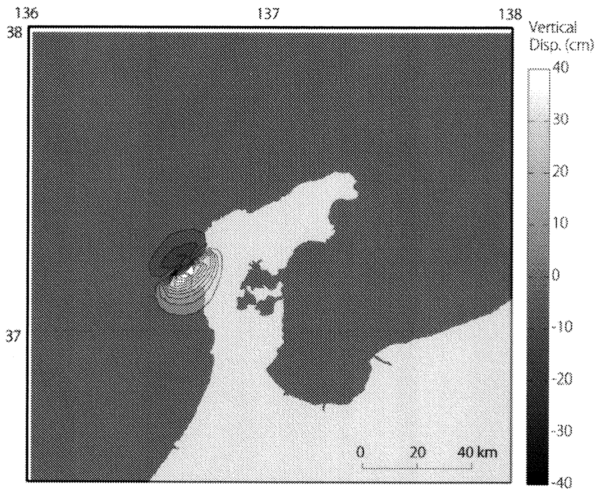

Figure 4 Vertical displacement due to the fault dislocation

Table 2 Fault parameters

Strike	55 (deg)
Dip	63 (deg)
Rake	137 (deg)
Max Dislocation	2.43 (m)
Length	27.5 (km)
Width	21.9 (km)
Depth of upeer edge	1.7 (km)

topography. Toyama Bay is deeper than off northwest of Noto Peninsula, and its unevenness is relatively rough compared to the topography near the epicenter.

We calculated the ground permanent displacement by Boundary Element Method (Kataoka and Ohmachi 1997). Fault parameters we used, shown in Table 2, are referred from GSI model (GSI 2007) that is estimated by GPS and SAR data. This fault model is not a uniform fault model, but is a complex one that has asperities. From the calculation of the ground, vertical displacement of Figure 4 is obtained. We can find large displacement of about 40cm concentrate on

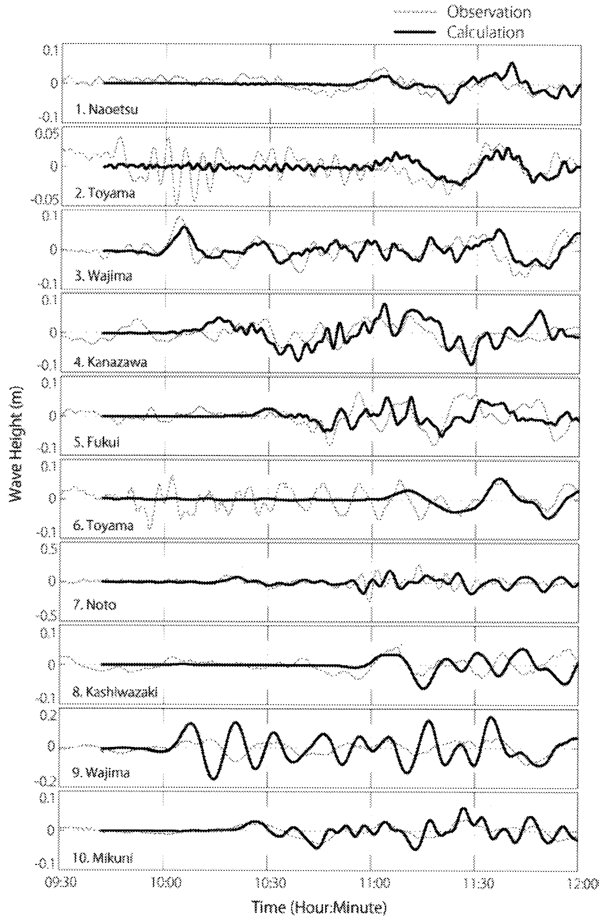

Figure 5 Comparison of observed waveforms (dashed lines) and calculated waveforms (solid lines)

the left side of Noto Peninsula but less displacement on Toyama Bay.

We performed tsunami simulation with the vertical displacement as its initial tsunami profile. The calculating waveforms are shown in Figure 5 with observed waveforms. From this figure, in No. 1-6 calculating waveform roughly agree with the observed one except for early arrival tsunami at Toyama. A Calculating waveform of No.6 Toyama also corresponds to observed one except for first arrival waves. On the other hand, in No. 7-10 calculating waveforms necessarily do not agree with observe waveforms well. The reason is thought that observation points of No .7-10 are located along shoreline, but the calculating points are not exactly on shoreline but on offshore. The disagreement should be considered more in the future.

4. EFFECT OF HORIZONTAL DISPLACEMENT

First arrival tsunami seems to have reached Toyama about 5 to 10 minutes after the occurrence of earthquake from figure 2. To investigate the source of the early arrival tsunami at Toyama, we drew inverse propagation diagrams from Toyama (Figure 6). From this figure, it is presumed

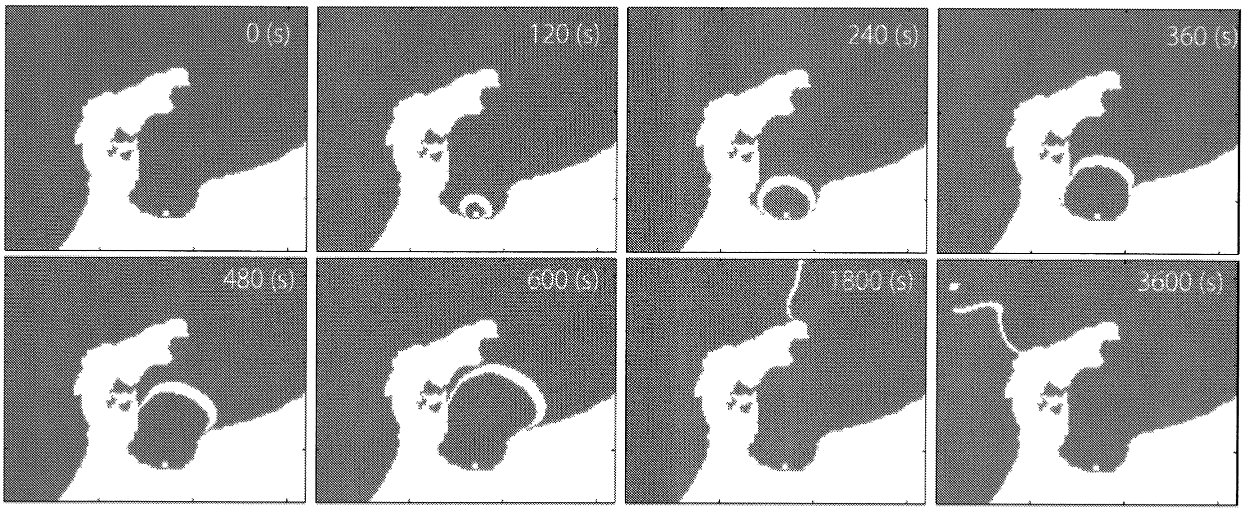

Figure 6 Inverse propagation diagrams from Toyama

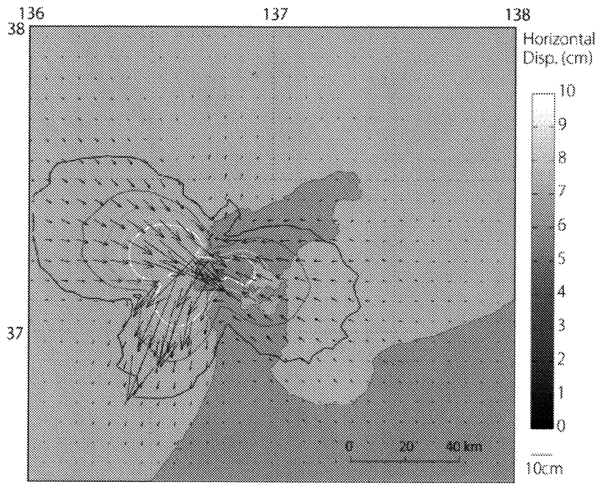

Figure 7 Horizontal displacement due to fault dislocation

that the source was located off east of middle Noto Peninsula.

As the source of east, we thought an effect of horizontal displacement due to fault movement. This effect was discussed by Tanioka and Satake (1996). The vertical displacement due to horizontal displacement of the slope, u_h is expressed by

$$u_h = u_x \frac{\partial H}{\partial x} + u_y \frac{\partial H}{\partial y}, \qquad (1)$$

where H is the water depth and u_x and u_y are the horizontal displacements due to faulting.

Figure 7 shows horizontal displacement due to fault dislocation (u_x and u_y), and Figure 8 and 9 illustrate slope of EW and NS-direction, respectively. We can find horizontal displacement of 2 to 4 cm and slope of 30 % in Toyama Bay. We obtain vertical displacement (u_h) of Figure 10 by applying eq. (1). The displacement is not large compared to

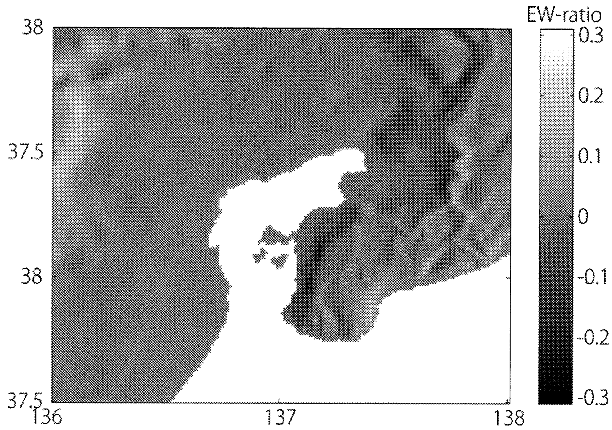

Figure 8 Slope of EW-direction

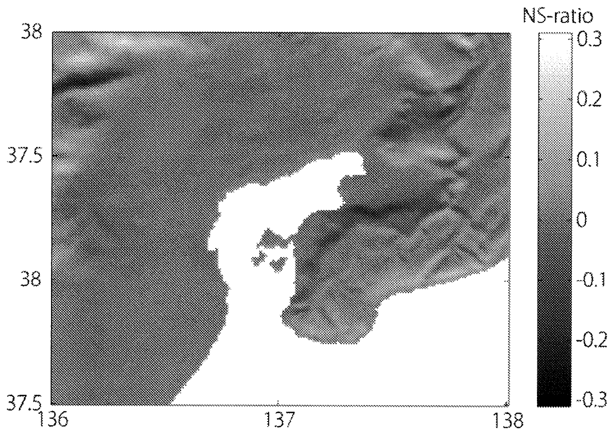

Figure 9 Slope of NS-direction

the displacement of western side of Noto. Figure 11 shows the wave height of calculated waveform by considering only u_h. However, the calculated wave height did not become as large as observed one.

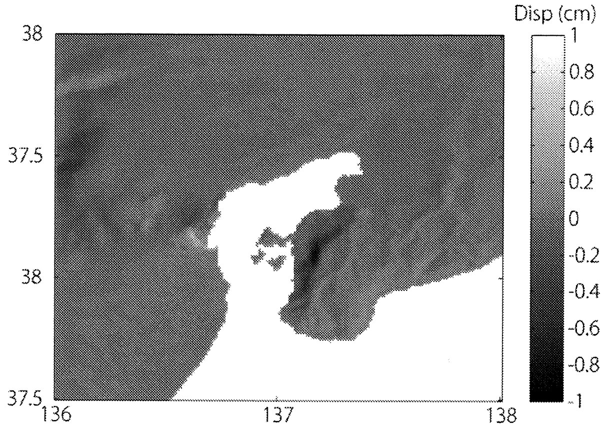

Figure 10 Vertical movement due to horizontal movement of steep slop

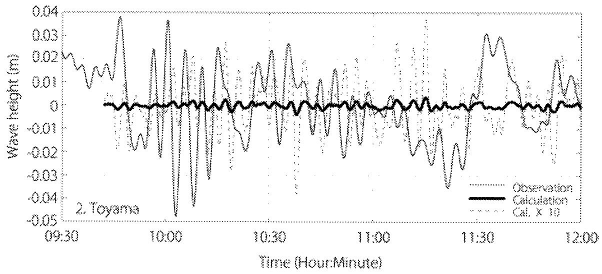

Figure 11 Comparison of observed waveform (solid line), calculated waveform (bold solid line) and calculated waveform multiplied by 10 (dashed line) at Toyama (PARI).

5. CONCLUSIONS

In the 2007 Noto Hanto earthquage, a tsunami was excited and an early arrival tsunami was observed at Toyama. We simulated the main part of the tsunami by considering the vertical displacement of fault model derived from GPS and SAR data. In addition, we assumed the source of early arrival tsunami by inverse propagation diagrams and performed the simulation by considering the effect of horizontal displacement of faulting. However, we could not express the first arrival tsunami at Toyama well.

Acknowledgements:

We are grateful to Dr. Nagai and his colleagues for providing their NOWPHAS data and their useful discussions. We additionally thank Japan Meteorological Agency and Geographical Survey Institute for their tide and wave height records. We acknowledge support from the Center for Urban Earthquake Engineering (CUEE) in Tokyo Institute of Technology. This research was supported by the Ministry of Education, Culture, Sports, Science and Technology (MEXT), Grant-in-Aid for Young Scientists (B) KAKENHI (19760311).

References:

Tanioka, Y. and Satake, K. (1996), "Tsunami generation by horizontal displacement of ocean bottom," *Geophysical Research Letters*, **23**(8), 861-864.

Nagai, T., Nozu, A., Lee, J. H., Kudaka, M., Adachi, S., and Ohmachi, T. (2007), "Characteristics of the Observed Pre-Tsunami Dynamic Seabed Pressure Wave Records," *Doboku Gakkai Ronbunshuu B*, JSCE, **63**(4), 368-373. (in Japanese)

Japan Meteorological Agency (2007), "Special Edition of the 2007 Noto Hanto Earthquake," http://www.seisvol.kishou.go.jp/eq/2007_03_25_noto/index.html. (in Japanese)

Geographical Survey Institute (2007), "Estimated dislocation distribution on the earthquake source fault (temporary)," http://www.gsi.go.jp/WNEW/PRESS-RELEASE/2007/0412/0412-5.htm. (in Japanese)

Geographical Survey Institute (2007), "Tide data: list of GSI tidal stations," http://tide.gsi.go.jp/furnish.html. (in Japanese)

Hashimoto, N., Mistui, M., Goda, Y., Nagai, T., and Takahashi, T. (1996), "Improvement of Submerged Doppler-Type Directional Wave Meter and its Application to Field Observation," *Proceedings of 25th International Conference on Coastal Engineering*, **1**, 629-642.

Nagai, T., Ogawa, H., Nukada, K., and Kudaka, M. (2004), "Development and Operation of the Japanese Tsunami Observation System by Using Nationwide Coastal Wave Gauges," *Journal of Civil Engineering in the Ocean*, JSCE, **20**, 173-178. (in Japanese)

Kataoka, S., and Ohmachi, T. (1997), "3-D simulation of near-field motion in irregular ground," *J. Struct. Mech. Earthquake Eng.*, JSCE, **556**, 139-149.

Japan Society of Civil Engineers and Japanese Geotechnical Society (2007), "Report of the 2007 Noto Hanto Earthquake damage investigation," JSCE.

PHYSICAL MODELING: AN ESTIMATION OF WAVE FORCES ON AN INLAND BRIDGE SUBJECT TO TSUNAMI BORES

Tze Liang Lau[1], Panitan Lukkunaprasit[2], Anat Ruangrassamee[3], and Tatsuo Ohmachi[4]

1) Graduate Student, Department of Civil Engineering, Chulalongkorn University, Thailand
2) Professor, Department of Civil Engineering, Chulalongkorn University, Thailand
3) Assistant Professor, Department of Civil Engineering, Chulalongkorn University, Thailand
4) Professor, Department of Built Environment, Tokyo Institute of Technology, Japan
celau@eng.usm.my, lpanitan@chula.ac.th, Anat.R@eng.chula.ac.th, ohmachi@enveng.titech.ac.jp

Abstract: Both tsunami bores and tsunami bore-induced forces on bridges are complex and they can hardly be theoretically predicted at this moment. As a result of the paucity of the tsunami wave force study on bridges, physical modeling was carried out to investigate the occurrence of tsunami bores acting on an inland bridge. The experimental setup and the characteristics of the simulated tsunami wave were discussed. The measured forces on bridge deck in this study were then compared to the calculated forces which were adapted from the proposed pressure distribution used on vertical wall and land structures in previous studies. The preliminary results show that some of these formulations can estimate the wave forces on the bridge deck at a certain wave height up to a certain extent. Hence, the formulation of tsunami wave forces on bridges needs to be studied further.

1. INTRODUCTION

The devastating 2004 Indian Ocean tsunami demonstrated its disastrous impact on civil engineering structures including bridges (Unjoh, 2005; Sengara et al., 2006; Sheth et al., 2006; Ballantyne, 2006) in both near and far fields by tsunami waves. Either the bridge decks were significantly displaced in their transverse direction or decks were completely washed away their decks from their foundations. This event has attracted the attention of scientists and engineers in conducting research that yields findings enabling them to estimate tsunami wave loads and to design bridges which have sufficient strength to withstand the predicted loading in order to save these structures.

Tsunamis are not new phenomena but they are well-known as destructive waves which comprise a series of long waves. One of the most potential causes of tsunamis in a water body is through an impulsive disturbance of the seafloor by a shallow undersea earthquake that vertically displaces the water column. They are distinguished from other water waves caused by a wind, storm and flood because they propagate at high speeds and travel great and transoceanic distances with limited energy losses. When tsunamis approach a shore, their energy flux remains nearly constant and with tremendous amount of energy. They can inundate a run-up height past the typical high-water level and the fast-moving water can cause a catastrophe to the coastal structures and the loss of life. Numerical simulations have been developed comprehensively in predicting the wave generation and propagation with encouraging outcomes. However, the terminal effect of tsunami on structures remains a challenge due to its complication and dependence on the factors such as the topography of the shoreline and the configuration of the structures.

This study focuses on the bridges that have to be constructed near to the coastline and they are possibly subjected to a tsunami wave attack. Bridges are used as lifeline structures when the coastal areas are inundated by a flood after the tsunami occurrence. If the bridges do not designed to resist tsunami wave forces, the operation of bridges will probably be disrupted and the emergency efforts that are essentially needed immediately after the disaster may be hampered. Hence, an estimation of tsunami wave forces on bridges is crucially needed to be studied in order to gain deeper insight of the structural responses to a tsunami attack.

2. EXPERIMENTAL STUDY

2.1 Background

Since the past few decades, tsunami waves on wall-type and land structures have been studied expansively in the laboratory. The wave forces on a vertical breakwater or building by a tsunami bore or surge advanced a dry bed have been investigated by Cross (1967), Togashi (1986), Ramsden (1996), Asakura et al. (2002), Ikeno and Tanaka (2003) and Arikawa et al. (2006). Fukui et al. (1963), Tanimoto et al. (1984), Ramsden and Raichlen (1990), Ramsden (1996), Hamzah et al. (2000), Mizutani and Imamura (2000, 2002) and Ikeno et al. (2001) studied the wave forces on a submerged vertical dike or seawall by a tsunami. Out of these studies, Togahsi (1986), Tanimoto et al. (1984), Asakura et al. (2002) and Arikawa et al. (2006) allowed the wave to overtop the structures and flow away into the further downstream end in their experiments whereas in other previous studies, the wave reflected and collided with the progressing incident waves after hitting the structures. The latter circumstances of the study may not applicable to the bridges as the wave can pass through the lower part of the bridge deck and overtop it after striking the deck.

Apart from Togashi (1986) and Hamzah et al. (2000), previous studies proposed formulations to estimate tsunami wave forces which were mainly expressed in some proportions of hydrostatic pressure distributions. Fukui et al. (1963) suggested pressure distributions for impulsive and continuous pressures based on the experimental results on dike with various slopes which could be adapted for a vertical wall. Tanimoto et al. (1983) recommended wave pressure distributions on a vertical breakwater. The formulation was then improved by Ikeno et al. (2000) and Ikeno and Tanaka (2003) for offshore and onshore vertical walls, respectively. Asakura et al. (2002) proposed a formulation to predict the wave force on land structures while the formulation of dynamic wave force on prevention structures such as seawalls and breakwaters was studied by Mizutani and Imamura (2000, 2002). Arikawa et al. (2006) related the sustainable pressure on the seawall to the tsunami height offshore but no further correlation between offshore and onshore wave heights was made.

Studies on tsunami-induced forces on bridge structures have not been sufficient up to date. Kataoka et al. (2006) and Iemura et al. (2007) studied a tsunami wave action on a submerged bridge and a bridge over a dry bed, respectively. According to Kataoka et al. (2006), their experimental results showed the slow-varying wave forces which were relatively small as compared to impulsive forces were in good agreement with some safety margin with the force estimated by the standard formula in Japan Port and Harbour Association (JPHA, 1999). On the other hand, the drag force as stipulated in CCH (2000), FEMA-55 (2000), FHWA (2001) and ASCE-7 (2005) could be sufficiently estimated by using the drag coefficient that equals to 1.1 for the bridge subjected to tsunami surge (Iemura et al., 2007). In contrast, the current study experimentally investigated and measured the forces and pressures on a bridge over a dry bed caused by tsunami bores which had not been thoroughly explored by previous researchers.

2.2 Physical Modeling

Due to the complexity of tsunami waves on structures, physical modeling is one of the practical approaches to study the tsunami-induced forces on bridges. In this study, a wave flume experiment is conducted to obtain the time histories of wave pressures and responses of a bridge structure subject to a tsunami force that cannot be theoretically predicted adequately. Bridge models is designed and constructed to represent a typical full-scale bridge and the results are scaled to the prototype based on the Froude Number similitude criteria.

2.3 Test Setup

Hydraulic model experiments were carried out in a 1.0 m wide by 40 m long by 1.0 m deep wave flume at the Hydraulic Laboratory, Asian Institute of Technology. The flume was situated in the horizontal position. It had clear acrylic side walls and a painted structural steel bed. A two-dimensional fixed bed model was performed. The still water level was set at 47.5 cm deep throughout the tests. Figure 1 illustrates the experimental setup of this study.

The experiment hypothetically simulated a bridge located at inland on Kamala Beach, Phuket. It was one of the coastal areas that were drastically hit in Thailand. Kamala Beach with the bed slope of 1:115 (0.5^0) was adopted as the typical coastline profile around this region in this study. These coastal geometries were downscaled in the model study with the length scale of 1-to-100.

The 1-to-100 reduced scaled bridge model was constructed from clear acrylic glass based on a typical bridge section constructed in Thailand. The total height of the bridge was 8.4 cm including the thickness of the deck of 2.8 cm as shown in Figure 2. There were six girders and two side parapets attached at the bridge deck. The girders were denoted as girders G1 to G6 in the direction of the wave propagation. The bridge model was installed at the downstream (left end of Figure 1) of the flume. Three spans of bridge deck with each span of 30 cm long were positioned across the width of the flume. Only the middle span was instrumented. Pressure gauges were placed at the front and/or back faces of the bridge deck and the front face of the bridge column to measure the time-histories of pressure acting on bridges. A high frequency load cell underneath the 15 cm by 15 cm load measuring plate of the model was utilized to determine the physical quantities of structural responses. The wave passed through the model and overflowed the flume to the pump sump under the ground floor level.

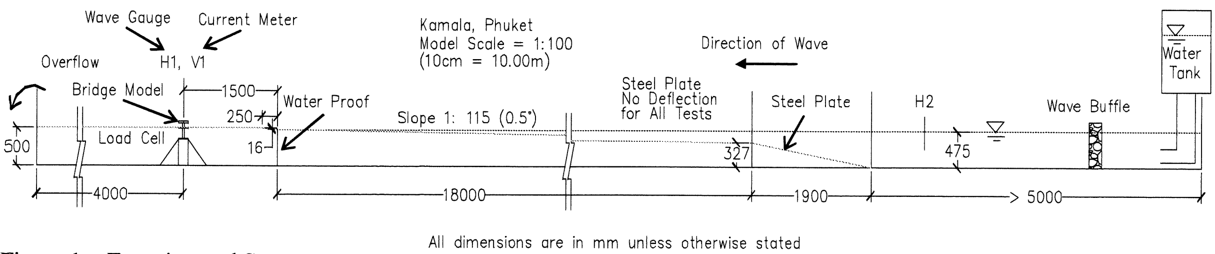

Figure 1 Experimental Setup

Solitary wave-like tsunamis were generated by an abrupt release of a known water volume in the elevated water tank situated at the upstream (right end of Figure 1) of the flume in the laboratory. By varying the released volume of water from the elevated tank, different waves with various wave heights and wave velocities were generated. The relationship of water volume and the wave height at the location of the model was calibrated prior to the installation of the model in the flume.

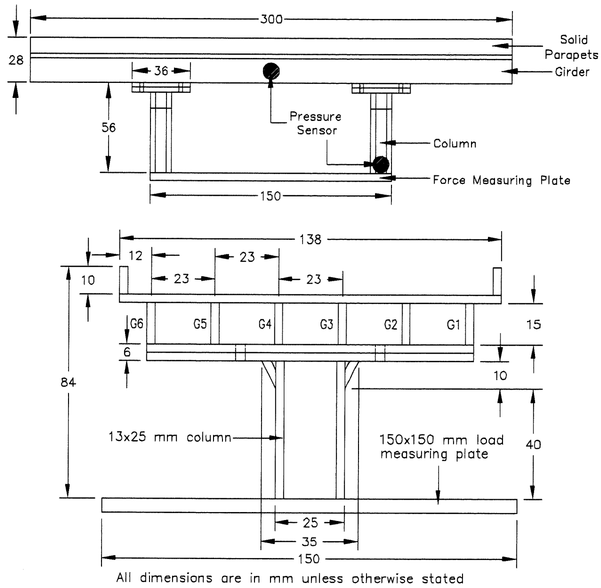

Figure 2 (a) Front and (b) Cross-Sectional Views of Bridge Model

2.4 Instrumentation and Measurement

The wave height, velocity, pressure and force were measured during the experiment by installing appropriate instrumentations. Data of wave heights and periods were collected on the DHI Wave Meter and Synthesizer. The propeller type current meter was used to measure the velocity of wave in the flume for various wave heights. The wave pressures were attained by attaching pressure gauges (SSK Type) at the locations on the bridge model where the pressures were needed to be determined. The pressure gauges were connected to the data logger, Kyowa EDS-400A Compact Recorder, where the measured physical quantities by the pressure gauge were collected and stored. The data were then converted into pressures using the calibrated factors and a spreadsheet program on a computer. The time histories of wave pressures acting on the bridge model were obtained.

A load cell was used to measure the force at the base of the bridge column. The load cell was constructed using the stain gauges mounted on the steel cylinder and placed underneath the model. The force and moment that caused changes in resistance of strain gauges were converted to electrical signals. These signals were collected and stored in the Kyowa PCD-300A Sensor Interface. By applying Wheatstone bridge relationship, the electrical resistance of the circuit was measured and the output voltage was proportional to the wave force that acted on the model.

2.5 Test Combination

The combination of six tests that consist of various placements of pressure gauges on the deck was carried out at two nominal wave heights, i.e. 6.5 cm and 8 cm. The combination of each test was repeated for at least three times. A total of 38 experimental runs were performed throughout the study.

3. RESULTS AND DISCUSSION

3.1 Wave Simulation

Figure 3 depicts the simulated wave forms at the upstream (H2) before wave breaking and the model location (H1) at the downstream of the flume. The time shown indicates the starting time of data sampling. Solitary-like waves are simulated as shown in Figure 3(a) at both nominal wave heights. This single wave travels along the flume and breaks into bore like a plunging breaker at the location near the first one-third of the flume when the still water depth becomes shallower as shown in Figure 4. The broken wave with random wave forms (Figure 3b) then travels toward the downstream of the flume and attacks the bridge model which is installed at the platform of 2.5 cm above the still water level. The tips of tsunami surges with 1.5 cm height in nearly vertical wave front are recorded at both nominal wave heights. Tsunami bore heights increases subsequently and reaches the peak.

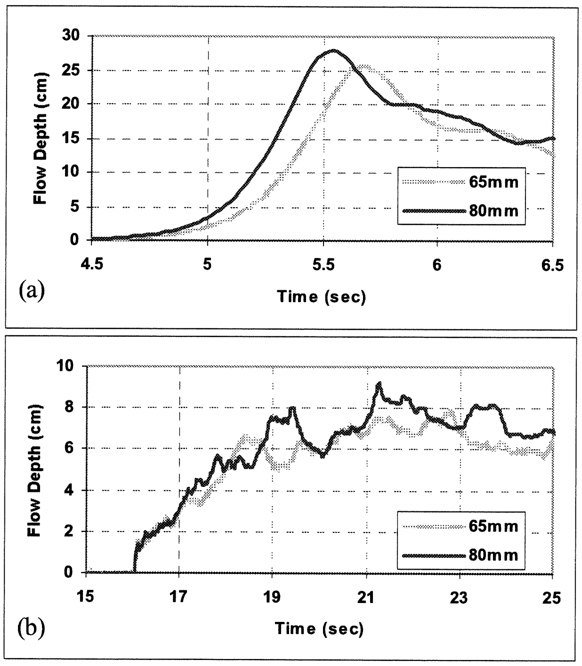

Figure 3 Wave Form at (a) H2 and (b) H1

3.2 Wave Velocity, Wave Height and Shear Forces

Time histories of flow depth, flow velocity and shear force on bridge deck are determined from the experiment.

The time histories of flow depth and velocity at the location of the model are measured without the presence of the model. Figure 5 demonstrates the relationships among these recorded parameters at both nominal wave heights. It reveals the maximum flow velocity is found at the leading tongue of the wave whereas the peak wave height reaches some times later after the wave passes through the same location. Even though with the maximum velocity at the tip of the wave, lower shear force on the deck is attained due to the relatively low wave height and small hit area at the bridge column at the initial moment of wave attack. The shear force achieves its peak value when the wave height reaches the deck level. The second peak is also observed at the later state which is mainly because of higher wave height but with lower wave velocity. This peak is not the concern of the present study.

Figure 4 Plunging Type Wave Breaking

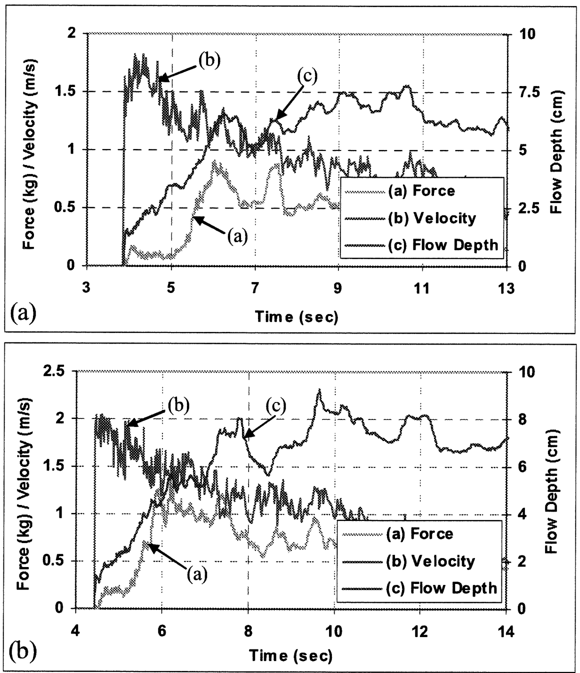

Figure 5 Correlations among Flow Depth, Velocity and Shear Forces at (a) 6.5 cm and (b) 8 cm Nominal Wave Heights

The flow velocity and flow depth can be related and expressed in terms of Froude Number (Fr). The Froude Number is defined physically as the square root of the ratio of inertia force to gravity force. In a mathematical form, it is determined as the ratio of flow velocity to the square root of product of the gravitational acceleration and flow depth. In this study, the maximum flow velocity and the maximum flow depth are used. The recorded flow velocity is considered high as the average Froude Number at both nominal wave heights of 2.27 is observed. This value is higher than one recommended by FEMA-55 (2000) if the maximum values of those parameters are adopted as the design values. However, the Froude Number is likely to be reduced as the roughness of the coastal bed is taken into consideration.

Hydrodynamic forces or usually known as drag forces are the forces caused by moving water around a structure or structural element at moderate and high velocities. Drag force is a function of flow velocity and structure geometry. It is determined from Eq. (1) as stipulated in various design guidelines (FEMA-55 2000, CCH 2000, FHWA 2001, ASCE-7, 2005). The standard formula for drag force is given by

$$F = \frac{1}{2}\rho C_d A v^2 \tag{1}$$

where A is the projected area of the body on the plane normal to the flow direction, v is the velocity of flow and C_d is the drag coefficient.

By adopting the maximum flow velocity in this study as the design velocity, the drag coefficient (C_d) of bridge deck is determined from Eq. (1) as 0.85. This value seems slightly lower than the proposed value by Iemura et al. (2007). However, as discussed in the earlier section, the peak force of the deck happens at a comparatively low flow velocity. In this context, if the corresponding velocity at the peak force is used as the design velocity, the lower Fr of 1.7 is obtained and the C_d of the deck calculated from Eq. (1) is 1.5.

Eq. (1) involves the application of the design flow velocity which makes the determination of the drag coefficient become velocity dependence. The usage of the calculated C_d from the experiment for other different cases may produce misleading results if the conditions of the experiment are not taken into account. Yeh (2007) points out the ideal way to determine the drag force from Eq. (1) is to use the maximum momentum flux from the detailed numerical simulation rather than the product of the maximum velocity and the maximum flow depth. Therefore, the appropriate C_d for the deck needs to be further investigated.

3.3 Wave Pressure

Apart from the forces, the pressures acting on the bridge structures were obtained from the pressure gauge installed at few orientations on the bridge deck. The pressure profiles at different girders which were subjected to the same wave height were measured by installing pressure gauges at the mid span of the girders. The net pressure acting on each girder was investigated by measuring the pressure at both front and back faces of the girders G1, G2 and G3. Figure 6 presents the net pressure profiles of bridge girders G1, G2 and G3 with the time history of shear forces plotted at the same time domain. The positive and negative values of net pressures represent the wave pressures acting on the front and back face of the girder, respectively. The plots show that the shear force and the pressure at the girder G1 of the bridge vary in the same trend. The girder G1 was subjected to the highest wave forces compared to other girders (girders G2 and G3) because it was exposed to the direct wave attack. The net pressures on the girders G2 and G3 are insignificant. Based on these results, the forces on the bridge deck can be estimated by assuming the pressure exerted on the vertical projection area of the deck.

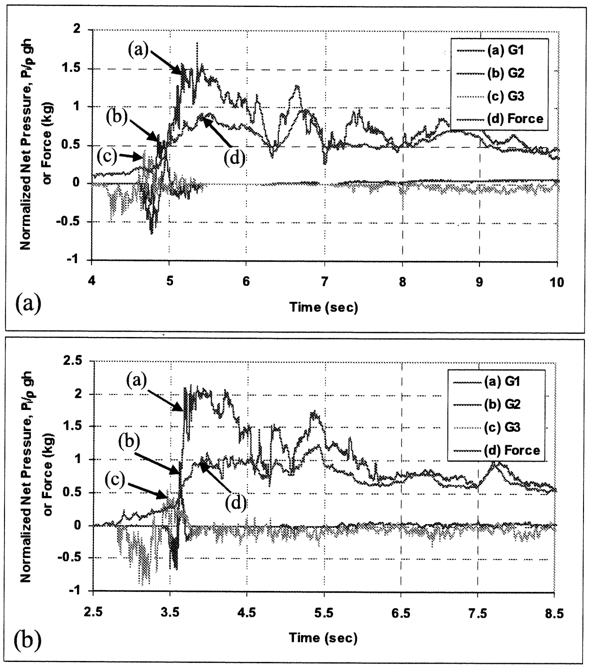

Figure 6 Net Pressure and Shear Force Time Histories for (a) 6.5 cm and (b) 8 cm Nominal Wave Heights

3.4 Comparison of Measured and Calculated Shear Forces

Due to the paucity of the tsunami wave forces on bridges, some formulations proposed for vertical wall and building type structures are adapted to be used with the case in this study based on their similarity of the consideration. For bridge deck with the ratio of its height to the wave height more than 0.5, the impulsive pressure is not effective and the formulations proposed by Asakura et al. (2002) for wave without fission, Ikeno et al. (2001) and Ikeno and Tanaka (2003) give the same results. Okada et al. (2004) suggested a specific formulation for the pressure acting on the building where the wave is allowed to flow through the bottom of the building with the height less than the inundation height based on the result of Asakura et al. (2002). This condition is close to the bridge deck study. Other than the above-mentioned studies, the results yielded from the study of Tanimoto et al. (1984) and the standard formula for drag force are also adopted for this comparison purpose.

Figure 7 presents the plot for the comparison of the computed and measured shear forces on the bridge deck for the wave height between 6.5 cm to 8.5 cm. From the chart, the forces calculated from the standard drag formula based on the values of C_d and Fr calculated from this study give almost the same values. In general, the standard drag formula, Asakura et al. (2002), Ikeno et al. (2001) and Ikeno and Tanaka (2003) overestimate the shear forces while the lower shear force is predicted by Tanimoto et al. (1984) and Okada et al. (2004). However, Tanimoto et al. (1984) gives a closer estimate for wave height of 6.5 cm and the other studies except Okada et al. (2004) show better agreement at the higher wave heights. An interesting point is the values computed from Okada et al. (2004) are distributed in the same trend as the experimental results even though the values are relatively underestimated.

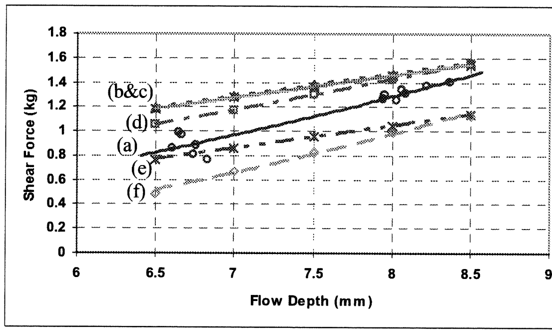

Figure 7 Comparison of Shear Force Estimation [(a) Experimental Data, (b) Drag Formula (v=2.27/(gd)^0.5, C_d=0.85), (c) Drag Formula (v=1.7/(gd)^0.5, C_d=1.5), (d) Asakura et al. (2002) & Ikeno et al. (2001) & Ikeno and Tanaka (2003), (e) Tanimoto et al. (1984), (f) Okada et al. (2004)]

4. CONCLUSIONS

Tsunami-induced forces are complex and cannot be adequately predicted theoretically. For designing tsunami resistant structures, the estimation of wave forces is vital. The physical modeling was adopted to investigate the wave forces acting on an inland bridge. The experimental results were compared with the findings obtained from previous studies which have the similar objectives to this study. The preliminary analysis reveals that some of these formulations can estimate the wave forces at a certain wave height up to a certain extent. It indicates that no single formulation can sufficiently estimate the measured wave forces on bridge deck from the experiment. Therefore, the formulation of tsunami wave forces on bridges needs to be studied further.

Acknowledgements:

The authors would like to express sincere gratitude to the JICA AUN/SEED-Net for funding this research through the Collaborative Research Project and the first author's study. The appreciations are also extended to Mr. Pairoj Anantasetakul, Dr. Tayagorn Charuchaimontri, Mr. Nuttawut Thanasisathit, Mr. Surakai Banchuen and Mr. Ha Duyen Trung for their assistance in constructing bridge model and conducting wave flume experiment.

References:

Fukui, Y., Nakamura, M., Shiraishi, H. and Sasaki, Y. (1963), "Hydraulic Study on Tsunami," *Coastal Engineering in Japan*, Japan Society of Civil Engineers, **6**, 67-82.

Cross, R.H. (1967), "Tsunami Surge Forces," *Journal of the Waterways and Harbors Division*, Proceedings of the America Society of Civil Engineers, **WW4**, 201-231.

Tanimoto, K., Tsuruya, K. and Nakano, S. (1984), " Tsunami Force on Nikonkai-Chubu Earthquake in 1983 and Cause of Revetment Damage (in Japanese)," *Proceeding of the 31st Japanese Conference on Coastal Engineering*, Japan Society of Civil Engineers.

Togashi, H. (1986), "Wave Force of Tsunami Bore on a Vertical Wall," *Science of Tsunami Hazards*, **4**(1), 25-38.

Ramsden, J.D. and Raichlen, F. (1990), "Forces on a Vertical Wall Caused by Incident Bores," *Journal of Waterway, Port, Coastal and Ocean Engineering*, American Society of Civil Engineers, **116**(5), 592-613.

Ramsden, J.D. (1996), "Forces on a Vertical Wall due ti Long Waves, Bores and Dry-Bed Surge," *Journal of Waterway, Port, Coastal and Ocean Engineering*, American Society of Civil Engineers, **122**(3), 134-141.

JPHA (1999), "Technical Standards and Commentaries of port and Harbour Facilities (in Japanese)," Japan Port and Harbour Association.

Hamzah, M.A., Mase. H. and Takayama, T. (2000), "Simulation and Experiment of Hydrodynamic Pressure on a Tsunami Barrier," *Coastal Engineering*, 1501-1507.

Mizutani, S. and Imamura, F. (2000), "Experiment on the Bore Wave Force Acting on Structures (in Japanese)," *Coastal Engineering*, Japan Society of Civil Engineers, **47**, 946-950.

FEMA-55 (2000), "Coastal Construction Manual: Principles and Practices of Planning, Siting, Designing, Constructing and Maintaining Residential Buildings in Coastal Areas," Federal Emergency Management Agency.

CCH (2000), "The City and County of Honolulu Building Code," Chapter 16, Article 11, Department of Planning and Permitting of Honolulu, Hawaii.

FHWA (2001), "Evaluating Scour at Bridges," Federal Highways Administration, U.S. Department of Transportation, Publication No. FHWA NHI 01-001 (Hydraulic Engineering Circular No. 18). 4th Edition, Authored by Richardson E.V. and Davis S.R.

Ikeno, M., Mori, N. and Tanaka, H. (2001), "Experimental Study on Tsunami Force and Impulsive Force by a Drifter under Breaking Bore Like Tsunami (in Japanese)," *Coastal Engineering*, Japan Society of Civil Engineers, **48**, 846-850.

Asakura, R., Iwase, K., Ikeya, T., Takao, M., Kaneto, T., Fujii, N. and Ohmori, M. (2002), "The Tsunami Wave Force Acting on Land Structures," *Coastal Engineering*, 1191-1202.

Mizutani, S. and Imamura, F. (2002), "Design of Coastal Structure Including the Impact and Overflow of Tsunami (in Japanese)," *Coastal Engineering*, Japan Society of Civil Engineering, **49**, 731-735.

Ikeno, M. and Tanaka, H. (2003), "Experimental Research on Tsunami Running Up on the Land and the Impact Force of Drifting Objects (in Japanese)," *Coastal Engineering*, Japan Society of Civil Engineers, **50**, 721-725.

Okada, T., Sugano, T., Ishikawa, T., Ohgi, T., Takai, S. And Hamabe, C. (2005), "Structural Design Method of Buildings for Tsunami Resistance (Proposed)," Building Technology Research Institute, The Building Center of Japan.

ASCE-7 (2005), "Minimum Design Load for Buildings and Other Structures," American Society of Civil Engineers Committee 7.

Unjoh, S. (2005), "Damage to Transporation Facilities," The Damage Induced by Sumatra Earthquake and Associated Tsunami of December 26, 2004, A Report of the Reconnaissance Team of Japan Society of Civil Engineers, 66-76.

Sheth, A., Sanyal, S., Jaiswal, A. and Gandhi, P. (2006), "Effects of the December 2004 Indian Ocean Tsunami on the Indian Mainland," *Earthquake Spectra*, Earthquake Engineering Research Institute, **22**(S3), S435-473.

Senggara, I.W., Puspito, N., Kertapati, E. and Hendarto. (2006) "Survey of Geotechinical Engineering Aspects of the December 2004 Great Sumatra Earthquake and Indian Ocean Tsunami and the March 2005 Nias-Simeulue Earthquake," *Earthquake Spectra*, Earthquake Engineering Research Institute, **22**(S3), S495-509.

Ballantyne, D. (2006), "Sri Lanka Lifelines after the December 2004 Great Sumatra Earthquake and Tsunami," *Earthquake Spectra*, Earthquake Engineering Research Institute, **22**(S3), S545-559.

Arikawa, T., Shimosako, K. and Imamura, F. (2006), "Large Model Test of Tsunami Pressure on a Seawal and on Land Structures," The Second International Workshop on Coastal Disaster Prevention – Tsunami and Storm Surge Disaster Mitigation, 2006.

Kataoka, S., Kusakabe, T. and Nagaya, K. (2006), "Wave Force Acts on a Bridge Girder Struck by Tsunami (in Japanese)," *Proceeding of the 12th Japan Earthquake Engineering Symposium*.

Iemura, H., Pradono, M.H. and Tada, T. (2007), "Experiments of Tsunami Force Acting on Bridge Models," *Journal of Structural and Earthquake Engineering*, Japan Society of Civil Engineers.

Yeh, H. (2007), "Tsunami Load Determination for On-shore Structures," *Proceedings of the 4th International Conference on Urban Earthquake Engineering*, Tokyo, Japan, 415-422.

Fifth International Conference on Urban Earthquake Engineering
March 4-5, 2008, Tokyo Institute of Technology, Tokyo, Japan

DAMAGE TO REINFORCED CONCRETE BUILDINGS WITH ELEVATED LOWER LEVELS IMPACTED BY TSUNAMI WATER-BORNE MASSIVE OBJECTS

Kavinda M. Madurapperuma [1] and Anil C. Wijeyewickrema [2]

1) Graduate Student, Department of Civil Engineering, Tokyo Institute of Technology, Japan
2) Associate Professor, Department of Civil Engineering, Tokyo Institute of Technology, Japan
ma.k.aa@m.titech.ac.jp, wijeyewickrema.a.aa@m.titech.ac.jp

Abstract: Buildings, bridges and other infrastructure located in the coastal zone are usually severely damaged due to tsunamis. To mitigate building damage, tsunami resistant building designs where the lower level is elevated by means of RC columns to allow the free flow of tsunami waves, have been recently proposed. However these columns are very vulnerable to impact due to water-borne massive objects. Tsunami field survey observations show that building destruction is often exacerbated by the impact of tsunami water-borne massive objects such as boats, shipping containers, barges, automobiles and empty storage tanks. In this paper, impact of tsunami water-borne massive objects on a RC frame structure is considered by using a fiber-based discretization model in OpenSEES. Two RC frame systems are considered, namely ordinary moment frame (OMF) and special moment frame (SMF) for low seismic risk zones and high seismic risk zones, respectively. Parametric studies are conducted to investigate nonlinear response of the RC frame systems due to impact of fishing boats. Numerical results show that in contrast to the OMF system, the SMF system can resist the impact load without strength degradation for the range of boats that are considered.

1. INTRODUCTION

Tsunami field surveys have reported severe destruction of coastal communities as a result of the Indian Ocean tsunami of December 26, 2004 (Inoue et al. 2007). In order to mitigate building damage, new tsunami resistant building design concepts have been proposed, where the lower level of the building would be elevated to allow the free flow of tsunami waves by means of RC columns (MIT Tech Talk 2005 and Okada et al. 2005). However, these buildings are very vulnerable to impact from tsunami water-borne massive objects. Failure of a single column due to such impact may lead to collapse of the building. Tsunami field survey observations show that building damage is often exacerbated by the impact of tsunami water-borne massive objects such as boats, shipping containers, barges, automobiles and empty storage tanks (Ghobarah et al. 2006). Therefore, it is of paramount importance to consider the effect of impact forces due to water-borne massive objects when designing buildings in tsunami inundation zones.

Numerical modeling of impact on structures from tsunami water-borne massive objects is complex because of the associated uncertainties in the determination of the impact force-time history. Previously the authors (Madurapperuma et al. 2007) considered impact due to shipping containers on a RC building which was designed only for gravity loads (following BS 8110-1:1997 which is used in certain Asian countries) and not for seismic loads. In addition, the hydrodynamic force which should be combined with the impact force due to water-borne massive objects for better response simulation, was not considered.

In this paper, the impact of tsunami water-borne massive objects on a RC building with elevated lower level which allows free flow of tsunami waves, is considered. Two RC frame systems are considered, namely ordinary moment frame (OMF) and special moment frame (SMF) for low seismic risk zones and high seismic risk zones, respectively (IBC 2003). The hydrodynamic force and the impact force due to fishing boats are considered in the analysis. The displacement, shear force and moment-curvature responses at the column impact section are investigated for the OMF system. Furthermore, the stress-strain behavior of cover concrete, core concrete and tension reinforcement at the impact section are studied. Finally, the behavior of the OMF and SMF systems are compared.

2. BUILDING DESCRIPTION AND STRUCTURAL DESIGN

The building considered is a three-story school building, located in a tsunami inundation zone that can also be used for vertical evacuation in the event of a tsunami. The RC building configuration is shown in Figure 1. The first floor is open space with only columns allowing free flow of tsunami waves. The building was analyzed and designed

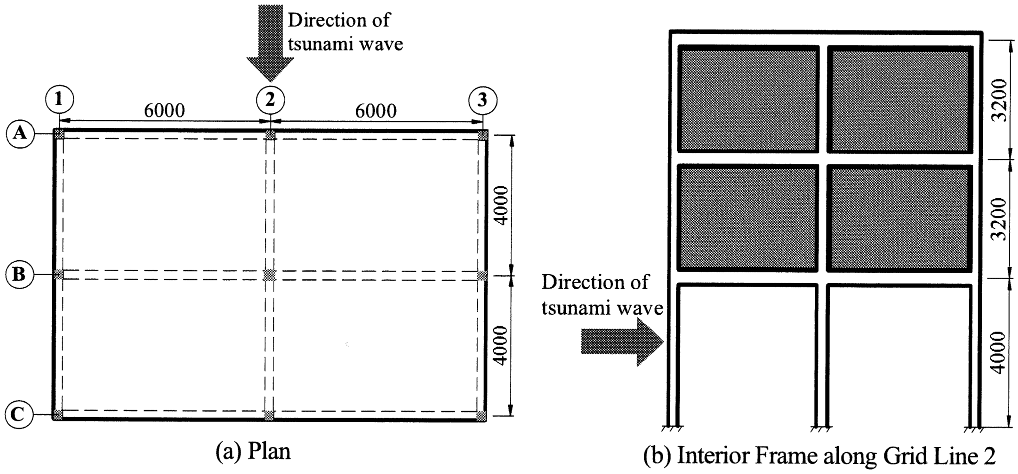

Figure 1. Building Configuration used in the Study (All Dimensions in mm)

Table 1. Section Details of Interior Frame along Grid Line 2 of Building

Frame System	Exterior Columns		Interior Columns		Beams		
	Size[a]	Steel[b]	Size[a]	Steel[b]	Size[a]	Top Steel[b]	Bottom Steel[b]
OMF	250×250	6-No. 5	300×300	8-No. 5	400×250	3-No. 5	3-No. 5
SMF	300×300	8-No. 5	300×300	8-No. 5	400×250	3-No. 5	3-No. 5

[a] All dimensions in mm. [b] Number of bars-diameter; No. 5: 16 mm.

according to the strength design method specified in ACI 318-02 (ACI 2002) using SAP2000 (2004). Design live loads and earthquake loads were determined using code provisions IBC 2003. The design live loads consisted of uniformly distributed loads of 0.96 kPa (20 psf) on roof slab and 1.91 kPa (40 psf) on floor slabs. The OMF and SMF systems are located in a low seismic risk zone (SDC A or B) and a high seismic risk zone (SDC D), respectively and designed for site class D (stiff soil) and seismic use group II (school occupancy). Normal weight concrete with a specified compressive strength of 27.6 MPa (4 ksi) and reinforcing steel with a yield strength of 414 MPa (60 ksi) were used. In this paper the water-borne boat is assumed to impact on column A2 (Figure 1(a)), hence only the frame along grid line 2 (Figure 1(b)) is analyzed. Section details for this frame are given in Table 1.

3. EVALUATION OF TSUNAMI FORCES

Some of the main forces acting on structures due to a tsunami are breaking wave force, buoyant force, hydrostatic force, surge force, hydrodynamic (drag) force and debris impact force. If the flood level is below the elevated floor level the dominant forces are the hydrodynamic force and the impact force from tsunami water-borne massive objects.

The hydrodynamic force F_H exerted on first floor columns can be evaluated from

$$F_H = \frac{1}{2}\rho C_D A u^2, \tag{1}$$

where ρ = fluid mass density, C_D = drag coefficient (2.0 for square columns), u = tsunami flow velocity, and A = wetted area of the object projected on the plane normal to the flow direction i.e., $A = hb$, in which h = flow depth and b = breadth of the object (pg 11-21, FEMA 2000). Yeh (2006) suggested that the Eq. (1) is applicable for evaluating the hydrodynamic force with a proper estimation of flow velocity. In the present study, it is necessary to calculate flow velocity for a given maximum inundation depth at the building location. The maximum inundation depth at a site of interest is evaluated from the difference between the site elevation and the runup for a given tsunami (i.e., h). Therefore, based on analytical solutions of Yeh (2006), the expression used to estimate maximum runup flow velocity on a uniformly sloping beach is

$$u = 2\sqrt{gh}. \tag{2}$$

The estimation of impact force on the structure is complex because force generated during the impact is influenced by the properties of the water-borne object, particularly its mass, velocity, and orientation on impact; and the properties of the structure itself. In this study the impact force-time history is based on the impulse-momentum approach that equates the change in linear momentum of the water-borne object and the impulse imparted on the structure during the impact. This results in the following expression for time varying impact force F_I

$$\int_0^{t_I} F_I dt = \Delta(m u^{obj}) = mu, \tag{3}$$

where m = mass of the object, u^{obj} = velocity of the object and t_I = impact duration. In Eq. (3) it is assumed that the velocity of the object before impact is the same as tsunami flow velocity u for the given inundation depth, and that linear momentum of the object after impact is zero. The impact force-time history is assumed to be of triangular shape and the impact duration is taken as $t_I = 0.1$ s following the recommendation for RC construction in CCH (2000).

4. FINITE ELEMENT MODELING OF IMPACT

Impact simulation of the two-dimensional structural frame along grid line 2 in Figure 1(b) is carried out using OpenSEES, an analysis platform that uses fiber models (Mazzoni et al. 2006, OpenSEES 2006). The frame structure is modeled using the "nonlinear beam column" element which is a distributed plasticity type element, with fiber sections accounting for the spread of plasticity along the member length. These elements take into account the spread of inelastic behavior both over the cross-section and along the deformable region of the member length. However, the stiffness and strength of floor slabs are not considered in the present study, which results in a conservative analysis. In order to accurately model the actual behavior of the column, in the area that impact takes place, the deformable height of the column is divided into a number of elements. Material properties for concrete and reinforcing bars are defined through conventional stress-strain models available in OpenSEES. The concrete material response is simulated using the *Concrete02* material model. The model proposed by Mander et al. (1988) is used to estimate core concrete strength accounting for the amount of confinement provided by transverse reinforcements. The *Steel02* material model is used to simulate the steel material response. The material properties for nonlinear material modeling of concrete and reinforcing bars are given in Madurapperuma (2007).

The gravity loads on the frame are evaluated according to roof and floor tributary areas. The hydrodynamic force on a column is evaluated using Eqs. (1) and (2), and applied on first floor columns as a uniform load from the column base to the tsunami flood level. Equations (2) and (3) are used to calculate the maximum impact force based on which the impact force-time history is obtained. The impact force is applied at the maximum flood level assuming that the boat carried by tsunami impacts the column at the tsunami flood level.

5. NUMERICAL ANALYSIS AND RESULTS

Nonlinear dynamic analysis is carried out with the modified Newton-Raphson iterative scheme and the Newmark method for time integration with $\beta = 0.25, \gamma = 0.5$. The Rayleigh damping parameters are calculated assuming a 5% damping ratio. The time step is taken as $\Delta t = 0.0005$ s for all analyses. The nonlinear response of the impacted column is investigated using different masses of fishing boats impacting at maximum tsunami flood levels of 2.0 m and 3.0 m above ground level, with impact initiated at $t = 0$. The hydrodynamic force which acts before time $t = 0$ for these tsunami flood levels are given in Table 2. In the present analysis fishing boats that could impact on buildings located in tsunami hazard zones are considered to have masses of 1250 kg, 1625 kg and 2025 kg and the maximum impact forces are given in Table 3. The response of the column at the impacted cross section is studied.

Table 2. Hydrodynamic Force (kN) for Different Columns and Water Depths

Water Depth from GL (m)	Flow Velocity (m/s)	Section Size (mm^2)	
		250×250 (OMF)	300×300 (SMF)
2.0	6.26	20.19	24.23
3.0	7.67	45.40	54.48

Table 3. Maximum Impact Force (kN) for Different Masses and Water Depths

Water Depth from GL (m)	Boat Velocity (m/s)	Mass of Boat		
		1250 kg	1625 kg	2025 kg
2.0	6.26	156.60	203.59	253.70
3.0	7.67	191.80	249.34	310.72

The impact on column A2 of the OMF system is considered first. In Figure 2(a) the column displacement at 2.0 m above ground level attains a peak value of 27.4 mm after 0.0715 s due to impact of the 2025 kg boat. Beyond this time the OpenSEES program is unable to compute compatible element forces and deformations for the element just below the node at which impact acts, due to extensive inelastic deformation at the impacted point. It is expected that the spalling of cover concrete followed by the yielding and buckling of steel reinforcements cause this large inelastic deformation. However, lesser damage can be seen due to impact of the 1625 kg boat at 2.0 m above ground level which results in a peak displacement of approximately 14 mm and a constant displacement of approximately 5 mm which is not equal to that before impact (i.e., displacement due to hydrodynamic force only). In Figure 2(b) where the impact is at 3.0 m above ground level, peak displacement is smaller than that when impact is at 2.0 m above ground level due to the 2025 kg boat. The shear force in Figure 3(a) indicates a sudden drop with extensive shear failure at the impacted section causing strength degradation due to impact of the 2025 kg boat. The failure starts 0.05 s when the maximum impact force is acting on the impacted point. In Figure 3(b) where the impact is at 3.0 m above ground level the shear force increases with increase in impact force up to a certain magnitude and then a sudden drop of shear force can be seen for the 2025 kg boat. However, the impacted column can resist the shear force even after the impact indicating lesser damage at 3.0 m above ground level compared to that at 2.0 m above ground level due to impact

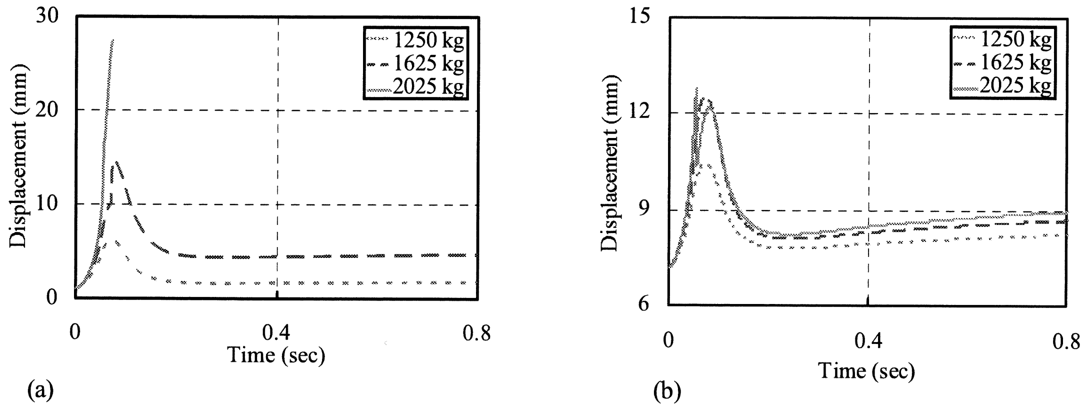

Figure 2. Displacement Response at Impacted Sections of Column A2 of OMF at Different Heights above GL: (a) 2.0 m and (b) 3.0 m

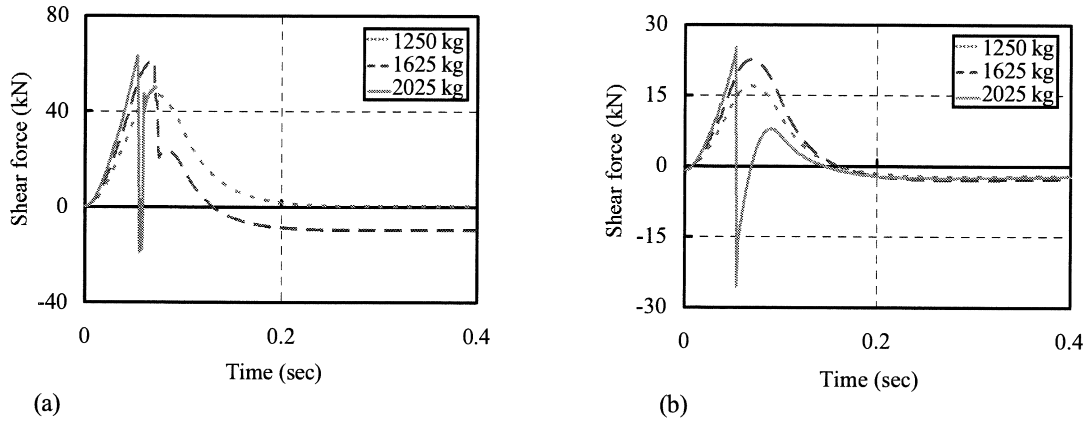

Figure 3. Shear Response at Impacted Sections of Column A2 of OMF at Different Heights above GL: (a) 2.0 m and (b) 3.0 m

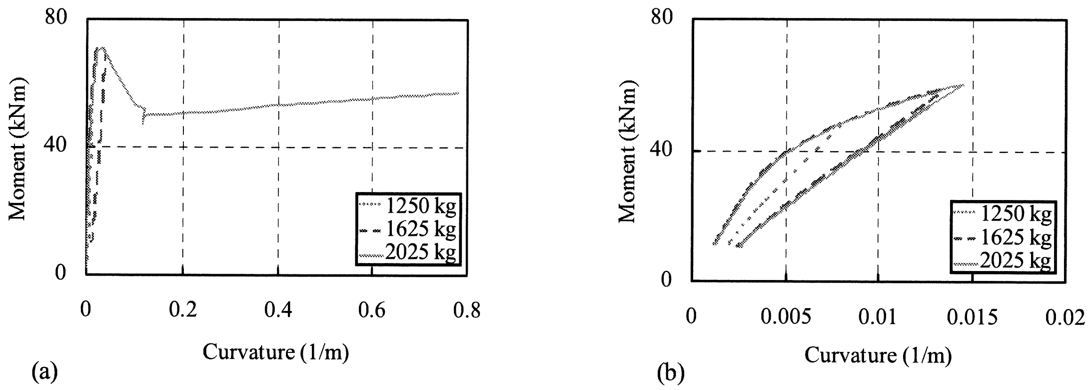

Figure 4. Moment-Curvature Response at Impacted Sections of Column A2 of OMF at Different Heights above GL: (a) 2.0 m and (b) 3.0 m

of 2025 kg boat. To investigate plastic hinge formation and flexural behavior, moment-curvature response of impacted sections at 2.0 m and 3.0 m above ground level are considered (Figure 4). When the 2025 kg boat impacts the column at 2.0 m above ground level, the moment drops after the spalling of the cover concrete with further increase in curvature forming a plastic hinge at the impacted section with extensive inelastic behavior. The reinforcements at the impacted section could have buckled or ruptured with further increase in curvature. However, in Figure 4(b) it can be seen that the inelastic behavior in the moment-curvature response at the section 3.0 m above ground level is very small compared to that of 2.0 m above ground level.

The stress-strain behavior of the cover concrete at extreme fibers in compression, the core concrete at extreme

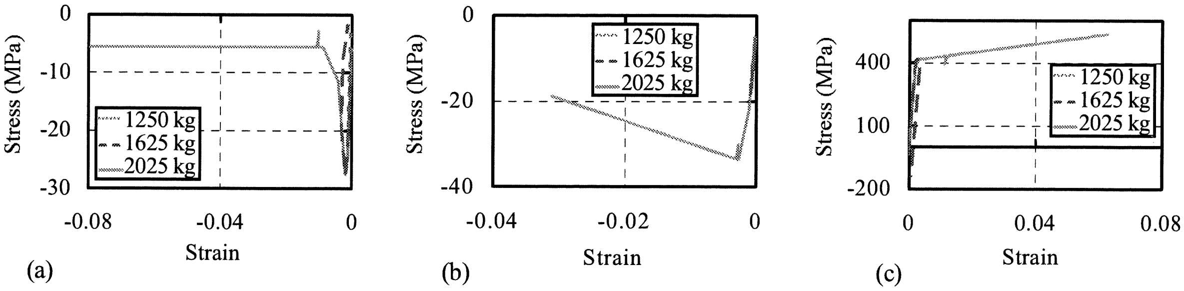

Figure 5. Stress-Strain Behavior of Column A2 of OMF at Impacted Section 2.0 m above GL: (a) Cover Concrete at Extreme Fiber in Compression, (b) Core Concrete at Extreme Fiber in Compression and (c) Longitudinal Bar in Tension

fibers in compression, and the longitudinal bar in tension are plotted in Figure 5, for the impact at 2.0 m above ground level. When column displacement reaches its peak value due to impact of the 2025 kg boat (Figure 2(a)), the cover concrete stress at the extreme fiber in compression has already exceeded the compressive strength −27.579 MPa and reaches its crushing strength of −5.516 MPa. This starts spalling of cover concrete at the compression side followed by yielding of tension reinforcements at the impacted section. However, the cover concrete stress due to impact of 1625 kg boat does not deteriorate to the crushing strength although it reaches to the compressive strength (Figure 5(a)). The stress in the core concrete compression fibers reaches to its compressive strength −33.646 MPa and deteriorates to stress of −18.8 MPa with a strain −0.003 (Figure 5(b)). The final stress of −18.8 MPa, which is 3.8 times the initial stress of −4.99 MPa before impact, shows degradation of the axial load carrying capacity due to impact of the 2025 kg boat. However, stress-strain response in core concrete behaves elastically due to impact of 1250 kg and 1625 kg boats. From Figure 5(c) it can be seen that the longitudinal bar in tension has yielded and the maximum strain is 0.06 which is 30 times the yield strain, due to impact of the 2025 kg boat. The computed stress-strain behavior of the cover concrete, core concrete and longitudinal bar shows failure of the impacted section in column A2 of the OMF system when impacted by the 2025 kg boat at 2.0 m above ground level.

The effectiveness of the SMF system compared to the OMF system for impact resistance is considered next. The comparison is carried out by investigating the response of column A2 at a section 2.0 m above ground level (i.e., for a maximum tsunami flood level of 2.0 m) when impacted by the 2025 kg boat. Figure 6(a) shows displacement response for the two different systems. Use of the SMF system reduced the maximum displacement at the impacted point by approximately 80% when compared to the use of the OMF system. The computed displacement response for the SMF system indicates that, after impact the displacement is nearly equal to that before impact (i.e., displacement due to hydrodynamic force only). Since the shear capacity of the SMF system is higher than that of the OMF system a sudden drop in shear force cannot be seen in Figure 6(b) for the SMF system. In Figure 6(c) the moment capacity at the impact section of the SMF system is increased by 20% without forming a plastic hinge compared to maximum moment reached in the OMF system. This behavior is also seen in Figures 7(a) and 7(b) where the stress in the cover concrete and core concrete at the extreme fiber is below the compressive strength, and the strain in the tension reinforcement in Figure 7(c) is in the elastic range. Therefore, it is seen that the SMF system performs very well compared to the OMF system when impacted by boats up to 2025 kg.

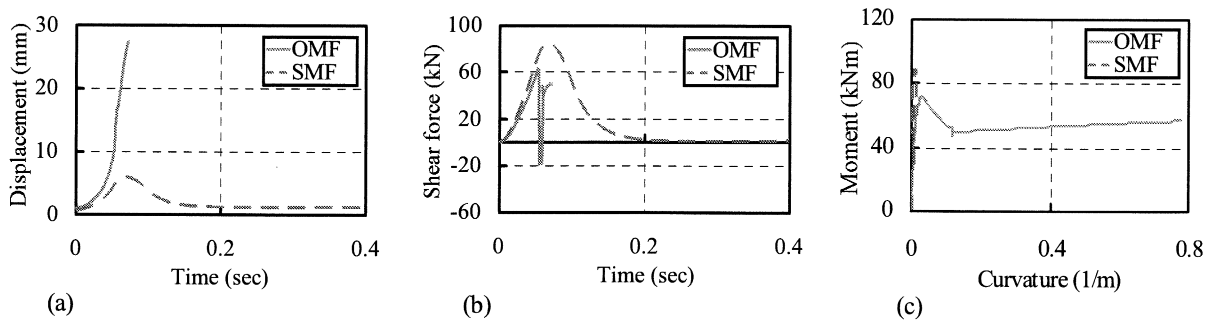

Figure 6. Response of Column A2 at Impacted Section 2.0 m above GL when Impacted by 2025 kg Boat: (a) Displacement (b) Shear and (c) Moment-Curvature

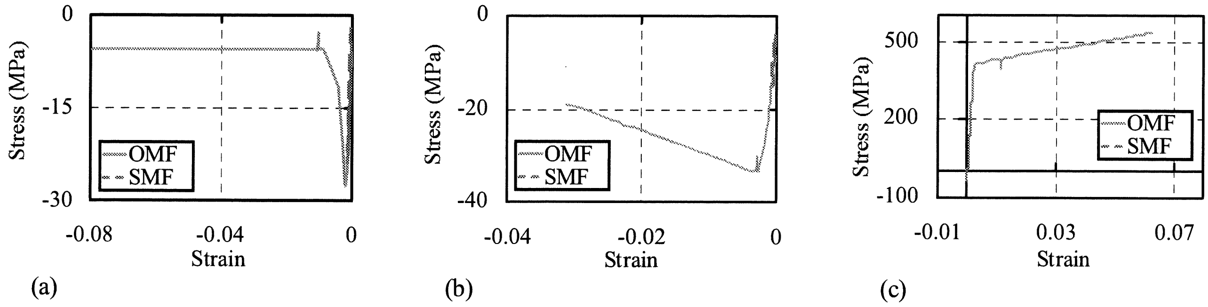

Figure 7. Stress-Strain Behavior at a Impacted Section 2.0 m above GL when Impacted by 2025 kg Boat: (a) Cover Concrete at Extreme Fiber in Compression, (b) Core Concrete at Extreme Fiber in Compression and (c) Longitudinal Bar in Tension

3. CONCLUSIONS

The impact of tsunami water-borne massive objects on a 2D RC frame structure is considered using a fiber-based discretization model in OpenSEES. It is found that impact at the mid section of the column is more critical than impact close to the floor level. Numerical results show that the OMF system is safe when impacted by boats with a mass less than or equal to 1250 kg. But the OMF system suffers extensive damage when impacted by 1625 kg and 2025 kg boats. However, the SMF system can resist the impact load without strength degradation for the boat masses considered i.e., the SMF system which provides high seismic resistance will also provide sufficient resistance against impact up to 2025 kg boats. Hence for RC buildings in tsunami hazard zones, SMF systems will provide better resistance to impact due to water-borne massive objects than OMF systems.

Therefore, it can be concluded that impact may cause devastating damage to the critical structural members of the building according to the mass of water-borne objects and the structural system. Hence, one of the impact mitigation strategies for critical buildings that may be used for tsunami evacuation purposes is to locate the building in an area that will have a low probability of impact by tsunami water-borne massive objects. Furthermore, orientation of the impact, uniformly distributed impacts and multiple impacts can also be considered for further analysis of impact on structures from tsunami water-borne massive objects.

Acknowledgements:

The first author gratefully acknowledges a Monbukagakusho scholarship from the Japanese government. The authors are very grateful to Prof. Tatsuo Ohmachi, COE Program Leader of Center for Urban Earthquake Engineering (CUEE), Tokyo Institute of Technology, and Prof. Kohji Tokimatsu, COE Program Sub-leader of CUEE, for their advice and support. Financial support from CUEE is gratefully acknowledged.

References:

American Concrete Institute (ACI). (2002), "Building Code Requirements for Structural Concrete," ACI 318-02, Farmington Hills, Mich.

BS 8110 (1997), "Structural Use of Concrete," Part 1: Code of Practice for Design and Construction, British Standard Institution.

CCH. (2000), "Regulations within Flood Hazard Districts and Developments adjacent to Drainage Facilities in the Revised Ordinances of Honolulu," City and Country of Honolulu Building Code, Department of Planning and Permitting of Honolulu Hawaii, Honolulu, Hawaii, Chapter 16, Article 11.

Federal Emergency Management Agency (FEMA). (2000), "FEMA Coastal Construction Manual," Publication number FEMA55, Washington, D.C.

Ghobarah, A., Saatcioglu, M. and Nistor, I. (2006), "The Impact of the 26 December 2004 Earthquake and Tsunami on Structures and Infrastructure," *Engineering Structures*, **28**, 312-326.

Inoue S., Wijeyewickrema, A. C., Matsumoto, H., Miura, H., Gunaratna, P., Madurapperuma, K. M., and Sekiguchi, T. (2007), "Field Survey of Tsunami effects in Sri Lanka due to the Sumatra-Andaman Earthquake of December 26, 2004," *Pure and Applied Geophysics*, **164**(2-3), 395-411.

International Building Code (IBC). (2003), International Code Council, Inc., Country Club Hills, Illinois.

Madurapperuma, K. M. (2007), "Impact Response of Buildings due to Tsunami Water-Borne Massive Objects," M.Eng. Thesis, Dept. of Civil Engineering, Tokyo Institute of Technology, Tokyo, Japan.

Madurapperuma, M. A. K. M., Wijeyewickrema, A. C., and Shakya, K. (2007), "Dynamic Impact of Tsunami Waterborne Massive Objects on Structures," *Proceedings of fourth International Conference on Urban Earthquake Engineering*, Tokyo, Japan, 475-482.

Mander, J. B., Priestly, M. J. N. and Park, R. (1988), "Theoretical Stress-Strain Model for Confined Concrete," *Journal of Structural Engineering*, ASCE, **114**(8), 1804-1826.

Mazzoni, S., McKenna, F., Scott, M. H., Fenves, G. L. (2006), "OpenSEES Command Language Manual," <http://opensees.berkeley.edu/OpenSees/manuals/HTML/> (Jan. 6, 2007).

MIT Tech Talk. (2005), "Waves will Flow through MIT Team's New Homes." Tech Talk Serving the MIT Community, **49**(30), <http://web.mit.edu/newsoffice/2005/saferhouse.html> (Dec. 6, 2006).

Okada, T., Sugano, Ishikawa, T., Ohgi, T., Takai, S. and Hambe, C. (2005), "Structural Design Method of Buildings for Tsunami Resistance (proposed)," The Building Center of Japan, 15 pp.

OpenSEES. (2006), "Open system for earthquake engineering simulation," <http://opensees.berkeley.edu> (Jan. 6, 2007).

SAP2000. (2004), "Integrated Finite Element Analysis and Design of Structures," Computers and Structures, Inc., Berkeley, Calif.

Yeh, H. (2006), "Maximum Fluid Forces in the Tsunami Runup Zone," *Journal of Waterway, Port, Coastal, and Ocean Engineering*, ASCE, **132**(6), 496-500.

Fifth International Conference on Urban Earthquake Engineering
March 4-5, 2008, Tokyo Institute of Technology, Tokyo, Japan

SEISMIC RESPONSE OF BRIDGE WITH C-BENT RC COLUMN BY DISTRIBUTED HYBRID SIMULATION

Yoshikazu Takahashi[1], Stephen A. Mahin[2], Gregory L. Fenves[2], and Hirokazu Iemura[3]

1) Associate Professor, Disaster Prevention Research Institute, Kyoto University, Japan
2) Professor, Dept. of Civil and Environmental Engineering, University of California, Berkeley, USA
3) Professor, Department of Urban Management, Japan
yos@catfish.dpri.kyoto-u.ac.jp, mahin@berkeley.edu, fenves@berkeley.edu, iemura@catfish.kuciv.kyoto-u.ac.jp

Abstract: To evaluate a seismic response of bridge systems, it is important to adopt the most appropriate model for each component. In this study, the seismic response of a bridge with a C-bent and a single RC pier and a steel pier is evaluated. Whereas the single RC pier is modeled by the fiber model, the C-bent RC and the steel pier are modeled by the hybrid experimental models because any numerical models cannot take into account their strong nonlinear behavior. OpenSees and OpenFresco are used to conduct the international hybrid simulation. As the results of the international hybrid simulation between Kyoto Univ. and UC Berkeley, the nonlinear seismic response of the bridge system can be obtained and the distributed hybrid simulation is found to be a powerful tool for the evaluation of structural systems.

1. INTRODUCTION

C-bent columns are usually constructed in an urban expressway because available space is very limited in urban area. Not only eccentric vertical load but also the coupling of flexural, shear and torsion deformation applies C-bent columns. Therefore the residual deformation tends to accumulate in the eccentric side (Kawashima et al. 2003). Since a bridge consists of multiple piers, girders and bearings, the behavior of one component has an interaction to others and it is important to evaluate the seismic performance of the bridge as the system, including multiple piers. For the simulation, it is important to adopt the most appropriate model for each component. Hybrid simulation was developed to take into account the seismic behavior of a structure, including components that are difficult to model numerically. Recently a distributed hybrid simulation method has been very actively developed, and this hybrid simulation is now one realistic option to evaluate the whole structural systems.

2. BRIDGE SYSTEM

2.1 Two-Span Continuous Bridge

The bridge system in this study is a two-span continuous bridge (Figure 1). It consists of a RC single pier (P1), RC C-bent pier (P2) and steel single pier (P3). The height of these piers is 10 m. The girder of 60 m is supported by elastomeric bearings.

2.2 Defects of Pure Numerical Model

The objective of this study is to evaluate the seismic behavior of the bridge system in the longitudinal direction. Although the input earthquake motion is inputted in the longitudinal direction, a 3-dimensional model has to be used because P2 is the C-bent type. In this study, the piers and the girder are modeled by line-type models and the bearings are modeled by springs. The beam of the C-bent pier is modeled by a rigid beam. When the girder responds due to the earthquake, P1 and P3 deforms flexural in the longitudinal direction. Therefore P1 can be modeled by a fiber model, and P3 can be modeled by a spring model with steel material model. However P2 deforms not only flexural but also torsional. The most critical defect of the pure numerical model of this bridge is that there is no appropriate numerical model for the coupling of flexural and torsional behavior of RC structure. In order to evaluate the bridge system, another model of P2 is needed.

3. FRAMEWORK OF DISTRIBUTED HYBRID SIMULATION

3.1 Distributed Hybrid Simulation System

Hybrid simulation provides a versatile, realistic and cost-effective method for simulating the seismic response of structural systems experimentally. A hybrid simulation is a combination of physical simulation of a specimen in a laboratory, using standard servo-controlled actuators, with computational simulation of the system to provide information about performance due to earthquake ground motion. The hybrid simulation is very powerful system but since it need to control experimental equipments, very simple analytical models were used in the previous studies. The conventional hybrid systems cannot collaborate the

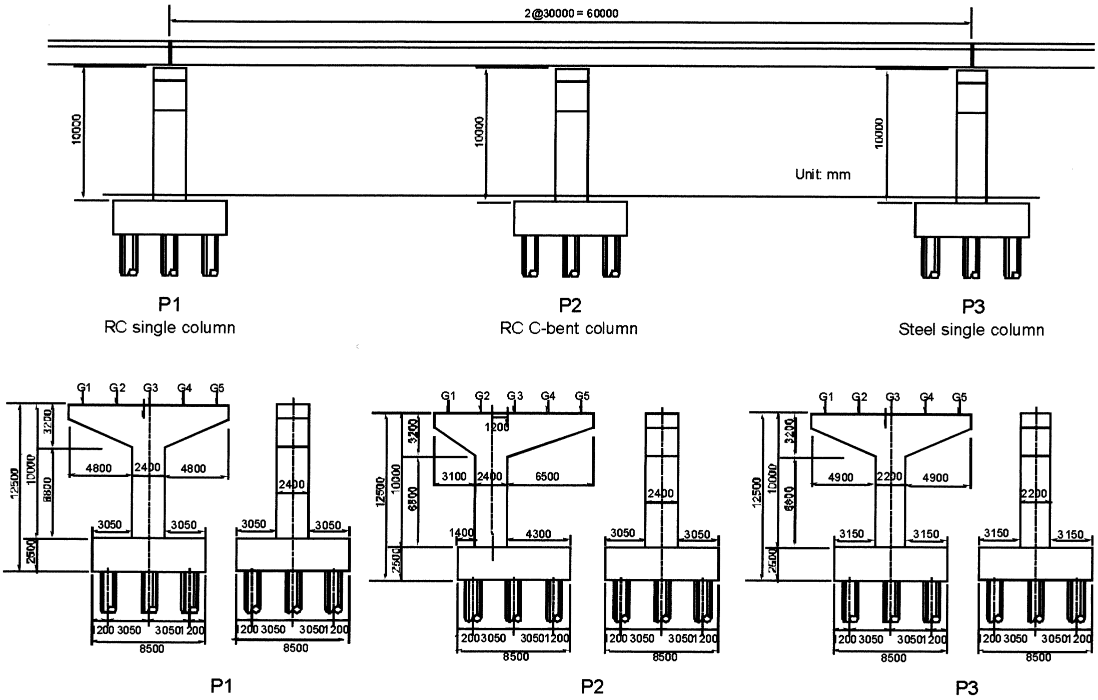

Figure 1 Bridge System

existing powerful numerical analysis and cannot control multiple experimental equipments. The more flexible software for the hybrid simulation had been requested.

3.2 OpenFresco

The Open Framework for Experimental Setup and Control (OpenFresco) is a software system for hybrid simulation of structural systems. For the earthquake engineering user, OpenFresco is a practical and easy to use software package that allows a wide variety of hybrid simulation algorithms, laboratory and control systems, experimental setups, and computational simulation models to be combined for a specific hybrid simulation. For the researcher or developer interested in new hybrid simulation methods, the architecture of OpenFresco provides a great deal of flexibility, extensibility, and re-usability through an object-oriented software framework. The design, implementation, and proof-of-concept of OpenFresco was described in Takahashi and Fenves 2006. Schellenberg and Mahin 2006 provided a complete summary of the progress using OpenFresco for a range of hybrid simulation applications.

An important aspect of OpenFresco is that the finite element software uses a general form of an element, termed the Generic-Client Element. The user does not have to create an experimental element in the finite element software when the Generic-Client Element is used. The Generic-Client Element can be easily implemented into any finite element software that allows user-defined elements. This feature allows OpenFresco to be used with a wide variety of computational software packages, such as LS-DYNA® or ABAQUS®. For developers and advanced users, experimental elements can be created for more sophisticated applications, but for most users interested in hybrid simulation, the Generic-Client Element should be sufficient.

OpenFresco v 2.5 can be downloaded from OpenFresco web site at NEESit repository (OpenFresco2008)

4. DISTRIBUTED HYBRID SIMULATION OF BRIDGE SYSTEM

4.1 Hybrid Modeling

Since P1 is expected to be flexural during earthquake, the fiber model with stress-strain relationships of concrete and steel bar is adopted. Since P2 is expected to behave complicatedly, the hybrid experimental model is adopted. The coupling of flexural and torsional deformation automatically satisfies the deformation of the experimental C-bent RC column specimen. P3 can be modeled by the spring model, but it is also modeled by the hybrid experimental model to take into account the bucking and/or breakage of the steel pier. The C-bent RC specimen of P2 was tested at Kyoto University, Japan, and the steel single specimen was tested at nees@berkeley, USA. The other components are modeled as linear system.

80% and 100% JR Takatori records (NS), Kobe Earthquake 1995, are inputted in the longitudinal direction of the bridge systems. The analytical time interval is set to 0.01 sec and the equation of motion is solved by the alpha-OS method.

4.2 Simulation System

(a) Specimens

A C-bent RC column at Kyoto University has a square cross-section of 320mm and a height of 1255mm. A steel column at nees@berkeley consists of a replaceable nonlinear

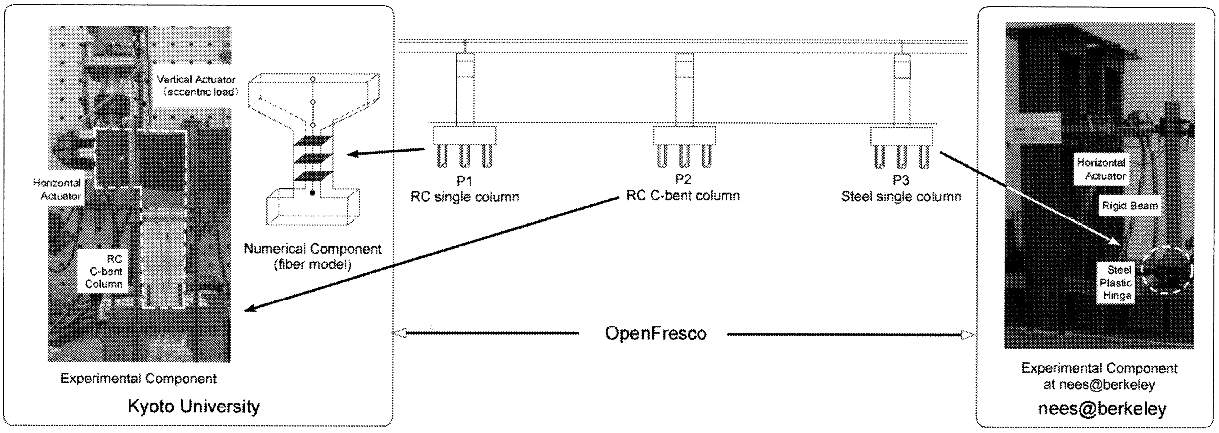

Figure 2 Hybrid model of Bridge Systems

steel plastic hinge with a rigid column.

(b) Hardware

Two actuators are used for loading at Kyoto University: One applies the eccentric vertical load and the other applies the horizontal deformation. These actuators are controlled by analog signal from National Instruments AD/DA board in the experimental computer. The vertical load is 90 kN. One actuator is used at nees@berkeley for loading of the deformation and controlled by digital signal from xPC target system.

(c) Software

OpenFresco is used for managing the distributed hybrid simulation. TCP/IP network is used for communication between Kyoto University and nees@berkeley. Open System for Earthquake Engineering System (OpenSees) is adopted as the numerical program. OpenSees is an object-oriented framework for numerical seismic analysis (Fenves et al. 2004) and developed at the Pacific Earthquake Engineering Research Center, USA. OpenSees is adopted as the numerical program of NEES (Network for Earthquake Engineering Simulation), USA and now widely used worldwide.

4.3 Results of Hybrid Simulations

The load-deformation hysteresis loops of piers and the displacement response of the girder in case of 80% input are shown in Figure 3. Torsional cracks were observed in the RC specimen and the hysteresis loop of P2 show narrow inverted-S shape because of the coupling of flexural and torsional deformation. Although P3 shows relatively large nonlinearity, it behave stable.

Following 80% input test, 100% input test was conducted (Figure 4). Since P2 had been already damaged by 80% input test, the hysteresis loop shows much narrower than before. And also the plastic hinge of P3 broke and the hysteresis loop changed into the small loop. Even in such a strong nonlinear case, the distributed hybrid test can be conducted stable.

In these tests, the time for solving the equation, communication between USA and Japan, controlling the test setups and measuring data during the analytical time step 0.01 sec. could be completed within 1.0 sec. As the results, the 20-second simulation could be 30-minute hybrid simulation. This test speed is almost the same as the conventional hybrid test at local test facility.

5. CONCLUSIONS

In this study, the seismic response of two span continuous bridge with C-bent column are examined by distributed hybrid simulation. It can be concluded as follows:

1 The hybrid simulation with OpenFresco and OpenSees can simulate the complicated structural system with the most appropriate model. In this study, the RC single column was modeled by the fiber model and the RC C-bent and the steel single column are modeled by the hybrid experimental models. As the results, the coupling of flexural and torsional behavior of the C-bent pier and the breakage of the Steel columns can be evaluated.

2 Since this framework is very stable even in these strong nonlinear cases, the distributed hybrid simulation is found to be a powerful tool for the evaluation of structural systems.

Acknowledgements:

This research was partially supported by the Japan Ministry of Education, Culture, Sport, Science, and Technology, Grant-in-Aid for Young Scientists (A), 16686029, 2004-2007 and the bridge program in NEES/E-Defense Collaboration Research, NIED, Japan.

References:

Kawashima, K., Watanabe, G. et al. (2003), "Seismic performance of C-bent columns based on a cyclic loading test," *Journal of JSCE*, **I-65**(745), 171-189.

Takahashi, Y. and Fenves, G.L. (2006), "Software framework for distributed experimental-computational simulation of structural systems," *Earthquake Engineering and Structural Dynamics*, **35**,

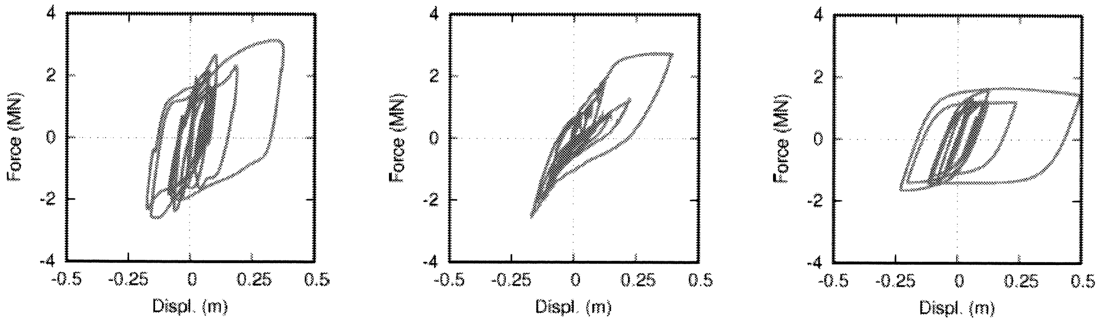

(a) P1 Pier (b) P2 Pier (c) P3 Pier

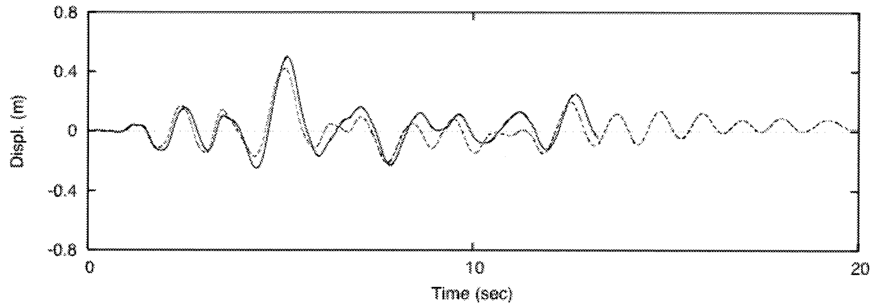

(d) Displacement Response of Girder

Figure 3 Results of Hybrid Simulation (80% input test)

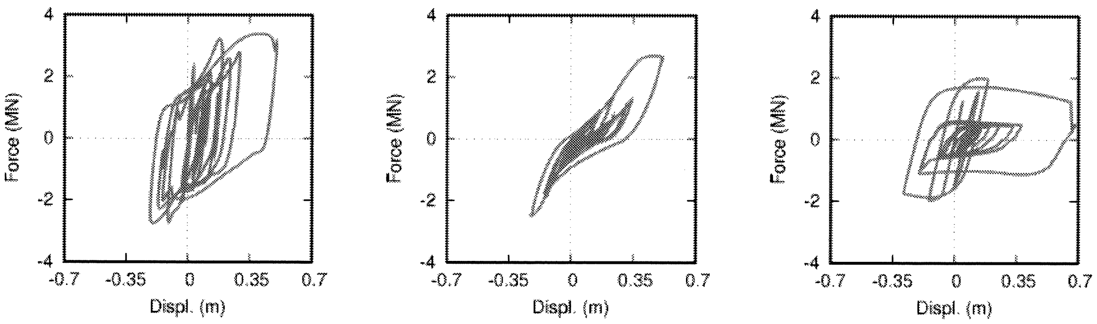

(a) P1 Pier (b) P2 Pier (c) P3 Pier

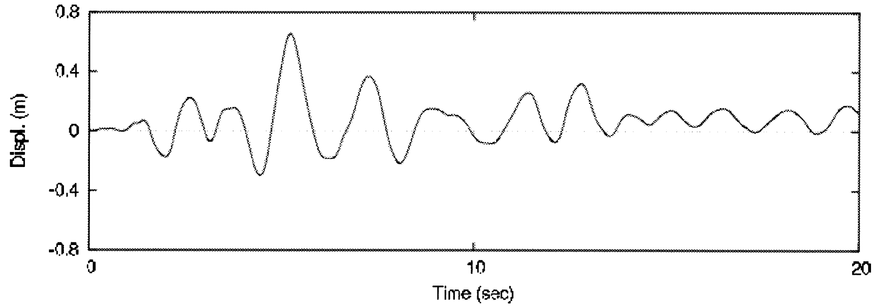

(d) Displacement Response of Girder

Figure 4 Results of Hybrid Simulation (100% input test)

267-291.

Schellenberg, and Mahin, S.A. (2006), "Application of an Experimental Software Framework to Hybrid Simulation of Structures through Collapse," *Proc. of 1st European Conference on Earthquake Engineering and Seismology, paper number 1221.*

Fenves, G.L., McKenna, F., Scott, M.H., and Takahashi, Y.. (2004), "An object-oriented software environment for collaborative network simulation," *Proc. of 13th World Conference on Earthquake Engineering, paper number 1492.*

OpenFresco web site. (2006), https://neesforge.nees.org/project/openfresco/.

Fifth International Conference on Urban Earthquake Engineering
March 4-5, 2008, Tokyo Institute of Technology, Tokyo, Japan

NONLINEAR DYNAMIC ANALYSIS OF ISOLATED BRIDGES WITH UNSEATING PREVENTION DEVICES

Tzu-Ying Lee[1)] and, Po-Hung Chen[2)] and Ren-Zuo Wang[3)]

1) Assistant Professor, Department of Civil Engineering, National Central University, Taiwan
2) Graduate Student, Department of Civil Engineering, National Central University, Taiwan
3) Associate Researcher, National Center for Research on Earthquake Engineering, Taiwan
tylee@ncu.edu.tw, c0937823804@gmail.com, rzwang@ncree.org.tw

Abstract: This study is aimed to analyze the isolated bridges with unseating prevention devices which may exhibit nonlinear dynamic behavior under large earthquakes. Since the Vector Form Intrinsic Finite Element (VFIFE) has the superior in managing the engineering problems with material nonlinearity, discontinuity, large deformation, large displacement and arbitrary rigid body motions of deformable bodies, it is selected to be the analysis method in this study. However, the VFIFE is in its infant stage as compared to the conventional Finite Element. There are still a number of elements and analysis method to be developed. Two new VFIFE elements and Rayleigh damping analysis method are herein developed for analyzing the target bridges. Through numerical simulation of examples and comparison with the Finite Element analysis, the developed elements and Rayleigh damping analysis method are verified to be feasible and accurate. The results also confirm that the VFIFE can be extended to investigate the extreme functions of the isolators, columns and unseating prevention devices and to predict the collapse situation of target bridges.

1. INTRODUCTION

Isolated bridges have been extensively used to mitigate the induced seismic forces by a shift of natural period. However, the trade-off is that the deck displacement becomes excessively large when subjected to a ground motion with large intensity or unexpected characteristics. Such a large displacement may result in the unseating of the deck. Therefore, unseating prevention devices are important for isolated bridges in particular (Kawashima and shoji 2000). Lately, modern bridge seismic design has been developed toward the seismic performance design on whole bridges as well as their elements. Understanding of the performance of the components of isolated bridges, such as bearings, unseating prevention devices, columns, under extreme condition shall be favorable to determine the goal of performance. In this paper, a new nonlinear structural dynamic analysis method is studied to simulate the dynamic behavior of the isolated bridges under large earthquakes.

The Vector Form Intrinsic Finite Element (VFIFE), a new computational method developed by Ting et al. (2004), is adopted in this study because the VFIFE has the superior in managing the engineering problems with material nonlinearity, discontinuity, large deformation, large displacement and arbitrary rigid body motions of deformable bodies. Since the VFIFE is in its infant stage, there are still a number of undeveloped elements. To analyze isolated bridges with unseating prevention devices, two kinds of new elements, an element with a gap or a hook and a bilinear element, are developed in this study. Additionally, the Rayleigh damping is first considered in VFIFE. Because it is not necessary to assemble the global stiffness matrix in the computational procedure of the VFIFE, structural damping was regarded as proportional to mass matrix only.

2. LINK ELEMENTS

This study is aimed to analyze the isolated bridges with unseating prevention devices under extreme earthquakes. Two new nonlinear VFIFE elements, an element with a gap or a hook and a bilinear element, are herein developed to simulate the unseating prevention devices, isolators and columns which may undergo nonlinear behavior to large earthquakes.

2.1 Elements with a Gap or a Hook

The unseating prevention devices are generally with non-working length before they are triggered to function. There are two categories of the unseating prevention devices, compression and tension. The compression device, such as a stopper, is idealized as an element with a gap, whereas the tension device is idealized as an element with a hook, showed in Figure 1. The mathematical model of force versus displacement of the plane compression device is as follows:

$$\begin{Bmatrix} f_x^s \\ f_y^s \\ m_z^s \end{Bmatrix} = \begin{Bmatrix} 0 \\ 0 \\ 0 \end{Bmatrix} \quad \text{if } \mathbf{d}^s + \mathbf{d}^{open} > 0$$

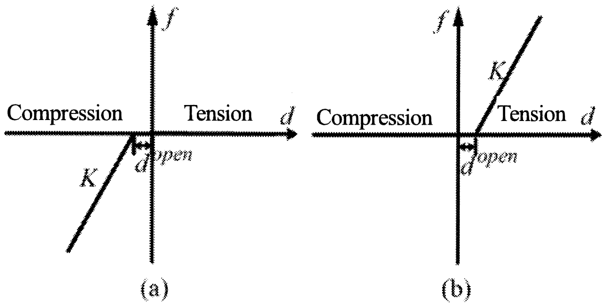

Figure 1 (a) an Element with a Gap (b) an Element with a Hoop

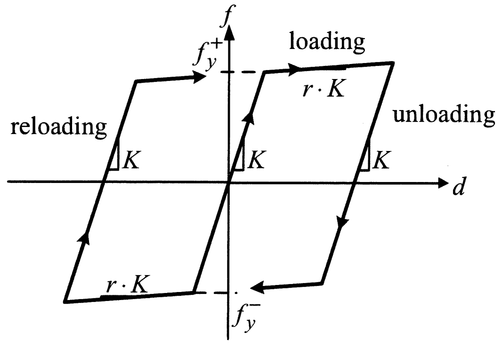

Figure 2 Model of Bilinear Elements

$$\begin{Bmatrix} f_x^s \\ f_y^s \\ m_z^s \end{Bmatrix} = \begin{bmatrix} K_x & 0 & 0 \\ 0 & K_y & 0 \\ 0 & 0 & K_z \end{bmatrix} \begin{Bmatrix} d_x^s + d_x^{open} \\ d_y^s + d_y^{open} \\ \theta_z^s + \theta_z^{open} \end{Bmatrix} \quad \text{if } \mathbf{d}^s + \mathbf{d}^{open} < 0 \tag{1}$$

where $d_x^{open}, d_y^{open}, \theta_z^{open}$ are the openings in direction x and y, and rotational direction z, respectively, which should be larger or equal to zero. Similarly, the mathematical model of force versus displacement of the plane tension device is as follows:

$$\begin{Bmatrix} f_x^s \\ f_y^s \\ m_z^s \end{Bmatrix} = \begin{Bmatrix} 0 \\ 0 \\ 0 \end{Bmatrix} \quad \text{if } \mathbf{d}^s - \mathbf{d}^{open} < 0$$

$$\begin{Bmatrix} f_x^s \\ f_y^s \\ m_z^s \end{Bmatrix} = \begin{bmatrix} K_x & 0 & 0 \\ 0 & K_y & 0 \\ 0 & 0 & K_z \end{bmatrix} \begin{Bmatrix} d_x^s - d_x^{open} \\ d_y^s - d_y^{open} \\ \theta_z^s - \theta_z^{open} \end{Bmatrix} \quad \text{if } \mathbf{d}^s - \mathbf{d}^{open} > 0 \tag{2}$$

2.2 Bilinear Elements

The first design principle of isolated bridges is the appropriate utilization of isolators and dampers to shift the main periods of vibration and increase the energy-dissipation capacity of the structures (Priestley et al. 1996). High damping rubber bearings and lead-rubber bearings, which have both the functions, are commonly utilized. Both bearings can be idealized by a bilinear model as shown in Figure 2. In addition, it has been shown in the past study that the columns of isolated bridges may exhibit nonlinear behavior under extreme earthquakes (Lee and Kawashima 2007). The bilinear model can also be used to idealize reinforced concrete columns and steel columns. It must be carefully managed in constructing the bilinear element of VFIFE is the loading, unloading and reloading paths.

3. RAYLEIGH DAMPING

In the present developed VFIFE analysis, the structural damping of multi-degree-of-freedom systems is regarded as proportional to mass matrix only. The reason is that it is not necessary to assemble the global stiffness matrix in the computational procedure of the VFIFE. However, the structural damping of MDOF systems is generally idealized by using Rayleigh damping which is proportional to both mass matrix and stiffness matrix. In this study, the Rayleigh damping is first considered and the analytical method is developed in VFIFE.

The first step in VFIFE analysis is to construct a discrete model for a continuous structure. It is noted that the continuous element mass must be lumped into the adjoining nodes. The equations of motion are established at every node for all degrees of freedoms by using Newton's Second Law of Motion. Applying the time-stepping method, the discrete motion equations is as follows:

$$\mathbf{M}\ddot{\mathbf{u}}_i + \mathbf{f}_{Di} + \mathbf{f}_{Si} = \mathbf{P}_i \tag{3}$$

where $\ddot{\mathbf{u}}_i$ is the acceleration vector at time i; $\mathbf{f}_{Di}, \mathbf{f}_{Si}, \mathbf{P}_i$ are the damping force, resisting force and applied nodal force vectors, respectively.

The central difference method, an explicit time integration method, was proposed to solve the equations of motion Eq. (3) by Ting et al. (2004). The acceleration $\ddot{\mathbf{u}}_i$ and velocity $\dot{\mathbf{u}}_i$ can be approximated as

$$\ddot{\mathbf{u}}_i = \frac{\mathbf{u}_{i+1} - 2\mathbf{u}_i + \mathbf{u}_{i-1}}{(\Delta t)^2} \qquad \dot{\mathbf{u}}_i = \frac{\mathbf{u}_{i+1} - \mathbf{u}_{i-1}}{2\Delta t} \tag{4}$$

where Δt is the incremental time.

Assume that the structural damping is simulated as Rayleigh damping. The damping force $\mathbf{f}_{Di}$ is denoted as

$$\mathbf{f}_{Di} = (a_0\mathbf{M} + a_1\mathbf{K})\dot{\mathbf{u}}_i \tag{5}$$

Instead of calculating resisting forces $\mathbf{f}_{Si}$ by using stiffness matrix $\mathbf{K}$ as in the traditional finite element analysis, the resisting forces are calculated through assuming the nodal displacements to obtain the element resisting forces and then assembling the related element resisting forces in VFIFE analysis. Therefore, it is needed to deal with the damping forces $a_1\mathbf{K}\dot{\mathbf{u}}_i$ particularly.

Since all element stiffnesses are assumed to be constant on each time interval $t_i \le t \le t_{i+1}$, the damping force $a_1\mathbf{K}\dot{\mathbf{u}}_i$ can be rewritten as $a_1\dot{\mathbf{f}}_{Si}$, the rate of change of element resisting force. Consider if $\dot{\mathbf{f}}_{Si}$ is approximated by central difference, it is impossible to obtain the element resisting force $\mathbf{f}_{S(i+1)}$ at time $i+1$. Thus it is proposed to approximate the $\mathbf{f}_{Si}$ only by using the rate of change of element resisting force on the time interval $t_{i-1} \le t \le t_i$ as

$$\dot{\mathbf{f}}_{Si} = \frac{\mathbf{f}_{Si} - \mathbf{f}_{S(i-1)}}{\Delta t} \tag{6}$$

Substituting Eqs. (4) and (6) into Eq. (5) yields

$$\mathbf{f}_{Di} = a_0\mathbf{M}\left(\frac{\mathbf{u}_{i+1} - \mathbf{u}_{i-1}}{2\Delta t}\right) + a_1\left(\frac{\mathbf{f}_{Si} - \mathbf{f}_{S(i-1)}}{\Delta t}\right) \tag{7}$$

Then, substitution of Eqs. (4) and (7) into Eq. (3) gives

$$\hat{\mathbf{K}}\mathbf{u}_{i+1} = \hat{\mathbf{P}}_i \tag{8}$$

where

$$\hat{\mathbf{K}} = \left[\frac{1}{(\Delta t)^2} + \frac{a_0}{2\Delta t}\right]\mathbf{M} \tag{9}$$

$$\begin{aligned}\hat{\mathbf{P}}_i &= \mathbf{P}_i - \mathbf{f}_{Si} - a_1\left(\frac{\mathbf{f}_{Si} - \mathbf{f}_{S(i-1)}}{\Delta t}\right) \\ &\quad + \frac{2\mathbf{M}}{(\Delta t)^2}\mathbf{u}_i - \left(\frac{1}{(\Delta t)^2} - \frac{a_0}{2\Delta t}\right)\mathbf{M}\mathbf{u}_{i-1}\end{aligned} \tag{10}$$

The above process successfully introduces Rayleigh damping into the VFIFE analysis so that the VFIFE can be applied to analyze more practical and broad engineering problems.

4. NUMERICAL EXAMPLES

4.1 Verification of Rayleigh Damping Analysis

A two-story reinforced concrete building, shown in

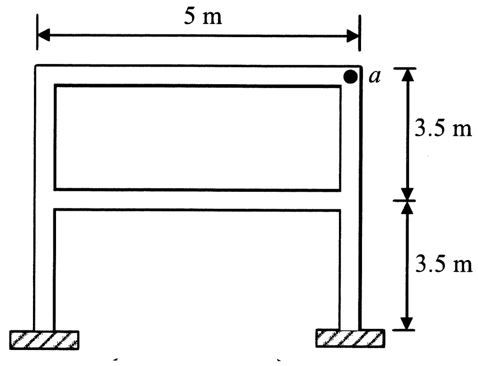

Figure 3 A Two-story Reinforced Concrete Building

Figure 3, is selected to verify the accuracy of the developed Rayleigh damping analysis in VFIFE. The beams are of 5 m span and the sections are $25\ \text{cm} \times 30\ \text{cm}$ ($\text{B} \times \text{H}$). Each story is 3.5 m high. The column sections are $30\ \text{cm} \times 30\ \text{cm}$. Assume that the damping ratios of the first and second modes of the structure are identical to be 15%. The input ground motions were measured at JMA Kobe Observatory in the 1995 Kobe, Japan earthquake shown in Figure 4(a). The VFIFE analytical results are compared with those by the conventional Finite Element analysis. Figure 4(b) presents the comparison of the displacement time history at the right corner of the top floor, indicated by point a. It is observed that both results by the VFIFE and the Finite Element (SAP2000) are almost identical. Therefore the developed Rayleigh damping analysis in VFIFE is feasible and accurate.

4.2 An Isolated Bridge with Unseating Prevention Devices

A three-span isolated bridge with a total length of 3@40 m = 120m, as shown in Figure 5, is analyzed to verify the accuracy of the developed elements and to investigate the seismic responses under extreme earthquake. The columns and isolators are assumed to be perfect elastoplastic and

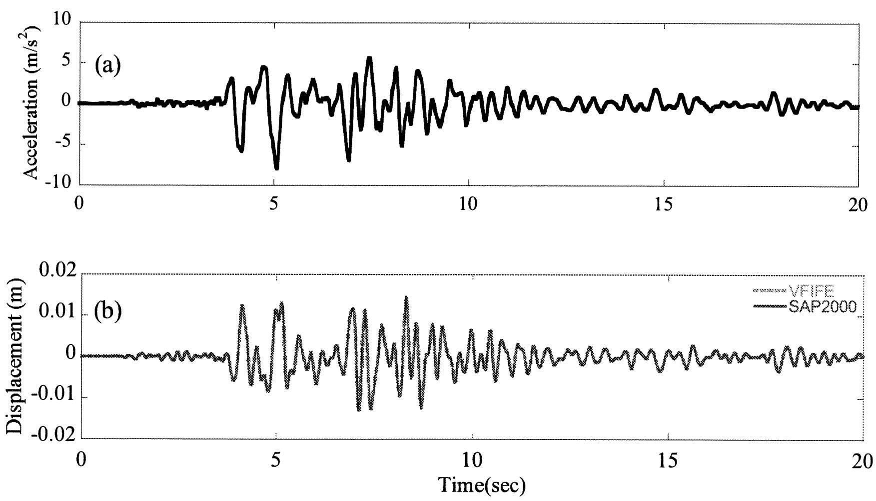

Figure 4 (a) JMA Kobe Ground Motion (b) Displacement Time History at point a

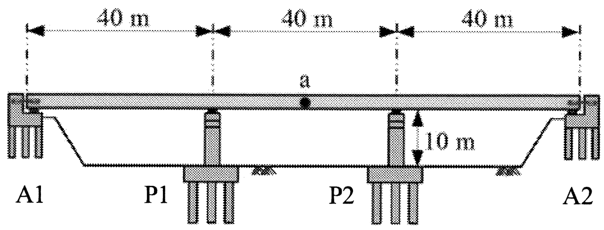

Figure 5 An Isolated Bridge with Unseating Prevention Devices

bilinear elastoplastic, respectively. The unseating prevention devices are installed at both end abutments. The devices are simulated as elements with a hook. The damping ratios of the system are assumed 5% for the first and second modes. In simulation, the isolated bridge is subjected to near-field ground motions recorded at Sun-Moon Lake in the 1999 Chi-Chi, Taiwan earthquake.

Also to verify the accuracy of the VFIFE the analytical results are compared with those by the conventional Finite Element analysis. Figure 6 shows the comparison of the displacement at the midpoint of the deck, the force of unseating prevention device at the A1 and A2 abutments. The hysteretic loops of the isolators at A1 abutment and P1 column and the bottom of P1 column are compared in Figure 7. It is revealed that both results by the VFIFE and the Finite Element (SAP2000) agree very well and that the developed VFIFE elements are accurate. Accordingly, the VFIFE analysis can be extended to take the fracture into account for simulating the ultimate situation.

5. CONCLUSIONS

Since the VFIFE has the advantages in managing the engineering problems with material nonlinearity, discontinuity, large deformation, large displacement, arbitrary rigid body motions of deformable bodies and even fracture and collapse, it is adopted in this study to analyze the isolated bridges with unseating prevention devices which exhibit nonlinear dynamic behavior under large earthquakes. As compared with the well-developed Finite Element analysis, the VFIFE analysis is in its infant stage. There are still a number of elements to be developed. Two new elements, elements with a gap or a hook and bilinear elements, and Rayleigh damping analysis in VFIFE are developed in this study for analyzing the target structures. The numerical simulation of examples verifies the feasibility and accuracy of the developed elements and Rayleigh

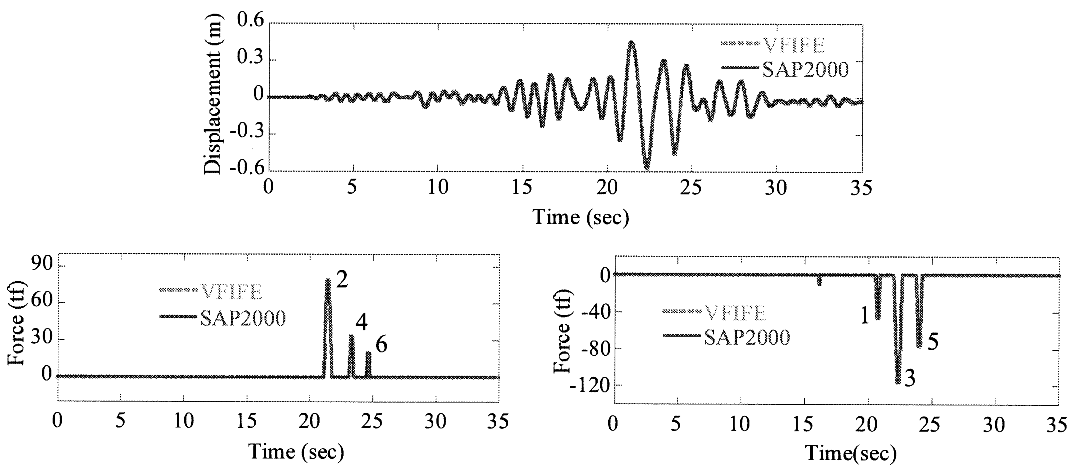

Figure 6 (a) The Displacement at Midpont of Deck (b) the force of Unseating Prevention Device at Abutment A1 (c) the force of Unseating Prevention Device at Abutment A2

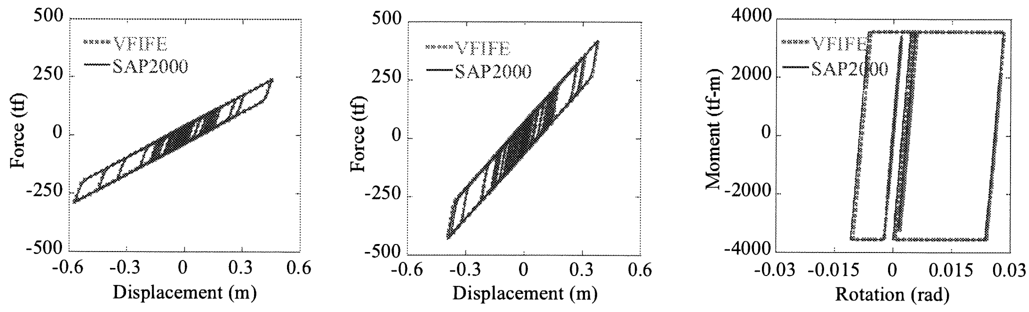

Figure 7 The Hysteretic Loops of the (a) Isolator at A1 (b) Isolator at P1 (c) Bottom of Column P1

damping analysis method through the comparison with the conventional Finite Element method. The results also confirm that the VFIFE can be extended to investigate the extreme functions of the isolators, columns and unseating prevention devices and to predict the collapse situation of target bridges.

References:

Kawashima, K. and Shoji, G. (2000), "Effect of Restraints to Mitigate Pounding Between Adjacent Decks Subjected to a Strong Ground Motion," *12th World Conference on Earthquake Engineering*, Paper No. 1435 (CD-ROM), Auckland, New Zealand.

Priestley, M. J. N., Seible, F. and Calvi, G. M. (1996), "Seismic Design and Retrofit of Bridges," John Wiley & Sons, New York, USA.

Ting, E. C., Shih, C. and Wang, Y. K. (2004), "Fundamentals of a Vector Form Intrinsic Finite Element: Part I. Basic Procedure and a Plane Frame Element," *Journal of Mechanics*, **20**(2), 113-122.

Lee T.-Y. and Kawashima K. (2007), "Semiactive Control of Nonlinear Isolated Bridges with Time Delay," *Journal of Structural Engineering*, ASCE, **133**(2), 235-241

Fifth International Conference on Urban Earthquake Engineering
March 4-5, 2008, Tokyo Institute of Technology, Tokyo, Japan

MULTI-DIMENSIONAL HYBRID SIMULATION USING MIXED LOAD AND DISPLACEMENT CONTROL: APPLICATION TO SKEW RC BRIDGES

Narutoshi Nakata[1), Bill F. Spencer, Jr.[2), and Amr S. Elnashai[2)

1) Assistant Professor, Dept. of Civil Engineering, Johns Hopkins University, USA
2) Professor, Dept. of Civil and Environmental Engineering, University of Illinois at Urbana-Champaign, USA
nakata@jhu.edu, bfs@uiuc.edu, aelnash@uiuc.edu

Abstract: This paper presents an application of the multi-dimensional hybrid simulation using mixed load and displacement control to the seismic assessment of complex structural systems. Mixed load and displacement control is critical to impose simultaneously the gravity load in the axial direction and the earthquake-induced displacement in other directions on test specimen. Following a description of the versatile mixed load and displacement control strategy, experimental setup for the multi-dimensional hybrid simulation that consists of six actuator self-reaction loading system is introduced. As an example of complex structural systems, skew RC bridge is investigated using the hybrid simulation method where an RC pier is experimentally tested and the rest of the bridge structure is computationally analyzed. The experimental results show that the multi-dimensional hybrid simulation with versatile mixed load and displacement control capability is a promising approach that provides a reliable means for evaluation of the seismic performance of large and complex structural systems.

1. INTRODUCTION

Hybrid simulation is an effective method for the assessment of seismic performance of structures. It combines laboratory testing, computational simulation, and numerical integration of the equations of motion at each time step to simulate dynamic response of structures. Because critical sections that are difficult to model or exhibit complex behavior are usually experimentally evaluated, simulation results provide more accurate response of structures than those in numerical analysis. Compared to quasi-static loading tests where the input loading on the structural components is predetermined, hybrid simulation can be seen as a sophisticated component test in which responses are evaluated at system level accounting for the input ground motion. Since its initial development (Takanashi et al. 1975), a lot of effort has been made towards improvement and verification of test methods, including numerical integration algorithms, etc (Mahin et al. 1985 and Shing et al. 1996).

While hybrid simulation has been used for evaluation of the seismic performance of a variety of structures, applications to date have been limited to planner loading and to relatively simple structural systems. In contrast, actions during strong earthquakes are three-dimensional and continuously varying. The seismic performance of structures under strong earthquakes is a highly coupled cause (action) –effect (behavior) problem. Thus, assessment of such multi-dimensionally varying actions is essential for understanding of the seismic behavior of structural components, especially for those in large and complex structural systems.

This paper reports a multi-dimensional hybrid simulation using mixed displacement and load control. As an example of complex structural systems, skew RC bridge is studied where one of the RC piers is experimentally tested and the rest of the bridge structure is computationally analyzed. Mixed displacement and load control is utilized to impose simultaneously the gravity load in the axial direction and the earthquake-induced displacement in other directions on the experimentally tested RC pier. Seismic behavior of the RC pier under spatial loading (i.e., axial, shear, flexural, and torsional loadings) is experimentally investigated.

2. MIXED LOAD AND DISPLACEMENT CONTROL

2.1 Introduction

Gravity load effects have been carefully considered in structural tests by many researchers (Kawashima et al. 2004, Lynn et al. 1996, and Pan et al. 2005). However, their test setups are combination of load-controlled actuators in the vertical direction and displacement-controlled actuators in the lateral direction of the specimen. Under large deformation, lateral actuators will have a force component in the vertical direction that should be considered.

Mixed load and displacement control in this study is defined as a combined control with either a load or displacement control in each Cartesian axis at a loading point. If a control system has coupling between actuator and Cartesian coordinates (i.e., x, y, z, $\theta_x, \theta_y, \theta_z$), mixed load and displacement control, including gravity loading and lateral displacement control, cannot be achieved with independent control of each actuator. The challenge is due to the contribution of unknown displacements in load-controlled actuator and unknown forces in displacement-controlled actuator to the target mixed load and displacement. In other words, mixed load and displacement commands cannot be explicitly decomposed into each actuator command without geometric approximation. Versatile and generally-applicable mixed load and displacement control algorithms need to be developed to take into account instantaneous and spatial coupling in the control system.

2.2 Control Algorithm

The proposed mixed load and displacement control method incorporates load-to-displacement command conversions in a mixed load and displacement control feedback loop. Figure 1 shows the main block diagrams for the proposed control method. The conversion is based on the incremental iteration process employing the Broyden (1965) update of the stiffness Jacobian of the tested structure. Because all actuator servo loops are closed with displacement output, the control system is extremely robust for mixed-mode control.

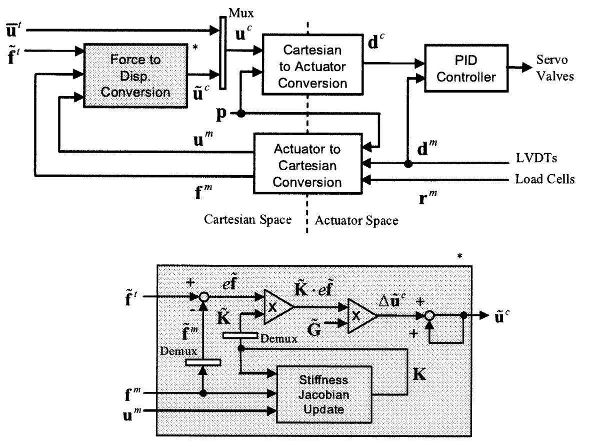

Figure 1. Block Diagram for the Mixed Load and Displacement Control: (a) Outer Loop, and (b) Force-to-Displacement Conversion

2.3 Iterative Procedure for the Mixed Load and Displacement Convergence

In the proposed method, target mixed load and displacement are achieved through a process that comprises directional and iterative ramps. First, the directional ramp is executed with an updated command in the displacement controlled axes whereas the command in the load control axes remains that at the end of the previous step. Then, iterative ramps are repeated with an updated command in the load controlled axes until convergence to the target load is achieved. After each ramp, an approximation of the stiffness Jacobian is updated using the Broyden's method. A single step in the mixed mode control procedure is described below:

(i) Directional Ramp at Step N:

$$\bar{\mathbf{u}}^{c}_{N(0)} = \bar{\mathbf{u}}^{t}_{N} \tag{1}$$

$$\tilde{\mathbf{u}}^{c}_{N(0)} = \tilde{\mathbf{u}}^{c}_{N-1} \tag{2}$$

where $\bar{\mathbf{u}}^{c}_{N(0)}$ and $\tilde{\mathbf{u}}^{c}_{N(0)}$ are the command displacement at the directional ramp in the N-th step in displacement- and load-controlled axes, respectively. $\bar{\mathbf{u}}^{t}_{N}$ is a target displacement in displacement controlled axes at step N. $\tilde{\mathbf{u}}^{c}_{N-1}$ is a command displacement in load controlled axes at step $N-1$.

(ii) Update the Stiffness Jacobian After the Directional Ramp:

$$\mathbf{K}_{N(0)} = \mathbf{K}_{N-1} + \frac{\left(\Delta\mathbf{f}^{m}_{N(0)} - \mathbf{K}_{N-1}\cdot\Delta\mathbf{u}^{m}_{N(0)}\right)\cdot\left(\Delta\mathbf{u}^{m}_{N(0)}\right)^{\mathrm{T}}}{\left\|\Delta\mathbf{u}^{m}_{N(0)}\right\|^{2}} \tag{3}$$

where $\mathbf{K}_{N(0)}$ is a updated stiffness Jacobian after the directional ramp at the N-th step. $\Delta\mathbf{u}^{m}_{N(0)}$ and $\Delta\mathbf{f}^{m}_{N(0)}$ are the measured incremental displacement and load vectors, respectively, and are written as follows:

$$\Delta\mathbf{u}^{m}_{N(0)} = \mathbf{u}^{m}_{N(0)} - \mathbf{u}^{m}_{N-1} \tag{4}$$

$$\Delta\mathbf{f}^{m}_{N(0)} = \mathbf{f}^{m}_{N(0)} - \mathbf{f}^{m}_{N-1} \tag{5}$$

Eq. 3 is known as Broyden update of the Jacobian. It satisfies the following relationship.

$$\Delta\mathbf{f}^{m}_{N(0)} = \mathbf{K}_{N(0)}\Delta\mathbf{u}^{m}_{N(0)} \tag{6}$$

(iii) Iterative Ramp at i-th Iteratoin at Step N:

$$\bar{\mathbf{u}}^{c}_{N(i)} = \bar{\mathbf{u}}^{t}_{N} \tag{7}$$

$$\tilde{\mathbf{u}}^{c}_{N(i)} = \tilde{\mathbf{u}}^{c}_{N(i-1)} + \tilde{\mathbf{G}}\cdot\tilde{\mathbf{K}}_{N(i-1)}\cdot\left(\tilde{\mathbf{f}}^{t}_{N} - \tilde{\mathbf{f}}^{m}_{N(i-1)}\right) \tag{8}$$

where $\tilde{\mathbf{G}}$ is a mixed-mode gain matrix in the load-controlled axes and $\tilde{\mathbf{K}}_{N(i-1)}$ is the updated stiffness Jacobian after the i-th iteration at the N-th step in the load controlled axes.

(iv) Update the Stiffness Jacobian After the i-th Iterative Ramp:

$$\mathbf{K}_{N(i)} = \mathbf{K}_{N(i-1)} + \frac{\left(\Delta\mathbf{f}^{m}_{N(i)} - \mathbf{K}_{N(i-1)}\cdot\Delta\mathbf{u}^{m}_{N(i)}\right)\cdot\left(\Delta\mathbf{u}^{m}_{N(i)}\right)^{\mathrm{T}}}{\left\|\Delta\mathbf{u}^{m}_{N(i)}\right\|^{2}} \tag{9}$$

where $\mathbf{K}_{N(i)}$ is an updated stiffness Jacobian after the i-th iterative ramp at the N-th step. The displacement and force increment vector $\Delta\mathbf{u}^{m}_{N(i)}$ and $\Delta\mathbf{f}^{m}_{N(i)}$ are written as follows:

$$\Delta\mathbf{u}^{m}_{N(i)} = \mathbf{u}^{m}_{N(i)} - \mathbf{u}^{m}_{N(i-1)} \tag{10}$$

$$\Delta\mathbf{f}^{m}_{N(i)} = \mathbf{f}^{m}_{N(i)} - \mathbf{f}^{m}_{N(i-1)} \tag{11}$$

(v) Convergence Evaluation:

$$\left|\tilde{\mathbf{f}}^{t}_{N} - \tilde{\mathbf{f}}^{m}_{N(i)}\right| \le e\tilde{\mathbf{f}} \tag{12}$$

where $e\tilde{\mathbf{f}}$ is a load tolerance vector in the load controlled axes. If Eq. 12 is not satisfied, the process goes back to (iii) and is repeated until the convergence criterion is satisfied. Following convergence, the process goes to the next step $N+1$ with following relationships:

$$\tilde{\mathbf{u}}^{c}_{N} = \tilde{\mathbf{u}}^{c}_{N(i)} \tag{13}$$

$$\tilde{\mathbf{f}}^{m}_{N} = \tilde{\mathbf{f}}^{m}_{N(i)} \tag{14}$$

Because of the updating feature, the proposed method takes into account material inelasticity and geometric nonlinearity and other abrupt effects, such as cracking, in the control process. Therefore, the proposed method is robust and efficient in terms of the load control in multi-axial control systems. Most importantly, with small increments in the directional ramp, this method is capable of producing the desired mixed load and displacement load history even for path-dependent structures.

3. EXPERIMENTAL SETUP

3.1 Six Actuator Self-Reaction Loading System

The state-of-the-art six actuator self-reaction loading system, referred to as Load and Boundary Condition Box (LBCB) at the University of Illinois at Urbana-Champaign (UIUC), is used as a platform for implementing the developed control strategies and hybrid simulation in the following section. Figure 2 (a) and (b) show the full-scale and 1/5th-scale LBCBs, respectively. Both units are servo hydraulic systems each consisting of a reaction box, a loading platform and six actuators with a servo valve, load cell and LVDT. The specifications of each LBCB are summarized in Table 1.

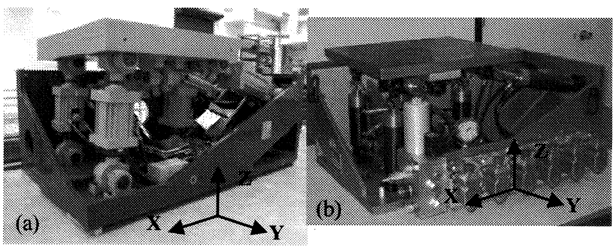

Figure 2. Load and Boundary Condition Boxes (LBCB): (a) Full-scale LBCB, and (b) 1/5th-scale LBCB

Table 1. Specifications of Full- and 1/5th-scale LBCBs

Full-scale LBCB					
Displacement (mm)	x	+-254	Force (kN)	x	+-2402
	y	+-127		y	+-1201
	z	+-127		z	+-3603
Rotation (degree)	x	+-16.0	Moment (kN*m)	x	+-862
	y	+-11.8		y	+-1152
	z	+-16.0		z	+-862
1/5th-scale LBCB					
Displacement (mm)	x	+-50.8	Force (kN)	x	+-8.9
	y	+-25.4		y	+-4.5
	z	+-25.4		z	+-12.3
Rotation (degree)	x	+-16.0	Moment (kN*m)	x	+-1.13
	y	+-12.0		y	+-2.03
	z	+-16.0		z	+-1.13

4. MULTI-DIMENSIONAL HYBRID SIMULATION OF SKEW RC BRIDGE

4.1 Prototype Bridge

Due to coupling of vibration responses, skew bridges are known to have complex behavior. To assess the seismic behavior of skew bridges and associated performance of RC piers, three-dimensional simulation is required to properly account for loading and boundary conditions.

Design Example No.4 (FHWA No.4 Bridge) from FHWA Seismic Design of Bridges (FHWA 1996) is selected as a reference skew bridge in the following multi-dimensional hybrid simulation. Figure 3 shows the plan and elevation views of the FHWA No.4 bridge. The bridge is a three-span, continuous, concrete box girder bride with a skew angle of 30 degree. Each bent consists of two circular reinforced concrete piers and cap beam integrated into the box girder.

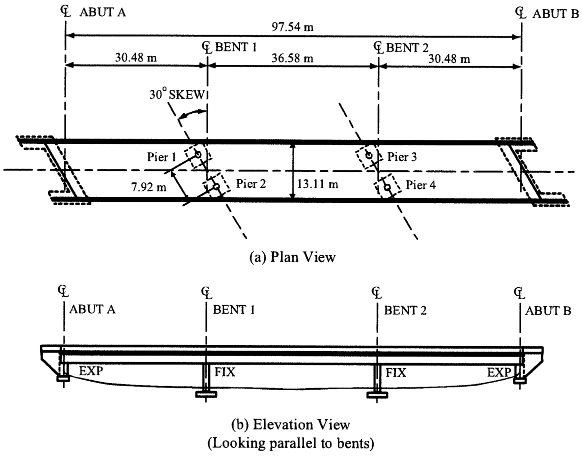

Figure 3. FHWA No.4 Bridge: (a) Plan View, and (b) Elevation View (Courtesy of FHWA)

4.2 Modeling and Substructures

The FHWA No.4 bridge is modeled using various elements to capture the fundamental and nonlinear behaviors. Figure 4 shows the schematic of the analytical model for the FHWA No.4 bridge.

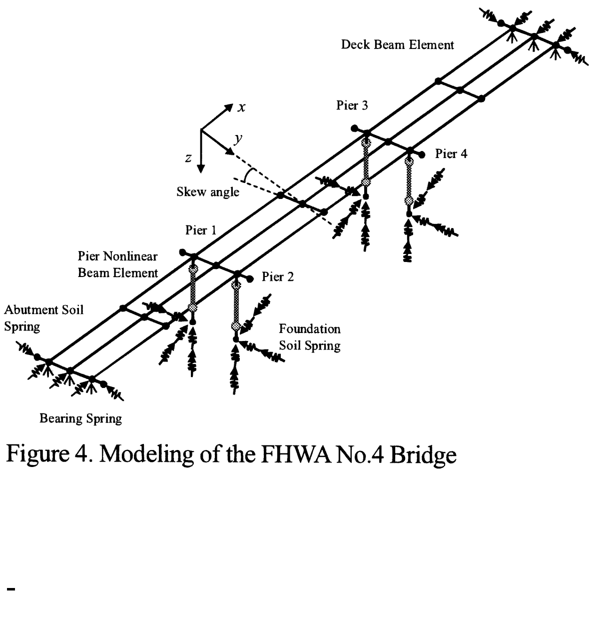

Figure 4. Modeling of the FHWA No.4 Bridge

RC piers are modeled with nonlinear fiber beam elements with cross sectional and material properties. ZeusNL is employed for the RC pier modeling. Because the superstructure usually remains elastic even during earthquake, the bridge deck, including the cap beams and end diaphragms, are modeled in linear beam elements. The bent foundations and abutment resistance are modeled as spring elements with equivalent stiffness for the spread footing and wingwall, respectively. The superstructure and foundations are modeled in Matlab. The substructuring technique is employed to combine the four RC pier substructures from ZeusNL and the rest of the structure from Matlab.

4.3 Small-scale RC Pier

In the hybrid simulation, one of the piers (Pier 4 in Figure 4) is experimentally modeled with scaling factor of 20. A small-scale RC pier is constructed with the original aspect and reinforcement ratios. Diameter and height of the specimen are 51 mm and 305 mm, respectively. Micro-concrete with a selected design mix is used for modeling of concrete at small-scale. The compressive strength of the micro-concrete mix is 31MPa. Heat-treated threaded rods and annealed steel wires are used as longitudinal and spiral transverse reinforcements. The yield strengths of the threaded rod and annealed wire are 345MPa and 414MPa, respectively.

4.4 Hybrid Simulation of Skew RC Bridge

The hybrid simulation model herein has five substructures: the bridge superstructure modeled in Matlab, three RC pier models in ZeusNL (Piers 1-3), and the small-scale RC pier model in experiment (Pier 4). Communication of all substructure models is coordinated by UI-SimCor developed at University of Illinois. The alpha-OS method with time increment of 0.01 sec is used as the time-step integration algorithm. For a loading scheme, traditional slow-rate ramp-hold loading procedure is employed.

The Morgan Hill earthquake record in 1984 at the station G06 is selected as the input ground motion. Two horizontal components of the record are considered with amplification factor. Based on the expected displacement feasible in the loading system from parametric study prior to the hybrid simulation, amplifications of the longitudinal and transverse components are determined to be 1.5 and 1.0, respectively. Figure 5 shows the amplified acceleration histories used in the hybrid simulation.

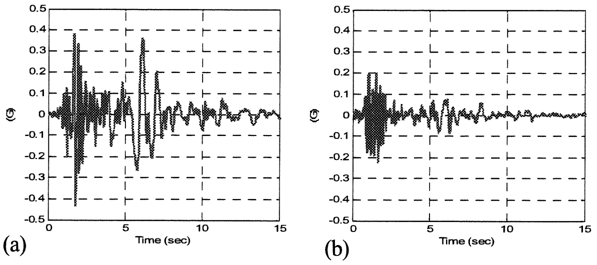

Figure 5. Input Ground Motion: (a) Longitudinal Direction, and (b) Transverse Direction.

4.5 Experimental Results

Hybrid simulation of the skew RC bridge is conducted using a 1/5th-scale LBCB combining mixed load and displacement control to impose constant axial load in the vertical direction and earthquake-induced displacements in the other directions on the experimentally tested RC pier. Figure 6 shows displacement and force time-histories of the RC pier. The x, y, and z-axes are in the longitudinal, transverse, and vertical directions of the bridge, respectively. Associated loading directions on the RC pier are shown in the Figure 7. As shown in the plots, the RC pier is subjected to three-dimensional deformation in all 6DOF due to the earthquake input and the gravity load effect. It is noted that the axial force in the z-axis remains constant at the initial gravity load level during the simulation regardless of the displacement in other five directions. The combined action of gravity load in axial direction and earthquake-induced deformation in other five directions on the RC pier is successfully achieved by the mixed load and displacement control capability. The variation in the axial displacement is a result of control of the axial force. This peculiar behavior cannot be simulated without the mixed load and displacement control capability.

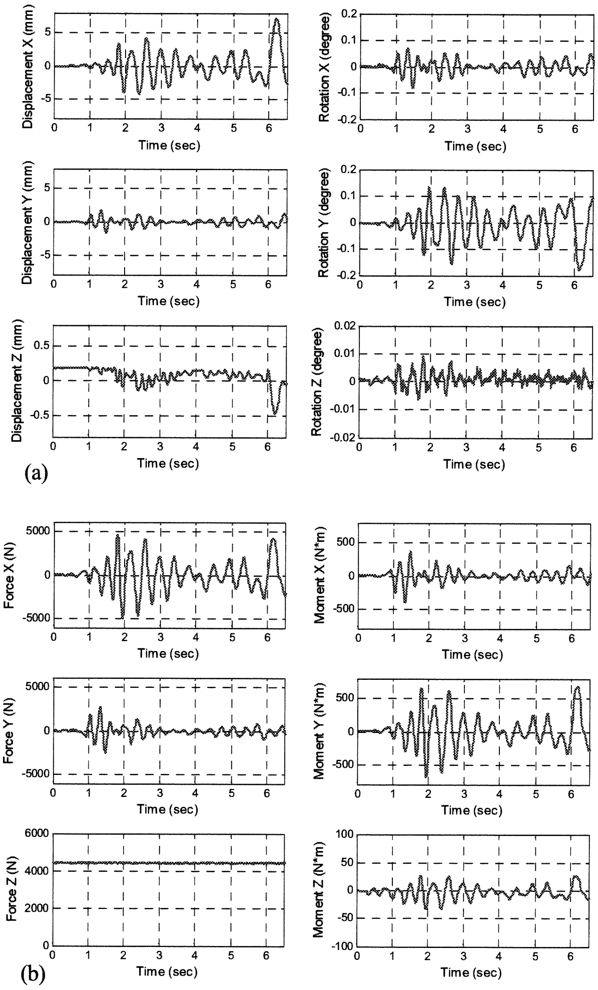

Figure 6. Displacement and Force Time-Histories: (a) Displacements and Rotations, and (b) Forces and Moments.

In-plane displacement trajectories are shown in Figure 7. These plots indicate a displacement path at the top of the RC pier in three-dimensional space. Figure 8 shows displacement and force relationships in the longitudinal and transverse directions. The longitudinal response exhibits an inelastic hysteresis loop including yielding and post-peak behavior. Although the transverse response does not exhibit significant inelastic behavior, the transverse stiffness reduces by about 50% after the peak strength in the longitudinal direction is reached. This result is due to the interaction between the longitudinal and transverse behaviors. Interactions among multiple directional behaviors cannot be evaluated in a simple in-plane simulation. As such, accounting for realistic loadings and boundary conditions is important for the assessment of seismic performance of critical structural components.

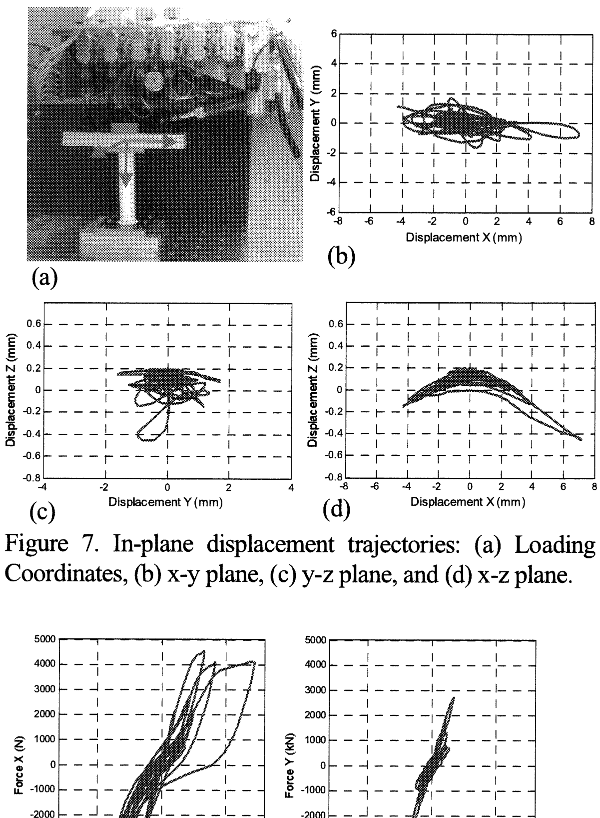

Figure 7. In-plane displacement trajectories: (a) Loading Coordinates, (b) x-y plane, (c) y-z plane, and (d) x-z plane.

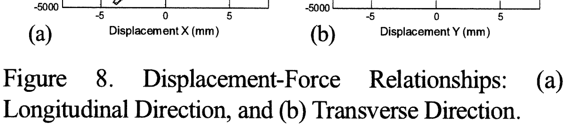

Figure 8. Displacement-Force Relationships: (a) Longitudinal Direction, and (b) Transverse Direction.

5. CONCLUSIONS

The paper presents the application of the multi-dimensional hybrid simulation using mixed load and displacement control to the complex structural systems. As an exapmle of the complex structural systems, skew RC bridge is investigated using the hybrid simulation method where an RC pier is experimentally tested and the rest of the bridge structure is computationally analyzed. The mixed load and displacement control is used to impose the gravity load in the axial direction and the earthquake-induced displacements in the other directions on the RC pier. The experimental results show that the multi-dimensional hybrid simulation with versatile mixed load and displacement control capability is a promising approach that provides a reliable means for evaluation of the seismic performance of large and complex structural systems.

Currently, a series of large-scale hybrid simulations using the full-scale LBCB are underway at UIUC. The same hybrid simulation methodology and control strategies presented in this study can be used for those large-scale experiments. Thus, the study presented in this paper lays the foundation for and provides smooth transition to the large-scale hybrid simulation including multi-dimensional simulation of complex structural systems.

Acknowledgements:

This research described in the paper is supported by the George E. Brown, Jr. Network for Earthquake Engineering Simulation (NEES) Program (NSF Award No. CMS-0217325) funded by the National Science Foundation (NSF) and the Mid-America Earthquake Center, an Engineering Research Center funded by the National Science Foundation under cooperative agreement reference EEC 97-01785.

References:

Broyden, C.G., (1965). "A class of methods for solving nonlinear simultaneous equations." Math. Comp. 19, 577-593.

Federal Highway Administration, (1996). "Seismic Design of Bridges -Design Example No.4 Three-Span Continuous CIP Concrete Bridge," FHWA-SA-97-009, Federal Way, Washington

Kawashima, K., Gakuho, W., Nagata, S., and Ogimoto, H., (2004). "Effect of Bilateral Excitation of the Seismic Performance of Reinforced Concrete Bridge Columns," Japan-Europe Seismic Risk Workshop, University of Bristol, UK

Kwon, O. S., Nakata, N., Elnashai, A. S., and Spencer, B. F., (2005). "A Framework for Multi-Site Distributed Simulation and Application to Complex Structural Systems." Journal of Earthquake Engineering, 9(5), 741-753.

Lynn, A.C., Moehle, J.P., Mahin, S.A., and Holmes, W.T., (1996). "Seismic Evaluation of Existing Reinforced Concrete Building Columns," Earthquake Spectra, 12(4), 715-739.

Mahin, S.A., and Shing, P.B. (1985). "Pseudodynamic Method for Seismic Performance Testing." Journal of Structural Engineering, 111(7), 1482-1503.

Nakata, N., Spencer, B. F., and Elnashai, A. S. (2004). "Mixed Load / Displacement Control Strategy for Hybrid Simulation." 4th International Conference on Earthquake Engineering, Taipei, Taiwan.

Pan, P., Nakashima, M., and Tomofuji, H., (2005). "Online test using displacement-force mixed control," Earthquake Engineering and Structural Dynamics, 34, 869-888.

Shing, P.B., Nakashima, M., and Bursi, O.S. (1996). "Application of Pseudosynamic Test Method to Structural Research." Earthquake Spectra, 12(1), 29-56.

Takanashi, K., Udagawa, K., Seki, M., Okada, T., and Tanaka, H. (1975). "Nonlinear Earthquake Response Analysis of Structures by a Computer-Actuator On-Line System." Bulletin of Earth-quake Resistant Structure Research Center 8, Institute of Industrial Science, University of Tokyo

Fifth International Conference on Urban Earthquake Engineering
March 4-5, 2008, Tokyo Institute of Technology, Tokyo, Japan

UPPER PART OF A HIGH-RISE BRIDGE AND ITS TIME-SERIES MOVEMENTS VIA GPS MEASUREMENT

Joz Wu[1)], Yi-Chi Li[2)], and Chi-Hsiu Hsieh[3)]

1) Professor, Center for Space and Remote Sensing Research and Department of Civil Engineering, National Central University, Taiwan
2) M. Sc. Candidate, Department of Civil Engineering, National Central University, Taiwan
3) Ph. D. candidate, Department of Civil Engineering, National Central University, Taiwan

jozwu@csrsr.ncu.edu.tw , 953202069@cc.ncu.edu.tw , jieshio.hsieh@msa.hinet.net

Abstract: GPS provides all-weather observations, and highly accurate positions. With a GPS model using carrier-phase observations containing integer-valued and real-valued unknown parameters, this paper presents a near-real-time data processing technique based on Bayesian statistics. Bayesian statistics analyzes data by using the posterior distribution of the data derived from prior knowledge. Based on the Bayesian principle and the integer property of phase ambiguities, the posterior density function of phase ambiguities and positioning parameters can be determined. The main aim of this research is to complete the adjustment by using Bayesian approach and to obtain the confidence regions for the position parameters by using a Monte Carlo method. Two bridges are tested in this research, and the test results indicate that the proposed method can supply positioning information about motion and displacement. Furthermore, confidence regions can be presented in real time by using a Monte Carlo method.

1. INTRODUCTION

Code and carrier phase observations can be used for positioning by using the GPS (Global Positioning System). Carrier phase observation is more precise than code observation, but it causes the problem of phase ambiguities. Ambiguities need to be estimated at their correct integer values, because incorrect integers generally bias the receiver coordinate considerably. However, because the GPS model containing integer-valued (phase ambiguities) and real-valued (baseline coordinates and ionospheric parameters) unknown parameters when using carrier phase observations, the statistical inference becomes difficult. The problem can be solved by using Bayesian statistics in this research (Gundlich and Koch, 2001).

Because of a different behavior between the GPS carrier-phase noise variance and the pseudorange noise variance, separate scaling factors are required. The algorithm of variance and covariance component unbiased estimation-Best Linear Unbiased Estimator (BLUE) is used here to render the stochastic model close to measurement reality (Wu and Yeh, 2005). Due to the high correlation problem between the ambiguity and geometry parameters, an ambiguity search region is large and it's hard to recognize the correct integer ambiguity. The whitening filter technique is used here (Mohamed and Schwarz, 1998) to solve above problems. Furthermore, for the sake of the fact that restricting the prior distribution of ambiguities is not consistent with the real data in Bayesian view, a theory of mixture model for a discrete-real ambiguity alternative based on Bayesian inference was proposed by de Lacy et al. (2001). Therefore, a Bayesian statistical discrimination test is also added in order to make the ambiguity and position results more reliable (Carlin et al., 2000). The main aim of this research is to complete the adjustment by using Bayesian approach and produce the confidence regions for GPS positioning parameter estimation by using a Monte Carlo method. The procedure of this study is shown in Figure 1.

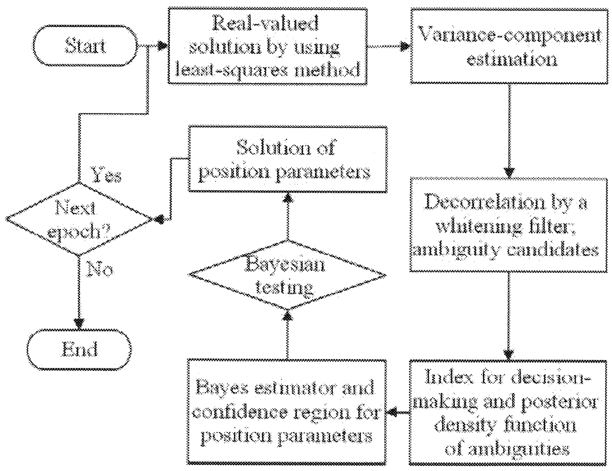

Figure 1 Workflow of the proposed scheme.

2. METHODOLOGY

In this section, the Bayesian principle is introduced first. Next, the real-valued solutions of unknown parameters can be obtained by using least-squares method. After computing the real-valued solutions, we can obtain the index for decision-making and construct the prior distribution of unknown parameters. Then, the posterior density function of ambiguities, Bayes estimators and confidence regions of positioning parameters are derived. Furthermore, confidence regions are produced by using a Monte Carlo method.

2.1 Bayesian statistics

Assuming that $\mathbf{l}$ is the observations and $\boldsymbol{\theta}$ is the unknown parameters, the posterior density function of $\boldsymbol{\theta}$ by Bayesian principle can be expressed as

$$p(\boldsymbol{\theta} \mid \mathbf{l}) = \frac{p(\boldsymbol{\theta}, \mathbf{l})}{p(\mathbf{l})} \tag{1}$$

where $p(\boldsymbol{\theta})$ is the prior density function and $p(\boldsymbol{\theta}, \mathbf{l})$ is the joint density function. Because $p(\mathbf{l})$ is independent of the unknown parameters, the posterior density function of unknown parameters can be written as

$$p(\boldsymbol{\theta} \mid \mathbf{l}) \propto p(\boldsymbol{\theta}) p(\mathbf{l} \mid \boldsymbol{\theta}) \tag{2}$$

The Bayesian principle has been applied to GPS phase ambiguity resolution by Betti et al. (1993). The unknown parameters are treated as random variables with probability density functions by Bayesian statistics. Starting to derive the posterior density functions of integer ambiguities, the Bayes estimator, covariance matrix and confidence region for the real-valued parameters are estimated.

2.2 Least-squares estimation

The mixed adjustment model with integer and real-valued unknown parameters of double-difference GPS observations can be expressed as (Teunissen, 1998)

$$\mathbf{v} + \mathbf{A}\mathbf{a} + \mathbf{G}\mathbf{x} = \mathbf{l}, \ D(\mathbf{l} \mid \sigma_0^2) = \sigma_0^2 \mathbf{P}^{-1} \tag{3}$$

where $\mathbf{l}$ represents the vector of reduced measurements. The vector $\mathbf{a}$ denotes the unknown integer phase ambiguities and $\mathbf{x}$ denotes the real-valued unknown parameters, such as baseline coordinates and ionospheric parameters. The corresponding design matrices of $\mathbf{a}$, $\mathbf{x}$ are $\mathbf{A}$ and $\mathbf{G}$, and the vector $\mathbf{v}$ stands for the vector of double-difference measurement noises. The stochastic model is given by the measurement covariance matrix which is defined by the given weight matrix and the prior variance factor. The optimal real-valued solution and covariance matrix for the unknown parameter vectors $\mathbf{a}$ and $\mathbf{x}$ by using least-squares method are defined as Eq. (4) and Eq. (5) (Gundlich and Koch, 2001)

$$\begin{bmatrix} \hat{\mathbf{a}} \\ \hat{\mathbf{x}} \end{bmatrix} = \begin{bmatrix} \mathbf{A}^T\mathbf{P}\mathbf{A} & \mathbf{A}^T\mathbf{P}\mathbf{G} \\ \mathbf{G}^T\mathbf{P}\mathbf{A} & \mathbf{G}^T\mathbf{P}\mathbf{G} \end{bmatrix}^{-1} \begin{bmatrix} \mathbf{A}^T\mathbf{P}\mathbf{l} \\ \mathbf{G}^T\mathbf{P}\mathbf{l} \end{bmatrix} \tag{4}$$

$$\sigma_0^2 \begin{bmatrix} \mathbf{A}^T\mathbf{P}\mathbf{A} & \mathbf{A}^T\mathbf{P}\mathbf{G} \\ \mathbf{G}^T\mathbf{P}\mathbf{A} & \mathbf{G}^T\mathbf{P}\mathbf{G} \end{bmatrix}^{-1} = \begin{bmatrix} \boldsymbol{\Sigma}_a & \boldsymbol{\Sigma}_{ax} \\ \boldsymbol{\Sigma}_{xa} & \boldsymbol{\Sigma}_x \end{bmatrix} \tag{5}$$

2.3 Prior and posterior distributions of unknown parameters

For the sake of solving the high correlation problem between the ambiguity and geometry parameters, the decorrelation technique is utilized. Teunisssen et al. (1997) explained how to obtain an integer set can by using the least-squares ambiguity deccorelation adjustment (LAMBDA) method. A whitening filter technique is used here (Mohamed and Schwarz, 1998) to acquire the same objective, it can look for the candidates of integer ambiguities more efficiently. After finding the candidate integer ambiguity sets, the posterior density functions of the ambiguity candidates are computed.

In general, the GPS observations are assumed to the normal distribution. In this research, the prior density function is taken as uniform distribution, namely non-information prior. This implies that the marginal density function of integer ambiguities can be transformed into as (Zhu et al., 2001)

$$p(\breve{\mathbf{a}} \mid \mathbf{l}) = \frac{\exp\{-\frac{1}{2}(\breve{\mathbf{a}} - \hat{\mathbf{a}})^T \boldsymbol{\Sigma}_a^{-1} (\breve{\mathbf{a}} - \hat{\mathbf{a}})\}}{\sum_{\breve{\mathbf{a}}} \exp\{-\frac{1}{2}(\breve{\mathbf{a}} - \hat{\mathbf{a}})^T \boldsymbol{\Sigma}_a^{-1} (\breve{\mathbf{a}} - \hat{\mathbf{a}})\}} \tag{6}$$

where $\breve{\mathbf{a}}$ is the vector of integer ambiguity candidate and $\hat{\mathbf{a}}$ is the real-valued solution for the vector of ambiguity. The conditional estimator corresponding to integer ambiguity candidate is written as Eq. (8) and the Bayes estimator is shown as Eq. (9) (Zhu et al., 2001).

$$\hat{\mathbf{x}}_{|a} = \hat{\mathbf{x}} - \boldsymbol{\Sigma}_{xa} \boldsymbol{\Sigma}_a^{-1} (\hat{\mathbf{a}} - \mathbf{a}) \tag{7}$$

$$\hat{\mathbf{x}}_{\mathrm{B}} = \hat{\mathbf{x}}_{\mathrm{Bayes}} = p(\mathbf{a} \mid \mathbf{l})_{\max} \hat{\mathbf{x}}_{|\{a|p(\mathbf{a}|\ \mathbf{l})_{\max}\}} \tag{8}$$

2.4 Index for decision-making

In performing the search space of ambiguities, one decision in a group of three should be adopt: (a) The information is sufficient to define a restricted confidence region around the floating solution, namely the search space, in which more than one integer components falls. (b) There is only one integer vector in search space. (c) No integer components fall in search space. However, restricting the prior distribution of ambiguities is not consistent with the real data in Bayesian view. A theory of mixture model for a discrete-real ambiguity alternative based on Bayesian inference was advanced by de Lacy et al. (2001). The mixture model is defined as

$$\varpi = \begin{cases} I, & \text{if } \mathbf{a} \text{ is integer} \\ F, & \text{if } \mathbf{a} \text{ is real} \end{cases} \tag{9}$$

In Eq. (9), ϖ is the discrete label variate. The index for decision-making is the marginal density function of ϖ shown as Eq. (10).

$$p(\varpi \mid \mathbf{l}) = \begin{cases} P_I = \dfrac{q}{q-1}\left(1 - \dfrac{1}{q-1}\log q\right), & \varpi = I \\ 1 - P_I, \ \varpi = F \end{cases} \tag{10}$$

where

$$q = \sum_{\boldsymbol{\beta}_I} \frac{\sqrt{|\boldsymbol{\Sigma}_{ar}|}}{(2\pi)^{m/2}\sigma_0^m} \exp\left(-\frac{1}{2\sigma_0^2}\boldsymbol{\beta}_I{}^T \boldsymbol{\Sigma}_{ar}^{-1} \boldsymbol{\beta}_I\right) \tag{11}$$

$$\boldsymbol{\beta}_I = \mathbf{a}_I - \hat{\mathbf{a}}, \ m = \dim \boldsymbol{\beta}_I \tag{12}$$

$$\boldsymbol{\Sigma}_{ar} = \mathbf{A}^T\mathbf{PA} - (\mathbf{A}^T\mathbf{PG})(\mathbf{G}^T\mathbf{PG})^{-1}(\mathbf{G}^T\mathbf{PA}) \tag{13}$$

If the marginal density function of ϖ approximates to zero, the search space of ambiguities contains no correct integer components. In this research, in order to find the correct fixed solution, the confidence region of ambiguities is expanded until the search-number of ambiguities is more than ten thousands when $p(\varpi \mid \mathbf{l})$ approximates to zero. Finally, a Bayesian statistical hypothesis test is used here to make the ambiguity and position results more reliable

2.5 Confidence regions of positioning parameters

In order to examine the precision of the parameter estimation, the confidence region for the positioning parameters are derived by using Eq. (14).

$$p(\mathbf{x} \in R \mid \mathbf{l}) = \sum_{a \in L^m} p(\mathbf{a} \mid \mathbf{l}) \int_{x \in R^u} p(\mathbf{x} \mid \mathbf{a}, \mathbf{l}) d\mathbf{x} = 1 - \alpha \tag{14}$$

In this research, confidence regions for positioning parameters can are obtained by using a Monte Carlo method. The procedure for confidence region is as follows. First, a random generator is used to generating n independent samples from the standard normal distribution. Then, collecting the n samples in a vector $\mathbf{w}$, and transforming the vector by means of $\mathbf{x} = \mathbf{wG} + \hat{\mathbf{x}}_{|a_i}$ with $\mathbf{G}$ the Cholesky factor of $\boldsymbol{\Sigma}_{x|a} = \mathbf{GG}^T$. The result is a sample vector $\mathbf{x}$ from $N(\hat{\mathbf{x}}_{|a}, \boldsymbol{\Sigma}_{x|a})$, where $\boldsymbol{\Sigma}_{x|a} = \boldsymbol{\Sigma}_x - \boldsymbol{\Sigma}_{xa}\boldsymbol{\Sigma}_a^{-1}\boldsymbol{\Sigma}_{ax}$ (Verhagen and Teunissen, 2005). Finally, the samples produce the confidence region for the positioning parameter by using Eq. (14).

3. EXPERIMENTS

Two experiments were made on 21 January in 2008 using dual-frequency Leica SR530 receivers with AT502 and AT504 antennas. The parameters of GPS receiver setting indicated a 1.0 Hz sampling rate and 15° cut-off angle. NTPU station is a permanent station located in National Taipei University. DZ01 and CY01 are temporary stations located on Da-Zhi bridge and Chong-Yang bridge. Distances from NTPU to DZ01 and from NTPU to CY01 are shown as Figure 2. Figure 3 shows the site of temporary stations of the two bridges, and Figure 4~Figure5 shows the values of DOP and the elevation angles of the satellite of the two temporary stations.

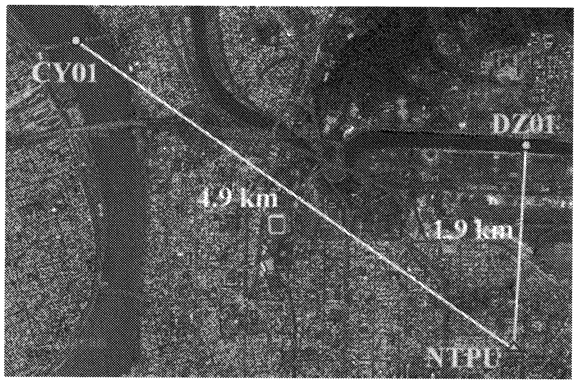

Figure 2 GPS baseline selected in this research.

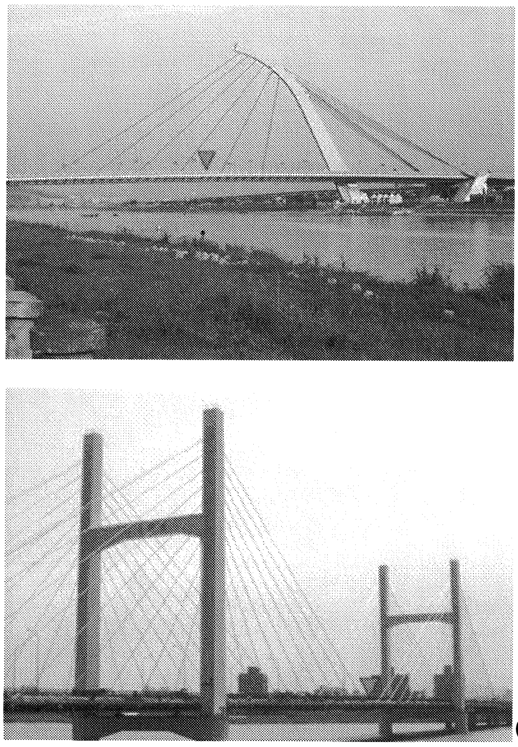

(a)

(b)

Figure 3 Site for temporary stations of the two bridges. (a) Da-Zhi bridge, and (b) Chong-Yang bridge

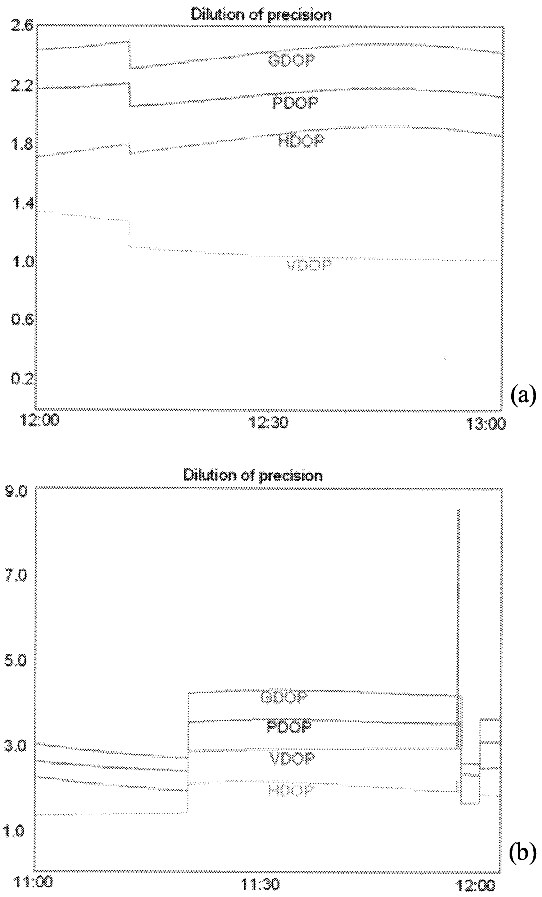

Figure 4 Values of DOP:
(a) Da-Zhi bridge, and (b) Chong-Yang bridge

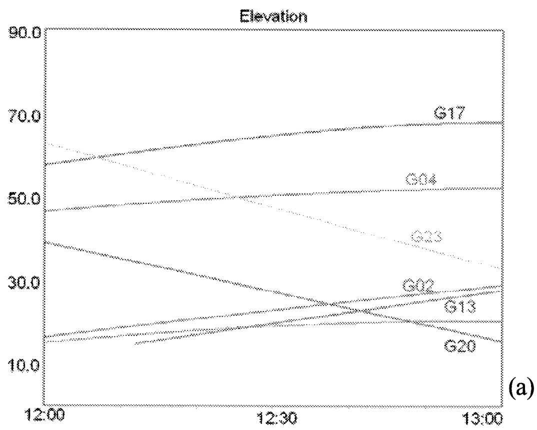

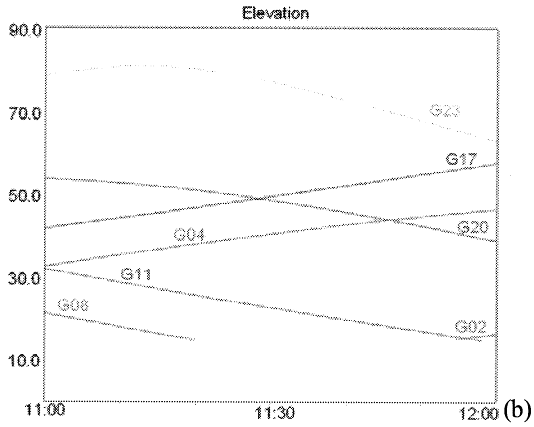

Figure 5 Elevation angles of the satellite:
(a) Da-Zhi bridge, and (b) Chong-Yang bridge

3.1 Performance of GPS positioning

The test in this research uses NTPU as reference station and DZ01/CY01 as rover station. The proposed method is used to solve the three dimensional coordinates. Figure 6 shows the positioning results of DZ01 at 12:48 ~ 12:51 p.m. and Figure 7 shows the positioning results of CY01 at 11:05 ~ 11:10 a.m. in TWD97 coordinate system epoch by epoch. The 3D graphs of positioning results for the two bridges are shown as Figure 8 and Figure 9. The results indicate that the degree of vibration of the Chong-Yang bridge is more violent.

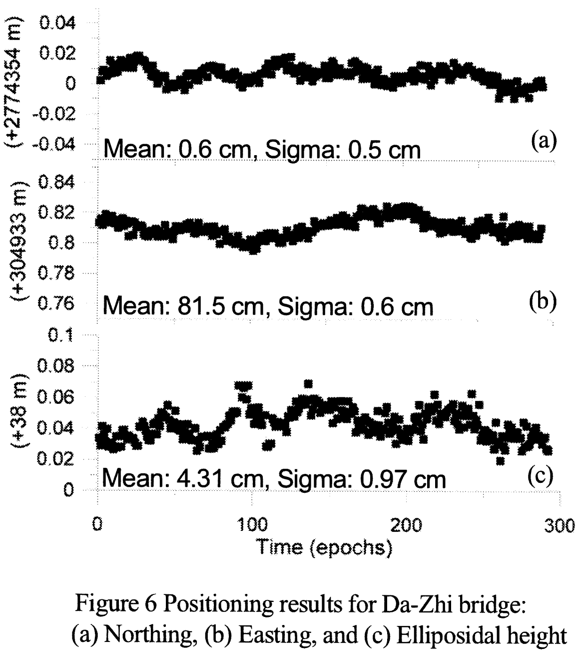

Figure 6 Positioning results for Da-Zhi bridge:
(a) Northing, (b) Easting, and (c) Elliposidal height

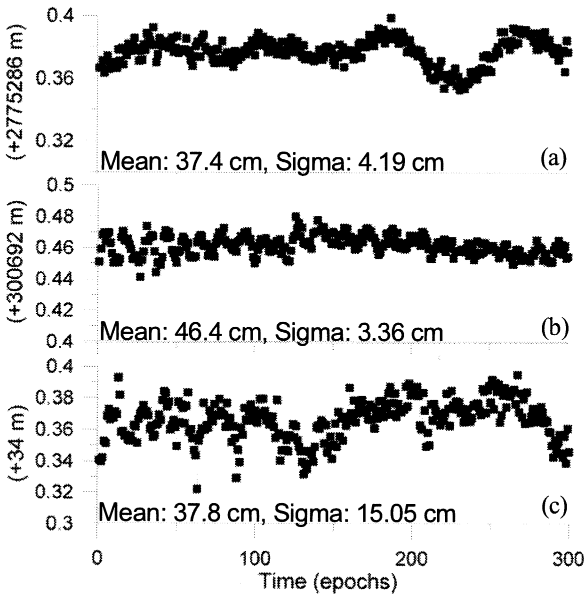

Figure 7 Positioning results for Chong-Yang bridge: (a) Northing, (b) Easting, and (c) Elliposidal height

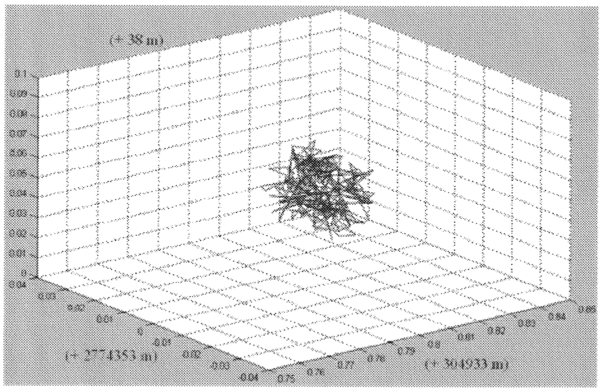

Figure 8 Positioning results for Da-Zhi bridge.

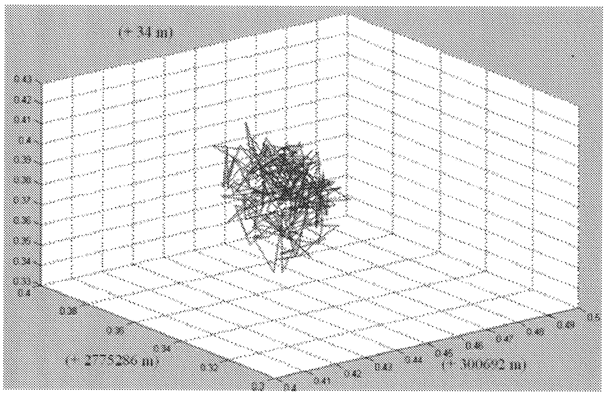

Figure 9 Positioning results for Chong-Yang bridge.

3.2 Performance of confidence region

In this test, two thousands samples are used to produce the confidence region with 95% confidence level. Figure 10 shows the confidence region for DZ01 and Figure 11 shows the confidence region for CY01 at 12:00:01 p.m.. The results indicate that the confidence region for Chong-Yang bridge is larger because the configuration of satellites is worse at 12:00:01 p.m..

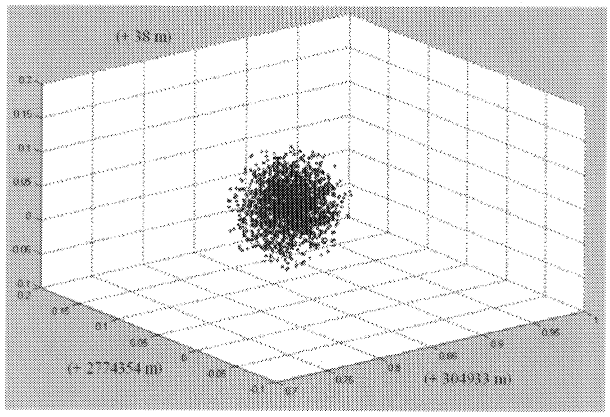

Figure 10 Confidence region for Da-Zhi bridge.

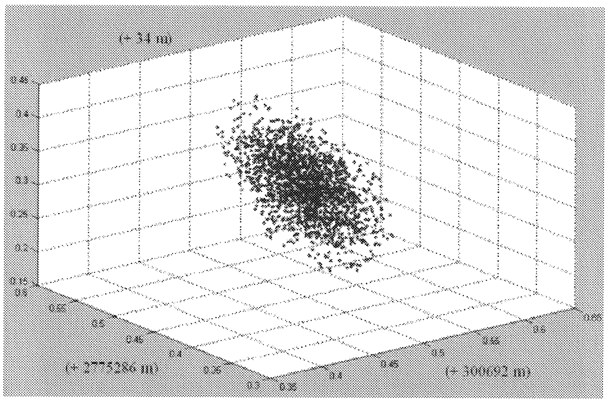

Figure 11 Confidence region for Chong-Yang bridge.

4. CONCLUSIONS

Preliminary test results for the two bridges present the advantage of GPS in near-real-time data processing. The high precision and high accuracy are suitable for monitoring the motion of large-scale structures. Furthermore, confidence regions can be presented by using a Monte Carlo method. However, the test results also show that the sampling rate is not enough for high-frequency movement. And the major problem of GPS technique now is GPS signal interruption, multipath effect, and interstation distance. Future work should involve raising the GPS sampling rate or adding high sampling rate IMU (Inertial Measurement Unit), and trying to optimize the data procession technique.

References:

Betti, B., Crespi, M., and Sanso, F. (1993), "A geometric illustration of ambiguity resolution in GPS theory and a Bayesian approach," *Manuscript Geodesy* 18(6), pp. 317–330.

Carlin, B. P., Louis, T. A., and Carlin, B. (2000), "Bayes and empirical Bayes methods for data analysis," Second Edition. Chapman & Hall/CRC, 38-42.

De Lacy, M. C., Sansò, F., Rodriguez-Caderot, G., and Gil, A. J. (2001), "The Bayesian approach applied to GPS ambiguity resolution. A mixture model for the discrete-real ambiguities alternative," *Journal of Geodesy*, 76(2), pp. 82-94.

Gundlich, B. and Koch, K -R. (2001), "Confidence regions for GPS baselines by Bayesian statistics," *Journal of Geodesy*, 76(1), pp. 381-391.

Mohamed, A. H. and Schwarz, K. P. (1998), "A simple and economical algorithm for GPS ambiguity resolution on the fly using a whitening filter," *Navigation*, 45(3), 221-231.

Teunissen, P. J. G., Jonge, P. J. de, and Tiberius, C. C. J. M. (1997), "Performance of the LAMBDA method for fast ambiguity resolution," *Navigation*, 44(3), 373-383.

Teunissen, P. J. G., (1998), "GPS carrier phase ambiguity fixing concepts. In: Teunissen PJG, Kleusberg A (eds) GPS for geodesy," Springer, 319–388

Verhagen S. and Teunissen, P. J. G (2006), "On the probability density function of the GNSS ambiguity residuals," *GPS Solutions*, 10(1), 21-28.

Wu, J. and Yeh, T. F. (2005), "Single-epoch weighting adjustment of GPS phase observables," *Navigation*, 52(1), 39-47.

Zhu, J., Ding, X. and Chen, Y. (2001), "Maximun-likehood ambiguity resolution based on Bayesian principle," *Journal of Geodesy*, 75(4), 175–187.

Fifth International Conference on Urban Earthquake Engineering
March 4-5, 2008, Tokyo Institute of Technology, Tokyo, Japan

SEISMIC BEHAVIOR OF BEAM-TO-COLUMN CONNECTIONS WITH FILLETS OF STEEL RIGID FRAME PIERS

Kiyoshi Ono[1) and Jun Tahara[2)

1) Associate Professor, Department of Civil Engineering, Tokyo Institute of Technology, Japan
2) Steel Structure Design Department, Hitachi Zosen Steel Structures Co., Ltd., Japan
ono.k.ae@m.titech.ac.jp, tahara_j@hitachizosen.co.jp

Abstract: The seismic design method of beam-to-column connections of steel bridge frame piers has not been established and it is necessary to develop it. Moreover the fatigue damage of beam-to-column connections of steel bridge frame piers is one of serious problems. It is proposed to install the fillets in beam-to-column connections of steel bridge frame piers for improving fatigue performance. The influence of fillets on seismic performance of beam-to-column connections must be considered in developing the seismic design method. In this study, cyclic loading experiments were conducted. Based on the experimental results, the seismic behavior of beam-to-column connections with fillets and the influence of fillets on seismic behavior of beam-to-column connections were investigated for developing the seismic design method in the future works.

1. INTRODUCTION

The Hyogo-ken Nanbu Earthquake occurred in January 1995, and it caused destructive damages to highway bridges (Ministry of Construction 1995), The specifications for highway bridges were revised in 1996 (Japan road association 1996a, 1996b) in consideration of the damage and the ductility design method was introduced to steel bridge piers. And the more detailed seismic design method for steel bridge piers was specified in the 2002 specifications (Japan road association 2002a, 2002b). Besides the specifications for highway bridges, some methods for estimating the seismic performance of steel bridge piers or steel members have been already proposed (Usami et al. 2001).

On the other hand, seismic design method of beam-to-column connections of steel bridge frame piers has not been established because the seismic behavior has not been investigated sufficiently and there are a lot of things to make clear for developing the ductility design method. Then beam-to-column connections of steel bridge frame piers are sometimes applied to elastic design method against level 2 Earthquake Ground Motions and it is not rational. It is necessary to clear up the seismic behavior of them in order to develop the ductility design method as the seismic design.

Moreover the fatigue damage of beam-to-column connections of steel bridge frame piers is one of serious problems. A lot of attempts have been conducted in order to improve the fatigue performance of beam-to-column connections. One of the methods for improving the fatigue performance is to install the fillets in beam-to-column connections. Fillets can reduce the high stress concentration by sheer lag at the corners in the beam-to-column connections and it can cause the improvement of the fatigue performance. However buckling at fillets is easy to occur and the buckling at fillets may have a bad influence on the seismic performance of beam-to-column connections. It is important to make clear the influence of fillets on the elasto-plastic behavior of beam-to-column connections.

In this study, cyclic loading experiments of beam-to-column connections of steel frame piers were carried out in order to grasp the seismic behavior of beam-to-column connections with fillets and the influence of fillets on it.

2. OUTLINE OF EXPERIMENTS

2.1 Test Specimens

Two types of test specimens were employed. One of them is with fillets and another is without fillets. Figure 1 shows R_R and steel grade of beam-to-column connections in previous experimental studies, actual steel rigid frame piers and this study. As shown Figure 1, R_R and steel grade in the previous experimental studies are different form those in actual beam-to-column connections. In this study, major buckling parameters such as R_R, R_F and γ_l^* of test specimens were decided in consideration of survey results of parameters of actual beam-to-column connections of steel frame piers which have been designed by the 1996 or the 2002 design specifications for high bridges in order that the parameters of test specimens could be similar to those of actual beam-to-column connections. R_R and R_F are the with-thickness ratio parameters of plate panels between longitudinal stiffeners and overall stiffened plate panels respectively. γ_l^* is relative stiffness ratio of a longitudinal

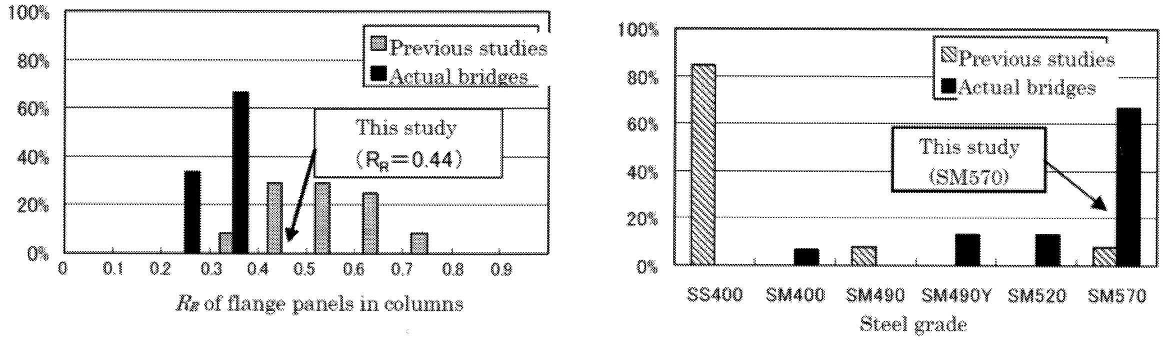

Figure 1 R_R and steel grade of connections in this study, previous studies actual bridges
(Note: R_R in Figure 1 is calculated by nominal yield stress σ_{yN})

stiffener based on the elastic buckling theory. The definitions of parameters mentioned above are identical to those stipulated in the 2002 specifications and given as follows.

$$R_R = \frac{b}{t}\sqrt{\frac{\sigma_y}{E}\frac{12(1-\nu^2)}{4n^2\pi^2}} \tag{1}$$

$$R_F = \frac{b}{t}\sqrt{\frac{\sigma_y}{E}\frac{12(1-\nu^2)}{4k_F\pi^2}} \tag{2}$$

$$\gamma_l^* = \begin{cases} \dfrac{1}{n}\left[\{2n^2(1+n\delta_l)-1\}^2-1\right] & \left(\alpha \geq \sqrt{1+n\gamma_l}\right) \\ 4\alpha^2 n(1+n\delta_l)-\dfrac{(\alpha^2+1)^2}{n} & \left(\alpha < \sqrt{1+n\gamma_l}\right) \end{cases} \tag{3}$$

where b = width of flange; t = thickness of plate; E = Young's modulus; σ_y= yield stress; ν = Poisson's ratio (=0.3) ; n = number of panels; k_R = bucking coefficient; α = aspect ratio; γ_l = relative stiffness ratio of an actual longitudinal stiffener.

Based on survey results shown in Figure 1, target values of major parameters of test specimen, R_R, R_F and γ_l/γ_l^* were selected as follows.

$$R_R\text{=0.5},\quad R_F\text{=0.5 and}\quad \gamma_l/\gamma_l^*<1.0 \tag{4}$$

Steel grade of test specimens was SM570 in consideration of the steel grade of actual beam-to-column connections as shown in Figure 1. The outside dimensions of specimens were made as large as possible in consideration of the capacity of the hydraulic jacks and frames.

It has been proposed that fillets are installed in beam-to-column connections in order to improve the fatigue performance. Fillets can reduce the high stress concentration at the corners of beam-to-column connections. The geometry of the fillets has been already prescribed in design specifications for Metropolitan Expressway as follows (The Metropolitan Highway Public Corporation 2003).

$$W \fallingdotseq 0.2H_b \quad \text{and} \quad R \fallingdotseq W \tag{5}$$

where W = width of fillet; R = radius at the end of fillet; H_b = height of web in column.

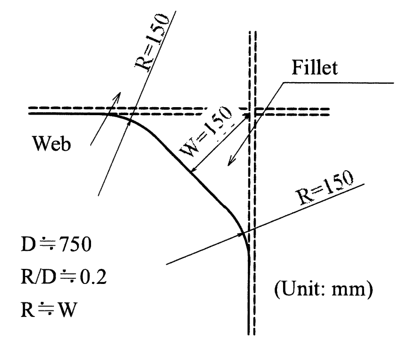

Figure 2 Geometry of fillets in test specimen

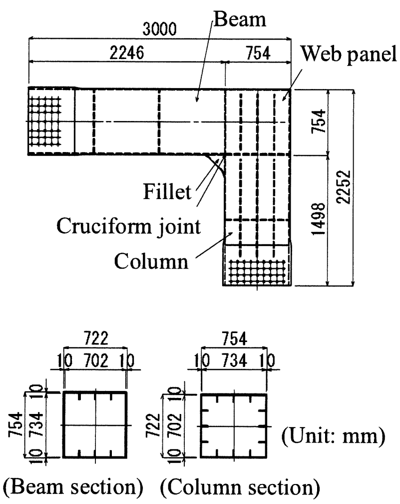

Figure 3 Geometry of test specimen C1

Geometry of fillets in specimens is shown in Figure 2.

The geometry of a test specimen C1 with fillets is given in Figure 3 and the values of major parameters and material properties of the test specimens are listed in Table 1. Here, C1 is a test specimen with fillets and C2 is a test specimen without fillets. The geometry of a test specimen C2 is the same as that of C1 except fillets.

Table 1 Major parameters of test specimens

	σ_{yM} (N/mm^2)	R_R	R_F	γ_l/γ_l*	γ_l/γ_{lreq}	δ_y (mm)
C1	562	0.48	0.52	0.85	1.38	8.8
C2	588	0.48	0.52	0.85	1.38	6.6

Note: R_R, R_F and δ_y was calculated by σ_{yM}

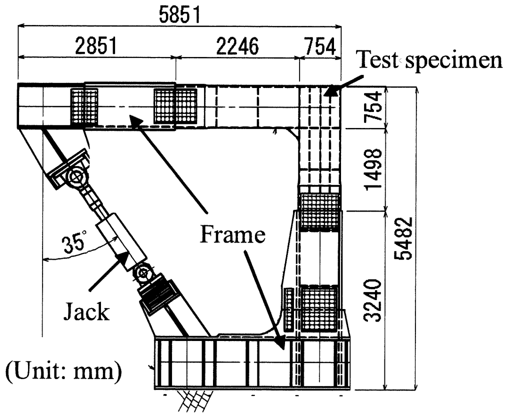

Figure 4 Outline of test setup

2.2 Cyclic loading Program

Figure 4 is an outline of test setup. Each specimen was set in fully stiff frames. A hydraulic jack was fixed at the end of each flame. The jack adapted an angle of about 35° to the vertical axis so that distribution of moment acting on beam-to-column connections of specimens and that of actual beam-to-column connections could be as approximate as possible.

Each experiment was controlled by the displacement δ_{cor}. δ_{cor} is a displacement as shown in Figure 5. The cyclic loading program is schematically shown in Figure 6. δ_y in Figure 6 is the yield horizontal displacement and it was decided by the following procedure. As shown Figure 7, strain gauges were attached on both surfaces of inner flange plates in the beam and the column and the distance between the gauges and the cruciform joint is 50 mm. The average values of all strain measured by strain gauges in the beam or the column were calculated respectively. The displacement δ_{cor} when the average value of the measured strain in the beam or the column reached to the yield strain ε_{ym} was defined as the yield displacement δ_y. Here, the yield strain ε_{ym} was obtained from the material test of each test specimen. The compressive force and the shrinking displacement from the neutral position were defined as the positive value respectively. By the way, yield displacement of a test specimen C1 is larger than that of a test specimen C2 in Table 1 because the average value of stress of C1 was smaller than that of C2 as the result of the fillets as described in the following section 3.3.

3. EXPERIMENTAL RESULTS AND COMMENTS

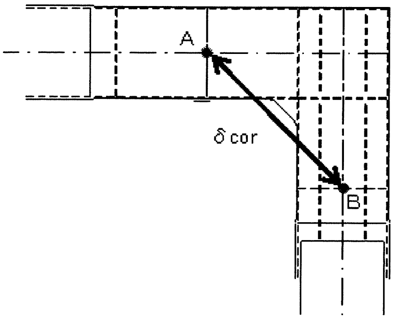

Figure 5 Displacement used for control of loading

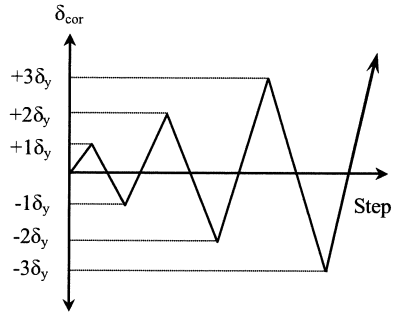

Figure 6 Cyclic loading program

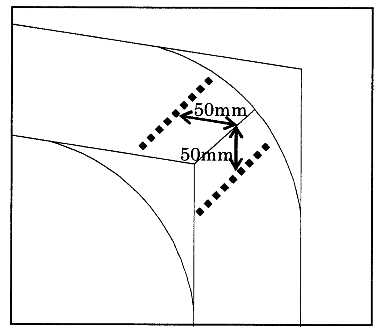

Figure 7 Distribution of Strain gauges for deciding δ_y

3.1 Feature of hysteretic curves

Figure 8 indicates a jack load P - displacement δ_{cor} relationship and Figure 9 shows the envelope curves of the test specimens. The square symbols (◆) in Figure 8 and Figure 9 exhibit the points where P_{max} appeared.

Figure 9 demonstrates that P_{max} and the displacement at P_{max} of C1 are a little larger than those of C2. However the envelop curve of C1 before P_{max} is almost identical with that of the specimen C2. Judging from the fact described above, fillets discussed in this paper have little effect on the overall load-displacement relationship of beam-to-column connections as far as the elasto-plastic behavior before P_{max}. On the other hand, difference between the envelop curve of

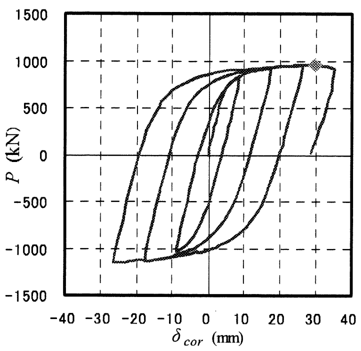

(Test specimen C1)

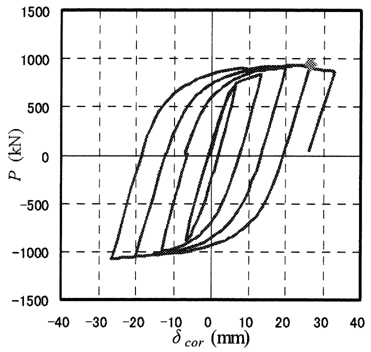

(Test specimen C2)

Figure 8 P- δ_{cor} relationship

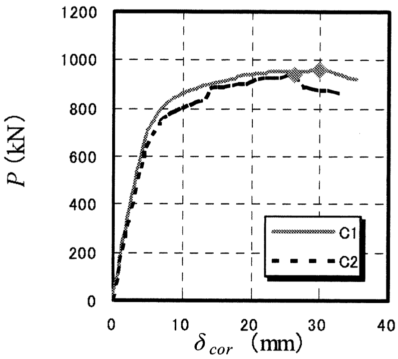

Figure 9 Envelop curves

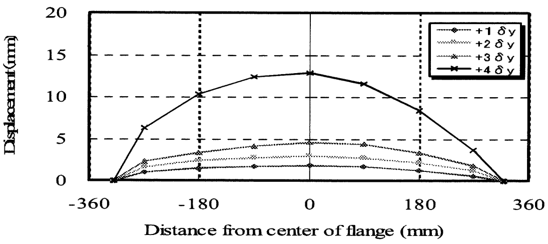

(a) Beam

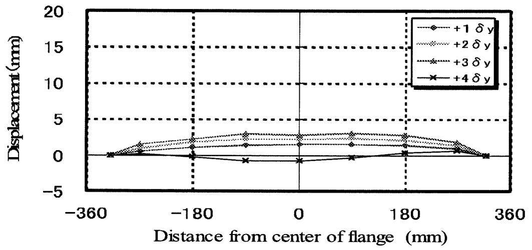

(b) Column

Figure 10 Progress of deformation on inner flange of C1

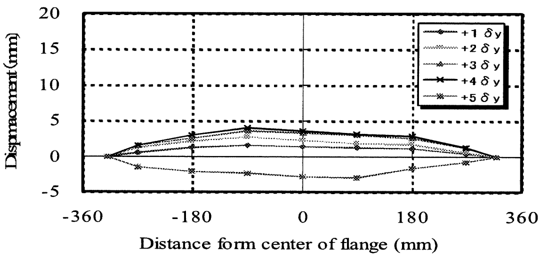

(a) Beam

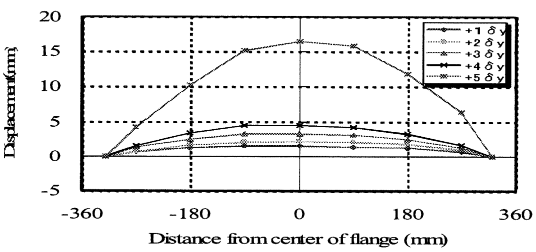

(b) Column

Figure 11 Progress of deformation on inner flange of C2

C1 and that of C2 after P_{max} is larger than that before P_{max}. The reason why the larger difference in the envelop curves after P_{max} occurred will be investigated in detail hereafter.

3.2 Buckling behavior

Figure 10 and Figure 11 show the progress of out-of-plane deformation of the inner flanges in the beam and the column at the end of each loop respectively. The points where the displacement was measured were 50 mm from the cruciform joint. And positive values of the deformation in Figure 10 and Figure.11 mean the out-of-plane displacement occurred into inside of flange plates.

As for a test specimen C1, the local buckling occurred with large deformation at the inner flange plates in the beam in the loading path of $+4\delta_y$ as shown in Figure.12. This bucking caused decline of strength and P_{max} appeared. The deformation of the inner flange plate in the beam in the loop of $+4\delta_y$ was much larger than that in the other loops as shown in Figure10(a).

Regarding a test specimen C2, the local buckling occurred with large deformation at the inner flange plates in the column in the loading path of $+5\delta_y$ as shown in Figure 13 and this bucking caused decline of strength and appearance of P_{max} as well as C1.

By the way, the deformation of the inner flange plate in the beam or the column was larger than that of another member and the direction of deformation in the beam was reverse to that in the column after P_{max}. As for a test specimen C1, the deformation of the inner flange in the beam was much larger than that in the column and the direction of deformation in the beam was reverse to that in the column in the loop of $+4\delta_y$ as shown in Figure 10. Moreover, Figure10 (b) indicates that the direction of the

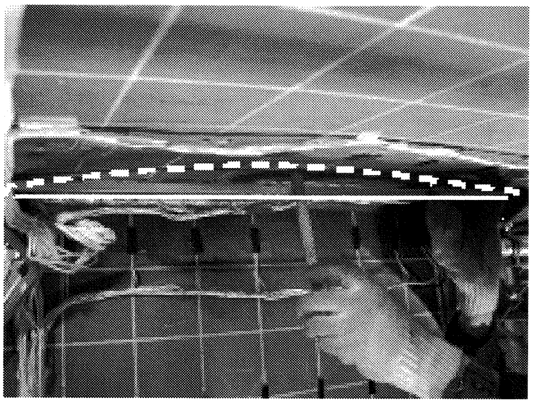

Figure 12 Local buckling at the inner flange in beam of C1 (+4 δ_y)

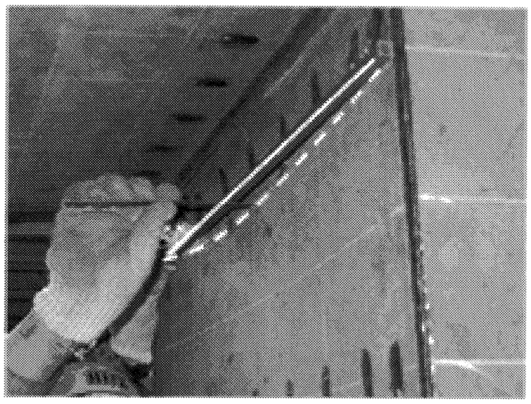

Figure 13 Local buckling at inner flange in column of C2 (+5 δ_y)

deformation of the inner flange in the column in the loops of +4δ_y was opposite to that of +1δ_y, +2δ_y and +3δ_y. The reason why this buckling behavior happened is supposed as follows. The rigid of the part of the cruciform joint is much larger than that of flange plates because of the weld bead, so the right angle of the cruciform joint tends to be kept even if the large deformation occurs at the inner flange plates. Therefore, if the buckling occurs with large deformation at the inner flange plates in the column or the beam, the large deformation of one member may cause deformation of another member in the reverse direction for keeping the right angle of the cruciform joint as shown in Figure 14.

Figure 15 shows the relationship between δ_{cor} and out-of-plane deformation of the fillets in the loops of +1δ_y and -1δ_y at the point shown in Figure 16. In Figure 15, the positive values of the deformation mean the out-of-plane deformation occurred inside. Figure 15 indicates that the maximum value of the deformation in the loop of +1δ_y is about 9mm. And residual deformation remains and the value is about 3mm even though δ_{cor} returns to zero. The large residual deformation at fillets after the earthquake is thought not to be desirable. It is important to consider the residual deformation of fillets in developing the seismic design method of beam-to-column connections with fillets.

According to fact mentioned above, fillets have little effect on buckling behavior of the inner flange plate and can improve the low cycle fatigue performance of the cruciform joint under the earthquakes but it is important to consider the residual deformation of fillets.

3.3 Feature of stress distribution on inner flanges in elastic range

Figure 17 and Figure 18 show the stress distribution on the outside surface of inner flange in the beam at 50 mm and at 280 mm from the cruciform joint respectively. The point at 280 mm from the cruciform joint corresponds to the edge of the fillets. The stress in Figure 17 and 18 was in the elastic range and the load corresponding to the stress in these figures was about 300kN in both C1 and C2.

Figure 17 demonstrates that stress of C1 is smaller than

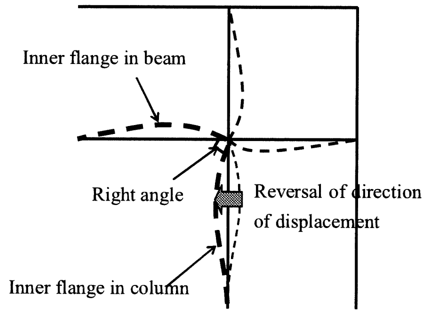

Figure 14 Process of appearance of reverse deformation

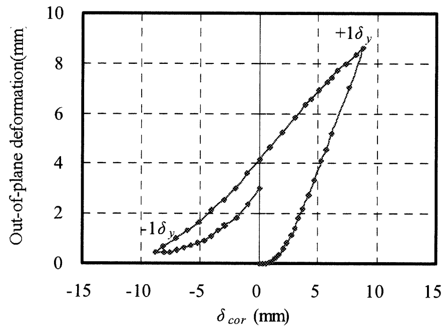

Figure 15 δ_{cor} - deformation of the fillets relationship

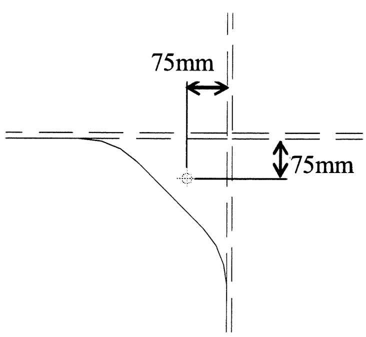

Figure 16 Measuring point of deformation

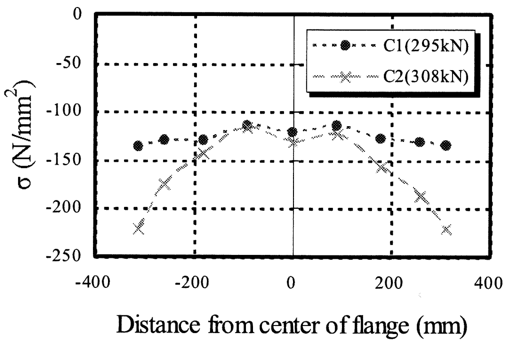

Figure 17 Stress distribution in beam at 50mm from cruciform joint

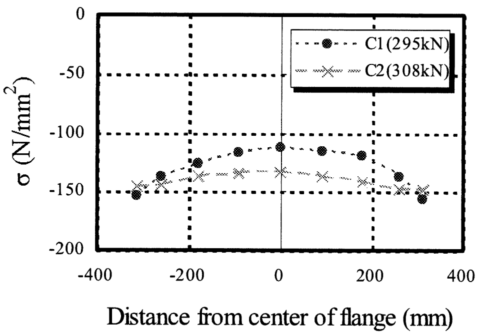

Figure 18 Stress distribution in beam at 280mm from cruciform joint

that of C2 and especially the high stress concentration at the corners of C1 is much smaller than that of C2 at 50mm from the cruciform joint. On the other hand, Figure 18 indicates that the stress of C1 is overall smaller than that of C2 but the stress concentration at the corners is a little larger than that of C2 at 280mm from the cruciform joint as the result of the edge of the fillets.

So fillets can reduce the stress near the cruciform joint overall. Especially, they can decrease stress concentration at the corners greatly. However they may slightly increase the stress concentration at the edge of fillets.

4. CONCLUSIONS

Cyclic loading experiments of beam-to-column connections of steel bridge frame piers were carried out in order to grasp the seismic behavior of beam-to-column connections with fillets and the influence of fillets on it. Based on the experimental results, the following conclusion can be drawn.

1) Fillets dealt with in this paper have little effect on the overall load – displacement relationship of beam-to-column connections before maximum load P_{max} and on buckling behavior of the inner flange plates of beam-to-column connections. However it is important to consider the residual deformation of fillets.
2) Fillets can reduce the stress near the cruciform joint overall. Especially, they can decrease stress concentration at the corners greatly.

References:

Japan Road Association (1996a), "Specifications for highway bridges, Part II Steel Bridges."

Japan Road Association (1996b), "Specifications for highway bridges, Part V Seismic Design."

Japan Road Association (2002a), "Specifications for highway bridges, Part II Steel Bridges."

Japan Road Association (2002b), "Specifications for highway bridges, Part V Seismic Design."

Ministry of Construction (1995), "Report on the damage of Highway Bridges by the Hyogo-ken Nanbu Earthquake," Committee for Investigation on the Damage of Highway Bridges caused by the Hyogo-ken Nanbu Earthquake.

The Metropolitan Highway Public Corporation (2003), "Design specifications for Metropolitan Highway Bridges, Part II Steel Bridges."

Usami, T. and Oda H. (2001), "Numerical analysis and verification methods for seismic design steel structures," J. Struct. Mech. / Earthquake Eng., JSCE, Vol.668/ I -54, pp.1-15, 2001.

Fifth International Conference on Urban Earthquake Engineering
March 4-5, 2008, Tokyo Institute of Technology, Tokyo, Japan

NONLINEAR RESPONSES OF BRIDGE PIERS CONSIDERING PERIODIC AND PHASE CHARACTERISTICS OF INPUT MOTIONS

Takeshi Kitahara[1)]

1) Associate Professor, Department of Civil & Environmental Engineering, Kanto Gakuin University, Japan
kitahara@kanto-gakuin.ac.jp

Abstract: In this study, a new estimation method for elasto-plastic maximum response displacements of bridge piers is investigated. Firstly, modified spectrum intensity, called Natural-Period-dependent spectrum intensity (SI), is proposed. Natural-Period-Dependent SI is a mean value of velocity response spectra in the natural period ranges corresponding to the target structure. It is clarified that Natural-Period-Dependent SI has a strong correlation with the non-linear response of structures. Secondly, we proposed an estimation method for non-linear response displacements of bridge piers using Natural-Period-Dependent SI. The accuracy of the proposed method is evaluated according to the results of non-linear dynamic analyses. Thirdly, the elasto-plastic responses of a single degree of freedom system subjected to the artificial seismic waves randomly generated having the same response spectrum are studied. Consequently, it is found that the proposed method for elasto-plastic maximum response displacements is better than the method using the equal energy assumption and using the equal displacement assumption in terms of the accuracy and the applicability. Moreover, it is clarified that the coefficient of variation is from 15 to 18 % for the maximum response displacements using the Level 2 Type I input earthquake motion.

1. INTRODUCTION

After the Great Hanshin-Awaji Earthquake Disaster in 1995, the importance of a dynamic analysis has increased in the seismic design of structures. In the seismic design of structures, the ductility design method is usually used. In the ductility design method of Japan specifications for highway bridges (2002), the equal energy assumption (as shown in the work by Housner, (1965)) is used in order to estimate the maximum response displacement. In the design specifications of CALTRANS (1999), the equal displacement assumption is suggested to evaluate the maximum response displacement of structures whose natural periods are from 0.7 to 3.0 second.

However, the estimation results using the equal energy assumption or equal displacement assumption are not always so accurate because the non-linear responses of structures are dependent on the periodic characteristics of input earthquake motions. In the previous works, it was found that the variations of estimation results using the equal energy assumption were large and that the applicable ranges of these equal assumptions were dependent on the natural period of structures and the input earthquake motions.

Therefore, this research aims to new estimation method for maximum response displacement that is more accurate than the equal energy assumption and equal displacement assumption. At first, the index of seismic motions, which has a strong correlation to the non-linear dynamic response of bridge piers, is investigated. The past studies (as shown in the work by Nagahashi et al. (1971) and Kitahara et al. (2000)) presented that the indices, which have strong correlation to dynamic response, are the PGA in the short period range, the PGV in the middle period range and the PGD in the long period range. However, the question is that the effective index varies according to the natural period of structures. Thus, it is important to find a new index, which has strong correlation to dynamic response over a wide range of natural period. In this study, modified spectrum intensity called natural-period-dependent SI (as shown in the work by Kitahara et al. (2000)) is proposed as the effective index of seismic motions. The natural-period-dependent SI, which is calculated as a mean value of velocity response spectra in the ranges corresponding to the structures, is an index value taking account of the prolongation of natural period with the damages.

Next, a new estimation method for non-linear maximum response displacement using natural-period-dependent SI is proposed. In this study, the precision of proposed method is appraised by the results of non-linear dynamic analyses using SDOF models with observed earthquake waves. In this case, the estimation results by proposed method are compared with the estimation results using the equal energy assumption and equal displacement assumption.

Moreover, many design codes are being revised into performance-based design. According to ISO2394 of the International Organization for Standardization (ISO), a reliability design method is endorsed in the seismic design of structures. These situations require estimating exactly the nonlinear seismic performance of structures.

However, non-stationary characteristics of seismic waves strongly affect nonlinear responses of structures so that elasto-plastic responses of the structure subjected to different seismic waves with the same response spectrum are not identical.

In order to take this effect into account, the Japanese Specifications for Highway Bridges (the Specifications) recommends evaluating seismic performances by averaging the results by three seismic waves. FEMA recommends evaluating seismic performances with the maximum value of results from three seismic waves or with the average of results from seven seismic waves. However, the background of these recommendations is not clear.

Therefore, this paper aims to clarify the influence of the non-stationary characteristics of input earthquake motions. The phase characteristics are considered as non-stationary characteristics. In this study, the variation of nonlinear response displacement subjected to a large number of artificial seismic waves randomly generated and having the same response spectrum is investigated. The seismic design method using a non-stationary coefficient is examined. A non-stationary coefficient is an index taking account of the influence of the non-stationary characteristics of input earthquake motions.

2. ANALYSIS METHOD

2.1 Analysis Model

Analysis targets are nine steel bridge piers as shown in Table 1. These bridge piers are designed on the type II ground by Design Specifications of Highway Bridges. The steel piers are stiffening box sections. The width-thickness parameter and the slenderness parameter of steel piers are set 0.3 to 0.6 and 0.25 to 0.65, respectively. Natural periods of steel bridge piers are from 0.38 to 1.41 second. The width-thickness parameter and the slenderness parameter are defined as follows:

$$R_f = \frac{b_f}{t}\sqrt{\frac{\sigma_y}{E}\cdot\frac{12(1-\mu^2)}{\pi^2 k}} \quad (1)$$

$$\bar{\lambda} = \frac{2h}{r}\cdot\frac{1}{\pi}\sqrt{\frac{\sigma_y}{E}} \quad (2)$$

where, b_f: flange plate width, t: flange plate thickness, σ_y: yield stress, E: Young's modulus, μ: Poisson's ratio, $k=4n^2$: buckling coefficient, h: length of member, r: radius of gyration.

The single degree-of-freedom model is adopted as shown in Fig. 1(a) because the target structures are single column type bridge piers. The bases of models are fixed in the analysis. As the hysteresis characteristics of steel piers, a 2-parameter model proposed by Suzuki et al.1996 is used. This model can be presented the degrading of stiffness and strength with local buckling of plates. The skeleton curve is assumed as tri-linear model as shown in Fig. 1(b). In Fig. 1(b), the example of hysteresis loop of S6025 is presented. The vertical axis shows the generalized horizontal force by the yield horizontal force H_y and the horizontal axis shows the generalized horizontal displacement by the yield horizontal displacement δ_y. H_m and δ_m in Fig. 1(b) indicate maximum horizontal force and maximum horizontal displacement, respectively.

The damping ratio is 5% at the damping term of dynamic equation. Linear acceleration method is used in time history analysis. The peak ground velocities of all input seismic waves, which are described in 2.1 and the total number is eighteen, are set 25, 35, 50 and 75cm/s. Thus, non-linear analyses are performed seventy-two times against one analysis model. The relevance of responses and indices of seismic motions is discussed using seventy-two results of dynamic analyses against each pier.

Table 1 Analysis Target

Model Name	Width-Thickness Parameter	Slenderness Parameter	Natural Period
S3025	0.30	0.25	0.38
S3045	0.30	0.45	0.69
S3065	0.30	0.65	1.02
S4525	0.45	0.25	0.47
S4545	0.45	0.45	0.86
S4565	0.45	0.65	1.26
S6025	0.60	0.25	0.53
S6045	0.60	0.45	0.96
S6065	0.60	0.65	1.41

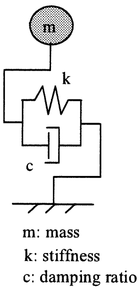

(a) SDOF Model

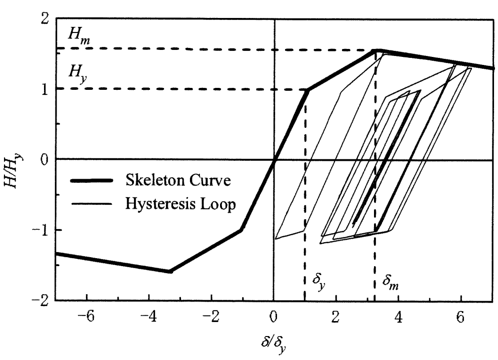

(b) Hysteresis Loop

Fig. 1 Analysis Model

2.2 Input Earthquake Wave

The observed waves and simulated waves in the Design Specifications of Highway Bridges are used as input earthquake waves. Table 2 shows the features of input earthquake motions. The original intervals of each seismic wave shown in Table 2 are 0.01 second or 0.02 second. All data are used as 0.005 second interval data by linear interpolation.

In this study, the PGA, PGV, PGD and SI are first considered as the basic indices of seismic motions. Time histories of velocity and displacement are calculated from acceleration time history using fast Fourier transformation (FFT) integration. SI is calculated by integration of velocity response spectrum.

Table 2 Earthquake Motions

Earthquake	Abbreviation	Type	Direction
Hyogoken-nanbu (1995, Japan)	JMA-NS	Near Field	NS
	JMA-EW	Near Field	EW
	FUKI-x	Near Field	(x)
	FUKI-y	Near Field	(y)
	TAK-NS	Near Field	NS
	TAK-EW	Near Field	EW
Imperial Valley	EL-NS	(Far Field)	NS
	EL-EW	(Far Field)	EW
Kern County (1952, USA)	TAFT-NS	Far Field	NS
	TAFT-EW	Far Field	EW
Tokachioki (1968, Japan)	HACHI-NS	Far Field	NS
	HACHI-EW	Far Field	EW
(Simulated Wave)	Typ1	Far Field	-
	Typ2	Near Field	-

2.3 Proposed Spectrum Intensity

Housner defined that the integration range of velocity response spectrum was from 0.1 to 2.5 second because he assumed that natural periods of the general structures were from 0.1 to 2.5 second. Thus, a seismic wave has a unique SI value independent of target structures and SI has generality as index of seismic motions.

The response spectrum at the neighborhood of natural period is meaningful against a certain structure. However, the integration range of SI extends to the region unrelated with the natural period. Therefore, the periodic characteristics against a certain structure are not effectively innovated into SI. That is to say, SI is the effective index of seismic motions in order to evaluate the mean responses of many structures. However, SI is not the effective index of seismic motions to estimate responses of a certain structure.

In this study, natural-period-dependent SI, which is calculated by the integration of the velocity response spectrum in the range corresponding to the natural period of structures, is proposed and presented as Eq. (3) and Fig. 2. For instance, in Fig. 2, two shaded areas indicate $SI_{n.p}$ corresponding to structures of natural period T_1 and T_2, respectively.

$$SI_{n.p.} = \frac{1}{(\beta-\alpha)T}\int_{\alpha T}^{\beta T} S_v(\tau,h)d\tau \tag{3}$$

where, $SI_{n.p.}$: natural-period-dependent SI,
S_v: velocity response spectrum,
h: damping ratio, α,β: constant.
τ: integration parameter (natural period),
T: natural period of the target structure.

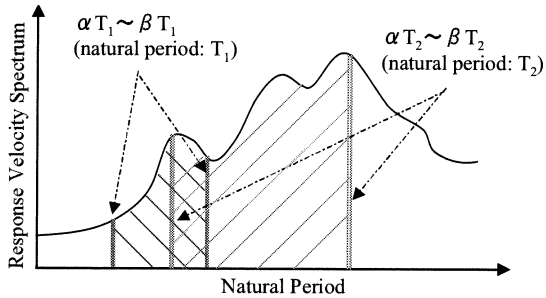

Fig. 2 Concept of Natural-Period-Dependent SI

It is generally accepted that the natural period of structures is prolonged because the stiffness of structures is degraded with damage. Therefore, it is likely that α=1.0 and β>1.0 in Eq. (3) are the optimal values. However, it is possible that the component in the short period range affects on the dynamic response due to the effect of damping and so on. Thus, the optimal α and β are evaluated from the results of non-linear dynamic analyses against steel bridge piers. Further, the effectiveness of natural-period-dependent SI is discussed.

3. ANALYSIS RESULTS AND DISCUSSION

3.1 Correlation between Response and Index of Earthquake Motion

It is assumed that the distributions of the dynamic responses and the indices of seismic motions are logarithmic normal distribution because the dynamic response values and the indices of seismic motions are not negative values. With this assumption, the correlation is calculated by Eq. (4):

$$\log R = a + b \cdot \log I \tag{4}$$

where, R: dynamic response value,
I: index of seismic motions,
a, b: regression coefficient.

The result of S6025 is shown in Fig. 3. Fig. 3 shows the relationship between the maximum response displacement and the PGA. In this figure, the solid line presents the regression line and the dash-dotted lines represent the logarithmic standard deviations. The symbols of circle and square denote the results of near-field type earthquake and far-field type earthquake, respectively. N shows the number of analysis case and R shows the correlation coefficient.

Fig. 3 indicates that there are no significant difference between the results of near-field type and far-field type. Thus, in the further discussions, all the seismic waves are not separated into near-field type and far-field type and are treated as a population. The correlation between the maximum response displacement and the PGA is strong such as its coefficient is 0.886. The scatter diagram (Fig. 3) also shows that there is obviously the linear relationship between maximum response displacement and the PGA.

Against all the target piers, the correlation between maximum response displacement and the other indices of seismic motions is calculated by Eq. (4). In such cases, it is verified that the regression results are fit under significant level 0.01(1%) using t-distribution.

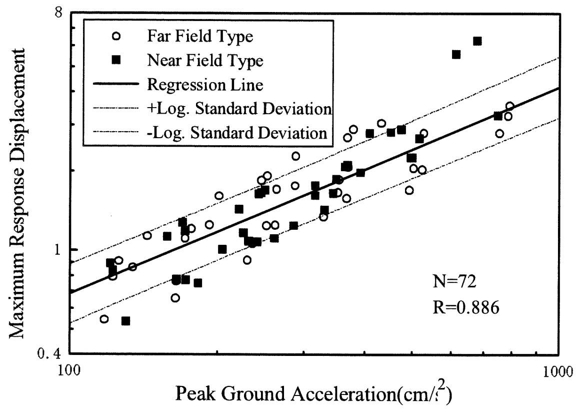

Fig. 3 Scatter Diagrams

3.2 Variation of Correlation due to natural period

The optimum parameters of α and β, which indicate integration ranges of natural-period-dependent SI shown in Eq. (3), are investigated. Fig. 4 indicates the results in the case of $\alpha \leq 1.0$ and $\beta \geq 1.0$. In this figure, the vertical axes show the mean values of correlation coefficient between maximum response displacement and natural-period-dependent SI and the horizontal axes show the parameter β. The square, closed circle, triangle and open circle denote the results of α = 0.7, 0.8, 0.9 and 1.0, respectively.

The values of α and β at the point the correlation coefficient is maximum can be regarded as the optimum parameters. For Fig. 4, the optimum parameters are α=0.9 and β=1.2 for steel piers. However, the optimum integration ranges decided here is effectively only for bridge piers of single column which are predominated by the first-order mode. For other bridge types, which are predominated by highly-order modes, it might be necessary to investigate against each bridge type.

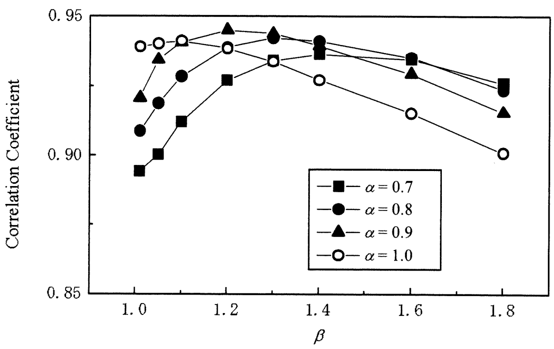

Fig. 4 Relationship Between α,β and Correlation Coefficient

Fig. 5 shows the correlation coefficient between the maximum response displacement and the index of seismic motions regarding all analysis models. In this figure, the symbols of closed square, closed circle, triangle, opened circle and opened square denote the correlation coefficient of the PGA, PGV, PGD, SI and natural-period-dependent SI, respectively.

Fig. 5 indicates that the correlation between the PGA and the maximum response displacement is strong in the natural period range up to 0.9 second. However, the correlation decreases in reverse proportion to the natural period over 0.9 second. Fig. 5 also shows that the correlation coefficient of the PGV and the maximum response displacement is from 0.7 to 0.9 over a wide range of natural period. The relevance of the SI and maximum response is almost equal to one of the PGV and maximum response, though the SI is the index taking account of the periodic characteristics of seismic motions.

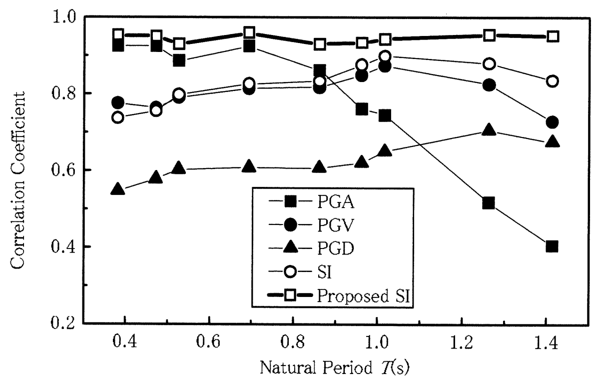

Fig. 5 Correlation Coefficient

(Maximum response displacement)

These results present that the correlation between the dynamic response and the basic index of seismic motions, such as PGA, PGV, PGD and SI, varies according to the natural period of bridge piers. In the other hand, Fig. 5 indicates that the correlation coefficient between the maximum response displacement and natural-period-dependent SI is from 0.93 to 0.95. Namely, it is clarified that the relevance of the maximum response displacement and natural-period-dependent SI is very strong for all the piers having different natural period. Therefore, it is fair to say that dynamic responses can be estimated adequately using natural-period-dependent SI as the index of seismic motions.

4. ESTIMATION METHOD

4.1 Estimation Equation

The relationship between the velocity response spectrum and the displacement response spectrum is shown in Eq. (5)

$$\delta = S_d = \left(\frac{T}{2\pi}\right) S_v \tag{5}$$

where, δ: maximum displacement,
S_d: displacement response spectrum,
S_v: velocity response spectrum,
T: natural period.

The natural-period-dependent SI is regarded as the mean value of the velocity response spectrum near the natural period during elasto-plastic response of the structure. Therefore, the estimation equation is conducted following Eq. (6) by replacing the velocity response spectrum with the natural-period-dependent SI and replacing the natural period with the equivalent period in Eq (5). It is difficult to exactly estimate the equivalent natural period during the elasto-plastic response.

$$\delta_{est.} = \left(\frac{T_{eq}}{2\pi}\right) S_{n.p.} \tag{6}$$

where, $\delta_{est.}$: estimated maximum displacement,
$SI_{n.p.}$: natural-period-dependent SI and
T_{eq}: equivalent period.

In this study, the equivalent period is simply regarded as the period using the secant modulus at $2\delta_y$ (δ_y is the yield displacement).

4.2 Estimation Results and Considerations

In order to evaluate the accuracy of the proposed method, the estimation results are compared with the maximum response displacements calculated by the elasto-plastic response analyses.

The results are shown in Fig. 6. In this figure, (a), (b) and (c) represent the results by the proposed method, the equal energy assumption and the equal displacement assumption, respectively.

The vertical axis denotes the estimation result divided by the maximum response displacement and the horizontal axis denotes the natural period of structures. The estimation result is in the underestimate range when the value of the vertical axis is less than 1.0. The symbols of square, circle, triangle and opposite triangle indicate the estimation results, the mean values and the means plus or minus the standard deviations, respectively.

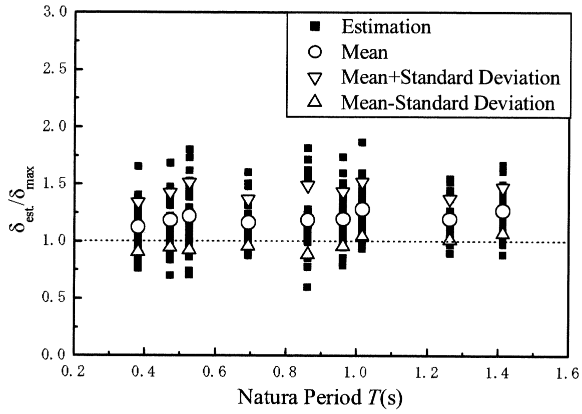

(a) Proposed Method

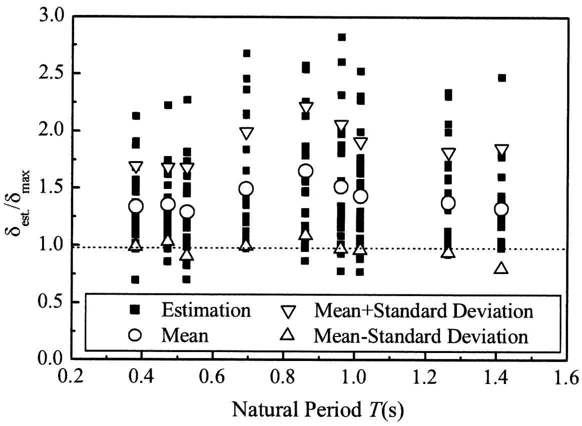

(b) Equal Energy Assumption

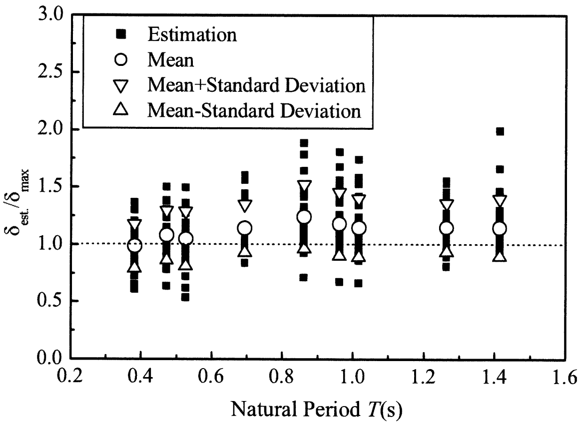

(c) Equal Displacement Assumption

Fig. 6 Estimation Results

In the case of steel piers, the results by the proposed method are from 0.6 to 1.8 and the mean values are from 1.1

to 1.3. Moreover, the means minus the standard deviations are nearly equal to 1.0. From these results, it is clarified that the risk of being underestimated by proposed is small.

The results using the equal displacement assumption are almost equivalent to the results of proposed method. However, the means minus the standard deviations in the short natural period range are smaller than by the proposed method. Therefore, the equal displacement assumption is not applicable to the structures in the short natural period range.

On the other hand, the results using the equal energy assumption are from 0.7 to 2.8. The risk of being overestimated by the equal energy assumption is likelihood. Moreover, the variation of estimation results is large.

4.3 Influences on Maximum Response Displacements

For the variation of nonlinear responses of steel bridge piers is investigated, one hundred waves with the same design spectrum are used as input earthquake motions. Fig. 7 shows the results on the variation of the maximum response displacements. In this figure, solid circles indicate analysis values and squares indicate mean values of each pier. Triangles and upside down triangles show the mean value minus the standard deviation and the mean plus the standard deviation, respectively. Stars show the coefficient of variation.

The graph shows that the mean values of the maximum response displacements are from 1.5 to 4.8 times as yield displacements and that the mean values vary according to the natural periods of each pier. On the other hand, it is found that the coefficient of variation does not vary much according to the natural periods and is from 15% to 18%. Compared with that the variations of the response acceleration spectra are from 2% to 7%, the variation of the maximum response displacements are amplified from 2 to 7 times.

Hence, the evaluations by the standard waves tend to risky depending on how things go. It may be that there are some cases in which such evaluations do not compensate enough for the influences of the non-stationary characteristics on nonlinear responses.

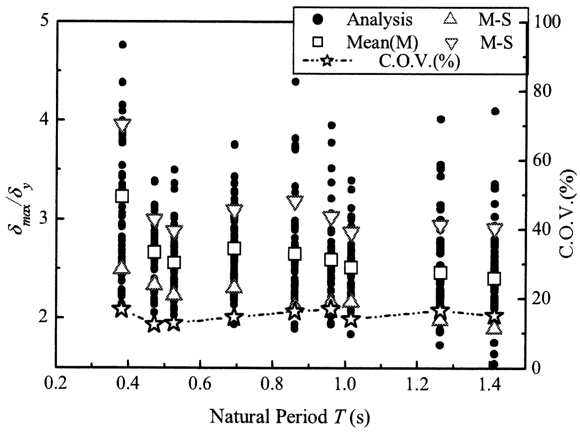

Fig. 7 Variation of Maximum Response Displacement

5. CONCLUSION

The following conclusions may be drawn from the present study:

1. Natural-period-dependent SI, which is calculated by the integration of the velocity response spectrum in the range corresponding to the natural period of the target piers, is proposed. The optimum integration ranges for natural-period-dependent SI are from $0.9T$ to $1.2T$ for steel piers.
2. The correlation between dynamic maximum displacement and natural-period-dependent SI is very strong over a wide range of natural period. The severe seismic waves against target structures can be selected by natural-period-dependent SI spectrum.
3. A new estimation method for maximum response displacement using the natural-period-dependent SI is proposed and the applicability for steel piers is proved.
4. The estimation method using the natural-period-dependent SI is better than using the equal energy assumption and equal displacement assumption in terms of the accuracy and applicability when the maximum response displacement is evaluated in the seismic design of structures.
5. The coefficient of variation of the maximum response displacement, subjected to one hundred simulated waves with the Level 2 Type I design spectrum specified by the Japanese Specification for Highway Bridges, is from 15% to 18%.
6. The variations of the maximum response displacement do not vary mach according to the natural periods of structures. It may be that there are some cases in which evaluations using the Japanese Specification standard three waves method do not adequately reflect the influences of the non-stationary characteristics on nonlinear responses.

References:

Japan Road Association (2002) "Specifications for Highway Bridges Part V Seismic Design", Maruzen, Tokyo.

Housner, G.W. (1965), "Intensity of Earthquake Ground Shaking near the Causative Fault", 3rd World Conference on Earthquake Engineering, Vol. 1(III), New Zealand, pp.94-115.

Caltrans (1999), "Memo to Designers 20-1 Seismic Design Methodology," Caltrans Metric, California.

Nagahashi S. and Kobayashi K. (1971), "Maximum Amplitude of Ground Motion as the Index Estimating the Intensity of Earthquake Motions", Transactions of the Architectural Institute of Japan, No. 181, Japan, pp.15-22 (in Japanese).

Kitahara T. and Itoh Y. (2000), "Correlation between Nonlinear Response of Bridge Piers and Natural-Period-Dependent Spectrum Intensity", 12th World Conference on Earthquake Engineering, New Zealand, CD-ROM Proceedings, 806/6/A.

Suzuki M., Usami T., Terada M., Itoh T. and Saizuka K. (1996), "Hysteresis Models for Steel Bridge Piers and Their Application to Elasto-Plastic Seismic Response Analysis", Journal of Structural Engineering /Earthquake Engineering, JSCE, No. 549/I-37, pp.191-204 (in Japanese).

Fifth International Conference on Urban Earthquake Engineering
March 4-5, 2008, Tokyo Institute of Technology, Tokyo, Japan

OPTIMAL BILINEAR MODEL OF HIGH DAMPING RUBBER BEARING FOR SEISMIC RESPONSE ANALYSIS

Junji YOSHIDA[1] and Toshiyuki SUGIYAMA[2]

1) Associate Professor, Dept. of Civil & Environmental Engineering, University of Yamanashi, Japan
2) Professor, Dept. of Civil & Environmental Engineering, University of Yamanashi, Japan
jyoshida@yamanashi.ac.jp t-sugiyama@yamanashi.ac.jp

Abstract: Bilinear hysteretic models are widely used for representing restoring forces of laminated rubber bearings. In this paper, the optimal bilinear model of a super high damping rubber bearing is proposed. At first, the bilinear model specified by the present design code is shown to be inaccurate especially in the large amplitude range. Then, optimal bilinear model under seismic excitations is obtained with the aid of the high order model and real-coded GA. Finally, equations for estimating the parameters of bilinear models are proposed, and they are found to be much more accurate than the present design code

1. INTRODUCTION

Base-Isolation system using laminated rubber bearings is considered to be an efficient technology of providing a mitigation of seismic damage for structures such as bridges and buildings, and has proven to be reliable and cost-effective. There are many structures in various countries, which concern not only new constructions but also existing structures (Skinner et al. 1993), especially after the Loma Prieta (1989), Northridge (1994) and Kobe (1995) earthquakes.

One of the most widely-used laminated rubber bearings is High Damping Rubber bearing (:HDR), which reduces the inertia force of the structure by extending the natural period and absorbs the earthquake energy by its hysteretic damping. Due to these dynamic effects, behavior of the bearings highly affects seismic response of base-isolated structures and, therefore, many hysteretic models of HDRs have been proposed, in order to accurately predict seismic response of base-isolated structures (Yasaka et al. 1988, Nagarajaiah et al. 1991, Sano and Pasquale 1995, Kikuchi and Aiken 1997, Hwang et al. 1997, Abe et al. 2004b). Although some of these models can well reproduce behavior of HDRs, they are so complex with many parameters that, instead of these models, simple bi-linear elasto-plastic model (called as "bi-linear model" in this paper) has often been employed in the actual design.

In this paper, optimal bi-linear model of HDR to accurately predict seismic response is developed with the aid of high order model, which was proposed by the authors (Abe et al. 2004b). At the first section, bi-linear model in the design code is shown to be inaccurate in seismic response analysis, especially when the displacement response becomes large. Then, optimal parameters of bi-linear model are found with genetic algorithm so that the seismic responses with the bilinear model become closer to that with the high order model. Finally, the optimal parameters are approximated by polynomial functions, and performance of bi-linear model with these functions in seismic response analysis is evaluated.

2. EVALUATION OF BI-LINEAR MODEL IN DESIGN CODE

2.1 Bearings used in the analysis

A HDR, which has rectangular cross-section of 400×400 mm, five layers of rubber with 10 mm thickness, is chosen as an example of typical bearings, and its load-displacement relation, which was obtained in advance through loading experiment, is modeled by the following high order model.

2.2 High order model

A hysteretic model proposed by Abe et al. (2004a,b) was proven to have capability of well representing load-displacement relations of HDRs. Therefore, the restoring force computed by the model is considered to be the "true" one of the HDR and called as "high order model" in this paper. Parameters of the model are identified so that difference of restoring forces by the experiment and the

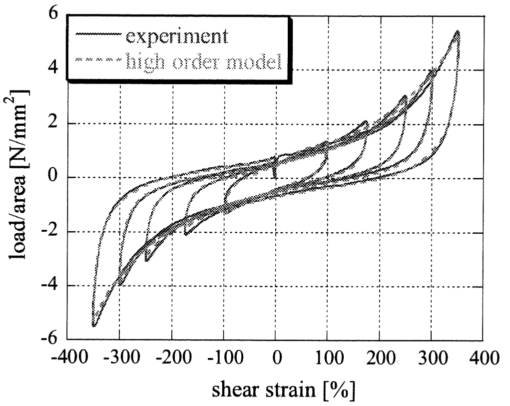

Figure 1 Restoring forces of HDR by loading experiment and high order model

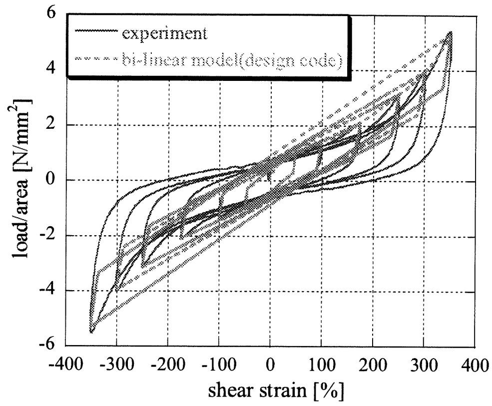

Figure 2 Restoring forces of HDR by experiment and bi-linear model in design code

Table.1 Coefficients in design equations of HDR with 1.2 N/mm^2 shear modulus

i	0	1	2	3	4	5
a_i	3.339	-5.201	4.113	-1.545	0.2808	-0.01933
b_i	5.128	-7.971	6.227	-2.331	0.4162	-0.02762
c_i	35.05	-54.61	43.19	-16.22	2.948	-0.2029

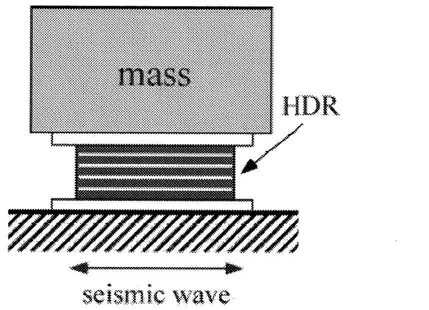

Figure 3 A SDOF system with HDR used in simulations

model is minimized with the aid of Real-Coded Genetic Algorithm (:RCGA), which was known to possess high ability of global searching in general parameter identification problems, even when they have strong non-linearity (Tsutsui et al. 1999 and Satoh et al. 2000).

Comparison of load-displacement relations by the experiment and the model with the identified parameters is shown in Figure 1, where shear strain in the horizontal axis is defined as "displacement over total thickness of rubber layers". From Figure 1, it is found that the model can express complex hysteretic loops accurately at several deformation levels.

2.3 Bi-linear model in design code

According to design code in Japan (JRA 2005), load-displacement relation of the HDR is approximated by a bi-linear model, whose elastic stiffness G_1 [N/mm^2], plastic stiffness G_2 [N/mm^2] and yielding force τ_Y [N/mm^2] in the normalized load-displacement relation ("force over area" and shear strain are used instead) are decided according to the following equations.

$$G_1(\gamma) := \sum_{i=0}^{5} a_i \gamma^i \ , \ G_2(\gamma) := \sum_{i=0}^{5} b_i \gamma^i \tag{1}$$

$$\tau_y := \frac{G_1(\gamma)}{G_1(\gamma) - G_2(\gamma)} \cdot \tau_d(\gamma) \tag{2}$$

with

$$\tau_d(\gamma) := \gamma \{ G(\gamma) - G_2(\gamma) \} \ , \ G(\gamma) := \sum_{i=0}^{5} c_i \gamma^i \tag{3}$$

$$\gamma := U_{\max} / \sum_{i=1}^{N} t_e^{(i)} \ , \ U_{\max} := \max_{0 \le t \le T_0} |U(t)| \tag{4}$$

where N is the number of rubber layers, $t_e^{(i)}$ is the thickness of i-th rubber layer and $U_{\max}$ is the maximum displacement response during seismic excitation ($0 \le t \le T_0$). On the other hand, a_i, b_i and c_i are coefficients, which was decided as in Table.1 from general experimental results of HDRs in the past. The hysteretic loops by the bi-linear model using Eqs.(1) and (2) are compared with that by the loading experiment in Figure 2.

2.4 Seismic response analysis with bi-linear model in design code

Accuracy of the bi-linear model in Eqs.(1) and (2) is evaluated through simulations with a Single Degree Of Freedom (:SDOF) system in Figure 3. In the system, a single structure (particle), whose mass is equivalent to "vertical load/area" of 4 N/mm^2, is supported by the HDR, and it is subjected to horizontal earthquakes as shown in Table.2.

Table.2 Earthquake acceleration data used in simulations

Name of earthquake	year	location	direction	Max acceleration [mm/sec^2]	dominated frequency [Hz]
Kobe	1995	Kobe marine	NS	8180	1.44
			EW	6170	1.42
Kobe	1995	East Kobe bridge	N12W	4430	0.513
			N78E	4250	0.391
Kushiro	1993	Kushiro marine	NS	8150	2.36
			EW	9190	2.75
Imperial Valley	1940	El Centro	NS	3400	1.46
			EW	2090	2.37
Sanfernando	1971	California	NS	11500	4.79
			EW	10500	2.33
Northridge	1994	Sylmar Parking Lot	NS	8270	0.635
			EW	5930	1.16
Kern Country	1952	Taft	NS	1520	1.37
			EW	1760	3.00

Table.3 Results of seismic response analysis with bilinear model in design code

Input earthquake		Kobe earthquake (1995) (East Kobe bridge, NS)				Kushiro earthquake (1993) (Kushiro marine, NS)				Imperial Valley earthquake(1940) (El Centro, NS)			
Vertical load /area [N/mm^2]		3.92		7.84		3.92		7.84		3.92		7.84	
Unit (displacement or shear strain)		mm	%	mm	%	mm	%	mm	%	mm	%	mm	%
Maximum of displacement	Bi-linear(design)	75.1	150	131	262	75.3	151	117	234	50.7	101	58.6	117
	High order	135	270	187	377	94.0	188	134	268	55.9	112	63.6	127
R.M.S of displacement	Bi-linear(design)	22.9	45.8	41.6	83.2	24.0	48.0	38.6	77.2	7.91	15.8	14.0	28.0
	High oder	45.0	90.0	77.9	156	30.7	61.4	48.9	97.8	8.81	17.6	15.3	30.6
Error (max displacement)		44.3 %		29.9 %		19.9 %		12.7 %		9.30 %		7.86 %	
Error (R.M.S displacement)		49.1 %		46.6 %		21.8 %		21.2 %		10.2 %		8.50 %	

In the first step of the simulations, the high order model is employed as the exact restoring force of the bearing in order to obtain the "true" responses, together with $U_{\max}$ in Eqs.(4). Then, the bi-linear model with parameters in Eqs.(1) and (2) is used as an approximated model for computing responses under the same seismic excitations, and they are compared with the "true" ones. The results of the comparisons are presented in Table.3, which imposes that there is much difference between the two responses. Figures 4 and 5 show two representative responses in the simulations and it is found that the bi-linear model in the design code is inaccurate under the specific seismic excitations.

3. OPTIMAL BI-LINEAR MODEL FOR SEISMIC REPONSE ANALYSIS

In this section, an optimal bi-linear model is constructed such that the model can predict displacement response of the SDOF system as close to the "true" one as possible.

3.1 Bi-linear model for seismic response prediction

Hysteresis by a bi-linear model could be computed, when its elastic stiffness, plastic stiffness and yielding force are given. In this research, these three parameters are considered to be unknown, and they are identified with the RCGA so that the following function E would be minimized.

$$E := \sum_i |U_b(t_i) - U_h(t_i)| \cdot |U_h(t_i)| \tag{5}$$

where $U_b(t_i)$ and $U_h(t_i)$ are displacement responses of the SDOF system by the bi-linear model and the high order model, respectively, at time t_i in the numerical computation. It is noted that, in Eq.(5), $|U_h(t_i)|$ is used as weight of the difference, because we usually need better agreement around peaks of the response.

Comparisons of the identified parameters and the present design code in Eqs.(1) and (2) are shown in Figs.6-8, where the normalized maximum displacement response defined in Eqs.(4) is used in their horizontal axis. From Figure 6-8, it is found that the optimal parameters are closely related to the maximum displacement response, and they are averagely smaller values than that by the design code.

3.2 New design equations of bi-linear model

Based on the identified parameters in Figure 6-8, new design equations for parameters of bi-linear model are constructed as functions of γ. The following second order

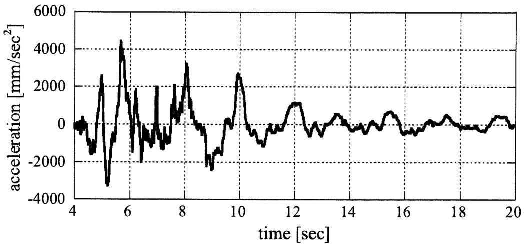

(a) seismic acceleration

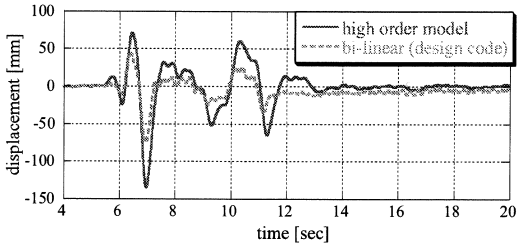

(b) displacement responses

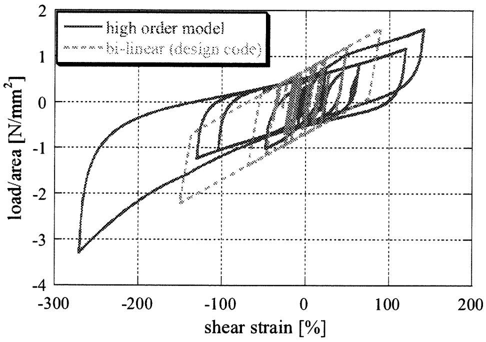

(c) restoring forces

Figure 4 Seismic responses of SDF system by high order model and bi-linear model in design code under East Kobe bridge (N12W)

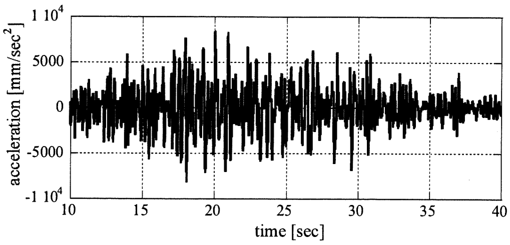

(a) seismic acceleration

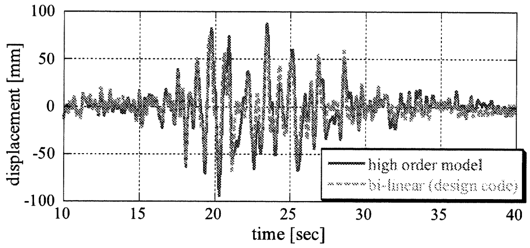

(b) displacement responses

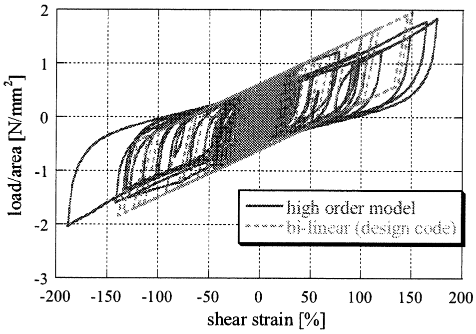

(c) restoring forces

Figure 5 Seismic responses of SDF system by high order model and bi-linear model in design code under Kushiro marine record (NS)

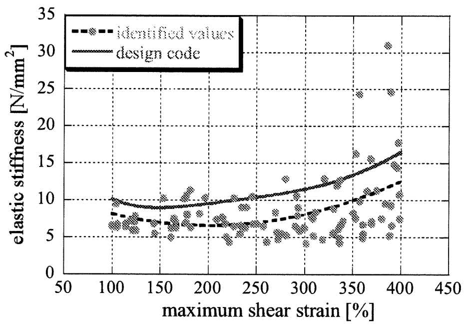

Figure 6 Identified values and design code of plastic stiffness

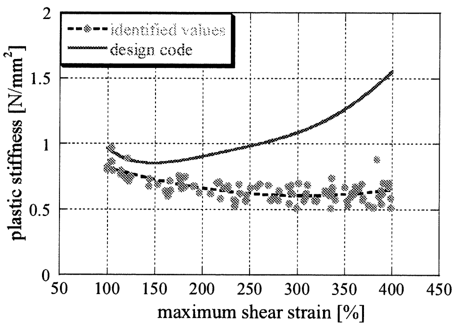

Figure 7 Identified values and design code of plastic stiffness

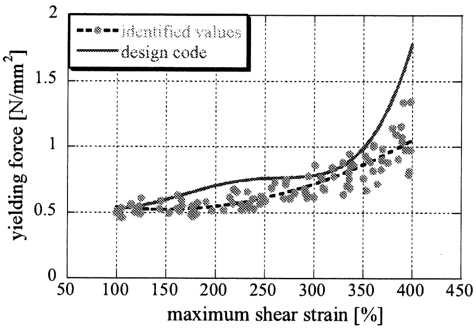

Figure 8 Identified values and design code of yielding force

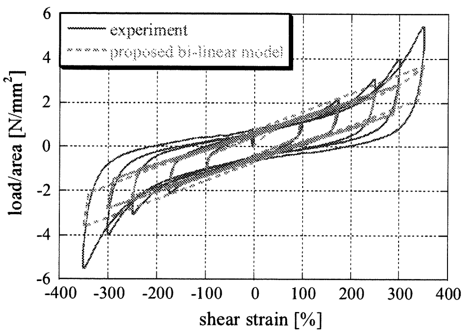

Fig.9 Restoring forces by proposed bi-linear model and experiment.

Table.4 Results of seismic response analysis with proposed bilinear model

Input earthquake		Kobe earthquake (1995) (East Kobe bridge, NS)				Kushiro earthquake (1993) (Kushiro marine, NS)				Imperial Valley earthquake(1940) (El Centro, NS)			
Vertical load /area [N/mm^2]		3.92		7.84		3.92		7.84		3.92		7.84	
Unit (displacement, shear strain)		mm	%	mm	%	mm	%	mm	%	mm	%	mm	%
Maximum of displacement	Bi-linear	134	268	197	394	96.0	192	134	268	51.8	103.6	58.9	118
	High order	135	270	187	374	94.0	188	134	268	55.9	112	63.6	127
R.M.S of displacement	Bi-linear	43.1	86.2	85.0	170	28.3	56.6	43.6	87.2	9.11	18.2	14.7	29.4
	High oder	45.0	90.0	77.9	156	30.7	61.4	48.9	97.8	8.81	17.6	15.3	30.6
Error (max displacement)		0.740 %		5.35 %		2.13 %		0.00 %		7.33 %		7.39 %	
Error (R.M.S displacement)		4.22 %		9.11 %		7.82 %		9.00 %		3.41 %		3.92 %	

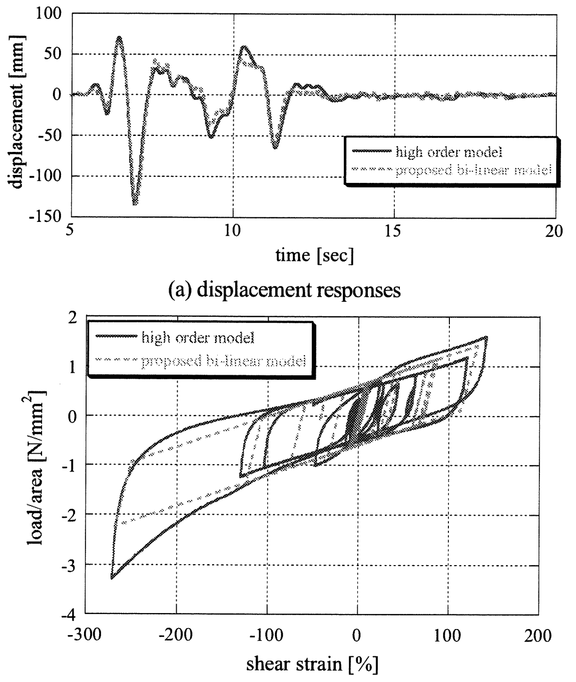

(a) displacement responses

(b) restoring forces

Figure 10 Seismic responses of SDF system by high order model and proposed bi-linear model under East Kobe bridge record (N12W)

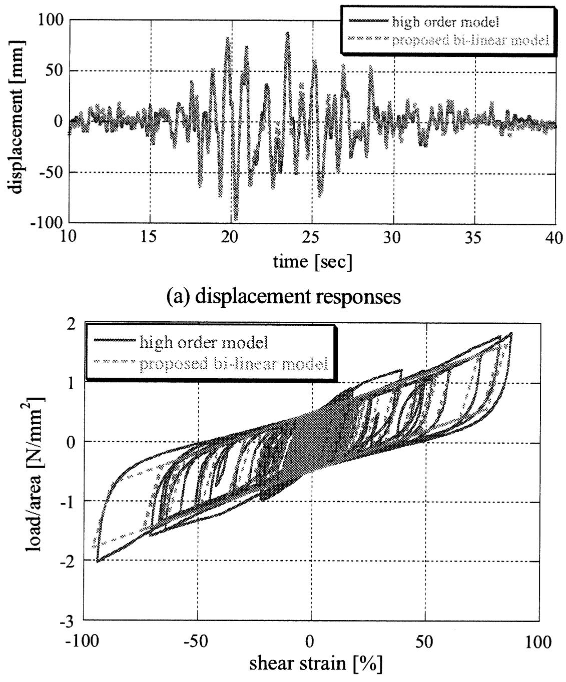

(a) displacement responses

(b) restoring forces

Figure 11 Seismic responses of SDF system by high order model and proposed bi-linear model under Kushiro marine record (NS)

polynomials are the equations, which are obtained by applying least square method (Press et al. 1988) to the identified parameters.

$$\bar{G}_1 := 12.7 - 6.06\gamma + 1.51\gamma^2 \quad (6)$$

$$\bar{G}_2 := 1.08 - 0.309\gamma + 0.0507\gamma^2 \quad (7)$$

$$\bar{\tau}_Y := 0.697 - 0.237\gamma + 0.0814\gamma^2 \quad (8)$$

where $\bar{G}_1$ [N/mm^2], $\bar{G}_2$ [N/mm^2] and $\bar{\tau}_Y$ [N/mm^2] are elastic stiffness, plastic stiffness and yielding force of the new bi-linear model, respectively, in the normalized load-displacement relation. The curves in the above equations are depicted as dot lines in Figure 6-8.

Figure 9 shows comparison of load-displacement relations by the proposed bi-linear model and the loading experiment.

3.3 Accuracy of the proposed design equations

Seismic response analysis with the new bilinear model is conducted under the same procedures in subsection 2.4, in order to evaluate performance of Eqs.(6)-(8).

Table.4 shows comparisons of displacement responses, when the HDR is modeled by the proposed bi-linear model or the high order model. Results in Table.5 indicate that error on maximum and R.M.S values of displacement responses are clearly decreased in comparison with those in Table.3. Representative displacement responses and load-displacement relations of both models are presented in Figure 10 and Figure 11 and, from these figures, it is understood that the proposed bi-linear model is much more accurate than the design code in seismic response analysis.

4. CONCLUSIONS

A new bilinear model of HDR is developed with the aid of high order model and genetic algorithm. Major findings are summarized as follows.

1) When a bi-linear model in the present design code is employed as a hysteretic model of HDR, responses in SDOF system show some error in comparison with those by high order model.
2) Optimal parameters of bi-linear model in order to predict accurate displacement response are found to possess high correlation with the maximum displacement response.
3) New equations for bi-linear model are proposed on the basis of the optimal parameters. These equations are so simple (2nd order polynomials) that they would be readily introduced in the actual design of base-isolated structures.
4) In seismic response analysis, bi-linear model with the proposed equations is found to be much more accurate than that with the present design code.

References:

Abe, M., Yoshida, J. and Fujino, Y. (2004a). "Multi-Axial Behaviors of Laminated Rubber Bearings and their Modeling: I Experimental Study", *Journal of Structural Engineering*, ASCE, 130(8), 1119-1132.

Abe, M., Yoshida, J. and Fujino, Y. (2004b). "Multi-Axial Behaviors of Laminated Rubber Bearings and their Modeling: II Modeling", *Journal of Structural Engineering*, ASCE, 130(8), 1133-1144.

Hwang, J.S. and Ku, S.W. (1997). "Analytical Modeling of High Damping Rubber Bearing." *Journal of Structural Engineering*, ASCE, Vol.128, No.8, 1029-1036.

Japan Road Association (2005). "*Handbook of Bearings for Highway Bridges*." (in Japanese).

Kikuchi, M. and Aiken, I.D. (1997). "An Analytical Hysteresis Model for Elastomeric Seismic Isolation Bearings." *Earthquake Engineering and Structural Dynamics*, Vol. 26, 215-231.

Nagarajaiah, S., Reinhorn, A.M., and Constantinou, M.C. (1991). "Nonlinear Dynamic Analysis of 3-D-Base-Isolated Structures." *Journal of Structural Engineering*, ASCE, Vol. 117, No.7, 2035-2054.

Press, H.W., Teukolsky, S.A., Vetterling, W.T. and Flannery, B.P. (1988). "*Numerical Recipes in C*." Cambridge University Press, New York.

Sano, T. and Pasquale, G.D. (1995). "A Constitutive Model for High Damping Rubber Bearings." *Journal of Pressure Vessel Technology*, ASME, Vol.117, 53-58

Satoh, H., Yamamura, M. and Kobayashi, S. (1996) "Minimal Generation Gap Model for GAs Considering Both Exploration and Exploitation." *Proceedings of IIZUKA '96*, 494-497.

Skinner, R.I., Robinson, W.H. and McVerry, G.H. (1993). "*An Introduction to Seismic Isolation*." John Wiley & Sons.

Tsutsui, S., Yamamura, M. and Higuchi, T. (1999). "Multi-parent Recombination with Simplex Crossover in Real-Coded Genetic Algorithms." *Proceedings of Genetic and Evolutionary Computation Conference*, Vol.1, 657-664.

Yasaka, A., Maeda, S. and Fujimoto, N. (1988). "Biaxial Hysteresis Model for Base Isolation Devices." Kajima Corporation, Tokyo, Japan.

Fifth International Conference on Urban Earthquake Engineering
March 4-5, 2008, Tokyo Institute of Technology, Tokyo, Japan

CRACK PROPAGATION IN UNDER-MATCHED JOINTS UNDER SEISMIC LOADING

Atsushi Tanabe[1)] and Worawit Padungsriborworn[2)]

1) Assistant Professor, Department of Civil Engineering, Tokyo Institute of Technology, Japan
2) Graduate student, Department of Civil Engineering, Tokyo Institute of Technology, Japan
tanabe@cv.titech.ac.jp, -

Abstract: There is a possibility of under-matched welded joint in case of high strength steel. When seismic force applied to under-matched joint, deposit metal yields first and it cause strain concentration and plastic constraint in the deposit metal. Previous study showed that the strain concentration at a weld defect reduces crack initiation life significantly and there is almost no crack initiation life. Therefore, evaluation of crack propagation behavior is important. This study is aiming to clarify the crack propagation behavior in the under-matched welded joint. Fracture mechanics approach showed that plastic constraint can extend propagation life, because plastic constraint reduces crack opening and crack propagation rate. However, the effect of the plastic constraint was small, thus the propagation life of under-matched joint was governed by yield strength of deposit metal.

1. INTRODUCTION

All of codes and specification request that the yield strength of the deposit metals should be higher than the yielding strength of base metals. However, this requirement cannot always be satisfied because of following reasons. (1) Softer welding materials are used intentionally in order to improve weldability, because stronger welding materials usually have bad weldability. (2) Actual yield strength of base metal can be significantly higher than the value in the provision for yield strength.

When seismic force is applied to under-match welded joints, deposit metal yields first and strain concentration occurs in the deposit metal. Such strain concentration possibly cause fracture of weld joint during earthquakes. Thus, evaluation of the strength of under-matched welded joint under seismic loading is important.

After yielding of deposit metal, the deformation of deposit metal is constrained by non-yielded base metal which called plastic constraint. Stress triaxiality, is introduced by the plastic constraint (Henry and Luxmoore 1997, Hancock et al. 1993). Because of stress triaxiality in deposit metal, under-matched welded joints had almost same tensile strength as usual welded joints, but it had a tendency of low elongation (Satoh and Toyoda 1971). This triaxiality may also affect to fatigue behavior.

Besides under-matching, weld joints may include weld defects such as blowholes, slag-inclusions, cracks, and so on, and these defects reduce fatigue strength (Miki et al. 2001). If defects exist in under-matched welded joints, fatigue strength under cyclic plastic strain may decrease because of strain concentration due to both of defects and under-matching. Furthermore, there is a possibility that stress concentration due to weld defect causes local yielding, even in service condition. In such case, high strain concentration may occur and it may affect fatigue strength.

Authors showed that under-matched welded joint had extremely low crack initiation life due to high strain concentration of under-matched welded joint (Tanabe and Long 2007). This result indicates that the crack propagation behavior is important to evaluate the fatigue performance of defect containing under-matched welded joints.

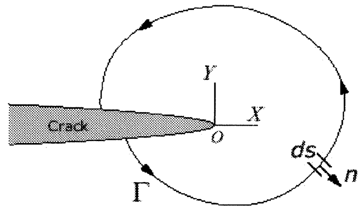

Figure 1 Definition of J-integral

Crack propagation under plastic strain can be evaluated by fracture mechanics parameter, J-integral and J-integral range. J-integral is defined as contour integral (see Eq. (1) and Figure 1), and it has path-independency (Rice 1978).

$$J = \int_{\Gamma}\left(Wdy - \sum_i T_i \frac{\partial u_i}{\partial x} d\Gamma \right) \qquad (1)$$

Where, T_i $(=\sigma_{ij}n_j)$ is surface force along the contour Γ, $\partial u_i / \partial x$ is gradient of stress in x direction (parallel to crack surface and perpendicular to crack front), W is strain energy density, defined as Eq. (2), for non-linear elastic material.

$$W = \sum_{i,j} \int_0^{\varepsilon_{ij}} \sigma_{ij} d\varepsilon_{ij} \tag{2}$$

Crack propagation life N_p can be calculated by Eq. (3) (Dowling and Begley 1976, Dowling 1977).

$$N_p = \int_{a_0}^{a_f} \frac{1}{\frac{da}{dN}} da \tag{3}$$

Where, a_0: initial crack size, a_f: final crack size, da/dN: crack propagation rate. The da/dN has relationship with ΔJ, da/dN was obtained by Eq. (4)

$$\frac{da}{dN} = C(\Delta J)^m \tag{4}$$

Where, C and m is material constant, in case of steel, $C = 3.32 \times 10^{-4}$, m=1.375.

ΔJ of plastic deformed material can not be calculated from the time history of J, because J-integral is defined for non-linear elastic material. Thus, ΔJ is calculated by summation of elastic part and plastic part as shown in Eq. (5) (Dowling and Begley 1976, Dowling 1977).

$$\Delta J = \Delta J^{(e)} + \Delta J^{(p)} = \frac{K_I}{E'} + \frac{Area}{Bb} \tag{5}$$

Where K_I: stress intensity factor (mode I), E': equivalent elastic constant, E for plain stress condition and $E/(1-\nu^2)$ for plain strain condition, *Area*: the area in load-crack opening curve considering crack closure (see Figure 2), B: width and b: ligament size. In this calculation, the equivalent load range ΔP_e, which considering crack closure, was used for calculation of stress intensity factor K_I.

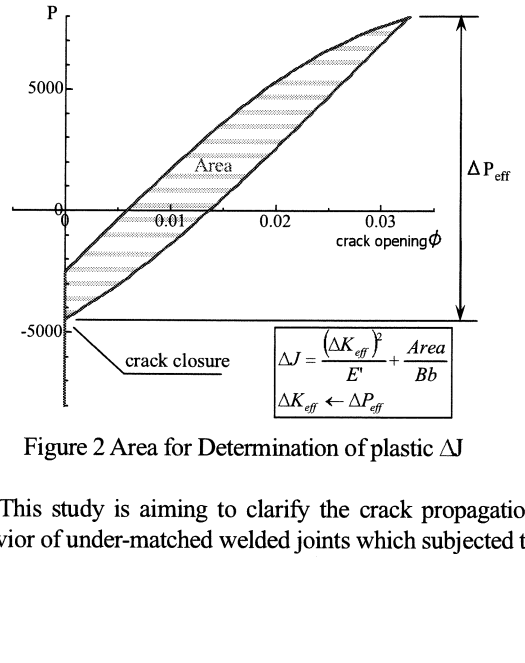

Figure 2 Area for Determination of plastic ΔJ

This study is aiming to clarify the crack propagation behavior of under-matched welded joints which subjected to plastic loading by fracture mechanics approach. At first, the effects of under-matching on J-integral development are discussed. Next, the under-matching effects on ΔJ were considered. And then, the effects on propagation life were evaluated.

2. EVALUATION OF EFFECT ON J-INTEGRAL

2.1 FEM Analysis

The parameters are groove shape, under-matching and weld size. FEM models are shown in Figure 3. I-groove and X- groove joint were considered. In case of I-groove model, weld size of 10, 20, 30 and 40 mm were modeled in order to evaluate the effects of weld size. X-groove model simulates actual weld joints.

Analysis code was ABAQUS (ABAQUS, Inc. 2004), second-order plane strain element was used. In order to evaluate singularity at crack tip, degenerate elements were used.

Bi-linear kinematic hardening is used. True stress-true strain relationships were shown in Figure 4. Yield strength of base metal was 500MPa. 10% and 20% under-match weld metal's yield strength were 450MPa and 400MPa, respectively. Hardening coefficient H is same for all material: 2000MPa (=E/100).

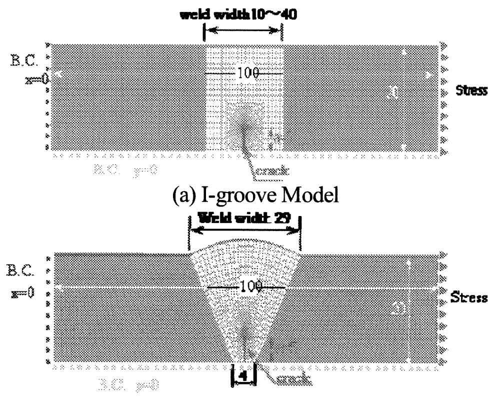

(b) X-groove model

Figure 3 FEM models for J-integral

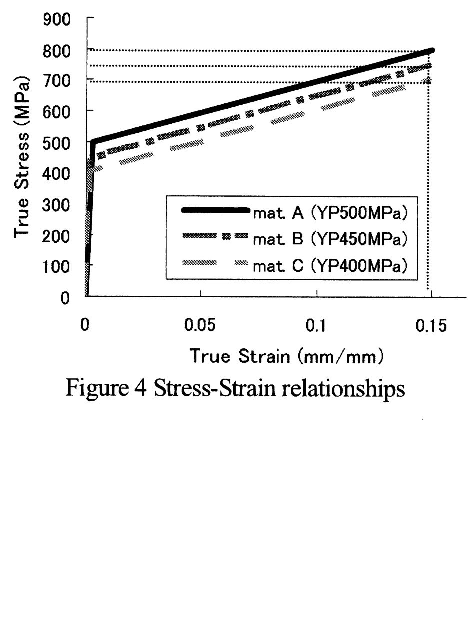

Figure 4 Stress-Strain relationships

2.2 Analysis Result

J-integral-Far field stress relationships of I-groove case were shown in Figure 5. J-integral of under-matched joints locates between the J-integral of base metal and J-integral of weld metal. Narrower weld width case was closure to base metal case. Narrower gap had high constraints and such high constraints may reduce J-integral.

FEA result of X-groove is shown in Figure 6. The under-matched case was almost same as weld metal case. Thus, constraint effect might be small in case of actual joints.

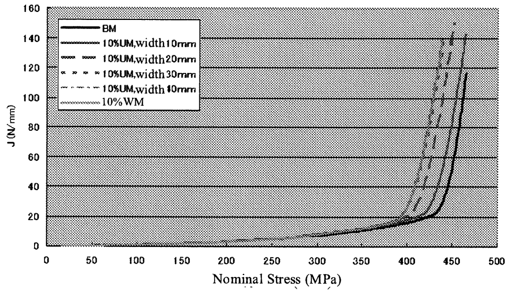

(a) I-groove

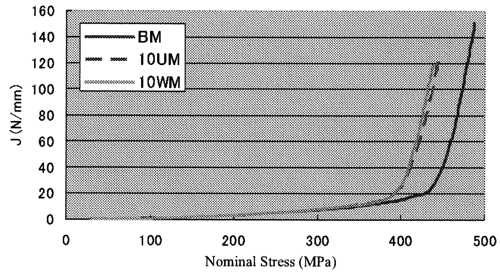

(b) X-groove

Figure 5 J-σn relationships

3. EVALUATION OF EFFECTS ON ΔJ

3.1 Parameters

Considered parameters are combination of material and nominal stress range.

Five matching conditions which made of three materials were considered. Figure 7 shows matching conditions. Considered combinations were: a) all base metal case (BM), b) 10% under-match case (10UM), c) 20% under-match case (20UM), d) weld metal for 10% under-match only case (10WM), and e) weld metal for 20% under-match only case (20WM).

Fig. 8 showed loading condition (stress history). Considered nominal stress range $\Delta\sigma_n$ were 8 cases (from 200 to 1000 MPa with R=-1).

3.2 FEM Model

Figure 9 shows FEM model for ΔJ and propagation analysis. Analysis code was ABAQUS, 2nd order plain strain 2D solid element was used. By considering symmetric condition, quarter model was used. Degenerate elements were used to around crack tip in order to consider singularity.

Weld joint of X-groove (45 degree) with 30mm thickness were modeled by second order plane strain element with degenerate element and gap element. The gap element was installed for crack face in order to simulate crack closure. Quarter model was used by considering symmetric condition.

Constitutive equation was same as previous analysis.

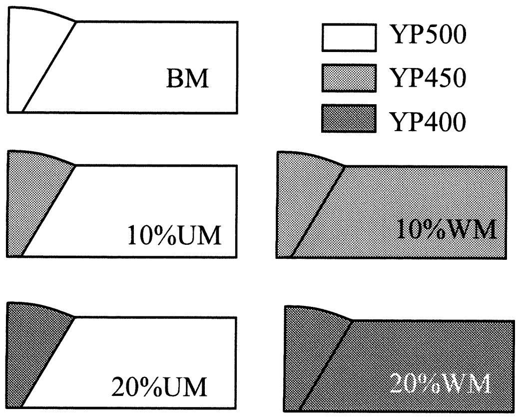

Figure 7 Matching condition

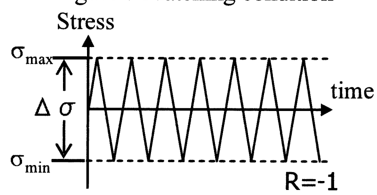

Figure 8 Loading condition

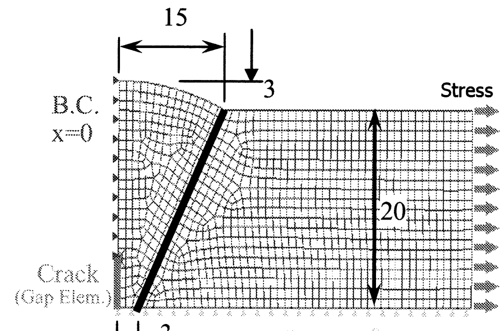

Figure 9 FEM model for ΔJ and propagation analysis

3.3 Analysis Result

Load-crack opening relationship of 800MPa range is showed in Figure 10. The loop of under-match case had smaller than weld metal case. This fact indicates that constraints due to under-matching reduces crack opening.

Figure 11 shows the relationship between ΔJ and $\Delta\sigma_n$. Under-match case had smaller ΔJ than base metal case when all section yield. This result indicates that constraint due to under-matching reduce crack opening and it results smaller ΔJ.

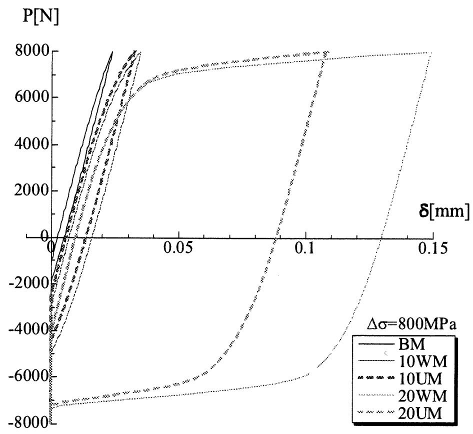

Figure 10 Load-crack opening relationship

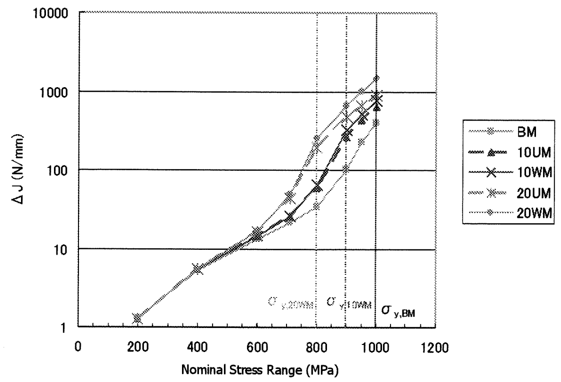

Figure 11 ΔJ-$\Delta\sigma_n$ relationships

4. PROPAGATION ANALYSIS

4.1 Parameters

Finally crack propagation life of under-matched joints was calculated. Parameters were initial crack size, nominal stress range and material combination.

Two initial crack sizes were considered: 1mm and 3.33mm. Where, 3.33mm is the allowable crack size for the joint which fatigue is considered ($2a=t/6$, t: plate thickness).

4.2 FEM Models

FEM models were similar with ΔJ analysis (see Figure 9). However, crack size a was changed from 1mm to 14 mm with 1mm pitch (14 models for each matching condition).

4.3 Determination of Final Crack Size a_f

In this study, final crack size a_f was determined from brittle fracture strength and maximum stress. Where, the brittle fracture strength is the far field stress when brittle fracture occurred. In this study, Crack Tip Opening Displacement (CTOD) δ_c=0.1mm was used as criterion of fracture toughness (Miki et al. 1999, Miki et al. 2000). The fracture toughness δ_c was converted to J_c by using Eq. (6) (ASTM 2006).

$$\delta = \frac{J}{m\sigma_Y} \tag{6}$$

$$\sigma_Y = \frac{\sigma_{YS} + \sigma_{TS}}{2} \tag{7}$$

$$m = A_0 - A_1\left(\frac{\sigma_{YS}}{\sigma_{TS}}\right) + A_2\left(\frac{\sigma_{YS}}{\sigma_{TS}}\right)^2 - A_3\left(\frac{\sigma_{YS}}{\sigma_{TS}}\right)^3 \tag{8}$$

$$\begin{Bmatrix} A_0 \\ A_1 \\ A_2 \\ A_3 \end{Bmatrix} = \begin{Bmatrix} 3.62 \\ 4.21 \\ 4.33 \\ 2.00 \end{Bmatrix}, \; when \; \left(\frac{\sigma_{YS}}{\sigma_{TS}}\right) \geq 0.5 \tag{9}$$

Where, σ_{YS}: Yield Stress, σ_{TS}: Tensile Strength.

Fracture strength can be obtained from J_c and far field stress-J relationship. The relationship between far field stress and J-integral was calculated by FEM analyses.

Fig. 12 showed the relationship between brittle fracture strength and crack size. Final crack size a_f can be obtained from maximum stress σ_{max} from this diagram.

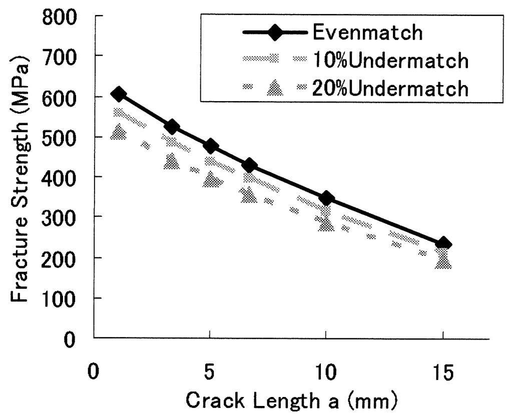

Figure 12 Fracture strength-Crack length

4.4 Procedure of Propagation Analysis

In order to carry out the propagation analysis, ΔJ for arbitrary a are required. Thus, FEM models with various crack length a were analyzed and the ΔJ-a relationships for each nominal stress and matching conditions were obtained.

Figure 13 shows ΔJ-a relationship when nominal stress range was 800MPa. In case of long crack model, ΔJ of under-match case had smaller value than weld metal case. Constraints were increased due to reduction of net section and it may result low ΔJ.

Crack propagation analysis was conducted by following procedure:

1) Initialize crack size a by a_0
2) Determine ΔJ related with crack length a
3) Calculate da/dN by Eq. xx
4) Append da/dN times 1 to a
5) Repeat 2) to 4) until a reaches a_f

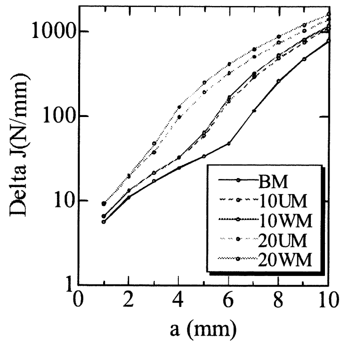

Figure 13 ΔJ-a relationship ($\Delta\sigma_n$=800MPa)

4.5 Propagation Analysis Results

Figure 14 and 15 shows crack propagation analysis results. Both initial crack sizes had same tendency. In elastic region, there is no difference among all cases. In plastic region, lower yield strength cases had shorter propagation life. Furthermore, under-matched cases had almost same but slightly longer propagation life than weld metal cases. This result indicates that crack propagation life depends on yield strength of crack material and the effect of constraint due to under-matching could be negligible.

5. CONCLUSION

In this study, crack propagation behavior of under-matched weld joint were evaluated by non-linear fracture mechanics approach. FEA and crack propagation analysis showed following result.

1. J-integral of under-matched welded joint is reduced by plastic constraints. Thus, narrower weld joint had smaller J-integral. However, in case of common weld joint such as X-groove joint had almost no effect by constraint.
2. After whole section yielding (stress range > $2\sigma_y$), plastic constraint reduces crack opening. This effect reduces ΔJ. Therefore, crack propagation rate decrease and N_p increases slightly.
3. The effect of plastic constraint on propagation life was small. Therefore, propagation life of under-matched joint might be governed by yield strength of deposit metal.

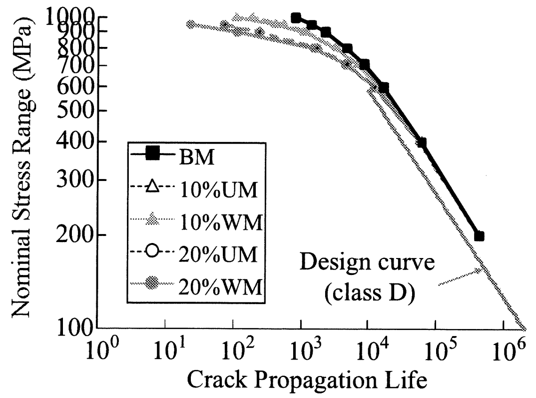

(a) Elasto-Plastic Region

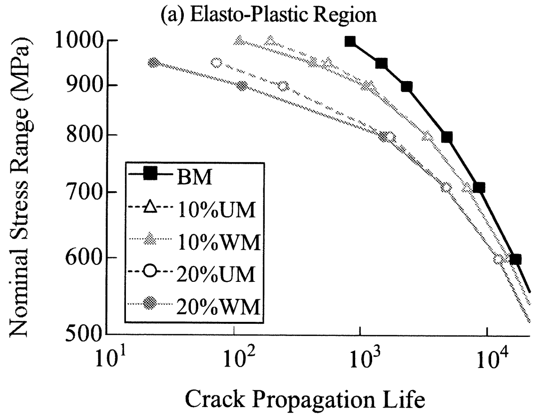

(b) Plastic Region (zoomed)

Figure 14 Propagation Analysis Result of a_0=1mm

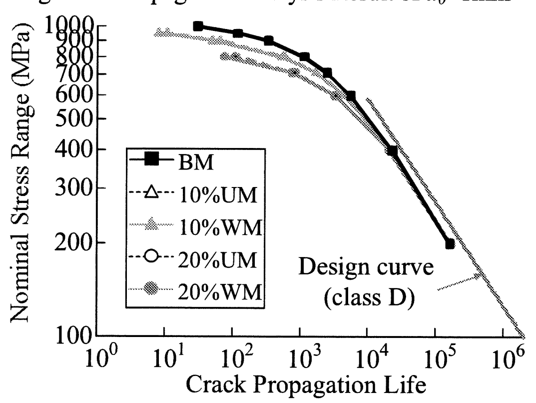

(a) Elasto-Plastic Region

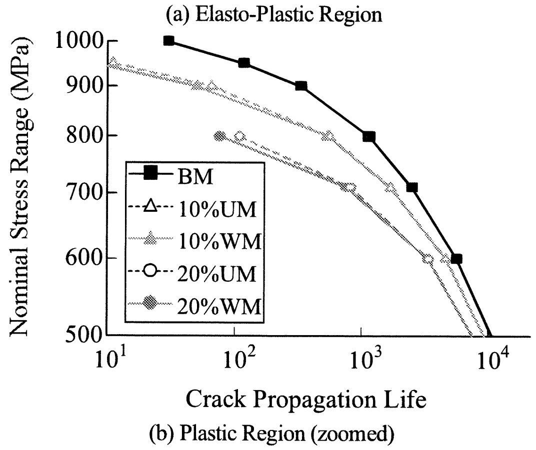

(b) Plastic Region (zoomed)

Figure 15 Propagation Analysis Result of a_0=3.33mm

References:

ABAQUS, Inc. (2004) ABAQUS Analysis User's Manual, Ver.6.5

ASTM (2006), "Standard Test Method for Measurement of Fracture Toughness", ASTM Designation: E1820-06, 2006

Dowling, N. E. and Begley, J. A. (1976), "Fatigue Crack Growth During Gross Plasticity and the J-Integral", *Mechanics of Crack Growth, ASTM STP 590*, 82-103

Dowling, N. E. (1977), "Crack Growth During Low-Cycle Fatigue of Smooth Axial Specimens", *Cyclic Stress-Strain and Plastic Deformation Aspects of Fatigue Crack Growth, ASTM STP 637*, 97-121

Hancock, J. W., Reiter, W. G. and Parks, D. M. (1993), “Constraint and toughness parameterized by T. Constraint Effects in Fracture”, *ASTM STP1171*, ASTM, 21–40

Henry, B. S. and Luxmoore, A. R. (1997), “The stress triaxiality constraint and the Q-value as a ductile fracture parameter”, *Engineering Fracture Mechanics*, **57**(4), 375–390

Miki, C., Kyuba, H. and Okinaka, K. (1999) A Study on the material of the brittle fractured bridge pier. Proceedings of JSCE, (612), 45-53

Miki, C., Sasaki, E., Kyuba, H. and Takenoi, I (2000) Deterioration of Fracture Toughness of Steel by Effect of Tensile and Compressive Prestrain, Proceedings of JSCE, (640), 165-175

Miki, C., Fahimuddin, F. and Anami, K. (2001), “Fatigue Performance of Butt-Welded Joints Containing Various Embedded Defects”, Structural Engineering / Earthquake Engineering of JSCE, **18**(1), 13s-28s

Rice, J.R. (1968), “A Path Independent Integral and the Approximate Analysis of Strain Concentration by Notches and Cracks”, *Journal of Applied Mechanics*, ASTM, **35**(2), 379–386

Satoh, K. and Toyoda, M. (1971), “Effect of Mechanical Heterogeneity on the Static Tensile Strength of Welded Joints”, Journal of the Japan Welding Society, **40**(9), 885-900

Tanabe, A. and Long, X. (2007), “Fatigue Behavior of Defect-containing Under-matched Welded Joints Under Plastic Strain”, *Proc. of Fourth International Conference on Urban Earthquake Engineering*, 261-268

EFFECT OF BACKFILL SOIL ON SEISMIC RESPONSE OF A HORIZONTALLY CURVED BRIDGE

Seiji Nagata[1], and Ian G. Buckle[2]

1) Research Engineer, Civil Engineering Research Laboratory, Central Research Institute of Electric Power Industry, Japan
2) Professor, Dept. of Civil and Environmental Engineering, University of Nevada, Reno
n-seiji@criepi.denken.or.jp, igbuckle@unr.edu

Abstract: This study focused on effect of reaction forces caused by backfill soil behind abutments on seismic performance of a horizontally curved bridge. A series of nonlinear dynamic response analyses were conducted on a three-span continuous concrete curved bridge supported by two single column bents and two integral abutments. Unilateral earthquake excitation was imposed in chord or radial directions to the analytical model with and without backfill soil. It was found that when the earthquake motion is only applied in the chord direction, the displacement response of the deck developed not only in the chord direction but also the radial direction due to the orientation of the abutments. In addition, the radial earthquake response is developed mainly in the positive side because the backfill soils are effective only in compression.

1. INTRODUCTION

The irregular geometry associated with horizontal curve of the bridge superstructure introduces complex force effects during earthquakes. Special design considerations for the structural components are thus needed to accommodate such force effects and to prevent undesirable failure mechanisms. Nevertheless, existing seismic specifications for bridges provide quite limited help for this type of bridges because little is known about their complex behavior during strong ground motions.

During the 1971 San Fernando earthquake, a number of reinforced concrete bridges with irregularity suffer extensive damage. Based on this experience, extended attention has been given to the study of seismic effects on irregular bridges such as horizontally curved bridges. Williams and Godden (1979) conducted shake table tests to clarify dynamic response of curved bridges, and these results were analytically simulated by Kawashima and Penzien (1979). Otsuka *et al.* (1997) investigated effect of various bearing conditions on nonlinear dynamic behavior of a continuous curved viaduct system. Sextos *et al.* (2004) analytically evaluated effect of wave passage, ground motion angle, and ground motion characteristics on seismic response of a curved, twelve-span bridge. With the same bridge, application of the multi-mode pushover analysis was evaluated by Paraskeva *et al.* (2006).

The previous studies described above mainly focused on the effect of the complicated seismic action due to the curvature on the design of columns, bearings and joints. However, the knowledge for the curved bridge system is insufficient especially for effect of the backfill soil reaction. For example, when a bridge superstructure has a sharp curve and the abutments at both ends are normal to the bridge centerline, the seismic performance of this type of bridges is highly dependent on the abutment/backfill interaction. Due to the sharp curve, the structure will experience different resistances depending on whether it is moving away from the backfill soil behind the abutment end-walls or into the backfill soil. In this study, seismic performance of curved bridge systems with and without backfill soil is analytically investigated.

2. TARGET BRIDGE AND IDEALIZATION

2.1 Target Bridge

A curved bridge illustrated in the Seismic Design of Bridges Design Example No. 6 (FHWA, 1996) is used in this study as a target structure. Figure 1 provides configuration of the bridge. This is three-span, concrete box girder bridge supported by reinforced concrete single columns and abutments. The girder is constructed monolithically with the column bents as well as the abutments. The columns and the abutments are founded on drilled shafts and steel pipe piles respectively. The bridge is assumed to be located on a site underlain by a deep deposit of cohesionless material. The alignment of the roadway over the bridge is sharply curved, horizontally (104 degree), but there is no vertical curve. The total span length of the deck is 88.5 m along the centerline and the curve radius is 48.8 m. The substructure elements are oriented at right angle to the bridge centerline at each substructure station.

Figure 2 shows the cross-section of the column and the pile shaft. The column is 6.7 m tall and has a 1.07 m by 1.68 m square cross section. An 18.3 m long reinforced concrete

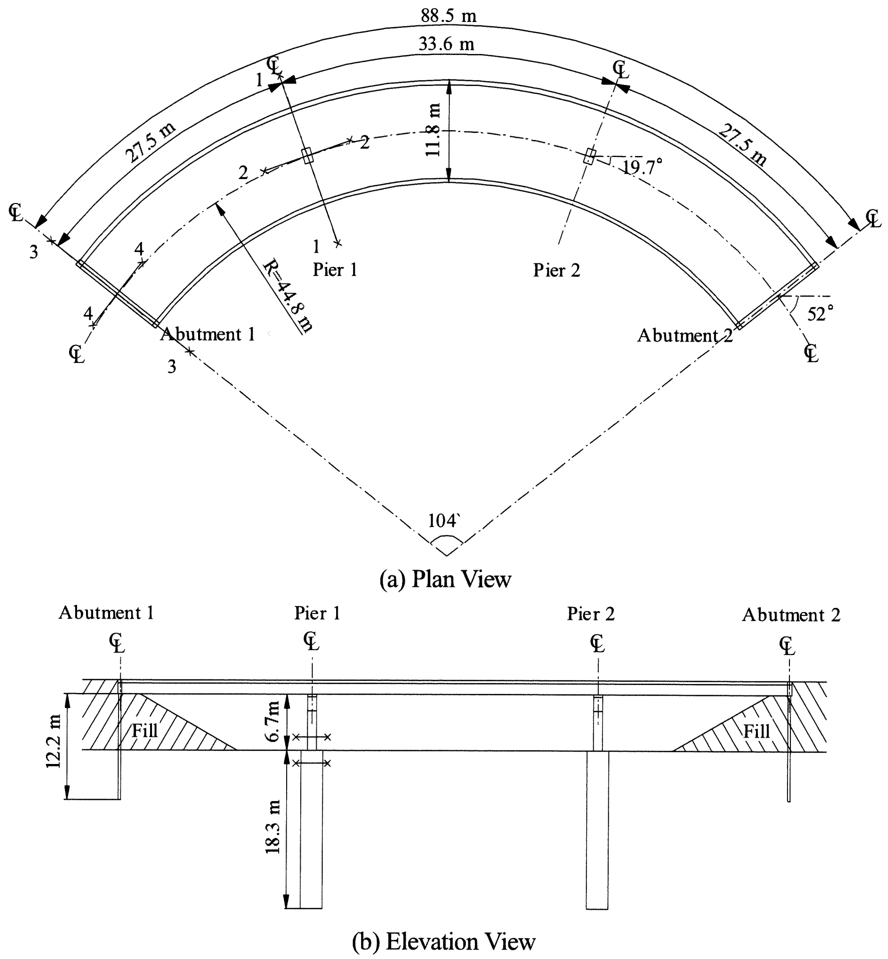

Figure 1 Three-Span Continuous Curved Bridge

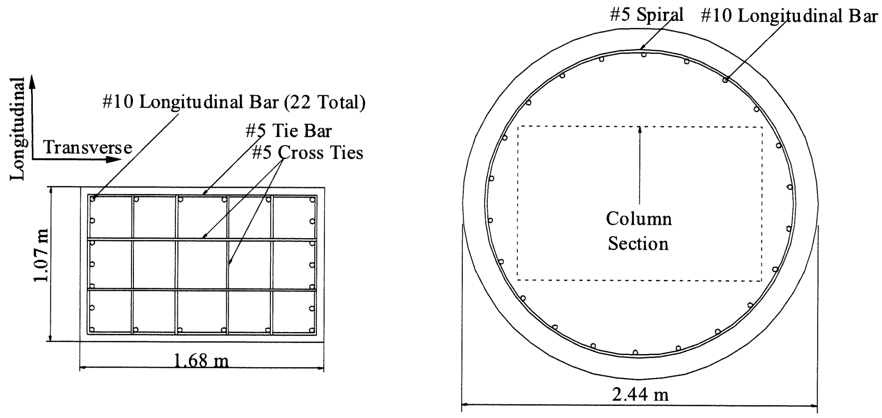

Figure 2 Cross-Sections of the Column and Drilled Shaft

pile shaft with a diameter of 2.4 m supports the column. The bridge is assumed to be built in the Northwestern United States in a seismic zone with an acceleration coefficient of $0.2\,g$. The bridge components are designed based on the 1993 edition of the Specifications (AASHTO, 1993). In the design procedure the earthquake loading was considered in two orthogonal directions, which was taken along the chord between the two abutments and along a line perpendicular to the chord. These two directions are called hereinafter the chord direction and the radial direction respectively.

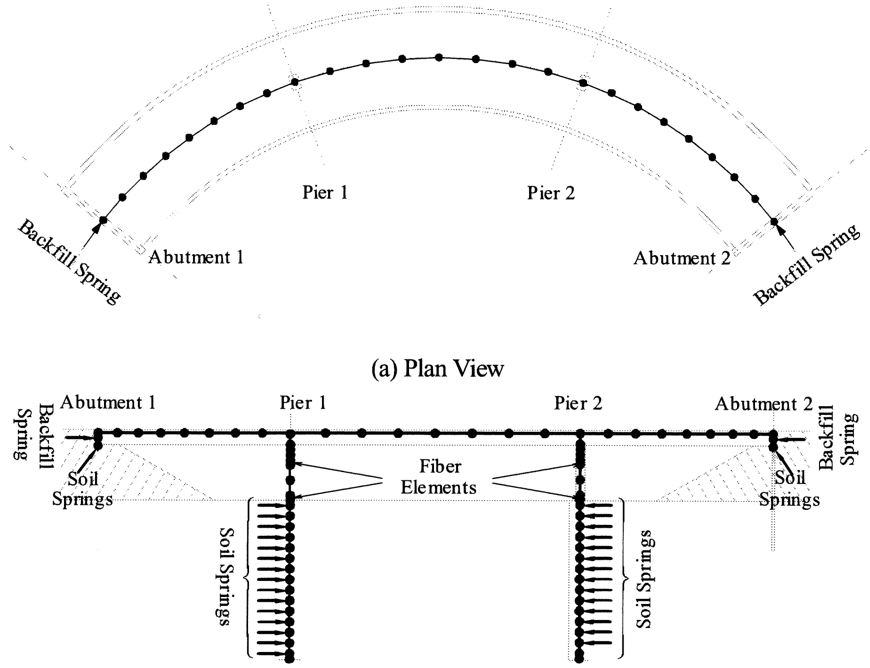

(a) Plan View

(b) Elevation View

Figure 3 Analytical Idealization of the Curved Bridge

2.2 Analytical Idealization

The structural analysis program OpenSees version 1.7.3 (Mazzoni *et al.*, 2006) was used for the analysis. The mathematical model used here is shown in Figure 3. This model includes a single line of beam elements with the cracked stiffness (one-half of the gross section stiffness) for each of the superstructure and the substructures including the full length of the drilled shafts. The drilled shafts are restrained by sets of uniformly spaced elastic springs oriented in the two orthogonal directions. The abutments are supported by elastic springs that represent the resistance due to the steel pipe piles. To include the biaxial bending as well as axial force variation, fiber elements were employed for the plastic hinge region of the columns.

To study effect of the backfill reaction forces, two version of the model are considered. The first model includes only the pipe pile resistance for the abutments, and is called the "without-backfill model". For the second model, which is called the "with-backfill model," the resistance due to the backfill soil behind the abutment is added to the pipe pile contribution. To represent backfill soil resistance, compression only spring was employed. The fundamental natural periods for the without-backfill model are 0.74 sec and 0.70 sec in the radial and chord directions respectively, while those for the with-backfill model are 0.63 sec and 0.23 sec in the chord and the radial directions respectively. The backfill resistance significantly reduces the natural period for the radial direction.

The NS (stronger) component of the 1940 El Centro ground motion was selected for the input ground motion. The intensity of the ground acceleration was increased by 1.5 times in order to give significant plastic behavior at the columns.

3. CHORD EARTHQUAKE RESPONSE

The NS component of the 1940 El Centro ground motion, scaled by 150%, was applied in the chord direction to the curved bridge with or without-backfill. In this case, the displacement response was principally in the chord direction. Figure 4 shows the displacement time history at mid-span of the deck in the chord direction. The maximum positive and negative displacements of the deck in this direction are almost the same, 0.321 feet (0.098 m) and 0.338 feet (0.103 m), respectively, in "without-backfill model". As for "with-backfill model", they are 0.197 feet (0.060 m) and 0.177 feet (0.054 m) respectively. These displacements are 62% and 52% respectively of those calculated for the bridge without backfill. Since the backfill forces have two components in both the chord and radial direction due to the orientation of the abutments, the displacement response of the deck also has two components (chord and radial) as shown in Figure 4(b). This is true even though the earthquake motion is only applied in the chord direction. In addition, the radial response is developed mainly in the positive side because the backfill soils are effective only in compression. It is noted that the

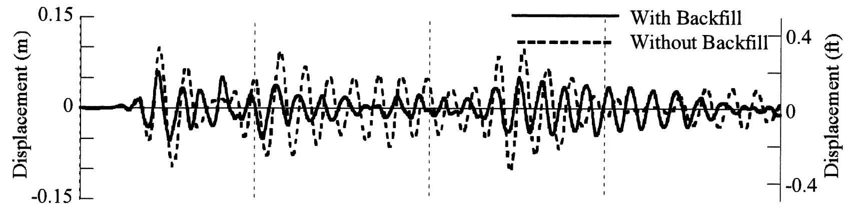

(a) Chord Direction

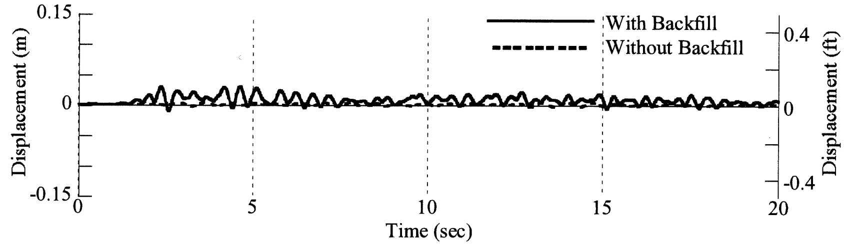

(b) Radial Direction

Figure 4 Displacement Response of Deck at Mid-Span under Chord Earthquake

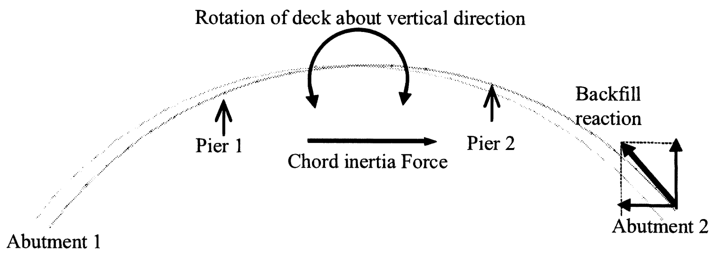

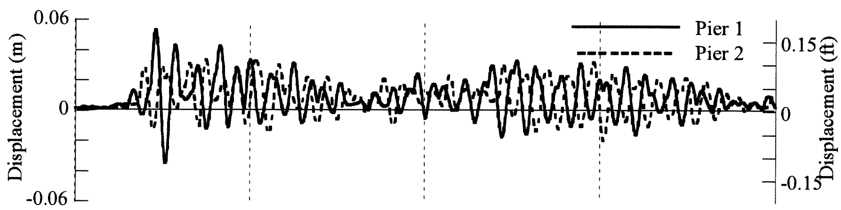

(a) Displacement response of deck at pier 1 and pier 2 in radial direction

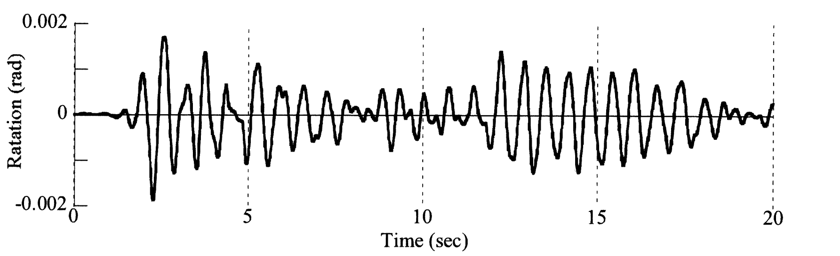

(b) Rotation of deck obtained from relative displacement at pier 1 and pier 2

Figure 5 Rotation of Deck about Vertical Axis under Chord Earthquake

compression-only resistance of the backfill (with such an orientation) results in the rotation of the superstructure about the vertical axis. Figure 5 shows the radial displacement responses of the superstructure at Pier 1 and Pier 2 and the rotation of the superstructure developed in "with-backfill model". This rotation is calculated by dividing the relative displacement response of Pier 1 and Pier 2 by the distance between the two stations. The displacements at Pier 1 and Pier 2 are different because of the deck rotation. The maximum rotation of the deck is 0.0019 radian.

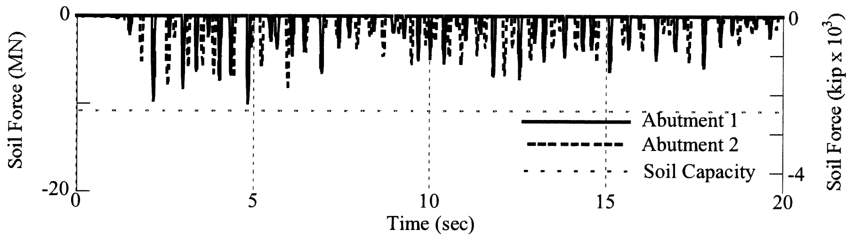

Figure 6 Backfill reaction forces at abutments under chord earthquake

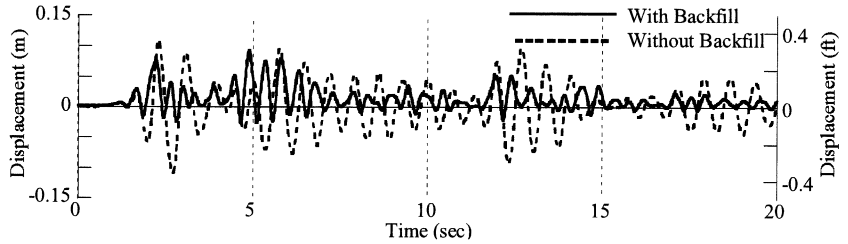

Figure 7 Radial Displacement Response of Deck at Mid-Span under Radial Earthquake

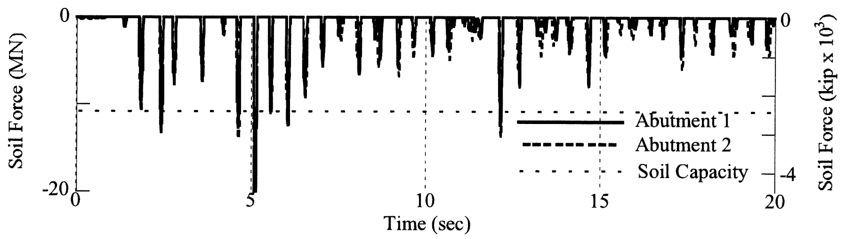

Figure 8 Backfill Reaction Forces at Abutments under Radial Earthquake

Figure 6 shows the backfill reaction forces in the longitudinal direction at the both abutments. Only negative (contact or pounding) forces are developed because compression-only springs were used to model the backfill resistance. The maximum capacity for the backfill is also shown in this figure. The maximum soil forces are 2,232 kip (9.932 MN) and 1,805 kip (8.032 MN) at the Abutments 1 and 2, respectively, and do not exceed the estimated soil capacity.

4. RADIAL EARTHQUAKE RESPONSE

The curved bridge model with or without the backfill effect was subjected to the same earthquake ground motion in the radial direction. The displacement response at mid-span of superstructure in the radial direction is shown in Figure 7. The maximum displacement responses at the positive and negative sides of the radial direction are 0.354 feet (0.108 m) and 0.361 feet (0.110 m) respectively, in "without-backfill model", while they are 0.302 feet (0.092 m) and 0.092 feet (0.028 m) respectively, in "without-backfill model". The displacement response were reduced by 15 percent and 75 percent at the positive and negative sides of the chord direction due to the backfill restraints. It is obvious that the reduction of the displacement response is more significant at the negative side than the positive side. This is because the backfill forces are effective only for the compression. Such a backfill resistance results in the bias of the displacement response in the radial direction.

Figure 8 shows the backfill reaction forces in the longitudinal direction at the both abutments. The maximum soil forces are 5,160 kip (22.96 MN) and 4,685 kip (20.85 MN) at the Abutment 1 and 2, respectively, and they exceed the maximum soil capacity that corresponds to 2,427 kip (10.80 MN). To clarify more realistic seismic behavior, the yield of the backfill soil should be included. These reaction forces are larger than the results under the chord earthquake that was presented in the previous section. This is because the orientation angle of the abutment between the chord and the longitudinal direction is more than 45 degree, therefore the backfills act more effectively for the radial earthquake than the chord earthquake.

5. CONCLUSIONS

To clarify effect of backfill soil on seismic performance of curved bridges, a series of dynamic response analyses were conducted. The conclusions from the analytical results presented herein are:

- Even though the earthquake motion is only applied in the chord direction, the displacement response of the deck has two components in both the chord and radial direction because the backfill forces developed have two components due to the orientation of the abutments. In addition, the radial response is developed mainly in the positive side because the backfill soils are effective only in compression.

- Under the chord earthquake, the compression-only resistance of the backfill with such an orientation results in the rotation of the superstructure about the vertical axis. Because of the deck rotation, the displacements at Pier 1 and Pier 2 are different.

- Although the backfill resistance reduces the radial displacement response of the deck as well as the moment developed at the columns under the radial earthquake, these responses have a bias because the backfill soils are effective only in compression.

Acknowledgements:

This research was supported from Center for Urban Earthquake Engineering (CUEE) in Tokyo Institute of Technology (TITech), and was carried out when the first author was 21st century COE post-doctoral researcher of TITech. The opportunity for the first author to study abroad at University of Nevada, Reno was provided by Professor Kazuhiko Kawashima (TITech). The authors express sincere appreciation for this invaluable support.

References:

American Association of State Highway and Transportation Officials (AASHTO), (1993), "Standard Specifications for Highway Bridges-Division I-A," Washington, DC.

American Association of State Highway and Transportation Officials (AASHTO), (1993), "Guide Specifications for Horizontally curved Highway Bridges", Washington, DC.

Federal Highway Administration (FHWA), (1996), "Seismic Design of Bridges - Design Example No. 6 Tree-Span Continuous CIP Concrete Box Bridge," Report No. FHWA-SA-97-011, McLean, VA, September.

Kawashima, K., and Penzien, J. (1979), "Theoretical and Experimental Dynamic Behavior of a Curved Model Bridge Structure," *Earthquake Engineering and Structural Dynamics*, 7, 129-145.

Kawashima, K., (1980). "Seismic response analysis of bridges with emphasis on discontinuous behavior in expansion joints and soil-structure interaction", Nagoya University.

Mazzoni, S., McKenna, F., Scott, M., S., Gregory, L., Fenves, G., L., et al., (2006), "Open System for Earthquake Engineering Simulation User Command-Language Manual" Pacific Earthquake Engineering Research Center (PEER), University of California, Berkeley.

Otsuka, H., Kanda, M., Suzuki, M., and Yoshizawa, T. (1997), "Dynamic Analysis of Sliding Behavior of Curved Bridge Superstructure caused by Horizontal Ground Motion," *J. of Structural Mechanics and Earthquake Engineering*, JSCE, 570 (I-40), 305-314 (in Japanese).

Paraskeva, T.S., Kappos, A.J., and Sextos, A.G. (2006), "Extension of Modal Pushover Analysis to Seismic Assessment of Bridges," *Earthquake Engineering and Structure Dynamics*, 35(10), 1269-1293.

Sextos, A., Kappos, A.J., and Mergos, P. (2004), "Effect of Soil-Structure Interaction and Spatial Variability of Ground Motion on Irregular Bridges: the Case of the Krystallopigi Bridge," *Proc. of 13th World Conference on Earthquake Engineering*, Paper No. 1156, Vancouver, Canada, August.

Williams, S., and Godden, W. (1979), "Seismic Response of Long Curved Bridge Structures: Experimental Model Studies," *Earthquake Engineering and Structural Dynamics*, 7, 107-128.

Fifth International Conference on Urban Earthquake Engineering
March 4-5, 2008, Tokyo Institute of Technology, Tokyo, Japan

VERTICAL RESPONSE CHARACTERISTICS OF RUBBER BEARINGS WITH ASYMMETRIC-NONLINEAR-ELASTICITY

Kahori Iiyama[1), Tatsuo Ohmachi[2)

1) Research Fellow, Center for Urban Earthquake Engineering, Tokyo Institute of Technology, Japan
2) Professor, Department of Built Environment, Tokyo Institute of Technology, Japan
iiyama.k.aa@m.titech.ac.jp, ohmachi@enveng.titech.ac.jp

Abstract: Recently, many kinds of rubber bearings have been installed in highway bridges. A rubber bearing shows the advantages for horizontal or compressional forces whereas its property still remains unclear under tensile forces. When we estimate vertical response force of a rubber bearing, we often regard only a compressive stiffness as a spring constant and ignore a tensile stiffness. However, some of tension experiment of rubber bearings presented that their tensile stiffness is elastic under small tensile stress and lower than compressive one. Therefore, the actual relation of vertical force-displacement of a rubber bearing shows asymmetric, nonlinear and elastic behavior. As a preliminary study, we analyzed the vertical seismic behavior of a bearing which have asymmetric and nonlinear elasticity by using SDOF models.

1. INTRODUCTION

In the 1995 Hyogoken-Nanbu earthquake, many metal bearings which connected superstructures and piers were much damaged. Hence the bridge design code has been changed and required us to install rubber bearings into bridges. As shown in Figure 1, a rubber bearing contains inside layers of metal plates. This structure enables to perform as an isolator against horizontal forces and support large load of a superstructure. In this way, the advantages of rubber bearings for large horizontal or compressional force were demonstrated whereas the advantages for tensile force still remain unclear. The design code basically requires bearings to resist uplift forces as little as possible. In case of calculating the vertical response force, compressive stiffness value based on experimental regression formula is widely considered.

However, some of load tests indicated the following results: i) The relation of tensile force-displacement is almost elastic under a low tensile stress. ii) Tensile stiffness is much lower than compressive one. These mean that their vertical performance may show nonlinear behavior, if they resist both uplift and compressive force.

We focus on this kind of behavior and set another vertical stiffness model. To find the relationship between response force and tensile stiffness, we compare two vertical seismic responses of two models by using single-degree-of-freedom (SDOF) simulation.

2. MODELING

1) Outline of Tensile Performance of Rubber Bearings

We set the vertical tensile stiffness based on the result of static load test (Uno et al., 2003) for three types of rubber bearing (NR, HDR, S-HDR). In this test, the shape of sample bearings was $350\times350\text{mm}^2$, 11mm×5 layers of rubber and 1st shape coefficient $S_1 \fallingdotseq 8$. According to the results of the force-displacement as shown in Figure 2, it exhibits inelastic hysteretic behavior under large stress. However, it is almost elastic under small stress.

2) Vertical Stiffness Modeling

In bearing design codes, experimental regression formula of vertical compressive force K_v^C is defined as follows.

$$K_v^C = \frac{E \cdot A_e}{\Sigma t_e}, \quad E = \alpha \cdot \beta \cdot S_1 \cdot G_e \tag{1}$$

where A_e is plane area; t_e is thick of one rubber; α is bearing type coefficient; β is planar shape coefficient, G_e is shear modulus. According to the force-displacement relation, the tensile stiffness K_v^T is about $0.2\sim0.3\,K_v^C$ when the stress is less than tolerable stress. This seems independent of bearings type, and we set the ratio s as follows.

$$s = \frac{K_v^T}{K_v^C} = 0.25 \tag{2}$$

The vertical force-displacement diagram of rubber bearing is shown in Figure 3. Figure 3(a) shows a typical linear-elastic model (L-model) with primary stiffness K_v^C, and Figure 3(b) shows an asymmetric-nonlinear-elastic model (NL-model) with secondary stiffness K_v^T. P_y in the figure corresponds to Mg (M : mass of superstructure, g : gravitational acceleration), therefore as long as the force is less than P_y, the bearing behaves elastically just like L-model. In this study, P_y is expressed as Eq.(3).

$$P_y = Mg = \frac{g}{4\pi^2} K_v^C \cdot T_0^2 \tag{3}$$

where T_0 is a structural period.

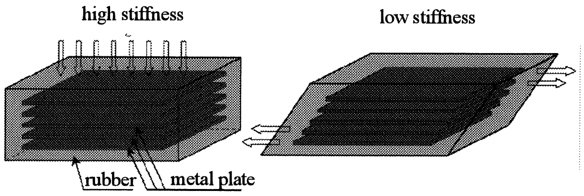

Figure 1 Rubber Bearing with Metal Plates

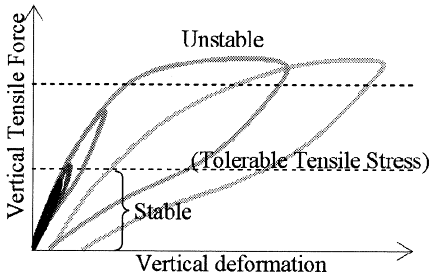

Figure 2 Result of Tensile Tests for Rubber Bearing

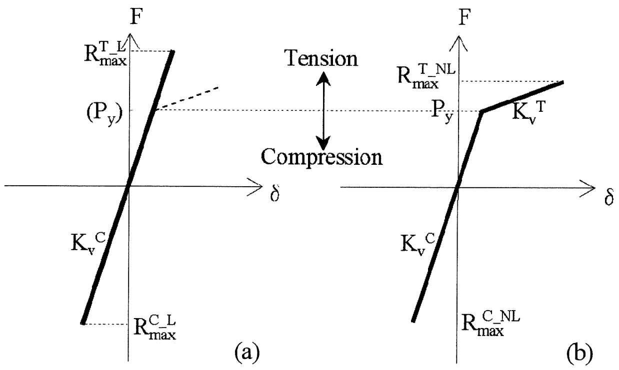

Figure 3 Models for Vertical Stiffness
(a) L-model, and (b)NL-model

3. SIMULATION

3.1 Analytical Conditions

In the SDOF analysis, 12 records having strong vertical acceleration and variable period characteristics are used (see Table 1). To confirm the contribution of input motion intensity, these records are classified into two groups based on maximum acceleration; the group I is less than 500 cm/s^2 and the group II is more than 500 cm/s^2.

As for other conditions, we set K_v^C=500000 kN/m, equivalent damping factor h =1%, time step dt = 0.001sec. Damping factor h is used for stability of calculation, in spite of the actual hysteretic damping being lower than 1%.

3.2 Maximum Response Forces

As an example, maximum response force against T_0 for input II-5 is shown in Figure 4. The upper figure refers to the maximum tensile response forces of L-model $R^{T\_L}_{max}$ and NL-model $R^{T\_NL}_{max}$. On the other hand, the lower figure refers to the maximum compressive response forces of

Table 1 Input Motions (vertical acceleration)

Group	Record ID	Date, Observation site	Max(gal)
I	wave I-1	1995/ 1/17, JR-Takatori sta.	290
	wave I-2	2007/04/15, K-net MIE004	323
	wave I-3	2003/09/26, K-net HKD091	325
	wave I-4	1995/ 1/17, JMA Kobe	332
	wave I-5	1995/ 1/17, Higashikobeohashi	395
	wave I-6	2000/10/06, K-net TTR007	404
II	wave II-1	2007/ 3/25, K-net ISK005	556
	wave II-2	Wave I-2 record × 2	645
	wave II-3	Wave I-3 record × 2	650
	wave II-4	Wave I-6 record × 2	808
	wave II-5	2004/10/23, K-net NIG019	820
	wave II-6	2003/ 5/26, K-net MYG011	825

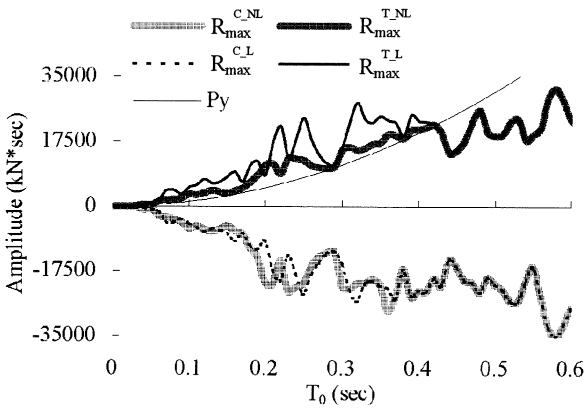

Figure 4 Force Response Spectra (Input : wave II-5)

L-model $R^{C\_L}_{max}$ and NL-model $R^{C\_NL}_{max}$. Here, $R^{T\_L}_{max}$ and $R^{C\_L}_{max}$ are perfectly proportional to displacement response spectrum for input II-5. The curved thin line in upper figure indicates P_y calculated by Eq.(3). In this case, $R^{T\_L}_{max}$ often exceeds P_y during $T_0 \leq 0.42$sec, therefore some differences occur between the two models. It seems that $R^{T\_NL}_{max}$ tends to be less than $R^{T\_L}_{max}$ whereas $R^{C\_NL}_{max}$ basically tends to be equal or more than $R^{C\_L}_{max}$.

To analyze the differences between L-model and NL-model under various input motions, the ratio of maximum response forces expressed as Eq. (4-1), (4-2) are introduced.

$$\gamma_C = R^{C\_NL}_{max} / R^{C\_L}_{max} \quad (4\text{-}1)$$

$$\gamma_T = R^{T\_NL}_{max} / R^{T\_L}_{max} \quad (4\text{-}2)$$

The ratios γ_C and γ_T indicate the ratio of nonlinear compressive or tensile response force to linear one for each T_0, respectively.

Figure 5.1 and 5.2 show the ratios γ_C and γ_T against T_0 for 12 input accelerations. In these figures, (a) shows the result for the group I, while (b) shows for the group II. As shown in Figure 5.1(a), the ratio γ_C is once exceeds 2.0 (at T_0 =0.11sec) for input I-5, however, mostly less than 1.5. In contrast, as shown in Figure 5.1(b), γ_C for group II is basically less than 2.0 and ranges from 1 to 1.5 over wide region of T_0.

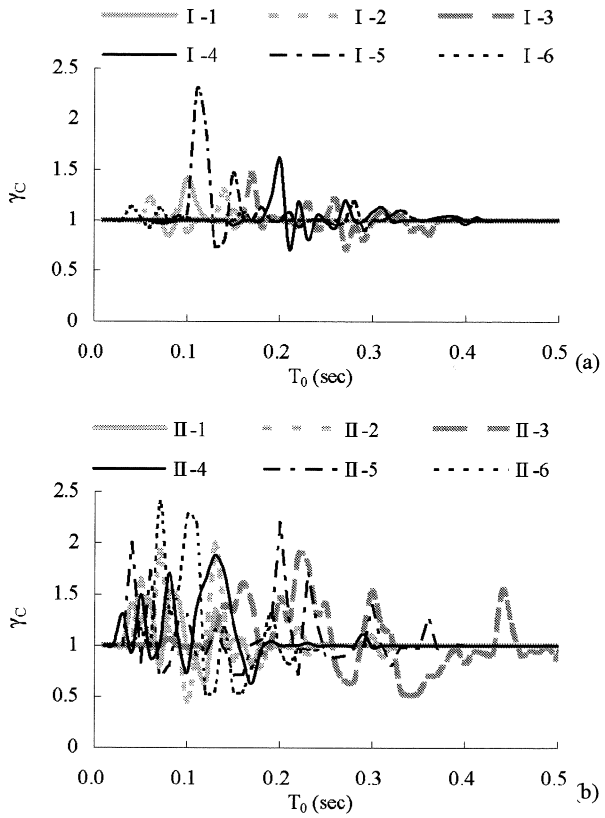

Figure 5.1 Spectral Ratio of Compression Forces
(a) Input: group I, (b) Input: group II

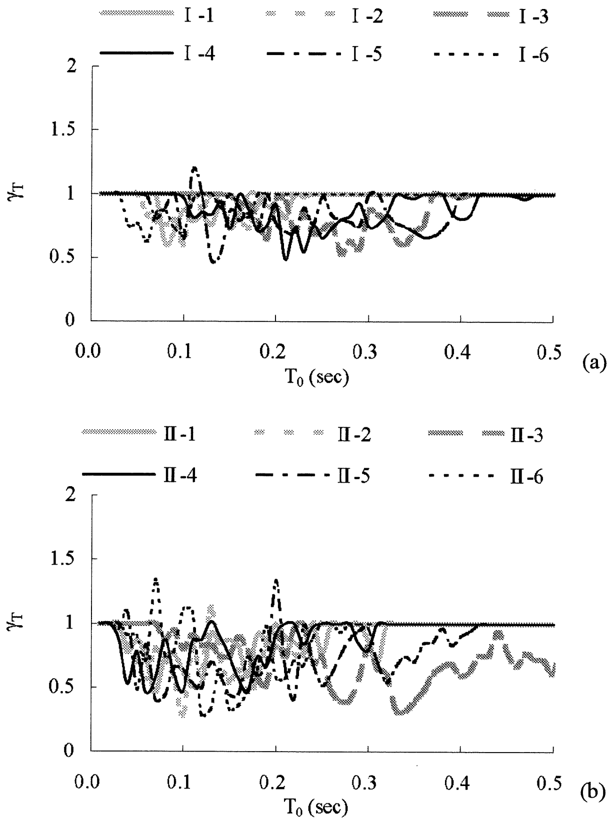

Figure 5.2 Spectral Ratio of Tensile Forces
(a) Input: group I, (b) Input: group II

On the other hand, as shown in Figure 5.2(a), the ratio γ_T for group I once exceeds 1.0 (at T_0 =0.11sec) for input I-5 but mostly less than 1.0. Likewise, the ratio γ_T for group II is basically less than 1.0 as shown in Figure 5.2(b). However, the range of γ_T value is wider than for the group I and occasionally exceeds 1.0. A possible interpretation of these results is that the difference of response force for L-model and NL-model tends to increase with a large acceleration of input motion as group II. However, the tensile response force of NL-model $R_{\max}^{T\_NL}$ is basically less than that of L-model $R_{\max}^{T\_L}$.

3.3 Prediction of Response Amplification

To analyze the dependence of the input motion intensity on the response force for NL-model, the parameter ξ defined as Eq.(5) is introduced.

$$\xi = R_{\max}^{T\_L} / P_y \qquad (5)$$

The parameter ξ indicates the ratio of compressive response force of L-model to yield force P_y (see Eq.(3)).

The ratio γ_C and γ_T against ξ for all input motions was plotted as shown in Figure 6.1, 6.2 for various T_0 from 0.05 to 1.0sec for every T_0 =0.01sec. In addition, to confirm the influence of the stiffness ratio s (see Eq.(2)), not only the case of s =0.25 (in Figure(b)) but s =0.1 and 0.4 is also shown in (a) and (c). The smaller s is, the stronger the nonlinearity becomes.

As shown in Figure 6.1(b), γ_C is almost equal to 1 for ξ <1.2, whereas for $1.2 \le \xi$ it scatters a little, and occasionally exceeds 2.0 for $\xi \ge 1.6$. The scattering is a little different for each s (Figure 6.1(a) and (c)), however, the scattering for ξ <1.2 is very small among all s. These results suggest that $R_{\max}^{C\_NL}$ is almost equal to $R_{\max}^{C\_L}$ while the stiffness remains to show weakly-nonlinear behavior. In addition, the upper of amplification of the $R_{\max}^{C\_NL}$ for $R_{\max}^{C\_L}$ is less than 2.0 in the range of ξ <1.6.

The ratio γ_T against ξ for all input motions was plotted in Figure 6.2. In the same way Figure 6.1, (a), (b) and (c) show the results for s =0.1, 0.25 and 0.4, respectively. Gray solid lines in the figures show the relationship between γ_T and ξ by assuming the property of energy conservation (PEC) shown in Figure 7. This relationship is defined as Eq.(6).

$$\gamma_T = \sqrt{s + (1-s)/\xi^2} \qquad (6)$$

As is evident from Figure 6.2(b), γ_T agrees well with PEC for ξ<1.3. Whereas γ_T scatters around PEC for $1.3 \le \xi$, sometimes beyond 1.0 for $\xi \ge 1.6$. This trend also appears in the case s = 0.1 and 0.4 (Figure 6.2(a) and (c)). These results indicate that we can estimate $R_{\max}^{T\_NL}$ from $R_{\max}^{T\_L}$ by applying PEC as long as the uplift force $R_{\max}^{T\_L}$ is lower than about 1.3 P_y. However, under the stronger tensile force, it is difficult to estimate the response amplification. Because it depends on not only phase and period characteristics of input motion but uncertainty of the structural response due to its strong nonlinearity.

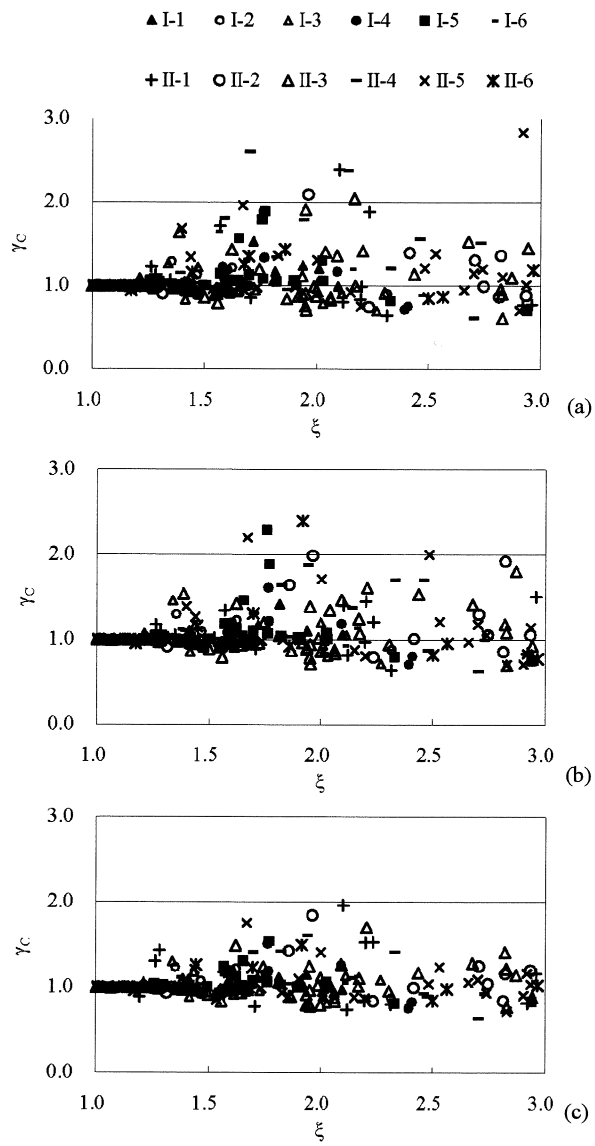

Figure 6.1 Ratio of Compressive Response Forces
(a) s=0.1, (b) s=0.25 and (c) s=0.4

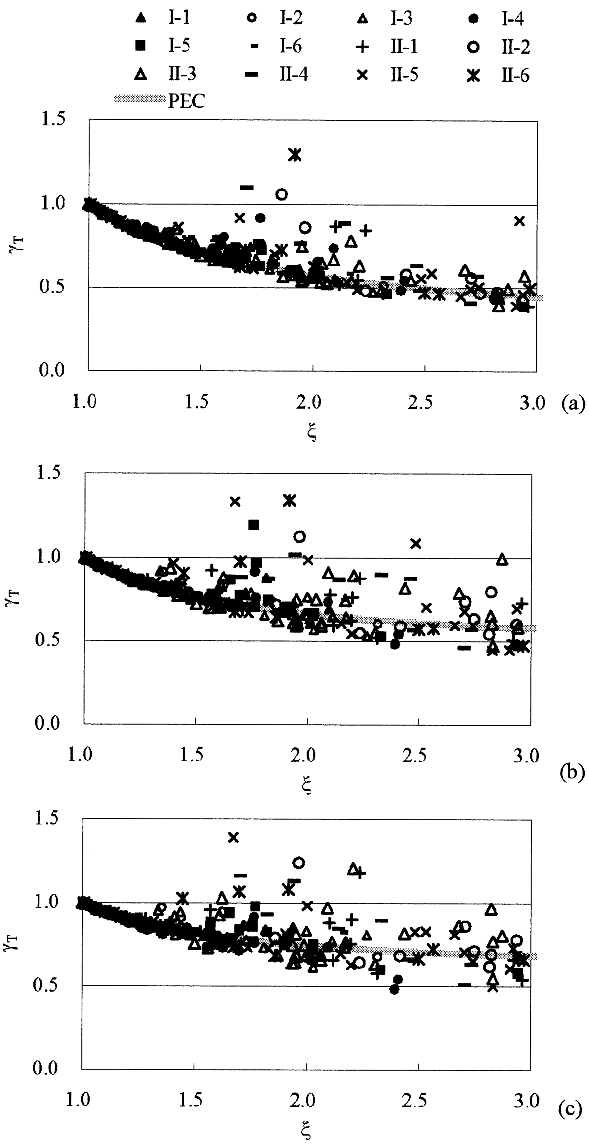

Figure 6.2 Ratio of Tensile Response Forces
(a) s=0.1, (b) s=0.25 and (c) s=0.4

4. CONCLUSIONS

The conclusions of this study using SDOF simulation with 1% damping can be summarized as follows.

1) If a rubber bearing is subject to small uplift during vertical ground motion, the amplification of vertical response force of NL-model can be estimated from L-model. Whereas if a rubber bearing is subject to large uplift, it is difficult to estimate because of large scattering.
2) If the tensile response force for L-model is less than $1.2P_y$, the compressive response force of NL-model is almost equal to that of L-model.
3) If the tensile response force of L-model is less than $1.3P_y$, that of NL-model is able to be roughly estimated by applying the property of energy conservation.

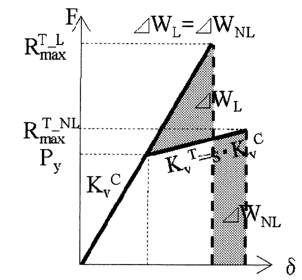

Figure 7 Property of Energy Conservation

Acknowledgements:

The writers acknowledge furnishing experimental data for Mr. Uno, a member of Japan bearing association.

References:

Y. Uno, T. Sumimura, H. Kanai (2003), "A study of the horizontal characteristics of several kinds of rubber bearings under tensile force", Journal of earthquake engineering, No.190 (in Japanese)

Fifth International Conference on Urban Earthquake Engineering
March 4-5, 2008, Tokyo Institute of Technology, Tokyo, Japan

EARTHQUAKE RISK MODELING AND ITS APPLICATION IN CHINA

Zifa Wang[1], Weimin Dong[2], Chris Mortgat[3] and Mohsen Rahnama[4]

1) Professor, Institute of Engineering Mechanics, China Earthquake Administration, Harbin, China
2) Chief Risk Officer, Risk Management Solutions, Inc., Newark, California, USA
3) Vice President, Risk Management Solutions, Inc., Newark, California, USA
4) Vice President, Risk Management Solutions, Inc., Newark, California, USA
zifa@iem.ac.cn, Weimin.Dong@rms.com, Chris.Mortgat@rms.com, Mohsen.Rahnama@rms.com

Abstract: Ground motion, vulnerability and exposure are the three key components in earthquake risk modeling. Probabilistic method is used to predict the ground motion at a given site with detailed consideration of seismic source parameters, attenuation and the effect of local site conditions. Vulnerability of different types of structures within China is derived based on a combination of historical loss information and the extensive numerical analysis of 9 buildings. Exposure in China is compiled based on the annals published by the Chinese government. Six historical events are used to calibrate the proposed model to prove its feasibility. The model is used to simulate the recurrence of both the 1679 Sanhe-Pinggu event and the 1976 Tangshan event. The simulation results demonstrate both the applicability and feasibility of the earthquake risk modeling in China. Finally the model is used to predict the actual loss of Pu-er earthquake which occurred in 2007 in the southwestern part of China. The relative good comparison between the predicted and the actual loss proves again the applicability of the model in loss modeling in China.

1. INTRODUCTION

Earthquake loss estimation is an important component to reduce earthquake risk in preventive measures, emergency response and resource planning as well as setting up financial countermeasures such as earthquake insurance. Earthquake loss estimation is a complex process that is evolving with the accumulation of human knowledge about earthquakes and their hazard. Earthquake risk modeling is one of the major methods to carry out earthquake loss estimation. There are three components in earthquake risk modeling: the ground motion, the vulnerability and the exposure. The earthquake risk modeling framework utilized in this paper is the standard one popularly adopted worldwide in products by Risk Management Solutions, Inc. The paper applies the same methodology directly to China with detailed local information vastly available in China for all the three components.

2. Ground Motion

Ground motion is the excitation on the ground resulted from the occurrence of an earthquake. To estimate the ground motion, the parameters of seismic sources that cause the earthquake, the attenuation of the excitation due to earthquake energy wave propogation in the earth's media and the local site condition that affects excitation to engineering structures and infrastructures.

The seismic sources used in this paper are derived based on a number of data sources. The original earthquake source data comes from the China Seismic Ground Motion Zonation Map (China Earthquake Adminstration 2001) with modifications based on new knowledge coming from active fault detection, recent seismic activity and latest research results on seismicity and source parameter determination. The modified seismic sources in China are shown in Figure 1, which shows that the potential sources are divided into smaller line sources for the simplicity of seismicity estimation. To account for the fact of the wide occurrence of M5 class earthquakes in China, a nationwide background source is added for the occurrence of these "out-of-range" earthquakes with magnitude up to 5.5.

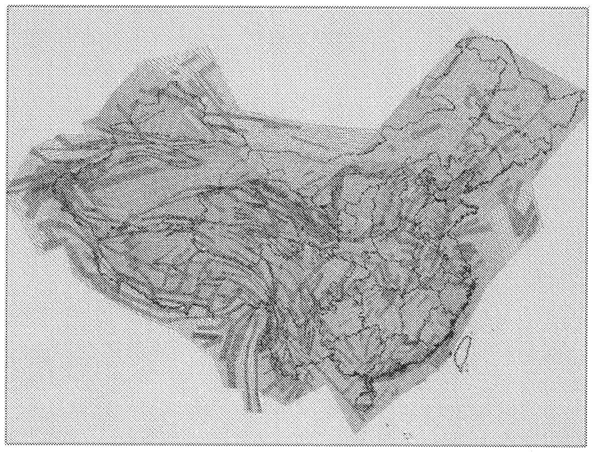

Figure 1 Seismic sources in China with background sources

Figure 2 shows the result for a typical G-R curve, which is the rate of occurrence for different magnitude bins. G-R curves are given for each belt, which is then sub-divided into different sources. From the map we can conclude that the G-R curve used in the model lies between the catalogue database and that used for the zonation map. With the rate of occurrence within a belt given, the seismicity for different sources in the belt can be calculated based on the area of each source within the belt. Thus, for a given source, the rate of occurrence for any magnitude bin can be determined.

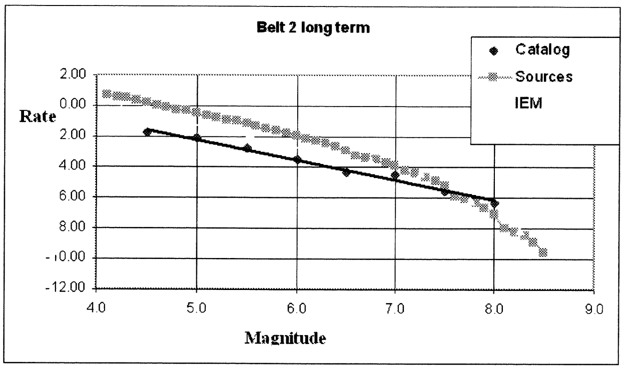

Figure 2 Seismicity map for Tancheng-Lujiang belt

The ground motion at a given site for hard soil can be calculated based on the following elliptical attenuation equation (China Earthquake Administration 2001) for a specified magnitude M and epicentral distance R:

$$\ln Y = 6.0805 + 0.5438M - 1.1924\ln(R+20) \quad (1a)$$

$$\ln Y = 4.7868 + 0.5715M - 1.0727\ln(R+5) \quad (1b)$$

where (1a) is used for long axis and (1b) is for short axis, Y is the equivalent ground motion in acceleration.

To account for the effect of local site conditions, we also obtained the digital soil map with resolution up to 1:200,000. RMS soil classification method is applied to determine the site amplification and potential liquefaction effect.

3. Vulnerability

To study the effect of vulnerability, building classification is first revised for application in China. Special consideration is given to China specific structures such as the old Russian style plant and the hybrid structure composed of RC, brick and masonry components. 8 designed buildings and 1 real one are used for the time-history numerical analysis. Historical loss information from Tangshan Earthquake, Haicheng Earthquake and Jiji Earthquake in Taiwan is used to calibrate and modify the vulnerability functions. Figures 3 and 4 show, respectively, the damage state and damage ratio for typical RC structures.

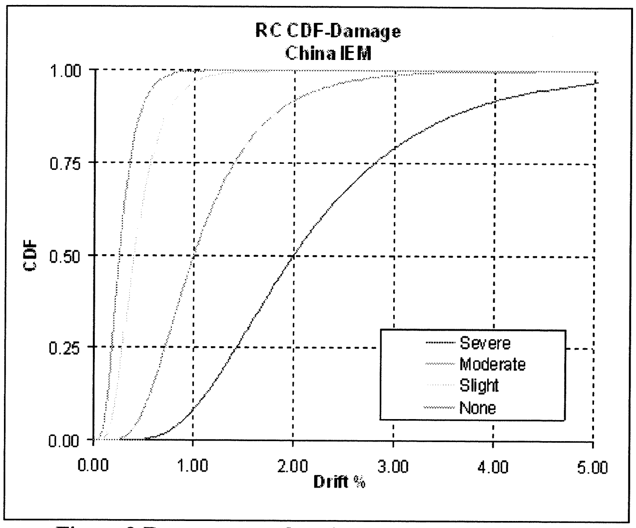

Figure 3 Damage state functions for RC structures

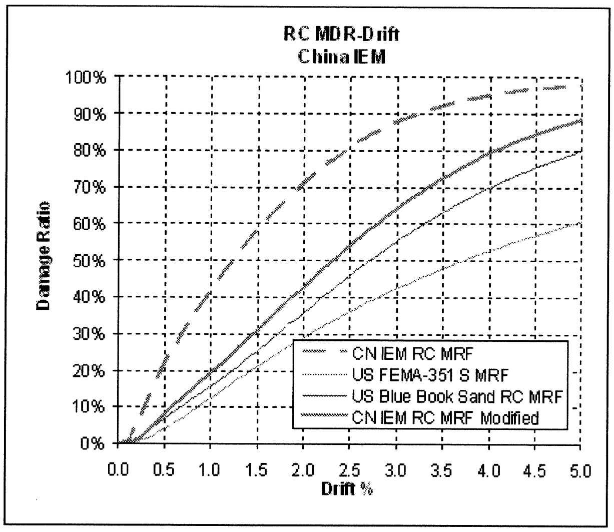

Figure 4 Damage ratio for RC structures in China

In addition to building classification, the height, year of construction, occupancy type and other secondary factors such as configuration, etc are also considered to modify the vulnerability functions in order to account for completeness of the study.

4. Exposure

Based on census data and the 2004 year book for all the provinces and whole China, 11 different inventory classes are proposed to account for different combinations inside China. 5 classes are designed for central business districts which are represented by Beijing, Shenyang, Tianjin, Tangshan and Hong Kong, respectively. 2 classes are designed for mid-size cities for highly developed areas and the developing areas. 4 classes are designed for rural areas to represent the whole range from the most developed areas in Zhejiang and Jiangsu Province to the developing areas in the western part of China. Figure 5, for example, shows the height, year and material distribution of the Shenyang-style city.

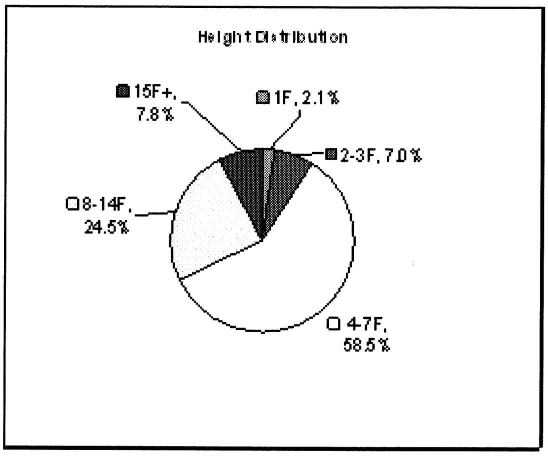

(a) Height distribution

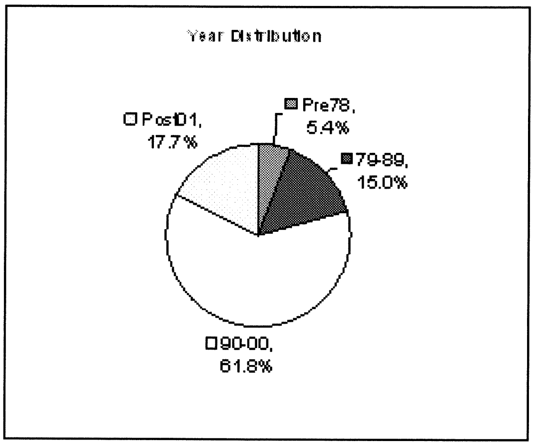

(b) Year distribution

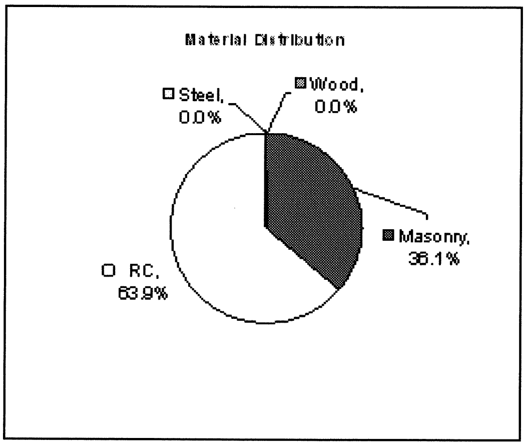

(b) Material distribution

Figure 5 Typical inventory for Shenyang-type city

5. Validation

With the information of ground motion, vulnerability and exposure from previous sections, we can easily assemble to estimate earthquake losses in China. For a single event with given magnitude and location, we can use equation (1) to estimate the ground motion, and then apply the exposure with its corresponding vulnerability to directly derive the loss amount for this given event. For the stochastic analysis, different magnitude bins with their corresponding rate are used to simulate all the events. The loss amount for all the events can be derived using the same approach for a single event, then different types of slice and dice analysis on the probabilistic loss amount can be readily carried out.

Whereas, before using the information, there is a need to validate and calibrate the proposed risk modeling methodology. In order to calibrate this model, six events are used to evaluate the proposed model. The selected six events are listed in table 1.

Table 1 Six selected events for validation

Name	Estimated	Modeled	Mod/Est
Tangshan 1976 M7.8	120,951	133,971	1.11
Haicheng 1975 M7.3	22,168	19,397	0.87
Lijiang 1996 M7.0	968	1,177	1.22
Baotou 1996 M6.4	2,572	2,229	0.87
Datong 1989 M6.1	182	203	1.12
Jiujiang 2005 M5.7	943	726	0.77
Six Event Combined	**147,784**	**157,703**	**1.07**

From table 1, it can be inferred that the proposed model can well simulate the recurrence of historical loss data. While there is a variation of less than 23% difference for a single event, the overall difference is only 7%. Figure 6 demonstrates the comparison of estimated and modeled loss distribution along the epicental distance. It can be seen from the figure that the result looks reasonable given the complexity in the modeling process.

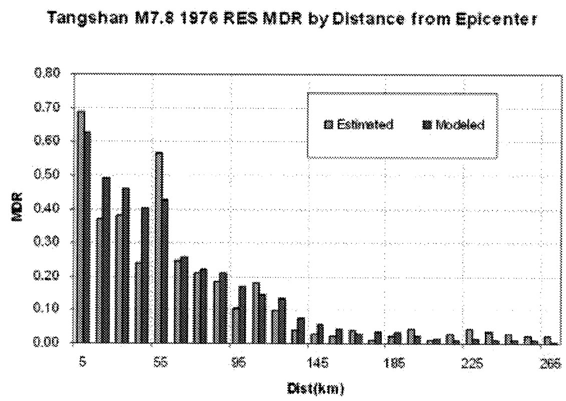

Figure 6 Validation along the epicentral distance

6. Application

Given the proposed earthquake risk modeling methodology, we can now apply it into real and assumed events for two different reasons. One, what would the disaster look like if a historical event happens again? Two, if there is a real event, how would the predicted result compare with the real numbers? To accomplish these two goals, the proposed model is first applied to predict the earthquake loss for the recurrence of both 1976 Tangshan and 1679 Sanhe-Pinggu earthquakes. Figure 7 and 8 show, respectively, the residential loss distribution for the recurrence. The total loss for the two events is 414billion and 1.31 trillion RMB, respectively, making them the 3rd and worst event in China's history.

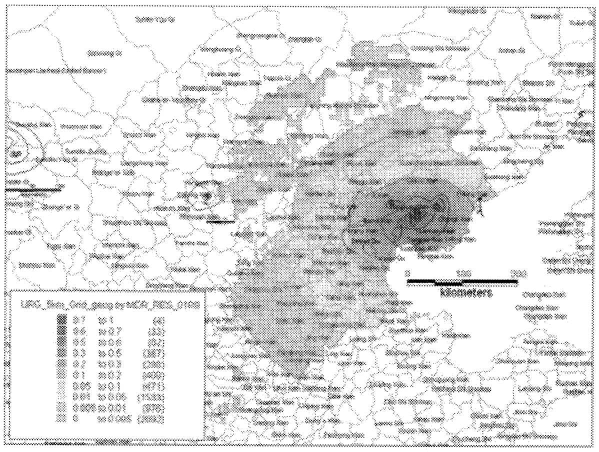

Figure 7 Residential loss for 1976 Tangshan Earthquake

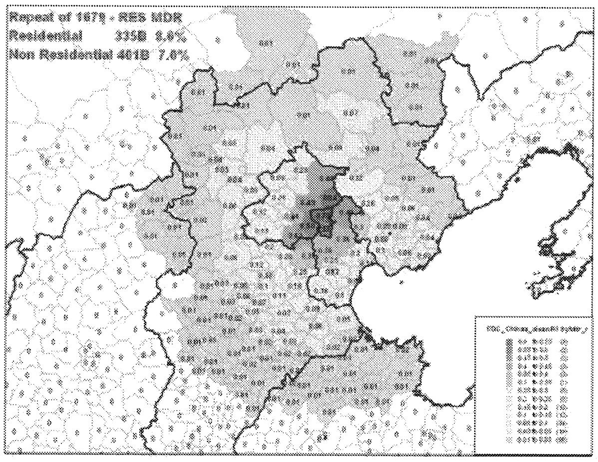

Figure 8 Residential loss for 1679 Sanhe-Pinggu Earthquake

On June 3, 2007, an Ms 6.4 event occurred in Pu-er county of Yunnan Province in the southwestern part of China. Institute of Engineering Mechanics (IEM) has sent a few researchers to the field to survey the real damage. The total loss for residential houses is about 1.035B RMB. For comparison, we only use the location, magnitude and epicentral depth of the event to predict the residential loss of the event and the predicted loss is about 880 million RMB, which is about only 15% less than the real loss number. Considering the fact that local governments always push for higher end of loss estimate for better central government support, the predicted number compares pretty well with the actual loss number, which again proves the applicability and feasibility of the proposed model.

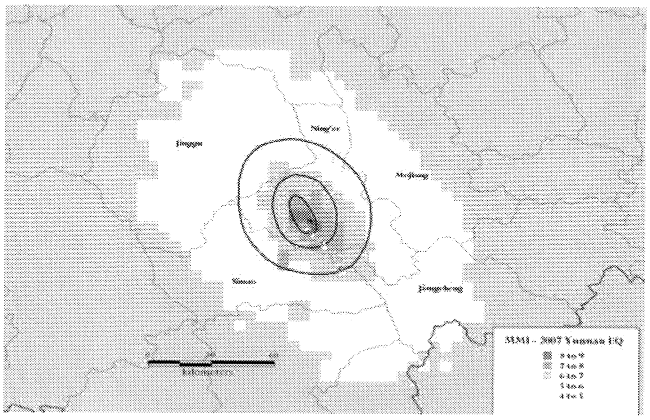

Figure 9 Predicted intensity versus actual intensity

7. CONCLUSIONS

This paper assembles China specific ground motion, vulnerability and exposure information, which are essential components to a typical earthquake risk modeling framework. Detailed validation is carried out to evaluate the proposed model. Initial application of the model to a real event in China demonstrates both its potential applicability and the validity of the proposed model.

Acknowledgements:

The authors acknowledge support from Ministry of Science and Technology of China for a 973 program under the grant number 2007CB714205.

References:

Wang, Z (2006), "Consequence-based and Fully Probabilistic Seismic Design Methodology," *Proceedings. 7th National Conference on Earthquake Engineering*, Volumn A, 627-633.

Liu R.S., Wang Z. and Zhu M. (2006), "A Study on Financial Loss and Its Adjustment in Earthquake Insurance," *Acta Seismologica*, **28**(2), 197-205.

Guo E.D., Wang Z., Mortgat C. and Dong W.M. (2006), "Study on Historical Earthquake Loss Reconstruction", *World Earthquake Engineering*, **22** (3), 10-13.

Grossi, P., Re D. D and Wang Z. (2006), "The 1976 Great Tangshan Earthquake 30-Year Retrospective", IEM-RMS Joint Report.

China Earthquake Administration (2001), "China Seismic Ground Motion Zonation Map, 2001", China Standard Press.

Fifth International Conference on Urban Earthquake Engineering
March 4-5, 2008, Tokyo Institute of Technology, Tokyo, Japan

DISASTER EDUCATION USING A PORTABLE VIRTUAL-REALITY SYSTEM AND ITS EFFICIENCY

Ryuzo Ohno[1] and Jaeho Ryu[2]

1) Professor, Dept. of Built Environment, Tokyo Institute of Technology, Japan
2) Research Fellow, Center for Urban Earthquake Engineering, Tokyo Institute of Technology, Japan
rohno@n.cc.titech.ac.jp, jaehoryu@enveng.titech.ac.jp

Abstract: We have designed and created a portable immersive virtual-reality system that enables people to have disaster education without going to the remote disaster education facilities. The system is composed of three sets of projector and screen, which can show a wide view image with the size of 6.0M (width) x 1.8M (height). This system can display both the real-timely generated computer graphics and moving picture on the screen. To make this system portable we carefully designed the size and weight of the parts as well as simplicity of the frame structure, electrical connections. The easiness of assembling and disassembling parts and compactness for transportation were essential design criteria of the system. As effective disaster education contents, we have developed a program for the users to examine safety of their own room using virtual-reality technology. The program helps people reconsider the arrangement of furniture by demonstrating real-time physics simulation of objects' behavior in the immersive virtual-reality system. The expected advantages of this interactive program for disaster education are: (1) people can have a virtual experience of disaster situation with higher sense of presence, (2) people can imagine and recognize the risk of future earthquake, and (3) people can take effective measures to mitigate the disaster. Using this system, we have carried out disaster educations in several places for various audiences including children, teachers, and citizen in general. Also, we have examined efficiency of the disaster education for children using this system through a series of questionnaire surveys.

1. INTRODUCTION

Given that the probability of a catastrophic earthquake occurring is quite high in Japan compared to other countries, major cities like Tokyo operate many disaster-education facilities for informing citizens about earthquake preparedness. Since an earthquake occurs suddenly with almost no time to react, daily preparation plays a greater role in reducing damage than for other types of disasters. In fact, statistics from the Kobe earthquake in 1995 show the largest cause of injury to have been falling furniture, something that could have been prevented with proper precautionary measures (AIJ, 1996).

The present article describes a portable immersive virtual-reality (VR) system that promotes earthquake preparedness by enabling people to receive effective training without having to travel a long way to a disaster-education facility. Also outlined are the contents of some educational materials that are currently being developed for this system.

2. PORTABLE VR SYSTEM

The system is composed of three sets of projectors and screens, which together can show a wide-view image 6.0m in width and 1.8m in height. Each LCD projector has SXGA resolution (1280 x 1024 pixels). Thus the total resolution of the connected screens comes to about 3000 x 1000 pixels, which is nearly comparable vertically and much higher horizontally to that for high-definition (HD) video images (1920 x 1080 pixels). The three rendering computers that each controls one projector are connected to one another via Gigabit Ethernet. This broadband network allows rapid transfer of data for synchronizing images.

The projectors and screens are housed inside a frame given a hexagonal shape in order to make for easier assembly while also providing structural stability and economy of space. Front instead of rear projection was adopted to minimize lighting and space requirements. (Rear projection requires darkness and extra space behind the screen.) To avoid casting shadows of viewers on the screens, mirrors were installed to heighten the projection point without having to lift up the heavy projectors. The entire system, including the computers and other necessary hardware, can be installed in a space of 4m x 4m. The individual parts are small and light enough for a single person to carry, and the whole ensemble may be loaded into a minivan with a cargo space of 3.0m x 1.3m x 1.5m.

The dismantling and assembling process requires less than two hours, thus reducing the burden of transporting the system from place to place. A plan and section of the system showing the hexagonal frame design and mirror projection method are given in figure 1. The setup holds 15 audience members at a time.

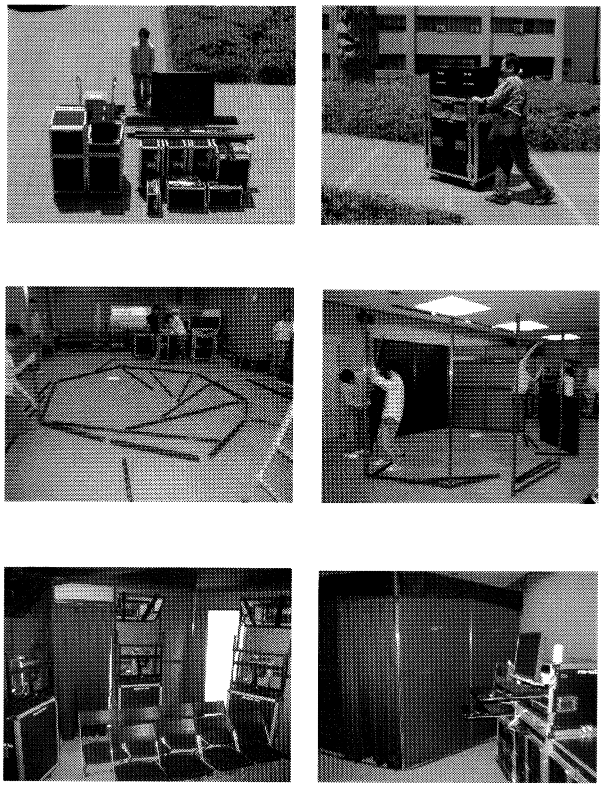

Figure 1. Process of Transporting/Assembling the Portable VR System

3. DISASTER-EDUCATION CONTENTS FOR THE SYSTEM

3.1 Movie and still images

As contents for the system, we are developing two types of materials for disaster education.

The first is a set of high-quality movie and still images of past disasters such as the 1995 Kobe earthquake and the tsunami generated by the 2004 northern Sumatra earthquake presented with scientific explanations.

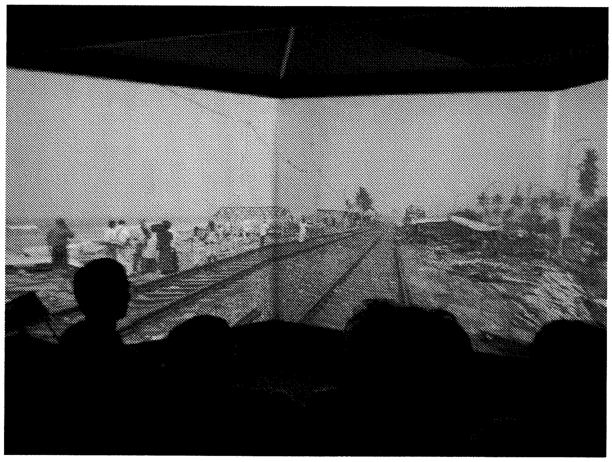

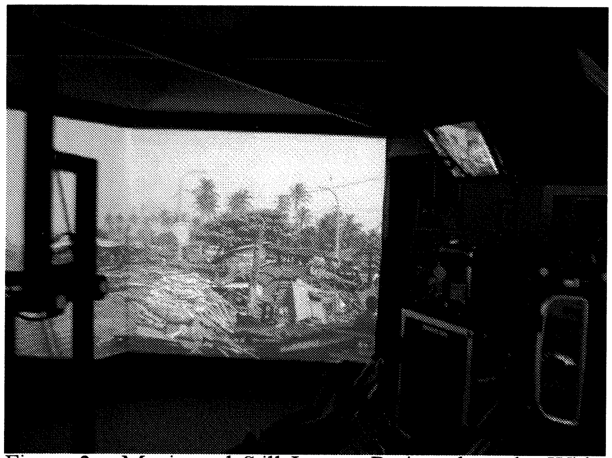

Figure 2. Movie and Still Images Projected on the Wide Screen

3.2 Real-time computer-graphics images

The other program currently under development employs wide-angle computer-graphics images that synchronize data from three rendering computers. The images will present real-time physics simulations of object motion during an earthquake, in this way allowing participants to interactively examine the safety of their own rooms and reevaluate how they arrange their furniture.

Our simulator is a VR substitute for the "shaking room model" using scale-model furniture typically found at earthquake-education facilities such as the Disaster Reduction and Human Renovation Institution in Kobe (figure 5). To use this tool, the participant first sets up some scale-model furniture in the room, then turns a handle and shakes the room to see the damage that can be caused by inappropriately placed furniture. The simulator makes it easy to see, for example, that tall furniture that could collapse across a wide portion of the room should not be installed near sitting or sleeping areas. Thus by trying out the model to evaluate the dangerousness of their own rooms during an earthquake, participants are encouraged to rearrange their furniture in safer ways.

This hands-on simulator is quite popular at earthquake-education facilities because it is fun and clearly illustrative and therefore highly effective. Replacing actual scale models with virtual reality, as in our program, should lead to several advantages, making it possible to (1) simulate different types of rooms and furniture layout, (2) more precisely control seismic forces, (3) use real-time physics simulation to depict object motion more accurately, and (4) give participants an immersive visual experience that enhances the realism and immediacy of the demonstration.

Notwithstanding the many difficulties still involved, we are currently in the process of developing a room re-layout tool that manipulates furniture in a virtual room using a popup menu or force-feedback interface (Ryu et al., 2004).

3.3 Real-time physics simulation

A longtime challenge in the field of VR technology has been to depict object motion in a realistic manner capable of making viewers feel as if they are actually experiencing what they are seeing. Before the advent of real-time physics simulation, pre-calculated animated sequences were used to realistically portray the behavior of objects in a virtual environment. One obstacle to applying real-time physics simulation to virtual reality was calculation time, which was much too long to be able to create continuous movie sequences.

The solution to this problem has been to have the engine simplify its calculation and lower accuracy so that it can render the scene at a rate acceptable for presenting a continuously moving image. Thanks to rapid advances in related algorithms and hardware, real-time physics simulation is now increasingly being incorporated into VR and game applications. The accuracy in object movement thus achieved greatly enhances viewers' sense of "actually being there." A wide variety of physics engines are currently available, from open-source products such as ODE (Open Dynamic Engine), Bullet, and OPAL to commercial options such as Havok and PhysX (formerly called NovodeX). In our case, we chose PhysX for its performance stability and the availability of many developing-support documents to help us write new codes for our system. Using PhysX to calculate object motion will endow our images with greater realism and immediacy.

4. IMPLEMENTATION OF DISASTER EDUCATION USING THE SYSTEM

4.1 Practice of the portable VR system

After the system was completed in April of 2007, we have implemented the disaster education in several places for various audiences. Table 1 shows a selected list of occasions in which the system was used although there were many other casual occasions for visitors to our laboratory.

Table 1 Selected List of Education Program of Portable VR System in 2007

Date	Event	Participants
12th of May	Open Laboratory Day: Suzukake-dai Festival	General Citizen (about 100 persons)
3rd of August	Inter-COE at Okayama Campus of TIT	Visitors of the Inter-COE Program (about 30)
14th of September	Yokohama City, Kamiooka Elementary School	Elementary school students (about 60)
7th of November	Structure Specialist Visit	Architectural Structure Experts (about 20)
28th of November	Foreign Visitors from Taiwan	Staffs and Students of NCU of Taiwan (about 20)
8th of December	Kanagawa-Ken Bouasi Fair	General Citizen (about 100)

4.2. Efficiency of the disaster education with the system for children

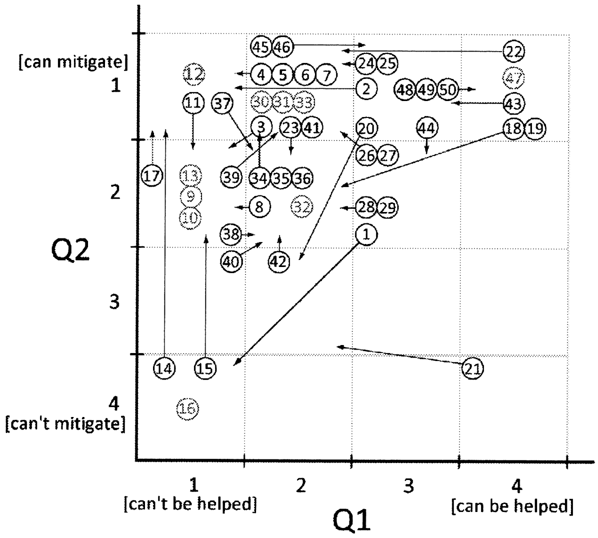

Figure 3 Changes in Attitude toward Disaster on the first and second Survey about Q1 and Q2

On the occasion of the disaster education in the Kamiooka elementary school, we conducted a series of questionnaire surveys to examine how this disaster education program affected children. Subjects were 50 pupils (the 6th year boys/girls). The surveys were conducted with the cooperation of teachers for three times: before, right after and two month after the implementation of the disaster education. In the first and third survey, the questionnaire consisted of the same questions asking about (1) attitudes towards disaster, (2) practice of counter measures, and (3) knowledge about earthquake. In the second survey conducted right after the education, the impressions of the visual demonstration were asked.

As the result of the second survey, almost all pupils seemed to be impressed by and to understand the content of visually presented images. Comparing the results of the third survey with the first one, the improvements of knowledge about earthquake and practice of counter measures were found only in limited responses. However, interesting changes in the attitudes towards disaster were noticed. We examined the respondent's attitude by asking whether he/she would agree or not the following statements: (1) "Since an earthquake is a natural phenomenon, there is no hope to avoid damage caused by it", and (2) "We can minimize the damage if we properly prepare for it". When we made the questions, we thought an affirmative answer for the first question indicated retrograde or negative attitude, while for the second one indicate positive attitude.

The result of the survey, however, revealed that most of the pupils responded affirmatively to both questions and this tendency became more evident as shown in Figure 3. After the disaster education many pupils seemed to start thinking that the damage caused by an earthquake was unavoidable and at the same time they thought they could minimize the damage by proper preparations. We were first puzzled with these seemingly inconsistent results. However, if we carefully consider their twisted attitude, the result may be interpreted as follows: (1) Viewing the images presented by the VR system and being impressed strongly by the disastrous situations, they have seriously recognized the reality that they cannot deny possibility of some damage. Nevertheless, (2) knowing some information about earthquake, they still have and even increase their confidence that they can reduce the damage by proper preparations. According to this interpretation, the disaster education with this VR system can lead most of children to positive attitude toward the earthquake, although this interpretation should be verified through more empirical research.

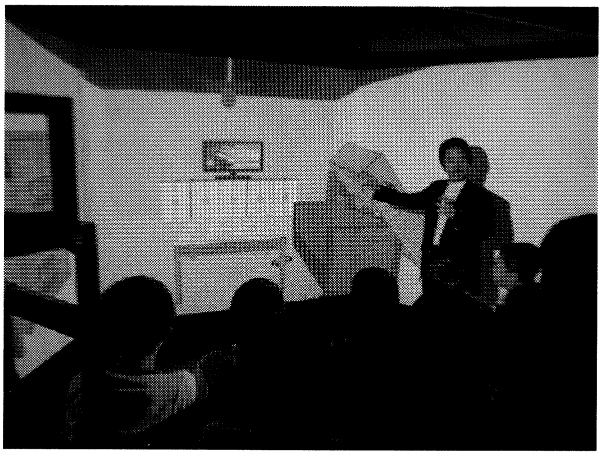

Figure 4 Discussion with the Participants about Safer Arrangement of Furniture using Interactive Real-Time Simulator Images

5. CONCLUSIONS

Our immersive VR system is very compact and portable and capable of presenting high-quality images. As contents for this system, we are developing a program that uses real-time physics simulation to show how furniture moves during an earthquake, thus encouraging participants to reevaluate the dangers present in their daily environment. Through this interactive program, it is expected that people will (1) be able to gain a more immediate experience of what it might be like to be in a disaster situation, (2) be prompted to think about and recognize the risks of future earthquakes, and (3) be able to test effective measures for lessening earthquake damage.

After completing the VR system, we implemented the disaster education in several places for various audiences and examined the effectiveness of it. The result of a series of questionnaire surveys showed that children tended to have more positive attitude toward the earthquake after participating in the disaster education.

In the future, we plan to upgrade our educational materials as well as work on the technical aspects of our furniture-manipulation interfaces. A follow-up survey of program participants will also be needed to evaluate the effectiveness of our system as compared to other text or image-based educational media in prompting people to actually alter their living environments, which is, after all, what will be needed to mitigate damage from a real-life earthquake.

References:

Architectural Institute of Japan (AIJ) (1996), "Hanshin-Awaji daishinsai jutaku naibu higai chosa hokokusho" (Report on damage inside houses during the Great Hanshin-Awaji Earthquake), AIJ, (in Japanese)

Ryu, J., Soeda, M. and Ohno, R. (2006), "Development of an effective tool for virtual experience of environmental hazards: A survey of disaster education facilities in Japan," *Proceedings of the Third International Conference on Urban Earthquake Engineering*, March 6–7, , Tokyo, Japan, 197–203.

Ryu, J., Hasegawa, S., Hashimoto, N., and Sato, M. (2004), "Multi-projection display system for architectural design evaluation, *Proceedings of the Ninth Conference on Computer-aided Architectural Design Research in Asia (CAADIRA)*, Paper Number 81, 901–910.

Acknowledgements:

The authors acknowledge support from Japan Ministry of Education, Culture, Sport, Science, and Technology (MEXT) for establishing the Center for Urban Earthquake Engineering (CUEE) in Tokyo Institute of Technology. The support has made possible this international conference, as well as international joint research projects and exchange programs with foreign universities. They also thank teachers and pupils of the Kamiooka Elementary School for cooperation in the survey.

Fifth International Conference on Urban Earthquake Engineering
March 4-5, 2008, Tokyo Institute of Technology, Tokyo, Japan

TRUST, SECURITY, AND PEACE OF MIND WITH RESPECT TO SEISMIC RISK

Satoshi Fujii[1)]

1) Professor, Dept. of Civil & Environmental Engineering, Tokyo Institute of Technology, Japan
fujii@plan.cv.titech.ac.jp

Abstract: This study sought to understand the determinants of risk acceptance. Thus, we implemented a survey (n = 200) to ask participants which policy measures would make approve each of the following risks: nuclear power plants, traffic accidents, food safety, electrical appliances, and medical mishaps. These results indicate that risk acceptance cannot be fully explained only by objectively achieved security, but other factors, such as scientific understanding and trust in workers and organizations, were also found to be important for increasing risk acceptance. It was also found from the other survey that seismic risks were perceived as medium risk in terms of fear and scientific unknown.

1. INTRODUCTION

Daily life incurs many risks. For example, a large earthquake may strike Japan in the next twenty to thirty years, traffic accidents occur daily, and human error has led to nuclear power plant disasters, such as at TMI or Chernobyl; furthermore, no one knows when the next infectious disease, such as SARS, will emerge. Unfortunately, few Japanese have the option of living in a place without earthquakes; we cannot drive a car without traffic accident risks, and our energy-consuming lifestyles lead us to rely on nuclear power plants. Even eating the food we need to survive incurs the slight risk of food poisoning. We can never truly free ourselves from risk.

There is a growing concern with risk and safety in Japan. This concern has been attributed to an increase in technological accidents that have occurred in recent years, as well as to scientific uncertainty over the probability of risks. While we must assiduously work to reduce technological risks, we still have to accept these risks, to some extent, because it is impossible to eliminate such risks completely.

Therefore, the practical problem with which this research was concerned was to understand how people accept risks, given the impossibility of achieving zero-risk status. To examine determinants of risk acceptance for several risk events, we surveyed 200 Tokyo residents to find their response to a variety of risks.

2. 2. RISK ACCEPTANCE

When do people accept risks? Researchers have investigated this question for decades (e.g., Slovic et al., 1976). The simplest answer is that people do not accept risks and, instead, work to eliminate risk. If all risks are eliminated, security is guaranteed and a zero-risk state is achieved. Although risk-reduction efforts are necessary, society will always face some risks. Achieving zero-risk status might not be a realistic aim to strive for.

Another answer is that people rationally accept risks if they expect the benefit of an activity to exceed the cost (Fischhoff et al., 1978). For example, people may drive a car, knowing the risk of a traffic accident, if they believe that car use is beneficial. People may also accept nuclear plants, as long as the energy produced improves the quality of their lives.

However, many empirical studies (c.f. Dawes, 1998; Kahneman, Knetsch, & Thaler, 1991; Payne, Bettman & Johanson, 1993; Slovic, 1995) have contradicted the above claims. These studies have found that personal decision making frequently deviates from theories such as the "expected utility theory," (Von Neumann & Morgenstern, 1947) or the "subjective expected utility theory," (Savage, 1954), which assume rational, cost-benefit decision making. Cost and benefit expectations can be important determinants of risk acceptance, but they do not fully explain the process. No one yet knows the probabilistic distribution of some risks, such as endocrine-disrupting chemicals. Other risks, such as risks from electromagnetic fields, remain controversial. We cannot evaluate these risks by science, or by costs and benefits, alone.

We compared the relative weight of two components of risk: the possibility of risk and the damage from risk. These two possible determinants are closely related to cost expectation, which is assumed to determine decision making in rational choice models, such as the expected utility theory. We also investigated the effects of compensation after risk events have occurred. Compensation is expected to reduce or to eliminate the cost of risks. Additionally, we examined how understanding the scientific causes of a risk affected risk acceptance. Scientific understanding may reduce the extent of unknown risks (Fischhoff et al., 1978) and may lead to risk acceptance.

3. TRUST AND RISK ACCEPTANCE

We presumed that trust in workers and regulatory agencies constitutes another important determinant of risk acceptance. Instead of controlling risks by themselves, individuals may trust in, and delegate power to, organizations or institutions. This situation can be represented through the "Trust Game" (Kreps, 1990).

The Trust Game has two players: Player A (the truster) and Player B (the trusted). Player A can "trust" Player B by sending a monetary endowment X (see Fig. 1). Player B then receives double what player A has sent (i.e., 2X). Player B must choose between "reciprocating" (returning X and taking X for himself) and "betrayal" (taking all he has received--2X). In this game, if Player A trusts Player B, the total monetary amount that Player A and Player B have increases by X. However, if Player A does not trust Player B, there is no collective increase. In this situation, trusting behavior is collectively beneficial. However, if Player B betrays Player A, Player A loses X. If Player A fears this risk, he does not trust Player B, which results in no collective benefit.

The basic structure underlying risk problems in our society may be seen as resembling that of the Trust Game, assuming that lay people represent Player A and risk experts represent Player B. Social benefits may increase if lay people "trust" risk experts by asking them to administer risks. Risk experts may "reciprocate" by successfully managing the risk, or "betray" by failing to effectively manage risks. If people expect experts to reciprocate, trust and social benefits may increase. However, if people expect betrayal by the experts, trust and social benefits may not increase. For example, social benefits could increase if electricity companies repay the trust of the public by managing nuclear plants successfully. Social benefits would not increase if nuclear plants ceased operations due to a lack of public trust. If electricity companies fail in repaying public trust due to a serious nuclear plant problem, social benefits will decrease.

4. METHOD

We presumed that trust in workers and regulatory agencies constitutes another important determinant of risk

4.1. Sample

Tokyo residents living within 50 km of the city center were randomly selected as participants for the August 2002 survey. A surveyor first visited the residents to ask them if they would participate in the survey. If the resident agreed to participate, a questionnaire was left at the home. After a few days, the surveyor again visited the home and collected the questionnaire.

4.2 Measures

As discussed above, we assumed that risk acceptance is determined by factors beyond subjective expectations of costs and benefits. We assumed that trust in persons and regulatory agencies in charge of risk would be another important determinant. Thus, we asked respondents to evaluate political policies or decisions implemented by administrators and the government. In the questionnaire, we asked respondents to consider six risk management measures and to choose three out of the six measures that would increase their risk acceptance for each of the following risks: nuclear power plants, traffic accidents, food safety, electrical appliances, and medical mishaps. The six choices were:

(1) Decrease the probability that the risk occurs.
(2) Minimize the damage when the risk occurs.
(3) Compensate for damages when the risk occurs.
(4) Know that the government adequately manages the risk.
(5) Know that workers and regulatory agencies are trustworthy.
(6) Know that scientific mechanisms of accidents and mishaps are well understood.

These six measures correspond to determinants of risk acceptance, as discussed in the first section. In the questionnaire, the following phrasing framed the question related to each risk:

With respect to (type of risk inserted here), how do you achieve a feeling of "an-shin"? Of the following six statements, which do you consider the first-, second-, and third-most important factors in creating a sense of "an-shin"?

An-shin in Japanese corresponds to "security" in English, but connotes, additionally, peace of mind. People may lack an-shin even when they are guaranteed security. People may have peace of mind, even when they are not guaranteed security from risks.

To ask participants directly whether they would be willing to accept certain risk events might not be appropriate, as almost all risks in our society exist as if they have already been accepted. Therefore, we measured an-shin instead of directly asking about risk acceptance. Note, that in the next section, we use the term "risk approval" for this measure of an-shin.

5. RESULTS

Table 1 shows the distributions and mean ranks of the six risk management measures, according to perceived effectiveness with regard to increased risk approval. The table shows that measures to decrease the probability of risk occurrence and measures to minimize damages from risk were evaluated as effective in increasing risk approval for the risks listed in the questionnaire. The former was the most

Table 1 Distributions and means of ranks of the six policy actions according to perceived effectiveness to increase risk approval.

		medical mishaps		food		electric appliance		nuclear plants		traffic accidents	
		freq.	%	freq.	%	freq.	%	freq.	%	freq.	%
decrease the probability that the risk occurs.	1st	46	23.0	55	27.5	51	25.5	49	24.5	103	51.5
	2nd	49	24.5	43	21.5	55	27.5	24	12.0	45	22.5
	3rd	44	22.0	39	19.5	43	21.5	48	24.0	29	14.5
	>=4th	61	30.5	63	31.5	51	25.5	79	39.5	23	11.5
	mean rank	2.91**		2.87**		2.73***		3.18**		1.98***	
minimize the damage when the risk occurs.	1st	23	11.5	19	9.5	36	18.0	42	21.0	31	15.5
	2nd	37	18.5	45	22.5	49	24.5	57	28.5	79	39.5
	3rd	48	24.0	31	15.5	47	23.5	40	20.0	30	15.0
	>=4th	92	46.0	105	52.5	68	34.0	61	30.5	60	30.0
	mean rank	3.51*		3.64		3.08*		2.91***		2.90**	
compensate for the damages when the risk occurs.	1st	6	3.0	3	1.5	8	4.0	1	0.5	15	7.5
	2nd	18	9.0	10	5.0	28	14.0	10	5.0	26	13.0
	3rd	37	18.5	39	19.5	40	20.0	24	12.0	66	33.0
	>=4th	139	69.5	148	74.0	124	62.0	165	82.5	93	46.5
	mean rank	4.24		4.40		4.02		4.59		3.65*	
know that the government adequately manage the risk.	1st	7	3.5	38	19.0	11	5.5	40	20.0	18	9.0
	2nd	17	8.5	28	14.0	8	4.0	21	10.5	13	6.5
	3rd	18	9.0	23	11.5	8	4.0	28	14.0	21	10.5
	>=4th	158	79.0	111	55.5	173	86.5	111	55.5	148	74.0
	mean rank	4.43		3.59*		4.58		3.61		4.24	
know that workers and regulatory agencies are trustworthy.	1st	99	49.5	74	37.0	30	15.0	38	19.0	20	10.0
	2nd	45	22.5	47	23.5	30	15.0	34	17.0	19	9.5
	3rd	23	11.5	30	15.0	26	13.0	20	10.0	26	13.0
	>=4th	33	16.5	49	24.5	114	57.0	108	54.0	135	67.5
	mean rank	2.12***		2.52***		3.69		3.53		4.06	
know that scientific mechanisms of accidents and mishaps are well understood	1st	19	9.5	11	5.5	64	32.0	30	15.0	13	6.5
	2nd	34	17.0	27	13.5	30	15.0	54	27.0	18	9.0
	3rd	30	15.0	38	19.0	36	18.0	40	20.0	28	14.0
	>=4th	117	58.5	124	62.0	70	35.0	76	38.0	141	70.5
	mean rank	3.81		4.00		2.91**		3.19*		4.19	

Note: For calculating mean ranks, ranks for options that were not selected as top three options were assumed as "5.5" that is mean ranks between 4^{th} and 7^{th}.

*** the highest-ranked policy, ** the second-highest-ranked policy, * the third-highest-ranked policy

effective in increasing risk approval for electrical appliance and traffic accidents, while the latter was the most effective in increasing risk approval for nuclear plants.

Respondents indicated that measures that decrease the expected cost of the risks (that is, measures minimizing the damage and probability of the risks) were also effective for medical mishaps and food risks. However, increasing trust in workers and regulatory agencies was evaluated as more effective than decreasing expected costs. Thus, increasing trust is the most effective risk management measure with regard to food risks and medical mishaps. Regarding electrical appliance and nuclear power plant risks, respondents chose scientific understanding and explanation of accident mechanisms. These two risks differ from the other risks, such as traffic accidents, food, and medical mishaps, in that they are caused by more advanced technologies, which are less likely to be understood, even by risk experts.

Compensation for risk damages was not chosen as effective in increasing risk approval, except for the traffic accident risk. Respondents indicated that risk approval for traffic accidents may increase with the compensation measure. This may be because damage from traffic accidents is generally less than damage from the other risks presented in the questionnaire. Additionally, it is likely that many people will actually face traffic accidents in their lives.

6. ATTITUDE TOWARD SEISMIC RISK

Table 2 shows relative ranking with respect to attitude toward various hazard including seismic hazard. This table was reported in Fujii, Kikkawa and Takemura (2003). They implemented a survey to investigate attitude toward various hazard in Tokyo. The hazard surveyed was nuclear-power plant, terrorism, seismic hazard, medical accidents, traffic accidents, food accidents, electric-goods accident. They found that seismic risk was perceived as less "fear" risk than nuclear power plant and terrorism, but was more "fear" than the others. They also found that seismic risks were perceived as less "scientific unknown" than terrorism and traffic accident, but more scientific unknown than the others. Thus, it was found that seismic risks were perceived as "medium" risk in terms of fear and scientific unknown. This implies that people would prepare against seismic risks somehow, but the preparation would not be so strong.

Table 3 Ranks of fear and scientific unknown of various risks (Fujii, Kikkawa and Takemura, 2003)

	fear	scientific unknown
nuclear power plant	1st	6th
terrorism	2nd	1st
seismic risks	**3rd**	**3rd**
medical accident	4th	5th
traffic accident	5th	2nd
food accident	6th	4th
electric good accident	7th	7th

7. DISCUSSION

This study sought to understand the determinants of risk acceptance. Thus, survey participants were asked which policy measures would make them feel "an-shin", as an indicator of risk approval. The results showed that the risk management measures that would increase risk approval depended on the respective risks. The following three findings emerged from the survey.

1) For traffic accidents, nuclear power plants, and electrical appliance risks, the most effective measure for risk approval was that of minimizing the damage or the probability of accidents.
2) For food and medical mishap risks, the most effective policy was that of increasing trust in workers and regulatory agencies, rather than that of minimizing the damage or the probability of accidents.
3) Risk approval for electrical appliances and nuclear power plants could increase if people knew that the scientific mechanisms of accidents and mishaps were well understood.

A possible reason why trust in workers and organizations is so important for food and medical mishap risks is that medical and food workers, and their organizations, are assumed to have relatively more control over these risks, unlike the other risks presented here. Electrical appliance and nuclear accidents, on the other hand, are assumed to stem more from mechanical error than from human error. This explanation also agrees with the finding that better understanding of scientific mechanisms is important for electrical appliance and nuclear plants risks. Conversely, the mechanisms of food and medical mishaps may be simpler than problems associated with nuclear power and electrical appliances. Thus, people may believe that increasing accident prevention among workers and organizations is most effective in this case. Traffic accidents were assumed to be less under the control of workers and organizations (such as the police in charge of traffic) than accidents from medical mishaps and foods. We believe this is why trust was not considered as an important determinant for traffic accident risk approval.

These results indicate that risk acceptance cannot be fully understood by adopting a rational choice theory, which assumes that people maximize the expected benefits and/or minimize the expected costs. Minimizing damage and the probability of accidents were assumed to be just two examples of effective risk management measures for increasing risk approval or, in more commonly used words, risk acceptance. In other words, the feeling of an-shin, or risk approval, cannot be explained only by objectively achieved security. Other factors, such as scientific understanding and trust in workers and organizations, were also found to be important for increasing risk acceptance.

This indicates that those who wish to increase the public's risk acceptance should appear trustworthy and try to understand the scientific mechanisms of accidents; they should also try to minimize risk damage and probability. Trust is important, especially for risks where accidents can be prevented relatively easily by workers and/or organizations. These risks include those associated with food and medical mishaps. Scientific understanding of risk mechanisms is also important for risk acceptance, especially for risks involving mechanisms that are relatively complex, such as nuclear power and electrical appliance risks.

Acknowledgements:

A part of this paper was also presented at *the First International Symposium on Systems & Human Science: For Safety, Security, and Dependability*, Osaka, Japan, 2003 and was included in its proceedings (pp. 81-85).

References:

Dawes, R. M., Behavioral decision making and judgment. In D. T. Gilbert, S. T. Fiske, & G. Lindzey (Eds.), Handbook of Social Psychology (4th ed.), McGraw-Hill, Boston, MA, pp. 497-548, 1998.

Fischhoff, B., Slovic, P., Lichtenstein, S., Read, S., & Combs, B., How safe is safe enough? A psychometric study of attitudes toward technological risks and benefits, Policy Sciences, 9, pp. 127-152, 1978.

Payne, J. W., Bettman, J. R. and Johnson, E. J., The Adaptive Decision Maker, Cambridge University Press, New York, 1993.

Kahneman, D., Knetsch, J.L., and Thaler, R.H., Anomalies: The endowment effect, loss aversion and status quo bias, Journal of Economic Perspectives, 5, pp. 193-206, 1991.

Kreps, D., Corporate culture and economic theory. In J. Alt and K. Shepsle (Eds.), Perspectives on Positive Political Economy, Boston: Harvard Business School Press, 1990.

Slovic, P., The construction of preferences. American Psychologist, 50, pp. 364-371, 1995.

Slovic, P., Fischhoff, B., and Lichtenstein, S. Cognitive Processes and Societal Risk Taking. In J.S. Carroll, & J.W. Payne (Eds.), Cognition and Social Behavior, Potmac, MD: Lawrence Earlbaum, 1976.

Von Neumann, J., and Morgenstern, O., Theory of Games and Economic Behavior, 2nd ed., Princeton University Press, Princeton, 1947.

Savage, I.R., The Foundations of Statistics, Wiley, New York, 1954.

Fifth International Conference on Urban Earthquake Engineering
March 4-5, 2008, Tokyo Institute of Technology, Tokyo, Japan

DISASTER MANAGEMENT SYSTEM USING MOVING OBJECTS DATABASE

Chien-Cheng Chou[1], Yi-Ping Chen[2], and Hsiao-Ai Mu[3]

1) Assistant Professor, Department of Civil Engineering, National Central University, Taiwan
2) Graduate Research Assistant, Department of Civil Engineering, National Central University, Taiwan
3) Undergraduate Research Assistant, Department of Civil Engineering, National Central University, Taiwan
ccchou@ncu.edu.tw, vicky74722@yahoo.com.tw, gifanser@yahoo.com.tw

Abstract: Critical infrastructure is broadly defined as a set of important assets for producing or distributing a continuous flow of essential goods or services of a country. As the complexity and interconnectedness of a country's critical infrastructure evolve, threats and vulnerabilities for the country increase. When a disaster engenders failure of one critical infrastructure system, it can be expected that other critical infrastructure systems that need services or goods originally provided by the discontinued system will stop shortly, exacerbating the damage caused by the disaster. In fact, modeling critical infrastructure interdependencies (CIIs) is the most fundamental task to create a disaster management system (DMS). Without accurate, timely, and accessible CII data, a government could not help reducing damage caused by natural or artificial disasters. However, less research utilized a thorough methodology to model CII data. A comprehensive understanding of how networked critical infrastructure systems work can provide the means to better evaluate vulnerabilities related to hazards. This research analyzed and designed an integrated information model that is expected to best characterize CIIs for disaster mitigation. The mechanisms of Unified Modeling Language (UML) and Moving Objects Database (MOD) were employed to derive new model elements that can describe CIIs. A literature review of current CII-related studies was conducted. Functional and non-functional requirements and measures were determined, followed by conclusions and recommendations for the research.

1. INTRODUCTION

Critical infrastructure is broadly defined as a set of important assets for producing or distributing a continuous flow of essential goods or services of a country (Fisher and Peerenboom 2000). These assets include, but are not limited to, facilities for transportation, telecommunications, electric power systems, gas and oil storage and transportation, water supply systems, and wastewater treatment systems (Chou et al. 2007). Since most critical infrastructure systems interact with each other, these interactions often create complex relationships or so-called interdependencies that cross system boundaries (Haimes 2005). As the complexity and interconnectedness of a country's critical infrastructure systems evolve, threats and vulnerabilities for the country increase. When a disaster engenders failure of one critical infrastructure system, critical infrastructure interdependencies (CIIs) undoubtedly exacerbate the degree and scope of the damage caused by the disaster. For example, a power generation plant has only one entrance road, which was torn down by an earthquake and is scheduled to be opened one month later. It can be expected that since fuel for the plant can no longer be transported through the road, shortage of electric power will soon spread along the power transmission lines. Furthermore, any critical infrastructure systems that need electricity provided by the plant may not function well unless the problems of the entrance road can be fixed.

Although owners of critical infrastructure systems have created and maintained their individual facility data for supervising the operation of the systems, they usually do not care much about CII data due to economical or security issues (Rinaldi et al. 2001). Past research has shown that in order to actively reduce a disaster's impact, disaster management officials should focus more on the damage caused during and after the disaster (Laefer et al. 2006). Since the majority of the damage after a disaster are derived from CIIs, CIIs are hence the topic that needs more comprehensive and systematical studies (MRA 2005). In fact, complete and accurate CII data are fundamental to develop a disaster management system (DMS) (Pederson et al. 2006). Without accurate, timely, and accessible CII data, a government could not help reducing the damage caused by natural or artificial disasters.

Recent research has designed several modeling approaches to describe CIIs; however, these models could not precisely render actual relationships between critical infrastructure systems and/or their components in accordance with the interdependency types and attributes (Pradhan et al. 2007). In addition, after one critical infrastructure system stops, it may take some time to let another system cease to function. The spatial dimension has been incorporated into most of the CII models; nevertheless, the time dimension is required to record every event during and after a disaster but currently exists in none of the CII models proposed (Peachavanish et al. 2006). A comprehensive understanding of how networked critical infrastructure systems work and interact with respect to time can provide the means to better evaluate vulnerabilities related to hazards. The research aims to analyze and design an integrated information model that is expected to best characterize CIIs for disaster mitigation. This paper thus outlines the development of an integrated information model for CII data. The study methodology began with a literature review, followed by analysis of CII requirements. The research team then incorporated the requirements into the design of the model. Finally, model verification and validation were performed and conclusions were made.

2. RELATED WORK

2.1 Critical Infrastructure Interdependencies

Critical infrastructure systems have been regarded by several researchers as complex adaptive systems due to the fact that change often occurs. Each critical infrastructure system has its own way to evolve (Rinaldi et al. 2001). For example, in a water supply system, adding a new water pump station can serve more nearby communities but also creates a dependent relationship with a power system (Kranc et al. 2007, Kraus et al. 2007). Interdependency is defined as two or more relationships among critical infrastructure systems; that is, critical infrastructure system i depends on j through some links, and j likewise depends on i through other links. Types for describing CIIs have been suggested and are summarized as follows (Rinaldi et al. 2001):

- Physical Interdependency: two critical infrastructure systems are physically interdependent if the state of each is dependent on the materials outputs of the other.
- Cyber Interdependency: a critical infrastructure system has a cyber interdependency if its state depends on information transmitted through another information infrastructure system. Cyber interdependencies connect critical infrastructure systems to one another via informational links, and the outputs of the information infrastructure system are inputs to the other critical infrastructure system. The commodity passed between the systems is information.
- Geographic Interdependency: critical infrastructure systems are geographically interdependent if a local environmental event can create state changes in all of them.

There are interdependencies between critical infrastructure systems that cannot be classified as physical, cyber, or geographic interdependencies (Uddin and Engi 2002). More investigations should be conducted to divide ambiguous interdependencies discovered into several direct interdependencies combined. Lastly, attributes data should be associated with a CII, e.g., the time when the interdependency is enacted, or the information exchanged in a cyber interdependency. CII's attributes enrich the capability of a CII model to describe more information concerning the CII. However, current CII models such as the one proposed by Kruchten et al. (2007) cannot accommodate this requirement.

2.2 The Disaster Management Process

The disaster management process consists of six disaster-related phases (USFDA 2003): (1) identification; (2) prediction; (3) mitigation; (4) preparation; (5) response; and (6) recovery. The identification phase involves ascertaining any opportunity pertaining to community assets, i.e., critical infrastructure systems, fire trucks, hospital beds, etc., that may be affected by a disaster. The prediction phase consists of scientific analysis tasks, including meteorological, geologic, hydrologic, agricultural, environmental, epidemiologic calculations and simulations. The mitigation phase concerns active reductions of a disaster's impact, whereas the preparation phase includes needed actions to contend with the portion of a disaster's impact that cannot be mitigated. The response phase focuses on real-time actions as a disaster evolves, whereas the recovery phase deals with how to restore community assets affected by a disaster (Pradhan et al. 2007).

Researchers have also analyzed requirements of a DMS covering all six phases of the disaster management process (Pradhan et al. 2007). Briefly, a DMS is designed to significantly lessen the loss of human life and the economic costs of a disaster, and should have three components (Uddin and Engi 2002): (1) a baseline database: which contains the basic information of the community assets affected by a disaster; (2) spatial querying: which can provide disaster management officials with a graphical interface showing designated geographical information of the disaster and community assets, e.g., locating the shortest evacuation path and optimizing the resource distribution; and (3) ubiquitous computing: which means redundant computing resources should be allocated to execute the DMS simultaneously (Pradhan et al. 2007).

Although most of the current DMSs have stored critical infrastructure baseline data for disaster management purposes, CII data have not been rigorously documented and analyzed. The rescue operations after September 11, 2001 were recognized as lack of an integrated data repository that can be used to predict possible subsequent infrastructure failures. CII data can play a major role in establishing the knowledge base for the rescue operations during and after a disaster. Disaster management officials or decision makers need to know not only direct impact on community assets of a disaster but indirect impact on other critical infrastructure systems that may be shut down due to CII. However, since managing the interdependencies of critical infrastructure systems is not their owners' top priority, the only way to collect CII data is for transportation agencies to ask infrastructure owners to upload interdependency data as a part of the rights-of-way permitting process. Some infrastructure owners build very detailed computerized models describing their own facilities, but this kind of information may involve a company's confidential data and cannot be completely shared with the others. Security concerns regarding CII data must be addressed in advance of data collection from different infrastructure owners. A formal model that can describe CIIs and predict a disaster's impact on critical infrastructure systems is highly desired.

2.3 The Time Dimension

Each event during and after a disaster may be associated with a different time scale (Chen et al. 2006). For example, if an accident destroys a power switch facility, the failure due to switching over voltages may ruin other power facilities within milliseconds. Shortage of fuel support as a result of road blockage may take months to fix the problem but might not affect the power generation process immediately. The need of the multi-scale time hierarchy associated with CIIs was reported as one of the most difficult research challenges in this area.

One advanced database technique that has emerged as a main focus of many spatial-temporal information systems such as the digital battlefield in the military is to keep track of object locations over time and to support temporal queries about future locations of the objects (Wolfson 2002, Wolfson et al. 1998). Called moving objects database (MOD), this technique aims to deal with geometries changing over time and to simplify the data update process through use of dynamic attributes (Guting and Schneider 2005), thereby having the potential for eliminating or reducing some of the associated challenges and complications. The way MOD employs to process the time dimension for each moving object may serve as a starting point for CII data modeling.

3. THE CII MODEL

The proposed CII model is shown in Figure 1. Elaboration of each class in the model is described in the following sections. Basically, the model consists of three main parts: (1) infrastructure and management classes; (2) interdependency classes; and (3) infrastructure type classes. The infrastructure and management classes contain information regarding an infrastructure system itself and the owners' organization. The interdependency classes are designed to capture requirements of the three CII types. The infrastructure type classes are the reflection of the need that each type of critical infrastructure systems has its own attributes. The mechanisms of the model are described as follows.

3.1 Infrastructure and Management Classes

Three classes pertain to this part:

- Organization: this class represents the owner of a critical infrastructure system. It includes a person's contact information so that disaster management officials can get in touch with him or her when potential damage of the infrastructure occurs.
- Enterprise: this class represents the concept of the organization's business entity. For example, a city government may be responsible for the water supply system, the wastewater treatment system, and the power distribution system. There must be three engineering divisions in the city government, so "Enterprise" represents the city government whereas "Organization" represents each engineering division. The "Enterprise-Organization" structure can be easily extended to model any infrastructure owners' organizations.
- Infrastructure: this class represents the most important concept in the CII model, i.e., infrastructure. It consists of six fundamental attributes:

1. Name: the name of the infrastructure.
2. Description: notes or other information regarding this infrastructure.
3. Location PolygonZ: the location and shape of the infrastructure, including the vertical dimension. It should be noted that since an infrastructure object may contain a set of other infrastructure objects via composition, the shape and base reference point of the object should be changed accordingly.
4. ServicePeriod T: the expected service period of the infrastructure. Sometimes an infrastructure service may be stopped due to maintenance. The discontinued service may cause a serious problem if a disaster strikes an area where the regular backup infrastructure is working. In the theory of temporal database or MOD, there are two time dimensions associated with each time-sensitive attribute: valid time and transaction time (Tansel et al. 1993, Guting and Schneider 2005). The valid time refers to the time in the real world when an event occurs or a fact is valid. The transaction time refers to the time when a change is recorded in the database. For example, the service period of an infrastructure is defined by a manager as from 2009/1/1 to 2009/5/1. The manager knows the plan on 2008/11/1, but the plan is changed by another manager on 2009/3/1. Hence, the infrastructure will not provide service after 2009/3/2, although the original plan does not say so (see Figure 2). Same rules can be applied to the transaction time dimension. Traditional database techniques do not consider such requirements because only the newest status of an object is recorded.
5. Status T: the working status of the infrastructure. This attribute is also time-sensitive. For example, disaster management officials might want to know when the status of an infrastructure is "Working" or "Stopped." They might want to know when the status data is updated. Persisting historical data of the infrastructure status in a database can help decision makers understand past experience.
6. EstimateStatus T: the estimated status of the infrastructure. Because the CII model is designed to predict the interdependencies between critical infrastructure systems, this attribute will be used to record the predicted status of an infrastructure.
7. RecoveryStatus T: the recovery progress of the infrastructure. If an infrastructure is out of order, its recovery plan will be executed. If RecoveryStatus is

equal to "Complete," the Status of the infrastructure should be "Working."

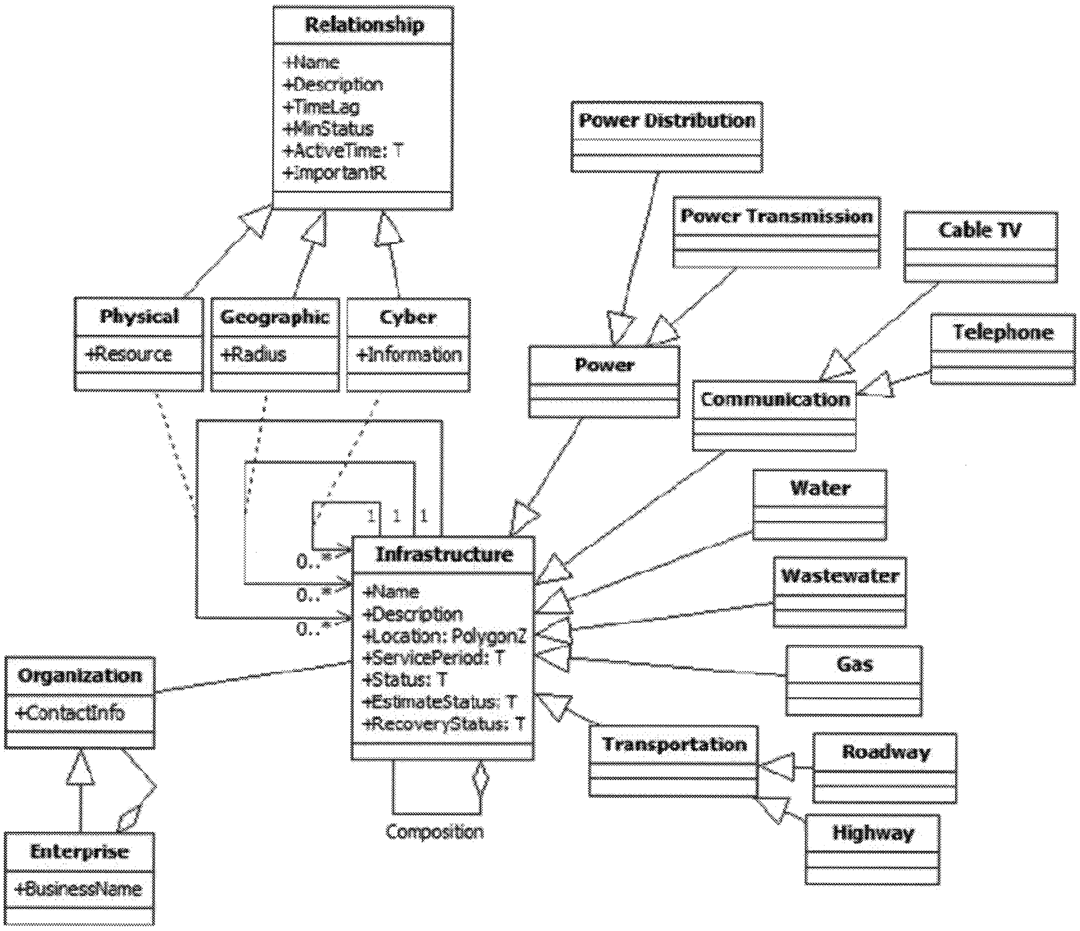

Figure 1 UML Class Diagram of the CII Model

3.2 Interdependency Classes

Four classes pertain to this part:

- Relationship: this class represents the concept of a relationship in the CII model. In the one end of the relationship, it is the dependent infrastructure that needs services or resources provided by the supporting infrastructure. For example, the operation of a power plant depends on the entrance road, whereas the traffic control system on the road needs electricity provided by the plant. Two relationship objects should be created for this interdependency. Additionally, the class consists of six attributes:

1. Name: the name of the relationship.
2. Description: notes or other information regarding this relationship.
3. TimeLag: the time span of the relationship that will cause the dependent infrastructure to stop or reduce the service level.
4. MinStatus: the minimum status of the supporting infrastructure that will activate the relationship, i.e., to shut down the dependent infrastructure.
5. ActiveTime T: the time when the relationship is activated. This attribute is time-sensitive and can provide detailed records of how a disaster propagates.
6. ImportantR: the weight or ratio of the relationship with respect to the dependent infrastructure. For example, two infrastructure systems support the operation of the third infrastructure. The two infrastructure systems may play different roles in supporting the third one. Hence, the weight for each supporting infrastructure is different.

- Physical: this class represents the physical relationship type in the CII model. Relationship attributes can be easily modeled in the class. In the proposed model, the resource that bridges the two infrastructures is recorded here.
- Geographic: this class represents the geographic relationship type in the CII model. In the proposed model, the radius defining the boundary of two infrastructures that may work or stop at the same time is recorded here.
- Cyber: this class represents the cyber relationship type in the CII model. In the proposed model, the information that is consumed by the dependent

infrastructure is recorded here.

3.3 Infrastructure Type Classes

This part defines various infrastructure types. Specific attributes pertaining to a certain type of critical infrastructure systems are recorded in respective classes. Additionally, because the structures and functions of a power distribution network is quite different that a power transmission network, two classes are designed to accommodate this requirement.

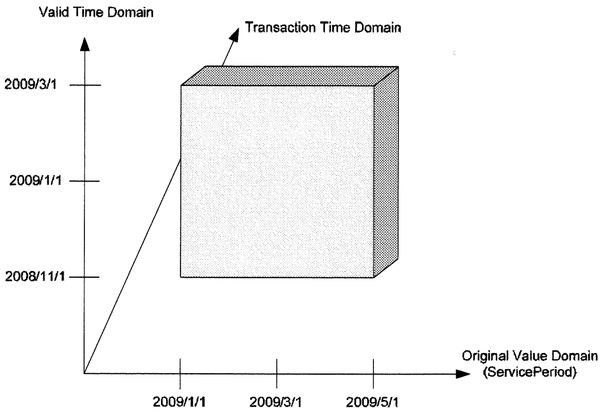

Figure 2 The Valid Time Dimension of ServicePeriod

4. EXPLOITING THE MODEL

A simulation tool is currently under development. The tool will use the CII model to simulate events of each critical infrastructure system under an earthquake disaster in a small town in Taiwan. The water supply system, power distribution lines, communication lines, and natural gas pipelines are depicted in the tool. Their baseline and interdependency data are recorded in the database.

With interdependency data in the database, users can find out when the scope of the disaster's impact with respect to the time dimension. A "firewall" concept may be added to an interdependency relationship to have the disaster propagation suspend. Other applications such as querying a certain type of infrastructure failure can be implemented.

5. CONCLUSIONS

With the ever-increasing demand for a streamlined analysis of CII, disaster management officials and decision makers are making substantial efforts to improve the disaster mitigation technology. Because CII data are fundamental to develop a full-fledged DMS and because the management of the time dimension is the most difficult task in modeling CIIs, a rigorous model with time processing capabilities such as the one in this paper can help disaster management officials retrieve relevant information on demand. This research has designed a UML-based model that can describe CIIs with the time-sensitive attributes. Further implementation and evaluation of the CII model proposed is needed in order to demonstrate how such information technology can mitigate a disaster's impact.

References:

Chen, L.C., Wu, J.Y., and Lai, M.J. (2006) "The Evolution of the Natural Disaster Management System in Taiwan." *Journal of the Chinese Institute of Engineers*, 29(4), 633-638.

Chou, C.C., Caldas, C.H., and O'Connor, J.T. (2007) "Decision Support System for Combined Transportation and Utility Construction Strategy." *Transportation Research Record: Journal of the Transportation Research Board*, TRB, 1994, 9-16.

Fisher, R., and Peerenboom, J. (2000) "Interdependencies: A DOE Perspective." *16th Annual Security Technology Symposium & Exhibition*, Office of Critical Infrastructure Protection, June 28, 2000, Williamsburg, Virginia.

Guting R.H., and Schneider, M. (2005) *Moving Objects Databases*, Morgan Kaufmann, San Francisco, CA.

Haimes, Y. (2005) "Infrastructure Interdependencies and Homeland Security." *Journal of Infrastructure Systems*, ASCE, 11(2), 65-66.

Kranc, S.C., Yalcin, A., Tsalatsanis, A., and Collier, N.O. (2007) "The Efficacy of Utility Data Management." *FDOT Research Project BD544-27 Report*, University of South Florida, Tampa, FL.

Kraus, E., Quiroga, C., Brown, R., Stevens, C., and Koncz, N. (2007) "Development of a Utility Conflict Management Tool." *TxDOT Research Project 0-5475 Report*, Texas Transportation Institute, College Station, TX.

Laefer, D., Koss, A., and Pradhan, A. (2006) "The Need for Baseline Data Characteristics for GIS-Based Disaster Management Systems." *Journal of Urban Planning and Development*, ASCE, 132(3), 115-119.

MRA. (2005) *Joint Infrastructure Interdependencies Research Program (JIIRP) Symposium*, the Department of Public Safety and Emergency Preparedness Canada (PSEPC), November 10, 2005, Ottawa, Ontario, Canada.

Peachavanish, R., Karimi, H., Akinci, B., and Boukamp, F. (2006) "An ontological engineering approach for integrating CAD and GIS in support of infrastructure management." *Advanced Engineering Informatics*, Elsevier, 20, 71-88.

Pederson, P., Dudenhoeffer, D., Hartley, S., and Permann, M. (2006) "Critical Infrastructure Interdependency Modeling: A Survey of U.S. and International Research." *INL/EXT-06-11464*, Idaho National Laboratory: Critical Infrastructure Protection Division, Idaho Falls, Idaho.

Pradhan, A., Laefer, D., and Rasdorf, W. (2007) "Infrastructure Management Information System Framework Requirements for Disasters." *Journal of Computing in Civil Engineering*, ASCE, 21(2), 90-101.

Rinaldi, S., Peerenboom, J., and Kelly, T. (2001) "Identifying, Understanding, and Analyzing Critical Infrastructure Independencies." *IEEE Control Systems Magazine*, 21, 11-25.

Tansel, A., Clifford, J., and Gadia, S. (1993) *Temporal Databases: Theory, Design, and Implementation*, Benjamin-Cummings, San Francisco, CA.

Uddin, N., and Engi, D. (2002) "Disaster Management System for Southwestern Indiana." *Natural Hazards Review*, ASCE, 3(1), 19-30.

USFDA. (2003) *Disaster preparedness phases*, U.S. Federal Drug Administration, Rockville MD.

Wolfson, O., Xu, B., Chamberlain, S., and Jiang, L. (1998) "Moving Objects Databases: Issues and Solutions." *Proceedings of the Tenth International Conference on Scientific and Statistical Database Management*, IEEE, Capri, Italy, 111-122.

Wolfson, O. (2002) "Moving Objects Information Management: The Database Challenge." *Lecture Notes in Computer Science*, Springer Berlin / Heidelberg, 2382, 15-26.

Fifth International Conference on Urban Earthquake Engineering
March 4-5, 2008, Tokyo Institute of Technology, Tokyo, Japan

A SIMPLE METHOD TO EVALUATE POTENTIAL PHYSICAL DAMAGE IN URBAN AREAS FOR RISK MANAGEMENT PURPOSES

Francisco Vidal [1)], Mercedes Feriche[2)], Manuel Navarro[3)], Lola Vidal[4)], Jose Morales [1)]

1) Professor, Andalusian Institute of Geophysics, Granada University,18080 Granada, Spain
2) Technical, Department of Disaster Prevention, Andalusian Institute of Geophysics, Granada University,Granada, Spain
3) Professor, Department of Applied Physics, Almeria University, 04120 Almeria, Spain
4) Assistant, Department of Economics, Granada University,Granada, Spain
fvidal@iag.ugr.es, feriche@ugr.es, mnavarro@ual.es, lvidal@ugr.es, jmorales@iag.ugr.es,

Abstract: A modular methodology for creating earthquake-damage scenarios adapted to urban areas of southern Spain has been developed. The seismic motion on rock is taken from probabilistic seismic hazard, deterministic methods or historical earthquakes intensity data. Site classification use seismo-classification soils and V_S^{30} obtained directly or indirectly. PGA amplification factors are obtained from UBC-97 and intensity from PGA an SA(T) data or qualitatively from empirical intensity data. Building vulnerability is obtained after building up a Building Typology Matrix and using the vulnerability index of Risk-UE project. Probability Damage Matrix is applied to estimate building damage. This single methodology has been applied to Granada and Velez Malaga cities (southern Spain). The assessment of the potential damage of possible seismic events and its detailed distribution affecting earthquake-prone cities are useful for seismic-risk reduction and risk management.

1. INTRODUCTION

The evaluation of potential earthquake damage in urban areas provides a basis for seismic risk reduction and generally for earthquake risk management. In regions with moderate to low seismic hazard level but moderate to high seismic risk level, like the western Mediterranean region, the application of single methods to perform a reliable forecast of the amount and distribution of future earthquake damage in urban areas is an adequate way for reducing the impact of future earthquakes. Single methods of Earthquake Damage Scenarios (EDS) mean less work time and lower economic cost and may be considered as the first level evaluation of earthquake impact. Furthermore, Emergency Planning and Earthquake Disaster Prevention measures should be based on those earthquake damage estimates.

The Andalusian region (Southern Spain), located in the European and African interaction zone, is the most hazardous seismic zone of Spain, especially the Granada, Malaga and Almeria provinces (Vidal, 1986). More than ten destructive historical earthquakes have occurred in these provinces in the last five centuries. Nevertheless, only a few earthquake risk evaluation studies have been developed recently in the urban areas of Malaga (Irizarry et al, 2006, 2007), Barcelona (Irizarry, 2004; Lantada et al., 2007) and Motril (Perez et al., 2007). In these cases the soils were classified in four classes according to Spanish seismic code NCSE-02. The building vulnerability were evaluated using typologies classification in the first case, and vulnerability index and capacity spectrum method in the others ones.

The accurate prediction of building damage during a future strong earthquake is difficult because it depends on the characteristics of earthquake source, the site conditions, and the building itself. However, at present and for risk management purposes, it is possible to estimate seismic motion in solid bedrock and surface soil at each urban area point. Furthermore, it is also possible accounting for more probable damage in homes, buildings, and lifelines for power, water, communication, and transportation.

In this work the methodology to obtain amplification factors from seismo-geotechnical classification of soils, building vulnerability evaluation from Building Tipology Matrix and vulnerability index (Milutinovic & Trendafiloski, 2003) of Risk-UE and earthquake damage estimation using Probability Damage Matrix for future earthquakes using a Geographical Information System (GIS) it is presented. This methodology has been applied to Granada and Velez Malaga cities, two Andalusian moderate-sized urban areas. The EDS were estimated in function of probable macroseismic intensity in 475 years in each ones.

2. THE EDS SINGLE METHOD

2.1 Soil classification, amplification factor and seismic hazard map.

If data on the thickness and nature of the geologic materials and soils of an urban area are available, several phenomena with a strong influence on ground shaking characteristics and damage distribution can be evaluated before the occurrence of an earthquake. These effects related with local ground conditions are: Amplification of ground motion by soft soils, liquefaction of water-saturated thick soils (sand, silt, gravel) and landslides triggered by shaking.

The ground shaking amplification is determined by thickness and physical properties of near surface geologic materials (Vidal et al, 1996). The Uniform Building Code (UBC-97) and Eurocode 8 (EC8) use average shear-wave velocity in the upper 30 m of soil, V_S^{30}, for site classification sites according soil type. A small variation of this classification has been applied for site conditions mapping in this work (Table 1). Our classification is a variation of the four types of soil considered by the Spanish Seismic Code NCSE-02, dividing I and IV soil categories in two new ones. Thus, materials of different lithology are grouped in six soil categories: Hard Rock (I_A), Rock (I_B), Very Dense Soil and Soft Rock (II), Stiff Soil (III), Soft Soil (IV_A), and Special Soils (IV_B).

Table 1. Soil types according UBC (*Uniforming Building Code*), EC8 (*Eurocode 8*) and PW (*Present Work*) and PGA Amplification Factors (AF) used in this work.

SOIL TYPE			**Description**	**V_S^{30} m/s**		**AF**
UB	**EC**	**PW**		**UBC**	**EC8**	
S_A	A	I_A	Hard rock	> 1500	>800	0.9
S_B		IB	Rock	760 - 1500		1.0
S_C	B	II	Very dense soil and soft rock	360 - 760	360-800	1.2
S_D	C	III	Stiff soil	180-360	180-360	1.4
S_E	D	IVA	Soft soil	<180	<180	1.8
S_F	E	IVB	Special soils		S_1<100 S_2 liq.	2.0

The structure and characteristics of soils has been mainly obtained by borehole data. Velocity data are determined by soil type-V_S relationships, SPT data or V_S seismic profiles. The predominant period from microtremor data (Cheddadi, 1996; Vidal et al, 1998) has been also considered in soil classification in Granada. Only soil type I_B, II and III are found in Velez Malaga and Granada urban areas. In Granada there are 3 to 8 m thick quaternary soft soils (sand, mud, clay, silt) in several places of the urban area but the V_S^{30} correspond to type III; only two small zones, located in the Beiro and Genil river alluvial fans, have soft soil 20 m thick or more and it is classified as type IV_A (Figure 1).

The shear-wave velocity is here used to characterize the liquefaction potential (Andrus and Stokoe, 1997; Seed et al, 2003). Although young, loose and granular soils are present in Granada city, these are unsaturated soils and consequently will not liquefy, but they may settle, mainly at riversides; however, liquefaction could occur outside the urban area.

The earthquake-induced landsliding has been assessed with slope data derived from digital cartography, geologic maps and from mapping of existing slides, from air photo interpretation. No landslides were found inside the studied urban areas but could occur in slopes near the rivers.

The seismic motion on rock is taken from probabilistic seismic hazard map, or from historical earthquakes intensity data, or by using deterministic methods. To calculate seismic ground motion in each point of the urban area we use PGA and SA(T) values in the bedrock multiplied by the amplification factors of the upper 30 m soil columns. The intensity is obtained from PGA and SA(T) data applying Okada et al (1991) relationship. When seismic hazard in rock is given by EMS intensity values the final intensity on soil is estimated increasing 0.5 and 1 degree for soils III and IV_A, respectively, and ≥1.5 for soils type IV_B (Tiedemann, 1992)

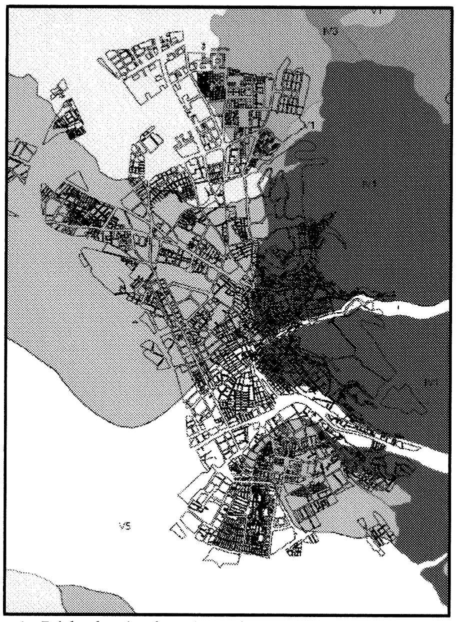

Figure 1. Lithological units of Granada city. Dark colour IVi units (half right part in the figure) correspond to column of soils type I_B and II (A and B in EC8). Light colour IVi units are soil type III (C of EC8).

2.2 Building vulnerability assessment.

Building vulnerability is the degree of damage to given building subjected to ground shaking of a given intensity. Vulnerability assessment based on past earthquake damages is called observed or empirical vulnerability. This approach assumes that certain groups of buildings characterized by a similar seismic behaviour tend to experience similar earthquake damage also and constitute vulnerability classes. Thus a series of empirical vulnerability functions can be obtained for these vulnerability classes from field damage observations (e.g. the ATC-13, 1985 functions).

To proceed to the vulnerability evaluation for each individual building of Granada and Velez Malaga cities, the Risk-UE project methodology named level I (based on vulnerability indices and damage functions) has been used. Thus, structural typology, age and other characteristics (as regularity, position, ..) of the buildings have been considered. First step has been to define a Building Typology Matrix (BTM) from specific features of buildings of each city, considering the BTM established by Risk-UE project and assigning average vulnerability indices to the vulnerability classes according to proposal of Milutinovic & Trendafiloski (2003). Risk-UE define 23 building classes for European countries: 10 classes for masonry (M), 7 for reinforced concrete (RC), 5 for steel (S) and 1 for wooden (W) buildings

Vulnerability index V_I values are arbitrary (Bernardini, 2000), as it represents only a score that quantifies the seismic behaviour of the building. These indices range between 0 and 1, being their higher values for the most vulnerable buildings and lower to strong earthquake resistant buildings. For each building type Risk-UE calculates four vulnerability indices: V_I* most probable value of V_I; [V_I^- ; V_I^+] bounds of the plausible range of V_I (usually obtained as 0.5-cut of the membership function); [V_I^{min}; V_I^{max}] upper and lower bounds of the possible values of V_I (Giovinazzi y Lagomarsino, 2004).

The vulnerability index value V_I for each building is calculated simply summing to the characteristic vulnerability index V_I* (according to the building type) two modifier factors ΔV_R and ΔV_m:

$$\overline{V}_I = V_I^* + \Delta V_R + \Delta V_m \quad (1)$$

The Regional Vulnerability Factor ΔV_R is introduced to take into account the particular quality of building construction at a regional level. Behaviour Modifier ΔV_m is assigned on the basis of particular attributes of each building, and take into account the effects due to the different behavior modifiers: state of preservation, seismic design level, number of floors, irregularity, soft-story, foundation an soil morphology. For building in aggregates it is also taken into account the effects due to different heights of adjacent buildings when there is insufficient aseismic joint in aggregate building. The main vulnerability modifier is seismic design level being 0.16 for pre or low code level and -0.16 for high level. The remainder modifiers have lower values, generally 0.04, except for buildings with 6 or more stories and low code level that reach 0.08. For these reasons a first simplified estimate of the vulnerability index is performed considering typologies, periods of construction according to seismic design level and taking into account also the following factors: bad maintenance, more than 6 stories, serious irregularity, and soft-story in the building.

2.3 Earthquake damage evaluation.

In order to obtain expected damage in a city as a function of the intensity once the vulnerability index is known the Risk-UE Level I methodology (Vacareanu et al, 2004) is applied. In this method the seismic action at each site is characterized by means of EMS-98 intensity scale (Grünthal, 1998) and the building vulnerability with vulnerability index. Six damage states are considered: a no-damage state, labelled as None and five more damage states, termed as Slight, Moderate, Substantial to Heavy, Very Heavy and Destruction. We apply a semiempirical function that correlates the mean damage degree μ_D with the macroseismic intensity I and the vulnerability index V_I, (Fig. 2) function based in observed damage in past earthquakes (Giovinazzi & Lagomarsino, 2002; Giovanazzi, 2005).

$$\mu_D = 2.5\left[1 + \tanh\left(\frac{I + 6.25\, V_I - 13.1}{2.3}\right)\right] \quad (2)$$

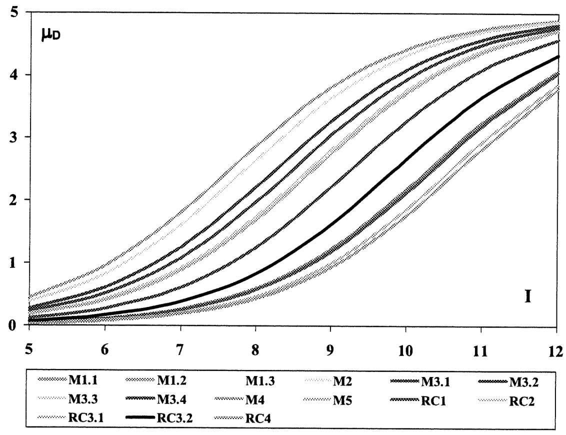

Figure 2. The mean semi-empirical vulnerability functions for the most common Risk-UE building typologies.

The probability of each state of damage, or the damage probability matrix (DPM), can be calculated from mean damage μ_D using the beta distribution. Thus potential physical damage scenarios can be obtained and plotted for the city (or for any selected area of the city) in mean damage values or in terms of each damage state of EMS scale.

3. EARTHQUAKE DAMAGE SCENARIOS IN TWO SOUTHERN SPAIN URBAN AREAS.

3.1 EDS for Granada city.

The population and building data are taken from the INE (Spanish National Statistics Institute) survey, (a nation-wide census carried out every 5 years). The most recent data, from the 2001 general census indicate 240.661 inhabitants and 21.377 buildings.

An analysis of the features characterizing the buildings of the city of Granada has recognized the following 13 BTM classes: 7 for Masonry (M), 4 for Reinforced Concrete (RC) and 3 of Steel (S). Structures of unreinforced masonry bearing walls: M1.1(rubble stone, fieldstone), M1.2 (simple stone), M1.3 (massive stone), M3.1 (wooden slabs), M3.2 (masonry vaults), M3.3 (composite steel and masonry slabs), M3.4 (RC slabs) and M4 (reinforced or confined masonry walls). Structures of Reinforced Concrete (RC): RC1 (buildings with RC moment frames), RC2 (buildings with RC shear walls), RC3.1 (buildings with RC frame and regular infill walls), RC 3.2 (buildings with RC irregular frame and masonry infill walls). Only a very small number of Steel (S) buildings have been identified: S1 (steel moment frames) S2 (steel braced frames) S1 (steel frames with unreinforced masonry infill walls).

A total of 16.233 buildings were tested; more than 60 % were RC buildings and masonry the remainders, mainly of brick walls. 47.5% of the buildings have one or two stories and 14% have 6 or more stories. The minimum typology vulnerability index V* is 0.35 and the maximum 0.87. When modifier factors are considered the minimum total vulnerability index V_I is 0.40 and the maximum is 1.00. According to EMS scale, the buildings of the old quarters and those built before 1974 are of vulnerability class A and B, and the constructions built after that date are generally class C and D and exceptionally of class E.

Using a preliminary 1:10.000 geological and geotechnical map as a guide, borehole database, SPT data, Vs of top 15 m from refraction seismic profiles measured at 28 different locations, and two N-S geological cross-sections, a ground amplification map of the urban area has been obtained from Figure 1. From these geotechnical zonation, and the detailed cross-sections, a map of soil types based on V_S^{30} (weighted average of Vs in the uppermost 30 m) values has been obtained. Soils type II and III are found. Only small zones at riversides are V_S^{30}classified as IV_A category.

Seismic hazard values on rock has been computed using Seismic Source Zones of the Spanish Seismic Code NCSE-02 and using Cornell's (1968) approach to hazard evaluation for different return periods.

Two earthquake damage scenarios with rock intensities of VII (EDS 1) and VIII (EDS 2) has been estimated in terms of probability damage; the first one corresponding to frequent destructive event and the second one to probabilistic ground motion (475 years return period) due to a rare event. Historical examples of these events are 1806 and 1431 earthquakes with epicenters near Granada. Distribution of final ground motion values has been obtained applying amplification factors. The mean degree of damage μ_D is computed with the expression (2) and the probability distribution of the degree of damage is calculated using the beta distribution (Mouroux, and Lebrun, 2006; Vacareanu et al, 2004). The results of both damage scenarios for Granada city are presented in Table 2 and in Figures 3 and 4. The number of casualties can be estimated using the percentage proposed by ATC-13 and FEMA 2003 for each grade of damage or by Coburn and Spence (2002).

Table 2. Number of buildings of each EMS damage degree for Granada damage scenarios (only of tested buildings).

EMS Damage degree	EDS 1 (I_r = VII)		EDS 2 (I_r = VIII)
	Using V* only	Using total V_I	Using total V_I
0	567	145	-
1	10.661	3.799	1.047
2	5.005	3.390	2.867
3	-	8.890	3.420
4	-	9	8.887
5	-	-	12

The number of uninhabitable buildings can be estimated suming buildings suffering damage degree 4 and 5 and the 50% of those with damage degree 3. The number of uninhabitable buildings for the EDS1 case is 4.454 of the tested buildings (27%) and 10.609 (65%) for the EDS2.

For both EDS considered, soil liquefaction could exists but appears outside the urban area (western side) and landslides occur at eastern part of the city in the hills nearby Beiro, Darro and Genil rivers. Historical documents indicate that such phenomena occurred during the maximum historical earthquake (1431) and during the moderate shaking of 1806. Landslide also occurred at north-eastern of Granada during the small quake of 1956 (M5.2).

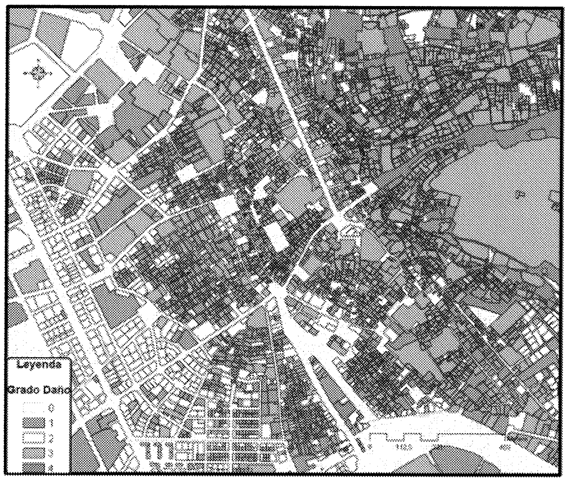

Figure 3. Distribution of average damage level for the Granada down-town zone estimated for frequent scenario earthquake EDS1 considering total V_I.

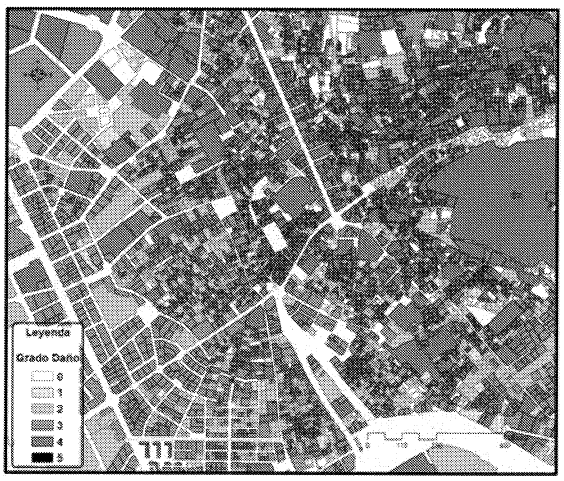

Figure 4. Distribution of average damage level for the Granada down-town zone estimated for the most severe scenario earthquake EDS2 considering total V_I.

3.2 Velez Malaga city.

In the case of Velez Malaga city, the population and building data of INE 2001 census are 35.322 inhabitants and 5.520 buildings. The typology and vulnerability of 4.957 buildings were evaluated; more than 65 % are RC buildings and masonry the remainders (mainly of brick walls). 72% of the buildings have one or two stories and 3% have 6 or more stories. 7 BTM classes were identified: 4 for Masonry (M1.2, M1.3, M3.1, M3.4) and 3 for Reinforced Concrete (RC1, RC3.1, RC3.2).

The minimum typology vulnerability index V* is 0.40 and the maximum 0.74. When modifier factors are considered minimum total vulnerability index V_I is 0.40 and the maximum is 0.94. According to EMS scale, the majority of the buildings belong to the A, B, and C classes, and less frequent to D class (Figure 5).

Figure 5. EMS-98 Vulnerability classes of the buildings of Velez Malaga down-town.

A column soils classification based on V_S^{30} values (estimated from geotechnical, borehole and SPT data) was performed and a detailed ground amplification map has been obtained. Soils type I_B, II and III are found inside the urban area, and outside the western zone of the city appear soils of type IV_A, and soil liquefaction could be possible for strong shakings.

We have used the largest historical event affecting Velez Malaga city as a scenario earthquake. This historical event corresponds to the 1884 Andalusia earthquake (M~6.8) located around 15 km far away from Velez Malaga. Thus, an intensity of VII-VIII on bedrock has been considered to estimate the EDS in terms of probability of damage.

The damage distribution for tested buildings is shown in Table 3. For damage estimation two typology vulnerability indices, V_I* and V_I^+, have been considered; V_I* is the most probable value of the Typology Vulnerability Index V_I, and V_I^+ is the maximum plausible value of the V_I (as it is said before, V_I^+ is usually obtained as 0.5-cut of the membership function). The total V_I has been calculated in both cases taken into account the modifiers.

The more serious damage appears in the old buildings located in the northern part of the city. The number of uninhabitable tested buildings is 589 (12%) and as far as 1.159 (23%) when V_I^+ it is used.

No landslides are predicted for the earthquake scenario considered and soil liquefaction has a low probability to occur at riverside zone outside of the city.

Table 3. Number of buildings affected for each EMS damage degree at Velez Malaga (only of tested buildings).

EMS Damage degree	EDS (I_r= VII-VIII)	
	Using V* + modifiers	Using V^+ + modifiers
0	231	1.129
1	2.377	1.391
2	1.188	231
3	1.145	2.094
4	16	112
5	-	-

3. CONCLUSIONS

The proposed modular methodology has been applied to estimate Earthquake Damage Scenarios (EDS) of two moderate-sized cities of the South of Spain with a moderate seismic hazard: Granada and Velez Malaga. From the point of view of methodology assessment, it is remarkable the opportunity to use heterogeneous data, derived from a variety of sources, and the possibility to apply different approaches to estimate earthquake ground motion, vulnerability and finally potential building damage and casualties. The application of this methodology gives reasonably scenarios with reliable results very useful to improve implementation policies for risk mitigation at the local level.

Several aspects seem worth emphasizing also in the way of concluding remarks. Firstly, when V_S^{30} data are used instead of shallow lithological data a more consistent soil classification is obtained and consequently more accurate soil amplification factor can be applied. Thus, a more reliable ground motion and intensity values distribution is obtained and a better final prediction of damage distribution is performed. For example, thin surface layers of dry loose soils (generally less than 5 m thick) overlying deposits (of sand, gravel or stiff clay) of high density (soils type III) or very high density (type II) are detected in Granada and Velez Malaga cities, in consequence the soil columns have V_S^{30} values corresponding to soil class III.

Secondly, the use of vulnerability index method achieves more accurate vulnerability assessment of the building. The total vulnerability indices of the buildings of the old quarters are high in both studied cities, generally with V_I values greater than 0.8. The highest mean damage are predicted in those quarters putting in evidence building vulnerability has a higher influence on damage distribution than ground amplification in these urban areas.

Thirdly, EDS obtained using only typological index V_I* or straightforward building vulnerability classification of EMS scale provide lower prediction of earthquake damage.

It is neccesary to enphasize that the final predictions of damage, fatalities, homeless etc. are crucially sensitive to use behaviour modifiers in vulnerability assessment. In the EDS1 estimation for Granada urban area the buildings suffering damage of grade 2 and 3 go from 31% and 0% (using V_I*) to 21% and 55 % (using total V_I), respectively.

The worst scenarios calculated for Granada and Velez Malaga (I_{rock} of VIII and VII-VIII, respectively) they forecast heavy and very heavy damage of 21% and 55 %, respectively for Granada city and 23% and 0.3%, respectively for Velez Malaga city.

The evaluation of physical damage to the built environment and the direct human consequences of the earthquakes considered constitute a reasonably forecasting of earthquake impact on these cities of moderate seismic hazard useful and necessary for seismic-risk reduction and risk management.

Acknowledgements:

The authors would like to show their sincere gratitude to all those who helped us during the surveys, specially to specially to Dr. J.A. Pérez for the development of the software used in this work, and the Civil Protection Staff from Granada's and Velez Malaga's cities and members of Andalusian Institute of Geophysics. This research was supported by the CICYT project *CGL2007-66745-C02-01/BTE.*

A particular gratitude goes to professors Kazuoh Seo (Tokyo Institute of Technology, TIT) and Takahisa Enomoto (Kanagawa University) for their continuous collaboration with in Andalusian risk analysis. The Center for Urban Earthquake Engineering (CUEE) is also acknowledged for support the expenses to assist to the 5th International Conference on Urban Earthquake Engineering.

References:

Andrus, R.D., and Stokoe, K.H., (1997), Liquefaction resistance based on shear-wave velocity. in Youd, T.L., and Idriss, I.M., eds., *Proceedings of the NCEER Workshop on Evaluation of Liquefaction Resistance of Soils*, National Center for Earthquake Engin. Research Technical Report NCEER-97-0022, 89-128.

ATC-13, (1985), Earthquake damage evaluation data for California, ATC-13, *Applied Technology Council*, Redwood City, CA.

Bernardini, A. (2000), The vulnerability of buildings - Evaluation on the national scale of the seismic vulnerability of ordinary buildings, CNR-GNDT, Rome.

Borcherdt, RD. (1994). Estimates of Site-Dependent Response Spectra for Design (Methodology and Justification). *Earthquake Spectra*, 10, pp 617-673.

CEN Comité Européen de Normalisation, (2003). *Eurocode 8: Design of structures for earthquake resistance,* Doc CEN/TC250/SC8/N335, January.

Coburn, A.; Spence, R. (2002). *Earthquake Protection.* Second edition. Ed.: Wiley.420 pp.

Cornell, C.A., 1968. Engineering seismic risk analysis, *Bulletin of the Seismological Society of America*, Vol 58, pp. 1583-1606.

Giovinazzi, S. y Lagomarsino, S. (2004), A macroseismic method for vulnerability assessment of buildings, *Proceedings of the 13th World Conference on Earthquake Engineering.* Vancouver, B.C., Canada, August 1-6, 2004, Paper ID 896.

Giovinazzi, S., (2005), *The vulnerability assessment and damage scenario in seismic risk analysis*, Ph. D. Thesis, Technical University of Braunschweig. Alemania, 300 pp.

Grünthal, G. (editor) (1998), *European Macroseismic Scale 1998.* Cahiers du Centre Européen de Géodynamique et de Séismologie, 7, Luxembourg, 99 pp.

Irizarry, J. (2004), *An Advanced Approach to Seismic Risk Assessment. Application to the Cultural Heritage and Urban System of Barcelona*, Ph. D. Thesis, Universitat Politècnica de Catalunya, 406 pp.

Irizarry, J., A. Macau, T. Goded, D. Clavero, A. Pazos , S. Figueras, R. Garcia, and ERSE Working Group (2006), Preliminary Seismic Risk Scenarios for Malaga, Spain, *8th U.S. National Conf. on Earthquake Engineering*, San Francisco, USA, 10 pp.

Irizarry, J., A. Macau,, Susagna T., García R., Figueras S., Goded T,Clavero, D. y Pazos, A. (2007). Escenarios de riesgo sísmico para la ciudad de Málaga. *3er Congreso Nacional de Ingenieria Sismica*, 8-11 Mayo 2007,Girona, 11 pp.

Lantada, N., Pujades L. G. Y. Barbat A.H (2007)."Métodos avanzados para la obtención de escenarios de riesgo sísmico. Aplicación a Barcelona (España)". *3er Congreso, Nacional de Ingeniería Sísmica*, Girona, Mayo de 2007.

Milutinovic Z. V. and G. S. Trendafiloski (2003). WP4: Vulnerability of current buildings. *Risk-UE project Handbook.* September 2003. Risk-UE project report. 111 pp.

Mouroux, P. and Lebrun, B. (2006), "RISK-UE project: an advanced approach to earthquake risk scenarios with application to different european towns", In: C. S.Oliveira, A. Roca and X. Goula, (Editors), *Assessing and Managing Earthquake Risk,* pp 479 - 508, Springer.

Navarro, M., Enomoto, T., Sánchez, F.J., Matsuda, I., Iwatate, T., Posadas, A., Vidal, F., Seo, K. (1998). Study of site effects in Almería City with comparison of geotechnical conditions and microtremor observation results. *Bulletin of Institute of Science and Technology of Japan.* Vol. 25, 59-67.

NCSE-02 (2002). "Normativa de Construcción Sismorresistente Española. Comisión Permanente de Normas Sismorresistentes", Real Decreto 997/2002. *Boletín Oficial Del Estado* No. 244, 11 October, 2002, Spain.

Okada, S.; Pomonis, A.; Coburn, A.W.; Spence, R.J.S.; Ohta, Y. (1991). *Factors Influencing Casualty in Buildings Damaged by Earthquakes.* Collaborative Report. Hokkaido University, University of Cambridge, University of Tokio, 16 pp.

Pérez-Ruiz, J. A., Posadas, A., Lantada N. Y L. G. Pujades (2007) "Un método avanzado de generación de escenarios de riesgo sísmico. Aplicación a la ciudad de Motril (España)". *3er Congreso Nacional de Ingeniería Sísmica*, Girona, 2007.

Seed, R. B., Cetin, K. O., Moss, R.E.S., Kammerer, A.M., Wu, J., Pestana, J.M., Riemer, M.F., Sancio, R.B., Bray, J.D., Kayen, R.E., Paris, A. (2003): Recent advances in soil liquefaction engineering: an unified and consistent framework. *Keynote presentation, 26th Annual ASCE Los Angeles Geotechnical Spring Seminar,* Long Beach.

Tiedemann, H. (1992). *Earthquakes and Volcanic Eruptions, a Handbook on Risk Assessment.* Swiss Re Publication, Zurich. 951 pp.

Vacareanu, R., Lungu, D., Aldea, A. y Arion, C. (2004). *WP07. Report Seismic Risk Scenarios Handbook.* Risk-UE Project, Bucarest. 50 pp.

Vidal, F. (1986) *Sismotectónica de la región Béticas-Mar de Alborán.* Tesis Doctoral, Universidad Granada, 457 pp.

Vidal, F., Feriche, M., Navarro, M., (1996). Estimación de daños sísmicos en áreas urbanas para la planificación de emergencias sísmicas, in *Homenaje al Prof. F. de Miguel*, p. 769-808.

Vidal F., M.D. Romacho; M. Feriche, M. Navarro, N. Abeki (1996). "Seismic microzonation in Adra and Berja Towns, Almería (Spain)". *Proc. of the 11th World Conference on Earthquake Engineering.* Acapulco, Mexico, June 23-28, 1996.

Vidal F., Navarro M., Cheddadi A., Mourabit T, Sánchez F., Enomoto E. And Seo K. (1997). Site response evaluation of surface soil using microtremor data in Berja town (Almería-Spain). *The XXII General Assembly of European Geophysical Society.* Vienna (Austria). 21-25 April 1997.

Vidal, F. Alguacil, G., Morales, J., Feriche, M., Mourabit, T., Cheddadi, A., Seo, K., Suzuki, K., Kobayashi, H., Samano, T., (1998): Study on Seismic Risk Assessment in Granada City, Spain. *II International Symposium on the effects of Surface Geology on Seismic Motion (ESG),* Vol.2, 1221-1228.

Fifth International Conference on Urban Earthquake Engineering
March 4-5, 2008, Tokyo Institute of Technology, Tokyo, Japan

TOWARDS INCOMBUSTIBLE CITIES: PROBABILITY FUNCTION OF REMAINDER FOR ESTIMATING THE LIFE SPAN OF BUILDINGS

Toshihiro Osaragi

Associate Professor, Department of Mechanical and Environmental Informatics, Tokyo Institute of Technology, Japan

osaragi@mei.titech.ac.jp

Abstract: Conversion of building structures or materials to an incombustible state is one of the most important issues in the field of disaster prevention planning. Changes in building structures or materials generally arise when older style buildings are demolished and replaced by contemporary buildings. The direction and the speed of the changes in building structures or materials are, therefore, deeply dependent on the possibility and probability that buildings will be demolished or will remain in the future. In this paper, we propose a statistical model that can describe the life span of buildings in order to evaluate the probability and the speed of conversion of buildings. We include an application of the model to actual data taken from densely built-up areas of Tokyo, and new results are presented.

1. INTRODUCTION

A large number of people have lost their lives in the fires that have followed earthquakes. Such fires are particularly destructive in densely built-up city-center areas, where building structures and materials are predominantly made of wood. The 1995 Hanshin-Awaji great earthquake that killed more than 6,300 people may be included in this category of disasters. Approximately 100 fires broke out in the initial stages of the earthquake, and then spreaded due to radiant heat and flame impingement. In total, 175 fires were observed within the 10 days following the earthquake, and an estimated one million square meters of land, including over 7,300 buildings, was burnt (Borden 1995, Takai et al 1998).

Conversion of building structures or materials to an incombustible state is one of the most important issues (Sekito et al., 1999; Yokota et al., 1999). Although research regarding the provision of fire-fighting services is of relevance to these disasters (Adrian et al.,1983, Richard et al., 1990; Wallace, 1993), we should discuss fire prevention rather than control in order to comprehensively address the problem of multiple uncontrolled fires following large earthquakes (Wallace et al., 1983; Wallace et al., 1984; Wallace, 1991). The process of conversion of cities to an incombustible state has not thus far been strongly promoted, because of the large amount of resources necessary for rebuilding. Conversion of buildings to an incombustible state is generally achieved when older style buildings are demolished and replaced with contemporary buildings. The speed at which building structures or materials may be changed is thus dependent also on the possibility and probability that buildings will be demolished.

Various studies about the life span of buildings have been carried out (Kaplan et al., 1992), since the life span of buildings is one of the basic concerns in various fields including urban economics and management, land use change, and disaster prevention planning. Reliability theory has been applied in many studies, and they, in turn, proposed methods for assessing the probability that buildings will be demolished or remain in the future (Komatsu, 1958, Osaragi et al., 2002). However, most of these studies have considered the case that the life span of buildings is a simple, single-variable function dependent only on the age of the building. Given this background, Osaragi (2004) proposed a statistical model that can evaluate characteristics of buildings and location, which in turn affect the life span of buildings. In particular, he examined characteristics of buildings (age of building, construction materials, building type, etc.) and characteristics of locations (land use zoning, building area to plot ratio, accessibility to railway stations, etc.), and evaluated how these factors affected the life span of buildings. Furthermore, Osaragi (2005) proposed a mathematical model, referred to as the "*interval probability function of remainder*", that can stably estimate the probability that buildings will be demolished or will remain within a time interval. That is, if information about the age of each building is acquired, the demolished/remaining probability can be estimated and applied in a variety of micro-simulation models.

However, in the general use of the model, the age of each building must be known in order to estimate the value of the probability. This requirement is an impediment to the application of the proposed model to actual urban data. In this article, in order to modify this disadvantage and extend applications of the model, an alternative method of the model is proposed using the concept of the "*average decrepitude of buildings*", which can be estimated from series of digital maps of cities over time. The average decrepitude of buildings can be considered as a quasi-average-age of buildings in an area, which can be calculated from the number of buildings that remain in a time interval. The utility and the efficiency of the alternative method are examined by consideration of numerical examples based on actual data taken from densely built-up areas of the Tokyo metropolitan area. Furthermore, simulations of the spatio-temporal distributions of buildings in Tokyo are demonstrated, and some new findings about the spatial distribution of old buildings, which will remain for a long time, are introduced.

2. MODELING OF THE PROBABILITY FUNCTION OF REMAINDER

The age of buildings is denoted by t ($t>=0$), and the category of buildings is denoted by j ($j=1,2,...,m$). The probability that a building of category j exists at age t is expressed by $P_j(t)$. This function is labeled the "*probability function of remainder*". It is assumed that derivative of $P_j(t)$ with respect to age t can be obtained. Moreover, "*the density function of life span*" is expressed by $f_j(t)$, and "*the demolition function*" which expresses the ratio of buildings being demolished is denoted by $h_j(t)$. The following relations exist between the above functions,

$$f_j(t) = \frac{-dP_j(t)}{dt}, \tag{1}$$

$$h_j(t) = \frac{f_j(t)}{P_j(t)}. \tag{2}$$

On the substitution of the expression for $f_j(t)$ derived from Eq. (2) for $f_j(t)$ in Eq. (1), we obtain,

$$P_j(t) = \exp\left[-\int_0^t h_j(x)dx\right]. \tag{3}$$

Although it is important to investigate the characteristics of demolition function $h_j(t)$, for the present purposes it is assumed that $h_j(t)$ can be expressed by the following equation using Taylor's expansion,

$$h_j(t) = \sum_{k=0}^{K-1} \frac{h_j^{(k)}(a)}{k!}(t-a)^k, \tag{4}$$

where $h^{(k)}_j(a)$ is the derivative of $h_j(t)$ with respect to time at the age $t=a$, and K is a constant sufficiently large to ensure a satisfactory approximation. Expressing the demolition function $h_j(t)$ as a polynomial of age t in this way, Eq. (3) can be rewritten as follows:

$$P_j(t) = \exp\left[-\sum_{k=1}^{K} a_{jk}t^k\right], \tag{5}$$

where a_{jk} is a constant coefficient corresponding to the coefficients of the powers of t in Eq. (4). Specifically, the demolition function, $h_j(t)$, can be expressed using the coefficients a_{jk} as follows:

$$h_j(t) = \sum_{k=1}^{K} k a_{jk} t^{k-1}. \tag{6}$$

The probability that a building, which has survived to age t, continues to survive to age $t+\Delta t$ ($\Delta t>0$) is expressed by $P_j(t+\Delta t|t)$. This function is hereafter called "*the interval probability function of remainder*". Since $P_j(t+\Delta t|t)$ is a conditional probability, it has the following relationship with the probability function of remainder, $P_j(t)$,

$$P_j(t+\Delta t \mid t) = \exp\left[-\sum_{k=1}^{K} a_{jk}\{(t+\Delta t)^k - t^k\}\right]. \tag{7}$$

Thus, the values of $P_j(t)$ and $P_j(t+\Delta t|t)$ can be obtained and applied to a variety of simulation models, if the coefficients a_{jk} are estimated.

Although age, t, is a continuous variable, in the following discussion we will model it as a discrete variable in order to correspond with the actual data that has been collected. That is, without loss of generality, t will be expressed as $t=0,1,2,...,n$. The number of buildings of age t is expressed as $N_j(t)$, and the number of buildings demolished at age $t+1$ is expressed as $d_j(t)$. The simultaneous probability, denoted by P, that the data are observed under the above probability distributions can be described as follows:

$$P = \prod_{j=1}^{m}\prod_{t=0}^{n-1} \frac{N_j(t)!}{d_j(t)!\{N_j(t)-d_j(t)\}!} \cdot \{1-P_j(t+1|t)\}^{d_j(t)} P_j(t+1|t)^{N_j(t)-d_j(t)}, \tag{8}$$

where n denotes the age of the oldest buildings. On the substitution of Eq. (7) for $P_j(t+1|t)$ in Eq. (8), the simultaneous probability P can be obtained as a likelihood function dependent only on the unknown coefficients a_{jk}. Maximum likelihood estimators of a_{jk} can be obtained by maximizing the value of P under the data obtained.

The values of $P_j(t)$ and $P_j(t+1|t)$ lie in the closed interval [0,1], while the value of $h_j(t)$ is nonnegative. Hence, the coefficients a_{jk} must satisfy the following three conditions:

$$\sum_{k=1}^{K} a_{jk}t^k \geq 0 \quad \textit{for all } j, t \tag{9}$$

$$\sum_{k=1}^{K} a_{jk}\{(t+1)^k - t^k\} \geq 0 \quad \textit{for all } j, t \tag{10}$$

$$\sum_{k=1}^{K} k a_{jk} t^{k-1} \geq 0 \quad \textit{for all } j, t \tag{11}$$

However, Eq. (3) shows that the values of $P_j(t)$ and $P_j(t+1|t)$ always lie in the closed interval [0,1], if the value of $h_j(t)$ is nonnegative. Hence, we have only to consider the condition described by Eq. (11). Thus, the undetermined multipliers method of Lagrange will be applied, since the coefficients a_{jk} are subject to the constraints Eq. (11). It is also possible to show that Lagrange function is a convex function of the coefficients a_{jk}. Thus a local minimum solution, which is a typical problem in optimization by the Hill-climbing method, does not exist in the present problem.

3. METHODS FOR ESTIMATING THE NUMBER OF BUILDINGS THAT WILL REMAIN

We describe four methods, shown in Figure 1, for predicting the number of buildings that will remain through a time interval. First, if information about ages of buildings is acquired, the following two methods are available, which use the probability function of remainder directly.

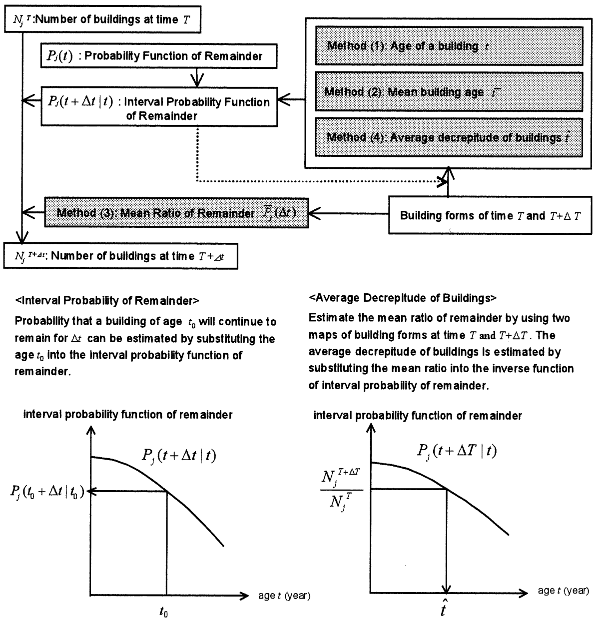

Figure 1 Methods for Estimating the Number of Buildings that will Remain

Method (1): Substituting the age of each building for the variable t in $P_j(t+\Delta t|t)$, the value of the interval probability of remainder is then predicted for each building. This method thus requires detailed information about building ages to be effective in predicting the demolished/remaining status of each building, one by one.

Method (2): Substituting the mean value of buildings age in a study area for the variable t in $P_j(t+\Delta t|t)$, the average value of the interval probability function of remainder is then derived. This method can be used in situations where not all of the ages of the buildings are known, but the mean value of the ages of buildings in the study area is known. It differs from method (1) in that the value of the interval probability function of remainder is therefore assumed to be the same constant value for all buildings of the same type in the area. Accuracy is thus expected to diminish when the actual age of a building differs significantly from the mean value of building age in the study area.

If no information about ages of buildings is available, the following two methods can be applied by using digital maps of building forms at the two points of time.

Method (3): By comparing building forms at time T and time $T+\Delta T$ on geographic information systems (GIS), we can extract data for the number of buildings in existence at time T, N_j^T, and at time $T+\Delta T$, $N_j^{T+\Delta T}$, (the details of the extraction method will be described later). From these two values, the value of the mean ratio of remainder $\bar{P}_j(\Delta T)$ of term ΔT can be derived. Furthermore, the value of the mean ratio of remainder $\bar{P}_j(\Delta t)$ of term Δt can also be estimated by calculating the $\Delta t/\Delta T$ power of the value $\bar{P}_j(\Delta T)$. However, since the value of the mean ratio of remainder is assumed constant across any given interval, this method is not therefore considered to be suitable for long-term predictions.

Method (4): Substituting the value of $\bar{P}_j(\Delta T)$ for the inverse function of $P_j(t+\Delta T|t)$, the average decrepitude of building $\hat{t}$ at time T can be estimated. The average decrepitude of buildings $\hat{t}$ is considered as a quasi mean-age of buildings in the area. Note that the value may be larger or smaller than the actual mean age of the building. Substituting this value $\hat{t}$ for the variable t of $P_j(t+\Delta t|t)$, the value of the interval probability function of remainder in term Δt will be obtained.

4. VALIDATION OF METHODS

4.1 Estimation Accuracy

Using the data for M-city in Tokyo, the number of buildings that remain in given specific time intervals is estimated using the four methods, and their accuracy is examined. The interval probability function of remainder according to building type is constructed using data from 1994 and 1996. Then, the number of buildings existing in 1994 that are expected to remain four years later (in 1998), is estimated by the four methods. Estimated values according to the building type for each town (the number of towns is 11) are compared with the actual observed values. Here, the accuracy of the estimates is evaluated by the following absolute error rates,

$$e_i = \frac{1}{M}\sum_{j=1}^{M}\left|\frac{N_{ij}-\hat{N}_{ij}}{N_{ij}}\right| \times 100\,[\%], \tag{12}$$

where a suffix j ($j = 1, 2, \ldots, M$) denotes a building type and a suffix i denotes a town ID number. The value N_{ij} is the actual observed value, while $\hat{N}_{ij}$ is the corresponding estimated value.

The absolute error rate of the number of remaining buildings estimated by each method is shown in Figure 2. For "commercial buildings", the estimation accuracy of method (1) is superior to that of the other methods. Before performing this analysis, we expected that method (1), using the age of each building, would offer the highest stability and accuracy for all building types. However, the results show that these expectations are not fulfilled. With this method, the same interval probability function of remainder is assumed across the whole area for buildings of the same type. In a small area like a town, however, the influence of the regional gap of demolition characteristics should not be ignored. Therefore, the estimation accuracy is not as high as was expected, even if detailed information of buildings' ages is used in the estimation. That is, we can conclude that the study area should be divided into sub areas in order to estimate the interval probability function of remainder more accurately if the demolition characteristics of building type are strongly dependent on local characteristics.

According to the results of "detached houses", "flats", and "others", the estimation accuracy of method (4) is higher than methods (1) and (2). As described in the above paragraph, the average decrepitude of buildings in each area used in method (4) reflects the demolition characteristics in the object area. Therefore, even if an area includes many comparatively new buildings, in practice, if the rate of demolition is high in the area, the degree of demolition might also be relatively high. Consequently, even if the same interval probability function of remainder is used, the estimate of method (4) may be of higher accuracy than methods (1) or (2), which do not incorporate the local characteristics of locations.

Next, the correspondence between the estimated values of the number of demolition buildings and the actual observed values are examined. The results are shown in Figure 3. Each point in Figure 3 corresponds to one town. Although some towns show large estimation errors, overall the estimated values and the actual observed values correspond well.

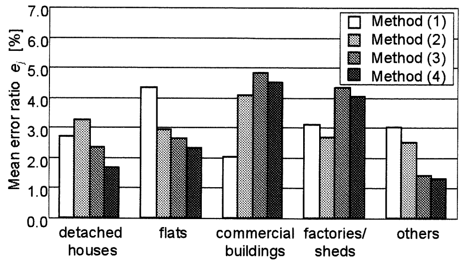

Figure 2 Accuracy of Estimates for the Number of Buildings that will Remain Obtained by the Four Methods

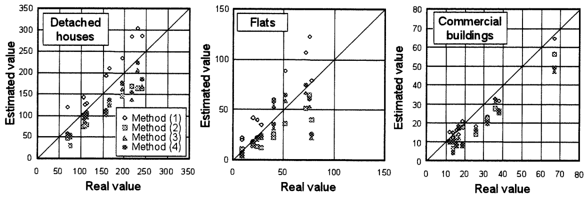

Figure 3 Accuracy of Estimates of the Number of Buildings Demolished Obtained by the Four Methods (Each Point Corresponds to A Single Towns in M-City)

4.2 Estimation Accuracy when Applying Model to Other Areas

In this section the interval probability function of remainder estimated from the data of M-city is applied to other areas, and the resultant estimation accuracy is examined. That is, the model estimated by using the data of a specific area is examined by checking whether or not it is also effective for other areas. Specifically, we apply the methods to data taken from the principal 48 cities of Japan, where the original data is derived from the fixed asset ledger of 1987.

The number of buildings of age t and type j is denoted by $N_j(t)$. Of these buildings, the number of buildings demolished in one year is denoted by $d_j(t)$. The values of $N_j(t)$ and $d_j(t)$ observed in 1987 are used for validation. That is, the values of $d_j(t)$ ($t \leq 35$) are estimated using the interval probability function of remainder for M-city, and are then compared with the observed values. The relationships between the actual values and the estimated values of $d_j(t)$ for each building age, t, are shown in Figure 4. Clearly the estimated values are in good agreement with the observed values for every building type. We can conclude, therefore, that the interval probability function of remainder estimated from the data of M-city can accurately express the demolition characteristics of buildings in all the principal cities in Japan.

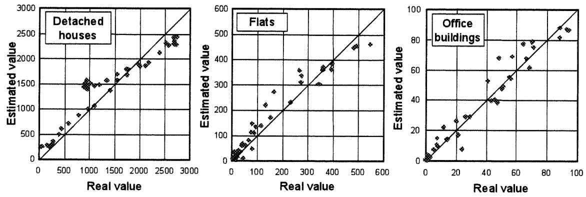

Figure 4 Accuracy of Estimates of the Number of Buildings Demolished Obtained by Method (1) (Each Point Corresponds to a Set of Buildings of the Same Age)

4.3 Estimation Accuracy when Using Average Decrepitude of Buildings

We consider here the flexibility of application of the method of the interval probability function of remainder. The number of remaining buildings in Tokyo's Setagaya ward is estimated by method (4) using the interval probability function of remainder of M-city. A corresponding estimate is also derived from method (3), and then the estimation accuracies of these two methods are compared. That is, the estimation accuracy is examined for the case when the ages of the buildings are unknown. By overlaying the building forms of 1991 and 1996 using the data of the Tokyo city planning geographic information system (hereafter called the Tokyo GIS data), information of whether buildings are demolished or remain is obtained. By using the conditions shown in Figure 5, we can correctly distinguish whether buildings are demolished or remain to an accuracy of 81.6%.

With the above preparation, the number of buildings of remaining for 10 years is estimated, considering 1991 as the initial year. Specifically, since the mean ratio of remainder for ten years is required to apply method (3), the squared value of the mean ratio of remainder for five years is estimated. In the process of applying method (4), first, the average decrepitude of buildings $\hat{t}$ in 1991 for each town is estimated by using the interval probability function of remainder. By substituting this value $\hat{t}$ for the interval probability function of remainder $P_j(t+10|t)$, the probability that each building will continue to remain after ten years is estimated. The rate of the mean absolute error is calculated by Eq. (3), and the results are shown in Figure 6 (the number of towns in Setagaya ward is 62). It is learned that the rate of the mean error of method (4) is smaller than that of method (3), i.e. method (4) is superior to method (3). For detached houses, flats, and commercial buildings, the rate of the mean error is around 5 percent or less. Since the study area is different from the area from which the parameters are estimated, the results are inferior to those shown in Figure 2. However, the results shown in Figure 6 are sufficiently accurate for practical purposes. In the above validation, the number of remaining buildings after a ten-year interval is estimated. For longer estimations, estimation accuracy will diminish, since method (3) assumes constancy of the mean ratio of remainder. On the other hand, since method (4) uses the average decrepitude of buildings, it is possible to describe the probability of remaining precisely, using an expression that varies with time. Therefore, method (4) shows a higher degree of accuracy than method (3).

Next, in order to examine the estimation accuracy of the number of demolition buildings, the actual and estimated values for each town are compared. The results are shown in Figure 7. For the case of detached houses, since the actual values of the demolition rate in 1991 - 1996 are lower than those of 1997-2001, the estimated values are a little smaller in many towns. We can say, however, that overall there is good agreement between the estimated and actual values.

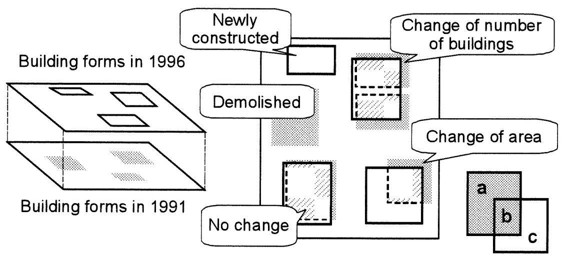

		Estimated value		
		demolition	remaining	total
Real value	demolition	10,157	5,546	15,703
	remaining	5,206	37,366	42,572
	total	15,363	42,912	58,275

<condition>

$$\frac{a+c}{a+b+c} > 20\%$$

$$a+c \geq 20\,[m^2]$$

Figure 5 Discrimination of Demolished/Remaining by Using Digital Maps of Cities

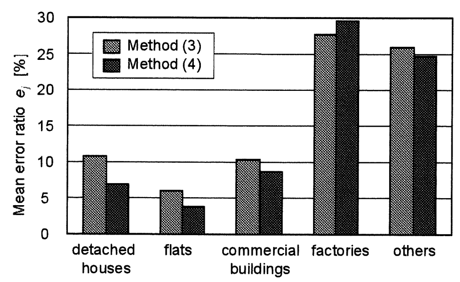

Figure 6 Accuracy of Estimates of the Number of Buildings that will Remain Obtained by Methods (3) and (4) (Shibuya city)

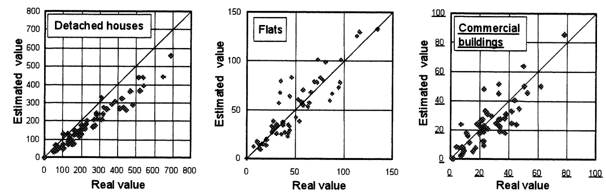

Figure 7 Accuracy of Estimates of the Number of Buildings Demolished Obtained by Method (4) (Each Point Corresponds to a Town in Shibuya Ward)

5. SPATIAL DISTRIBUTION OF AVERAGE DECREPITUDE OF BUILDINGS

The number of demolished/remaining buildings is calculated by the method shown in Figure 5 using the Tokyo GIS data (1991 and 1996), and the average decrepitude of buildings for each town in 23 wards of Tokyo is estimated. The results of three building types are shown in Figure 8. For flats, the degree of decrepitude is high in almost all the towns in wards such as the Katsushika ward and the Nerima ward. The degree of decrepitude is high in the Omori station and the Kamata station circumference, exhibiting values of 45 years or more. There are also many commercial buildings demolished before their structural life span is complete. A very high degree of decrepitude is estimated in areas where buildings are intensively demolished. That is, the decrepitude estimated age is likely to be larger than the actual age in such areas. Moreover, in many areas, the degree of decrepitude of detached houses is higher than that of flats. This tendency is remarkable especially in the Chiyoda ward, Suginami ward, and Setagaya ward.

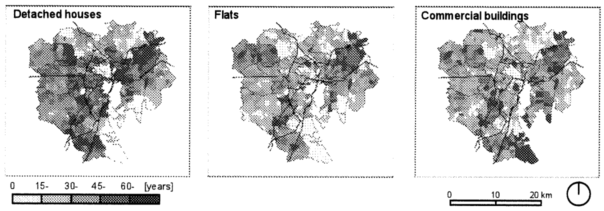

Figure 8 Spatial Distribution of the Average Decrepitude of Buildings

6. SPATIO-TEMPORAL DISTRIBUTION OF NUMBER OF REMAINING BUILDINGS

Based on method (4), an estimation of the number of remaining buildings in the future is performed using the average decrepitude of buildings of each town. That is, the number of buildings predicted to continue to remain in 2001, 2006, 2011, and 2016 is estimated for each town, considering 1991 as the initial year. Figure 9 and Figure 10 demonstrate the results for detached houses and commercial buildings, respectively. Many detached houses will remain in a northern part and eastern part of Tokyo. Many commercial buildings will remain around the northeastern section of the Yamanote Line, and an eastern part of Tokyo.

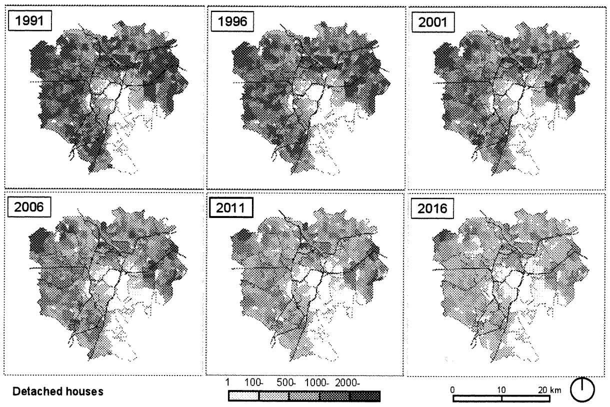

Figure 9 Spatio-temporal Distribution of Remaining Buildings (Detached Houses)

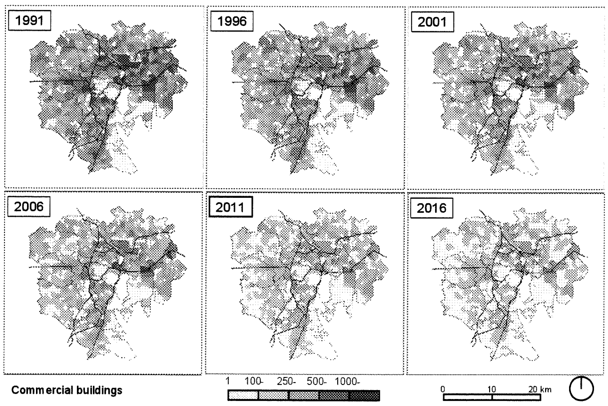

Figure 10 Spatio-temporal Distribution of Remaining Buildings (Commercial Buildings)

7. SUMMARY AND CONCLUSIONS

In this research, a method for extending the application of the interval probability function of remainder is proposed, in order to facilitate the incorporation of this function into micro-simulation models, such as disaster prevention planning for established city areas. In particular, it is shown that the average decrepitude of buildings can be calculated if the data of building forms at two points of time can be obtained, even if information about the age of buildings is not available. Moreover it is shown that the number of remaining buildings can be estimated to a high degree of accuracy (the rate of error is about 1 - 4%) in a comparatively small spatial unit like a town. Furthermore, by using the interval probability function of remainder and the average decrepitude of buildings, estimations of the number of demolished/remaining buildings in the future can be achieved with a high degree of accuracy.

Acknowledgements:

The author would like to give his special thanks to Ms. Shiori Kamata for computer-based numerical calculations.

References:

Adrian, C. (1983), "Analysing service equity: fire services in Sydney," *Environment and Planning A*, **15**, 1083-1100.

Borden, F. W. (1995), The Kobe earthquake: Lessons for the United States. *Fire Engineering*, 148-5, 43-48.

Kaplan, E.L. and Meier, P. (1958) "Nonparametric Estimation from Incomplete Observations," *Journal of American Statistic Association*, **53**, 457-481.

Komatsu, Y. (1992), "Some theoretical studies on making a life table of buildings," *Journal of Architectural Planning and Environmental Engineering*, **439**, 91-99 (in Japanese).

Osaragi, T. and Shimizu, T. (2002), "Related factors to demolishing of buildings and estimation of subsistence probability," *Journal of Architectural Planning and Environmental Engineering*, **560**, 201-206 (in Japanese).

Osaragi, T. (2004), "Factors leading to buildings being demolished and probability of remainder," *Proceedings of The Sustainable City III*, 325-334, WIT Press, June 2004.

Osaragi, T. (2005), "The life span of buildings and the conversion of cities to an incombustible state," *Proceedings of Safety and Security Engineering IV*, WIT Press, 495-504, June 2005

Richard, D., Beguin, H. and Peeters, D. (1990), "The location of fire stations in a rural environment: a case study," *Environment and Planning A*, **22**, 39-52.

Sekito, M., Koshiyama, K., Hokugo, A. and Murosaki, Y. (1999), "Analysis on shape of flame and effect of fire-spreading interception in urban conflagration of Hanshin-Awaji great earthquake," *Papers on City Planning*, **34**, 673-678 (in Japanese).

Takai, H., Yano, K., Matsui, T., Bouike, M. and Uemura, Y. (1998), Study on fires outbreaks and spread caused by the great Hansin and Awaji earthquake in Kobe city. *Journal of Architectural Planning and Environmental Engineering*, **508**, 137-144 (in Japanese).

Wallace, R. and Wallace, D. (1983), "Urban fire as an unstabilized parasite: the 1976-1978 outbreak in Bushwick, Brooklyn," *Environment and Planning A*, **15**, 207-226.

Wallace, D. and Wallace, R. (1984), "Structural fire as an urban parasite: population density dependence of structural fire in New York City, and its implications," *Environment and Planning A*, **16**, 249-260.

Wallace, R. (1991), "A stochastic model of the propagation of local fire fronts in New York City: implications for public policy," *Environment and Planning A*, **23**, 651-662.

Wallace, R. (1993), "Recurrent collapse of the fire service in New York City: the failure of paramilitary systems as a phase change," *Environment and Planning A*, **25**, 233-244.

Yokota, H., Koshiyama, K., Hokugo, A. and Murosaki, Y. (1999), "Analysis on fire-spreading to fire-resistant building in the city fire after the Hanshin-Awaji earthquake," *Papers on City Planning*, **34**, 679-684 (in Japanese).

Fifth International Conference on Urban Earthquake Engineering
March 4-5, 2008, Tokyo Institute of Technology, Tokyo, Japan

EARTHQUAKE RISK ASSESSMENT AND OPTIMAL RISK MANAGEMENT STRATEGIES FOR HI-TECH FABS IN TAIWAN

Wen-Ko Hsu[1], Wei-Ling Chiang[2], Dung-Mou Hung[3] , Y-Y Chiu[4]

1) Research Fellow, Research Center for Hazard Mitigation and Prevention, National Central University, Chungli, Taiwan,
2)Professor, Department of Civil Engineering, National Central University, Chungli, Taiwan,.
3)PhD Candidate, Department of Civil Engineering, National Central University, Chungli, Taiwan,
4)Principal Engineer, Risk Management & Corporate ESH Division, TSMC, Taiwan

Abstract: Taiwan lies at earthquake-prone area. More than 200 sensible earthquakes occurred every year. Average annual loss due to 83 disastrous earthquakes since 1900 is about NT$19 billion dollars which equals to 0.7% GDP. Taiwan is home to over 30 plants that make semiconductor wafers and Taiwan's factories account for more than half of the world's semiconductor contract manufacturing and more than ten percent of the world's silicon area processing capacity. The Richter magnitude 7.3 Chi-Chi Earthquake struck Taiwan on September 21, 1999. The overall impact to semiconductor companies in Taiwan was estimated approach US$1 Billion. The property damage (e.g., facilities and equipment) only was about 5% of the total; the rest was due to business interruption. In addition to business interruption, there are possible impacts due to loss of market share. According to the impact of the Chi-Chi earthquake, the most of Taiwan's Hi-Tech companies have more seriously concerned about and worked to mitigate earthquake risk. In this paper, we have built up an event-based seismic hazard assessment and financial analysis model for Hi-Tech Fabs in Taiwan. As we know, low occurrence rate, tremendous loss and high uncertainty are characteristics of earthquake disasters. For the above issues, the model we built integrates knowledge from many fields including earth science, seismology, geology, risk management, structural engineering, the insurance profession, financial engineering and facility management. Based on the portfolio data from the site survey, the model can be used to calculate the event losses (include building, content, and business interruption losses), furthermore the average annual loss and loss exceeding probabilities also can be calculated. The total earthquake risk cost, which includes earthquake insurance premium, average annual retained loss, and equivalent annual retrofit cost, was defined to be an indicator for selection of optimal risk management strategies.

1. INTRODUCTION

Taiwan is home to over 30 plants that make semiconductor wafers and Taiwan's factories account for more than half of the world's semiconductor contract manufacturing and more than ten percent of the world's silicon area processing capacity. In addition Taiwan produces 80% of the motherboards used in PC manufacturing, and most of the computer keyboards and mice, and a large portion of the video display terminals. At the moment, most of Taiwan's electronics production capacity was concentrated at Hsinchu Science-Based Industrial Park, located on the west coast of the

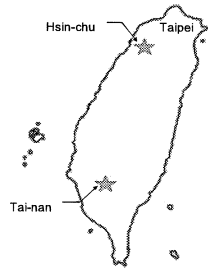

Figure 1. The Locations of Hsin-Chu and Tai-Nan Science-Based Industrial Park in Taiwan

island, and a second industry park has also been constructed on Taiwan since Chi-Chi earthquake, Tai-nan, located in the southwest of the island. Tai-Nan Science-Based Industrial Park provides a valuable source of backup production; many Hi-Tech companies have opened second facilities in the new park to spread their exposure. Figure 1 shows the locations of these two science-based industrial parks.

Taiwan is at Pacific Ocean earthquake zone and the boundary between Eurasia Plate and Philippine plate. There are more than 200 sensible earthquakes every year in Taiwan. Average annual loss due to 83 disastrous earthquakes since 1900 is about NT$19 billion dollars which equals to 0.7% GDP. The Richter magnitude 7.3 Chi-Chi Earthquake struck Taiwan on September 21, 1999. The total financial and property losses from the Chi-Chi earthquake are estimated to be about US$10 billion. Direct property losses are estimated to be US$8 billion of total losses, while indirect business interruption losses are estimated to be US$2 billion. Insured losses are estimated to only be about US$700 million, and most of this payment will go to manufacturing industries for business interruption losses associated with the extensive power disruption. Only 7% of total losses are covered by commercial insurance. The claims are expected to mostly pass through to global reinsurance companies, with local insurance companies only retaining about 10% to 25% of the insured losses.

Short-term loss for the semiconductor industry (damage to equipment and to wafers-in-progress) was only USD 7.7 million, but that represent less than 1.5 percent of the total loss. The real damage came from the indirect losses attributable to loss of power and business interruption; totaling over USD 525 million, this was the largest loss ever experienced by the industry (Erik Ruttener et al., 2003). In addition to business interruption, there are possible impacts due to loss of market share.

In this paper, we have established an event-based seismic hazard assessment and financial analysis model for Hi-Tech Fabs in Taiwan. As we know, low occurrence rate, tremendous impact and high uncertainty are characteristics of earthquake disasters. For the above issues, the model we built integrates knowledge from many fields including earth science, seismology, geology, risk management, structural engineering, the insurance profession, financial engineering and facility management. Based on the portfolio data from the site survey, the model can be used to calculate the event losses (include building, content, and business interruption losses), furthermore the average annual loss and loss exceeding probabilities also can be calculated. The total earthquake risk cost, which includes earthquake insurance premium, average annual retained loss, and equivalent annual retrofit cost, was defined to be an indicator for selection of optimal risk management strategies.

2. EARTHQUAKE RISK MANAGEMENT

According to the impact of the Chi-Chi earthquake, reinsurers are no longer offering cat protection on a proportional basis, and have taken natural perils out of the property treaties. Insurers are taking a bigger piece of the risk, and underwriting has improved considerably. Similarly, as deductible move up, insureds are taking a more active hand in corporate risk management, which has accelerated some of the mitigation measures. Most of Taiwan's Hi-Tech companies have more seriously concerned about and worked to manage earthquake risk.

The risk managers of HI-Tech companies should find out the optimal strategies between risk control and insurance within limited budget. The optimal strategies aim at the best applicability and balance between risk control and insurance capability. A proper setup of risk management program not only can eliminate or reduce the severity of unfavorable consequences but also reduce the amount of financing that will be required following and event (PIANC. 2001). The cost of such program can be easily justified by the avoidance of losses and many times can be partially undertaken by the parties responsible for loss financing, i.e., insurance companies. The mechanisms available for loss control include avoidance, prevention, reduction and separation. Risk avoidance means that managers would stop the operations whose exposure to risk is substantial and of high frequency. Also, it could mean that it would avoid taking responsibility for the consequences towards third parties. This technique is very useful for minimizing the liability exposure of the building authority. Risk reduction is a technique that pertains to engineering the various processes so that there are redundancies in the system and further loss is avoided. Loss reduction usually refers to reducing the losses after the event has occurred. For enterprise managers, there are several kinds of actions for earthquake risk controlling as followed. Seismic upgrading or retrofitting of existing enterprise facilities and structures to higher standards can reduce the risk exposure. Or having a backup power system in standby mode would prevent equipment loss. Other prevention measures would be plans to avoid fire after an earthquake. Loss reduction technique would be emergency reaction plans or to change the operation mode of the enterprise so that it can continue its operations with reduced capacity. Emergency plans are a series of standard of procedure to monitor disasters, but requires comprehensive planning and continuous modification and practice. Emergency response procedures include the initial response within the first hours after the earthquake, emergency management steps and recovery plans (Werner et al., 1997).

Purchasing earthquake insurance to transfer risk, or adopting retrofit measures to upgrade earthquake resistance capacity of facilities (building or equipment/content) to mitigate earthquake losses, both are risk treatment methods that often be used to reduce earthquake risk. An optimal strategy of earthquake risk management can be approached by adopting the proper combination of different feasible risk treatment methods with the lowest total risk cost. This paper presents an indicator of total annual earthquake risk cost for selection of optimal strategy of earthquake risk management. As shown in the Eq. (1) below:

$$r_{total} = r_{premium} + r_{retrofit} + r_{retained} \tag{1}$$

r_{total}: total annual earthquake risk cost; $r_{premium}$: the premium of given earthquake insurance coverage, it can be acquired from the insurer or insurance broker according to different suggested policy conditions; $r_{retrofit}$: the equivalent annual retrofit cost, it equals to the total cost of the retrofitting program divides by the remaining time of amortization of the HI-Tech Fabs; $r_{retained}$: the average annual retained loss, it means the earthquake loss that will be undertaken by HI-Tech companies itself, and it will be calculated by the model considering the given insurance policy conditions.

In addition, the calculation of losses exceeding probabilities will be helpful to understanding the PML (Probable Maximum Loss) and to design the appropriate risk protection level. The efficiency of different risk management strategies can be clearly realized through the comparison of curves of losses exceeding probabilities. The calculation of average annual loss will be helpful to understand the reasonable insurance premium and can be a bargaining base with insurance companies.

3. EARTHQUAKE VULNERABILITY OF HI-TECH FABS IN TAIWAN

3.1 Vulnerability of Facilities

A semiconductor plant, whose product is worth billions of USD annually, relies on a highly specialized manufacturing process which must be meticulously maintained in an environment 1,000 times cleaner than a hospital surgical suite. The total building costs for one 200-mm fab (a facility that

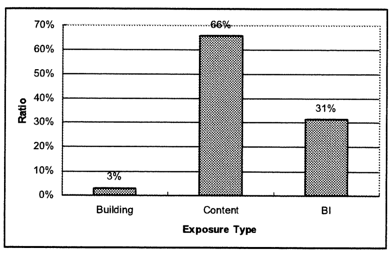

Figure 2 Percentage of Exposure Value by Exposure Type of HI-Tech Fabs (Semiconductor Fabs)

produce 200-mm (8-inch) wafers) lie between USD$ 1.2 and 1.5 billion. New 300-mm fabs cost more than twice as much, reaching USD$ 3 billion. Like any other factory, a typical fab building includes support facilities-offices, storage rooms, and testing and packaging areas. The extra is the clean room that the heart of every fab plant. (Pui Fong et al., 2001). As shown in the Figure 2, the total cost of buildings of a semiconductor company is only 4%-5% of total cost of content.

The double fab structures are uniquely seen in Taiwan's semiconductor industry restricted by shortage of land resource and in response to a rapid growth of demands or strategic business planning of the enterprise. Common structural layout for standard fabs is like that the first two stories of the fab are generally reinforced concrete structures with heavy shear walls and closely spaced columns. Moreover, the deep and stiff waffle slab with holes on the surface panels is built for ventilation purpose and high rigidity demands. Framing above the waffle slab are long span steel mega trusses supported by braced steel frames at the periphery of the plant to reserve a considerably column-free space for manufacturing process. Unlike the standard fab whose clean room supports only a relatively light roof level, double fab structures contain two clean rooms where most of the columns have been removed to comply with the manufacturing process, which must carry considerable gravity load and seismic lateral load transmitted from the stories above. As the plan area of today's hi-tech fab has been increasingly wider, it is insufficient to brace only the peripheral frames to maintain rigidity and strength, and soft stories are inevitably formed at the clean room levels. As a result, the double fab structures become seismically vulnerable once encountered with severe earthquakes. Excessive story drifts are to be focused on the clean room levels during the earthquakes. As a consequence, the floor accelerations are amplified and the secondary (P-) effects further deteriorate the earthquake-resisting capability of the fab and exaggerate the seismic risk. Even if the earthquake is moderate enough to be structurally harmless, the floor acceleration could be amplified and damage the delicate manufacturing tools due to a soft-story configuration. (Wang et al., 2003)

Non-linear Push-Over analysis was performed to establish the fragility curves for the fabs. As shown in the figure 3, the curves present the damage probability of the sample fab at given seismic intensity.

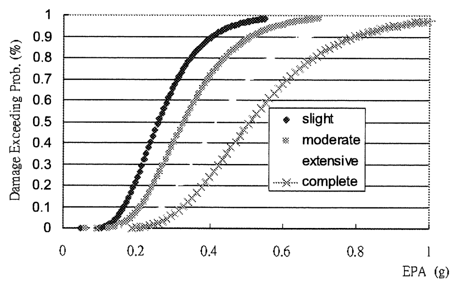

Figure 3 Examples of Fragility Curves of HI-Tech Fabs

In HI-Tech fabs, there are a number of expensive process equipments that are susceptible to damage. Before Chi-Chi earthquake, most of the installations of seismic anchorage of the equipments are improper or even lack. The results of the Chi-Chi earthquake confirmed that long quartz tubing used in reaction chambers are susceptible to damage. The types of process equipment that suffered the most quartz damage were vertical diffusion furnaces (VDFs). In some facilities, more than 90% of VDF quartz chamber were damaged. While there were a large number of quartzware vendors, the need to replace hundreds of these at one time likely placed a burden on the supply. Even without business interruption due to power failure, it could be assumed that the operation of many production lines would have been impacted by this situation. (Brian Sherin, 1999)

In our study, the equipments of HI-Tech fabs were classified according to sensitivity of vibration damage (sensitive and insensitive) and anchorage situations (poor, normal, and good). There are totaling six classes of fragility of equipments defined. curves of fragility of each equipment class, that represent the probabilities of damage of equipment at a given floor acceleration, were established.

3.2 Business Interruption

According to the statistics of Industrial Development Bureau of Ministry of Economic Affairs, the output value of semiconductor industry is USD$470 billion in 2007, and was estimated USD$530 billion will be achieved in 2008. Along with rapid growth of output value of semiconductor industry, the impact of business interruption also will become huge. Business interruption is commonly known difficult to model. Interruption of utility and supply chain, and damage of facilities or process equipment may cause business interruption. In this paper, we present a simplified business interruption model only considered the effect of damage of building and equipment, as shown in the Figure 4. Probabilities of damage of equipments will be estimated according to the calculated floor acceleration, and then expected restoration time of process equipment ($\overline{T}_M$) and support equipment ($\overline{T}_S$) will be calculated. Eq(2) to Eq(6) show the formula of the restoration time needed to completely recover the function of the fab considering the damage state of building and equipments. Finally, $\overline{T}$ the expected restoration time of fab can be calculated by Eq(7). P_i are probabilities of different damage states of building.

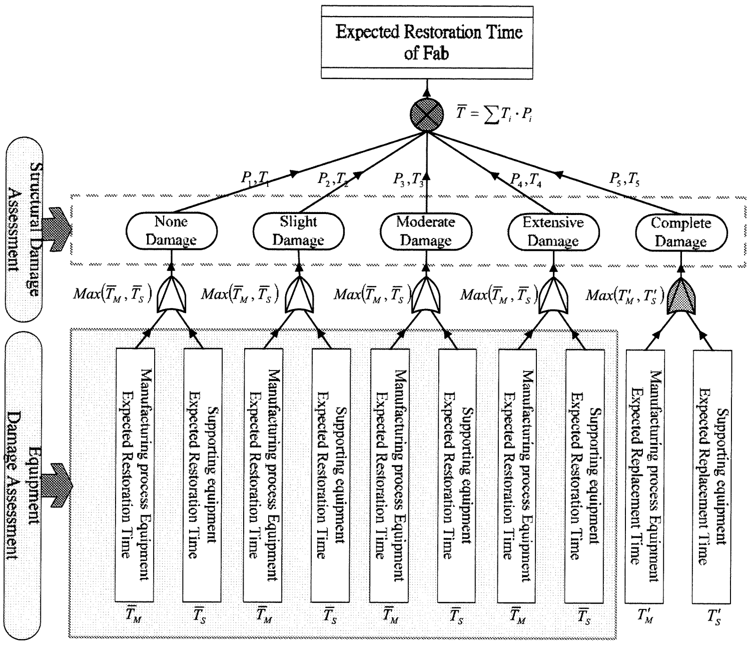

Figure 4 Simplified Business Interruption Model of Hi-Tech Fab

$$T_1 = Max(\overline{T}_M, \overline{T}_S) \quad (2)$$

$$T_2 = Max(Max(\overline{T}_M, \overline{T}_S), T'_{Bldg,Slight}) \quad (3)$$

$$T_3 = Max(Max(\overline{T}_M, \overline{T}_S), T'_{Bldg,Morderate}) \quad (4)$$

$$T_4 = Max(T'_{Bldg,Extensive} \times 0.8 + Max(\overline{T}_M, \overline{T}_S), T'_{Bldg,Extensive}) \quad (5)$$

$$T_5 = Max(T'_{Bldg,complete} \times 0.9 + Max(T'_M, T'_S), T'_{Bldg,complete}) \quad (6)$$

$$\overline{T} = \sum_{i=1}^{5} T_i \times P_i \quad (7)$$

4. CATASTROPHE MODEL FOR EARTHQUAKE RISK

Within our Earthquake Loss Model, we have four separate modules. The first module being the Stochastic earthquake event generator. This module will generate a series of all possible earthquakes in and around the island of Taiwan. The second module is the Hazard module. This module will assess the intensity of ground shaking at any given location for any given event. The third module is vulnerability module. The Vulnerability module will assess the possible structural and content damage with regards to the intensity of a predicted event at a location. The final module is the financial module. This module will assess possible economic loss according to different financial perspectives (i.e. total loss or insured loss).

As shown in the Figure 5, we begin by generating about 18000 possible events by using the stochastic event module. From here we move to the Hazard Module, where we analyze the intensity distribution of each possible event. Based on the analyzed hazard information and portfolio database, we can use the Vulnerability Module to assess the possible damage to property and business interruption. Finally, we calculate the economic loss of each event with the financial module to generate the Event-Loss Table. This table includes the average loss and the deviation of loss. Furthermore, we can also calculate the loss of differing insurance policy conditions.

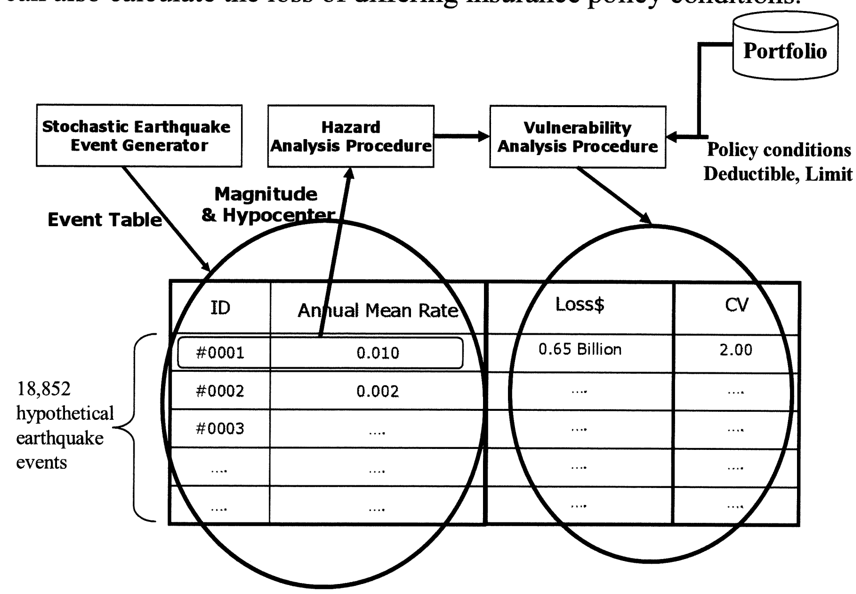

Figure 5 Building the event loss table

Furthermore, as shown in the Figure 6, based on the Event-Loss Table, we can generate the severity distribution and frequency distribution with the Poisson Model. From here, we use the Monte Carlo simulation technique to establish the exceeding probability curves. This will show us the Aggregate exceeding probability (AEP) and the Occurrence exceeding probability (OEP). First, we use the Poisson distribution to describe the earthquake occurrence times. According to the occurrence rate of each event, we can get the occurrence times N in every simulation and simulate the

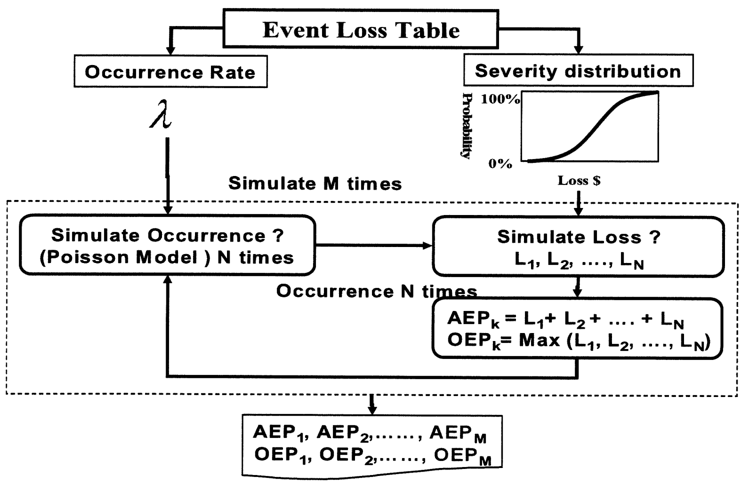

Figure 6 Building the aggregate/occurrence loss exceeding probability curve

accumulative probability of severity distribution randomly.

When the losses for all locations in a portfolio are calculated, the financial analysis procedure allocates the losses to different participants, i.e., insured, insurer, and re-insurer through various insurance and treaty structures. Because there are many sources of uncertainty in modeling (from attenuation, vulnerability and incompleteness of data), the loss at the location level is treated as a random variable.

5. ANALYSIS RESULTS OF EXAMPLE PORTFOLIO

Through detail site survey and interview with site engineer, an example portfolio includes over 60 building was built. For each building, structural type, built year, height and replacement cost of building was investigated and recorded. In addition to building information, the sensitivity and anchorage situation of equipments and its exposure value were recorded too. Because of the concern of commercial confidentiality, the exposure values were reform to build a hypothetical example portfolio. Using the established earthquake risk model to assess earthquake risk of the example portfolio, the loss exceeding probability curves according to different financial perspective could be calculated as show in the Figure 7. Loss exceeding probability curves were shown by the form of loss ratio versus return period.

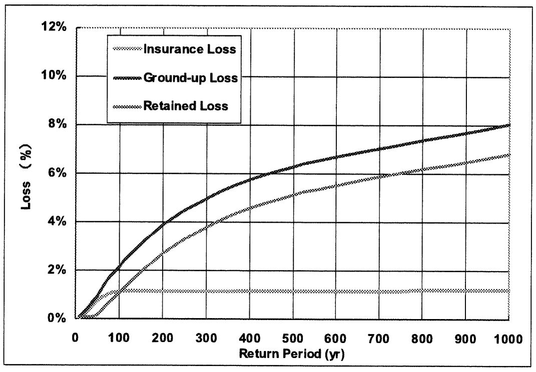

Figure 7 Loss exceeding probability curve

As shown in the Eq. (1), total annual earthquake risk has been defined to be sum of the insurance premium, the equivalent annual retrofit cost, and the average annual retained loss. As shown in Table 1, we define 3 insurance proposals with different policy conditions and premiums, 3 retrofitting proposals and totaling 4 risk management strategies were selected to evaluate. Figure 8 shows the results of total annual earthquake risk cost of each risk management strategies. Figure 8 also shows strategy-3 will be the optimal risk management strategy.

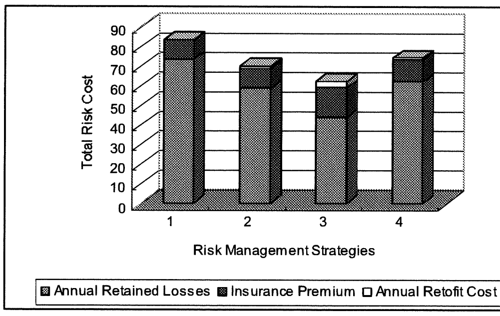

Figure 8 Total Annual Earthquake Risk Cost of Different Risk Management Strategies

Table 1 Earthquake Risk Management Strategies considering Retrofit and Insurance

	Strategy-1	Strategy-2	Strategy-3	Strategy-4
Annual Retained Losses	73	59	44	62
Insurance Premium	10	10	15	11
Annual Retofit Cost	0	1	3	1
Total Annual Risk Cost	83	70	62	74
Description	w/o retrofit- Present insurance policy	w/partial retrofit- Present insurance policy	w/retrofit - insurance I- with lower retention value	w/retrofit - insurance II- with lower deductible of BI

7. CONCLUSIONS

In this paper, we propose a framework for assessing the earthquake risk of HI-Tech fabs in Taiwan. Furthermore, the result of risk assessment can be extended to calculate the total annual earthquake risk cost for selection of optimal strategy of earthquake risk management. The total annual earthquake risk has been defined to be sum of the insurance premium, the equivalent annual retrofit cost, and the average annual retained loss.

Business interruption is commonly known difficult to model. Interruption of utility and supply chain, and damage of facilities or process equipment may cause business interruption. In this paper, we also present a simplified business interruption model only considered the effect of damage of building and equipment. How to consider the power supply as a factor of business interruption assessment will be the future research topic.

Because of the concern for uncertainty and engineering model, the earthquake loss assessment model can provide more information than the traditional method. For example, the loss exceeding probability curve can offer the policymaker to determine the earthquake protection capacity according to their tolerance of risk. On the other hand, the traditional method only can give us the single value for the possible maximum loss due to earthquake disaster.

References:

Brian Sherin, Stacy Bartoletti, TAIWAN's 921 QUAKE: Effect on the Semiconductor Industry and Recommendation for Preparing for Future Earthquakes, 1999.

Erik Ruttener, Linus Phoon, Chi-Chi – Three Years On, Global Reinsurance.

Gutenberg, B., Richter, C. F., "Frequency of Earthquake in California", Bull. Seism. Soc. Amer. 1991, Vol. 34, 185~188.

Lin B. S, Lee C.T., Cheng C .T ,"Strong Ground-Motion Attenuation Relationship for Subduction Zone Earthquakes in Taiwan", 9th Conf. on Geophysical Society, China, 2002, 24-31.

Pui Fong Han, May Ong, Risks in Semiconductor Fabrication Plants, 2001.

Risk Management Solutions, Event Report- Chi Chi, Taiwan Earthquake, 2000.

Dong, Weimin, Building a More Profitable Portfolio-Modern Portfolio Theory with Application to Catastrophe Insurance, Risk Management Solutions, 2001.

Wang, Yen-Po, Liao, Wei-Hsin, Chien-Liag Lee, Seismic Risks of Typical Double Fabs in Taiwan's HI-Tech Industry, 2003.

Young , "Subduction Slabs in Taiwan Region", Jour. Geol. China, 40, 1997 , 653-670.

Fifth International Conference on Urban Earthquake Engineering
March 4-5, 2008, Tokyo Institute of Technology, Tokyo, Japan

SOCIAL DIFFICULTIES INDUCED BY RECENT EARTHQUAKES IN JAPAN

Kazuoh SEO

Professor, Department of Built Engineering, Tokyo Institute of Technology, Japan
seo@enveng.titech.ac.jp

Abstract: When we visit the district heavily damaged by an earthquake, we often find several reasons why the damage became so big. In general, they are seismicity, geological and geomorphological condition, local soil condition, engineering problems about structures in buildings and houses, and so on. On the other hand, local society itself may have some problem to continue their daily lives after the damage. In this paper, some of such kind of social difficulties those could be found in recent Japanese earthquake disasters since the 1995 Kobe earthquake will be introduced. The biggest social problem is pointed out that the tendency of decreasing in population and aging of people often prevent the quick recovery from earthquake disasters.

1. INTRODUCTION

It is believed in general that we will learn much more lessons through a failure rather than a success. For this reason, it is very important to visit a damaged district just after an earthquake disaster and to have some kind of new findings in such failures. After that, we will make very careful evaluation to identify them, what are very useful even in the future, what are solved already, and what are not so important anymore. In the process of such integration among Japanese earthquake disasters since the 1995 Kobe earthquake, we will find some important lessons about the features of local community how residential people suffered the damage, how they recovered from the damage and how they restarted their daily lives after the damage. Some of the lessons look quite similar among different and distant districts. Examples about social difficulties, induced by individual earthquake disasters, will be introduced in the following chapters.

2. HOW TO COUNT THE NUMBER OF VICTIMS

Thirteen years have already passed since the 1995 Kobe earthquake. Every year on January 17th, local governments and organizations around Kobe hold some memorial events to keep the disaster in their mind. One of the biggest problems about the Kobe earthquake has been reported that the definition counting the number of victims is not clear (Seo, 2007). For example, some of researchers in the field of seismology and earthquake engineering say "the 80% of 6434 deaths were killed by the failure of their own houses and furniture." A newspaper reports "Just thirteen years have passed since the Kobe earthquake which brought 6434 victims." It is true that there were 5,500 deaths, most of them were buried under collapsed houses and furniture, and some others by big fires. Additional 900 were regarded as indirect deaths (some of them are called as solitary deaths) caused by illnesses, alcohol dependencies and even suicides within five years in temporal evacuation houses those were completely closed after five years from the earthquake.

It was so good that the government took such indirect victims into account as the first attempt. But one question remains why they stopped counting the number of victims after five years? Maybe we need a definition identifying indirect victims. Otherwise the number of indirect victims will increase year by year. According to recent newspaper, additional 400 and more deaths were confirmed after five to ten years from the 1995 earthquake in reconstructed houses. Such condition looks very uncertain, doesn't it?

Photo 1. Temporal houses prepared after the 1995 Kobe earthquake. They were kept using for maximum five years , where the number of indirect victims increased year by year because of illnesses, alcohol dependencies and even suicides .

3. RECOVERY FROM EARTHQUAKE DISASTERS IN UNDER-POPULATED AREAS

Recent Japanese earthquakes often hit under-populated local country districts, such as the 2004 Chuetsu (Niigata) earthquake, the 2007 Noto Peninsula (Ishikawa) earthquake, and again the 2007 Chuetsu-Oki (Niigata) earthquake. In such areas, countermeasures in recovery and reconstruction after the disasters are not so easy because of very serious tendency that the population is decreasing and people are aging year by year. For example, old ages with heavy damage in their houses will hesitate the reconstruction of their own houses, or feel almost impossible to do it. Besides the economic reason, there are no prospects in their future lives. That is actually the biggest social difficulty induced by recent earthquakes in Japan.

Photo 2. A village named Yamakoshi, Niigata pref., was completely damaged during the 2004 Chuetsu earthquake, because of land failures. The people have to spend three years in distant temporal houses.

Photo 3. Some of villages in the mountain area sank down in the water due to landslides after the 2004 Chuetsu earthquake. The residential people could never return back to their own houses.

Photo 4. Typical failure of wooden houses those were found quite often in the 2007 Noto Peninsula earthquake.

Photo 5. Many wooden houses were crushed again in the 2007 Chuetsu-Oki earthquake. Reconstruction of such houses looked very difficult for old ages.

4. SO-CALLED NON-STRUCTURAL FAILURES IN CONDOMINIUMS DURING EARTHQUAKES

According to the review after the 1995 Kobe earthquake, the revision of the Japanese Building Code in 1981 was very successful. They say buildings and houses with the newer building code suffered only a slight damage during the 1995 Kobe earthquake, although buildings and houses with the older building code did suffer heavy damage. On the other hand, the impression about the 2005 M7 Fukuoka-Oki earthquake was quite different. In this case, most of the failures on reinforced concrete condominiums were moderate or slight, where 70% of the citizens were living in such condominiums. The point in this case was that such damage could be found mostly in non-engineering parts of the newer buildings, constructed within five years, rather than the older ones. It means that the structural design of modern buildings became very critical, and therefore they have become more vulnerable than before.

For example, a new condominium suffered shear cracks on non-structural walls. As the second effect, the walls crashed the neighboring entrance doors, and they disturbed evacuation activities those should have been made after the earthquake immediately by the residential people. In case of another new condominium, the expansion joints were crashed between bumping two buildings, and a peace of concrete fence with 500kg in weight fell down from the 10^{th} floor to the ground level. Although it was not a case of new building, outer window glasses of a 10 stories office building were broken, and numbers of fragments fell down to the sidewalks like a shower. Needless to say, non-structural failures are serious enough because they can kill residential people quite easily. It was just fortunate that the 2005 Fukuoka-Oki earthquake did not kill the people, only because the earthquake took place in a Sunday morning.

The experience in the 2005 Fukuoka-Oki earthquake looks very important for the future earthquakes those could be expected in mega-cities like Tokyo metropolis. We can imagine the similar non-structural failures in great number of condominiums. Recently the usage of expansion joints, for example, is becoming uncertain just to get permission for new constructions of tall and dense condominiums.

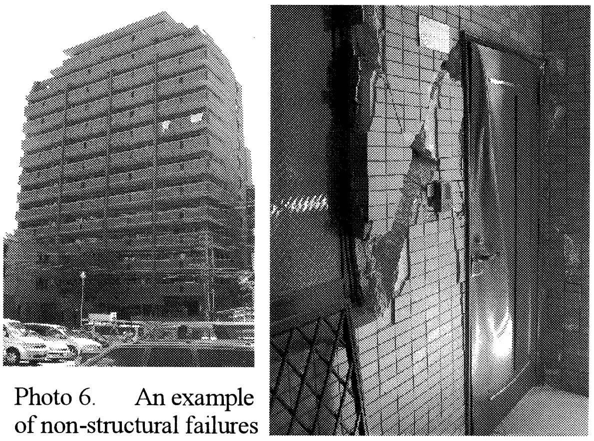

Photo 6. An example of non-structural failures that could be seen in the 2005 Fukuoka-Oki earthquake. Crashed entrance doors disturbed evacuation activities.

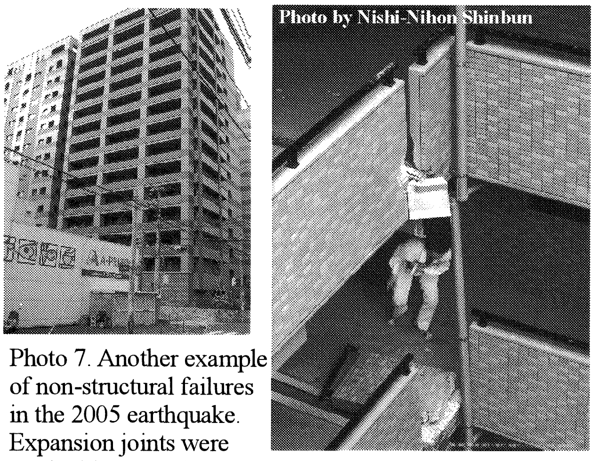

Photo 7. Another example of non-structural failures in the 2005 earthquake. Expansion joints were crashed between bumping two buildings, and a peace of heavy concrete fence fell down to the ground level.

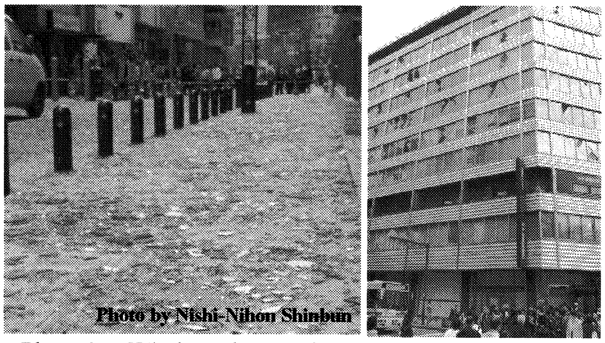

Photo 8. Window glasses of a 10 stories office building were broken and numbers of glass fragments fell down to the sidewalks like a shower.

5. SOCIAL PROBLEMS INDUCED BY NUCLEAR POWER PLANTS DURING EARTHQUAKES

We believe that there was no earthquake damage in nuclear power plants before the 2007 Noto Peninsula (Ishikawa) earthquake and the 2007 Chuetsu-Oki (Niigata) earthquake. Therefore the failures in such nuclear power plants during the both 2007 earthquakes brought us a very serious confusion. It may be true that the failures themselves were not so severe from the engineering point of view. The most important problem was that the authorities and related companies on electric power plants did not take any kind of urgent countermeasures. We want to believe they did, but we could not confirm them at all. It does not look funny because they have the constitution to keep the silence about their inconvenient facts, even criticality accidents, in their history.

There is no doubt that nuclear power plants are quite important in Japan. Therefore they have been constructed with the agreement among the government, related electric company, and local government as the representative of the citizens in the district. In deed, construction sites must be chosen very carefully not to have every kind of accidents, environmental pollutions and natural disasters like earthquakes and volcanic eruptions. Most of all, the evaluation of seismic activities around the site should be made very carefully. Recently the improvements in seismology, geology and geography are requiring re-examination about the safety of nuclear power plants against the possible future earthquake around the individual sites.

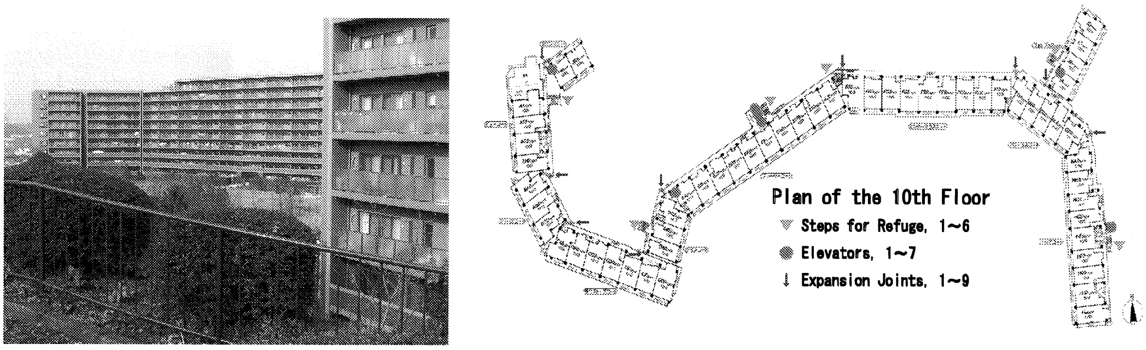

Photo 9. A new condominium constructed in Tokyo metropolis that has number of expansion joints without refuge steps.

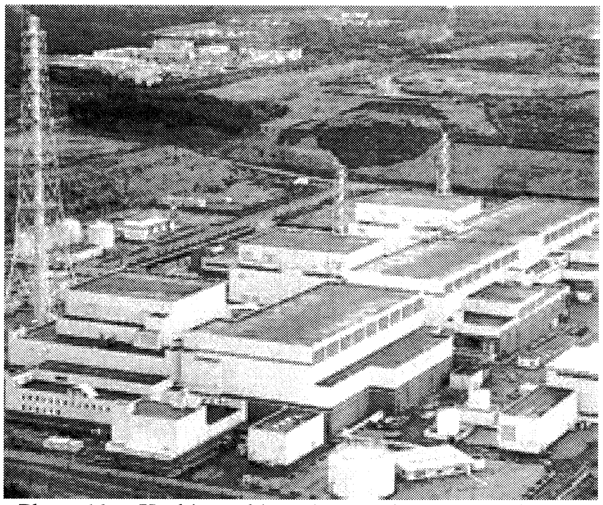

Photo 10. Kashiwazaki-Kariwa nuclear power plant of Tokyo Electric Power Company (TEPCO) suffered the damage during the 2007 Chuetsu-Oki earthquake.

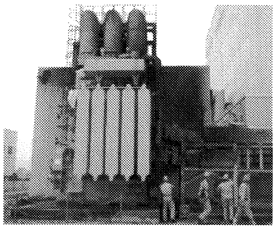

Photo 11. No one could not put off the fire for long time after the earthquake.

Photo 12. Vessels for atomic waste collapsed under the weight.

Photo 13. Sloshing phenomena was observed in a water pool for spent fuels during the earthquake. The water showed overflow from the pool. (Photos 10 to 13 were referred from the website prepared by TEPCO.)

6. CONCLUSIONS

In this paper, some of typical examples about social difficulties were introduced and discussed, those could be found in recent Japanese earthquake disasters since the 1995 Kobe earthquake.

First of all, the author stressed the importance to define the way, how to count the exact number of victims after catastrophic earthquakes. In the 1995 Kobe earthquake, we have noticed about the existence of indirect deaths with about 900 people. Most of them were found as solitary deaths in temporal evacuation houses from a few months to a few years after the earthquake. The question is how long time we need to count the number of such victims. In case of the 1995 earthquake, the authority stopped counting on the half way without making clear the reason.

Second, the author pointed out the tendency that decreasing in population and aging of people often prevent the quick recovery from earthquake disasters. As they cannot survive by themselves, the governments must prepare a support system to help them.

Third, according to the experience during the 2005 M7 Fukuoka-Oki earthquake, citizens living in modern cities may have another kind of social problem. Many of new and tall condominiums will have non-structural failures such as the collapse of non- engineering walls or bumping of buildings at expansion joints even in moderate M7 earth-quakes, as they are often built with the critical structural design.

Finally the author pointed out some kind of social problem about nuclear power plants during earthquake disasters. Actually there were very sensitive discussions not only for the case of Kashiwazaki-Kariwa nuclear power plant but also for similar facilities distributed in the country. Some of them were installed in the areas with very high seismicity. Now the concerning authority has just started reviews about them, although some of them are working and some others are waiting for reviewing results.

Acknowledgements:

The author acknowledges the financial supports from Japan Ministry of Education, Culture, Sport, Science, and Technology (MEXT) and the Center for Urban Earthquake Engineering (CUEE) in Tokyo Institute of Technology to have made a number of field surveys in damaging regions since the 1995 Kobe earthquake. The author would like to express his sincere appreciation to the citizens in damaged areas, who showed as possible as cooperation in spite of their very hard situation after the serious damage.

References:

Seo, K., Motoki, K., and Eto, K. (2006), "Lessons Learned from Recent Earthquake Disasters – for Mega-Cities on Huge Sedimentary Basins – ," *Proceedings of the 3rd International Conference on Urban Earthquake Engineering*, 593-600.

Seo, K., Motoki, K., and Ueda, R. (2006), "Non-Structural Damage of Residential RC Buildings during the 2005 Fukuoka-Oki Earthquake as a Typical Urban Disaster," *Proceedings of the 12th Japan Symposium on Earthquake Engineering*, Paper No.0056 CD-ROM (in Japanese)

Seo, K. (2007), "Some Examples Showing Very Vulnerable Condition in Earthquake Countries," *Proceedings of the 4th International Conference on Urban Earthquake Engineering*, 231-236.

Fifth International Conference on Urban Earthquake Engineering
March 4-5, 2008, Tokyo Institute of Technology, Tokyo, Japan

SEISMIC MICROZONATION OF ADDIS ABABA BY COMBINING ANALYTICAL PROCEDURE AND MICROTREMOR MEASURMENTS

Messele Haile [1]

1) *A/Professor, ,Department of Civil Engineering, Addis Ababa University, Ethiopia*

messele.haile@ethoinet.et

Abstract: An attempt to produce seismic microzonation maps for cities exposed to seismic risk has been attempted by using different methods. In places like Addis Ababa, the capital city of Ethiopia, where strong ground motions records are rare, the use of recorded strong motion for seismic microzonation is not an option. The use of analytical procedure combined with microtremor measurements is practical and economical. Soil profile data and parameters are collected form previously done soil investigations for other purposes. Analytical procedure was used to determine site period and amplification. Microtremor measurements were made on spots where periods and amplifications were determined by analytical procedures. Comparison was made between the periods and amplifications obtained both by analytical methods and microtremors. Good agreement was obtained. Wider area measurement of microtremors was made over many points where soil date is not available. The Fourier amplitudes and predominant periods of microtremors are plotted on a GIS based map of the City and a seiesmic microzonation map of the city is produced.

1. INTRODUCTION

The city of Addis Ababa, which is located at about N9.02 and E38.45 is near the western escarpment of the rift valley system of East Africa, which passes through Ethiopia. Is proved to be seismically active from different studies(Gouin, 1976, 1979; Olive and Boyed, 1970). Addis Ababa is the Economic, Political and Social center of the Country - a center where catastrophe of any sort will have a server consequences. Since its founding a century ago, a number of seismic activities have occurred. An earthquake of lesser magnitude occurring near a population center will have a significant effect while an earthquake of magnitude hundred times bigger in a remote place will pass un-noticed except by seismic stations and seismologists. Addis Ababa has witnessed a number of earthquakes in 100 years of its existence, some are: the 1906 earthquake of magnitude 6.8 at epicentral distance of about 100 km south of Addis , the 1961 an earthquake of magnitude 6.6 which occurred at a distance of 200km (Karakore Earthquake), the July 1997 an earthquake with magnitude 4.0 at a distance of 22 km to the south west of the city. Some other earthquakes of smaller magnitude and at far distance (in 1977, 1984 and 1985) were felt at upper story of high rise buildings, (Asfaw , 1985a,b)

A critical case for Addis Ababa could be the reoccurring of an earthquake like that of 1906. In 1906 an earthquake of magnitude 6.8 occurred at epicentral distance of 100 kms or less from Addis Ababa. From such earthquakes an intensity of greater than VII (M.M) is expected. With concentration of population and multi-story buildings here and there the life loss and property damage could be disastrous unless the awareness and the preparedness exists.

In regions where seismicity is low to moderate, recording a representative earthquake is difficult. Moreover, it may be difficult to obtain simultaneous records on the soft soil stations and on the hard rock reference stations. A proposed alternative is to use analytical method in combination with records of ambient seismic noise called microtremors. This technique is used in this study because of the following reasons:

1. The city of Addis Ababa has moderate seismicity and strong ground motion data are not available.

2. Even if low to moderate earthquake occurred several times in the past they were not recorded so as to be used for microzonation purpose.

3. Existing soil data is used for the analytical approach. Therefore no additional cost is incurred.

4. Microtremor reading does not need subsurface exploration, expensive laboratory tests and expensive computation. It is also possible to cover a large area within a short period of time.

From the above it was more apparent that the seismic microzonation of Addis Ababa by using analytical procedure and microtremors is the most suitable

2. Analytical procedure

Soil profile and soil parameter data was collected for sites where earlier geotechnical investigation was carried out. These are site where soil investigation was done for the purpose of building construction. Among the numerous data, emphasis was made on soil profile, Standard Penetration Test (N) values which are converted to shear wave velocity(Vs) and density. For analysis purposes one dimensional vertical shear wave propagation was used as given in the program SHAKE(Schnabel, 1972) . In the absence of locally recorded strong ground motions, commonly available strong ground motion records were used as bed rock input motion. These records are; the 1941 Elcentro record of the Imperial Valley Earthquake, The 1952 Taft record of the Kern Country Earthquake, the 1968 Hachinohe record of the Tokachi-Oki Earthquake and The 1995 Kobe JMA record of the Hyogoken-nanbu Earthquake. These earthquakes were deconvolved to the bedrock at their place of recording to take out the site effect at their place of recording. The deconvolved earthquake records were input as bed rock motion at the respective sites chosen for analysis.

All the above records were capped to maximum acceleration of 0.2g to calibrate to local hazard levels. Analysis was done for 5 sites for which soil data is available and responses are obtained. Focus was made on the free field response which corresponds to the exact position where the microtremors are later measured. Among the different response values the predominant periods are chosen for ease of comparison with the periods obtained from microtremor measurements.

Table 1 Predominant period for the top layers obtained from analytical procedure

Location of site in Addis Ababa	T_{AP} in sec.
NISCO Head office building	0.1
Finfine Furniture Factory	0.06
Awash Insurance/Bank Building	0.1
Alem Building	0.1
Bekele Abshiro building	0.08

T_{AP} =period obtained from Analysis

3. MICROTREMOR MEASUREMENTS AND ANALYSIS

3.1 background

Once the analytical procedure was completed for the five sites, micrtremore measurements were done for the five sites at surface. In regions where seismicity is low to moderate, recording a representative sample of earthquake is difficult. Moreover, it may be difficult to obtain simultaneous records on the soft soil stations and on the hard rock reference stations; a proposed alternative is to use records of ambient seismic noise called microtremors. This technique is used in this study because of the following reasons:

1. The city of Addis Ababa has moderate seismicity and strong ground motion data are not available.

2. Even if low to moderate earthquake occurred several times in the past they were not recorded so as to be used for microzonation purpose.

3. Microtremor reading does not need subsurface exploration, expensive laboratory tests and expensive computation. It is also possible to cover a large area within a short period of time.

From the above it was more apparent that the seismic microzonation of Addis Ababa by using analytical method and microtremors is suitable.

3.2 Microtremor Instrument Used and it's Operations

Microtremor Instruments used for this study can generally be presented schematically as shown in (Fig. 1). A set of three highly sensitive seismometers which are arranged in two orthogonal directions i.e., UD (up-down) and NS (north-south), were used to pick up the noise from the ground.

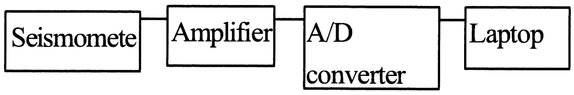

Figure 1. Instrument Arrangements for Microtremor readings

3.3 Comparison of periods obtained form analytical procedure and microtremor measurements

The microtremor measurements were recorded on laptop as time histories. The records were filtered for noise. Fourier analysis of the records was done and the predominant periods and Fourier amplitudes of microtremors were obtained. The predominant periods obtained from the analysis and microtremor measurements are compared for the five sites were soil date is available and good agreement is obtained between the two methods. The comparisons are given in table 2 below.

Table 2 Comparison of predominant period for the top layers obtained from analytical procedure and microtremor measurements.

Location of site in Addis Ababa	T_{AP} in sec.	T_M in sec
NISCO Head office building	0.1	0.1-0.13
Finfine Furniture Factory	0.06	0.05
Awash Insurance/Bank Building	0.1	0.11
Alem Building	0.1	0.1
Bekele Abshiro building	0.08	0.1

T_{AP} =period obtained from analysis

T_M =period obtained from microtremors

Comparison of the predominant period by the analytical and microtremor measurements showed good agreement. This showed the potential for the applicability of microtremors for seismic microzonation purposes in the city of Addis Ababa. Therefore, an attempt was mode to prepare seismic microzonation map for the city of Addis Ababa.

3.4 Preparation of Seismic Microzonation maps by Using Microtremor Measurments.

The next step was to take microtremor readings of point data at selected p laces far apart but which cover the city. A grid of 5 by 5 km was taken. The points of measurement are given in Figure 2. The result gives an idea on amplitude and predominant period of microtremors in the city. This two values are good indicators for the possible amplifications and predominant periods that may be observed during strong ground motion. However, it is important to note that microtremors give values at low strain level within the linear range. One has to consider the effect of non linearity when extrapolation these results for strong ground motion response

The exact location of the points of microtremor measurements is determined as marked with GPS receiver. Microtremor measurements were made for many points in the city. The obtained rmicrotremor time history records were filtered and Fourier analysis was made to determine predominant periods and the Fourier Amplitudes were determined. Seismic microzonation maps for the city are prepared based on these two parameters. The seismic microzonation maps prepared using the Fourier Amplitude and predominant period are given in Figures 3 and 4.

Fig 2. Points of Measurements of Microtremors

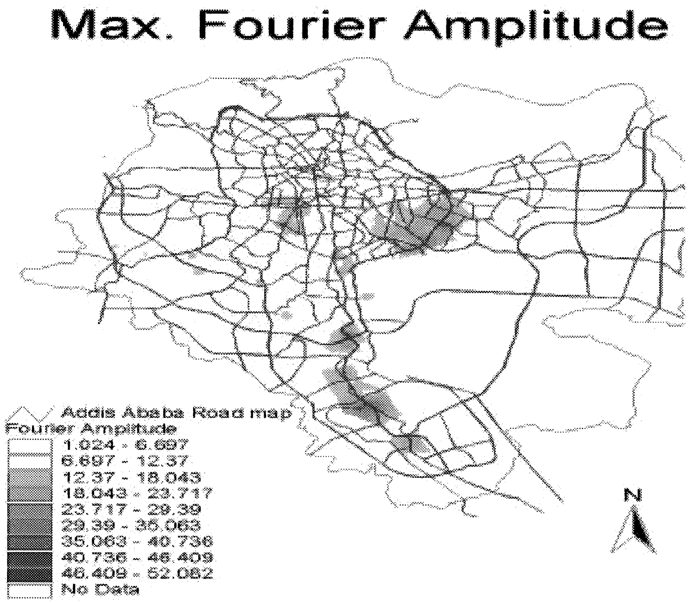

Fig 3. Fourier Amplitude Spectra of Microtremor Measurements for The City of Addis Ababa

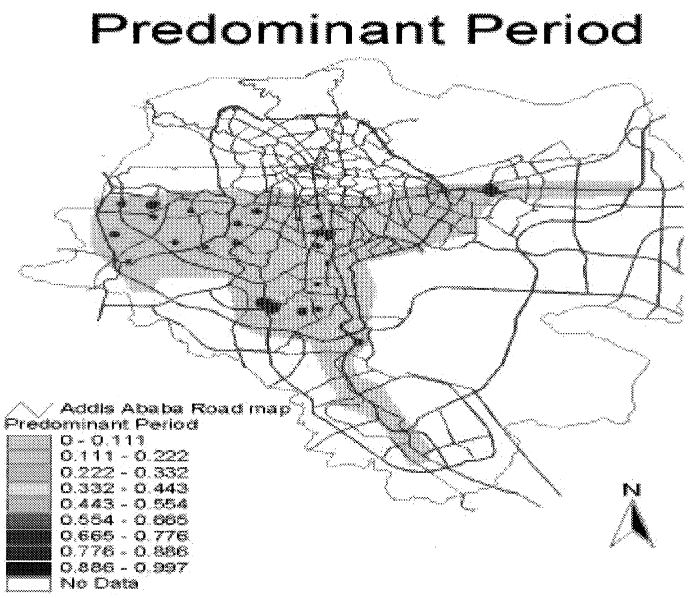

Fig 4 Predominant Period of Microtremor Measurements for The City of Addis Ababa

4. CONCLUSION

1. The above study showed that microtremors are applicable for seismic microzonation proposes in the city of Addis Ababa
2. It showed that carefully measured microtremors and analytical method based on borehole date could give close results
3. The study clearly showed that microtremors are effective in areas where strong ground motion is scares or is not available, specially in areas of moderate seismicity.

4. ACHNOWLDEGMENT

The Author would like to express its gratitude and acknowledge the contribution made by MSc students, of the Civil Engineering Department of The Addis Ababa University, who worked their thesis on the subject under the advisorship of the Author. These are 1. Mr. Daniel Aberra, 2. Mr. Henock Wondimu and3 . Mr. Gezahegn Ayele

6. REFERENCES

1. Guine P. Seismic Zoning in Ethiopia",(1976). Bull, Geophysical Observatory Addis Ababa
2. Guine P.(1979) Earthquake History of Ethiopia and the Horn Of Africa" IDR Publication, Ottawa.
3. Olive and Boyed(1970). African Magnetism and Tectonics, Ednberg.
4. Asfaw L.(1985 a). Seismicity and Seismic risk in Addis Ababa region" Bull, Geophysical Observatory Addis Ababa.
5. Asfaw L.(1985 b). Catalogue of Ethiopian Earthquake, Parameters, strain release and Seismic risk" Bull, Geophysical Observatory Addis Ababa.
6. Schnabel P.P., J. Laysmer, H.B. Sead(1972). SHAKE, Acomputer program for the earthquake response Analysis of of Horizontally Layered Sites. Report No EERC 72-12, UC Berkely

Fifth International Conference on Urban Earthquake Engineering
March 4-5, 2008, Tokyo Institute of Technology, Tokyo, Japan

DETECTION OF SLOPE FAILURE AREAS USING HIGH-RESOLUTION SATELLITE IMAGES AND DIGITAL ELEVATION MODEL FOR THE 2004 NIIGATA-KEN CHUETSU, JAPAN EARTHQUAKE

Hiroyuki Miura[1] and Saburoh Midorikawa[2]

1) Assistant Professor, Department of Built Environment, Tokyo Institute of Technology, Japan
2) Professor, Department of Built Environment, Tokyo Institute of Technology, Japan
hmiura@enveng.titech.ac.jp, smidorik@enveng.titech.ac.jp

Abstract: A methodology to detect slope failure areas from pre-, post-event high-resolution satellite images and digital elevation model is introduced in this study. The IKONOS images observed before and after the 2004 Niigata-ken Chuetsu, Japan earthquake are used in this study. The slope failures are extracted as the areas where normalized difference vegetation index (NDVI) is remarkably decreased after the earthquake because the vegetation is flowed out and the surface soil is exposed in the failure areas. The flat areas are eliminated in the analysis using slope angle computed from the digital elevation model. The result shows that the distribution of the detected areas agree with the distribution of slope failure areas extracted by manual interpretation of aerial photographs.

1. INTRODUCTION

The Niigata-ken Chuetsu, Japan earthquake on October 23, 2004 (Mw6.6) produced many slope failures and the associated building and road damage. For the emergency response, it is important to rapidly comprehend the extend and the severity of the damage. The identification of the distribution of the slope failures, however, is not easy because of the difficulty of gathering data in mountainous areas by field survey.

Remotely sensed data is useful to detect the distribution of slope failures and the damage. Slope failure areas usually have been identified from aerial photographs by manual interpretation. Since the interpretation requires great demand for labor and time in a large-scale disaster, automated or semi-automated detection would be necessary for more rapid response.

Authors examined a method to semi-automatically detect slope failure areas by using high-resolution satellite images [Miura and Midorikawa, 2006]. A lot of mis-detections, however, were produced in flat areas because the terrain information was not included in the analysis. In this study, a methodology to detect slope failure areas is proposed by using the digital elevation model as well as the high-resolution satellite IKONOS image observed before and after the earthquake.

2. DATA AND METHODOLOGY

Figure 1 shows the pre-, post-earthquake IKONOS images and digital elevation model used in this study. The area covers the epicentral areas such as Kawaguchi town and Yamakoshi village, extending 9km in NS direction by 6.5km in EW direction. Two pre-event images are used in this study because a single image does not cover the entire target area. The image A observed in Apr. 29, 2002 covers the western part from the dotted line in Fig. 1 while the image B observed in Apr. 15, 2002 covers the eastern part of the area. The post-event image was observed a day after the earthquake. The spatial resolution of the images is 1m and the images consist of 4 spectral bands (Blue, Green, Red and Near infrared). The characteristics of the images are shown in Table 1. The digital elevation model is constructed from airborne laser scanner data observed in Oct. 28, 2004. The spatial resolution of the DEM is 2m.

Figures 2(a-1) and (a-2) show the close-up of the IKONOS images in slope failure areas. In the post-event image, the vegetations such as trees are flowed out and the soils are exposed on the surface due to the slope failure as shown in the dotted circle. Figures 2(b-1) and (b-2) show the distribution of NDVI (Normalized difference of vegetation index [e.g., Tucker, 1979]) computed from the images by the equation (1).

$$NDVI = (DN_{NIR}-DN_{Red}) \ / \ (DN_{NIR}+DN_{Red}) \qquad (1)$$

Here, DN_{NIR} and DN_{Red} represent digital number of a pixel in the near infrared band and the red band image, respectively. NDVI is related to the amount of biomass within a pixel and yields a number from −1 to +1. A higher NDVI indicates a higher density of green leaves. In the slope failure area in the post-event image, NDVI is remarkably decreased due to the flow out of the vegetation. This suggests that slope failure areas can be detected using

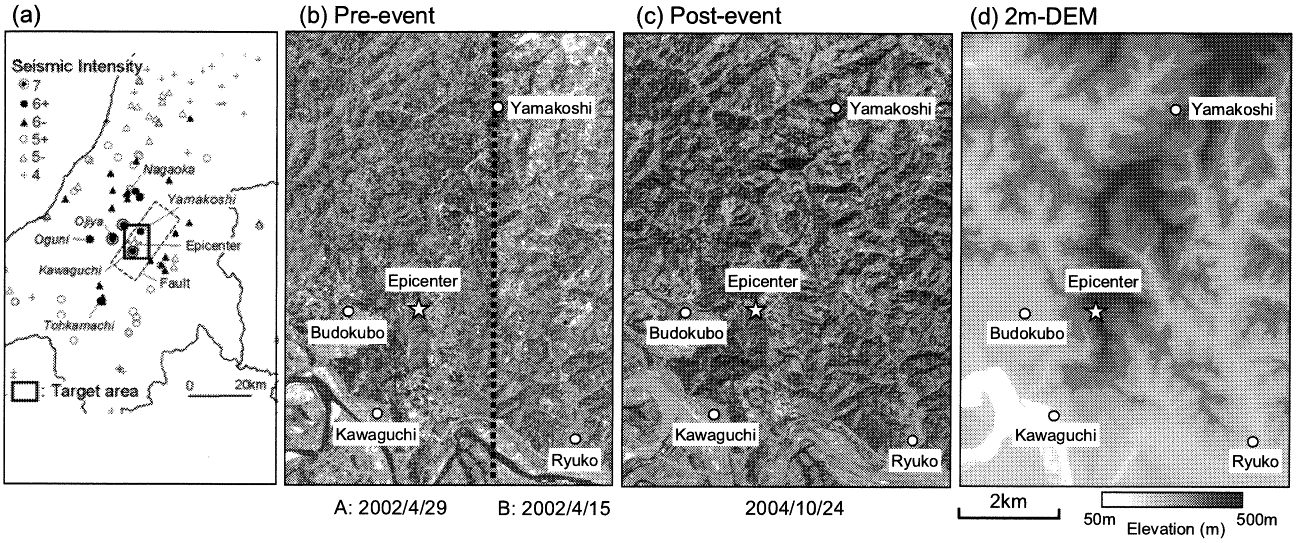

Figure 1 (a) Target Area with Distribution of Seismic Intensity of The 2004 Niigata-ken Chuetsu, Japan Earthquake, (b) Pre-event IKONOS Images, (c) Post-event IKONOS Image, (d) Digital Elevation Model (DEM)

Table 1 Characteristics of IKONOS Images

		Date	Time	Satellite Angle (deg.)	Satellite Elevation (deg.)	Sun Angle (deg.)	Sun Elevation (deg.)	Spatial Resolution
Pre-	A	Apr. 29, 2002	AM 09:48	N226E	78	N148E	64	1 m
	B	Apr. 15, 2002	AM 09:38	N117E	77	N147E	59	1 m
Post-		Oct. 24, 2004	AM 10:03	N250E	54	N172E	41	1 m

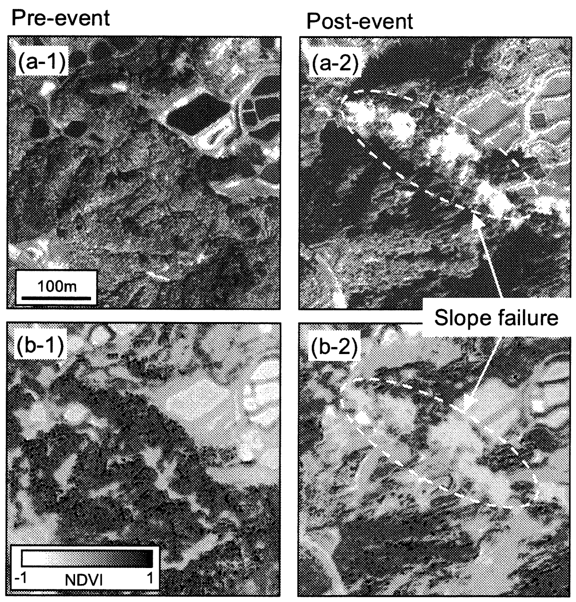

Figure 2 (a) Comparison of Panchromatic Images
(b) Comparison of NDVI Images

the difference of NDVI.

Figure 3 shows the flow of the detection of slope failure areas adopted in this study. First, the pre- and post-event IKONOS images are geometrically rectified using the DEM. After eliminating the shadow areas, NDVI is computed in

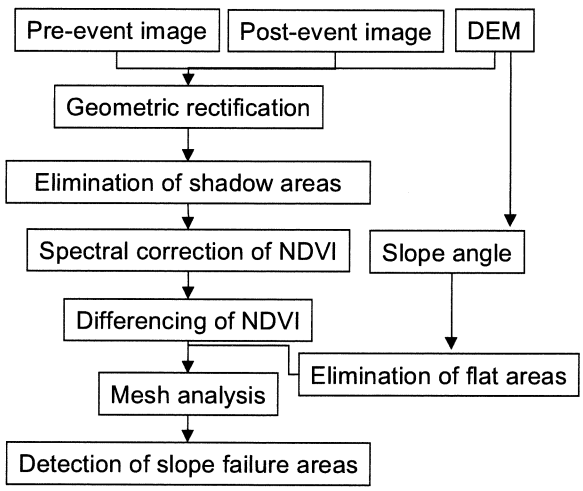

Figure 3 Flowchart for Detection of Slope Failure Areas

each pixel. The NDVI in the post-event image is spectrally corrected to reduce the effect of seasonal change between the images. In order to reduce mis-detections, the flat areas are eliminated in the analysis using the slope angle of the terrain computed from the DEM. Finally, the slope failure areas are detected by thresholding of the difference of NDVI.

3. DETECTION OF SLOPE FAILURE AREAS

3.1 Preprocessing of IKONOS Images

The IKONOS images are geometrically rectified using the DEM to precisely overlay the images. In the rectification, about 50 reference points are used for the ground control points. The horizontal positional error between the images is about 3.5m in the rectification with using DEM while the error is about 13m in the rectification without using DEM.

It is difficult to accurately evaluate the difference of NDVI in the areas covered with shadow. The shadow areas are eliminated in the analysis by extracting the shadows from threshold of the near infrared band images. The threshold value is selected from the trough of the histogram of the digital numbers. The pixels whose digital number is lower than the threshold are classified as the shadow area.

Since the activity of the vegetation is seasonally changed between the images even in unaffected area, NDVI is spectrally corrected to reduce the effect of the seasonal change. NDVI of about 100,000 pixels in the pre- and post-event images is selected from unaffected areas. Figure 4 shows the comparison of NDVI of the selected pixels before and after the earthquake. Figure 4(a) indicates the comparison in the area of the image A shown in Fig. 1, while Fig. 4(b) indicates the comparison in the image B. The range of NDVI in the post-event image is narrow compared with that in the pre-event image. This would be because that the observation condition such as the atmospheric condition and the sun elevation in the post-event image is not fine.

NDVI of the post-event image is spectrally corrected using the linear relationship shown in Equation (2) computed by the least square regression of NDVI before and after the earthquake.

$$NDVI_{After\_corrected}=(NDVI_{After}-0.266) / 0.519 \quad \text{(for Image A)}$$

$$NDVI_{After\_corrected}=(NDVI_{After}-0.219) / 0.689 \quad \text{(for Image B)} \qquad (2)$$

Figure 5 shows the comparison of histograms between original pre-, post-event images and spectrally corrected post-event image. After the correction, the distribution of the digital number of the post-event image comes to be closer to that of the pre-event image.

3.2 Characteristics of Difference of NDVI

The difference of NDVI, defined as D value, is computed in each pixel. The histograms of D value are shown in Fig. 6. Since the shape of the histogram is almost the normal distribution, it is not easy to determine the threshold value to discriminate slope failure areas with the other areas simply from the histogram shape. In order to examine the effect of the threshold value, the slope failure areas are estimated by using four threshold values as shown below.

Case 1: Threshold value = Ave.+1.0σ
Case 2: Threshold value = Ave.+1.5σ
Case 3: Threshold value = Ave.+2.0σ

Here, Ave. and σ indicate the average of D value and its standard deviation, respectively. The distribution of the slope failure areas estimated by the threshold values is shown in Fig. 7. The comparison with the distribution of actual slope failure areas reveals that the result in the Case 3 shows better agreement than the other cases. The value in the Case 3 is selected as the threshold to discriminate slope failure areas with other areas. The pixels whose D value is lager than the threshold value are classified as the slope failure pixels, defined as PF.

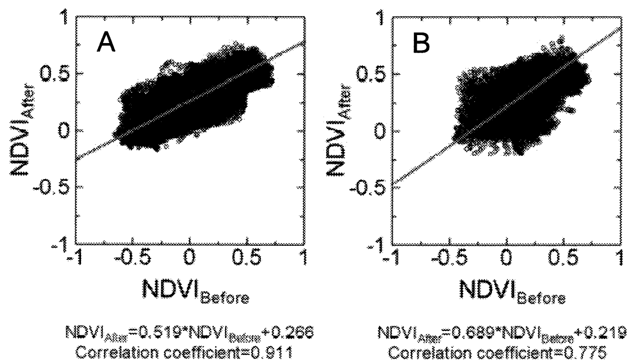

Figure 4 Comparison of NDVI Before and After the Earthquake

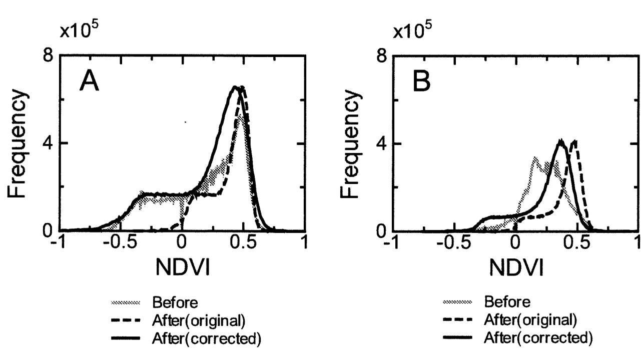

Figure 5 Comparison of Histograms of NDVI

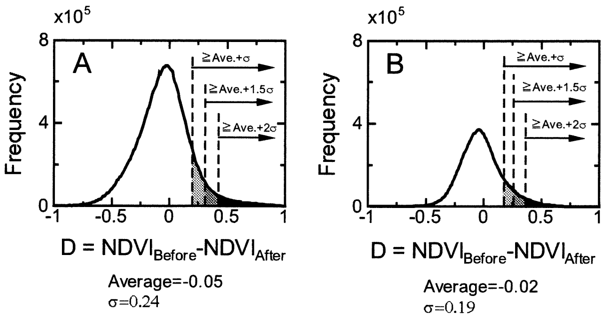

Figure 6 Histograms of D-value

3.3 Elimination of Flat Areas

In this study, the terrain information computed from the DEM is included in the analysis to reduce mis-detections in flat areas. Figure 8(a) shows the close-up of slope failure areas. The dotted circles indicate the locations of the slope failures. Figures 8(b) and (c) show the distribution of the elevation and its slope angle in each pixel, respectively. Figure 8(d) indicates the distribution of the originally detected PF. The flat areas located in the central part of the image are mis-detected because NDVI in the area is decreased after the earthquake. These mis-detected areas are eliminated using the slope angle.

The comparison between the slope angle (Fig. 8(c)) and the actual slope failures (Fig. 8(a)) shows that slope angles in most of slope failures is more than 10 degrees. Therefore, the areas whose slope angle is less than 10 degrees are classified as the flat areas unaffected by the slope failures. Figure 8(e) shows the distribution of PF after the elimination of the flat areas, showing good agreement with the distribution of the actual slope failures.

In order to eliminate small-scale change other than slope failures, the detected slope failure pixels are evaluated by 20m-mesh system. The mesh size is determined from the reason that the scale of the slope failures are more than

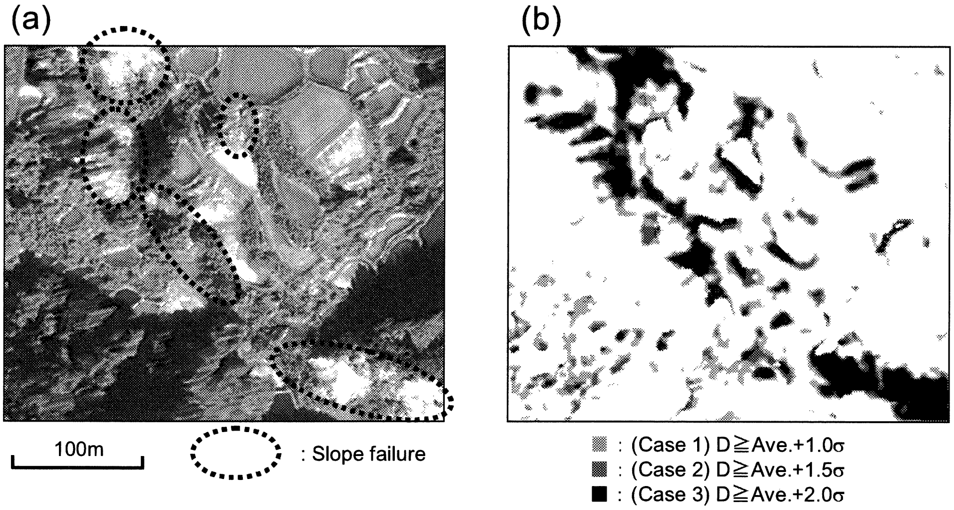

Figure 7 (a) Post-event Image, (b) Detected Pixels for Each Case

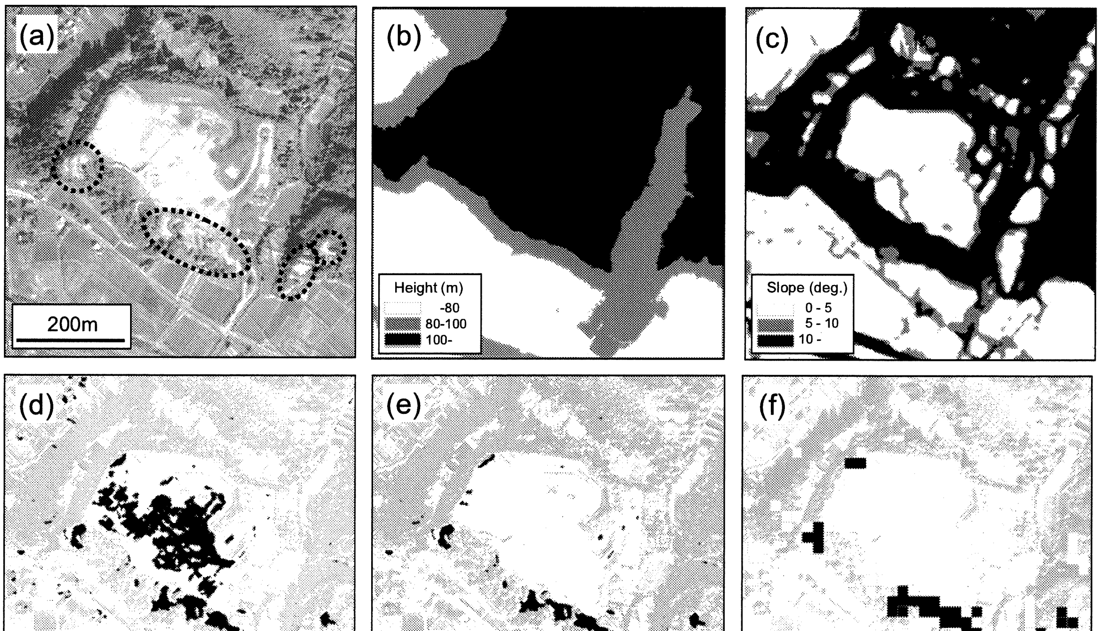

Figure 8 (a) Post-event Image, (b) Distribution of Elevation, (c) Distribution of Slope Angle
(d) Distribution of Initially Detected PF, (e) Distribution of PF After Elimination of Flat Areas, (f) Distribution of Detected Meshes

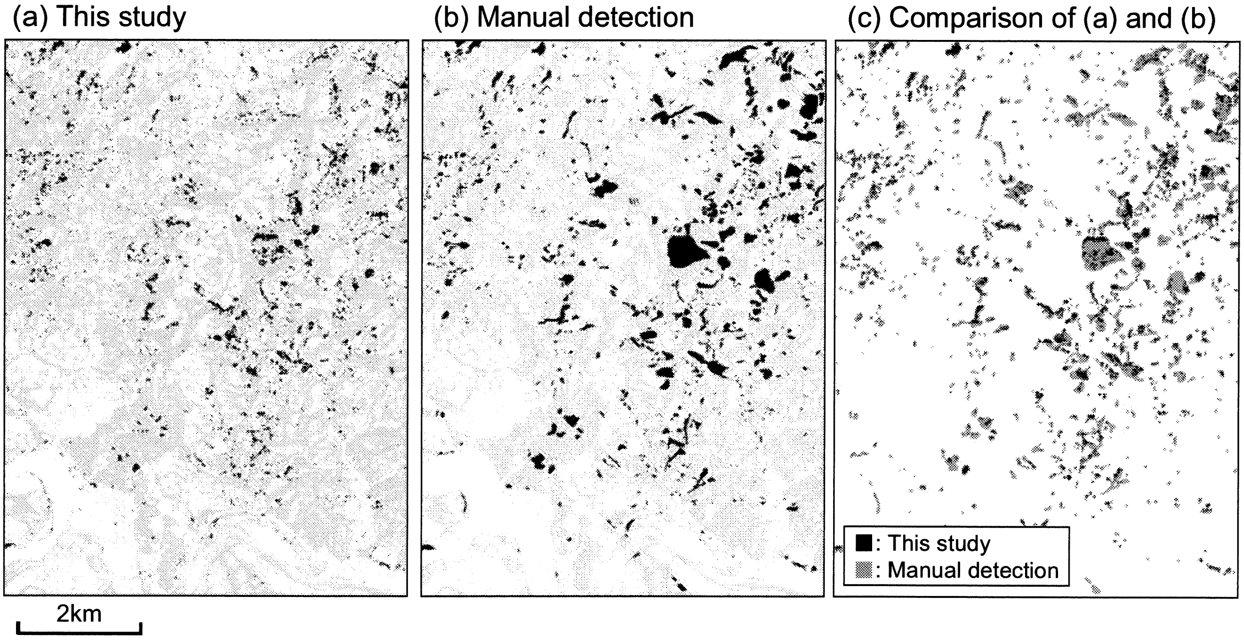

Figure 9 (a) Distribution of Slope Failure Areas Detected in This Study, (b) Distribution of Slope Failure Areas Manually Detected Using Aerial Photographs [Geographical Survey Institute, 2006], (c) Comparison of (a) and (b)

20m for almost 95% of the failures by the manual interpretation of aerial photographs [Geographical Survey Institute, 2006]. The ratio of the number of PF is computed for each mesh. From the comparison with the distribution of the actual slope failures, the meshes whose ratio of PF is more than 20% are classified as the slope failure areas. The distribution of the detected meshes is shown in Fig. 8(f).

4. EVALUATION OF RESULTS

Figure 9(a) and (b) show the distribution of the slope failure areas detected in this study and that by the manual interpretation of the aerial photographs [Geographical Survey Institute, 2006], respectively. Figure 9(c) shows the overlay of the areas detected in this study and the manually detected areas.

The detection percentage of this analysis is calculated from the number of correctly detected areas and that of un-detected areas. Table 2 shows the relationship between the detection percentage and the scale of the slope failure. The detection percentage is almost 90% for the slope failures whose area is more than 1,000m^2 while the percentage is about 50% for the slope failure smaller than 500m^2. Totally 85% of the slope failures are correctly detected in the analysis.

The causes of these un-detections are broadly classified into three categories. Category 1 is that the flow out of vegetation is not clearly observed. Category 2 is that the difference of NDVI in the slope failure is less than the threshold value. Category 3 is that the slope failure itself is covered with shadow. Table 3 shows the relationship between the scale of slope failure and the number of the un-detections classified into each category.

Table 2 Detection Percentage of the Analysis

Failure area (m^2)	No. of Detected areas	No. of Un-detected areas	Detection percentage(%)
~500	58	48	54.7
500~1,000	128	37	77.6
1,000~2,000	180	26	87.4
2,000~5,000	189	19	90.9
5,000~	169	5	94.1
Total	724	135	84.3

Table 3 Number of Un-Detected Areas Classified into Three Categories

Failure area (m^2)	Categoy 1	Category 2	Category 3	Total
~500	0	45	3	48
500~1,000	4	26	7	37
1,000~2,000	4	14	8	26
2,000~5,000	10	3	6	19
5,000~	3	1	1	5
Total	21	89	25	135

Category 1: Flow out of vegetation is not clearly observed.
Category 2: Difference of NDVI in slope failure is less than the threshold.
Category 3: Slope failure area itself is covered with shadow.

According to the classification of failure type [Chigira and Yagi, 2006], the failure type of the Category 1 is the landslide. In some cases of the landslide, the flow out of the vegetation is not clearly observed because the distance of the soil movement is relatively small. It is difficult to detect such kind of landslide by the proposed method.

The comparison of the pre- and post-event images shows that the contrast of NDVI of post-event image is relatively low. Besides, many shadows are observed in the post-event image. These are due to the low observation elevation and the low sun elevation as shown in Table 1. One of the reasons for the un-detections of the Category 2 and 3 might be the low quality of the image.

Regarding the mis-detections, the detected meshes are classified into correct detection or mis-detection by comparing the distribution of slope failures manually detected from aerial photographs. Totally 6019 meshes are detected as the failure area in the analysis while the number of mis-detected meshes is 595. About 90% of the detected meshes are the correct detection. The mis-detected meshes represent a part of paddy field, water area, roofs of buildings and roads. The difference of NDVI between the slope failure areas and the mis-detected areas is low in the post-event image. One of the reasons for the mis-detections might be the low quality of the post-event image. These results show that the number of the mis-detections and un-detections would be reduced if the higher quality image is obtained.

5. CONCLUSIONS

In this study, a methodology to detect slope failure areas using high-resolution satellite images and digital elevation model is introduced. The IKONOS images observed before and after the 2004 Niigata-ken Chuetsu, Japan earthquake are used. The areas whose NDVI computed from the images is remarkably decreased after the earthquake are detected as sloe failure areas. The digital elevation model is used to geometrically rectify the images and to eliminate mis-detection in flat areas. The result shows that the distribution of the detected areas shows good agreement with distribution of the slope failures manually extracted by aerial photographs. Totally 85% of the slope failures are correctly detected in the analysis.

References:

Chigira, M. and H. Yagi (2006), "Geological and Geomorphological Characteristics of Landslide Triggered by the 2004 Mid Niigata Prefecture Earthquake", *Engineering Geology*, 82, 202-221.

Geographical Survey Institute (2006), "1/25,000 Scale Disaster Map in the 2004 Mid-Niigata Prefecture Earthquake" (in Japanese).

Miura, H. and S. Midorikawa (2006), "Slope Failures by the 2004 Niigata-ken Chuetsu, Japan Earthquake Observed in High-Resolution Satellite Image", *Proc. of 5th International Workshop on Remote Sensing for Post Disaster Response*, Paper No. 7, 6pp.

Tucker, C.J. (1979), "Red and Photographic Infrared Linear Combinations for Monitoring Vegetation", *Remote Sensing and Environment*, 8, 127-150.

AN EVACUATION SIMULATION FROM SPREADING FIRE AFTER AN EARTHQUAKE IN AN AREA DENSELY CROWDED WITH WOODEN HOUSES

Yumi MABUCHI[1], Kazuoh SEO[2], Kentaro MOTOKI[3] and Ryo UEDA[4]

1) Graduate Student, Tokyo Institute of Technology, Japan
2) Professor, Tokyo Institute of Technology, Japan
3) Assistant Professor, Tokyo Institute of Technology, Japan
4) Division of Architectural Design and Engineering, Kajima Corp , Japan
mabuchi@enveng.titech.ac.jp, seo@enveng.titech.ac.jp, kmoto@enveng.titech.ac.jp, uedar@kajima.com

Abstract: This study aims to propose an effective evacuation method against spreading fire after an earthquake in an area densely crowded with wooden houses. Firstly, detailed fire risk of the research area is shown using Monte Carlo method. Secondly, multi-agent model is applied for the simulation of evacuation from the fire spreading. And then a case study comparing two evacuation routes is carried out. The case study showed that the evacuation on the eastern route, which is avoiding high-fire risk area, is better than the western route, which is recommended as a main route by the local government, although it includes high-fire risk area. It is concluded that the evacuation planning using practical simulation like this study looks very important and effective.

1. INTRODUCTION

In the 1923 Great Kanto Earthquake, widely spreading fire destroyed the eastern half of Tokyo City, and it made tremendous victims about 80 thousands. Receiving instructions from this experience, Tokyo Metropolitan Office is planning "2-step evacuation system", where people evacuate firstly from their own houses to the nearest temporal gathering space, and secondly from there to much wider regional evacuation space prepared by the local government. However, the government has never try precise check about the risk of confronting fire and/or congestion on the evacuation route. It can be foreseen that evacuating people may encounter fires and cause congestion when they choose the same route at the same time. It could be useful to know the risk of fire spreading after an earthquake in detail in order to evacuate more safely and effectively.

Thus this study aims to propose effective evacuation plan by evaluating the risk of fire spreading and setting up a 2-step evacuation model for the fire risk. In previous research, Aoki et al. (1992) considered an effective guide strategy in evacuation focusing on information and communication. In their model, however, people were expected to go to wide regional evacuation spaces directly without following the 2-step evacuation. And their model did not consider the risk of confronting fire. This study is going to focus on the way people in the research area safely get the wide regional evacuation space in the second step.

2. RESEARCH AREA AND SCENARIO EARTHQUAKE

Research area is installed in Taishido district of Setagaya, Tokyo. The area is densely crowded with wooden houses and very narrow streets, and is considered as the most dangerous areas in Tokyo during a major earthquake, according to the estimation by Tokyo Metropolitan Office (2006) and The Cabinet Office of Japan (2005).

Now the worst fire case is assumed as; a M7.3 earthquake will happen just beneath the northern Tokyo bay, at 18:00 in winter (already very dark, and families are preparing their dinner maybe), accompanied by strong wind of 15m/sec in average velocity. Soil condition in the area will be classified into two different types. Some parts are located in soft soil condition because they have been developed with rice fields. Another parts are located in hard soil condition on the hilly zone. Such different soil condition is identified in Fig.1 with other necessary information.

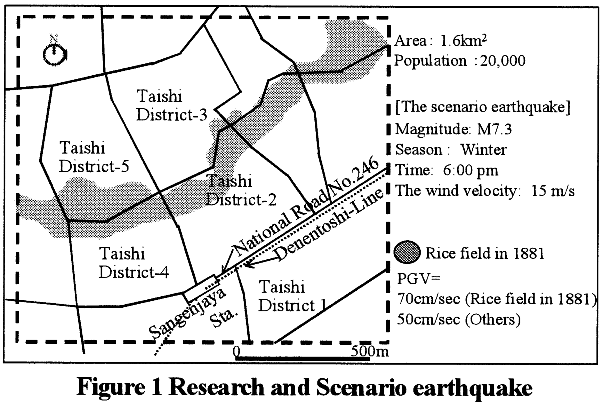

Figure 1 Research and Scenario earthquake

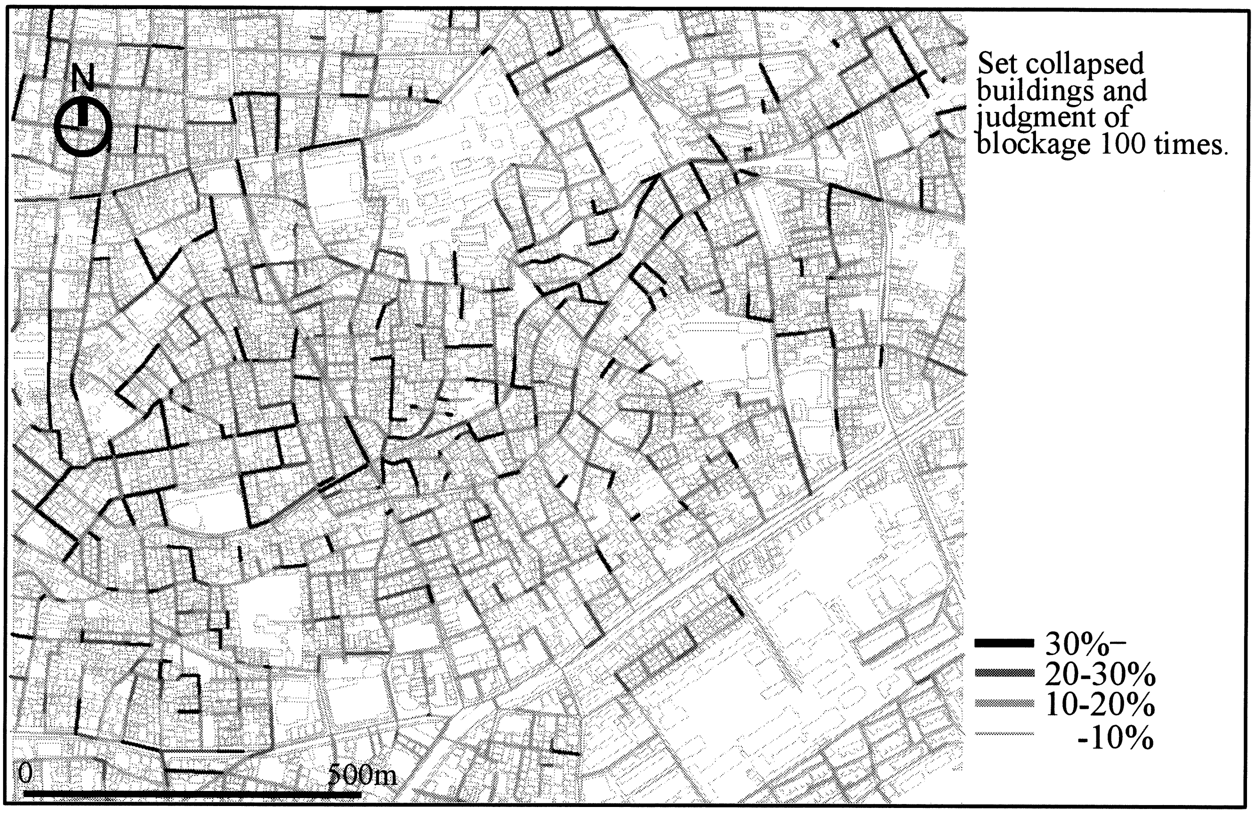

Figure 2 Probability of "Street Blockage"

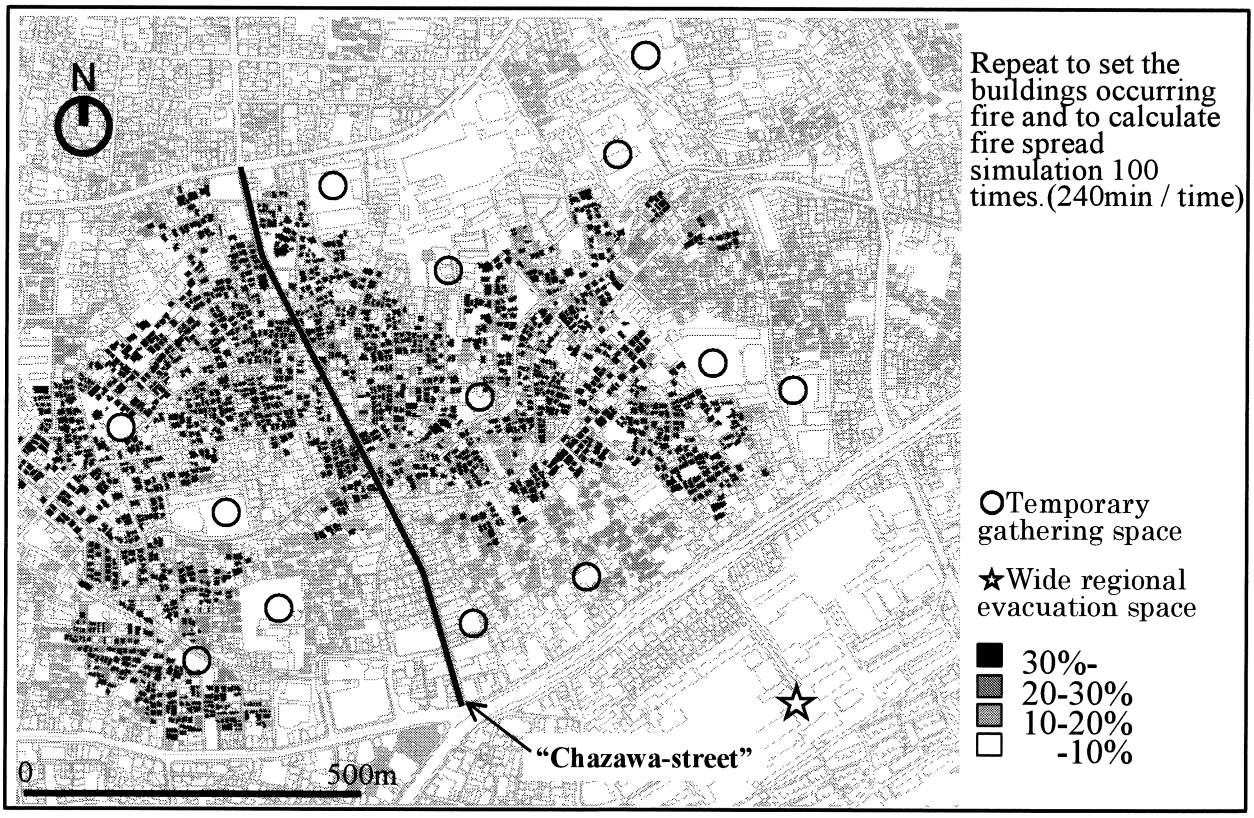

Figure 3 Probability of "Spreading Fire"

3. PROBABILLITY OF "STREET BLOCKAGE" AND "SPREADING FIRE"

When the earthquake happens, spreading fire and street blockage will disturb the evacuation activities. For estimating these risks, firstly the probability of total collapse in buildings and houses was assumed based on the results by the Cabinet Office in Japan (2001). Basic information about existing individual buildings and houses was referred in detail from the survey of land and building made by Setagaya Ward Office. "The street blockage" will be defined by the following method: If a building collapses, rubbles are scattered within the distance as same as the height of the building. If rubbishes cover all width of a street, it is judged as "blocked". "Spreading fire" can be defined by the following method: Buildings with outbreak of fire will be defined using the empirical probability studies about post-earthquake fire disasters in Japan, referring Kanagawa Prefecture (1986). The process of fire spreading after the outbreak can be simulated also if the tolerance of spreading fire from a burning building to another could be assumed. Imagining the worst case, fire-fighting activity is not considered in this study. The first procedure of Specifying collapsed buildings and judging the blockages and the second procedure to specify outbreak fire in some buildings and to make fire spread simulation were carried out a hundred times respectively with Monte Carlo method. Probability of street blockage is presented in Fig.2, and probability of spreading fire is shown in Fig.3 with the locations of evacuation spaces.

4. QUESTIONNAIRE TO LOCAL DISASTER MITIGATION ORGANIZATION

In Setagaya district, local disaster mitigation organization is expected to associate with disaster management. Then questionnaire survey was carried out against the organization members in the research area to obtain resources for evacuation modeling. Table.1 shows the out line of the questionnaire. The aim of the questionnaire is just to confirm the preparedness for a future earthquake, because the area is well known as one of the most dangerous area about the fire spread after a major earthquake. But their response was quite different from expects. For example, the approval time to start the first evacuation from individual home to the nearest temporal gathering spaces (the 1st-Step Evacuation) was obtained in Fig.4, where 54% of answerers chose "When the government urges to start evacuation". It was followed by 28% as "When I notice the damage of my own building or house". Figure 5 shows the person who will lead people in the 1st-step, where around 60% chose "Neighborhoods", "Local Community", or "Local Disaster Management Organization".

The approval time to start the second evacuation, from a temporal gathering space to the wide regional evacuation space (the 2nd-Step Evacuation), was obtained in Fig.6. Answers were mainly divided into two groups, "When fire approaches close to the temporal gathering space" or "When

Table1 The outline about questionnaire

Distribution period	2007/9/1～/9/31
Subject	80 members of LDMO※ in research area ※ Local Disaster Mitigation Organization
Abstract of questionnaire	•Basic information about LDMO •How to evacuate just after earthquake etc.
Distribution method / Correction method	by Hand / by Mail
Collection rate	69% (55/80)

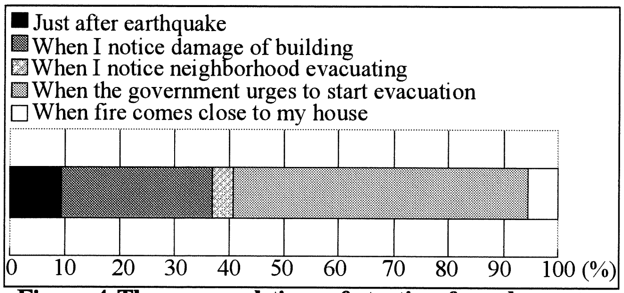

Figure 4 The approval time of starting from home to temporal gathering space (1st-Step Evacuation)

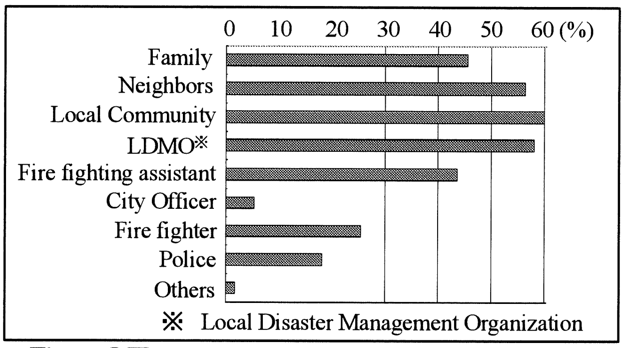

Figure 5 The person who will lead people in 1st-step Evacuation

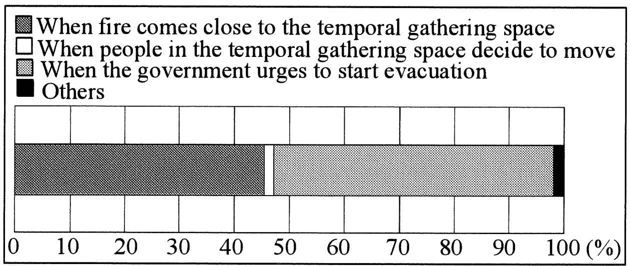

Figure 6 The approval time of starting from temporal gathering space to wide regional evacuation space (2st-Step Evacuation)

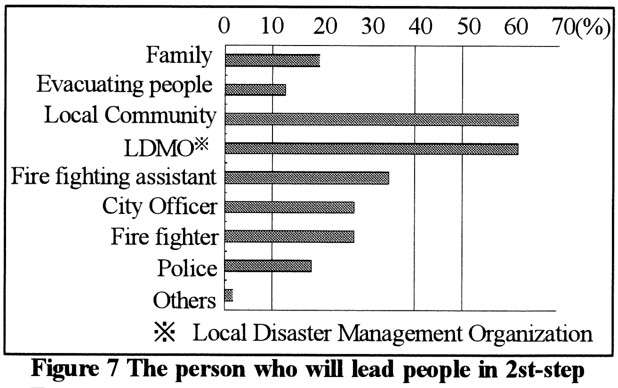

Figure 7 The person who will lead people in 2st-step Evacuation

the Government urges to start evacuation". Fig.7 shows the person who will lead people in the 2nd-step. Around 60% chose "Local Community", or "Local Disaster Management Organization"; they look to depend too much on the local government and local disaster management organization. But they are the leaders in such organization.

Local Disaster Management Organization (LDMO) is expected as the leader of residential people when a disaster happens. Therefore evacuation planning which was made by LDMO is really expected. But from this survey, it was found that LDMO* entrusts the judgment of starting time for evacuation to the Government. However it is almost impossible for the Government to urge people to evacuate just after an earthquake. Actually it should be necessary for LDMO to instruct people at the right time to start evacuation instead of the government. In the simulation of this study, LDMO instructs evacuation activities when the people recognize the fire within 200m in distance in the both cases of the 1st evacuation and the 2nd one.

5. MULTI-AGENT MODEL

The multi-agent model is composed of a lot of agents interacting each other. Agent is a model of human or something that thinks, behaves, and change condition by him/herself. This model is sometimes very useful in the research to modify a complicated human action and so on. Therefore we will apply the multi-agent model in this study.

5.1. EVACUATION MODELING OF AGENT

Model of evacuation after the earthquake is built up with the results mentioned above and the other resources. First of all, the primal settings will be made after the individual preparedness about "Street Blockage", "Fire breakout and spread" and "Primal position of agents" as shown in Fig.8. Then the simultaneous simulation between "Fire spread simulation" and "2-step evacuation with multi-agent model" can be made in deterministic way for individual cases.

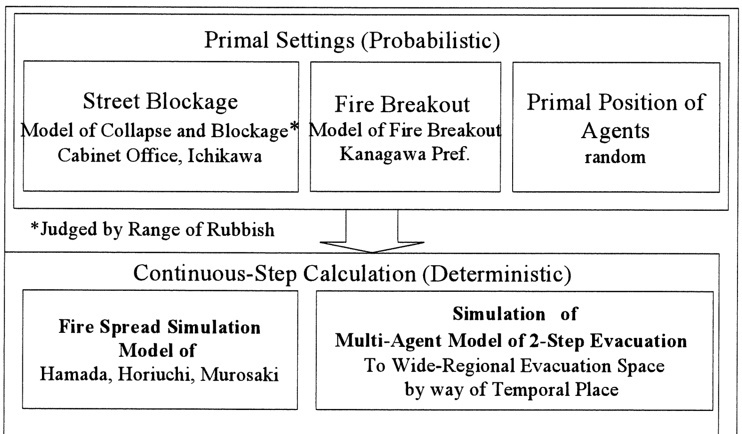

Figure 8 Concept of Multi-Agent Model of 2-step Evacuation

There are 20,000 evacuation agents in the area shown in Figs. 1, 2 and 3. According to the questionnaire survey, the local disaster management organization in this area has not prepared reasonable strategy for urgent evacuation against the fire spread during an earthquake. But they are strongly expected to take the leadership for residential people. Thus in this model, agents start the first evacuation to the nearest temporal gathering space when spreading fire is recognized within 200m in distance. In the same way, agents start the second evacuation from the temporal gathering space to the wide regional evacuation space, that has been prepared by the government, when the fire approaches within 200m to the temporal gathering space. If an agent encounters the fire within 50m on the way to the evacuation space, he or she need to back from the fire and selects another direction that minimizes the distance to the destination. Walking velocity of an agent decreases with the congestion of individual streets following Fruin's model. Merely because of saving the computing time, 40 people are regarded as one group (one agent represents 40 people); the authors of this study has made a careful checking about the stability of the results by changing the number of agents, and confirmed there was no bad effects among them. Simulation duration after the earthquake was also confirmed that 4 hours were sufficient enough.

5.2. CASE STUDY

A case study assuming two different evacuation routes was examined in this study. One idea is to take "Chazawa Street" (we define it as "the western route"), and the other one is to take the eastern route avoiding high risk area against the fire, (we call it as "the eastern route"). The western route is recommended as the main route for evacuation by the local government. The concept showing different rules between two evacuation routes can be seen in Fig.9.

As shown in Fig.10, the ratio of people who have completed the evacuation was compared between two different routes, by taking the average among ten different patterns of fire spread. The ratio of people going on the way was also indicated in Fig.10. It may be sure that the ratio of people who have completed evacuation increases in case of the eastern route much faster than the case of the western route. The western route leads people to wide regional evacuation space with the shorter distance than the eastern route. However the result shows that the eastern route looks much better than the western route. For this result it is considered that: In the western route, fire risk is so high that many people start evacuation almost at the same time and there is only one major evacuation street named "Chazawa Street", therefore they cause congestion around there. And the risk of encountering fire in the western route is high and people are obstructed by it. On the other hand, the risk on the eastern route is lower, and route is separated into 3 streets.

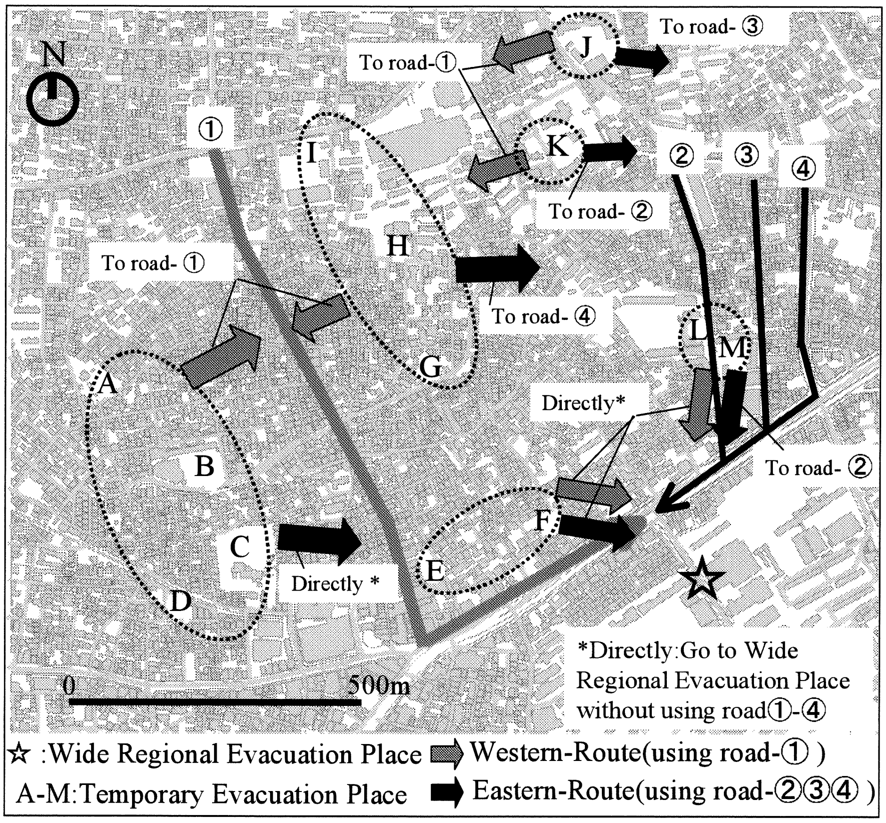

Figure 9 Rules of Evacuation Route

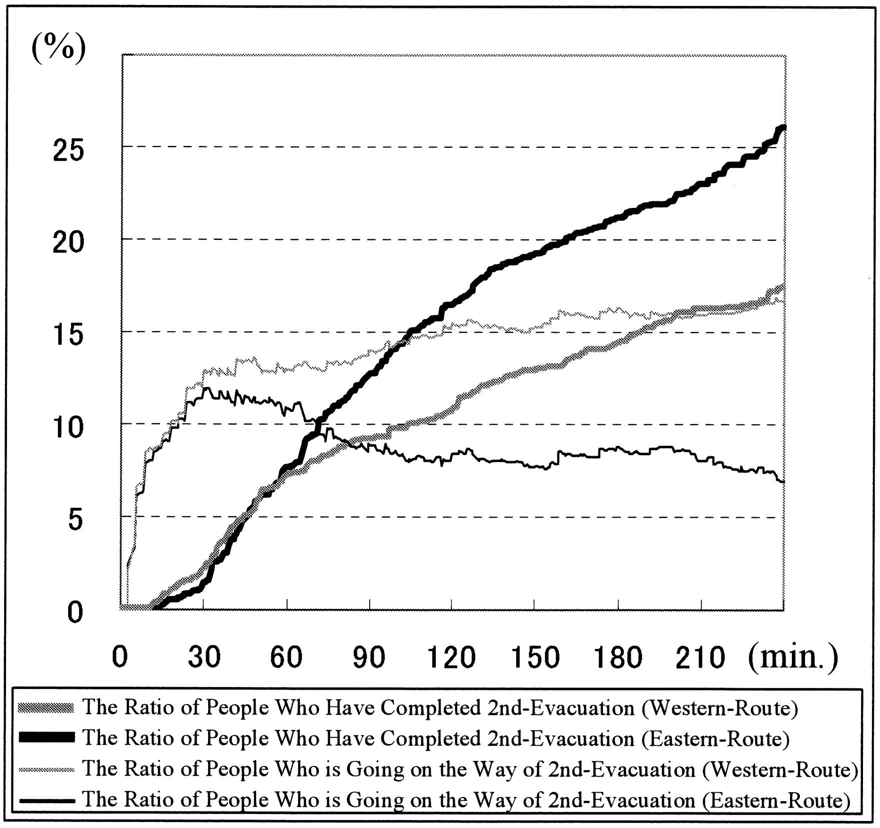

Figure 10 The ratio of people who have completed evacuation and that of people going on the way

The evacuation planning with considering risk of fire spread looks very important and useful after the comparison of the results about evacuation simulation mentioned above.The ratio of people going on the way of the second step gradually increases on the western route after one hour from the earthquake (see Fig.10). It is considered that the congestion became very serious around this time. This congestion is also certified on the view of simulation as shown in Fig.11. This result may support the consideration about obstructions on the western route.

When the time of congestion is found like this way, it will become possible to cope with congestion by emphasizing control of congestion. On the other hand, the ratio of people going on the way of the second evacuation on the eastern route at 30 minutes is around 12%, and after that the ratio is gradually getting down. Finally after 4 hours it becomes only 7%. It means that wide regional evacuation has almost finished. In addition to this result it was found that most of agents about 7% have already moved to the safer place..

6. CONCLUSIONS

A model of the 2-step evacuation in the area densely crowded with wooden houses has been built up, and simulation has been carried out in Taishido district, Setagaya, Tokyo. Since the risk of spreading fire is relatively high in the central and the western area of the district, it is shown that the evacuation on the eastern route is much safer and effective, and also the 2-step evacuation will be able to be finished within 4 hours after the earthquake by using the eastern route. In addition to prepare wide regional evacuation spaces, it is necessary and very important to examine whether they are actually useful or not by making as many as possible simulation studies.

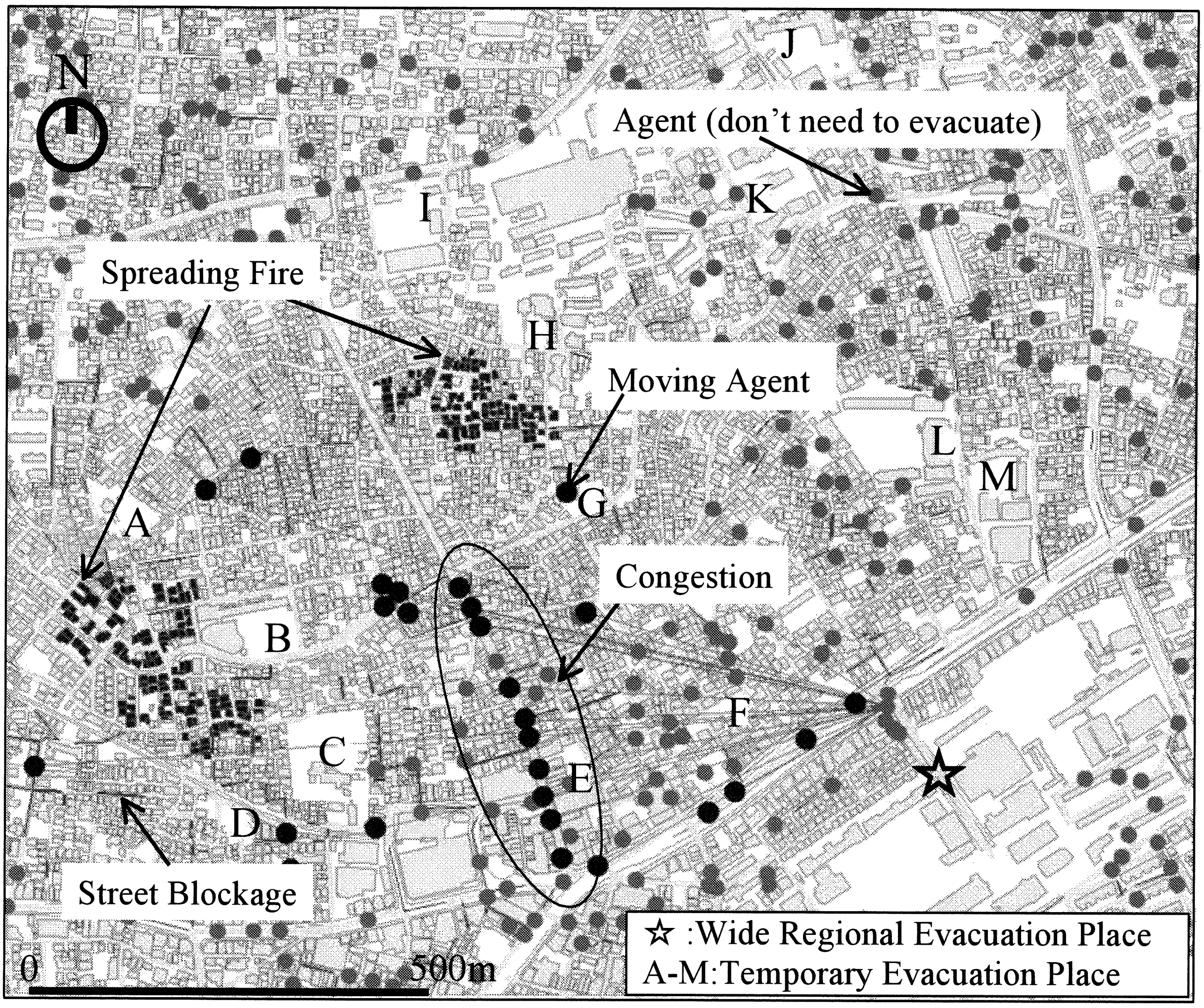

Figure 11 The view of simulation that is shown "Congestion" (Western-route after 120min.)

Acknowledgements:

The authors would like to express their sincere appreciations to the officers in Setagaya Ward and the members of Local Disaster Management Organization for very kind cooperation to our questionnaire survey and to our interviews. The authors acknowledge the financial support from Japan Ministry of Education, Culture, Sport, Science, and Technology (MEXT) for research project "Development of Practical Urban Earthquake Engineering for Disaster Mitigation in Metropolitan Area" at the Center for Urban Earthquake Engineering (CUEE) in Tokyo Institute of Technology.

References

Aoki, Y. Osaragi, T. and Hashimoto, K. (1992) "A Simulation Model Of Evacuation Behavior In The Fire-Spread Urban Area Following Earthquake: Effects Of Hearsay Information Process And Geographical Urban Image", *Journal of architecture, planning and environmental engineering. Transactions of AIJ*, No.140, pp.111-118 (in Japanese)

Cabinet Office of Japan (2005), "Report by Research Conference for Prevention against Earthquake Directly Under the Capital" (in Japanese)

Tokyo Metropolitan Office (2006), "Report about Estimation of Damage in Tokyo by Earthquake Directly Under the Capital" (in Japanese)

Cabinet Office of Japan (2001), "Supporting Manual for Estimation of Damage by Earthquake, Web Site of Cabinet Office of Japan (in Japanese)

Ichikawa et. al. (2001) "Study about Location of Evacuation Space Considering Risk of Street Blockage on Evacuation Route" , *Technical Paper of Annual Meeting AIJ*, F1, pp.489-499 (in Japanese)

Disaster Mitigation Conference of Kanagawa Prefecture (1986), "Report about Estimation of Damage in Kanagawa by Earthquake"

Hamada, M. (1951), "Study about Fire Vol. I" pp.183-188 (in Japanese)

Horiuchi, S. (1994), "Fire Prevention on Architecture -New Edition" pp.183-188 (in Japanese)

Ueda, R. et. al. "Risk Evaluation of Street Blockage and Fire during Earthquake at Densely Populated Wooden District in Suginami, Tokyo" *Japan Earthquake Engineering Symposium*, pp.1374-1377 (in Japanese)

Takahama, T. (2006),"A Study on Railroad Traffic Interruption After an Earthquake. Based on the Questionnaire Survey to Railway Companies" *Journal of Institute of social safety science* No.8,2006.11 pp.253-258 (in Japanese)

Fifth International Conference on Urban Earthquake Engineering
March 4-5, 2008, Tokyo Institute of Technology, Tokyo, Japan

COMPARISON OF SEISMIC BEHAVIOR OF ECCENTRICALLY BRACED STEEL FRAMES WITH FIXED BASE AND PARTIALLY UPLIFT COLUMNS

Midorikawa, M.[1], Toyomaki, S.[2], Hori, H.[3] and Asari, T.[4]

1) Professor, Division of Architectural and Structural Design, Hokkaido University, Japan
2) Takenaka Corporation (Former Graduate Student), Japan
3) Graduate Student, Graduate School of Engineering, Hokkaido University, Japan
4) Assistant Professor, Division of Architectural and Structural Design, Hokkaido University, Japan
midorim@eng.hokudai.ac.jp, toyomaki.shingo@takenaka.co.jp, taikenhirotake@yahoo.co.jp, asari@eng.hokudai.ac.jp

Abstract: Previous studies have suggested that rocking vibration accompanied with uplift motion might reduce the seismic damage of buildings subjected to strong earthquake motions. In this paper, the seismic response of a braced steel frame with partial columns allowed to uplift is evaluated and compared with that of a fixed-base frame by numerical analyses, whose prototype test frame of a full-scale six-story eccentrically braced steel building structure was tested by the pseudo-dynamic testing system in Tsukuba in early 1980's. The results show that the base shears in the column-uplift frame are significantly reduced as compared to the fixed-base frame, while the maximum roof drifts of the column-uplift frame are larger than those of the fixed-base frame regardless of the ground motion intensity because of the reduction of the rotational rigidity at the uplift-column bases.

1. INTRODUCTION

It has been pointed out by past studies (Housner 1963, Rutenberg et al. 1982, Hayashi 1999) that the effects of rocking vibration accompanied with uplift motion might reduce the seismic damage to buildings subjected to strong earthquake ground motions. The influence of uplift motion on the seismic behavior of building structures has been reasonably explained through the simple analysis (Meek 1975).

Based on these studies, structural systems have been studied and developed which allow the rocking and uplift motion under proper control during strong earthquake motions. One of the features of an uplift structural system is that the maximum strain energy associated with the horizontal deformation of a superstructure is reduced, because a portion of the total earthquake input energy exerted to the structural system is dissipated by the potential and kinetic energy associated with the vertical motion of the structural system as shown in the previous work. The references mentioned above are listed in other publication (Midorikawa et al. 2006).

An uplift structural system under research and development by the authors (Azuhata et al. 2004, Midorikawa et al. 2006) makes use of the uplift yielding mechanism of specially designed flexing base plates. When the base plates yield due to column tension during a strong earthquake motion, the columns uplift and allow the building structure to rock.

In this paper, presented are the comparison of the analytical results of the seismic behavior of six-story braced-steel structures with fixed base and partially uplift columns and also the evaluation of analytical results as compared with the full-scale seismic tests on an eccentrically braced steel structure (Foutch 1989), which were carried out in Tsukuba in 1982 to 1984. The objectives of the study are to improve the understanding of the dynamic response of a structure with partially uplift columns subjected to earthquake motions, and to validate analytical models to simulate the response of partial rocking through column uplift.

2. FULL-SCALE SEISMIC TEST STRUCTURE

The full-scale test structure was originally designed as a six-story concentrically braced-steel building with fixed base. An eccentric bracing system was installed in the center frame (Frame B) following the removal of the concentric braces from Frame B upon completion of Phase I test (Foutch 1989). The design and construction of the test structure, test program, test procedure, and instrumentation are described in detail in other publication (Foutch 1989).

In the tests, the simulated seismic forces by the pseudodynamic test system were applied in the direction

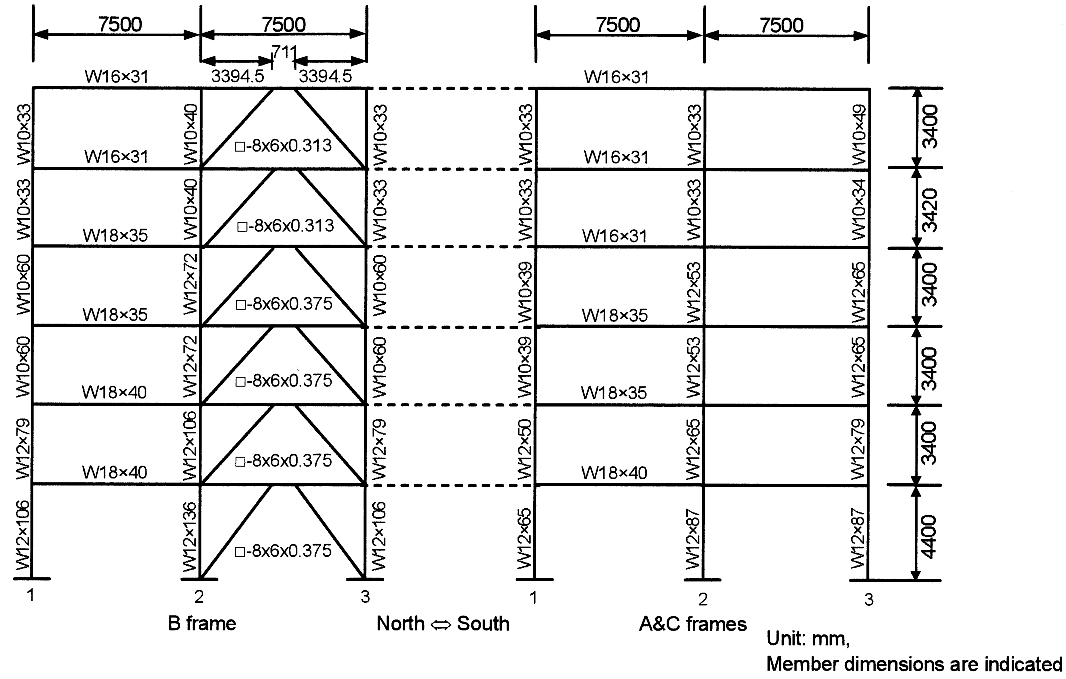

Figure 1 Analytical Model

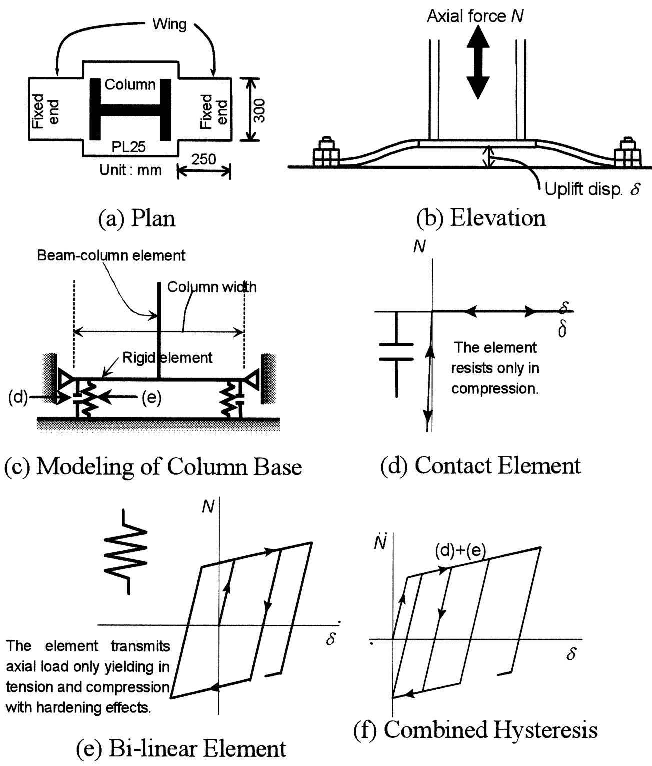

Figure 2 Uplift Yielding Base-plate

Table 1 Earthquake Ground Motions

Seismic motion	Year	PGA (cm/s²)	PGV (cm/s)
Taft S21°W	1952	173	15.4
El Centro NS	1940	342	33.1
JMA Kobe NS	1995	818	84.7

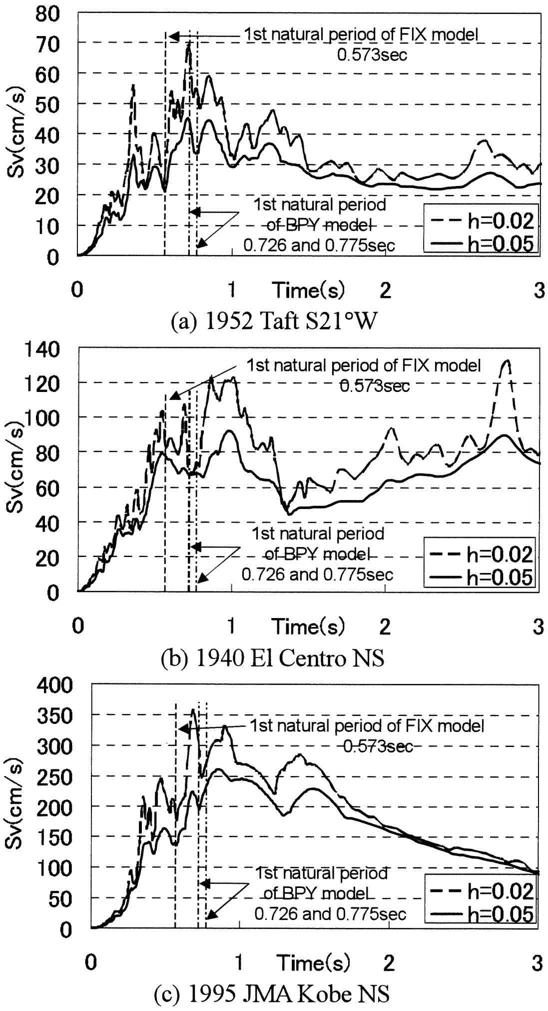

Figure 3 Velocity Response Spectra

of Frames A, B and C. The response of the structure to the 1952 Taft S21°W record scaled to 65 cm/s^2 for the elastic test and to 500 cm/s^2 for the inelastic test was simulated. Since relatively small damage was observed in the structure during the inelastic test, a series of three tests using sinusoidal input motions were carried out.

3. ANALYTICAL MODELLING AND ANALYSES

3.1 Fixed-base Model

The modified version of the two-dimensional nonlinear dynamic analysis program DRAIN-2DX, originally developed by Kanaan and Powell (1973), was used to evaluate and compare the seismic response of the analytical models. The mathematical idealization of the structure is illustrated in Fig. 1. All column bases of this model were fixed and referred to as Fixed-base model.

Two element types, beam-column and beam elements, were used to model the columns, composite girders, braces, and shear links located at midspan of the girders in the braced bay.

The main assumptions used to model the test structure are followed by the previous work (Midorikawa et al. 1989) except for the assumption that the restraint on axial deformation of columns by diagonal cross-bracing and girders in the transverse direction were neglected.

It is assumed that the viscous damping resulted from a combination of the mass-dependent and initial stiffness-dependent effects (Rayleigh-type viscous damping). The critical damping ratio of 2.0% was introduced to the first two vibration modes referring to the previous work (Goel 1989).

3.2 Column-uplift Base-plate Yielding Model

The main assumptions used to model the structure with partially uplift columns and yielding base-plates were the same as Fixed-base model except for the following.

The yielding base-plates to allow the column uplift as shown in Figs. 2(a) and (b) were installed at the bottom of two columns of the braced bay at the first story in Frame B. The base-plate configuration was determined so that its uplift yield strength was approximately 10% of the column axial load. This base-plate yielding structure was referred to as BPY model.

Fig. 2(c) shows the mathematical model of a yielding base-plate which represents its deformation mechanism as shown in Fig. 2(b). This model was assumed to have two sets of a parallel combination of contact and bi-linear elements, as shown in Figs. 2(d) and (e), at both ends of rigid element whose length is equal to the column width. Fig. 2(f) shows the combined hysteresis model of the yielding base-plate that used the kinematic hardening scheme whose strain hardening stiffness was set at 15% of the initial elastic stiffness, referring to the previous study (Ishihara et al. 2003).

3.3 Earthquake Ground Motions

Three sets of earthquake ground acceleration records listed in Table 1 were selected for the seismic response analyses. The elastic velocity response spectra of three earthquake ground motions are shown in Fig. 3. The maximum ground velocity of each record with the duration time of 20 seconds was scaled to 30 through 150 cm/s in the analyses.

4. ANALYTICAL RESULTS AND DISCUSSION

4.1 Natural Periods and Pushover Analyses

The natural periods from the analytical and test results of the fixed-base structure are listed in Table 2. The fundamental natural period of of BPY model is 0.726 and 0.775 s.

Fig. 4 shows the story shear versus interstory drift relationships at each floor level from the pushover analysis for Fixed-base model under the A_i distribution of story shears along the height. The story shear versus roof drift relationships from the pushover analyses for Fixed-base and BPY models are shown in Fig. 5.

Table 2 Natural Periods of Fixed-base Model

Mode	1st	2nd	3rd
Model (s)	0.573	0.207	0.115
Test (s)	0.545	0.193	0.106

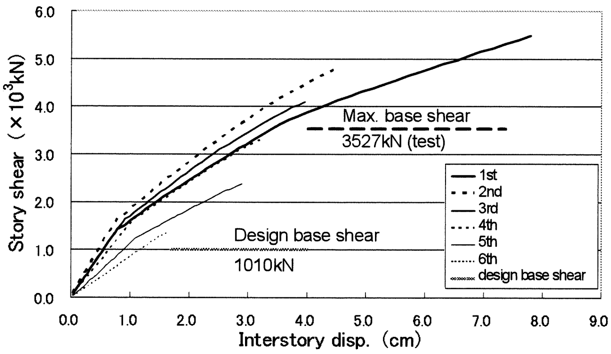

Figure 4 Story Shear versus Interstory Drift Relations

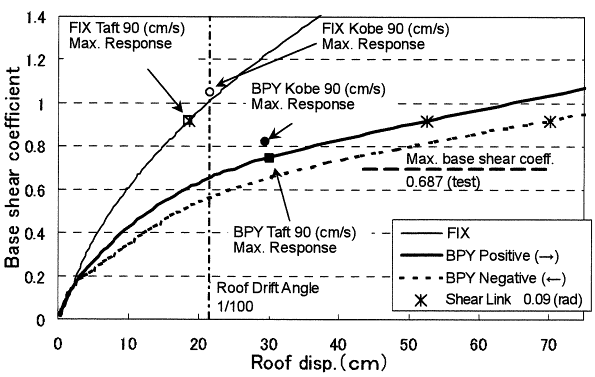

Figure 5 Base Shear Coefficient versus Roof Drift Relations

4.2 Seismic Response of Fixed-base Structure

Comparison of fixed-base model and test structure

The time histories of the roof drifts of BPY model and the test structure subjected to the Taft record are shown in Fig. 6. The both results harmonize well with each other in the inelastic response. Fig. 7 shows the shear force versus shear deformation relationships of the 2FL shear link to the Taft record of 500 cm/s^2. The maximum deformation from the analysis is slightly smaller than that from the test. The shear link attains the ultimate shear strength at the shear deformation of 0.09 rad. during the sinusoidal tests. It is reported in the previous test (Popov et al. 1987) that the ultimate and design-limit shear deformation of a fully stiffened shear link are 0.10 and 0.06 rad., respectively.

Maximum responses versus input ground velocity

The maximum shear deformation of the second-floor (2FL) shear link (SL) versus input ground velocity relationships of Fixed-base model are shown in Fig. 8, and the maximum roof drift versus input ground velocity relationships in Fig.9. The maximum roof drift angle to the Taft record of 500 cm/s^2 is 1/272 (7.9 cm), while it is 1/108 (19.8 cm) when the shear deformation of 2FL shear link reaches the test-ultimate value of 0.09 rad.

4.3 Comparison of Seismic Response of Fixed-base and BPY Models

Time histories of roof drifts and uplift displacements

The roof drift time histories of Fixed-base and BPY models subjected to the Taft record of 90 cm/s are shown in Fig. 10, and the uplift displacement time histories at the column bases of the braced bay of BPY model in Fig. 11. The roof drift of BPY model is considerably larger than that of Fixed-base model. The maximum uplift displacement of BPY model is 8.56 cm corresponding to the rocking angle of 1/88 in the braced bay.

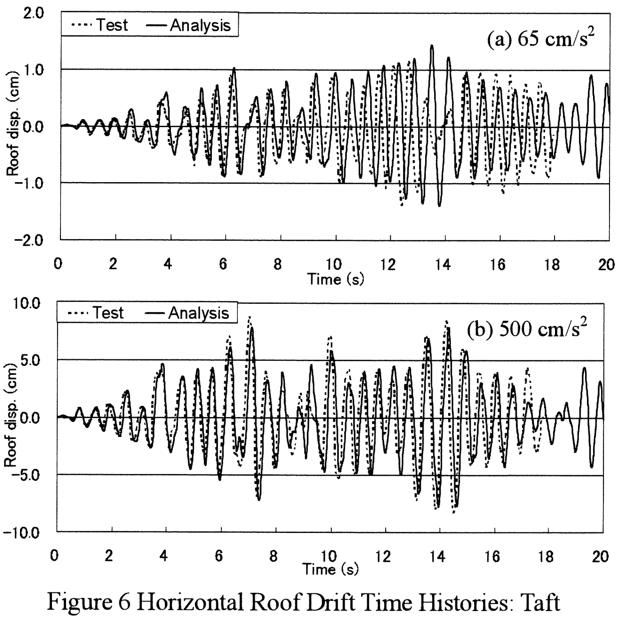

Figure 6 Horizontal Roof Drift Time Histories: Taft

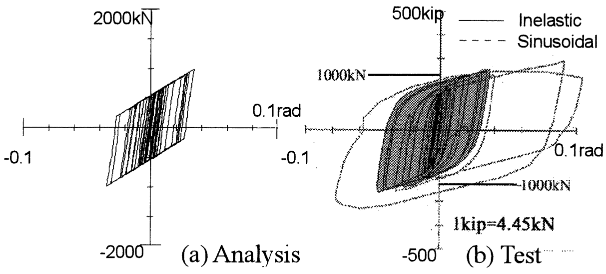

Figure 7 Shear Force versus Shear Deformation Relations of 2nd-floor Shear Link

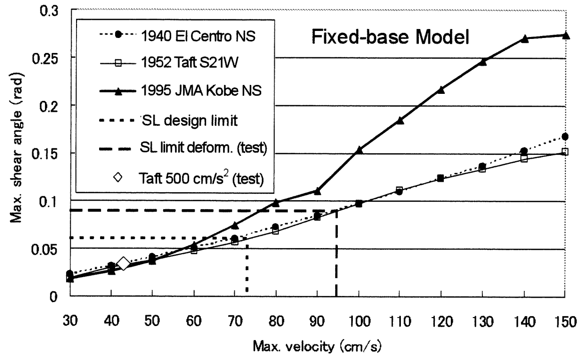

Figure 8 Maximum Shear Deformation versus Input Ground Velocity Relations of 2nd-floor Shear Link

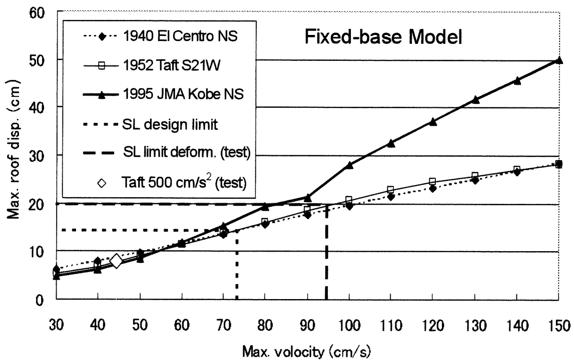

Figure 9 Maximum Roof Drift versus Input Ground

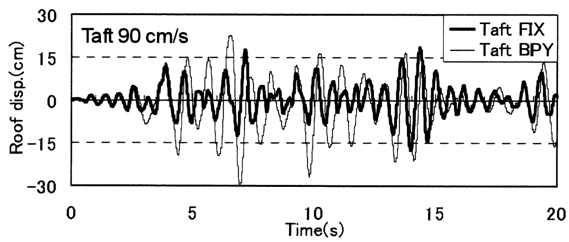

Figure 10 Horizontal Roof Drift Time

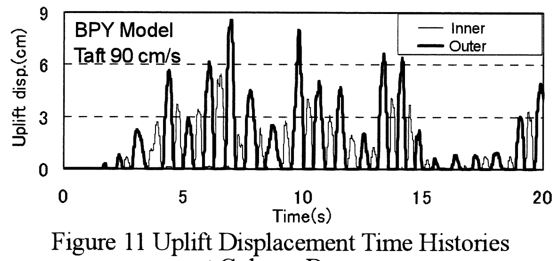

Figure 11 Uplift Displacement Time Histories at Column Bases

Maximum responses versus input ground velocity

The maximum uplift displacement at the column bases of BPY model versus input ground velocity relationships are shown in Fig. 12. The maximum uplift displacements subjected to the JMA Kobe record of 90 cm/s are 10.4 and 8.35 cm at the inner and outer column bases, respectively, that correspond to the rocking angle of 1/72 and 1/90, respectively, in the braced bay.

The maximum roof drift versus input ground velocity relationships of Fixed-base and BPY models are shown in Fig. 13. The roof drift of BPY model is considerably larger than that of Fixed-base model because of the reduction of the rotational stiffness at the uplift-column bases in BPY model.

The maximum base shear coefficient versus input ground velocity relationships of Fixed-base and BPY models are shown in Fig. 14. The base shear coefficient of BPY model is limited to a relatively constant value over the input ground velocity of about 90 cm/s, while that of Fixed-base model increases monotonously.

Envelopes of maximum responses

The envelopes of the maximum interstory drifts, story shears and overturning moments (OTMs) of Fixed-base and BPY models are shown in Fig. 15.

The maximum interstory drifts of BPY model to the Taft and JMA Kobe records of 90 cm/s are much larger than those of Fixed-base model as shown in Fig. 15(a). As a result, the inelastic deformation of structural members in the moment-resisting frames of BPY model becomes larger than that of Fixed-base model.

The maximum story shears at the lower stories of BPY model are definitely smaller than those of Fixed-base model, while they become nearly equal at the upper stories, as shown in Fig. 15(b).

The OTMs of BPY model are certainly smaller than those of Fixed-base model as shown in Figs. 15(c) and (d). There is no significant difference between the input ground velocity of 90 and 120 cm/s^2 in OTM of BPY model. On the other hand, there is a definite difference in OTM of Fixed-base model.

Hysteretic behavior of Fixed-base and BPY models

The base OTM versus roof drift relationships to the Taft record of 90 cm/s are shown in Fig. 16. The restoring force versus deflection relationship of Fixed-base model remains quite stable, whereas that of BPY model shows the attribute of the fluctuation in the restoring force. This is probably the effect of higher mode vibration induced in uplift structures as pointed out by the previous studies (Meek 1975, Ishihara et al. 2006).

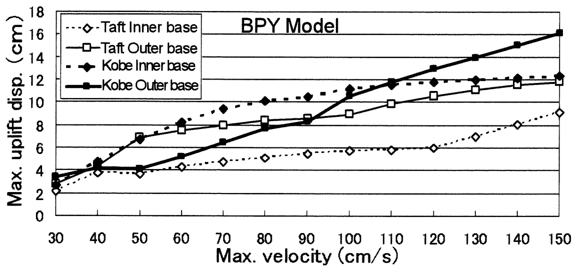

Figure. 12 Maximum Uplift Displacement versus Input Ground Velocity Relations at Column Bases

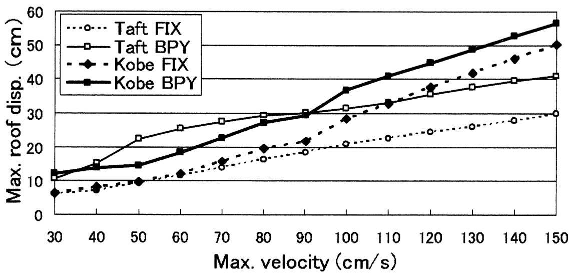

Figure 13 Maximum Roof Drift versus Input Ground Velocity Relations

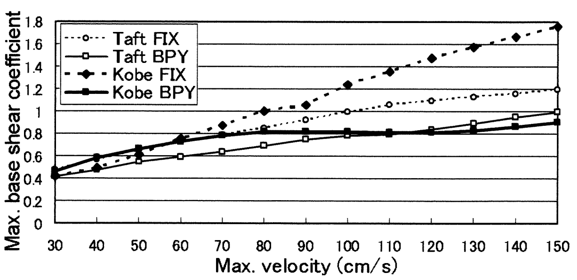

Figure 14 Maximum Base Shear Coefficient versus Input Ground Velocity Relations

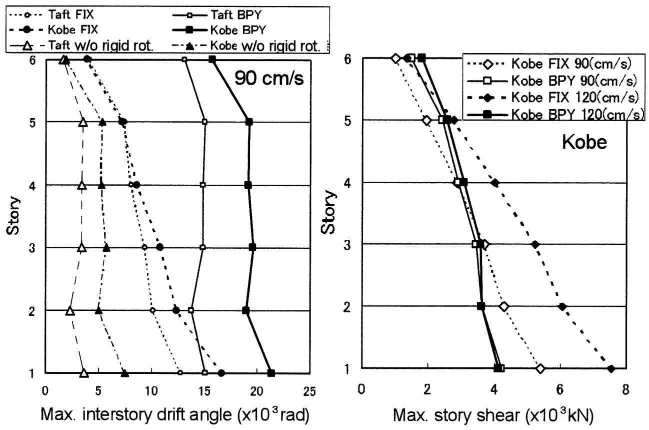

(a) Maximum Interstory Drifts (b) Maximum Story Shears

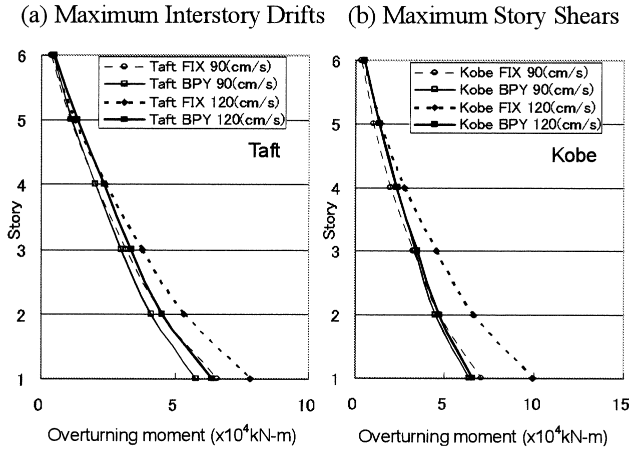

(c) Max. Overturning Moments (d) Max. Overturning Moments

Figure 15 Envelopes of Maximum Responses

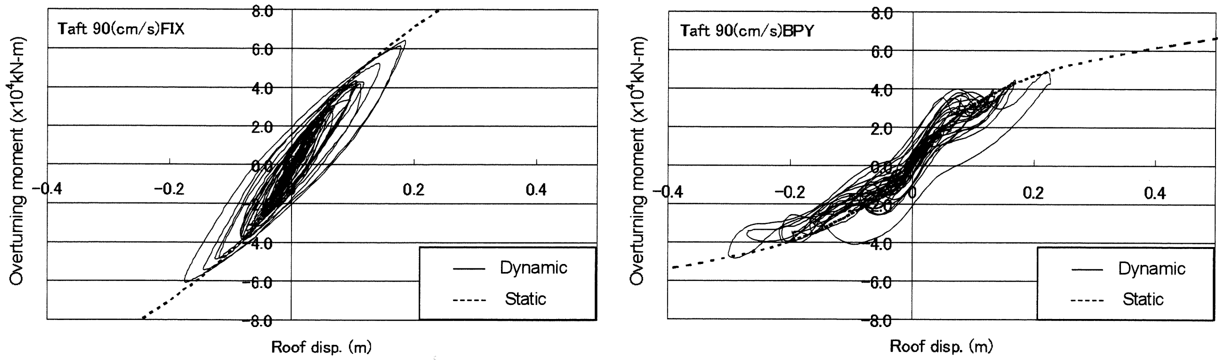

(a) Fix-base Model: Taft S21°W; 90 cm/s (b) BPY Model: Taft S21°W; 90 cm/s

Figure 16 Base Overturning Moment versus Roof Drift Relations

5. SUMMARY AND CONCLUSIONS

The results of this study are summarized below.

(1) The analytical results of the fixed-base structure subjected to the Taft record of 500 cm/s^2 show good agreement with the inelastic test results of the full-scale test structure. In addition, the seismic behavior of the prototype test structure subjected to an earthquake ground motion of intensity greater than that used in the tests is validated by the analyses, which was not accomplished in the seismic tests.

(2) The base shears in the column-uplift structure are significantly reduced as compared to the fixed-base structure, whereas the maximum roof drifts of the column-uplift structure are considerably larger than those of the fixed-base structure regardless of the ground motion intensity because of the reduction of the rotational rigidity of the uplift-column bases of the braced bay. As a result, the inelastic deformation of structural members of the column-uplift structure becomes larger than that of the fixed-base structure.

The results discussed above regarding the seismic behavior of a partial-column uplift system are not directly relevant to the practical design of structures. Further study is needed to establish the optimal range of design parameters of partial-column uplift systems to achieve the desired system performance under various intensities of earthquake ground motions.

References:

Housner, G. W. (1963), "The behavior of inverted pendulum structures during earthquakes," *Bulletin of the Seismological Society of America*, 53(2), 403-417.

Rutenberg, A., Jennings, P. C. and Housner, G. W. (1982), "The Response of Veterans Hospital Building 41 in the San Fernando Earthquake, *Earthquake Engineering and Structural Dynamics*, 10(3), 359-379.

Hayashi, Y., Tamura, K., Mori, M. and Takahashi, I. (1999), "Simulation analyses of buildings damaged in the 1995 Kobe, Japan, earthquake considering soil-structure interaction," *Earthquake Engineering and Structural Dynamics*, 28(4), 371-391.

Meek, J. W. (1975), "Effect of foundation tipping on dynamic response," *Journal of the Structural Division*, ASCE, 101(7), 1297-1311.

Azuhata, T., Midorikawa, M. and Ishihara, T. (2004), "Energy dissipation mechanism and maximum response displacement prediction of steel frames with yielding base plates in uplift motion for seismic response reduction," *Journal of Structural and Construction Engineering*, AIJ, 583, 61-68 (in Japanese).

Midorikawa, M., Azuhata, T., Ishihara, T. and Wada, A. (2006), "Shaking table tests on seismic response of steel braced frames with column uplift," *Earthquake Engineering and Structural Dynamics*, 35(14), 1767-1785.

Foutch, D. A. (1989), "Seismic behavior of eccentrically braced steel building," *Journal of Structural Engineering*, ASCE, 115(8), 1857-1876.

Kanaan, A. E. and Powell, G. H. (1973), "General purpose computer program for inelastic dynamic response of plane structures," *Report No. UCB/EERC-73/6*, EERC, University of California, Berkeley, CA.

Midorikawa, M., Nishiyama, I. and Yamanouchi, H. (1989), "Analytical evaluation of K-braced structure seismic test," *Journal of Structural Engineering*, ASCE, 115(8), 1930-1948.

Goel, S. C. and Boutros, M. K. (1989), "Analytical modeling of Phase 2 steel structure," *Journal of Structural Engineering*, ASCE, 115(8), 1949-1959.

Ishihara, T., Midorikawa, M., Azuhata, T. and Wada, A. (2003), "Hysteresis characteristics of column base for rocking structural systems with base plate yielding," *Journal of Constructional Steel*, 11, 51-56 (in Japanese).

Popov, E. P., Kasai, K. and Engelhaldt, M. D. (1987), "Advances in design of eccentrically braced frames," *Earthquake Spectra*, 3(1), 43-55.

Ishihara, T., et al. (2006), "Shaking table tests on uplifting responses of reduced-scale models of multi-story buildings considering stiffness distribution," *Journal of Constructional Steel*, 14, 327-334 (in Japanese).

Fifth International Conference on Urban Earthquake Engineering
March 4-5, 2008, Tokyo Institute of Technology, Tokyo, Japan

MODE CONTROL SEISMIC DESIGN WITH DYNAMIC MASS

Takeshi Furuhashi[1) and Shinji Ishimaru[2)

1) Associate Professor, College of Science and Technology, Nihon University, Tokyo, Japan
2) Professor, College of Science and Technology, Nihon University, Tokyo, Japan
furuhashi@arch.cst.nihon-u.ac.jp, ishimaru@arch.cst.nihon-u.ac.jp

Abstract: This paper presents a new response control method for building structures against earthquakes by making use of the inertia element connected between mass points. The device is named as the dynamic mass which generates the force to be proportional to the acceleration difference between mass points. In this paper, two topics are introduced. One of them is the method which the natural period of structure can be elongated keeping its mode shapes. Next topic is the method that can be made all participation factors of higher modes 0 except the 1st mode. It is very simple to make the suitable combination of the dynamic mass of each story which is satisfied to the above situation. As the result, response shear coefficients of all stories become same, because the response for higher modes does not occur.

1. INTRODUCTION

In general, seismic designs of buildings are performed by adjusting the stiffness and the strength and, in recent years, by artificially giving the damping. The response control by making use of these devices means to design the stiffness factor and the damping factor in the equation of motion.

On the other hand, there are studies to control the response by making supplementary masses behave according to the displacement difference between mass points.

Kawamata has researched the effect of the input decrease and the elongation of the natural period by making use of a supplementary mass produced by movement of the fluid [1].

Okumura has proposed the vibration interception connection mechanism produced by idealizing the function of the supplementary mass between mass points [2].

Ishimaru has proposed the mode control method by adjusting participation factors of structures, on a basis of getting knowledge of the fact that supplementary masses change the mass distribution in the equation of motion [3].

These response control methods using the supplementary mass induce characteristic changes of the vibration system like a decrease effect for ground motion input etc., which can not be obtained by only controlling the stiffness and damping.

Rightly, the damping element and the stiffness element each generate the forces to be proportional to the velocity difference and the displacement difference between mass points. After the above expression, the authors newly defines "the dynamic mass" (the inertia connection element between mass points) that generates the force to be proportional to the acceleration difference between mass points.

The high performance "dynamic mass" to be much greater than its actual mass can be realized by using the displacement amplification mechanism such as the rotation mechanism etc.

Thus, we can gain a quite new response control method. That is, the three main factors of mass, damping and stiffness in the equation of motion can be adjusted in order to satisfy the engineer's target design performance for structures.

This paper introduces two topics. One of them is the method which the natural period of structure can be elongated keeping its mode shapes. Next topic is the method that can be made all participation factors of higher modes 0 except the 1st mode.

2. DYNAMIC MSSS (INERTIA CONNECTION ELEMENT BETTWEEN MASS POINTS)

Fig.1 shows the concept of the dynamic mass which is composed of the rotation body with combined the inner wheel and the outer wheel. And mass m is concentrated at the outer wheel.

Now, we define the amplification ratio β which is the ratio of the radius of the outer wheel to the inner wheel. When the inner wheel is pushed in the direction of the tangent with the acceleration α, the inertia force of the mass m of the outer wheel is $m\beta\alpha$. And the reaction force to push the inner wheel becomes $\beta^2 m\alpha$.

As a result, the mass m of the outer wheel can display the magnitude of $\beta^2 m$ at the position of inner wheel which means the formation of mass amplification device.

If β is large enough, this mechanism can be assumed as the dynamic mass that generates the force to be proportional to the acceleration difference between mass points.

Rightly, if the small damping element and stiffness element are installed at the position of the outer wheel, we can create the damping and stiffness amplification devices. Now, we express the magnitude of dynamic mass as m' ($=\beta^2 m$) in distinction from the real mass m of the structure.

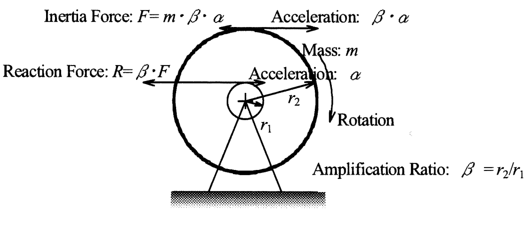

Figure 1 Rotation Body

The practical device of dynamic mass is composed by a little improvement for a viscous damping device called "Rotary Damping Tube" (RDT) which can convert an axial movement into the gyration of the inner cylinder with a ball screw, and generates the resistance force from the viscous body filled between the rotating inner cylinder and the fixed cover cylinder. The displacement of the direction of the tangent of the inner cylinder is amplified to about 5 to 40 time of axial displacement. The effect of the inertia mass of the rotating inner cylinder is amplified to the square of the displacement amplification ratio. It becomes 1,000 times or more the mass of the inner cylinder.

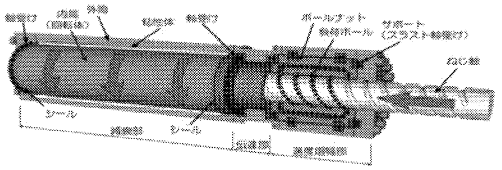

Figure 2 Rotary Damping Tube (RDT)

Thus, if the mass at the rotating inner cylinder is designed with a little larger magnitude, the device can be applied for the practical use. The dynamic mass device with 1,000 ton has been made for trial purposes, and an experiment was executed successfully [4].

3. SINGLE DEGREE OF FREEDOM SYSTEM WITH DYNAMIC MASS

Considering the single degree of freedom vibration system that the above-mentioned rotation body is built into shown in Figure 3(a), or the single degree of freedom vibration system that has the dynamic mass shown in Figure 3(b)

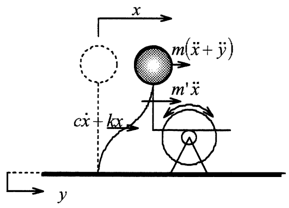

Figure 3(a) Single Degree of Freedom Vibration System with Rotation Body

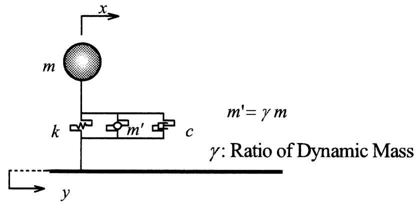

Figure 3(b) Single Degree of Freedom Vibration System with Dynamic Mass
(Hereafter, dynamic mass is shown by ─○─ .)

The equation of motion is given by Eqs.(1),(2) and (3) below:

$$(m+m')\ddot{x}+c\dot{x}+kx=-m\ddot{y} \tag{1}$$

$$(m+m')\ddot{x}+c\dot{x}+kx=-(m+m')\eta\ddot{y} \tag{2}$$

$$\ddot{x}+2h\omega\dot{x}+\omega^2 x=-\eta\ddot{y} \tag{3}$$

in which, $\omega^2=\dfrac{k}{m+m'}=\dfrac{m}{m+m'}\dfrac{k}{m}$

$$h=\frac{c}{2\omega(m+m')}=\frac{c}{2\sqrt{k(m+m')}}=\sqrt{\frac{m}{m+m'}}\frac{c}{2\sqrt{km}}$$

$$\eta=\frac{m}{m+m'}$$

From Eq.(3), it is understood that dynamic mass induces the following characteristic changes to vibration systems.

(1) Elongation of the natural period,
(2) Decrease of damping effect
(3) Decrease effect for acceleration of ground motion.

Considering Eq.(1), in case of k=0 and c=0, the absolute acceleration A becomes Eq.(4) that is not 0. This means that the ground motion acceleration is transmitted through the dynamic mass. As a result, it appears another vibration mode that represents "acceleration transmitted directly through the dynamic mass". However, this effect doesn't become visible at the left side of Eq.(1).

$$A=\ddot{x}+\ddot{y}=-\frac{m}{m+m'}\ddot{y}+\ddot{y}=\frac{m'}{m+m'}\ddot{y}=(1-\eta)\ddot{y} \tag{4}$$

In order to clearly specify the effect of dynamic mass, the equation of motion for two mass system, in which a dummy mass may be added to one mass system as shown in Figure 3, is given by Eq.(5) as follows:

$$\begin{bmatrix} m+m' & -m' \\ -m' & m'+m_0 \end{bmatrix}\begin{Bmatrix} \ddot{x}_1 \\ \ddot{x}_0 \end{Bmatrix}+\begin{bmatrix} c & -c \\ -c & c \end{bmatrix}\begin{Bmatrix} \dot{x}_1 \\ \dot{x}_0 \end{Bmatrix}+\begin{bmatrix} k & -k \\ -k & k+k_0 \end{bmatrix}\begin{Bmatrix} x_1 \\ x_0 \end{Bmatrix}$$
$$=-\begin{Bmatrix} m \\ m_0 \end{Bmatrix}\ddot{y}=-\begin{bmatrix} m+m' & -m' \\ -m' & m'+m_0 \end{bmatrix}\begin{Bmatrix} 1 \\ 1 \end{Bmatrix}\ddot{y} \tag{5}$$

in which, m_0 is dummy mass, $m_0 << m$
k_0 is dummy spring constant, $k_0 >> k$
x_0 is displacement of dummy mass from the ground, $x_0 << 1$

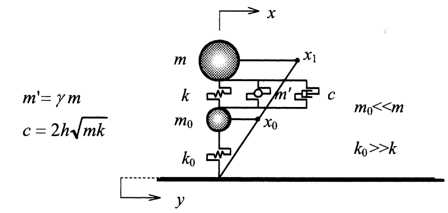

Figure 3 Addition of Dummy Mass

Considering the eigenvalue problem of the left side of Eq.(5) under the condition with disregard of the viscous damping term, the eigenvalues ω, the eigenvectors $\{u\}$, the participation factors β and the participation vectors $\beta\{u\}$ are the following.

$${}_1\omega^2=\frac{k}{m+m'}=\eta\frac{k}{m},\quad {}_2\omega^2=\infty \tag{6}$$

$$\begin{Bmatrix} {}_1u_1 \\ {}_1u_0 \end{Bmatrix}=\begin{Bmatrix} 1 \\ 0 \end{Bmatrix},\quad \begin{Bmatrix} {}_2u_1 \\ {}_2u_0 \end{Bmatrix}=\begin{Bmatrix} 1-\eta \\ 1 \end{Bmatrix} \tag{7}$$

$${}_1\beta=\frac{\{{}_1u\}^T[M]\{1\}}{\{{}_1u\}^T[M]\{{}_1u\}}=\eta,\quad {}_2\beta=\frac{\{{}_2u\}^T[M]\{1\}}{\{{}_2u\}^T[M]\{{}_2u\}}=1 \tag{8}$$

$${}_1\beta\{{}_1u\}=\begin{Bmatrix} \eta \\ 0 \end{Bmatrix},\quad {}_2\beta\{{}_2u\}=\begin{Bmatrix} 1-\eta \\ 1 \end{Bmatrix} \tag{9}$$

Now, the symbol η is defined as the decrease effect of input. The 1st mode is "the mode of the response to the decreased input" and the 2nd mode is "the mode of the acceleration that acts directly through dynamic mass".

4. TWO DEGREE OF FREEDOM SYSTEM WITH DYNAMIC MASS

The equation of motion for two mass system with the dynamic mass shown in Figure 4 is expressed as two mass system of Eq.(10) and as three mass system with a dummy mass of Eq.(11).

In the expression of two mass system Eq.(10), an input index vector at the right side of the equation becomes $\{\eta\}$. Each element of $\{\eta\}$ is a value of 1 or less. The 1st mode and the 2nd mode are the modes of the response to the decreased input.

In the other expression of three mass system Eq.(11), the vector is $\{1\}$, and it has the third mode of the rigid body which directly transmits the acceleration of ground motion in the ratio of the mode shape through the dynamic mass devices.

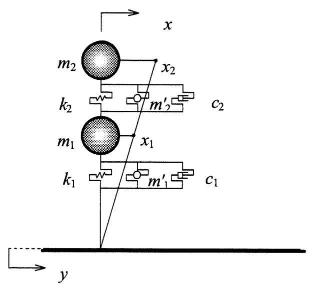

Figure 4 2-Mass System with Dynamic Mass

$$[\hat{M}]\{\ddot{x}\}+[\hat{C}]\{\dot{x}\}+[\hat{K}]\{x\}=-[\hat{M}]\{\eta\}\ddot{y} \tag{10}$$

in which,

$$[\hat{M}]=\begin{bmatrix} m_2+m'_2 & -m'_2 \\ -m'_2 & m'_2+m_1+m'_1 \end{bmatrix},\quad [\hat{C}]=\begin{bmatrix} c_2 & -c_2 \\ -c_2 & c_2+c_1 \end{bmatrix}$$

$$[\hat{K}]=\begin{bmatrix} k_2 & -k_2 \\ -k_2 & k_2+k_1 \end{bmatrix},\quad \{\eta\}=[\hat{M}]^{-1}[\hat{M}_0]\{1\}$$

$$[\hat{M}]=[\hat{M}_0]+[\hat{M}']$$

$[\hat{M}_0]$ is ordinary mass matrix, $[\hat{M}_0]=\begin{bmatrix} m_2 & 0 \\ 0 & m_1 \end{bmatrix}$

$[\hat{M}']$ is dynamic mass matrix, $[\hat{M}']=\begin{bmatrix} m'_2 & -m'_2 \\ -m'_2 & m'_2+m'_1 \end{bmatrix}$

$$[M]\{\ddot{x}\}+[C]\{\dot{x}\}+[K]\{x\}=-[M]\{1\}\ddot{y} \tag{11}$$

in which,

$$[M]=\begin{bmatrix} m_2+m'_2 & -m'_2 & 0 \\ -m'_2 & m'_2+m_1+m'_1 & -m'_1 \\ 0 & -m'_1 & m'_1+m_0 \end{bmatrix}$$

$$[C]=\begin{bmatrix} c_2 & -c_2 & 0 \\ -c_2 & c_2+c_1 & -c_1 \\ 0 & -c_1 & c_1 \end{bmatrix},\quad [K]=\begin{bmatrix} k_2 & -k_2 & 0 \\ -k_2 & k_2+k_1 & -k_1 \\ 0 & -k_1 & k_1+k_0 \end{bmatrix}$$

$[M_0]$ is ordinary mass matrix, $[M_0]=\begin{bmatrix} m_2 & 0 & 0 \\ 0 & m_1 & 0 \\ 0 & 0 & m_0 \end{bmatrix}$

$[M']$ is dynamic mass matrix, $[M']=\begin{bmatrix} m'_2 & -m'_2 & 0 \\ -m'_2 & m'_2+m'_1 & -m'_1 \\ 0 & -m'_1 & m'_1 \end{bmatrix}$

$m_0 << m_1$, $k_0 >> k_1$

5. RESPONSE CONTROL OF TWO DEGREE OF FREEDOM SYSTEM WITH DYNAMIC MASS

There are some effective uses of the dynamic mass for the response control of the structure against earthquakes.

5.1 Response Control Changing Eigenvalues without Changing Eigenvectors

The natural period can be elongated without changing eigenvectors by adding the dynamic mass proportional to the stiffness of each story of the vibration system. Assuming the following eigenvalue problem from Eq.(10),

$${}_s\omega^2[\hat{M}]\{{}_s\hat{u}\}=[\hat{K}]\{{}_s\hat{u}\}$$

Add $\alpha\cdot{}_s\omega^2[\hat{K}]\{{}_s\hat{u}\}$ to the both sides of the equation.

$$
{}_s\omega^2[\hat{M}]\{{}_s\hat{u}\}+\alpha\cdot{}_s\omega^2[\hat{K}]\{{}_s\hat{u}\}=[\hat{K}]\{{}_s\hat{u}\}+\alpha\cdot{}_s\omega^2[\hat{K}]\{{}_s\hat{u}\}
$$
$$
{}_s\omega^2\left([\hat{M}]+\alpha[\hat{K}]\right)\{{}_s\hat{u}\}=\left(1+\alpha\cdot{}_s\omega^2\right)[\hat{K}]\{{}_s\hat{u}\}
$$
$$
\frac{{}_s\omega^2}{\left(1+\alpha\cdot{}_s\omega^2\right)}\left([\hat{M}]+\alpha[\hat{K}]\right)\{{}_s\hat{u}\}=[\hat{K}]\{{}_s\hat{u}\}
$$
$$
\therefore {}_s\omega'^2\left([\hat{M}]+[\hat{M}']\right)\{{}_s\hat{u}\}=[\hat{K}]\{{}_s\hat{u}\} \tag{12}
$$

in which dynamic mass matrix $[\hat{M}']=\alpha[\hat{K}]$

changes eigenvalue to $\quad {}_s\omega'^2=\dfrac{{}_s\omega^2}{\left(1+\alpha\cdot{}_s\omega^2\right)}$

When the dynamic mass $[\hat{M}']=\alpha[\hat{K}]$ is added to the system, the eigenvalues change from ${}_s\omega^2$ to ${}_s\omega'^2$ without changing eigenvectors.

5.2 Response Control Adjusting Participation Factor of 2nd Mode to 0

The participation factor of the 2nd mode can be adjusted to 0 by operating eigenvectors by adding the dynamic mass. If the 1st eigenvector of Eq.(10) is $\{\eta\}$, the 2nd participation factor shown by Eq.(13) becomes 0 because of the orthogonality between the eigenvectors. And the response of the 2nd mode disappears.

$$
{}_2\beta=\frac{\{{}_2\hat{u}\}^T[\hat{M}]\{\eta\}}{\{{}_2\hat{u}\}^T[\hat{M}]\{{}_2\hat{u}\}}=0 \tag{13}
$$

The required conditions to keep this situation can be solved as shown below.

$$
\left.
\begin{aligned}
&\frac{{}_2u_2}{{}_2u_1}=-\frac{m_1}{m_2}\\
&{}_2\omega^2=k_2\left(\frac{1}{\dfrac{m_2\cdot m_1}{m_2+m_1}+m'_2}\right)\\
&m'_1=\frac{k_1}{{}_2\omega^2}=\frac{k_1}{k_2}\left(\frac{m_2\cdot m_1}{m_2+m_1}+m'_2\right)
\end{aligned}
\right\} \tag{14}
$$

in which, the value of m'_2 is arbitrary.

In this condition, the eigenvector of the 1st mode is $\{\eta\}$, and the participation factor of the 2nd mode is 0. The eigenvalue problem of the 1st mode is given by Eq.(15).

$$
{}_1\omega^2[\hat{M}]\{\eta\}=[\hat{K}]\{\eta\} \tag{15}
$$

From Eq.(15), considering $\{\eta\}=[\hat{M}]^{-1}[\hat{M}_0]\{1\}$, the following relations are obtained.

$$
{}_1\omega^2=\frac{k_2(\eta_2-\eta_1)}{m_2},\quad {}_1\omega^2=\frac{k_1\cdot\eta_1}{m_2+m_1} \tag{16}
$$

$$
{}_1\omega^2=\frac{1}{\displaystyle\sum_{i=1}^{2}\left(\frac{1}{k_i}\sum_{j=i}^{2}m_j\right)} \tag{17}
$$

That is, when the 2nd participation factor is 0 by adding the proper combination of the dynamic mass, the 1st eigenvalue is Eq.(17). And from Eq.(16), response shear coefficients of 1st and 2nd stories are the same value.

6. MULTI DEGREE OF FREEDOM SYSTEM WITH DYNAMIC MASS

The equation of motion of n mass system with dynamic mass shown in Figure 6 is given by Eq.(18). The difference between Eq.(18) and a conventional equation of motion, the vector of the right side is not $\{1\}$ but $\{\eta\}$. Each element of $\{\eta\}$ is a value of 1 or less. This indicates the decrease effect of the input.

$$
[\hat{M}]\{\ddot{x}\}+[\hat{C}]\{\dot{x}\}+[\hat{K}]\{x\}=-[\hat{M}]\{\eta\}\ddot{y} \tag{18}
$$

in which,

$[\hat{M}]=[\hat{M}_0]+[\hat{M}']$

$[\hat{M}_0]$ is ordinary mass matrix,

$$
[\hat{M}_0]=\begin{bmatrix}
m_n & 0 & \cdots & & \cdots & 0\\
0 & m_{n-1} & & & & \vdots\\
\vdots & & m_{n-2} & & & \\
 & & & \ddots & & \\
 & & & & m_3 & \vdots\\
\vdots & & & & m_2 & 0\\
0 & \cdots & & \cdots & 0 & m_1
\end{bmatrix}
$$

$[\hat{M}']$ is dynamic mass matrix,

$$
[\hat{M}']=\begin{bmatrix}
m'_n & -m'_n & 0 & \cdots & & \cdots & 0\\
-m'_n & m'_n+m'_{n-1} & -m'_{n-1} & & & & \vdots\\
0 & -m'_{n-1} & m'_{n-1}+m'_{n-2} & \ddots & & & \\
\vdots & & \ddots & \ddots & \ddots & & \vdots\\
 & & & \ddots & m'_4+m'_3 & -m'_3 & 0\\
\vdots & & & & -m'_3 & m'_3+m'_2 & -m'_2\\
0 & \cdots & & \cdots & 0 & -m'_2 & m'_2+m'_1
\end{bmatrix}
$$

$$
[\hat{C}]=\begin{bmatrix}
c_n & -c_n & 0 & \cdots & & \cdots & 0\\
-c_n & c_n+c_{n-1} & -c_{n-1} & & & & \vdots\\
0 & -c_{n-1} & c_{n-1}+c_{n-2} & \ddots & & & \\
\vdots & & \ddots & \ddots & \ddots & & \vdots\\
 & & & \ddots & c_4+c_3 & -c_3 & 0\\
\vdots & & & & -c_3 & c_3+c_2 & -c_2\\
0 & \cdots & & \cdots & 0 & -c_2 & c_2+c_1
\end{bmatrix}
$$

$$
[\hat{K}]=\begin{bmatrix}
k_n & -k_n & 0 & \cdots & & \cdots & 0\\
-k_n & k_n+k_{n-1} & -k_{n-1} & & & & \vdots\\
0 & -k_{n-1} & k_{n-1}+k_{n-2} & \ddots & & & \\
\vdots & & \ddots & \ddots & \ddots & & \vdots\\
 & & & \ddots & k_4+k_3 & -k_3 & 0\\
\vdots & & & & -k_3 & k_3+k_2 & -k_2\\
0 & \cdots & & \cdots & 0 & -k_2 & k_2+k_1
\end{bmatrix}
$$

$\{\eta\}=[\hat{M}]^{-1}[\hat{M}_0]\{1\}$

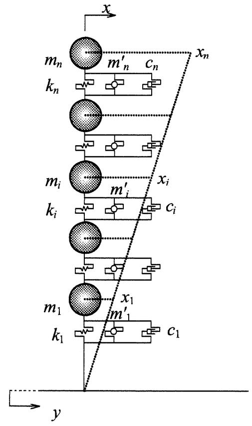

Figure 6 n-Mass System with Dynamic Mass

The equation of motion of n mass system with the dynamic mass is also expressed as $(n+1)$ mass system with a dummy mass. In this expression of $(n+1)$ mass system, the vector of the right side is $\{1\}$, and it has the $(n+1)$th mode of the rigid body.

$$
[M]\{\ddot{x}\}+[C]\{\dot{x}\}+[K]\{x\}=-[M]\{1\}\ddot{y} \tag{19}
$$

in which,

$$[M]=\left[\begin{array}{c:c} [\hat{M}] & \begin{matrix}0\\ \vdots\\ 0\\ -m'_1\end{matrix} \\ \hdashline 0\ \cdots\ 0\ \ -m'_1 & m'_1+m_0 \end{array}\right]=[M_0]+[M']$$

$[M_0]$ is ordinary mass matrix, $[M']$ is dynamic mass matrix.

$$[M_0]=\left[\begin{array}{c:c} [\hat{M}_0] & \begin{matrix}0\\ \vdots\\ \vdots\\ 0\end{matrix} \\ \hdashline 0\ \cdots\ \cdots\ 0 & m_0 \end{array}\right],\quad [M']=\left[\begin{array}{c:c} [\hat{M}'] & \begin{matrix}0\\ \vdots\\ 0\\ -m'_1\end{matrix} \\ \hdashline 0\ \cdots\ 0\ \ -m'_1 & m'_1 \end{array}\right]$$

$$[C]=\left[\begin{array}{c:c} [\hat{C}] & \begin{matrix}0\\ \vdots\\ 0\\ -c_1\end{matrix} \\ \hdashline 0\ \cdots\ 0\ \ -c_1 & c_1 \end{array}\right],\quad [K]=\left[\begin{array}{c:c} [\hat{K}] & \begin{matrix}0\\ \vdots\\ 0\\ -k_1\end{matrix} \\ \hdashline 0\ \cdots\ 0\ \ -k_1 & k_1+k_0 \end{array}\right]$$

$m_0 << m_1$, $k_0 >> k_1$

7. RESPONSE CONTROL OF MULTI DEGREE OF FREEDOM SYSTEM WITH DYNAMIC MASS

As well as the case of two mass system, there are some effective uses of the dynamic mass for the response control of the structure to earthquakes.

7.1 Response Control Changing Eigenvalues without Changing Eigenvectors

The natural period can be elongated without changing eigenvectors by adding the dynamic mass proportional to the stiffness of each level of the vibration system. The proof is similar to the previous case.

7.2 Response Control Adjusting Participation Factors except the 1st Mode to 0

The participation factors of from 2nd to n-th mode can be adjusted to 0 by operating eigenvectors by adding the dynamic mass. The combination of the dynamic mass can be evaluated easily by the following procedure. The detailed procedures can be found in the references 5]-7].

$$\left.\begin{array}{l}
{}_1\omega^2=\dfrac{1}{\sum\limits_{i=1}^{n}\left(\dfrac{1}{k_i}\sum\limits_{j=i}^{n}m_j\right)} \\
\eta_0=0 \\
\eta_i=\eta_{i-1}+\dfrac{{}_1\omega^2}{k_i}\sum\limits_{j=i}^{n}m_j \qquad (1\le i\le n) \\
\{{}_{n+1}u\}^T=\{\{1-\eta\}^T\ 1\} \\
D_i=\dfrac{{}_{n+1}u_i}{{}_{n+1}u_{i-1}} \qquad (1\le i\le n) \\
m'_n=0 \\
m'_i=\dfrac{m_i+m'_{i+1}(1-D_{i+1})}{\dfrac{1}{D_i}-1} \qquad (1\le i\le n-1)
\end{array}\right\} \tag{20}$$

7.3 Example of Response Control with Dynamic Mass

Table 1 shows the process and the result of obtaining the combination of the dynamic mass that adjusts the participation factor of all higher modes of the example vibration system to 0.

Table 1 Evaluation of Dynamic Mass

${}_1\omega$	5.6381	${}_1T=$	1.1144
${}_1\omega^2$	31.788		

i	m_i (ton)	k_i (kN/m)	Σm_i (ton)	$\Sigma(1/k_i\Sigma m_i)$	${}_1u_i = \eta_i$	${}_{n+1}u_i = 1-\eta_i$	D_i	m'_i (ton)
8	750.0	820,000	750.0	0.00091	1.0000	0.0000	0.0000	0
7	760.0	830,000	1,510.0	0.00273	0.9709	0.0291	0.3346	382.09
6	770.0	840,000	2,280.0	0.00545	0.9131	0.0869	0.5018	1,031.66
5	780.0	870,000	3,060.0	0.00897	0.8268	0.1732	0.6077	2,004.36
4	790.0	890,000	3,850.0	0.01329	0.7150	0.2850	0.6745	3,267.00
3	800.0	900,000	4,650.0	0.01846	0.5775	0.4225	0.7201	4,793.33
2	850.0	910,000	5,500.0	0.02450	0.4133	0.5867	0.7533	6,693.43
1	900.0	920,000	6,400.0	0.03146	0.2211	0.7789	0.7789	8,985.31
0	—	—	—	—	0.0000	1.0000	—	—

Table 2 Eigenvalue Analysis of Original System

	1st	2nd	3rd	4th	5th	6th	7th	8th	9th
T	1.000	0.348	0.215	0.159	0.130	0.113	0.103	0.096	0
ω	6.283	18.05	29.28	39.57	48.52	55.79	61.30	65.13	∞
β	1.286	-0.432	-0.251	0.165	0.107	0.072	0.039	-0.019	1.000
u_8	1.000	1.000	-0.918	-0.815	0.720	-0.541	0.392	0.165	0.000
u_7	0.964	0.702	-0.198	0.352	-0.830	1.000	-0.955	-0.475	0.000
u_6	0.893	0.198	0.669	1.000	-0.572	-0.327	1.000	0.738	0.000
u_5	0.791	-0.359	1.000	0.205	0.917	-0.705	-0.512	-0.932	0.000
u_4	0.665	-0.792	0.552	-0.850	0.420	0.898	-0.247	1.000	0.000
u_3	0.518	-0.986	-0.306	-0.700	-0.944	-0.016	0.836	-0.876	0.000
u_2	0.355	-0.893	-0.921	0.423	-0.317	-0.875	-0.885	0.572	0.000
u_1	0.180	-0.529	-0.792	0.915	1.000	0.820	0.519	-0.262	0.000
u_0	0.000	0.000	0.000	0.000	0.000	0.000	0.000	0.000	1.000

Table 3 Eigenvalue Analysis of Controlled System

	1st	2nd	3rd	4th	5th	6th	7th	8th	9th
T	1.114	0.621	0.539	0.459	0.381	0.302	0.220	0.135	0
ω	5.638	10.12	11.66	13.70	16.51	20.83	28.53	46.61	∞
β	1.000	0.000	0.000	0.000	0.000	0.000	0.000	0.000	1.000
u_8	1.000	-0.663	-0.663	-0.669	-0.693	-0.733	-0.816	1.000	0.000
u_7	0.971	-0.601	-0.580	-0.554	-0.521	-0.442	-0.208	-0.987	0.029
u_6	0.913	-0.477	-0.416	-0.325	-0.177	0.137	1.000	0.000	0.087
u_5	0.827	-0.293	-0.172	0.015	0.336	1.000	0.000	0.000	0.173
u_4	0.715	-0.054	0.145	0.457	1.000	0.000	0.000	0.000	0.285
u_3	0.578	0.239	0.535	1.000	0.000	0.000	0.000	0.000	0.423
u_2	0.413	0.590	1.000	0.000	0.000	0.000	0.000	0.000	0.587
u_1	0.221	1.000	0.000	0.000	0.000	0.000	0.000	0.000	0.779
u_0	0.000	0.000	0.000	0.000	0.000	0.000	0.000	0.000	1.000

Table 2 shows the results of the eigenvalue analysis of the original vibration system. The 9th mode doesn't have the meaning in this case.

Table 3 shows the result of those of the vibration system with the dynamic mass. And the participation factors of 2nd to 8th mode of the controlled vibration system are 0. The 9th mode of rigid body (i.e., $\omega=\infty$)appears, and it has the physical meaning of transmit of the acceleration related to the ground motion.

Figure 7 shows comparisons of time history response analysis results of the original vibration system and the controlled vibration system. The input earthquake motion is El Centro 1940 NS (A_{max}=510.8 cm/s^2).

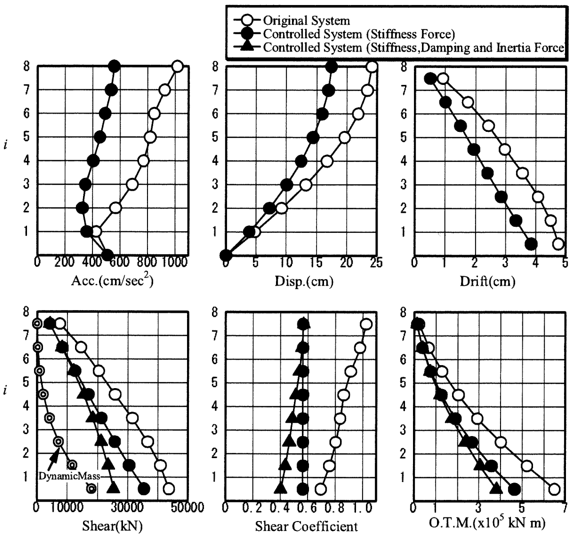

Figure 7 Comparisons of Maximum Response

The damping is assigned h=0.05 for the first mode in proportion to the stiffness of the original vibration system. By adding the dynamic mass, the first period is elongated from T=1.00 [sec] to T=1.11 [sec]. The damping factor of the 1st mode has decreased from h=0.05 to h=0.045.

As a result of mode control, the response of the higher mode disappears. Response accelerations decrease. Response shear coefficients of all stories are the same. It shows the unique and effective response control.

8. MODEL VIBRATION EXPERIMENT

A 4-story model vibration experiment that confirms the effect of the mode control by the dynamic mass was executed. Participation factors of all higher modes are adjusted to 0 by adding the dynamic mass. The resonance of higher modes is lost as a result of the sine wave excitation experiment, and the response only of the 1st mode is remained. The absolute acceleration amplification ratio of each mass point shown in Figure 9 agrees with the calculation value very well.

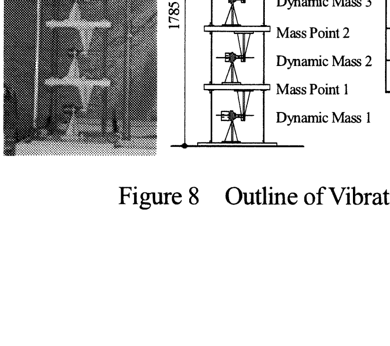

i	m_i(kg)	k_i(N/m)	m'_i(kg)
4	54.7	23,819	37.7
3	54.7	23,819	50.3
2	54.7	23,819	91.3
1	54.7	23,819	151.1

Figure 8 Outline of Vibration Model

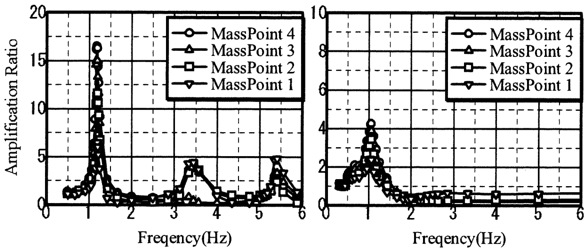

Figure 9 Amplification Ratio of Absolute Acceleration

9. CONCLUSIONS

The dynamic mass (the inertia connection element between mass points) is defined as an element between mass points of vibration systems that generates the force to be proportional to the acceleration difference between mass points. Such an element can be put to practical use with an inertia mass amplification device that uses a displacement amplification mechanism.

Dynamic mass is useful to control response of structures. The characteristic changes are induced to the vibration system, such as the elongation of the natural period, the damping decrease, and the input decrease.

By adjusting the value of the dynamic mass of the each story, the natural period can be changed without changing the eigenvector of the multi mass vibration system and the participation factor of a higher mode can be adjusted to 0. Especially, the combination of the dynamic mass can be evaluated easily, that makes all participation vectors of higher modes zero except the 1st mode .

References:

1] kawamata, S., et al. (1986), "Control of Structural Vibration by Inertia Pump Damper Part(1), Part(2)", Summaries of Technical Papers of Annual Meeting, Architectural Institute of Japan, August 1986, 771-774

2] Okumura, A. (2000), "Vibration Interception Connection Mechanism", Waseda Univ. Science & Technology Seeds, NO. TLO 2000-002, March 2000

3] Ishimaru, S. (1994), "Outline of Response Control of Structures against Earthquakes, Design Mechanism and Control Dynamics of Building Structure", Architectural Institute of Japan, November 1994, 199-202

4] Nakaminami, S., et al. (2005), "Development of Viscous Damping Device with Inertia Mass Element", REPORTS OF TECHNICAL RESERCH INSTITUTE OF SUMITOMO MITSUI CONSTRUCTION CO., LTD. No.3, September 2005

5] Furuhashi, T. and Ishimaru, S. (2004), "Mode isolation by inertial mass, Study on response control by inertial mass no.1," Journal of Structural and Construction Engineering, Architectural Institute of Japan, February 2004, 55-62

6] Furuhashi, T. and Ishimaru, S. (2006), "Response control of multi-degree system by inertial mass, Study on response control by inertial mass no.2," Journal of Structural and Construction Engineering, Architectural Institute of Japan, March 2006, 83-90

7] Saiki, K., Mitsusaka, Y., Furuhashi, T. and Ishimaru, S. (2004), "Study on Characteristic of SDOF system response with Inter-story Inertial Mass Part 1, Part 2 and Part 3", Summaries of Technical Papers of Annual Meeting, Architectural Institute of Japan, August 2004, B-2, 241-246

SHAKING TABLE TEST USING MULTIPURPOSE TEST-BED

Toru Takeuchi[1], Kazuhiko Kasai[2], Mitsumasa Midorikawa[3], Yuichi Matsuoka[4], Takeshi Asakawa[5], Isao Kubodera[6], Yuji Kurokawa[6], Hirotaka Ando[7] and Shoichi Kishiki[8]

1) Associate Professor Tokyo Institute of Technology, Japan
2) Professor, Structural Engineering Research Center, Tokyo Institute of Technology, Japan
3) Professor, Hokkaido University, Japan
4) Nat. Res. Inst. for Earth Science and Disaster Prevention
5) Nikken Sekkei Co., Ltd.
6) General Manager, Tomoe Corporation.
7) Graduate student, Tokyo Institute of Technology
8) Assistant Professor, Tokyo Institute of Technology
ttoru@arch.titech.ac.jp, kasai@serc.titech.ac.jp, midorim@eng.hokudai.ac.jp, pinehill@bosai.go.jp, asakawa@nikken.co.jp, i_kubodera@tomoegiken.co.jp, kurokawa@tomoegiken.co.jp, ando3@mail.arch.titech.ac.jp, kishiki@serc.titech.ac.jp

Abstract: This paper presents a multipurpose set-up system called "test bed" for large shaking table tests. The test-bed is composed of multistory box-trusses with concrete mass of inertia supported by linear slider bearings in each layer. It supports self-weight, however, gives horizontal inertia force to the frame specimen when they are connected and placed on the shaking table. In this paper, shaking table tests with a single-story sample frame with beam-end damper are carried out. Their results are compared with the analytical results and the performances of the set-up system are discussed.

1. INTRODUCTION

The E-Defense shake table facility, the world's largest earthquake simulator, is being utilized for a major research project on steel buildings in Japan. E-Defense can shake a large specimen with a complete three-dimensional configuration. However, since the cost of such a specimen can be very high, testing a part of the specimen such as the plane frame of a building would be much more economical and can still produce meaningful data. Such test methods would also enable parametric studies requiring multiple specimens. Accordingly, the authors are currently constructing a so-called "test bed" having a multipurpose inertial mass system (Takeuchi, Kasai, et. al. 2007). The test bed will be utilized for the aforementioned study on innovative methods, involving researchers from both US and Japan, as a part of the NEES / E-Defense Collaboration Research Program.

The test-bed system under planning is shown in Figure 1. One unit of the test bed is composed of steel truss boxes with a plan of 6 m × 4.5 m and a height of 2.7 m. Each unit comprises a concrete slab with dimensions of 3000 mm × 4000 mm and a mass of 30 metric ton. In the case of unidirectional movement, one unit of the test bed is supported by two unidirectional linear sliders and two bidirectional linear sliders. If additional horizontal stiffness

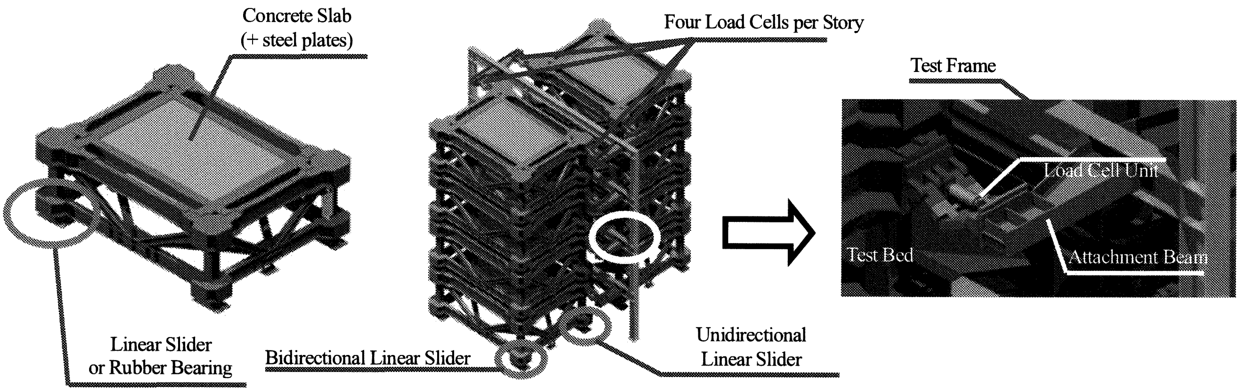

Figure 1 Test bed Set-up for Unidirectional Shaking Table Tests

is required, rubber bearings can be replaced instead of linear sliders. The inertial forces are transferred to the test frame through load-cell units, which can automatically measure the shear forces introduced in each floor. Also the story drift between each floor is measured by LVDTs placed between each layer of unit.

In this study, two units of the test bed are constructed, and several types of trial tests using plane steel frame are carried out. The dynamic characteristics and response of the system, including the smoothness of the linear slider and equivalent damping ratio of the system is evaluated. Also the performance and accuracy of the load-cell units and story-drift measuring system are confirmed.

2. DESIGN OF THE TEST FRAME

The sample plane frame used in these tests comprises one of passive response control structure systems developed for medium-scale building. Figure 2 shows the elevation of a four-story office building frame with two spans. The beams with the longer span are rigidly-connected to the columns, while the beams in the core part are connected to the columns by "beam-end dampers" (Kishiki et. al. 2006) as shown in Figure 2. This connection system is composed of an elastic split-tee at the top flange and replaceable plastic split-tee at the bottom flange of the beam. With the concrete floor slab, the center of rotation of the beam ends stays at the level of the elastic split-tee, and the plastic split-tee perform as a plastic damper, dissipating seismic energy. The plastic split-tee has "dog-bone" shaped plastic area and restrained from buckling by the additional restrainer and the lower flange of the beam. In this system, seismic energy input into the building is dissipated by plastic split-tees, and replaced after they are damaged.

Cyclic test and fatigue test has been previously carried out for this system, and their basic characteristics have been confirmed.

The set-up of the shake table test using test bed system is shown in Figure 3, and the test frame using beam-end

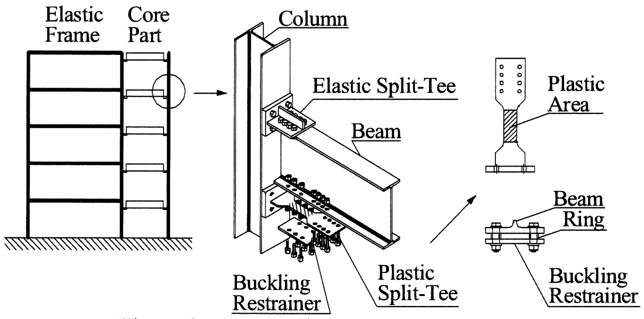

Figure 2 Beam-End Dampers System

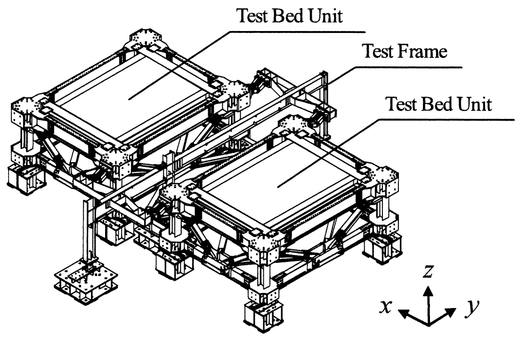

Figure 3 Test Set-up of Single Story Frame

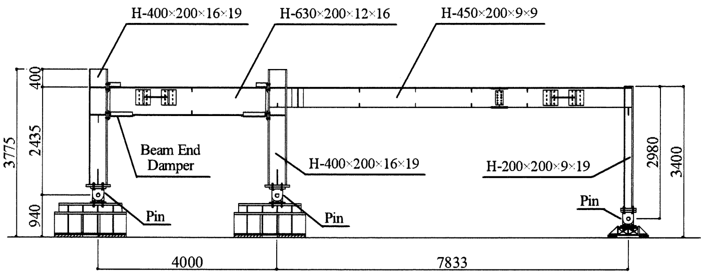

Figure 4 Test Frame Diagram

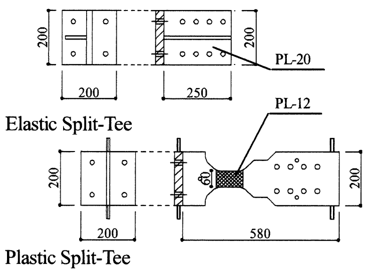

Figure 5 Beam End Damper

CODE	DIMENSION	STEEL PRODUCT
C1	H-700×300×19×25	SS400
C2	H-300×300×12×29	SS400
G1	H-600×300×12×29	SS400
G2	H-900×200×16×22	SS400
ST	PL-16~22×93	LY225

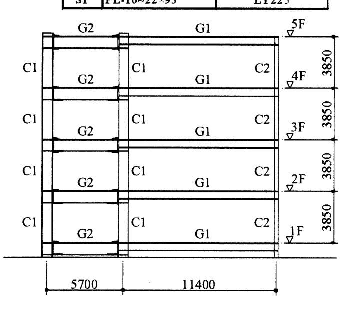

Figure 6 4-story Model Frame

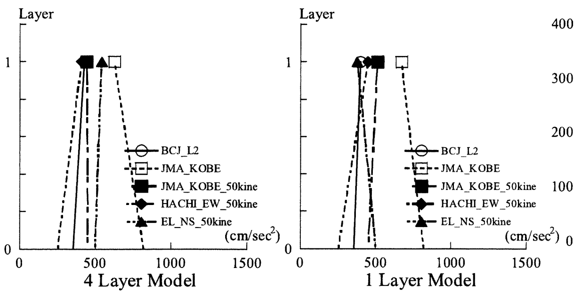

Figure 7 Highest Acceleration Response Value

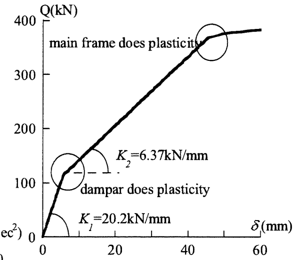

Figure 8 Shear Force–Story Drift Relationship

dampers are shown in Figure 4. The test frame is reduced to 70% scale. Detailed drawings of elastic split-tee and plastic split-tee are shown in Figure 5. Elastic area of the plastic split-tee has two-levels of hunch to measure axial force of the damper by the strain gauges.

The single-story test frame was designed referring the response of 4-story building as shown in Figure 6. The natural period of this 4-story building is about 0.6 second, while that of the test frame is 0.36sec in elastic condition. So time scale of earthquake input is reduced by half to model the response of 4-story building.

The results of time history analyses for the real-size 4-story building and single-story test frame is compared in Figure 7. In this figure, the maximum acceleration responses of these models generally consists each other, and designed test frame is considered to well simulate real-size 4-story building. The shear force – story drift relationship in the test frame is shown in Figure 8. This figure shows that plastic split-tee start yielding at a story drift of about 6mm (0.25% angle), and test frame start yielding at a story drift of 40mm (1.8% angle).

Nest, the fracture point of the plastic split-tees at beam ends is evaluated. The equation for evaluating cumulative deformation capacity for buckling restrained braces has been proposed by Takeuchi and Ida (2006) as in equation (1).

$$\chi(\%) = \frac{1}{\alpha_s/35 + (1-\alpha_s)(\varepsilon_{ph}^{(1+m)}/(C_2/2))^{1/-m_2}} \tag{1}$$

χ : cumulative plastic strain
ε_{ph} : averaged plastic strain amplitude
α_s : skeleton hystereis ratio

C_2 and m_2 in equation (1) is the value obtained from fatigue curve of the member, and this equation show that cumulative plastic strain of buckling restrained braces is able to be calculated from ε_{ph} and α_s. For the plastic split-tee, C_2 =43.9 and m_2=-0.57, have been obtained by Takeuchi and Shirabe (2006).

$$\chi(\%) = \frac{1}{\alpha_s/35 + (1-\alpha_s)(\varepsilon_{ph}^{0.756}/904)} \tag{2}$$

Using this equation, N_{seis}; the numbers of earthquake until the fracture is obtained from equation (2). From above method, it is expected that the plastic split-tees will fracture at 2nd or 3rd times of BCJ-L2 wave, or 1st time of JMA-KOBE wave.

3. SHAKING TABLE TEST

3.1 ELASTIC SHAKING TEST

First, the white noise test containing the frequency range of 0.1 to 30Hz is performed with a goal of 100gal in each direction to confirm the natural period of the system. The obtained acceleration transfer function is shown in Figure 12. Those results show that the natural frequency of test frame in Y-direction is 3Hz generally meets the designed value.

Then the sin wave test is performed to confirm damping performance of the system. Three sin waves of 5Hz was input, with the amplitude of 120gal. The time-history of the displacement in Y-direction is shown in Figure 11. This figure shows that the displacement of the test beds and test frame is almost consistent. Amplitude ratio d is estimated from Figure 11, and equivalent damping constant h is derived from the equation (3).

$$h = \left(\frac{\ln d}{2\pi}\right) \Big/ \sqrt{1+\left(\frac{\ln d}{2\pi}\right)^2} \tag{3}$$

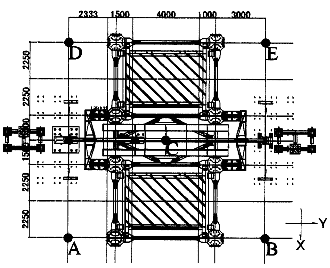

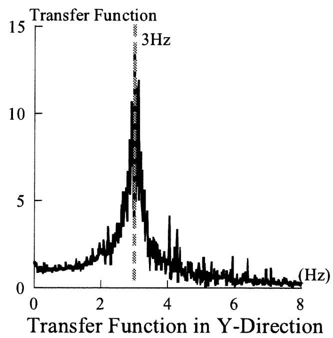

Figure 9 Transfer Function

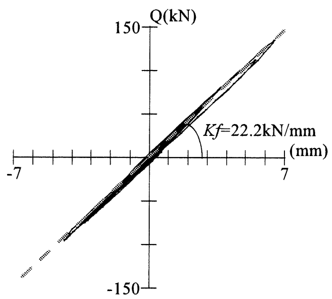

Figure 10 Shear Force-Displacement Relationships

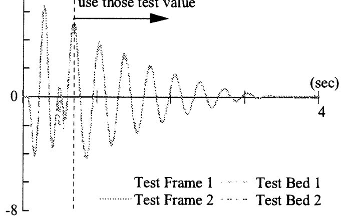

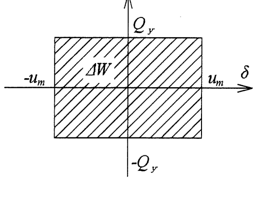

Figure 11 Acceleration Time History of Shaking Table

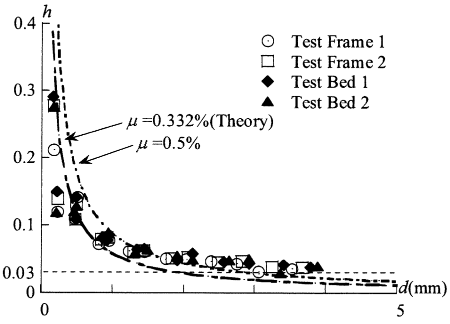

Figure 12 Equivalent Damping Ratios

It is expected that this damping is produced by the friction of linear sliders, so the equivalent damping ratio can be estimated by equation (4).

$$h_{eq} \approx \frac{1}{4\pi}\left(\frac{\Delta W}{W}\right) \qquad \begin{cases} \Delta W = 4u_m Q_y \\ W = \dfrac{1}{2}K_f u_m^{\;2} \end{cases} \tag{4}$$

Where, ΔW (shadow area in Figure 12) is one cycle energy produced by friction force of linear sliders, and W is the potential energy of the test frame in amplitude of u_m. Maximum friction force Q_y is obtained from the mass of the system multiplied by the dynamic friction coefficient μ obtained from equation (5).

$$\mu = 0.0028907 + 5.6114\times10^{-6}\times \mathrm{P} \tag{5}$$

Estimating the mass as 62.5ton and μ as 0.00332, Q_y becomes 2.034kN and horizontal stiffness of test frame K_f becomes 22.2kN/mm. The damping constant h obtained from those figures is shown in Figure 14.

The result shows that the damping constant of the system is affected by the amplitudes, however, convergences to 0.03 when the amplitude becomes larger. Also the test results is consistent with the theory (eq.(4)).

4.2 BCJ-L2 LOADING TEST

Next, artificial seismic wave of BCJ-L2 (Amax=356cm/s^2) whose time axis is reduced by half is applied to the system. The shear force measured by the load From this figure, the load cell system is confirmed to be cell is compared with those derived from the strain gauges on the columns of the test frame, and shown in Figure 13. accurate enough to measure the share force. The relationship between shear force and displacement obtained by the test is shown in Figure 14, while the hysteretic curves of plastic split-tee 1 and 2 are shown in Figure 15 and 16, respectively. The split-tee 1 fractured at the third wave of BCJ-L2, which is the same as expected in eq. (2), however until the fracture, the split-tee showed stable hysteretic curve.

The simple analytical model is created to evaluate the test result. The analytical model is shown in Figure 17, and the member size of the model is shown in Table 1. The yield strength of each member is shown in Table 1, which is derived from the coupon tests. The mass of the test beds of 62.5 ton is divided equally in each node points, and the damping constant is set as 0.02 from the result of sin wave loading test.

The response spectrum of the target earthquake wave is compared with that of measured earthquake wave in the test. As shown in Figure 18. The figure shows that the response spectrum of observed earthquake wave is larger than that of target earthquake wave. However, in elastic natural period, the response spectrum is generally consistent. Wherein the measured earthquake wave is used for analyses.

The time histories of the displacement in Y-direction obtained from test and analysis are compared in Figure 19. This figure shows that the test results and the analysis analytical results agrees each other, and the test bed system

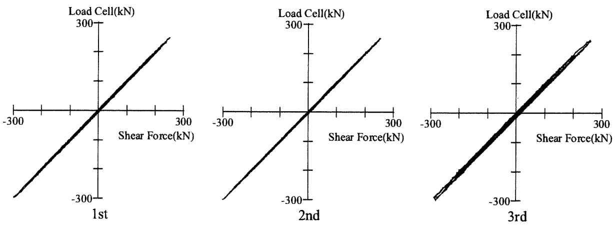

Figure 13 Load Comparison

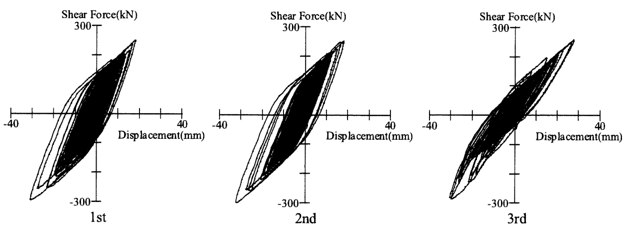

Figure 14 Shear Force-Displacement Relationships

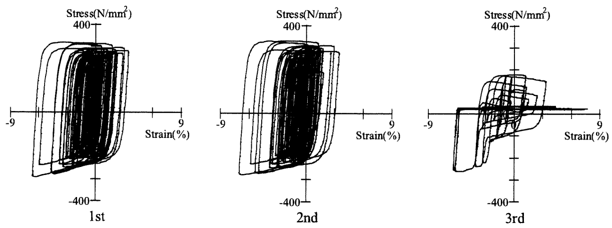

Figure 15 Hysteretic Curve of Plastic Split-Tee 1

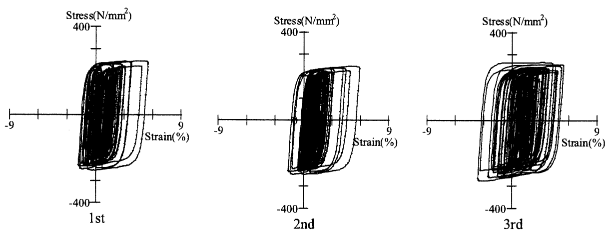

Figure 16 Hysteretic Curve of Plastic Split-Tee 2

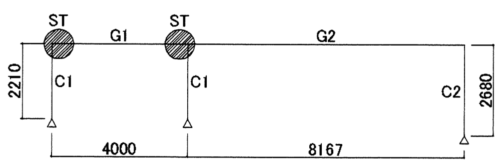

Figure 17 Analysis Model

Table 1 Member Characteristic

CODE	DIMENSION	STEEL PRODUCT	YIELD POINT(N/mm2)
C1	H-400×200×16×19	SS400	300
C2	H-200×200×9×19	SS400	300
G1	H-630×200×12×16	SS400	300
G2	H-450×200×9×9	SS400	300
ST	PL-60×12(Plastic Area100mm)	LY225	225

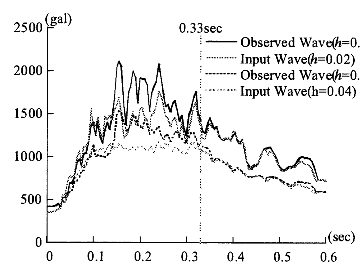

Figure 18 Response Spectrum

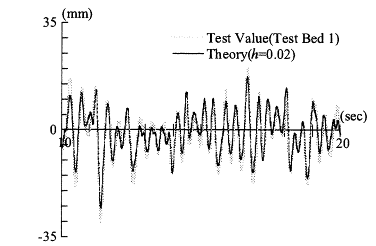

Figure 19 Displacement in Y-Direction Time History

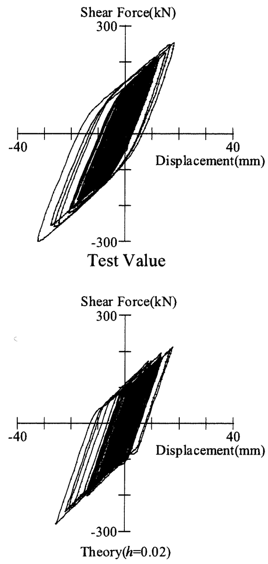

Figure 20 Shear Force-Displacement Relationship

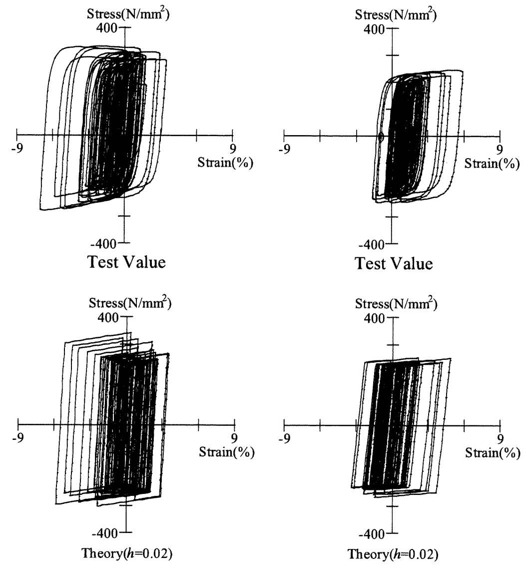

Plastic Split-Tee 1 Plastic Split-Tee 2

Figure 21 Hysteretic Curve of Plastic Split-Tee

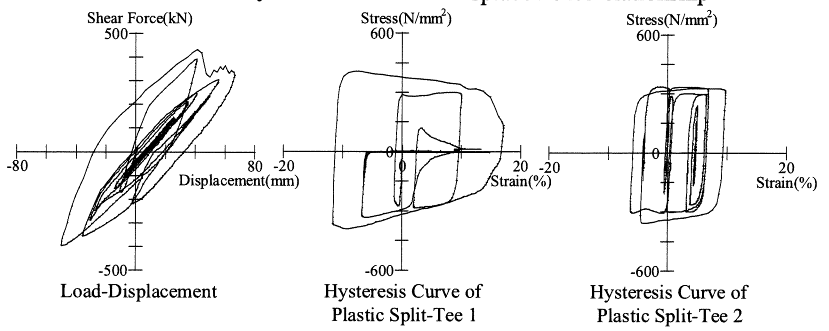

Figure 22 Test Result input JMA-KOBE

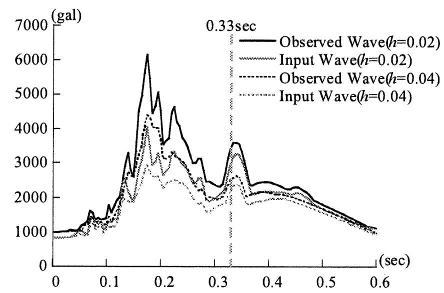

Figure 23 Response Spectrum

to work effectively.

The shear force and displacement relationship of the test frame is shown in Figure 20. From these figures, it is confirmed that the test results are generally consistent with the analytical results. The horizontal stiffness of the test frame before the fracture of the plastic split-tee is 22.2kN/mm, which is almost as same as value in elastic loading test. The horizontal stiffness of the test frame after the fracture of the plastic split-tee is reduced to 6.31kN/mm. The hysteretic curves of plastic split-tee obtained from the analyses are shown in Figure 21. These figures show that the response of plastic split-tee in the test is also consistent with the analysis results.

4.2 JMA-KOBE LOADING TEST

After the fractured plastic split-tees are replaced, the same test frame is tested against JMA-KOBE earthquake wave (A_{max}=818cm/s^2) whose time axis is decreased by half. The part of results is shown in Figure 22. In the third cycle of the first earthquake, the plastic split-tee 1 and the connecting bolts of the elastic split-tee 2 fractured. However, the maximum response was consistent with expected values in analyses, and effective response reduction by the beam-end dampers were observed.

The response spectrum of target earthquake wave is compared with that of observed earthquake wave in Figure 23. This figure shows that the response spectrum of measured earthquake wave is larger about 10% than that of target earthquake wave. The measured wave is used for the following analyses. Time history of axial force between load cells around the fracture of split-tees is shown in Figure 24. From this figure, it is observed that the axial force is decreased by 360kN after the fracture of the plastic split-tee 1 and the connecting bolts of the elastic split-tee 2. It means axial forces were initially introduced to the beam at assembly stages, and released at the fracture of the split-tees.

Next, the shear force and the displacement in Y-direction relationship and the hysteretic curve of the plastic split-tee 1 and 2 until the fracture are shown in Figure 24. I these figures, the test results are compared with that of analyses until the fracture. The figure shows that the analytical results are generally consistent with the analytical results. Also the fracture point is roughly as same as expected by eq. (2)

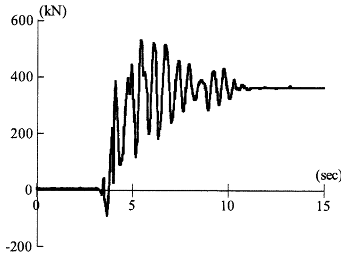

Figure 24 Axial Loads between Load Cells Time History

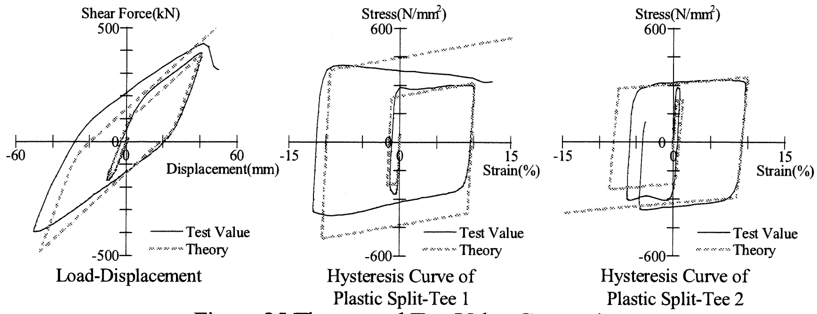

Figure 25 Theory and Test Value Comparison

5. CONCLUSIVE REMARKS

The multipurpose inertial mass called "test bed" was constructed, and shaking table tests of single story test frame with beam-end dampers are carried out using this system. As results, the following conclusions are obtained.

1) The dynamic characteristics of the set-up system are consistent with the value as designed. Equivalent damping constant is derived from the friction force of the linear slider, which is 0.03 when amplitude is larger than 3 mm.
2) It was confirmed that the shear force measured by the load cells corresponded to that delivered from the strain gauges on the test frame columns.
3) From shaking table test using seismic waves, it was confirmed that the obtained response value was consistent with the analysis value.
4) Also, it was confirmed that the hysteretic curve and fracture point of plastic split-tees obtained by the test is consistent with the analysis value.

From above, the shaking table test using constructed test-bed system is considered to be effective to simulate the dynamic response of structural systems.

Acknowledgements:

The authors acknowledge support from Japan Ministry of Education, Culture, Sport, Science, and Technology (MEXT) for establishing the Center for Urban Earthquake Engineering (CUEE) in Tokyo Institute of Technology. The support has made possible this international conference, as well as international joint research projects and exchange programs with foreign universities.

References:

Takeuchi, T., Ida, M., Yamada, S., Suzuki, K., (2006) : Estimation of Cumulative Deformation Capacity for Elasto-plastic Dampers, STESSA 2006 (Yokohama, Japan), pp.793-799, 2006. 8

Takeuchi, T., Shirabe, H., Yamada, S., Kishiki, S., Suzuki, K., Saeki, E., Wada, A., (2006) : Cumulative Deformation Capacity and Damage Evaluation for Elast-Plastic Dampers at Beam Ends, J. Struct. & Constr. Eng., A.I.J., No.600, pp.115-122, 2006.2

Takeuchi, T., Kasai, K., Midorikawa, M., Matsuoka, Y., (2007) :E-Defense Tests on Full-Scale Steel Buildings Part 4 - Multipurpose Test Bed for Efficient Experiments, ASCE, Structural Congress 2007(Long Beach, USA), 247-20, 2007. 5

Fifth International Conference on Urban Earthquake Engineering
March 4-5, 2008, Tokyo Institute of Technology, Tokyo, Japan

A REVIEW OF THE SEISMIC PERFORMANCE OF THE CEILING-PIPING-PARTITION NONSTRUCTURAL SYSTEMS

E. "Manos" Maragakis[1]

1) Professor, Civil and Environmental Engineering Department, University of Nevada, Reno, Reno, Nevada, maragaki@unr.edu

Abstract: Nonstructural components and systems in a building are not part of the structural load-bearing system, however they are subjected to the same dynamic environment experienced by the building caused by an earthquake. These elements almost always represent the major portion of the total investment in buildings. Furthermore, damage to nonstructural elements occurs at response intensities much lower than those required to produce structural damage. A very widely used nonstructural system, which always represents a significant investment in a structure, is the *ceiling-piping-partition* system. Past earthquakes and numerical modeling considering potential earthquake scenarios show that the damage to this system causes the preponderance of US earthquake losses. Nevertheless, due to the lack of system-level research studies, its seismic response is poorly understood. Consequently, its seismic performance contributes to increased failure probabilities and damage consequences, loss of function, and potential for injuries. All these factors contribute to decreased seismic resilience of both individual buildings and entire communities.

This paper summarizes damage of ceilings, piping and partitions in recent earthquakes and its impact on all categories of seismic risk and demonstrates the importance of these elements on the functionality of buildings. Furthermore, it summarizes some major analytical and experimental research studies on the seismic response of these elements and discusses a major recent research project on this topic.

1. INTRODUCTION

Nonstructural components and systems are defined as the elements of a building that are not part of the main gravity and/or seismic loading resisting structural system. Nonetheless, these elements are typically supported by the structural frame of the building and are subjected to the same dynamic environment experienced by the building caused by an earthquake. Typical examples of nonstructural components and systems include:
(i) architectural components such as cladding, ceilings and lights, racks and shelves and partition walls; (ii) equipment and piping such as electrical power, fire protection system, and mechanical piping; and, (iii) building contents and inventory such as record storage, production and computer equipment.

Sample data from Miranda (2003) illustrates the typical investment in structural framing and nonstructural components in office, hotel and hospital construction. It is clearly demonstrated (Figure 1) that the investment in nonstructural components is far greater than that for structural components. The *ceiling-piping-partition* system is a very widely used nonstructural system that has been a main contributor to both seismic damage and associated property damage. All of its subsystems (i.e. piping, partitions and ceilings) have suffered significant damage in recent earthquakes. Such damage has resulted in property loss, loss of function, increased fire hazard and has shown potential for loss of life.

This paper summarizes damage of the components of the ceiling-piping-partition nonstructural system in recent earthquakes and its impact on all categories of seismic risk such as property loss, loss of function, fire hazard and potential for injury and loss of life. Furthermore, the paper summarizes some major analytical and experimental research studies on the seismic response of these nonstructural elements and discusses a major recent research project on this topic.

2. NONSTRUCTURAL DAMAGE IN RECENT EARTHQUAKES AND ASSOCIATED SEISMIC RISK

Recent earthquakes have demonstrated that poor performance of ceiling-piping-partition nonstructural systems can result in significant damage.

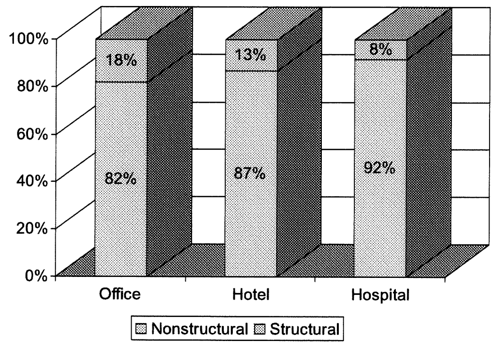

Figure 1 Typical investments in building construction (after Miranda, 2003)

2.1 Damage to Piping Subsystems and Components

In the recent 2006 Kiholo Bay (Kona, Hawaii) Earthquake, widespread piping damage was reported (RMS, 2006). Water damage from sprinkler leakage was the main problem at the Mauna Kea Beach Resort, the

Fairmont Orchid and the Hapuna Beach Prince Resort. Broken pipes and sprinkler failures were also reported in other commercial and residential buildings. Similarly, Ayres et al. (1998) indicated that water damage was one of the most significant types of damage that occurred in the 1994 Northridge Earthquake. This damage was mainly caused by the failure of components of service and safety pipelines. Reitherman et al. (1995) tabulated water damage at a number of hospitals and other facilities during the Northridge Earthquake, including complete collapse of lines as large as 12 inches in diameter, demolishing an area of a shopping mall. The Fire Sprinkler Advisory Board of Southern California (FSABSC, 1994) survey of contractors and insurers following the Northridge Earthquake found an extensive variety of failures, including fractures in the piping and at heads, failure of braces, and in one case the complete collapse of sprinkler piping in a large warehouse damaging over 2,000 linear feet of piping. Sekizawa et al. (1998) reported that 40.8% of sprinkler systems sustained damaged in Kobe following the 1995 earthquake.

2.2 Damage to Suspended Ceilings

Failure of suspended ceiling systems has been one of the most widely reported types of nonstructural damage in buildings following earthquakes. For example, in the recent 2006 Kona, Hawaii Earthquake, extensive ceiling damage (Figure 2) was reported (EERI, 2006; RMS, 2006; Robertson et al., 2006). Multiple classrooms at the Waimea Elementary School had ceiling panels along the perimeter of the room that were cracked or had completely fallen out. The metal hanging systems for the ceiling panels were bent and had pulled the anchors out of the wall. Similar damage was observed at the Waikoloa Elementary School. The Kona Community Hospital suffered extensive ceiling damage due to interaction effects between the lay-in suspended ceilings and the partition walls. Ceiling damage was also reported in several other commercial and residential buildings. Several ceiling failures were observed in the 1971 San Fernando earthquake (Fierro et al., 1994). Gates et al. (1998) reported that during the Northridge Earthquake millions of square feet of ceiling tiles were dislodged along with lighting fixtures and air vent ducts (Figure 3). Similarly, suspended ceiling damage was observed in the e 2001 Nisqually Earthquake (Filiatrault et al., 2001).

2.3 Damage to Partitions

Past earthquakes have shown widespread damage to partitions in various types of buildings including hospitals, schools, offices and stores. Partition walls are either partial or full-height. In the former case, adverse interaction with hung ceilings and other suspended elements occurs and in the latter case inter-story drift has been cited as the main cause of failure. In the recent 2006 Kona, Hawaii Earthquake several partition walls were cracked, while interaction between partitions and ceilings resulted in extensive ceiling damage (RMS, 2006; Robertson et al. 2006).

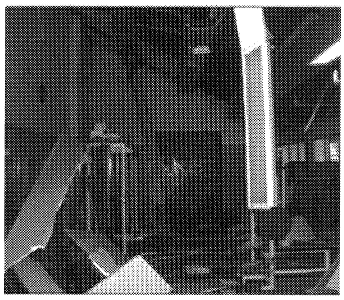

Figure 2 Ceiling damage in 2006 Hawaii Earthquake (EERI, 2006)

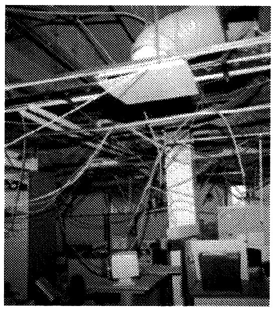

Figure 3 Ceiling damage in the 1994 Northridge Earthquake.

2.4 Property Loss

Since most nonstructural systems have higher fragilities than the structures that house them, actual losses from past US earthquakes and projected losses from future ones are dominated by nonstructural property losses. Of the $2.4 billion in predicted annualized loss in the US due to structural damage and damage to built-in nonstructural features of buildings, nonstructural damage accounts for 78.6% of the total; the structural loss accounts for the remaining 21.4% of the total loss (FEMA 366, 2000; as calculated for the 11 states accounting for the majority of the nation's seismic risk). Preliminary reports from the recent 2006 Kona, Hawaii Earthquake, indicate that the total damage at the Waikoloa Elementary School was $2 million for ceiling and light fixtures (RMS, 2006). The same reconnaissance report states that the Kona Community Hospital suffered physical nonstructural damage of around $5 million and revenue loss of $150,000 per day while not fully operational.

2.5 Loss of Function

Loss of function includes business interruption, loss of habitability, and essential services downtime, which impact commercial, residential, and utility/public critical facility occupancies respectively. Ayres et al. (1996) found that 10 of 12 sprinkler equipped hospitals they surveyed suffered significant leaks and loss of function in the Northridge Earthquake. Similar findings were reported in hospitals damaged by the Kobe earthquake (Ukai, 1997). In the recent 2006 Kona, Hawaii Earthquake, several schools remained closed for several days after the earthquake due to ceiling damage. The Kona Community Hospital, which also suffered significant ceiling damage, had to evacuate its long-term care patients and their caretakers to a nearby hotel for five days (RMS, 2006). The hospital was not operational for twelve weeks after the earthquake.

2.6 Fire Hazard

Damage to fire sprinkler distribution lines, ceilings and partitions results in a decrease or loss of functionality of the fire protection systems of buildings, and an increase in the fire hazard. Fire spread resistance is compromised by damage to ceilings and partitions, many of which are fire-rated assemblies, and obviously the entire fire sprinkler system loses its function by damage to sprinkler heads and distribution lines. Following the Kobe Earthquake, several fires occurred as a result of this (Sekizawa et al., 1998). Reports have also documented the loss of function of fire protection systems following earthquakes (Kobe City Fire Department, 1995).

2.7 Potential for Loss of Life

The ceiling-piping-partition system is associated with the most commonly found nonstructural safety risks, because ceiling-related components are overhead and when they fall the potential for injury is obvious (Figure 4). A study of the damage conditions in buildings after the Northridge Earthquake, which fortunately occurred at 4:31 AM, estimated that had the earthquake occurred in the middle of the day approximately 25 children located in schools at that time would have been killed because of falling light fixtures alone (Holmes, 1994). Other similar estimations have been reported in the literature.

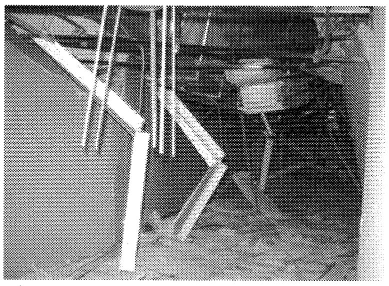

Figure 4 Fallen ceiling components

3. RESEARCH ON THE SEISMIC RESPONSE OF CEILING-PIPING-PARTITIONS NONSTRUCTURAL SYSTEMS

Despite the prevalence of damage and the potential for future losses, limited research studies have been conducted in the past on the seismic response of nonstructural systems. However, in recent years considerable attention has been given to this area in order to study the seismic response of nonstructural systems and develop better strategies for their seismic rehabilitation.

3.1 Research on Piping

The most comprehensive design pipe specifications are provided by ASME 31.1, which are applicable to pressurized power plant piping. These requirements focus on the design of pipe components and have evolved through experimental and analytical research in the nuclear power industry. In these nuclear power plant studies, however, the pipes and braces were designed to remain elastic and interactions with the structure and surrounding nonstructural components, which are ubiquitous in ordinary buildings, were neglected. Gupta (2004) has shown that seismic responses evaluated by ignoring these interactions can be excessively higher than those calculated in a coupled system analysis. However, there is a lack of significant experimental data to verify such models. Most of the original experimental work was focused on the evaluation of failure modes associated with individual pipe components, without considering system performance. (e.g. Masri et al., 2002). Some shake table studies have also been conducted on piping subsystems. Nims (1991) concentrated on the effectiveness of mechanical snubbers, seismic stops and energy dissipating restraints. Shimizu et al. (1998) investigated the response of a piping system that was simultaneously subjected to shake table excitation and an actuator load, simulating the displacement of a support structure during an earthquake. Chiba et al. (1998) performed shake table tests to study the behavior of a piping system colliding with its support structure. Maragakis et al., 2003, investigated the seismic behavior of welded and threaded hospital piping systems.

3.2 Research on Ceilings

Examples of experimental and analytical studies to date on suspended ceiling systems are reported by ANCO (1993), Yao (2000), and Badillo et al. (2006). Some of these studies served to qualify ceiling systems for use in building projects. Only the studies by Badillo involve the development of experimental fragility curves for typical installations of suspended ceilings in buildings. Recently, a hospital ceiling experiment was conducted by Masri (2005). The ceiling covered an area of about 20 ft by 50 ft.

3.3 Research on Partitions

Most of the research on stud walls has been on wood-framed shear walls and partitions that are the primary lateral load carrying systems in residential construction such as single-family and low-rise multi-family dwellings (e.g. Filiatrault et al., 2002; Kanvinde et al., 2006). Reported experimental and analytical work on steel stud partitions, which are common in commercial, hospital and school occupancies, is very scarce. Available research includes standard in-plane shear resistance tests based on ASTM E 72 8 ft x 8 ft panels by Serrette et al. (1996) and out-of-plane in-situ tests on partitions in a hospital building by Elhassan et al. (2003). Experiments have also recently been conducted on steel stud partitions by Restrepo et al. (2005).

3.4 Fragility and Risk Assessment Studies

Largely due to the lack of data, the development and availability of fragility curves for nonstructural systems is very limited. A recent ATC-sponsored workshop (ATC-29-2, 2003) presented select efforts to develop these curves for systems such as ceilings, critical facilities such as hospitals, elevators and building contents. Alternatively, methods have been explored for extending the typical 2D representation to a surface (3D) fragility for nonstructural systems based either on Monte Carlo Simulation or the crossing theory for stochastic processes (Kafali et al., 2003).

3.5 Recent Design Guidelines

The FEMA Performance-Based Seismic Design Guidelines Project (ATC-58/FEMA 445) is an important national-scale engineering advancement that explicitly includes nonstructural systems within its scope. The ATC-58 project, and other guidelines on nonstructural components, are discussed by Bachman et al. (2003), as well as in ATC (2003), ATC-51 (2000) and ATC-51-1 (2002).

4. A RECENTLY FUNDED PROJECT BY THE NATIONAL SCIENCE FOUNDATION (NSF).

In August 2007 NSF funded a project entitled "NEESR-GC: Simulation of the Seismic Performance of Nonstructural Systems". The main objectives of the project are:

1. To study the seismic response and failure mechanisms of ceiling-piping-partition systems including their interaction with the structural system.
2. To develop an experiment-based simulation platform, which accurately and effectively evaluates responses and fragilities associated with system-level failure modes.
3. To develop visualization tools to improve the efficiency of the evaluation of the seismic performance of nonstructural systems.
4. To identify the impact on public policy at the building and metropolitan scale levels and address implementation barriers.
5. To provide extensive outreach and facilitate implementation of the research findings.

To accomplish these objectives the project includes the following major research tasks:

4.1 Experimental Studies

An experimental program has been developed including subsystem and full-scale system level experiments. The subsystem experiments include testing of partition, pipes and ceilings using the Nonstructural Component Simulator (NCS) and the shake tables at the University at Buffalo (UB) NEES site. A large rigid testing frame will be constructed and will be mounted on the two shake tables at the UB NEES site to allow for testing of ceiling/piping/partition subsystems (Figure 5). The system experiments include the design and construction of a large scale test-bed with tunable frequencies and yielding characteristics. This will be mounted on the three shake tables at the University of Nevada, Reno (UNR) NEES site and will allow the simulation of different structural dynamic environments (Figure 6). It will be used to study the seismic response of full scale ceiling-piping-partition nonstructural systems and their interaction with the structure.

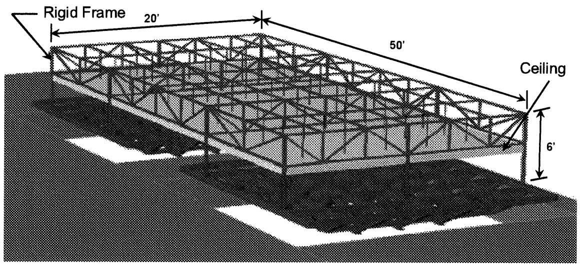

Figure 5 Large scale ceiling / sprinkler / piping / partition walls experiment at UB-NEES Site

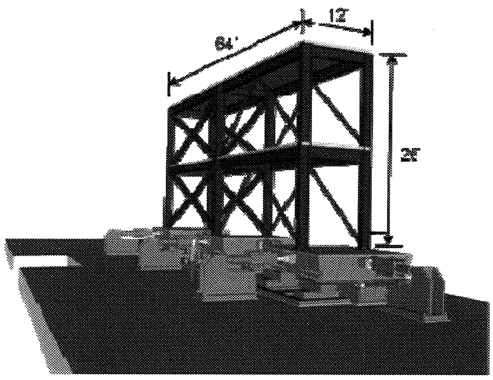
Figure 6 System level experiments at the UNR-NEES Site

4.2 Simulation Studies

The objective of the simulation studies is to develop an experiment-based simulation platform that accurately evaluates response and fragilities associated with system-level failure modes of ceiling-piping-partition nonstructural systems. To accomplish this objective the following tasks have been planned:

1. Experimentally validated analytical models of ceiling-piping-partition nonstructural systems will be developed using macro and/or discrete element formulations, also considering existing response data from the literature survey.
2. Algorithms for fragility evaluation and experimental validation of global system fragilities will be developed.
3. Tools will be developed for the visualization of the experimental and simulation data.
4. Representative index-buildings, representing three different occupancies (office, hospital, school) will be developed and modeled with or without improvements to their nonstructural systems and will provide input into the public policy investigations (section 4.3).

4.3 Public Policy Investigations

This task will determine the impact of the experimental and simulation research on seismic vulnerability over time and quantify the impacts of the research on the seismic resilience of buildings and communities. In the first step of this process, Index Buildings will be introduced and analyzed to apply the research results at the individual building level. Then the project will go beyond the single building scale to explore how improved design and construction of the ceiling-piping-partition system over a large number of buildings affect the seismic vulnerability at the metropolitan scale over time as new buildings are added incrementally. These studies will provide information to support the adoption of the project's research findings and provide a solid foundation for the implementation of the research results

In addition to these major research tasks the project includes a series of educational tasks as well as implementation, data archiving and management plans (www.nees-nonstructural.org)

5. CONCLUSIONS

Nonstructural components and systems represent approximately 80% of the loss exposure of US buildings in earthquakes and account for over 78% of the total estimated national annualized earthquake loss. The ceiling-piping-partition nonstructural system has suffered major damage in recent earthquakes. This damage has resulted in property loss, loss of function, increased fire hazard and potential for injury. Major research studies at the system level are needed to better understand the seismic response of nonstructural systems and develop better strategies for their seismic rehabilitation. Such a study has been recently funded recently by NSF to study the system-level response of ceiling-piping-partition systems. This study includes an extensive integrated research program consisting of component and system-level experimental studies, simulation studies and public policy investigations.

Acknowledgements

The author acknowledges A. Filiatrault, S. French, W. Holmes, T. Hutchinson and R. Reitherman for their contributions to several sections of this paper.

References

ANCO (1993), "Earthquake Testing of a Suspended Ceiling System," ANCO., Culver City, CA.

Applied Technology Council (ATC-51) (2000), "US-Italy Collaborative Recommendations for Improved Seismic Safety of Hospitals in Italy," ATC.

Applied Technology Council (ATC-51-1) (2002), "Recommended US-Italy Collaborative Procedures for Earthquake Emergency Response Planning for Hospitals in Italy," ATC.

Applied Technology Council (ATC) (2003), *Program Plan for Development of Next-Generation Performance-Based Design Guidelines.* ATC, January, 2004. Redwood City, CA.

Applied Technology Council (ATC-29-2) (2003), *Proceedings of the Seminar on the Seismic Design, Performance and Retrofit of Nonstructural Components in Critical Facilities,* ATC, October 23-24, 2003, Newport Beach CA.

Ayres & Ezer Associates (1996), "Northridge Earthquake Hospital Water Damage Study," Office of Statewide Health Planning and Development, State of California.

Ayres, J. M. and R. J. Philips (1998), "Water Damage in Hospitals Resulting from Northridge Earthquake," *ASHRAE Transactions*, American Society of Heating and Refrigerating and Air Conditioning Engineers, Vol. 104, Part I, Atlanta, GA.

Bachman, R., R. O. Hamburger, C. D. Comartin, C. Rojahn, and A. S. Whittaker (2003), "ATC-58 Framework for Performance-Based Design of Nonstructural Components," *Proceedings of Seminar on Seismic Design, Performance, and Retrofit of Nonstructural Components in Critical Facilities.* Redwood City, CA: Applied Technology Council.

Badillo-Almaraz, H., A. S. Whittaker, and A. M. Reinhorn (2006), "Seismic Fragility of Suspended Ceiling Systems," *Earthquake Spectra*, Vol. 23, No.1, Earthquake Engineering Research Institute, Oakland, CA.

EERI (2006), "Preliminary Observations on the Hawaii Earthquakes of October 15, 2006", EERI Special Report, *EERI Newsletter*, December 2006.

Elhassan, R., C. Tokas, and B. Faircloth (2003), "Analytical and Experimental Seismic Assessment of Existing and Retrofitted Metal-Stud Partitions," *Proceedings of Seminar on Seismic Design, Performance, and Retrofit of Nonstructural Components in Critical Facilities*, ATC-29-2, pp. 243-255, October 23-24, 2003, Newport Beach CA.

FEMA (Federal Emergency Management Agency) (2000), *HAZUS 99 Estimated Annualized Earthquake Losses for the United States.* (FEMA 366).

Fierro, E. A., C. L. Perry, and S. A. Freeman (1994), "Reducing the Risks of Nonstructural Earthquake Damage: A Practical Guide," Third Edition, FEMA 74, September 1994.

Filiatrault, A., D. Fischer, B. Foltz, and C.-M. Uang (2002), "Seismic Testing of Two-Story Woodframe House: Influence of Wall Finish Material," ASCE *Journal of Structural Engineering*, Vol. 128, No. 10, pp. 1337-1345.

Filiatrault, A., C.-M. Uang, B. Folz, C. Christopoulos, and K. Gatto (2001), "Reconnaissance report of the February 28, 2001 Nisqually (Seattle-Olympia) earthquake," Structural System Research Project Report No. SSRP-

2000/15, Department of Structural Engineering, University of California, San Diego, La Jolla, CA, 62 p.

FSABSC (Fire Sprinkler Advisory Board of Southern California) (1994), *Report on the 1994 Northridge Earthquake.*

Gates, W. E., and G. McGavin (1998), "Lessons learned from the 1994 Northridge Earthquake on the Vulnerability of Nonstructural Systems," *Proceedings of the Seminar on Seismic Design, Retrofit, and Performance of Nonstructural Components*, ATC 29-1, pp. 93-106, San Francisco, CA.

Gupta, A. (2004), "Recent Developments in Seismic Analysis and Design of Multiply-Supported Piping Systems", *Proceedings of Pressure Vessel and Piping Conference,* ASME, La Jolla, CA.

Holmes, W. (1994), "Lessons Learned," *1994 Structural Engineers Association of Northern California Spring Seminar.* San Francisco, CA.

Kafali, C. and M. Grigoriu (2003), "Fragility Analysis for Nonstructural Systems in Critical Facilities," *Proceedings of Seminar on Seismic Design, Performance, and Retrofit of Nonstructural Components in Critical Facilities*, ATC-29-2, pp. 375-385, October 23-24, 2003, Newport Beach CA.

Kanvinde, A. M. and G. G. Deierlein (2006), "Analytical Models for the Seismic Performance of Gypsum Drywall Partitions," *Earthquake Spectra,* Vol. 22, No. 2, pp. 391-441, Earthquake Engineering Research Institute, Oakland, CA.

Kobe City Fire Department (1995), "Investigation Report on Damages to Fire Protection Systems Caused by the Hanshin-Awaji Earthquake in Kobe," 1995.

Maragakis, E., A. Itani, and E. Goodwin (2003), "Seismic Behavior of Welded Hospital Piping Systems," *Proceedings of Seminar on Seismic Design, Performance, and Retrofit of Nonstructural Components in Critical Facilities,* ATC-29-2, pp.321-333, October 23-24, 2003, Newport Beach CA.

Masri, S. F., J. P. Caffrey, R. Myrtle, R. Nigbor, M. Agbabian, E. Johnson, W. Petak, M. Shinozuka, R. Tranquada, and L. Wellford (2002), "Nonstructural Mitigation in Hospitals: the FEMA-USC Hospital Project," *Proceedings of the Seventh US National Conference on Earthquake Engineering*, Boston, July, 2002, CD.

Masri, S.F. (2005), "Experiments of a Hospital Ceiling", *Oral Communication,* June.

Miranda, E. (2003), "Building Specific Loss Estimation for Performance Based Design," *2003 Pacific Conference on Earthquake Engineering.* University of Canterbury, Christchurch, New Zealand.

Nims, D. K. (1991), "Large Scale Experimental Studies of Two Alternate Support System for the Seismic Restraint of Piping," PhD Dissertation, University of California, Berkeley, CA.

Reitherman, R. and T. Sabol (1995), "Nonstructural Damage," in *Northridge Earthquake of January 17, 1994 Reconnaissance Report*, Vol. 1, Supplement C to Vol. 11 of *Earthquake Spectra,* Earthquake Engineering Research Institute, Oakland, CA.

Restrepo, J. I. and A. F. Lang, (2005), "Interim Report to PEER Advisory Board Year 7: Performance Evaluation of Gypsum Wallboard Partitions. Results of Test 1," PEER Interim Report, Department of Structural Engineering, UC-San Diego, January 16, 2005, La Jolla, CA.

RMS (2006), "2006 Kiholo Bay, Hawaii Earthquake," RMS Event Report, Risk Management Solutions.

Robertson, I. N., P. G. Nicholson, and H. G. Brandes, 2006. "Reconnaissance Following the October 15th, 2006 Earthquake on the Island of Hawaii," Report No. UHN/CEE/06-07, University of Hawaii, October 26, 2006.

Sekizawa, A., M. Ebihara, and H. Notake (1998), "Development of Seismic-induced Fire Risk Assessment Method for a Building," Fire Safety Science, *Proceedings of the Seventh International Symposium,* pp. 309-320, 1998.

Serrette, R and K. Ogunfunmi (1996), "Shear Resistance of Gypsum-sheathed Light-gauge Steel Stud Walls," ASCE *Journal of Structural Engineering*, Vol. 122, No. 4, pp. 383-389.

Shimizu, N. and Y. Hanawa (1998), "Seismic Experiment of Piping Systems Simultaneously Subjected to Shake Table Excitation and Actuator Input," American Society of Mechanical Engineering, *Seismic Engineering*, Vol. 364.

Ukai, T. (1997), "The Great Hanshin-Awaji Earthquake and the Problems with Emergency Medical Care," *Ren Fail,* 1997, Vol. 19, pp. 633-645.

Yao, G.C. (2000), "Seismic Performance of Direct Hung Suspended Ceiling Systems," ASCE, *Journal of Architecture Engineering*

Fifth International Conference on Urban Earthquake Engineering
March 4-5, 2008, Tokyo Institute of Technology, Tokyo, Japan

Variation of supplemental stiffness and damping using adjustable fluid spring and damper

J. Dyck[1], S. Nagarajaiah[2] and D. Taylor[3]

1) Formerly, Graduate Research Assistant, Dept. of Civil & Environmental Engineering, Rice University, Houston, TX 77005
2) Professor, Dept. of Civil & Environmental Engineering and Mechanical Engineering & Material Science, Rice University
3) President, Taylor Devices Inc., Buffalo NY
Lack Email Address

Abstract: In this paper a new adjustable passive fluid spring and damper (apsd) is studied experimentally. The apsd is capable of varying the stiffness and damping independently; thus, the device can be used as an adjustable damper or as an adjustable fluid spring or as a combined stiffness and damping device. This allows a range of possibilities to modify structural stiffness and damping properties by placing the apsd at appropriate locations in the bracing system of the structure. In this paper the experimental results of the apsd under cyclic and ramp loading are presented. The versatile properties of the apsd are shown by means of experimental force - displacement loops.

1. INTRODUCTION

Passive fluid viscous dampers have been implemented in a number of structures with the primary objective of response reduction due to energy dissipation during earthquakes or wind gusts. In the case of earthquakes, the dampers prevent or limit structural damage, whereas, for wind gusts, the dampers reduce vibration levels to relieve occupant discomfort. The testing of passive fluid dampers, developed by Taylor Devices, for seismic applications was performed by Constantinou and Symans (1993) and clearly demonstrated the ability of such dampers to improve the performance of building structures. Fluid viscous dampers consist of a metallic cylinder, filled with a low-viscosity fluid, containing a piston head which separates the two sides of the cylinder. For the range of frequencies typical of the fundamental mode of most structures, fluid dampers can be designed to exhibit insignificant restoring forces, resulting in behavior that is essentially linear viscous. Fluid dampers also offer the advantage that they provide high-energy dissipation density (i.e., due to the high internal fluid pressures, they are able to dissipate large amounts of energy for their size).

Various semi-active devices that can change stiffness and damping have been developed (Spencer and Nagarajaiah 2003). The variable stiffness systems (VS) developed by Kobori et al. (1993) at Kajima Research Institute, Japan, maintain non-resonant state under seismic excitations by altering the building's frequencies and stiffness based on the nature of the earthquake. The stiffness is varied by engaging and disengaging the braces in each story of the structural framing system. The hydraulic device connected between inverted V-shaped bracing system and floor beams is used to engage and disengage the bracing system in an on-off manner and thus leading to abrupt changes in stiffness.

To overcome the limitation of the VS system, Nagarajaiah and Mate (1998) have developed a new semi-active variable stiffness (SAIVS) system, which varies the structural stiffness and frequency continuously and smoothly, and maintains non-resonant state. The mechanical SAIVS device has been developed, tested, and shown to be effective by Nagarajaiah and Mate (1998).

Yang et al. (2000) and Jabbari and Bobrow (2002) have developed and shown the effectiveness of a resetting semi-active stiffness damper system. The resetting semi-active stiffness damper system consists of a cylinder-piston system with an on-off valve in the by-pass pipe connecting two sides of the cylinder filled with hydraulic oil. During the operation in the resetting mode, the valve is always closed, and hence the energy is stored in the hydraulic damper (hydraulic cylinder and bracing) in the form of potential energy. At appropriate time instants, the valve is pulsed to open and closed quickly so that the pressure difference across the cylinder is eliminated, and the energy stored in the entire damper is released. Hence, by regulating the resetting damper at appropriate time instants, the structural response is reduced by withdrawing energies from the vibrating structure. It is not possible to vary the stiffness with this device as it can only operate in the lock or unlock mode.

Variable damping systems that utilize variable orifice fluid dampers have been developed for structural systems by Symans and Constantinou (1997). The variable damper is made up of a metallic cylinder which contains a piston rod/head assembly, a piston rod make-up accumulator (to minimize restoring forces), and is filled with a thin silicone oil. An external bypass loop containing a control valve is attached to the damper for modulating fluid flow. The pressure differential across the piston head, and thus the output force, was therefore modulated by the external control valve. Depending on the type of valve used, either two-stage damping or continuously variable damping was generated. Symans and Constantinou (1997) have shown by means of shaking table test that the peak response of the uncontrolled structure could be reduced dramatically with the use of the variable damper control system.

MR fluid dampers (Spencer et al. 1997) are relatively new semi-active devices that utilize MR fluids to provide controllable damping forces. These devices overcome many of the expenses and technical difficulties associated with semi-active devices previously considered. For improving the scalability of MR fluid technology to devices of appropriate sizes for civil engineering applications, a large-scale 20-ton MR fluid damper has been designed and built (Spencer et al. 1998). The damper uses a particularly simple geometry in which the outer cylindrical housing is part of the magnetic circuit. The effective fluid orifice is the entire annular space between the piston outside diameter and the inside of the damper cylinder housing. The damper has an inside diameter of 20.3 cm and a stroke of ±8 cm. The electromagnetic coils are wound in three sections on the piston, resulting in four effective valve regions as the fluid flows past the piston. At the maximum magnetic field, the output force of the damper is 201 kN, which is within 0.5% of the design specification 200 kN. Moreover, the on/off range of the damper is well over the design specification of 10 (Spencer et al. 1998, Sodeyama 2003).

Although variable stiffness devices and variable damping devices have been developed separately, both features have not been considered in a single device. In this paper a new adjustable passive fluid spring and damper (APSD) is studied experimentally. The APSD is capable of varying the stiffness and damping independently; thus, the device can be used as an adjustable damper or as an adjustable fluid spring or as a combined stiffness damping device. This allows a range of possibilities to modify structural stiffness and damping properties by placing the APSD at appropriate locations in the bracing system of the structure. In this paper the experimental results of the APSD under cyclic and ramp loading are presented. The versatile properties of the APSD are shown by means of experimental force - displacement loops.

2. ADJUSTABLE STIFFNESS AND DAMPING DEVICE

Initial tests of the APSD device are conducted under cyclic loading, in order to determine the variation of stiffness and energy dissipation capabilities. The adjustable stiffness and damping properties of the damper are controlled by two separate valves, as shown in Fig. 1. Stage one consists of a fluid spring with an accumulator and an adjustable spring valve and stage two consists of a variable damper with an adjustable bypass damper valve, as shown in Fig. 1 and Fig. 2. The damper is designed for an allowable stroke of 4 inches. The dynamic damping function is approximately 1933 $v^{0.9}$ with the damping valve closed, where v is the velocity in inches per second. The damping can be reduced by opening the damping valve, which allows addition flow through a 0.19 inch diameter orifice in the bypass. By adjusting the spring valve, the spring's properties can be turned on or off. When the spring valve is closed, the low pressure accumulator is removed from participation, which allows for the generation of high liquid spring forces under full stroke of the piston. Approximately 9,500 pounds of liquid spring force is generated when the damper is stroked for full 4 inches with the spring valve closed. The low pressure accumulator is reactivated when the spring valve is opened and the force in the liquid spring is negligible—only 19 lbs force under a 4 inch stroke with spring valve fully open. The spring valve can be closed at any intermediate stroke (for example two inches) leading to lower liquid spring force due to shorter stroke lengths.

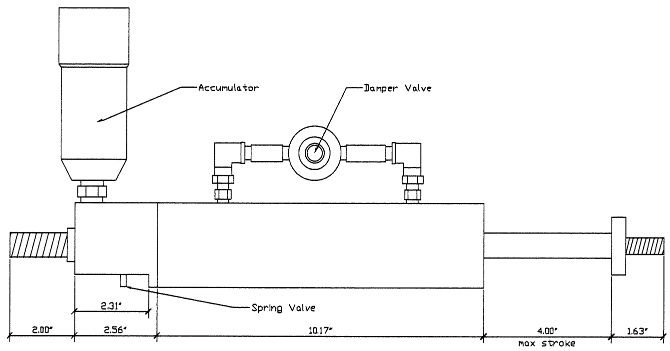

Figure 1. Dimensions of the APSD Device, with the Location of the Spring Valve, Damper Valve, and Accumulator Shown.

3. TEST SETUP

The experimental testing setup is specifically designed to be able to test the prototype device at peak dynamic conditions. The setup, shown in Fig. 2, allows for velocities of up to 21 inches per second and loading in excess of 30 kips.

The data is collected by MATLAB/SIMULINK in conjunction with dSPACE data acquisition software from the load cell, with a maximum dynamic capacity of 56 kips dynamic and maximum static capacity of 110 kips, and LVDT. The instrumented channels include force and displacement measurements from the actuator and a LVDT to measure the displacement of the damper. Processed data is used to generate force displacement loops.

4. TYPES OF LOADING

In order to properly understand and model the properties of the damper, cyclic and ramp loadings of various frequencies and amplitudes are applied to the damper. Test signals shown in Fig. 3 are applied (via dSPACE) to the damper and force – displacement response data, under various loadings, is recorded.

Tests are conducted using cyclic loading ranging in frequency from 1/2 to 3 Hz and amplitudes from 1/4 to 1 inch. Thirteen different high velocity ramp tests are conducted—for details refer to Table 1.

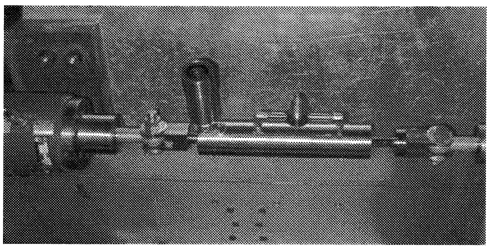

(a) APSD Device Connected to Load Cell

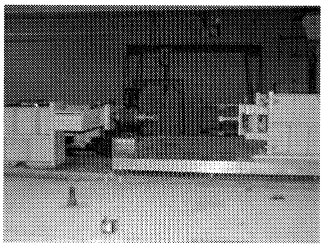

(b) Side View

Figure 2. Test Setup for the APSD Device

5. TEST RESULTS

Initial testing of the APSD device is conducted with the damper positioned in the "neutral stroking position" located at the midpoint of the stroke, i.e. at 2 inches. Systematic testing with full sine pulse loading is conducted for the various damping and stiffness settings.

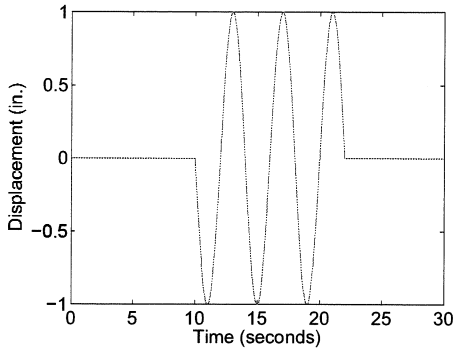

(a) Full Sine Pulse Loading

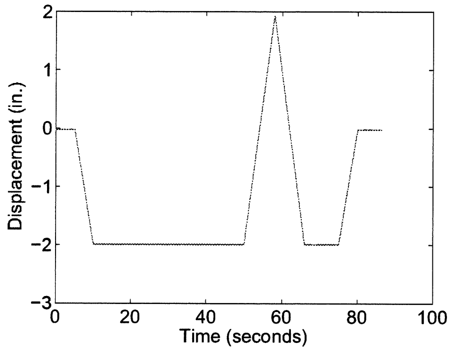

(b) Ramp Pulse Loading

Figure 3. Sample Loading used for Dynamic Testing of the APSD Device.

Force displacement loops with damper valve closed and the stiffness valve open, are shown in Fig. 4 (a). The test resulted in a maximum force of ~7.5 kips as shown in Fig. 4 (a), for 0.5 Hz; also shown are force displacement loops for 1 Hz and 1.5 Hz. The variable damping capability is clearly evident. Force displacement loops for the case with damping valve at 2 revolutions and stiffness valve closed at 4 inches is shown in Fig. 4 (b). With the stiffness accumulator valve closed at 4 inches and the damping valve at 2 complete revolutions, the maximum force achieved by the damper is approximately 2.75 kips and the corresponding stiffness is 2.75 kips/inch—note preloading of ~3 kips exits when the valve is closed at any position beyond the 2 inch neutral mark.

The second stage of testing involves ramp pulse loading of various velocities and amplitudes. In order to protect the APSD device, all ramp loadings are centered about the neutral stroking position, as illustrated by the ramp pulse in Fig. 3(b).

Two tests are conducted to determine the spring accumulator's strength at a velocity of 1/4 inch per second. With the damping valve closed and the accumulator valve open, the prototype damper produces approximately 1/2 kip of force, and with the spring accumulator closed at full stroke, the damper produces approximately 9.5 kips of force (refer to Fig. 5 (a)). The variable stiffness is clearly evident in Fig. 5 (a).

For the high velocity ramp loadings, two settings are tested as listed in Table 1. The force displacement loops for the second setting (21 inch/sec compression velocity and 10 inch/sec tension velocity) are shown in Fig. 5 (b). The damper is capable of producing nearly 20 kips force with damper valve closed and spring valve open.

The effects of the "high/low" stiffness capabilities of the prototype damper are evident in Figs. 4 (b) and 5 (a). Depending on the spring valve setting, damper valve setting, and the frequency of the cyclic test, the sharpness and the shape of the hysteresis or force-displacement loop changes—thus the stiffness and damping changes. The maximum liquid spring force and the amount of damping are the direct result of where the spring valve is closed and the position of the damping valve, as shown in Figs. 4 and 5.

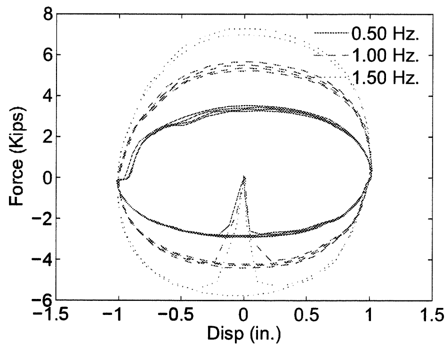

(a) Damping Valve Fully Closed and Stiffness Valve Open

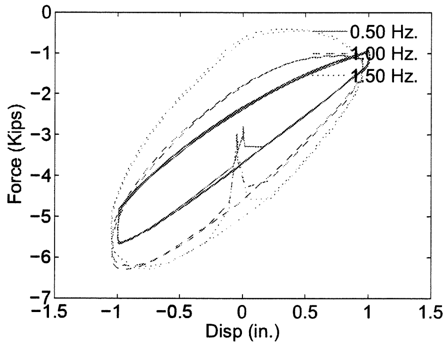

(b) Damping Valve at 2 Revolution and Stiffness Valve Closed at 4~inches

Figure 4. Force Displacement Loops under Full sine pulse loading

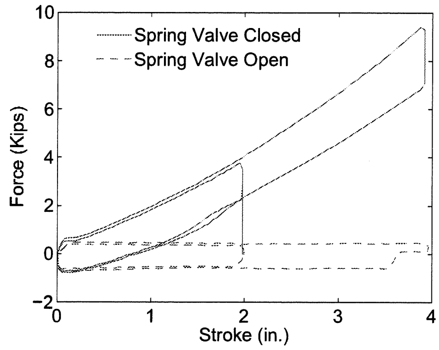

(a) At 1/4 inch per second

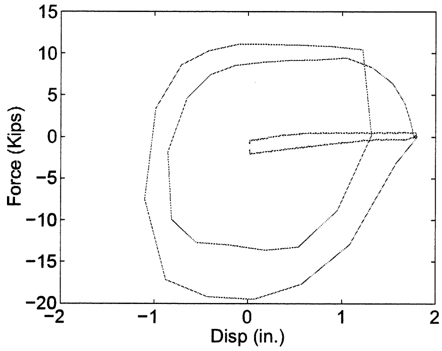

(b) Compression Velocity of 21~inch/sec and Tension Velocity of 10~inch/sec with Damping Valve closed and Stiffness Valve Open

Figure 5. Force Displacement Loops under Ramp Loading

6. CONCLUSIONS

The testing of a prototype APSD device has been presented. Tests were conducted at various amplitudes, frequencies, and for various types of loading. The following conclusions can be drawn based on the test results.

1. The APSD device can alter damping and stiffness properties quite effectively.
2. The maximum liquid spring force obtained under dynamic loading of APSD, with spring valve closed (at full 4 inch stroke) and with the damping value fully open, is approximately 9.5 kips.
3. The maximum damping force obtained under 21 inch/sec dynamic loading of APSD, with damping valve closed and stiffness valve open, is approximately 20 kips.
4. Significant changes in the shape of the force-displacement or hysteresis loops, with different stiffness and damping, can be obtained by adjusting the spring valve and damping valve settings.

Table 1. Ramp pulse excitation tests conducted on APSD device.

Compression Velocity	Tension Velocity	Spring Valve	Damping Valve	Amplitude
Inches/sec	Inches/sec			Inches
0.25	0.25	Open	Closed	±2.00
0.25	0.25	Closed	Closed	±2.00
15.0	15.0	Closed	Closed	±0.25
15.0	15.0	Closed	Closed	±0.50
15.0	15.0	Closed	Closed	±0.75
15.0	15.0	Closed	Closed	±1.00
21.0	10.0	Open	Closed	±0.25
21.0	10.0	Open	Closed	±0.50
21.0	10.0	Open	Closed	±0.75
21.0	10.0	Open	Closed	±1.00
21.0	10.0	Open	Closed	±1.25
21.0	10.0	Open	Closed	±1.50
21.0	10.0	Open	Closed	±1.75

ACKNOWLEDGMENTS

The authors wish to acknowledge the support of NSF CAREER grant CMS 9996290.

REFERENCES

Constantinou, M. C., and M. D Symans (1993). Experimental study of seismic response of buildings with supplemental fluid dampers, *Struct. Des. Tall Build.*, 2, 93–132.

Jabbari, F., and J. E. Bobrow (2002). Vibration suppression with resettable device, *Journal of Engineering Mechanics*, 128(9), 916-924.

Kobori, T., M. Takahashi, T. Nasu, N. Niwa, and K. Ogasawara(1993). Seismic response controlled structure with active variable stiffness system, *Earthquake Engineering and Structural Dynamics*, 22, 925-941.

Nagarajaiah, S., and D. Mate (1998). Semi-active control of continuously variable stiffness system, *Proc., 2nd World Conference Structural Control*, 1, 397-405.

Sodeyama H., K. Sunakoda, H. Fujitani, S. Soda, N. Iwata, and H. Hata (2003). Dynamic tests and simulation of magneto-rheological dampers, *Computer-Aided Civil and Infrastructure Engineering*, 18, 45–57.

Spencer, B. F., S. J. Dyke, M. K. Sain, and J. D. Carlson (1997). Phenomenological model of a magnetorheological damper, *Journal of Engineering Mechanics*, 123(3), 230-238.

Spencer Jr., B. F., G. Yang, J. D. Carlson, and M. K. Sain (1998). Smart Dampers for Seismic Protection of Structures: A Full-Scale Study, *Proc. of the 2nd World Conference Structural Control*, 1, 417–426.

Spencer, B. F., and S. Nagarajaiah(2003). State of the art of structural control, *Journal of Structural Engineering*, 129(7), 845-856.

Symans, M. D., and M. C. Constantinou (1997). Seismic testing of a building structure with a semi-active fluid damper control system, *Earthquake Engineering and Structural Dynamics*, 26(7), 759–777.

Yang, J. N., J. H. Kim, and A. K. Agrawal (2000). A Resetting Semi-Active Stiffness Damper for Seismic Response Control, *Journal of Structural Engineering, ASCE*, 126 (12): 1427-1433.

Fifth International Conference on Urban Earthquake Engineering
March 4-5, 2008, Tokyo Institute of Technology, Tokyo, Japan

FULL-SCALE TESTS OF FRAME SUBASSEMBLIES AND DAMPERS TO BE USED FOR E-DEFENSE 5-STORY BUILDING SPECIMEN

Kazuhiko Kasai[1], Yoji Ooki[2], Shojiro Motoyui[3], Toru Takeuchi[4], Kensaku Kaneko[5] and Yu Azuma[6]

1) Professor, Structural Engineering Research Center, Tokyo Institute of Technology, Japan
2) Assistant Professor, Structural Engineering Research Center, Tokyo Institute of Technology, Japan
3) Associate Professor, Dept. of Build Environment, Tokyo Institute of Technology, Japan
4) Associate Professor, Dept. of Architecture and Building Engineering, Tokyo Institute of Technology, Japan
5) Postdoctoral Research Fellow of COE, Center for Urban Earthquake Engineering, Tokyo Institute of Technology, Japan
6) Graduate Student, Dept. of Build Environment, Tokyo Institute of Technology, Japan
kasai@serc.titech.ac.jp, ooki@serc.titech.ac.jp, motoyui@enveng.titech.ac.jp,
ttoru@arch.titech.ac.jp, kensaku@enveng.titech.ac.jp, azuma.y.ad@m.titech.ac.jp

Abstract: E-Defense is the Japanese three-dimensional shaking table, the largest in the world. Using the table, a full-scale passively controlled 5-story building will be tested in 2008 or later. Five damper types will be considered and 16 dampers per each type will be installed into the building. Full-scale tests of such dampers as well as those on steel beam-column-gusset subassemblies were conducted in 2007, and the results are explained in the present paper.

1. INTRODUCTION

Wide-ranging participation from the US and Japan is being encouraged in the NEES/E-Defense Collaboration Research Program using the E-Defense shaking table. The facility is the largest earthquake simulator capable of subjecting full-scale structures to the strongest earthquakes recorded in the world.

Relatively short term collaboration has already taken place involving geo-structures, wooden buildings, and reinforced concrete buildings. Currently, more emphasis is made on steel buildings and bridges. The steel building projects focus on moment-resisting frames, innovative methods for new or existing buildings, nonstructural elements, and protective systems (Kasai et al. 2007). This paper discusses the project on a protective system utilizing the passive control scheme.

2. FULL- SCALE 5-STORY FRAME SPECIMEN

Passive control scheme is typically used for numerous major Japanese buildings and even many small residential buildings after the 1995 Kobe earthquake, in order to better protect the building and its contents (JSSI 2003, 2005, Kasai & Kibayashi 2004a). However, very little information has been available regarding their actual performance at both major and frequent minor earthquakes, since histories of the new schemes are short.

Hence, realistic 3-D shaking table tests of full-scale building specimens utilizing the new schemes will be conducted in order to assess their performance and enhance analysis/design methods. The performance will be verified through a series of time history analyses. The building is 5-story with two bays in each direction. The seismically active weight of the superstructure will be about 6,500 kN for the passively controlled specimen, and 8,000 kN for the base isolated specimen. Tests of the passively controlled buildings are scheduled for fall 2008, considering four different damper types (oil, viscous, viscoelastic, and steel dampers).

Detailed tests and analyses have been conducted for three damper sizes per damper type, as well as many beam-column-gusset subassemblies. As shown in Figure 1, the plan dimension of the 5-story building is 12 m × 15 m, and total height from center line of the foundation beam is 18.1 m. Two bays are considered for each of x- and y-directions, respectively. Details for the frame are given elsewhere (Kasai et al. 2007).

3. FULL-SCALE DAMPER TESTS AND ANALYSES

3.1 Outline of Damper Tests

Four major types of dampers are considered for the experiment. They are steel, viscoelastic, viscous, and oil dampers (Figures 2). See JSSI (2003, 2005) for their mechanisms and characteristics:

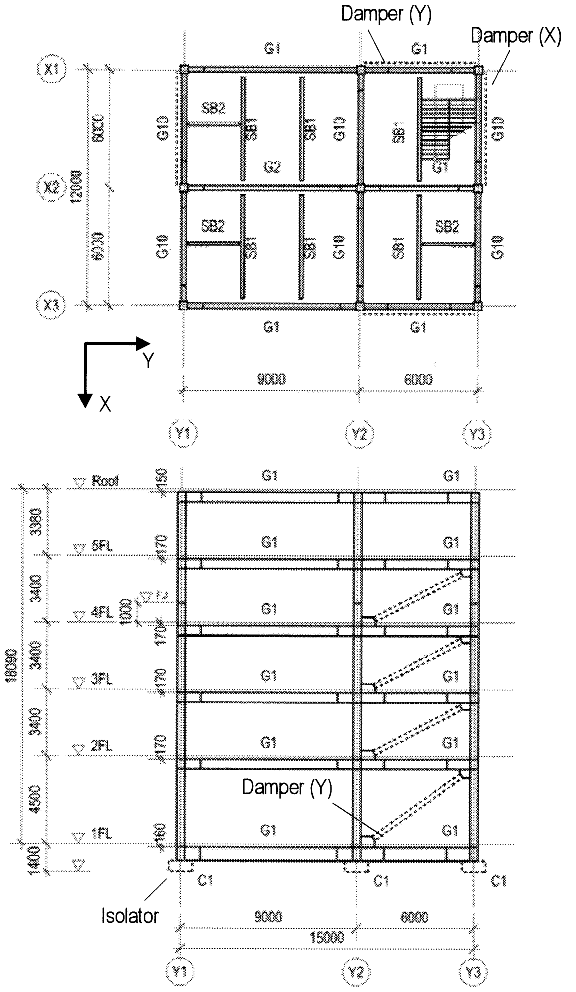

Figure 1 Full-Size 5-Story Frame: (a) Plan of A Typical Floor, and (b) Elevation (Damper and Isolator Shown by

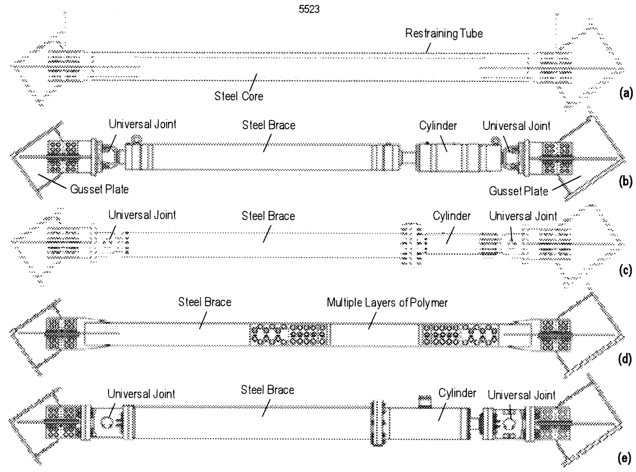

Figure 2 Sizes and Configurations of 5 Types of Dampers to be Used (between 2nd and 3rd Floors): (a) Steel, (b) Oil, (c) Viscous (US), (d) Viscoelastic, and (e) Viscous (Japanese) Dampers

For each damper type, three different damper sizes are considered. They are identical with those at 1st, 3rd, and 4th stories of the full-scale 5-story building specimen (Figure 1). Since the length of the specimen is restricted by that of the loading apparatus (Figure 3), the yielding part of the steel damper is reduced to 4.2 m. As for the others, the length of the brace is adjusted. As shown by Figure 3, the test set-up utilizes two parallel dynamic actuators whose maximum possible stroke, velocity, and load are 400 mm, 500 mm/s, and 2000 kN, respectively.

As shown in Figure 4, deformations of various components of the damper-brace assembly were measured, and are used to estimate properties of the analysis models depicted by Figure 5. Sinusoidal and random deformation tests are performed as the "basic dynamic tests".

For sinusoidal deformation tests, four different peak displacements (0.5, 12, 24, 36 mm) and four frequencies (0.2, 0.5, 1, 2 Hz) are combined, and total of fifteen cases are considered. Note that the loading with combination of 36 mm and 2 Hz exceeds the performance limit of most dampers, and was not performed.

The deformations correspond to drift angles of 1/300, 1/150, and 1/75 at 1st story of the 5-story building specimen, respectively. The deformation control was done for u_d , u_m , u_m , and u_d (Figures 5a to 5d), respectively for the steel, oil, viscous, and viscoelastic dampers, respectively.

As for random deformation tests, the 1st story drift history that is obtained from each analysis of 5, 12, and 24-story building models is normalized and applied to damper-brace assembly. The drifts due to JMA Kobe NS record and Taft EW record are considered. Peak deformations of 12 and 24 mm, and only for JMA Kobe 36 mm, are considered, thus, total number of cases considered is fifteen.

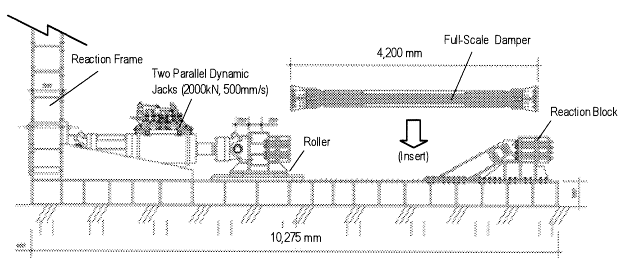

Figure 3 Damper Test Set-Up

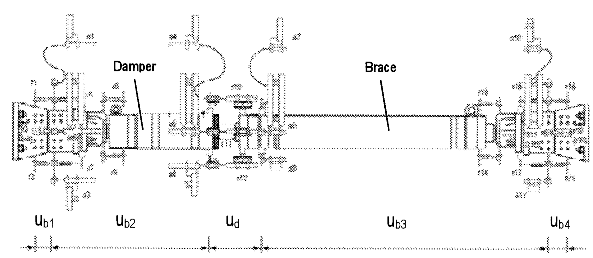

Figure 4 Oil Damper and Instrumentation

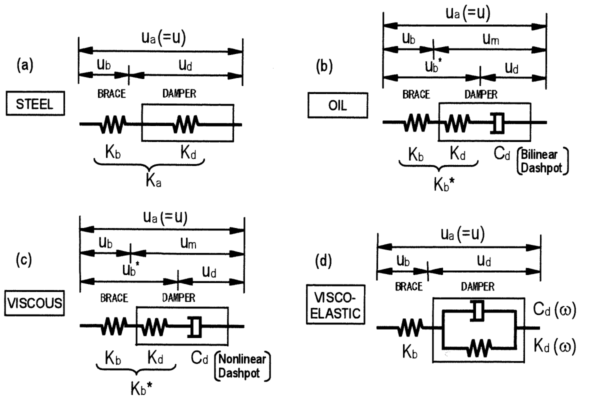

Figure 5 Added Component Combining Brace and Damper in Series (for Analysis)

Various additional tests are performed on a damper-by-damper basis. Steel damper is statically tested prior to the above dynamic tests, in order to estimate the basic parameters for the analytical model. The test applies cyclic deformation of gradually increased peak magnitude, i.e., the peak average strain over the yielding part of the buckling-restrained brace is varied from 0.02% to 2%. Also, the total number of the dynamic tests is reduced to about 1/3 times those for the velocity dependant dampers, in order not to exceed low cycle fatigue life of the specimen. After the dynamic tests were completed, the specimens still survived, and the sinusoidal deformation with peak magnitude of 36 mm and frequency 1 Hz was applied until fracture. For both the oil and the viscous dampers, sinusoidal deformations of 1, 2, and 4 mm with 1 Hz are applied to examine trends of deviations from the ideal performance. For viscoelastic damper, ambient temperatures of 22 and 30°C are considered, because of the temperature sensitivity of the viscoelastic material.

3.2 Damper Test Results and Correlative Analyses

Figure 6a shows the hysteretic curves obtained from test and analysis of the steel damper. Analytical model is given in the reference (Kasai et. al. 2004a, Yamazaki et. al. 2006). The model is based on Menegotto-Pinto Model, and it matches very well with the static test result, as evidenced by Figure 6. The damper force under dynamic loading appears to be somewhat larger, as has been realized, and analytical model for such behavior is being developed by the writers.

Figures 6b to 6d show the hysteretic curves obtained from tests and analyses of the oil, viscous, and viscoelastic dampers, respectively. Analytical models are given in the references (Kasai et. al., 2004b, 2004c, and 2004d). The analytical model appears to be accurate (Figure 6b). However, although not shown, the oil damper hysteresis at small deformation of 0.5 mm and/or velocity is not well predicted by the analysis, which must be considered when designing against wind and traffic vibration.

As for the viscous damper, its hysteresis at velocity less than 20 mm/s differs considerably from analytical prediction (Figure 6c left). Further, the spring stiffness K_d of the nonlinear Maxwell model for the viscous damper (Figure 5c) appears to be even smaller than that of the oil damper (Figure 5b). This should be considered in design, since, assuming $K_d \approx \infty$ as recommended elsewhere, can lead to overestimate of control performance. In the present study, a finite value of K_d is estimated from the tests, and is used for the analysis model. Thus-obtained model matches well with the actual damper, demonstrating F_d vs. u_d curve that is inclined (Figure 6c) due to the deformation of the spring mentioned above. Analytical model for the viscoelastic damper appears to be accurate from extremely small to large deformation (Figure 6d). Unlike other dampers, increase of force at the first half cycle is remarkable.

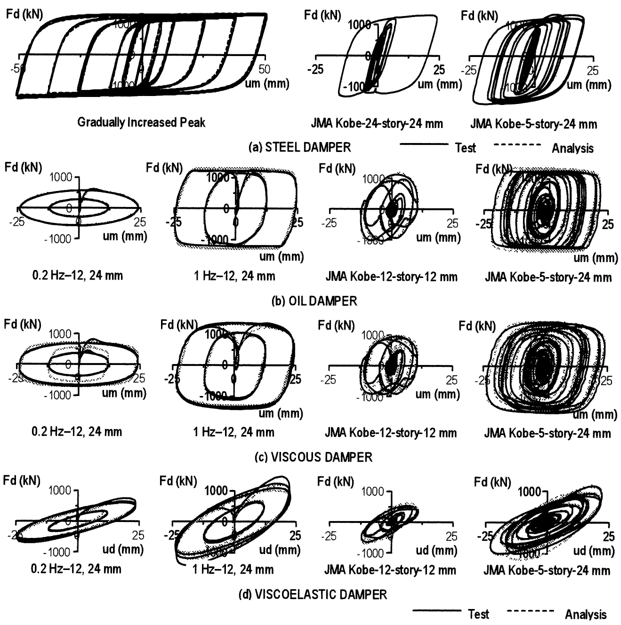

Figure 6 Steel, Oil, Viscous, and Viscoelastic Dampers to be Used For 1st Story: Test and Analysis

4. FULL-SCALE SUBASSEMBLY TESTS AND ANALYSES

4.1 Hybrid Test Combining Subassembly and Virtual Damper

The performance of passively-controlled building depends not only on damper but also on frame members and connections. In addition to the bending moment and shear caused by the story drift, relatively large axial force develops in the elements because of the damper force. The axial force can cause earlier yielding and possibly buckling in the elements. In order to develop a design method to control such failure, full-scale tests and analyses have been conducted on subassemblies consisting of beam, column, and gusset plate, and interim results are reported here.

Figure 7 shows the concept of a simplified hybrid test method combining a subassembly and a virtual damper. The subassembly is of L-shape, representing a quarter portion of the frame. We define "positive loading" when the beam is in positive (tension) axial force and positive moment, and vice versa (Figure 7).

Figure 8a shows the test-set-up, where laterally supported L-shape specimen is connected to Link-1 and Link-2 that keep the distance between the midpoint of the brace and inflection points in beam and column, respectively, see Figure 7. Two parallel actuators (total 3,000 kN capacity) are used for the displacement control to satisfy the target story drift, and one actuator diagonally placed (1,000 kN capacity) for the force control simulating damper force. The target story drift is given, but target damper force depends on the change Δu_a in diagonal distance (Figure 8a). The target damper force is calculated by substituting the measured Δu_a into the mathematical model of the damper at every step of the test, and the actuator applying such a force is called the "virtual damper". The virtual damper can apply the force of any damper type, as long as the mathematical model is available. The steps for displacement control, force control, and damper force calculation are schematically shown in Figure 8b.

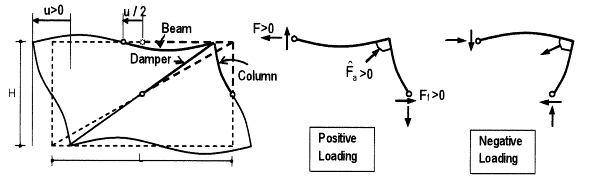

Figure 7 Concept of Hybrid Test and Definitions of Positive Loading

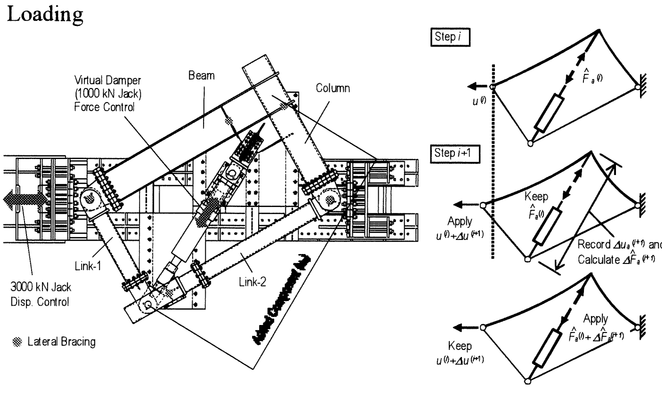

Figure 8 (a) Set-Up, and (b) Procedure of Hybrid Test

Note that under the positive and negative loading cases (Figure 7), the bottom flange of the beam near the gusset tends to develop relatively large tension strain and compression strain, respectively. This is analytically illustrated in Figure 9, where possibility of local buckling under negative loading is clearly shown by our extensive nonlinear finite element analysis.

4.2 Specimens and Loading Schemes

Figure 10 shows a typical specimen. The beam is of a built-up section of 500 mm depth, 12 mm web

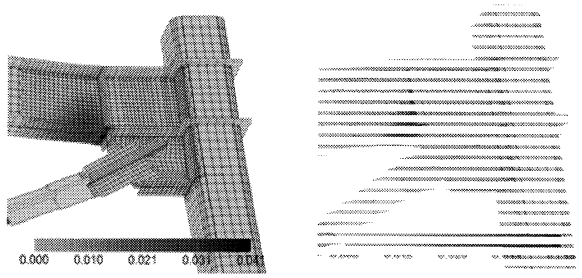

Figure 9 FEM Analysis Results for Positive and Negative Loading Cases

thickness, 250 mm flange width, and 22 mm flange thickness. The column is a square box section of 400 mm × 400 mm × 19 mm. The nominal yield strength of the steel material is 325 MPa for all the elements, and actual yield stresses are 371, 357, 351, and 372 MPa for the beam web, beam flange, column, and gusset plate, respectively, unless noted. The beam satisfies the Japanese compact section requirement for a beam as well as a beam-column. The beam-column connection is a fully-restrained type.

Table 1 summarizes the specimen types. Specimen 1 has neither gusset plate nor stiffeners, and is not subjected to the damper force. Specimens 2 to 6, and 9 have a common configuration depicted by Figure 10.

Specimen 2, however, is not subjected to the damper force, and only the effect of story drift is examined. Specimens 3 and 4 are benchmark specimens, meaning that they have the typical

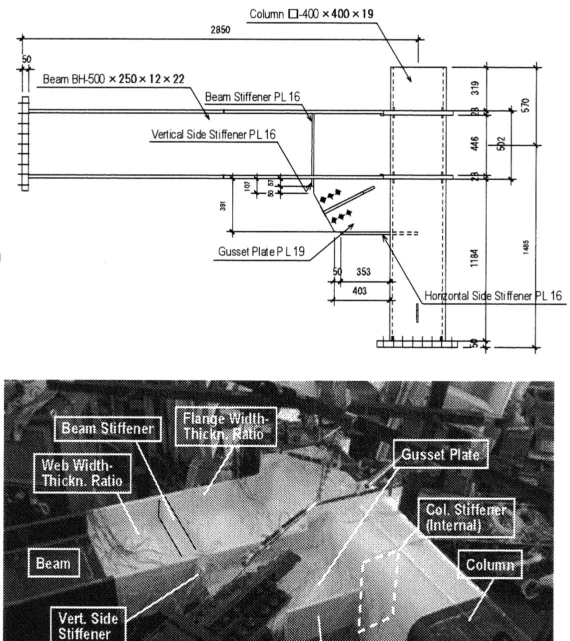

Figure 10 Typical Full-Scale Subassembly Specimen

Table 1 Specimen Types and Cumulative Deformation Capacities

No.	Specimen Type	N_f	N_f'	N_f''	θ^*
1	No Damper Force, No Gusset	111	118	120	±1/50
2	No Damper Force	123	125	126	±1/50
3	Benchmark (EP Damper / EP Damper)**	55	101	104	±1/50
4	Benchmark (VE Damper / EP Damper)***	4	8	45	±1/33
5	Large Width-Thickness Ratio for Web	0	3	24	±1/33
6	Large Width-Thickness Ratios for Web and Flange	0	0	6	±1/33
7	No Horizontal Side Stiffener, No Column Stiffener	11	22	45	±1/33
8	No Stiffeners at All	6	16	43	±1/33
9	Thin Gusset Plate	6	17	18	±1/33

* Story drift θ* indicated in this column was applied repeatedly until failure.
** EP (steel) damper force was considered for both loading cases, with gradually increased peak story drift and with constant peak story drift, respectively.
*** VE damper force was considered for loading with gradually increased peak story drift, and EP damper force considered for loading with constant peak story drift, respectively.

configuration (Figure 10), subjected to the damper force.

In specimen 5, the web is thinner (9 mm) and does not meet the Japanese code requirement for a beam-column compact section, while barely satisfying the requirement for a beam. In specimen 6, both web and flange are thinner (9 mm and 16 mm, respectively), and the flange slightly violates the compact section requirement for a beam. Specimen 7 has neither horizontal side stiffeners nor column stiffener, and specimen 8 has no stiffeners at all. Specimen 9 has a gusset plate of thickness less than 0.5 times (9 mm) the typical value of 19 mm.

All specimens are loaded with two cycles of story drift of ±1/800, ±1/400, ±1/200, ±1/100, and ±1/50 rad (0.00125, 0.0025, 0.005, 0.01, and 0.02 rad), respectively. Further, specimens 1 to 3 are loaded with multiple cycles of ±1/50 rad (0.02 rad) until failure. Specimens 4 to 9 are loaded with multiple cycles of ±1/33 rad (0.03 rad) until failure. In general, the steel (elasto-plastic, EP) damper force is considered. Exceptionally, for specimen 4, the viscoelastic (VE) damper force is considered during application of the gradually increased peak drift, and it is switched to the steel damper force during ±1/33 rad (0.03 rad).

4.3 Test Results – Failure Mode

Figure 11 shows the failure modes due to multiple cycles of ±0.03 rad. Specimens 2, 3, and 7 showed failure mode 1 in Figure 11, that is, the bottom flange failed at the welded and thus heat-affected zone near the gusset plate, vertical side stiffener, and beam stiffener. Flange local buckling was less severe due to the smaller drtft ±0.02 rad applied to specimens 2 and 3, as well as due to reduced deformation demand caused by the increased joint flexibility at the column tube wall and gusset plate in specimen 7. Thus, the strains are concentrated in the region immediately outside the gusset area where maximum moment develops on the beam.

Specimens 5 and 8 showed mode 2, where the bottom flange failed at more than 130 mm away from the gusset (Figure 11). Since local buckling is very severe in specimen 5, and since amount of welding is minimum in specimen 8, the strain concentration occurred due to localized and severe bending of the flange plate. Specimens 4, 6, and 8 showed mode 3, where the weld connecting the flange and web fractured due to sever local buckling of both the flange and web. Flange buckling was the most severe in specimens 4 and 6.

Specimen 9 showed mode 4, where tearing of the gusset plate progressed in the horizontal direction from the edge of the vertical side stiffener and gusset plate. Strain gage records indicate large shear strains at the upper portion of the gusset, where horizontal component of the virtual damper force is transmitted to the beam. The tension force, developed along the inclined gusset edge during the positive loading, might have caused the crack initiation at the vertical side stiffener.

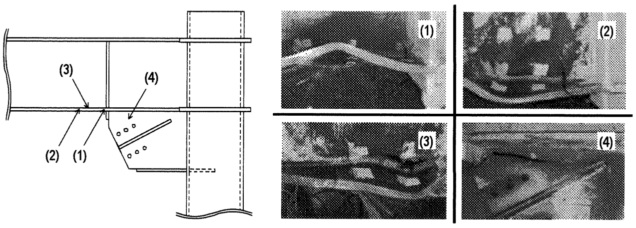

Figure 11 Various Failure Modes Observed

4.4 Test Results – Cumulated Deformation Capacity

Table 1 also summarizes the numbers of cycles applied up to certain failures defined. For specimens 1 to 3, the story drift angle of ±0.02 rad is used as mentioned. For specimens 4 to 9, ±0.03 rad is used. Note that N_f, N_f', and N_f'' are the numbers of cycles where the absolute peak force becomes 0.8, 0.7, and 0.5 times the largest magnitude experienced at the earlier cycle, respectively. At cycle number N_f'', significant tearing occurred in the subassembly.

There is remarkable difference of number of cycles to the failure between the story drift angles of ±0.02 and ±0.03 rad, as seen from specimens 3 and 4. The specimens are believed to be at almost the same condition, before applying such cycles with the common EP damper force. They show more than ten-fold difference of N_f = 55 and 4, respectively (Table 1). When applying ±0.02 rad, flange local buckling was slight, and the peak force remained stable during many repeated cycles (Figure 12a).

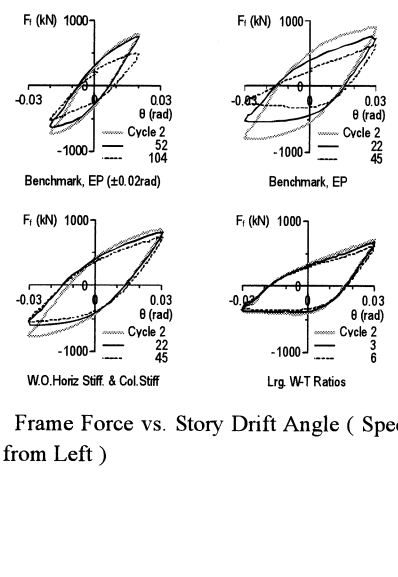

Figure 12 Frame Force vs. Story Drift Angle (Specimens 3, 4, 7, and 6 from Left)

As for ±0.03 rad, the flange local buckling occurred from the first cycle, and the beam kept deteriorating at the subsequent cycles, resulting in significantly lowered peak force of the frame at the negative loading (Figure 12b).This trend becomes more significant when the width-thickness ratios of the flange and web are large, like specimens 5 and 6 (Figure 12d). The peak forces of these specimens at negative loading case decreased to 0.8 or 0.7 times the largest peak force during application of the cyclic deformation with increasing peak drift angle, prior to application of ±0.03 rad story drift angle. Note that specimen 7 with no horizontal stiffener and no column stiffener survived much longer than the others (Figure 12c), since the beam deformation demand decreased due to the increased joint flexibility at the column tube wall and gusset plate, as mentioned earlier.

4.5 Test Results – Hysteretic Behavior

In Figure 13, the horizontal forces of the system (F), frame (F_f), and damper (F_a) are plotted against the story drift angle (θ). The positive directions of the forces are already defined in Figure 7, where $\hat{F}_a$ indicates the force at an inclined brace angle.

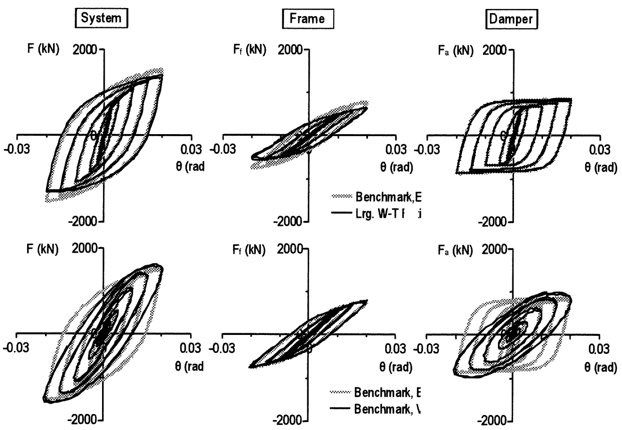

Figure 13 Forces of System, Frame, and Dampers with Respect to Story Drift Angle (Specimens 3 Vs. 6, and Specimens 3 Vs. 4)

The top row of Figure 13 shows the effect of local buckling, up to story drift of ±0.02 rad. The effect is not as great as the case of ±0.03 rad discussed earlier (Figures 12b-d)), but is still obvious from both F_f-θ and F-θ curves. Although the flange and web thicknesses are reduced by about 25%, the damper force has not changed appreciably (right figure), thus, the beam axial stress has increased by about 25%. This and moderate local buckling have caused reduction in the beam moment, and consequently horizontal force F_f of the frame.

The bottom row of Figure 13 compares of effects of EP damper and VE damper. The VE damper force is larger than the EP damper force at story drift angle of ±0.02 rad. The systems combining the subassembly and these virtual dampers show clearly different hysteretic behavior, but the inelastic strains of the beams and gusset plate were similar in both cases, as can be understood from F_f-θ curves. Note, however, that VE damper force can be larger than considered in the present study, and such a case will be investigated later by using a larger jack.

5. CONCLUSIONS

Passive control scheme is considered to better protect buildings and contents, and has been increasingly used in Japan. Since little information is available regarding its actual performance, realistic 3-D shaking table tests will be conducted for a full-scale building with the passive control scheme. The tests are scheduled for fall 2008, considering four different damper types, namely the oil, viscous, viscoelastic, and steel dampers. Detailed tests and analyses have been conducted for several damper types, as well as beam-column-gusset subassemblies of different details and thicknesses. This paper has explained interim results from such studies.

Acknowledgements:

This study is a part of "NEES/E-Defense collaborative research program on steel structures". The writers acknowledge financial support provided by the National Research Institute for Earth Science and Disaster Prevention. The study was pursued by the Damper and Isolation System Working Group (WG). Both the overall research program and the study by this WG are led by Kazuhiko Kasai, Tokyo Institute of Technology. Special thanks are given to Messrs. Sueoka, Ozaki, and Ishii at Nikken Sekkei Ltd. and to other WG members for their analysis and design. s

References:

Kasai, K., Ooki, Y., Motoyui S., Takeuchi T., and Sato, E., "E-Defense Tests on Full-Scale Steel Buildings: Part 1 – Experiments Using Dampers and Isolators", ASCE Str. Congress, Long Beach, CA, May 16-19, 2007

JSSI Manual, Design and Construction Manual for Passively Controlled Buildings, Japan Society of Seismic Isolation (JSSI), Tokyo, JAPAN, 1st Ed., 405 pages, 2003, 2nd Ed., 515 pages, 2005 (in Japanese)

Yamazaki, H., Kasai K., Ono Y., Kaneko H., and Sadasue K., "Curved Hysteresis Model of Structural Steel under Cyclic Loading, Part 3 Modify of Analysis Model", *Summaries of Technical Papers of Annual Meeting*, Architectural Institute of Japan (AIJ), C-1, September 2006, 935-936

Kasai, K., and Kibayashi, M., "JSSI Manual for Building Passive Control Technology: Part-1 Manual Contents and Design/Analysis Methods", 13WCEE, Aug. 1-6, Vancouver, 2004a, No. 2989 (Note: Papers below are the companion papers, and are listed in an abbreviated fashion.)

Kasai, K., Takahashi, O. and Sekiguchi, Y., "Part-10 Time-History Analysis Model for Nonlinear Oil Dampers", 13WCEE, Aug. 1-6, Vancouver, 2004b, No. 1283

Kasai, K., Oohara, K., and Sekiguchi, Y., "Part-11 Time-History Analysis Model for Viscous Dampers", 13WCEE, Aug. 1-6, Vancouver, 2004c, No. 1427

Kasai, K., Ooki, Y., Tokoro, K., Amemiya, K. and Kimura, K., "Part-9 Time-History Analysis Model for Viscoelastic Dampers, 13WCEE, Aug. 1-6, Vancouver, 2004d, No. 1507

Fifth International Conference on Urban Earthquake Engineering
March 4-5, 2008, Tokyo Institute of Technology, Tokyo, Japan

SEISMIC RETROFITTING OF LOW-RISE BUILDINGS VIA OUT-FRAME SYSTEMS CONNECTED BY VISCOUS DAMPERS

Masaaki Tsuji[1] and Izuru Takewaki[2]

1) Associate Professor, Dept. of Urban and Environmental Engineering, Kyoto University, Japan
2) Professor, Dept. of Urban and Environmental Engineering, Kyoto University, Japan
mtsuji@archi.kyoto-u.ac.jp, takewaki@archi.kyoto-u.ac.jp

Abstract: The purpose of this paper is to disclose the fundamental properties of a new seismic retrofit method of connecting an existing building with an adjacent outer frame using viscous dampers. The mass ratio and stiffness ratio of the outer frame to the building are introduced as the key parameters for representing the dynamic properties of such retrofit system. The damping ratio evaluated under the assumption that the outer frame is rigid is used to express a quantity of damping of the added connecting dampers. It is shown that the stiffness ratio and the damping ratio defined above play a central role in the seismic response reduction due to the proposed retrofit method. The approximate formula of the response reduction ratio is proposed and is validated through numerical examples. It is concluded that the proposed method is an effective seismic retrofit method for existing buildings.

1. INTRODUCTION

Various seismic retrofit methods for existing buildings with insufficient seismic capacity have been proposed and applied to a large number of such buildings. For example, a method of additional steel framed braces to reinforced concrete building is commonly used in Japan. The construction and design method of such additional bracing are well established. However, the method of additional braces may cause large changes in usage and appearance of a target building, since additional braces are usually installed at opening or inside of the target building.

Recently, authors proposed a new seismic retrofit method of connecting an existing building with an adjacent outer frame using viscous dampers (Tsuji *et al.* 2005), and applied the method to a real 5-story building in Japan (Kataoka *et al.* 2007). The architectural characteristics of the proposed method can be summarized as follows: (1)retrofit construction is almost limited to outside of a target building; (2)changes in usage and appearance of a target building are very small; (3)no temporal moving is required under retrofit construction.

The purpose of this paper is to disclose the fundamental properties of the proposed seismic retrofit method and to show the efficiency of the retrofit method.

Many researches have been made on seismic or modal properties of connected structures with viscous, visco-elastic, or hysteretic dampers. Kobori *et al.* (1988) presented a practical application of hysteretic damper connection between two adjacent buildings. Luco and De Barros (1998) showed an optimal damping distribution between two adjacent elastic structures of different heights. For simplicity, two buildings are represented as uniform damped shear beams. Kageyama *et al.* (2000a) showed an optimal solution of damping coefficient and stiffness between two adjacent elastic single-degree-of-freedom structures derived from the theory of stationary points of transfer functions. Furthermore, Kageyama *et al.* (2000b) proposed a method of obtain an optimum damper arrangement between two adjacent elastic multi-degree-of-freedom structures based on the stationary point theory.

The connected structure system analyzed in this paper is different from the other connected structure systems treated in the former studies in the sense that the mass of one structure representing outer frame is quite smaller than that of another structure representing target building and seismic response reduction is only required for the target building, not required for the outer frame, since the frame is built for retrofit of the target building. In this paper, two basic parameters that characterize the reduction effect on seismic response of the target building are introduced: mass ratio and stiffness ratio of the outer frame to the target building. Time history analyses and complex eigenvalue analyses are performed to disclose the fundamental properties of the retrofit method. Based on the disclosed properties, approximate formula is derived for the response reduction effect.

2. SEISMIC RESPONSE EVALUATION METHOD

2.1 Structural Model

In this paper, the building for retrofit, referred to as "target building", and the outer frame are modeled both as elastic planar shear structures. Viscous type dampers connect the two structures at the same floor level. The concept of the retrofit method is shown in Figure 1(a) and (b). The structural model is shown in Figure 1(c). The lumped mass, the damping coefficient, and the story stiffness of the jth story are denoted as m_j^S, c_j^S, and k_j^S, respectively, for the building and m_j^{OF}, c_j^{OF}, and k_j^{OF}, respectively, for the outer frame. Here and in the following, the superscripts S and OF denote that the variables belong to the target building and the outer frame, respectively. The structural damping characteristics of the both structures are assumed here to be stiffness-proportional of 3% critical damping ratio in the fundamental vibration mode when the structures are not connected. The damping coefficient of connecting damper at the jth story is denoted as c_j^I.

In order to evaluate the response reduction effect, the following dimensionless quantity δ_j referred to as "response ratio" is introduced:

$$\delta_j = \Delta_j^S / \bar{\Delta}_j^S \tag{1}$$

where Δ_j^S and $\bar{\Delta}_j^S$ denote the maximum interstory drift of the jth story of the target building with damper connection and that without damper connection, respectively.

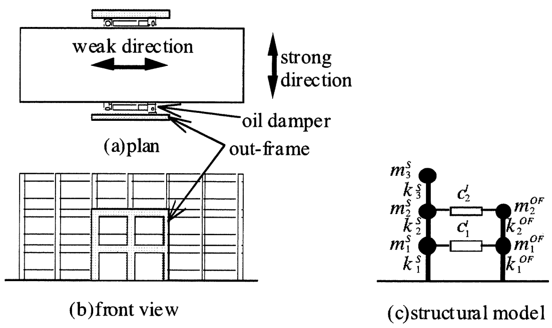

Figure 1 Concept of Retrofit via Damper Connection to Outer Frame

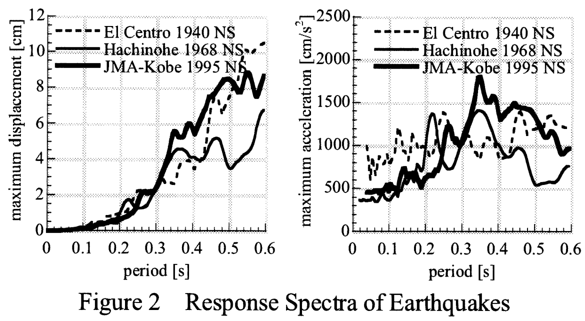

Figure 2 Response Spectra of Earthquakes

2.2 Earthquake Input and Response Analysis Method

Three recorded earthquake motions, El Centro 1940 NS, Hachinohe 1968 NS, and JMA-Kobe 1995 NS, are adopted here to evaluate the seismic response reduction effect. Each earthquake motion is normalized such that the maximum velocity of ground motion would be 50cm/s.

Maximum response subject to these earthquakes is calculated using time-history analysis. The Newmark-β method is used as the numerical integration scheme. Response spectra of maximum displacement and maximum absolute acceleration in 3% critical damping ratio are shown in Figure 2.

Because the system of connected structures may possess a strong non-proportional damping characteristic, modal damping ratios of the system are calculated by means of complex eigenvalue analysis. The rth damping ratio of the connected system is denoted by $h^{(r)}$.

3. CONNECTION EFFECT FOR SDOF MODELS

The target building and the outer frame are treated as elastic single-degree-of-freedom (SDOF) structures in this section. The following dimensionless parameter h^R is introduced here to represent the capacity of the connection damper:

$$h^R = \frac{1}{2\omega^S}\frac{c^I}{m^S} \tag{2}$$

where ω^S denotes the circular frequency of the target building without damper connection. The parameter h^R denotes the damping ratio when the outer frame is assumed to be rigid. The mass ratio μ and the stiffness ratio κ of the outer frame to the target building are defined as follows:

$$\mu = \frac{m^{OF}}{m^S} \quad , \quad \kappa = \frac{k^{OF}}{k^S} \tag{3a,b}$$

It should be noted that when κ coincides with μ, no connection effect is obtained since each lumped mass vibrates synchronously.

Detailed results are shown in the case that the natural period of the target building without connection T^S is specified as 0.5[s], which corresponds to the fundamental natural period about 5-story reinforced concrete or steel building.

Relationships between modal damping ratios $h^{(r)}$ of the connected system and h^R are shown in Figure 3(a) (μ = 0.05) and 3(b) (μ = 0.10). It can be observed that (1)when mass ratio μ is small compared with unity, variation of damping ratio with μ is very small, (2)the 1st damping ratio $h^{(1)}$ varies inmonotonically with respect to h^R, and the 2nd damping ratio $h^{(2)}$ increases monotonically with h^R, (3)the maximum value of $h^{(1)}$ and the corresponding value of h^R increase with stiffness ratio κ.

Relationships between the maximum displacement of the connected system and h^R are shown in Figure 4(a), (μ = 0.05, Kobe wave), 4(b) (μ = 0.10, Kobe wave), 5(a) (μ = 0.05, El Centro wave), and 5(b) (μ = 0.05, Hachinohe wave). It can be observed that (1)the maximum displacement of the target building Δ^S varies inmonotonically with respect to h^R and the maximum displacement of the outer frame Δ^{OF} almost increases monotonically with h^R except in the region of small h^R, (2)the minimum value of Δ^S decreases with κ and the corresponding value of h^R increases with κ, (3)although the value of h^R which minimizes Δ^S is significantly greater than that of h^R which maxmizes $h^{(1)}$, the value of Δ^S corresponding to the maximum $h^{(1)}$ seems to be a good approximation of the minimum Δ^S.

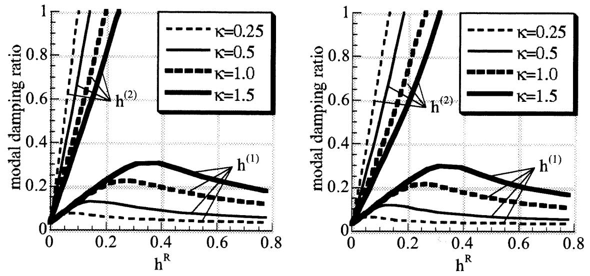

(a)μ=0.05 (b)μ=0.10

Figure 3 Relationships between Damping Ratio $h^{(r)}$ and h^R

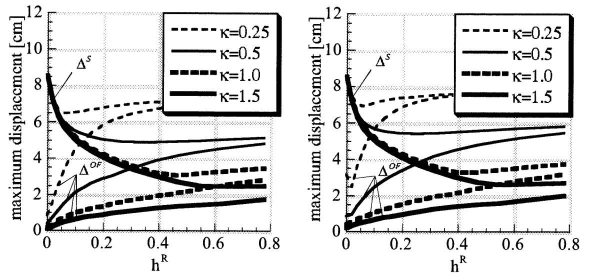

(a)μ=0.05 (b)μ=0.10

Figure 4 Relationships between Maximum Displacement of Building Δ^S, that of Outer Frame Δ^{OF} and h^R (Kobe Wave)

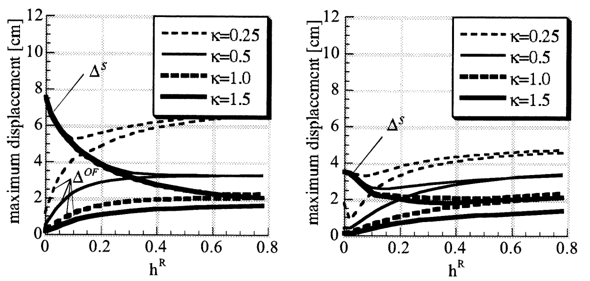

(a)El Centro 1940 NS (b)Hachinohe 1968 NS

Figure 5 Relationships between Δ^S, Δ^{OF} and h^R ($\mu = 0.05$)

Relationships between Δ^S and stiffness ratio κ are shown in Figure 6(a) (μ = 0.05, Kobe wave) and 6(b) (μ = 0.05, Hachinohe wave). It can be observed that (1)the value of Δ^S almost decreases with κ except in the region of small κ with very large h^R such as h^R = 0.39, (2)the value of Δ^S becomes almost constant when κ exceeds about 1.0.

Displacement time histories of the target building due to two different earthquake motions are shown in Figure 7 (Kobe and Hachinohe waves, μ = 0.05, κ = 1.0). Solid lines show the time histories with connection of h^R = 0.2 and dotted lines show those without connection. It can be observed that vibration period of the target building with damper connection is about the same as that without connection.

Results for the target building of T^S = 0.25[s] are shown briefly. The representative results of T^S = 0.25[s] and T^S = 0.5[s] are summarized in Table 1. Italic numbers in Table 1 denote the response ratio δ defined in Eq. (1). The term "rigid connection" in Table 1 means that the target building and the outer frame are connected by rigid member. It can be observed that the damper connection to outer frame with sufficient stiffness such as $\kappa \leq 1$ shows enough response reduction effect for building with very short natural period.

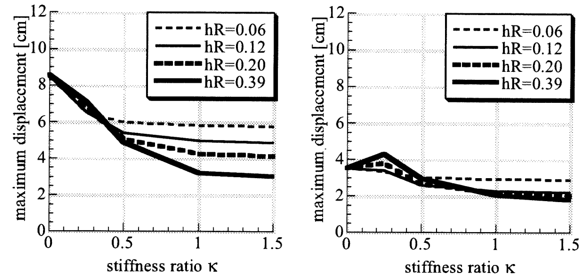

(a)JMA-Kobe 1995 NS (b)Hachinohe 1968 NS

Figure 6 Relationships between Δ^S and κ ($\mu = 0.05$)

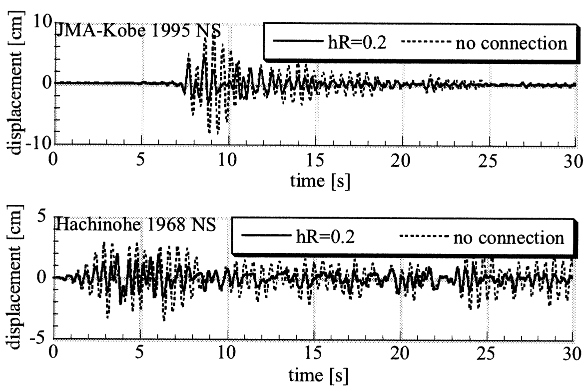

Figure 7 Time Histories of Displacement ($\mu = 0.05$, $\kappa = 1.0$)

Table 1 Comparison of Response Ratio

			TS=0.25[s], μ=0.05			TS=0.5[s], μ=0.05		
			Kobe	El Cen.	Hachi.	Kobe	El Cen.	Hach.
Δ (no connection)			1.4cm	2.2cm	1.3cm	8.5cm	7.5cm	3.5cm
δ	hR=0.10	κ=1	*0.62*	*0.52*	*0.85*	*0.61*	*0.66*	*0.69*
		$\kappa=\infty$	*0.64*	*0.51*	*0.83*	*0.58*	*0.67*	*0.68*
	hR=0.20	κ=1	*0.50*	*0.40*	*0.71*	*0.50*	*0.51*	*0.62*
		$\kappa=\infty$	*0.52*	*0.38*	*0.67*	*0.47*	*0.53*	*0.52*
	hR=0.40	κ=1	*0.50*	*0.31*	*0.56*	*0.37*	*0.36*	*0.58*
		$\kappa=\infty$	*0.48*	*0.32*	*0.48*	*0.35*	*0.37*	*0.46*
	rigid connection	κ=1	*0.38*	*0.40*	*0.51*	*0.64*	*0.47*	*1.37*

4. CONNECTION EFFECT FOR MDOF MODELS

4.1 Scope of this section

In this section, only the basic property of response reduction effect of damper connection for multi-degree-of-freedom (MDOF) structures is presented. The degrees of freedom of the target building and the outer frame are denoted as N^S and N^{OF}, respectively, where $N^{OF} \leq N^S$. For MDOF structures with viscous or visco-elastic dampers, including connected structures by dampers, many researches have been made on optimum damper distribution or placement (*e.g.,* Zhang and Soong 1992, Tsuji and Nakamura 1996, Luco and De Barros 1998, Kageyama *et al.* 2000b, Takewaki 2000).

Even if the outer frame is assumed to be rigid, the connected system which consists of two or more MDOF structures possesses a non-proportional damping characteristic, except the distribution of damping coefficients of the connection dampers is proportion to the distribution of lumped masses of the target building. For weakly non-proportional damped system, decoupling approximation is often used to evaluate the modal damping ratios (Thomson *et al.* 1974). In this section, the following dimensionless parameter h^R is introduced based on the decoupling approximation to represent the capacity of the connection dampers:

$$h^R = \frac{\sum_{j=1}^{N^{OF}} c_j^I u_j^{S(1)2}}{2\omega^{S(1)} \sum_{j=1}^{N^S} m_j^S u_j^{S(1)2}} \tag{4}$$

where $\omega^{S(1)}$ and $u_j^{S(1)}$ denote the fundamental circular frequency and the jth element of the fundamental natural mode of the target building without damper connection, respectively. The parameter h^R defined in Eq. (4) denotes the approximate fundamental damping ratio when the outer frame is assumed to be rigid.

The mass ratio μ and the stiffness ratio κ are defined as follows:

$$\mu = \frac{\hat{M}^{OF}}{\hat{M}^S} \quad , \quad \kappa = \frac{\hat{K}^{OF}}{\hat{K}^S} \tag{5a,b}$$

where $\hat{M}^{OF}$ and $\hat{M}^S$ denote the equivalent mass with respect to the fundamental natural mode of the outer frame and that of the target building, respectively and $\hat{K}^{OF}$ and $\hat{K}^S$ denote the equivalent stiffness with respect to the fundamental natural mode of the outer frame and that of the target building, respectively. Note that the fundamental participation function of each structure without connection is used here as the natural mode.

4.2 Connection of two structures of the same heights

For a representative model of connected structures of the same heights, two elastic 3-story structures with uniform mass and uniform stiffness are considered in this section. The fundamental natural period of the target building is specified as T^S = 0.5[s]. Mass ratio defined in Eq. (5a) is specified as μ = 0.05; Stiffness ratio defined in Eq. (5b) is specified as κ = 0.05 or 0.10. Two cases of damper distribution are considered: the case that the connection damper is installed only the top floor, *i.e.*, $c_1^I = c_2^I = 0$ (Case A); the case that the connection dampers with the same damping coefficients are installed in all floors, *i.e.*, $c_1^I = c_2^I = c_3^I$ (Case B).

Relationships between modal damping ratios $h^{(r)}$ and h^R defined in Eq. (4) for Case A and Case B are shown in Figure 8 and Figure 10, respectively, and relationships between maximum interstory drift Δ_j^S and h^R for Case A and Case B are shown in Figure 9 and Figure 11, respectively. In Figures 8 and 10, "h*r*" (r = 1, 2, ..., 6) denotes $h^{(r)}$; in Figures 9 and 11, "ΔS*j*" (j = 1, 2, 3) denotes Δ_j^S. Time histories of interstory drift of the 1st story in Case B are shown in Figure 12. It should be noted that the damping coefficient of each connection damper is different between Case A and Case B of the same h^R, *e.g.*, the damping coefficient per unit floor mass of the target building c_j^I / m_j^S at h^R = 0.2 is 9.3[kNs/m/t] in Case A or 5.0[kNs/m/t] in Case B. Therefore, the total sum of the damping coefficients of connection dampers in Case A is smaller than that in Case B.

It can be observed that (1)although a general tendency of variation of damping ratios with respect to h^R is quite different between Case A and Case B, variation of the fundamental damping ratios $h1$ in Case A and that in Case B are quite similar, (2)although the response reduction effect depends on damping coefficient distribution of connecting dampers, the effect in Case A and that in Case B are almost the same with respect to h^R when h^R is smaller about than 0.2, (3)when h^R is smaller about than 0.2, distribution of reduced interstory drifts is almost proportion to the distribution of interstory drifts of h^R = 0, (4)similar to the results of section 3, the value of Δ_j^S corresponding to the maximum $h^{(1)}$ seems to be a good approximation of the minimum Δ_j^S, (5)predominant vibration period of the target building with damper connection is about the same as that without connection.

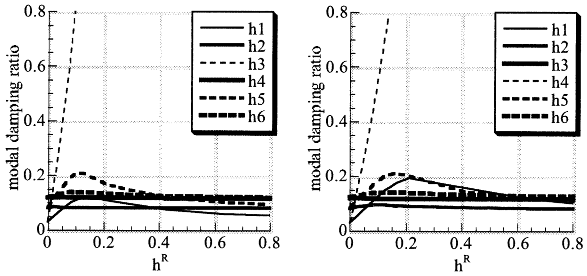

(a)stiffness ratio κ=0.5 (b)stiffness ratio κ=1.0

Figure 8 Relationships between Damping Ratio $h^{(r)}$ and h^R of Case A (Damper Connection only at Top Floor)

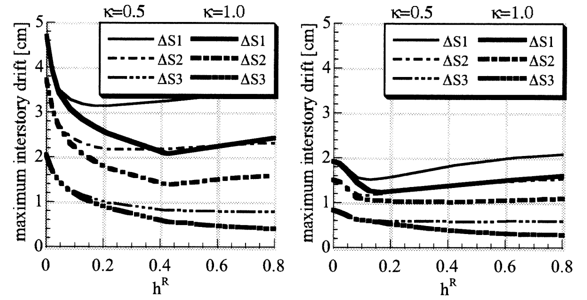

(a)JMA-Kobe 1995 NS (b)Hachinohe 1968 NS

Figure 9 Relationships between Maximum Interstory Drift of Target Building Δ_j^S and h^R of Case A

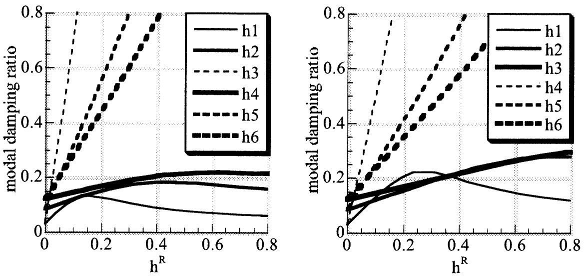

(a)stiffness ratio κ=0.5 (b)stiffness ratio κ=1.0

Figure 10 Relationships between $h^{(r)}$ and h^R of Case B (Uniform Damper Connections in All Floors)

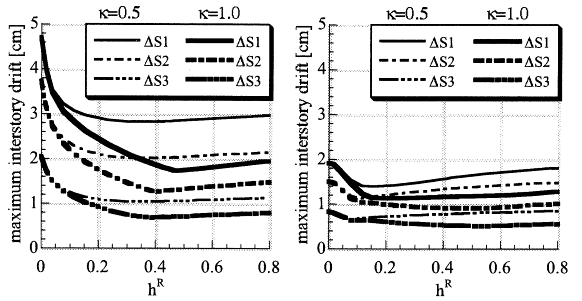

(a)JMA-Kobe 1995 NS (b)Hachinohe 1968 NS

Figure 11 Relationships between Δ_j^S and h^R of Case B

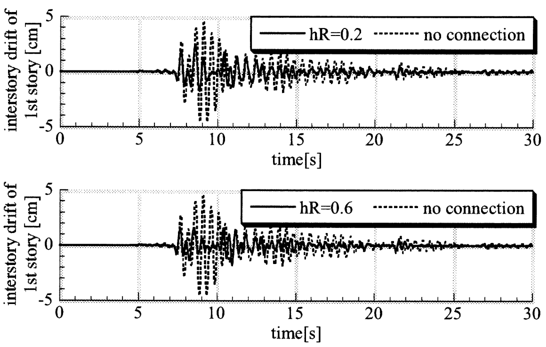

Figure 12 Time Histories to Kobe Wave (Case B, $\kappa = 1.0$)

4.3 Connection of two structures of the different heights

For a representative model of connected structures of different heights, an elastic 3-story structure as target building and an elastic 2-story structure as outer frame are considered. Uniform mass and uniform stiffness are specified to the both structures. The fundamental natural period of the target building is specified as T^S = 0.5[s]. Mass ratio is specified as $\mu = 0.05$; stiffness ratio is specified as $\kappa = 0.05$ or 0.10. Only one case of damper distribution is considered: the case that the connection dampers with the same damping coefficients are installed in all floors, *i.e.*, $c_1^I = c_2^I$ (Case C).

Relationships between $h^{(r)}$ and h^R and relationships between Δ_j^S and h^R are shown in Figure 13 and Figure 14, respectively. Note that the damping coefficient per unit floor mass of the target building c_j^I / m_j^S at h^R = 0.2 is 11.0[kNs/m/t].

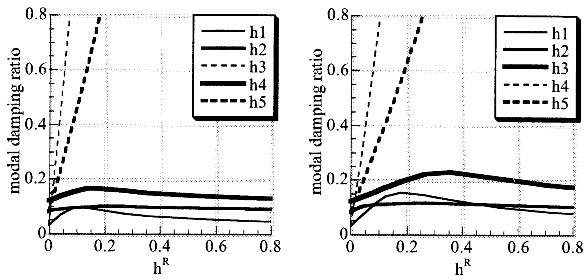

(a)stiffness ratio κ=0.5 (b)stiffness ratio κ=1.0

Figure 13 Relationships between $h^{(r)}$ and h^R of Case C (Connected to Two Story Outer Frame)

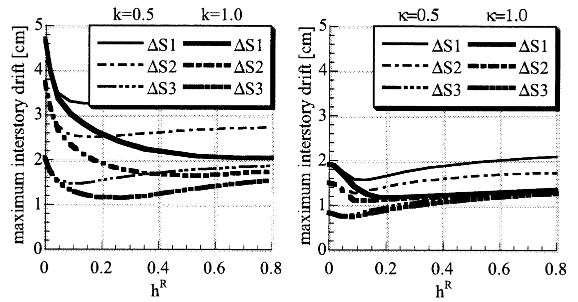

(a)JMA-Kobe 1995 NS (b)Hachinohe 1968 NS

Figure 14 Relationships between Δ_j^S and h^R of Case C

It can be observed from Figure 13 and Figure 14 and from comparison with the results of section 4.2 that (1)similar to the results in section 4.2, the value of Δ_j^S corresponding to the maximum $h^{(1)}$ seems to be a good approximation of the minimum Δ_j^S. (2)when h^R is smaller than about 0.2, the response reduction effect in Case C is almost the same as that in Case A and Case B, but when h^R becomes larger than about 0.2, the effect becomes relatively small compared with that in Case A and Case B, especially in the 3rd story, (3)when h^R is smaller than about 0.2, distribution of reduced interstory drifts is almost proportion to the distribution of interstory drifts of $h^R = 0$.

4.4 Summary

The results of this section are summarized as follows: (1)The basic properties of connected MDOF structures are quite similar to those of connected SDOF structures; (2)The response reduction effect depends on height of the outer frame or damping coefficient distribution of connecting dampers. For instance, the effect for interstory drift of the story under unconnected floor to outer frame tends to be smaller than that of the story under connected floor. However, when h^R is not excessively large, such as $h^R \leq 0.2$, and κ is enough large, such as $\kappa \geq 0.5$, the effect for every story can be roughly estimated only using h^R.

5. APPROXIMATION OF CONNECTION EFFECT

According to the results of section 3 and 4, the following approximations for the response reduction effect due to the proposed retrofit method are introduced: (1)the relationship between $h^{(1)}$ and h^R for connected MDOF structures is assumed to be agree with that for connected SDOF structures; (2)the distribution of reduced interstory drifts is assumed to be proportion to the distribution of interstory drifts without damper connection; (3)the vibration period of the target building with damper connection assumed to be agree with that without damper connection.

Combination of the above approximations and the predominant property of the fundamental vibration mode in seismic response leads to the following approximate formula for reduced interstory drift of the target building:

$$\Delta_j^S = R\left(h^{(1)}, h_S^S\right)\overline{\Delta}_j^S \tag{6}$$

where h_S^S denotes the fundamental damping ratio of the target building without damper connection, and $R(h^{(1)}, h_S^S)$ denotes the ratio of maximum seismic displacement of SDOF system with critical damping ratio $h^{(1)}$ to that with h_S^S. This approximate formula means that the response ratio δ_j defined in eqn. (1) is assumed to be equal to $R(h^{(1)}, h_S^S)$.

Various formulas for such ratio $R(h^{(1)}, h_S^S)$ have been proposed; the following equation is a well-known example in Japan:

$$R\left(h^{(1)}, h_S^S\right) = \sqrt{1+30h_S^S} \Big/ \sqrt{1+30h^{(1)}} \tag{7}$$

Figure 15 shows comparison between the response ratio given by Eq. (6), shown by solid lines, and simulated one, shown by dotted lines, of the interstory drift of the 1st story subject to Kobe wave and Hachinohe wave for Case B in section 4.2. The relationship between $h^{(1)}$ and h^R shown in section 2 and Eq. (7) are used to calculate $R(h^{(1)}, h_S^S)$. It can be observed that when stiffness ratio κ is enough large such as $\kappa \geq 0.5$ and when h^R is smaller about than 0.2, the response ratio δ_j can be roughly estimated using the proposed approximate formula.

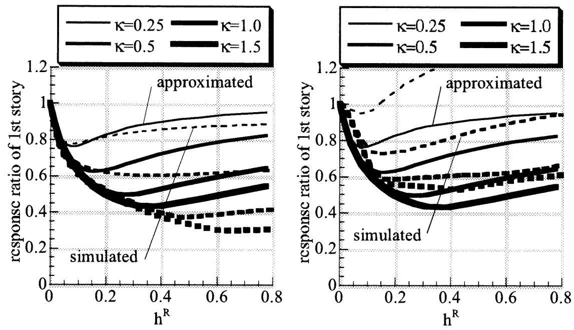

(a)JMA-Kobe 1995 NS (b)Hachinohe 1968 NS

Figure 15 Approximated and Simulated Response Ratio of interstory drift of 1st story (Case B in section 4.2)

6. CONCLUSIONS

Fundamental properties of a new seismic retrofit method of connecting an existing building with an adjacent outer frame using viscous dampers have been disclosed as follows:

(1)The response reduction effect for existing building increases with stiffness ratio of outer frame to existing building. However, the effect becomes almost constant when the stiffness ratio exceeds about 1.0.

(2)The response reduction effect hardly depends on mass ratio of outer frame to existing building when the ratio is small enough compared with unity.

(3)The response reduction effect depends on height of the outer frame or damping coefficient distribution of connecting dampers. However, when a representative damping ratio which corresponds to the fundamental damping ratio estimated under the assumption that the outer frame is rigid is not excessively large, such as less than 0.2, and the stiffness ratio is enough large, such as greater than 0.5, the effect for every story can be roughly estimated only using the representative damping ratio.

Based on the fundamental properties of the retrofit method, approximate formula for reduced interstory drift of the target building is derived. The validity of the formula has been presented through numerical simulations.

Acknowledgements:

This research was carried out as a part of joint research by Kyoto university and Konoike Corporation, Japan. Some useful comments have been provided by Dr. Kenichi Katagihara of Konoike Corporation. The authors are grateful to Konoike Corporation for these supports.

References:

Kageyama, M., Yasui, Y., and Seto, K. (2000a), "The Principal Solutions of Connecting Spring and Damper for Optimum Vibration Control under Several Criteria," *J. Structural and Construction Engineering*, AIJ, **529**, 97-104. (In Japanese)

Kageyama, M., Yasui, Y., and Seto, K. (2000b), "A Study on the Optimum Arrangement of Connecting Springs and Dampers for Multi-Mode Vibration Control," *J. Structural and Construction Engineering*, AIJ, **538**, 79-86. (In Japanese)

Kataoka, T., Ohta, T., and Kuroki, Y. (2007), "Seismic Retrofit of Building Structures by Out-Framed Viscous Damping System," *Konoike Technical Research Report*, 17, 25-28. (In Japanese)

Kobori, T., Yamada, T., and Takenaka, T. (1988), "Effect of Dynamic Tuned Connection on Reduction of Seismic Response -Application to Adjacent Office Building-," *Proc. 9WCEE*, Tokyo-Kyoto, Japan, **V**, 773-778.

Luco, J. Enrique and De Barros, F. C. P. (1998), "Optimal Damping Between Two Adjacent Elastic Structures," *Earthquake Engrg. Struct. Dyn.*, **27**, 649-659.

Takewaki, I. (2000), "Optimal Damper Placement for Planar Building Frames Using Transfer Functions," *Structural and Multidisciplinary Optimization*, **20**, No.4, 280-287.

Thomson, W. T., Calkins, T., and Caravani, P. (1974), "A Numerical Study of Damping," *Earthquake Engrg. Struct. Dyn.*, **3**, 97-103.

Tsuji, M. and Nakamura, T. (1996), "Optimum Viscous Dampers for Stiffness Design of Shear Buildings," *Structural Design of Tall Buildings*, **5**, 217-234

Tsuji, M., Takewaki, I., Takahashi, K., and Katagihara, K. (2005), "Seismic Retrofitting via Out-Frame Systems Connected by Viscous Dampers," *Proc. Annual Meeting of Japan Association for Earthquake Engineering*, 392-393. (In Japanese)

Zhang, Ri-Hui, and Soong, T. T. (1992), "Seismic Design of Viscoelastic Dampers for Structural Applications," *J. Struct. Engng.*, **118**, 1375-1392.

Fifth International Conference on Urban Earthquake Engineering
March 4-5, 2008, Tokyo Institute of Technology, Tokyo, Japan

CURRENT IMPLEMENTATION PRACTICES OF PASSIVE ENERGY DISSIPATERS IN THE UNITED STATES

H. Kit Miyamoto[1] and Amir S.J. Gilani [2]

1) President, Miyamoto International, Inc., Los Angeles, CA, USA
2) Structural Specialist, Miyamoto International, Inc, Sacramento, CA, USA
kit@miyamotointernational.com, agilani@miyamotointernational.com,

Abstract: Performance based design (PBD) and a system of steel special moment resisting frames with viscous damping devices were used for the seismic design of two new multi-story midrise buildings in California. The first structure is located in Los Angeles Basin, in a region of high seismicity. The second building, which is located in Central Valley, a region of moderate seismicity, is one of the first structures in the United States to apply 2005 ASCE 7-05 procedure to design In accordance with ASCE 7-05, the steel frames were sized and designed with strength requirements of the static force level force. Dampers were provided to control displacement of the structures. Earthquake performance and cost effectiveness were the primary concerns in designing the buildings. However, long-term performance was also assessed. Comparative analyses of the PBD and conventional design (CD) buildings showed that the PBD building had superior seismic performance. PBD approach lead to a longer period structure reducing seismic demand and floor accelerations. Dampers reduced the story drift ratios below the design limits. A cost study shows that much of the damper expense is offset by decrease in the weight of the steel members and reduction in foundation costs while providing a immediate occupancy performance.

1 INTRODUCTION

Provisions of ASCE/SEI 7-05 (ASCE 2005) were used to design two new steel framed multi-story buildings. Both structures were analyzed and designed using Performance Based Design (PBD). However, Code Design (CD) was used for comparison. The steel members were sized using conventional code design procedures [2]. Viscous Damping Devices (VDDs) were sized to control the story drift. The dampers were placed only at the lower stories. Building 1 is located in region of high seismicity, whereas, Building 2 is situated in a moderate zone.

VDDs are devices, originally developed for the defense and aerospace industries. They are activated by the transfer of incompressible silicone fluids between chambers at opposite ends of the unit through orifices. During seismic events, the devices become active and the seismic input energy is used to heat the fluid and is thus dissipated. The application of VDDs for seismic design of steel Special Moment Frames (SMRFs) is one of the recommended practices of the SAC Joint Venture (FEMA 2000) and has been successfully implemented by the authors in both new construction and in rehabilitation.

Two levels of seismic hazard were investigated in design: the design basis earthquake (DBE) with a return period of 475 years, and the maximum considered earthquake (MCE) with a 2500-year recurrence interval. The response spectra for the two sites are shown in Figure 1. For Building 1, the seismic demand was obtained from ASCE 7-05 maps and methodology. The peak DBE and MCE spectral accelerations were 1.4g and 2.1g, respectively. For Building 2, geotechnical investigations were undertaken to prepare the site specific seismic information. The peak spectral acceleration for DBE and MCE spectra were 0.5g and 0.9g, respectively. Spectrum-compatible records were synthesized using seeds from past earthquake records and having response spectra closely matching the target. The records have a typical duration of 30 sec.

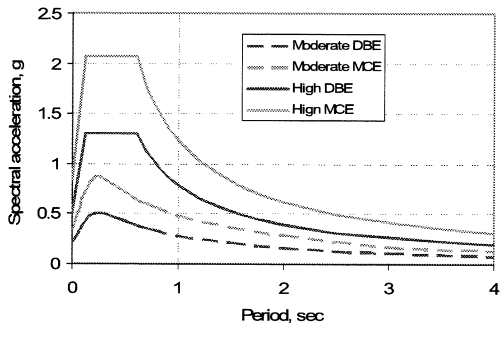

Figure 1. Seismic demand for buildings

Two performance levels were used in evaluation of buildings. For Building 1 the objectives were life safety

(LS) at DBE and collapse prevention (CP) at MCE. For Building 2, the performance goals were more stringent and were Immediate Occupancy (IO) at DBE—to ensure steel members remained elastic and limit story drifts to 1% —and LS at MCE.

Computer program SAP (CSI 2005) was used to prepare three-dimensional models of the buildings. The steel beams and columns were modeled using the program's beam-column elements, centerline dimensions and spans, and nominal member sizes (AISC 2005). Two-dimensional shell elements were used to model floors. P-Δ effect was included in the analysis. Sufficient modes were used to ensure that over 90% of the building mass participated in response. For the PBD model, the bases of columns were modeled as pinned. A similar model without the VDDs and with base fixity was prepared to simulate CD. The CD model was designed to satisfy the conventional code (CBC 2001) strength and drift requirements. The PBD models have longer periods than the CD models.

Nonlinear response history analysis was performed to evaluate the response of the buildings. The damper nonlinear force-deformation response was modeled. The models were first preloaded with ASCE 7-05 gravity load combinations. For each combination, three pairs of DBE and three pairs of MCE analyses were performed, with different components of the ground motioned aligned with building principal directions. Maximum responses (floor displacement and accelerations, story shears, VDD forces, and member stresses) were extracted. The extreme values from all analyses were then used for evaluation.

2 ASCE 7 -05 PROCEDURE FOR VDD DESIGN

Chapter 18 of ASCE 7-05 details the seismic design requirements for structures with supplementary damping. When using the equivalent lateral load procedure, the base shear can be reduced to 75%. Site-specific ground motions can be used to determine the seismic demand. Nonlinear response history analysis procedure accounting for damper behavior is used. The inherent damping in the structure is limited to 5% of critical. When the demand to capacity ratio (DCR) in a member is below 1.5, that member is allowed to be modeled as linear element. In analysis, a strength reduction factor, ϕ, of unity is used to evaluate the response of members. Prior to installation, production tests are required to ensure that the constitutive relation for dampers is acceptable.

3 DESCRIPTION OF BUILDINGS

3.1 Building 1

This four-story commercial building is located in Southern California. It is 18.5 m tall and has a total floor space of 8,000 m^2. Architectural rendering of the building (Ware Malcomb 2005) is presented in Figure 2.

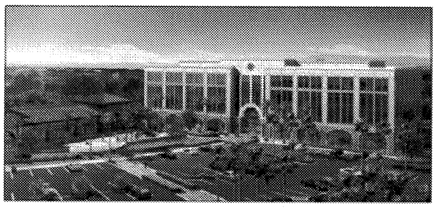

Figure 2. Architectural rendering of the Building 1

Figure 3 depicts the mathematical model of the building. SMRFs resisted lateral loading and 16 first-floor nonlinear VDDs controlled story drifts. The seismic mass of the building was approximately 9 MN.

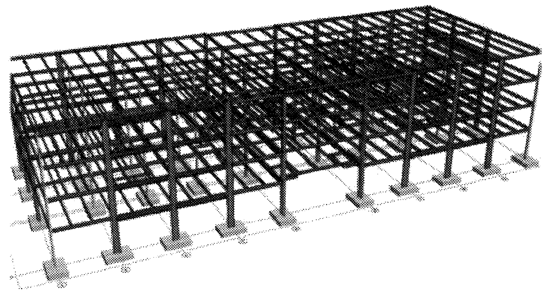

Figure 3. Mathematical model of Building 1

3.2 Building 2

The $50 million building is part of the expansion of a medical facility located in central California. Figure 4 (Boulder 2006) presents an architectural rendering of the building. The medical office building is a five-story structure. It is 21 m tall with a typical story height of 4.3 m. The total building area is approximately 13,000 m^2.

Figure 4. Architectural rendering of the Building 2

The building's lateral loading system is comprised of ASTM Grade 50 SMRFs, using ductile and laboratory tested beam-to-column slotted web connections, and VDDs. Forty nonlinear VDDs, comprised of ten units in each-direction for the first and second floors were used. The VDDs were arranged in the inverted V (Chevron) configuration. For the first mode, the equivalent-damping ratio produced by the FVDs is approximately 35% of critical.

Figure 5 presents the three-dimensional mathematical model of the building. Gravity loading on the building consisted of selfweight of members, uniformity distributed nonstructural load, perimeter wall load, and mechanical equipment loads from HVAC and air conditioning units at the roof. The seismic weight of the structure is estimated to equal approximately 55 MN.

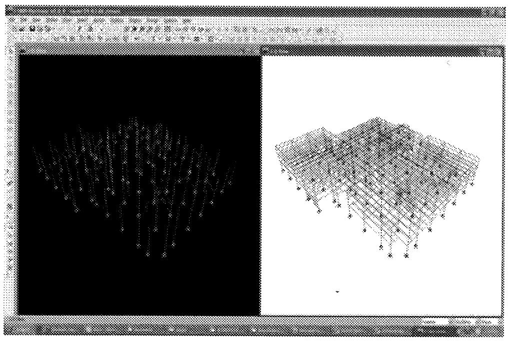

Figure 5. Mathematical model of Building 2

4 ANALYTICAL RESULTS

4.1 Story drifts

Figure 6 depicts the computed DBE drift ratios for Building 1. The PBD and CD models have similar drifts. Base fixity controls drift for the CD model. VDDs do such control for the PBD model. For Building 2, an additional analysis was performed to simulate the CD response. In this model, VDDs were removed, however, the base of the columns were left as pinned. Figure 7 depicts the computed DBE ratios for the models. The addition of VDDs reduces the floor displacements and drifts significantly.

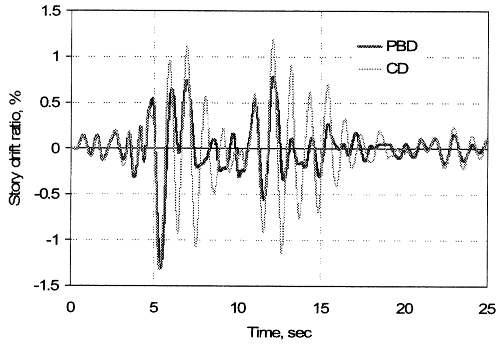

Figure 6. DBE story drift ratio, Building 1

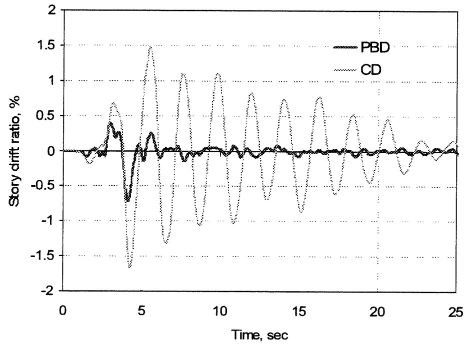

Figure 7. DBE displacement responses, Building 2

Table 1 lists the story drift ratios. The computed story drifts satisfy the CBC 2001 limits. Furthermore, for Building 2, the computed DBE and MCE level values were below 1.0- and 1.5-%, respectively, satisfying the drift targets.

Table 1. Computed story drift ratios, PBD models

	Top	Roof	L4	L3	L2
Building 1		1.2	1.3	1.1	1.4
Building 2	0.7	0.7	0.5	0.5	0.8

4.2 Base shear

The PBD models have smaller story shears due to two factors. Releasing the fixity at the base of columns elongates the building period and reduces seismic demand by traveling on the 5%-damped spectra from left to right. Second, the addition of VDDs increases the equivalent damping of the structure by traveling down, at a given period, from the 5%-damped to a highly damped spectrum. Figure 8 presents the computed DBE base shear coefficient for the two models of Building 1. Figure 9 presents the computed base shear in at the MCE level for Building 2.

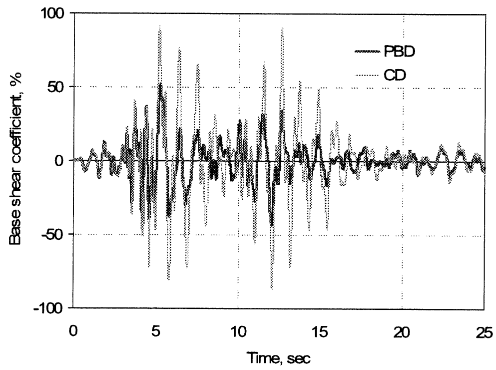

Figure 8. DBE base shear coefficient, Building 1

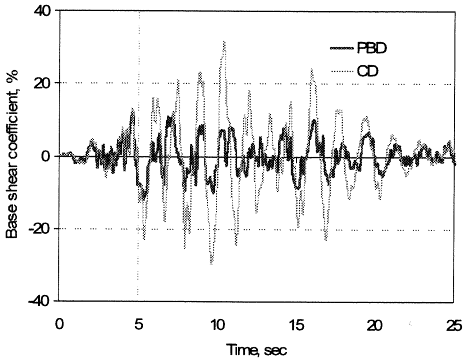

Figure 9. MCE base shear response, Building 2

4.3 Floor accelerations

The acceleration traces at the center of the roof for Building 1 and the Building 2 in x-direction are presented in Figure 10 and Figure 11, respectively. The PBD structures have significantly lower accelerations.

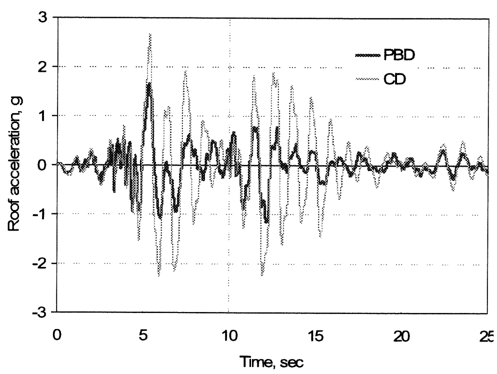

Figure 10. DBE roof acceleration, Building 1

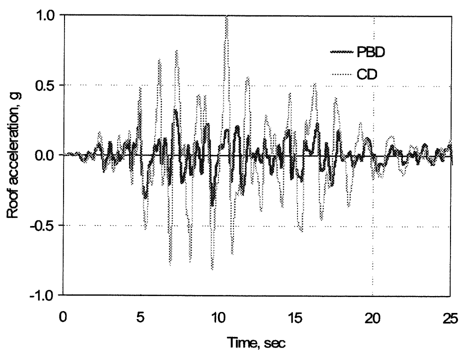

Figure 11. MCE roof acceleration, Building 2

The horizontal roof accelerations for the CD and PBD models are presented in Table 2. The PBD accelerations are less than 60% of the CD. Floor acceleration can damage acceleration-sensitive nonstructural components such as piping and ceilings. Hence, the PBD structures protect both the structural and nonstructural components.

Table 2. DBE maximum roof accelerations (g)

	CD	PBD
Building 1	2.7	1.7
Building 2	0.62	0.23

4.4 Steel member DCRs

Figure 12 shows the plastic hinge formations for Building 1 at the MCE level. The CD model meets CP, whereas, the PBD model meets LS. Additionally, the columns of the PBD model remain elastic. Table 3 summarizes plastic hinge rotations for the two models

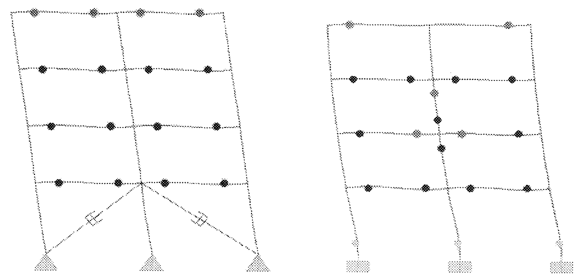

a. PBD b. DC

Figure 12. MCE plastic hinge rotations, Building 1

Table 3. MCE plastic hinge rotations, % radian

	CD	PBD
Beam	1.7	1.3
Column	2.6	0

DCR values for Building 2 were computed. At the DBE event, all members had a DCR of less than unity, satisfying the first design criterion. At the MCE event, see Figure 13, all member stresses are below the target value of 1.5, meeting the second design criterion.

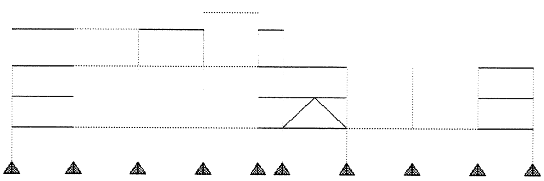

Figure 13. Member stress check, MCE event

5 PROTOTYPE TESTS

Prior to construction, prototype tests of the dampers is required to ensure that they have adequate capacity and stroke, to verify the force-velocity relations, and to check the endurance of units for seismic loading. The prototype tests of one damper of each size are typically conducted by the manufacturer. Sample laboratory hysteretic data for Building 2 VDDs are shown in Figure 14 (Taylor 2007). The damper constitutive force-displacement relation closely correlated to the theoretical values used in analysis.

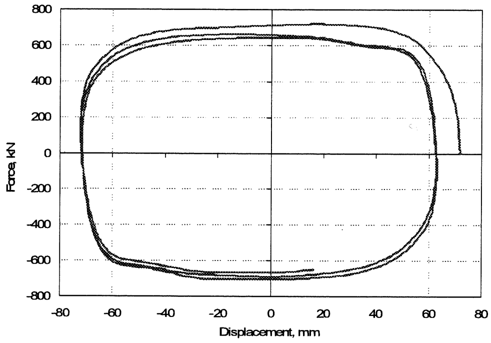

Figure 14. Experimental hysteresis

6 SEISMIC RESILIENCY

The additional cost of the dampers is offset by the savings in steel tonnage and foundation concrete volume. Hence, the two buildings have similar initial costs. However, the PBD building has superior performance and lower long-term costs. Following a design earthquake, the CD building will provide life safety, but will sustain significant damage. In a well-designed CD building, ductile beam-column connection details are used to prevent premature brittle failure. In these buildings, the seismic energy is dissipated by ductile yielding in the steel members; see Figure 15 (SSDA 2005).

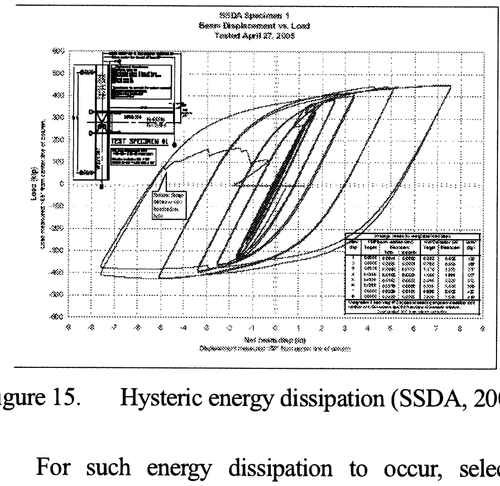

Figure 15. Hysteric energy dissipation (SSDA, 2005)

For such energy dissipation to occur, selected members must yield. This behavior can be simulated in laboratory tests, as shown in Figure 16 (SSDA 2005) A preferable approach is to use ductile beam-column combination in conjunction with seismic protection devices such as VDDs. The VDDS will reduce inelastic behavior and the ductile connection ensures that no brittle failure would occur even for large seismic events.

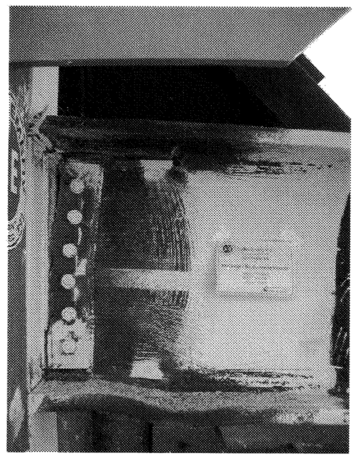

Figure 16. Ductile yielding and of beam (SSDA 2005)

This PBD building will dissipate the seismic energy by the nonlinearity in the VDD force-deformation response. Such response is depicted in Figure 17 for Building 1. As shown in Figure 18 for Building 2, the dampers are effective in dissipating the largest portion of seismic energy. Hence, the PBD structure is expected to sustain little damage after the DBE event.

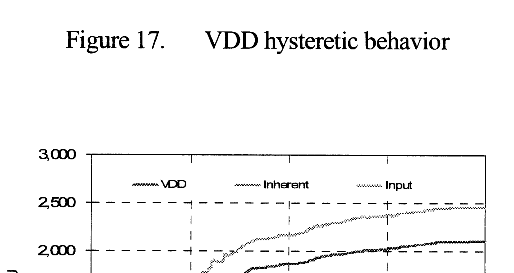

Figure 17. VDD hysteretic behavior

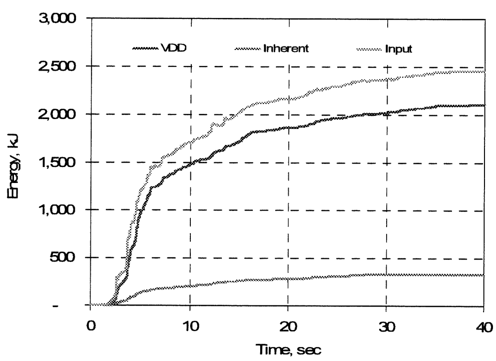

Figure 18. Components of seismic energy, DBE event

The long-term performance of PBD and CD building following major earthquakes is qualitatively illustrated in Figure 19. The buildings have similar performances at construction time. Sometime later, a seismic event occurs. This reduces the quality level of the buildings. The degradation for CD building is greater, resulting in larger repair cost and downtime. The long-term relative efficacy of the seismic design is inversely proportional to the areas under the curves of Figure 19, which accounts for severity of damage and repair time, i.e., cost and loss of operation. The PBD structure is a more robust design or it has a higher seismic resiliency.

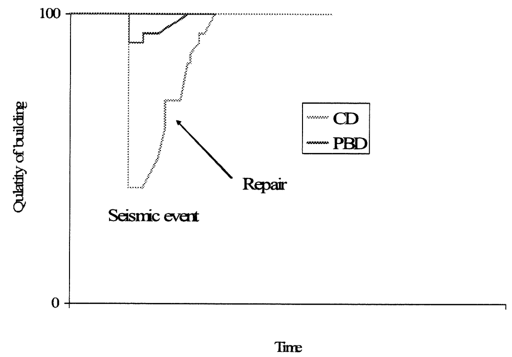

Figure 19. Qualitative resiliency curves

7 SAMPLE STRUCTURES IN THE US

In the past several years, the authors have had the opportunity to work on structures incorporating passive energy devices (Miyamoto and Gilani 2007). For a more detailed listing of the buildings with seismic protective devices in the United States, the reader is referred to PEER (2007) or Taylor (2007). A partial list of structures with VDDs from Taylor (2007) is tabulated in Table 4.

Table 4. Sample US application of VDDs

Structure	Stories	Area, m^2	Date
Sutter Gold, Modesto	5	13,000	2007
Mills Peninsula Hosp.		45,000	2007
926 J Street, Sacramento	14	10,000	2006
Bayer Building, UC Berkeley	2	3,500	2005
Semiconductor Building, Silicon Valley	2		2005

8 SUMMARY AND CONCLUSION

Two steel buildings were designed using PBD and provisions of ASCE 7-05. SMRFs were used to provide strength; VDDs were used to control story drifts. Key findings are summarized below.

- PBD building using VDDs is superior to the CD structure. The demand on both structural and nonstructural components is reduced.
- The additional cost of VDD is offset by the decrease in structural and foundation costs. In the long-term, it is expected that the PBD building will have lower repair costs and higher extended performance quality.
- The PBD approach and VDDs as drift control devices is applicable to the full spectrum of seismicity
- VDDs provide non-intrusive and reliable toll for seismic design. The VDD force demand is controlled by using nonlinear damping properties. These forces are out-of-face with elastic forces and do not increase the demand on members.

9 REFERENCES

ASCE (2005), "ASCE/SEI 7-05: Minimum design load for buildings and other structures," American Society of Civil Engineers, Reston, VA

FEMA (2000), "FEMA 351: Recommended Seismic Evaluation and Upgrade Criteria for Existing Welded Steel Moment-Frame Buildings," Federal Emergency Management Agency, Washington, D.C., 2000

CSI (2006), "SAP: structural analysis program," Computers and Structures Inc., Berkeley, CA.

AISC (2005), "Manual of Steel construction, American Institute of Steel Construction," Chicago, IL

CBC (2001), "California Building Code," California Building Standards Commission, Whittier, CA

Ware Malcomb (2005), personal communications

Boulder Associates Inc (2006), Personal communications

Taylor (2007a), "Acceptance test plan for 160-kip dampers," Taylor Devices Inc., North Tonawanda, NY

Seismic Structural Design Associates (SSDA) (2007) http://www.slottedweb.com/dtd.htm

Miyamoto and Gilani (2007), "Earthquake hazard mitigation using performance based engineering," Proceedings of West Sumatra Earthquake Conference, Public Works Department, Padang, Indonesia.

PEER (2007), "Structures in North America with Supplemental Energy Dissipation Devices," Earthquake Engineering Research Center, University of California, Berkeley, CA.

Taylor (2007b), "Structural Applications of Fluid Viscous Dampers," Taylor Devices Inc., North Tonawanda, N

Fifth International Conference on Urban Earthquake Engineering
March 4-5, 2008, Tokyo Institute of Technology, Tokyo, Japan

A STUDY ON RESPONSE CHARACTERISTIC OF SEISMICALLY ISOLATED TALL BUILDING

Daiki Sato[1], Yoji Ooki[2], Hitoshi Morikawa[3], Satoshi Yamada[4], Hiroyasu Sakata[4], Hiroaki Yamanaka[5], Kazuhiko Kasai[6], Akira Wada[6] and Haruyuki Kitamura[7]

1) Assistant Professor, Department of Architecture, Tokyo University of Science, Japan
2) Assistant Professor, Structural Engineering Research Center, Tokyo Institute of Technology, Japan
3) Associate Professor, Department of Built Environment, Tokyo Institute of Technology, Japan
4) Associate Professor, Structural Engineering Research Center, Tokyo Institute of Technology, Japan
5) Associate Professor, Department of Environmental Science and Technology, Tokyo Institute of Technology, Japan
6) Professor, Structural Engineering Research Center, Tokyo Institute of Technology, Japan
7) Professor, Department of Architecture, Tokyo University of Science, Japan

daiki-s@rs.noda.tus.ac.jp, ooki@serc.titech.ac.jp, morika@enveng.titech.ac.jp,
naniwa@serc.titech.ac.jp, hsakata@serc.titech.ac.jp, yamanaka@depe.titech.ac.jp,
kasai@serc.titech.ac.jp, wada@serc.titech.ac.jp, kita-h@rs.noda.tus.ac.jp

Abstract: Recently, the number of monitoring reports of seismically isolated building is gradually increasing. In this paper, a long-term dense monitoring system of seismically isolated tall building in Tokyo Institute of Technology is introduced. In this monitoring system, the acceleration at ground surface, 1st, 2nd, 7th, 14th and 20th floor is recorded in detail, as well as the story drift and acceleration at the floor where the base isolators are located. Using the data, the response characteristics of the building are evaluated.

1. INTRODUCTION

The seismic isolation building in Japan had been initiated from the Yachiyo-dai-house in 1982. Recently, the number of the tall buildings having the seismically isolation system are gradually increasing in Japan. The traditional fixed based structures had many experiences of collapses or damage for the major earthquake. However, because the seismic isolated structures are new technology and these are not encountered with the major earthquake and large damage, the investigations and researches of the response characteristic about the full-scale isolated structures are not sufficient yet.

In 2005, 20-story seismically isolated building was constructed in Tokyo Institute of Technology Suzukake-dai Campus. As the one of the main themes of the Center for Urban Earthquake Engineering (CUEE) in Tokyo Institute of Technology which is the 21st Century COE program, a long-term dense monitoring of this building is carried out. The observed data are used to define the characteristic of the isolated tall building including the ground motion.

In this paper, a long-term dense monitoring system of this building is presented. The dynamic characteristics of the building evaluated based on the long-term monitoring results are discussed in this paper.

2. SEISMICALLY ISOLATED TALL BUILDING AND MONITORING SYSTEM

2.1 Seismically Isolated Tall Building

Figure 1 illustrates the elevation of the 20-story seismically isolated building, and it is called as "J2-building" in this paper. Figure 2 shows the plan of the isolation floor of J2-building. The foundation and 1st floor of this building are RC structure. The other floors are hybrid with steel beams and CFT columns.

In the isolator floor of this building, several types of dampers are installed. The 1,200ϕ rubber bearing with conical spring (Figure 3 (a)) is installed in the position A as shown in Figure 2. In the position B, the steel dampers (Figure 3 (b)) are attached, and the 1,100ϕ rubber bearing with the steel dampers (Figure 3 (c), (d)) are installed in the position C and D, respectively. In the position E, the 1,000kN oil dampers (Figure 3 (e)) are installed.

The mega-braces (□ - 500mm x 160mm x 19 to 32mm) are installed on the both sides of building because the horizontal stiffness is necessary to maintain the seismic isolation effects. Because this building is very slender shape with the height of 91m and aspect-ratio of 5, tensile force in the rubber bearing becomes a critical design problem. If this tall seismic isolated building suffers a

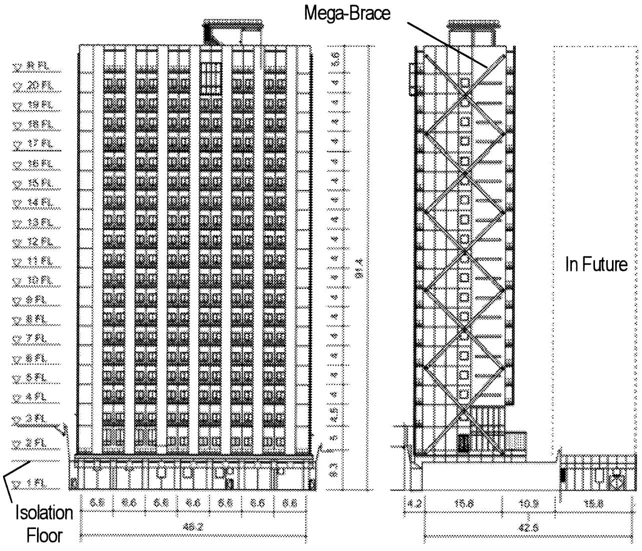

(a) East Side Elevation

(b) West Side Elevation

Figure 1 J2-building (unit: m)

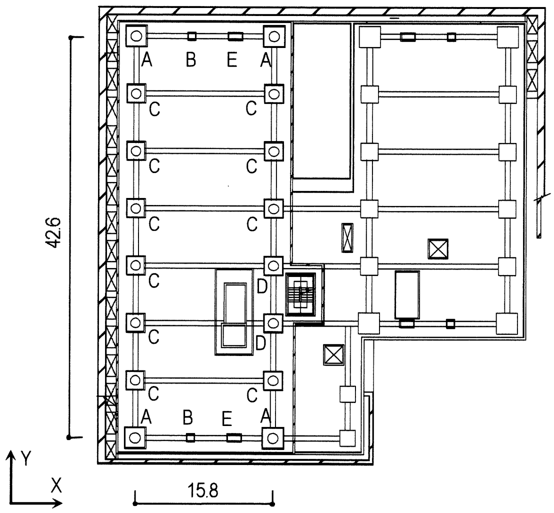

Figure 2 Seismic Isolation Floor (unit: m)

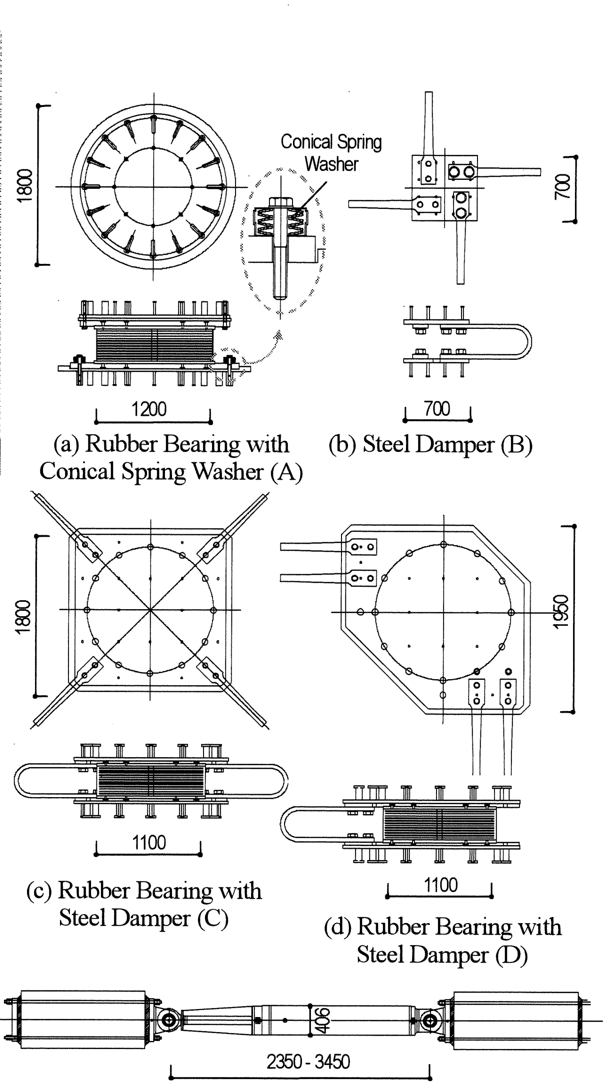

(a) Rubber Bearing with Conical Spring Washer (A)

(b) Steel Damper (B)

(c) Rubber Bearing with Steel Damper (C)

(d) Rubber Bearing with Steel Damper (D)

(e) Oil Damper (E)

Figure 3. Rubber Bearing & Damper (unit: mm)

major earthquake, the large up-lift forces may develop at the multi-layer rubber bearings due to the tensile force cause by the large overturning moment. To avoid the large tensile forces, the bearings are enabled to do up-lift in this isolated system (Figure 3 (a)).

2.2 Monitoring System

Figure 4 shows the monitoring system and the list of the sensors are indicated in Table 1. In this long-term monitoring system, the accelerometers are placed on the ground surface, 1st, 2nd, 7th, 14th, 20th floor. This instrument is broad, thus the time history of displacement can be computed by numerical integration. The displacement transducers are installed to measure the displacement of the isolation devices. To measure the large and/or small inter-story displacement in the isolated story level between 1st and 2nd floors, a trace recorder is used in combination with the other measurement devices. The trace recorder is fixed to a bottom steel beam of the superstructure, while the stainless steel board for trace recording is fixed to the concrete slave the top of the substructure, and the displacement of the isolated story is drawn on the board. The strain gages are installed at the columns and the Mega-Braces. Oil damper force and deformation are measured. To measure the up-lift of the isolator as shown in Figure 3(a), the displacement transducers and the video camera are placed.

Output voltage of accelerometers, displacement transducers and strain gages are A/D converted by data loggers installed at each floor, transmitted to data servers through a LAN, and recorded continuously. The clock on data server is set using a GPS signal data on each data logger via the LAN.

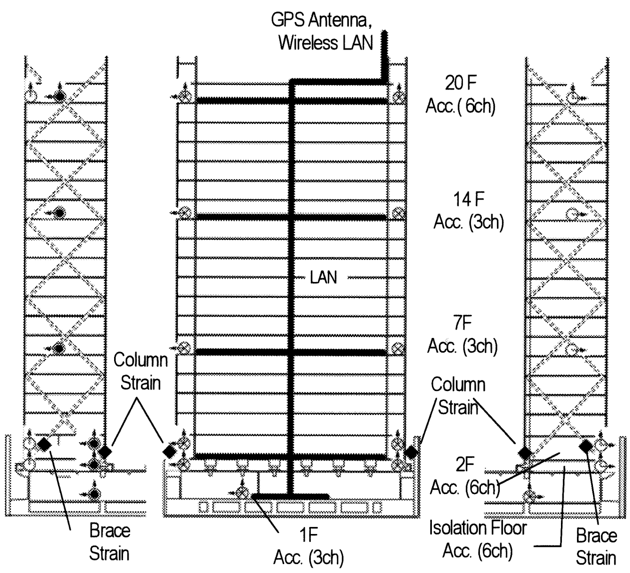

(a) Elevation

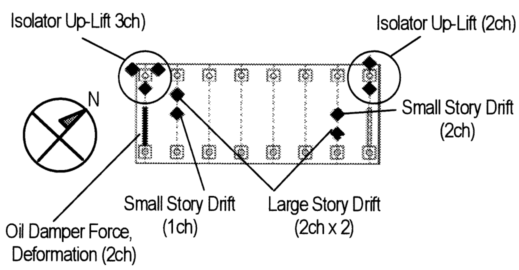

(b) Plan of Isolation Floor

Figure 4 Monitoring System

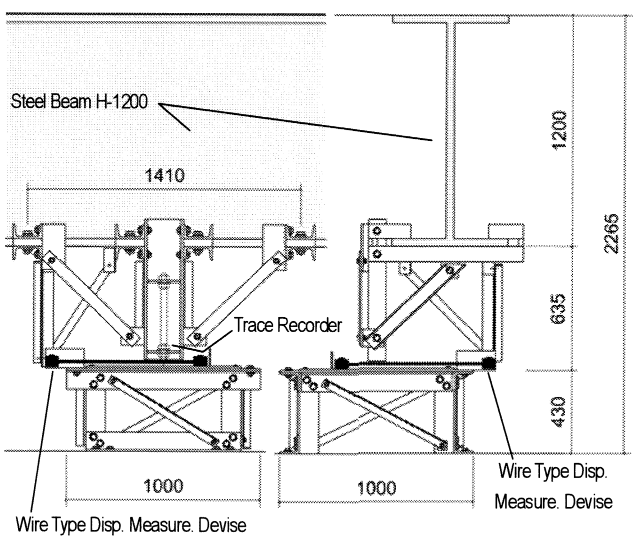

Figure 5. Measurement Device for Large Story Drift in Isolated Story (unit: mm)

Table 1 List of the Sensors

Floor	Item	Capacity	Sensitivity
7, 14, 20F	Acc.	2G	1 μG
	Column, Brace Strain	(Strain Gauge)	1 μstrain
Isolation Floor	Acc.	2G	1μG
	Small Story Drift	±100 mm	0.05 mm
	Large Story Drift	±500 mm	0.5 mm
	Drift Trace	-	-
	Damper Force	(Strain Gauge)	1 μstrain
	Damper Deformation	1000mm	0.5mm
	Isolator Up-Lift	50mm (Video)	0.03mm -
1F	Acc.	2G	1 μG
Ground	Acc.	2G	1 μG

3. RESPONSE CHARACTERISTICS

3.1 Observed Earthquake-induced Response

After installing this monitoring system, some earthquakes-induced responses of the isolated building have been measured. This paper summarizes two observed earthquake-induced response, which are the Chiba Hokuseibu Earthquake on July 23, 2005 and the Miyagi-ken Oki Earthquake on August 16, 2005.

Figure 6 shows the recorded acceleration data at 1F and 20 F during the Chiba Hokuseibu Earthquake. Likewise, Figure 7 illustrates the observed acceleration record at 1st and 20th floor during the Miyagi-ken Oki Earthquake. It is recognized that the vibrations of 20th floor are continued though the ground acceleration decreases sufficiently, especially, in Miyagi-ken Earthquake as shown in Figure 7.

Figure 8(a), (b) respectively plot the maximum acceleration and absolute displacement response distribution of J2-building. These maximum displacements are calculated by the numerical integration from the acceleration data using band-pass filter from 0.1Hz to 30Hz. As seen in Figure 8, the response of acceleration and displacement both are concentrated in the isolated floor.

The isolated story drift traces during the Miyagi-ken Oki Earthquake are shown in Figure 9(a), (b). These traces are obtained from the trace recorders as shown in Figure 5 in the position SW and NE (See Figure4). Figure 10(a), (b) show the comparison of the isolated story drift during the Miyagi-ken Oki Earthquake obtained from the small inter-story device and the numerical integration of the acceleration time history. As shown in Figure 10, these are almost identical, it is consequently indicate that these measurement devices are accurate. As can be seen from Figure 9 and 10, the isolator devices are deformed 11.1mm to X-direction and 8.8mm to Y-direction, these are the elastic range (= 31.7mm) of the steel damper installed in the isolated floor.

Figure 11(a), (b) respectively depict the power spectrum density of the 20th floor X-direction and Y-direction acceleration during the Chiba Hokuseibu

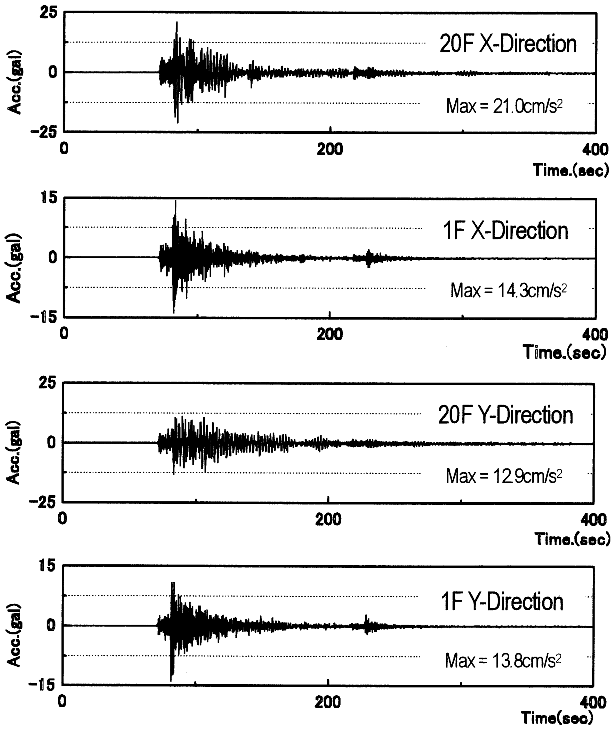

Figure 6 Acceleration Time History
(Chiba Hokuseibu EQ.)

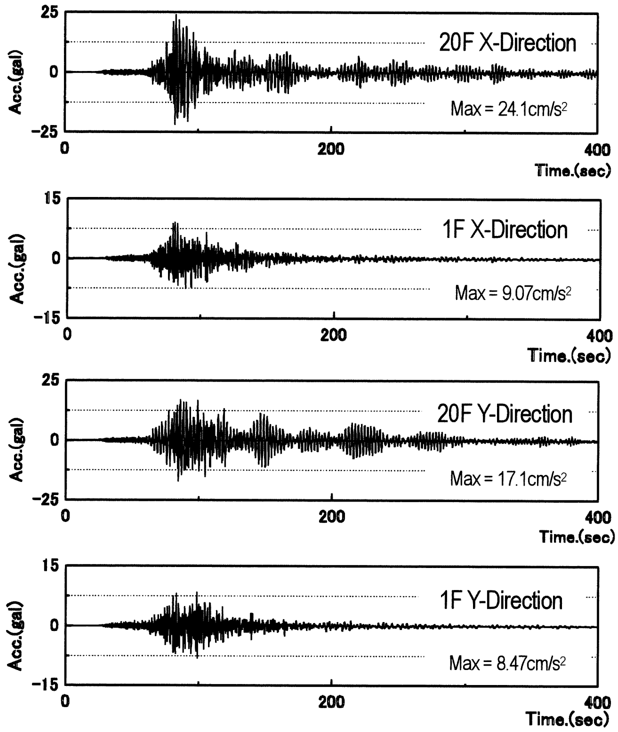

Figure 7 Acceleration Time History
(Miyagi-ken Oki EQ)

Earthquake. As can be seen from Figure 11, 1st and 2nd mode frequency of X-direction obtained from the peak of the power spectrum density are 0.39Hz and 1.19Hz, respectively. Likewise, 1st and 2nd mode frequency of Y-direction are 0.42Hz and 1.31Hz, respectively.

Likewise, Figure 12(a), (b) illustrate the power spectrum density of the 20th floor X-direction and Y-direction acceleration during the Miyagi-ken Oki Earthquake, respectively. 1st and 2nd mode frequency of X-direction are, respectively, 0.41Hz and 1.15Hz, and Y-direction are 0.43Hz and 1.22Hz, respectively. These 1st mode frequencies are low in comparison with the analysis results of status fixing the isolator which are calculated by Kikuchi (2005), (See Table 2).

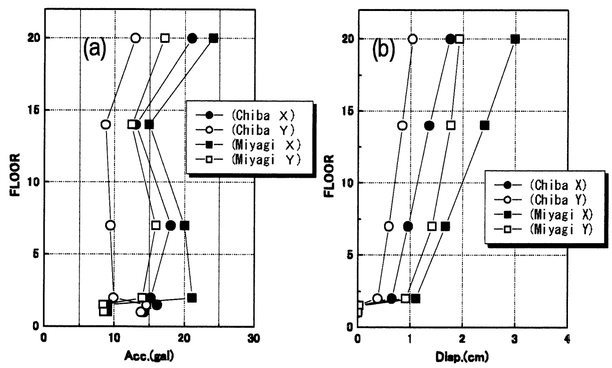

Figure 8 Maximum Response (Earthq.):
(a) Acceleration, (b) Displacement

From the results of the calculating displacement by using the 2 types of the band pass filters range, which, respectively, are from 0.3Hz to 0.5Hz and from 1Hz to 2Hz, it is identified that the responses around the two peaks are the sway vibration.

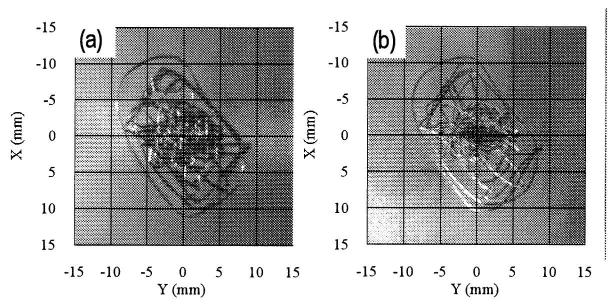

Figure 9 Drift Trace Obtained from Trace Recorder
(Miyagi-ken Oki EQ.): (a) SW, (b) NN

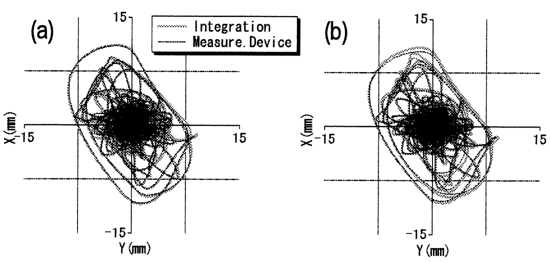

Figure 10 Comparison of Drift Trace Obtained from
Integration and Measurement Device
(Miyagi-ken Oki EQ.): (a) SW, (b) NN

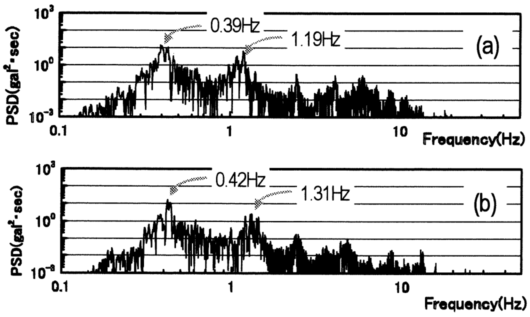

Figure 11 20F Acc. PSD (Chiba Hokuseibu EQ.): (a) X-direction, (b) Y-direction

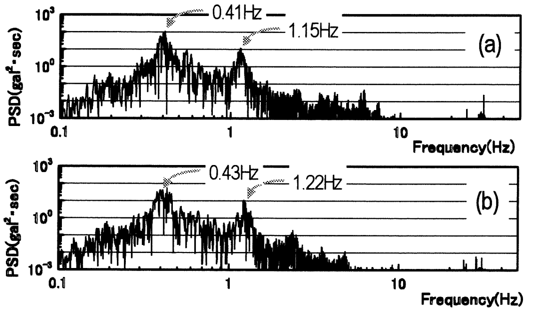

Figure 12 20F Acc. PSD (Miyagi-ken Oki EQ.): (a) X-direction, (b) Y-direction

3.3 Observed Wind-induced Response

Figure 13(a), (b), respectively, show the wind-induced maximum acceleration and absolute displacement response of the 20th floor on Mar. 17 and 19 in 2005. These maximum displacements are computed by numerical integration from the 10 minute acceleration data using the band-pass filter from 0.1Hz to 30Hz. In case of the wind-induced response, the isolators almost are not deformed.

Figure 14(a), (b) show the power spectrum density X and Y-direction wind-induced response acceleration of the 20th floor on Mar. 17, respectively. Figure 15(a), (b) depict the power spectrum density of the 20th floor X and Y-direction wind-induced response acceleration on Mar. 19, respectively.

In X-direction power spectrum density as shown in Figure 13(a) and 14(a), there are two peaks of less than 1Hz. However, as can be seen from Figure 14(b) and 15(b), the power spectrum of density of Y-direction has only one peak of less than 1 Hz.

From the results of the calculating X-direction displacement by using the 0.4Hz to 0.6Hz band pass filters, it is defined that the responses in this range are the sway vibration. However, in case of using the band pass filter from 0.4Hz to 0.6Hz , the torsion vibrations are recognized.

Because the isolators almost are not deformed in case of the wind-induced response, 1st mode frequency during the wind response is higher than 1st mode frequency during the earthquake-induced response that the isolator is deformed. The natural frequency obtained from the observed data and from the analysis result calculated by Kikuchi (2005) are indicated in Table 2.

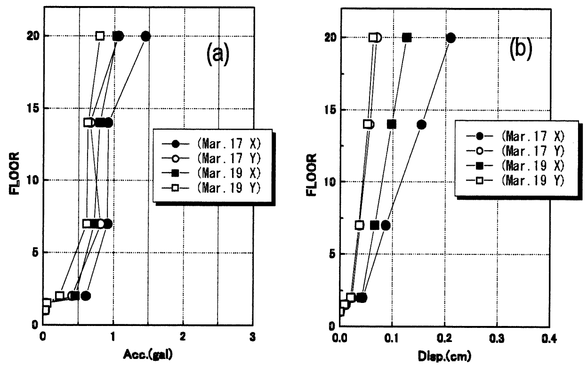

Figure 13 Maximum Response (Wind): (a) Acceleration, (b) Displacement

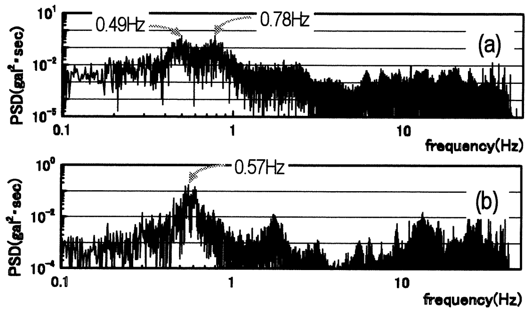

Figure 14 20F Acc. PSD (Mar. 17, Wind): (a) X-direction, (b) Y-direction

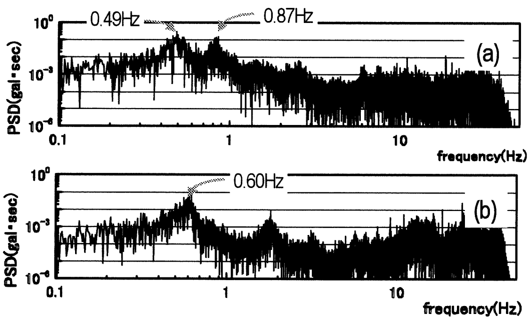

Figure 15 20F Acc. PSD (Mar. 19, Wind): (a) X-direction, (b) Y-direction

Table 2 Comparison of Natural Frequency

	Direction	Sway	Tortion
Chiba Hokusei-bu	X	0.39Hz	-
(Earthq.)	Y	0.42Hz	-
Miyagi-ken Oki	X	0.41Hz	-
(Earthq.)	Y	0.43Hz	-
Mar. 17	X	0.49Hz	0.78Hz
(Wind)	Y	0.57Hz	-
Mar. 18	X	0.49Hz	0.87Hz
(Wind)	Y	0.60Hz	-
Analysis	X	0.46Hz	-
(Isolatro Fixed)	Y	0.40Hz	-
Analysis	X	0.28Hz	-
(γ = 50%)	Y	0.26Hz	-

3.4 Torsion Vibration of Wind-induced Response

In case of the wind-induced response, not only the sway but also the torsion vibration is identified. In this section, the torsion vibration is focused. Figure 16(a), (b) show the torsion ratio α_θ and the center of torsion, respectively. These are obtained from the ensemble average using 13 data. The torsion ratio α_θ is calculated as follows,

$$\alpha_\theta = \frac{\sigma_{\theta X}}{\sigma_X} \tag{1}$$

where, $\sigma_{\theta X}$ = the standard deviation of the torsion response of X-direction, σ_X = the standard deviation of the X-direction response. The center of the torsion is obtained from the method suggested by Arakawa (2005). This method is explained briefly as follows: Firstly, the time history of the torsion response is calculated by using 2 points X-direction data and the distance of 2 points. Secondly, the natural frequency of the torsion response is obtained from the peak of the power spectrum density of the calculated torsion response. Next, each of the torsion components included in X-direction's response at the natural frequency are estimated from 2 points X-direction power spectrum density, respectively. Then the center of the torsion is obtained by using the distance of 2 points and the ratio of torsion components.

As can be seen from Figure 16(a), in North side (N) on Mar. 17, the torsion vibration components included in X-direction response of 7-20th floor and 2nd floor are about 60% and 42%, respectively. However, in the South side (S), the characteristic of the torsion ratio are different from North side. The torsion components of 7-20th floor are 30-40%, and the torsion component of 2nd floor is 65%. In addition, the torsion responses on Mar. 17 and 19 show the different property. These differences may be caused by the wind direction, wind force and so on. However to clear these reasons, it calls for further investigation.

From what has been discussed above, the torsion vibration cannot be neglected to evaluate wind-induced response of the isolated tall building.

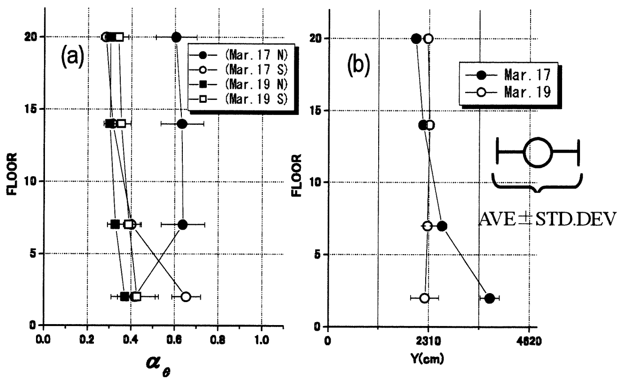

Figure 16 Torsion Response (Wind): (a) Torsion Ratio, (b) Center of Torsion

4. CONCLUSIONS

A long-term dense monitoring system of the seismically isolated tall building in Tokyo institute of technology is presented in this paper. Based on the observed data obtained from earthquake and wind-induced response, the response characteristics of the building are evaluated. 1st mode natural frequency during wind-induced response is higher than earthquake-induced response case. It is recognized that the torsion vibration occurs only in wind-induced response, and it cannot be ignored in evaluating for the wind-induced response of the isolated tall building.

Acknowledgements:

This paper is the part of the results of joint-research project by the 21st Century COE program, the Center for Urban Earthquake Engineering (CUEE) in Tokyo Institute of Technology and Kitamura Lab., Tokyo University of Science. The authors would like to express their thanks to the people engaged in this research. The author would like to thank for Mr. Takahiro Ebihara, Kitamura Lab., for the assistance in this study.

References:

Arakawa, T., and Yoshise, S. (2005), "A Study on the Evaluate on Vibration Characteristics and Amplitude Dependences for a Steel Building Based on Measuring Data," *Journal of Technology and Design*, Architectural Institute of Japan, No22, 157-162, Dec.

Kikuchi, T., Fujimori, S., Takeuchi, T., and Wada, A. (2005), "Design of High Rise Seismic Isolated Steel Building with Mega-Bracing System," *Journal of Technology and Design*, Architectural Institute of Japan, No20, 217-222, Dec.

Ooki, Y., Yamashita, T., Morikawa, H., Yamada, S., Sakata, H., Yamanaka, H., Kasai K., and Wada, A. (2005), "Concete Approach on Long Term and Dense Monitoring System of Seismically Isolated Tall Building," *Journal of Technology and Design*, Architectural Institute of Japan, No21, 73-77, Jun.

NUMERICAL INVESTIGATION OF BEAM-COLUMN-GUSSET COMPONENTS IN VALUE-ADDED FRAMES

Kensaku Kaneko[1)], Kazuhiko Kasai[2)], and Shojiro Motoyui[3)]

1) Post doctoral fellow of COE, Center for Urban Earthquake Engineering, Tokyo Institute of Technology, Japan
2) Professor, Structural Engineering Research Center, Tokyo Institute of Technology, Japan
3) Associate professor, Dept. of Built Environment, Tokyo Institute of Technology, Japan
kaneko.k.aa@m.titech.ac.jp, kasai@serc.titech.ac.jp, motoyui.s.aa@m.titech.ac.jp

Abstract: L-shape subassemblies in passive controlled bulging were investigated using finite element analysis. Results obtained by using finite element analysis were compared to experimental results. Influence of gusset connection on plastic deformation capacity was investigated through parametric study.

1. INTRODUCTION

Passive control schemes, where dampers in frames are expected to absorb a part of vibration energy, are commonly used in seismic design. The performance of the passively-controlled building depends not only on damper but also frames members and connections.

Premature failure or fracture of the frames or the connections results in poor performance of the system. Relatively large axial force develops in the beams because of the damper force in addition to bending moment and shear caused by the story drift. The axial force can cause earlier yielding and possibly buckling in the elements.

The objective of this study is to investigate seismic performance of the passively-controlled building through a parametric study of numerical analysis.

2. TEST SPECIMEN AND ANALSYS MODEL

2.1 Outline of subassembly

Figure 1 shows the concept of subassembly consisting of beam, column, and gusset plate. The subassembly has a configuration of L-shape, and it represents a quarter portion of the frame. The L-shape specimen is connected to Link-1 and Link-2 in order to simulate the damper force.

Positive loading, where the beam is subjected to positive (tension) force and positive end moment, is defined as shown in Figure 2, and verse versa.

Figure 3 shows a typical specimen. The beam is of a wide flange built-up section of 500mm deep, 12mm thick web, 250mm wide flange, and 22 mm thick flange. Square box column section of 400mm×400mm×19mm is used. Table 1 summarizes the specimen types. Specimen 1 has neither gusset plate nor stiffeners, and is not subjected to the

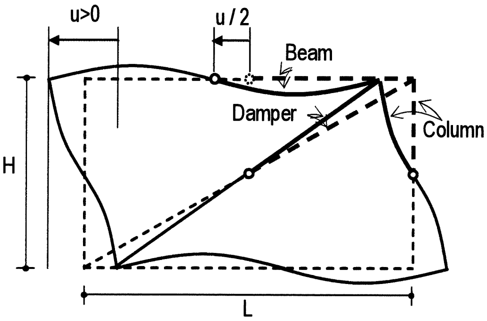

Figure 1 Concept of subassembly

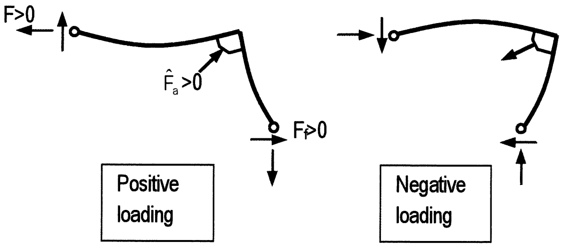

Figure 2 Loading preterm

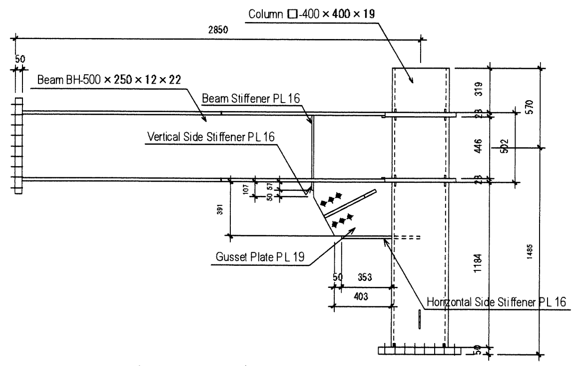

Figure 3 Reference specimen

damper force.

Specimen 1 is to be compared with those having gusset plate. The geometries of other specimens 2 to 6, and 9 commonly follow Figure 3. Specimen 2, however, is not subjected to the damper force, and only the effect of story drift is examined. Specimen 3 and 4 are benchmark specimens, meaning that they have the typical configuration (Figure 3) and are subjected to the damper force.

In specimen 5, the web is thinner (9mm) and it dose not meet the Japanese code requirement [JASS6, 1996] for a beam-column compact section, while barely satisfying the requirement for a beam. In specimen 6, both web and flange are thinner (9mm and 16mmm, respectively). The flange slightly violates the compact section requirement for beam-column and beam. Specimen 7 has neither horizontal side stiffeners nor column stiffener (Figure 3) and specimen 8 has no stiffeners at all. Specimen 9 has a gusset plate of thickness less than 0.5 times (9mm) the typical one mentioned above. Such deference is summarized in Table 1.

Table 1 Specimen types

No.	Specimen Type
1	No Damper Force, No Gusset
2	No Damper Force
3	Benchmark (EP Damper / EP Damper)**
4	Benchmark (VE Damper / EP Damper)***
5	Large Width-Thickness Ratio for Web
6	Large Width-Thickness Ratios for Web and Flange
7	No Horizontal Side Stiffener, No Column Stiffener
8	No Stiffeners at All
9	Thin Gusset Plate

2.2 Analysis model

Finite element analysis is conducted to simulate the behavior of the specimens. Both the material and geometric non-linearities are considered. The von Mises yield criterion with associated flow rule and isotropic hardening rule are employed in the material model. An overlay model is used to characterize the material behaviors as shown in Figure 6. A four node quadrilateral shell element is used to model the beam, the column, the gusset plate, and the stiffener. A truss element is also used to model the link element. The bolts and the splice plates for connecting the dumper and the gusset plate are neglected for simplicity.

The force of the damper in the FE model is obtained from the inner fore of the damper, while the damper force were applied by force control of a actuator in the experiment Boundary conditions simulated the test restraints, including translational degrees of freedom.

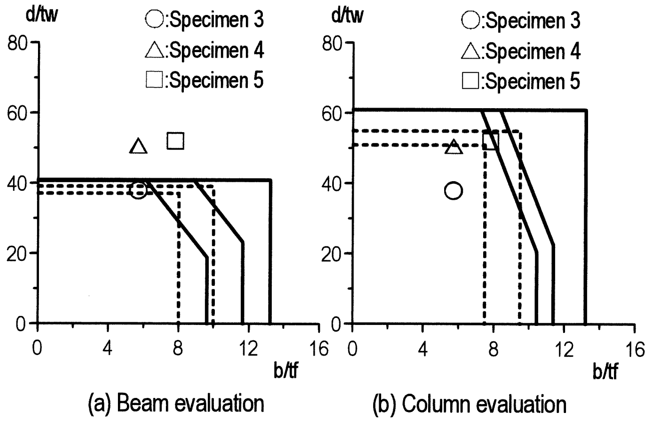

Figure 4 Classification of width/thickness ratio

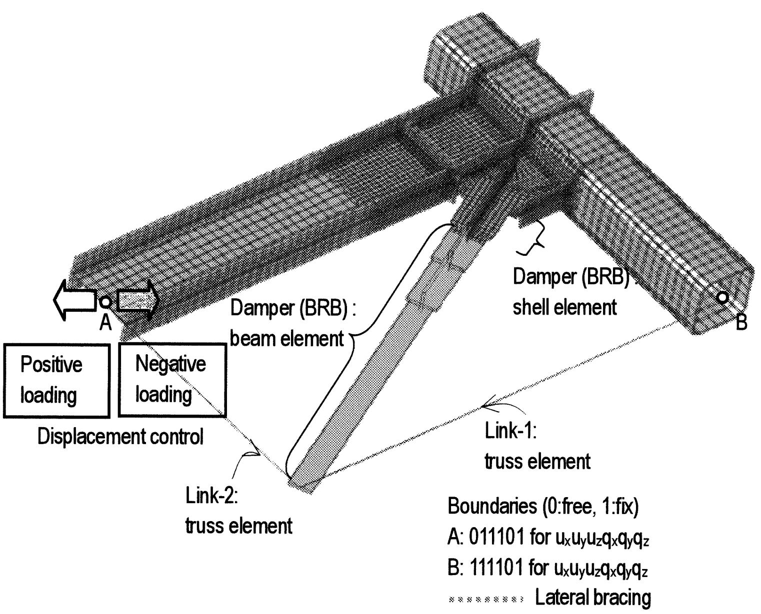

Figure 5 Finite element model

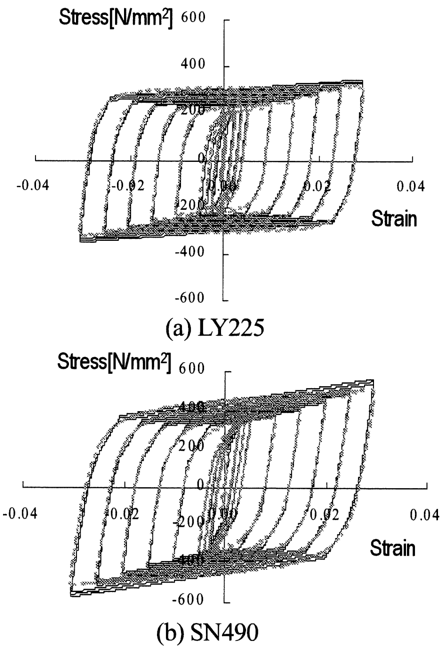

(Solid line: analysis, dash-line: experiment)

Figure 6 Material model

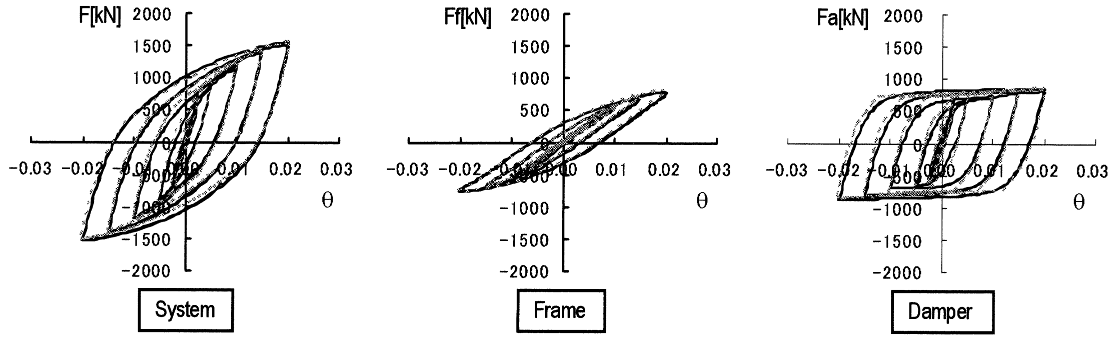

(Dash line: analysis, solid line: experiment)

Figure 7 Forces with respect to drift angle in benchmark specimen

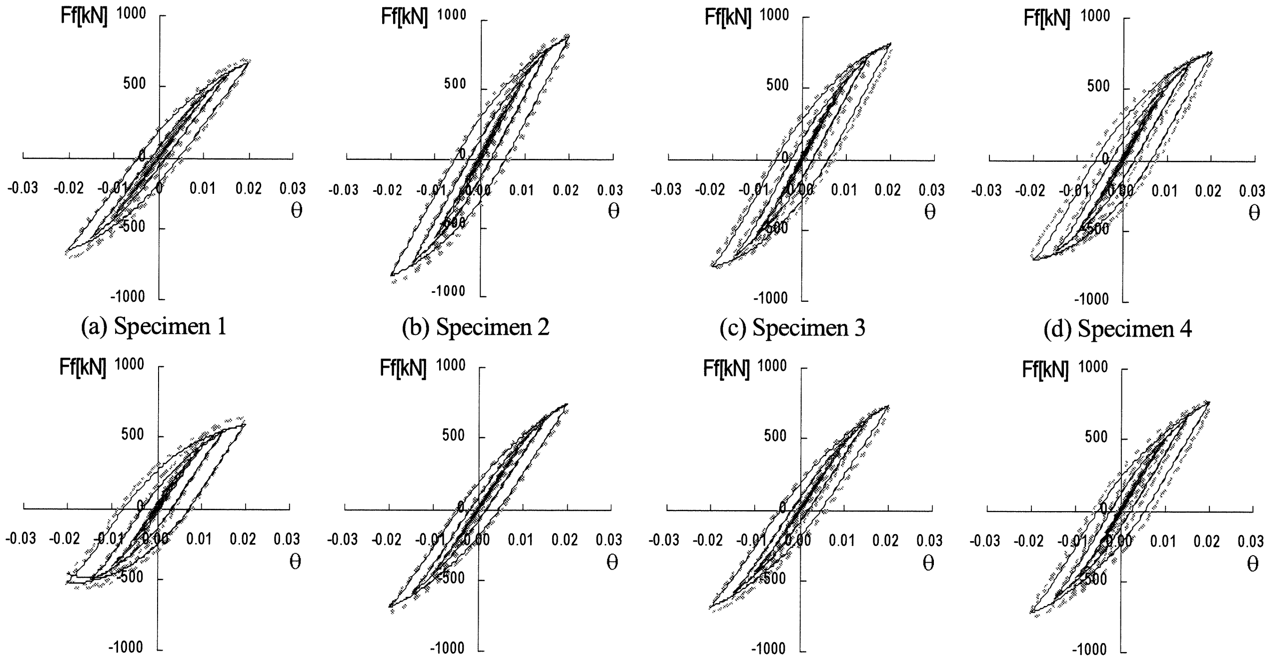

(a) Specimen 1 (b) Specimen 2 (c) Specimen 3 (d) Specimen 4

(e) Specimen 6 (f) Specimen 7 (g) Specimen 8 (h) Specimen 9

(Dash line: analysis, solid line: experiment)

Figure 8 Forces of frame with respect to drift angle

3. COMPARISON BETWEEN TEST AND ANALYSIS RESULTS

Figure 7 shows the forces of the system, the frame, and the damper with respect to drift angle. Figure 8 shows the forces of the frame. The comparison with experimental results showed the finite element model accurately predicted the cyclic inelastic response of the test specimens.

Figure 9 shows failure modes of the frame. Specimen 3 showed the failure mode, where the bottom flange of the beam subjected to axial stress and bending stress buckled. In specimen 7, plastic strain was concentrated on the corner of the gusset plate as shown in Figure 9(b). In specimen 8, the web plate of the beam buckled in shear because of the concentrated shear force from the gusset plate, and tore in the orthogonal direction to buckling waves as shown in Figure 9(b). Plastic hinges in the beams were formed at the position of the beam stiffener in case of any specimen.

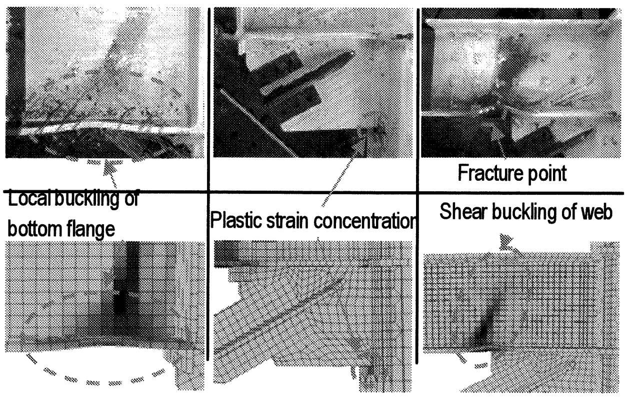

(a) specimen 3 (b) specimen 7 (c) specimen 8

* Shading represents magnitude of equivalent plastic strain

Figure 9 Failure mode
(upper row: experiment, lower row: analysis)

4. PARAMETRIC STUDY USING FE ANALSYS

Type of specimens is increased for investing influence of gusset connections on the frame. Figure 10 represents influence of thickness/width ratio of beam on plastic deformation capacity of frame. Specimens with thinner web plate showed local buckling in web. Specimens with thinner flange plate showed local buckling in bottom flange, where shear force of the column decreased dramatically.

Figure 11 represents influence of gusset connection on stiffness and plastic deformation capacity of the frame. Specimens without horizontal side stiffener and column stiffener had the same frame stiffness as the specimen without the gusset connection. Plastic deformation capacity of frame was slightly improved compared to the benchmark specimen. Specimens without vertical side stiffener and beam stiffener showed lower deformation plastic capacity. The beam web buckled early in shear at the gusset tip. A beam stiffener was effective for preventing web buckling. In both of the case, plastic hinge of beam was formed at the gusset tip even if frame stiffness is not increased due to gusset connection.

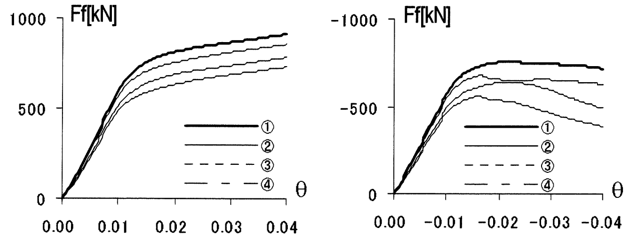

(a) Positive loading (b) Negative loading

①: benchmark, ②: large width-thickness for web

③: large width-thickness for web and flange

④: large width-thickness for web

Figure 10 Influence of thickness/width ratio of beam

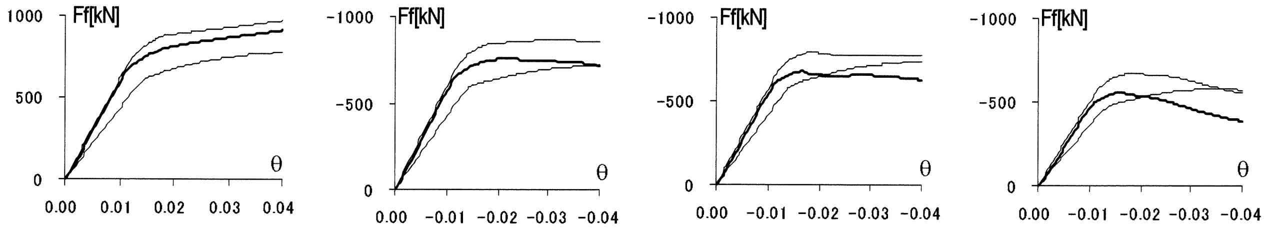

(Solid line: with damper force, dot line: without damper force, dash line: without damper force and without gusset connection)

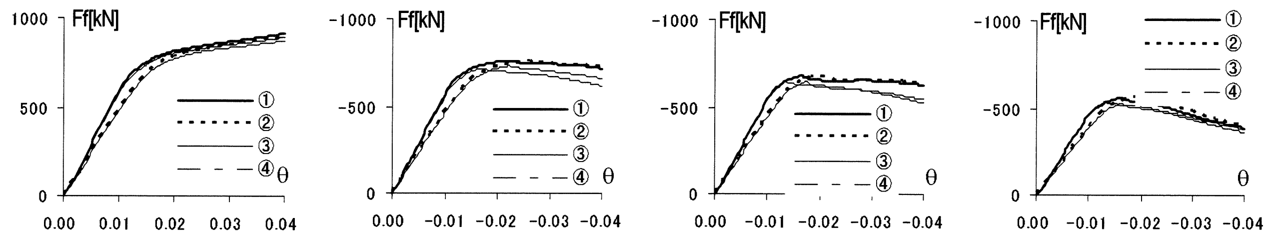

①: all stiffeners, ②: without column stiffener and horizontal side stiffener

③: non stiffeners at all , ④:without beam stiffener and vertical side

(a) Benchmark thickness (positive loading)

(b) Benchmark thickness (negative loading)

(c) Large width-thickness for web (negative loading)

(d) Large width-thickness for web and flange (negative loading)

Figure 11 Influence of gusset connection and damper force on stiffness and plastic deformation capacity of frame

5. CONCLUSION

Subassemblies in passively controlled buildings were investigated using finite element analysis. Summaries are as follows.

- Gusset connection with horizontal side stiffener and column stiffener increase frame stiffness.
- Gusset connection shift plastic hinge location in beam from column face in L-shape specimen.
- Gusset connection decreases plastic deformation capacity of beam even if beam is not subjected to axial force due to damper force.
- Beam web without beam stiffener easily buckle in shear due to concentrated force from gusset tip.
- Beam stiffener prevent web buckle in shear.
- Specimens with vertical side stiffener have better plastic deformation capacity, but column wall yield column early before yield hinge is formed.

Acknowledgements:

This study is a part of NEES/E-Defense collaborative research program on steel structures. The study was pursued by the Damper and Isolation System Working Group (WG). Special thanks are given to Yu Azuma, graduate students at Tokyo Institute of Technology, who produced experimental results.

References:

Cheol-Ho Lee and Chia-Ming Usang (2001), "Analytical Modeling and Seismic Design of Steel Moment Connections with Welded Straight Haunch", *Journal of Struct. Eng.* , **127**(9), 1028-1035.

Fifth International Conference on Urban Earthquake Engineering
March 4-5, 2008, Tokyo Institute of Technology, Tokyo, Japan

EQUIVALENT LINEARIZATION OF SYSTEM WITH NONLINEAR VISCOELASTIC DAMPERS AND ITS APPLICATION TO PASSIVE CONTROL DESIGN

Yoji Ooki[1] and Kazuhiko Kasai[2]

1) Assistant Professor, Structural Engineering Research Center, Tokyo Institute of Technology, Japan
2) Professor, Structural Engineering Research Center, Tokyo Institute of Technology, Japan
ooki@serc.titech.ac.jp, kasai@serc.titech.ac.jp

Abstract: In this paper, passive control design for linear viscoelastic damper system is extended to that for nonlinear viscoelastic damper system. The nonlinear damper is replaced to Kelvin model that has equivalent stiffness and damping based on the hysteresis including the peak response. This equivalent linearization rule is verified using time-history analysis of SDOF models. Simplified theories on seismic peak response evaluation and preliminary design of the viscoelastically damped building based on SDOF idealization are introduced. A rule to convert to MDOF system is also presented. The verification of the accuracy of design approach is demonstrated via time-history simulations.

1. INTRODUCTION

Passively controlled structures with viscoelastic dampers are one of the major systems in Japan. As for the rational design method by which designers can find the damper size of these systems, Kasai et al. proposed the method that combines the equivalent linearization and the response spectrum method regarding the system with steel dampers, nonlinear oil dampers, nonlinear viscous dampers, and linear viscoelastic dampers (JSSI, 2005). On the other hand, since almost all the viscoelastic dampers have strain sensitivities, that contributes to the nonlinearity of the material, it has great significance to design the structure with nonlinear viscoelastic dampers based on the same technique as Kasais'

Nonlinear viscoelastic damper considered in this paper is composed of isobutylene and styrene polymer. Through the linearization process, the damper is replaced into Kelvin model with equivalent stiffness and damping, and the "control performance curve" of linear viscoelastic damper system proposed by Kasai (1998, 2006,) is applied. Since the authors proposed the model for time-history analysis of the nonlinear viscoelastic damper in high accuracy (Ooki et al. 2007, Kasai et al. 2003), applicability of the equivalent linearization can be discussed by using it.

2. EQUIVALENT LINEARIZATION OF NON -LINEAR VISCOELASTIC DAMPER

2.1 Temperature, Frequency, and Strain Sensitivities of Nonlinear Viscoelastic Material

Characteristics of isobutylene-styrene viscoelastic material are explained at the beginning. Figure 1 shows the time-history model of the material by Ooki et al (2007). It is a parallel combination that consists of viscoelastic, viscous, and spring element. Storage modulus G'_d and loss factor η_d under sinusoidal loading are evaluated as shown below;

$$G'_d(\omega,\gamma_{\max}) = G'(\omega,\gamma_{\max}) + G_s(\gamma_{\max}) \tag{1a}$$

$$\eta_d(\omega,\gamma_{\max}) = \frac{G''(\omega,\gamma_{\max}) + C_d(\gamma_{\max})\cdot\omega^{\zeta}/\gamma_{\max}^{1-\zeta}}{G'_d(\omega,\gamma_{\max})} \tag{1b}$$

where ω, $\gamma_{\max}$ = circular frequency and peak shear strain of material under sinusoidal loading, G' = storage modulus of viscoelastic element, G_s = storage modulus of spring element, G'' = loss modulus of viscoelastic element, C_d = damping coefficient of viscous element (force of viscous element is proportional to ζ power of strain rate). As for the details of these properties, please refer the original paper.

Figure 2 shows the frequency and strain sensitivities of the storage modulus and loss factor. Since the temperature sensitivity has the conversion rule between the frequency sensitivities that is so-called 'temperature -frequency equivalency principle' (Kasai et al. 2003), the temperature is fixed to 20 degrees and its change due to energy dissipation is not considered in this paper.

The loss coefficient tends to rise in this material while the storage modulus decreases according to the increase of the strain when the frequency is larger than about 0.4 Hz. Due to this, the hysteresis like the bilinear shape is observed under large strain, and the excessive increase of damper force can be avoided.

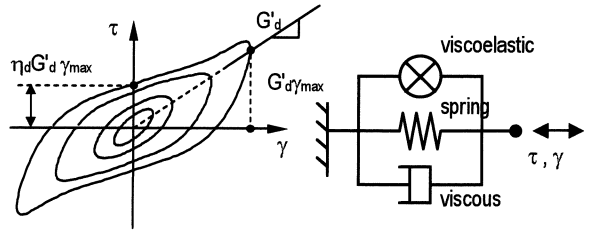

Figure 1 Model of Nonlinear Viscoelastic Material and Typical Hysteresis under Sinusoidal Loading

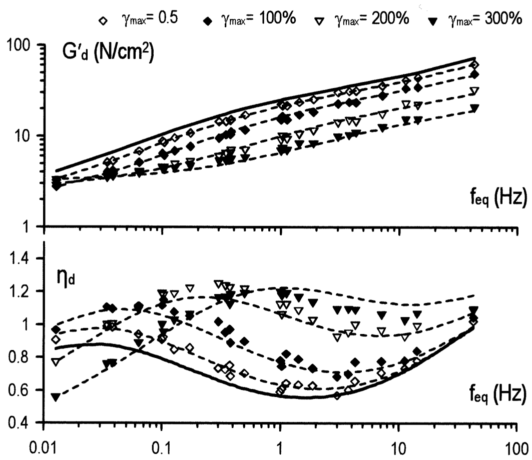

Figure 2 Sensitivities on Equivalent Frequency and Strain of Nonlinear Viscoelastic Material

2.2 Equivalent Linearization of Damper Hysteresis

In order to apply the equivalent linearization method to the analysis of the system with nonlinear viscoelastic damper, the bilinear-like hysteresis in steady state is replaced into an ellipse provided by equivalent Kelvin model.

Figure 3 shows the ratio of energy dissipation of hysteresis by Ooki's model (strict model) to that of equivalent Kelvin model (approximate model) having the same storage modulus and loss factor as strict model. Since the material under $\gamma_{\max} < 0.5$ shows elliptical hysteresis (Kasai, Ooki, and et al. 2003), the results under such a small strain are eliminated. The ratio is nearly uniform over the applicable range of the strict model. This means that the hysteresis of the strict model is equivalent and replaceable to the approximate model in case of steady state.

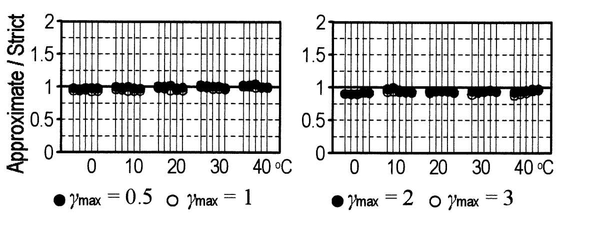

Figure 3 Comparison of Dissipated Energy of Viscoelastic Material under Stationary Condition between Strict and Approximation Model

3. SEISMIC RESPONSE CHARACTERISTICS OF NONLINEAR VISCOELASTIC DAMPER SYSTEM

When the seismic response of nonlinear viscoelastic damper system is considered using the equivalent damper previously mentioned, it is necessary to pay attention to the change of the storage modulus and loss factor with not only frequency, but also strain. In this section, using SDOF model reproducing the passive control system, how to set the strain that is required to linearization of the damper is discussed.

3.1 Structural Characteristics of SDOF Passive Control System

Definitions of structural characteristics for nonlinear viscoelastic dampers are introduced here. They are based on the linear damper case (Kasai et al. 2006).

Figure 4 shows SDOF model of the passive control system. M is mass of the system. K_f = stiffness of the frame, $K'_d(\omega_n, \gamma_{\max})$ = damper stiffness, K_b = brace stiffness, K'_a = stiffness of added component (combination of K_d and K_b in line) A_s, d = shear area and thickness of viscoelastic material. All of them are representing the contribution to lateral component.

Circular frequency of the system is obtained shown as follows;

$$\omega_n = \sqrt{(K_f + K'_a)/M} \tag{2}$$

$$\begin{aligned} K'_d &= K'_d(\omega_n, \gamma_{\max}) \\ &= G'_d(\omega_n, \gamma_{\max}) A_s / d \end{aligned} \tag{3}$$

$$K'_a = \frac{\{(1+\eta_d^2)K'_d + K_b\}K'_d K_b}{(K'_d + K_b)^2 + (\eta_d K'_d)^2} \tag{4}$$

Relationship of the loss factor among damper (η_d), added component (η_a), and system (η) are shown as follows;

$$\eta_a = \frac{\eta_d}{1 + (1+\eta_d^2)K'_d / K_b} \tag{5}$$

$$\eta = \frac{\eta_a}{1 + K'_f / K'_a} \tag{6}$$

3.2 Parametric Analysis Using SDOF Passive Control Systems

Parameters of the models are set to K'_{d0}/K_f, K_b/K_f, and $T_{n0} = 2\pi/\omega_{n0}$, where K'_{d0} = initial damper stiffness and T_{n0} = corresponding system period. $\gamma_{\max}$ is set to 0.1 to get K'_{d0} (Eq.(3)). And T_{n0} changes according to the property of the SDOF system. This means that iterative procedure using Eqs. from (2) to (4) is necessary for calculating T_{n0}.

The earthquakes used here are JMA Kobe (NS component) and artificial wave which has ideal response spectrum (Figure 5). Table 1 indicates the properties of the strict SDOF models, and shear strains of viscoelastic material of the strict model are set to $\gamma_{max} = 0.1, 1, 2, 3$ by adjusting the magnitude of the acceleration of the earthquakes. Total number of the analysis is 128. On the other hand, the approximate model has the equivalent stiffness and damping defined based on the peak response of the damper to strict model

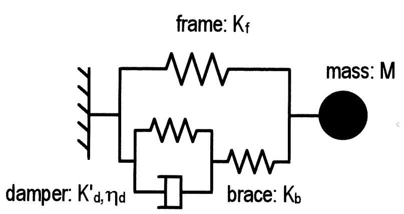

Figure 4 SDOF Passive Control System

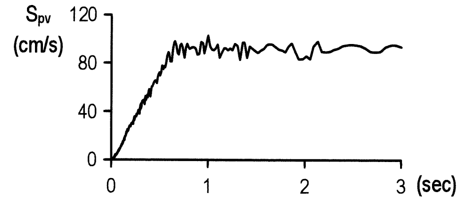

Figure 5 Response Spectrum (Damping = 2 %) of Artificial Wave

Table 1 Properties of SDOF Models (Strict Model)

	K'_{d0}/K_f	K_b/K_f	T_{n0} (sec)	γ_{max} (rad)	Earthq.
Case 1	0.4	∞	0.3, 1, 2, 3	0.1, 1, 2, 3	JMA Kobe, Artificial Wave
Case 2	2	∞			
Case 3	0.4	3			
Case 4	2	3			

3.2 Accuracy of Approximate Model

Figure 6 shows the comparison between strict model and approximate model in parametric analysis. It can be said that the approximate model is roughly predictable of peak response of the strict model.

In case of Kobe earthquake, the system reaches to peak response with a few cycles because of the impulsive acceleration. And the peak stands out as compared with those in other cycles. On the other hand, in case of artificial wave, the peak of almost the same size is observed in the around the maximum value. Since the nonlinear viscoelastic damper system has strain and frequency sensitivity, the system shows a little bit different behavior from the steady state under impulsive excitation. The fact does not coincide with the premise of the equivalent linearization, and it causes the result that the accuracy in artificial wave is better than that of Kobe wave case.

As discussed above, there is still room for improvement of the methodology especially in setting the frequency and strain of approximate model. However, if we take account of its simplified process and the fact that the current model can reproduce mostly the behavior of the strict model, the equivalent linearization method in this paper can accept the method based on the property at peak response, which is applied to the passive control design described in the next section.

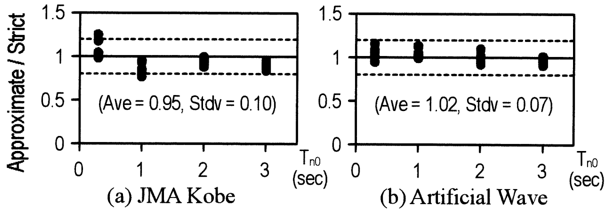

Figure 6 Comparison between Strict Model and Approximate Model in Parametric Analysis ($\gamma_{max} = 1, 3$)

4. PASSIVE CONTROL DESIGN OF SYSTEM WITH NONLINEAR VISCOELASTIC DAMPER

From the discussion in the section 2 and 3, it is found that the peak response of the system with nonlinear viscoelastic damper can be predicted based on the equivalent linearization method. In this section, the passive control design procedure for the system with linear viscoelastic damper (JSSI 2005, Kasai et al. 2006) is extended upgraded case in which the nonlinear damper is considered.

4.1 Control Performance Curve of SDOF Passive Control System

Kasai et al. proposed the response reduction ratio (R_d, R_{pa}) of passive control system based on the response spectrum method. R_d and R_{pa} are the reduction ratio of displacement spectrum S_d and pseudo acceleration spectrum S_{pa}, respectively.

$$R_d = D_h \frac{T_{eq}}{T_f}, \quad R_{pa} = R_d \left(\frac{T_f}{T_{eq}} \right)^2 \qquad (7a, b)$$

$$D_h = \sqrt{\frac{1 + \alpha h_0}{1 + \alpha h_{eq}}} \qquad (8)$$

where T_f = natural period of original frame, h_0 = damping factor of original frame, T_{eq} = equivalent period of passive control system, h_{eq} = equivalent damping factor of passive control system, respectively. Furthermore, D_h represents the effect of the response reduction aroused by damping and α = 75 is recommended in case of artificial earthquake. Eqs. (7) and (8) are applicable to the case where pseudo velocity spectrum S_{pv} = constant. This condition is generally considered to the design of middle and high rise building.

T_{eq} and h_{eq} in Eqs. (7) and (8) are given as below;

$$T_{eq} = T_f \sqrt{\frac{K_f}{K_f + K'_a}} \qquad (9)$$

$$h_{eq} = h_0 + 0.92 h'_{eq}, \quad h'_{eq} = \eta/2 \qquad (10a, b)$$

Using Eqs. from (7) to (10), control performance curve R_{pa} vs. R_d is obtained as shown in Figure 7. Response spectrum of BCJ-L2 wave, which is an artificial design earthquake provided by The Building Center of Japan (BCJ), is applied in this case.

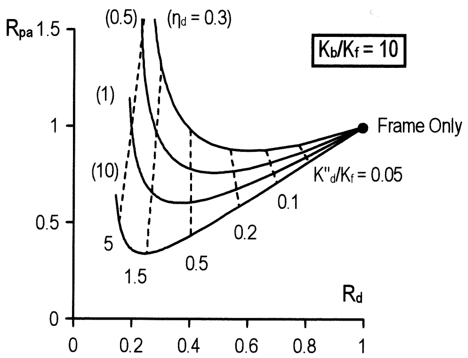

Figure 7 Control Performance Curve of Passively Controlled Structure with Nonlinear Viscoelastic Damper

4.2 Procedure of Passive Control Design (SDOF)

The control performance curve is originally for linear viscoelastic damper system and it can be extended to nonlinear case, directly.

Firstly, SDOF passive control system is designed by using the control performance curve. The curve is based on the case $K_b/K_f = 10$

1) Get the elastic response of the original frame (no damper) and obtain θ_f using the equation below. Displacement reduction ratio R_d is calculated according to the target inter-story drift θ of passive control system.

$$\theta_f = S_d(T_f, h_0)/H_{eff} \qquad (11)$$

$$R_d = \theta/\theta_f \qquad (12)$$

where H_{eff} = effective height.

3) Get required stiffness ratio K''_d/K_f from control performance curve base on the target R_d.

4) Set the target shear strain γ_{max} of viscoelastic damper. Using γ_{max}, T_{eq}, and ambient temperature (= 20 degrees), obtain η_d from Eq. (1b).

5) Simultaneously, T_{eq} is re-calculated using Eq. (9). This process is repeated until T_{eq} is converged.

6) After the step 5), from converged T_{eq} and target γ_{max}, correct η_d is finally obtained. $K'_d/K_f = K''_d/K_f/\eta_d$ is used for deciding the i-th story damper stiffness K'_{di} in the next stage.

In Kasai's method, R_d is modified according to an index regarding the effect of the second mode of the passive control system, but the process is eliminated here.

4.3 Procedure of Passive Control Design (MDOF)

Secondly, based on the properties of the SDOF system, damper size of MDOF system is decided. This procedure aims at satisfying the two conditions; a) equivalent damping factor between SDOF and MDOF system is identical. b) inter-story drifts of MDOF system caused by the design lateral force are uniformly distributed and they are equivalent to the target θ of SDOF (Kasai et al. 2006).

The i-th story damper stiffness K'_{di} and brace stiffness K_{bi} are decided using Eqs. from (13) to (15).

$$K'_{di} = \frac{Q_i}{h_i}\frac{\sum K_{fi} h_i^2}{\sum Q_i h_i}\left(\beta + \frac{1}{\Gamma_b} + \frac{K'_d}{K_f}\right) - K_{fi}\left(\beta + \frac{1}{\Gamma_b}\right) \qquad (13)$$

$$K_{bi} = K'_{di}/\beta \qquad (14)$$

$$\beta = K'_d/K_b, \quad \Gamma_b = 1 + \frac{\eta_d^2}{1 + K_b/K'_d} \qquad (15a, b)$$

where Q_i = i-th story design force, h_i = i-th story height. From the target inter-story drift θ, i-th story maximum deformation $u_{i,max}$ is obtained (= $h_i\theta$) and we have relationship between $u_{i,max}$ and the maximum damper deformation $u_{di,max}$ as shown below;

$$u_{di} = \sqrt{K''_a/K''_d}\, u_{ai} \qquad (16)$$

Thickness d_i and shear area A_{si} of viscoelastic material at i-th story are obtained as follows.

$$\hat{d}_i = u_{di,\max}\cos\varphi_i/\gamma_{\max} \qquad (17)$$

$$\hat{A}_{si} = K'_d \hat{d}_i/\cos^2\varphi_i/G'_d \qquad (18)$$

where φ_i = i-th story damper angle. The symbol "^" indicates the contribution to longitudinal component of the damper.

5. EXAMPLE OF PASSIVE CONTROL DESIGN AND VERIFICATION OF ACCURACY

In this section, by using four kinds of 10-story structures with different frame stiffness, the passive control design and its verification are demonstrated.

Inter-story drift by 1/150 is the target here. Figure 8 shows the distribution of lateral stiffness of four building models. The distribution of lateral frame stiffness of S-Type is in proportion to that of the design shear force. On the other hand, in L-Type and U-Type, the frame stiffness is insufficient at upper or lower portion of the structure, respectively. JSSI Type is a realistic frame designed by a committee of Japan Society of Seismic Isolation (JSSI). Natural period of original frame is 2 sec. in these models and dampers are designed according to the procedure previously mentioned in section 4. If $K'_{di} < 0$ is true in Eq. (13), the damper will not be installed to the floor concerned.

Figure 9 shows the comparison between the target inter-story drift and the result from time-history analysis. BCJ-L2 wave is applied to the analysis. Average of inter-story drift distribution is nearly identical to the target, and it does not depend on the difference of the frame stiffness too much.

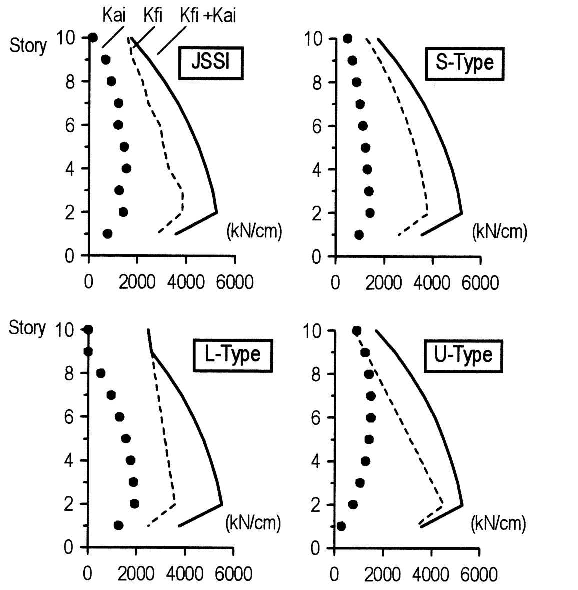

Figure 8 Distribution of Lateral Stiffness of Four Building Models

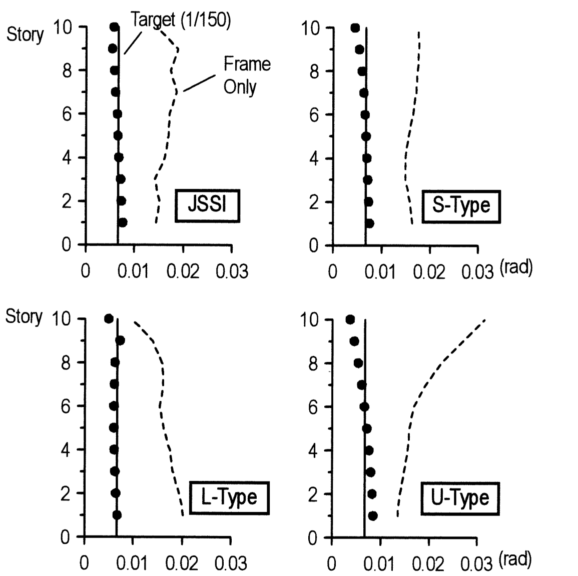

Figure 9 Comparison between Target Inter-Story Drift and Analytical Result

6. CONCLUSIONS

Based on the equivalent linearization technique, simplified design procedure for nonlinear viscoelastic damper system is discussed.

1) The equivalent stiffness and damping of the nonlinear viscoelastic damper is decided based on the hysteresis including the peak response. The equivalent Kelvin model obtained by this approach can approximate the behavior of the strict model.

2) By using the control performance curve of passively damped system with linear viscoelastic damper, the procedure of passive control design for the system with nonlinear viscoelastic damper is explained.

3) 10-story buildings with different four kinds of lateral stiffness of the frame are designed according to the proposed method and its accuracy is validated by means of the time-history analysis.

References:

Japan Society of Seismic Isolation (2005), "Manual for Design and Construction of Passively-Controlled Buildings (2nd Edition", JSSI. (in Japanese)

Kasai, K., Fu, Y., and Watanabe, A. (1998), "Passive Control Systems for Seismic Damage Mitigation," *Journal of Structural Engineering*, American Society of Civil Engineers, **124**(5), 501-512.

Kasai, K., Ooki, Y., Amemiya, K., and Kimura, K. (2003), "A Constitutive Rule for Viscoelastic Materials Combining Iso-Butylene and Styrene Polymers: Part 1 Linear Model Considering Temperature And Frequency Sensitivities", *Journal of Structural and Construction Engineering (Transaction of AIJ)*, **569**, 47-54. (in Japanese)

Ooki, Y., Kasai, K., Amemiya, K., and Kimura, K. (2007), "A Constitutive Rule for Viscoelastic Materials Combining Iso-Butylene And Styrene Polymers: Part 2 Non-Linear Model Considering Temerature, Frequency, and Strain Sensitivities", *Journal of Structural and Construction Engineering (Transaction of AIJ)*, **617**, 77-85. (in Japanese)

Kasai, K., Minato, N., and Kawanabe, Y. (2006), "Passive Control Design Method Based on Tuning of Equivalent Stiffness of Viscoelastic Damper", *Journal of Structural and Construction Engineering (Transaction of AIJ)*, **610** 75-83. (in Japanese)

Fifth International Conference on Urban Earthquake Engineering
March 4-5, 2008, Tokyo Institute of Technology, Tokyo, Japan

PASSIVE CONTROL DESIGN METHOD FOR BUILDING STRUCTURE WITH BILINEAR OIL DAMPER

Hiroshi Ito[1], Kazuhiko Kasai[2], and Takayuki Ogura[3]

1) Post-doctoral Research Fellow, Center on Urban Earthquake Engineering, Tokyo Institute of Technology, Japan
2) Professor, Structural Engineering Research Center, Tokyo Institute of Technology, Japan
3) Farmer Graduate Student, Department of Built Environment, Tokyo Institute of Technology, Japan
ihiroshi@enveng.titech.ac.jp, and kasai@serc.titech.ac.jp

Abstract: This paper proposes a practical theory for peak response evaluation method and a design approach for system with bilinear oil damper in preliminary seismic design. The proposed theory is based on the single-degree-of-freedom (SDOF) idealization of multistory building structure, and uses the so-called "performance curve" which simultaneously expresses the seismic performance as a function of stiffness parameter, properties of damper, and seismic response spectrum. A rule to convert a SDOF design to a multistory design and arrangement of damper stiffness over the height of structure is also presented. The accuracy of this method is validated via extensive time history simulations over a wide range of building models.

1. INTRODUCTION

In recent years passively-controlled building structures by incorporating various energy dissipation devices (dampers) have become common in Japan. In particular, the use of oil dampers in passively-controlled building has gained widespread practical applications. The oil dampers can substantially reduce story drift and member force by adding viscous damping to the primary structure (frame) against earthquake ground motion and wind vibration. In general, oil damper consists of a series of an elastic spring element and a bilinear viscous element which has relief mechanism to control the damper force. In preliminary seismic design, however, lack of comprehension of the relationship among response reduction, amount of damper and seismic ground motion induces an irrational approach, which requires numerous time history simulations.

Objectives of this paper are to propose a simplified prediction theory for peak seismic response and a design approach for building structure with bilinear oil damper in preliminary seismic design, and to verify the accuracy of this method. The proposed theory employs the single-degree-of-freedom (SDOF) model idealization of multi-story building structure and equivalent linearization technique. A rule to convert a SDOF design to a multi-story design including the arrangement of damper stiffness over the height of building is also presented. The accuracy of this design approach is validated via time history simulations over a wide range of MDOF models.

2. DYNAMIC PROPERTIES OF SDOF SYSTEM WITH OIL DAMPER

2.1 Response of SDOF System with Bilinear Oil Damper at Steady State

To fully comprehend the dynamic properties of the multi-story building structures with oil dampers, consider the idealized SDOF model of system with oil damper as shown in Figure 1. Figure 2 and 3 show the hysteretic curve of viscous element and components of system at steady state, respectively. For viscous element, added component and system, their forces at zero deformation and maximum deformation divided by maximum deformation of each are defined as "loss stiffness", "storing stiffness", respectively.

Viscous element behaves bilinearly for velocity as shown in Figure 2, 3. Viscous damping coefficient, second viscous damping coefficient ratio, relief velocity, relief force, maximum velocity, maximum deformation of viscous element are defined as C_d, p, $\dot{u}_{dy}$, F_{dy}, $\dot{u}_{d,\max}$, $u_{d,max}$, respectively. In addition, considered circular frequency ω, relief factor of viscous element μ_d is defined as ratio of maximum deformation $u_{d,max}$ to relief deformation u_{dy} ($= \dot{u}_{dy}/\omega$) corresponding to relief velocity $\dot{u}_{dy}$. For the cases of both linear and bilinear behavior, loss stiffness of damper K''_d is defined as follows.

$$K''_d = C_d\omega \quad (\mu_d \le 1)$$
$$K''_d = \{p + (1-p)/\mu_d\}C_d\omega \quad (\mu_d > 1) \qquad \text{(1a,b)}$$

Oil damper consists of a series of a bilinear viscous element and an elastic spring which shows internal stiffness K_d of damper. In addition, internal stiffness factor of damper β is defined as Eq. (2b).

Added component consists of a series of Maxwell body of oil damper and elastic spring which shows brace stiffness

K_b. Equivalent brace stiffness K^*_b is defined as a series of internal stiffness of damper K_d and brace stiffness K_b as following equation.

$$K_b^* = \frac{K_b \cdot K_d}{K_b + K_d} = \frac{\beta / \omega \cdot K_b C_d \omega}{K_b + \beta / \omega \cdot C_d \omega}, \quad K_d = \beta C_d \quad \text{(2a,b)}$$

In addition, λ factor which is an index of effectiveness of energy dissipation of added component is defined as K''_d / K^*_b. Relief factor of added component μ_a is approximately obtained as following equation.

$$\mu_d - 1 = (\mu_a - 1)(1 + 0.25\lambda + 0.15\lambda^2) \quad (3)$$

In addition, for the case of linear behavior, storing stiffness and loss stiffness of added component K'_a, K''_a are expressed as following equations, respectively.

$$K'_a = \frac{\lambda}{1+\lambda^2} K''_d, \quad K''_a = \frac{1}{1+\lambda^2} K''_d \quad \text{(4a,b)}$$

Moreover, for the case of bilinear behavior, K'_a, K''_a are approximately obtained as following equations, respectively.

$$K'_a = \frac{\lambda \zeta^2}{1+(\lambda\zeta)^2} C_d \omega \ ,$$
$$K''_a = \min\left[\frac{\zeta}{1+(\lambda\zeta)^2} C_d \omega, \left(p + \frac{1-p}{\mu_a \sqrt{1+\lambda^2}}\right) C_d \omega\right] \quad \text{(5a,b)}$$

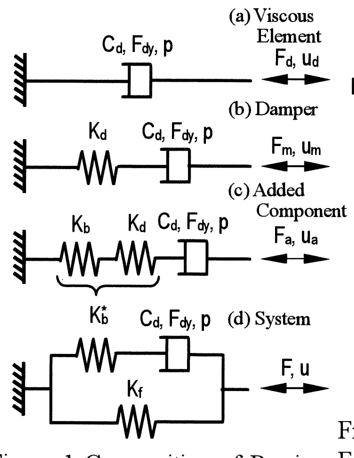

Figure 1 Composition of Passive Control System with Oil Damper

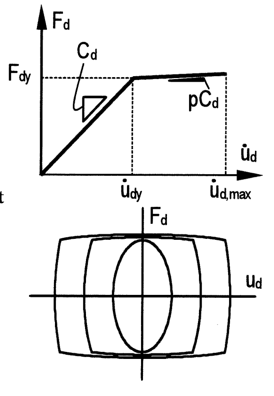

Figure 2 Relationship of Force – Velocity and Deformation of Viscous Element

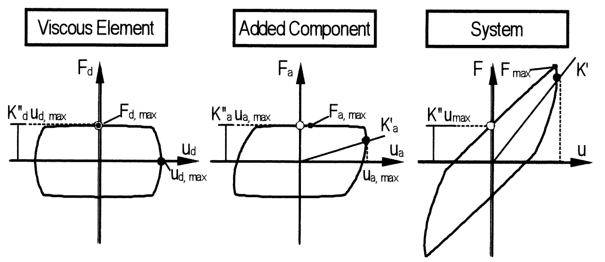

Figure 3. Hysteretic Curve of Viscous Element, Added Component and System at Steady State

where

$$\zeta = p + (1-p)\exp[-R(\mu_a - 1)^S],$$
$$R = \min[0.05 + 0.4\lambda, 0.5\lambda^2 + \lambda^4] \quad (\lambda \leq 7),$$
$$S = \max[-2.5\log\lambda, 0.67 - 0.43\log\lambda] \quad (\lambda \leq 7) \quad \text{(6a-c)}$$

SDOF model of system consists of a mass and combination of elastic spring which shows frame stiffness K_f and added component connected in a row to the mass. Finally, storing stiffness and loss stiffness of system K', K'' are expressed as following equations, respectively.

$$K' = K_f + K'_a \ , \quad K'' = K''_a \quad \text{(7a,b)}$$

2.2 Dynamic Properties of SDOF System with Bilinear Oil Damper

By equivalency between bilinear and linear viscous elements based on passive control effectiveness (Kasai et al. (2007)) shown in Figure 4, viscous damping coefficient of equivalent linear viscous element C_{dL} is approximately estimated as follows.

$$\frac{C_{dL}}{C_d} = p + \frac{2(1-p)}{\mu_d} - \frac{1-p}{\mu_d^2} \cong \frac{K''_{dL}}{K''_d} \quad (8)$$

where subindex "L" means properties of equivalent linear element.

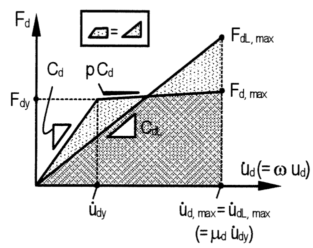

Figure 4. Equivalency for Bilinear and Linear Viscous Elements Based on Passive Control Effectiveness

By converting bilinear to linear viscous element based on equivalency between both elements, equivalent period T_{eq} and damping h_{eq} of SDOF system with oil damper can be estimated readily. Firstly, for system with equivalent linear viscous element, storing stiffness ratio of added component K'_{aL}/K_f and λ_L factor are expressed as Eq. (9a,b).

$$\frac{K'_{aL}}{K_f} = \frac{\lambda_L^2}{1+\lambda_L^2} \cdot \frac{K_b^*}{K_f} \ , \quad \lambda_L = \frac{C_{dL}}{C_d} \cdot \frac{K''_d}{K_f} \cdot \frac{K_f}{K_b^*} \ ,$$
$$\frac{K_b^*}{K_f} = \frac{\beta/\omega \cdot (K_b/K_f)(K''_d/K_f)}{K_b/K_f + \beta/\omega \cdot (K''_d/K_f)} \quad \text{(9a-c)}$$

In the same way for added component, storing stiffness ratio of system K'_L/K_f is expressed as Eq. (10).

$$K'_L / K_f = 1 + K'_{aL} / K_f \quad (10)$$

Defining fundamental vibration period and damping ratio of frame as T_f, h_0, equivalent period T_{eq} and damping h_{eq} of equivalent linear system is estimated as following equation.

$$T_{eq} = T_f \Big/ \sqrt{1 + \frac{K'_{aL}}{K_f}} \ ,$$

$$h_{eq} = h_0 + 0.8 \times \frac{1}{2} \cdot \frac{\lambda_L}{K_f / K_b^* + (1 + K_f / K_b^*) \lambda_L{}^2} \quad \text{(11a,b)}$$

3. SYMPLIFIED RESPONSE EVALUATION FOR SDOF SYSTEM WITH BILINEAR OIL DAMPER

3.1 Response Reduction Factor of Displacement and Acceleration

Peak response of the system with oil damper will be obtained from a linear response spectrum using T_{eq} and h_{eq} indicated above. We define S_d, S_{pv} and S_{pa} as response displacement, response pseudo velocity and response pseudo acceleration spectra, respectively. For the frame, their values are obtained from an expected seismic response spectrum, T_f and h_0. With the response of frame, peak response of the system with bilinear oil damper is expressed by considering following two effects due to inserting the damper. They are shortening of vibration period (from T_f to T_{eq}) and viscous damping increase (from h_0 to h_{eq}). The latter is represented by damped effect factor D_h, which is an "average" reduction of S_d, S_{pv} and S_{pa} (Eq. (12)).

$$D_h = \sqrt{(1 + a h_0)/(1 + a h_{eq})} \quad \text{(12)}$$

where $a = 25$ (for an ensemble of 31 observed earthquake motions (Kasai et al. (2003))) and 75 (for most artificial ground motions). Peak responses of the system with oil damper $S_d(T_{eq}, h_{eq})$ and $S_a(T_{eq}, h_{eq})$ normalized to those of the frame S_d (T_f, h_0) and S_{pa} (T_f, h_0) are defined as displacement reduction R_d and acceleration (base shear) reduction R_a, respectively. Considered the two effects indicated above, also S_{pa}, S_{pv} will be assumed to be period-independent as for short period, medium-long period structure, respectively. R_d and R_a are given as Eq. (13a-c).

$$R_d = D_h \left(\frac{T_{eq}}{T_f} \right)^2 \ (S_{pa}{=}const.) \ , \ D_h \frac{T_{eq}}{T_f} \ (S_{pv}{=}const.) \ ,$$

$$R_a = \sqrt{\left(\frac{K'_a}{K_f} + 1 \right)^2 + \left(\frac{K''_a}{K_f} \right)^2} \, R_d \quad \text{(13a-c)}$$

3.2 Performance Curve of SDOF System with Bilinear Oil Damper

The previous equations can clarify the complex interactive effects of stiffness parameter, properties of damper, vibration period, damping and seismic response spectrum on the response reduction of the system with bilinear oil damper. Figure 5 shows the curves for drift reduction R_d and acceleration (base shear) reduction R_a of SDOF system with bilinear oil damper under a period-independent S_{pv}, and S_{pa}, respectively. The initial damping ratio of frame is $h_0 = 0.02$.

The performance curves for system with bilinear oil damper depend strongly on five parameters: loss stiffness ratio of viscous element K''_d/K_f, brace stiffness ratio K_b/K_f, ratio of second viscous damping coefficient of viscous element p, relief factor of viscous element μ_d, and internal stiffness factor of damper β.

In Figure 5, the point $K''_d / K_f = 0$ gives the frame response $R_d = R_a = 1$. In case of independent-period S_{pv}, to a point, larger K''_d/K_f (larger damper) and K_b/K_f (stiffer brace) lead to smaller drift (R_d) and force (R_a) (Figure 5(b)). Thereafter, the drift continues to decrease, but base shear increases sharply. In case of independent-period S_{pa}, larger K''_d/K_f (larger damper) and K_b/K_f (stiffer brace) lead to even smaller R_d and R_a (Figure 5(a)). As indicated above, the performance curve clearly shows the trade-off between drift and base shear, and can provide readily the design solution to satisfy the desired response.

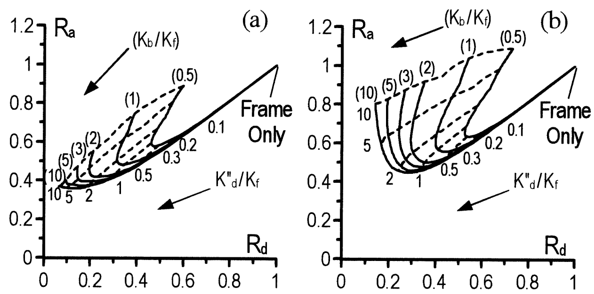

Figure 5. Performance Curve ((a) independent-period S_{pa} and (b) independent-period S_{pv})

4. DESIGN PROCEDURE FOR MDOF SYSTEM WITH BILINEAR OIL DAMPER

Design procedure for the MDOF system with oil damper is summarized below:

Step 1. Obtain the peak drift angle θ_f of the SDOF frame (without damper) from the design response spectrum, assuming the equivalent height H_{eff} of the frame:

$$\theta_f = \frac{T_f \cdot S_{pv}(T_f, h_0)}{2\pi \cdot H_{eff}} \ ,$$

$$H_{eff} = \frac{\sum_{i=1}^{N} (m_i \hat{\phi}_i H_i)}{\sum_{i=1}^{N} (m_i \hat{\phi}_i)} = \frac{\sum_{i=1}^{N} (m_i H_i{}^2)}{\sum_{i=1}^{N} (m_i H_i)} \quad \text{(14a,b)}$$

Step 2. Evaluate the target displacement reduction ratio R_d based on the target story drift angle θ. Evaluate the required loss stiffness ratio of viscous element K''_d/K_f for the brace stiffness K_b / K_f and target displacement reduction ratio R_d based on the SDOF idealization. Required K''_d/K_f may be obtained by dynamically analyzing a SDOF structure on a trial-and-error basis, or much more efficiently, by using the "performance curve" that is shown in Figure 5.

Step 3. Estimate the loss stiffness of viscous element K''_{di} at i-th story by Eq. (15), which converts the required ratio K''_d/K_f of the SDOF system to those of the MDOF system. Calculate equivalent brace stiffness K^*_b by using λ factor.

$$K''_{di} = \left\{\lambda + \left(\frac{C_d}{C_{dL}}\right)^2 \frac{1}{\lambda} + \frac{K''_d}{K_f}\right\} \frac{Q_i}{h_i} \frac{\sum_{i=1}^{N}(K_{fi}h_i^2)}{\sum_{i=1}^{N}(Q_i h_i)},$$
$$-K_{fi}\left\{\lambda + \left(\frac{C_d}{C_{dL}}\right)^2 \frac{1}{\lambda}\right\}$$
$$K^*_{bi} = \frac{K''_{di}}{\lambda} \tag{15a,b}$$

Step 4. Calculate the peak deformation of viscous element $u_{di,max}$, viscous damping coefficient of viscous element C_{di}, internal stiffness of damper K_{di} and brace stiffness K_{bi} at ith-story. If the higher modes effect must be included, take additional steps and repeat 3rd and 4th steps only once.

$$u_{di,\max} = h_i\theta \frac{1+0.25\lambda+0.15\lambda^2}{\mu_d+0.25\lambda+0.15\lambda^2} \cdot \frac{\mu_d}{\sqrt{1+\lambda^2}},$$
$$C_{di} = \frac{K''_{di}}{\omega_{eq}}, \quad K_{di} = \beta C_{di},$$
$$K_{bi} = K_{di}K^*_{bi}/(K_{di} - K^*_{bi}) \tag{16a-d}$$

Step 5. Evaluate the peak damper force $F_{di,max}$ and peak story shear $V_{i,max}$ at i-th story.

$$F_{di,\max} = K''_{di}\, u_{di,\max},$$
$$V_{i,\max} = h_i\theta\sqrt{(K_{fi}+K'_{ai})^2 + (K''_{ai})^2} \tag{17a,b}$$

Step 6. Determine the size and detail of each oil damper. See for instance the JSSI manual (JSSI, 2003, 2005)

5. VALIDATION OF THE PROPOSED DESIGN APPROACH

5.1 Frame Models and Design Earthquake Ground Motions

In order to verify the accuracy of response control design in the previous chapter, MDOF shear-bar models (JSSI-Type), which are based on full-frame models of 4, 10 and 20-story steel moment-resisting frame designed by JSSI (JSSI (2005) and Kasai et al. (2005)), are utilized. In addition, 3 types of story stiffness distribution for these 4, 10 and 20-story buildings are considered, which have mass distribution m_i, story height distribution h_i and fundamental vibration period T_f identical to JSSI-Type. The three types are called as standard (S-Type), upper-deformed (U-Type) and lower-deformed (L-Type). Story stiffness distribution of 4 types of frame for 4, 10 and 20-story buildings are shown in Figure 6. The frame stiffness K_{fi} at ith-story of S-Type is designed such that story drift becomes uniform under the A_i lateral force distribution (BCJ (2004)). In U-Type frame, story drift at upper stories increases, whereas in L-Type frame, story drift at lower stories increases. As mentioned above, story stiffness distributions of S, U and L-Type frame are obtained such that fundamental vibration period of them are identical to JSSI-Type. Fundamental vibration period of frame T_f, the total building height H and drift angle of frame obtained from design response spectrum (Figure 7) utilizing Eq. (14) are shown in Table 1. The viscous damping ratio of frame is $h_0 = 0.02$.

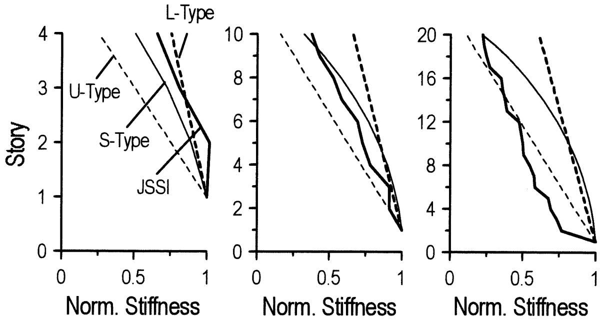

Figure 6. 4 Story Stiffness Distributions of Frames for Various Building Heights

Table 1. Fundamental Vibration Period of Frame and Drift Angle of Frame Obtained from Design Response Spectrum

	4-Srory	10-Story	20-Story
T_f (sec)	0.640	2.012	3.704
H (m)	18.0	42.0	82.0
T_f / H	0.036	0.048	0.045
$S_d(T_f, h_0)$ (cm)	14.26	44.83	82.53
θ_f (rad.)	0.0101	0.0149	0.0146

Design response spectrum and response spectra of 4 artificial earthquake motions for 2% damping (Table 2), which are considered as extremely severe earthquake level, are shown in Figure 7. S_{pv} of 4 artificial earthquake motions will be assumed to be period-independent in the range greater than 0.64 sec, S_{pa} of 6 artificial earthquake motions will be also assumed to be period-independent in the range of shorter vibration period (0.16 – 0.64 sec). Peak ground acceleration (PGA) and coefficient a (Eq. (12)) of 4 artificial earthquake motions are shown in Table 2. It is clarified that coefficient a (Eq. (12)) related to damped effect factor D_h for each artificial ground motion tends to be higher than an ensemble of 31 observed earthquake motions.

5.2 Analysis Results

In order to verify the accuracy of response control design, time history analyses were carried out for 432 MDOF system with oil damper designed: 4 types of frame which are JSSI, S, L and U-Type shown in Figure 6, 3 building heights which are 4, 10, 20-story, 3 target drift

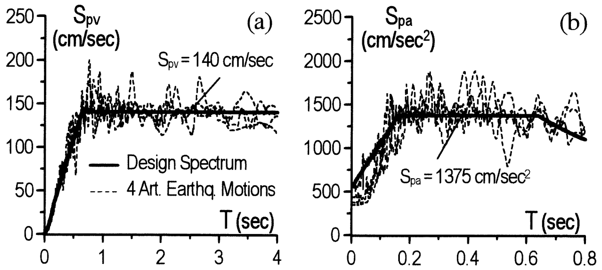

Figure 7. Response Spectrum of 6 Artificial Earthquake Ground Motions (h_0=0.02) ((a) S_{pv} and (b) S_{pa})

Table 2. List of Input Artificial Earthquake Ground Motions

	PGA (cm/sec^2)	a
BCJ-L2	346.59	75
Hachinohe EW (1968) Phase	435.07	75
Tohoku Univ. NS (1978) Phase	370.97	75
Taft N111E (1952) Phase	548.50	75

angles θ= 1/200, 1/150 and 1/125, and 4 artificial earthquake ground motions shown in Figure 7 and Table 2. The required loss stiffness ratio of viscous element K''_d/K_f for the brace stiffness K_b/K_f and target displacement reduction ratio R_d is determined to be K''_d / K_b = 0.5 based on the SDOF idealization. MDOF shear-bar models are used in dynamic analysis and viscous damping ratio h_0 is set 0.02 for each vibration periods of frame corresponding 1st and 2nd mode as a rayliegh damping. The average value of peak drift angle obtained from time history analysis under 4 artificial earthquake ground motions and design target, in case of 4 types of 4, 10, 20-story frame, θ= 1/200, 1/125 are shown in Figure 8. As you can see Figure 8, analysis results fairly meet the design target due to inserting a sufficient amount of damper. In addition, distributions of peak drift angle become uniform regardless of the deformation shape of each frame without damper. Table 3 summarizes the average accuracy of the peak drift angle for each frame type and building height. "Average" in Table 3 indicates the total average of the ratio of analysis to design target at every story for 12 cases: 3 target drift angles and 4 artificial earthquake ground motions. Compared between 4, 10 and 20-story models, the peak drift angle of the taller building tends to be underestimated.

Figure 9 shows comparison between prediction by Eq. (17a,b) (solid line) and analysis results (symbol) of story shear force and damper force for 4 earthquake motions, it can be seen that the prediction gives good estimation.

As a whole, the proposed design approach based on behavior of SDOF system with bilinear oil damper can control peak response of MDOF system with bilinear oil damper. It demonstrates that the simple rule to arrange the damper stiffness shown in Eq. (15) can produce the uniform distribution of peak story drift under earthquake excitation.

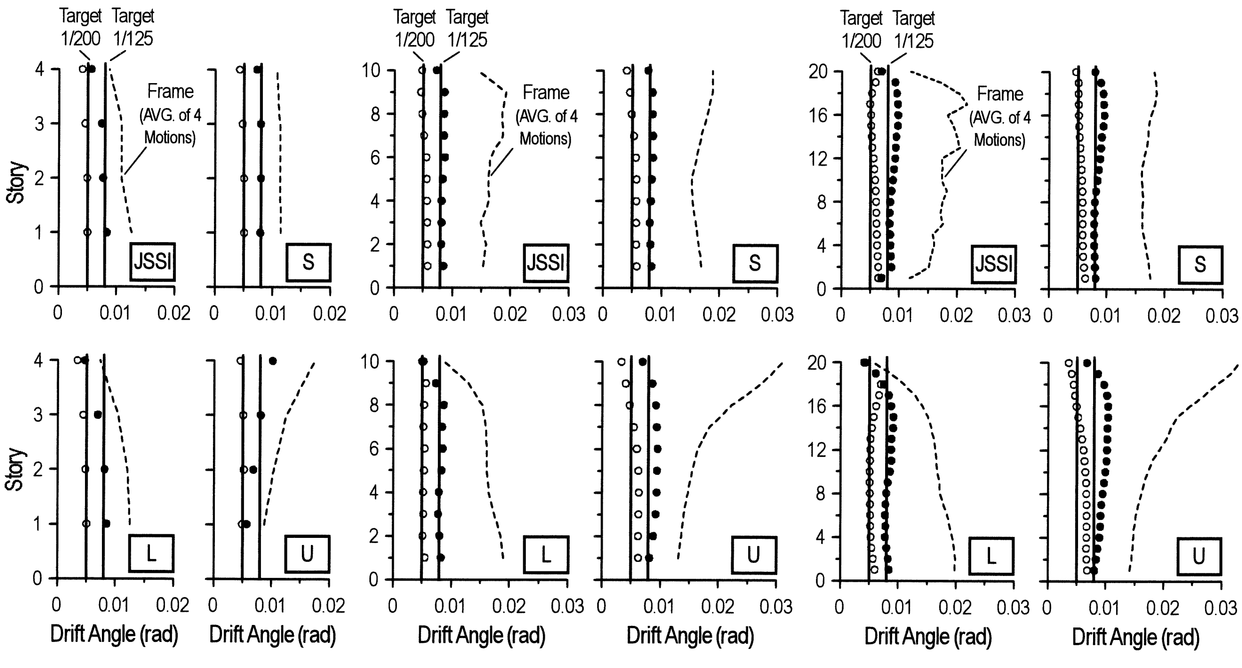

Figure 8. Comparison between Analysis Results (Symbol) and Design Targets (Solid Line) for Peak Story Drift Angle (average of 4 ground motions, θ= 1/200, 1/125rad)

Table 3. Average Accuracy of Peak Story Drift Angle

	4-Story				10-Story				20-Story			
	JSSI	S	L	U	JSSI	S	L	U	JSSI	S	L	U
AVG.	0.916	0.962	0.882	0.973	1.053	1.043	1.010	1.106	1.147	1.096	1.049	1.253
STD.	(0.119)	(0.081)	(0.170)	(0.166)	(0.104)	(0.113)	(0.131)	(0.180)	(0.157)	(0.149)	(0.131)	(0.170)

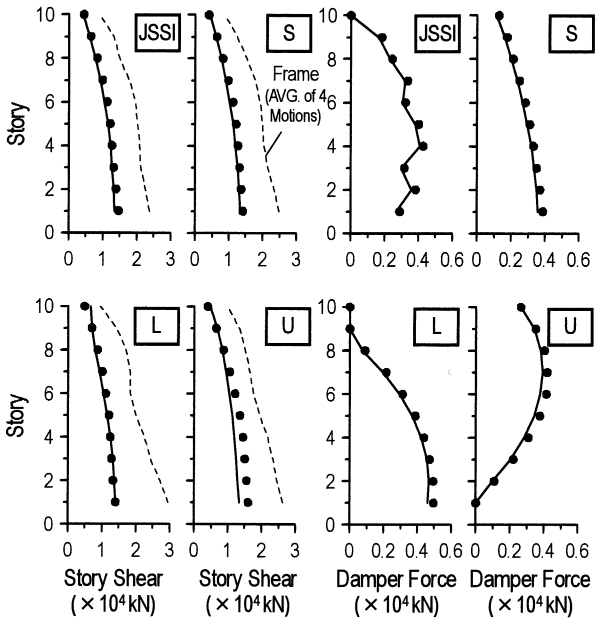

Figure 9. Comparison between Analysis Results (Symbol) and Prediction (Solid Line) on Story Shear Force and Damper Force (average of 4 ground motions, 10-story building, θ= 1/150 rad)

6. CONCLUSIONS

This research is aimed toward developing design approach for passive control system with bilinear oil damper in preliminary seismic design. The proposed method is based on the SDOF idealization of multi-story building structure, performance curve and a rule to convert a SDOF design to a multi-story design by tuning the equivalent stiffness of system.

The conclusions are as follows:

1. Arrangement of damper stiffness tuning the equivalent stiffness at each story for design shear force based on A_i lateral force distribution can give nearly uniform distribution of peak story drift, and prevent concentration of damage in particular story level.

2. Accuracy of proposed design approach is demonstrated via numerous time history analysis of a wide range of building height, frame stiffness distribution, design target drift angle, peak ductility demand and earthquake type using multiple-degrees-of-freedom (MDOF) models.

It is noteworthy that the findings given by this paper as well as the performance curves are adopted by the design specifications published by design manuals 1st and 2nd editions published by the Japan Society of Seismic Isolation (JSSI, (2005)).

References:

Building Center of Japan. (2004), "The Building Standard Low of Japan" (In English)

Hata, I., Ishimaru, S., and Hasegawa, J. (2007), "On Performance Based Design Method for System with Non-linear Viscous Damper and Elasto-plastic Damper," *Journal of Structural Engineering Architectural Institute of Japan*, Vol. 617, 47-54. (In Japanese)

Japan Society of Seismic Isolation (2005), "JSSI Manual for Design and Construction of Passively-Controlled Buildings 2nd Edition" (In Japanese)

Kasai, K., Ito, H., and Watanabe A. (2003), "Peak Response Prediction Rule for a SDOF Elasto-plastic System Based on Equivalent Linearization Technique," *Journal of Structural Engineering Architectural Institute of Japan*, Vol. 571, 53-62. (In Japanese)

Kasai, K., and Ito, H. (2005), "Passive Control Design Method Based on Tuning of Stiffness, Yield Strength, and Ductility of Elasto-Plastic Damper," *Journal of Structural Engineering Architectural Institute of Japan*, Vol. 595, 45-55. (In Japanese)

Kasai, K., Minato, N., and Kawanabe, Y. (2006), "Passive Control Design Method Based on Tuning of Equivalent Stiffness of Visco-Elastic Damper," *Journal of Structural Engineering Architectural Institute of Japan*, Vol. 610, 75-83. (In Japanese)

Kasai, K., and Nishimura, T. (2004), "Equivalent Linearization of Passive Control System with Oil Damper Bilinearly Depend on Velocity," *Journal of Structural Engineering Architectural Institute of Japan*, Vol. 583, 47-54. (In Japanese)

Kasai, K., Ogura, T. and Nishimura, T. (2007), "Equivalency between Linear and Bi-linear Viscous Elements Based on Passive Control Effectiveness," *Journal of Structural Engineering Architectural Institute of Japan*, Vol. 583, 47-54. (In Japanese)

Kasai, K., Ogura, T. and Suzuki, A. (2007), "Passive Control Design Method Based on Tuning of Equivalent Stiffness of Nonlinear Viscous Damper," *Journal of Structural Engineering Architectural Institute of Japan*, Vol. 618, 97-104. (In Japanese)

Niwa, N. (2001), "Research on Required Damping Force of Oil Damper Installed in Buildings," *Journal of Structural Engineering Architectural Institute of Japan*, Vol. 545, 43-50. (In Japanese)

Fifth International Conference on Urban Earthquake Engineering
March 4-5, 2008, Tokyo Institute of Technology, Tokyo, Japan

PERFORMANCE-BASED SEISMIC DESIGN FOR HIGH-RISE BUILDINGS IN METROPOLITAN CITY

Xilin Lu[1] and Huanjun Jiang[2]

1) Professor, State Key Laboratory for Disaster Reduction in Civil Engineering, Tongji University, Shanghai 200092, China
2) Associate Professor, State Key Laboratory for Disaster Reduction in Civil Engineering, Tongji University, Shanghai 200092, China
lxlst@mail.tongji.edu.cn, jhj73@mail.tongji.edu.cn

Abstract: Performance-based seismic design provides the means for designing structures with desired levels of seismic performance. This paper presents the methodologies of performance-based seismic design (PBSD) for high-rise buildings in metropolitan city. The PBSD approach involves selection of performance objectives, establishment of design criteria for structural components and systems consistent with desirable performance objectives, and validation of the design through structural analysis and evaluation of the response of all structural components and systems. An 18-story Shanghai Gateway Service Apartment Building retrofitted by energy-dissipation braces is introduced as an engineering example of high-rise buildings where the performance-based seismic analysis and design are followed. The example demonstrates that the performance-based design approach is an appropriate way to control efficiently the seismic damage on the structures.

1. INTRODUCTION

After a great deal of damage caused by earthquakes in the last two decades which was increasing rather than decreasing, there is general agreement in the world that the current seismic design process is necessary to be upgraded so as to be capable of designing a structural system with predictable seismic performance in the future earthquake. In several countries, seismic design is in the process of fundamental change, with the emphasis changing from "strength" to "performance" (Priestley 2000). The need to improve seismic performance of the structures through the development of performance-oriented procedures and guidelines has been repeatedly highlighted (Chandler and Lam 2001). Up to now, the philosophy of performance-based seismic design (PBSD) has been sufficiently developed. There have been different interpretations of what is meant by PBSD. To the authors' understanding, the appropriate definition is that it refers to the methodology in which seismic design criteria are expressed in terms of achieving a set of performance objectives. The most suitable approach to achieve the objectives of PBSD appears to be the displacement-based design method to which the most attentions have been paid by researchers so far. To some extent, performance-based design and displacement-based design can be used interchangeably.

The general methodology for PBSD can be classified into two types. In the first type of approaches, traditional forced-based analysis is conducted, and after the design is completed, the deformation and damage may be estimated and checked against pre-established limit (Arzoumanidis et al. 2005). It can be easily applied therefore appropriate in the current practice. The other type of approaches start by predetermined displacement or damage index consistent with the design performance level, proportion the structure, and then conduct the response analysis. In the latter type of approaches, the direct displacement-based seismic design is one of the most suitable procedures which can easily be incorporated into PBSD philosophy (Priestley and Kowalsky 2000). Although the direct displacement-based seismic design procedure appears promising, several areas require further investigation before it can be applied in practice. The Pacific Earthquake Engineering Research Center has embarked on a more robust methodology, the second generation of PBSD procedures for performance-based earthquake engineering (Moehle 2004). A consistent probabilistic framework underpins the methodology so that the inherent uncertainties in earthquake performance assessment can be presented.

Since 1980's, with the rapid growing of economy and the acceleration of urbanization, a large number of high-rise buildings have been constructed in metropolitan cities of China and other countries. Owing to the wide variety of social requirement for commercial or aesthetic purposes, the limited availability of land, and the preference for centralized services, the height of tall buildings has grown taller, and the configuration has become more complex in recent years. The uniqueness in these structures brings new challenges to engineers, since their structural behavior are difficult to predict and evaluate. The performance-based seismic design is a powerful new approach to control the seismic damage and economic loss efficiently. The performance-based seismic analysis and design of high-rise buildings consistent with the current Chinese national design code is presented in this study. It is an extension of the traditional strength-based seismic design with the detailed evaluation of seismic performance.

2. PERFORMANCE OBJECTIVES

The Structural Engineers Association of California has defined the coupling of expected performance levels with expected levels of seismic ground motions as seismic performance objectives (SEAOC 1996). The minimum seismic performance objective for ordinary buildings specified in the current Chinese national code for seismic design of buildings issued in 2002 is as follows:

(1) During a minor or frequent earthquake with the exceeding probability of 63.2% in 50 years corresponding to a mean return period of 50 years, the building should not be damaged, or should be only slightly damaged and continue to be serviceable without any repair (fully operational performance level).

(2) During a moderate or basic earthquake with the exceeding probability of 10% in 50 years corresponding to a mean return period of 475 years, the building may be damaged but should still be serviceable after ordinary repair (Repairable performance level).

(3) During a strong or rare earthquake with the exceeding probability of 2% in 50 years corresponding to a mean return period of 2475 years, the building should neither collapse nor suffer severe damage that would endanger human lives (life safety performance level).

For special buildings with higher importance class or higher performance levels required by the owners, the performance objective should be enhanced. The relationships between these performance levels and earthquake design levels are summarized in Figure 1.

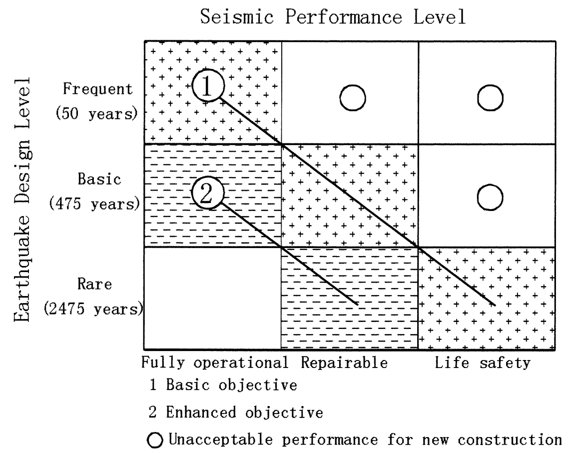

Figure 1 Seismic Performance Objectives for Buildings

3. DESIGN CRITERIA AND SEISMIC PERFORMANCE EVALUATION

3.1 Design Criteria

The design criteria are established corresponding to the desired performance objectives. These minimum acceptance criteria ascertain that the performance objective will be accomplished. The criteria are set in terms of limit values of configuration, distribution of stiffness and strength along the height of the structure, axial load ratio (specified for RC columns and shear walls), stresses, strains, inter-story drift, ratio between the maximum lateral displacement of the vertical structural members (maximum floor displacement) to the average floor displacement to control the torsional response, etc. The design philosophy of weak beam and strong column, weak flexural strength and strong shear strength, and weak member and strong joint, is commonly employed to adjust the strength and then the reinforcement. In addition, the constructional measures, such as minimum reinforcement ratio, minimum material strength grade, reinforcement detailing, etc., are required to reduce seismic structural damage.

The building configuration is generally defined as the size, shape and proportions of the three-dimensional form of the building. The extended definition of configuration also includes the nature, size and location of the structural members. The configuration establishing conceptual design is often determined by architectural design of the building, and is a subject of mutual agreement between architect and engineer. It plays an important role in determining the building's seismic performance. It has been well accepted that the configuration should be as regular as possible. In Chinese national design code, two types of irregularities, plan and vertical irregularities, are defined. The code approach reducing the detrimental effect of irregularity is to require more advanced methods of analysis and even carry out structural tests if necessary.

3.2 Seismic Performance Evaluation

(1) Numerical analysis

After the preliminary design phase is completed with the basic configuration of the structure selected, the seismic effects under the frequent earthquake and the effects of other actions are determined on the basis of linear-elastic behavior. The dimensions and reinforcement of structural members are selected by using the conventional strength-based design code. The general method for determining the seismic effects is the modal response spectrum analysis using elastic design spectra.

Verifying analysis ranging from simple frame procedures to an elaborate finite element analysis is performed in the next phase. The performance is checked under the frequent earthquake and the rare earthquake respectively. The performance under the basic earthquake is regarded as satisfactory if the requirements of constructional measures can be met and the performance under other two levels of design earthquake has been verified. The elastic analysis is conducted under the frequent earthquake while nonlinear analysis, including nonlinear static (pushover) analysis and time history (dynamic) analysis, is done under the rare earthquake. Nonlinear analysis should be properly substantiated with respect to the seismic input, the constitutive model used, the method of interpreting the results of the analysis and the requirements to be met. The earthquake responses, plastic mechanism, distribution of damage, etc., are estimated against the preset allowable limit.

(2) Structural tests

Physical testing is important to structural engineering because it helps establish fundamental understanding about the behavior and failure mechanism of structures. For high-rise buildings it generally involves both static tests on joints and members and dynamic tests on complete structural models for overall assessment since the scale in the structural model test is too small to reflect the local behavior precisely. For joint and member test the challenge is to produce the real stress field and boundary conditions.

Structural model testing is often used to help structural engineers directly acquire the knowledge about the prototype, especially in the case of complex tall buildings for which the numerical simulations are considered unreliable. Shaking table model test has been considered an economical, accurate, and practical way to evaluate the seismic performance of structures. To ensure that the model behaves in a similar manner as the prototype, the model designed should meet the requirements of dynamic similitude theory. By shaking table tests, the earthquake responses and dynamic characteristics are derived, the failure process, failure mechanism, and structural weak positions are discovered, and then the overall seismic performance of the prototype structure can be evaluated accordingly.

4. THE DESIGN PROCEDURE

The performance-based seismic design procedure consists of two design phases. In the first phase, the seismic performance objectives are selected and elastic analysis under the frequent earthquake is performed to determine the dimensions and reinforcement of structural members by using the conventional strength-based design code. In the second phase, the seismic performance of the target building is evaluated by numerical analysis. For the complex high-rise buildings, if necessary, structural testing including joint, member, and structural model test should be conducted to study the structural behavior and check the seismic performance directly. If the pre-defined seismic objectives can not be satisfied, design iteration should be done until satisfied. Figure 2 represents the flowchart of the overall design procedure.

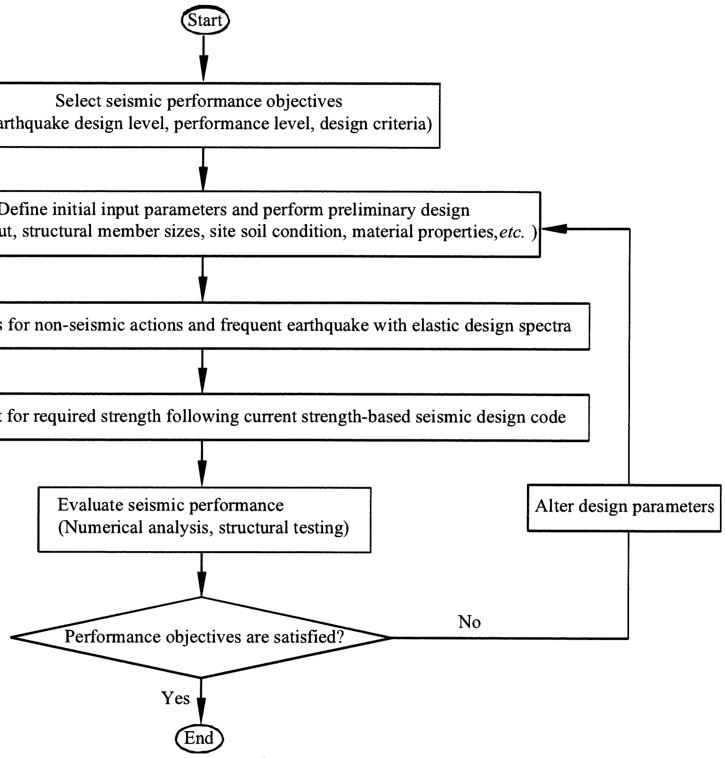

Figure 2 Flowchart of Performance-based Seismic Design Procedure

5. AN ENGINEERING EXAMPLE

5.1 Seismic Retrofit

Eight-story Shanghai Gateway Service Apartment Building (SGSAB) with the total height of 42.25m was completed in 1999 for commercial use. The main structure is RC frame with several RC shear walls. The plan as shown in

Figure 3 is roughly square, and the structure is regular.

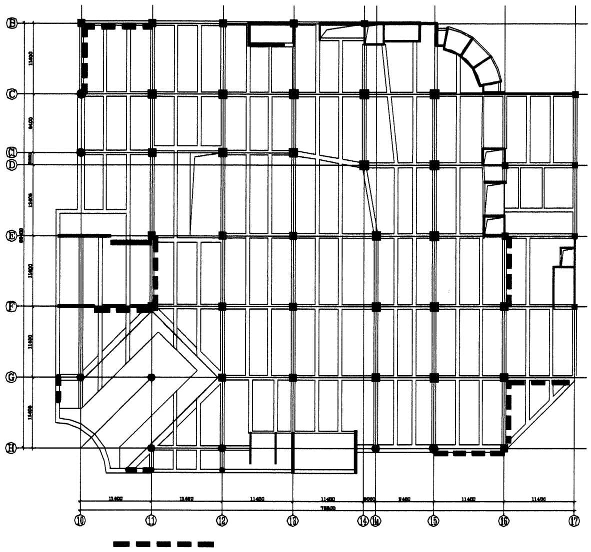

Figure 3 Structure and Energy-Dissipation Device Plan Layout of 2nd Floor

The continuation of this building is to add 10 stories on it, resulting in the total height of 77.85m beyond the maximum allowable height of 55m for RC frame structure specified in Chinese design code. The new upper part is L-shaped in plan and setback in elevation. In addition, there are several transfer girders in Floor 9. The structure after continuation is classified as both plan and vertical irregularity. The perspective view of this building after continuation is shown in Figure 4.

In order to meet the performance objective set for ordinary buildings, basic objective as shown in Figure 1, the seismic retrofit work is first undertaken to improve the seismic performance of the original structure. The main measures are taken as follows:

(1) The cross sections of some columns are enlarged to reduce the compressive axial load ratio and increase the strength as well. Carbon fiber sheet is also used to increase the strength of some beams and columns.

(2) Thirteen sets of steel braces are installed in appropriate positions distributed at the 1st, 2nd and 7th story to reduce the torsional responses caused by the eccentricity between the mass center and rigid center of the structure after continuation.

(3) Eighty-eight sets of combined energy-dissipation system consisting of oil damper and rubber bearing are installed in 1st to 7th story to dissipate seismic energy and therefore reduce earthquake responses.

Figure 4 Perspective View of SGSAB

The plan layout of the steel braces and energy-dissipation devices in 2nd floor is illustrated in Figure 3. The typical elevation view of the brace with energy-dissipation devices is shown in Figure 5. Due to the very limited space available for retrofit construction to keep the building still operational during construction, the amount and position of braces and energy-dissipation devices are not optimum but feasible.

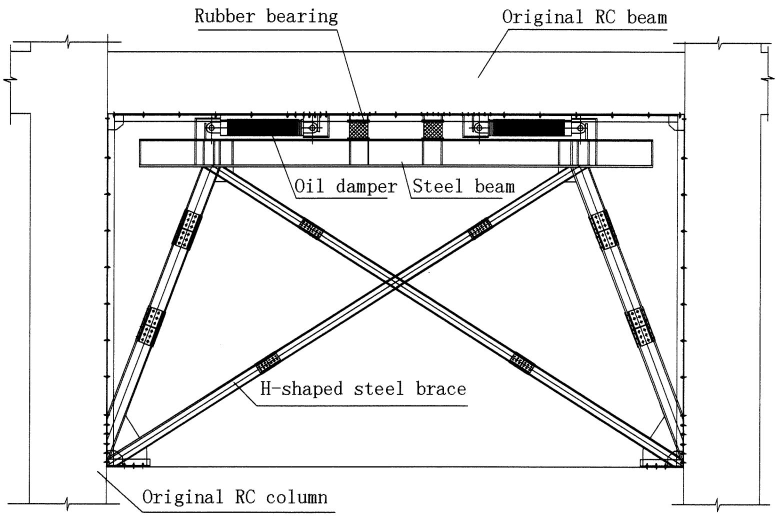

Figure 5 Elevation View of Brace with Energy-Dissipation Device

5.2 Numerical Analysis

The program SAP2000 is employed to establish the analytical model for the structure after retrofit and continuation as shown in Figure 6. The seismic performance under the frequent and rare earthquake of intensity 7 is checked through time history analysis. Four sets of earthquake ground motions, El Centro waves (1940), Taft waves (1952), and two Shanghai artificial waves (named SHW1 and SHW2) are used as input motions.

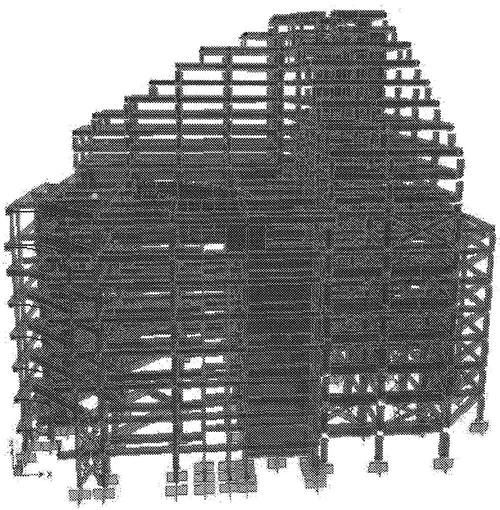

Figure 6 Analytical Model for SGSAB

The structural dynamic characteristics and earthquake responses are obtained as follows:

(1) The first two modes are translation, corresponding to the periods of 1.6440s and 1.3725s respectively. The third mode is torsion with the period of 1.0997s. The ratios of the first torsional period to the first two translational periods are 0.669 and 0.801 respectively, less than the maximum limit of 0.85 stipulated in the design code.

(2) The critical damping ratio is increased by 3.5% and 1.5% compared with that of the structure without steel braces and energy-dissipation devices during the frequent earthquake and rare earthquake respectively.

(3) Under the frequent earthquake, the maximum inter-story drifts in two horizontal directions are both 1/977, less than the maximum limit of 1/550. The maximum ratio of the maximum floor displacement to the average value is 1.30, less than the maximum limit 1.4. The structure behaves elastically.

(4) Under the rare earthquake, the maximum inter-story drifts in two horizontal directions are 1/133 and 1/148 respectively, less than the maximum limit of 1/80. Most of the plastic hinges occur at the ends of the beams. For the continuation part, most of the plastic hinges appear at the beams in the two flanges of L-shaped plan.

The numerical analysis results demonstrate that through seismic retrofit the seismic performance objectives can be realized for the building after continuation.

6. CONCLUSIONS

Performance-based seismic design has already achieved extensive acceptance as the goal of the next generation of seismic design codes. Performance-based seismic analysis and design of high-rise buildings consistent with the current Chinese national design code is presented in this study. It is an extension of the traditional strength-based design with upgrades by the check of definite performance objectives. At the current state of arts, it is more practical as well as feasible than the direct PBSD. The performance objectives, design criteria and design procedure are proposed. The practice of this method is shown by an engineering example of seismic retrofit of an existing building. Although the performance-based seismic design appears promising, further research and development remain to be done before it can be generally accepted and extensively applied in engineering practice. For example, much research is needed to associate different response limits with the damage states and performance levels, quantification of the relationship between building restoration time/costs and earthquake hazard level.

Acknowledgements:

The authors are grateful to the support from the following organizations: The Ministry of Science and Technology of China under grant No. 2007CB714202, The National Natural Science Foundation of China under grant No. 50621062 and No. 50708081, and Shanghai Grand Gateway Real Estate Development Corporation, Limited.

References:

Arzoumanidis, S., Shama, A., and Ostadan, F. (2005), "Performance-based Seismic Analysis and Design of Suspension Bridges," *Earthquake Engineering and Structural Dynamics*, **34**, 349-367.

Chandler, A.M. and Lam, N.T.K. (2001), "Performance-based Design in Earthquake Engineering: A Multi-disciplinary Review," *Engineering Structures*, **23**, 1525-1543.

Moehle, J.P. (2004), "A Framework for Performance-based Earthquake Engineering," *Proceedings of the 1st International Conference on Urban Earthquake Engineering*, Tokyo, Japan, 7-17.

Priestley, M.J.N. (2000), "Performance Based Seismic Design," *Proceedings of the 12th World Conference on Earthquake Engineering*, Paper No. 2831.

Priestley, M.J.N. and Kowalsky, M.J. (2000), "Direct Displacement-based Seismic Design of Concrete Buildings," *Bulletin of the New Zealand Society for Earthquake Engineering*, **33**(4), 421-444.

SEAOC, Structural Engineers Association of California (1996), "Vision 2000: Performance Based Seismic Engineering of Buildings," Sacramento, CA.

Fifth International Conference on Urban Earthquake Engineering
March 4-5, 2008, Tokyo Institute of Technology, Tokyo, Japan

TRENDS IN THE STRUCTURAL DESIGN OF HIGH-RISE STEEL BUILDINGS IN JAPAN

Toru Kobori

Managing Director and Representative, Structural Engineering Department, Nikken Sekkei Ltd., Tokyo, Japan
kobori@nikken.co.jp

Abstract: This paper describes the structural design philosophy and concept for a precise and rational structural planning which does not depend on simulations of complex structural configuration that tends to rely on "black box" of computer technology.

1. INTRODUCTION

An unprecedented building boom is underway in Dubai in the UAE, one of the oil-producing nations of the Middle East. Many buildings with unusual, impressive shapes are being constructed in rapid succession. One of the reasons seems to be to achieve a distinctive building that attracts attention, as a means of increasing property value. Similar examples are being seen in China, and this trend is also gradually emerging in Japan. Many architects share a fascination with buildings that are freeform in shape, rather than rectangular. In an age when the development of computer technology makes it seem as if anything is possible, the philosophy of structural designers is more important than ever before.

2. HISTORY OF HIGH-RISE STEEL BUILDINGS IN JAPAN

Tokyo Tower, with a height of 333 meters, was built exactly 50 years ago. However, Japan's first actual building with a height exceeding 100 meters was the Kasumigaseki Building. This 36-story, 147-meter-tall building was completed in 1968. These accomplishments in Japan came more than 50 years after a series of challenges including Chicago's Home Insurance Building, completed in 1885; the Eiffel Tower, completed in 1889; and the skyscrapers which began appearing in Chicago and New York in the 1930s.

The Japanese economy ballooned during a period of rapid growth that began in the latter half of the 1950s, and there was an increasing demand for higher buildings. The World Conference on Earthquake Engineering was held in 1954 and 1960, and research on a 24-story virtual high-rise building was performed over a three-year period beginning in 1959. The study of dynamic analysis began in the 1960s as the environment became more conducive, including the maturation of construction technologies such as the fabrication of heavy-section thick steel plate. Many high-rise buildings including the Hotel New Otani (72 meters) were constructed after a 31-meter height restriction had been abolished in 1964 under the "special block" system.

The Hotel New Otani has a distinctive shape with three wings, but most early high-rise buildings were

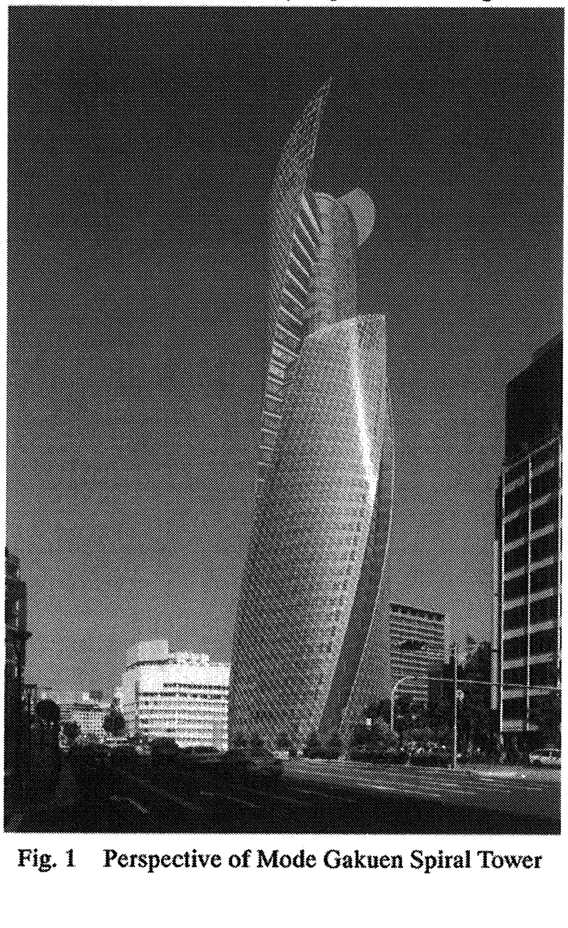

Fig. 1 Perspective of Mode Gakuen Spiral Tower

built on a rectangular plan with two bisecting axes to provide a structurally stable frame, as in the Kasumigaseki Building. Architects stuck to these straightforward configurations to avoid the kinds of problems that could result from asymmetry, such as twisting during earthquakes. This was a judicious policy for the structural planning of early skyscrapers.

Later, in the 1970s, Keio Plaza Hotel featured towers with slender proportions; Shinjuku Sumitomo Building was built with a three-layered tubular structure inside a hexagonal layout; and the height of 240 meters was attained in Sunshine 60 in 1978. In 1982, the Shinjuku NS Building was completed with a large open atrium at its center, and the NEC Super Tower applied to a skyscraper the concept of a superframe formed by large-assembly construction, placing the columns in a consolidated arrangement to achieve much greater plan flexibility around the base of the building. In recent years, the use of megaframe construction has been a trend in skyscrapers.

Since the 1995 Great Hanshin (Kobe) Earthquake, the concept of damping and seismic isolation structures has begun to be applied to skyscrapers in order to minimize the damage that a major earthquake would cause to the basic frame, including the columns and beams that support a building's weight; and to improve safety, maintenance of building functions, and asset preservation in case of an earthquake. Structural planning has more frequently shown a clear orientation toward separation of seismic energy absorption mechanisms, with performance design and damage control as key themes. In other words, the aim is to reduce the amount of energy borne by general columns and beams at the time of an earthquake, through the active utilization of members which absorb seismic energy.

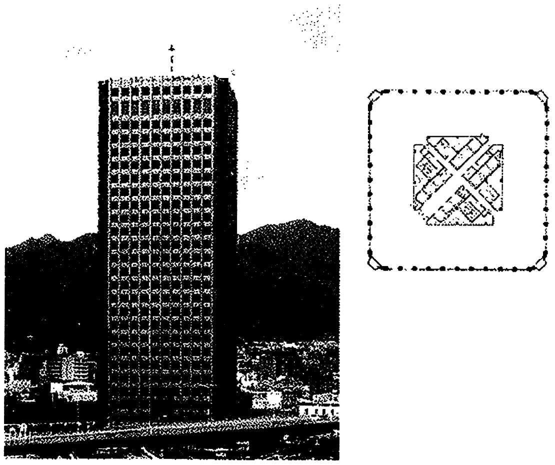

Fig. 2 Kobe Commerce, Industry and Trade Center

3. FLEXIBLE CONFIGURATION AND STRUCTURAL PLANNING

As a design trend in this context, architects have been designing more and more freeform shapes. Mode Gakuen Spiral Towers, under construction near Nagoya Station, is named with the plural "Towers" because its design includes three towers intertwined in a spiral form, suggesting the intertwined rising energy of the students of Mode Gakuen's three schools: its fashion school (MODE), computer and animation school (HAL), and medical school (ISEN). For this concept to get beyond merely playing with shapes, its configuration needs to be coordinated by engineers in a planned manner. In the case of a highly difficult structural design for a building having an organic spiral shape, instead of relying on the capabilities of advanced computers to perform the analyses needed to apply a structural frame to that shape, the structural design must be created on the basis of clear intention in order to create a rational, strong, yet delicate expression.

This building has 36 floors above ground, 3 basement levels, and 2 penthouse levels. Its height is 170 meters above ground and 21 meters underground. A central core having an oval cross-sectional shape consists of three wings having fan-shaped cross sections, radially arranged next to each other. The planar configuration changes with height. Three classrooms are arranged in the respective wings around the central core, which includes stairwells and elevator shafts. Ascending higher in the building in a spiral pattern, the rooms gradually become smaller in size. Displacement of the centers of rotation of the three wings produces an external appearance of organic curves.

The interior frame is coordinated with the vertical elements such as stairwells, elevators, and equipment shafts in the center of the building; 12 straight columns are arranged around this core, and braces are connected to these columns in a mesh network, forming the thick central trunk of the tubular structure (called an "inner truss tube"). This tubular structure is highly strong and rigid with regard to horizontal and twisting forces exerted on the building by earthquakes and high winds, providing the necessary structural performance. With no braces around the outside, a transparent appearance is achieved; and minimal, thin-diameter columns provide lower rigidity for a light frame that does not bear seismic forces.

Horizontal forces continually act on the diagonal columns around the outside because of their twisted configuration. To deal with these horizontal forces, flat beams are arranged in a truss pattern to increase rigidity and transmit the horizontal forces generated around the outside to the inner truss tube. At the connection of the columns and beams with the braces at the inner truss tube on the ground floor, an earthquake would produce a high level of stress in addition to the constant twisting forces. Therefore, cast blocks are used at the six brace connections of the inner truss tube to easily transmit the forces of the columns, beams, and braces. The outer frame, which provides a distinctive shape, serves strictly to support the weight of the building, while the tube resists twisting and seismic forces with a central brace structure.

In a tower-shaped building, there is a great deal of bending deformation in the building as a whole and a high level of axial expansion and contraction on the outer columns, resulting in greater deformation at the top of the building. To efficiently attenuate earthquake energy, the building employs two new control systems that make use of this configuration. Quantitative analysis has confirmed that deformation during an earthquake can be reduced by up to 20% compared to the case of not adding any damping system.

The outer columns, which undergo a high level of axial expansion and contraction, are left out every four to seven stories in order to consolidate axial deformation; and viscous dampers are instead placed in those locations, providing a high attenuation effect. These control columns are arranged in 26 locations of the building overall. Since simulations indicate that the control columns would expand and contract by 40 mm at the ground floor and about 20 mm on other floors during a major earthquake, the exterior finish used near the control columns is able to follow interlaminar deformation in both the horizontal and vertical directions. Since the viscous dampers normally do not bear weight, braces are installed at the upper floors equipped with control columns, with a cantilever truss structure from the inner truss tube for ordinary weight support.

Considering the large extent of deformation at the top of the building, a weight corresponding to 1% of the building's weight is placed on the rooftop and

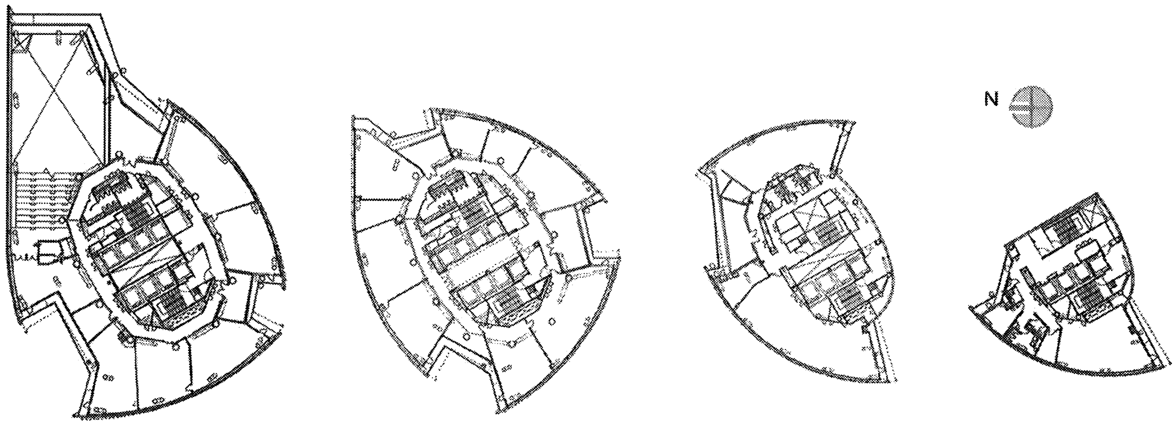

Fig. 3 Floor plans of Mode Gakuen Spiral Tower

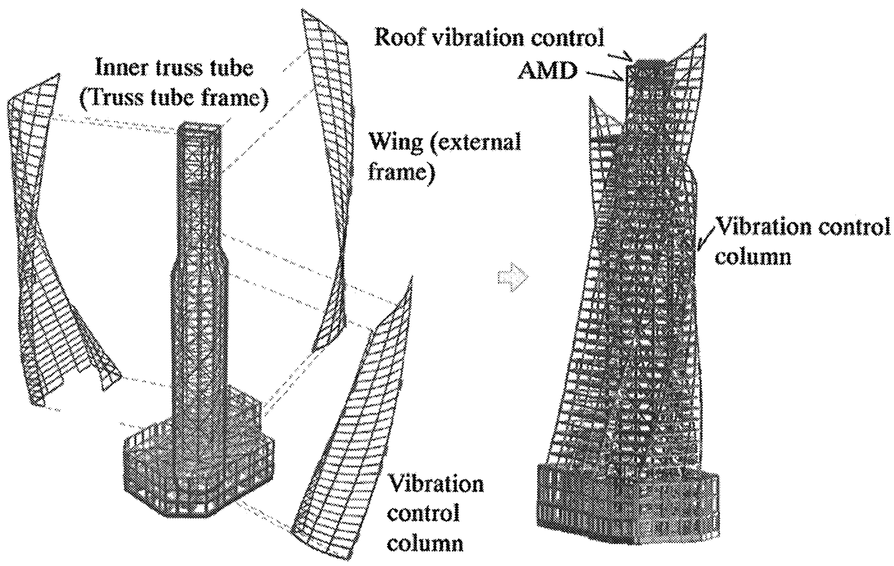

Fig. 4 Conceptual system of framing

coordinated to the frequency of the building by means of roller bearings and a laminated rubber isolator. In the case of a major earthquake, the relative displacement of the added mass with regard to the building would be a large movement of 500 mm in the reverse direction. In this way, the lead damper efficiently absorbs seismic energy.

The laminated rubber isolator does not bear the weight of the added mass, but functions only as a stability spring. Its two-layered structure serves to adjust the horizontal rigidity and double its movable deformation. This system uses a lead damper, which can absorb a great deal of energy; and a roller bearing mechanism which can resist up-and-down forces of 1 G in movement of the added mass (without becoming detached and falling off).

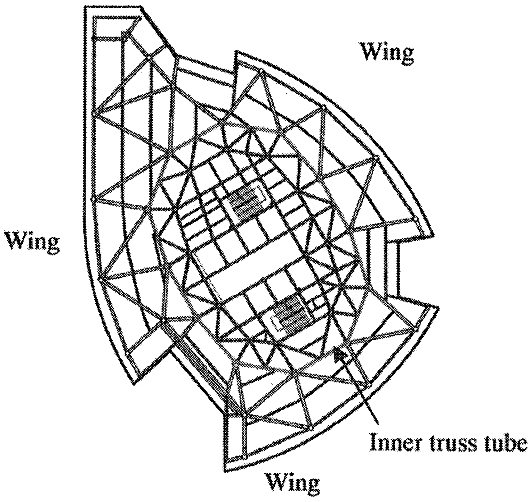

Fig. 5 10th floor beam framing plan
Horizontal forces on outer framing are transmitted to inner truss tube through steel truss beams

The safety margin of each member is set according to its importance. In order to enable the building to tenaciously resist even stronger earthquakes than the anticipated levels, a large safety margin of strength is assigned to the foundation and inner truss tube, which are the most important members. To provide good earthquake performance even in stronger earthquakes than anticipated, the design ensures that practically no elasticity would be lost even in an earthquake measuring 1.4 times the level of earthquake ground motion that can be anticipated to occur only very rarely; and the inner truss tube is designed with a margin of rigidity and strength to withstand 1.8 times that level.

4. CONCLUSION

In the simulation of complex structural configurations, there is a tendency to rely on the "black box" of computer technology; but when structural systems are made more easily understandable, the flow of forces can be grasped in a sensory manner. In the Spiral Towers, which have a freeform external appearance, we have incorporated concepts that are as clear-cut and straightforward as possible. We prefer to think of computer analysis as merely a tool to confirm the validity of these concepts.

I am confident that the Spiral Towers, as an embodiment of clear-cut and rational structural planning in a freeform skyscraper, will lead the way to a new flow of structural design.

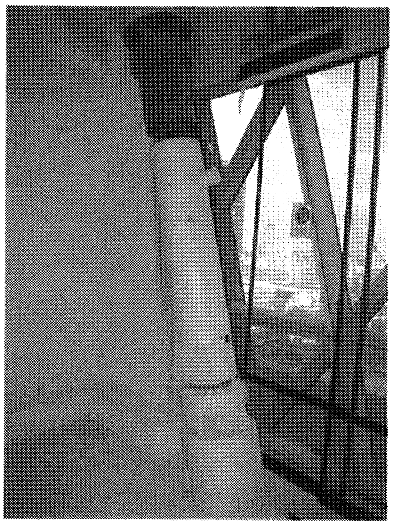

Fig. 6 Vibration control column
(using a damping system with amplifying mechanism)

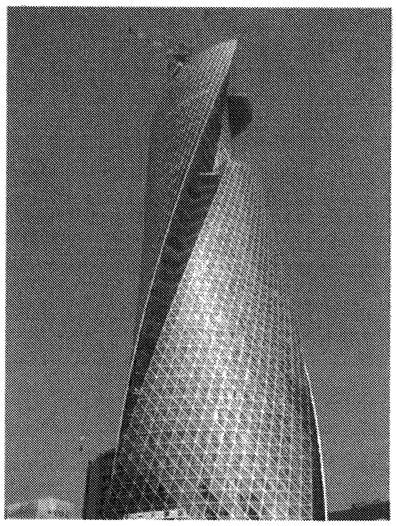

Fig.7 Construction work in progress
(erection completed)

Fifth International Conference on Urban Earthquake Engineering
March 4-5, 2008, Tokyo Institute of Technology, Tokyo, Japan

RETROFIT DESIGN OF OFFICE BUILDING USING SEISMIC RESISTANT FACADE

Yoshiharu Kanebako[3], Kiwako Kamo[2], Masashi Sogabe[2], Masayoshi Takeuchi[2], and Manuel Tardits [2]

1) Structural Engineer, Kanebako Structural Engineers, Tokyo, Japan
2) Architect, Mikan, Yokohama, Japan
kanebako@kanebako-se.co.jp, info@mikan.co.jp

Abstract: This paper reports our practice of an idea called "Seismic Resistant Façade", which integrates earthquake strengthening and façade design in retrofitting an office building in an urban area. The existent building was composed of columns with small ductility and shear walls, and eccentricity of the building was large due to uneven wall distribution. Seismic resistance capacity was improved by retrofit work.

1. INTRODUCTION

Building Retrofitting Promotion Act obliges an owner of the building to ensure the required earthquake resistance of a building where public gathers. Frequent earthquakes accompanied by enormous damages in recent years draw building owners' attention to earthquake resistance of the building. They start to recognize the difference in the earthquake resistance as difference in property, not only as a part of ensuring safety. From these situations, demands for seismic retrofit and reconstruction of the buildings in an urban area are expected to emerge. The goal of seismic retrofit is achieved if earthquake resistance is ensured. Additionally, reconstruction provides freshness with the building and enhances a quality of space at the same time. From this perspective, reconstruction seems to have more advantages. However, reconstructing a number of buildings leads to enormous loss of resources, being of a problem from a standpoint of sustainability. Also in the eyes of global environmental problems , it is necessary to consider extending the life span of buildings. Even for a case that reconstruction for a functional or structural problem could have been planned; retrofitting and utilizing the existing building will be required. To obtain advantages equal to the reconstruction, the retrofit that has better design enhancing the space quality or creating a new façade, besides increasing the earthquake resistance, is desired. The seismic retrofit is required as various practical exercises and structural design of the seismic retrofit should be acknowledged.

Photo 1 Outer View of the Retrofitted Building

This paper reports our practice of an idea called "Seismic Resistant Façade", which integrates earthquake strengthening and façade design in retrofitting an office building in an urban area. One of the features of the practice is that the building was retrofitted under the condition that almost half of the areas were used by tenants although the retrofit construction was executed while some of the tenants were relocated.

2. OUTLINE OF THE EXISYENT BUILDING AND RETFOFIT DESIGN

2.1 Outline of the Building

The target building was an office building located in front of Kanda station and completed in 1965(Photo 2,Figure 1). The building had the SRC structure, rising 9 stories above the ground and 2 underground stories. The northern and western sides of the building faced roads and had PC curtain walls while the southern side and the eastern side faced the next building and the back street respectively with RC exterior wall. The building had the SRC structure with grid-type reinforcing steel using two angle bars as a flange embedded in the columns and lattice-type reinforcing steel using two pairs of angle bars as a flange embedded in the beams in the same way. This structure contained small

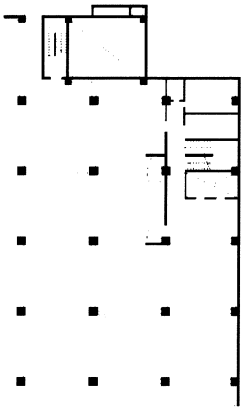

Photo 2 The existent Building Figure 1 Plan of The Existent Building

Table 1 Outline of The Building

Name of building	Ueno Building
Designers	MIKAN Kanebako Structural Engineers Kankyo Engineering inc.
Location	Kaji-machi, Chiyoda-ku, Tokyo
Scale	9 stories above the ground 2 underground stories
Total floor area	8001.94 m^2
Structure	SRC structure, RC structure

ductility. The existent building had a seismic weak point in that the bearing walls are placed eccentrically in both of the directions. According to the result of the seismic diagnosis shows, seismic index of structure (Is value) derived from Secondary Diagnosis was 0.28 to 0.41 in the X-direction (narrow side) and 0.33 to 0.77 in the Y-direction. Shear columns and flexural columns mingled, and most of the flexural columns had small ductility index. Considering the earthquake resistance of the building as a whole, the building was composed of columns with small ductility and shear walls, and eccentricity of the building was large due to uneven wall distribution.

From this aspect, adding some seismic factors to the two sides facing on the roads in the retrofit design was expected to improve exponentially the earthquake resistance of the building. Our main subject was to integrate the earthquake strengthening and façade design, and renovewte the appearance of the building by removing the existing PC curtain walls and creating a new façade with the earthquake resistance. This façade is called “Seismic Resistant Façade”.

2.2 Seismic Resistant Façade

The following requirements must be considered in designing the Seismic Façade.

- -Freshness of the design
- -Dynamic efficiency
- -Steel processability and Field workability
- -Cost

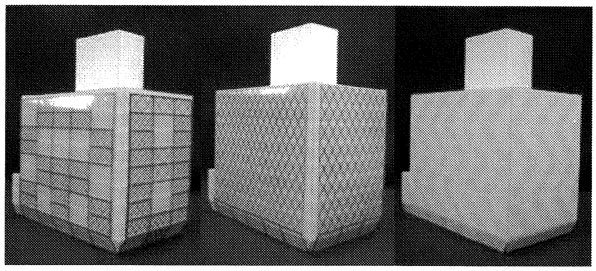

(1) (2) (3)

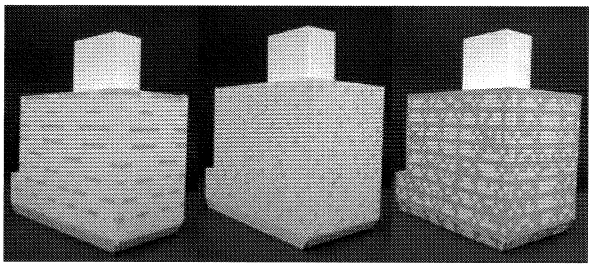

(4) (5) (6)

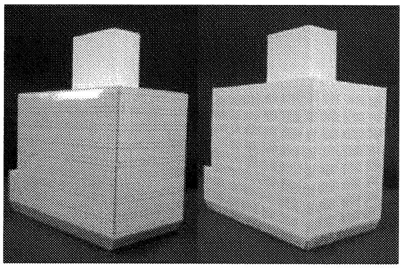

(7) (8)

Photo 3 Frame Patterns of Seismic Façade

These requirements are partially inconsistent with one another and it is necessary to evaluate the design paying attention to maintaining balance. Photo 3 shows concrete seismic façades discussed by our design team. These facades are roughly classified into three types: schemes of using braces (1 to 4), using panels (5, 6), and using frames (7, 8). Keywords of the design are “construction of delicate materials”, “aggregation of structure” and “atypical configuration”. Although breaking the repetitive patterns enhances the freshness of the design, it decreases dynamic and economic efficiency. As the result of our discussion, the scheme of “dogleg braces”, which has an impressive design despite the simple structure, were adopted. This brace is a kind of brace reinforcement in terms of dynamics. This scheme is excellent in economic efficiency and workability, providing a sense of streaming motion by its design.

2.3 Outline of Retrofit Design

Our policy of the building retrofit was to perform maximum earthquake strengthening under the three conditions: the retrofit should not affect the space of the office room, the retrofit should be done to the extent people can stay in the building, and the retrofit should not require the foundation reinforcement of the existing building. The target Is value was determined to be 0.65 or higher based on the preliminary examination, because we and the client

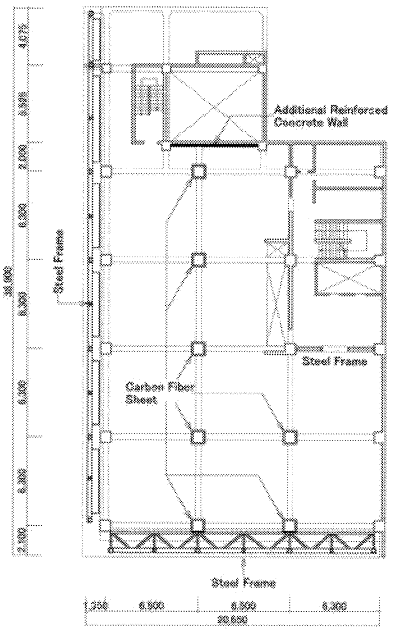

Figure 2 Structural Plan

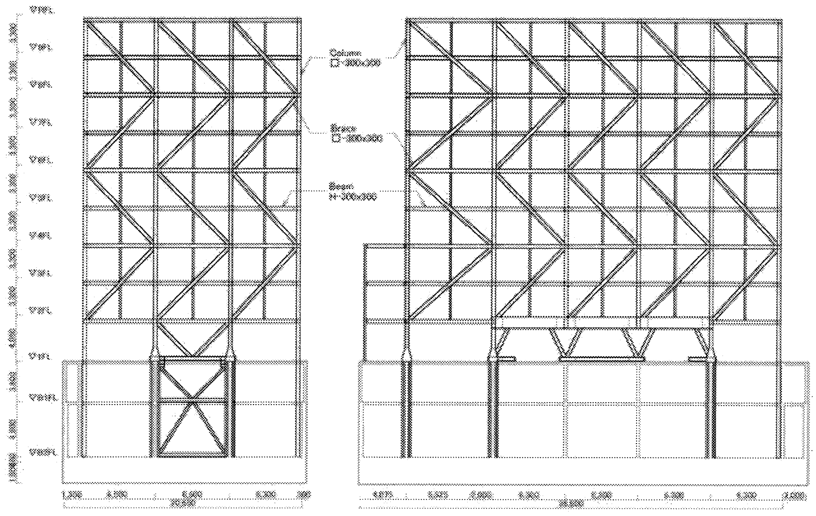

Figure 3 Framing Elevation

agreed with adding about 10 % of bias due to the evaluation method to the standard value 0.6.

The following four earthquake strengthening items including the Seismic Resistant Façade described above were implemented. The strengthening method and pertinent parts are shown in the figure 2 and 3.

1) Newly set up the steel frame with the brace to the exterior walls of the western and northern sides. Lower the steel column down to the underground and integrate it with the existing underground RC building frame so that the brace strength can be maximized.
2) Reinforce the RC seismic wall of the existing building to enhance the strength as well as increase ductility
3) Wind carbon fiber sheets around the existing independent column for reinforcement to increase ductility of the column
4) Set up a reinforcing steel frame to the boarder area between the interior elevator hall and a tenant room.

3. DESIGN OF STEEL FRAMES

3.1 Above-ground Steel

The columns of the two road-facing aspects were located at the inside of the building rather than at the external wall, and the cantilevered slab was placed. The slab head was removed by 40 cm and the steel frame composed of the column, beam, and brace was set there. The shape of the material of the column and the brace were 300 mm × 300 mm box-section, and a H-shaped steel with the depth of 300 mm (H-300 ×300, H-300×150) was used for the beam and intermediate post. The beam was used with the orientation to making the flange face vertical, and the two sides of the column, the brace and the flange face of the beam were set on the same flat in order to clarify the force transmission as

Photo 4 Steel Frame and horizontal truss

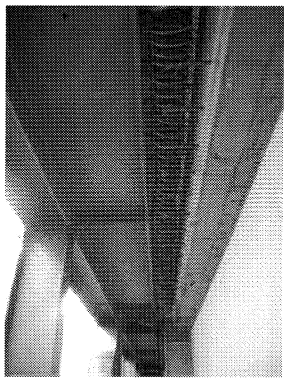

Photo 5 Steel Frame and anchor detail

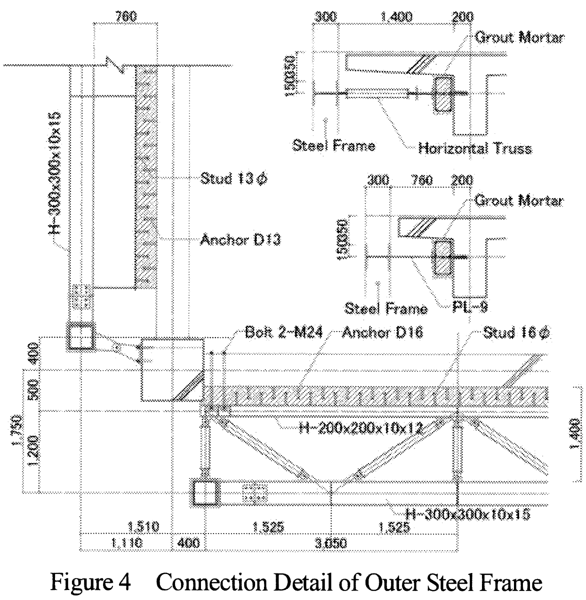

Figure 4 Connection Detail of Outer Steel Frame

well as to make the appearance simple. The "dogleg" pattern set on the 2nd story and above could not be formed on the 1st story as the entrance and exit needed to be ensured. A type of an eccentric brace was used for the longitudinal face and the section of the girder on the 2nd story was enlarged. On the crosswise face, a V-shaped brace with a large section was set in the center with an image of successive "dogleg" braces.

It is essential to transmit the force on the steel frame and existing building frame. Thus, enough attention was paid to the connection method. Because the clearance between the steel frame and the RC girder was 0.7 to 1.4 m, a connecting steel material with stud bolts was added between the steel beam and the existing girder, and the steel beam and the main girder anchor were integrated by grout mortars. A horizontal truss was set to the western side of the building since the clearance between the exterior surface of the existing girder and the interior surface of the steel frame was 1.4m. The clearance of the northern side was 0.76 m and a full-web horizontal beam was set. These horizontal members transmit the shear force from the main body of the building to the steel frame. However, the distance between the existing girder and the steel frame generates the eccentric moment. This moment becomes push-pull force into the orthogonal direction of the building exterior wall at the both ends of the steel frame. Thus, pull-resistant bolts were attached to the frame ends.

3.2 Underground Steel

When the brace is attached within the framework of the existing frame, axial force due to overturning moment rests on the existing frame. However, this steel frame is independent and requires a foundation structure to transmit the overturning moment to the ground. The underground parts of the building extended across the boarder of the site from the exterior of the columns. Utilizing this situation, the steels were extended to the interior of the underground external wall and integrated with the underground columns and walls. By adding the stud bolts to the steel columns and the anchors to the existing RC column in the 2nd basement, and integrating these columns, the compressing force was applied to the existing foundation and the tension force was resisted by using the weight of the building frame. Because the steel column contacted the RC beam on the 1st story, the column size was enlarged at the plinth on the 1st story and the column was changed to two channel steel in the underground across the existing RC girder on the 1st story. The steel column at the end was moved to the inside of the existing column grid. The box column was extended to the underground. In order to transmit the shear force resting on the steel frame to the 1st story floor of the existing building frame, the steel beam stud set directly above the 1st story floor and the anchor set on the floor slab were integrated by grout mortars. Furthermore, the steel braces were added in the 1st and 2nd basement fore reinforcement because of the insufficient shear force only with the existing RC underground exterior wall in the crosswise direction. Figure 5 shows detail of steel frames.

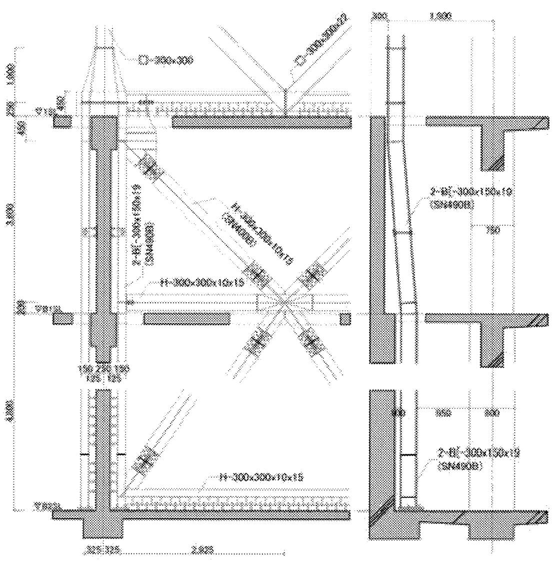

Figure 5 Detail of Underground Steel Frame

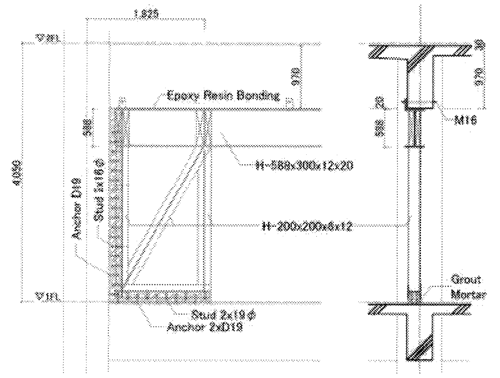

Figure 6 Detail of Steel Brace Reinforcement

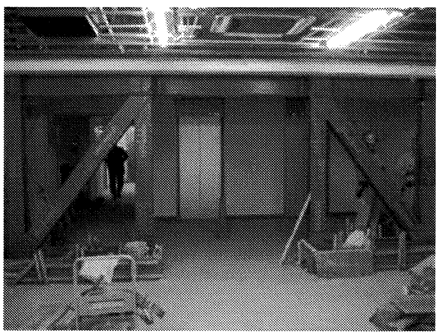
Photo 6 Steel Brace Reinforcement

4. INTERIOR STEEL-FRAME REINFORCEMENT

The building is a rectangular plan form. Therefore, strength in the longitudinal direction is sufficient with the circumferential steel reinforcement, but it is relatively small in the crosswise direction. To supplement the strength and decrease the burden of the horizontal force transmission of the floor slab, the steel frame reinforcement was performed in the crosswise direction of the interior building. The steel brace reinforcement was set up in the existing beam-to-column frame of the boarder wall between the elevator hall and the tenants on the 1st to 6th stories, as well as in the existing frame of the entrance hall on the 1st story. The eccentric brace was used to provide an opening in the center. To minimize the mounting dimension, an epoxy bonding method was applied to the upper part. Figure 6 and Photo 6 show the steel brace reinforcement.

Although the steel brace holds the shear force with this reinforcement method, the axial force in the orthogonal direction due to the overturning moment rests on the existing column. Therefore, the horizontal force that the frame can hold is also determined by the axial bearing force of the existing column. The examination of the steel frame strength was incorporated in modeling the whole building. The Ai distribution earthquake load was set and the relation between the shear force and column axial force of each layer was computed. The frame strength was determined in consideration of both the sear force (brace axial force) and the RC column axial bearing force.

5. EFFECT OF REINFORCEMENT

Figure 7 shows the change of the Is index before and after the reinforcement. 0.65 or higher Is index is ensured in all the stories after the reinforcement. E_0 index was increased because the strength was improved by the structure reinforcement of the circumference frame, interior steel frame, and the existing wall and the ductility of the column was improved by winding the carbon fiber sheets around the column. The eccentricity ratio was improved by reinforcing the northern and western aspects with the steel frames. The SD index of the X-direction was 0.90 to 1.20 after the reinforcement while it was 0.80 before. The SD index of the Y-direction was improved to 0.87 to 1.20 while 0.80 before.

By changing the façade from the PC curtain wall to the glass, sunlight shines into the office room. Accordingly, the goal of improving the interior space is achieved. The two-row reinforcing frame shown as photo 7 was added to the entrance of the 1st story to ensure the strength. The entrance was renewed as a unique space by highlighting the reinforcing brace as a part of design. In this façade, the braces are recognized through the glass with the background of the blind during the daytime, while they are impressively expressed with blue LED lights during the nighttime, giving a new impression to the surrounding streets (photo 8).

6. CONCLUSION

The method used in the project was an applied technology that has been conventionally used, and an individual solution. This study succeeds in pointing out the possibility to scheme not only improvement of earthquake resistance but also enhancement of the interior space and acquisition of the façade design. The scope of seismic retrofit design is proven to be wide. This method shall be familiarized in the seismic retrofit of the urban area in the future.

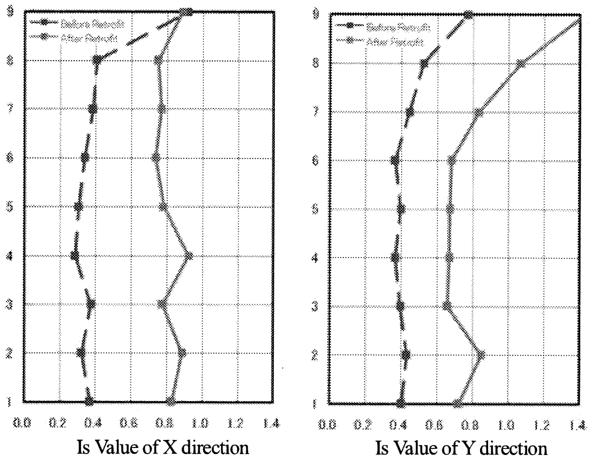

Figure 7 Seismic Index


Photo 7 Steel Brace Reinforcement in the Entrance Hall

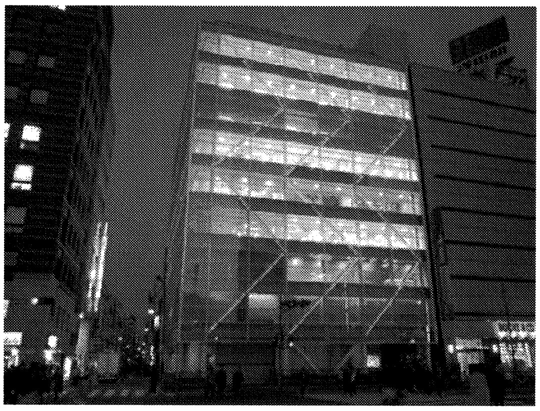
Photo 8 Outer View During Night

Acknowledgements:
We would like to appreciate all the persons concerned, especially Ueno & Co. Inc., the client of this project, Takafumi Wada from Kankyo Engineering Inc., who was in charge of facility design, and Fujita Corporation in charge of construction.

Fifth International Conference on Urban Earthquake Engineering
March 4-5, 2008, Tokyo Institute of Technology, Tokyo, Japan

SOME NEW DEVELOPMENTS IN EARTHQUAKE AND HEALTH MONITORING OF BUILDINGS

Robert L. Nigbor[1]

1) Research Engineer, Civil Engineering Department, University of California, Los Angeles
nigbor@ucla.edu

Abstract: As part of the U.S. Advanced National Seismic Network (ANSS), several buildings have now been instrumented with advanced systems that allow both earthquake recording and real-time, continuous, high-resolution data collection for health monitoring. One such building is the Factor Building on the UCLA Campus. This brief paper describes the instrumentation and some developments in the processing of both earthquake and continuous ambient data from this building. Methods include classical global modal analysis and a novel local identification method that takes advantage of the complete sensor array. Use of elevators as a repeatable quasi-deterministic excitation is also described.

1. INTRODUCTION

Seismic instrumentation has advanced rapidly in the past decade, following advances in the more general fields of instrumentation and communications. It is now possible to have sensors and data acquisition units that have sufficient range to cover both low-level ambient or microtremor vibrations as well as high-level earthquake shaking. It is also possible to have both on-site recording of event or continuous data and remote monitoring, recording, and analysis of continuous data in real-time.

However, there is a lack of robust analysis methodologies for application to these data. An ultimate goal for such monitoring systems is to provide practical information products to the building owner and occupants, both immediately after an earthquake and also for long-term assessment of building condition. Research is needed to develop these methodologies.

Within the U.S. Advanced National Seismic System (www.anss.org), a few buildings are being densely instrumented with modern, high-resolution data acquisition systems to act as testbeds for the development of new analysis methodologies. One such building is the Factor Building on the campus of the University of California at Los Angeles (UCLA). This brief paper describes the instrumentation of the Factor Building and presents some of the ongoing research into the use of the earthquake and ambient data from this building.

2. MONITORING OF THE FACTOR BUILDING

2.1 ANSS Background

The ANSS concept was developed over a decade ago by the US Geological Survey (USGS) and the U.S. seismological and earthquake engineering communities. ANSS has become an international focal point for earthquake monitoring, with products such as ShakeMap (see www.anss.org) openly providing new levels of earthquake information.

While ground motion monitoring is the most visible product of ANSS, structural response monitoring is also an important part of the ANSS mission. To date, 12 structures, a mix of buildings and bridges, have been monitored through the ANSS structural response monitoring program. Guidelines for monitoring of engineered civil systems are provided in ANSS (2005).

2.2 Factor Building Instrumentation

The experiments discussed in this paper take place in the UCLA Doris and Louis Factor Building ("Factor Building"), a 15-story steel-frame structure with two underground levels. It is the tallest building on the UCLA campus. Figure 1 shows a photograph of the building, and Figure 2 shows its dimensions.

In 2002-2003, the U.S. Geological Survey, in partnership with the UCLA Center for Embedded Networked Sensing (CENS), deployed a 24-accelerometer in Factor Building. In 2004 the system was upgraded to 72 accelerometers with sensors on every floor, making it one of the most heavily instrumented buildings in North America. The design of the sensor array is simple: There are four accelerometer channels per floor - two horizontal NS and two horizontal EW components. In 2006 ANSS upgraded all of the accelerometers to Kinemetrics ES-T, with bandwidth 0-200 Hz, 4g clip level, and sub micro-g resolution. Data acquisition is done using Quanterra 4128 digitizers, with 24-bit resolution and GPS-synchronized timing to provide <10 microseconds of time synchronization. The array operates continually, generating data that are continuously recorded in real-time both on a local disk array and remotely at the IRIS Data Center (www.iris.edu). Initially, data were recorded at 500 samples per second per channel for almost one year; data are now recorded at 100 samples per second.

Data from Factor are openly available to researchers through IRIS; the array name is "FAC". This is indeed an excellent resource for earthquake and structural monitoring research, and is a testbed for data analysis methodologies.

Figure 1. Factor Building

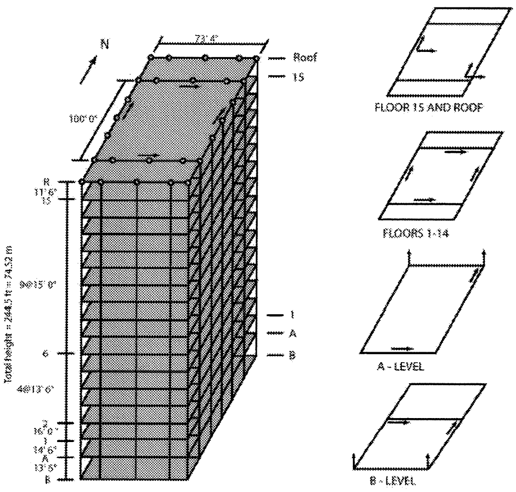

Figure 2. Diagram of Factor building showing dimensions and sensor locations

3. ANALYSES OF FACTOR BUILDING DATA

3.1 Earthquake Data

The Factor Building array has been in operation for about 8 years. However, Southern California has been in a relatively quiet period for earthquakes in the past decade. While dozens of small earthquakes have been recorded by the system (Kohler et al., 2005), maximum peak accelerations to date are small, less than 0.1g.

Kohler et al. has analyzed the building's motions and modal properties during many earthquakes from the first two years of operation. Dominant frequencies and corresponding motion shapes are presented, with animated shapes available at http://factor.gps.caltech.edu. The fundamental horizontal mode frequencies are about 0.5Hz, and the fundamental torsional mode is at 0.7Hz. Significant variation in the mode frequencies was observed for different earthquakes; this variability continues to be investigated.

Skolnik et al.(2006) looked at data from the 2004 M6 Parkfield Earthquake, 260km from the Factor building with peak response acceleration of 0.003g – small but above ambient vibrations. Applying advanced system identification methods, they determined the fundamental mode frequencies to be 0.47Hz EW, 0.51Hz NS, and 0.68Hz torsion. They used the system identification results to validate a SAP2000 finite element model of the building, which was in turn used to estimate response of the building to the 1994 Northridge Earthquake.

3.2 Ambient Data

The continuously-recorded high-resolution data provide an excellent database for ambient vibration analyses. Several researchers have taken advantage of this resource to investigate different methodologies for obtaining dynamic properties of the Factor Building.

Kohler et al. (2005) analyzed selected subsets of ambient vibration data from the Factor Building using simple frequency domain methods. They find the fundamental horizontal frequencies to be 0.55-0.6Hz, slightly higher than those from earthquake recordings. Some post-earthquake "healing" was observed during one of the stronger recorded earthquakes.

Skolnik et al.(2006) applied advanced system identification techniques to selected subsets of ambient data in addition to the Parkfield Earthquake data. They found similar results to Kohler et al., with ambient modal frequencies from 5-15% higher than Parkfield Earthquake frequencies.

Nayeri et al. (2008) have looked very closely at 50 days of continuous ambient vibration data from the Factor Building. Using several advanced system identification methods, including both global methods and a novel local method, they tracked the modal properties of Factor in 1-hour intervals. This allowed a very thorough statistical study of the variability of identified frequencies, damping rations, and mode shapes. They found basic variabilities in the modal frequencies to have coefficients of variation from

1-3%, but damping ratio estimates had coefficients of variation from 20-70%. They also found a strong temperature-correlated variability of as much as 6% in the higher mode frequencies. This temperature variation lagged the air temperature by as much as 12 hours. Only with continuous data recording could such thorough analyses be accomplished.

3.3 Elevator Vibrations

The Factor Building's dense, real-time monitoring allows study of details of structural vibration that have not been previously observable. One can, with such continuous high-resolution data, attempt to parse the ambient vibrations into their various source components. The hope is to find statistically separable components of ambient vibrations in buildings for use in Structural Health Monitoring (SHM), the repeated monitoring of building response characteristics that can possibly be used to detect degradation or other changes in the structure.

In its most direct implementation, SHM involves excitation with a (known) repeatable source of vibration. In inhabited buildings like Factor (which houses auditoriums, classrooms, laboratories, and offices) this kind of experimentation is not feasible, and SHM researchers look to ambient vibrations. Unfortunately, the many sources of ambient vibrations are inherently variable: the movements of people in the building, the operation of lab equipment, and even the traffic patterns outside the building. Explicit knowledge of the inputs to the structural system, robust identification of dynamic properties is difficult.

In recent and continuing work by the author and colleagues (Nigbor et al. 2008), elevator motion are examined as a potentially repeatable source of vibrations to support SHM efforts. In tall buildings like Factor, elevators move at sufficient speeds to generate observable vibration patterns. The elevator counterweight is a primary source of horizontal forces to the structure.

There are two primary sources of vibration associated with an elevator counterweight: First, the wheels that guide the counterweight can develop flat spots, producing vibrations at high speeds; and second, the track itself can have irregularities that introduce vibrations at specific locations along the shaft. From an SHM perspective, this excitation source is repeatable (and in fact repeats many times over the course of a day on its own) although it's precise spectral characteristics are not known and may change slowly over time.

A series of experiments were conducted to help characterize the building's response to elevator activity. These included a series of forced vibration studies, a more detailed analysis of the building's response to elevator movement, and finally measurements taken on the counterweight itself to help describe the excitation is provided.

Initial experiments with timed elevator runs showed very promising results. At quiet times in the building (middle of night, no wind), as much as 74% of the measured ambient vibration rms acceleration (about 50% of the signal power) could be attributed to a single elevator traveling up and down the building, as shown in Table 1 below.

Table1. Elevator contribution to total RMS acceleration for the four accelerometers on floor 4

Frequency Range	Direction			
	North	South	East	West
Broadband 0-80Hz	22.60%	8.30%	6.40%	14.40%
Low Frequency 0-5Hz	30.30%	21.00%	38.20%	27.00%
High Frequency 37-43Hz	58.20%	29.20%	21.50%	74.10%

A small (400N) electromagnetic shaker was temporarily installed on the floor near the elevators and run at known time intervals. Data from the Factor array were obtained for those same intervals. Even with the small shaker force the shaker signal was clearly observed in the ambient vibration data as shown in Figure 3. This important result showed that forces on the order of those expected from the 2-ton counterweight are observable in the ambient vibration data.

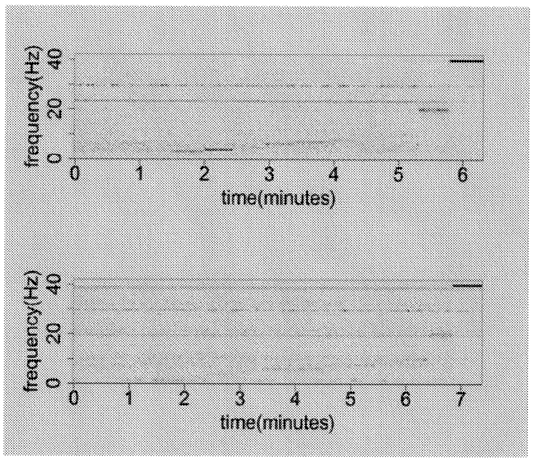

Figure 3. Spectrogram of shaker experiment on 4th floor (top) and 8th floor (bottom)

A new instrumentation system was then temporarily installed on the elevator counterweight. This consisting of a triaxial accelerometer, a 24-bit data logger with 200 Hz sampling rate and a battery attached to the counterweight of the west elevator in the building. A series of single-elevator tests was conducted late at night and a combined data set of elevator vibrations and building responses was assembled.

Data from the counterweight system and the Factor instrumentation were time-aligned so that subsets of known elevator motion could be parsed. Vertical acceleration of the counterweight was double-integrated to provide elevator position – this proved surprisingly accurate. So, vibration data could be compared directly to elevator position.

Figures 4 and 5 show data from six different elevator trips (ground floor to top floor and back). Figure 4 is the elevator counterweight acceleration and Figure 5 is the building response at the 4th floor in the NS direction. The horizontal axis is height in meters.

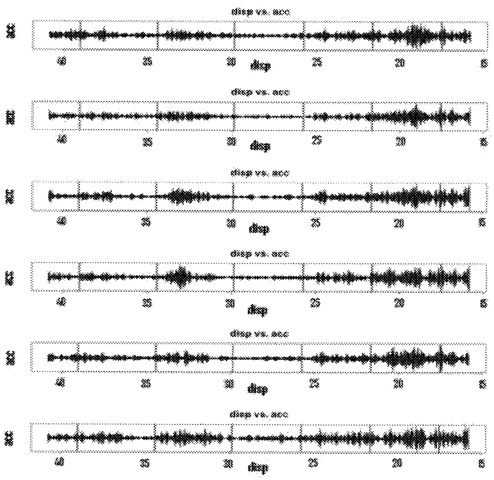

Figure 4. Acceleration of the counterweight as a function of position of the counterweight along the elevator shaft.

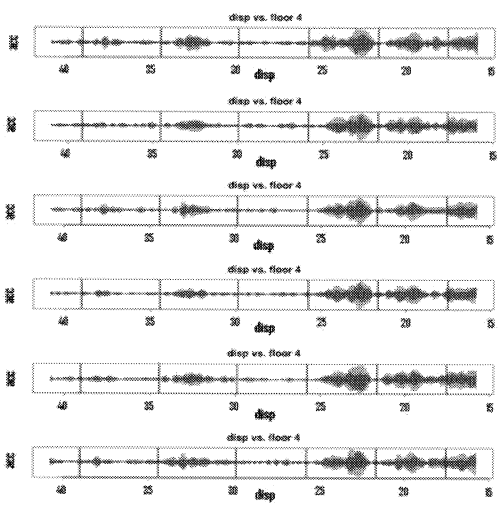

Figure 5. Acceleration of the 4th floor (NS) as a function of displacement of the counterweight along the elevator shaft.

Of note is the consistent, repeatable character of the counterweight and building vibrations. This provides evidence that the quasi-deterministic elevator motions can be separated from the remaining random ambient vibrations through time domain or frequency domain averaging.

Of course, one will need to know the forcing function (counterweight force) if the elevator-induced vibration is to be used in input-output analyses. The author and his colleagues continue to refine this method. At present, studies are underway to better characterize the elevator's effect on building vibrations. Additional instrumentation is being developed that will track the location of the elevators in the building and provide automatic tagging of long sweeps through the building. In parallel, statistical modeling is being developed to characterize propagation of this vibration source as it moves through the building.

4. DISCUSSION

Data from the Factor Building's dense array, operated through the U.S. Advanced National Seismic System (ANSS), are openly available to the research community. This includes both earthquake event data and continuous data. To date, several researchers have taken advantage of these data in their much-needed studies of analysis methodologies for building response.

The current state-of-the-art seismic instrumentation for buildings, as now used in ANSS, can provide a wealth of information not only for post-earthquake analysis of building response for research and code development (the traditional purpose of seismic instrumentation) but can also provide a wealth of data for use in structural health monitoring. As shown in the Factor Building example, it is possible to continuously record high-resolution, dense array data in a building and to provide these data to the research community. Such data can even be provided in real-time for alerting and post-earthquake assessment purposes.

The various analyses of Factor building data mentioned herein are examples of what can now be done with such data. What is needed are robust methodologies for the analysis and evaluation of such monitoring data, with the purpose of producing products useful to building owners and occupants.

Acknowledgements:

The author acknowledges support and assistance from the Center for Embedded Networked Systems (CENS), the George E. Brown Jr. Network for Earthquake Engineering Simulation (NEES), and ANSS. The contributions of Salih Tileylioglu, Mark Hansen, Joon-Ho Baek, Derek Skolnik, and Monica Kohler are also gratefully acknowledged.

References:

ANSS, (2005), "Guideline for ANSS Seismic Monitoring of Engineered Civil Systems Version 1.0", USGS Open-file Report 2005-1039.

Kohler, M., Davis, P., Safak, E. (2005), "Earthquake and Ambient Vibration Monitoring of the Steel-frame UCLA Factor Building", *Earthquake Spectra* 21 715–36

Nayeri, R., Masri, S., Ghanem, R., Nigbor, R.(2008) "A Novel Approach for the Structural Identification and Monitoring of a Full-Scale 17-story Building Based on Ambient Vibration measurements", Smart Materials & Structures 17.

Nigbor, R., Hansen, M., Tileylioglu, S., Baek, J-H, (2007), "Elevators as a Repeatable Source for SHM in Buildings", *Proc. 6th Intl Workshop on Structural Health Monitoring*, Palo Alto, CA, USA, Sept. 2007.

Skolnik, D., Lei, Y., Yu, E. and Wallace, J. (2006), "Identification, Model Updating, and Response Prediction of an Instrumented 15-story Steel-frame Building", *Earthquake Spectra* 22 781–802.

Fifth International Conference on Urban Earthquake Engineering
March 4-5, 2008, Tokyo Institute of Technology, Tokyo, Japan

MODELLING OF PLAN IRREGULAR BUILDING SUBJECTED TO DESIGN RESPONSE SPECTRA FOR IPOH (MALAYSIA)

Taksiah A. Majid[1)], Shaharudin Shah Zaini[2)], Mohd Rashwan Arshad[3)] and Salmia Beddu[4)]

1) Associate Professor, School of Civil Engineering, Universiti Sains Malaysia, Penang
2) Lecturer, School of Civil Engineering, Universiti Sains Malaysia, Penang
3, 4) Postgraduate Student, School of Civil Engineering, Universiti Sains Malaysia, Penang
taksiah@eng.usm.my, shaharudin@eng.usm.my, rashwan_arshad@yahoo.com

Abstract: Normally in Malaysia, lateral force that is taken into consideration in design is wind load. Tremors that felt by Malaysians from the Sumatran Earthquake on the 26th December 2004 was a "wake up call" for engineers, architects and local authorities to accept the importance of understanding potential seismic hazard that can occur to buildings and other structures. The effect on irregular building behavior may be even severe when subjected to lateral forces because it is easily to rotate and twist. Such buildings are prone to earthquake damage due coupled lateral and torsional movements producing non-uniform displacement demand in building elements and concentrations of stresses as well as forces on structural members. This study focuses on the behavior of a 'T-shape' plan irregular building with various heights and different lift core positions when subjected to lateral force due to wind and earthquake. Seismic load in the form of response spectrum is applied for the purpose of this study. The design response spectrum was developed for Ipoh site on a very dense soil and soft rock (soil class C). The result confirm that asymmetrical positioning of different lift core have significant effect on the building response especially to the column bending moment.

1. INTRODUCTION

Structural irregularities are commonly found in constructions and structures. Architectural demands are usually the cause of such irregularities. Most of the buildings have some degree of irregularities in the geometric configuration, distribution of mass, stiffness and strength. These buildings display asymmetry to some extent, due to either unsymmetrical arrangement of vertical members such as columns, cores, shear walls, unsymmetrical elevation (set-backs) or unsymmetrical load distribution on floors. Shaharudin et al., (2007) reported that 1132 of 2696 buildings surveyed in Penang (Malaysia) having plan irregularities. Most plan irregularities can affect all building types. Plan irregularities causing torsion are especially prevalent among corner buildings, in which the two adjacent street sides of the building are largely windowed and open whereas the other two sides are generally solid. Wedge shape buildings, triangular in plan, on corners of streets, not meeting at 90 are similarly susceptible.

Structural asymmetry can be a major reason for the building's poor performance under severe lateral loads. Yoon and Smith (1995) stated that asymmetry contributes significantly to the potential for translational-torsional coupling in the dynamic behavior of structure which can lead to increase in lateral deflection and member forces as well as the possibility of member failure and ultimately initiating collapse.

Lateral loads due to wind or earthquake are the major factors to be considered in design, especially for high-rise buildings. According to Smith and Coull (1991), for building up to 10 stories and of typical proportions, the design is rarely infected by wind loads. Great Sumatran-Andaman earthquake disaster occurred on 26 December 2004, becomes an important issue in Malaysia especially on the effect of the existing RC structure due to earthquake. Identification of the weakest elements of the existing reinforced concrete structure were necessary for further actions to be taken, in order to reduce the number of structural and non-structural damages, casualties, loss of live and others.

A number of research works have been carried out on the behavior of building with symmetric and asymmetric wall frame structure. However, less research works have been carried out on the behavior of wall frame in high-rise, medium-rise and low-rise buildings together with different lift core arrangement in resisting the lateral loads. Thambiratnam (1996) had performed the study on response of tall buildings to earthquake. He has developed a simple computer based three dimensional model for analyzing the earthquake response for some tall buildings. Two buildings are considered in this study, the first one is 10 storey symmetric rectangular building, where asymmetry is brought about by placing the core in an eccentric position.

The second example is a 15 storey "L" shaped building and is therefore unsymmetrical in plan to begin with. The positioning of the lift core brings about a further degree of asymmetry. Both static and dynamic analyses give results that the responses are greatly influenced by the degree of the asymmetry in the building. From the study, the deflection, moment, shear and the column twisting due to lift core position are obtained.

Wilkinson and Thambiratnam (1993) have studied mode coupling in the vibration response of asymmetric buildings using simple three-dimensional computer models. The purpose of this study is to predict the torsional coupling due earthquake response to the building. The study included three types of plan arrangement, which are 10 storey square building, 10 storey rectangular building and 15 storey L-shape building. In these buildings, the position of the core is varied to obtain different degrees of asymmetry and the consequent coupling of the modes of vibration. It can be seen that period of vibration increase slightly with the increase in eccentricity. The building response is obtained by using response spectrum. Bugeja et al., (1997) have studied the effects of stiffness and strength due to eccentricities on inelastic earthquake response of asymmetric structures. The objective of the study is to asses the influence of stiffness and strength due to eccentricities on the inelastic earthquake response of asymmetric structures. The numerical study presented in the paper was conducted using a model consists of single-storey structure with perfectly rigid floor diaphragm, supported by moment-resisting frames.

2. MODELLING AND ANALYSIS

The analysis in this study has been carried out using STAADPro 2006 computer software under linear elastic condition. This analysis has been carried out using buildings of three different heights, i.e 25, 15 and 5 storeys, with five different lift core positions.

Figure 1 and Figure 2 show the elevation and floor plan for the building, respectively. The building plan was modified from Thambiratnam (1996) study where the original L-shape building has been converted to T-shape building.

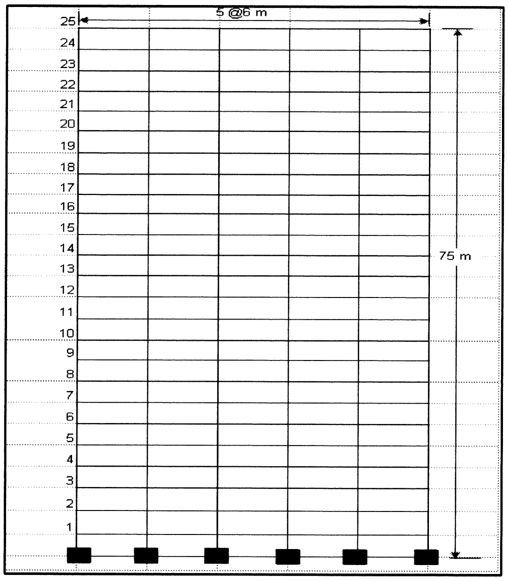

Figure 1: Elevation of 25-storey Building (unit in Meters)

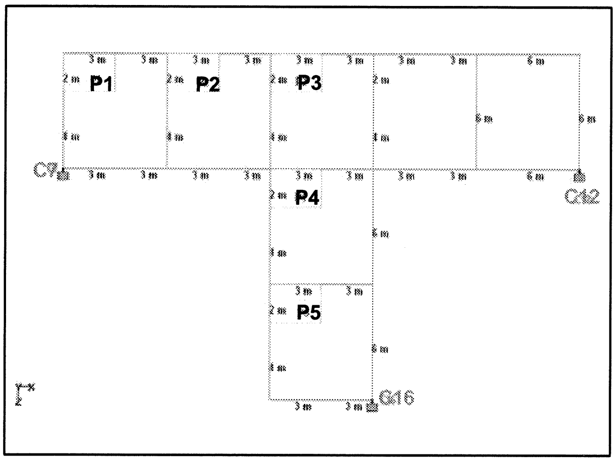

Figure 2 Building plan with lift core position (P1, P2, P3, P4 and P5)

In this study, 3-dimensianal T-shape building with various heights subjected to lateral loads are investigated and compared in terms of column deflection, moment and shear. Wind load is determined using MS 1553 and seismic load determined using response spectra taken from Rashwan et al., (2007).The typical dimensions of the structural members are shown in Table 1.

Table 1: Dimension for beams, slabs and lift core.

Member/Element	Size (mm)
Beams	500 x 200
Slabs	175 (thickness)
Lift Core	200 (thickness)

3. LOAD DETERMINATION

The load specified in this study is suitable for use either with strength design or with allowable stress design criteria. The load consists of dead load; G_k, live load; Q_k and wind load; W_k. Three load combinations have been considered. The load combination used in this study is based on Uniform Building Code (UBC) 1997. Ultimate Load Combinations for concrete structure are as follows:

i. $U = 1.4DL + 1.7WL$ (1)

ii. $U = 0.75\ (1.4DL + 1.7LL + 1.7WL)$ (2)

iii. $U = 0.9DL + 1.0EQ$ (3)

3.1 Gravity Load

i. Dead Load
ii. Live load

3.2 Wind Load (MS 1553: 2002)

i. Site Wind Speed, V_{sit}

$$V_{sit}=V_s \times M_d \times M_{z,cat} \times M_h \times M_s \quad (4)$$

ii. Design Wind Speed, V_{des}

$$V_{des}=V_{sit} \times I \quad (5)$$

iii. Design Wind Pressure, P

$$P=(0.5\rho_{air})\ (V_{des})^2\ C_{fig}\ C_{dyn} \quad (6)$$

iv. Wind Actions

$$F=\sum p_z A_z \quad (7)$$

v. Minimum Design Wind Load
The minimum design wind pressure is taken as 0.65 kN/m^2 as specified.

3.3 Seismic Design

During the earthquake, the ground surface moves in all directions. The movements parallel to the ground surface generally cause the most damaging effects on stationary structures, because structures are ordinarily designed to support vertical gravity loads (Ambrose and Vergun, *1995*). Seismic load in the form of response spectrum is applied in this analysis for the purpose of this study.

In this study, the building is assumed to be located on a very dense soil and soft rock (soil class C). The design response spectrum is shown in Figure 3.

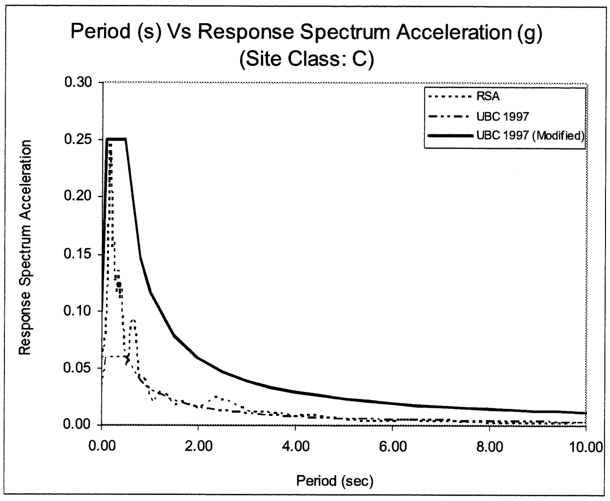

Figure 3 Design spectra acceleration for soil class C (Rashwan et al., 2007)

4. RESULTS

In this study the important parameters to be determined are deflection, moment, shear, torsion, of the column and time period of the building with different lift core position and different height of building. Three columns C12, C16 and C7 were selected for this purpose.

4.1 Deflection of Column

The result shows that the deflection in X and Z direction for column C12 and C16 of 5, 15 and 25 stories building model start to decrease as the lift core moves to near the centroid or the center of stiffness of building which is at P3 and P4. The deflection decrease approximately 100% for column C12 of 5 storey building 21% and 17% for 15 storey and 25 storey respectively. Column C16 also shows the same trend as C12 but the percentage decrease is smaller. The deflection of column C7 increase when the core moves to the centroid at P3 and P4. The deflection increase approximately 68%, 31% and 14% for 5, 15 and 25 storey respectively. The increase is due to the fact that column C7 is nearest to the core position P1. As the lift core position move, column becomes further away from the core resulting in the increase of deflection.

The maximum deflection in X and Z direction are also significantly affected by the height of the building. For example at lift core position P1, deflection at column C12 in X direction is 10.339 mm, 23.65 mm and 9.314 for 5, 15 and 25 storey building respectively. Deflection in Z direction for column C12 is 44.071 mm, 127.995 mm and 210.135 mm for 5, 15 and 25 storey building respectively. Deflection in X direction is found to increase as the height changes from 5 to 15 storeys. However, the increase in X direction is smaller for 25 storey building compared to 15 storey building. Deflection in Z direction drastically increases from 5 to 25 storey building. Table 2 shows the result of the maximum deflection for 5, 15 and 25 stories building models with different lift core position for selected columns.

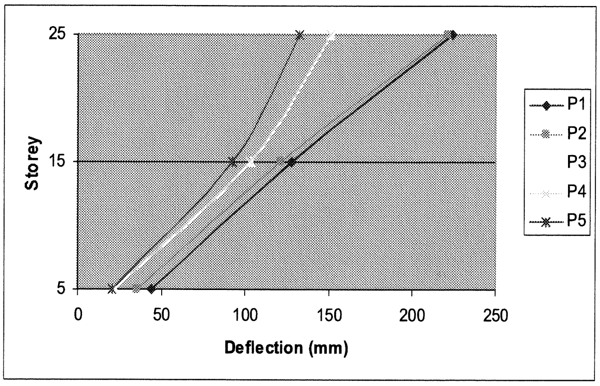

Figure 4 Deflection of column C12 with different building heights.

4.2 Bending Moment of Column

The result shows that the minimum bending moment, M_y occurs when the lift core is located at P3 and P4 which is close to the centroid hence the center of stiffness of the building. Bending moment, M_y at column C12 increase up to 81%, 54% and 27% for the case of 5, 15 and 25 storey building, respectively. The result shows that the bending moment of column decreases as the core moves nearer to the centroid. It can be seen that significant variations in bending moment when the lift core position is varied. The result is shown in Figure 5.

Bending moment is also significantly affected by the height of the building. For instance, maximum bending moment, M_y in column C12 with core position P1 is 54.873 kNm, 413.614 kNm and 1831.019 kNm for the case of 5, 15 and 25 storey respectively. The difference in terms of bending moment, M_y is higher with the increase in height. Figure 5 shows the bending moment for column C12 with respect to different building height and different core position.

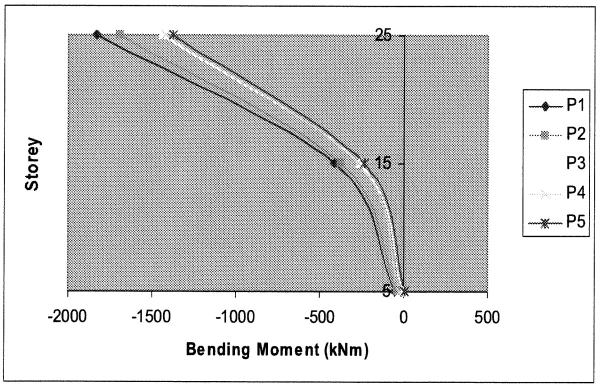

Figure 5 Bending moment of column C12 with different building heights.

It is noted that this behavior is a direct consequence of the effect of asymmetry and the resulting torsional coupling which occurs in the case of lift core position at the edge where the distance is furthest from the centroid.

4.3 Shear Force of Column

From the results obtained, it is seen that shear force for column C12 and C7 decrease as core position moves from P1 to P4. Core position P3 gives the minimum F_y. The trend of shear force is the same as deflection of the building as discussed before. Shear force in Z direction, F_z is larger than F_y. **This is due to the fact that shear force is large in the direction of loading.** F_z is observed to decrease as the lift core move from P1 to P3. Minor variation in shear force observed when the lift core position is varies.

Heights of the building give significant effect to the shear force. As the building become higher, shear force increases. Figure 6 shows the shear force in column C12 with different building heights.

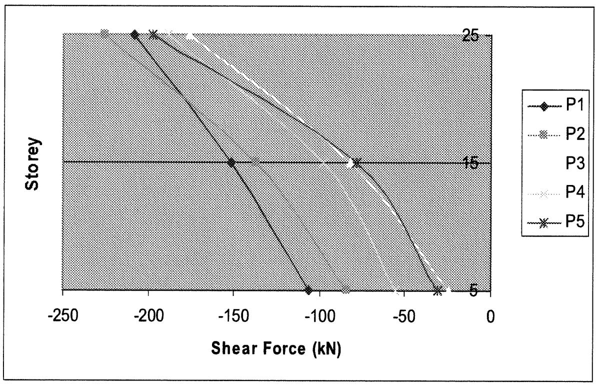

Figure 6 Shear force of column C12 with different building heights.

The above behavior of shear force is also expected as the consequence of the effect of asymmetry and the resulting torsional coupling. The effect of asymmetry and torsional coupling is obvious when the core is located furthest from the centroid of the building.

4.4 Torsion in Column

Torsion in selected column, C12, C16 and C7 increase with respect to the building height. When the lift core moves to P3, the torsion in all selected column becomes smaller. This is due to the fact that when the lift core moves nearer to the centroid, the stiffness of the building is larger and the twisting deformation will be reduced. From the result shown in Table 2, it can be seen that the torsion of selected column becomes larger as the building height increase.

Table 2 Torsion for selected column.

No. of Stories	Selected Column	Lift core Position	Torsion (kNm)	% Different in Torsion compared to P3
5	C12	1	-5.927	142
		2	-6.137	150
		3	-2.451	-
		4	-3.853	57
		5	-1.856	-24
	C16	1	-5.985	137
		2	-6.186	145
		3	-2.523	-
		4	-3.947	56
		5	-1.927	-24
	C7	1	-6.449	138
		2	-6.39	136
		3	-2.704	-
		4	-4.409	63
		5	-2.504	-7
15	C12	1	-40.832	-16
		2	-40.804	-16
		3	-48.412	-
		4	-37.617	-22
		5	-39.302	-19
	C16	1	-40.73	-11
		2	-40.47	-11
		3	-45.669	-
		4	-34.49	-24
		5	-38.817	-15
	C7	1	-40.735	-13
		2	-39.937	-15
		3	-46.985	-
		4	-39.854	-15
		5	-39.946	-15
25	C12	1	-134.04	214
		2	-101	136
		3	-42.733	-
		4	-30.264	-29
		5	-29.129	-32
	C16	1	-134.04	222
		2	-100.29	141
		3	-41.626	-
		4	-26.454	-36
		5	-28.611	-31
	C7	1	-137.09	227
		2	-97.447	133
		3	-41.901	-
		4	-33.666	-20
		5	-30.259	-28

4.5 Period and Frequency of the building

The building frequency inversely related to the building height where, the lowest building recorded the highest frequency value. The building period is simply the inverse of the frequency. This means that a low building with a high natural frequency will have a shorter period.

Frequency of the building increases as the core moves nearer to the centroid. This means that the stiffness of the building increases as the lift core is located nearer to the centroid hence the center of stiffness of the building. Table 3 shows the building frequency and period for all buildings.

Table 3 Frequency and period of 5, 15 and 25 building models

No. of Storey	Lift Core Position	Frequency, ω (Hz)	Period, T(s)
5	1	1.180	0.847
	2	1.268	0.789
	3	1.381	0.724
	4	1.451	0.689
	5	1.330	0.752
15	1	0.416	2.047
	2	0.433	2.312
	3	0.454	2.202
	4	0.459	2.178
	5	0.454	2.202
25	1	0.232	4.304
	2	0.236	4.238
	3	0.238	4.200
	4	0.242	4.126
	5	0.240	4.160

5. CONCLUSIONS

STAADPro 2006 has been use to analyze three reinforced concrete building with 5, 15 and 25 storeys heights. Fifteen models have been generated and analysed. From the analysis it can be concluded that the responses are greatly influenced by the degree of asymmetry in the building. The result proved that overall deflection, bending moment, shear force and torsion of column and column moment increase as the lift core moves further away from the centroid of the building.

It is evident from this study that degree of asymmetry can bring about changes in the deflection and internal forces in the building when subjected to earthquake load. The effect can be severe (deflection, bending moment and torsion) as the height of the building increase.

The study shows that the most efficient lift core position for this T-shape building model in order to attain high performance is at core P3 and P4 because the magnitude of deflection, bending moment, shear force and torsion of the building become smaller. The lift core position should be located as close as possible to the centroid of the T-shape building.

The governing deflected shape with central lift core position is a combination of flexural and shear mode. As the degree of asymmetry increases, the governing deflected shape changes and is greatly influenced by the frame action. Thus, the function of lift core as a lateral load resisting member becomes ineffective.

Building period is increase with the building height. At the same building height, the building period decrease as the lift core position moves closer to the building centroid.

Acknowledgements:
Authors would like to thank Universiti Sains Malaysia for granted a short grant for the study. The sponsorship from Center for Urban Earthquake Engineering (CUEE), Tokyo and Tokyo Institute of Technology also gratefully acknowledge.

References:

Ambrose, J., Vergun D. (1995). "Simplified Building Design for Wind and Earthquake Forces". 3rd Edition, John Wiley and Sons, pp 33–37.

Bugeja M.N., Thambiratnam D.P and Brameld G.H.1998. "The influence of stiffness and strength eccentricities on the inelastic earthquake response of asymmetric structures," Elsevier Science Ltd, Engineering Structures, pp 856 – 863.

Malaysia Standard Institution, MS 1553: 2002, Code of Practice on Wind Loading for building structure. MSI. Pp 1-47.

Rashwan, A. and Taksiah, A. M. (2007), "Development of Design Response Spectra for Ipoh", Persidangan Kebangsaan Kejuruteraan Awam (AWAM '07), Hotel Helang, Langkawi, 29-31 May 2007.

Smith, B. S and Coull, A., 1991." Tall Building Structures: Analysis and Design". Jone Willey & Sons Inc., New York.

Thambiratnam, D.P. (1996), "Response of Tall Buildings to Earthquakes," *2nd International Conference on Multi-Purpose High-Rise Towers and Tall Buildings,* CI-Premier Conference Organization, Singapore, pp 259-264.

Uniform Building Code Earthquake regulations for seismic isolated structures. Whittier (CA); 1997.

Wilkinson S.M. and Thambiratnam D.P. (1993) "Mode Coupling in the Variation Response of Asymmetric Buildings" Elsevier Science Ltd, Engineering Structures, pp 1039 – 1051.

Yoon Y.S. and Smith B.S. (1995), "Assessment of Translational-Torsional Coupling in Asymmetric Uniform Wall-frame Structure", *Journal of Structural Engineering*, McGill University, Vol. 121, No. 10, pp 1488 – 1496.

Zaini S.S, T.A. Majid, T.L. Lau and M.N. Fadzli (2007) "Study on Irregularities of Building Structure Under the Effect on Long Distance Sumatran Earthquakes", Persidangan Kebangsaan Kejuruteraan Awam (AWAM07), Hotel Helang, Langkawi, 29-31 May 2007.

WELD ACCEPTANCE CRITERIA FOR BEAM-END BUTT JOINTS IN SEISMICALLY LOADED STEEL STRUCTURES

Yukihiro Harada[1], Tadao Nakagomi[2], and Tsuyoshi Tanaka[3]

1) Professor, Dept. of Design and Architecture, Faculty of Engineering, Chiba University, Japan
2) Professor, Dept. of Architecture and Civil Engineering, Faculty of Engineering, Shinshu University, Japan
3) Associate Professor, Dept. of Architecture, Faculty of Engineering, Kobe University, Japan
yharada@faculty.chiba-u.jp, nakagom@gipwc.shinshu-u.ac.jp, tanaka@arch.kobe-u.ac.jp

Abstract: It is widely known that weld defects are likely to occur at welding ends in beam-end butt joints with ceramic end tabs, and inspection methods and acceptance criteria for the defects have not been investigated well. The object of the present study is to propose weld acceptance criteria for the welding ends of the beam-end butt joints with the ceramic end tabs. According to the studies on the mechanical influence and the inspection technique of the weld defects at welding ends, weld acceptance criteria and a guideline for a supplemental inspection of welding end zone in butt weld joints are proposed.

1. INTRODUCTION

In steel frameworks of low- or mid-rise building structures in Japan, a welded through-diaphragm-to-beam flange joint is widely used in H-shaped beam-to-square tube column connection (Figure 1). In Hyogo-ken Nanbu Earthquake, brittle fractures of the beam-end butt joints were observed in many steel buildings, and after that various investigations to prevent the brittle fracture of the beam-end welding connections have been conducted (BCJ 2003).

At welding ends of the beam-end butt joints, ceramic end tabs are widely used to omit fabrication process about steel end tabs and to finish stress concentrating reentrant part smoothly (Figure 2); on the contrary, weld defects are likely to be included at the welding ends with the ceramic end tabs, because starting and ending of the welding are within the flange width (BRI 2002). The weld defects at the welding ends are difficult to inspect by conventional ultrasonic testing (AIJ 1996), and quality control of the welding ends with ceramic end tabs remained to be done.

The object of this study is to propose weld acceptance criteria for the welding ends of the beam-end butt joints with the ceramic end tabs. Many previous experimental and analytical studies pointed out that the defects at the welding ends can cause the brittle fracture even if the defect size is relatively small, and a supplemental inspection to measure the defect size (not only the length, but also the height, Figure 3) thus should be established, although measuring the defect height is not required in the conventional ultrasonic inspection. By combination of the knowledge about mechanical influence of the defect and the defect sizing technique, acceptance criteria for welding ends of beam-end butt joints are proposed.

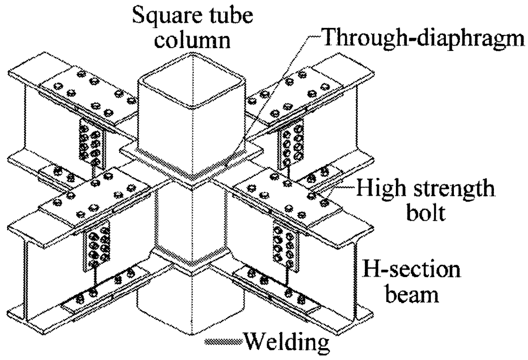

Figure 1 Beam-to-Column Connection Widely Used in Japan

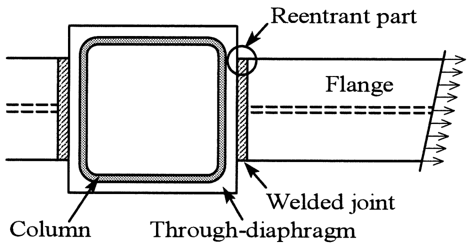

Figure 2 Through-diaphragm-to-beam flange butt

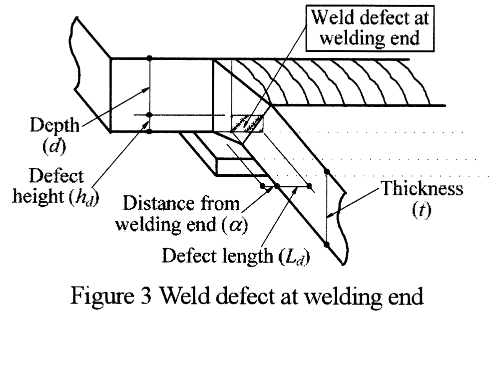

Figure 3 Weld defect at welding end

2. RELATIONSHIP BETWEEN WELD DEFECT SIZE AND BUTT JOINT STRENGTH

2.1 Previous Experimental Studies

In this section, the previous experimental studies on the influence of the weld defect at welding ends are introduced. Eight series of experimental studies are selected for the discussion in this study: pull-plate specimens with welded butt joints (Ozawa 2005, Hiroshige 2005, Suzuki 1999, Kato 2006), notched pull-plate specimens (Shimokawa 2004), beam-to-column subassemblage specimens (Yoshimura 2002, Nakagomi 2002), and beam specimens with welded butt joint (Ozawa 2004). Number of the selected specimens is 86 (50 pull-test specimens for tensile tests and 36 beam-to-column connection ones for cyclic loading tests). Detailed information (weld defect size, Charpy absorbed energy of the steel material, size of marginal weld, for example) needed in the later analytical investigation is given in the selected specimens.

The shapes of the selected specimens are shown in Figure 4. The sizes and mechanical properties of the specimens are shown in Table 1. Groove shape is a single bevel groove with 35 degrees groove angle and with 7mm root gap. All the welded joints are full penetration welding. The weld defects are partial (i.e. non-through-thickness) artificial defects created by embedded steel or copper wedge on root face. Surface flaw of steel plate specimen was notched by a saw blade.

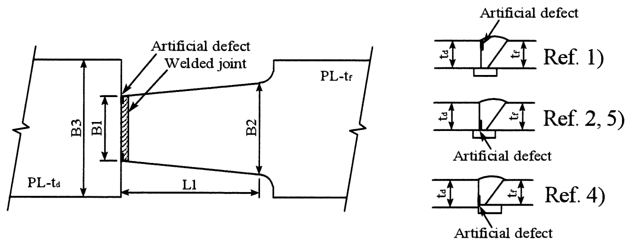

(a) Pull-Plate Specimens with welded butt joints[1, 2, 4, 5]

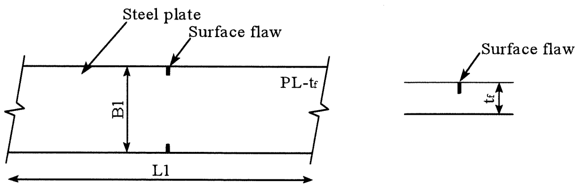

(b) Notched Pull-Plate Specimens[3]

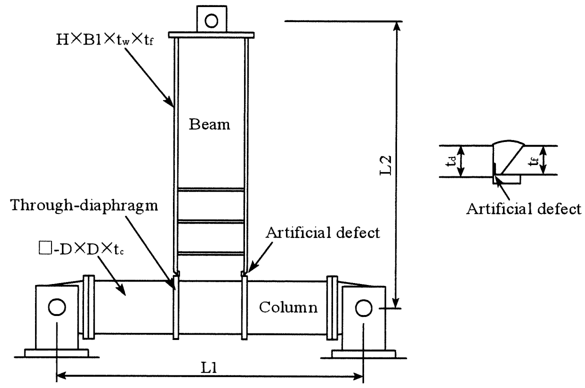

(c) Beam-to-Column Subassemblage Specimens[6, 7]

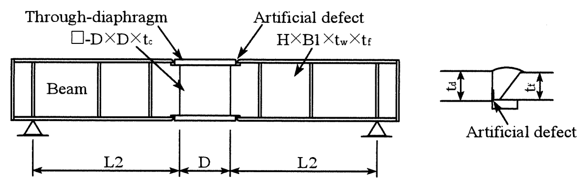

(d) Beam Specimens with welded butt joint[8]

Figure 4 Test specimens

(Ref. No.: 1) Ozawa 2005, 2) Hiroshige 2005, 3) Shimokawa 2004, 4) Suzuki 1999, 5) Kato, 2006, 6) Yoshimura 2002, 7) Nakagomi 2002, 8) Ozawa 2004)

Table 1 Sizes and mechanical properties of specimens

(a) Welded butt joints and steel plate

Ref.	Measureing side							Fixing side					Weld metal		Remarks
	Steel	t_f	B1	B2	L1	σ_y	σ_u	Steel	t_d	B3	σ_y	σ_u	σ_y	σ_u	
1)	SN490B	19	125	180	380	381	567	SN490B	25	200	339	566	374	536	-
2)	SN490B	25	200	252	300	328	582	SN490B	25	350	328	582	460	559	L
						369	539				369	539	494	542	H
3)	SN490B	25	140	-	800	328	582	-					-		-
4)	SN490B	25	200	286	500	328	582	SN490B	25	480	328	582	460	559	L
						359	554				359	554	469	566	H
						321	510				321	510	529	599	A3
						361	535				361	535	529	599	A4
5)	SN490B	25	200	252	300	328	582	SN490B	25	350	328	582	460	559	-

L1, L2: Length of specimens (mm)
B1, B2, B3: Width of specimens (mm)

${}_f\sigma_y$: Yield stress of beam flange (N/mm^2)
${}_f\sigma_u$: Tensile strength of beam flange (N/mm^2)
${}_d\sigma_y$: Yield stress of diaphragm (N/mm^2)
${}_d\sigma_u$: Tensile strength of diaphragm (N/mm^2)
σ_y: Yield stresst of weld metal (N/mm^2)
σ_u: Tensile strength of weld metal (N/mm^2)

t_f: Thickness of beam flange (mm)
t_d: Thickness of diaphragm (mm)

(b) Beam-to-column connections

Ref.	Beam					Diaphragm				Weld metal		Column		Remarks
	Steel	Size	L2	${}_f\sigma_y$	${}_f\sigma_u$	Steel	t_d	${}_d\sigma_y$	${}_d\sigma_u$	σ_y	σ_u	Size	L1	
6)	SN490B	H-500×200 ×10×16	3500	352	535	SM490A	19	396	584	378	524	□-350×12	3000	M/M
										516	620			H/M
7)	SM490A	H-400×200 ×13×21	2100	369	541	SN490B	25	374	529	412	521	□-400×25	2000	FaS1, FaM1,M3
										404	520			-
8)	SM490A	H-280×200 ×12×22	845	381	525	SM490A	25	338	569	433	551	□-250×16	-	S
				362	530			356	520					W

2.2 Analytical Prediction of Butt Joint with Defects

In this study, fracture strength of the butt joint is predicted by applying linear fracture mechanics (Shimokawa 2006). The basic idea of the linear fracture mechanics is that a brittle fracture occurs when a stress intensity factor K reaches a fracture toughness K_c of the material.

The brittle fracture stress of a pull-plate with through-thickness notch (Figure 5) is given as follows, according to the linear fracture mechanics (Okamura 1976):

$$\sigma = \frac{K_c}{F_K(\xi)\cdot\sqrt{\pi \cdot a}} \tag{1}$$

$$\xi = 2\cdot a/B \tag{2}$$

where B, a, and $F_K(\xi)$ are a plate width, a notch length, and a non-dimensional factor determined by the ratio $2a/B$, respectively. The fracture toughness K_c can be estimated as follows (JWES 1997):

$$K_c = \sqrt{\frac{2\cdot\delta_c\cdot\sigma_{yT}\cdot E}{1-\nu^2}} \tag{3}$$

$$\delta_c = F_c\left({}_vT_E, {}_vE_{br}/\sigma_{yT}\right) \tag{4}$$

where δ_c, σ_{yT}, ${}_vE_{br}$, E, ν, and ${}_vT_E$ are a critical CTOD estimate, a yield stress at the temperature T(°C), a Charpy absorbed energy of the fractured point, Young's modulus, Poisson's ratio, and a transition temperature of Charpy absorbed energy (°C), respectively. The function F_c can be approximated by an exponent function of $T-{}_vT_E$ (Shimokawa 2006), and then the estimated fracture stress σ_{pr} is derived as follows:

$$\frac{\sigma_{pr}}{\sigma_{uT}} = \frac{341}{\sigma_{uT}}\cdot\frac{\sqrt{EXP\left(-0.0097\cdot\left(T-{}_vT_E\right)\right)\cdot{}_vE_{br}}}{F_K(\xi)\cdot\sqrt{\pi\cdot A_{eq}}} \tag{5}$$

$$\xi = 2\cdot A_{eq}/B \tag{6}$$

where σ_{uT} and A_{eq} are a maximum stress and an equivalent through-thickness flaw length defined for the partial (non-through-thickness) flaw; A_{eq} is determined so that the pull-plate with the partial flaw and the one with the through-thickness flaw have the same intensity factor K (JWES 1997). A_{eq} thus depends on the length a, the height b,

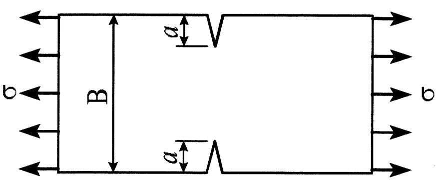

Figure 5 Pull-plate with through-thickness notch

and the position of the flaw.

When the weld defect is small or the toughness of the material is high, not brittle fracture but ductile fracture will occur. The ductile fracture strength is simply determined by the product of the maximum stress of the material and net sectional area of the joint, and then the ratio of σ_{pr}/σ_{uT} is equal to the ratio of section area deficit. At the same time, it is experimentally known that the strength of the butt joint is about 10% larger than the tensile strength of the steel material due to restraining effect around the butt joint. When the ratio of that strength rise is α, the ductile fracture strength is as follows:

$$\frac{\sigma_{pr}}{\sigma_{uT}} = \alpha\cdot\frac{B-2\cdot a\cdot b/t}{B} \tag{7}$$

The fracture strength of the butt joint is predicted as the smaller one between the brittle fracture strength (Eq. (5)) and the ductile one (Eq. (7)).

Comparisons between the experimental fracture stress σ_{max} and the prediction σ_{pr}, where α is assumed to be 1.05, are shown in Fig. 6 (Shimokawa 2006). In almost all the specimens, the predictions are slightly smaller than the experimental results, and thus give safe estimate.

2.3 Relationship between Strength Deficit and Defect Size

In this section, the relationship between strength deficit of butt joint and defect size is analytically investigated according to the knowledge obtained in the previous section.

To obtain the estimated brittle fracture stress, the transition temperature of Charpy absorbed energy ${}_vT_E$ should be determined first. In this study, an estimated ${}_vT_E$ from predicted Charpy energy transition curve by curve-fitting with a master transition curve (JWES 2003) is used. The relationship between Charpy absorbed energy of the fracture

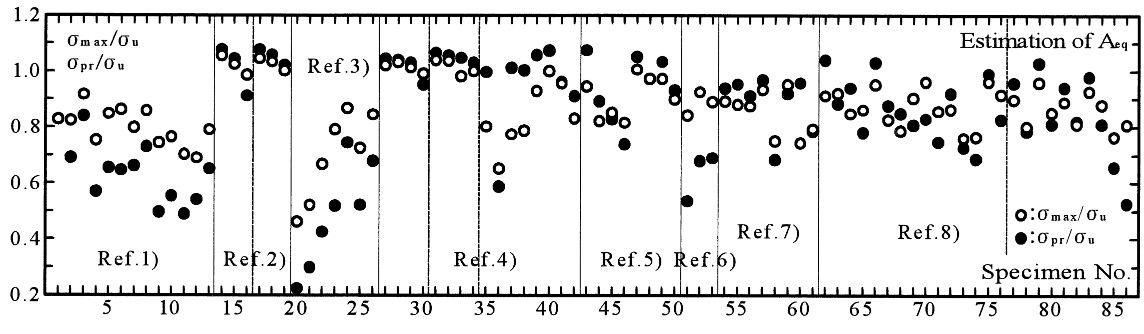

Figure 6 Comparison between experimental results and predictions of the strength of the butt joints

points at tested temperature ${}_vE_{br}$ and experimental $T-{}_vT_E$ was shown in Fig. 7. The fitted master curve of transition curve is also shown. The master curve was given as follows:

$$ {}_vE(T) = \frac{225}{EXP\left(-0.05\cdot\left(T - {}_vT_E\right)\right)+1} \tag{8} $$

where ${}_vE(T)$ is Charpy absorbed energy at temperature T. It is confirmed that the experimental results almost corresponds to the master curve. From Eq. (8), the temperature shift $T-{}_vT_E$ is derived as follows.

$$ T - {}_vT_E = -20\cdot\ln\left(\frac{225}{{}_vE(T)} - 1\right) \tag{9} $$

The brittle fracture stress in Eq. (5) can be calculated by using the temperature shift $T-{}_vT_E$; derived temperature shift is shown in Table 2.

<u>(a) Influence of fracture toughness of material</u>

The relationship between the equivalent through-thickness flaw length A_{eq} and the strength ratio γ, which is defined by σ_{pr}/σ_{uT} or σ_{max}/σ_{uT}, is shown in Figure 8, varying the value of ${}_vE_{br}$ at 0°C as 27, 47, or 70 J. The width of the member of the investigated weld joint is 200mm, and the tensile strength σ_u is 490N/mm^2. It is observed that the maximum strength is determined by the ductile fracture for smaller A_{eq}, and by the brittle fracture for larger A_{eq}.

From Figure 8, the minimum A_{eq} to occur brittle fracture is observed to get larger as ${}_vE_{br}$ is larger, and thus the strength ratio γ gets larger for larger ${}_vE_{br}$. The minimum A_{eq} to occur brittle fracture is 12mm in the case ${}_vE_{br}$ is 70 J, although 5mm in the case ${}_vE_{br}$ is 27 J. This tells us an importance to retain the fracture toughness of the material around butt weld joint to prevent brittle fracture.

<u>(b) Influence of defect size</u>

The relationship between the defect length a and the equivalent through-thickness defect length A_{eq} is shown in Figure 9, varying the defect height b as 5 or 6 mm which corresponds to the bead height in the butt joint. The width of the member of the investigated joint is 200mm, and the thickness t is 19 or 28mm. A_{eq} becomes larger as the defect size, the length a or the height b, is larger.

The relationships between the defect length a and the estimated strength ratio γ with different ${}_vE_{br}$ (27, 47, or 70 J) and different thickness t (16 to 40 mm) are shown in Figure 10. The defect height b is 5 mm, and the tensile strength σ_u is 540 N/mm^2. When ${}_vE_{br}$ is 27 J, the brittle fracture dominates the maximum strength under the defect length a larger than 12 mm. On the contrary, when ${}_vE_{br}$ is 47 or 70 J, the estimated maximum strength is determined by ductile fracture despite of the defect length a or the thickness t. These results give us a rough idea about the weld acceptance criteria to prevent brittle fracture.

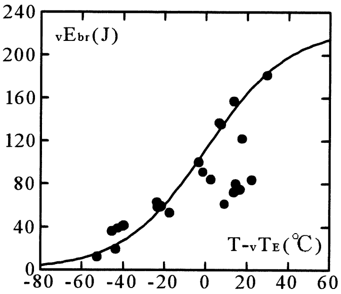

Figure 7 Relationship between ${}_vE_{br}$ and $T-{}_vT_E$

Table 2 Estimated temperature shift $T-{}_vT_E$

${}_vE(T)$	27J	47J	70J
$T-{}_vT_E$	-39.8	-26.6	-15.9

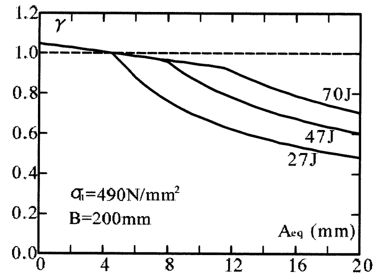

Figure 8 Relationship between A_{eq} and strength ratio γ

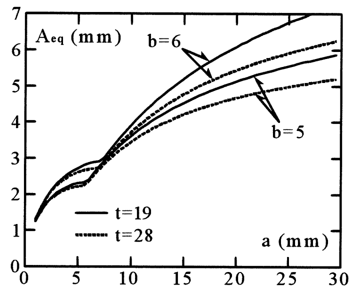

Figure 9 Relationship between the length a and A_{eq}

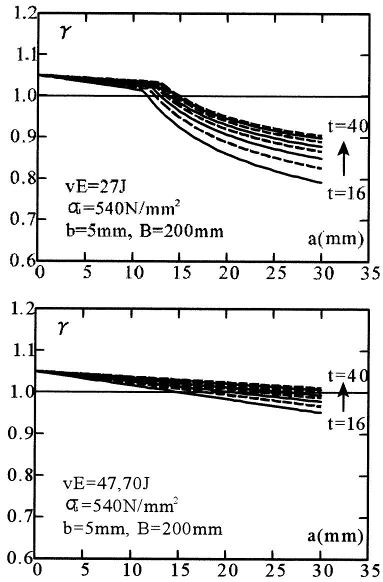

Figure 10 Influence of defect size on joint strength

3. ULTRASONIC INSPECION OF WELDING ENDS OF BEAM-END BUTT JOINTS

As already mentioned, weld defects may occur in the welding ends with ceramic end tabs, and the weld defects in the welding ends are difficult to detect by the conventional ultrasonic angle beam testing (AIJ 1996). One of the most appropriate methods to improve flaw detection reliability is thought to be an advanced tip echo technique (Mak 1985), and the feasibility of the inspection method was investigated (Kasahara and Nakagomi 2006). According to Kasahara and Nakagomi, the advanced tip echo technique is available without any special instruments, and is easy to acquire for the ultrasonic inspection engineers who have been familiar with the conventional inspection method.

Outline of the advanced tip echo technique is shown in Figure 11. The defect height is determined by the difference between the beam path distance from the top and bottom of the weld defect; the advantage of the technique is to be able to simultaneously detect the top and bottom of the defect. Display outputs of ultrasonic detector are shown in Figure 12. Two peaks, which correspond to tip echoes from the top and bottom of the defect, are observed in the outputs, and the height of the defect is determined by the difference in the beam path distances corresponding to the two peaks. By the inspections of the multiple specimens with natural flaws or embedded artificial flaws, the defect heights can be measured by the probes with 65-degrees refracting angle, not by the ones with 70-degrees refracting angle which is ordinarily used in the conventional inspection (Kasahara and Nakagomi 2006).

4. WELD ACCEPTANCE CRITERIA AND INSPECTION FOR BEAM-END BUTT JOINTS WITH CERAMIC END TABS

According to the studies on the mechanical influence and the inspection technique of the weld defects at welding ends in the butt weld joints with ceramic end tabs, weld acceptance criteria and a guideline for a supplemental inspection of end zone in butt weld joints are proposed (JSSC 2008). In the guideline, the width of inspected end zone is defined by 25mm or plate thickness t (16 to 40 mm), whichever is larger (Figure 13); this is because 80% of the weld defects exist within 20mm from the flange edge (BRI 2002).

In the supplemental inspection, the height of weld defect is measured with the advanced tip echo technique, although the defect height is not measured in the conventional inspection. Allowable length and height of the weld defect are specified in the guideline, as shown in Table 3. These acceptance criteria are classified into two cases: (a) the case where Charpy absorbed energy of heat affected zone (HAZ) in the butt weld joint ${}_{v}E_{br}$ is not specified, and (b) the case where weld condition is specified so as to ensure ${}_{v}E_{br}$ larget than 70 J. In the latter case (b), the allowable size is larger in accord with high fracture toughness. In the

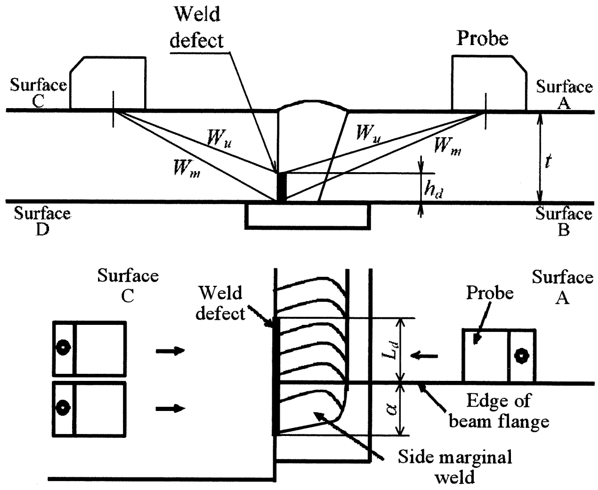

Figure 11 Advanced Tip Echo Technique

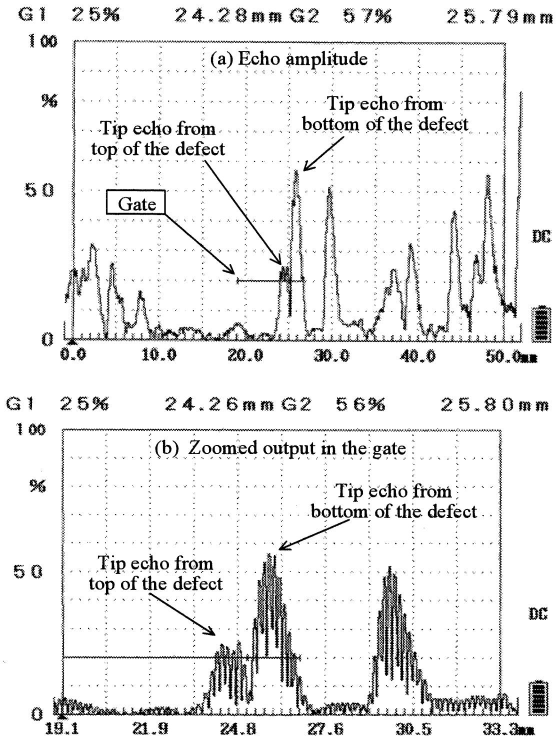

Figure 12 Example of Display Output of Instruments

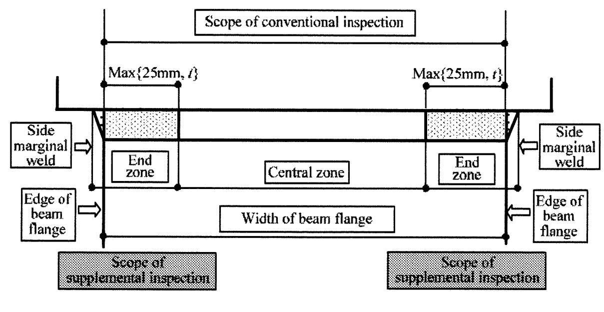

Figure 13 Welding Ends for the Supplemental Inspection

Table 3 Allowable defect size in the end zone

(a) Standard case (when HAZ's $_vE_0$ is not specified)

Welding type and portion	Allowable limit of height	Allowable limit of length
Shop welding (upper and lower flange) Site welding (upper flange)	5mm	12mm
Site welding (lower flange)	5mm	1mm

(b) The case where HAZ's $_vE_0$ >70J (or expected to have equivalent toughness)

Welding type and portion	Allowable limit of height	Allowable limit of length
Shop welding (upper and lower flange) Site welding (upper flange)	5mm	Max{15mm, 0.8*t*} (25mm maximum)
Site welding (lower flange)	5mm	Max{8mm, 0.4*t*} (12mm maximum)

(*t*: thickness of beam flange)

former case (a), very small allowable size is specified for site welding at the lower flange; this is because the bottom of the groove is at the lowest edge of the beam in this case, and then the weld defect is under high tensile stress.

The supplemental inspection is not needed if the width of the beam flange is increased at the beam-end (i.e., horizontal haunch) and thus the tensile stress in the beam flange is kept lower; it should be noted that controlling the tensile stress, as well as the quality of weldment, is important to prevent brittle fracture at the butt joints.

Acknowledgements:

This study has been accomplished by Research Committee for Weld Acceptance Criteria and Inspection for Beam-End Butt Joints, which is organized under Japan Society of Steel Construction. The authors thank all of the members of the Committee and working groups for their helpful contributions.

References:

Building Center of Japan (BCJ) (2003), "Guideline for Prevention of Brittle Fracture at Beam End Welded Connections," Tokyo. (in Japanese)

Building Research Institute (BRI), Japan Iron and Steel Federation (JISF), and The Japan Welding Engineering Society (JWES) (2002), "Welding Material for Steel for Building Structure and Performance of Welding Connection," commission's report. (in Japanese)

Architectural Institute of Japan (AIJ) (1996), "Standard for the ultra sonic inspection of weld defects in steel structures," 3rd Ed., Tokyo (in Japanese)

Shimokawa, H., Nakagomi, T., Harada, Y., Hiroshige, T., Fujita, T., Ishihara, K. and Okamoto, H. (2006), "Estimation of Fracture Strength of Butt Joints with Weld Defects," *Proceedings of the 4th International Symposium on Steel Structures*, 210-219.

C. Ozawa, T. Nakagomi, K. Hattori, Y. Ichikawa, K. Matoba, T. Kitazawa, and S. Nakamura. (2005), "Experimental Study of Butt Joints with Surface Defects at Welding End", *Annual assembly of AIJ, C-1 Structure III*, 543-548. (in Japanese)

T. Hiroshige, K. Morita, K. Ishihara, M. Kato, M. Okano, T. Kojo, Y. Tsuchiya, T. Shima, and H. Hattori. (2005), "Experimental Study of Butt Joints with Surface Defects at Welding End," *Annual assembly of AIJ, C-1 Structure III*, 531-534. (in Japanese)

H. Shimokawa, T. Nakagomi, H. Okamoto, and K. Morita (2004), "Estimation of Fracture Strength Applying Linear Fracture Mechanics," *Journal of Structural and Construction Engineering (Transactions of AIJ)*, No. 585, 169-175. (in Japanese)

T. Suzuki, T. Ishii, K. Morita, and K. Takanashi (1999), "Experimental Study on Fracture Behavior of Welded Beam-to-column Joint with Defects," *Steel Construction Engineering*, **6**(23), 149-164. (in Japanese)

T. Kato, K. Morita, K. Ishihara, T. Hiroshige, M. Okano, T. Furuki, Y. Tsuchiya, and T. Shima. (2006), "Experimental Study of Butt Joints with Surface Defects at Welding End," *Annual assembly of AIJ, C-1 Structure III*, 977-980. (in Japanese)

T. Yoshimura, M. Tabuchi, T. Tanaka, and K. Yasui (2002), "Influence of Weld Defects on Fracture of Beam-to-Column Welded Connections for Steel Frame Structures," *Journal of Constructional Steel*, Vol. 10, 21-26. (in Japanese)

T. Nakagomi, K. Hattori, Y. Ichikawa, K. Matoba, and M. Iwata (2002), "Experimental Study on Deformation Capacity of Welded Beam-to-Column Connection with Weld Defects," *Journal of Structural and Construction Engineering (Transactions of AIJ)*, No. 556, 145-150, 2002.6 (in Japanese)

C. Ozawa, T. Nakagomi, Y. Ichikawa, T. Mutaguchi, M. Suemori. (2004), "Experimental Study on Deformation Capacity of Welded Beam-to-Column Model Connection with Weld Defects," *Annual assembly of AIJ, C-1 Structure III*, 569-572. (in Japanese)

Okamura, H. (1976), "Approach of Linear Fracture Mechanics – Lecture 1 of Fracture Mechanics and Material Strength," Baifukan, Tokyo. (in Japanese)

Mak, D. K. (1985), "Ultrasonic methods for measuring crack. location, crack height and crack angle," *Ultrasonics*, **23**, 223-226.

Kasahara, M. and Nakagomi, T (2006), "Experimental Studies about Evaluation of Defects by Advanced Tip Echo Technique in the End Zone of Beam-to-Column Weld Joints," *Journal of Structural and Construction Engineering (Transactions of AIJ)*, No. 607, 167-174. (in Japanese)

The Japan Welding Engineering Society (JWES) (1997), "Method of Assessment for Flaws in Fusion Welded Joints with respect to Brittle Fracture and Fatigue Crack Growth," WES 2805:1997, Tokyo.

The Japan Welding Engineering Society (2003), "Method of assessing brittle fracture in steel weldments subjected to large cyclic and dynamic strain," WES 2808:2003, Tokyo.

Japan Society of Steel Construction (JSSC) (2008), "Guideline for Weld Acceptance Criteria and Inspection for Beam-End Butt Joints in Steel Structures," Tokyo. (in Japanese)

Fifth International Conference on Urban Earthquake Engineering
March 4-5, 2008, Tokyo Institute of Technology, Tokyo, Japan

APPLICATION OF A WEDGE DEVICE TO STEEL STRUCTURES

Takao Takamatsu[1], Hiroyuki Tamai[2], Teruaki Yamanishi[3] and Akira Matsuo[4]

1) *Professor, Faculty of Engineering, Hiroshima Institute of Technology, Japan*
2) *Associate Professor, Faculty of Engineering, Hiroshima Institute of Technology, Japan*
3) *Graduate Student, Graduate School of Engineering, Hiroshima Institute of Technology, Japan*
4) *Professor, Graduate School of Engineering, Hiroshima University, Japan*

takamatu@cc.it-hiroshima.ac.jp, tamrix@cc.it-hiroshima.ac.jp, tv-hit@cc.it-hiroshima.ac.jp, matu12@hiroshima-u.ac.jp

Abstract: A wedge device consisting of a wedge, a counter-wedge and a spring, has been proposed by the authors. The device is applied to earthquake resistant elements to assist more effective capability of energy absorption under seismic ground motion. New structural elements, a non-slip-type column base, non-compression braces, a self-centering beam-to-column connection and non- compression knee-braces, have been proposed. Experimental results of each element subjected to cyclic loadings were good agreement with the corresponding analytical ones.

1. INTRODUCTION

A wedge device has been proposed to minimize slip of an anchor-bolt-yield-type exposed column base. This new column base is called a non-slip-type column base and it has many advantages over a conventional exposed column base(Takamatsu et al. 2001, 2002, 2003a, 2004, 2005a-e, 2006a, Yamanishi et al. 2007a-b). Furthermore, this wedge device can be applied to brace members to eliminate slip. These brace members are called non-compression braces and they have many advantages including no slipping and no buckling(Kobata et al. 2006, Takamatsu et al. 2003b, 2006c, Tamai et al. 2005a-b, Yamanishi et al. 2007a). Beam-to-column connections used the wedge device can minimize beams and columns yielding and reduce residual deformation in a building after an earthquake. These connections are called self-centering connections(Kobata et al. 2006, Takamatsu 2005e, 2007a). Finally, knee-braces with the wedge device called non-compression knee-braces can strengthen moment-resisting connections under an earthquake(Kobata et al. 2006, Takamatsu 2005f. 2007a-b). The specimens with the wedge device are experimented to obtain restoring force characteristics under cyclic loadings.

Models of the restoring force characteristics are compared with the experimental results to examine applicability of the wedge device to the earthquake-resistant elements.

2. NON-SLIP-TYPE COUMN BASE

2.1 Function of Non-Slip-Type Column-Base

The non-slip-type column base proposed by the authors is shown in Figures 1 and 2. Slip behavior is prevented by simply setting the wedge device between the nut and the base plate. A gap generated between the nut and the base plate due to plastic elongation of the anchor-bolt can be eliminated by the wedge moving into the gap under spring compression. The restoring force characteristics of the column base show non-slip-type behavior, linear from the origin. The non-slip-type column base has the following advantages over the conventional column base. 1) No gap appears between the nut and the base plate, so that no looseness is generated in the column base. 2) Since the anchor-bolt can absorb plastic energy without pinching behavior, the column base can play the role of an energy absorption damper during earthquakes of all levels. 3) The wedge device can be easily installed in existing column bases and is thus applicable to rehabilitation of conventional column bases. 4) Since a column base with multi-rows of anchor-bolts shows cyclic curves returning to the origin during unloading, unless the rotation of the column base exceeds the elastic limit of rotation, the column base has self-centering capability. Since the cyclic curves become linear from the origin, the self-centering capability can survive after any large-amplitude of main shock.

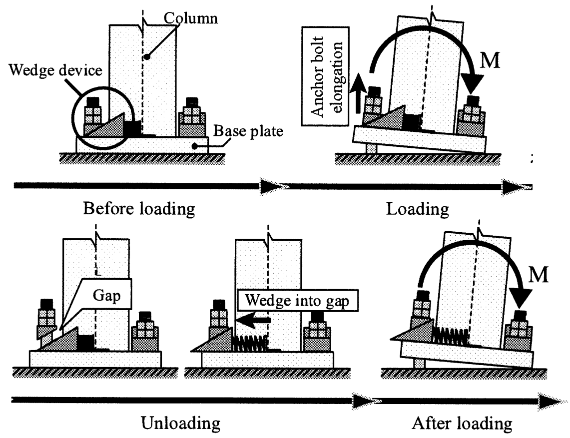

Figure 1 Function of Non-Slip-Type Column-Base

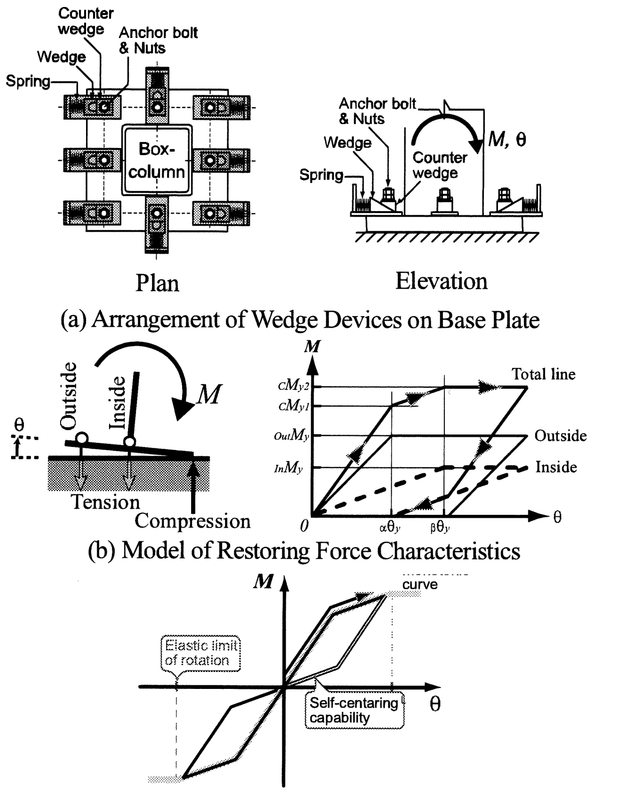

(a) Arrangement of Wedge Devices on Base Plate

(b) Model of Restoring Force Characteristics

(c) Model of Restoring Force Characteristics under Cyclic Loading

Figure 2 Restoring Force Characteristics

2.2 Experiment

Horizontal loading apparatus was used on the experimental studies. Apparatus and specimen shape show in Figure 3. The specimens were designed as anchor-bolt-yield-type column bases, in which the anchor bolts were considered as yielding elements but the base plate, the column member and the foundation were considered as elastic elements. A steel foundation was employed instead of a concrete one, and the anchor bolts were rolled thread anchor bolts standardized by the Japanese Society of Steel Construction.

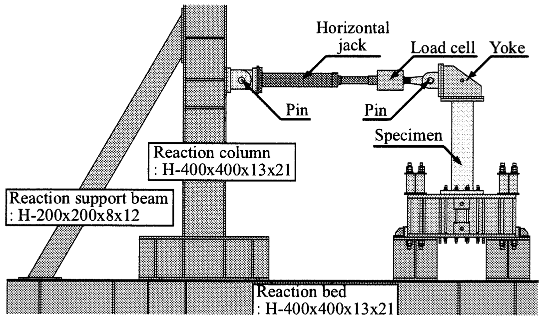

Figure 3 Apparatus

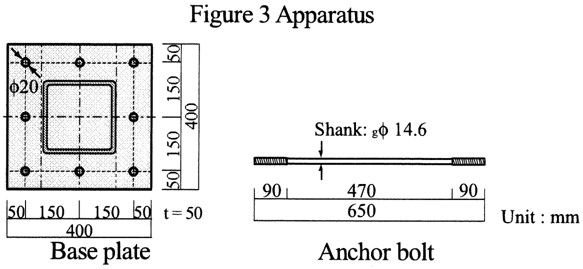

Figure 4 Shape of Specimen

2.3 Results AND Discussions

The experimental results are shown in Figure 5. The relationships between the bending moment M and the base-plate rotational angle θ of column base are shown as the restoring force characteristics. The dotted line in the figure shows the result given by the model of restoring force characteristics, and the solid line shows the result of the loading test.

In the cyclic loading tests, the loads built up from the origin at each loading cycle, and returning to the origin during unloading. Self-centering performance was shown until the elastic limit of rotation was exceeded. The models of the restoring force characteristics showed fairy good agreement with the experimental results.

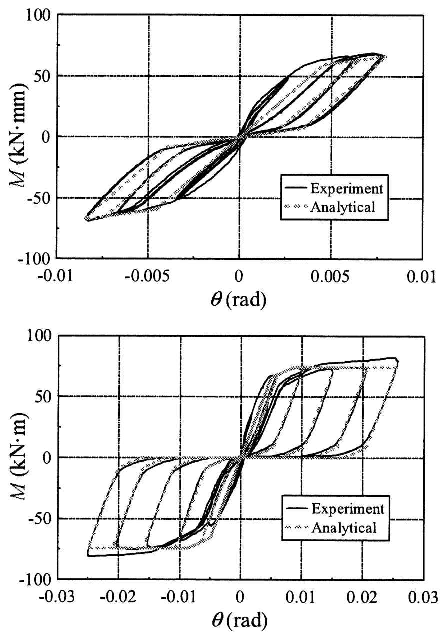

Figure 5 Bending Moment : M v.s. Rotational Angle : θ

3. NON-COMPRESSION BRACES

3.1 Function of Non-Compression Brace

The non-compression brace proposed by the authors is shown in Figures 6 and 7. It consists of a slender rod with tensile-connected ends installed with the wedge device. One end of the brace is pinned and the other with the wedge device is designed as a roller moving only in the compressive direction. The brace can only resist tensile force so there is no buckling caused by compressive force. The tensile force exceeds the yield axial force and the brace elongates plastically. In cyclic loadings the plastic elongation of a conventional brace causes slip-type restoring force characteristics, but the wedge of the non-compression brace under spring compression slides into a gap between the counter-wedge and the wedge-stand to prevent looseness of the brace. A pair of non-compression braces subjected to seismic loadings shows perfectly elasto-plastic restoring force characteristics. The non-compression brace has the following advantages over conventional braces. 1) It shows no buckling and no looseness in the tensile direction. 2) A pair of them shows perfectly elasto-plastic curves, so that an analytical model of cyclic behavior can be easily formulated. 3) The brace end connection can be simply designed as a tensile connection. 4) The sliding displacement of the wedge is the most significant measure for design of the non-compression brace. The plastic deformation capacity or the energy absorption capacity of the non-compression brace depends upon the movable length of the wedge. Therefore, the non-compression brace is suitable for performance-based design.

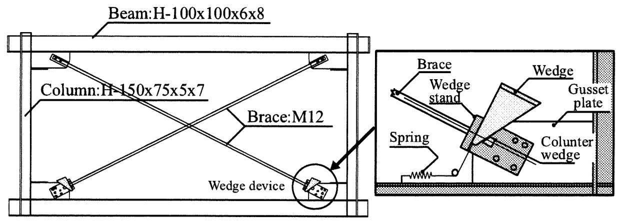

(a) Arrangement of Wedge-Device on Brace End

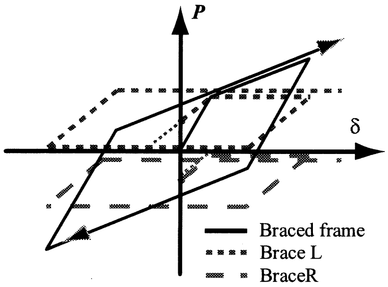

(b) Model of Restoring Force Characteristics

Figure 6 Restoring Force Characteristics

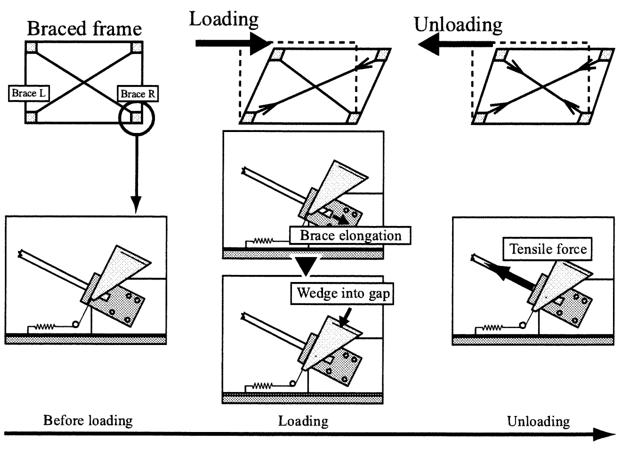

Figure 7 Function of Non-Compression Braces

3.2 Experiment

Horizontal loading apparatus was used on the experimental studies. Apparatus and a brace member show in Figures 8 and 9. The specimen was a portal frame with non-compression braces. The specimens subjected to cyclic loadings and braces were pre-tensioned 50% of brace yield-axial-force.

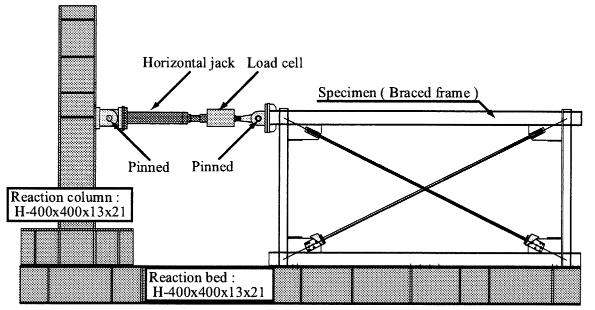

Figure 8 Apparatus

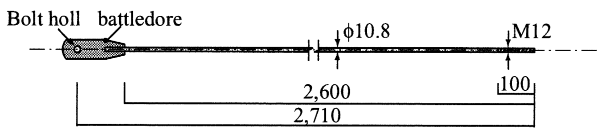

Figure 9 Shape of Specimen

3.3 Results and Discussions

The experimental results are shown in Figure 10. The relationships between the horizontal load P and the horizontal displacement δ of frame with braces are shown as the restoring force characteristics. The dotted line in the figure shows the result given by the model of restoring force characteristics, and the solid line shows the result of the loading test.

In the cyclic loading tests, the braced frame showed the spindle type restoring force characteristics at each loading cycle, and constant elastic-stiffness curves.

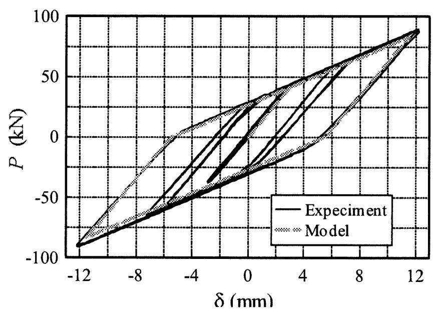

Figure 10 Horizontal Load : P v.s. Horizontal Displacement : δ

4. SELF-CENTERING CONNECTION

4.1 Function of Self-Centering Connection

The self-centering connection proposed by the authors is shown in Figures 11 and 12. It consists of end-plate type beam-to-column connection using normal-strength bolts with the wedge device. This connection has the same resistant mechanism as non-slip-type column base.

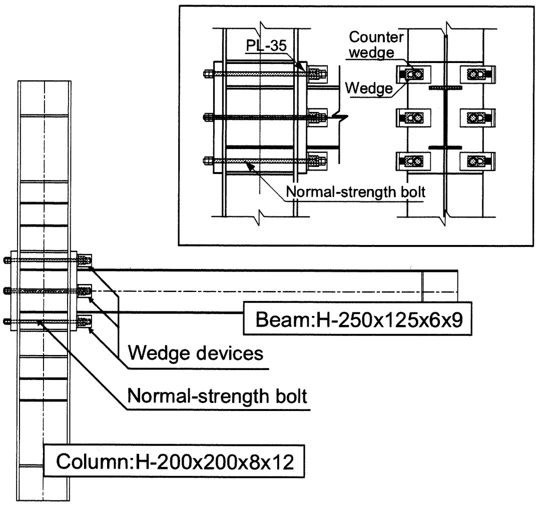

(a) Arrangement of Wedge Devices on End-Plate

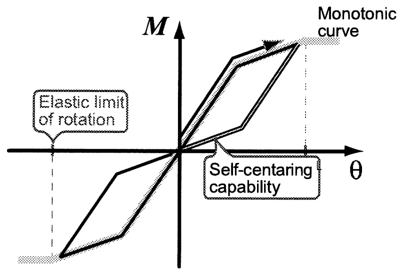

(b) Model of Restoring Force Characteristics

Figure 11 Restoring Force Characteristics

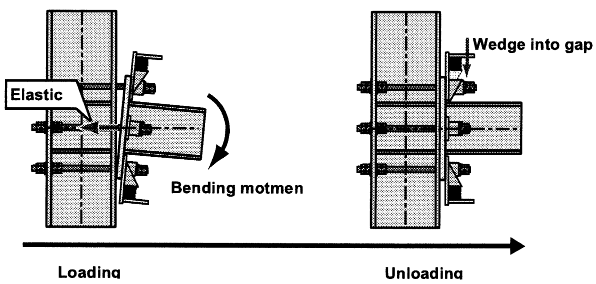

Figure 12 Function of Self-Centering Connection

4.2 Experiment

Horizontal loading apparatus was used on the experimental studies. Apparatus and a normal-strength bolt show in Figures 13 and 14. The specimen was rotated 90 degrees and the top of the beam was subjected to cyclic vertical loadings by horizontal jack. The specimen was T-shaped beam-to-column connection with the wedge devices.

4.3 Result and Discussions

The experimental results are shown in Figure 15. The relationships between the horizontal load P and the horizontal displacement δ of frame with the self-centering connection are shown as the restoring force characteristics. The bold-solid line in the figure shows the result given by the model of restoring force characteristics, and the thin-solid line shows the result of the loading test.

In the cyclic loading test, the restoring force characteristics showed the same cyclic behavior as the non-slip-type exposed column base. The rotation of the connection did not exceed the elastic limit of rotation so that the connection sustained self-centering capability, returning to the origin after unloading. The elastic stiffness was higher than the analytical stiffness owing to the pre-tension of the bolts. The cyclic behavior was in good agreement with the analytical curves. The members other than the bolts were in the elastic region.

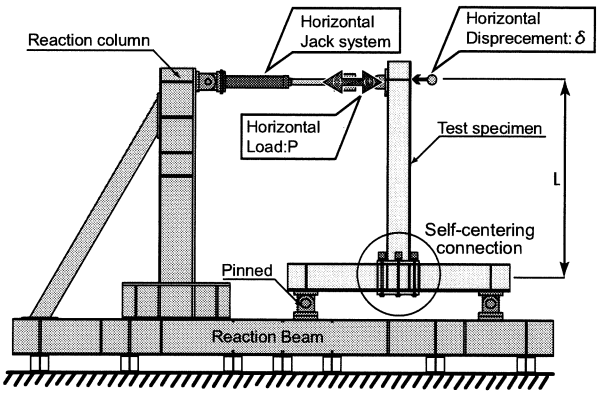

Figure 13 Apparatus

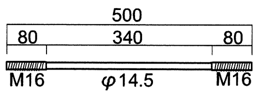

Figure 14 Shape of Normal-Strength Bolt

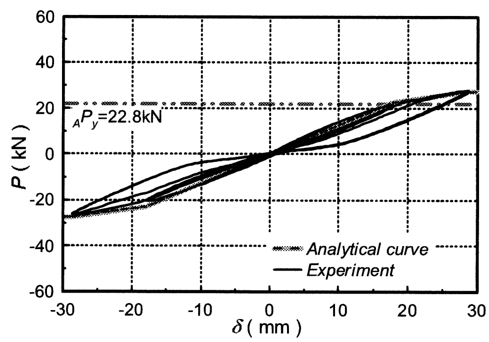

Figure 15 Horizontal Load : P v.s. Horizontal Displacement : δ

5. NON-COMPRESSION KNEE-BRACES

5.1 Function of Non-Compression Knee-Brace

The non-compression knee-brace proposed by the authors is shown in Figures 16 and 17. It consists of a rigid connection with the non-compression knee-braces. This knee-brace has the same resistant mechanism as the non-compression brace.

5.2 Experiment

Horizontal loading apparatus was used on the experimental studies. Apparatus and a knee-brace show in Figures 18 and 19. The specimen was rotated 90 degrees and the top of the beam was subjected to cyclic vertical loadings by horizontal jack. The specimen was T-shaped beam-to-column connection with non-compression knee-brace.

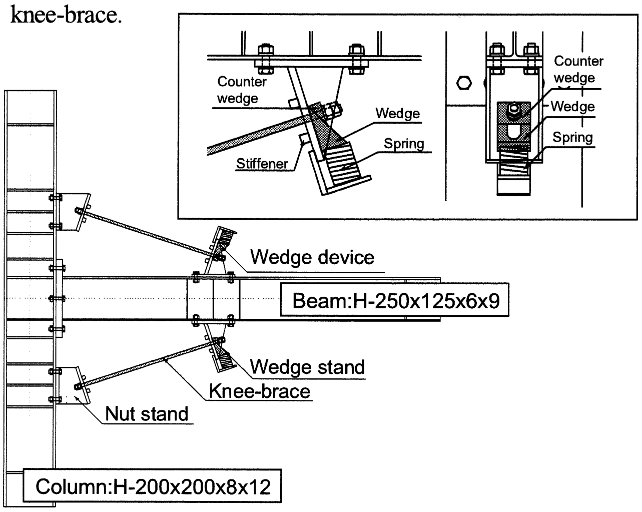

(a) Arrangement of Wedge-Device on Knee-Brace End

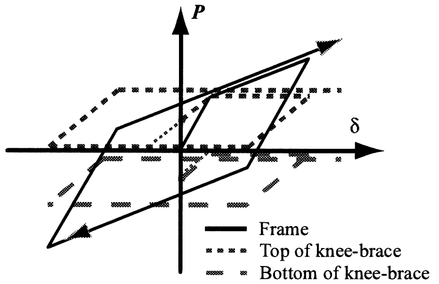

(b) Model of Restoring Force Characteristics

Figure 16 Restoring Force Characteristics

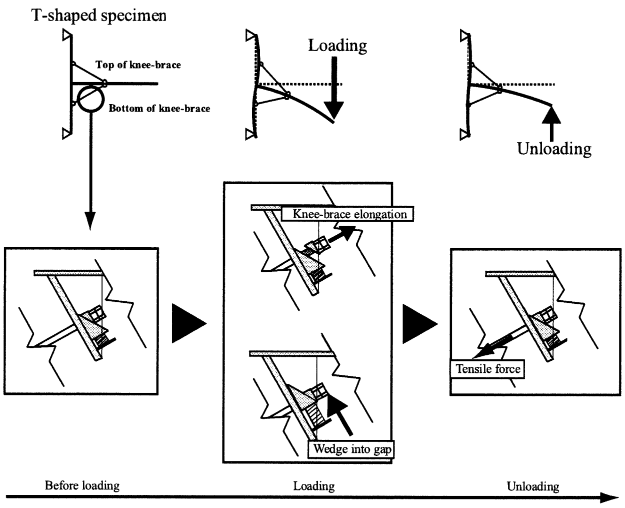

Figure 17 Function of Non-Compression Knee-Brace

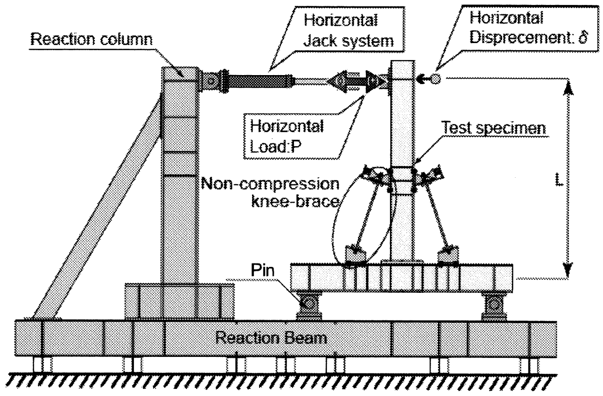

Figure 18 Apparatus

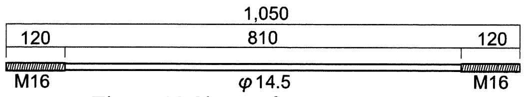

Figure 19 Shape of Knee-Brace

5.3 Results and Discussions

The experimental results are shown in Figure 15. The relationships between the horizontal load P and the horizontal displacement δ of frame with non-compression knee-braces are shown as the restoring force characteristics. The bold-solid line in the figure shows the result given by the model of restoring force characteristics, and the thin-solid line shows the result of the loading test.

In the cyclic loading test, the restoring force characteristics became bi-linear curves. The elastic stiffness was in accordance with the analytical elastic stiffness of the rigid connection with the non-compression knee-braces. The second stiffness coincided with the analytical elastic stiffness of the frame. The yield load was equal to the yield load of the non-compression knee-brace. The members other than the knee-braces were in the elastic region.

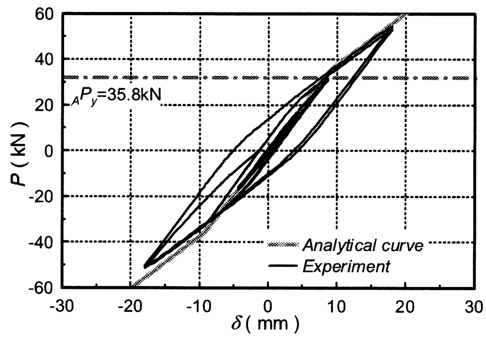

Figure 20 Horizontal Load : P v.s. Horizontal Displacement : δ

6. SUMMARY AND CONCRUSIONS

An experimental study was performed on the structural elements with the wedge device under cyclic loadings to investigate the restoring force characteristics. Based on the test results the following conclusions were drawn:

1) The non-slip-type column base and the self-centering

beam-to-column connection showed non-slip-type behavior, linear from the origin and had the self-centering capability.

2) The non-compression braces and the non-compression knee-braces showed perfectly elasto-plastic cyclic behavior without buckling and slipping.

ACKNOWLEDGEMENT

This research was carried out as a part of the Project of the Research Center for Development of High-Performance-Oriented Structural System (Head : Prof. Takamatsu , T.) at the Hiroshima Institute of Technology. The authors express their sincere appreciation to the Center. They also express their gratitude to their colleagues at the Center, who helped them carry out the research.

Reference

Kobata, H., Takamatsu , T., Tamai, H., Yamanishi, T., & Matsuo, A. 2006. A *experimental study on rehabilitation and new joint system of T-shaped beam-to-column connection*, Journal of Constructional Steel, Japanese Society of Steel Construction: Vol. 14, 717-724. (in Japanese)

Takamatsu , T., Douki, H. & Nakamura, S. (2001). *Experimental study on restoring force characteristics of exposed-type column base*, Journal of Constructional Steel, Japanese Society of Steel Construction: Vol. 9, 415-422. (in Japanese)

Takamatsu , T., Douki, H. & Nakamura, S. (2002). *A study on restoring force characteristics of steel exposed-type column base*, Journal of Constructional Steel, Japanese Society of Steel Construction: Vol. 10, 499-506. (in Japanese)

Takamatsu , T., Douki, H. & Nakamura, S. (2003 a). *A study on exposed-type column bases with improved restoring force characteristics*, Journal of Constructional Steel, Japanese Society of Steel Construction: Vol. 11, 563-570. (in Japanese)

Takamatsu , T., Tamai, H. & Komochi, A. (2003 b). *Histeresis characteristics and energy absorption capacity of non-compression brace*, Journal of Constructional Steel, Japanese Society of Steel Construction: Vol. 11, 129-136. (in Japanese)

Takamatsu , T., Tamai, H., Yamanishi, T., S. Ishihara & Matsuo, A. (2004). *Restoring force characteristics of exposed-type column bases in an existing gymnasium*, Journal of Constructional Steel, Japanese Society of Steel Construction: Vol. 12, 281-288. (in Japanese)

Takamatsu , T. & Tamai, H. (2005 a), *Non-slip-type restoring force characteristics of exposed-type column base*, Journal of Constructional Steel Research, Vol. 60. 942-961.

Takamatsu , T., Tamai, H. & Yamanishi, T. (2005 b), *Models of restoring force characteristics of non-slip-type exposed column base in steel structures*, Journal of Structural Engineering, Architectural Institute of Japan: Vol. 51. 293-302. (in Japanese)

Takamatsu , T., Tamai, H., Yamanishi, T., Matsuo, A. (2005 c), *Models of Restoring Force Characteristics for Exposed Column Base with Wedge Device*, Third International Symposium on Steel Structure, Seoul, Korea, pp497-504.

Takamatsu , T., Tamai, H., Yamanishi, T., Matsuo, A. (2005d), *Rehabilitation Technique of Exposed-type Column Base in an Existing Gymnasium by Wedge Device*, Proceedings of IABSE Symposium, Lisbon, Vol.61.

Takamatsu , T., Tamai, H., Yamanishi, T., & Matsuo, A. (2005 e). *A study on self-centering performance of non-slip-type exposed column-base*, Journal of Constructional Steel, Japanese Society of Steel Construction: Vol. 13, 173-180. (in Japanese)

Takamatsu , T., Tamai, H. Kobata, H. & Takeuchi, I. (2005 f). *Rehabilitation for H-Shaped beam-to-column conecction by means of non-compression knee-brace*, Journal of Constructional Steel, Japanese Society of Steel Construction: Vol. 14, 717-724. (in Japanese)

Takamatsu , T., Tamai, H., Yamanishi, T. & Matsuo, A. (2006 a), *Self-centering performance of non-slip-type exposed column-base*, Proceeding of fifth international conference on "Behaviour of Steel Structures in Seismic Areas(STESSA2006)", Yokohama, Japan, 357-362.

Takamatsu , T., Tamai, H., Kato, T. & Kobata, H. (2006 b). *Restoring force characteristics of steel framed structure strengthened by non-compression brace*, Journal of Constructional Steel, Japanese Society of Steel Construction: Vol. 14, 429-436. (in Japanese)

Takamatsu , T., Tamai, H., Okabe, M. & Koga, T. (2006 c). *Shaking table test of steel framed structure with non-compression braces*, Journal of Constructional Steel, Japanese Society of Steel Construction: Vol. 14, 349-356. (in Japanese)

Takamatsu , T., Tamai, H. & Kobata, H. (2007 a). An Experimental Study on Seismic Rehabilitation and a New Beam-to-column Connection, PSSC, Wairakei, NewZealand, Vol. 2, 297-302.

Takamatsu , T., Tamai, H., Kobata, H., & Hiyamoto, K. (2007 b). *A study on rehabilitation technique of steel framed structure by means of knee-brace*, Journal of Constructional Steel, Japanese Society of Steel Construction: Vol. 15, 113-120. (in Japanese)

Tamai, H., Takamatsu , T. & Matsuo, A. (2005 a). *Improvement of a seismic performance on non-compression brace*, Journal of structural and construction engineering, Architectural Institute of Japan: No. 595, 131-138 (in Japanese)

Tamai, H. & Takamatsu , T. (2005 b), *Cyclic loading tests on a non-compression brace considering performance-based seismic design,* Journal of Constructional Steel Research, Vol. 61. 1301-1317.

Yamanishi, T., Takamatsu , T., Tamai, H., Kato, T. & Matsuo, A. (2007 a). *Earthquake-resistance design method for steel structure with wedge device based on energy balance*, Journal of Constructional Steel, Japanese Society of Steel Construction: Vol. 15, 447-454. (in Japanese)

Yamanishi, T., Takamatsu , T., Tamai, H. & Matsuo, A. (2007 b). *Restoring force characteristics of non-slip-type exposed column-base with multi-rows of anchor-bolts -Self-centering performance in case of no-axial force-*, Journal of structural and construction engineering, Architectural Institute of Japan: No. 621, 155-162, 2007.11. (in Japanese)

Fifth International Conference on Urban Earthquake Engineering
March 4-5, 2008, Tokyo Institute of Technology, Tokyo, Japan

SEISMIC PERFORMANCE OF A MULTI-TOWER HYBRID STRUCTURE

Ying Zhou[1] and Xilin Lu[2]

1) Lecturer, Research Institute of Structural Engineering and Disaster Reduction, College of Civil Engineering, Tongji University, China
2) Professor, State Key Laboratory for Disaster Reduction in Civil Engineering, Tongji University, China
yingzhou@mail.tongji.edu.cn, lxlst@mail.tongji.edu.cn

Abstract: In China, the irregular high-rise buildings are becoming more extensive. Considering the irregularities and complexities of these buildings, it is significant to verify the safety and rationality of their seismic design through effective means including small scale dynamic model tests, refined numerical analysis and large scale joint tests. The target building of this paper is Shanghai International Design Center (SHIDC), which has two different-height connected towers designed by Japanese Architect Tadao Ando. The hybrid system of reinforced concrete core walls in conjunction with perimeter steel frames is out of Chinese code in the plan and elevation layouts. Thus, scaled model was carefully tested on the shaking table to obtain the weak position, dynamic characteristics, inter-story drift, and shear force of the structure. A linear dynamic analysis by ETABS was performed to compare, check, and support the experimental results. On the basis of those results, the seismic performance of the complex irregular structure was evaluated and the suggestions to the same type of structural design were given.

1. INTRODUCTION

China has been building up a large number of novel high-rise buildings under an increasing requirement of architectural aesthetics. Most of these buildings have irregular structures against traditional structural concept. Their irregularities may exist in configuration of the building, in differences between the storey heights, in distribution of masses and rigidities, in creating short columns, and also in nonorthogonal placement of columns and shear walls (Tezcan and Alhan, 2001). According to the past experience, it is the irregularities in the structural design that directly or indirectly cause the collapse or severe damage of the buildings under strong earthquake. Detailed investigation is thus necessary to verify the safety and rationality of the seismic performance of the irregular buildings.

In the past several decades, substantial progress has been made in computer-based procedure for analysis of structures. Using one analytical method, however, it is still difficult to predict the seismic performance of irregular structures. Shaking table test is another useful procedure to examine the structural seismic performance. Several shaking table facilities have lately been constructed, including E-defence shaking table (Katayama, 2005), EU Center shaking table (Pavese et al. 2005), shaking table at Montreal Structural Engineering Laboratory (Tremblay, 2005), shaking table at China Academy of Building Research, etc. Researchers have more and more investigated the earthquake-resistant behaviors of irregular buildings by shaking tables, as shown in the work by Ko and Lee, (2006), Lu et al. (2007a, 2007b), and Tong et al. (2007).

To study the seismic performance of irregular structures, shaking tables tests are used in conjunction with the numerical analysis. First, preliminary analysis is carried out for the peer review on the irregular structure. Then, shaking table model test is carried out to find the weak positions and to obtain the structural parameters of the building, which are the basis for the further experiment on the weak joint and refined analysis of the overall structure.

The target building of this paper is a high-rise multi-tower building, whose hybrid structure is out of Chinese code. A detailed shaking table model test was performed by the working group at the State Key Laboratory for Disaster Reduction in Civil Engineering of Tongji University, China. The calculation from the model responses, such as displacement and shear force, to the prototype responses was made according to the similitude law. The numerical analysis is then carried out to carefully compare, check, and support the experimental results, based on which, measures for improving the seismic performance of the structure were given at the last part of the paper.

2. DISCRIPTION OF THE BUILDING STRUCTURES

Shanghai International Design Center (SHIDC) is an office building which is built for the centennial anniversary of Tongji University in 2007. For its significant background, prestigious Japanese Architect Tadao Ando was invited to design the architecture of SHIDC. He finally decided to apply the overturned Arabic number "4" as the main elevation of SHIDC, as shown in Figure 1.

It is structural engineers' responsibility to realize the design of the architects. In SHIDC, reinforced concrete (RC) core wall-steel frame hybrid structures were employed, as shown in Figure 2 and Figure 3.

Figure 1 Architectural Visualization of SHIDC

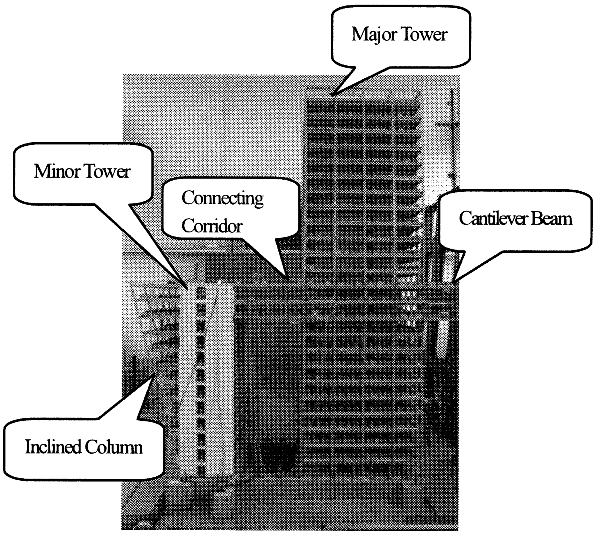

Figure 2 Structural Elevation of SHIDC Model

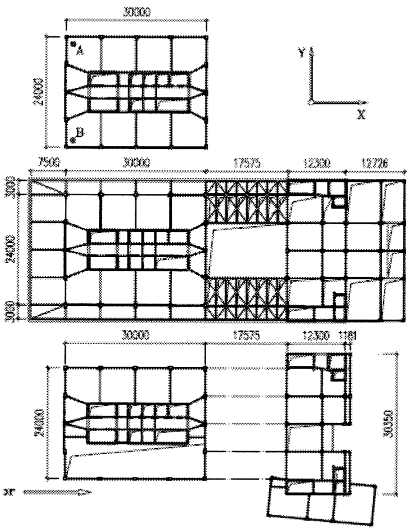

Figure 3 Plan Layouts of SHIDC

The structure consists of a major tower, a minor tower and a 4-storey podium adjacent to the minor tower. The major tower is 25-storey with a height of 99m, while the minor tower is 12-storey with a height of 48m. Both towers are steel frame-reinforced concrete tube system. There are 7.5m-span cantilever floors at the middle height of the major tower from story 11 to story 13. Five inclined columns (the inclined angle is 15°) in the east of the minor tower support cantilever beams at each storey. The connecting corridor consisting of steel trusses spans 17.5m to join the two towers rigidly between storey 11 and storey 12.

According to Chinese Code for Seismic Design of Buildings (GB50011-2001, 2001) and Technical Specification for Concrete Structures of Tall Building (JGJ3-2002, 2002), the main characteristics of SHIDC structure can be summarized as follows.

1. In the plan layouts, there are large openings exist in continuous seven stories of the Major Tower, whose area is over 30% floor area and beyond the limitation of the Chinese Code. Second, the length of the cantilever floor adds up to 7.5m and it locates at 50m above the ground, which may potentially vibrate during the strong earthquake.
2. In the elevation, SHIDC is a two-tower-connected hybrid structure and structural height of the Major Tower is two times of the Minor Tower. China has built many single-tower buildings using RC core walls in conjunction with steel perimeter steel frame, but it has no experience in designing a different-height multi-tower hybrid systems. And, there are five inclined steel columns in the Minor Tower, which are easier to buckling under non-uniformly distributed loads.

Given the above irregularities and complexity of the structure, it is necessary to precisely study SHIDC seismic behavior and evaluate its performance to resist designed earthquakes.

3. SHAKING TABLE TEST OF SHIDC

3.1 Shaking Table Facility

The MTS shaking table used for the testing can input three-dimensional and six degree-of-freedom motions. It has a dimension of 4m × 4m with a maximum payload of 250 kN. With a 150kN payload, the maximum accelerations are 1.2g, 0.8g and 0.7g for the horizontal, transverse and vertical directions, respectively. Its working frequency ranges from 0.1Hz to 50Hz and 96 channels are available for data acquisition. (SLDRCE, 2003)

3.2 Building Model Material

Material properties are very important in the dynamic model tests. According to the purpose of experiment, shaking table models can be classified into two categories: elastic model and strength model. The material of the former does not need to be exactly the same as that of the prototype provided that it remains elastic during testing and has the same distribution of mass and rigidity as the prototype structure. However, the similitude of elastoplastic material between the model and the prototype is essential in the strength model. (Lu et al. 2007a) Thus, based on past experiences, copper plates were applied to simulate the steel structural members and fine-aggregate concrete with fine wires were chosen to construct the RC components in SHIDC model.

3.3 Similitude Relationship

Corresponding to the fact that the dynamic behavior of a structure is fully described by means of three basic quantities, only three model quantities can be arbitrarily selected in dynamic problems. (Sabnis et al. 1983) Practically, the similitude equilibrium in the dynamic test is given in Eq. (1), where S_l, S_E, S_a, S_ρ is scaling factor of dimension, elastic modulus, acceleration, density, respectively.

$$\frac{S_E}{S_\rho \cdot S_a \cdot S_l} = 1 \tag{1}$$

First, based on the capacity and the size of the shaking table, the scaling factor of dimension S_l was chosen to be 1/15. SHIDC model was thus built with a height of 6.6m. Second, since the prototype structure was made of concrete and steel, the overall scaling factor of elastic modulus S_E should be determined by two kinds of materials. It also should be noted that there is a distinct decrease in elastic modulus when copper is welded. According to the material test results, the overall scaling factor of elastic modulus was determined to be 0.35. Third, considering the capacity of the shaking table and avoiding the disturbance of the noise, the scaling factor of acceleration was set to be 2.5. The total height of the model, including the additional artificial mass, was estimated to be 195 kN. All the other scaling factors could be derived and the typical factors are listed in Table 1. It is still difficult to have the same stress scaling factor for both aggregate and steel bars. Therefore, the strength alternation in structural members should be considered in the model design, as shown in the work by Lu et al. (2007a).

The complete elevation of SHIDC test model is shown in Figure 2.

Table 1 Typical Scaling Factors of SHIDC Model

Parameter	Relationship	Model/prototype
Length	S_l	1/15
Elastic modulus	S_E	0.35
Stress	$S_\sigma = S_E$	0.35
Strain	S_σ / S_E	1.00
Density	$S_\sigma / (S_a \cdot S_l)$	2.10
Force	$S_\sigma \cdot S_l^2$	1.56E-03
Frequency	$S_l^{-0.5} \cdot S_a^{0.5}$	6.12
Acceleration	S_a	2.50

3.4 Test Program

There were 70 sensors in total installed on the SHIDC model structure, which include 29 accelerometers on the ground, 6th, 9th, 11th, 13th, 15th, 20th and 25th story, respectively; 16 displacement transducers on the ground, 6th, 11th, 13th, 20th and 25th story, respectively; and, 25 strain gauges on surfaces of a few structural members such as lower shear walls and connecting trusses.

Base on the soft site condition of Shanghai, three ground motions were input during the test, include two strong earthquake records (El Centro record from California Imperial Valley earthquake and Pasadena record from California Kern County earthquake) and one Shanghai artificial accelerogram.

In Chinese Codes, Shanghai is assigned to earthquake zone of intensity 7 with peak ground acceleration (PGA) of 0.10g. A summary of the test inputs is listed in Table 2. The test was carried out in 5 stages. The first two stages represented frequent occurrence of intensity 7, while the next two stages simulated basic and rare occurrences of intensity 7, respectively. The last one represented the rare occurrence of intensity 8, which was utilized for further investigation of the SHIDC structure subjected extremely strong earthquakes.

Table 2 Test Program

Test Case	Stage	Input Signal	Peak value of input accel. (g)			Note
			Principal Direc.	Dire. Y	Dire. X	
1	Frequent Earthquake	WN 1		0.07	0.07	2D
2		El Centro	Y	0.09	0.07	2D
3			X	0.07	0.09	2D
4		Pasadena	Y	0.09	0.07	2D
5			X	0.07	0.09	2D
6		Shanghai Wave	Y	0.09		1D
7			X		0.09	1D
8	Frequent Earthquake 45°	WN 2		0.07	0.07	2D
9		El Centro	Y	0.06	0.06	1D
10			X	0.06	0.06	1D
11		Pasadena	Y	0.06	0.06	1D
12			X	0.06	0.06	1D
13		Shanghai Wave	Y	0.06	0.06	1D
14			X	0.06	0.06	1D
15	Basic Earthquake	WN 3		0.07	0.07	2D
16		El Centro	Y	0.25	0.21	2D
17			X	0.21	0.25	2D
18		Pasadena	Y	0.25	0.21	2D
19			X	0.21	0.25	2D
20		Shanghai Wave	Y	0.25		1D
21			X		0.25	1D
22	Rare Earthquake	WN 4		0.07	0.07	2D
23		El Centro	Y	0.55	0.47	2D
24			X	0.47	0.55	2D
25		Pasadena	Y	0.55	0.47	2D
26			X	0.47	0.55	2D
27		Shanghai Wave	Y	0.55		1D
28			X		0.55	1D
29	Rare Earthquake of Intensity 8	WN 5		0.07	0.07	2D
30		El Centro	Y	1.00	0.85	2D
31			X	0.85	1.00	2D
32		Pasadena	Y	1.00	0.85	2D
33			X	0.85	1.00	2D
34		Shanghai Wave	Y	1.00		1D
35			X		1.00	1D
36		WN 6		0.07	0.07	2D

4. EXPERIMENTAL RESULTS OF SHIDC MODEL STRUCTURE

4.1 Cracking and Failure Patterns

At the test stage of frequent earthquakes of intensity 7, no visible damage was observed. After the white noise 3 scanned the model, it was found that the frequencies in both Y and X directions reduced slightly. That is to say, micro-cracks of the model had already developed inside.

At the test stage of basic earthquakes of intensity 7, shear wall concrete of the Minor Tower first appeared cracks at storey 3 while the Major Tower remained undamaged. Steel beams at the connecting corridor began to buckling. The results of the white noise showed the stiffness of the structure decreased noticeably.

At the test stage of rare earthquakes of intensity 7, existing crack developed. For the Major Tower, cracks appeared at the RC coupling beam ends from storey 10 to storey 13. An obvious crack was observed at the connected end of the cantilever slabs at story 13 due to negative moment (Fig. 4(a)). For the Minor Tower, new cracks appeared at the coupling beam ends from storey 4 to storey 12 and at the bottom corner of the shear walls. More beams of the connecting corridor buckled.

At the test stage of rare earthquakes of intensity 8, existing cracks remarkably propagated. For the Major Tower, more cracks spread at the coupling beam ends and new cracks were also found on the shear walls at storey 5 and storey 15. The Minor Tower damages badly in the middle and bottom part of the shear walls and at most of the coupling beam ends (Fig. 4(b)). For the connecting corridor, welded beams of the steel truss ruptured at joints (Fig. 4(c)), and steel beams buckled obviously out-of-plane (Fig. 4(d)).

From the observation, it can be concluded as follows.

1. The RC core wall of the Major Tower stayed undamaged until the rare earthquake of intensity 7, while that of the Minor Tower cracked at the former stage, i.e., basic earthquake stage.
2. There is no obvious buckling observed in the perimeter steel frame members, even in the inclined steel columns.
3. Rigid joints between the steel truss and the core walls worked well but steel members buckled under the earthquakes.
4. Those cantilever slabs located so high that they damaged more severely than those in the expected design.

4.2 Experimental Dynamic Characteristics

The first three vibration modes were translation in Y, translation in X, Torsion, respectively. Figure 5 gives the values of the first three frequencies at different experimental stages. It can be seen that all three frequencies decreased with the increase of the strong earthquake input. The first frequency decreased from 2.382Hz to 1.191Hz and the second frequency from 3.573Hz to 1.786Hz. Thus, the equivalent stiffness decreased about 75% when the model underwent the earthquake of intensity 8.

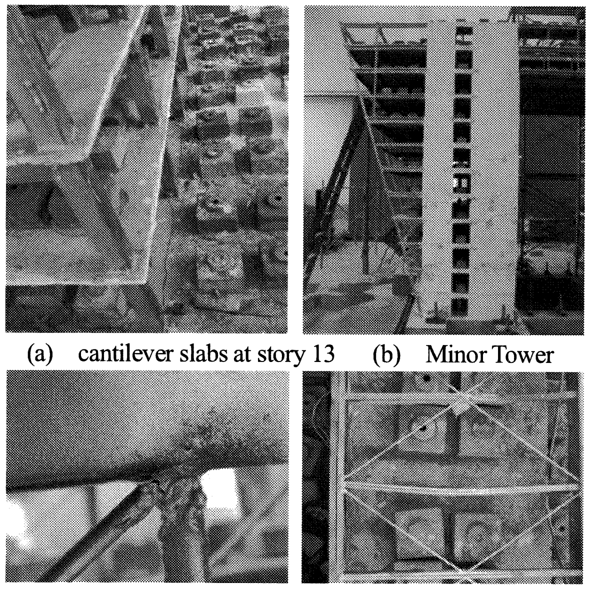

(a) cantilever slabs at story 13 (b) Minor Tower

(c) joint at the corridor (b) steel beams at the corridor

Figure 4 Failure Pattern of SHIDC Model

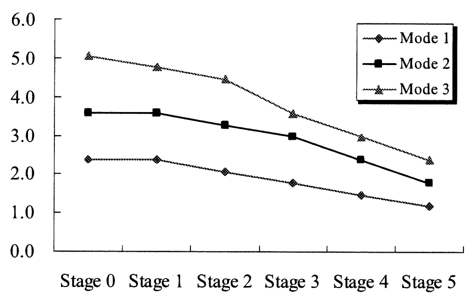

Figure 5 Frequencies at Different Stages

5. EXPERIMENTAL RESULTS OF SHIDC PROTOTYPE STRUCTURE

5.1 Dynamic Characteristics

Model frequencies can be extrapolated to the prototype structure by the similitude relation (Eq. 2). The first six experimental frequencies are summed up in Table 3.

$$f_p = f_m / S_f \tag{2}$$

Table 3 Dynamic Characteristics

Period	Test (s)	Analysis (s)	Mode
T1	2.571	2.37	Translation in Y
T2	1.715	1.42	Translation in X
T3	1.211	1.18	Torsion
T4	0.734	0.73	Translation in Y
T5	0.587	0.62	Torsion
T6	0.467	0.47	Translation in X

5.2 Inter-story Drift

The method of acceleration integration is used here to achieve the final results of displacement. The inter-story drift is calculated by subtracting the lateral displacements of two adjacent floor levels. Table 4 presents the maximum displacement, total displacement/height, maximum inter-story drift, and base shear force/weight of the prototype structure.

It can be shown that the inter-story drifts under frequent earthquake occurrence are 1/778 in direction Y and 1/ 1234 in direction X, which in direction Y is slightly beyond the code requirement of 1/800. At the rare earthquake stage of the designed intensity 7, inter-story drift increase to 1/114 in direction Y and 1/235 in direction X, both of which are smaller than the elastoplastic inter-story drift limitation of 1/120 for hybrid systems.

Table 4 Displacement Responses and Base Shear Force/Weight Ratios

		Stage 1: F7	Stage 2: F7	Stage 3: B7	Stage 4: R7	Stage 5: R8
Max. Dis. (mm)	Y	97.98	63.14	235.43	581.04	1502.68
	X	34.79	46.32	127.21	278.85	722.96
Total Dis. /Height	Y	1/981	1/1522	1/408	1/165	1/64
	X	1/2762	1/1949	1/755	1/344	1/133
Max. Inter-story Drift	Y	1/778	1/841	1/293	1/114	1/46
	X	1/1234	1/866	1/178	1/235	1/86
Base Shear Force/ Weight (%)	Y	3.16	2.94	8.96	15.02	29.98
	X	3.26	2.40	6.12	11.92	23.47

5.3 Shear Force

The story shear is calculated by summing the individual floor inertia forces at each floor above that story; these inertia forces are calculated by multiplying the measured absolute acceleration by the floor weight. Distributions of storey shear force in direction Y and direction X are figured in Figure 6. The base shear force/weight ratios are listed in Table 4.

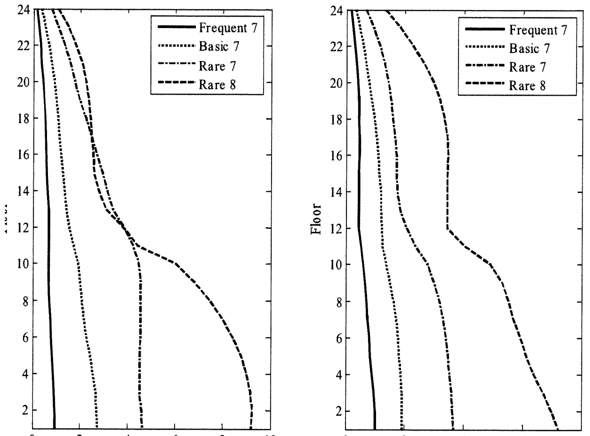

(a) direction Y (b) direction X
Figure 6 Storey shear force distribution

6. NUMERICAL ANALYSIS OF SHIDC STRUCTURE

The computer program ETABS was employed for the elastic dynamic analysis of the prototype structure (ETABS, 2000). The steel frames were modeled by the frame elements in the program, and for the slabs and RC tubes, the shell elements were employed to simulate their mechanical behaviors.

6.1 Dynamic Characteristics

The first three modes of vibration obtained from the numerical analysis are shown in Figure 7. The comparison of the analytical periods to the experimental results is shown in Table 3 and they agreed well with each other. The ratio of the first torsion period to the first translational period is 0.5, which is less than the Chinese code limitation of 0.9.

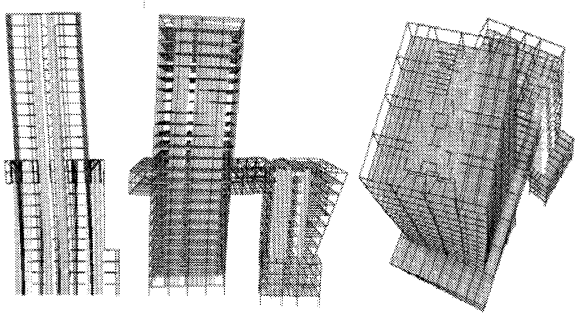

(a) first mode (b) second mode (c) third mode
Figure 7 Mode Shapes of SHIDC Analytical Model

6.2 Time History of the Displacement

Based on the results of the dynamic characteristics, the time history analysis was carried out. Figure 8 shows the time history of the roof displacement of the Major Tower under Shanghai accelerogram input. The numerical results are in fair agreement with the experimental ones. The maximum value in X direction is about one third of that in Y direction, which implies the greater lateral stiffness in X direction contributed by the connecting trusses.

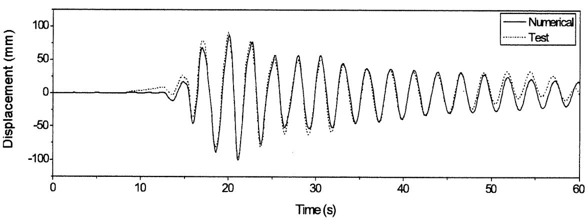

(a) Direction Y

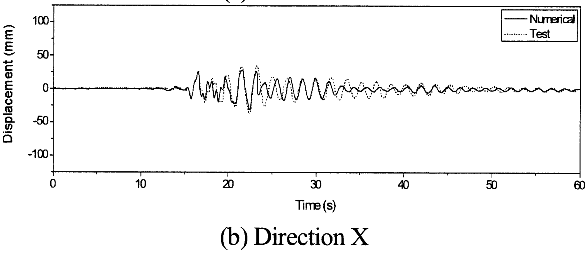

(b) Direction X
Figure 8 Time History Comparison of the Displacement

6.3 Time History of the Shear Force

Figure 9 is the comparison of the time history of the base shear forces obtained from the numerical simulation and the shaking table test under Shanghai accelerogram input. The maximum ratios of base shear to structural weight in both X and Y directions met the code requirement of 1.6%.

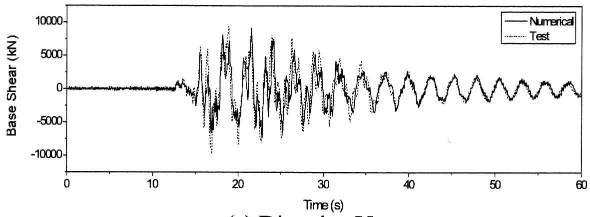

(a) Direction Y

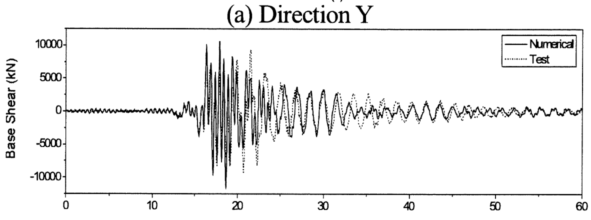

(b) Direction X

Figure 9 Time History Comparison of the Shear Force

7. CONCLUSIONS

Shanghai International Design Center (SHIDC) is a hybrid tall building with two different-height towers connecting together, which is extremely irregular in both plan and elevation. As suggested by the peer review committee, shaking table model test was carried out at the State Key Laboratory for Disaster Reduction in Civil Engineering, Tongji University, China. And linear dynamic numerical analysis was also performed to compare with the experimental results. The seismic performance of SHIDC structure was evaluated based on the dynamic test and numerical analysis as follows.

1. The irregular structure can resist designed frequent earthquakes without damage, resist basic earthquakes with some structural cracking and deformation, and resist rare earthquakes with some major damage, but without catastrophic collapse.
2. When the structure is subjected to earthquake waves of frequent stage, the maximum inter-storey drift in direction Y is 1/778, which is slightly greater than the allowable value of 1/800 according to Chinese code.
3. The RC core wall of the Major Tower stayed undamaged until the rare earthquake of intensity 7, while that of the Minor Tower cracked at the basic earthquake stage. Steel columns are suggested to be encased as the boundary columns of the Minor Tower, as shown in the work by Wada and Wallace (1998), which will contribute to the seismic behavior of the Minor Tower and to the displacement of the overall building.
4. There is no obvious buckling observed in the perimeter steel frame members and the force distribution between the core walls and steel frames is reasonable.
5. Rigid joints between the steel truss and the core walls worked well but steel members buckled under the earthquakes, which successfully denote the structural strong-columns-weak-beam concept.
6. The strength and the stiffness of the cantilever floors need to be improved considering the dynamic effect.
7. Nonlinear numerical analysis will be performed for better evaluating the structural performance.

Acknowledgements:

The authors are grateful for the financial support in part from the National Natural Science Foundation of China (Grant No. 50708071), National Key Technology R&D Program (Grant No. 2006BAJ13B01), 973 Program (Grant No. 2007CB714202), Shanghai Educational Development Foundation, and Program for Young Excellent Talents in Tongji University. Doctoral students and professor contributed to the research presented here are also acknowledged, including Zhihua Huang, Linzhi Chen, and Prof. Wensheng Lu.

References:

ETABS. (2000), "ETABS Integrated Finite Element Analysis and Design of Structures", Computer and Structure Inc, Berkeley, CA, USA.

Katayama, T. (2005), "Construction of E-Defense - A Large-sized 3-dimensional Shaking Table," *Proceedings of the First Conference on Advances in Experimental Structural Engineering*, **1**: 29-37.

Ko, D. W. and Lee, H. S. (2006), "Shaking table tests on a high-rise RC building model having torsional eccentricity in soft lower storeys," *Earthquake Engineering and Structural Dynamics* , **35**(11), 1425-1451.

Lu, X. L., Zhou, Y. and Lu, W. S. (2007a), "Shaking table model test and numerical analysis of a complex high-rise building," *The Structural Design of Tall and Special Buildings*, **16**(2), 131-164.

Lu, X. L., Zou, Y., Lu, W. S., *et al.* (2007b), "Shaking table model test on Shanghai World Financial Center Tower," *Earthquake Engineering and Structural Dynamics*, **36**, 439-457.

Pavese, A., Lai, C. G., Calvi, G. M., *et al.* (2005), "Reaction Mass and Foundation Design of the High Performance, One-degree-of-freedom EUCENTRE Shaking Table, in Pavia (Italy)," **1**, 513-524.

Sabnis, G. M., Harris, H. G., White, R. N., *et al.* (1983), "Structure Modeling and Experimental Techniques," Englewood Cliffs, NJ.

Tezcan, S. S. and Alhan, C. (2001), "Parametric analysis of irregular structures under seismic loading according to the new Turkish earthquake code," *Engineering structures*, **36**(6), 600-609.

Tong, D. L., Xi, C. W., Li, J. G., *et al.* (2007), "Shaking Table Model Test of the Twin-Tower Connecting Tall Building with Transfer Story," *Proceedings of the Second International Conference on Advances in Experimental Structural Engineering*, **1**, 338-345.

Tremblay, R., Velev, N., Merzouq, S., *et al.* (2005), "Multipurpose Earthquake Simulation Testing Set-up for Seismic Force Resisting Systems of Multi-Storey Buildings," *Proceedings of the Second International Conference on Advances in Experimental Structural Engineering*, **1**, 533-540.

SLDRCE. (2003), "Introduction of Shaking Table Testing Division," State Key Laboratory for Disaster Reduction in Civil Engineering, Shanghai, China.

Wada, A. and Wallace, J. (1998), "Report of the Working Group on Hybrid Wall Systems", U.S.-Japan Cooperative Earthquake Research Program on Composite and Hybrid Structures, Tokyo, 23-36.

"Code for Seismic Design of Buildings," (GB50011-2001), China Ministry of Construction, Beijing, 2001.

"Technical Specifications for Concrete Structures of Tall Building," (JGJ3-2002), China Ministry of Construction, Beijing, 2002. (In Chinese)

CYCLIC TESTS ON WOOD PANEL RESTRAINED STEEL SHEAR WALLS WITH SLITS

Toko Hitaka[1] and Taketo Soejima[2]

1) Associate Professor, Disaster Prevention Research Center, Kyoto University, Japan
2) Graduate, Faculty of Human Environmental Studies, Kyushuo University, Japan
toko.h@ay2.ecs.kyoto-u.ac.jp

Abstract: A new type of earthquake-resisting element, consisting of a steel plate shear wall with vertical slits, is studied. In this system, the steel plate segments between the slits behave as a series of flexural links, which provide a fairly ductile response without the need for significant out of plane stiffening of the wall. In order to extend this system, thin steel plates (1.2 – 2.3 mm) are used as opposed to thicker plates. To avoid premature failure due to global out of plane buckling, the steel plates are restrained by 12 to 24 mm thick wood panels. Wood panels are attached by sliding bolts, ensuring that no additional lateral stiffness is provided. Of these shear walls, eight specimens are tested under cyclic lateral loading; the results show hysteretic loops that are stable and mostly independent of the thickness of the wood panel, negligible strength degradation, associated to material hardening compensating strength loss due to buckling, and a significant improvement in the energy dissipation capacity when compared to the unrestrained steel shear walls.

1. INTRODUCTION

The subject of this paper is the hysteretic characterization of thin steel plate shear walls with slits ("Slit walls" hereafter) which use wood panels to restrain out of plane buckling. These earthquake resisting elements are connected to moment frames by high-strength tension friction bolts. The wood panels provide out of plane buckling confinement to the slit walls, but do not participate in any direct way in the lateral load resistance. The basic concept behind these walls is for the steel plate between the slits to behave as a series of flexural links, which undergo large flexural deformations relative to their shear deformation..

Figure 1(a) shows the floor schematics of a Japanese residential building (AIJ 2005). Two particular characteristics can be observed in the direction perpendicular to the beams:

1. Openings for window are large and abundant, with RC walls placed between this openings to provide lateral resistance. Also,
2. RC walls are relatively thin (an average of 150 mm) when compared to typical structural RC walls.

Generally speaking, existing damping devices' cross section is large, and to have a significant effect on the structure they must be placed on every span of the building. These shortcomings make the installation of such devices difficult in buildings that comply with restrictions 1 and 2. In response, the purpose of this research is to develop a new hysteretic damper for such structural typology. The proposed device is easier to fabricate and install.

In the framework of this research, 9 specimens featuring thin steel plates (1.2 and 2.3 mm) and different levels of out-of-plane restraining provided by wood panels, were tested under cyclic loading. Non-linear FEM analysis is being performed on equivalent models that will provide an analytical verification to the

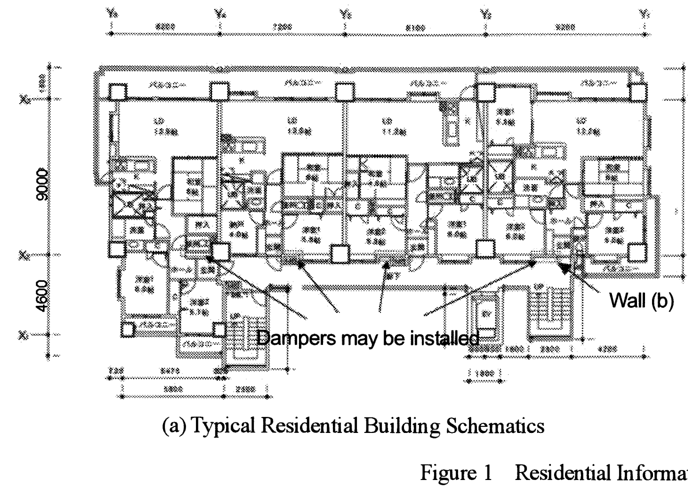

(a) Typical Residential Building Schematics

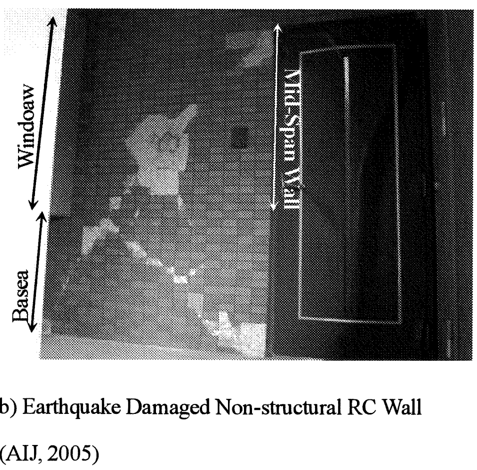

(b) Earthquake Damaged Non-structural RC Wall

Figure 1 Residential Information (AIJ, 2005) experimental background for the development of these devices.

2. Behavior characterization of slitted shear walls

The slitted shear walls, as shown in Figure 2, are made of a steel plate with a series of slits. When subjected to seismic input, the links formed by the slits bend. The elastic stiffness (K_{wt}) and the ultimate force (Q_{wtu}) are calculated using the following equations (Hitaka 2003) :

$$K_{wt}=\frac{1}{\frac{\kappa(h-ml)}{GBt}+\frac{\kappa l}{Gbt}\cdot\frac{m}{n}+\left(1+\alpha^{-1}\right)^2\cdot\frac{l^3}{Etb^3}\cdot\frac{m}{n}}$$
$$\cong\frac{1}{1+\frac{G}{\kappa E}\cdot\left(1+\alpha^{-1}\right)^2\cdot\alpha^2\beta}\cdot K_{wo} \qquad (1)$$

$$Q_{wtu}=\alpha^2\left(1-cos\frac{\sqrt{3}}{\alpha}\right)\cdot Q_{wty} \qquad (2)$$

where, E = Young's Modulus, G = shear modulus, κ = shear deformation shape factor (=1.2 for rectangular section), α = aspect ratio of the shear links (=l/b, where l = length and b = width of flexural links) and β = ratio of total link length in the vertical direction to the wall height (= ml/h), for other parameters, refer Figure 2. In Eq. (2), Q_{wty} is the yield strength, calculated with Eq. (3),

$$Q_{wty}=\frac{ntb^2}{2l}\cdot\sigma_y\cong\frac{\sqrt{3}}{2\alpha}\cdot Q_{wo} \qquad (3)$$

In Eq. (3), Q_{wo} is the shear yield force of the steel plate (without slits) ($=Bt\sigma_y/\sqrt{3}$). In addition, the following equation is proposed to calculate the horizontal displacement (δ_{wtu}) from the previously calculated value of Q_{wtu}. In Eq. (4), ε_y is the yielding strain of the steel plate.

3. TESTS

3.1 Design of Shear Walls

As shown in the floor schematics of the apartment building in Figure 1(a), the floor area (including balconies and aisles) of each story is 412 m^2, and there are 3 to 4 locations in the sides of the aisles, where the proposed damper can be installed. The gravity loads due to dead and live cases is 1.3 t/m^2, base shear factor is 0.3. The design goal for the dampers intervention is to sustain a 10% of the total building shear force. This can be achieved by using 3 dampers with a capacity of 630 kN. The test specimen was fabricated in a 1:2 scale with the original shear wall needed ($630/2^2$ = 160 kN). Japanese standard SS400 steel was used for the plates, with a total width of 800 mm; as for the shape of the slits (*m, b, l, α* in Figure 2) is the same for all the specimens (see Figure 3(a)). Plate thickness for the specimen is 2.3 mm and, in this case, by assuming a yield stress of 300 $N=mm^2$ for the steel, the ultimate force of the shear wall calculated according to Equation 1 is 128 kN. A total of 9 specimens were tested, divided into 6 element specimens and 3 combined-wall specimens.

3.2 Specimens

Regarding the element specimens, shown in Figure 3(a), the connection to the reaction frame is done at the top and bottom 100 mms of the plate by steel angles with friction connections. The remaining height between the steel angles (600 mm) sustains the shear deformation. The objective behind the element specimen test is to study the efficacy of wood panels as an out-of-plane deformation restrainer. Consequently, the first parameter of the experiment is the thickness of the wood panel (12-24 mm), and the second parameter is the thickness of the slitted steel plate (1.2 or 2.3 mm).

The proposed use for combined-wall specimen is in nonstructural walls as an amalgam of a base wall and a midspan wall. Damage in RC nonstructural walls (as reported in Reference 1), is small in the base wall and mainly concentrated in the midspan wall. The same principle applies to the combined walls.

Considering that the combined-wall specimens (1100 mm in height), the part corresponding to the midspan wall is slitted (600 mm) and the base wall is not (500 mm). For out-of-plane deformation restraining, two different methods were adopted: the first method consists of restraining the slitted section with wood panels, and embedding the non-slitted section in an RC wall (tests specimens E-SW and UBWP). The second method is restraining both the slitted and the non-slitted parts with wood panels, where the steel plate of the non-slitted section is thicker than the slitted section to avoid buckling (E-WP, F-WP). Taking into account preliminary experimental results obtained for the E-WP series (see below for further explanation), the F series studies dampers with welded connections to the steel frame, and uses thicker steel plates in the non-slitted section and wood panels than those used for the E-WP series (see Table 2). In this paper, details about the reaction frame have been omitted. The column shear force (equivalent to the shear force in the wall) is calculated indirectly by measuring the strain in the column flange, which works only for elastic behavior.

Mechanical characteristics of the steel used for the walls and bolts are shown in Table 3. Wood panels are made of 5-12 layers thick plywood. Flexural behavior of these panels were studied prior to the tests, which was linear elastic until, maximum strength, was reached. At this point the plywood layers separate and the moment decreases.

Nineteen SS400 (JIS) 8mm diameter steel bolts are used to attach the wood panels to the steel plates in each specimen. The bolts are passed through perforations in the steel plates. These perforations are oversized with respect to the bolt diameter in order to avoid transference of the lateral force to the wood panel during loading.

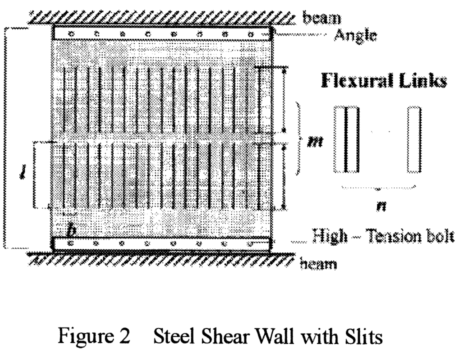

Figure 2 Steel Shear Wall with Slits

Table 1 Specimens

	Specimen	OPS	SPH (mm)	WPT (mm)	SPT (mm)	CUS (kN)	EUS (kN)	CS (kN/mm)	ES (kN/mm)
Element	NST-s23	no	600(+100x2 connection)	-	23	115	42	56	67
	WP12-s12	wood panel		12	12	71	81	32	37
	WP21-s12			21	12	71	76	32	28
	WP18-s23			18	23	123	131	60	76
	WP24-s23			24	23	123	118	60	58
Wall	E-WP		1100	18	23	123	113	48	61
	E-SW-WP			18	23	123	132	60	75
	F-WP			24	23	135	149	47	46

OPS: out of plane stiffening, SPH: steel plate height, WPT: wood panel thickness, SPT: steel plate thickness, CUS: calculated ultimate strength, EUS: experimental ultimate strength, CS: calculated stiffness, ES: experimental stiffness

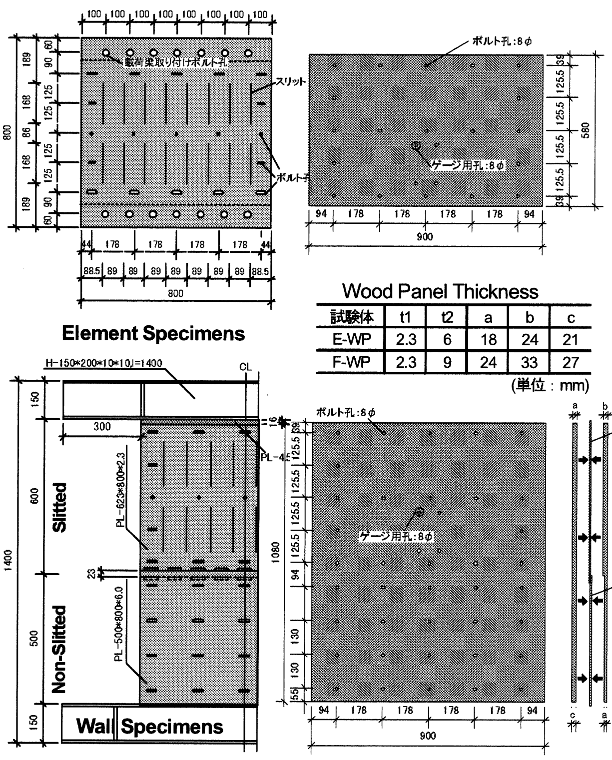

Figure 3 Specimens

Table 3 Steel Mechanical Properties

	σ_y (N/mm^2)	σ_u (N/mm^2)	Elongation (%)
s12	297	370	32.2
s23	278	359	40.0
s23(F)	310	387	35.9

Considering the relatively small piercing strength of the plywood panels, 3 mm (F-WP) and 2.3 mm (others) thick, 30mm long square washers were used. The test setup did not affect the maximum tensile strength of the bolt. An average maximum of 9 kN was obtained with a low dispersion, whereas the dispersion of maximum extension was large.

3.3 Loading and Measurement

Loading procedure for the frame specimen F-WP consisted of three cycle at every 0.25% of drift angle (3mm for the test specimen) up to a 2%. For the E-series combined-wall specimens and the element specimens, two cycles at every 3 mm of lateral deformation (to perform the conversion between drift angle R and lateral deformation, divide the lateral deformation by 1200 (i.e. 3mm 3/1200=0.25%)). However, specimen E-WP, when R=-1% (second cycle), a malfunction in the lateral deformation measuring device increased the drift angle to -2%. Lateral and vertical displacement measurement was done using transducers.

4. TEST RESULTS

4.1 Hysteretic Characterization and Damage

The relation between the lateral force and drift angle for each specimen is shown in Figure 4. In the plots, the horizontal dashed line shows the ultimate force (Q_{wtu}) calculated with Equation 2; vertical dashed line shows the drift angle corresponding to δ_{wtu} (R_{wpt}) calculated with Equation 4. In addition, Table 1 shows Q_{wtu} and initial stiffness (K_{wt}) calculated with Equation 1. Also, Figure 6 shows pictures of different element specimens after the conclusion of the experiment.

Element Specimens: In the specimen without out of plane restraining, the initial stiffness is almost the same as K_{wt} but after the drift angle reached R=0.2% buckling occurs and the stiffness decreased along the global buckling as shown in Figure 5(a). Specimens with out-of-plane restraining sustained similar behavior and deformation (Figure 5(b)), independent of the thickness of the steel plate and wood panel. Plastic behavior initiates for a drift angle of 0.1% and Q_{wtu} is closely related to R_{wpt}. After yielding, further hysteretic cycles are of stable slip type despite small strength deterioration and out of plane deformation.

A possible explanation for the slip behavior of the specimens, is based on local out of plane buckling of the steel plate in the vicinity of the end of the slits, which was observed after the experiments (Figure 6(a)). The specific strength of wood is large, but the piercing strength is very small (around 3 N/mm^2). On the

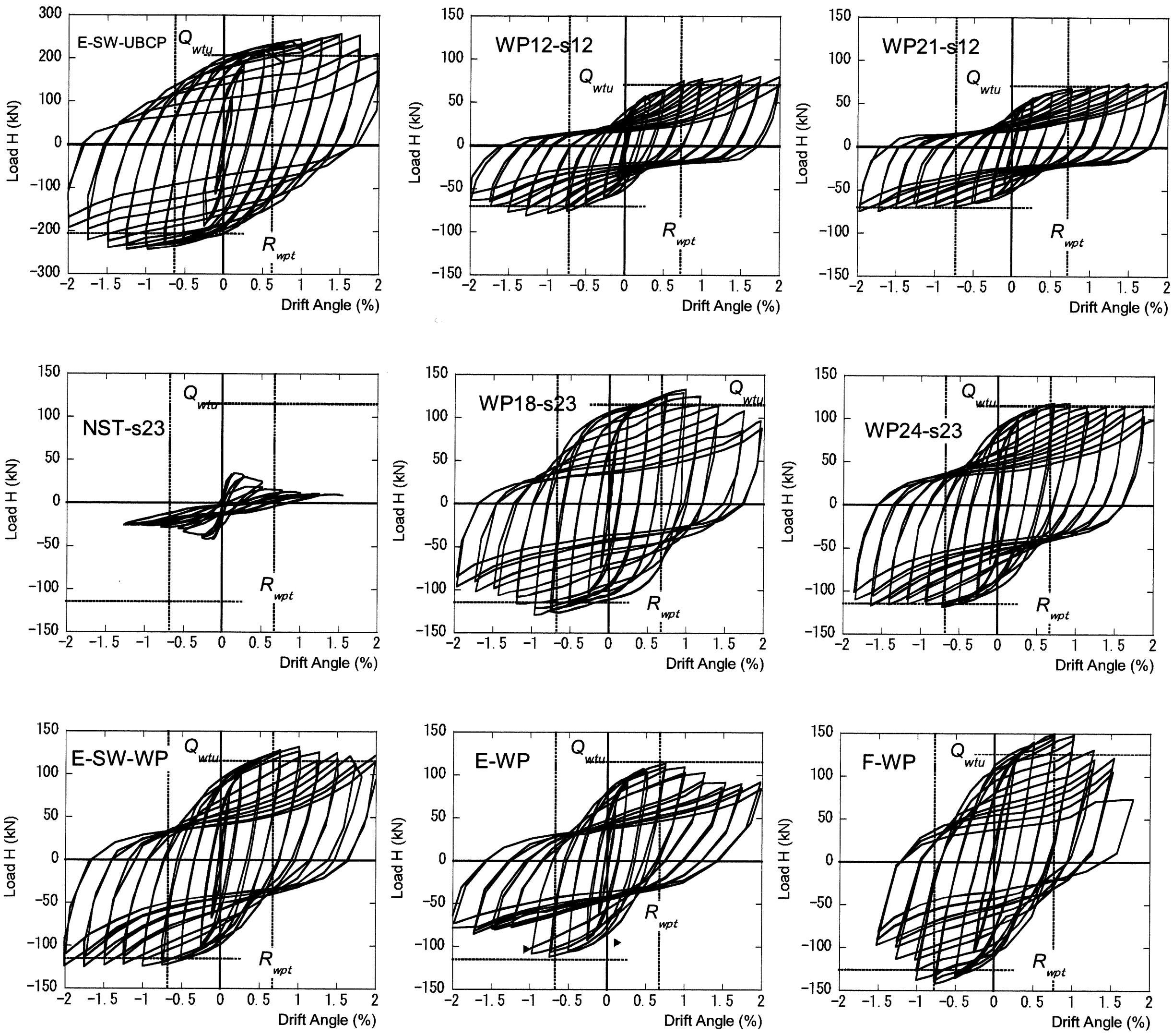

Figure 4 Horizontal Force –Story Drift Relation

other hand, because the steel plates are thin (less than 2.3mm) the buckling wavelength occurs inside the plastic zone. Therefore, local out of plane buckling is likely to occur. The data measured from strain gages attached to both faces of the steel plate at the end of the slits suggests that such local buckling initiated at the same time as the slip behavior began.

Fractures spread from the end of the slits along the local out of plane buckling zone (Figure 6(b)). These fractures are likely to have caused deterioration of strength. For the other specimens, although there seems to be no damage on the wood panels, fractures appeared, starting at the bolt perforation and advanced to the side of the steel plate, as is can be seen in Figure 7(b). However, there is almost no strength deterioration because the wood panels remain undamaged.

The behavior of specimens WP18-s23 and WP12-s12 particularly differs from the other specimens. In specimen WP18-s23 the hysteresis loop has a rounded shape until R=1%, but when R 1.25% the strength notoriously deteriorates. Also, as shown in Figure 6(c), cracks develop at mid-height between the end of the slits on both upper and lower ends, constituting one slit with a length of $2l+b$, instead of two l long slits. If the length of the shear links is changed from l to $2l+b$, the ultimate strength changes from $tb^2\sigma_y/(2l)$ to $tb^2\sigma_y/(4l + 2b)$, in other words, the strength of WP18-s23 decreases. In the experiment using 4.5 mm thick steel plates restrained by mortar panels, crack development and strength deterioration also occurs in a similar fashion as seen on specimen WP18-s23 (the hysteresis loop is shown the Figure 4 (E-SW-UBCP)). As it can be observed in Figures 5(c) and 5(b), out of plane deformation of WP18-s23 is smaller than WP24-s23, and also, buckling initiates at a larger drift angle than for the other specimens. A possible explanation for the delayed initiation of out of plane deformation of specimen WP18-s23 is that original imperfections of this test specimen are smaller than in the other test specimens.

In addition, in specimen WP12-s12, when loading in the negative direction to a drift angle larger than 1.25%, the strength also deteriorates slightly. As explanation for this strength deterioration (better use other expression) is the damage sustained

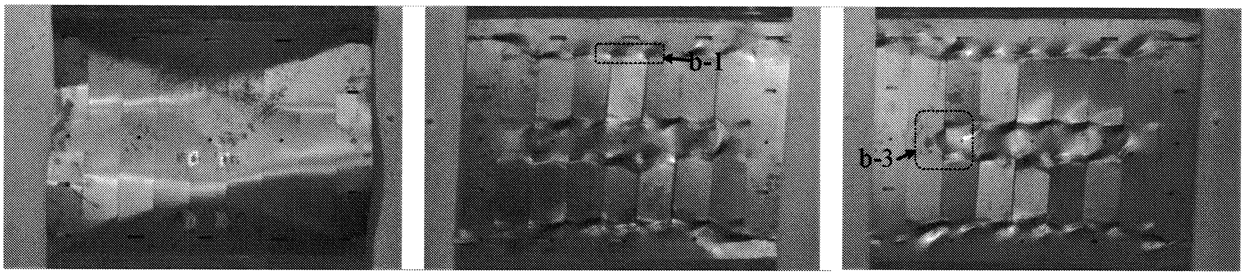

(a) NST (b) WP24-s23 (c) WP18-s23

Figure 5 Damaged state (panoramic view of test specimens)

(a) Local buckling (WP24-s23) (b) Buckling cracking along the slit edges (c) Fracture of WP18-s23

Figure 6 Damage (cracking and deformation in the slit edges)

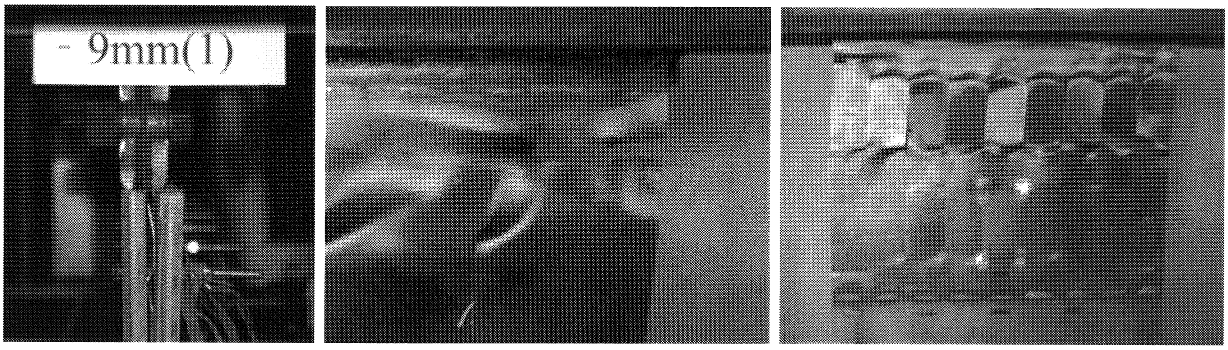

(a) Local buckling (WP12- s12) b) Fracture of steel plate (E-WP) (c) Out of plane deformation concentrated in the upper section

Figure 7 Damaged state (Bolt perforation vicinity)

by the wood panels in the vicinity of the corner bolts. A detail of this is shown in Figure 7(a) for R=+0.75%. The steel plates are affected by compression forces originated by the bending moment on both ends of the wall, where large plastic deformation occurs. The s12 series is particularly affected by this phenomenon, mainly because of the small thickness of the steel plate. As shown in Figure 7(a), out of plane deformation occurs with a very short wavelength. In specimen WP12-s12 wood panel thickness is small, so that the damage sustained by the wood panels after cycle R=+1.25% causes the strength deterioration.

Combined-wall Specimen: In the case of the combined-wall specimen, the behavior observed for specimen E-WS-WP is similar to the one of the element specimen. In the non-slitted mortar restrained part, cracking mainly occurs on the sides of the steel plate.

On the other hand, for E-WP specimens, strength at R_{wpt}, is a 9% less than the expected value for Q_{wtu}. A possible explanation for this is the larger out of plane deformation that takes place in E-WP specimens, as explained in the next section (refer to the next section). In addition, it is difficult to compare the hysteretic loops when R≥1% because the loading procedure differs from the other specimens, nonetheless, strength deterioration is larger than in E-SW-WP specimen. A possible explanation is that out of plane deformation takes place only (i.e. deformation concentrates in the uppermost links. So the maximum scale of out-of-plane disp. is larger in these two specimens than the others) on the uppermost shear links, shown in Figure 7(c) (as seen after the experiment). Figure 6(b) shows crack initiation at the end of the slits for specimen E-WP, where intensive out of plane deformation is observed, crack length is around twice as long as for specimen E-WS-WP. As Figure 6(b) shows, crack causes a decrease of b in Equation 3 (therefore, the ultimate force decreases). It is thought by the authors that strength deteriorates as cracks advance. Taking the large out of plane deformation of specimen E-WP into consideration, a thicker wood panel and steel plate for the non slitted section are used in the F- WP specimen. The maximum strength of specimen F-WP is larger than the ultimate strength in Equation 3. Until R=1%, the hysteretic behavior is similar to specimen E-SW-WP and the out of plane deformation is not as large as in specimen E-SW-WP. Therefore, the effect of increasing the element sections is recognized as out of plane stiffness increases. However, from R≥1.25% strength remarkably deteriorates and, as observed for specimen E-WP, intensive out of plane deformation is observed in the upper side shear links. As a consequence, the uppermost bolts reach failure stress for R≥1.0%. And, considering that for R=1.75% all the upper side bolts had failed, loading was stopped. Bolt failure causes the out of plane stiffening to deteriorate and utterly disappear; hence specimen F-WP strength deterioration.

5. CONCLUSIONS

Seismic behavior of the wood panel restrained slitted steel plates were studied through tests on five element specimens and three wall specimens.

Wood panel restrained slitted steel plates were testeshow plastic behavior in early stages (drift angle around 0.1%) and the behavior shown does not present major strength deterioration until the drift angle is larger than 1.5%, hence, slitted steel plates are appropriate to use as hysteretic dampers.

Out of plane restraining by wood panels provides sufficient control over buckling for the proposed application. However, since the piercing resistance of wood is small, it is difficult to control local out of plane buckling in the plastic zone in the vicinity of the slit ends. Therefore, the slip shape observed for the hysteretic loops. In spite of this fact, it was observed that the slip occurs after the ultimate strength is reached at 0.6 - 0.7% story drift.

The combination of slitted and non-slitted sections can be interpreted as the combination of a midspan wall and a base wall, and the behavior of the damper is similar to the use of an element specimen in combination with an RC wall. Out of plane restraining by wood panels is viable for controlling the bucking of the entire damper. However, since the out of plane deformation is concentrated in the upper side shear links, the deformation capacity is inferior.

Acknowledgements:

This research was funded by The Japan Iron and Steel Federation. The authors would express gratitude to the technical stuff and a graduate of Kyushu-university, Takayuki Iiya for their cooperation in test preparations. The authors would also thank Prof. Kawano of Kyushu University for his suggestions and Andres Jacobsen of Kyoto University for his help in writing this paper.

References:

Hitaka, T. and Matsui, C. 2003. Experimental study on steel shear wall with slits. *Journal of Structural Engineering, ASCE* Vol. 129, No. 5: pp.177-184.

AIJ. 2005. Report on the Damage Investigation of the 2005 West off Fukuoka Earthquake.

Fifth International Conference on Urban Earthquake Engineering
March 4-5, 2008, Tokyo Institute of Technology, Tokyo, Japan

EFFECT OF ASPECT RATIOS ON THE SEISMIC PERFORMANCE OF STEEL-CONCRETE COMPOSITE MEMBERS

H.-L. Hsu[1], J.-L. Juang[2], K.-T. Luo[3] and D.-S. Juang [1]

1) Professor, Dept. of Civil Engineering, National Central University, Taiwan
2) Post-doctoral research fellow, Research Center for Hazard Mitigation and Prevention, National Central University, Taiwan
3) M.S., Dept. of Civil Engineering, National Central University, Taiwan
t3200178@ncu.edu.tw, jjl1@ncu.edu.tw, t320006@ncu.edu.tw

Abstract: This study focuses on the seismic performance evaluation of hollow composite members composed of steel tubes and high-strength reinforced concrete. A series of tests on composite members with various sectional compositions were conducted. Test results showed that the member's strength could be evaluated by the method of superposition. Test results also showed that the strength deterioration rate of composite members increased when the sectional aspect ratio was increased. Finally, an interaction expression between bending and torsion was proposed for engineering practice references.

1. INTRODUCTION

Steel-concrete composite members, particularly those with thin-walled hollow sections, are widely used in building and bridge constructions. Hollow composite members possess effective torsional resistance, and high strength/mass ratios and significant ductility in the sections' two principal directions; thus are suitable designs for earthquake-resistant purposes. Benefits in using the hollow composite members include the light member weight to reduce the demand in lateral load resistance, and the performance enhancement from steel-concrete interaction. In order to accomplish these goals, the effective integration of the comprising steel and concrete must be sustained.

Current studies on the seismic behavior of hollow composite members are mostly focused on their responses under axial load, flexural load, or the combination [Lachance 1982; Qiu et. al. 2002; Mirza and Skrabek 1991; Ricles and Paboojian 1994]. However, for structures subjected to earthquakes, combined loads involving torsion are usually parameters that govern the performance of the structures [Hsu and Wang 2000], because the concrete is low in shear resistance. Once the torsion-induced shear is presented in the composite members, premature diagonal cracks in concrete will hamper the sectional integrity, increase the local buckling potential of the encased steel tubes, and subsequently affect the members' seismic performance in the inelastic stages. Therefore, investigation on the effect of torsion to the member performance is essential to the effective designs of hollow composite members.

It has been indicated in several studies that the tosional resistance and the cyclic behavior of steel tubes are related to the geometries, particularly the aspect ratio, of the sections. This concern remains in the seismic design of hollow steel-concrete composite members, because various stress states will be induced in sections with different aspect ratios when torsion or loads coupled with torsion is presented. As a result, the member performance is affected. In order to evaluate the effectiveness of the design, the relationship between the aspect ratio and the member performance must be defined.

This study focuses on the torsional-flexural behavior of hollow steel-concrete composite member. A series of tests on composite members with various sectional compositions subjected to eccentric cyclic loading were conducted. Relationships among member performance, sectional aspect ratios, and magnitude of torsion were quantitatively investigated so that design references can be established.

2. EXPERIMENTAL PROGRAM

2.1 Specimens

Fourteen specimens, including 12 composite members, one steel tube, and one hollow reinforced concrete member, were fabricated for testing. The composite members were composed of reinforced concrete and various steel tubes. Steel tubes used for composite member fabrications were JIS-SS400 150x150x6, 200x100x6 and 200x150x6, respectively. The concrete thickness for the hollow reinforced concrete member and all composite specimens was 110 mm. These compositions yielded three series, namely series A, B, and C, of composite sections with aspect ratios (depth/ width; D/B) equaling 1, 0.76, and 0.88, respectively. Specimen labels are described in Table 1. These arrangements were used to investigate the effect of aspect ratios in affecting the members' performance when loads coupled with torsion were presented. The reinforced concrete of the member was composed of #5 longitudinal bars and #3 stirrups, respectively. Yield strengths of the steel, the longitudinal bar, and the stirrups were 346.5MPa, 366.9MPa, and 353.7MPa, respectively. Compressive strength of the concrete was 55.7 MPa, determined from cylinder tests after 28-day curing. The specimen details are shown in Figure 1.

Table 1 Specimen Labels

Specimen	Composite section (B x D) (*mm*)	Steel tube (b x d) (*mm*)	Aspect ratio (D/B)	Loading type	Eccentricity ($\frac{e}{h}$)
M-A11	370x370	150x150	1	Bending	0
M-B11	420x320	200x100	0.76		
M-C11	420x370	200x150	0.88		
T-S	----	150x150	----	Torsion	0.5
T-RC	370x370	----	---		
T-A11	370x370	150x150	1		
T-B11	420x320	200x100	0.76		
T-C11	420x370	200x150	0.88		
TM92-A11	370x370	150x150	1	Combined bending and torsion	0.5
TM92-B11	420x320	200x100	0.76		
TM92-C11	420x370	200x150	0.88		
TM46-A11	370x370	150x150	1		0.25
TM46-B11	420x320	200x100	0.76		
TM46-C11	420x370	200x150	0.88		

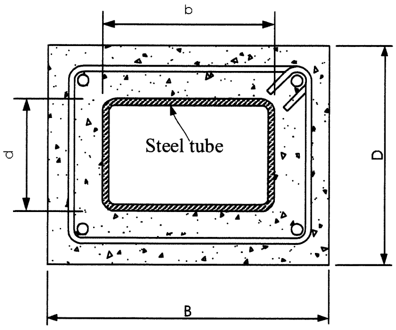

Figure 1 Specimen Details

2.2 Test set-up

Four types of loads were considered in this study. They included bending tests, pure torsion tests, bending with smaller torsion, and bending with larger torsion. These combinations were designed to evaluate the member strengths and the strength interaction under various load combinations. In each test, the specimen bottom was fastened to a stiffened base platform and the member top was attached to a stiffened loading beam for load transmission.

For bending tests, a servo-controlled actuator was attached to the loading beam driven by desired displacement commands. For pure torsion tests, the actuator was moved to one side of the loading, and a stiffened strut with both ends hinged was placed at the center of the loading beam, so that the desired torsion could be achieved through the coupled action of the actuator and the strut. For combined bending and torsion tests, the strut was removed and the actuator was driven by the prescribed displacement command to generate the required combined loads. Figure 2 shows the test set-up..

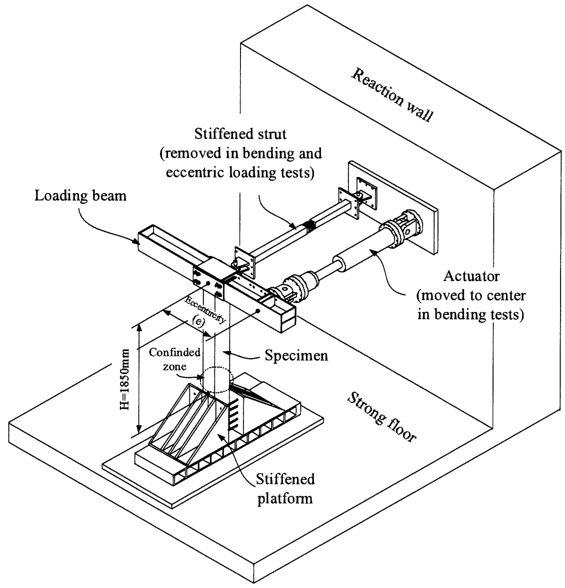

Figure 2 Test Set-up

3. EXPERIMENTAL OBSERVATIONS

For members subjected to torsion, diagonal cracks were first observed at the center of the members. Subsequent local buckling of steel tubes was observed when the twist angles were increased. It was found from the tests that the extents of distortion in the encased steel tubes were related to the aspect ratios of the sections. For example, when steel tubes with same cross-sectional areas, however different aspect ratios, were used to fabricate the composite sections, various torsional responses, such as twist angles and damage extents, were exhibited when the same magnitude of torsion was applied. This phenomenon can be attributed to the different torsional rigidity resulted from the various aspect ratios. Therefore, the effect of aspect ratios on the performance of members subjected to earthquake loads, particularly those coupled with torsion, must be adequately defined.

4. COMPARISONS AND INTERPRETATIONS

4.1 Torsional behavior of members

Figure 3 shows the typical load-deformation relationships for the steel tube, the reinforced concrete member, and the composite member composed of the previous ones. It can be found from the figure that torsional responses of members can be approximated by tri-linear expressions. These relationships could be distinguished by the deformations at which members reached the crack state and the ultimate strength, respectively. For members with extreme aspect ratios, the achievable deformation, such as the crack angle and the deformation at which steel tube buckled, would be altered. Consequently, the member responses at each stage would be affected. Figure 4 shows the comparisons of the torsional responses of the three test series.

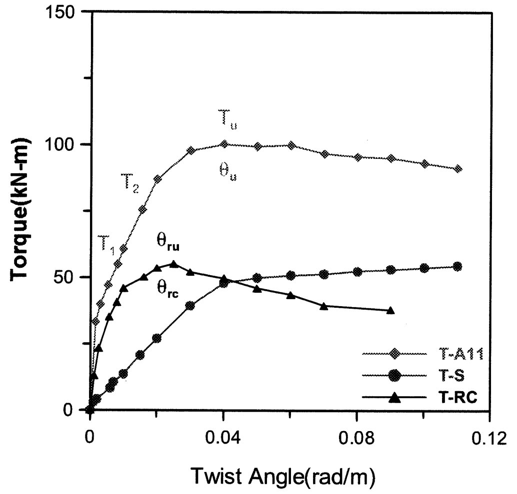

Figure 3 Typical Load-deformation Relationships for Members Subjected to Torsion

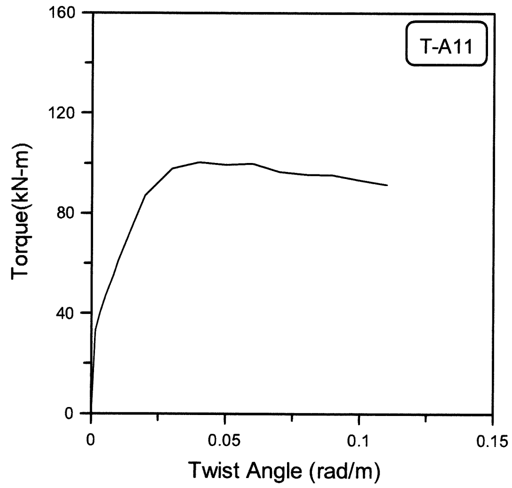

(a)

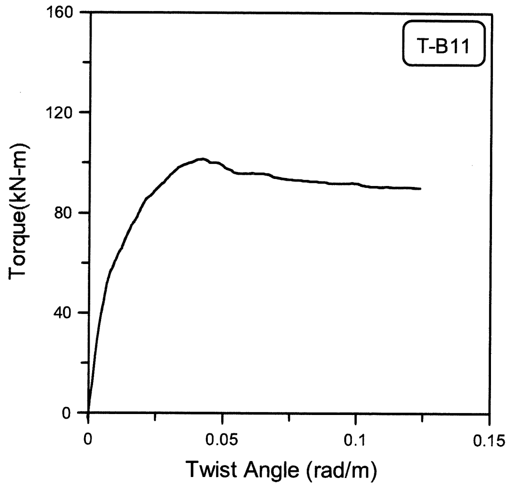

(b)

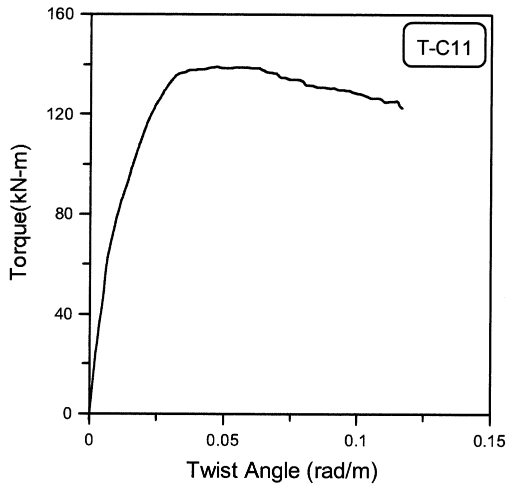

(c)

Figure 4 Torsional Responses of Test Specimens: (a) A11; (b) B11; (c) C11

4.2 Effect of aspect ratios on the flexural-torsional performance

Figure 5 shows the typical hysteretic relationships for members subjected to various load combinations. It can be found from the figure that the achievable member strength decreased when the magnitude of torsion increased. The member strengths for the three test series under combined loads were further normalized with respect to the flexural strength of the corresponding members. Figure 6 shows the relationships between the normalized flexural and torsional strengths of the three test series. It can be observed from the figure that a linear relationship between the normalized bending and the normalized torsion existed. It is also found that the interaction between bending and torsion was related to the aspect ratios of the members. The interaction can be described by the following expression:

$$\frac{M}{M_u} = 1 - \alpha_r \frac{T}{T_u} \qquad (1)$$

In which α_r is an interaction coefficient accounting for the influence of aspect ratio. As shown in Figure 7, the interaction coefficient can be linearly related to the aspect ratio by the following:

$$\alpha_r = 0.477 \frac{D}{B} \qquad (2)$$

The above information can be used to estimate the member's flexural-torsional performance, and can be further improved by more test information.

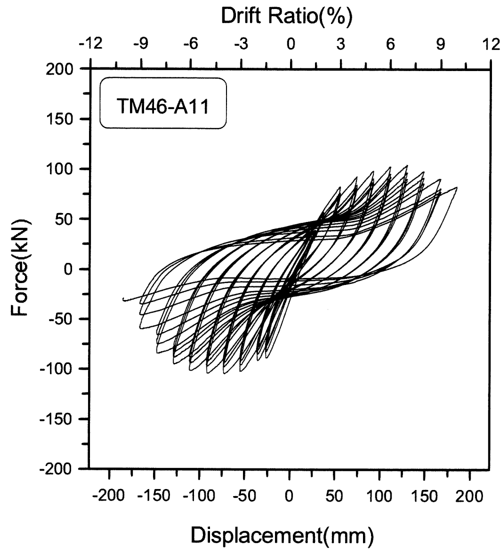

(a)

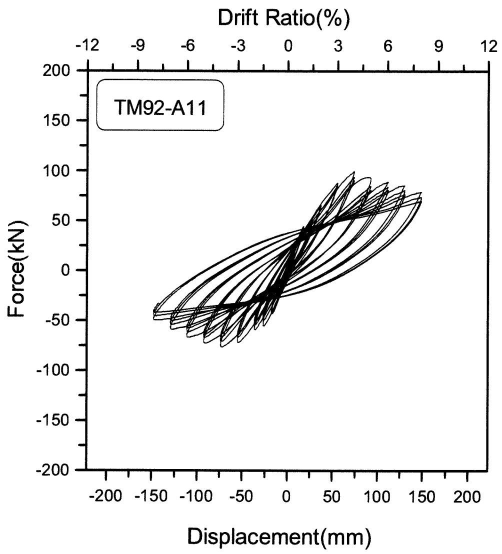

(b)

Figure 5 Typical Hysteretic Relationships for Members Subjected to Combined Loads: (a) Bending with Smaller Torsion; (b) Bending with Larger Torsion

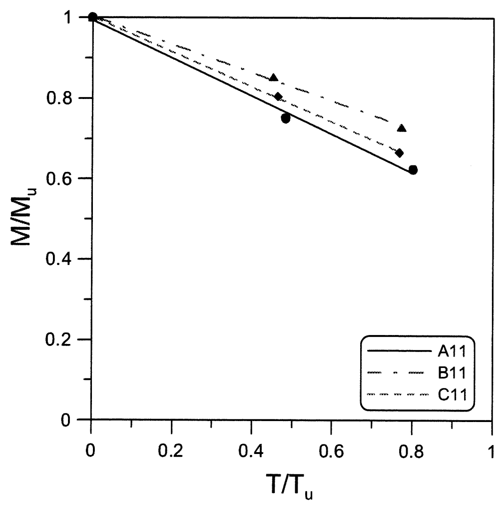

Figure 6 Relationships between Normalized Flexural and Torsional Strengths

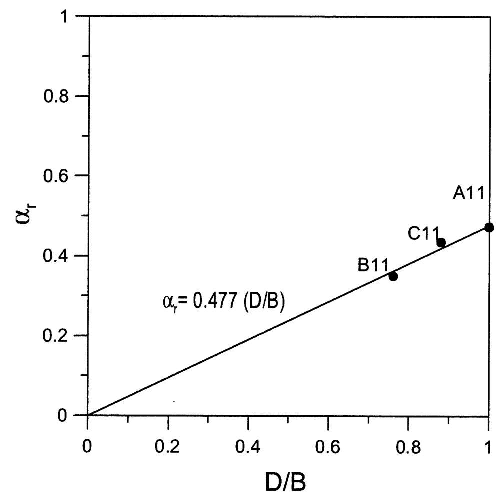

Figure 7 Relationships between the Interaction Coefficients and The Aspect Ratios

5. CONCLUSIONS

This paper presented the test information of hollow steel-concrete composite members subjected to combined bending and torsion. Relationships between member performance and the aspect ratios of the composite sections were evaluated. Test results showed that the member's strength could be evaluated by the method of superposition. Test results also showed that the strength deterioration rate of composite members increased when the sectional aspect ratio was increased. Finally, an interaction expression between bending and torsion was proposed for engineering practice references.

Acknowledgements:

This study was partially supported by the National Science Council of the Republic of China under Grant No. NSC 95-2221-E-008-099, which is gratefully acknowledged.

References:

Lachance, L. (1982), "Ultimate Strength of Biaxially Loaded Composite Sections," *Journal of the Structural Division,* American Society of Civil Engineers, **108**(ST10), 2313-2329.

Qiu, F., Li, W.F. , Pan, P., and Qian, J. (2002), "Experimental Tests on Reinforced Concrete Columns Under Biaxial Quasi-static Loading," *Engineering Structures*, **24**(4), 419-428.

Hsu H-L. and Wang C-L. (2000), "Flexural-Torsional Behaviour of Steel Reinforced Concrete Members Subjected to Repeated Loading" *Earthquake Engineering and Structural Dynamics*, **29**(5), 667-682.

Mirza, S. A. and Skrabek, B. W. (1991), "Reliability of Short Composite Beam-Column Strength Interaction" *Journal of Structural Engineering*, American Society of Civil Engineers, **117**(8), 2320-2339.

Ricles, J. M. and Paboojian, S. D. (1994), "Seismic Performance of Steel-Encased Composite Columns" *Journal of Structural Engineering*, American Society of Civil Engineers, **120**(8), 2474-2494.

Fifth International Conference on Urban Earthquake Engineering
March 4-5, 2008, Tokyo Institute of Technology, Tokyo, Japan

Seismic Isolated Structures Applied to from Detached Houses to High-rise Apartments in Japan

A. Wada [1], N. Kani[2], S. Hirano [3], H. Kamikouchi [4] , M. Kimura [5]

1) Professor, Tokyo Institute of Technology, Japan, Yokohama
2) Japan Society of Seismic Isolation, Tokyo
3) Ichijo Housing Co. Ltd., Hamamatsu
4) Nikken Housing System Ltd., Tokyo
5) Mitsubishi Jisho Sekkei Inc. Tokyo

wada@serc.titech.ac.jp kani@jssi.or.jp s-hirano@ichijo.co.jp
kamikouchi_nhs@nikken.co.jp masato.kimura@mj-sekkei.com

Abstract: Japan was a country of the wooden architecture. Superior earthquake engineering such as Five Story Pagoda was possessed. In Europe countries where the earthquake is few, their technology is starting from stone structures, and it is basic to make structures of architectures strong, stiff and tight. On the contrary, it can be said that the wooden structures of Japan was a technology that allows deformation and enables the energy absorption. Japan opened the country to the world in 1867, and new architectural technologies were introduced from Europe and America. A lot of buildings were constructed by using new technology, new materials of steel and concrete. These many buildings were damaged and collapsed by earthquakes in these 140 years. It was clear that the earthquake engineering had advanced greatly in the 20th century. Although, there is a limit in the earthquake performance of conventional method, that fix the building to the foundation. It entered 1980's that the seismic isolated structures were put to practical use, and it has been arriving now. The current state of the seismic isolated structures of Japan is discussed here, and three examples of the seismic isolated structures to the housing are introduced.

1. INTRODUCTION

The next three stages are in the performance levels of defence of building structures to big earthquakes:

1) **Function maintenance**: Function of building and activity of every day can be maintained after the earthquake.

2) **Property value**: It is possible to use it again if it suffered big earthquake. After some repair of the building, the property value of building can be kept.

3) **Life safety**: It must defend people's safeties though building may become a demolition after the earthquake.

The performance is different though the seismic structures can be greatly classified into the following four:

1) **Strength oriented structures**: The structure is constructed enough and strongly, and a large plastic deformation is not caused due to the big earthquake. Because the acceleration in the building grows very high, the function maintenance is difficult though the property value and the life safety can be maintained.

2) **Ductility oriented structures**: The structure is made not too strongly, and a large plastic deformation is allowed during big earthquakes. After the earthquake, the building might be demolished though only the life safety is performed.

3) **Passive controlled structures**: Earthquake energy is absorbed by the various dampers installed into the building. Because the acceleration in the building is not small, the maintenance of the function partially becomes difficult. In some case after the earthquake, it is necessary to repair.

4) **Seismic isolated structures**: The building is isolated from the foundation, and the earthquake energy could not enter to the building. It has the highest earthquake resistance to be able to defend three items such as function, property and life. Thus, it is an earthquake engineering to be able to trust the seismic isolated structure under the present situation.

2. FEATURES OF SEISMIC ISOLATED STRUCTURES

The acceleration in the seismic isolated building becomes 10% of the fix based conventional buildings, and becomes 100cm/sec2 to 200cm/sec2. The story drift angles would be 1/1000 to 1/200 in the seismic isolated buildings though a usual building generated exceeding 1/100 to 1/50. Base shear coefficient becomes about 0.1 to 0.13 in the seismic isolated structure, and it makes easy to design columns and beams though the base shear coefficient becomes 0.25 to 0.55 in a usual building. It can be said that the seismic isolated structure becomes cheap from the fixed base building when the number of stories exceeds 8 or 10.

The seismic design regulation of Japan demands only life safety, neither the function maintenance nor the property value are demanded. Because it costs enormous for the individual to buy the house, the second cannot be bought. It is necessary to maintain the function maintenance and the property value. It is a reason why this presses the spread of seismic isolated houses. Still, it is an amount of about 1% of buildings constructed in a year. We want to extend this up to 10%

3. STATISTIC DATA OF SEISMIC ISOLATED HOUSES IN JAPAN

The number of seismic isolated buildings has been increasing, since the 1995 Hyogo-ken Nanbu Earthquake. The number of detached houses with seismic isolation has been increasing also. This progress is according to the frequent occurrences of big earthquakes in Japan. Figure 1 shows construction of buildings with seismic isolation (SI) except detached houses. The first seismic isolated building was built in 1983. Half of them are condominiums shown in Figure 2. Figure 3 shows the number of detached houses with SI of which capture ratio is 60%. Very recently high-rise buildings with SI have been built as offices or condominiums shown in Figure 4, mostly they are condominiums.

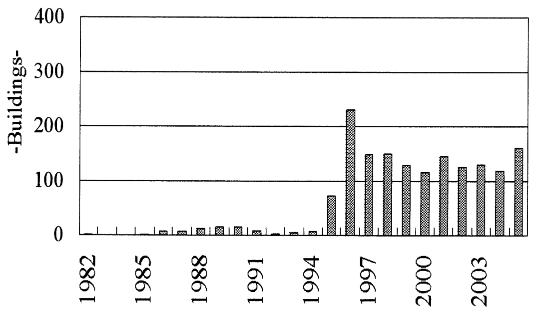

Figure 1 Number of SI Buildings by year in Japan
(Not including detached houses)

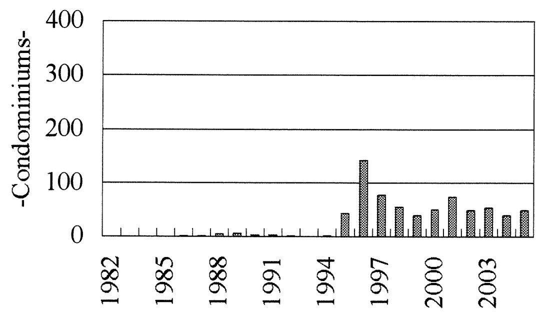

Figure 2 Number of SI Condominiums by year in Japan

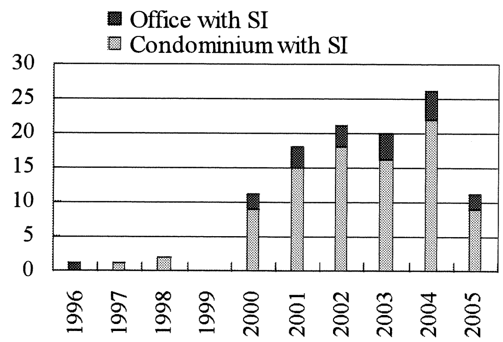

Figure 3 Number of SI Detached Houses by year in Japan

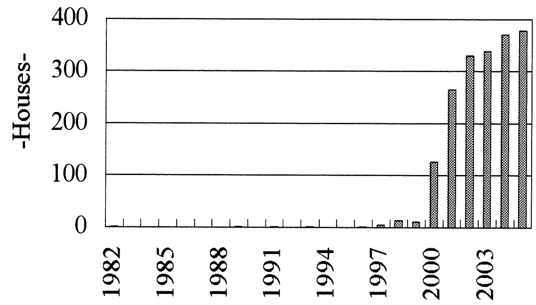

Figure 4 Number of SI High-rise Buildings by year

4. DETACHED WOODEN HOUSES ON SEISMIC ISOLATE SYSTEM

More than 2200 seismic isolated wooden houses were designed and constructed by One Company, Ichijo Housing Co. Ltd. in Japan. Many photographs and figures of a typical example of them in Toyota City are introduced here. The areas of ground floor and second floor are $108m^2$, $63m^2$ in respectively. The structure supported by 21 small sliding devises, which friction coefficient is about 4%. The 4 elastic rubbers stabilize the structure in horizontal large movement.

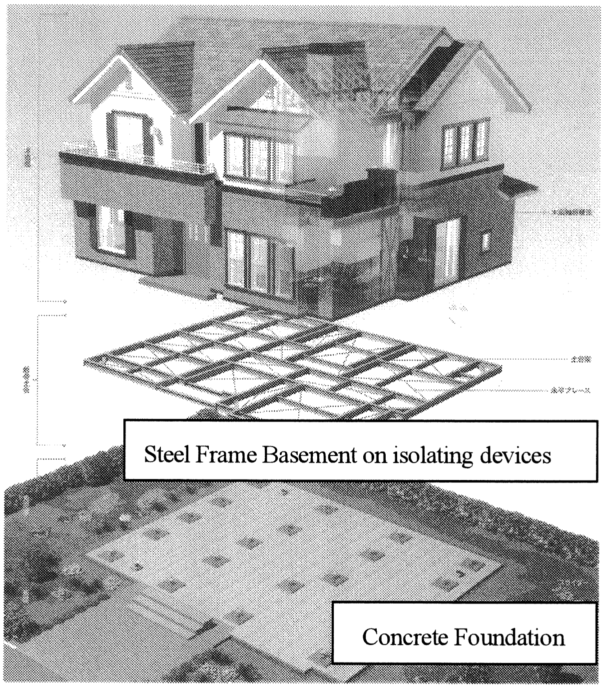

Steel Frame Basement on isolating devices

Concrete Foundation

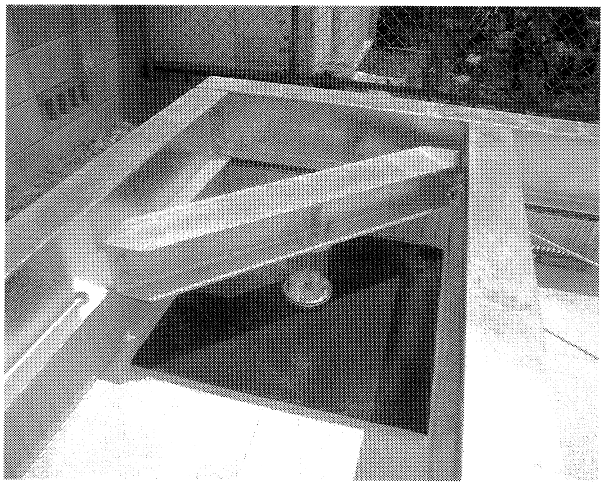

Small Sliding Device

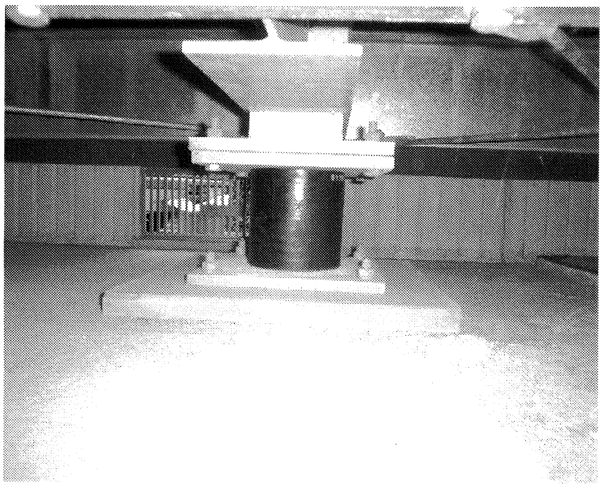

Elastic Rubber Spring

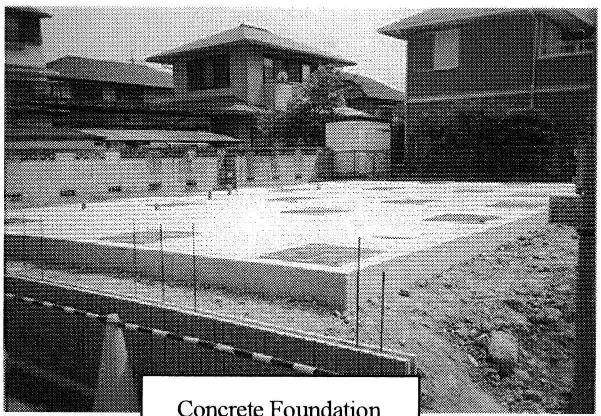

Concrete Foundation

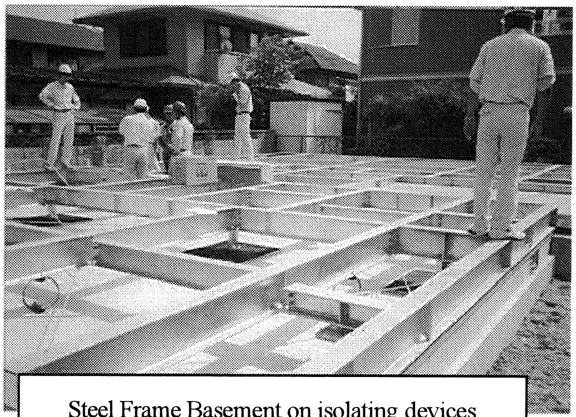

Steel Frame Basement on isolating devices

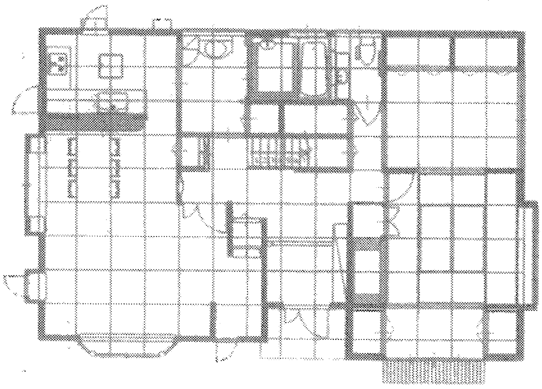

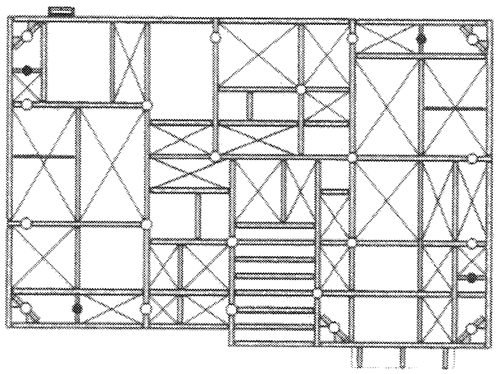

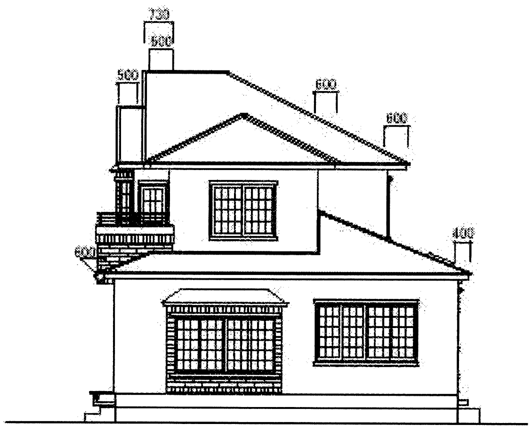

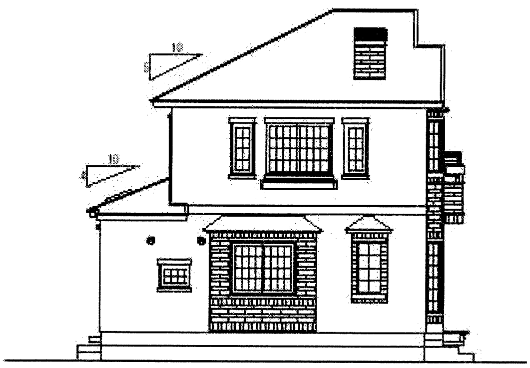

5. CONDOMINIUM OF CHUORINKAN CONSIDERING ENVIRONMENT

Architects: Hiroyuki Usami, Kazunori Shirabe, Nikken Housing System Ltd.

Structural Engineers: Hirofumi Kamikouchi, Yuji Yokoyama, Nikken Housing System Ltd.

Contractor: Tokyu Construction Co. Ltd.

This project has 7 apartment buildings. Environmental aspects and seismic safety are most important issues in the design process of the project. Then, the height and the shape of each building were designed to be deferent and these complex configurations are very comfortable for the residents. San shine effects and wind flow effects are very nice for them. For the earthquake issue, the seismic isolation system is applied to each building. The natural rubber bearings, the lead dampers and the steel dampers are installed as seismic isolation devices. The tallest of them is 17story building. The weight of this super structure is 10,200 tons. While we are taking in to account only the flexibility of rubbers and we assume that the super structure is perfectly rigid, the first natural period of the building is 4.8 sec. The sum of yield force of the dampers is 215tons, and then yield shear force coefficient of dampers is 2.1%.

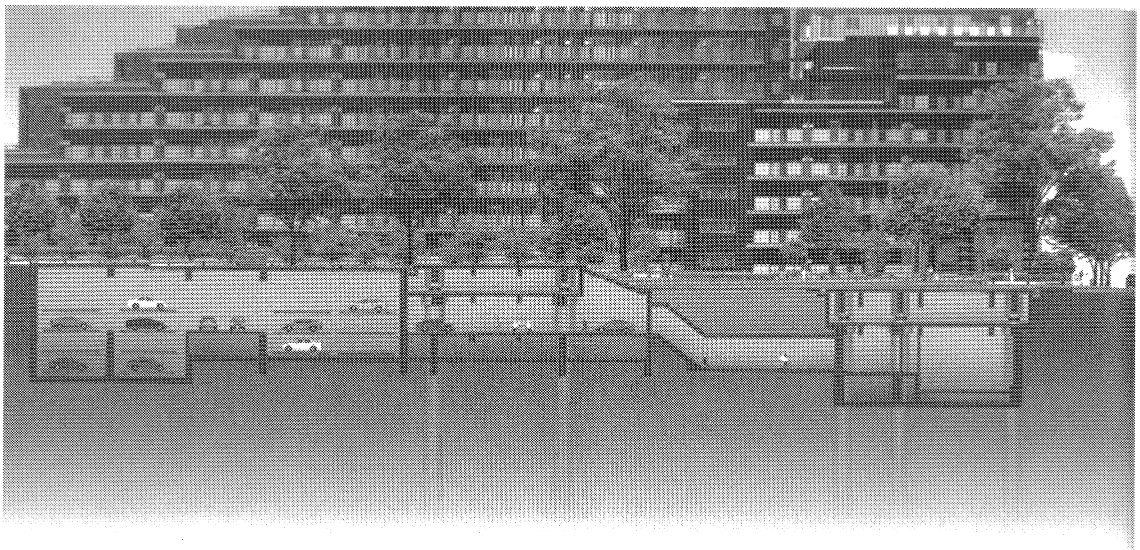

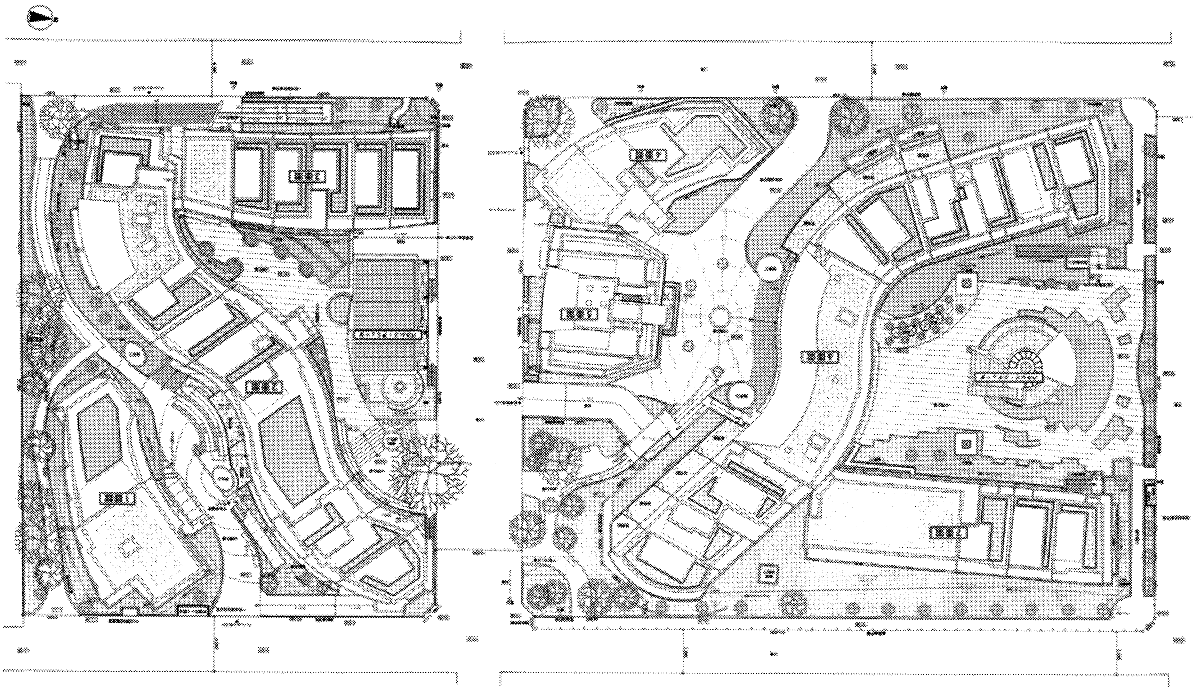

Global Plan

Comfortable Courtyard

Expansion around buildings

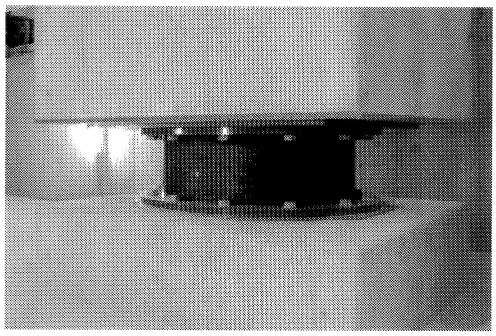

Natural Rubber Bearing

6. THREE RESIDENTIAL TOWERS ON THE YOKOHAMA BAY

Three high-rise apartments of reinforced concrete structure and seismic isolation system were constructed on the Yokohama Bay Area. Architects and structural engineers are the excellent members of the Mitsubishi Jisho Sekkei Inc. in Tokyo. The sizes of a typical building are 33.3m x 32.6m and the height is 99.8m, and the total weight of this building is a 61,339 tons. The lead dampers and the steel dampers are installed, sum of yield forces is 1,152 tons and it is 1.87% of the weight of super structure. An equivalent period when rubber bearing deformed 100% shear is 5.42sec. The core wall and the perimeter framework combine up this structure. This structural system raises flexibility of design of habitation area. Concrete was formed into the pre-cast and rational construction was performed.

REFERRENCE

Kani, N., Takayama, M. and Wada, A. (2006), Performance of Seismically Isolated Buildings in Japan - Observed records and vibration perception by people in buildings with seismic isolation -, *Proceedings of the 8th U.S. National Conference on Earthquake Engineering*, paper No. 2181

Construction

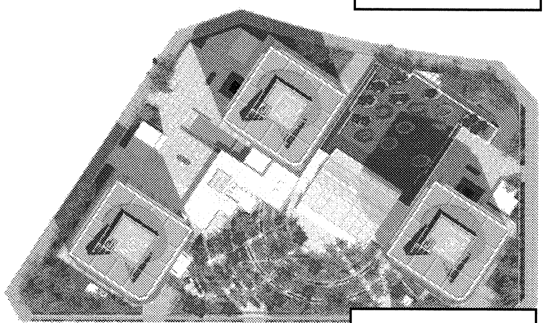

Global Plan

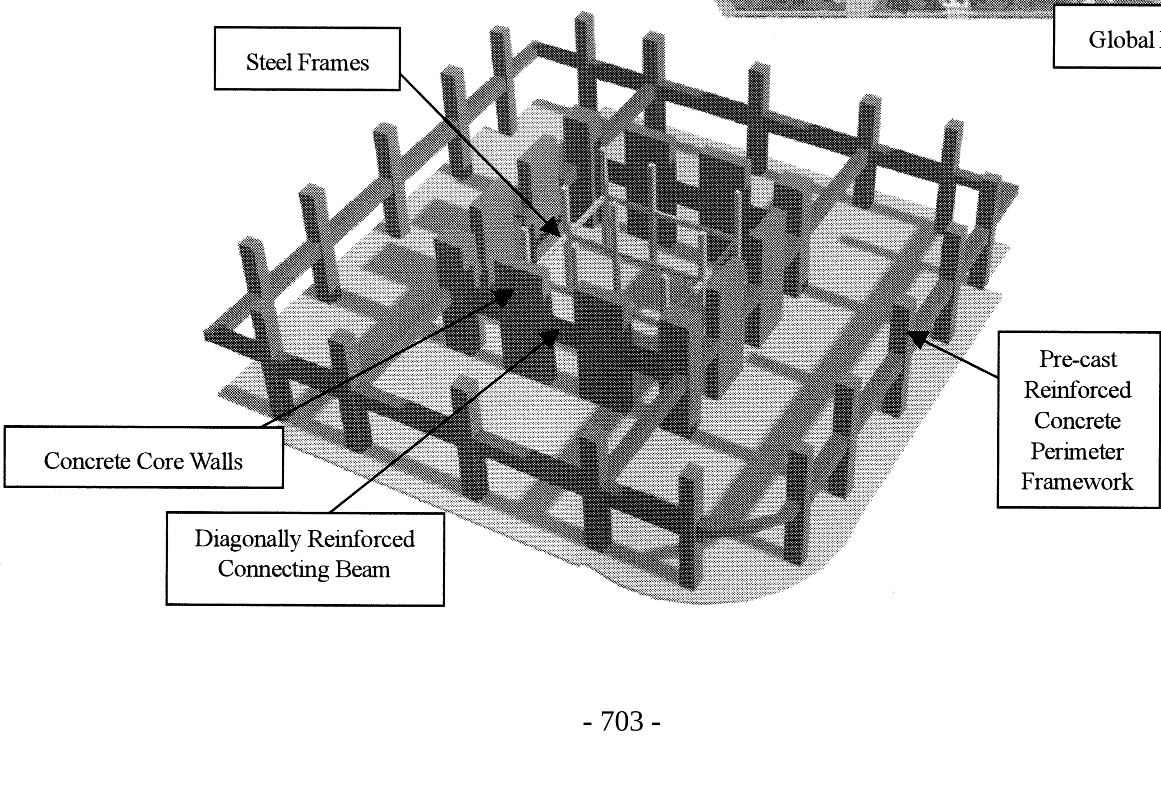

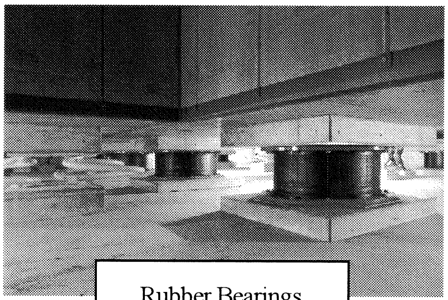

Rubber Bearings

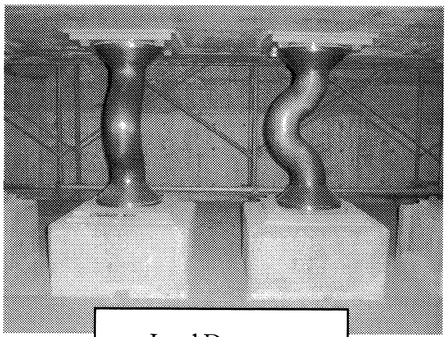

Lead Dampers

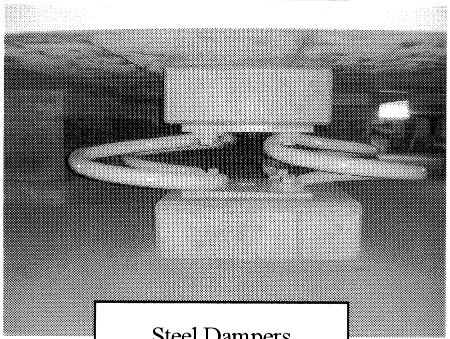

Steel Dampers

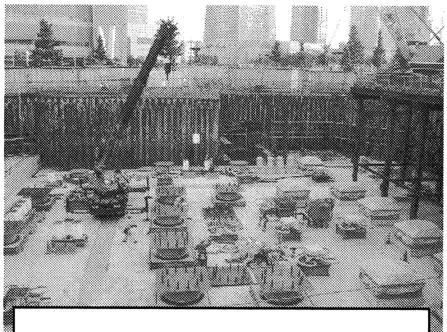

Isolating Devices set on Foundation

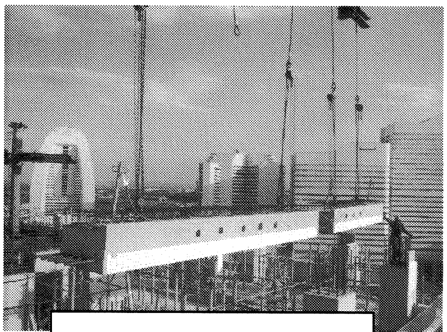

Pre-cast Concrete Slab

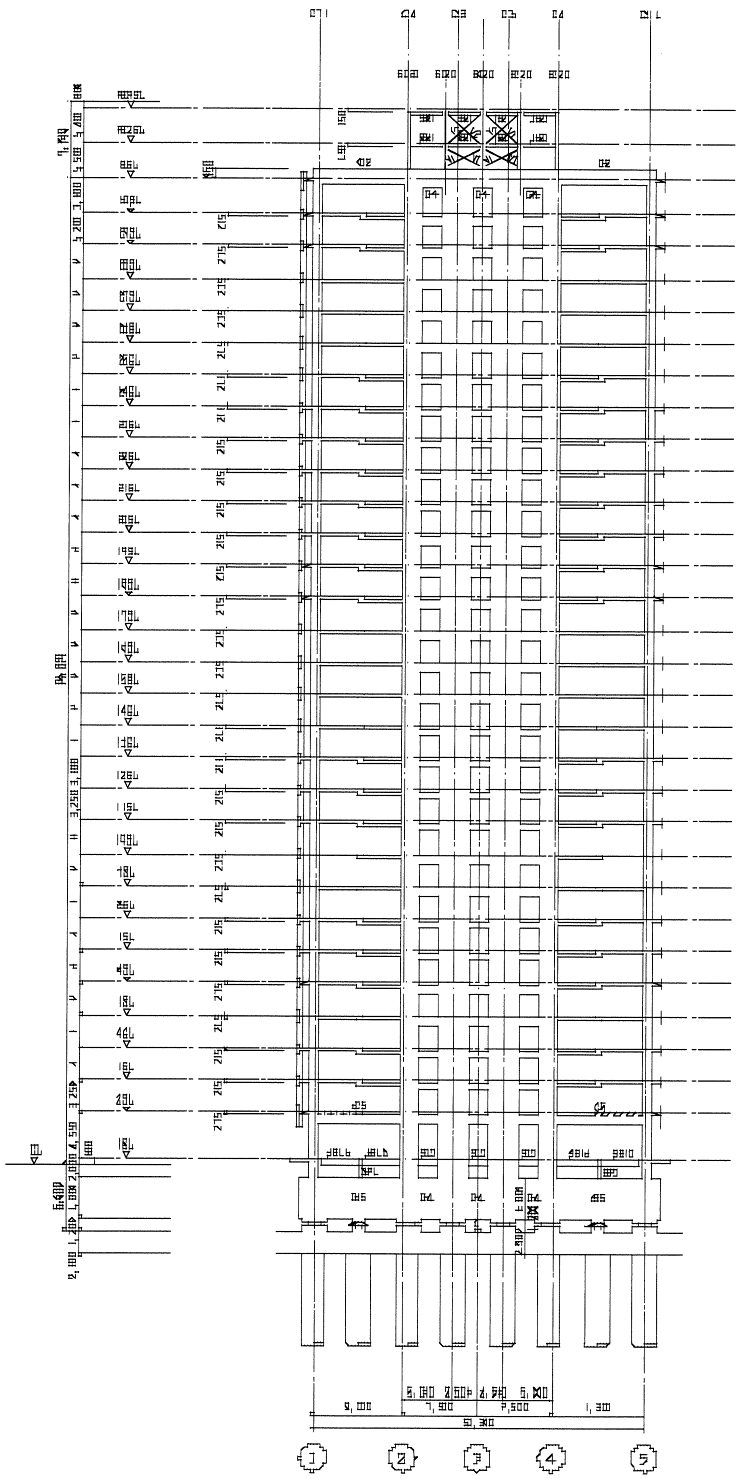

Framing Elevation

DYNAMIC COLLAPSE BEHAVIOR OF 3-D STEEL FRAME MODEL

Yuko Shimada[1], Yuichi Matsuoka[2], Satoshi Yamada[3], and Keiichiro Suita[4]

1) Graduate Student, Tokyo Institute of Technology, Japan
2) Nippon Steel Engineering Co. Ltd., Japan
3) Associate Professor, Structural Engineering Research Center, Tokyo Institute of Technology, Japan
4) Associate Professor, Dept. of Structural and Geotechnical Engineering, Kyoto University, Japan
yuko_shimada@serc.titech.ac.jp, yuivhi.matsuoka@msc.co.jp, naniwa@serc.titech.ac.jp, suita@archi.kyoto-u.ac.jp

Abstract: In order to evaluate the capacity to collapse behavior of steel building under exceedingly large ground motion, the shaking table test of a full-scale building at E-Defense was conducted. Small-scale shaking table test was conducted to address following technical issues; (1) acquisition of 3-D behavior of specimen frames up to collapse; and (2) efficiency of safeguard system to protect shaking facilities. Obtained results are effective to verify not only the instrumentation methods but also numerical analytical methods for collapse simulation.

1. INTRODUCTION

Behavior of steel building under severe earthquake and final collapse process are not clarified. In order to clarify them, full-scale steel building collapse test was executed at E-Defense in 2007. This study was conducted as pre-consideration experiment of full-scale collapse test to verify measurement instrumentation and examine the scenario of 3-D steel frame collapse. The result of this experiment is also contributed to calibration of simulating collapse behavior.

2. EXPERIMENT PROCEDURE

2.1 Specimen

Specimen designed aim to collapse. It isn't meant to replicate full-scale frame building. As shown in Figure 1, specimen is 2-story, 1×1 span 3-D steel flame. Span length in each horizontal axis are 1.25m×2.25m, and each story height is 1.0m. The frame members consist of square hollow section column □-60x60x1.6 (STKR400), steel beam BH-75x50x4.5x4.5 (SS400), and steel block 70x70x95 (SS400) as beam-to-column connection. Column base is exposed type with enough stiffness. Counter weight on each floor is about 15kN, and total frame weight is 31.0kN. Calculated value of the fundamental natural period is 0.302s (Y-dimension), base shear from Mp (column full-plastic moment) is 0.85, and ratio yield axial force of column is 0.05.

2.2 Measurement

In order to follow 3-D behavior of specimen from elastic range to collapse, measurement instruments settled as follows;

・Strain-type acceleration transducers set on the surfaces of shaking table and faces of connection block in order to measure their 6 DOF accelerations.

・Potentiometer-type displacement transducers fasten on safety guard and their targets are put on connection blocks as shown in Figure 2. Displacement of each story is calculated from displacements of each target points.

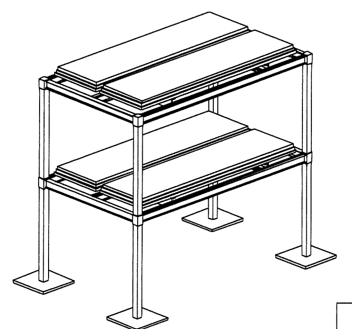

Figure 1 Specimen

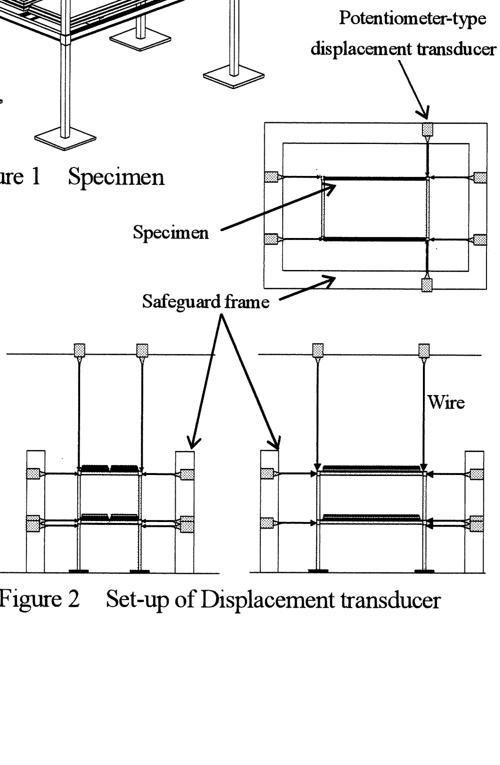

Figure 2 Set-up of Displacement transducer

・Elastic strain gauges are put on two section in elastic potion of each member. Figure 3 shows the calculating method of inertial force from strain. Q is shear force acting in each column, and it's sum of *Wsin θ* (orthogonal component in the column axis of gravity) and *Qrcos θ* (resistant component in the column axis of horizontal applied force) as shown in Figure 4. In the following consideration, Qr is used as story shear.

2.3 Characteristics of material and member

Before shaking table test, coupon test of material and cyclic loading test of simple supported beam and column is carried out as shown in Figure 5. Result of coupon test is shown in Table 1. Loading history used in the cyclic loading test is controlled by rotation angle of member. End moment corresponding to the rotation angle is calculated as shown in Figure 6. Strength ratio of column and beam at full plastic moment is 2.5. Results of the cyclic loading test are shown in Figure 7. In the moment-rotation angle relationship of the beam, deterioration is not significant. That is because lateral support set at same point with frame specimen (Figure 8) resists against lateral buckling. On the other hand, column loses restoring force remarkably after local buckling is occurred. Finally, restoring force of column settles about 40% of the maximum strength.

2.4 Excitation

In the shaking table test, NS, EW, and UD components of 1995 Kobe Record are used as input wave. Input acceleration data is shorten 0.5 times in the time domain, considering the spec of the shaking table and natural period of the specimen. Excitation is carried out as following step;

(1) Free vibration in one direction. (X and Y)
(2) Elastic excitation in one direction and three directions. Input wave used in the excitation is 0.125 times multiplied JMA Kobe record.
(3) Elasto-plastic excitation. Input level is changed step by step as shown in Table 2. (JMA Kobe × 1.00, 1.25・・・)

When specimen touches the safeguard frame, excitation is finished. Excitation list is shown in Table 2.

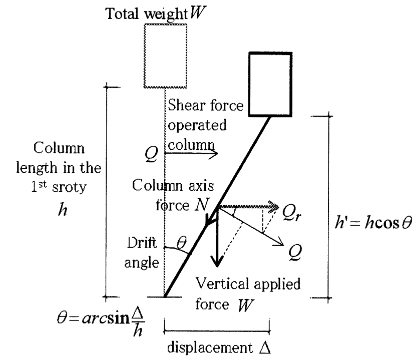

Figure 3 Calculation of story shear

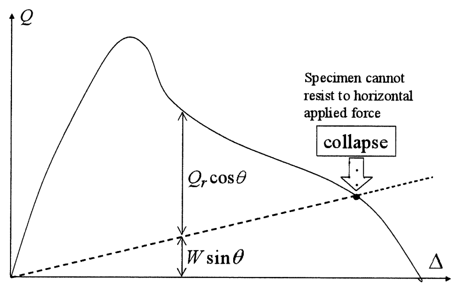

Figure 4 Components of Q

Table 1 Material property of steel members

	σy	σu
Beam	306	432
Column	427	481

Table 2 Excitation list

No.	Input
1	Free vibration (X dimention)
2	Free vibration (Y dimention)
3	JMA Kobe(Elastic:1 axis)
4	JMA Kobe(Elastic:3 axis)
5	JMA Kobe×1.00
6	JMA Kobe×1.25

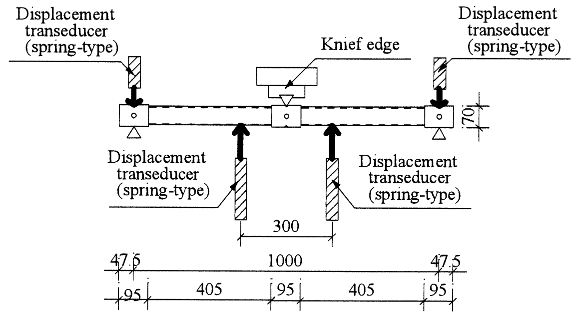

Figure 5 Set-up of cyclic loading test

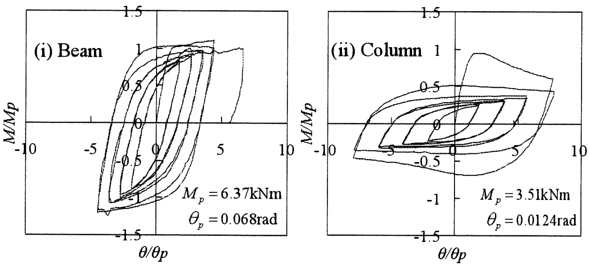

Figure 7 Characteristics of steel member

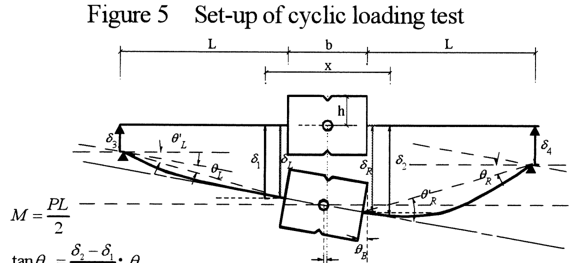

$$M = \frac{PL}{2}$$

$$\tan\theta_B = \frac{\delta_2 - \delta_1}{x} \cdot \theta_B$$

$$\delta_L = \delta_1 + \left(\frac{x-b}{2}\right) \cdot \theta_B \qquad \delta_R = \delta_2 + \left(\frac{x-b}{2}\right) \cdot \theta_B$$

$$\theta_L' = \frac{\delta_L - \delta_3}{L} = \frac{2\delta_1 + (x-b)\theta_B - 2\delta_3}{2L} \qquad \theta_R' = \frac{\delta_R - \delta_4}{L} = \frac{2\delta_2 + (x-b)\theta_B - 2\delta_4}{2L}$$

$$\theta_L = \theta_L' - \theta_B = \frac{2\delta_1 + (x-b)\theta_B - 2\delta_3}{2L} - \theta_B \qquad \theta_R = \theta_R' - \theta_B = \frac{2\delta_2 + (x-b)\theta_B - 2\delta_4}{2L} - \theta_B$$

Figure 6 Calculation of end moment and rotation angle

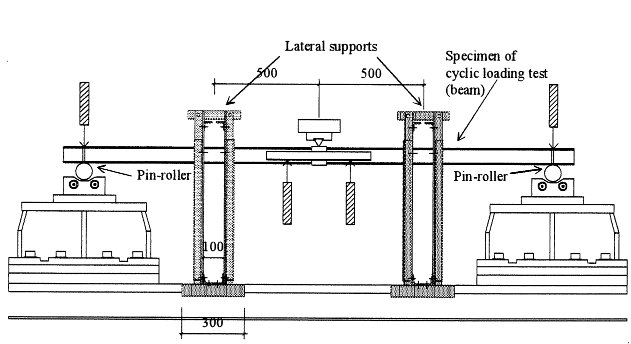

Figure 8 Lateral support

3. EXPERIMENTAL RESULTS

3.1 Examination of measurement

Measurement system of displacement is settled couple of displacement transducers. Comparing both measured results, they are almost same at any couple, and very few error caused by slack of wire in potentiometer-type displacement transducer is observed (Figure 9).

Shear force calculated by measured acceleration or strain (Qr). Figure 10 shows examination of both results. At JMA Kobe × 1.00 excitation, the both results almost equal in X and Y direction respectively. However, at JMA Kobe × 1.25 excitation, shear force in X direction calculated by acceleration is unsteady in the deteriorating range. It's because acceleration transducers pick up vertical vibration of connection block. On the other hand, Qr is almost steady. According to the behavior of the specimen, it is considered that Qr is correct.

3.2 Spectrum of input wave

Fourier spectrum of measured input wave and original acceleration data (Target) are compared in Figure 11. In X and Y-direction, measured spectrum is 10% larger than each Target spectrum. Distribution of both spectrum in X-direction generally corresponds. While a part of measured spectrum of Y-direction doesn't correspond so much to target spectrum around fundamental natural period of the specimen.

3.3 Natural period and damping factor

Natural period and damping factor of the specimen is calculated by the result of free vibration. The fundamental natural period is 0.33s, and damping factor is 0.9% in X-direction and 0.11% in Y-direction. From observed natural period and Fourier spectrum of the input energy, specimen is considered to be able to receive enough energy to collapse.

3.4 Collapse behavior of story

In this study, collapse is defined as specimen loses its resistance against gravity. In the excitation, specimen collapse in the first story and the second story is kept in elastic range. Therefore in this study, behavior of the first story is considered.

In this section, Qr (horizontal applied force calculated from strain of column) and θ (drift angle) relation is focused. Figure 12 shows Qr- θ relation. Broken line shows

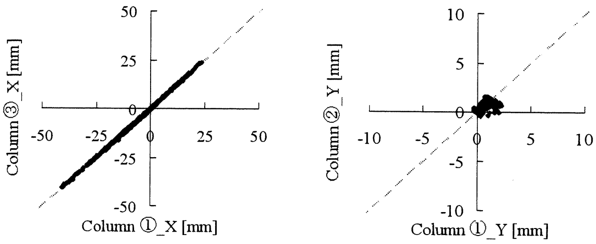

Figure 9 Examination of measurement (displacement)

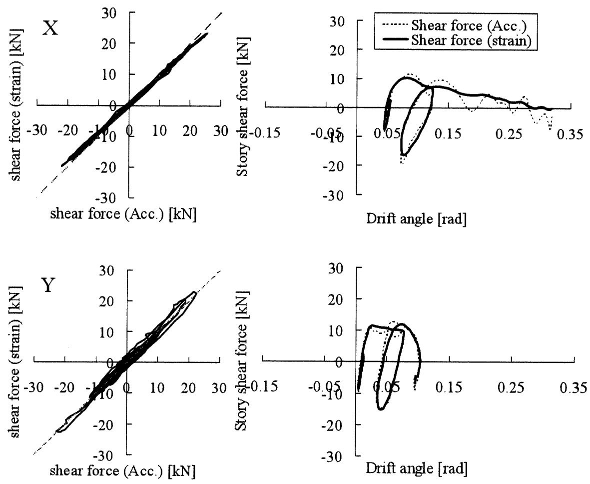

Figure 10 Examination of measurement (story shear)

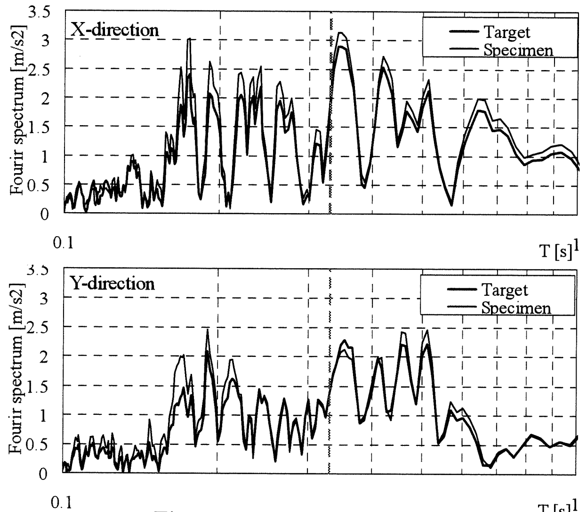

Figure 11 Fourier spectrum

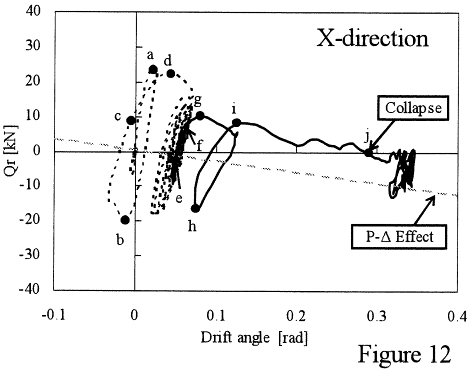

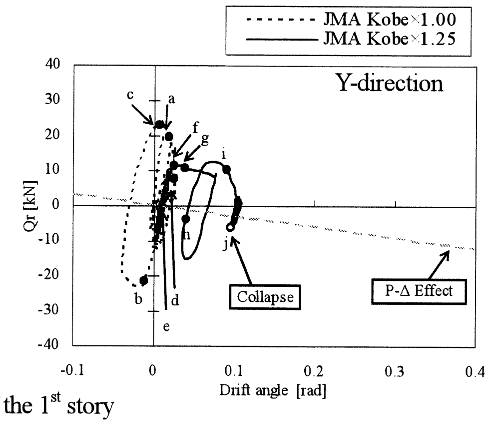

Figure 12 Behaviors of the 1st story

P-Δ effect, and points named a ~ j corresponds to the behaviors of X-direction and Y-direction at same time. At JMA Kobe × 1.00 excitation, specimen reach the maximum strength of Qr. The maximum strengths are about 23kN both in X and Y-direction, however the maximum strength observed in each direction at different time (X-direction: point a, Y-direction: point c). After this excitation, local buckling is observed at both top and end of all columns in the first story.

At JMA Kobe × 1.25 excitation, Qr raised only 50% of maximum strength (X-direction: point f, Y-direction: point e). After that, deformation in X-direction significantly increase and Qr decrease by P-Δ effect (point g ~ point i), finally specimen lose restoring force. Specimen touches safeguard frame after the time of point j, therefore excitation finished.

3.5 Behavior of X-Y plan

Figure 13 shows orbit of the center of 2nd floor (10 times expanded to the real displacement). And it shows also orbit of the 2nd floor frame rotates around Z axis. Points a ~ j are same as **3.4**. Point a and point g are same time; 1.50s, point b is 1.66s, point h is 1.78s, and point c and point i are 1.96s after input started. In orbit of the 2nd floor frame, gray thick line is 0.0s (start time of input), black thick line is 30.0s (finish time of input), and doted lines show the displacements of the specimen at 1.0s ~ 5.0s respectively with 0.2s step.

At JMA Kobe × 1.00 excitation observed maximum strength, from point O to point a, the center of 2nd floor moves to the direction of 45° against X axis and Y axis. The center keeps moving on the direction of 45° until point b. After it reached point c, moving direction of the center changes to X-direction. And at this excitation, the 2nd floor frame doesn't rotate so much before it reaches maximum strength. However after it reached maximum strength, the 2nd floor frame rotates constantly up to about 0.004rad. At JMA Kobe × 1.25 excitation collapse behavior is observed. Center of the 2nd floor also moves to the direction of 45° after it passed point g as same time as point a. After it reached point i, moving direction of the center changes to almost X-direction. While increasing deformation of specimen, rotation of the 2nd floor frame also increases, and it rotates about 0.015rad at collapse time.

3.6 Correspondence between frame and member

Behavior of column based on the cyclic loading test shown **2.3** is simplification of column behavior in the frame. In this section, whether behavior of column in the frame corresponds with the result of cyclic loading test or not is examined. Before examination, the result of cyclic loading test needs to be corrected as shown Figure 14 to correspond to column in frame.

Firstly, comparing skeleton curve, stiffness of column in the frame is lower than the result of cyclic loading test both in X and Y-direction. It's considered that moment distribution of column in frame isn't ideal reverse-symmetry. And maximum strength in the frame is 30% lower than the result of cyclic loading test (Figure 15-(i)). According to **3.5**,

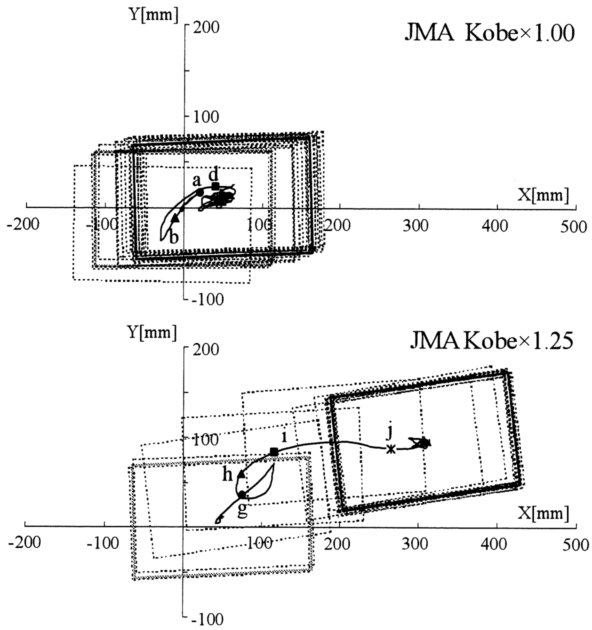

Figure 13 Orbit of center in the 2nd floor and frame

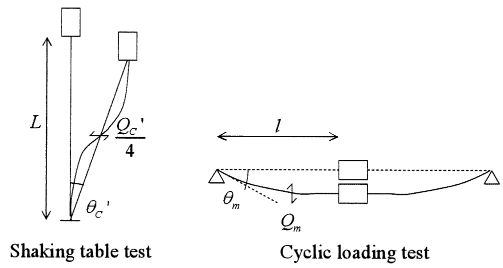

Q_m and θ_m in Cyclic loading test correspond to Q_c and θ_c in Cyclic loading test

$$Q_c' = \frac{8l}{L} Q_m \qquad \theta_c' = \frac{L}{2l} \theta_m$$

Figure 14 Correction of result in cyclic loading test

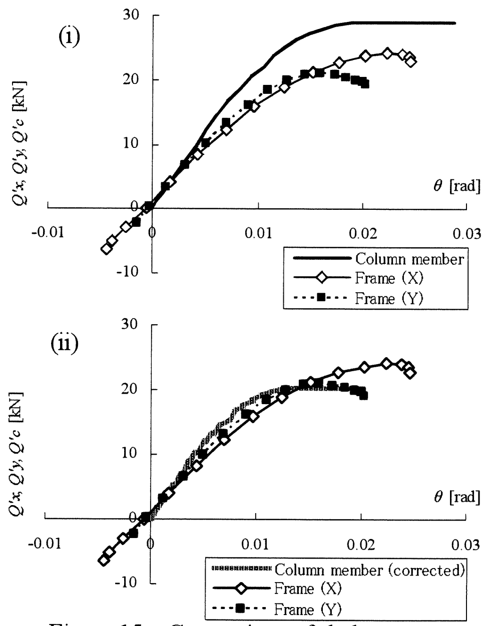

Figure 15 Comparison of skeleton curve

frame specimen in this range moves to the direction of 45° against X axis and Y axis. Therefore, horizontal component of restoring force in the frame is considered as projection of story shear on each direction. Multiplied $1/\sqrt{2}$ by the result of cyclic loading test, it corresponds with both horizontal components of frame (Figure 15-(ii)).

Secondly, behaviors after it reach maximum strength are focused. In this study, story shear and drift angle relationship acquired from the result of cyclic loading test approximates the three lines named 'column member approximate envelope lines'. And each area divided these three envelope lines call 'Elastic area', 'The 1st deteriorating area', 'The 2nd deteriorating area' as shown in Figure 16. Comparing story shear and cumulative displacement relationship of the frame and 'column member approximate envelope lines', decreasing of story shear in the frame correspond to the 1st deteriorating area after it reach maximum strength. And after frame displacement begins to increase in X-direction, loss of restoring force corresponds to the 2nd deteriorating area is observed as shown in Figure 17.

3.7 Collapse energy

Equation of energy under earthquake is given by Eq. (1) below:

$$E = W_{ek} + W_{es} + W_p + W_h \tag{1}$$

E : Full energy input

W_{ek} : Kinetic energy

W_{es} : Elastic strain energy

W_p : Plastic strain energy

W_h : Damping energy

Generally damping force is contained in the measured restoring force in shaking table test. So *Wes+Wp+Wh* can get by integration of story shear force and drift angle relationship. *Wek* can get by velocity from differential calculation. *Wpd* is given by Eq. (2) below:

$$W_{pd} = \int \frac{W \Delta_1}{h_1'} \, d\Delta \tag{2}$$

Figure 18 shows time history of absorbed energy around collapse time in X, Y-direction. Solid line shows E that is sum *Wek* and *Wes+Wp+Wh*, broken line shows *Wpd* energy lost by P-Δ effect. *Wpd* is so small before specimen begin to deteriorate, however at JMA Kobe × 1.25 excitation, shows a remarkable increase corresponding with increase of displacement in X-direction. And at collapse time, account 19% for E. Increment of E during 1.9 ~ 2.4s just before collapse is as much as increment of *Wpd*.

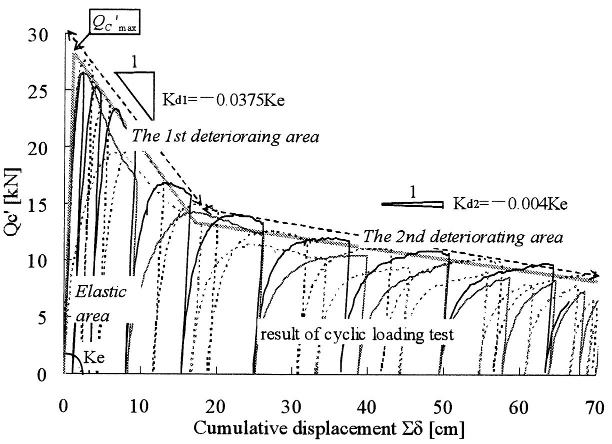

Figure 16 Method of column member approximate envelope lines

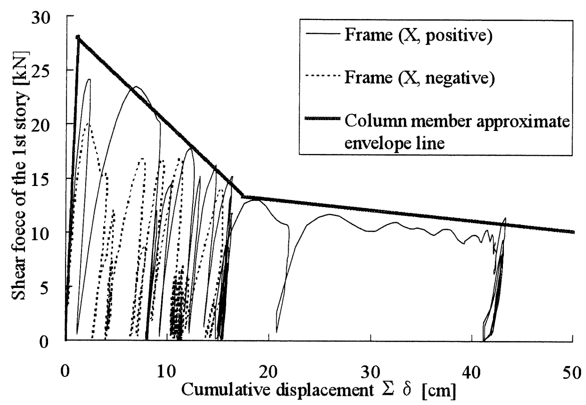

Figure 17 Comparison of Frame and column member approximate envelope lines

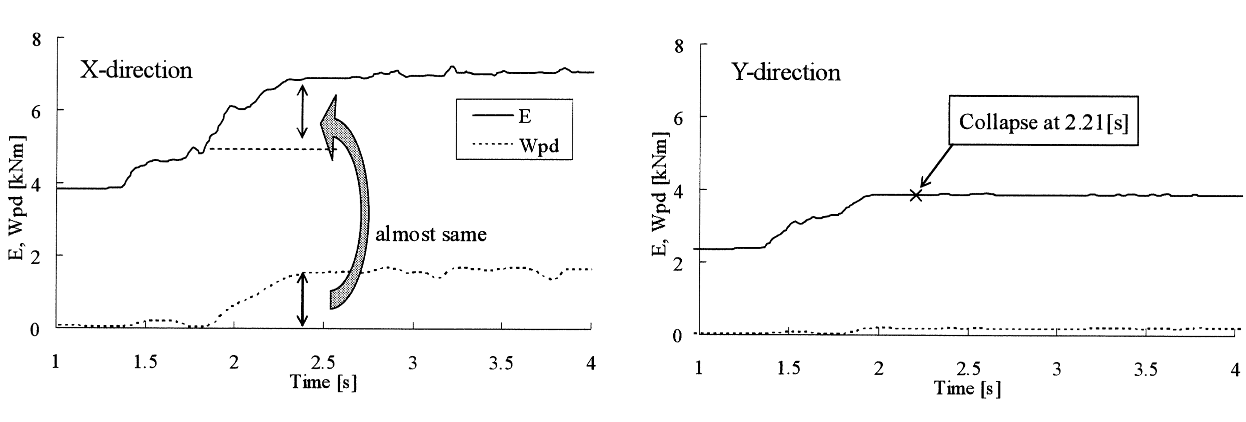

Figure 18 Time history of absorbed energy around collapse time

4. CONCLUSIONS

Dynamic behavior of small-scale 3-D steel frame model from elastic range to collapse with column collapse mechanism in the 1st story could be generally identified by shaking table test.

The important findings are follows;

1) Inputting earthquake wave adjusted JMA Kobe record to 3-D steel frame model, local buckling observed at tops and ends of columns in the 1st story. After that, input level increased, resistance of the specimen decreased. And finally, specimen lost restoring force.
2) As calculation of story shear contained deteriorating behavior, the method used column strain is better than the method used acceleration transducers. And potentiometer-type displacement transducers are effective to measure large displacement up to collapse.
3) Before it reaches maximum strength, specimen moves to the direction of 45° against X axis and Y axis. In this area column receive bending forces in two directions. $1/\sqrt{2}$ multiplied result of cyclic loading test corresponds to X and Y components of frame.
4) In the deteriorating range, behavior of column in the frame correspond to corrected result of the cyclic loading test. It's because specimen behave mainly X-direction up to collapse.

Acknowledgements:

This study is a production of the Building Collapse Simulation Working Group (WG) in 'NEES/E-Defense collaborative research program on steel structures'. The Japan team leader for overall program is Kazuhiko Kasai, Tokyo Institute of Technology, and the WG leader is Keiichiro Suita, Kyoto University. This study acknowledge financial support provided by the National Research Institute for Earth Science and Disaster Prevention, and utilization of shaking table based on 18G-01, general collaborative study in the Disaster Prevention Institute of Kyoto University. Special thanks are given to many WG members and students, staffs of the Disaster Prevention Institute of Kyoto University.

References:

Kasai, et. al. (2006), "E-Defense Experimental Projects for Steel Buildings – Part 1 ~ 5", *Summaries of Technical Papers of Annual Meeting Architectural Institute of Japan*

Fifth International Conference on Urban Earthquake Engineering
March 4-5, 2008, Tokyo Institute of Technology, Tokyo, Japan

DYNAMIC BEHAVIOR OF WOOD FRAMES WITH PASSIVE CONTROL MECHANISM AND NONSTRUCTURAL WALLS USING SHAKING TABLE

Kazuhiro Matsuda[1), Hiroyasu Sakata[2), Kazuhiko Kasai[3), and Yoji Ooki[4)

1) Graduate Student, Department of Built Environment, Tokyo Institute of Technology, Japan
2) Associate Professor, Structural Engineering Research Center, Tokyo Institute of Technology, Japan
3) Professor, Structural Engineering Research Center, Tokyo Institute of Technology, Japan
4) Research Associate, Structural Engineering Research Center, Tokyo Institute of Technology, Japan
matsuda@serc.titech.ac.jp, hsakata@serc.titech.ac.jp, kasai@serc.titech.ac.jp, ooki@serc.titech.ac.jp

Abstract: In Japan there are 10 million inadequate wooden houses against building standard law and most of them (approximately 90 percent) are composed of conventional post-and-beam. Passive control schemes to mitigate their seismic damage are important. In order to reduce seismic response and damage of wooden houses effectively, a series of so-called shear-link-type passive control systems, which include both velocity- and deformation-dependent dampers were proposed. A number of shaking table tests of the full-scale two-story wooden frame specimens were carried out and the dynamic behavior of the specimen having only structural elements were figured out. However nonstructural element is had to consider when passive control system is applied to wood frames. In this study, a number of shaking table tests of the full-scale two-story wooden frame specimens with inner and outer walls were carried out. The amount of inner and outer walls of the specimens is determined by the amount of inner and outer walls of real house. The performance of the specimens is discussed by referring to story drifts, story shear forces, damper deformations and forces with a focus on behavior of inner and outer walls. The dynamic properties of the structures such as equivalent periods and damping ratios are also discussed.

1. INTRODUCTION

In the Hanshin-Awaji (Kobe) Earthquake that occurred in 1995, the number of collapses or seriously damaged of wooden houses were approximately 250,000. It is said that approximately 10 million wooden houses are insufficient for earthquake resistant in Japan, and those houses need to be reinforced immediately. Moreover, to design new wooden houses to be resistant to earthquakes, it is important to investigate rational methods applying the passive control to wooden houses.

In order to mitigate the damage of wooden houses and seismic response, dynamic cyclic loading tests for wooden frames with passive controls (Kasai et al. 2005) and shaking table tests for one-story wooden frames that corresponded to mass for two-story were carried out (Sakata et al. 2007). And shaking table tests for two-story wooden frames (figure 1(a)) were also carried out (Matsuda et al. 2007). In this way, a number of shaking table tests of the full-scale wooden frame specimens were carried out and the dynamic behavior of the specimen having only structural elements were figured out. However nonstructural element is had to consider when passive control system is applied to wood frames. There are a lot of influences of nonstructural element and it's contemplated that the most is inner and outer wall. Therefore the inner and outer walls were adopted as nonstructural element. In this study, a number of shaking table tests of the full-scale two-story wooden frame specimens with inner and outer walls were undertaken (figure 1(b)). The objective of this study is to figure out the dynamic behavior of these specimens by shaking table tests.

2. OUTLINE OF SHAKING TABLE TEST

2.1 Specimen Concept

Figure 2 illustrates the building frame of the structural element. The specimen is composed of conventional post-and-beam and has a configuration of piled-up two

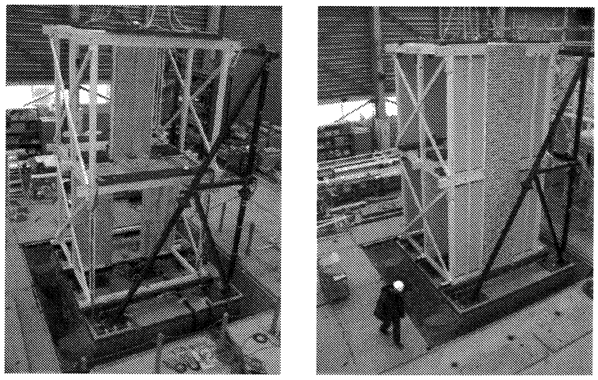

(a) Only Structural Elemenet (b) Having Nonstructural Element

Figure 1 Experimental Overview

cubes with 2730mm length on each side. The wooden frame has glulam spruce timber for the post (105×105mm), glulam red pine timber for the groundsill (105×105mm), glulam red pine timber for the beam (180×105mm), and structural plywood for the floor slabs (thickness of 28mm).

The seismic resistant frame is allocated in the center plane in the shaking direction, and the nonstructural element is allocated in the outside planes. The weight of the specimen is determined so that the two structural elements of the wall-strength-factor 2 have the resistance equivalent to the design lateral force for one story. Design lateral force for one story is obtained as a product of the weight of the specimen and the standard base shear coefficient (= 0.2). Here, the bracing-unit-multiplier is defined as the value of the lateral force corresponding to the 1/120rad. story drift angle deformation of 1m structural element divided by 1.96kN (= shear force which 1m wall can resist). The mass ratio of the 2nd-floor to the 1st- floor is 0.9, assuming the heavy roof and house where the area of the 1st- floor is equal to that of the 2nd- floor. The weights over the structural element have an effect on the pull-out of the post of the structural element. Therefore, the weights over the structural element are determined so that permanent axial load of the post of structural element is approximately equal to the dead load of the post of real houses. In the plane orthogonal to the shaking direction, the wood braces are set up to prevent torsion.

2.2 Parameter of Specimen

Specimen parameter is listed in Table 1. The wall-quantity in Table 1 is represented by the product of the bracing-unit-multiplier of structural element and the length.

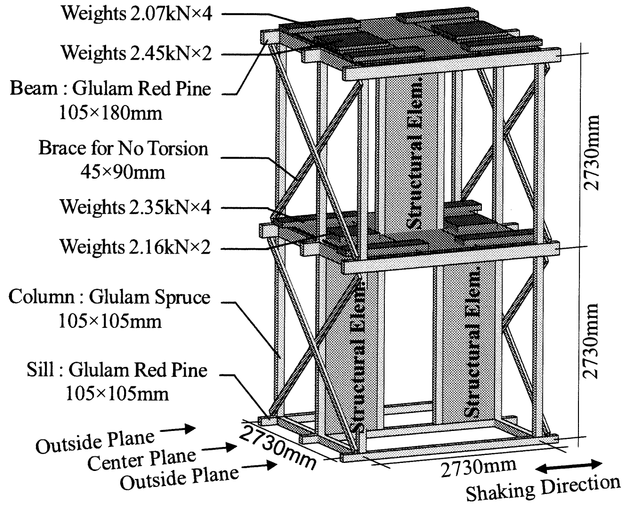

Figure 2 Building Frame of Structural Element

The shear link type "K-brace" is used as passive control system. For wood panel of the 2nd-floor, the wall is represented by the value considering the strength-factor at the adjustment since stiffness and strength by the number of nails obtained by Murakami and Inayama's equations were changed (Murakami et al. 1999). In addition, the letters of W means wood panel, V means viscoelastic damper, F means friction damper, S means siding, G means gypsum board, and M means mortar. The structural elements are arranged in center plane and the nonstructural elements are arranged in outside planes.

2.3 Measurement and Vibration Scheme

Figure 3 illustrates the measurement. Laser

Table 1 Parameter of Specimens

WQ means "Wall-Quantity"

No.		1	2	3	4			5
Name		-FW-/FW-FW	-F-/F-F(S+G)	-1.2W-/W-W(S+G)	-V-/V-V(S)	-V-/V-V(G)	-V-/V-V(G+S)	-V-/V-V(M)
Center Plane	2nd Floor	F + W	Friction Damper	Wood Panel	Viscoelastic Damper	Viscoelastic Damper	Viscoelastic Damper	Viscoelastic Damper
		WQ = (6+3.6)×0.91	WQ = 6×0.91	WQ = 3.6×0.91	WQ = 5×0.91	WQ = 5×0.91	WQ = 5×0.91	WQ = 5×0.91
	1st Floor	F + W	Friction Damper	Wood Panel	Viscoelastic Damper	Viscoelastic Damper	Viscoelastic Damper	Viscoelastic Damper
		WQ = (6+3)×0.91×2	WQ = 6×0.91×2	WQ = 3×0.91×2	WQ = 5×0.91×2	WQ = 5×0.91×2	WQ = 5×0.91×2	WQ = 5×0.91×2
Outer Plane	Innner	-	Gypsum Board	Gypsum Board	-	Gypsum Board	Gypsum Board	-
	Outor	-	Ceramic Siding	Ceramic Siding	Ceramic Siding	-	Ceramic Siding	Mortar
Last Schedule		14	16	14	12	12	16	18

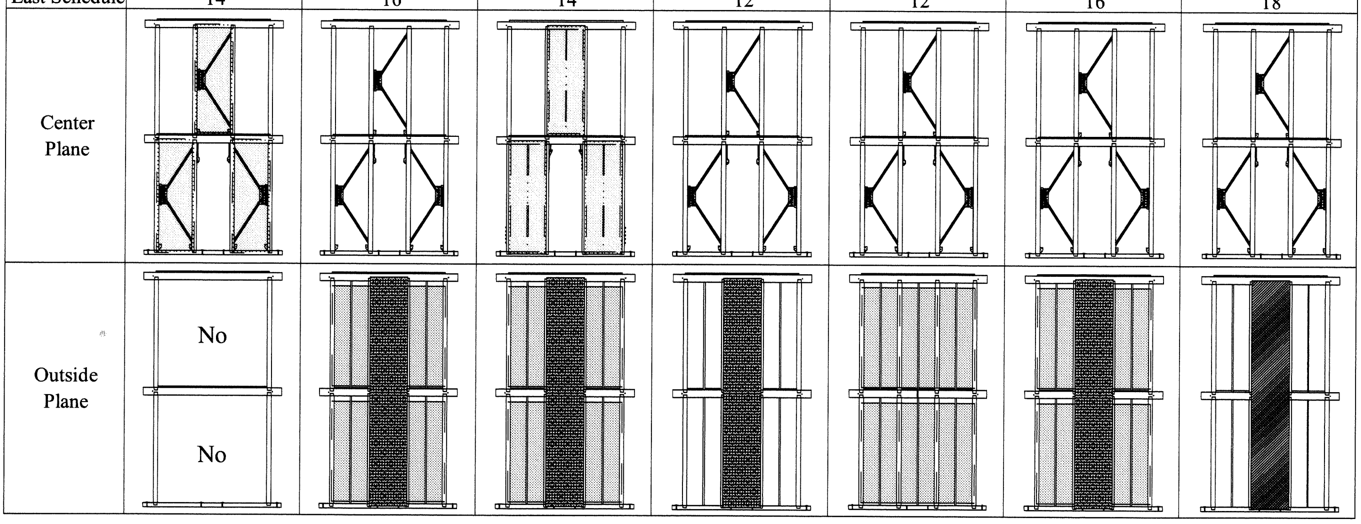

displacement sensors on the measurement frame built in the shaking table were used to measure the relative displacement of the specimen to the shaking table, and story drifts u_1, u_2 are calculated by using Eq. (1). There are acceleration sensors at the specimen's groundsill, beams on the 1st-story and the 2nd-story, and the story lateral force, F_1 and F_2, are calculated by using Eq. (2). The calculation of the story lateral force is found to be correct since Eq. (3) was verified by using the data of the shear-type load-cell arranged under the basement.

$$u_2 = d_2 - d_1 \qquad u_1 = d_1 - d_0 \qquad (1)$$
$$F_2 = m_2 \times a_2 \qquad F_1 = F_2 + m_1 \times a_1 \qquad (2)$$
$$F_1 + m_0 \times a_0 = \Sigma F_{load} \qquad (3)$$

Vibration scheme is listed in Table 2. For all earthquakes, the coefficient of variation of the displacement response spectrum and the pseudo-acceleration response spectrum obtained from the acceleration at the specimen's groundsill against target spectrum was checked to be within 5% for the natural period from 0.1 to 1.0 second. The eigenfrequency of specimens was measured in subjected to whitenoise which has maximum acceleration 0.1g before or after earthquakes. All specimens were not carried out all earthquakes since each specimens have different strength. The last vibration scheme number is indicated on table 1. The specimens of frame number 4 (table 1) were carried out according to -V-/V-V(S), -V-/V-V(G), -V-/V-V(S+G).

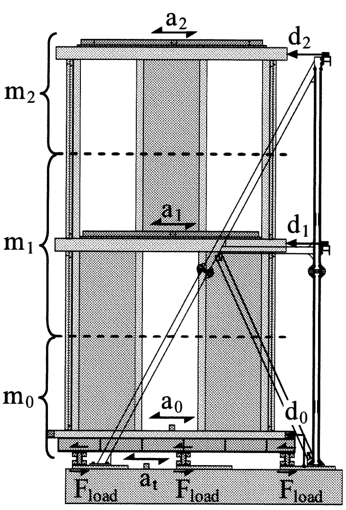

Figure 3 Measurement

Table 2 Vibration Scheme

No.	Name	Maximum Acc.(g)
1	W1	0.1
2	Taft-0.2g	0.2
3	W2	0.1
4	Kobe0.2g	0.2
5	W3	0.1
6	Kobe0.6g	0.6
7	W4	0.1
8	Kobe0.2g(2nd)	0.2
9	W5	0.1
Bolt The Joint Again		
10	W6	0.1
11	Kobe0.83g	0.83
12	W7	0.1
13	Kobe0.83g(2nd)	0.83
14	W8	0.1
15	Kobe1.08g	1.08
16	W9	0.1
17	Kobe1.08g(2nd)	1.08
18	W10	0.1

2.4 Amount and Sort of Inner and Outer Walls

Amount of inner and outer walls which are arranged in real house are investigated in order to determine amount of inner and outer walls which are arranged in the specimens. Here is the procedure to determine amount of inner and outer walls.

Regarding the weight of specimen, 1st floor is 18.8kN and 2nd floor is 16.8kN. Regarding the weight per unit area which is assumed to calculate necessary wall-quantity, 1st floor is 1.67kN/m^2 and 2nd floor is 1.44kN/m^2. The floor area of the specimens correspond to 11.5m^2 1st floor and 2nd floor alike because of dividing the weight of 1st and 2nd floor by per unit area. According to the investigation of four real houses using the opening reduction coefficient K_0, amount of inner and outer walls per unit area is generally equal and the average is listed in table 3(a). Multiplying the value of table 3(a) by 11.5m^2 corresponding to floor area of specimens gives the value of table 3(b). Therefore, 1st floor and 2nd floor alike, 6P inner walls and 2P outer walls are arranged in the specimens.

Table 3 Amount of Inner and Outer Walls (Average)

Unit : P (= 910mm)

(a) Per 1m^2

	Inner Wall	Outer Wall
1st Floor	0.443	0.144
2nd Floor	0.515	0.171

(b) Per 11.5m^2

	Inner Wall	Outer Wall
1st Floor	5.10	1.66
2nd Floor	5.92	1.97

Here is the detail of inner and outer walls.

(1) Inner Wall

The gypsum board was used. The side is 910×2420×12mm. The gypsum boards are screwed to the column and the intermediate column at 150mm intervals.

(2) Outer Wall

The details of outer walls are illustrated to figure 4 and used staple is illustrated to figure 5. There are a lot of construction methods of outer walls, the commonest construction method is adopted. The ceramic siding walls

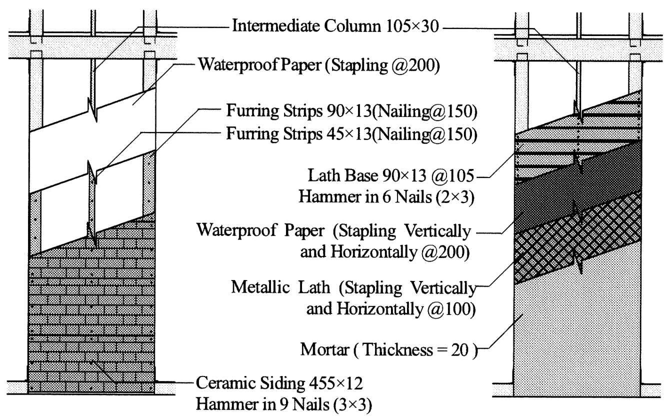

(a) Ceramic Siding (b) Mortar

Figure 4 Details of Outer Walls

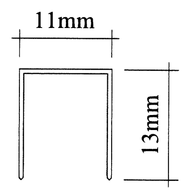

Figure 5 Used Staple

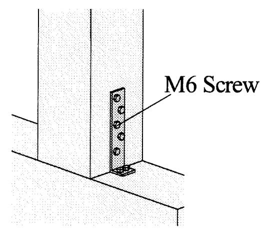

Figure 6 L type Joint Metal

are composed of ventilatory method by arranging the furring strips vertically. The mortar walls were given a first coat on March 8th, were given a final coat on March 14th and shaking table test of the specimen applied mortar walls are carried out on April 9th. In case of using inner walls or outer walls, L type joint metal (figure 6) is arranged in the junction of column with horizontal member.

3. TEST RESULTS AND COMSIDERATION

3.1 Time History of Story Drift

Figure 7(a) indicates the time history of story drift in case -FW-/FW-FW was subjected to Kobe0.83g. And for comparison, figure 7(b) indicates the time history of story drift in case -1.6W-/F-F which is included in the reference (Matsuda et al. 2007) was subjected to same earthquake.

In case of -1.6W-/F-F, the 1st floor with only friction damper had residual story drift angle of approximately 1/45rad. and the 2nd floor with only wood panel had long natural period because of the heavy damage. On the other hand, in case of -FW-/FW-FW, although the 1st floor has story drift angle of approximately 1/90rad., the floor has little residual story drift and stable natural period.

In case of no elasticity element, there is a high possibility that the floor with only friction damper has residual story drift because the secondary stiffness of friction damper is low. It is possible to confirm that the wood panel serves as elasticity element effectively.

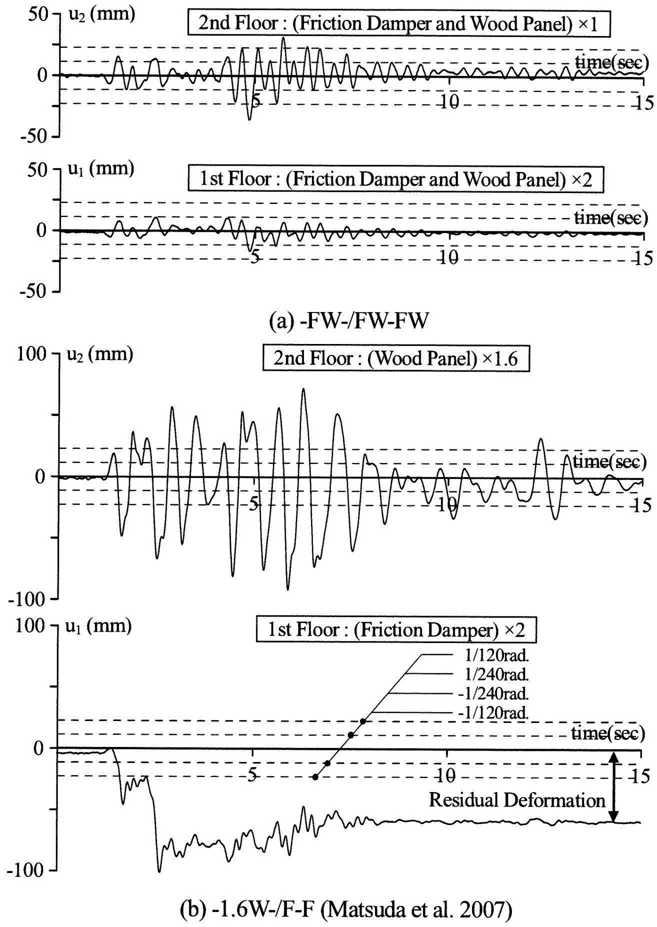

Figure 7 Time History of Story drift

3.2 Relationships Between Lateral Force and Displacement

In case the specimens were subjected to Kobe0.6g and

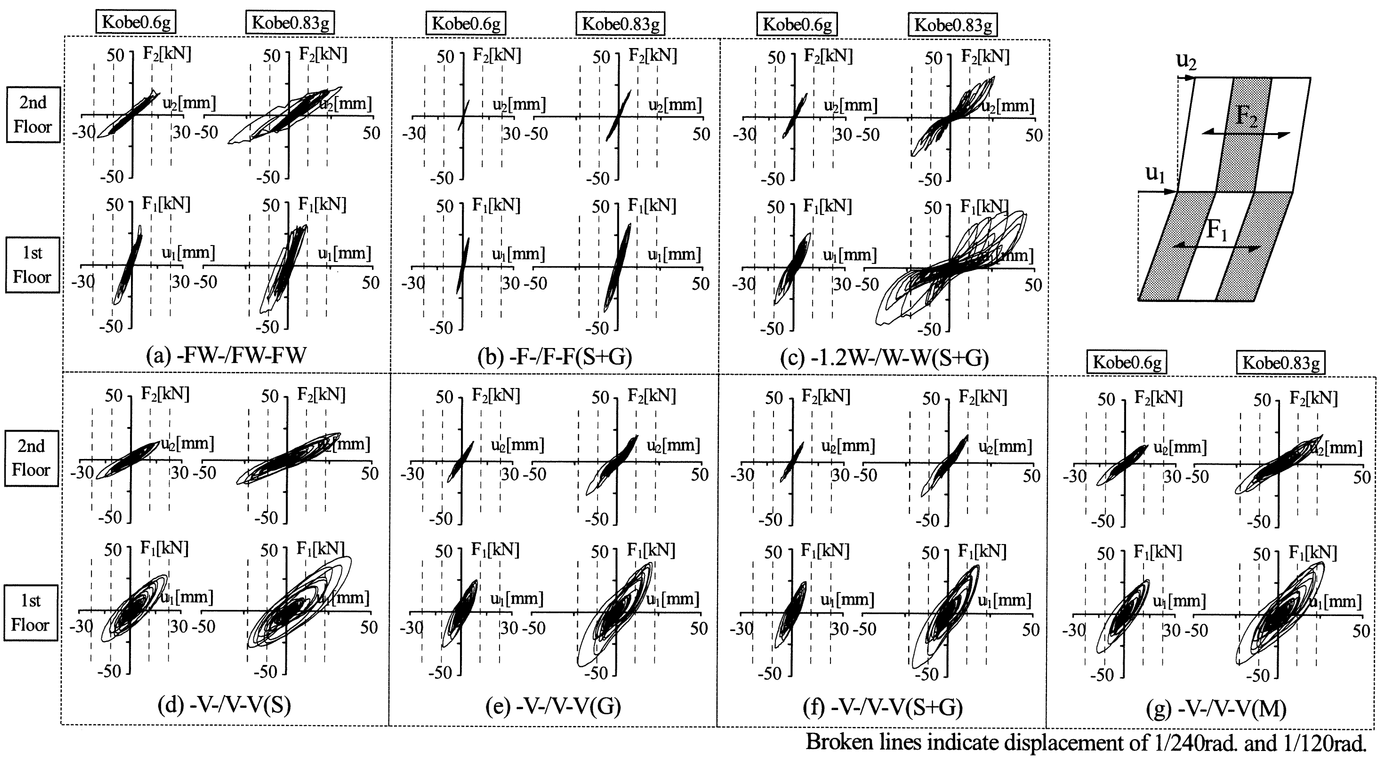

Figure 8 Relationships Between Lateral Force and Displacement

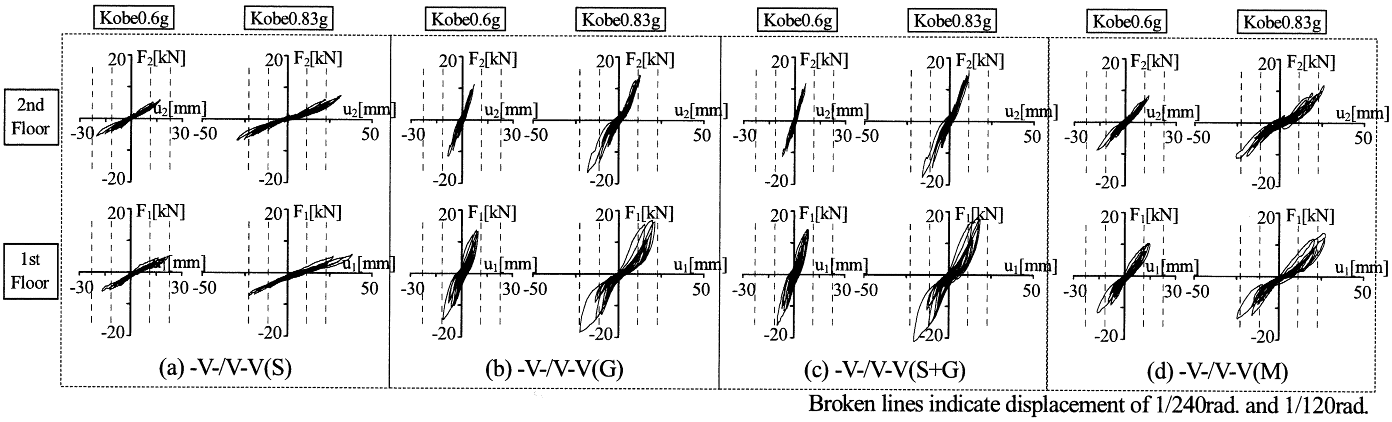

Figure 9 Relationships Between Lateral Force of Outside Planes and Displacement

Kobe0.83g, the relationships between lateral force and displacement are illustrated in figure 8. -FW-/FW-FW behaved with elasto-plastic hysteresis when it is subjected to Kobe0.6g. However -F-/F-F(S+G) behaved with elastic hysteresis when it is subjected to Kobe0.6g because of high initial stiffness. When -1.2W-/W-W(S+G) was subjected to Kobe0.83g, it behaved with pinched hysteresis having slippage after nails came off structural plywood. The hysteresis of the specimens with viscoelastic damper formed the ellipsoid.

3.3 Relationships Between Lateral Force and Displacement of Outside Planes

When the center plane has K-brace, the lateral force which the center plane bears approximately equal to third part of damper force (Sakata et al. 2007). Subtracting the third part of damper force from lateral force of figure 8, it is possible to calculate the lateral force which the outside planes bear. Figure 9 illustrates the relationships between lateral force of outside planes and displacement.

-V-/V-V(S) which has only ceramic siding in outside planes behaved with elastic hysteresis if the story drift angle was over 1/120rad. On the other hand, -V-/V-V(G) which has only gypsum board in outside planes behaved with high initial stiffness, however it behaved with pinched hysteresis having slippage after the screws dug into the gypsum board. -V-/V-V(M) which has only mortar in outside planes behaved with higher initial stiffness than ceramic siding, however it behaved with pinched hysteresis having slippage after the staple came off the lath base in small deformation.

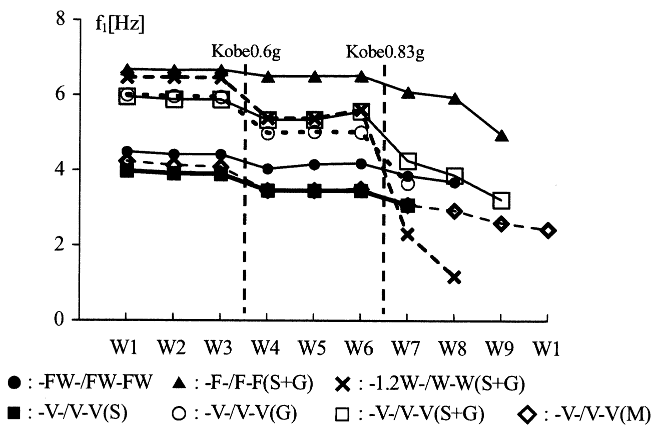

Figure 10 Variation of First Eigenfrequency

3.4 Variation of First Eigenfrequency

The variation of first eigenfrequency is illustrated in figure 10. The value was evaluated by whitenoise. When -V-/V-V(S) and -V-/V-V(M) are compared, -V-/V-V(M) slightly had higher than -V-/V-V(S) at first. However the two were approximately equal after Kobe0.6g. In spite of -1.2W-/W-W(S+G) had high value at first because of gypsum board, the more it was shaked, the more the value dropped away. In particular, after Kobe0.83g the value dropped away considerably. In case of -V-/V-V(G) and -V-/V-V(S+G), the value gradually dropped away because gypsum board had damage in small deformation. However they had higher value than the specimens which have only outer walls. Therefore the influence of inner walls is larger than that of outer walls, regarding real house.

4. CONCLUSIONS

A number of shaking table tests of the full-scale two-story wooden frame specimens with inner and outer walls were carried out. Major finding are

1) In case of the friction damper, it is possible to reduce the residual story drift by combining with the wood panel as elasticity element.
2) The difference of hysteresis of between gypsum board, ceramic siding and mortar were figured out.
3) The influence of inner walls is larger than that of outer walls, regarding real house. And in this experiment, the specimen which has gypsum board in outside planes behaved with eigenfrequency over 6Hz at first

Acknowledgements:

This study is program supported by a grant from "Electric Power Development Co., Ltd". We would like to express our appreciation to the company.

References:

1 Kasai, K. and Sakata, H. and Wada, A. and Miyashita, T. (2005): "Dynamic behavior of a wood frame with shear link passive

control mechanism involving k-brace", Journal of Structural and Construction Engineering, No.598, 2005.12, pp.51-60 (In Japanese)

2. Sakata, H. and Kasai, K. and Wada, A. and Midorikawa, M. and Ooki, Y. and Nakagawa, T. and Matsuda, K. (2005): "Shaking table tests of wood frames with velocity-dependent dampers", Journal of Structural and Construction Engineering, No.615, 2007.5, pp.161-168 (In Japanese)
3. Matsuda, K. and Kasai, K. and Sakata, H. and Ooki, Y. and Wada, A. (2007): "Shaking table tests of two-story frames with passive control system", Proceedings of 4th International Conference on Urban Earthquake Engineering, Center on Urban Earthquake Engineering, 2007.3, pp.369-374, Yokohama, JAPAN
4. Murakami, M. and Inayama, M. (1999): "Formulae to predict the elastic and plastic behavior of sheathed walls with any nailing arrangement pattern", Journal of Structural and Construction Engineering, No.519, 1999.5, pp.87-93 (In Japanese)

BCP IN JAPAN: DIFFUSION AND EXPECTATION

Hiroaki Maruya[1)]

1) Professor, Institute of Economic Research, Kyoto University, Japan
maruya@kier.kyoto-u.ac.jp

Abstract: BCP and BCM are gradually recognized and accepted by Japanese companies in several years. Main reason for the diffusion of BCP/BCM is risk recognition of large-scale earthquake, such as Tokyo Inland Earthquakes, Tokai Earthquake, etc. It contains not only direct damage of quake or tsunami, but also indirect damage thorough economic transactions or by suspend of supply chain. Government, both central and local, has promoted BCP by official guidelines and manuals. Ministries and some prefectural governments have started to formulate BCP. Additionally, a non-profit organization BCAO has acted as a promoter of BCM and started a certification system of BCM experts.

1. Background of Diffusion of BCP

Business Continuity is essentially a management strategy for corporations and organization to facilitate the rapid recovery and restoration of services and operations with minimum interruption in the aftermath of an accident or disaster. This is achieved through Business Continuity Management (BCM) for the development, execution, exercising and review of Business Continuity Plans (BCP). In the wake of the computer millennium bug problem and the terrorist attack on September 11 in New York, the importance of BCM and BCP has been the focus of increasing attention, and the USA and UK have taken the lead in widespread adoption of BCM. For this reason, cases of Japanese companies that are requested by overseas trading partners to furnish their BCP are on the rise. In addition, because it is necessary to tackle the issue of Business Continuity throughout the supply chain, major domestic companies are beginning to demand BCP from their suppliers.

Since 2004, Japan has experienced a string of large-scale disasters, and companies have a renewed recognition of the importance of corporate disaster and crisis management measures. Also from the standpoint of information security governance, the continuity of information system operations is vital. With this in mind, the government has been announcing Business Continuity guidelines one after another since 2005, stressing the importance for all companies including small- and medium-scale businesses to come to grips with BCM. Furthermore, the government positions BCP as a key pillar of corporate disaster management in their policy for national countermeasures in the event of a large-scale earthquake.

2. What is Business Continuity?

Figure 1 shows a concept of Business Continuity. If a company has no countermeasures to continue its operation: the operation degree of the 'critical operations' turns to be zero % by a disaster or an accident, and gradually recovers. However, such a late recovery seems to cause 1) losing customers to other companies, 2) decline in market share, 3) serious social inconvenience and 4) negative impact on a company's reputation due to the interruption of critical operations. Therefore, the company should recognize the

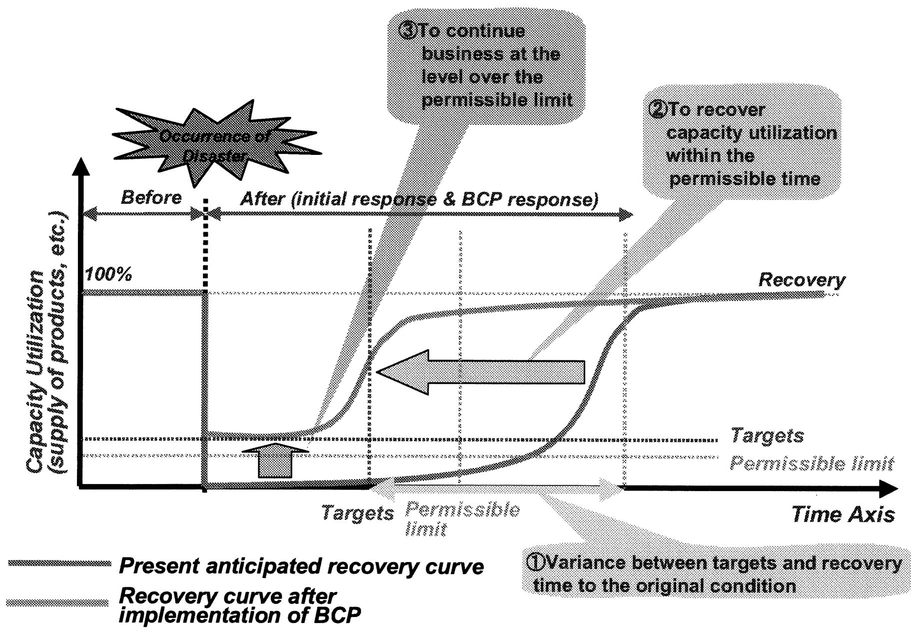

Figure 1 Concept of Business Continuity

'permissible limit of recovery time', and should recover the operation degree before the limit. Additionally, even shortly after a disaster or an accident, the company should keep the operational degree above the permissible level.

Business Continuity is to be ranked by companies as a strategic issue at a management level. Their interested parties, including clients, require that after damage is incurred, companies do not suspend critical operations, or if they are suspended, they resume operations as soon as possible. Concern of interested parties is not only the direct damage by disasters or accidents.

Important articles of Business Continuity are;

1) Clarifying the chain of command
2) Securing the functions of the head office and other key sites
3) Transmitting information outside and information sharing
4) Backing up the information system
5) Supplying products or services

Suspension of 5) may be allowable, provided 1) to 4) have already been established, and the suspension time is within the allowable period

Main items and measures for Business Continuity are;

a) Emergency response team/system, contact place of communication
b) Safety confirmation of company members, replacement of personnel
c) Alternative facility, seismic strengthening
d) Financial consideration
e) Alternative suppliers, request of BCM to suppliers
f) Alternative production agreement with other companies of the same trade

Many of these items and measures do not need large expense. Therefore, BCP should be prepared by every company and organizations.

3. Difference between Disaster Prevention and BCM

In Japan, a main factor for most companies and organization to introduce BCM is risk recognition of large-scale earthquakes. Therefore, to make clear the difference between traditional disaster prevention countermeasures and BCM measures is important. Without such explanation, BCM may be misunderstood as something similar to seismic strengthening or simple recovery plans.

Traditional Disaster Prevention and BC

	Disaster Prevention	BCM
Point of view	◆Safety of life ◆Reduction of material damage ◆Reaction in each business base ◆Mainly done by safety-related/facility department	Additional new points of view ◆Continuity and early recovery of the important operations ＜management view＞ ◆Countermeasures in supply chain
Index	◆Numbers of casualties ◆Amount of material damage	◆Recovery time/level ◆Management, Effect to stakeholders

特定非営利活動法人 事業継続推進機構

Table 1 Disaster Prevention and BCM

Table 1 shows an example to clarify the difference. Key words of BCM compared to disaster prevention are 'critical operations', 'supply chain', 'recovery time', 'effect to stakeholders' and so on.

3. Present Situation of BCM Acceptance in Japan

Several research firms have conducted BCP/BCM surveys in Japan, and most of them show that diffusion rate has been considerably lower than that of USA and United Kingdom. In addition, number of companies that already formulated BCP is not increasing rapidly in these two or three years. A questionnaire survey by the Development Bank of Japan (Sep, 2007) is one of most reliable. It covers companies whose capital is more than one billion yen. Number of response was 1,573. The result shows;

- Companies already formulated BCP: 8 %
- Those already started to formulate BCP: 18 %
- Those without BCP but with disaster prevention plan including emergency response plan: 53 %
- Those having no plan of disaster prevention: 21 %.

Additionally the rate of 'already formulated BCP' is almost the same percent point with a survey of previous year.

However, based on discussions with a lot of firms and related organization, the author believes that most of Japanese big companies have already known what BCP/BCM is and understand the importance. The reasons of these low diffusion rate include the fact that the BCP/BCM for large-scale of earthquakes is more difficult to formulate, compared to those for a fire or an electric power failure. Firms and Organization have to estimate the damage of infrastructure, suppliers and customers and neighborhood. Many Japanese companies that stared to execute BCP/BCM seem to be facing a large number of problems in time of a big earthquake, and lose serf-confidence to publish that they have started to formulate BCP for large-scale earthquakes.

4. Promotion Policy of Japanese Government

The author was a person in charge of drafting the "Business Continuity Guideline[1]" of Cabinet Office in 2005. One of the important trigger to make the guideline was publication of the estimated damage of the Tokyo Inland Earthquakes. If it occurs, by way of suspend of critical supply in wide range of business transactions, expansion of economic damage is strongly concerned, to all over Japan or worldwide Therefore Japanese government is promoting BCP and BCM in addition to the traditional disaster prevention countermeasures.

At present, feature of BCP policy of Japanese government is as follows;

1) Formulation of BCP is not legal obligation by laws
2) Governments urge companies to introduce voluntarily

BCP by Business Continuity guidelines[2]

3) The Basic Disaster Management Plan (based on the Disaster Countermeasures Basic Act) officially requested enterprises to make effort to formulate BCP

Governmental organizations themselves have also started to formulate BCP. "Business Continuity Guidelines for Ministries" was published in June, 2007. Following to the guideline, all central government ministry and agency are requested to formulate their BCP in fiscal year 2007. Prior to this, Ministry of Land, Infrastructure and Transport (MLIT) published its basic BCP in Jun, 2007, and its regional bureau for Kanto area (including Tokyo) revised its basic BCP in July, 2007[3]. The other Regional Bureaus of MLIT are now formulating.

As for prefectural government, Tokushima is under way of making its BCP, and Tokyo and Osaka have started to make in this fiscal year.

Regional government and public organization also began the promotion of BCP/BCM to companies in their own region. The author and BCAO (explained later) originally developed a BCP manual for small and medium-sized enterprises (SMEs): "BCP Step-up Guide for SME." It has 3 parts and 24 steps, to help gradual advancement of SMEs. With the help of the author, Tokushima prefecture[4] published its BCP guideline in April, 2007, which utilized the BCP Step-up Gide and customized considering local situations. One similar case is the "Prepare to the Disaster! BCP Step-up Guide for Small and Medium-sized Enterprises in Tokyo"[5] by Chamber of Commerce and Industry, Tokyo, published in December, 2007. Another similar case is "Simple Gide for Business Continuity for Construction Companies in Case of Disasters"[6], by Kanto Regional Bureau, MLIT, published in December, 2007.

To promote BCP/BCM especially to SMEs, effective incentives must be necessary. Development Bank of Japan (DBJ) started low interest loan for companies that have a special rating of disaster preparedness including BCP in 2006. This rating for each company is decided by DBJ itself on a case-by-case basis. Several private regional banks are now offering low interest loan for companies with BCP or having schedule to introduce BCP. However, number of the companies using this loan system is very small at this moment.

Other ways to promotion probably include awarding SMEs for their good practices, and priority public procurement from SMEs having BCP; an example should be procurement of disaster prevention related goods and services. For these promotion systems including low interest loans, the author believes that a clear/objective evaluation tool of BCM level of each company is necessary. The author is now discussing and drafting with CCI, Tokyo, Tokushima Prefectural Government and a NPO members stated later.

5. Establishment of BCAO

Business Continuity Advancement Organization, Japan (BCAO)[7] was established based on the proposal of the experts and scholars associated with the formulation of the above mentioned Business Continuity governmental guidelines and with the cooperation of many others with a high degree of interest in the field of Business Continuity.

The roles and activities of BCAO include: activities to educate companies and promote widespread adoption of BC; fostering BC specialists; standardization; awards; research; information dissemination; publishing, seminars; and support for companies and organizations that are embarking on BCP.

As of the end of December, 2007, the organization has the participation of over 1,000 individual members (including persons registered under the corporate membership).

BCAO has published the Introductory Standard Textbook that serves as BCM teaching material and has been continuously revised. Figure 2 and 3 show examples of slides from the text. Content of each has been originally produced by BCAO.

Figure 2 Text Example 1

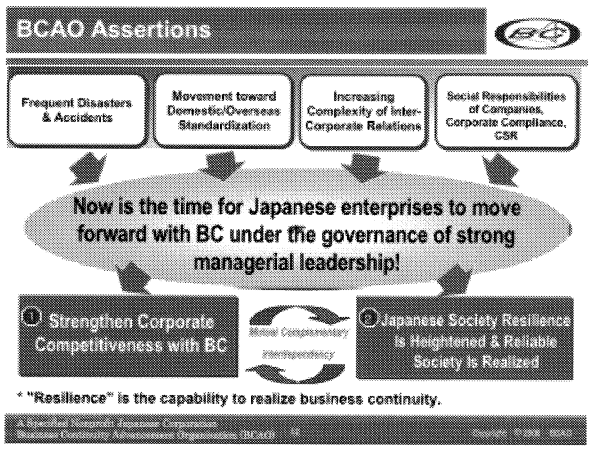

Figure 3 Text Example 2

These text examples show that the needs of BCP/BCM are not only generated by the increase of disasters or concern of disasters. Vulnerability for continuity of critical operation is generated by the companies' efforts of rationalization of business, such as limiting the number of suppliers, outsourcing, introducing information and communication technology, and so on. Therefore, every organization is recommended to secure some part of resources to strengthen the ability of Business Continuity.

Current committees of BCAO are as follows:

1) Standardizing & Education
2) Promotion of BC Understanding & Adoption
3) Committee on International Affairs
4) BC Fundamentals – Business Impact, Information System, Backup Office, Finance, Natural Disaster Study, Natural Disaster Information, Terrorism & Accidents
5) Research & Analysis Issues

These five committees have subcommittees and their number is about 20. Additionally, for members who wish to acquire fundamental knowledge about BCP/BCM, a Fundamentals Study Group has been established. These various committees and subcommittees generally will meet on a monthly basis.

Also BCAO has regional blanch in Kansai (Osaka), and some regional activity groups.

6. Certification System of BCAO

With the aims of facilitating the acquisition of basic knowledge by those charged with the management and supervision of BC in companies and organization and providing those with practical BC experience with a way to enhance their specialty, BCAO has structured a system of certification for Business Continuity specialists.

BCAO has already implemented a certification system of 'Business Continuity Specialist Grade I', and is in the process of preparing a curriculum for the training of 'Business Continuity Specialist Grade II.

Certification System for Business Continuity Specialists and Respond Director is shown in Figure 4.

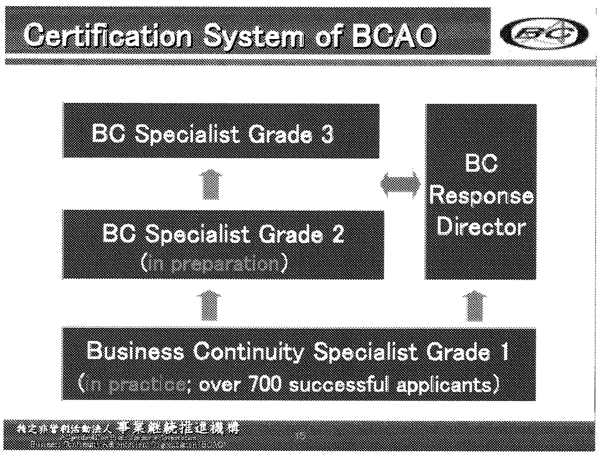

Figure4 Certification System of BCAO

Number of successful applicants of Business Continuity Specialist Grade I is over 1,000. The training course and examination of Business Continuity Specialist Grade II will be expected in the end of fiscal year 2007.

7. Conclusion

These days, introducing BCP/BCM is 'finally' one of hot issues of business leaders and large companies after warming-up of several years. However, it seems that executives of companies do not easily admit the cost of investment for Business Continuity because they always face severe competition in their market. To get over this problem, the author believes that merit of BCM should be more recognizable and countable, not only in time of disasters or accidents, but also in ordinal/peace times. For this, evaluation and appreciation of Business Continuity in market and regional society should be very important.

Large scale natural disasters including big earthquakes are inevitable in Japan. Additionally we should consider the risks of terrorism, new influenza, etc. All disaster-related specialists are requested to contribute the continuity of Japanese social and economic activities in time of disasters and accidents.

References:

Maruya, H and Sashida, T. (2006), "Commentary and Q&A of Business Continuity Guideline of Central Disaster Prevention Council," Nikkagiren Inc

Maruya, H. (2007), "Study of the Step-up Introduction Measures of BCP for Small and Medium Enterprises," Proceedings of the Annual Conference, Institute of Social Science, No.20, 41-16

Maruya, H. (2007), "The Present State and Regional Difference in the Assistance Measures Provided by the Prefectural Government, etc. for SMEs to Introduce a BCP," Journal of Social Safety Science, Institute of Social Science, No.9, 37-46

Maruya, H., Mori, S., Arai, N., Tawa, J., and Amakuni, K. (2007), "Characteristics of BCP of Local Governments and Consideration on Promotion of its Development," Proceedings of the Annual Conference, Institute of Social Science, No.21, 95-100

Maruya, H. (2006), "Study on the Situation and Difficulty of Introducing Important Elements of Business Continuity Management, Considering Dissemination of BCM to SMEs in Japan," Journal of Social Safety Science, Institute of Social Science, No.8, 269-278

Additional Note

[1] Cabinet Office, Japan (2005), "Business continuity Guide line, 1st edition", http://www.bousai.go.jp/MinkanToShijyou/guideline01.pdf

[2] The guidelines are that of 'Cabinet Office' (see note 1), 'Ministry of Economy and Trade' (focusing on IT security), and 'Small and Medium Enterprise Agency.

[3] The author helped to formulation works of BCP of MLIT and BCP of Kanto Regional Bureau.

[4] http://www1.pref.tokushima.jp/005/01/kibou/

[5] http://www.tokyo-cci.or.jp/chiiki/bcp/

[6] http://www.ktr.mlit.go.jp/kyoku/saigai/bcp/kanigaido.pdf

[7] http://www.bcao.org/

Fifth International Conference on Urban Earthquake Engineering
March 4-5, 2008, Tokyo Institute of Technology, Tokyo, Japan

EVALUATION OF EARTHQUAKE RESISTANCE CAPACITY OF BUSINESSES: DEVELOPMENT OF CMP-METHOD

Hideki Kaji [1], Jun Mihira [2], and Yoshinari Takanashi [3]

1) Professor, Center for Urban Earthquake Engineering (CUEE), Tokyo Institute of Technology, Japan
2) Doctoral Student, Graduate School of Media and Governance, Keio University, Japan
3) Chief Project officer, Iota Co. Ltd, Ikebukuro, Tokyo, Japan
hkaji@plum.ocn.ne.jp, jmihira@sfc.keio.ac.jp, takanasi@iota-lab.com

Abstract: This paper describes a new method, named CMP and developed by the author, which is applied to evaluate the capacity of earthquake resistance of business enterprises. On the bases of their emergency governance, including earthquake resistance of the buildings and facilities, preparedness for relief, daily practice of training exercise in emergency, their potential capacity of earthquake resistance can be extracted as the five dimensions of integrated, structural, planning preparedness and response capacity.

1. INTRODUCTION

The needs of disaster management of business enterprises can be discussed from three different aspects (Figure 1). The first and most primary need is to mitigate property damage caused by disasters in order to reduce economic loss. This may directly bring benefit to enterprises. The disaster mitigation plan (DMP) should be prepared for measurement. The second need is to share disaster mitigation efforts with community they belong for fulfillment of their social responsibility that is current requisite by society. One of the typical contributions of business enterprises to the society may be to conclude mutual-help agreement with the community. The third and the most recent interest are to continue their businesses even after a disaster for securing their social credibility as well as for contributing to quick recovery of social functions. The business continuing plan (BCP) is thus to be prepared.

These three interests, however, are not perfectly independent but overlapping each other. The common part of the damage mitigation and social responsibility includes the relief and rescue responses to customers who are often neighbors of the enterprises. The enforcement or perfect back-up of the most fundamental function of the business enterprise is important for both DMP and BCP. Because the severe damage to such function, if occurs, must bring extreme economic loss to the enterprise, and at the same time must make the recovery delay, resulting in long suspension of businesses. The overlapping part of credibility security and social responsibility includes protective measures to production or service operation in general, as immediate resumption of supply of products or services is no other than the aim of BCP and also the best way to fulfill the social responsibility. The central part of the figure 1, on which three interests are overlapped, includes information management system which consists of data base on customers, inventories, list of supply chain, employees, operation manuals, and so on so force. It is expected for all business enterprises to prepare the disaster management plan from these three different points of views.

This paper focuses on the damage mitigation capacity of businesses. In order to evaluate their capacity, CMP method has been developed. The CMP stands for Capital, Manpower and Planning, respectively. About 600 business enterprises of Mie prefecture were surveyed in March 2005, on earthquake resistance of their building and facilities, equipment, disaster drill, preparedness for relief, emergency governance, and so on. The paper examines the results.

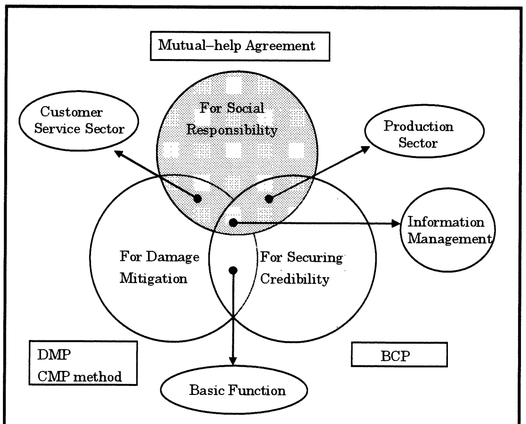

Figure 1 Disaster Management Planning of Business

2. CMP MEASUREMENTS

2.1 Twelve measurements

In order to expose the potential capacity of earthquake resistance of business enterprises, their current status of emergency governance in terms of facility and equipment (Capital), human resources (Manpower), and emergency planning (Planning) is surveyed. These three emergency governances are further broken down to four measurements respectively. They are as follows:

Capital Status -- Strength of facilities to earthquake and preparation of equipment for emergency:
- Proportion of earthquake resistant buildings and facilities,
  Structure of building and elevator, furniture protection from falling down, and inspection
- Preparation of fire proof equipment,
  Sprinkler, fire extinguisher, and emergency route
- Installation of emergency information equipment,
  Power source and extra computers for emergency
- Preparation of relief and rescue equipment,
  15 kinds of emergency equipment, including chain sow, jack, electric generator, and so on

Manpower Status – Empowerment of human resources:
- Practice of disaster drills,
  Frequency, participation ratio, practice of 9 contents and collaboration with community
- Practice of disaster education to employees,
  7 subjects, including lectures on earthquake disaster, first-aid, and emergency contact, and so on
- Special stuff for emergency management,
  Self-help fire brigade and regular person in charge
- Leadership of top management to disaster,
  Awareness, cooperation, and grasp of emergency plan

Planning Status – Formulation of emergency plan:
- Flexibility to diverse disaster occasions,
  Variety of disaster scenario, measures to changing disaster phase, and frequent amendment
- Richness of planning contents,
  9 plans on responses to the employees, their families, customers, business partners, and neighbor communities
- Establishment of information network system,
  9 plans on communication with the top managers, the employees and families, business partners, hospitals, local governments, and news media
- Preparation for recovery,
  Data back-up and storage of water, food, and medicine,

The current status of emergency governance of enterprises can be surveyed on these measurements.

2.2 Sampling and Data Collection

On March, 2005, the questionnaire sheets were distributed to 1,283 major enterprises of Mie Prefecture as samples. Out of them, 569 enterprises answered. The collection ratio was 44 per cent.

Reflecting the regional characteristics of the prefecture, about half of samples collected were manufacturing industries and concentrated in a particular district.

3. RESULTS

3.1 Capacity Dimensions

Above mentioned twelve measurements are overlapped and correlated each other. Moreover, they can not be directly summed up or multiplied as the scale dimension of respective measurements are not the same. Thus the component analysis was applied to extract the latent axes, which reflected common dimensions of these twelve measurements.

As a result, three principal components were extracted. The first principal component implied the dimension of integrated capacity of earthquake resistance as all twelve measurements had positive factor loadings to this axis. Therefore, the bigger the principal component score (called as a factor score hereafter) of this component of an enterprise is, the bigger the earthquake resistance capacity on the said enterprise is. The second component was interpreted as the two polar axes with structural and planning capacity dimensions. The positive side implied structural capacity as the measurements on capital status had high factor loading, while the negative side implied planning capacity as the factor loadings of measurements on planning status were very high.

The third component was also polar axis with response and preparedness capacity dimensions. The positive side implied the capacity of actual battle after an earthquake occurred, that was the capacity of response to earthquake damage. The negative side implied rather defensive activities prior to an earthquake such as preparation of defense equipment and planning formulation, and thus was interpreted as preparedness capacity.

The feature of earthquake resistance capacity of individual enterprise can then be illustrated in a pentagon diagram by using factor sores on these five capacity dimensions (Figure 2). In case of the figure 2, the capacity of this company is relatively higher than the regional average on all dimensions. Out of four dimensions excluding the integrated, structural capacity is dominated and planning capacity is rather weak.

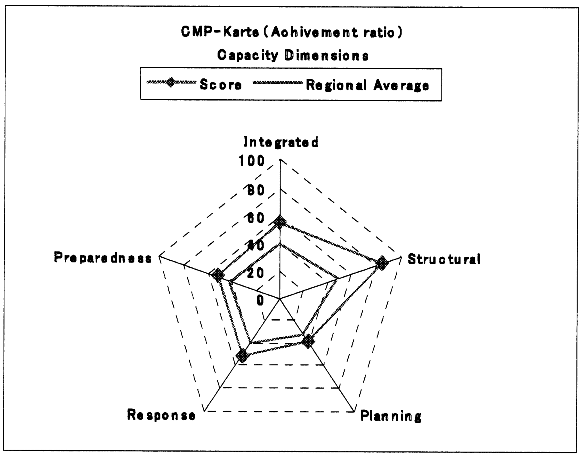

Figure 2, Pentagon diagram of earthquake capacity of business enterprise

3.2 Distribution of capacity score

Table 1 shows the outline of capacity scores of five dimensions in this region. The full sores of five capacity dimensions vary due to different factor loadings of twelve measurements to each axis extracted by the component analysis. The average score of 569 enterprises on each component is about 40 % in terms of achievement ratio. Among them, structural capacity is the highest, while planning capacity is the lowest. It implies that the enterprises of this region make their efforts to strengthen their buildings and facilities, but little attentions are paid to formulate an emergency plan.

Table 1, Outline of the region

Score	Full (A)	Highest	Average (B)	Achievement (B/A*100)
Integrated	746	684	300	39.3 %
Structural	172	158	83	48.3
Planning	130	123	42	32.4
Response	159	134	62	39.1
Preparedness	95	85	39	41.4

Figure 3 illustrates the distribution of the integrated capacity scores of the sample enterprises surveyed. It can be observed in this figure that about half of enterprises concentrate in the category of 400s point. Only 10 % of the enterprises exceeded at the level of more than 500 points in their integrated capacity. It is, therefore, recommended that all enterprises should up-grade their integrated capacity to more than 500 points, which is about 65 % in terms of the achievement ratio.

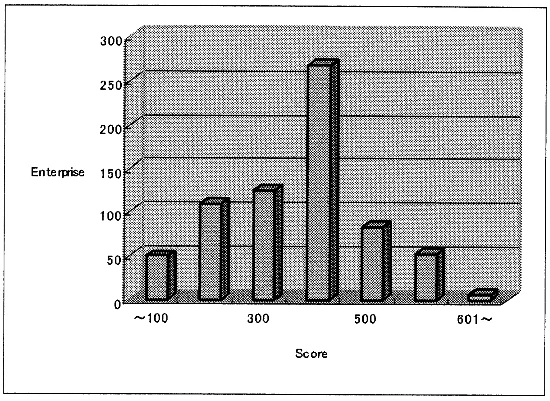

Figure 3, Distribution of integrated capacity

Figure 4 is the distribution of all enterprises on the graph of two dimensions with structural capacity score for X-axis and planning capacity score for Y-axis. This figure represented the unique characteristics of this sample region. That is, so many enterprises have no emergency plan, even though they have certain structural capacity. Some of them exceed more than 100 points with the structural capacity, which is measured as about 60 % in achievement score, while less than 10 % with planning capacity. In order to mitigate the earthquake damage, the certain extent of structural capacity may be a necessary condition, but may not be a sufficient one, because the structural protection can only reduce damage with limitation. It is recommended that more than 120 points of structural capacity score and 80 points of planning capacity score should be achieved respectively.

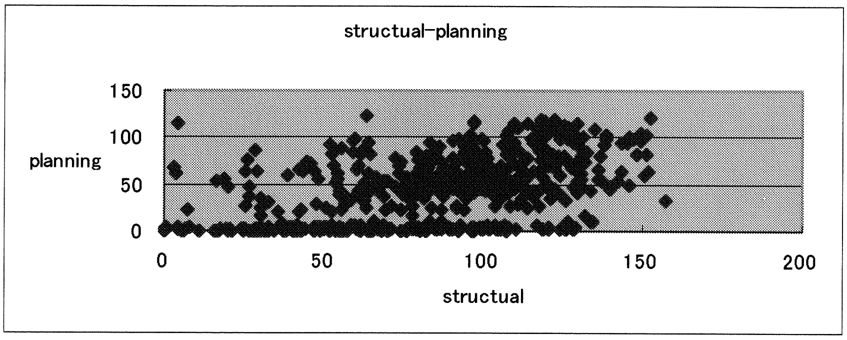

Figure 4, Balance between structural and planning capacity

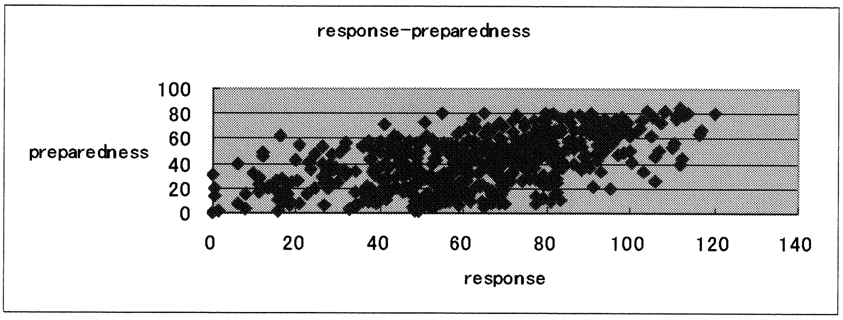

Figure 5, Balance between response and preparedness capacity

Figure 5 is also the distribution of all enterprises on the graph of two dimensions with response capacity score for X-axis and preparedness capacity score for Y-axis. As far as these two capacities are concerned, not so much unbalance between them is observed, though some have low preparedness capacity with high response one, while others are converse. As a recommendation, more than 90 points of response capacity score and more than 60 points of should be targeted.

3.2 Capacity score by attribute of enterprises

The capacity score strongly depends on the attributes of enterprises, in particular by size (the number of employees) and by the type of industry.

Figure 6 shows the bar graph of the integrated capacity by size of enterprise in terms of the number of employees. It is obviously shown that the bigger the size, the bigger the capacity is. The enterprises with less than 100 employees have only half capacity of those with more than 1000 employees. In other words, the middle and small industries may suffer severer damage than big ones. The detail observation, however, indicates that structural and response capacities are not so much different between middle and small enterprises and large ones, while their planning and preparedness capacities are almost 30 to 40 % of the large ones. Thus, more intensive instructions in these aspects and financial support to them are strongly recommended.

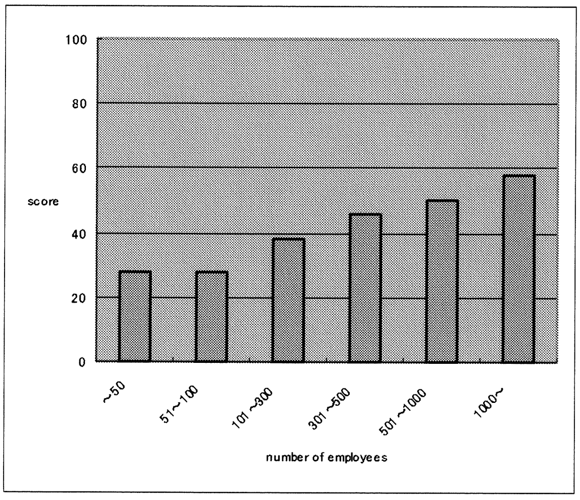

Figure 6, Integrated capacity by size of enterprise

The figure 7 shows also the bar graph of the integrated capacity by types of industry. This graph also exposes an interesting or rather common result. The power plant and gas distribution companies, which are responsible to so called life-line, have extremely higher capacity than other types of industries. The communication service companies have also higher capacity than the others. The finance, manufacturing, retail, and insurance companies are a bit higher among others. It should be noted, however, that transport and construction companies, which must have important functions after an earthquake, have relatively lower capacity. Restaurants have the lowest capacity among all types of industries. This fact gives the important warning because they are responsible for taking care of their customers.

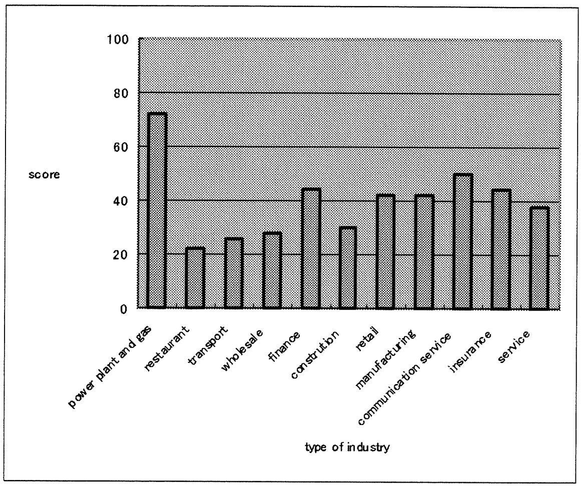

Figure 7, Integrated capacity by type of

4. CONCLUSIONS

It must have been popular concern to know of how far enterprises prepare for an earthquake and to what extent they will be able to respond to damage after the event. However no simple method to evaluate the earthquake resistance capacity of these enterprises has been developed so far. Most of enterprises must take some countermeasures to cope with an anticipated earthquake. Department sores must train their employees for guiding their customers to a safe place, and manufacturing industries which are using hazardous materials must formulate a perfect manual in case of emergency. The question is how to evaluate such different types of practices and integrate or compile to the capacity of earthquake resistance as their potential capability.

This paper is one of the challenging attempts to this question. The five potential capacities of enterprises have been extracted on the basis of their emergency governance and daily practice for disaster training exercise. The results indicate that middle and small enterprises are far behind large ones in planning and preparedness capacities, though structural and response capacities are not so much different.

The paper has not referred to the relation with BCP. Need-less- to-say, however, the protection or back-up of the basic functions of the said enterprises, which is the common part of BCP, are given the highest priority when some capacity up-grading actions are taken.

References:

SFC Research Institute of Keio University and Office of Earthquake Disaster Management of Mie Prefecture, (2005), "Evaluation of Earthquake Resistance Capacity of Business Enterprises," Keio University (Japanese)

Hideki Kaji and Takashi Yamaki (2004), "Development of CMP-Method – Evaluation of Earthquake Resistance Capacity of Business Enterprises," *Yobou-Jihou*, **219**, 40-48 (Japanese)

Fifth International Conference on Urban Earthquake Engineering
March 4-5, 2008, Tokyo Institute of Technology, Tokyo, Japan

THE CURRENT STATUS AND IMPACT OF PERFORMANCE-BASED EARTHQUAKE ENGINEERING IN CALIFORNIA RELATIVE TO SUSTAINABLE (GREEN) BUILDING DESIGN

Linden T. Nishinaga, P.E., LEED A.P.

Senior Civil Engineer, Department of Public Works, City of Long Beach, California U.S.A. and Co-Chair, California Seismic Safety Commission's Review Committee on the Pacific Earthquake Engineering Research Center.
linden_nishinaga@longbeach.gov

Abstract: This paper will describe and draw parallels between the current situation of two of our latest professional building design methodologies, namely performance-based earthquake engineering (pbee) and sustainable "Green" building design in the United States and the State of California. It will do this by defining and describing both state-of-the-art design methodologies; characterizing their benefits, successes, and impacts so far; and then providing insights as the reasons why. Independently both pbee and green design have started out at the same time in the mid 1990's; however their implementation paths and success rates have been very different. Pbee has provided solid development, merit, and promise; however to this day it is still not widely known, understood, nor practiced by the majority in the California structural engineering building community. Green building design on the other hand has made quantum steps forward to becoming well known, widely accepted, part of the fabric of everyday architectural practice, and is the current buzzword of public and private managers and even elected officials. Pursuant to the better understanding of the relative impacts and successes of disparate professional disciplines for similar built environments, my paper will take the reader through this scenario and suggest possible reasons and remedies.

1. INTRODUCTION:

Headquartered in Berkeley, California the Pacific Earthquake Engineering Research Center (P.E.E.R.) is a major U.S. regional engineering research center established in 1997 by the State of California and the United States National Science Foundation. P.E.E.R.'s mission is to develop and disseminate performance-based earthquake engineering (pbee) technology throughout the Western USA in general and California in particular.

P.E.E.R.'s main product, peformance-based earthquake engineering (pbee), is a revolutionary new structural engineering design methodology that goes beyond traditional prescriptive design procedures and current building code force-based approaches. Pbee design decisions are based on establishing specific performance objectives, functional statements, and performance level requirements in connection with the impact of expected probabilistic-based earthquakes in the building area in question. These performance levels include operational, immediate occupancy, life safety, and collapse prevention, which in turn are associated with accepted earthquake hazard levels based on their predicted chances of occurrences over certain time periods. Pbee is involved with not only the prevention of loss of life and protection of structures and their contents but also the ability to repair and use facilities after earthquake events. It attempts to do this by specifying and predicting certain facility performance parameters such as story drifts, deflections, periods of oscillation, etc. and building damage scenarios in terms of casualties, dollar loss, and disruption of functions, etc. This information allows the designer in coordination with facility owners to make better decisions about the effectiveness of various alternatives in controlling those consequences. As a result, pbee can be more efficient from a construction cost standpoint, perform more predictably, and be more reliable as a risk management tool than traditional, prescriptive, and force-based design methods. In the long run pbee will result in safer, more reliable structures with lower life-cycle costs.

2. CALIFORNIA EARTHQUAKES:

In the State of California the following is past and projected casualty losses from specific earthquakes:

Table 1: Causalities and Losses from Specific Earthquakes and Earthquake Scenarios

	Earthquakes	**Deaths**	**Property Damage & Economic Loss**
Past	1971 Sylmar, CA Earthquake (EQ)	65	$0.5 billion
	1989 Loma Prieta, CA EQ	62	$10 billion
	1994 Northridge, CA EQ	57	$20 billion
	1995 Kobe, Japan EQ	>5,500	$250 billion
Projected	Scenario 7.0 Hayward fault, CA	>4,000	$100 billion
	Scenario 7.4 event on the Puente Hills fault, Los Angeles, CA	3,000-18,000	$80-250 billion
	Repeat of the 1906 San Francisco, CA EQ	800-3,400	$90-120 billion
	Scenario 7.0 Newport-Inglewood fault, Long Beach, Los Angeles, & Orange County, CA	2,000-6,000	$200 billion

According to the United States Geologic Survey (USGS) and its Earthquake Shaking Potential map of California, the California Coastline is the highest region of earthquake shaking potential because they are nearest to major, active faults. These are areas of many major population centers and will on average experience stronger earthquake shaking more frequently. This intense shaking can damage even strong, modern buildings. Relative earthquake shaking hazard potential in California is indicated by the following ground shaking intensity map:

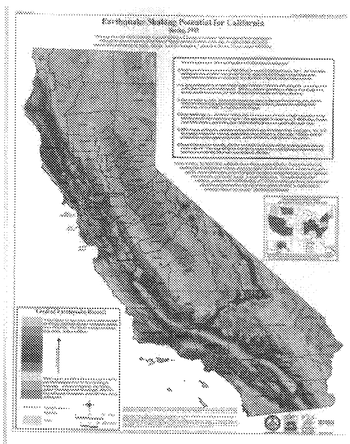

Figure 1: California EQ Shaking Potential

3. PBEE's IMPACT IN CALIFORNIA:

To address all this P.E.E.R. and others have so far applied pbee on an apparent impressive looking number of achievements throughout the State of California. Strong examples of these include the following:

Example #1: Located near downtown San Francisco, The One Rincon Hill condominium complex is 60 Stories and is currently under construction.

Example #2: Also located near downtown San Francisco, The Infinity is new 38-Story condominium residence and retailing twin tower complex. It is scheduled to be complete in 2008.

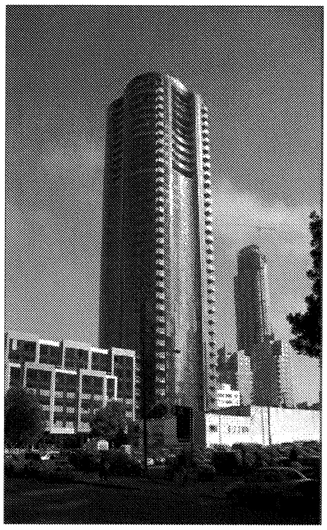

Figure 2: The Infinity Tower Building

Example #3: The Bay Area Rapid Transit (BART) system was constructed in the 1960s and 1970s. Built to seismic standards considered high for the time, recent research indicates that the system has both life safety and post-earthquake operability deficiencies. PEER helped develop a cost-effective program using performance-based procedures to meet life safety objectives and shorten times for restoration of train service after earthquakes.

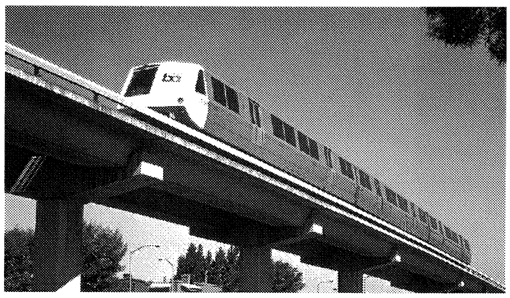

Figure 3: BART System Overpass

Example #4: The earthquake safety and sustainability of California's institutions of higher learning have also benefited tremendously from the use of performance-based earthquake engineering and PEER's research results. In 1997, the University of California at Berkeley (UC) embarked on an aggressive program to upgrade seismically deficient buildings using PBEE. Costs for these improvements were substantially less than bringing UC's buildings into compliance with older, prescriptive, force-based codes for new buildings. UC was able to be more flexible in its allocation of funds, meet its budget, tailor its building performance objectives, and spend its retrofit funds more efficiently with PEER's help.

Example #5: PEER has developed the OpenSees computer program for simulating the complex performance of structural systems in earthquakes. OpenSees has become a widely accepted, web-based application for analyzing structures under various loading conditions.

Example #6: Recent physical experiments at the University of San Diego have indicated structural-portion construction savings in the range of 15 to 25% for tall reinforced concrete buildings.

These good pbee success examples however are often concentrated in specific niche sectors of the structural engineering community. Among most California practicing structural engineers, building owners, and in the public at large, however, the overall impact of pbee is not as impressive. All in spite of pbee's great promise and potential.

It is reported that only approximately 1% of the new California buildings have been designed so far using pbee. What's more, other unofficial surveys and anecdotal accounts of practicing structural engineers reveal that so far approximately 10 to 15% of them have heard of pbee and that around 5% truly understand and have used pbee in their design practice. A past unofficial survey of the number pbee designs that went through building departments of three of California's largest cities including Los Angeles, San Francisco, and Long Beach resulted in the following:

Los Angeles:	0
Long Beach:	6
San Francisco:	2

There is presently no apparent far-reaching, effective, and comprehensive pbee education and technology transfer system throughout California. Notable exceptions include the Port of Los Angeles, which has staged public workshop seminars and established its own set of pbee design guidelines for the design of reinforced concrete container wharves and the California Department of Transportation, which has developed a Seismic Design Criteria based on pbee. But for building design, most rank and file practicing structural engineers for the most part would have to go out of their way in order to become effectively familiar with pbee. The building code doesn't provide much help as it still does not prescribe pbee except to treat it as an alternative design method. As such, understaffed building departments are often not equipped to handle pbee designs and would have to hire special contract consultants to perform the necessary plan checking. A building owner would have to hire both qualified pbee designers and independent design peer reviewers who are approved by the building department but paid for by the owner.

All this would result in pbee costing more for pbee-based design than conventional code-based design. Design cost increases are estimated at from 50 to 100%, depending on the practitioner's "learning curve." Given the lack of knowledge by most building owners, this in turn puts the pbee structural engineer at a distinct competitive economic disadvantage in the highly competitive design market. The end result of these and other practical issues is that California structural engineers still tend to shy away from pbee.

4. SUSTAINABLE (GREEN) DESIGN:

As with pbee, sustainable a/k/a Green design also began in the early to mid-1990's. Its principal sponsor has been the United States Green Building Council (USGBC) headquartered in Washington, D.C. (ref. www.usgbc.org). This program addresses the fact that in the U.S. buildings account for 65% of electricity consumption, 36% of total energy use, 30% of greenhouse gas emissions, 30% of raw material use, 30% of waste output (or 136 million tons/year), and 12% of potable water consumption. Its principles include meeting the needs of the present without compromising the ability of future generations to meet their own needs, improving the quality of life, stabilizing the use of our environment's natural resource supply, revising policies and practices at all level, understanding the consequences of inaction, innovating changes needed to institutional structures, and educating to influence individual citizen behaviors. The USGBC's mission is to promote the design and construction of buildings that are environmentally responsible, profitable, and healthy places to live and work. The definition of a Green building is a structure that more efficiently uses valuable resources such as energy, water, materials, and land compared to buildings constructed to basic building codes. Green buildings are better for the environment, and provide healthy comfortable, productive indoor spaces.

In order to define, qualify, quantify, and certify Green buildings, the USGBC created the LEED system. LEED, which stands for Leadership in Energy and

Environmental Design, takes into account energy & atmosphere, land conservation, water quality, water quality, waste reduction, transportation, infrastructure, and permaculture, i.e. approach for permanence of sustainable practices in the future. LEED encourages a holistic approach that guides an integrated and collaborative design, construction, and O&M process throughout the building's life cycle. Typically Green buildings cost between 1 and 5% more to design and construct but this premium is outweighed by the overall cost benefits. Benefits of Green buildings include competitive first costs, reduced operating expenses including significant lower utility costs (30 to 50% typical), decreased occupant vacancy rates, and reduced liability. Occupant-related benefits include increased productivity, improved occupant performance (student performance increases in day-lighted schools), reduced worker absenteeism, retail sales increase with daylighting of store spaces, and general increased health and happiness of workers.

An overview of the three-step LEED registration process fosters a whole building collaborative integrated design and construction process approach. There are six main areas covered: a) sustainable sites, b) water efficiency, c) energy and atmosphere, d) materials and resources, e) indoor environmental quality, and f) innovation and design process. The following is the LEED point rating system:

Certified:	26 – 32 Points
Silver:	33 – 38 Points
Gold:	39 – 51 Points
Platinum:	52 + Points (69 Possible)

Including the Cities of Santa Monica, Long Beach, San Francisco, and others, many California cities have adopted official Green building policies. Many public managers and elected officials are in fact not only calling for Green Building policies but also insisting that new building be LEED certified. The City of Long Beach is presently going through this process. Long Beach has also constructed its first LEED certified new building, namely Mark Twain Branch Library. This 16,000 square-foot state-of-the-art new library is currently completed and is submitted for application as a LEED "Silver" building. It has sustainable features including but not limited to waterless urinals, daylighting of the interior, refurbished carpet tiles from old PVC irrigation pipes, other recycled materials usages throughout building, low VOC paints, no CFC hvac refrigerants, water efficient landscaping, storm water runoff management (via Stormceptors), optimized mechanical energy performances, urban and Brownfield redevelopment, public transportation access, and innovative sustainable design education display for the public.

Some Mark Twain Branch Library photos:

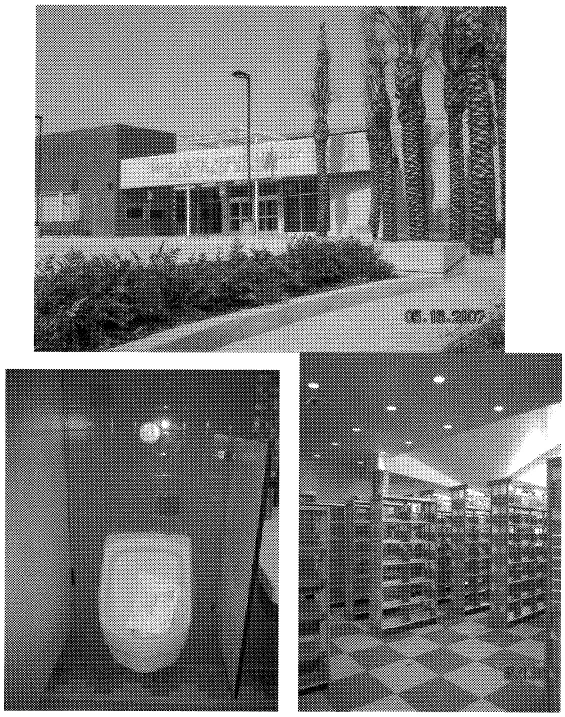

Figure 4: Mark Twain Library Photos

A great number of private firms have also jumped on the Green bandwagon. For example, the City of Torrance's Toyota Motors complex has a LEED Gold Certified building that they proudly showcase.

As such the impact and growth in the United States of sustainable "Green" design has been astounding. As opposed to only a handful of pbee designed buildings, there are already over 400 registered and certified buildings in California. This accounts for over 40 million square feet of space. What's more new buildings have been certified in 50 U.S. States and in 14 countries and there are now over 30,000 LEED accredited professionals. California leads the nation in the number of LEED certified buildings. Thus, there is today widespread knowledge and popularity of Green design by a growing number of practitioners, building owners and managers, elected officials, and the public at large.

5. CONCLUSIONS:

Why has Green design taken off while pbee hasn't? The reasons are complex. The basic approach of U.S. engineers and U.S. architects are different and may offer a clue. Engineers tend to be cautious with their peers and stakeholders, so much so that often they are waiting for the "other parties" before moving forward and making design policy decisions. An example is the U.S. and California building code adoption process relative to new design methods. When a new methodology is researched by a center such as P.E.E.R.

they then often refer the new method to their peers including institutions such as FEMA pursuant to establishing new guidelines. Later these guidelines may become engineering standards via such organizations as ASCE. All along other organizations including building code committees comprised of diverse individuals, are also often reviewing the new method. By this long, discordant, and complicated process the time required for a promising new design methods to become part of an adopted building code may be 10 or 15 years or longer. Presently California has just adopted the 2007 California Building Code largely based on the 2006 International Building Code. But despite this new code and the years spent so far on research, development, and review, pbee is still not prescribed.

Furthermore, similar or parallel engineering institutions such as P.E.E.R., the Consortium of Universities for Research in Earthquake Engineering (CUREE), National Earthquake Engineering Symposium (NEES), Southern California Earthquake Center (SCEC) and others sometimes have apparent overlapping missions. Duplication of effort, non-standardized technical terminologies of similar methods, and public and professional confusion is sometimes the result.

Architects, on the other hand, by first establishing a central and well-accepted organization such as the USGBC have effectively led and accelerated not only the development of Green design but also their implementation via public outreach and education and training. Their approach has been so successful that as opposed to engineering professionals waiting for the building code committees to finally insert new methods into the building code, Green architectural professionals have instead gone forward relatively independently eventually "forcing" the building departments and code committees to "catch up." Architects' apparently more "liberal", market drive, and aggressive approach stands in stark contrast with engineers' more conservative and cautious approach. Added to this the fact that Green design is somewhat more tangible to the average person compared to earthquakes, which are less understood and sporadically occurring in nature. The attention span of the public is consistent for Green design, especially in this day of pollution, limited natural resources, and Global Warming; whereas the attention for earthquakes diminishes non linearly with the passage of time after the last major event. For example in California there were several major events that occurred in the 1990's, which in turn resulted in very strong public attention and concern for earthquakes and earthquake safety at the time. Presently however given it's been over 14 years since the last major earthquake (Northridge, January 1994) public attention to earthquakes is relatively very low.

6. RECOMMENDATIONS:

In order to rectify this scenario, we California engineers need to adopt new and different strategies and approaches including a) adopting more aggressive, holistic, and less cautious new design implementation methods, b) leading society and not following, c) taking more calculated risks based on knowledge, social integration, and confidence, d) implementing much better marketing, public outreach, and education strategies, e) collaborating with owners, practitioners, managers, code officials, and other key stakeholders in establishing buy-in, consensus, public mandates and policies, and incentives for enhanced professional usage of pbee, and e) thinking more idealistically about the building occupants who're apparently at greater risk by not having appropriate pbee designs in their structures and buildings, i.e. how many lives would be lost and dollars expended needlessly by not using our best design methodology available?

Finally, consideration needs to be made for the near-term establishment of a permanent private non-profit engineering design and construction organization similar to the USGBC. Given seismic design is most serious and applicable to areas of highest seismic activity, an organization as such for the State of California could be an effective beginning—ala the **California Seismic Building Council** (CSBC). Like USGBC, the CSBC would:

- Be a non-profit organization committed to expanding seismically safe building designs and practices,
- Have members including structural and civil engineers, architects, MEP engineers, contractors, building owners, real-estate developers, construction and facility managers, building code committee members, and governmental agency representatives,
- Have as is core mission to transform the way buildings are designed, built and operated, enabling seismically safe, healthy, and prosperous environment that improves the quality of life,
- Be driven by the building business and insurance market industries, therefore economically sustainable and risk management correct, respectively,
- Be independent of but in close cooperation with the multitude of existing State and national structural and earthquake engineering research bodies, organizations, universities, and code committees that would provide support, expertise, research, and development information,
- Have a comprehensive and effective Education and Outreach program dedicated to

the effective transfer of performance-base earthquake engineering technology and other state-of-the-art non-prescriptive and advanced deflection-based structural and civil design methodologies. This education system would focused on the transfer and practical application of pbee within the practicing private and public sector design, building code regulatory, and construction industry communities. Focus would also be place on educating owners, risk managers, and other building business industry interests; public agencies; and local elected officials. Examples of such outreach programs may include Statewide pbee seminars, lectures, workshops, conferences, retreats, guidelines, publications, etc.,

- Be a close partner with the USGBC given both organizations are involved in the exact same built environment, i.e. buildings. Ensure that sustainable structural and civil engineering proposals be incorporated into the LEED Rating System, thereby finally creating incentive for their applications.
- And be also a close collaborating partner of relevant international organizations and institutions including but not limited to those in Japan, Taiwan, India, Turkey, South Korea, Mongolia, Mexico, etc. pursuant to the mutually beneficial exchanges of technical information.

It seems apparent that it makes no sense to build energy efficient and environmentally sophisticated LEED Certified green buildings that nonetheless fails and hurts people upon the first major earthquake event in the area just because it wasn't designed using the best seismic design technology available. A wasted collapsed building would be diametrical to the cause of Green. Given that the majority of people in California spend over 90% of their lives within buildings it is reasonable and compelling that the same widespread attention, education, and application that's currently placed on Sustainable (Green) building design should also be placed on the latest state-of-the-art seismic design methods for these very same buildings.

References:

California Seismic Safety Commission, Review of the Pacific Earthquake Engineering Research Center (PEER), Years 7-9, March 8, 2007, Report No. CSSC 07-04.

United States Green Building Council, New Construction & Major Renovation, Version 2.2 Reference Guide, 2nd Edition, September 2006.

Fifth International Conference on Urban Earthquake Engineering
March 4-5, 2008, Tokyo Institute of Technology, Tokyo, Japan

REGIONAL ECONOMIC MODELING FOR DISASTER ANALYSIS: TRENDS AND ISSUES

Yasuhide Okuyama[1)]

1) Associate Professor, Graduate School of International Relations, International University of Japan, Japan
okuyama@iuj.ac.jp

Abstract: Economic analysis of disasters has attracted interest from a wide audience in recent years, because not only of the frequent occurrence of large-scale natural disasters worldwide but also of the spread of international terrorism to a global scale. This paper reviews the past modeling studies for economic impact analysis of disasters, such as the input-output models, the social accounting matrix, and the computable general equilibrium models. The paper also discusses the current issues of disaster modeling raised by the literature, and proposes some future directions.

1. INTRODUCTION

Until the 1990s, the economic impacts of natural hazards and disasters received relatively little attention from research communities. A series of disasters in the mid 1990s, such as the Northridge Earthquake in 1994 and the Kobe Earthquake in 1995, that occurred in developed urban areas and brought considerable damages and impacts to the society, demonstrated how vulnerable modern industrialized cities are to severe natural hazards. Recent large-scale disasters, such as the 2004 Indian Ocean Earthquake leading to the Asian Tsunami and Hurricane Katrina in 2000, showed that the understanding of and the preparation for such hazards, including their impacts and effects to society and the economy, are urgent tasks around the globe.

Significant progress has been made in recent years in the economic analysis of disasters, especially in the field of economic modeling for disaster impact analysis in a regional context (for example, Okuyama and Chang, 2004; and an excellent compilation of related papers by Kunreuther and Rose, 2004a). Since the pioneering work by Dacy and Kunreuther (1969), a generalized framework for the economic analysis of natural disasters had been proposed (for example, Sorkin, 1982; and Albala-Bertrand, 1993). The recent advancements have been more toward empirical analysis and toward strategies for modeling extensions and modifications to fit them to disaster situations. This trend is due to improved data availability of disaster damages and losses and to increased multidisciplinary research activities about disasters, including sociology, economics, and psychology. The uniqueness of each hazard and of its damages and impacts presents enormous challenges for economic modeling of disasters; many issues remain unsolved.

In the following section, a brief history of economic modeling practice for disaster impact analysis is summarized. Then, the current issues of modeling, such as time and spatial dimensions, resiliency and counter actions, are discussed in Section 3. The final section concludes the paper with some future directions for this line of research.

2. ECONOMIC MODELING FOR DISASTERS: TRENDS

Disasters can cause physical destruction to built-environment and networks, such as transportation and lifelines, and these damages are called *direct losses*. Direct losses then lead to the interruptions of economic activities, production and/or consumption, and the losses from business interruptions are often called the *indirect effects* of disaster. While some critique that the indirect (or secondary) effects of disaster are "more a possibility than a reality" (Albala-Bertrand, 1993, p. 104), the estimation of indirect effects has been attempted to "gauge individual and community vulnerability, evaluate the worthiness of mitigation, determine the appropriate level of disaster assistance, improve recovery decisions, and inform insurers of their potential liability" (Rose, 2004, p. 13). This indirect effect includes a wide array of consequences caused by direct losses, and Rose (2004) suggested that the use of "*higher-order effects*" is more appropriate, because of the conflict with the terminology used in economic models, especially the input-output (IO) model.

Various economic modeling frameworks have been employed to estimate the higher-order effects of a disaster. Perhaps, the most widely used modeling framework is the IO model (for example, Cochrane, 1974, 1997; Wilson, 1982; Kawashima *et al.* 1991; Boisvert, 1992; Gordon and Richardson, 1996; Rose *et al.* 1997; Rose and Benavides, 1998; and Okuyama *et al.*, 1999), and the application of the IO model to disasters, including both natural and man-made ones, dates back to strategic bombing studies during the World War II (Rose, 2004). The popularity of IO model for disaster related research is based mainly on the ability to reflect the interdependencies within a regional economy in detail for deriving higher-order effects, and partly on its simplicity. The simplicity of the IO framework has enabled integrative approaches, in which IO models are combined with other modeling framework, such as engineering models, and/or data, in order to estimate higher-order effects that are more sensitive to the changes in physical destruction. Some examples of this approach include the links with transportation network models (Gordon *et al.*, 1998, 2004; Cho *et al*, 2001; Sohn *et al.*, 2004, among others), with lifeline network models (Rose, 1981; Rose *et al.* 1997; Rose and Benavides, 1998), and the comprehensive disaster assessment model, namely HAZUS (Cochrane *et al.*, 1997).

On the other hand, this simplicity of IO model creates a set of limitations, including its linearity, its rigid structure with respect to input and import substitutions, a lack of explicit resource constraints, and a lack of responses to price changes (Rose, 2004). In order to overcome these limitations under a disaster situation, several attempts of refinement and extension of the IO framework have been proposed. For instance, the shortage of regionally produced inputs under a disaster situation was dealt with by the integration of a methodology for more flexible treatment of imports (Boisvert, 1992; and Cochrane, 1997). The issue of supply-side constraints due to the damages to production facilities was addressed with the allocation model variant of IO model (Davis and Salkin, 1984); however, this modeling scheme has inherent deficiencies (Oosterhaven, 1988 and 1989; see Dietzenbacher, 1997, for a solution), and was later modified by Steinback (2004) to include only backward-linkage effects. The treatment of price has been transferred to computable general equilibrium (CGE) models, and the applications to disaster situations are discussed below.

An alternative modeling framework to the IO model is CGE analysis (for example, Boisvert, 1992; Brookshire and McKee, 1992; Rose and Guha, 2004; and Rose and Liao, 2005). Unlike IO models, CGE models are non-linear, can respond to price changes, can incorporate input and import substitutions, and can explicitly handle supply constraints. However, Rose and Liao (2005) claims that most CGE models are intended for long-run equilibrium analysis; hence, in contrast with the rigidity of the IO model, a CGE model generally leads to the underestimation of economic impacts due to its flexible adjustment feature. It is argued, however, that CGE models provide lower impact estimates than IO models, partly because "not all causations in CGE models are unidirectional, *i.e.*, functional relationships often offset each other" (Rose, 2004, p. 27). In addition, the more extensive data requirement for CGE modeling presents a major disadvantage for empirical analysis of disasters.

Other modeling frameworks have been also employed to estimate higher-order effects of disasters. The social accounting matrix (SAM) has been utilized to examine the higher-order effects across different socio-economic agents, activities, and institutions. Notable studies using a SAM or one of its variants include Cole (1995, 1998, 2004) among others. Like IO model, the SAM approach has rigid coefficients and it tends to provide upper bounds for the estimates. On the other hand, the SAM framework, as well as extended IO models and CGE models, can derive the distributional impacts of a disaster in order to evaluate equity considerations for public policies against disasters. Econometric models, which are based on time-series data that may not include any major disaster experiences, appear ill-suited for disaster impact analysis. Ellson *et al.* (1984), however, argue that they examined the damage estimates of major earthquakes in the United States and found that the damages do not appear really outside of the historical variability of the regional economy in response to more traditional shocks and cyclical fluctuations. Furthermore, econometric models are statistically rigorous, can provide stochastic estimates, and have forecasting capabilities. They do require a large data set (time-series as well as cross-section) though, and cannot easily distinguish between direct and higher-order effects (Rose, 2004).

3. ISSUES OF DISASTER MODELING

Some specific features under a disaster situation, such as negative (destruction) and immediately following positive (recovery and reconstruction) shocks to an economy in a short period of time, a wide range of simultaneous physical damages across multiple locations, and behavioral changes in a crisis situation, need to be incorporated into the modeling framework in order to visibly articulate the impacts and effects of a disaster. However, most economic models assume gradual and incremental changes over time and uniform impacts over space. Thus, when applying such models, it is difficult to cope with these features. In the following sub-sections, some attempts to extend the modeling framework to handle these issues are discussed.

3.1 Time Dimension

The duration of a hazard occurrence varies from one hazard to another: the ground shakes of an earthquake last around 30 seconds, while a large-scale flood can remain from a few weeks to a few months. However, these time frames are still considered short in an economic modeling sense. Mainly due to the data availability and to the equilibrium-oriented assumption, the time span of most economic models is annual while some models are operating with a quarterly or monthly frequency. Moreover, the activities of recovery and reconstruction after a hazard are conducted much more rapidly and simultaneously in multiple locations than usual construction activities. These features of a disaster generate seesawing temporal changes and lead to considerable temporally-intense interactions of economic activities. Hence, the use of static economic models potentially cancels out the positive and negative effects in the long run and then often ends up estimating insignificant total impacts (Albala-Bertrand, 1993).

A few attempts to incorporate the dynamic nature of disaster situations have been made. Cole (1988 and 1989) proposed lagged expenditure models through extending the standard IO framework. Concerning the time necessary to produce goods and taking into account the process of labor market adjustment, among other things, Cole's lagged IO models aim to capture the process of impact (or growth) from a factory closure (or production expansion) within the IO framework. With a similar objective, but putting more emphasis on production chronology and production modes, Okuyama *et al.* (2004) employed the Sequential Interindustry Model (SIM) for disaster impact analysis, creating a quarterly IO model with the SIM modification. The SIM framework was originally introduced by Romanoff and Levine (for example, Romanoff and Levine, 1986) in response to the need to analyze interindustry production in a dynamic economic environment, such as large construction projects where the effects on production and employment are transitory. Okuyama (2006) later extended the SIM with the inclusion of an inventory function, and demonstrated the temporal distribution of higher-order effects from hypothetical lifeline disruptions.

While the SIM framework can handle a shorter time period better than the conventional economic models do, it is still not sufficiently flexible because of its discrete nature. In response to the need of a more flexible modeling scheme in terms of time, Donaghy *et al.* (2007) proposed a continuous-time formulation of a regional econometric-input-output model (REIM) to capture higher-order effects of unexpected and extreme events and of nonlinear continuous recovery processes. Another direction to this line of extension may be the application of dynamic CGE models; however, the issue of temporal substitution in a disaster situation can become troublesome, and its application has not been made to disaster situations to this date. While these extensions of the conventional economic models shed some light on the temporal feature of disaster impacts, the modeling scheme is still considered somewhat *ad hoc*, since no definitive theories have been established for their application to the idiosyncrasy of conventional models (Rose, 2004).

3.2 Spatial Dimension

Since disasters create a wide range of impacts over space, the spatial dimension of higher-order effects has been dealt in many ways. One way to do this is the development of an interregional impact analysis of a disaster, because a large natural hazard can create impacts that spread well beyond the boundary of the region in which the hazard occurred. For example, Okuyama *et al.* (1999) employed a two-region interregional IO table to estimate the higher-order effects of the 1995 Kobe Earthquake, both for the region where the earthquake occurred and for the rest of Japan. As mentioned above, various integrative approaches with transportation models have been attempted for analyzing the spatial distribution of higher-order effects. For instance, Sohn *et al.* (2004) calculated the multi-regional impact of a hypothetical New Madrid Earthquake in the United States, utilizing the interregional commodity flow model based on the Leontief-Strout-Wilson-type modeling framework. However, these studies are based on the IO framework, and the changes in interregional trade patterns are dealt with either in an *ad hoc* way or in a more transportation engineering way (minimizing the total transportation time).

The damages and losses of a disaster, such as a large earthquake or a tornado, are often not uniform across the region: some areas are heavily destructed, whereas other areas are virtually untouched. In order to analyze the sensitivity of spatial distribution of damages and higher-order effects, some extensions have been made using spatially disaggregated economic models. Cole's (1998) multi-county SAM was constructed based on county-level economic data and geographic information system (GIS) based location data, and was applied to lifeline failures in the Memphis region. Further disaggregating economic information to smaller geographical areas, van der Veen and Logtmeijer (2003) employed the concept of economic hot spots, through which multipliers from the IO table are visualized as a contour map using GIS. This visualization does not directly provide the detailed information about the higher-order effects of a disaster, but can illustrate which locations are more vulnerable (or important) in terms of economic interdependency. Extending the concept of economic hot spots, Yamano *et al.* (2007) proposed and demonstrated a disaggregation of their multiregional IO model to a district level (500-meter square) in order to show the spatial distributions of economic activities and of potential higher-order effects. The advantage of their finer geographical-scale model is to clearly identify which district is crucial in terms of economic losses. Their numerical case studies revealed that the total economic losses are not proportional to the distribution of population or of industrial activities. This is a particularly noteworthy finding for disaster management policy, because it suggests that countermeasures need to take more account of higher-order effects.

3.3 In-Built Counteractions

As mentioned before, Albala-Bertrand (1993, p. 104) claims that higher-order disaster effects are "often unimportant for the economy and society as a whole and rapidly counteracted within the disaster area," since "in-built societal mechanisms may prove sufficient to prevent most potential indirect (higher-order) effects on the economy and society". Meanwhile Dacy and Kunreuther (1969, p. 64) indicated the sympathetic behavior of mutual aid in a chaotic situation, leading to the situation that "the supply and demand curves may shift unexpected ways" in extreme circumstances. These counteract mechanisms and behavioral changes have started to receive increased attentions in recent years (Kunreuther and Rose, 2004b). Some attempts to incorporate behavioral changes in a disaster situation have been made. For example, Okuyama *et al.* (1999) included the final demand decrease in the rest of Japan after the Kobe earthquake, since people outside of the damaged region felt sorry for the event and for people in the Kobe area, due to the catastrophic destructions of a major city and a large number of casualties, and tended to reduce their discretionary purchases. Or, people may purchase necessary goods for the damaged area, such as blankets and/or food, and may donate them, instead of buying other goods for themselves. These types of behavioral changes (consumption pattern changes) have not been well studied or modeled yet, whereas these behavioral changes are a part of the in-built counteractions.

Another type of in-built counteractions is the so called economic resilience, "which refers to the inherent ability and adaptive response that enables firms and regions to avoid maximum potential losses" (Rose and Liao, 2005, p. 76). In the disaster related literature, Tierney (1997) studied the business coping behavior and community response in disaster situations, Bruneau *et al.* (2003) introduced community resilience as the in-built counteractions of a community, and Rose and Liao (2005) modeled economic resilience successfully in the CGE modeling framework. In the latter model, inherent resilience, *i.e.* the ability to substitute inputs and/or reallocate resources under normal circumstances, is embodied in the production function for individual businesses, while adaptive resilience, *i.e.* the ability in crisis situations with extra effort, is set as the changes in the parameters.

In a similar line of study, Steenge and Bočkarjova (2007) proposed a modified IO system that aims to incorporate imbalances (or disproportions) between demand and supply in an economy. Their extension starts from the standard open IO model and then transforms into a 'special' closed Leontief model, which is somewhat similar to the IO model that is closed with respect to household. Their study demonstrated the identification of imbalances due to disruptions by a disaster and proposed the countermeasures to alleviate the mismatches to regain the previous production level or proportion. These numerical demonstrations are useful for emergency management practitioners who need to quickly grasp the situation after a hazard has occurred and to prepare counteractions.

4. CONCLUSIONS

When the impact analysis of a disaster is presented, the issue regarding the accuracy of the impact estimates (especially higher-order effects) is often raised. Accuracy is one of the issues when discussing the advantages and limitations of various modeling frameworks. However, for the impact analysis of disasters, accuracy may not be the most important concern, since disasters are quite different phenomena from conventional economic events. Each disaster is unique, and exactly the same hazard will never occur again. Hence, the impact analysis of disasters is not a forecast of an event or of its consequences; rather, it suggests only what might happen. As Hewings and Mahidhara (1996) wrote, disaster impact analysis is "inexact science". What researchers need to concern then is how each model generally behaves with the same damage data. For example, researchers and emergency management practitioners should know that the estimation obtained from using an IO model yields the upper-bound results, and a CGE model derives what may be seen as the lower-bound results. In addition, the quality of input data is crucial for the legitimacy of results. As West and Lenze (1994) pointed out, the more sophisticated regional impact models become, the more precise numerical data will be required, while imperfect measurements of the damages and losses of a disaster are often the case.

Therefore, what the future research on economic modeling of disasters needs to focus on is more plausible theoretical foundations. Many of the extensions and modifications discussed above are still considered ad hoc, implying that those adaptations are not theoretically supported. For example, the theory of firm behavior needs to be extended so that economic resilience can be endogenized in the model, rather than just numerically adjusted. Theoretical formulations of mutual aid and sympathetic behavior, which may lead to behavioral changes under a disaster situation, require more research in order to be incorporated in the model. At the same time, the researchers should always keep in mind the users of the results of disaster impact analysis. Mantell (2005, p. 635) contended that "(i)t may be more useful in the aftermath of a disaster to have results for a 'quick and dirty' input-output model to give at least an upper end of the total loss, than to wait for results from some of the more complex model." Perhaps, Mantell's remarks were made with the needs in mind of emergency management practitioners who have to grasp the size and extent of disaster effects within a short period of time. By the same token, a standardized model of disaster assessment, like HAZUS, should be maintained and improved for this purpose. Yet, the *raison d'être* of complex models is to understand the nature of disaster situations and their economic effects, and to prepare for future disasters by providing more detailed information about the vulnerability of economies and the counteractive measures to be proposed. For this reason, the challenges of economic modeling for disasters are still many; however, the interface among theory, model development, and disaster management practitioners is probably one of the greatest challenges.

Acknowledgements:

The author would like to express the sincere gratitude to Geoffrey J.D. Hewings and to Erik Dietzenbacher for their helpful comments and support. This paper is based on the presentation made in the 53rd North American Meetings of the Regional Science Association International in Toronto, Canada, 2006. The author also would like to thank the participants of the disaster sessions for the useful comments.

References:

Albala-Bertrand, J.M. (1993) *The Political Economy of Large Natural Disasters: With Special Reference to Developing*

Countries (Oxford, UK: Clarendon Press).

Boisvert, R. (1992) Indirect losses from a catastrophic earthquake and local, regional, and national interest, in: *Indirect Economic Consequences of a Catastrophic Earthquake*, pp. 207-265 (Washington, DC: National Earthquake Hazards Reduction Program, Federal Emergency Management Agency).

Brookshire, D. and Mckee, M. (1992) Other indirect costs and losses from earthquakes: issues and estimation, in: *Indirect Economic Consequences of a Catastrophic Earthquake*, pp. 267-325 (Washington, DC: National Earthquake Hazards Reduction Program, Federal Emergency Management Agency).

Bruneau, M., Chang, S.E., Eguchi, R., Lee, G., O'Rourke, T., Reinhorn, A., Shinozuka, M., Tierney, K., Wallace, W. and von Winterfelt, D. (2003) A framework to quantitatively assess and enhance seismic resilience of communities, *Earthquake Spectra*, 19, pp. 733-752.

Cho, S., Gordon, P., Moore II, J.E., Richardson, H.W., Shinozuka, M. and Chang, S.E. (2001) Integrating transportation network and regional economic models to estimate the costs of a large urban earthquake, *Journal of Regional Science*, 41, pp. 39-65.

Cochrane, H.C. (1974) Predicting the economic impacts of earthquakes, in: H.C. Cochrane, J.E. Haas and R.W. Kates (Eds) *Social Science Perspectives on the Coming San Francisco Earthquakes—Economic Impact, Prediction, and Reconstruction*, Natural Hazard Working Paper No.25 (Boulder, CO: University of Colorado, Institute of Behavioral Sciences).

Cochrane, H.C. (1997) Forecasting the economic impact of a Midwest earthquake, in: B.G. Jones (Ed.) *Economic Consequences of Earthquakes: Preparing for the Unexpected*, pp. 223-247 (Buffalo, NY: National Center for Earthquake Engineering Research).

Cochrane, H.C., Chang, S.E. and Rose, A. (1997) Indirect economic losses, in: *Earthquake Loss Estimation Methodology: HAZUS Technical Manual, Volume 3* (Washington DC: National Institute of Building Sciences).

Cole, S. (1988) The delayed impacts of plant closures in a reformulated Leontief model, *Papers of the Regional Science Association,* 65, pp. 135-149.

Cole, S. (1989) Expenditure lags in impacts analysis, *Regional Studies*, 23, pp. 105-116.

Cole, S. (1995) Lifeline and livelihood: a social accounting matrix approach to calamity preparedness, *Journal of Contingencies and Crisis Management*, 3, pp. 228-40.

Cole, S. (1998) Decision support for calamity preparedness: socioeconomic and interregional impacts, in: M. Shinozuka, A. Rose and R.T. Eguchi (Eds) *Engineering and Socioeconomic Impacts of Earthquakes*, pp. 125-153 (Buffalo, NY: Multidisciplinary Center for Earthquake Engineering Research).

Cole, S. (2004) Geohazards in social systems: an insurance matrix approach, in: Y. Okuyama and S.E. Chang (Eds) *Modeling Spatial and Economic Impacts of Disasters,* pp. 103-118 (New York: Springer).

Dacy , D.C. and Kunreuther, H. (1969) *The Economics of Natural Disasters* (New York, The Free Press).

Davis, H.C. and Salkin, E.L. (1984) Alternative approaches to the estimation of economic impacts resulting from supply constraints, *Annals of Regional Science*, 18, pp. 25-34.

Dietzenbacher, E. (1997) In vindication of the Ghosh model: a reinterpretation as a price model, *Journal of Regional Science*, 37, pp. 629-651

Donaghy, K.P., Balta-Ozkan, N., and Hewings, G.J.D. (2007) Modeling unexpected events in temporary disaggregated econometric input-output models of regional economies, *Economic Systems Research*, 19, pp. 125-145.

Ellson, R.W., Milliman, J.W. and Roberts, R.B. (1984) Measuring the regional economic effects of earthquakes and earthquake predictions, *Journal of Regional Science*, 24, pp. 559-579.

Gordon, P., Moore II, J.E., Richardson, H.W., Shinozuka, M., An, D. and Cho, S. (2004) Earthquake disaster mitigation for urban transportation systems: an integrated methodology that builds on the Kobe and Northridge experiences, in: Y. Okuyama and S.E. Chang (Eds) *Modeling Spatial and Economic Impacts of Disasters*, pp. 205-232 (New York: Springer).

Gordon, P. and Richardson, H.W. (1996) The business interruption effects of the Northridge earthquake (Lusk Center Research Institute, University of Southern California, Los Angeles, CA).

Gordon, P., Richardson, H.W. and Davis, B. (1998) Transport-related impacts of the Northridge earthquake, *Journal of Transportation and Statistics*, 1, pp. 22-36.

Hewings, G.J.D. and R. Mahidhara. (1996) Economic impacts: lost income, ripple effects, and recovery, in: S. Changnon (Ed.) *The Great Flood of 1993*, pp. 205-217 (Boulder, CO: West View Press).

Kawashima, K., Sugita, H. and Kanoh, T. (1991) Estimation of earthquake induced economic damage, *Report of Public Works Research Institute*, 186, pp. 1-57. (In Japanese.)

Kunreuther, H. and Rose, A. (Eds) (2004a) *The Economics of Natural Hazards, Volume I & II* (Northhampton, MA: Edward Elgar).

Kunreuther, H. and Rose, A. (2004b) Introduction, in: H. Kunreuther and A. Rose (Eds) *The Economics of Natural Hazards, Volume I*, pp. xiii-xxxv (Northhampton, MA: Edward Elgar).

Mantell, N.H. (2005) Book Review of "Modeling Spatial and Economic Impacts of Disasters", *Journal of Regional Science*, 45, pp. 633-635.

Okuyama, Y. (2006) Sequential interindustry model and inventory function: sensitivity analysis, Paper presented at the 2006 Intermediate Input-Output Meetings on Sustainability, Trade & Productivity, Sendai, Japan.

Okuyama, Y. and Chang, S.E. (Eds) (2004) *Modeling Spatial and Economic Impacts of Disasters* (New York: Springer).

Okuyama, Y., Hewings, G.J.D. and Sonis, M. (2004) Measuring economic impacts of disasters: interregional input-output analysis using sequential interindustry model, in: Y. Okuyama and S.E. Chang (Eds) *Modeling Spatial and Economic Impacts of Disasters*, pp. 77-101 (New York: Springer).

Okuyama, Y., Hewings, G.J.D. and Sonis, M. (1999) Economic impacts of an unscheduled, disruptive event: a Miyazawa multiplier analysis, in G.J.D. Hewings, M. Sonis, M. Madden and Y. Kimura (Eds) *Understanding and Interpreting Economic Structure*, pp. 113-144 (Berlin: Springer).

Oosterhaven, J. (1988) On the plausibility of the supply-driven input-output model, *Journal of Regional Science*, 28, pp. 203-217.

Oosterhaven, J. (1989) The supply-driven input-output model: a new interpretation but still implausible, *Journal of Regional Science*, 29, pp. 459-465.

Partridge, M.D. and Rickman, D.S. (1998) Regional computable general equilibrium modeling: a survey and critical appraisal, *International Regional Science Review*, 21, pp. 205-248.

Romanoff, E. and Levine, S.H. (1986) Capacity limitations, inventory, and time-phased production in the sequential interindustry model, *Papers of the Regional Science Association*, 59, pp. 73-91.

Rose, A. (1981) Utility lifelines and economic activity in the context of earthquakes, in J. Isenberg (Ed.) *Social and Economic Impacts of Earthquake on Utility Lifelines*, pp. 107-120 (New York: American Society of Civil Engineers).

Rose, A. (2004) Economic principles, issues, and research priorities in hazard loss estimation, in: Y. Okuyama and S.E. Chang (Eds) *Modeling Spatial and Economic Impacts of Disasters*, pp. 13-36 (New York: Springer).

Rose, A. and Benavides, J. (1998) Regional economic impacts, in: M. Shinozuka, A. Rose and R.T. Eguchi (Eds) *Engineering and Socioeconomic Impacts of Earthquakes*, pp. 95-123 (Buffalo, NY: Multidisciplinary Center for Earthquake Engineering Research).

Rose, A., Benavides, J.,Chang, S.E., Szczesniak, P. and Lim, D. (1997) The regional economic impact of an earthquake: direct and indirect effects of electricity lifeline disruptions, *Journal of Regional Science,* 37, pp. 437-458.

Rose, A. and Guha, G.S. (2004) Computable general equilibrium modeling of electric utility lifeline losses from earthquakes, in: Y. Okuyama and S.E. Chang (Eds) *Modeling Spatial and Economic Impacts of Disasters*, pp. 119-141 (New York: Springer).

Rose, A. and Liao, S.Y. (2005) Modeling regional economic resilience to disasters: a computable general equilibrium analysis of water service disruptions, *Journal of Regional Science*, 45, pp. 75-112.

Sohn, J., Hewings, G.J.D., Kim, T.J., Lee, J.S. and Jang, S.G. (2004) Analysis of economic impacts of earthquake on transportation network, in: Y. Okuyama and S.E. Chang (Eds) *Modeling Spatial and Economic Impacts of Disasters*, pp. 233-256 (New York: Springer).

Sorkin, A.L. (1982) *Economic Aspects of Natural Hazards* (Lexington, MA: Lexington Books).

Steenge, A.E. and Bočkarjova, M. (2007) Thinking about imbalances in post-catastrophe economies: an input-output based proposition, *Economic Systems Research*, 19, pp. 205-223.

Steinback, S.R. (2004) Using ready-made regional input-output models to estimate backward-linkage effects of exogenous output shocks, *Review of Regional Studies*, 34, pp. 57-71.

Tierney, K. (1997) Impacts of recent disasters on business: the 1993 Midwest floods and the 1994 Northridge earthquake, in: B.G. Jones (Ed) *Economic Consequences of Earthquakes: Preparing for the Unexpected*, pp. 189-221 (Buffalo, NY: National Center for Earthquake Engineering Research).

van der Veen, A. and Logtmeijer, C.. (2003) How vulnerable are we for flooding? A GIS approach, in: A. van der Veen, A.L.V. Arellano and J.P. Nordvik (Eds) *In Search of a Common Methodology on Damage Estimation (EUR 20997 EN)*, pp. 181-193 (Ispra, Italy: European Commission, Joint Research Center).

West, C.T. and Lenze, D.G. (1994) Modeling the regional impact of natural disaster and recovery: a general framework and an application to hurricane Andrew, *International Regional Science Review*, 17, pp. 121-150.

Wilson, R. (1982) Earthquake vulnerability analysis for economic impact assessment (Information Resources Management Office, Federal Emergency Management Agency, Washington, DC).

Yamano, N., Kajitai, Y., and Shumuta, Y. (2007) Modeling the regional economic loss of natural disasters: the search for economic hotspots, *Economic Systems Research*, 19, pp. 163-181.

Fifth International Conference on Urban Earthquake Engineering
March 4-5, 2008, Tokyo Institute of Technology, Tokyo, Japan

A CONCEPTUAL DESIGN OF MOBILE GAMING SYSTEM ON PUBLIC EDUCATION OF EARTHQUAKE DISASTER

Masaki Fujioka[1], Hideki Kaji[2], and Jun Mihira[3]

1) Researcher, Center for Urban Earthquake Engineering (CUEE), Tokyo Institute of Technology, Japan
2) Professor, Center for Urban Earthquake Engineering (CUEE), Tokyo Institute of Technology, Japan
3) The Graduate Program of Media and Governance Keio University, Japan
fujioka.m.aa@m.titech.ac.jp, kaji@cuee.titech.ac.jp, jmihira@sfc.keio.ac.jp

Abstract: In this study we designed a conceptual Mobile Gaming System for the purpose of Public Education and the future's analysis of individual ability of disaster prevention. One of the effective ways to minimize earthquake damage is to maximize the knowledge level of each person within a specific regional society. Due to the passive essential of disaster subject, preventing disaster is hard to be understood by social awareness. In this aspect, one of the contributions of this mobile gaming system is to provide a user friendly platform, which attracts people's attention on disaster prevention.

1. Background

"Bousaishi" is a special license system for disaster prevention in Japan. "Bousaishi" not only evaluates the existing skill level of each individual but also offers training program to empower one's capabilities to rescue others. There are several ways to improve the learning of disaster prevention.

1. Go to the lessons which organized by government
2. Go to the Life safety leaning center.
3. Get information from web site or other publications.

Generally speaking, the existing learning materials of disaster prevention do not grab readers' much attention. It is mainly because the learning material is not easy to understand and "disaster" itself is not an interesting topic. Our project is to enthuse people's interest into disaster prevention in order to build up the awareness of risk management.

About computer based education system, there are several training system for professionals use such as for government and management of fire fighter who charge of emergency response using big simulation system (Jun Mihira 2004)

Moreover, TV game is the best acceptable interface for the younger generation. Recently, the concept of "Edutainment" which combines the words "Entertainment" and "Education" is prevailing. Our disaster prevention program for educational purpose is ought to be the solution of easy and wide acceptability.

2. Concept of Public Education for Earthquake Disaster.

There are four fundamentals for promoting public education on earthquake disaster.

2.1 User Friendly

Through the past experiences of holding public lecture of disaster drills, the participants are mostly the elder, excluding the younger people. One of the reasons is that for younger people spending time on disaster trainings held in public centers relatively lacks attractive. User friendly is an important fundamental which helps public education to cross age barrier of participation.

2.2 Customize Training

People have diverse lifestyles so that the disaster training has to satisfy different needs to seek effective disaster prevention.

2.3 Easy Access

Speaking of accessibility, the service should work on the widely used platform such as www and mobile phone interfaces.

2.4 Effectiveness

There are two aspects of effectiveness have to be considered. One is the effectiveness of training contents, which is about if the knowledge capacity is enough for users' needs during the emergency situation; also to compare and to cooperate with other educational method such as disaster drills.

The other aspect is the extendibility of service span. The bigger user population in one specific area is; the better effectiveness of disaster prevention will be. The ratio of service expending is also an important fundamental of public education in disaster prevention.

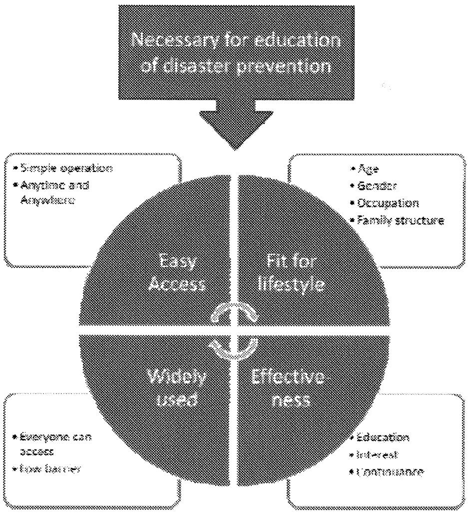

Figure 1

3. The procedure of accessing the system of mobile game in public education of earthquake disaster.

After the game system launched through personal mobile phone, with player's historical data player starts the first time educational game. Then, the score of this trial and the points which has to be improved by player next time will be reported. By the report and the playing experience, player should understand and accept his/her situation against earthquake disaster. So, most players will take measures to meet the situation on their own. The procedure should be run more than once in order to seek the best effectiveness.

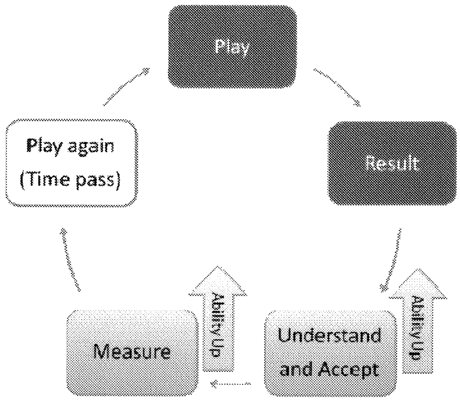

Figure 2

4. Indicators for estimating the ability of disaster prevention

There are two abilities which individual has to prepare as the response forces. They are ability for survive and ability for living.

Ability for survive equals the protection ability when the first impact of earthquake occurs. The indicators of ability for survive are:

A. Ability to escape from danger and evacuate to the safe area.

B. Ability to protect life during the shaking.

Ability for living is for the life after disaster happened.

A. Ability to recover from inconvenient life or uncomfortable surroundings like shelter.

B. Ability to rebuild the common life

As indicators, individual's capabilities of activeness and living are calculated by one's knowledge and tactics. The knowledge factor covers whole the information from disaster characteristics such as earthquake vibration, types of fire, the usage of extinguisher and so on. The tactic factor introduces all kinds of skills might be used during the disaster. For example, how to tie knots, extinguish a fire effectively, cook in the strict situation and so on.

Besides, it's not adequate that one holds abundant knowledge and tactics only. How to use this knowledge set in the real disaster situation is the purpose of our program. Because human living capability reflect the usage of knowledge and tactics, individual's living capability is indicated of individual information and preparation.

Individual information includes attributes of each person such as age, gender, family structure, and occupation. Living environment covers distances to working places or schools, commuters, and communication tools. The ratio of in danger is calculated by using above individual information.

The preparation is the indicator of instrument preparation against disasters. For example take antiseismic reinforcement work, prepare emergency place, foods, the fire alarm, and extinguisher.

There are two types of preparation. One is for extraordinary situation. The other one is for ordinary living use. The first type includes the tools for professional uses limited for disaster or emergency situation such as alarm, extinguisher, AED, and litter for carrying injured person. The ordinary type includes tools which can be used in common life, such as water stock, oils, jacking-up tools, and so on. The ratio of preparation leads to overcome the problems people will meet after disaster.

The four indicators in this program: Knowledge, Tactic, Individual information, and Preparation as figure 3.

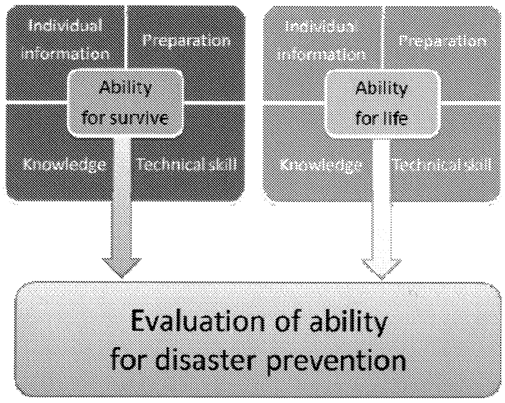

Figure 3

4. Prototype System

4.1 System design

On the prototype system we build, the system can be accessed by www anytime and anywhere for use as show in figure 4.

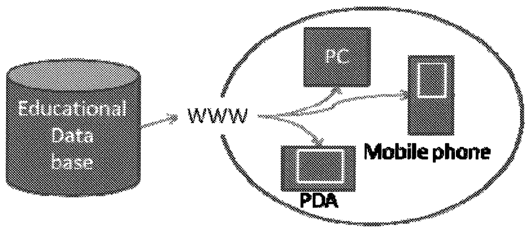

Figure 4

4.2 Interactive element in game

Compared with lecture textbook, game interface takes the advantage of dynamically expressing contents by using animation. Also, interaction between game and players reinforces the interest of leaning subject itself. With regard to these merits, we consider these:

A. Interestedness

B. Interaction

C. Dynamic changes

D. Quick response

4.3 Output image

Figure 5 shows the dictionary image which can be accessed in games. This dictionary includes following six sections.

A. Basic knowledge on earthquake which leads to exclude player's nonsense fear and have the right attitude when facing disasters.

B. Sufficient preparation before disaster occurs

C. Emergency response after disaster teaches the tangible methods of each process

D. Evacuation and shelter life teach basic knowledge for evacuation and the situation of shelter.

E. Rebuild the life explains how to rebuild the common life from the standpoint of planning and finance

F. History of disaster introduces the knowledge of experience of world catastrophic disaster.

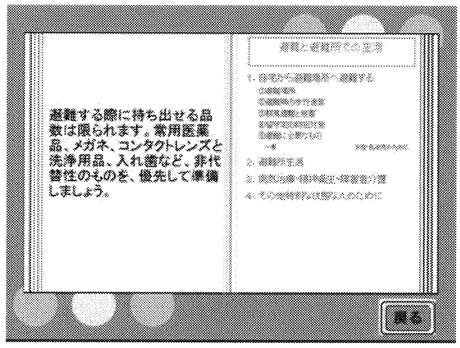

Figure 5 the image of Dictionary in the game

Figure 6, 7 show the game image which people escape from buildings and evacuate to the shelters in their region.

Figure 6 Evacuation simulations in room

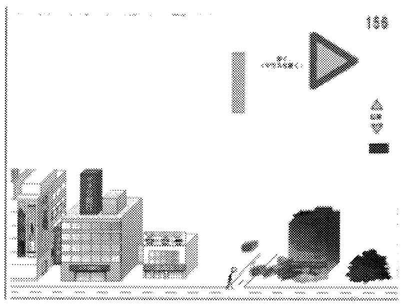

Figure 7 Evacuation simulations on the path

4.4 Calculation and estimation of the disaster prevention ability

There are two types of analyses: individual analysis and analysis for family as below:

A. Individual ability for disaster prevention

As shown as figure 2 the personal evaluation ability will be calculate automatically. The personal data will be stored into data server which will be used as the basic data for the next play. Also these data will become the dataset to calculate normalized ability of region by region.

B. Analyze for family

Using network games also make it possible for calculate whole the family ability. One topics should understand whole the family such as evacuation way or meeting location of this family. On the other hand, some topics are useful for the owners of housing such as insurance of housing. If whole the member of family play these games, it is possible to analyze effective method for this family and detect the parts should be improved.

5. Problem

5.1 Limitation of reality

The goal of this game is to reduce the damage from disasters not only for entertainment purpose. But if the entertainment level is too high in this game, player will not realize their situation of disaster prevention by their own. On the other hand, if the game lacks of reality, it cannot attract players' attentions. To keep the balance of game contents is very important.

5.2 Continuous usage

Player always has interest at the beginning playing game. But it's hard to persuade player keep playing once player feels not interested in anymore. Continuous usage is very important to provide the correct and on time knowledge to player. To do so, we need to create functions for keeping players' attention continuously. Additionally, we need to set the re-teaching logic for explaining player's misunderstanding.

5.3 Effectiveness evaluation

Thinking about personal indicator of disaster prevention ability, we need to set more diverse factors depending on the changes or lifestyles. Some research is needed for clarifying the definition of indicators and evaluation. Moreover, we need to analyze that this software is effective for public education of earthquake disaster and other natural disasters.

6. Future plan

6.1 Multi Platform

About accessibility, it is ideal that service provided by Multi-Platform with Multi-Media information, especially new media platform.

6.2 Data Update

When disaster happens, sometimes new knowledge has to be delivered in order to correct the old common sense. Also, when new disaster prevention system or service launch, it is necessary to provide the dynamical training information. Especially, the past research shows that the wrong education information affect people to be liable of mistakes.

6.3 Long term Survey for optimize the indicator

For ensure the indicator of disaster prevention ability, the longer the survey is held, the better.

References:

Matsumura K., Kaji H., Kaneda T., Kanegae H., Ishibashi K.," *A Simulation Model on the Three Days Consequences of Earthquake Damage for Gaming Exercise in Emergency Headquarter Responses*", 7th U.S./Japan Workshop on Urban Earthquake Hazard Reduction, Maui, Hawaii, March 23-26, 2003

Jun Mihira, Kaji H., Matsumura K., Takanashi Y., Sakahara S., "Development of a Gaming Model for Training Emergency Headquarter Staff in Responding to Large Scale Earthquake- the Virtual Earthquake Response Game:VEQRES/SAITAI-", Proceedings of the 15th Annual Workshop of Japan Institute of Social Safety Science, Shizuoka, November 2004 (Japanese)

Fifth International Conference on Urban Earthquake Engineering
March 4-5, 2008, Tokyo Institute of Technology, Tokyo, Japan

AN EXPERIMENTAL APPROACH TO PREDICTING HOUSING SITUATION FOLLOWING URBAN DISASTER

Keiichi Sato[1)], Itsuki Nakabayashi[2)], and Saburoh Midorikawa[3)]

1) Post-doctoral Research Fellow, Center for Urban Earthquake Engineering, Tokyo Institute of Technology, Japan
2) Professor, Graduate School of Urban Science, Tokyo Metropolitan University, Japan
3) Professor, Center for Urban Earthquake Engineering, Tokyo Institute of Technology, Japan
ksato@enveng.titech.ac.jp, nakabasi@comp.metro-u.ac.jp, smidorik@enveng.titech.ac.jp

Abstract: In the event of large urban disaster such as the Tokyo metropolitan earthquake, it is not clear whether the present system of temporary housing assistance will work effectively. In order to design institutional arrangements as well as to make preliminary considerations, an experimental policy simulation is one of the most useful research approaches. To construct reliable social simulation, we developed household's behavior model from discrete choice analysis. Also, we are constructing the database of rental housing and construction sites of prefabricated temporary housing. Based on these foundational works, the experimental simulation model which illustrates temporary housing situation was developed.

1. INTRODUCTION

The anticipated Tokyo Metropolitan Earthquake is approximately eight times of the Kobe Earthquake in the housing damage scale and it is called "Super Urban Earthquake Disaster". In such a situation, additional countermeasures will be required, and the further progresses of researches and prior considerations are expected.

In the Tokyo Metropolitan Earthquake, the number of about 300,000 to 850,000 complete-collapse buildings is predicted (Cabinet Office 2004). Considering the number of buildings and the number of households, about 500,000 to 1,500,000 households who lose their houses will appear, and they will have evacuation, temporary living, and housing reconstruction problem.

This paper focuses on temporary housing problem and gropes for the new research approach for the "Super Urban Earthquake Disaster". In Japan, the prefabricated houses (prefabs) act the central role in the temporary housing countermeasures. However, the supply limit of the prefabs is only about 120,000. Temporary housing is apprehensive about becoming insufficient when the Tokyo Metropolitan earthquake occurs. However, approximately 1,000,000 vacant rental housings are existed in the Tokyo metropolitan area. These vacant can be utilized as temporary housings for victims (Sato and Midorikawa 2007).

The argument of supply amount is not enough to solve the problem. Figure 1 expresses complexity of the temporary housing problem. There are many types of temporary housing, and each household have each choices. Also, central and local governments will have housing support. Now, in Japan, housing recovery countermeasures need more consideration for next disaster such as Tokyo

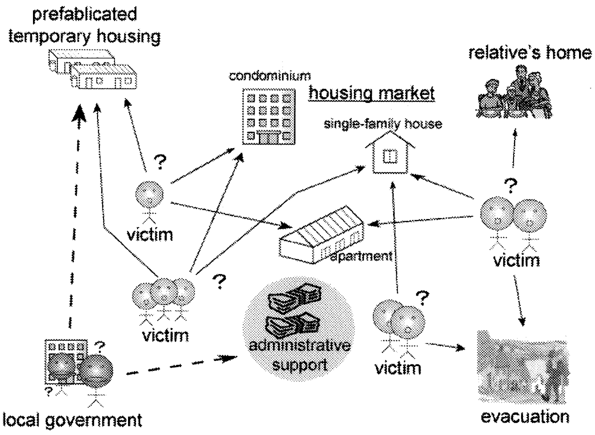

Figure1 Complexity of the temporary housing problem

Metropolitan Earthquake. It can be considered that an administrative support for temporary living in rental housing.

For develop the research for the problem as mentioned above, constructing a concrete experimental research for the social simulation of temporary housing situation following urban disaster is required. In this study, the following research step is considered to figure out the temporary housing problem.

1. Grasp the mechanism of the preference to the temporary housing of the disaster victim after the urban disaster.
2. A simulation about how to match many disaster victims and housings based on victim's preference and real housing data.
3. Evaluation of policy effect to disaster victims using constructed simulation.

2. DISCRETE CHOICE MODELING

To grasp the victim's preference and choice mechanism, discrete choice analysis is useful because it can treat many variables including policy variables. Also, discrete choice analysis creates choice probabilities and its results are suitable for prediction and simulation. For example, we constructed discrete choice model from internet-based questionnaire system showing in the Figure 2. In the system, common gateway interface (CGI) program which make conditions of temporary housing (such as location and rent) by a respondent's conditions and database of rental housing was developed. This system creates huge combinations of choice problems following household's attributes. The mechanism of the preference can be expressed from the data with variety.

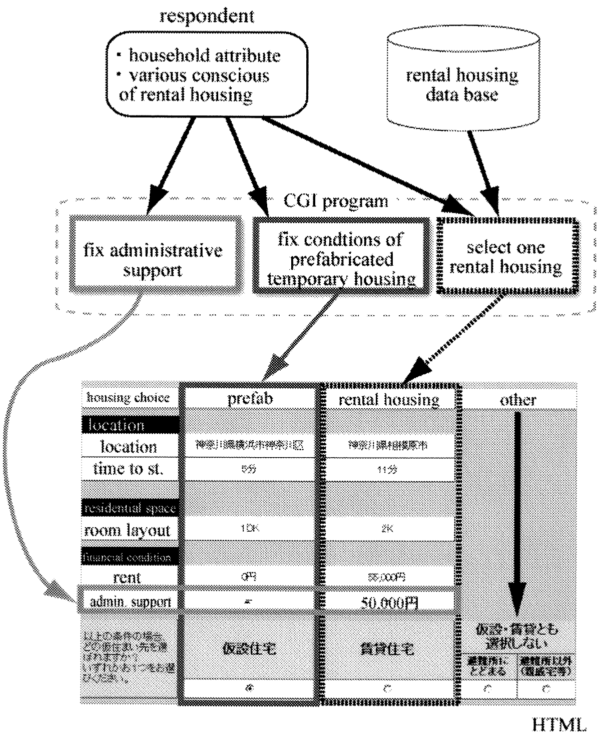

Figure2 Outline of Internet-based questionnaire survey

The internet-based questionnaire was conducted from January, 2007 and responses 2869 households were collected. Parameter estimation of discrete choice model was calculated using all questionnaire reply (Sato et al 2007).

Table 1 shows numerical examples of constructed discrete choice model. The choice probabilities can be calculated using household's attributes and conditions of temporary housing. In the case 1, the choice probability of the prefab is high and the probability of rental housing is low. However, the relation of choice probabilities changes in the case 2 which has governmental support to rental housing. In this approach, as shown in this table, any choice probabilities can be calculated under all settings (about housing conditions, household's attributes, and policy variables).

Table1 Numerical example of constructed choice model

household's attributes

householder's age	34
household number	3
housing ownership	rental
household income	4 million JPY
months passed	1month
leads on temporary housing	no
residential area	saitama2

case1

	prefabs	**rental housing**	shelter	other
time from neaby station	21minutes	12minutes	-	-
room layout	2DK	2DK	-	-
rent	0 JPY	100,000 JPY	-	-
location	saitama 4	saitama3	-	-
governmental support	-	-	-	-
A systematic component of utility	-0.31	-1.377	-2.204	-1.175
choice probability	**57.5%**	**19.8%**	8.6%	14.1%

case2

	prefabs	**rental housing**	shelter	other
time from neaby station	21minutes	12minutes	-	-
room layout	2DK	2DK	-	-
rent	0 JPY	100,000 JPY	-	-
location	saitama 4	**saitama 2**	-	-
governmental support	-	**rent subsidy 50,000 JPY per one month**	-	-
A systematic component of utility	-0.31	-0.132	-2.204	-1.175
choice probability	**38.6%**	**46.1%**	5.8%	9.5%

3. MICRO SIMULATION MODEL

After discrete choice analysis of victim's preference can be performed, the micro simulation that illustrates the situation of temporary housing can be constructed because any choice probabilities can be calculated under all settings. Then, the prototype of a micro simulation model as shown in the figure 3 was constructed. The simulation flow is summarised in below.

1. Fix the individual data of the household who lose their houses. Gather housing data about the prefabs and rental housing.

2. Extract the household who looks for a temporary housing at random.

3. Extract the rental housing using victim's preference and rental hosing data. Extract the prefabs from the supply role. In a severe situation, there is a possibility that rental housing and the prefab does not exist.

4. Compute choice probability to generated choice problem by constructed discrete choice model and assign of choice result using a random number.

5. Delete selected supply data.

6. Extract the next household who looks for a temporary housing at random and compute 3 to 5 again. The same calculation repeat to all households.

One calculation is completed above flow. Since the result of choices is assigned by the random numbers, calculation has to perform repeatedly. By totaling a repetition calculation result, we can grasp what kind of thing happens in the temporary housing situation.

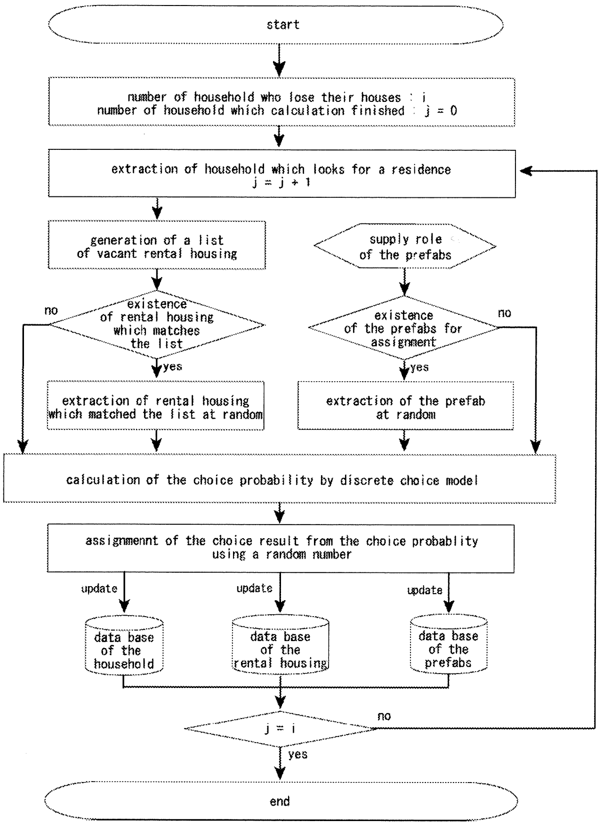

Figure3 Prototype of Micro Simulation Model

4. DATA SET AND MICRO DATA

In order to implement the constructed simulation model, it is necessary to set micro data. Generally, it is necessary to generate micro data from aggregate value since the individual data cannot be obtained. In this research, the aggregate value about households, rental housing, and temporary housing are required. The households who lose their houses and the rental housings which can be used following disaster are acquired from our survey (Sato and Midorikawa 2007). The supply amounts of the prefabs are placed from the temporary housing site lists of prefectural governments. Figure4 expresses what totaled values per original 24 areas of Tokyo metropolitan area. In the central area, households who lose their houses are huge amount and temporary housings are not enough.

Next, micro data were generated from the aggregate values mentioned above. The prefab's site lists were used for micro data of prefab's supply directly. The micro data of rental housing were generated using the information about rental housing on the internet. The micro data of the household who lose their houses were generated using national statistical data about housing and land. The attribute of each micro data was generated using random number and the ratio of the statistical data.

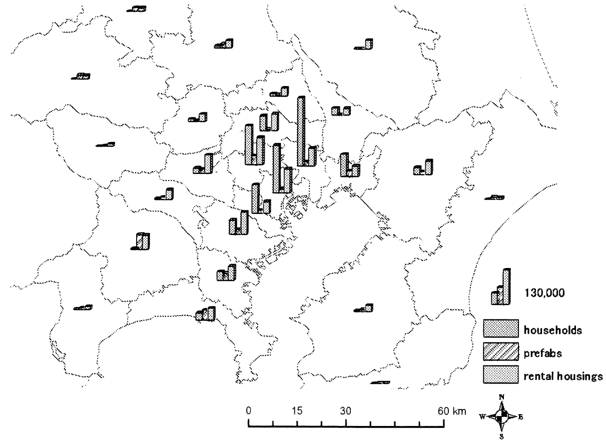

Figure 4 Temporary housing amount of TME M7.3

5. EXPERIMENTAL SIMULATION

5.1 Outline of the Simulation and Calculation Process

A simulation was performed using the constructed model and the generated micro data. First of all, we have to set the supply rule of the prefabs. In this paper, a simple rule which assigned by order of search was taken. As other examples, the supply rule which makes elderly-people households move in preferentially can be considered. However, since the development of the micro simulation is the purpose of this research, we do not treat various supply rules of the prefabs in this paper.

The simulation case is the Tokyo Metropolitan Earthquake M7.3 (winter, 18o`clock, wind speed 3 meter per a second). A calculation of one million households was required about one hour using the general workstation.

Figure5 shows the calculation process of the all households. Vertical axis indicates the number of households which moved in, and horizontal axis indicates the number of

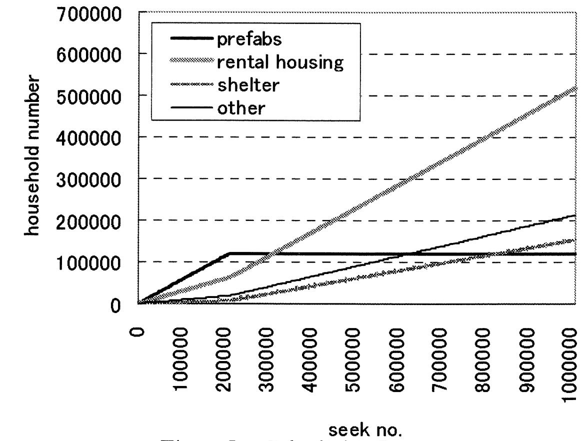

Figure5 Calculation Process

order which seek the house. To 200 thousands in seek no., there is a marked increase in the prefabs. After there are no prefabs, the number of rental housing increases rapidly. Also, the number of other housings and shelters increase gradually. As a result, the number of households who move in prefabs is about 120 thousands. The number of households who move in rental housing is about 500 thousands.

5.2 Stability of the Simulation

Checking the stability of the constructed simulation is required because many random numbers were used in the simulation such as choice making from calculated probability of the discrete choice model. Checking the stability needs many results of the simulation. However, there is a limitation of computational effort. In this paper, Figure 5 indicates the variation of ten times simulation results. The figure indicates that the number of prefabs and other housing are stable. Otherwise, the number of rental housing and shelters has a range about plus or minus 50 thousands.

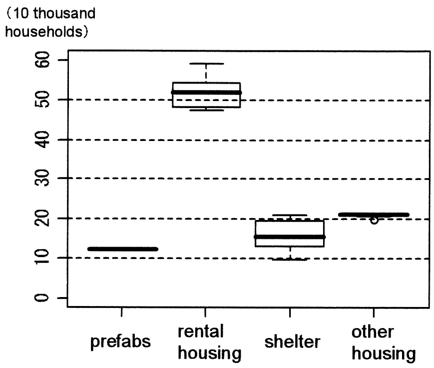

Figure6 Stability of the Simulation

5.3 Results of the Simulation

A result of the micro simulation is micro data. So we have to total by some variables if we want to summarize the result. In this paper, we only indicate choice results by residential area as shown in Figure 7. It can see that trends of choices have differences in each area. In tokyo1, tokyo2, and chiba1 area, there are many households who remain shelter. It can say that, if we provide more prefabs in these three areas, households who remain shelters can reduce gradually.

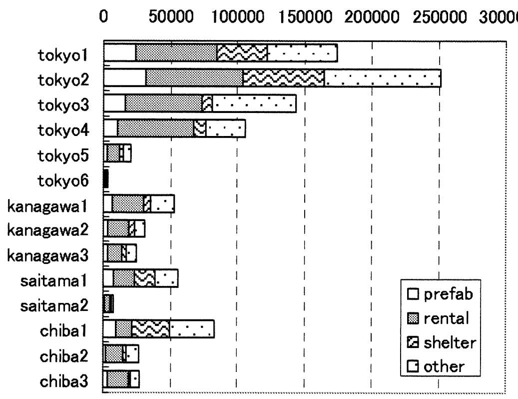

Figure7 Simulation Results by Residential Area

5.4 Trial of Policy Simulation

In the Internet-based questionnaire survey shown in Figure2, administrative support for rental housing was treated. We set 5 policy cases below for trial of the policy simulation.

- Case 1 : no administrative support
- Case 2 : disaster victims relief law which is revised in 2004
- Case 3 : rent subsidy 50 thousand JPY per a month
- Case 4 : rent subsidy 100 thousand JPY per a month
- Case 5 : governments hire all rental housings and rent free to disaster victims

Each micro simulation of 5 policy cases was calculated ten times, and average values of results were shown in the Figure 8. The number of households who move in rental housing changes from 484 thousands to 761 thousands by policy cases. These figures prove clearly that administrative supports have large impact to household number who move in rental housing. However, households who remain shelters still remain in any cases. It can say that other options such as more prefabs or evacuation for households who remain shelters are required.

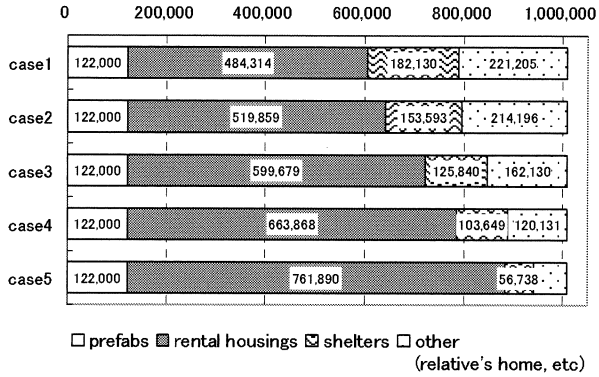

Figure8 Results of the Policy Simulation

6. CONCLUSION

In this paper, an experimental approach to predicting housing situation following urban disaster was developed. The introduced approach has following three phases. 1) Grasping the preference to the temporary housing of the disaster victim. 2) A simulation about how to match many disaster victims and housings based on victim's preference and real housing data. 3) Evaluation of policy effect to disaster victims using constructed simulation.

References:

Japanese Cabinet Office(2004), " Reference Data of Damage Assessment of Tokyo Metropolitan Earthquake", http://www.bousai.go.jp/jishin/chubou/shutochokka/13/shiryo2-2.pdf.

Keiichi Sato and Saburoh Midorikawa (2007), "Distribution characteristic of Vacancy on Rental Housing which can be used following the Tokyo Metropolitan Earthquake", *Journal of Social Safety Science*, No.9, 47-54

Keiichi Sato, Itsuki Nakabayashi and Saburoh Midorikawa (2007), "Discrete Choice Analysis of Temporary Housing Choice After Urban Earthquake Disaster", *Proc. Fourth International Conference of Urban Earthquake Engineering*, pp.553-560.

Center for Urban Earthquake Engineering (CUEE)
Tokyo Institute of Technology

Suzukakedai Office
Department of Built Environment
Tokyo Institute of Technology
G3-11 4259 Nagatsuta-cho, Midori-ku, Yokohama, Japan 226-8502
Tel: +81-(0)45-924-5576 Fax: +81-(0)45-924-5199

O-okayama Office
Department of Architecture and Building Engineering
Tokyo Institute of Technology
M1-39 2-12-1 O-okayama, Meguro-ku, Tokyo, Japan 152-8552
Tel: +81-(0)3-5734-3200 Fax: +81-(0)3-5734-3200

Email:office@cuee.titech.ac.jp
URL:http://www.cuee.titech.ac.jp